

Society of Automotive Engineers
of China (SAE-China)
International Federation
of Automotive Engineering Societies (FISITA)
Editors

Proceedings of the FISITA 2012 World Automotive Congress

Volume 8: Vehicle Design
and Testing (II)



Lecture Notes in Electrical Engineering

Volume 196

For further volumes:
<http://www.springer.com/series/7818>

Society of Automotive Engineers of China
(SAE-China) · International Federation of
Automotive Engineering Societies (FISITA)
Editors

Proceedings of the FISITA 2012 World Automotive Congress

Volume 8: Vehicle Design
and Testing (II)



 Springer

The Springer logo, which is a stylized white chess knight (horse) facing left, positioned to the left of the word 'Springer' in a black, serif font.

Editors
SAE-China
Beijing
People's Republic of China

FISITA
London
UK

ISSN 1876-1100
ISBN 978-3-642-33737-6
DOI 10.1007/978-3-642-33738-3
Springer Heidelberg New York Dordrecht London

ISSN 1876-1119 (electronic)
ISBN 978-3-642-33738-3 (eBook)

Library of Congress Control Number: 2012948289

© Springer-Verlag Berlin Heidelberg 2013

This work is subject to copyright. All rights are reserved by the Publisher, whether the whole or part of the material is concerned, specifically the rights of translation, reprinting, reuse of illustrations, recitation, broadcasting, reproduction on microfilms or in any other physical way, and transmission or information storage and retrieval, electronic adaptation, computer software, or by similar or dissimilar methodology now known or hereafter developed. Exempted from this legal reservation are brief excerpts in connection with reviews or scholarly analysis or material supplied specifically for the purpose of being entered and executed on a computer system, for exclusive use by the purchaser of the work. Duplication of this publication or parts thereof is permitted only under the provisions of the Copyright Law of the Publisher's location, in its current version, and permission for use must always be obtained from Springer. Permissions for use may be obtained through RightsLink at the Copyright Clearance Center. Violations are liable to prosecution under the respective Copyright Law.

The use of general descriptive names, registered names, trademarks, service marks, etc. in this publication does not imply, even in the absence of a specific statement, that such names are exempt from the relevant protective laws and regulations and therefore free for general use.

While the advice and information in this book are believed to be true and accurate at the date of publication, neither the authors nor the editors nor the publisher can accept any legal responsibility for any errors or omissions that may be made. The publisher makes no warranty, express or implied, with respect to the material contained herein.

Printed on acid-free paper

Springer is part of Springer Science+Business Media (www.springer.com)

Contents

Part I Vehicle Performance Development

A New Approach to Improve the Design Quality of Chinese National Brand Vehicle	3
F2012-E01-004 Du Cao, Jing Deng and Fengfei Fu	
The Process of Vehicle Dynamics Development	13
F2012-E01-011 Zhanglin Cai, Stephen Chan, Xiaofeng Tang and Jiang Xin	
Development of Methodologies for Evaluation, Simulation and Improvement of Cross-Wind Sensitivity.	23
F2012-E01-014 Guido Tosolin, Jonathan Webb, Alex Català, Alfonso Escuer and Young Jin Hyun	
Maneuvering Experiment of Personal Mobility Vehicle with CVT-Type Steering Mechanism	35
F2012-E01-016 Yoshihiro Suda, Hirayama Yuki, Masahiko Aki and Takafumi Takagi	
Vehicle Performance Objective Management in Automotive R&D . . .	45
F2012-E01-018 Xuezhen Wu, Haiqiang Han, Liqiang Dai, Linghua Zou and Fuquan Zhao	
Improving Energy Efficiency of Heavy-Duty Vehicles: A Systemic Perspective and Some Case Studies	51
F2012-E01-024 Juhani Laurikko, Kimmo Erkkilä, Petri Laine and Nils-Olof Nylund	

Study on the Active Front Steering System with Steady Gain	65
F2012-E01-025	
Youkun Zhang and Baohui Liu	
Design Optimization of Full Vehicle Suspension Based on Ride and Handling Performance	75
F2012-E01-026	
Tey Jing Yuen, Ramli Rahizar, Zainul Abidin Mohd Azman, Alias Anuar and Dzakaria Afandi	
Improve Fuel Economy of Commercial Vehicles Through the Correct Driving	87
F2012-E01-029	
Ping Guo, Zhenlei Li, Zhiwu Zhang, Jun Chi, Shuai Lu, Ye Lin, Zhengfa Shi and Jingcai Shi	
Research on Test Method of Off-road Vehicle Trafficability	97
F2012-E01-031	
Wenhu Qin, Zhanjun Guo and Weigong Zhang	
Part II Vehicle Integration Platformized and Universal Design	
A Design Method for Future Automobiles	109
F2012-E02-003	
Zhifeng Wang, Wu Yang, Zhiguo Le and Fuquan Zhao	
Effect of Engineering Materials for Vehicle Collision Simulation.	123
F2012-E02-005	
Yanling Huang, Gaoji Yin, Zhitao Wang, Juanli Ni, Li Li, Qiang Liu, Anzhi Yang and Fuquan Zhao	
Part III Development of CAD/CAE/CAM and CF Methods in Automotive Practice	
Simulation of Leaf Spring Balanced Suspension Based on Virtual Test-Rig	135
F2012-E03-002	
Xinpeng Tang and Kun Liu	
A Simulation Analysis and Optimization of Mode and Stiffness of BIW	145
F2012-E03-004	
Qiuxia Zhang, Leyi Zhang and Mingtao Guo	

Vehicle Wading Simulation with STRA-CCM+ 157
 F2012-E03-005
 Xin Zheng, Xin Qiao and Fanhua Kong

**Developing Low-Noise Low Back Pressure Intake System
 by CAE Technology** 167
 F2012-E03-006
 Yue Chang Chen, Haotian Shi and Yang Guang

Study on Vehicle Modeling and Steering Performance 177
 F2012-E03-009
 Minglun Cao and Cai Yang

**Surrogate Model for Aerodynamic and Handling Stability
 Optimization of a Tractor-Trailer in Crosswinds** 189
 F2012-E03-010
 Xu Gong, Zhengqi Gu, Jian Ye, Xu Yan and Zhiming Zhao

Calculation of Drum Brake Temperatures in Ten-Cycle Braking 201
 F2012-E03-013
 Kun Zhang and Cai Yang

Solution of the Glare Risk in Vehicle Inner Trim Designing 209
 F2012-E03-014
 Mengdong Mi, Yongqing Liu, Congwen Yu, Sujuan Peng, Bin Feng,
 Jian Shi and Pin Wang

Topology Optimization Design of a Heavy Truck Frame. 219
 F2012-E03-015
 Jingxin Wang, Tie Wang, Yanchao Yang, Zhaohui Peng,
 Zhi Li and Na Wang

**Bridging the Gap Between CAD and CAE in Composite
 Structures Development Process for the Automotive Industry.** 229
 F2012-E03-016
 Samouil Saltiel, Michalis Giannakidis and Nikos Toulas

**Ensuring Reliability of Automotive Electronics
 by Using Thermal Analysis** 241
 F2012-E03-019
 Boris Marovic and Alexandra Francois-Saint-Cyr

Effects of Frequency Response Spacing on Vibration Fatigue Analysis	253
F2012-E03-020	
Jasuk Koo	
CAE Supported ESC Development/Release Process	267
F2012-E03-021	
Yiqin Mao, Johannes Wiessalla, Jan Meier, Wolfgang Risse, Guy Mathot and Manfred Blum	
Application of Optimization Algorithm to HVAC Configuration Design	277
F2012-E03-023	
Tatsuro Kyuto, Motohiro Kitada and Hideo Asano	
Research of Flow Field Simulation for Lubrication System and Effect Evaluation on a 7-Speed Dual Clutch Transmission	285
F2012-E03-033	
Yinhui Lin, Zhihua Hu, Chaoqiang Xiong, Mengyan Zang, Yuan Jia, Yong Chen, Daguo Luo and Fuquan Zhao	
Application of Stiffness Estimation and Structure Optimization in Rubber Component Development.	299
F2012-E03-036	
Min Sun, Yuan Qu, Youfeng Qiu and Shenrong Wu	
Brake Cooling Simulation: A Combined Procedure of CFD, Thermal and 1D Software	309
F2012-E03-037	
Enric Aramburu and Roger Calvo	
BIW Optimization by Means of an Automated CAE Process for the Reduction of Welding Points	321
F2012-E03-038	
Pérez Mario, Calvo Roger and Hirschbeck Bernhard	
Establishing a Carbon Fiber Material Database for Crashworthiness Structural Development	329
F2012-E03-039	
Pablo Cruz and Raúl Ureña	
Full Vehicle Durability Analysis by Means of the IDIADA Virtual Proving Ground	337
F2012-E03-040	
Jordi Arbiol, José Antonio Muñoz, Xavierl Armengo and Enric Aramburu	

The Parametrical Design and Optimization of Body Frame Based on Crashworthiness and Lightweight 349
 F2012-E03-042
 Yongxin Men, Guojun Zheng, Huicai Zelong Lu and Zelong Wang

Development of Concept Analysis and Multi-Objective Optimization Platform for Body-In-White Structure 361
 F2012-E03-046
 Yiwen Li, Hongjian Li, Zuofeng Pan and Tao Xu

Fatigue Life Prediction of Spot-Weld for Auto Body Based on Multiple Load Cases 373
 F2012-E03-049
 Liling Zhang, Qing Jiang, Xuefeng Chen and Xu Wang

Acoustic Isolation Analysis of Weatherstrip Considering Door Opening Condition 383
 F2012-E03-050
 Tae Hyung Kim, Hak Jin Kim, Heon Young Kim, Joon Chul Park, Byung-Kwon Min and Chang-Kuk Yim

Assessment of Modeling Individual Physiological Differences when Predicting Thermal Comfort 393
 F2012-E03-053
 Curran Allen and Hepokoski Mark

The Multi-Physics Coupling Analysis Based on Electro-Magnetic, Structural and Acoustic Characters for a Drive Motor in EV 399
 F2012-E03-057
 Jinling Zeng, Yingzi Piao, Bingwu Lu, Fuxiang Huo and Qun Zhang

Modular Car Body Design and Optimization by an Implicit Parameterization Technique via SFE CONCEPT 413
 F2012-E03-058
 Fabian Duddeck and Hans Zimmer

A New Approach for Vibro-Acoustic Optimization Using Discrete and Continuous Shape Variables Applied to a Car Body 425
 F2012-E03-059
 Hans Zimmer, Arnold Gross-Thebing, Manohar Prabhu and Fabian Duddeck

Part IV Advanced Chassis, Body Structure and Design

Integrated Architectures for Third Generation Electric Vehicles: Technical Challenges Meeting Customer Requirements	437
F2012-E04-001 Micha Lesemann, Leif Ickert, Lutz Eckstein, Sven Faßbender, Michael Funcke and Jac Wismans	
The Ring-Shaped Route Body Structure Design and Evaluation Method	447
F2012-E04-002 Feng Xiao and XinHua Gao	
The Study of Wheeled Semi-trailer Design and Development Based on Scale Model	463
F2012-E04-003 Xiong Xin, Xuexun Guo and Libo Wang	
The Concept and Methodology of Creating the Universal Life-Saver with Rotary-Screw Mover	477
F2012-E04-004 Maxim Krashennikov, Anatoly Kulashov, Viktor Shapkin and Alla Koshurina	
Research on the Development Procedure of Light-Weight New Body Architecture	491
F2012-E04-005 Xiangyang Fu, Guohong Shi, Xin Jiang, Yunhui Duan and Zhengchao Song	
Control and Simulation of Regenerative Suspension Using Permanent Magnetic Synchronous Motor	505
F2012-E04-007 Weihua Wang and Songshan Liu	
The Application of Tolerance Analysis During Engineering Process. . .	515
F2012-E04-009 Wei Wang and ZhiHan Zhou	
Synchronized Design Optimization Method of Body Joints and Major Cross Sectional Members	531
F2012-E04-010 Jie Xiang, Yong Chen and Youmin Guo	

Design and Development of Contractive Suspension in Hill-Climb Races 539
 F2012-E04-014
 Antonini Pierluigi and Cibrario Valerio

Modularized Design of the Engine Compartment Design Based on the Theory of CBR 553
 F2012-E04-016
 Honghua Li, Wei Li and Fuquan Zhao

Development of First Order Analysis for Torsion Beam Suspension (FOA/TB) Corresponding to Modular Design 561
 F2012-E04-017
 Kazuaki Chiku, Hideki Sugiura, Takaaki Uno and Toshiji Hirotani

A Pillar Structure Optimization Design of Driving Safety 571
 F2012-E04-018
 Guolin Li, Jun Sui, Xiang Zheng, Honghua Li and Fuquan Zhao

A New Body Concept for Electric Vehicle: PBC-EV 579
 F2012-E04-020
 Jaehyun Kim, Hongwoo Lee, Kyunghwan Chung, Hyounyoung Lee, Yeonsik Kang and Jaebok Nam

The Study on Development of High Security and High Comfort Commercial Vehicle Cab 593
 F2012-E04-021
 Yuhai Chang and Xiaojun Yang

The Design and Simulation Analysis of Electromagnetic Energy Regenerative Suspension System 601
 F2012-E04-023
 Hongbin Ren, Sizhong Chen and Zhanzong Feng

Optimization of the Magnetic Property of a Magnetorheological Squeeze Mount 611
 F2012-E04-024
 Xinjie Zhang, Fangwu Ma, Fuquan Zhao, Konghui Guo and Mehdi Ahmadian

Semi-Active Suspension Adaptive Control Strategy Based on Hybrid Control 625
 F2012-E04-025
 Xinjie Zhang, Wuhui Yu, Fangwu Ma, Fuquan Zhao and Konghui Guo

Optibody Project: Optimizing Vehicle Structures for Electric Light Trucks and Vans 633
 F2012-E04-026
 Eduardo del Pozo de Dios, Arturo Dávila,
 Juan José Alba and Massimiliano Avalor

Linear Quadratic Gaussian Optimal Control Strategy for Four-Wheel Steering Vehicle 641
 F2012-E04-028
 Yan Chen, Wenqiang Chen, Xingmin Wei and Fuquan Zhao

Design and Validation of a Race Car with Respect to Aerodynamics and Body Styling 651
 F2012-E04-029
 Abdul Vaseem Akram, M. Ajay Kumar,
 K.C. Vora and Mohammad Rafiq

Part V Automotive Ergonomic, Interior and Exterior Trim Design

Driver Accommodation Assessment Using Physics-Based Posture Prediction Model 665
 F2012-E05-001
 Ozsoy Burak and Jingzhou (James) Yang

Design of the Adjustable Vehicle Seating Buck for Ergonomics Verification 677
 F2012-E05-002
 Hongfang Ling, Li Wu and Gang Li

Study on Preventing Dazzle of Meter 691
 F2012- E05-006
 Luo Pan, Xiaolin Liao, Guozheng Luo, Jing Wang,
 Dejian Cheng and Li Yu

A Study and Application of Optimization on Console Development. . . 701
 F2012-E05-009
 Ruiyan Zhang, Ni Cao and Miao Luo

Enhancing Vehicle Ingress/Egress Ergonomics with Digital Human Models 713
 F2012-E05-010
 Nanxin Wang, Ksenia Kozak, Jian Wan,
 Gianna Gomez-Levi and Gary Strumolo

Preliminary Research on Muscle Activity in Driver’s Steering Maneuver for Driver’s Assistance System Evaluation 723
 F2012-E05-011
 Ryouhei Hayama, Yahui Liu, Xuewu Ji, Takahiro Mizuno, Tomoyasu Kada and Liming Lou

Color TFT Instrument Clusters in the Chinese Market. 737
 F2012-E05-012
 Huibin Li, Gerhard Mueller, Karl Reich and Leo Glasenhardt

Color and Texture Design of Chinese Automobile Brand 747
 F2012-E05-014
 Yanhong Hao and Fuquan Zhao

Development of Shock-Absorbing Grip-Handle Structures on the Headliner 761
 F2012-E05-015
 Hee Sang Park, Yongsu Chang and Jun Ho Jung

SEMG Based Recognition for Lumbar Muscle Fatigue During Prolonged Driving 773
 F2012-E05-017
 Xin Tao, Bo Cheng, Bo Wang, Feiruo Zhang, Guofa Li and Chaoyang Chen

Part VI Vehicle Style and Aerodynamic Design

Aerodynamic Investigations in Conceptual Vehicle Development Supported by Integrated Design and Simulation Methods. 787
 F2012-E06-004
 Mario Hirz, Severin Stadler, Martin Prenner and Johannes Mayr

Research on Drag Reduction of Commercial Vehicle Based on Aerodynamics. 801
 F2012-E06-007
 Shijie Fan, Qiang Fu, Jialin Zhang, Jinying Ma, Jing Zhao and Kelong Lu

The State of Equilibrium in Car Body Design: The Application of Asymmetry for Enhanced Harmony. 811
 F2012-E06-009
 Liming Fu, Mingyang Sun and Alvin Chan

Part VII New Materials and Structures

The Analysis of Composite Leaf Spring by Finite Element Method and Experimental Measurements 823
F2012-E07-004
Jiashi Wang, Zaike Li and Qibin Jiang

Finite Element Analysis of Two Kinds of Dump Trunk. 831
F2012-E07-005
Zhi Li, Tie Wang, Jingxin Wang, Zhaohui Peng and Na Wang

Advanced Solid Lubricant Technology Improve Engine Performance 839
F2012-E07-006
Yupeng An, Kejin Zhang, Dan Wang, Junyan Zhang and Bin Zhang

Wrought Magnesium Alloy AZ31 Grain Refinement by Predeformation 851
F2012-E07-007
Fei Xiong, Lichun Cui and Ping Wang

Consideration of Biomimetics in Structural Design of Vehicle Side Intrusion Bars 859
F2012-E07-009
Yan Rui, Aleksandar Subic and Chunhui Wang

Development of High Performance FRP Crush Box: A Report of JSAE FRP Working Group Activity. Numerical Analysis of Fracture Behavior of FRP Crush Box with Tapered Trigger 869
F2012-E07-012
Reika Akita, Atsushi Yokoyama, Asao Koike, Kouji Kawamura, Yoshihiro Sukegawa and Hiromichi Oohira

Development of the High Performance FRP Crush Box: A Report of JSAE FRP Working Group Activity. Analysis of Collapse Mechanism of the Trigger Part of FRP Crush Box 879
F2012-E07-013
Asao Koike, Atsushi Yokoyama, Reika Akita, Yoshiro Sukegawa, Koji Kawamura and Hiromichi Oohira

Research of Application of Crash Durable Adhesive on a Chinese Domestic Car Body 889
 F2012-E07-020
 Zhongying Yue, Xiukui Yuan, Chaoqian Gao, Liantai Yuan, Qiang Liu, Fuquan Zhao, Yufei Wang, Xiaojun Yang and Jie Xu

The Study of Aluminum Alloy Application on Automotive Control Arm 901
 F2012-E07-021
 Juanli Ni, Li Li, Qiang Liu, Fuquan Zhao, Yi Xu, Shijie Guo and Bowen Changhai

Using Shape Memory Alloys in Automotive Safety Systems 909
 F2012-E07-023
 Viorel Gheorghita, Paul Gumpel, Joachim Strittmatter, Chiru Anghel, Thomas Heitz and Mathias Senn

Study on Electro Rheological Fluid Shock Damper and Adjustable Damping Performance 919
 F2012-E07-024
 Jianhua Wang, Fei Xie, Yuncheng Wang and Chunbao Guo

Cyclic Tension–Compression Test of Mg Alloy Sheet at the Elevated Temperature 927
 F2012-E07-029
 Oh Suk Seo, Heon Young Kim, Myoung-Gyu Lee, Ji Hoon Kim and Dae Yong Kim

The Third Generation Auto Sheet Steel: Theory and Practice. 933
 F2012-E07-030
 Shanqiang Ying and Han Dong

Part VIII Automotive Reliability Technology

Vehicle Usage Measurement and Analysis Based on the Random Retail Customer 951
 F2012-E08-001
 Yaozeng Pan, Feng Yang and Chenyang Li

Part IX Lightweight Design Technology

Design, Evaluation Methods and Parameters of Automotive Lightweight 965
F2012-E09-001
Mingtu Ma and Hongzhou Lu

Body Light Weight and Cost Control 977
F2012-E09-006
Dazhou Guo

Lightweight Design and Formability Analysis of Auto Body Aluminum Trunk Lid 987
F2012-E09-007
Zhao Liu, Ping Zhu and Xiaojing Zhu

Geometric Parameters Optimal Design of Variable Cross-Section Rim 1003
F2012-E09-009
Hongyu Wang

Lightweight Design for a FSC Car Based on Modal and Stiffness Analysis 1009
F2012-E09-012
Liman Jiang, Guoquan Wang, Guoqing Gong and Ruiqian Zhang

Application of Comprehensive Optimization into Bus Structure Lightweight Improvement in 3-Section Chassis Frame 1023
F2012-E09-014
Congcheng Ma and Fengchong Lan

Applying Agile Software Principles and Practices for Fast Automotive Development 1033
F2012-E09-015
David Socha, Tyler C Folsom and Joe Justice

Multi-Objective Evaluation Regulation Study of Automotive Lightweight 1047
F2012-E09-016
Hongzhou Lu, Zhiwen Wang, Ma Mingtu, Yilong Cheng and Guimin Lu

Future Mobility Requires Advanced Car Concepts and Power Train 1057
F2012-E09-025
Sven Augustin

A Lightweight Optimization Method of Vehicle Body Structure Design.	1063
F2012-E09-026	
Zhixiang Li and Jifa Mei	
Analysis of the Transient Thermomechanical Behaviour of a Lightweight Brake Disc for a Regenerative Braking System.	1075
F2012-E09-028	
S. Sarip, A. J. Day, P. Olley and H. S. Qi	
Concept Analysis of Automotive Aluminium Alloy Bumper	1089
F2012-E09-030	
Xinming Wan, Xiao Zhi, Qingjiang Zhao, Guangyao Wang and Xiaofei Xu	
Study on Lightweight of Vehicle Body Structure Based on Implicit Parametric Model	1101
F2012-E09-031	
Jiyou Zhang, Shudan Liu, Hong Peng, Yongxin Men and Fuquan Zhao	
Lightweight Design and Evaluation for Cab-in-White of Heavy-Duty Truck	1109
F2012-E09-034	
Xinyu Wang, Dengfeng Wang, Wanlai Sun and Peiwu Liu	
Research on Parameterized Structural Modeling for Carbody Lightweighting.	1119
F2012-E09-038	
Xin Chen, Fangwu Ma, Dengfeng Wang, Yongxin Men, Qiang Liu, Zaiqi Yao, Junlong Zhou and Chen Xie	
Reliability-Based Topology Optimization of Control Arm of Suspension for Lightweight Design.	1129
F2012-E09-039	
Qinghai Zhao, Xiaokai Chen and Yi Lin	
Structural Lightweight Design of Engine Connecting Rod.	1139
F2012-E09-042	
Fuxiang Huo, Jun Li, Yu Xu, Bing Wu, Yepeng Han, Peng Li and Qun Zhang	
Part X Design for Recycling	
Development of Environmental Assessment System of Vehicle	1151
F2012-E10-001	
Moosang Yu and Yunjong Kim	

Research on Hydraulic Regenerative Braking System for Pure Electric Vehicle Based on AMESim 1161
 F2012-E10-002

Junping Jiang, Xiaobin Ning, Yaoting Xu, Qiucheng Wang,
 Wei Liu, Zhijie Pan and Fuquan Zhao

Part XI Dynamic Modeling

Main Problems of Creating Surface Traction-Transport Vehicles with Mechatronic Systems 1173
 F2012-E11-001

Belousov Boris and Ksenevich Tatiana

Wheelbase Filtering Effect on Vehicle Ride Dynamics. 1183
 F2012-E11-007

Kang Song, Xiaokai Chen and Yi Lin

Part XII Simulation and Experimental Validation

Modeling and Experimental Research About a New Type of Vehicle Active Suspension Electromagnetic Actuator 1199
 F2012-E12-001

Lai Fei and Huang Chaoqun

Research on Nonlinear Characteristics of Hydro-Pneumatic Spring and Impact to Ride Performance of Vehicles. 1211
 F2012-E12-002

Junwei Zhang, Sizhong Chen, Zhicheng Wu, Lin Yang and Bin Zhang

Simulation Research on Car Suspension Durability Enhancement Test Based on Virtual Proving Ground 1223
 F2012-E12-003

Zhenglin Cao, Jun Li and Konghui Guo

Simulation Research on Strong Fluid–Solid Interaction of Hydraulic Engine Mount 1235
 F2012-E12-004

Zhenglin Cao, Jun Li, Konghui Guo and Qun Zhang

A Study on Battery Model Verification Using Battery HILS 1249
 F2012-E12-008

Hyun-Sik Song, Tae-Hoon Kim, Jin-Beom Jeong, Byoung-Hoon Kim,
 Dong-Hyun Shin, Baek-Haeng Lee and Hoon Heo

Extended Flexible Environment and Vehicle Simulation for an Automated Validation 1263
 F2012-E12-010
 Albert Albers, Rolf Hettel, Matthias Behrendt, Tobias Düser and Alexander Schwarz

Application of Energy Distribution Analysis During the Vehicle Development 1275
 F2012-E12-012
 Yongsheng Long, Jianpeng Shi, Li Xin, Xueen Zhang, Jun Wang and Shaoju Qu

Simulation and Correlation of Commercial Axle Banjo Housing Fracture Under Braking Fatigue Test 1287
 F2012-E12-013
 Ajay Guddeti and Abhijit Nilangekar

Development of a Vehicle Simulator Based on a Real Car for Research and Education Purposes 1301
 F2012-E12-015
 Zsolt Szalay, Péter Gáspár, Zoltán Kánya and Dávid Nagy

Early Verification of Complex Distributed Systems Using Model Driven Development and Virtual Engineering 1313
 F2012-E12-020
 Lance Brooks, Jun Wu and Darrell Teegarden

Research in the Impact of Curtain Airbag Deployment on Interior 1327
 F2012-E12-021
 Shuyuan Zhou, Liangming Xiang, Jie Lou, Wenwei Zhang and Min Xu

Multi-Domain Modeling and Simulation of Automotive Air Conditioning System Based On Modelica 1337
 F2012-E12-024
 Jing Li, Yunqing Zhang and Wei Chen

Predictive Energy Management Strategies in Virtual Driving Tests: Early Evaluation of Networked Controller Functions in Realistic Use Cases 1351
 F2012-E12-027
 Andreas Kunz, Bernhard Schick and Steffen Lange

Evaluation of Video-Based Driver Assistance Systems with Sensor Data Fusion by Using Virtual Test Driving	1363
F2012-E12-028 Bernhard Schick and Steffen Schmidt	
Vehicle Warm-Up Analysis with Experimental and Co-Simulation Methods.	1377
F2012-E12-029 Daniel Ghebru, Christian Donn, Wolfgang Zulehner, Heiko Kubach, Uwe Wagner, Ulrich Spicher, Wolfgang Puntigam and Klaus Strasser	
Modelling and Simulation of AMT Truck Clutch Actuating Mechanism	1391
F2012-E12-030 Yanying Guo, Xintian Lu, Tao Yan and Zhonghui Sun	
Vibration Fatigue Analysis of Adaptive Front Lighting System.	1401
F2012-E12-031 Yeon Gyoo Lee, Seungryul Choi and Tae Ryong Jeon	
Application of Two-Chamber Muffler to Reduce Car Noise in Engine Intake System	1411
F2012-E12-040 Zhihong Tang, Zhenying Zhu, Yongxin Men and Fuquan Zhao	
Ergonomic Simulation and Optimization During the Body Assembly	1419
F2012-E12-041 Yanjun Gao, Xianbo Wei, Beifang Ma, Yang Yu, Xingmin Wei and Fuquan Zhao	
Test and Analysis of the Mechanical Properties for Laser-Welding Seams and Spot-Welding Joints	1429
F2012-E12-046 Liling Zhang, Xuefeng Chen, Qing Jiang and Xu Wang	
Aerodynamic Design and Numerical Simulation Analysis of a Passenger Car's Defrosting Duct.	1441
F2012-E12-048 Bo Yang, Li-na Huang and Fengtao Ren	

An Operating System for the Optimization of Technical Systems Using the Example of Transmission Calibration 1449
 F2012-E12-051
 Albert Albers, Alexander Schwarz, Matthias Behrendt and Rolf Hettel

Model Structure, Realization and Learning Process For a Driver Model Being Capable to Improve Performance with Learning by Itself 1461
 F2012-E12-052
 Kazuhide Togai and Hisashi Tamaki

Part XIII Virtual Design, Testing and Validation

The Suspension Optimization of FSAE Racing Car Based on Virtual Prototyping Technology 1481
 F2012-E13-002
 Jun Ni, Sizhong Chen and Zhicheng Wu

The Study of the Impact of Aluminum Formability Parameters on its Stamping Formability 1491
 F2012-E13-003
 Jian Zhang, Mingtu Ma and Hongzhou Lu

Calculation of Shrinkage Rate for Injection Molding Based on Moldflow 1501
 F2012-E13-007
 Fangcheng Xiao, Lei Chen and Xiao Wang

A Study of Contact Condition in Vehicle Transmission Virtual Assembly System 1511
 F2012-E13-010
 Yan Chen, Shouwen Yao and Fei Liu

The Multi-Properties Modeling Technologies of Virtual Assembly for Vehicle Transmission Based on the Design 1521
 F2012-E13-011
 Fei Liu, Qingdong Yan, Shouwen Yao and Xin Zheng

New Technologies in Driving Dynamics Performance Simulation . . . 1531
 F2012-E13-012
 Cibrario Valerio and Cugnon Frederic

Transmission System Design and Manufacture in FSC Racing Vehicle. 1551
 F2012-E13-014
 Zhenpo Wang, Changfu Zou, Lei Yue and Lei Zhang

Parallel Design Optimization of Articulated Heavy Vehicles with Active Safety Systems 1563
 F2012-E13-015
 Manjurul Md. Islam, Steve Mikaric, Yuping He and Thomas Hu

The Application of Dual Limit Analysis Method in Physical Performance Characteristics Defining and Structural Designing 1577
 F2012-E13-016
 Chi Luo

Predicting Battery Pack Thermal and Electrical Performance in a Vehicle Using Realistic Drive Cycle Power Profiles 1587
 F2012-E13-017
 Allen Curran and Scott Peck

Virtual Test Drive in the Application Process of ESP[®]-Systems to Ensure Performance and Robustness. 1595
 F2012-E13-019
 Albert Lutz, Fabien Macaire and Walter My

The Test and Analysis of Car’s Brake Noise. 1611
 F2012-E13-020
 Qinghai Sui

Thermal Management Simulation of Passenger Car with Naturally Aspirated and Turbocharged Gasoline Engine 1621
 F2012-E13-021
 Haie Chen, Hongzhou Li, Xinxin Dai, Qun Chen and Kang Li

Part XIV Testing of Components, Systems and Full Vehicle

Research on User Vehicle Operation Regularity 1643
 F2012-E14-008
 Zhonggao Yu, Yutan Zhang, Yonghong Xu, Gan Chen, Jianguang Zhou, Jianxian Chen and Jie Bai

Acoustic Mode and Structure Mode Analysis of Heavy Duty Truck Muffler	1655
F2012-E14-011	
Guoquan Wang, Cheng Zhao, Liangcheng Zhang and Yong Chen	
Transient Thermal Measurement of Electronic Components and Radiometric Characterization of LEDs	1669
F2012-E14-013	
Boris Marovic and Alexandra Francois-Saint-Cyr	
Maneuver-Based Testing of Integrated, Highly Interconnected Safety Systems	1677
F2012-E14-019	
Kathrin Sattler, Andreas Raith, Thomas Brandmeier, Christian Schyr and Daouda Sadou	
Studying of Instantaneous Emissions Character for Hybrid Electric Vehicle	1691
F2012-E14-024	
Yanxin Nie, Baocheng Du, Peng Wan and Jingsi Xie	
Effect of Cryogenic Treatment on Retained Austenite and Fatigue Life of Gcr15 Wheel-Hub Bearing	1701
F2012-E14-025	
Qiucheng Wang, Xiaobin Ning, Qi Chen and Bintao Mao	
A Study on Analysis Method of Motion Characteristics in the Crash Test Based on Computer Vision	1709
F2012-E14-029	
Guohua Cao, Gang Han, Weiguo Liu and Fuquan Zhao	
Study of Optimized Tuning in Full AFLS Head Lamps	1719
F2012-E14-031	
Doohyun Kim	
Improvements in Test Protocols for Electric Vehicles to Determine Range and Total Energy Consumption	1733
F2012-E14-032	
Juhani Laurikko, Jukka Nuottimäki and Nils-Olof Nylund	
New AMFM Test Method with Android Operation System	1745
F2012-E14-038	
Yongqing Zhu, Kerun Xu, Lubing Zeng, Minjie Tian and Chendong Wang	

Part XV Subjective and Objective Evaluation of Performances

Ergonomic Evaluation System for Vehicle Package. 1755

F2012-E15-001

Shihai Li, Yongqing Liu, Zhongxian Chen, Mengdong Mi, Hao Chen,
Weiwei Du, Tingchuan Song and Huang Jian

Subjective and Objective Vehicle Tests, Two Parallel

Vehicle Handling Evaluations 1767

F2012-E15-004

Eric Chabrier and Michel Grima

**Subjective Evaluation and Modeling of Human Ride Comfort of
Electric Vehicle Using Tools Based on Artificial Neural Networks. 1777**

F2012-E15-005

Lerspalungsanti Sarawut, Albers Albert and Ott Sascha

**Torque Vectoring Control Design Based on Objective
Driving Dynamic Parameters. 1787**

F2012-E15-006

Michael Graf and Markus Lienkamp

**Integrated State Estimation with Driving Dynamic Sensors
and GPS Data to Evaluate Driving Dynamics Control Functions. 1797**

F2012-E15-013

Markus Bauer, Carlo Ackermann and Rolf Isermann

Evaluation Tool for Current and Future Powertrains. 1807

F2012-E15-016

Barak Adam

Part XVI Other

**Wet Handling Track: Utilities, Water System, Coefficient
of Adherence. 1825**

F2012-E16-005

Pinilla Marc, Carbonell Abel and Arango Luz A

**The Development of an Auxiliary Unloading Device
for Dump Trucks 1837**

F2012-E16-006

Guoxing Li and Tie Wang

Part VIII
Automotive Reliability Technology

Vehicle Usage Measurement and Analysis Based on the Random Retail Customer

Yaozeng Pan, Feng Yang and Chenyang Li

Abstract Customer vehicle real world usage is one of the most important foundations of vehicle development. It is the basis of setting vehicle, subsystem and component technical specification; the basis of developing product validation test procedure; the basis of product evaluation target. On the other hand, it is also the basis of product warranty system. This chapter introduces a random customer vehicle real world usage measurement and analysis method which is found on statistical sampling theory, vehicle CAN and signal measurement technical.

Keywords Real world · Usage · Random sample · Measurement · Analysis

1 Preface

China has become the largest automotive manufacturing country and the largest automotive market in the world. The rapid development of market not only improve product develop level, but also promote intensified market competition. Developing safety and reliable product which can meet all the customer's requirements with lower cost will became very considerable support for a company to win in so intensified market competition. Low cost has become a very important study subject in modern automotive development.

One of most important approaches to realize low-cost vehicle development is development and validation philosophy which based on customer real world usage.

F2012-E08-001

Y. Pan · F. Yang (✉) · C. Li
Pan Asia Technical Automotive Center Co., Ltd, Shanghai, China
e-mail: feng_yang@patac.com.cn

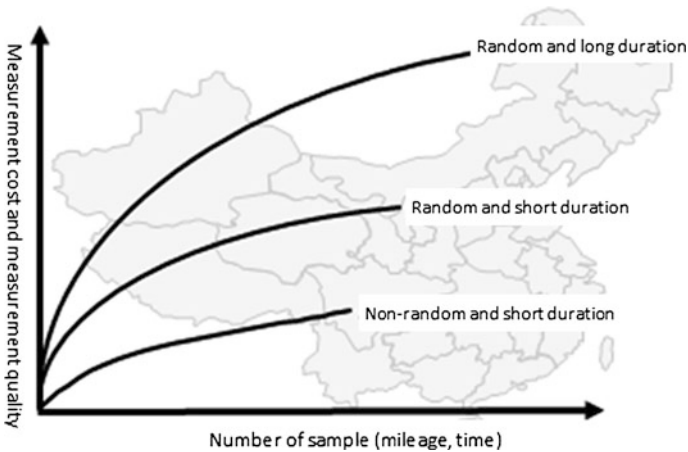


Fig. 1 Relationship between measurement cost and quality of different measurement methods

This philosophy based on customer real world usage is used to set up vehicle technical specification and related test procedure and validation assessment criteria. It not only avoiding conventional over-design, but also improving the correlation between vehicle validation and customer real world usage.

The key to develop and validate vehicle based on customer real world usage lies on measuring customer vehicle real world usage objectively. In some automotive technical developed countries, it has exceeded 40 years to measure customer real world usage. The measurement regions include almost all developed and potential vehicle market all over the world. By this way, those countries have accumulated abundant of fundamental data for product development and quality improvement.

As important basis of vehicle design and validation, the customer real world usage measurement should contain the working load and service condition of the full vehicle and component as far as possible. It includes road condition, service circumstance, full vehicle and main components working condition, driver's operation habits, and the usage of all on-board features, in order to obtain comprehensive and real world vehicle usage data.

As a face became known, the usage of vehicle, service condition and the driver's driving style differ in thousands ways. This determines the characters of vehicle usage are not only random, but also dispersed. Therefore, current vehicle real world usage measurement methods can be bracketed into several groups as follow: random and long duration; random and short duration; non-random and short duration. The relationship between measurement cost and quality of different measurement methods is mentioned in Fig. 1.

Considering the better support for vehicle development which face to china market, we adopted the method of "random retail customer and extended tracking measurement (random and long duration)" to study the measurement and analysis methods of China customer vehicle real world usage.

The study object is aimed at random retail customer's vehicle. The study theory was founded on statistical sampling theory. And the study is by means of obtaining vehicle CAN data, signal measurement technology and wireless data transmission technology to obtain customer vehicle usage data for study. So far as I know, it is the first time in china to study customer real world vehicle usage in such a systemic and integrated way. The study not only completes the independent development of main measurement system and entire measurement data analysis software, but also obtains abundant of measurement data.

2 Customer Vehicle Usage Measurement

As we know, there is no such tow customers have same vehicle usage. Customer vehicle real world usage measurement depends on accumulating tracking sample data from numerous customers, and then extrapolates the population customer usage information according to measurement data of limited samples. Following is detailed description of how to obtain population customer usage information by limited samples from overall customers.

2.1 Selection of Customers (Driver)

In order to ensure the selected customers are objective, complete and real, customer selection should coordinate following aspect: vehicle usage purpose, driving experience, gender, age, vocation and customers are unaware of the measurement content and details.

2.2 Selection of Measurement Area

Measurement area selection should coordinate geography and climate environment, and then divide overall area (China market) into several regions. At first, count vehicle quantity and related proportion of every region. Then distribute the measurement samples to every region proportional to the region vehicle quantity. With respect to special environmental area, the number of samples could be increased if necessary.

The above selection method of customers and measurement region not only coordinate the complete operating condition and environment, but also ensure the sampling is random and independent. Therefore, the samples which preform real world usage data acquisition can be considered as complete independent. Meanwhile, as a random process, the measurement data can be considered as ergodic and accord with normal distribution.

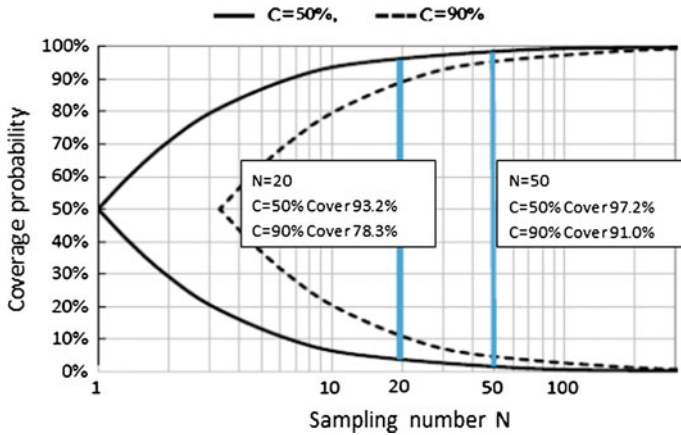


Fig. 2 Relationship between sampling number, confidence coefficient and measurement coverage probability

2.3 Selection of Sample Number (Number of Measurement Vehicle)

Sample number will decide the level of confidence of the measurement result, meanwhile; decide the probability of measurement data which can be covered by the customer usage. Due to the independence of sample, the number of sample, degree of confidence, and probability meet following binominal distribution Eq. (1):

$$\sum_{x=0}^r \binom{N}{x} R^{N-x} (1 - R)^x \leq 1 - C \tag{1}$$

Where N is sample number; r is the number of failure sample; R is the expected probability of customer usage; C is the expected level of confidence of measurement result [1].

When all the samples are available during the whole measurement (namely, there is no measurement vehicle be dropped out because fail to data sampling.), r is zero. Equation (1) is transformed to:

$$R^N \leq 1 - C \tag{2}$$

Figure 2 shows the relations between measurement coverage probability and the number of sampling in the context of confidence coefficient $C = 0.5$ and $C = 0.9$. As can be seen, when the expected confidence coefficient is certain, and coverage probability accumulates to certain quantity, the improvement of sampling number has limited influence to coverage probability. Secondly, when the coverage probability is certain, sampling number needs to be increased if expect higher confidence coefficient. That means in order to catch the special affairs which has

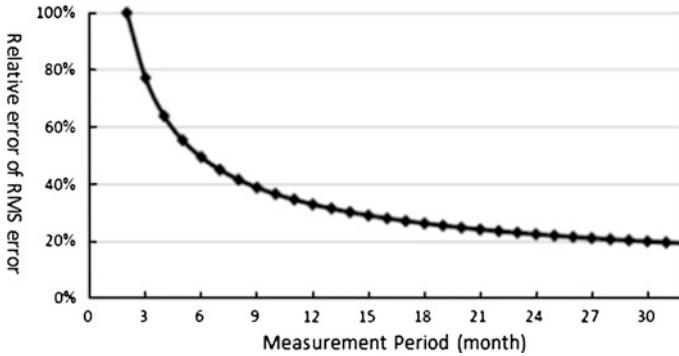


Fig. 3 Relationship between relative errors of sample RMS error and measurement period

little probability to happen, the number of sampling must be increased. And that will lead to increase the measurement cost and workload largely. Statistics shows base on finite sampling measurement method, the measured coverage probability is limited. It can be forecasted that it is impossible to obtain usage affair which the probability is less than 0.2 %.

2.4 Selection of Measurement Period

Assume the measurement parameter is random process X , and X comply with normal distribution with typical value μ_x and variance σ_x^2 , then according to independent measurement samples number N , the variance s^2 can be expressed as follow,

$$s^2 = \frac{\sigma_x^2 \chi_{n;\alpha}^2}{n}$$

$$s = \sigma_x \sqrt{\frac{\chi_{n;\alpha}^2}{n}}$$

$$\frac{(\sigma_x - s)}{\sigma_x} = 1 - \sqrt{\frac{\chi_{n;\alpha}^2}{n}}$$

Where $\chi_{n;\alpha}^2$ is the χ^2 distribution with degree of freedom $n = N - 1$ and probability α [2].

Figure 3 shows the relationship between the relative errors of sample RMS error and measurement period. This curve shows the relative error between RMS error of measurement data and RMS error of measurement population reduce gradually with increase of measurement period.

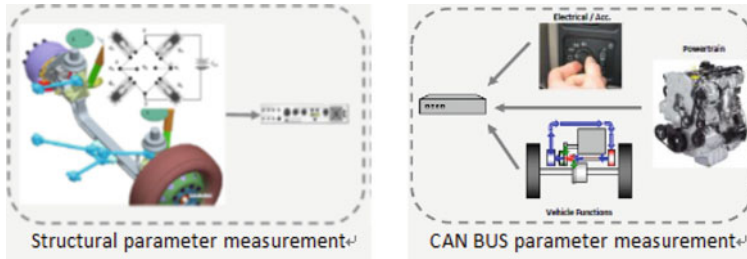


Fig. 4 Parameters acquisition and recording system

2.5 Measurement System and Data Acquisition

Early method of vehicle usage measurement mainly recurred to analog signals transmitted by vehicle harness. With the restriction of transducer, data recorder and transmit condition, this kind of measurement not only costly, but also results in the number of measureable parameters and sample number (the number of measured vehicle) are limited. Those restrictions will affect confidence level of the measurement result. With the application of CAN BUS technology, more and more vehicle signals can be measured by various kind of vehicle control transducers. On the other hand, due to the development of communications technology, the cost of data record and transmission is reduced greatly. Thereby, the number of measurable signals and the number of samples are increased greatly. Those technologies can not only improve the confidence level of measurement result, but also shorten the measurement period obviously [3].

Figure 4 shows the customer vehicle usage tracking measurement system, which based on CAN and strain transducers. It includes 2 parts as follow, Firstly, various kinds of transducer signal conditioning and acquisition devices which used to quantify the road condition, traffic situation and environment of vehicle usage. Sampling frequency is fixed to 256 Hz. It adopts P-V with time stamp format to record data, shows in Fig. 5. This format compresses data quantity enormously under conditions of keeping parameters' amplitude, moreover, data transmit speed was improved. Original data can be reconstruction by P-V with time stamp and sampling rate if necessary.

Secondly, data acquisition and record system which is based on vehicle controller network (vehicle CAN). The controller network is used to obtain not only driver maneuver information which include full vehicle, subsystem running situation and driving habits, but also vehicle feature usage information. Sampling frequency was fixed to 1 Hz. It adopts time history format to record data.

Figure 6 shows remote real time data transmitting and receiving system. Customer vehicle real world usage data is transmitted by on-vehicle electroplate, transferred by satellite communications system, received by remote server for data receive system real-timely.

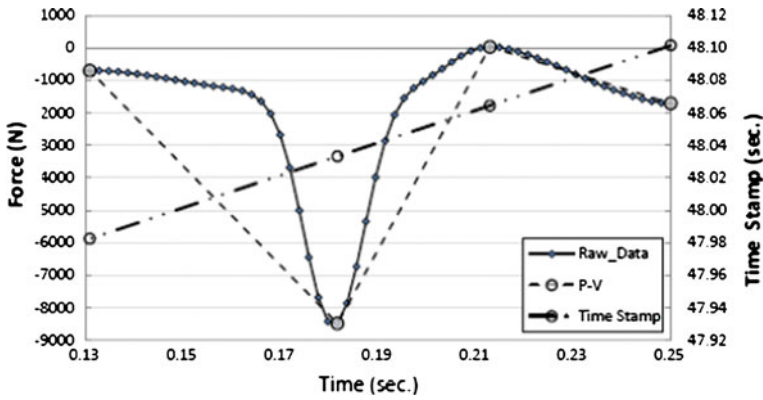


Fig. 5 Data format comparison between Original time history data and P-V

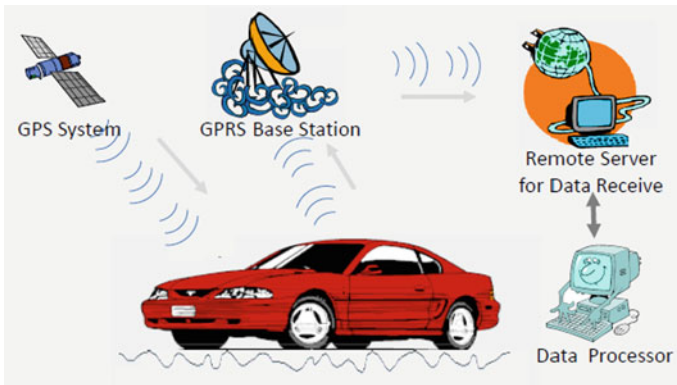


Fig. 6 Customer vehicle remote real time data transmitting and receiving system

The power consumption of the full measurement system is very low, due to the function of auto dormancy and activation. And this system is compact conformation and easy to install. Thereby, it ensures no impact to customer driving and vehicle service condition.

3 Measurement Data Analysis

3.1 Sample Data Analysis

According to various kinds of purpose and special requests from measurement result requestors, the original measured data can be processed into various formats. For the sampling data from every measurement vehicle, it was ordinarily

Average vehicle deceleration during brake activation
(Data unit: Occurrences)

Average Dec. (m/s/s)	-10	-9	-8	-7	-6	-5	-4	-3	-2	-1	Total
	to	to	to	to	to	to	to	to	to		
State	-9	-8	-7	-6	-5	-4	-3	-2	-1	0	
Off	0	0	0	0	0	0	0	0	0	0	0
On	0	0	0	1	0	1	2	5	130	1323	1462

Fig. 7 Column diagram example

Transmission Gear State
(Data unit: Occurrences)

To From	D 1	D 2	D 3	D 4	D 5	D 6	N	R	P	Total
D 1	0	390	1	0	0	0	19	58	21	490
D 2	147	0	264	0	0	0	0	0	0	412
D 3	244	21	0	298	0	0	0	0	0	563
D 4	1	0	297	0	152	0	0	0	0	450
D 5	0	0	1	151	0	88	0	0	0	240
D 6	0	0	0	1	87	0	0	0	0	88
N	15	0	0	0	0	0	0	13	4	32
R	63	0	0	0	0	0	7	0	20	90
P	18	0	0	0	0	0	6	17	0	40
Total	488	412	563	450	240	88	32	88	45	

Fig. 8 From-To 3D column diagram example

Vehicle speed vs. Gear state
(Data unit: km)

Gear state	Speed (km/h)																Total
	0	12	24	36	48	60	72	84	96	108	120	132	144	156	168		
D 1	9.0	2.5	0.0	0.0	0.0	0.0	0.0	0.0	0.0	0.0	0.0	0.0	0.0	0.0	0.0	11.5	
D 2	0.2	9.9	1.0	0.0	0.0	0.0	0.0	0.0	0.0	0.0	0.0	0.0	0.0	0.0	0.0	11.1	
D 3	0.1	11.1	20.2	1.8	0.1	0.0	0.0	0.0	0.0	0.0	0.0	0.0	0.0	0.0	0.0	33.3	
D 4	0.0	0.0	14.6	32.2	4.1	0.6	0.2	0.1	0.0	0.0	0.0	0.0	0.0	0.0	0.0	51.9	
D 5	0.0	0.0	0.0	8.8	35.3	14.7	2.2	1.0	0.5	0.2	0.1	0.0	0.0	0.0	0.0	62.8	
D 6	0.0	0.0	0.0	0.0	0.8	24.1	35.9	24.6	14.9	8.4	3.5	0.5	0.1	0.0	0.0	112.8	
N	0.0	0.0	0.0	0.0	0.0	0.0	0.0	0.0	0.0	0.0	0.0	0.0	0.0	0.0	0.0	0.0	
R	0.5	0.0	0.0	0.0	0.0	0.0	0.0	0.0	0.0	0.0	0.0	0.0	0.0	0.0	0.0	0.5	
P	0.0	0.0	0.0	0.0	0.0	0.0	0.0	0.0	0.0	0.0	0.0	0.0	0.0	0.0	0.0	0.0	
Total	9.8	23.5	35.8	42.8	40.4	39.4	38.3	25.7	15.5	8.6	3.6	0.5	0.1	0.0	0.0		

Fig. 9 Relevant running situation 3D column diagram example

processed into 2 dimensional or 3 dimensional chart, and even more complicated matrix diagram and histogram as follow. These analysis results not only present each parameter of operating situation, but also present the relationship between relevant parameters. For structural load data, more analysis can be done by spectrum, fatigue analysis etc. Figures 7, 8, 9, 10 show different kinds of data analysis result.

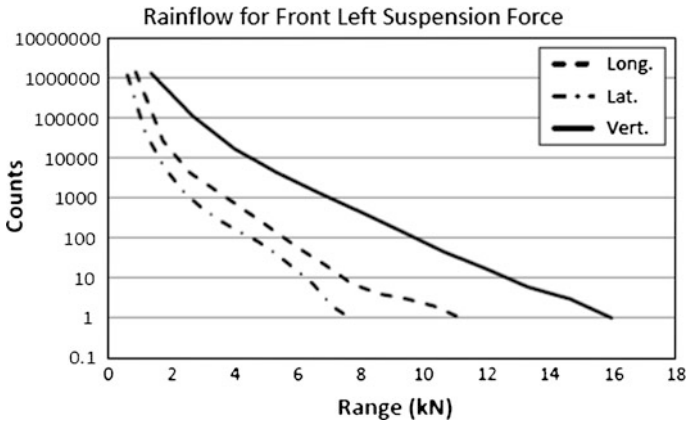


Fig. 10 Rain flow column diagram example

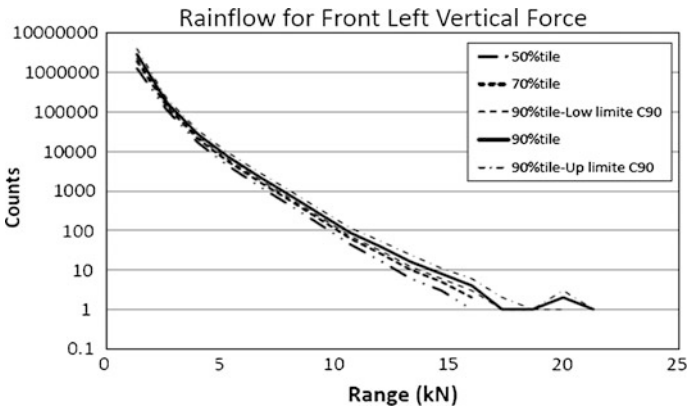


Fig. 11 Architecture load rain flow statistics-percentile estimation and confidence interval

- Parameter level—frequency
- Status change frequency of parameter
- Parameter status continuance period
- Fatigue statistics

3.2 Population Estimation (Sample Parameters Percentile Extrapolation)

As previous presentation, customer vehicle real world usage measurement is based on limited sample measurement data, and obtains the population parameter by assumed probability distribution model estimation. Practice shows normal

Fig. 12 Different status time-percentile estimation and confidence interval

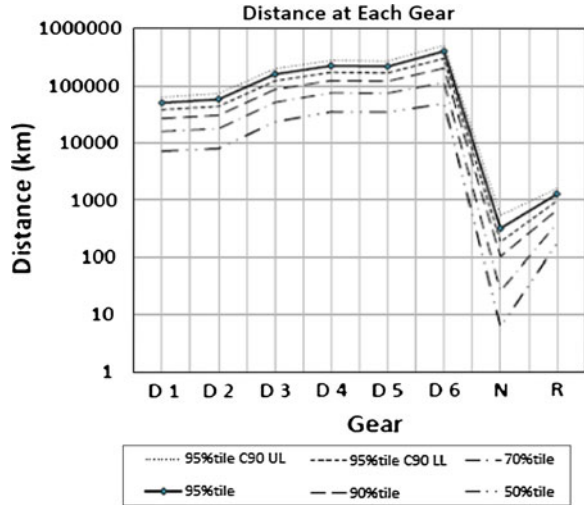
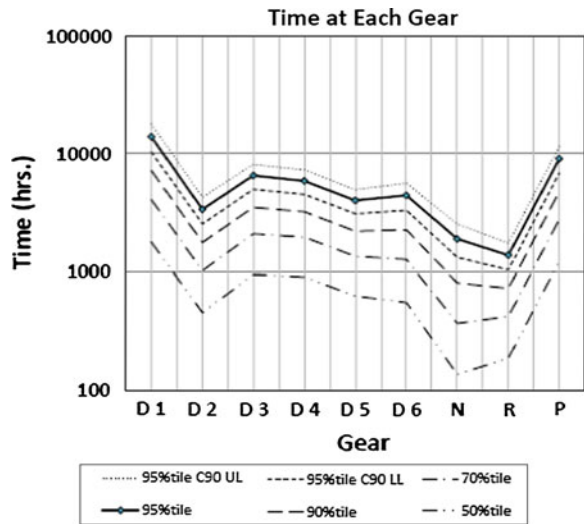
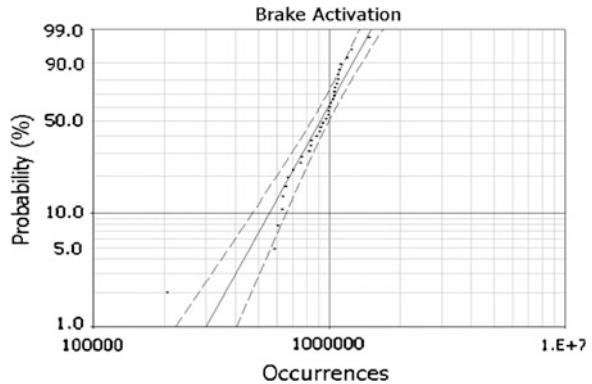


Fig. 13 Different status mileage-percentile estimation and confidence interval



distribution model which depends on the physical characteristics of measurement parameters and Weibull distribution model can describe customer vehicle usage data. For the estimation method selection, due to point estimation cannot provide estimation error, interval estimation method should be selected. From Figs. 11, 12, 13, 14 show several representative customer vehicle real world usages measured parameters 90 % confidence level population percentile estimation result base on weibull distribution model.

Fig. 14 Driving habits-percentile estimation and confidence interval



4 Conclusion

This chapter integrally describes the customer vehicle usage measurement method, which set random retail customer vehicle as object, based on statistics sampling theory, and in virtue of vehicle CAN system and signal measurement system, as well as wireless data transmission technology. This study not only provides the selection method of various kinds of factor which would impact measurement result, but also finished self-development of main measurement system and all data analysis and process software. So far, it's the first time to study the customer vehicle usage so systematically and integrally in China.

According to the method mentioned in this chapter, we have been performing continuous tracking measurement over 3 years which involve more than 30 random customers' vehicle and cover 20 provinces in China mainland. The accumulated data mileage is more than 600,000 km, and the coverage rate of usage measurement exceed 95 %. Now, various kinds of production technology specific and validation test standard which based on those measurement results have been extensively used to local production design, test validation and quality improvement for Chinese market. It provides important support to production cost reduction and pertinence of test and development improvement.

References

1. Lee YL, Pan J, Hathaway R, Barkey M (2005) Fatigue testing and analysis (theory and practice). Elsevier Butterworth Heinemann, Boston
2. Bendat JS, Piersol AG (1971) Random data: analysis and measurement procedures. Wiley, NY
3. 罗峰 孙泽昌 著 《汽车CAN总线系统原理、设计与应用》 电子工业出版社

Part IX
Lightweight Design Technology

Design, Evaluation Methods and Parameters of Automotive Lightweight

Mingtu Ma and Hongzhou Lu

Abstract Automotive lightweight is quite important and active demand, due to the requirements of automotive industry development, energy saving and emission reduction. This chapter illuminates the signification, the conception and comprehension, characterization parameters and execution methods about automotive lightweight and lightweight design. The physical and technical signification of parameters in the lightweight coefficient equation is explained also. A more direct parameter, lightweight exponent L^1 is suggested, and the physical and technique significations of those parameters in lightweight exponent L^1 equation are clarified for various conditions of lightweight. The execution approaches of automotive lightweight and the relationship of the performance of typical parts with the performance of materials are discussed. A life cycle analysis method is presented to evaluate the economy, selection and application of the lightweight materials and technologies.

Keywords Automotive lightweight · Lightweight coefficient · Lightweight exponent · Execution approach · Life cycle analysis

F2012-E09-001

M. Ma (✉) · H. Lu
China Automotive Engineering Research Institute, Chenjiaping,
Chongqing 400039, China
e-mail: mingtuma@126.com

H. Lu
e-mail: hong@126.com

1 Introduction

The automotive industry in the world is developing fast, and the annual output of automobiles in the world is 73 million and the retaining number is more than 500 million in 2007. The automotive industry is a principal industry in developed countries. Automotive industry impulses the progress of human civilization, and, however, also results in the problems including safety, fuel consumption and emissions [1]. Due to increasing the retaining number and annual output of automobiles, emissions of CO₂ and other environment pollutants become worse. Energy consumption and environment pollutants by automobiles have been a serious problem. At the same time, because the price of international oil climbs fast and the requirements of the whole performance by customer are much higher, automotive lightweight becomes more and more significant. This chapter illuminates the signification, conception and comprehension of automotive lightweight. Characterization parameters, and execution methods of automotive lightweight are also clarified.¹

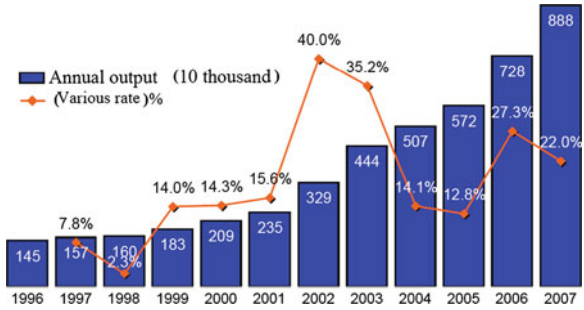
2 China Automotive Industry Development and Automotive Lightweight

China's automobile industry develops fast in these years. Figure 1 shows an obviously increasing trend in the annual output of automobiles in China [2]. In 1996, the output and sale number per year is about 1.0 million, but in 2007, the annual output will be near 9.0 million, a fast increase trend comes up. Since 2000, the purchasing power of personal cars and development of China automotive industry have been accelerated, and the annual output and sale number increase significantly. The output of automobiles in China in 2007 is about 8.88 million, and the output of automobiles in China for the 2008 will add up to more than 10.0 million. So it is quite important and active demand to save energy and reduce emissions.

In order to solve the problems of energy consumption and environment pollution produced by automobiles, the automotive lightweight has been attained much more attentions in China. To impulse the steps of automotive lightweight, an automotive lightweight creating alliance was established on 27 Dec 2007 in China. The automotive lightweight alliance leaguers include main carmakers of China and relational research institutes, and universities etc. The main aim to establish this alliance is to reduce the automotive weight for increasing fuel efficiency and decreasing CO₂ emissions by usage of optimization design, and advanced forming technologies, and high strength lightweight materials such as HSS (high strength steel) and aluminum alloy and magnesium alloy, plastic composites.

¹ This project is supported by the National High Technology Research and Development Program of China (863 program) (No. 2007AA03z551).

Fig. 1 Development of China automotive industry and annual output



3 Requirement for Design of Body-In-White

Several requirements should be put forward, including requirements of Body-In-White (BIW) for smooth going and stable property, requirements of body structure and sealing for acoustic and NVH (Noise, Vibration and Harshness), materials requirements of safety for crash performance (front crash, rear crash, side crash and roll, others), performance and technical requirements of body covers for geometry and dent resistance, performance and technical requirements of fatigue and antirust for some typical parts, protection requirements of BIW for roll, relational requirements of body for satisfy difference of profile, torsion stiffness and bending stiffness requirements of BIW for improving performance etc. These requirements are shown in Fig. 1. Besides those requirements, the engineering feasibility and cost must be considered. Under the condition of satisfying functions, the cost should be the lowest i.e. a high ratio of performance to cost (Fig. 2).

4 Conception of Automotive Lightweight and Automotive Lightweight Design

Lightweight design and weight reduction of the body-in-white (BIW) can not always be measured in kilograms, but they are related to the achieved vehicle dimension and functional requirements. Three aspects are used to expatiate on the conception of automotive lightweight and automotive lightweight design. Firstly, for a vehicle with fine functions, a automotive lightweight design is performed to reduce the mass but keep the whole performance, and this can be called direct lightweight. Secondly, for a vehicle without fine functions, a automotive lightweight design is performed to improve the whole performance but keep the mass, such as smooth going and stable property, acoustic and NVH safety, torsion stiffness and bending stiffness [3, 4]. Thirdly, an automotive lightweight design is performed not only to reduce the mass but also to improve the whole performance. From above discussion, the conception of automotive lightweight design should be a combination of mass, function, structure and cost. In the project of ULSAB

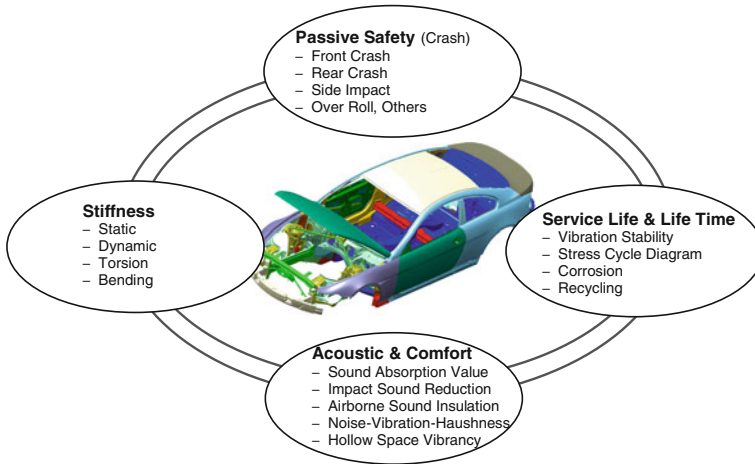


Fig. 2 Functional requirements for the body-in-white design

(Ultra Light Steel Auto Body) organized by internal steel association [5], the automotive lightweight is divided into ULSAB, ULSAC (Ultra Light Steel Auto Covers) and ULSAS (Ultra Light Steel Auto Suspension). The objects, materials and methods for the three kinds of lightweight are different, but the conception of automotive lightweight design is the same.

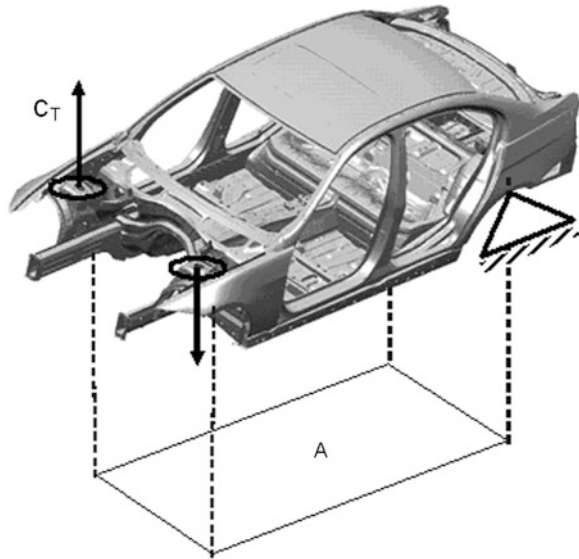
5 Characteristic Parameters of Automotive Lightweight

Lightweight design should include weight reduction of the body-in-white (BIW) and performance improvements. The functional requirements for stiffness, crash and car lifetime have to be considered in selection of the materials for a body in white. The stiffness of a structure can be influenced by the E-modulus and panel thickness and construction. Crash and vehicle lifetime are controlled by the strength of the material and thus affected by high strength steel grades. A specific lightweight coefficient L is suggested in literature [4]. The specific lightweight coefficient L is developed by Bruno Lüdke from BMW and is expressed by the formula (1). L is the ratio of structure weight m_{Ger} (excluding glass) to static torsion stiffness C_t (with glass) and the associated area A (footprint track \times wheelbase), it can be also as a customer benefits evaluating parameter. Increased customer benefits are reflected in a decreased lightweight coefficient.

$$L = \frac{m_{Ger}}{C_t \times A} \left[\frac{Kg}{Nm/^\circ \times m^2} \times 10^3 \right] \tag{1}$$

Figure 3.

Fig. 3 The specific lightweight coefficient



In order to reflect directly the lightweight effect, a lightweight exponent L^i is presented and suggested based on formula (1). Lightweight exponent L^i is expressed in formula (2),

$$L^i = \frac{L_1 - L_2}{L_1} = 1 - \frac{m_{Ger2}}{m_{Ger1}} \cdot \frac{C_{t1} \times A_1}{C_{t2} \times A_2} \tag{2}$$

where L_1 represents the lightweight coefficient of the original vehicle, and L_2 represents the lightweight coefficient of the lightweight vehicle. When the properties of BIW are invariable, the formula (2) can be simplified as formula (3),

$$L^i = 1 - \frac{m_{Ger2}}{m_{Ger1}} \tag{3}$$

Similarly, when the weight of the vehicle is invariable, but the properties of BIW are enhanced, a vehicle is also lightweight, and then formula (2) can be expressed as formula (4),

$$L^i = 1 - \frac{C_{t1} \times A_1}{C_{t2} \times A_2} \tag{4}$$

In order to reflect comprehensively the influence of lightweight on the whole performance, the ratio of loads for front axes to loads of rear axes must be kept to be 1:1, and the functions, cost and weight reduction all should be considered. Take an instance for ULSAB-AVC, three factors have been required, i.e. (1) lightweight of BIW must satisfy crash requirements, (2) mass relative to conventional vehicles should reduce 20 %, (3) no additional cost (Table 1).

Table 1 The targets of ULSUB and ULSUB-AVC

	2000 BIW	ULSAB	ULSAB-AVC
Crash requirements	2000 Year's law	2000 Year's law	2004 Year's law
BIW mass	270 kg	203 kg	218 kg
BIW costs	US\$979	US\$947	US\$972

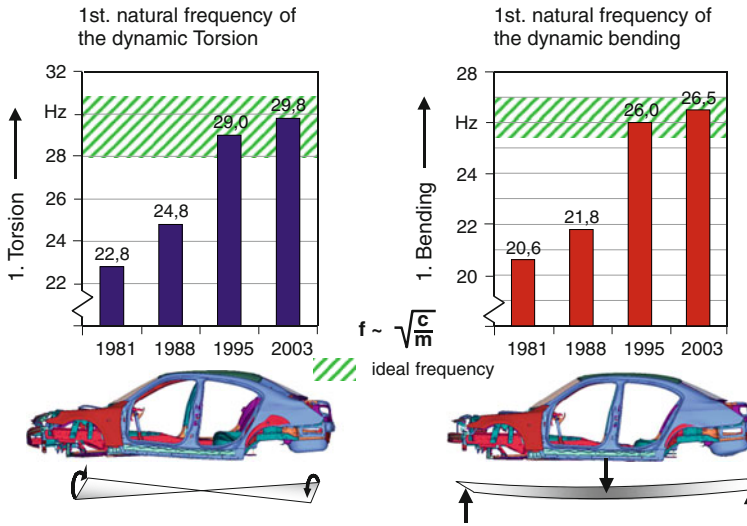


Fig. 4 The evaluation for NVH performance

However, not only the BIW, but also the auto-body covers and chassis should be lightweight. When the level of lightweight is increased due to other performance variation, the Ct in formulas should be replaced by other performance parameters.

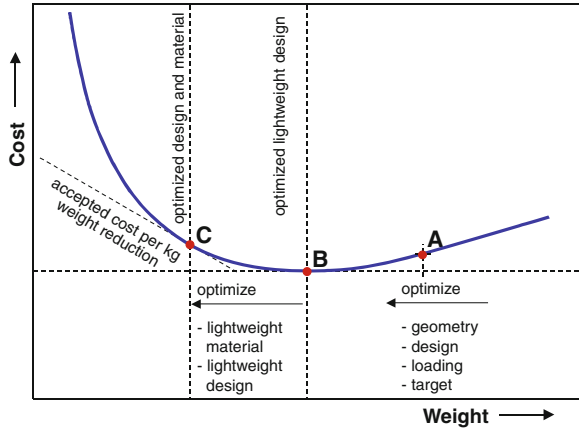
When the NVH performance is used to evaluate the effect of lightweight, the Ct in formula (1) should be replaced by f, i.e. the 1st nature frequency of dynamic torsion or 1st nature frequency of dynamic bending. The evaluation instance can be seen in Fig. 4, and it is expressed in formula (5).

$$L^i = \frac{L_1 - L_2}{L_1} = 1 - \frac{m_{Ger2}}{m_{Ger1}} \cdot \frac{f_1 \times A_1}{f_2 \times A_2} \tag{5}$$

When auto-body covers are lightweight, the Ct in formulas (2) should be replaced by the dent resistance value (DR), and it is expressed in formula (6).

$$L^i = \frac{L_1 - L_2}{L_1} = 1 - \frac{m_{Ger2}}{m_{Ger1}} \cdot \frac{DR_1 \times A_1}{DR_2 \times A_2} \tag{6}$$

Fig. 5 Relationship of the cost (R&D, material, process, and repair) and weight



In the same way, when suspending system of chassis is lightweight, the C_t in formulas (2) should be replaced by the stiffness and fatigue performance of spring.

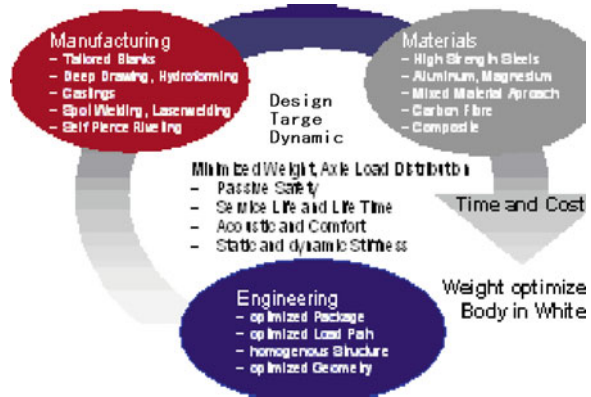
Another important factor for automotive lightweight engineering is cost. Particular care should be exercised when lightweight construction materials are used, because they not only increase the materials costs of the half finished products, but also the costs of manufacturing and repair. Relationship of the cost (R&D, material, process, and repair) with weight is shown in Fig. 5 [6]. Every effort should be made to get from status A to an optimal status B through “shape- and condition-related” lightweight structural design. Only then should status C be tried through material substitution. Cost should be controlled better.

6 Execution Approaches of Automotive Lightweight

From Fig. 6, a lightweight design should be a superior integration of different materials, a superiority integration of different specialties, a superiority integration of design, materials and advanced manufacture technologies. A lightweight design can be performed by optimized geometry to attain the effect of lightweight. But the better effect of lightweight can be able to perfect by the dominant integration of design, materials and manufacture.

From the formula (1), area A is an important parameter for the design of automobiles. The class of vehicles and the performance C_t of BIW are determined by this parameter. The parameter mass is related to the strength of materials, specific strength, ductility, modulus, geometry and forming technologies of materials. The choice of advanced forming technology is important, for the application of SHSS (super high strength steel) to improve the safety performance. Due to the poor formability of SHSS, the hot forming must be used in order to attain the strength more than 1,500 MPa. The high strength floor panels of vehicle body can be manufactured by roll forming. TWB (tailored welding blanks)

Fig. 6 Lightweight design approaches



technology can reduce the numbers of parts and weld points, resulting in improvement of the fatigue performance and sealing performance as well as reduction of weight. Hydroforming can reduce the numbers of parts and improve the performance of parts (for example, sub-frame of engine). These are the foundation of the design.

The computer simulation is an effective method in execution approaches of automotive lightweight. The load paths for crash and formability for a part can be simulated, and thus reasonable technological parameters can be attained for lightweight design and selection of materials and advanced forming technologies.

7 The Relationship of Performances of Typical Part with Properties of Materials

The relationship of performance of typical part with properties of materials is listed in Table 2, which shows how to choose a material according to the performance of various parts.

Application of lightweight materials is an important aspect of automotive lightweight, The aspect of material selection based on functionality of a body in white must be considered. The following six given characteristics have to be paid attention to for the purpose of lightweight design and selection in Fig. 6 [6]. A lightweight design is not only to choose some lighter materials to satisfy some performance of the part, but also to analyze the stress, optimize the design of structure, to select advanced manufacture technologies (Fig. 7).

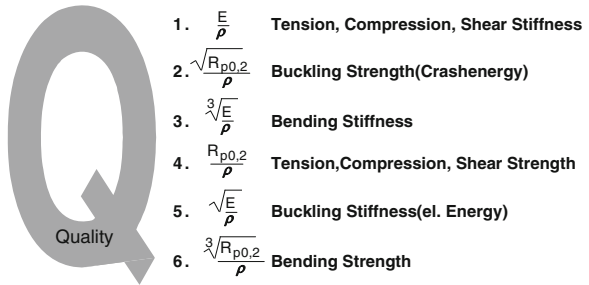
A life cycle analysis method should be used to evaluate the feasibility of the lightweight [7]. The life cycle analysis equivalent especially for energy consume equivalent and CO₂ emissions equivalent should be used as an evaluation parameter to evaluate the application of the lightweight materials and technologies. Of course such an evaluation method has to face much of complicated

Table 2 The relationship of performances of typical part with properties of materials [8]

Deformation	Typical part	Required performance of the parts	Relationship of thickness, strength and performance
Big plastic deformation	Bumper, reinforcement panel; Anti-collision pillar of door; Reinforcement rib of side beam	High collapse strength	$P_s \propto t(\sigma_b)^n$
		High absorb energy	$n \sim \frac{1}{2}$ $A_E \propto t^2(\sigma_b)^{2n}$ $n : \frac{1}{2} - \frac{2}{7}$
Small plastic deformation	Outer panel of roof and engine hood; Outer panel of door; Outer panel of luggage lid	High dent resistance	$P_t \propto t(\sigma_p)^n$ $n \approx \frac{1}{2.5}$
Smaller elastic and plastic deformation	Side beam of body; Cross beam	High modulus	$P \propto t \cdot E_D^n$ $(\frac{1}{E_D} = \frac{1}{E} + \frac{1}{E_s})$
Smaller deformation	Side beam Wheel	Fatigue strength	$\sigma_w \propto \sigma_b$

Note P_s collapse strength
 A_E collapse absorb energy
 P_t dent force
 P resistant force of smaller deformation
 σ_w fatigue strength
 σ_b tension strength
 t thickness
 σ_p the flow stress under the strain of some forming parts
 e dynamic modulus, e is constant

Fig. 7 Ranking of characteristic quotients for the purpose of lightweight design E elastic modulus P density $R_{p0.2}$ yield stress



factors, and a number of data are needed for this evaluation, but the life cycle analysis method will provide a crucial foundation for lightweight design.

8 Conclusion

1. Automotive lightweight is quite important and active demand due to the requirements of automotive industry development, energy-saving and CO₂ emission reduction;
2. Lightweight design should include weight reduction of the body-in-white (BIW) and performance improvements.
3. Based on the lightweight coefficient equation, a more direct parameter: lightweight exponent L_i is suggested. The physical and technical significations of the parameters in lightweight exponent L_i equation are clarified for various conditions of lightweight.
4. The execution approaches of automotive lightweight include geometry structure optimization, reasonable application of advanced forming technologies and lightweight materials, or a superior integration of design, materials and advanced manufacture technologies. The relationship of performances of typical parts with properties of materials is important for the selection of lightweight materials and should be considered.
5. The life cycle equivalent analysis especially for energy consuming equivalent and CO₂ emission equivalent should be used as an evaluation parameter to evaluate the application of lightweight materials and advanced forming technologies, and it will provide a crucial foundation for lightweight design.

References

1. Mingtu M, Baorong W (2008) Physical and mechanical metallurgy of double phase steel, 2008 Metallurgy Industry Press (Second edition)
2. Mingtu M, Hongzhou L, Zhigang L (2008) Automotive lightweight and advanced forming technologies. *Mater Mach Eng* 32:5–9
3. Mingtu M, Jianren B (2004) Research progress of automotive lightweight materials. *New Mater Ind* 6:42–48
4. Jianren B (2006) High strength steel and car body, annual proceeding of China SAE, Oct 2006, pp 30–45
5. Liu SD (2003) Application of advanced high strength steels in ULSAB-AVC. Program symposium of seminar about automotive materials of China and USA, 2003
6. Bruno L, Markus P (2006) Functional design of a *Lightweight Body in White*—How to determine body in white materials according to structural requirements, Niobium microalloyed sheet steels for automotive applications edited by TMS (The Minerals, Metals and Materials Society), 2006, pp 24–42
7. Mohrbacher H (2006) Niobium microalloyed automotive sheet steel—A cost effective solution to the challenges of modern body engineering, Niobium microalloyed sheet steels for automotive applications edited by TMS (The Minerals, Metals and Materials Society), 2006, pp 1–23
8. Mingtu M (2007) Advanced automotive steels, chemical industry press, 2007, Beijing, pp 18–31

Author Biography

Mingtu Ma is currently a professor in China Automotive Engineering Research Institute, China. He graduated from Shanghai Jiaotong University in 1964, and received his PHD degree from China Steel & Iron Institute, in 1985. His research interests include lightweight materials and technology of automotive, semi-solid technology, testing technology and DP steel etc. He has published more than 200 papers and 7 composing in public.

Hongzhou Lu is currently an engineer in China Automotive Engineering Research Institute, China. He received his Master's degree from College of Materials Science and Engineering, Shanghai Jiaotong University, China. His research interests include lightweight materials of automotive, semi-solid technology, testing technology, and recycling of end-of-life automotive and plastic, etc. He has published more than 20 papers in public and 10 papers have been indexed by SCI.

Body Light Weight and Cost Control

Dazhou Guo

Abstract Body light weight is optimization design of body performance under body cost control, which is also a system engineering balanced body performance and body cost. Making the best of application of computer aided software for design and analysis, contrast body performance is sensitive to steel thickness, carry through light weight design and cost control, combine application these methods: body structure optimization included body joints optimization, major section improvement and features betterment; using more thin steel with higher strength as advanced high strength steel, ultra high strength steel, even press hardened steel; using new kind of light material as plastic, various alloy; applying new manufacture process as TRB, TWB, hot stamping etc. Controlling body cost through these methods such as, body structure boundary well adjusted in order to improve material utilization ratio, removing those overmuch strength structure, using low price material with equal performance. Applying computer aided software, carried through system design and analysis, balanced advantage and disadvantage of these methods, can we realize the aim of body light weight and cost control. Researching and discovering body light weight has sameness with body cost control, but there are also some differences, because both of their purpose and method are different. At present, costliness of those advanced light material with higher strength is the developing bottle neck for vehicle bodywork light weight and body cost control. Only when more cheap materials with high strength appear, can automobile company farther realize reducing body weight and low cost body.

F2012-E09-006

D. Guo (✉)
SAIC Motor Technical Center, Shanghai, 201804, China
e-mail: gdz_xy@126.com

Keywords Light weight • Cost control • Combine • Balance • Material utilization ratio

1 Introduction

1.1 Background

With the development of society economy, automobile is more popularly used, but both of using and manufacturing car will use up finite resource. Under influence of oil and goods' price, and more understand for sustainable development, people begin to pay attention to their life style. Light weight of car can reduce the consume of the resource, according to stat. Body weight is 25 % of vehicle's total weight, so body light weight is one of the most of partial. Consume of car is multi-demand market, general people like bargain, cost control is the key factor to the successful of a car. This chapter will mainly describe how to lighten body weight and cost control.

1.2 Understand to Body Light Weight and Cost Control

Is a light car unsafe? Is "safe" in people's traditional thoughts safe? In second *CAR 168 PK*, people PK about "does thickness of steel decide the passive safe of car", as a result, two-part people think car passive safe is depend on steel thickness. It open out most people also think those cars with thinner thickness and heavier weight are safe, certainly this body will maintain the whole body when crash occur, but can it protect passenger? Which kind of body is safe? Well-known passenger safety depend on cabin of passenger, system of restrain and energy-absorption area etc. only one of the factors cannot ensure passengers' safety. The safety mainly consist protecting passenger, but not injured of car. The heaviest car have small injure while impact occur, but passenger injured extent depend on energy-absorption body design and passive configure, such as, optimization of body structure and force load transfer road, improve safety meanwhile reduce aggress to opponent. Cost control is a key factor, body cost consist of cost of purchase part, cost of production and investment for mould, jig, fixture and cubing etc. Price of a part depend on part weight and material utilization ratio.

There are certain differences between light weight and cost control for bodywork. Light weight is for the purpose of light body weight, not all of which can reduce cost of body, such as applying some unpopular material in body, weight is light, but cost has increased. Body cost control is for the purpose of reducing part cost and invests, not all of which can also light body weight, but carry over mature vehicle some part or component can save some invests while maintain the vehicle weight.

Light weight is different from jerry-build. Here light certainly is not some auto factory action which is jerry-build for profit neglect consumer benefit. The right way is to strengthen the place where is needed and weaken the place where is unimportant. Doing just right, mean how to light weight and reduce cost under maintain body safe performance, which is customer value maximization. The best structure should be:

$$\text{Customer value maximization} = \frac{\text{Performance}}{\text{Weight} \times \text{Cost}}$$

2 How to Light Weight and Cost Control for Bodywork

In general the methodology of body light weight is continually optimizing series of body part or component with light weight and cost control under ensure the variety performance of body. Designing and analysing through computer aided software is the basic method and tool, which do not need productive cost. Repeating to analyse variety of design case, can we get the best scheme. Light index is related with the three factors: M_{biw} -weight of body, C_t -torsion static stiffness of body, A -body projection area mean the product (Wheelbase \times Tread). After engineers' study the engineer find out the relationship as below: [4]

$$L = \frac{M_{biw}}{C_t \times A} \times 10^3$$

Body light weight is a complex system engineering activity. Only combine these methods as below, balance their advantage and disadvantage, can we really lighten body weight and control body cost. For a auto company, the greater the yield it is, the lower the cost will be.

2.1 Improve Steel Performance Reduce Steel Gauge

Applying those thinner steel with higher strength is currently popularly light weight method. Such as Press Hardened Steel (PHS), Ultra high strength steel (CP, MS), Advanced high strength steel (DP, TRIP), High strength steel (BH, HSIF, HSLA), as shown in Fig. 1 steels characteristic. Steel still have their advantages such as: cheap, mature process compared with alloy or macromolecule materials, so far, steel is also the most used material on body by right of steel high strength.

In 1990s, 35 steel companies worked together and finished "ULSAB-Ultrav Light Steel Auto Body research", which indicate 90 % of body steel using high strength steel with mature and mass production, body weight can be lighted 25 % of body self weight (sedan car) without cost increase, and torsion stiffness has

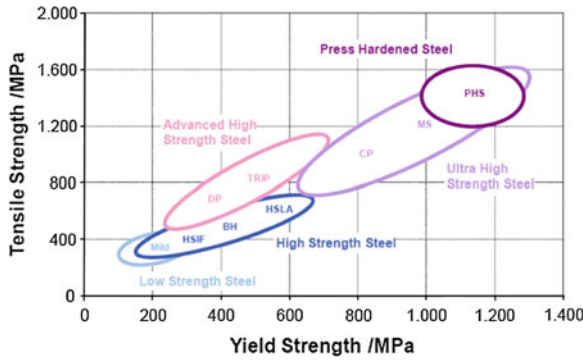


Fig. 1 Variety of steel characteristic

Table 1 Statistic body steel use instance from 2011ECB

Material (Steel)	Percentage (%)				
	Audi A6	BMW 1	Hyundai I40	Ford focus	Mazda CX5
Low strength	29.1	28	35.6	43.6	43
High strength	28.2	53	23.2	29.7	40
Advanced high strength	13.1	13	28.5	14.9	14
Ultra high strength	0	0	6.1	4.8	0
Press hardened	11.3	2	3.1	7	3

increased 80 %, bending stiffness increased 52 %, 1st mode of body increased 58 %, fulfil all requirement of impact rule and law. But this is only a study, it has not so widely applied high strength steel in body.

2011 European Car Body statistic indicated: so far low steel use ratio in high brand car body (Audi, BMW) is only 30 %, compared with 40 % of other brand car body, there is evident difference. High steel ratio is 68 % for BMW 1 Series, sum of high strength steel and alloy is 70 % for Audi A6. Hyundai I40 high strength steel ratio is 60.9 %,so body steel use higher and higher strength steel and more strength steel. As shown in Table 1, some automobile companies body steel use instance.

2.2 Alloy

Applying variety of alloy can lighten body weight but its price is bottleneck. As to passenger vehicle, static in 1973 alloy weight ratio in car all material is 5, 5.6 % in 1980, is 9.6 % in 1997. Variety of alloy is one of the lightest materials, which include aluminium alloy, magnesium alloy, and titanium alloy. Aluminium density is 2.7 g/cm³, about the third of steel density, mostly-used alloy material. Aluminium alloy mainly include cast aluminium, sheet aluminium and extrusion

aluminium. Magnesium alloy density is 1.8 g/cm^3 , also is the lightest metal. Titanium density is 4.51 g/cm^3 . Titanium's price is very expensive, so it's rarely used [2].

2.3 Plastic

The biggest advantage of plastic is light. Density of general plastic is only $0.9\text{--}1.5 \text{ g/cm}^3$, a more lighter material compared with metal density, so plastic is first selection light material for body light weight. So far plastic dosage exceed 120 kg per vehicle in some foreign automobile company, plastic dosage also exceed 90/vehicle in some domestic automobile companies. From some structure part inside to some panel outer side, plastic is more applied in vehicle, nowadays in developed country people regard plastic dosage as the symbol of design level and manufacture level. In Germany, average plastic dosage is nearly 300 kg, which occupy 20 % of vehicle weight. In China, average plastic dosage is only 78 kg. There is a big gap. Conventional plastics include: Polypropylene, polyurethane, PVC, Thermoset composites, ABS, nylon and polyethylene. Polypropylene has been mostly used in the last two years, and its growth rate is at 2.2–2.8 % per year. Estimate average plastic dosage reach 500 kg/vehicle by 2020 in developed country. Plastics range of applications in the automotive plastics is from mounted part outward to the interior parts, body and structure expansion. Focus on the development direction of the development of structural parts, exterior parts with reinforced plastic composites, high-performance resins and plastics and recyclability of the materials will be highly concerned.

2.4 Structural Optimization Design

Optimized body structure design contains the body joint optimization, major or minor section optimization and optimization feature of the body, the three different methods lead to the same destination, they are very important methods for body lightweight design and cost control.

2.4.1 Joint Optimization

The joint is the important position of the body structure, and it's very important for the global or local stiffness and mode. Joint can be understood that simple cross position of pillar and cantrail or the root of a cantilever. Only the good joint, pillar (cantrail) can play a role. There are nine big important joints on body in white without closures as Fig. 2: joint A consist of A pillar upper, front cross member of roof and cantrail front; B joint consist of B-pillar and cantrail; C joint consisted of sill and B pillar etc. [1].

Fig. 2 Joints of BIW

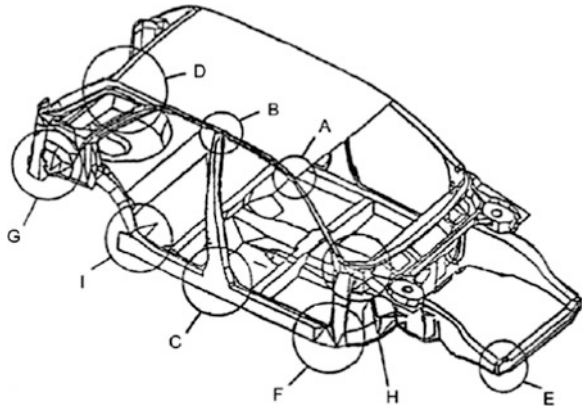
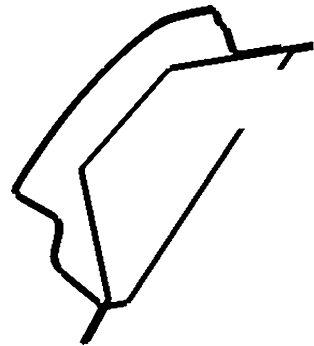


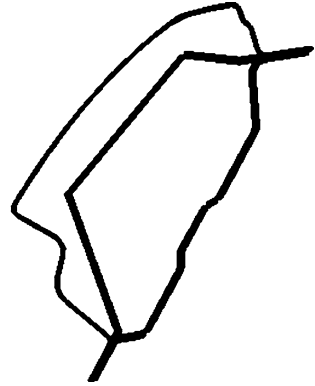
Fig. 3 Original section



There are also many minor joints on body besides major joints mentioned above, such as: joints on the four corners of shelf in sedan, joint consisted of cantrail and cross member of roof. The rootstalk of all cantilever is a minor joint, which is valuable to think about when body design. Firstly joints should be strong, then thinning cantrail or pillar which include reduce material gauge and cutout hole, meanwhile we can add or adjust muscles along the direction force load on part.

2.4.2 Optimization of Major or Minor Section

Section is a very important technique during body design, which is a simple engineering language. For example, section at cantrail (roof ditch), Fig. 3 is an original section, Fig. 4 is an optimized section. As to Fig. 3, the structure is big, heavy and high cost because the boundary is so big, otherwise as to Fig. 4, the structure is light and low cost but it can improve the body performance. Whether a structure is good or not, whether a structure is light or not, whether a structure

Fig. 4 Optimized section

material utilization ratio is high or low, all of them is depended on the shape and size of the section. Meanwhile body performance depends on the size of the section shapes and sizes, such as body mode, stiffness, durability etc.

2.4.3 Optimization Feature of Body

In general, the characteristic optimization is to increase local or resize the stiffener rib to achieve improvement of body stiffness or intensity with same material thickness. A good structure designing should be structural optimization design based on the path of force transfer. Applying Finite Element Method Analysis to optimize the structure of various options over and over again, we can find out how body structure stress distribute and where stress concentration area it is, bold open weight-cutout, and optimize the structure up to lightweight and cost control [3].

2.5 New Advanced Manufacturing Technology

Now new advanced manufacturing processes include Hot Stamping, Rolling, TWB (Tailor Welding Blank) and TRB (Tailor Rolled Blank), TWB appeared before TRB. Hot stamping generally used in A Pillar, B Pillar, Sill collision key area etc., but it's expensive. If general cost lower, hot stamping is also a good method. Rolling is a more appropriate method for threshold equal section part etc.

2.5.1 Application of TWB

TWB is integrating more than two sheets of steel together before form, usually the sheets which consisted of variety of equal or different thickness, yield or tensile strength, surface coating is welded together by laser welding process. TWB can reduce the number of part and the overlap of welding flange, light the weight of

Fig. 5 Example of TWB

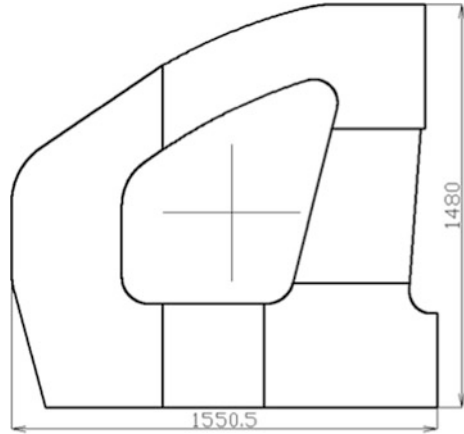
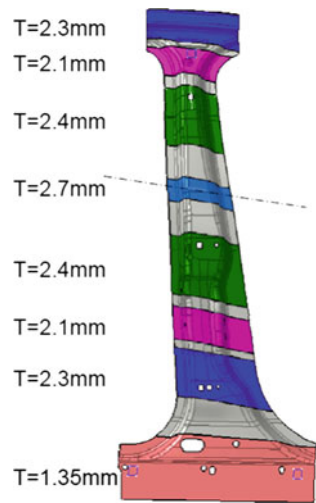


Fig. 6 Distribute of thickness

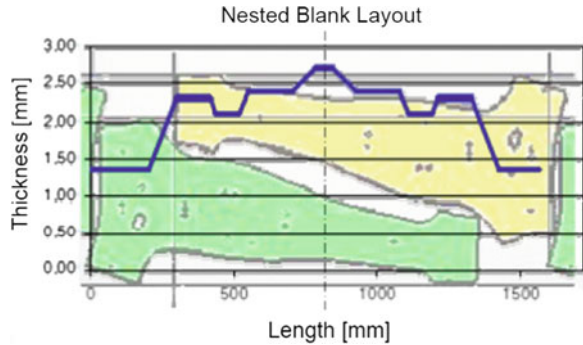


component, and improve body performance as a whole part with different strength property. Now some auto companies have began to apply TWB widely. According to the different need of different area of body, integrating several sheets together can significantly improve material utilization, effectively reducing the cost of parts and materials. As Fig. 5: five parts integrated into a big single part, which can save original welding flange and lighten the body weight.

2.5.2 Application of TRB

TRB is a kind of plate which has different thickness, sheet of steel has been rolled to a sheet with different thickness. TRB is a new technique which has been used widely, appeared after TWB. It means thickening where need strengthen, otherwise

Fig. 7 Layout of blank



reduce the thickness, such as applying TRB technique in Reinforcement B Pillar, which meet body performance, meanwhile light body weight. If this material is in mass production, it will certainly reduce the body cost. The following Fig. 6 shows the distribute of thickness of Reinforcement B pillar, Fig. 7 show the layout of blank, use TRB method can meet the performance requirements for body and achieve body light weight and cost control.

3 Summary

More and more auto companies pay attention to body light weight and cost control, which decided their competitive capacity. Body light weight and cost control are the Integration of multiple methods which are optimizing body structure, application of high strength steel and new light material, new advanced manufacture process. Only the light material is mass production and large output of the vehicle, can people buy a light car with high performance but cheap in the future.

References

1. Ling FF (2011) The automotive body (Volume I: Components Design) [M]. ISSN 0941-5122
2. Robert J (2000) Automotive handbook, 5th edn. [M]. Federal Republic of Germany, ISBN 7-5640-0209-3
3. Gu Zhengqi. "JIAOCHE CHESHEN" [M]. People's traffic Press, 2002, ISBN 7-114-04361-9
4. Niu Shengfu, Li Wei, "Lightweight technology of car body" [J]. SHANGHAI AUTO, 2009(9)

Lightweight Design and Formability Analysis of Auto Body Aluminum Trunk Lid

Zhao Liu, Ping Zhu and Xiaojing Zhu

Abstract Aluminum-alloy achieves more application in automobile industry as a kind of lightweight material. Auto body structures experience complex loads and performance requirements differ greatly among these conditions. In order to integrate all mechanical properties into initial design of Aluminum-alloy structure, a new optimization method is provided. With the prototype of a steel trunk lid, a new design based on original structure space using material replacement, structure optimizing and formability validation method is put forward. New Aluminum-alloy trunk lid matches both the performance and manufacturability requirement with weight reduction of 41.6 %. This method provides a referable way for lightweight design of aluminum-alloy trunk lid in initial design phase.

Keywords Automotive engineering · lightweight · Aluminum-alloy · FEM · Formability

1 Introductions

With the seriously increasing of world's energy shortage and environmental pollution, the people's environmental awareness is continuously improved and therefore the requirement of energy conservation and emission reduction become higher and higher. According to statistics, fuel consumption can be reduced by 6 to

F2012-E09-007

Z. Liu (✉) · P. Zhu · X. Zhu
Shanghai Jiao Tong University, Shanghai, China

8 % with every 10 % weight loss of cars [1], and as an effective way of energy conservation and emission reduction, lightweight is received more and more attention [2, 3]. There are two methods to achieve car's lightweight design: designing a more rational structure to avoid redundant location of the material distribution; using light material, such as aluminum alloy, magnesium alloy, engineering materials, composite materials, etc. or high strength steel instead of ordinary low-carbon steel to improve performance and reduce weight. The car's lightweight design is to reduce weight to the maximum extent under the premise of ensuring the structural performance and manufacturing cost [4, 5].

The trunk lid is the typical covering parts located in the back of the car body, the existing trunk lid design is often repair the original structure's problems and can not play the real role to guide design [6]. There still has difficult to analyze the most prominent problems of trunk lid, stiffness and dent resistance, at the preliminary design stage.

In order to solve the above problems, the method structural optimization with performance evaluation was used in the dissertation. Make one car's trunk lid as the object of study, and structural optimization with new aluminum material replaced were used to arrange the core area based on the original structure of space layout, and to achieve weight loss on the basis of specified performance; one-step forming method was used to analyze manufacturability of the newly structural aluminum trunk lid. The article provides a lightweight design method for the initial design phase of the trunk lid.

2 The Optimization Method of Trunk Lid

Three elements of optimal design: design objects, design constraints and design objective. Therefore, we must firstly determine the design of the three elements at the beginning of the trunk lid optimization program. Among them, the design constraints and objectives are often determined according to the corporation's requirements or experience. Because the design proposal needs to satisfy the boundary conditions of the original trunk lid, which means the spatial relationship with other parts cannot be changed, the optimization procedure should only be in the space within the scope of the original structure.

2.1 The Design Objective and Requirements of the Trunk Lid

The trunk lid design requirements of the stiffness and dent resistance are as follows:

1. The shear stiffness requirements: the connection bolt holes between the hinge and white body must be fully constrained, and also the support rod. Load along

the Y direction at the middle corner point of the trunk lid, and maximum deformation value must be less than 3.0 mm, and permanent deformation must be less than 1.0 mm.

2. The hinge and white body must be fully constrained, and also the support rod. Load along the closing direction at the right corner point of the trunk lid, and permanent deformation must be less than 1.0 mm.
3. The dent resistance requirements: the trunk lid should be closed, the connection bolt holes between the hinge and white body must be fully constrained, and also the sealing joint strip and the support bar's hole. The third degree of freedom of the buckle should be constrained. The weakest position of the trunk lid should be chosen to load vertical loading by probe at the outer plate surface, and permanent deformation must be less than 0.15 mm.

2.2 The Stiffness Performance Evaluation of the Original Trunk Lid

Because aluminum-alloy luggage still need to assemble in the original space, the performance of original structure should be evaluated firstly, and then the optimization design of the new structure is conducted on the basis of the original spatial layout.

1. Establish of the stiffness analysis FEM.

Trunk lid contains three parts including the inner plate, outer plate and reinforcing plate. Because of the different materials collocation, the connection between the inside and outside plate dissimilates. For steel structures, wrapping and welding technologies are mainly used. The embossment frame edge located at the middle area of the inner and outer plate connects with the outer plate through adhesive, and the reinforcing plate connects with the inner and outer plate by the welding spot or bolts.

The material of the original trunk lid is steel. When build model, the inner and outer plate and the reinforcing plate use shell element; the wrapping thickness is set to two layers of outer plate and a layer of inner plate, and shell elements are used to connect with the outer and inner plate by conode. The welding spot use the element spot weld; Solid element is used to model the structural adhesive, and connect with the corresponding nodes of outer and inner plate. The finite element model shows as Fig. 1, and the specification of the shell element is 5 mm, and the total number is 99072 in which the amount of triangular element is 3855 accounting for 3.9 %, and there are 41 spot welds. Build material model depending on the material information of component. A multi-linear elastic-plastic constitutive equation is used to model the inner, outer and reinforcing plate, and linear elastic constitutive equation is used to simulate structural adhesive. The two stiffness working conditions are shown as Fig. 2.

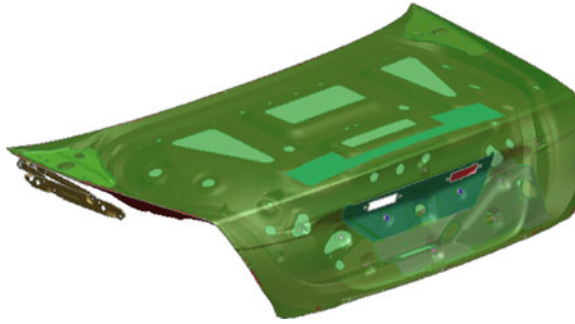


Fig. 1 The original trunk lid finite element model

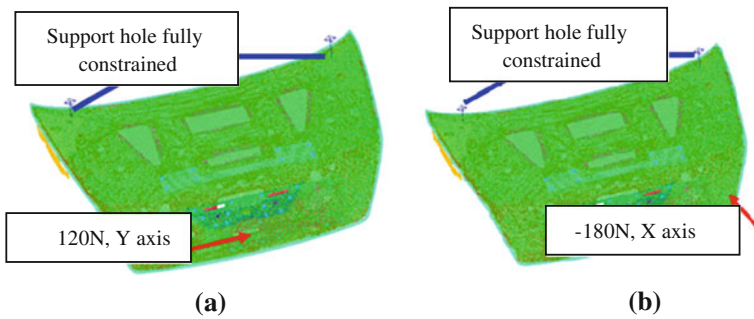


Fig. 2 The stiffness analysis simulation conditions of trunk lid a shearing condition b bending condition

2. Analysis of permanent deformation based on the Ls-Dyna implicit algorithm

The research uses the Ls-Dyna implicit algorithm for nonlinear solution in consideration of the local large deformation and the difficult to guarantee astringency during the loading procedure of the stiffness and dent resistance.

The kinetic equation of the system can be expressed as:

$$M\ddot{x}(t) + F(x, \dot{x}) - P(x, t) = 0 \tag{1}$$

Among the equation, x , \dot{x} and \ddot{x} , are displacement, velocity and acceleration vectors; M is the mass matrix; F stands for the internal force vector; P is on behalf of the resultant vector of physical force and external force; for elastic system:

$$F(x, \dot{x}) = Cx + K\Delta x \tag{2}$$

The C and K are the damping and stiffness matrix; no matter the implicit integral or the explicit integral, the residual vector is defined as:

$$Q = M\ddot{x} + f - p = 0 \tag{3}$$

For the implicit solver, the residual vector Q is an implicit function of x^{n+1} , and meets the following formula:

$$Q(x^{n+1}) = 0 \quad (4)$$

Use x_k^{n+1} to approximate x^{n+1} , which is $Q(x_k^{n+1})$ to approximate $Q(x^{n+1})$, $k = 1, 2, 3, \dots$. Expand the equation linear approximation at the neighborhood of $Q(x_k^{n+1})$, and can be expressed as:

$$Q(x_k^{n+1}) = Q(x_{k-1}^{n+1}) + J(x_{k-1}^{n+1})\Delta x_k \quad (5)$$

Its Jacobian matrix can be written as:

$$J = M \frac{\partial \ddot{x}}{\partial x} + \frac{\partial F}{\partial \dot{x}} \frac{\partial \dot{x}}{\partial x} + \frac{\partial F}{\partial x} - \frac{\partial P}{\partial x} = M \frac{\partial \ddot{x}}{\partial x} + C \frac{\partial \dot{x}}{\partial x} + K_t - \frac{\partial P}{\partial x} \quad (6)$$

The $C = \frac{\partial F}{\partial \dot{x}}$ is the tangential damping matrix, the $K_t = \frac{\partial F}{\partial x}$ is the tangential stiffness matrix.

Iterative solution:

$$x_k^{n+1} = x_{k-1}^{n+1} + \Delta x_k \quad (7)$$

$$J(x_{k-1}^{n+1}) = \left. \frac{\partial Q}{\partial x} \right|_{x_{k-1}^{n+1}} \quad (8)$$

The solution with load increment n is known, and to solve the solution with the incremental $n + 1$, using the following linear equation:

$$K_t \Delta u_0 = P(x^n)^{n+1} - F(x^n) \quad (9)$$

The Δu_0 is the expectation increment of displacement; the $P(x^n)^{n+1}$ is external load vector based on the location $n + 1$ of the geometry at the moment n ; the $F(x^n)$ is the divergence vector of the moment n . Displacement vector is updated as follows:

$$x_1^{n+1} = x^n + s_0 \Delta u_0 \quad (10)$$

The s_0 is the search factor between 0 and 1 for linear search.

Then start equilibrium iteration calculation:

$$K_{t_i} \Delta u_i = P(x_i^{n+1})^{n+1} - F(x_i^{n+1}) = Q_i^{n+1} \quad (11)$$

The subscript i represents the number of iterations. Convergence would be checked after every iteration, and define a small quantity ε as the convergence factor; Convergence is achieved if one of the following two conditions are satisfied.

$$\frac{\|\Delta u_i\|}{u_{\text{Max}}} < \varepsilon \quad (12)$$

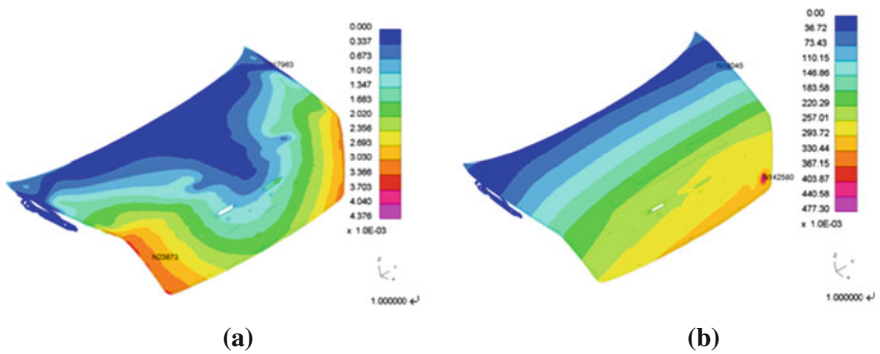


Fig. 3 The stiffness analysis results of the original steel trunk lid **a** shearing deformation (mm) **b** bending deformation (mm)

$$\frac{|\Delta u_i^t Q_i|}{\Delta u_0^t Q_0} < \varepsilon \tag{13}$$

If convergence is not reached, the displacement vector updated; when at the *i*th updating, the displacement vector is updated to:

$$x_{i+1}^{n+1} = x_i^{n+1} + s_i \Delta u_i \tag{14}$$

And go for a new iteration. If there is no convergence in the allowed number of iterations, or there appear:

$$\|Q^{n+1}\| < \|Q_{i+1}^{n+1}\| \tag{15}$$

The K_t is recalculated by the program. When the number of updates reaches a set value, the calculation terminates.

The load increases from 0 to the required value and then unload during the simulation, and keeping a period of time after unload to 0 ensure that the elastic deformation completely eliminate, calculating the final permanent deformation. The simulation results are shown in Fig. 3, and the deformation results are shown in Table 1. It can be seen that the stiffness properties of the original steel trunk lid meets the design needs, and the performance of the original trunk lid can be used as the reference to the design of the new one.

2.3 The Selection of Aluminum-Alloy Material

Comparing with traditional steel, The advantage of aluminum alloy is obvious: a higher specific strength (strength/density); the ability to absorb impact is twice that of steel; high recycling rates [7].

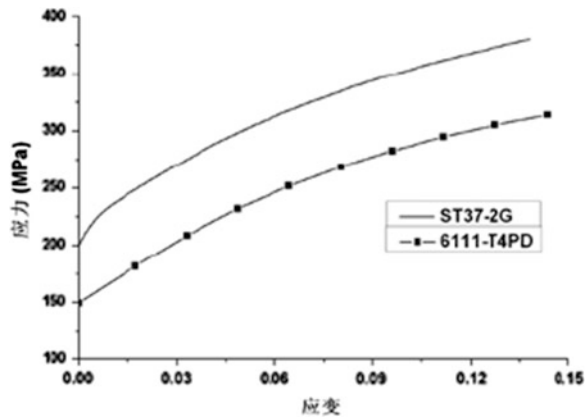
Table 1 The stiffness analysis results of the original steel trunk lid

	Shearing condition	Bending condition
Design requirements	Maximum deformation value <3.0 mm Permanent deformation value <1 mm	Permanent deformation value <1.0 mm
Results	Maximum deformation value is 0.442 mm Permanent deformation value is 0.0044 mm	Permanent deformation value is 0.477 mm

Table 2 The basic mechanical properties of 6111-T4PD aluminum-alloy

Material name	Modulus of elasticity (MPa)	Poisson’s ratio	Density (Kg/m ³)	Yield strength (MPa)
6111-T4PD	69,000	0.3	2,890	149.52
	Tensile strength (MPa)	Uniform elongation	Breaking elongation	work hardening coefficient
	290	18 %	25 %	0.23

Fig. 4 The effective stress–strain curve of 6111-T4PD aluminum-alloy



In order to ensure the stiffness and stamping performance of trunk lid, material must has the strength and ductility property, and 6111-T4PD type aluminum-alloy is chosen here. The basic mechanical properties of the materials are shown in Table 2, and the effective stress–strain curve is shown in Fig. 4. It can be seen that the stress–strain curve of the 6111-T4PD aluminum-alloy is just like the ST37-2G steel of the original structure, having a low yield ratio, and uniform elongation and breaking elongation rate can reach a higher level, so the formability is preferable; The yield strength of aluminum-alloy is close to 150 MPa and reach the level of the ordinary carbon steel; The 6111-T4PD aluminum-alloy has good strength and ductility.

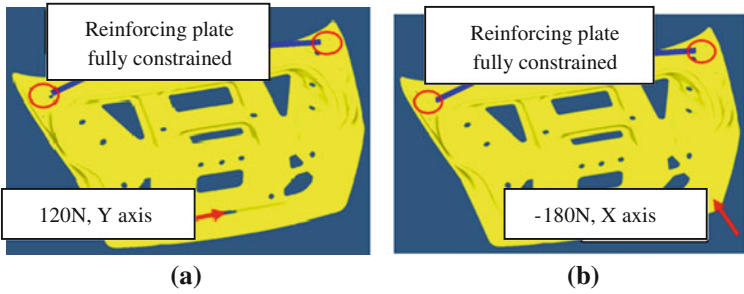


Fig. 5 The evaluation boundary conditions of the steel inner plate **a** shearing condition **b** bending condition

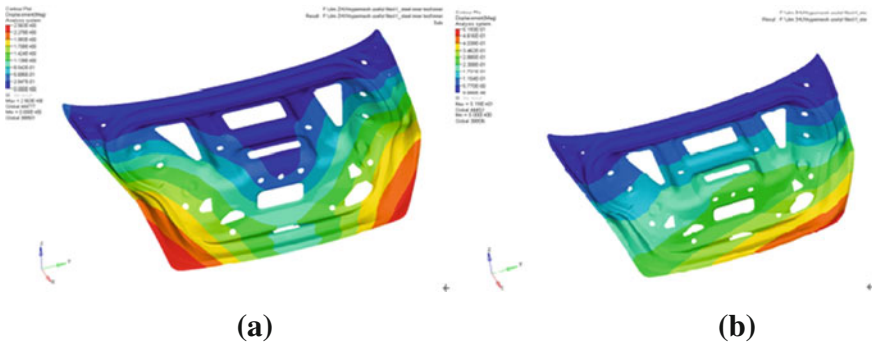


Fig. 6 The deformation contour of steel inner plate **a** shearing condition **b** bending condition

2.4 The Optimization Design of the Aluminum-Alloy Trunk Lid

Because of the functional differences between the inside and outside the plate, the main properties of the trunk lid is decided by the inner plate. Firstly, the topology optimization method is used to delete material, and then the topography optimization method is used to determine the board's reasonable location for reinforcing rib to guarantee the overall performance. The original structure can ensure the design requirements, so the inner plate performance of steel trunk lid will be evaluated at first, and then the performance will be the optimized design constraints to guide the inner plate of the aluminum trunk lid design.

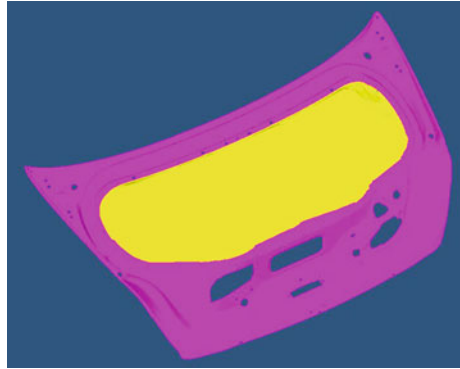
1. The performance evaluation of the steel trunk lid's inner plate

The constraint conditions remain as lateral load and bending condition. Loading conditions are shown in Fig. 5; the static analysis is used for structural elastic

Table 3 The deformation of the steel inner plate on two design conditions

	Shearing condition	Bending condition
Maximum deformation (mm)	2.56	51.9

Fig. 7 The optimization area of the inner plate



deformation, and the elastic deformation will be the design objective of the optimization program. The deformation cloud is shown in Fig. 6, and the result is in Table 3.

2. The optimization program of the aluminum trunk lid’s inner plate

Fill the center blank part of the original trunk’s inner plate, and remove the reinforcing ribs, where is set to be the new design area, shown as Fig. 7 which the yellow area is the target design area. Material is replaced by aluminum alloy. The thickness of the inner board is set to 1.0 mm, because of the different properties between the steel and aluminum and weight loss requirements of the optimization, meanwhile, in order to avoid the huge difference between the real performance and the design objective at initial iteration.

During the topology optimization, the optimization constraints are defined as: the maximum deformation of lateral bending should be less than 2.5 mm and bending should be less than 50 mm; design goals: minimum quality. The optimization result is shown in Fig. 8.

Conduct topography optimization for the model. Because one of the bosses locates in the bending area and has a great influence on manufacturability, the result is omitted. Final optimization proposal is shown in Fig. 9.

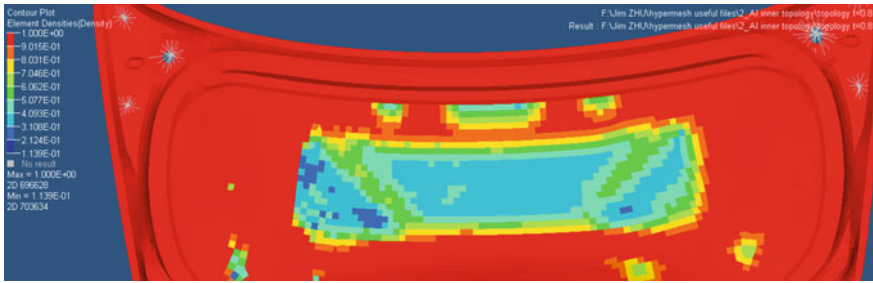


Fig. 8 The topology result of the inner plate

Fig. 9 The final optimization proposal



3 Verification of the Aluminum-Alloy Trunk Lid's Optimization Proposal

3.1 Stiffness Verification of the Aluminum-Alloy Trunk Lid

Calculate the deformation of the structure in shear and bending conditions separately, the same as the steel trunk lid. The results are shown in Fig. 10.

Table 4 is the deformation situations and design requirements of two conditions and the comparison between the steel and aluminum trunk lid about deformation. It can be seen that lightweight design of aluminum alloy trunk lid satisfies the stiffness requirements.

3.2 Dent Resistance Verification of Aluminum-Alloy Trunk Lid

Find the worst dent resistance location of the outer plate, according to the optimization results of the aluminum-alloy trunk lid. It's located in the center of the inner plate's convex part. Vertical load is imposed above the outer plate of the position. In order to match the probe size, and increase local flexibility, the place

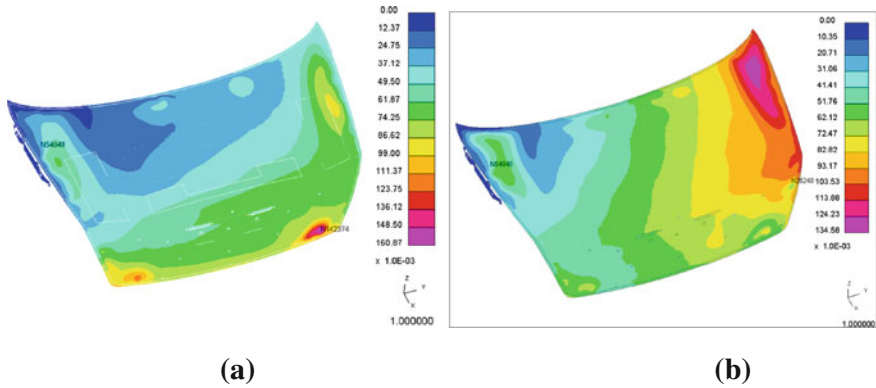


Fig. 10 Stiffness verification result of Aluminum trunk lid **a** shearing **b** bending

Table 4 Stiffness performance of aluminum trunk lid

	Design requirements		Stiffness performance of aluminum trunk lid		Stiffness performance of steel trunk lid	
	Permanent deformation (mm)	Maximum deformation (mm)	Permanent deformation (mm)	Maximum deformation (mm)	Permanent deformation (mm)	Maximum deformation (mm)
shearing	<1	<3	0.161	0.413	0.004	0.442
bending	<1		0.135		0.477	

for loading should be locally refined; the mesh size changes from 5 mm of the periphery to 2.5 mm of the middle, and then 1.25 mm of the central location.

To calculate the permanent deformation of the trunk lid uses implicit calculation method of DYNA after being loaded, and the simulation result is shown in Fig 11, and Table 5 shows the contrast of simulation result and dent resistance requirements. It can be seen the dent resistance of the aluminum trunk lid satisfies the requirements.

3.3 General Evaluation of the Aluminum-Alloy Trunk Lid's Optimization Proposal

In order to ensure the optimization design of the aluminum trunk lid to satisfy the needs of the stiffness and dent resistance, firstly, make the stiffness property of the original steel trunk lid as the reference, and proceed topology optimization of the aluminum trunk lid and ensure the performance of the inner plate at the same time; the shape of the surrounding area should not be changed; reasonable

Fig. 11 The simulation deformation contour of aluminum trunk lid's dent resistance

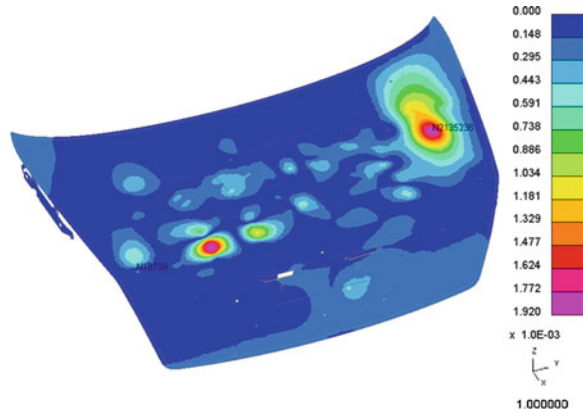


Table 5 The simulation result of aluminum trunk lid's dent resistance

Design requirement	Real permanent deformation
<0.15 mm	0.002 mm

thickness of internal and external plate is selected to verify the stiffness and dent resistance of the trunk lid.

The 6111-T4PD Aluminum alloy is selected in the optimization program, and the thickness of the outer plate is 1.1 mm, and the inner plate is 1.0 mm; the thickness of the reinforcing plate are 1.5 and 1.0 mm. The connections type: The edge of inner and outer plate use the flanging connection; the middle of inner and outer plate use the adhesive connection; the reinforcing plate connects to the inner and outer plate by welding spot.

The validation results show that the stiffness and dent resistance of the aluminum trunk lid satisfy the design requirements, and performance indicators are shown in Table 6. Trunk lid assembly, including inner and outer plate, flanging, and reinforcing plate, lose weight 5.92 kg, and weight loss ratio is 41.6 %; the inner plate lose weight 2.20 kg, and weight loss ratio is 44.3 %,which match the weight reduction requirements. So the optimization proposal of the trunk lid is feasible.

4 The Manufacturability Analysis of Aluminum Trunk Lid

Sheet metal forming is a complex process of plastic strain, and has geometry, material and contact nonlinear characteristics, and the incremental method is usually used for formability simulation. But the mould information needed for the incremental method often cannot be determined in the initial design phase, and the simulation time is long, while repeatedly modifying the parameters is needed for

Table 6 The stiffness and dent resistance performance of aluminum trunk lid

	Design requirement		The stiffness performance of steel trunk lid		The stiffness performance of aluminum trunk lid	
	Permanent deformation (mm)	Maximum deformation (mm)	Permanent deformation (mm)	Maximum deformation (mm)	Permanent deformation (mm)	Maximum deformation (mm)
	Shearing	<1	<3	0.004	0.442	0.161
Bending	<1		0.477		0.135	
Dent resistance	<0.15				0.002	

double counting; therefore, the one step forming is used for the initial design phase.

The one-step method bases on the total theory of plasticity. Assumed that the sheet metal forming process loads in proportion, and establish the relationship between the initial and final shape of the sheet; it can quickly calculate the stress–strain and the information of thickness distribution of the parts during the forming process to predict possible forming defects [8].

According to the principle of virtual work, known the initial and final shape of the sheet, and ignoring the intermediate state and the configuration change, the following relationship can be got:

$$\sum W_{in}^e - \sum W_{out}^e = \sum \left| \int_V \{\varepsilon^e\}^T \{\sigma\} - \int_A \{u^e\}^T \{f\} \right| = 0 \quad (16)$$

W_{in}^e is the element's internal forces of virtual work and W_{out}^e is the external force of virtual work; $\{\varepsilon^e\}$ is the virtual displacement and $\{u^e\}$ is the virtual strain vector; $\{\sigma\}$ and $\{f\}$ are the internal and external force vector respectively.

$$\text{Finite element equation for forming : } \{k\} \cdot \{u\} = \{P\} \quad (17)$$

$\{k\}$ is the stiffness matrix; $\{u\}$ is the displacement vector; $\{P\}$ is the external force vector.

Because the stiffness matrix and external force vector are the functions of displacement $\{u\}$, the Newton–Raphson method is need for the iterative solution, and when at the i times, the iteration equation can be expressed as:

$$\{k_T^i(u^i)\} \times \{\Delta u^i\} = \{P(u^i)\} \{u^{i+1}\} = \{u^i\} + \omega \{\Delta u^i\} \quad (18)$$

ω is the relaxation factor for the iteration; $\{k_T^i(u^i)\}$ is the tangent stiffness matrix for the i -th iteration; $\{\Delta u^i\}$ is the displacement increment of the i th; $\{P(u^i)\}$ is the external force vector of the current increment step.

The tangent stiffness matrix in global coordinates can be written as:

$$\{k_T^i(u^i)\} = \left[\frac{\delta P(u)}{\delta u} \right]_{u=u^i} \quad (19)$$

One-step formability simulation is used for the trunk lid inner plate's finite element mode. According to the manufacturing process of the inner plate, the blank holder area is set to the four edges; Adjust the direction of the inner plate for forming calculation; Set the coefficient of friction between the sheet and the mould, and adjust the blank holder force in order to obtain better formability.

Conduct one step forming for the performance analysis of the trunk lid's inner plate, and the results are shown in Fig. 12. From the figure, there is no trend of cracking during sheet metal forming, but more wrinkling defects (shown in purple),

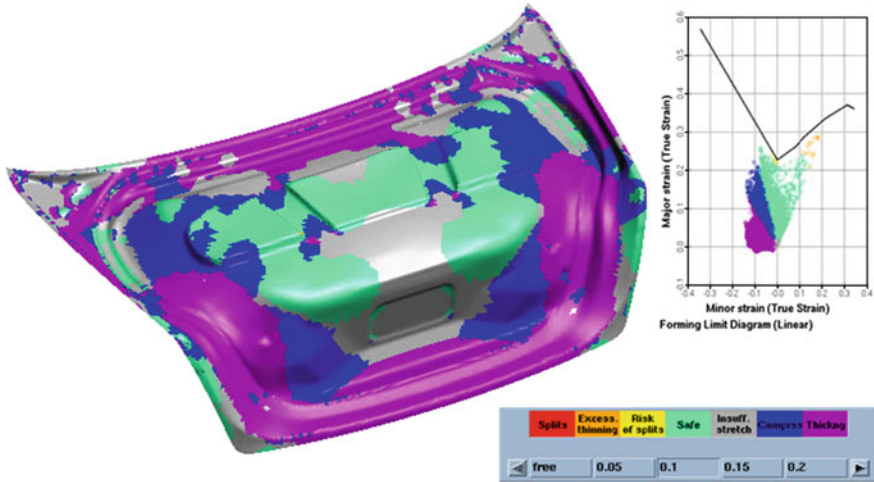


Fig. 12 Forming analysis chart of trunk lid' inner plate

and the wrinkling defects should be emphasisly concerned during stamping. These can be improved by adjusting the local blank holder force and changing the shape of the ribs; if you need to determine the formability of the specific location, mould design is needed when the process dimension is decided at detail design stage, and incremental method is used to conduct a detailed analysis.

5 Conclusions

Comprehensive consideration of the spatial layout, complex conditions and forming processes and other factors at the initial design of aluminum structures can effectively ensure performance of product, reduce design cycle time and manufacturing costs. The dissertation provides a reference method to achieve weight loss 41.6 % and at the same time ensure the mechanical properties and manufacturability of the trunk lid.

References

1. Benedict JC (2000) Light metals in automotive applications. [J] Light Metal Age 10(1):34–35
2. Merklein M (2002) New materials and production technologies for innovative lightweight construction. [J] J Mater Process Technol 125–126:532–536
3. Tamaki Y (1999) Research into achieving a lightweight vehicle body utilizing structure optimizing analysis:Aim for a lightweight and high and rigid vehicle body. [J] JSAE Rev 20(4):558–561

4. Jing-yu L, Shao-zeng W, Hong-min C (2008) Optimal design of heavy truck suspension[J]. J Chang'an University (Natural Science Edition), 8(5):103–106
5. Hong Z, Mao-hong Y (2002) Optimized design of steel frame structure using a genetic algorithm[J]. Journal of Chang'an University(Natural Science Edition), 22(5):65–67
6. Yu Z, Ping Z, Guan-long C, Zhong-qin L (2006) The lightweight design of bonnet in auto-body based on finite element method[J]. J Shanghai Jiaotong University, 2006, 40(1):163–166
7. Jun L (2008) Aluminum lighten weight material used in Automobile[J]. Automobile Technol Mater 2:8–10
8. Ke-su L, Quan-kun L, Liang M, Jun W (2009) Simulative analysis and optimization of formability of automotive b-pillar reinforced panel[J]. Automobile Technol 6:59–61

Geometric Parameters Optimal Design of Variable Cross-Section Rim

Hongyu Wang

Abstract In order to achieve the wheels lightweight design, the optimization software Isight integrated with SolidWorks and Abaqus. The parametric three-dimensional model of the rim section is built based on SolidWorks, the finite element method is used to analyze stress and displacement distributions in a variable cross-section rim subject to the conjoint influence of radial load and inflation pressure. The optimization methods which combined multi-island genetic algorithm (MIGA) with NLPQL algorithm is used for exploration. By adjusting control parameters of the rim shape quality is optimized. The results show that the optimization effect is good.

Keywords Variable cross-section rim · Lightweight · Parametric modeling · Finite element method · Optimal design

1 Introduction

Automobile Wheels are rotating parts between the tires and axle, which are important safety components in the vehicle driving system, plays a significant role in bearing, steering, driving and braking. Studies have shown that the energy saving effect of automobile rotating parts lightweight is equivalent to 1.2–1.3 times that of non-rotating parts. The equal strength design of wheels is an important way to achieve the wheels lightweight. The equal strength rim's thickness varies

F2012-E09-009

H. Wang (✉)
Beijing University of Aeronautics and Astronautics, Beijing, China
e-mail: wanghy.cool@yahoo.com.cn

according to the load size rim cross-section suffered, after a strong spinning the fatigue strength of the rim and resistance to stress corrosion can improve; therefore it has small quality, high strength, and good security. The equal strength rim research is still at the starting stage, the relationship between the change of cross-section and carrying capacity is not clear, resulting in a lack of theoretical guidance in variable cross-section rim design.

In recent years, domestic and foreign popular optimization design method provides new rim design ideas, that is, first through the initial design method to design the geometry of the rim, and then the cross-section can be expressed as the design parameters, performance is expressed as a objective function changing along with the design parameters [1]. So optimization design process is to select design parameters for the best performance based on the objective function. This process is an automated process, without manual intervention, therefore, the design cycle greatly shortens. According to the new rim design method, this article uses multi-island genetic algorithm (MIGA) combined with sequential quadratic programming (NLPQL) optimization method to generate the optimal rim model.

2 Design Parameters of Variable Cross-Section Rim

The sketch of constant cross-section rim (LT2745) consists of the arc and line, variable cross-section wheel rim design method is to use the spline curve instead of the arc lines, and add size constraints to achieve parametric modeling, so rim section shape can vary by changing design parameters. Take the cross-section control parameters D1, D7, D6 D2, D10, D3, D14, D15, D5, D17, D4, D19 and D18 as design parameters to optimize, as shown in Fig. 1.

3 Stress Analysis in a Rim Subject to the Radial Load

Under the influence of a radial load, the tensile strength of the rim exerts a profound influence on durability, that is, fatigue life of the automotive wheel [2]. In an actual automotive wheel, the radial load is applied at the bead seat with the tire. The distributed pressure is loaded directly onto the bead seat in the model used in this analysis. The pressure is assumed to have a cosine function distribution mode with a central angle of 36° in a circumferential direction [3], as shown in Fig. 2. Also, it is assumed that the contact patch width corresponds to the area of contact over the bead seat, as shown in Fig. 2. These calculations are based on segments of a circular geometry. By choosing a cosine load function, the distributed pressure (Wr) is given by the expression

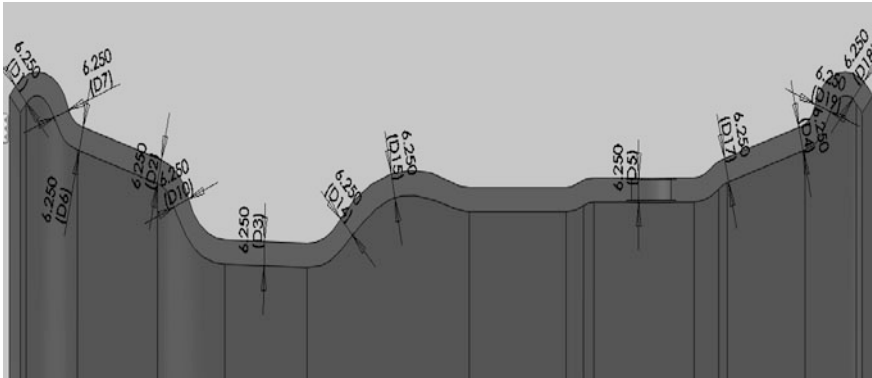


Fig. 1 The section parameters of variable cross-section rim

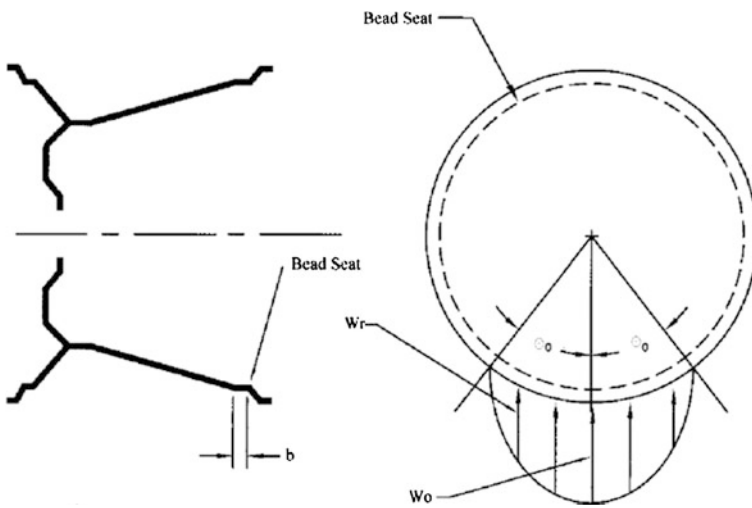


Fig. 2 Radial loading schematic

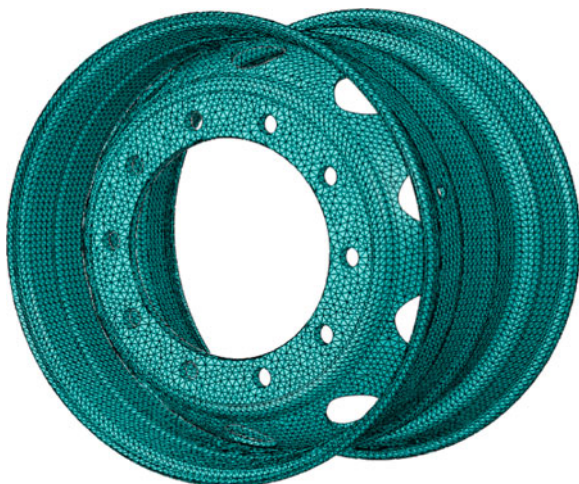
$$W_r = W_0 \cos\left(\frac{\pi \theta}{2\theta_0}\right) \tag{1}$$

From this equation, the total radial load W is calculated as follows.

$$W = b \int_{-\theta_0}^{\theta_0} W_r r_b d\theta \tag{2}$$

$$W = 4br_b\theta_0 \frac{W_0}{\pi} \tag{3}$$

Fig. 3 Finite element model



or

$$W_0 = \frac{W\pi}{4br_b\theta_0} \quad (4)$$

For LT2745, $W = 44100$ N, $b = 28$ mm, and $r_b = 280$ mm, the value of W_0 is 7.03 MPa, in Eq. (4), r_b is the radius of the bead seat, while b is its total width, θ_0 the loading angle, and θ_0 is the angle at maximum load. Furthermore, in this analysis a total radial load (W) of 44,100 N was applied to the model. The magnitude of this load is the same as that applied to the actual automobile wheel (tire–rim combination) in stress measurement experiments. The tire air pressure is applied directly on to the rim at its outer side and indirectly at the rim flange. In a three-dimensional analysis, the mesh subdivision is shown in Fig. 3.

4 Optimization Methods

In the size optimization of variable cross-section rim, take the cross-section control parameters D1, D7, D6, D2, D10, D3, D14, D15, D5, D17, D4, D19 and D18 as design variables, the rim mass as the optimization objective, and the maximum stress value in a rim subject to the radial load as constraints.

In this optimization, first multi-island genetic algorithm (MIGA) is used to look for global optimum, and then the MIGA algorithm optimum is the starting point for sequential quadratic programming to look for local optimum [4]. The optimization results are shown in Tables 1 and 2. After the optimization, the mass of the rim can decrease 7.1 %, while the maximum stress value in a rim subject to the radial load remain the same as the constant cross-section rim.

Table 1 Multi-island genetic algorithm optimization results

Design variables	Initial value	Lower bound	Upper bound	Optimal value
Mass [kg]	31.22	–	–	29.01
D1 [mm]	6.25	4.8	6.25	5.2
D7 [mm]	6.25	4.8	6.25	5.2
D6 [mm]	6.25	4.8	6.25	6.2
D2 [mm]	6.25	4.8	6.25	5.6
D10 [mm]	6.25	4.8	6.25	6.0
D3 [mm]	6.25	4.8	6.25	6.2
D14 [mm]	6.25	4.8	6.25	6.2
D15 [mm]	6.25	4.8	6.25	5.8
D5 [mm]	6.25	4.8	6.25	5.4
D17 [mm]	6.25	4.8	6.25	5.4
D4 [mm]	6.25	4.8	6.25	5.2
D19 [mm]	6.25	4.8	6.25	5.4
D18 [mm]	6.25	4.8	6.25	5.2
Maximum stress [Mpa]	349.49			357.17

Table 2 NLPQL optimization results

Design variables	Initial value	Lower bound	Upper bound	Optimal value
Mass [kg]	29.01	–	–	29.01
D1 [mm]	5.2	4.8	6.25	5.4
D7 [mm]	5.2	4.8	6.25	5.0
D6 [mm]	6.2	4.8	6.25	6.2
D2 [mm]	5.6	4.8	6.25	6.2
D10 [mm]	6.0	4.8	6.25	6.2
D3 [mm]	6.2	4.8	6.25	6.2
D14 [mm]	6.2	4.8	6.25	6.2
D15 [mm]	5.8	4.8	6.25	6.2
D5 [mm]	5.4	4.8	6.25	5.0
D17 [mm]	5.4	4.8	6.25	5.0
D4 [mm]	5.2	4.8	6.25	5.0
D19 [mm]	5.4	4.8	6.25	5.4
D18 [mm]	5.2	4.8	6.25	5.4
Maximum stress [Mpa]	357.17			349.93

5 Conclusions

Based on this study, using the technique of optimization and finite elements method in an automobile rim made from steel, the following are the observations.

1. Using spline curve parameters modeling method is simple and fast, parametric modeling for a rim is easy to optimize.

-
2. The optimization methods which combined multi-island genetic algorithm (MIGA) with NLPQL algorithm is used for exploration to avoid local optimum, and a good optimization effect is achieved.

References

1. Monedero J (2000) Parametric Design, a Review and Some Experiences. *Autom Constr* 9(4):367–377
2. Hsu YL, Hsu MS (2001) Weight reduction of aluminum disc wheels under fatigue constraints using a sequential neural network approximation method. *Computers in industry. Taiwan*. Vol. 46(2)
3. Stearns J, Srivatsan TS, Prakash A, Lam PC (2004) Modeling the mechanical response of an aluminum alloy automotive rim. *Mater Sci Eng A366*:262–268
4. Qiu Q, Feng P, Wu J (2002) Product mode structure for generalized optimal design. *Prog Nat Sci* 12(4):294–300

Lightweight Design for a FSC Car Based on Modal and Stiffness Analysis

Liman Jiang, Guoquan Wang, Guoqing Gong and Ruiqian Zhang

Abstract Based on the stiffness and vibration modal analysis for a FSC racing car frame with the FEA method and testing evaluation, the design parameters of optimal tubular space frame were determined through the sensitivity analysis. Oriented the minimizing the frame weight, the thickness of tubes was conducted under meet the requirements of stiffness and vibration modal. As a result, the frame weight was decreased by 7.18 %.

Keywords FSC racing car frame · Modal analysis · Stiffness calculation · Sensitivity analysis · Lightweight

1 Introduction

The FSC racing car frame is the installation base of the overall car assembly, which bears the gravity of all kind assembly such as engine, care body, wheel and tire, suspension and driver. Moreover, it bears the complex loads between the road surface and tire. The frame structural strength and dynamic characteristics have a great influence on the driver safety, power performance, handling and stability, ride comfort as well as other aspects of the car. It is necessary that frame structure possess sufficient stiffness to ensure the assembly accuracy of the motion system

F2012-E09-012

L. Jiang (✉) · G. Wang · G. Gong · R. Zhang
Beijing Information Science and Technology University, Beijing, China

and operating requirements. At the same time, the frame must have excellent dynamic characteristics to suppress vibration shock and reduce the noise [1]. Due to the power limitation, the frame should be lightweight as much as possible in order to increase the acceleration capability and better fuel efficiency.

2 Establishment of the Finite Element Model of the FSC Car Frame

In this chapter, the geometric model of the car frame was established by CATIA software, as shown in Fig. 1, it was a tubular space frame which designed according to the Rules of the Formula Student of China [2]. Then the model was imported into HyperMesh software to establish the corresponding finite element model. To reduce the calculation scale, the fuel tank, engine radiator and some smaller parts were left out on the premise as the small influence on the main mechanical properties of the frame. The finite element model was shown in Fig. 2.

The tubular space frame was welded steel tube. Since the tube wall is thinner, the methods of extraction the middle surface was used while meshing the element grid and the shell element was an average element size of 5 mm. Welding among circular tubes was simulated by shared nodes, while other soldered dots replaced by Spot-weld (1D element). Engine, differential gear, wheels, steering wheel and the driver were replaced with the lumped mass CONM2, which acted on corresponding nodes through the RBE3 element. The frame material is 30 CrMo, and the modulus of elasticity, the density, and the Poisson's ratio are 2.11×10^5 MPa, 7.9×10^{-3} kg/mm³, and 0.279, respectively.

3 Modal Analysis of the Frame

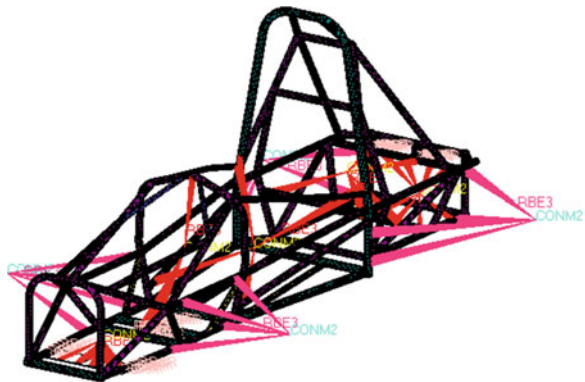
Uneven road and engine vibration caused the random excitation of the frame while the car driving on the road. If the frequency of the exciting force is coincided with a natural frequency of the frame, it may lead to resonance phenomenon, and then damage the frame. In order to avoid the resonance phenomenon, it is necessary to know the frame natural frequency and vibration mode. Here, the frame modal analysis was carried out in a way of combining test with simulation.

Boundary conditions of the free modal analysis were without any constraint and load. Radioss solver of HyperWorks (10.0) and the Block Lanczos arithmetic were used for the fine element modal calculation. As the car's speed is less than 200 km/h, the excitation caused by road will low at most 20 Hz. HONDA CBR600 four-cylinder gasoline engine was installed in this car, and the idle speed is 1,000 r/min, maximum power speed equipped with current limiting valve is 8,000 r/min, so the idle frequency of engine is about 33.3 Hz. The maximum operating frequency of the

Fig. 1 Geometric model of the FSC racing car



Fig. 2 Finite element model of the car frame



rotating components on transmission system and driving system is 15.36 Hz [3]. So, select 0–80 Hz as calculation frequency range, the first six modal shapes and frequencies (except the rigid body mode) are shown in Fig. 3.

To verify the results of finite element analysis, modal test of the frame was carried out using China Orient Institute of Noise & Vibration experimental system which consist of 98321ICP three—direction acceleration sensor, 3060A intelligence signal automatic gathering and processing system, DASP V10 modal calculation software and so on. There were twenty-four test points, and the vibration accelerations in vertical, longitudinal and transversal directions were collected for each point, so a total of 72 measurement signals were in this test. Release the tire pressure and then set the four tires on the sponge of 150 mm thickness to imitate the free case. Based on the fundamental principle of modal analysis, the method of force-hammer excitation was adopted, applying multiple points exciting forces method and collecting the responding signals from multiple points. The Varied-Time-Base analyzing method was used when collecting data. Modal parameters fitted through Poly IIR new algorithm which based on Padé approximation for MIMO test [4]. Figure 4 shows test mode shapes.

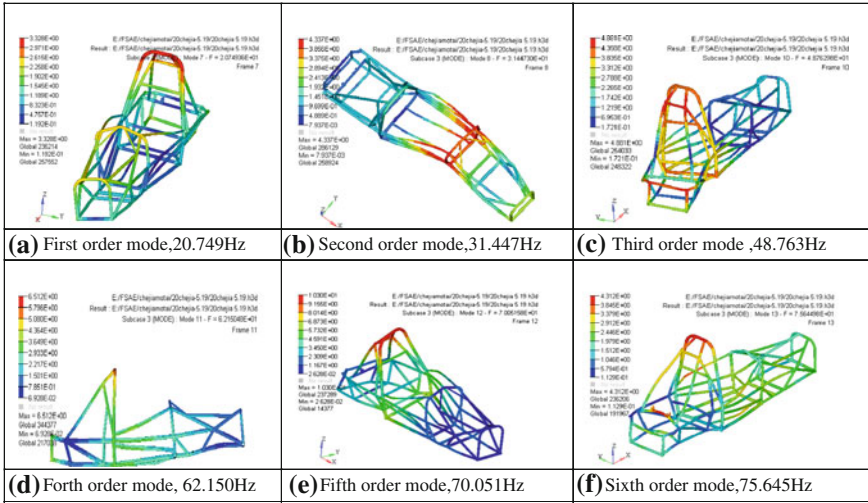


Fig. 3 FEM mode shapes of the FSC car frame

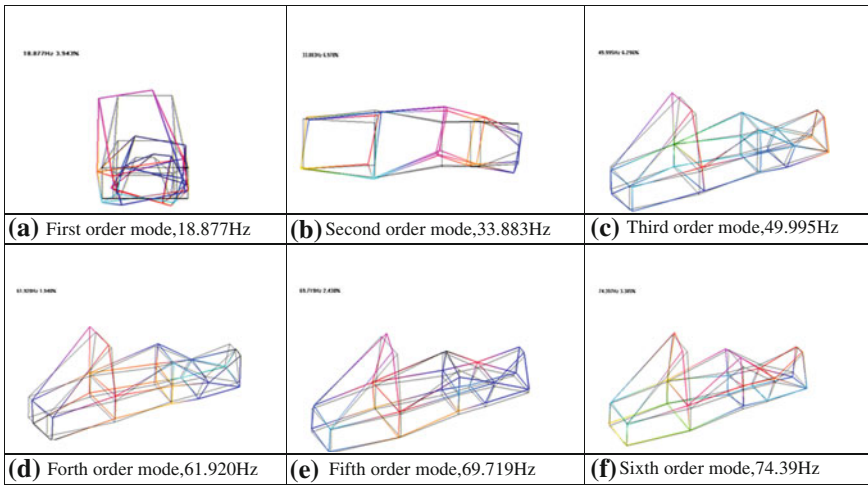


Fig. 4 Test modal shapes of the FSC car frame

Table 1 provided a comparison of the natural frequencies of the simulation and test. The results showed a good consistency of the two methods, so it indicated the finite element model was right.

To avoid the frame resonance, the first frequency should be between the non-spring load natural frequency and engine idle speed frequency [5]. Analysis indicates: (1) The first order frequency (20.749 Hz) avoids the engine idling

Table 1 Comparison of the natural frequency between the simulation and test

Order	Calculation results (Hz)	Test results (Hz)	Error (%)	Modal shapes
1	20.749	18.857	10.03	The first order torsion
2	31.447	28.852	8.99	The first order bend around z axis
3	48.763	49.995	2.46	Combined bending with torsion
4	62.150	61.920	0.37	The first order bend around y axis
5	70.051	69.719	0.47	The second order torsion
6	75.643	74.397	1.67	Local torsion

frequency but close to the road surface excitation frequency, it may cause the low-frequency resonance of the frame. (2) The second order frequency (31.447 Hz) is close to the engine idling frequency, resonance is likely to occur to the frame.

4 The Frame Stiffness Analysis

4.1 Torsional Stiffness Calculation and Analysis

The frame torsional stiffness influenced the positional accuracy of vehicle suspension hard points in the distorted road or steering quickly, it will affect the handling stability and driving safety. Therefore the torsional stiffness of car frame is a very important performance index.

As torsional deformation is relatively small compared to the size of the entire frame, the approximate torsion angled was calculated as follow:

$$\theta = 180(\delta_1 - \delta_2)/(L\pi) \tag{1}$$

The torsional stiffness [6] is:

$$K = \frac{\pi TL}{180(\delta_1 - \delta_2)} \tag{2}$$

Here, T is the torque acted on the frame, L is the distance between the two stress points of the frame, δ_1 and δ_2 are the maximum displacement in vertical direction and the minimum displacement respectively. K is the frame’s torsional stiffness.

All suspensions are four- pole double wishbone independent suspension and each one connected to the car frame through four hinge joints. During the analysis, the actual condition of the car was simulated by constraining the DOF (Degree of Freedom) of the connections between the frame and suspensions. To simplify the calculation process,project the two “outer” points of the upper swing arm and lower swing arm onto the frame and put them to the joint points. And now the boundary restraints should only be exerted to 8 points.

The frame torsional stiffness was analyzed under three different conditions [7]:

(I) Constrain xyz translational DOF of rear suspension connection points and z

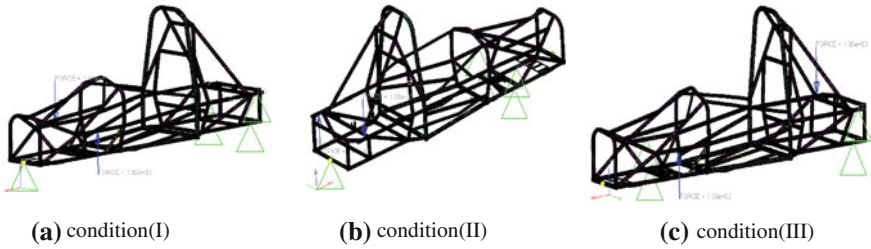


Fig. 5 Models under three conditions

direction translational DOF of the midpoint in the front cross beam. Exert the same force in opposite direction (z and $-z$) on the front suspension connection points left and right, respectively.

(II) Constrain xyz translational DOFs of front suspension connection points and z translational DOF of the midpoint in the rear cross beam. Exert the same force in opposite direction (z and $-z$) on the rear suspension connection points left and right, respectively.

(III) Constrain xyz translational DOFs of right anterior and left posterior suspension connection points. Exert the same force in opposite direction (z and $-z$) on the left anterior and right posterior suspension connection points, respectively. Models in above conditions are shown in Fig. 5.

The torsional stiffness under above conditions calculated according to the results of finite element calculation and the formula (2). Table 2 showed the deformation and torsional stiffness results.

The torsional stiffness of some other abroad formula racing car is designed in 1,000–4,000 N·m/deg [8]. It shows that this frame’s torsional stiffness within the normal range and the value under condition (III) is the smallest.

4.2 Bending Stiffness Calculation and Analysis

The bending stiffness of the frame refers to the degree of flexural deformation of the frame when bearing the vertical load. It will affect the wheelbase, wheel alignment parameters, as well as handling stability.

Take the frame, suspension and wheels as a whole simply supported beam. Approximate stiffness values can get according to the calculation method of beam deflection in material mechanics. The formula [9] is:

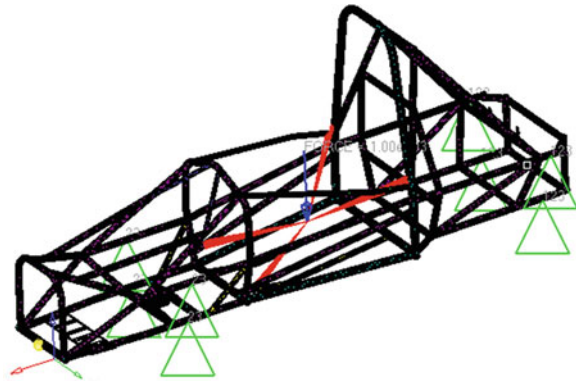
$$r_f = \frac{Fab(l^2 - a^2 - b^2)}{6fl} \tag{3}$$

Here, r_f is the bending stiffness, F is the vertical force of fulcrum, a is the distance between the force functional point and the confined point of rear suspension, b is

Table 2 The results of calculation in three conditions

	Condition (I)	Condition (II)	Condition (III)
δ_1 (mm)	0.9675	1.173	1.273
δ_2 (mm)	-1.314	-1.901	-2.225
L (m)	0.43	0.575	0.494
K (N·m/deg)	1414.47	1877.19	1217.62

Fig. 6 Model of the frame under bending condition



the distance between the force functional point and the confined point of front suspension, l is the distance between the confined points of front and rear suspension, f is the maximum deflection of the frame.

The boundary conditions were constrained xyz DOFs of rear suspension connection points and yz DOFs of front suspension connection points. Meanwhile, put $F = 1,000\text{ N}$ of $-z$ direction at the seat barycenter position, which acts on the connection points between the frame and the driver seat through the RBE3 element. The model is shown in Fig. 6.

Use HyperWorks software for finite element calculation got the deformation of the frame in bending condition. The bending stiffness parameters are shown in Table 3.

It can get the bending stiffness $r_f = 378827.71\text{ N} \cdot \text{m}^2$ based on the parameters in Table 3 and formula (3). The bending stiffness of the frame has smaller impact on the vehicle performance than the torsional stiffness, so there is less data about the bending stiffness of the FSC car frame. Therefore, the bending stiffness of the FSC car frame is reasonable [10].

Table 3 Bending stiffness parameters

F/N	a/m	b/m	l/m	f/mm
1,000	0.972	0.608	1.58	-0.1945

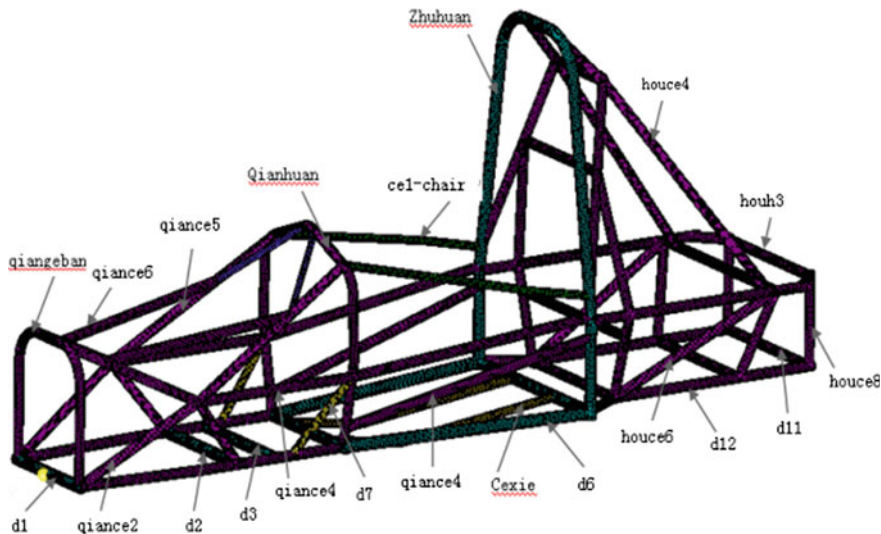


Fig. 7 The sketch of components number

5 Optimization Design of the Frame

5.1 Sensitivity Analysis of the Frame Structural Parameters

Through structural sensitivity analysis can find the most sensitive design values which influenced the structural performance and obtain the most concerned sensitivity coefficient and the best design parameters. Oriented the minimizing the frame weight, the thickness of tubes was conducted under meet the requirements of stiffness and vibration modal.

The sensitivity respect to the design variable of the frame can be defined as [11]:

$$Sen \left(\frac{u_j}{x_i} \right) = \frac{\partial u_j}{\partial x_i} \tag{4}$$

Where, u_j is the j th function, here stands for the objective function and constraint function of stiffness or modal. x_i is the i th variable, the thickness of the i th component.

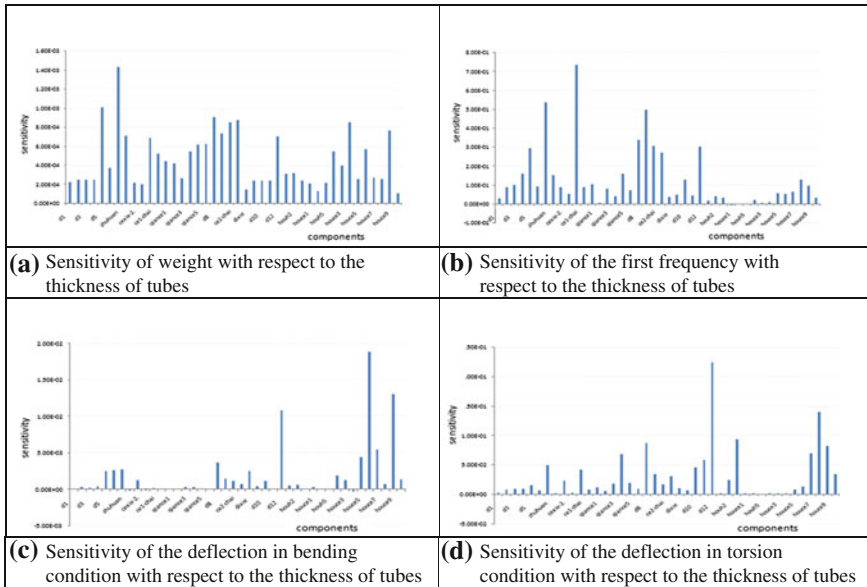


Fig. 8 The sensitivity histogram of various components

The frame consists of forty-two components, Fig. 7 is a sketch of components number. With the thickness of the structural parts as the design variable, the deflection of twisting and bending, and the 1st natural frequency as the restraint conditions, the minimum weight of the frame as the goal, the sensitivity analysis results can be defined and output using SENSITIVITY and OUTPUT cards in the finite element software HyperMesh. The sensitivity values that the deflection in bending condition, the deflection in torsion condition, the first modal frequency of different components and the weight of the frame with respect to the thickness of tubes were obtained, respectively. The sensitivity histogram of various components is shown in Fig. 8.

Figure 8 shows: under the freedom condition, the sensitivity values of the first torsional frequency with respect to the thickness of tubes are both positive and negative. The positive values indicate that the first torsional frequency will improve as the increase of the steel tubes thickness, while the negative values mean the first torsional frequency will decrease as the increase of the steel tubes thickness. The sensitivity values of main ring, side impact beams of the chair and part of bottom beams are relatively large, so the first torsional frequency can be improved by increasing the thickness of steel tubes. In bending and torsion conditions, the positive sensitivity values indicate that the increase of the steel tubes thickness will cause the decrease of the z-direction relative displacement at frame stress points, and then promote an increase in frame stiffness. The negative values

Table 4 Comparison of the optimized thickness with the original

Components	Original thickness (mm)	Upper limit (mm)	Lower limit (mm)	Optimized thickness (mm)
d1	2.5	2.5	2.4	2.4
d7,cexie	2.3	2.5	1.6	2.4
Shangxie	2.35	2.5	1.6	2.4
Ce1—chair	1.75	2.5	1.6	2.4
Qiance2, houce1-4, houh4,	2.4	2.5	1.6	1.6
Qiance6,houce6	2.4	2.5	2.4	1.75

indicate the opposite sense. The sensitivity values of bottom beams, side impact beams back are relatively large, thus changes in the thickness of the tubes will cause large changes in stiffness [12].

5.2 Lightweight Design of the Frame

The OptiStruct solver can firstly transform the nonlinear objective function or constraints into a linear expression by the approximate linear method for size optimization, and then use the Feasible Direction Method for solving. The basic idea of the FDM is: set a feasible point X^k which can meet the following iterative formula:

$$X^{k+1} = X^k + d^k s^{k+1} \tag{5}$$

Here, s^{k+1} is the search direction of the iteration $k + 1$, d^k is the step size. If the X^{k+1} is not the optimal solution, the above steps will repeat until the optimal point array appears. For the linear problem, s^{k+1} of the above iterative process should meet [13]:

$$\begin{cases} (S^{k+1})^T \nabla g_j \leq 0 \\ (S^{k+1})^T \nabla f \leq 0 \end{cases} \tag{6}$$

This chapter selected the bending, torsion and free conditions used in the analysis of static and dynamic characteristics, and established the model for size optimization according the results of stiffness, modal, and sensitivity analysis:

1. Objective function: weight minimum
2. Constraint condition: the lower limit of disp1—z directional displacement of node 236832 on the main ring is -0.1945 mm, the lower limit of disp2—z directional displacement of node 32768 on the connection of right posterior suspension is -2.225 mm, the upper limit of disp3—z directional displacement of node 298323 on the connection of left anterior suspension is 1.273 mm

Table 5 Comparison of the optimized weight with the original

	Original weight (kg)	Optimized weight (kg)	Variable quantity (kg)	Change rate (%)
Weight of the frame	46.385	43.056	3.329	7.18

3. Design variable: Pick components which have smaller sensitivity of stiffness and natural frequency but larger mass sensitivity, and have larger sensitivity of stiffness and natural frequency but smaller mass sensitivity as the design variables [14]. Here, the design variables are thickness of cone tubes. Considering the thickness of steel tubes is not continuous variation in the actual production, the amplitude of the thickness variation was set to 0.05 mm. Thus, the optimized thickness will be an integer multiple of 0.05.

The optimal calculation Since the FSC Chinese Rules have certain requirements on the size of the frame, it is necessary to adjust optimized thickness values according to the «Formula Student China Chinese Rules(2012 Version)» and the exited specifications on steel tubes. Table 4 gives a comparison of the optimized thickness with the original.

Table 5 gives a comparison of the optimized weight with the original, it shows the weight of the frame after optimization and adjustment is 43.056 kg, decreased by 7.18 %. Thus the objective of lightweight has realized.

6 Discussion

To evaluate the results of optimization and verify the reasonability of sensitivity analysis, modal characteristics and stiffness characteristics of the optimized frame were analyzed.

6.1 Modal Analysis of the Optimized Frame

Modal analysis of optimized frame is conducted through FEM again. The first six modal shapes and frequencies are shown in Table 6. As it can be observed from the Table 5, modal shapes of the optimized frame are similar with the original ones, the first two modal shapes still being first torsion and first bending. As there are some changes in the frame size and total mass, modal frequencies change, obviously. The first and sixth natural frequencies increase by 1.59 and 4.5 %, respectively, while the second, third, fourth and fifth natural frequencies are decrease in different degree.

Table 6 Modal shapes and frequencies of the optimized frame

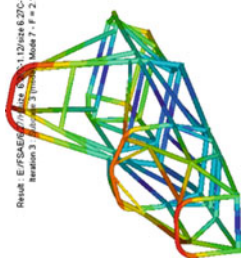
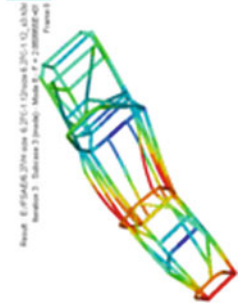
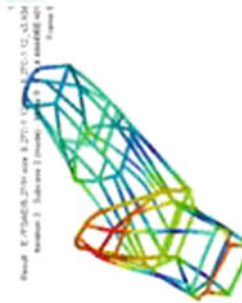
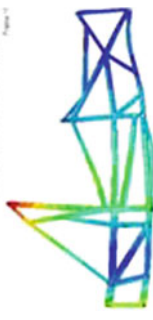
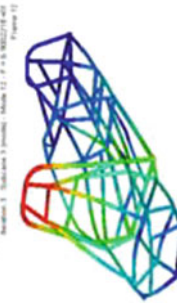
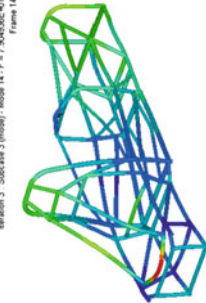
Order	1	2	3
Modal shapes after optimization			
Frequencies before optimization/Hz	20.749	31.447	48.763
Frequencies after optimization/Hz	21.079	28.690	44.445
Rate of change	1.59 %	-8.76 %	-8.85 %
Order	4	5	6
Modal shapes after optimization			
Frequencies before optimization/Hz	62.150	70.051	75.645
Frequencies after optimization/Hz	54.572	69.002	79.049
Rate of change	-12.19 %	-1.5 %	4.50 %

Table 7 Comparison of stiffness before and after optimization

Performance index	Original values (kg)	Optimized values (kg)	Variable quantity (kg)	Change rate (%)
Bending stiffness N·m ²	378827.71	351536.21	-27291.5	-7.2
Torsional stiffness N·m/deg	1217.62	1224.27	6.65	0.55

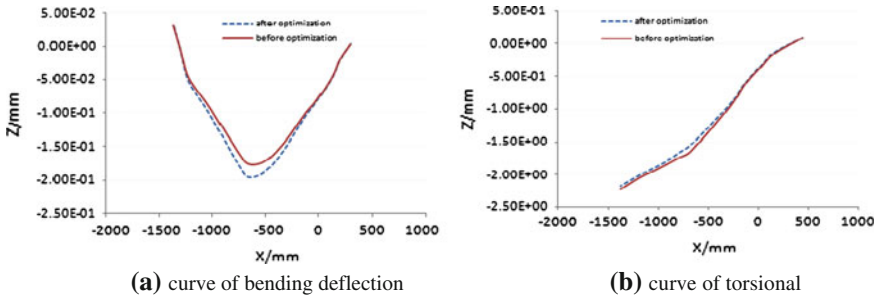


Fig. 9 Curves of static stiffness

6.2 Static Stiffness Analysis

Static stiffness analysis of the optimized frame is carried out through simulation. Table 7 summarized the bending stiffness, torsional stiffness and their comparison analysis before and after optimization.

Compared with the former frame, the bending stiffness of the optimized frame decreased by -7.2 %, but still higher than the design reference value of the other racing car. The torsional stiffness has a small change, increases by 0.55 %. Figure 9a and b depict the z directional displacements of nodes on right upper longitudinal beams in bending condition and torsion condition, respectively, that are the bending stiffness and the torsional stiffness of the frame. It can be seen from the figure that although stiffness values change a little after optimization, the bending stiffness curve gets smoother than that before optimization, and the torsional stiffness curve gets near linear. The above conclusions reveal that the overall stiffness of the frame is designed uniformly.

7 Conclusions

1. Vibration modes of the FSC racing car was analyzed in a way of combine test with simulation. Results shown a good consistency of the two methods, and indicated the finite model was reasonable.

2. Lightweight of the frame realized through size optimization under the premise of the stiffness and modal performance requirements. After optimization, the weight of the frame decreased 3.329 kg, the first torsional frequency increased by 1.59 %, torsion stiffness increased by 0.55 %.
3. Sensitivity analysis is an effective way for lightweight of frame, which can provide feasible foundation for realization of lightweight. The whole analysis and optimization process provides a valuable reference for the further optimization in collision, fatigue and NVH performance constraints.

Acknowledgments The authors would like to acknowledge the support of Beijing Information Science & Technology University graduate innovation fund project under the grant No.5028211000.

References

1. Yun-jiao Z (2010) Studies on lightweight design for bus bodies based on stiffness and modal analysis [J]. *Machin Des Manuf* 7:117–119
2. The Society of Automotive Engineers (2010) China Formula Student China Chinese Rules (2011 Version)[M]
3. Yin X (2007) Weight-light design on vehicle frame based on FEA method [D]. Wuhan University of Technology, Wu Han
4. Liu J (2011) Accurate and automatic parameters identification of structure dynamics[D]. Tsinghua University, Bei Jing
5. Wang X (2009) Modal analysis for frame of off-road racing car based on ANSYS[J]. *Tractor Farm Transporter* 36(4):28–29 (32)
6. Shuai Z, Xi D, Wang S, etc (2011) Strength and stiffness analysis on FSAE racing car frame[J]. *Comput Aided Eng* 20(4):53–56
7. Yu G, Huang H, Wu J (2009) Finite element calculation and analysis of FASE race car's frame strength and stiffness[J]. *J Xiamen University of Technol* 17(4):29–32
8. Riley WB, George AR (2002) Design, analysis and testing of a formula SAE car chassis[C]. *Motor Sports Eng Conf Exhibition, Indianapolis*, pp 382–399
9. Nie L, Meng G (2009) *Mechanics of materials*[M]. China Machine Press, Beijing
10. Yang L (2007) Structure analysis and optimization design of the frame of EV[D]. Jilin University, Chang Chun
11. Wang Z, Liu B, Ma S (2008) On body-in-white optimization based on bending stiffness and torsional stiffness [J]. *Mech Sci Technol Aerosp Eng* 27(8):1021–1024
12. Li Z (2010) FEM Analysis and optimization research on truck white body by hyperworks[D]. Southwest Jiao tong University, 2010
13. Liu L, Xin Y (2011) A study on the lightweight of vehicle frame based on sensitivity analysis[J]. *Mech Sci Technol Aerosp Eng* 30(10):1724–1727
14. Duan Y, Bi C (2010) Study on weight-reduction of car-body based on stiffness and modal sensitivity analysis [J]. *Noise Vib Control* 6:79–82

Application of Comprehensive Optimization into Bus Structure Lightweight Improvement in 3-Section Chassis Frame

Congcheng Ma and Fengchong Lan

Abstract This chapter presents the structural optimization and lightweight design of a bus chassis frame. Firstly, the static performance of the chassis frame is obtained using finite element analysis (FEA). A prototype of a chassis truss divided into three-sections is proposed based on the material distribution from the topology optimization. Comparative analysis between the optimized chassis structure and the original structure shows that the optimal chassis is superior to the original in terms of the rigidity, strength and mode performance. Compared to the results for the original frame, the maximum stress of the optimized chassis truss under the worst torsional loading case are reduced 23.4 MPa, the maximum stiffness increased 18.5 %. Moreover, a mass-saving with 196 kg, i.e., 14 % of the original chassis mass verifies the lightweight design performed in this study.

Keywords Bus body · Three-sectioned chassis frame · Lightweight design · Topology optimization · Finite element analysis

1 Introduction

Three-section chassis frame is used in the domestic bus. The frame possesses the characteristics of simple structure, high strength, high stiffness, and flexible and easy application in accordance with the modification in vehicle's wheel base, etc. [1]. On

F2012-E09-014

C. Ma (✉) · F. Lan
School of Mechanical & Automotive Engineering, South China University of Technology,
Guangzhou, China
e-mail: rongtingma@163.com

the contrary, the three-section chassis frame possesses the shortcoming of big weight, and comes short of the environmental requirements of energy saving, etc. [2]. Chassisless body structure is another type of frame, it possesses the characteristics of ingenious structure, light weight, reasonable structural-load-carrying form, etc. But the complex production process is not easy to achieve, it becomes bottleneck of restricting the domestic bus-worker enterprise. Chinese government has promulgated relevant regulations that request bus-worker must use chassisless body instead of semi-integral structural body in a few years. Therefore, in order to improve the existing bus chassis structure, scholars in china have discussed different approaches to the reform plans of weight reduction [3–7]. But there are few practical solutions. This paper puts forward a type of truss structural frame attempting to solve the problems in bus-worker at the present situation. The truss structural frame and ensure possesses the both of advantages lightweight and simple production process. There is great importance of analysing static mechanical property and modal on the frame [8], as the frame, after improvement should possesses the same or greater mechanical properties in strength, stiffness and modal, etc. the capacity compared to original. Finite element analysis (FEA) is used to calculate the new frame structure for avoiding blind design. The proposed prototype of the chassis truss which has the structure divided into three-sections by their own loading functions is based on the material distribution from the topology optimization. Comprehensive analysis methods are applied to reduce the structural weight and further improve some target parts. Finally, the truss structural frame is verified by analysis and calculation.

2 Simulation Analysis and Experimental Verification

A three-section chassis frame finite element model (FEM) has been built as shown in Fig. 1. The experimental verification to ensure using the laser scanner ATOS is carried out by the correctness of FEM, when the developer is sprayed on the location of frame beams in order to improve the experimental precision. No-load, 3000 and 5000 kg loads, in order, respectively were loaded on the bus luggage compartment for test in order to test under bending and torsion condition. The frame rails deformations in each case were scanned, experimental site as shown in Fig. 2. Different load condition is loaded. The vertical displacements are measured, i.e. seventeen testing points on the beams Z coordinate. The Z coordinates deformations of indication to verify each testing point. The location distribution of measuring point is shown in Fig. 3.

Experimental values which are on right stringer of the middle section are contrasted with simulation values. The results show that both of the deformation trends are consistent. As a result, the correctness of FEM of the frame has been verified.

Bending load condition is simplified when the static mechanical properties of the frame are calculated. The boundary conditions are: the center of the front suspension bracket Y and Z two level degrees of freedom are constraints. Both sides of the rear suspension imposed by the X, Y, and Z three parallel to moving

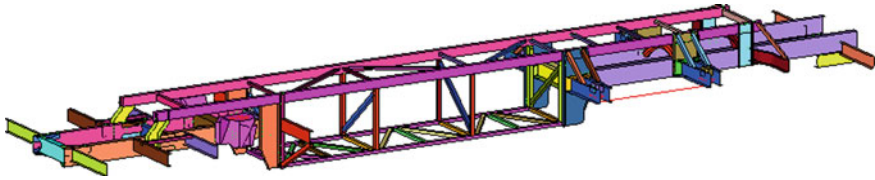


Fig. 1 Three-section frame FEM

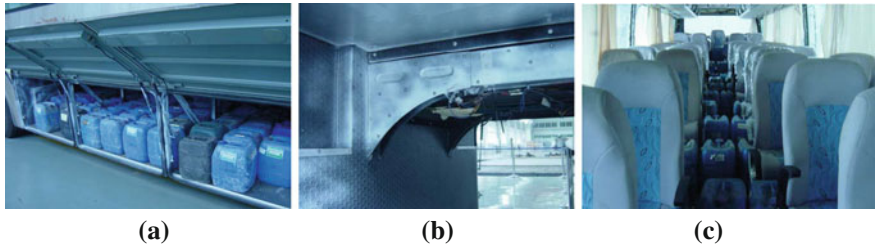


Fig. 2 Scene of test

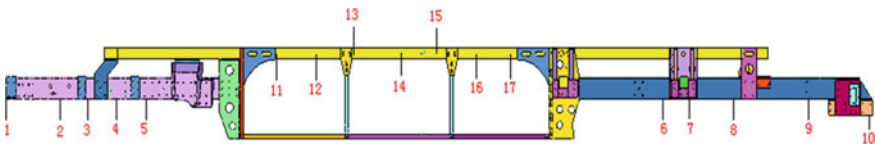


Fig. 3 Measuring point distribution

degrees of freedom were constraints. A total 40 KN distributed load was loaded on the frame, the form of load distribution as shown in Fig. 4.

The three-section chassis frame was calculated under bending conditions, concurrently, stress distribution cloud is obtained as shown in Fig. 5. The distribution cloud shows their stress distribution bilateral symmetry about left side carling and right side. Most of the regional stress level is lower. Region maximum stress concentration was emerged at the top of the luggage rack of the middle frame stringer. The maximum stress reaches 84.6 and 83.9 MPa, respectively, on the left and right sides of the stringer. It's within the bounds of the material limit of yielding.

The damage form of U-steel structural just general plastic limit of yielding, therefore, the fourth strength theory was applicable. When the bus is travelling on the rugged road the Speed is generally low velocity, the frame bear the torque this moment. The dynamic load vary with time-dependent is slows on the chassis frame. In addition, the inertia load is small. The simulation analysis result shows that the frame of the weak parts on the static load torsion test is the same with on dynamic load torsion. Therefore, on calculate use bending and torsional features of frame instead of static dynamic. The static torsional analysis results shows the strength and stiffness characteristics.

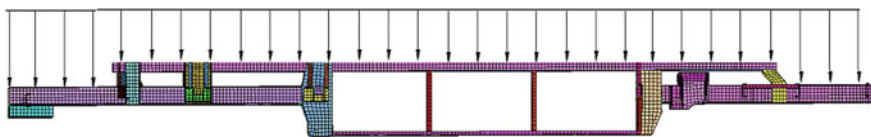


Fig. 4 The way of uniform load in bending conditions

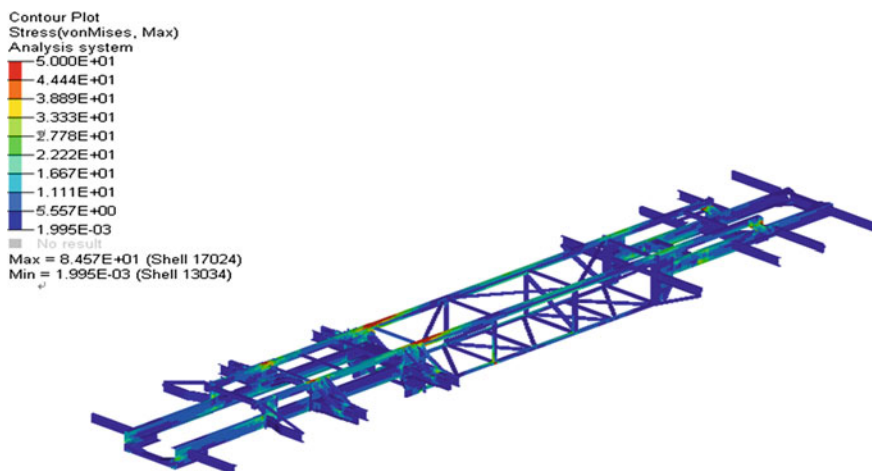


Fig. 5 The overall frame stress cloud in bending condition

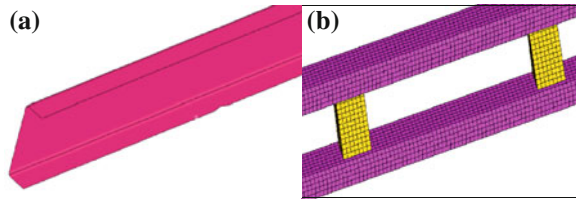
Under torsional condition, the boundary conditions are: both sides of rear suspension of all translational and rotational degrees of freedom were constraints. A pair of negative direction force 3000 N is loaded on the center of the both sides front suspension bracket. The same method as bending conditions the frame was calculated under torsional condition, the frame stress distribution cloud is obtained. The same as under bending condition, region of maximum stress concentration are emerged at the top of the luggage rack of the middle section frame stringer. The maximum stress was 84.1 MPa in stringer. The methods of analysis under torsional condition are same as bending condition, not any more elaborate hereinafter.

In summary, the results showed that the front and rear section frame possesses high stiffness and high strength. They should be the focus of lightweight and structural improvement next step.

3 Lightweight Design and Optimization Improvement

A type of topology prototype is obtained which material distribution is discrete and hollow get through use topology optimization analysis methods on front section frame. Several types of truss structure have been designed reference the topology

Fig. 6 Compared frame improve before and after, **a** appearance before improvement, **b** appearance after improvement



of prototype. The optimal solution is selected through simulation analysis and compare. The FEM of structure is shown in Fig. 6b. The original structural frame shown in Fig. 6a is replaced at now. The improved stringer graphics size as shown in Fig. 7. The improved structure is made of rectangular box welded truss structure, which wall thickness is 4 mm. Improved truss structure retain better static mechanical properties with original structure.

Simulation analysis shows the rigidity of middle section frame is insufficient, thus frame the overall resistance to bending and torsion stiffness is led to degradation. Therefore, the middle luggage rack must be increased some support, Fig. 8 shows the improvement of the rib.

Several types of chassis truss frames have been designed and verified, based on FE analysis above. The optimal chassis truss frame is selected through simulation analysis and compare. Truss frame as shown in Fig. 9. Both ends the middle beam of the frame is downward bending to weld with front section and rear section frame after improvement. The structure of front section and rear section frame are replaced by truss structure as shown in Fig. 7. Stress distribution cloud shows the static mechanical properties are superior to original frame. After improvement, the truss structure is lightweight 14 %, i.e. reducing 196 kg, than the original structure. Frame all weight down from 1360 to 1164 kg [9–11].

4 Compare and Analysis Static Mechanical Properties

The static mechanical properties of chassis truss frame must been calculated. The boundary conditions are same as the analysis of original frame, not elaborate any more.

The simulated results show that the overall stress of chassis truss frame is lower, under bending conditions, the maximum stress in 96.5 MPa. The maximum stress is slightly higher than the original. The stress is rose from 84.6 to 96.5 MPa, but still in the yield strength of material. The others stress is same as the original level. After improvement the overall front section frame sink, the end near the front axle reach maximum, both ends of subsidence over the middle section frame sink.

The Z-direction displacement basically is same with original frame in bending condition. The maximum Z-direction displacement is 6.65 mm before improvement, in 6.61 mm after improvement. The deformation of front section frame in

Fig. 7 Size of beam after improvement

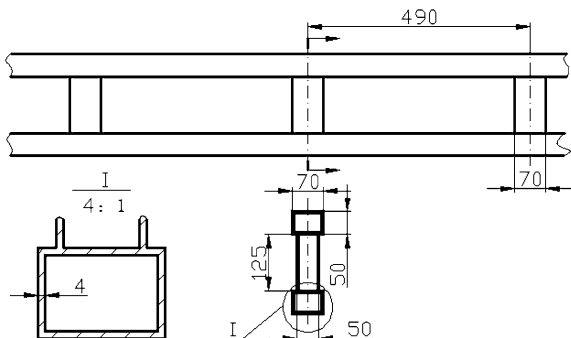


Fig. 8 Contrast of the luggage rack before and after improvement **a** appearance before improvement, **b** appearance after improvement

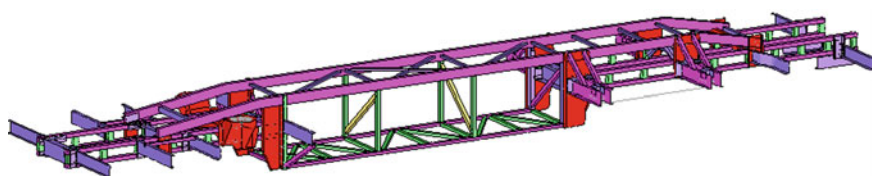
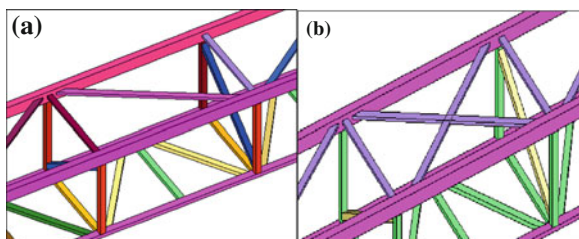


Fig. 9 The structure of three-section chassis frame after improvement

keeping with stress, the overall front section frame sink, the end near the front axle reach maximum, both ends of subsidence over the middle section frame sink. In the area of engine mount of rear section frame sinking deformation reach 6 mm. The Z-direction displacement of front section frame slight increase, displacement of middle section frame and end of the frame are declined. Overall, the bending stiffness of the truss frame is superior to before modification.

The right beam of middle section frame is more twists and turns, the end area near the rear section frame reach the maximum, there is part in the opposite direction bend between them.

The deflection curves deformation of rear section frame is simply. The deformation displacement area of engine mount is the maximum.

After improvement, the Z-direction displacement of middle section frame and front section frame is slight increase relative to original, the other way round, the rear section frame is decreased. Results show that the overall bending stiffness of truss frame remained essentially level in original frame.

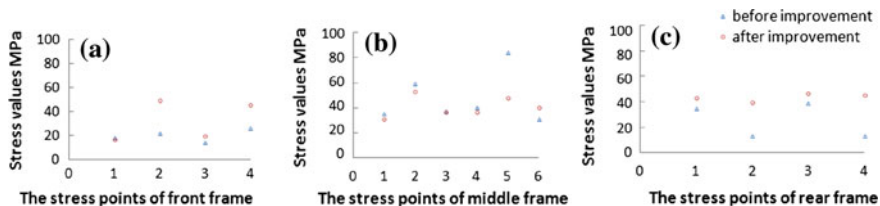


Fig. 10 The scatter plots of frame comparison before and after improvement

The stress level of whole truss frame decreased significantly under torsion condition, the maximum stress in 60.7 MPa. The stress is drop from 84.1 to 60.7 MPa, decreased by 27.8 %, i.e., decrease 23.4 MPa. The stress level of front section frame improved slightly increased, the maximum stress in 49.6 MPa. Some scatter stress of front section frame contrast original frame as shown in Fig. 10a. Other structures stress on the lower level.

The stress level of all middle section frame is lower than original, the maximum stress in 48.3 MPa. The stress is decrease from 84.1 to 48.3 MPa, decrease 42.6 %, i.e., decrease 35.8 MPa. Some scatter stress of middle section frame contrast original frame as shown in Fig. 10b.

The stress level of rear section frame is improved uniformity. Some scatter stress of rear section frame contrast original frame as shown in Fig. 10c. The location of scatter on the label in the frame is shown in Fig. 3.

Torsional rigidity of truss frame is increased after improvement. The displacement of left relative to right the front suspension bearing in 5.59 and -4.46 mm before improvement, it's in 4.47 and -3.375 mm after improvement. The stringer and the relative twist of left and right deflection on middle section frame have significant decrease. Relative torsion angle of middle section frame reduces after improvement. Obviously, the torsional stiffness of truss frame is increased.

The fulcrum spacing of front hanging around is 1250 mm, the relative displacement is 8.49 mm, 3750 Nm load torque is loaded under torsional condition. Function (1) and (2) can obtain the relative twist angle is 0.389°, the torsional stiffness is 9640.1 Nm/degree, i.e., increased by 18.5 % relative to original frame.

$$\text{relative twist angle : } \theta = \frac{180(d_1 - d_2)}{3.14L} \tag{1}$$

$$\text{torsional stiffness : } C_T = \frac{T}{\theta} \tag{2}$$

Where d_1 is the displacement of fulcrum at the left front overhang, d_2 is the displacement of fulcrum at the right front overhang, L is spacing of fulcrum, T is torque.

The performance parameters compare before and after improvement as shown in Table 1.

Table 1 The static mechanical properties compare before and after improvement

Contrast index	Before improvement	After improvement
Max stress of bending conditions	84.6 MPa	96.5 MPa
Max stress of reverse conditions	84.1 MPa	60.7 MPa
Relative displacement of reversing conditions	5.59/−4.46	4.74/−3.75 mm
Displacement of Z-direction	6.65 mm	6.61 mm

The maximum stress increase 11.9 MPa under bending conditions after improvement, the maximum displacement is reduced reach 1.56 mm. The maximum stress decrease 23.4 MPa under torsional condition. Overall, the stiffness and strength of truss frame possesses great static mechanical properties are superior to original frame.

5 Conclusion

- (1) A type of prototype truss-like chassis is proposed based on the material distribution from the topology optimization.
- (2) The static mechanical properties of three-section chassis frame are calculated and lightweight design through finite element analysis. The truss frame was obtained get through compare the properties of frame improvement before and after.
- (3) The quality of objective frame down from 1360 to 1164 kg, i.e., reduce 196 kg, decrease of 14.4 %, its effect to lightweight is obviously.
- (4) This chapter present one method and design a structure to transition from semi-integral body to chassisless body.

References

1. Yongli S (2001) A Design of frame with 3-section-chassis-frame for TJR6120D06 coach. *Bus Technol Res* 2001 (01)
2. Qing L (2009) Research of development of bus frame structure. *Auto Mobile Sci Technol* 2009(5):5–8
3. Guanliang Z, Jingyi L, Mingde Y (2006) Static and dynamic analysis of the bus-body based on FEM. *Comput Simul* 8(23):226–229
4. Kai L (2007) The exploration and research of two style bus structure of integral body. *JiLin University*, 04
5. Yue Y (2008) Struture optimization design for bus frame. *J HeFei Univ technol* 2008(09):1396–1398
6. Zuo K, Chen L, Zhang Y-Q (2007) Study of key algorithms in topology optimization. *Int J Adv Manuf Technol* 32:787–796
7. Zhang Z, Na J, He H (2010) Study on partial structural optimization design of some bus/coach chassis. *Bus Technol Res* 4:8–10

8. Liu S, Li F (2010) Finite element analysis of the structure of a bus frame. *J Mech Electr Eng* 4(27):20–23
9. Su R, Gui L, Wu Z (2010) Multidisciplinary design and collaborative optimization for bus body. *J Mech Eng* 09(46):128–133
10. Campanelli M, Shabana AA (1998) Chain vibration and dynamic stress in three-dimensional multi-body tracked vehicles. *Multi-body Sys Dyn* 2:277–316
11. Mikkola AM, Shabana AA (2003) A non-incremental finite element procedure for the analysis of large deformation of plates and shells in mechanical system applications. *Multi-body Sys Dyn* 9:283–309

Applying Agile Software Principles and Practices for Fast Automotive Development

David Socha, Tyler C Folsom and Joe Justice

Abstract This paper addresses lightweight designs both in terms of materials and processes. The study is based on the WIKISPEED SGT01 car, which was an entrant in the Progressive Insurance Automotive X-Prize contest to produce a full-sized road-legal car getting 100+ mi/gal (2.25 L/100 km). The 638 kg car is built from aluminum and composites. Agile Methods were introduced for software projects and give product cycle times measured in weeks, not years. Good software design demands modules that are loosely coupled and can be tested apart from the entire system. These principles have led to a modular automotive design. On the WIKISPEED car, major subassemblies such as suspension, motor, and body can be replaced in the time it takes to change a flat tire. The wheels and suspension bolt to the chassis and can be repositioned or replaced. The composite body bolts to the chassis and allows exchange of external shells. The same car can be a race car today and a pick-up truck tomorrow. This modularity allows for rapid iterations and experimentations during development, testing, and after purchase. A mid-engine design ensures that the center of gravity is well-positioned no matter what engine is used. Production does not use metal stamping, molds, or autoclaves.

Keywords Agile development • Fuel efficiency • Distributed design • Lightweight materials • Modularity

F2012-E09-015

D. Socha
University of Washington Bothell, Bothell, USA

T. CFolsom (✉)
QUEST Integrated Inc, Kent, USA

J. Justice
Team WIKISPEED, Seattle, USA

1 Introduction

This paper describes how a distributed, collaborative team of volunteers spread around the world is creating, on a shoestring budget, a potentially transformative model for how to design and manufacture a highly efficient automobile.

Team WIKISPEED entered the Progressive Insurance Automotive X-Prize contest which challenged entrants to build a full-size, road-legal car achieving fuel economy of better than 100 mi/gal (2.25 L/100 km). A total of 136 vehicles entered the X-prize competition; WIKISPEED was one of only 10 in the full-size division that made it to the Michigan International Speedway for the shakedown stage 26 April–7 May, 2010. Part of the competition included methods by which a practical car could be produced; few, if any, of the other finishers are believed to be pursuing production.

WIKISPEED achieved the X-prize objective by using lightweight processes and lightweight materials. The car weighs only 638 kg due to construction from aluminum and composites. Our capital costs of production are low:

- There are no specialized plastic parts requiring molds.
- There is no metal stamping equipment, since all body parts are composite.
- The composite process does not require an autoclave.

WIKISPEED is doing this by borrowing and evolving concepts from a variety of sources such as agile and lean software development. In particular, WIKISPEED is adapting aspects of agile software development principles and practices to the research, design and production of physical products.

Other design forces include:

- A shoestring budget (less than \$100,000 by the end of the X-prize) that places a premium on continually reducing costs, and avoiding expensive standard solutions.
- A geographically distributed all-volunteer team (41 volunteers in 4 countries by the end of the X-prize), which is coordinated by an e-mail distribution list, kanban board, and weekly conference call.
- Joe Justice's background in software engineering and infectious enthusiasm.

The WIKISPEED project and car pioneer novel concepts in automotive production that could transform the industry. As of July 2012, WIKISPEED's growing team of over 170 volunteers in 15 countries continues to evolve the design of the WIKISPEED automobile, production process, and business model. For instance, our production paradigm might revolve not around a few capital intensive factories, but around thousands of small garages each producing a few cars.

2 Design Principles

WIKISPEED follows most of the suggested design principles and stages for sustainability [1]. The car is agnostic on the question of whether it is based on purely renewable energy; the modular structure allows multiple choices of power plant. It would be possible to use an electric motor for local driving and switch to a gasoline engine for long-distance trips. If non-renewable energy is used, the car seeks to utilize it as efficiently as possible. It is well known that reduced weight and improved aerodynamics greatly contribute to energy efficiency, but many designers have not concentrated on fuel efficiency [2, 3]. Making sustainability a priority has major impacts on a vehicle's design.

Established automobile organizations use traditional business models, tools and processes for researching, designing and producing automobiles. The purpose of a start-up company like WIKISPEED is to search for unknown business models [4]. WIKISPEED chose to use a distributed all volunteer team with very little capital, focus continually on sustainability, minimize material consumption, favor modularity and loose coupling wherever possible, favor incremental, iterative processes with rich feedback loops that promote rapid learning and reduce cycle time, distribute decision-making to as close to the work as reasonable, use morale to multiply velocity, and experiment with different business models.

These design principles manifest themselves in a number of practices, including: using a highly modular system of components that bolt to the chassis, enabling more experiments and concurrent engineering, creating very low-cost designs for parts and production, minimizing material consumption, creating tests before modifying any part, usually working in pairs, swarming to solve problems and remove blockages, using Scrum to organize work, and using kanban boards to make the work visible.

3 Agile Development

In order to support WIKISPEED's goals, Joe Justice and the WIKISPEED team adopted a variety of principles and practices from the community of agile software development, and continue to evolve them in order to fit the context of automobile research, design, and production. Note that agile software development evolved independently from Agile Manufacturing, though both were in response to similar design forces. "Agile" was first applied to manufacturing as early as 1992 [5], and to software development processes as early as 1998 [6].

Agile software development has a long history. It derives from the iterative and incremental processes used since some of the earliest software development projects [7]. For a number of decades, however, the vast majority of software driven projects used heavyweight and document driven "traditional" or "waterfall" processes (first requirements, then design, then build, then test). In 2001, a group

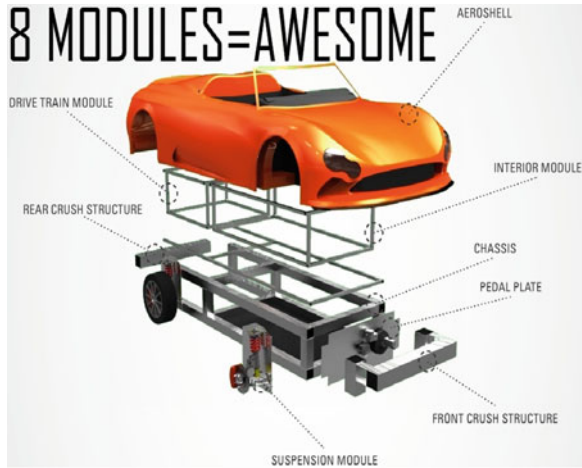
of 17 method leaders of “lightweight” software development processes met to find common ground against these “traditional” processes. The result was the Manifesto for Agile Software Development based upon twelve principles [8]. These twelve principles help guide WIKISPEED on a daily basis (when reading these, we can replace “software” with “product”):

1. *Our highest priority is to satisfy the customer through early and continuous delivery of valuable software.*
2. *Welcome changing requirements, even late in development. Agile processes harness change for the customer’s competitive advantage.*
3. *Deliver working software frequently, from a couple of weeks to a couple of months, with a preference to the shorter timescale.*
4. *Business people and developers must work together daily throughout the project.*
5. *Build projects around motivated individuals. Give them the environment and support they need, and trust them to get the job done.*
6. *The most efficient and effective method of conveying information to and within a development team is face-to-face conversation.*
7. *Working software is the primary measure of progress.*
8. *Agile processes promote sustainable development. The sponsors, developers, and users should be able to maintain a constant pace indefinitely.*
9. *Continuous attention to technical excellence and good design enhances agility.*
10. *Simplicity—the art of maximizing the amount of work not done—is essential.*
11. *The best architectures, requirements, and designs emerge from self-organizing teams.*
12. *At regular intervals, the team reflects on how to become more effective, then tunes and adjusts its behavior accordingly.*

Agile processes are now common in almost every sector of the software development industry, and continue to evolve to accommodate the diverse needs and constraints of the entire lifecycle of software development, diverse types of products, and the increasing complexity and size of software projects and products.

WIKISPEED is an experiment in applying those principles and processes to automobile research, design, and production. In particular, WIKISPEED borrows from extreme programming [9], Scrum [10], and radical management [11]. These processes have helped WIKISPEED create a research, design and production cycle in which changes can be made to any part of the automobile every week. While this paper is too short to cover the myriad of ways in which these principles inform and guide our day-to-day work, the following section describes some of the resulting innovations.

Fig. 1 Modular design



4 Lightweight Materials

The principles and practices mentioned above resulted in several innovations, including:

1. A highly modular automobile.
2. A lightweight (68 kg) aluminum load bearing chassis with high crash protection.
3. A low-cost process to create the car’s composite aeroshell without metal stamping, molds, or autoclaves.
4. A fuel-efficient engine control unit we call WIKISPEEDlet.

4.1 A Highly Modular Automobile

Modularity has been extremely important for creating large, high-quality software systems. It reduces complexity by hiding a module’s complexity behind an interface, divides the system into units that can be worked on by separate teams, and allows software engineers to more easily swap components.

The WIKISPEED car is modular to an unusual extent (Fig. 1). The wheels and suspension bolt to the chassis and can be repositioned or replaced. The composite body bolts to the chassis and allows exchange of external shells. The engine module uses a pedal plate incorporating the accelerator, braking system, and steering rack. This allows electrical, rather than mechanical control of the vehicle, which further reduces the weight. The mid-engine design locates the engine at the center of gravity, which means that the rest of the design can be independent of engine weight. Major subassemblies such as suspension, motor, and body can be replaced in the time it takes to change a flat tire. The same car can be a race car

Fig. 2 WIKISPEED chassis

today and a pick-up truck tomorrow. Modularity and drive-by-wire facilitates smart cruise control systems and additional driver-assistance systems such as collision avoidance, lane maintenance, or automated parking. The system is designed to allow fully autonomous driving with the addition of suitable sensor and software modules.

This modularity supports many of our design and process principles. It allows for rapid iterations and experimentations during development and testing. Loosely coupled components with simple and well-defined interfaces minimize system interdependencies, enabling more rapid and reliable software and hardware development. Modularity allows unit tests of individual systems, and supports concurrent engineering and experimentation. It leads to more innovation, which contributes to low design costs, low manufacturing cost, more long-term evolution and more consumer post-sale options.

4.2 A Lightweight Load Bearing Chassis

The principle of simplicity guided our design of a simple and lightweight chassis that has high impact ratings from a crash in any direction. The vehicle's chassis is a box formed by square aluminum 6,061 beams (see Fig. 2). The chassis and structural members were designed by several iterations of Computer Aided Design (CAD) and Finite Element Analysis (FEA). The car is a low-slung roadster with no door; stepping into it is no more difficult than mounting a motorcycle. Figure 3 shows great strength in a FEA simulated side impact; the force of impact is partially transferred to the opposite side.

The Center for Advanced Product Evaluation (CAPE) performed two physical impact tests on the WIKISPEED automobile in November 2011. While the structural carbon fiber aeroshell would have absorbed more impact force, it was

Fig. 3 Simulated side impact to chassis

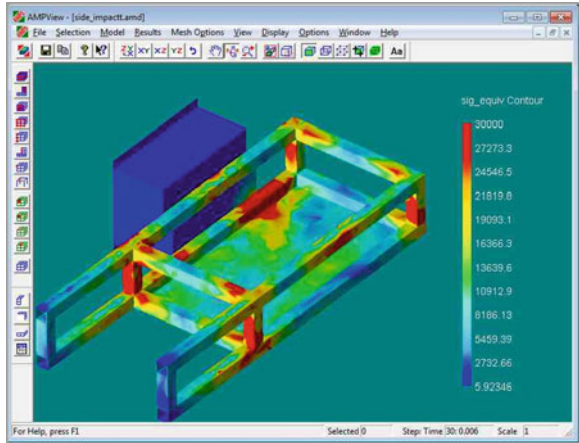
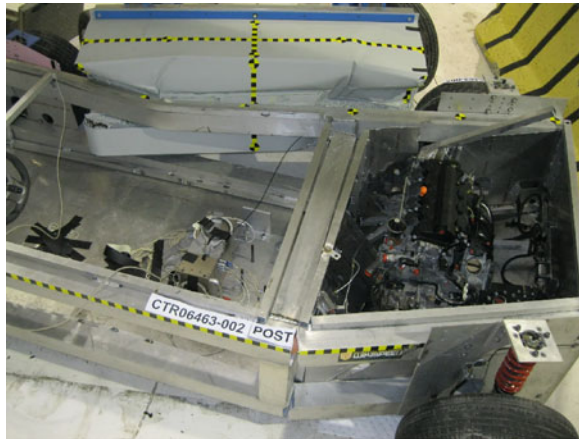


Fig. 4 Aftermath of side impact crash test



not included in the tests so that we could gain information on the chassis itself and thus verify full collision safety regardless of the additional benefit of the carbon fiber drop-on-body. This will allow us to change bodies and designs quickly without re-establishing impact safety.

Test 1 was a 40 mph frontal offset impact into a 40 % offset deformable barrier, as specified by the Insurance Institute for Highway Safety [12]. Test 2 was a side impact protection test hitting the side of the car with a movable deformable barrier to simulate a severe intersection collision between two passenger vehicles, as specified by the Federal Motor Vehicle Safety Standard FMVSS 214 [13].

These tests revealed failure modes at some welds (Fig. 4), and protrusion of the deformable barrier into the passenger compartment. We used the results of these tests to refine our simulation models leading to two changes:

Fig. 5 Side crush structure added after crash test



Fig. 6 Foam mold for composite layup



1. The original design uses front and rear crush structures of square tubes of 6063 aluminum. Aluminum side crush structures were rapidly retrofitted to the modular prototypes (Fig. 5).
2. Replacing the welds with riveted sockets in future versions.

4.3 A Low-Cost Composite Process

To minimize weight, we wanted to use a fully structural carbon fiber car body, however, the lowest bid of \$36,000 over three months (with waived labor costs) was beyond our budget. Fortunately, Robert Mohrbacher used his extensive composites experience to pioneer a composites process that takes considerably less time and money to go from a CAD drawing to a full structural carbon fiber car body. A key feature is a low-cost custom-built CNC machine for machining foam blocks. The process starts with a CAD drawing, which is verified against the module dimensions. The CNC machine then creates the body in foam (Fig. 6).

Fig. 7 Composite lay-up



Fig. 8 WIKISPEED car as of April, 2010, at progressive insurance automotive X-prize



Next, fibreglass is laid up over the foam to create a mold. Finally, carbon fibre is placed over the mold, air bubbles are squeezed out, and the body is heated by an electric blanket (Fig. 7). This process requires \$800 for materials, and takes three days; these significant savings in capital and time allow us to more quickly experiment and adapt.

Figures 8, 9 and 10 illustrate how the car’s aeroshell has evolved. The shell used in the Automotive X-Prize (Fig. 8) was the simplest and least complex solution. Subsequent iterations with the added criterion of aesthetic appeal produced the SGT01 race car design of Fig. 9. Greater emphasis on driver comfort and convenience led to the C3 comfy commuter car design of Fig. 10.

4.4 A Fuel-Efficient Engine Control Unit

The WIKISPEED STG01 X-Prize competition vehicle achieved 114 mi/gal highway in rigorous contest simulation. Although light-weight construction and efficient aerodynamics were contributing factors, much of this efficiency was

Fig. 9 WIKISPEED SGT01 car as of January, 2011, at the North American international auto show



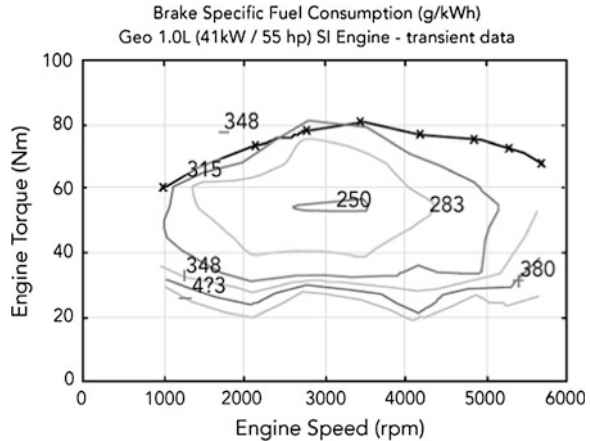
Fig. 10 WIKISPEED C3 car design, to be produced in July 2012



provided by the WIKISPEEDlet engine control system. This subsystem takes advantage of the well-documented fact that all internal-combustion piston engines have certain operating regimes with respect to engine rotational speed and dynamic loads at which the engine is considerably more efficient. Fuel efficiency can be measured by the Brake-Specific Fuel Consumption (BSFC), which is the ratio of fuel consumed to power produced. Each engine has different BSFC values at different speeds and loads. Typically, a reciprocating fossil fuel engine achieves maximum efficiency when the intake air is unrestricted, which means that the throttle valve is wide open, and the engine is running under fairly heavy load, or near its torque peak. For instance, Fig. 11 shows that the regime of greatest thermodynamic efficiency for a Geo Metro 1.0L engine is about 250 g of fuel per kilowatt-hour, when that engine is running at 3,000 revolutions per minute and producing 55 Newton-meters of torque.

The WIKISPEEDlet system uses sensor inputs, electronic control circuitry, and engine control outputs to keep the engine operating within its most fuel-efficient regime for a greater proportion of its running time. The result uses less fuel for a given amount of power output. WIKISPEEDlet operates on the principle of pulse and glide, a method by which a driver opens the throttle for efficient acceleration, and then lets the car coast to a lower speed. The strategy can double or triple fuel economy [15]. The result is that WIKISPEEDlet made an otherwise unmodified Honda R18A motor more fuel-efficient than any other production automotive engine, without wide swings in cruising speed.

Fig. 11 BSFC contour map for a geo metro 1.0L engine [14]



5 Conclusions

Based upon over two years of WIKISPEED experience, we summarize what has been important to date, and what might be applicable to other projects. The following were critical to the WIKISPEED project:

- Joe Justice’s persistently enthusiastic leadership.
- Borrowing and evolving principles and practices from agile software development, extreme programming, lean manufacturing, etc.
- Having access to little capital.

Would an organization of paid employees been able to be as innovative? We suspect the answer is no. In a volunteer organization, people work on what they are interested in doing; the power structure is very different than in an organization of work for hire. With very little capital, many standard solutions were too expensive, requiring the team to innovate dramatically less expensive (and often faster) solutions.

The term “extreme programming” was coined because the authors of that process combined 13 good practices to reap a synergistic result. The set of practices described in this paper may be the beginning of a similar set that could be called “extreme manufacturing” [16].

WIKISPEED is pioneering a qualitatively different approach to the research, design and production of automobiles. It has long been known that the Waterfall Method does not work well with software where requirements are unknowable and subject to rapid change. Lean product design and manufacturing both take a much more iterative approach to this work for physical products. WIKISPEED is trying to push this even further, largely by applying software design principles and practices to automotive engineering. Our experience indicates that this can dramatically speed up the automotive development time, reduce the need for expensive tooling, and potentially lead to a qualitatively different business model.

Our approach can set overly ambitious goals and not adhere to time estimates, but that is hardly unique in the industry. In a March 30, 2010 report Team WIKISPEED projected that in one month the car would be equipped with windshield wipers and defroster, filtered cabin air and heating, power mirrors, MP3/WMA player, navigation, driver eco-guide display, and a livable interior with cup-holders and cell phone storage nooks. As of July 2012 no prototype contains any of these features.

However, while it is possible to buy expertise and components, it is not possible to buy passion. Motivation is a multiplier for velocity, and the solid engineering accomplishments of the WIKISPEED car outweigh its Spartan interior. The WIKISPEED project has demonstrated how aluminum and composite structures can produce a lightweight vehicle. We designed a full-sized car, 1.96 by 4.22 m, weighing only 638 kg. The 68 kg aluminum chassis achieved high impact ratings from a crash in any direction. WIKISPEED offers prototype vehicles for \$25,000. Total expenditures through April 2012 were \$330,000, which resulted in construction of five prototype vehicles. We continue to innovate new and more effective ways to research, design and produce highly efficient roadworthy automobiles.

Acknowledgments This paper would not be possible without the continued support and effort of the growing team of WIKISPEED volunteers, whose passion and commitment to excellence is fundamental to the innovations described in this paper. The Automotive X-Prize provided the initial motivation to produce the WIKISPEED car, and our finish among the top ten resulted in free air bag design from Roush Enterprises.

References

1. Kor J et al (2010) Designing cars for renewable energy and the environment; describing a vehicle architecture appropriate for global markets in the 21st century, in FISITA 2010 World automobile congress
2. Amory B (2011) Lovins and rocky mountain institute, reinventing fire: bold business solutions for the new energy era. Vt.: Chelsea Green, White river junction
3. Folsom TC (2012) Energy and autonomous urban land vehicles. *IEEE Technol Soc Mag* 31(2):28–38
4. Blank S, Dorf B (2012) The startup owner's manual: the step-by-step guide for building a great company. K&S Ranch Press, Pescadero
5. Youssef M (1992) Agile manufacturing: a necessary condition for competing in global markets. *Ind Eng* 24(12):38–41
6. Dyba T (2008) Empirical studies of agile software development: a systematic review. *Inf Softw Technol* 50(9–10):833–859
7. Larman C, Basili VR (2003) Iterative and incremental development: a brief history. *Computer* 36(6):47–56
8. Beck K et al (2001) Manifesto for agile software development, Online available: <http://www.agilemanifesto.org/>. Accessed: 29 Jun 2012
9. Beck K (1999) Embracing change with extreme programming. *Computer* 32(10):70–77
10. Schwaber K, Beedle M (2002) Agile software development with scrum. Prentice Hall, Upper Saddle River

11. Denning Stephen (2010) *The leader's guide to radical management reinventing the workplace for the 21st century*. Jossey-Bass, San Francisco
12. IIHS (2008) *Frontal offset crashworthiness evaluation: offset barrier crash test protocol (Version XIII)*
13. U.S. department of transportation national highway traffic safety administration laboratory test procedure for fmvs 214s (STATIC) side impact protection, report TP-214S-05, 1992
14. Brake Specific Fuel Consumption (BSFC) Maps—EcoModder. Online available: [http://ecomodder.com/wiki/index.php/Brake_Specific_Fuel_Consumption_\(BSFC\)_Maps](http://ecomodder.com/wiki/index.php/Brake_Specific_Fuel_Consumption_(BSFC)_Maps). Accessed 12 Jul 2012
15. Lee J (2009) *Vehicle inertia impact on fuel consumption of conventional and hybrid electric vehicles using acceleration and coast driving strategy*, PhD. dissertation, Virginia polytechnic institute and state university, Blacksburg
16. Jakubowski M (2012) *Extreme manufacturing—open source ecology*. Online available: <http://blog.opensourceecology.org/2012/04/extreme-manufacturing/>. Accessed 05 Jul 2012]

Multi-Objective Evaluation Regulation Study of Automotive Lightweight

Hongzhou Lu, Zhiwen Wang, Ma Mingtu, Yilong Cheng
and Guimin Lu

Abstract Based on the multi-objective optimization and design of automotive body, the evaluation method of automotive lightweight is studied. An innovative evaluation method and the automotive lightweight comprehensive evaluation index E are presented, which is expressed by following formula $E = \frac{m_{\text{body}}}{C_t \times A \times [\text{ENCAP}] \times F} \left[\frac{\text{kg}}{\text{Nm}^{\sigma} \times \text{m}^2 \times \text{Hz}} \times 10^4 \right]$, and the weight of car body is associated with the model, stiffness of car body and safety of cars by this formula. The relationship between automotive lightweight and correlative functions is

F2012-E09-016

H. Lu (✉)

The School of Resources and Environmental Engineering, East China University of Science and Technology, Meilong Road 130, Xujiahui District, Shanghai 200237, People's Republic of China

e-mail: hongzhoulu@yahoo.cn

Z. Wang · Y. Cheng

Society of Automotive Engineers of China, 10/F, Tianlian Tower, No.102, Lianhuachi East Road, Xuanwu District, Beijing 100055, People's Republic of China

M. Mingtu

China Automotive Engineering Research Institute, No.101 Chaotiancun Chenjiaping, Jiulongpo District, Chongqing 400039, People's Republic of China

H. Lu

CITIC Metal Co., Ltd, Room 1901, Capital Mansion 6, Xin Yuan Nanlu, Chaoyang District, Beijing 100004, People's Republic of China

G. Lu (✉)

The School of Mechanical and Power Engineering, East China University of Science and Technology, Meilong Road 130, Xujiahui District, Shanghai 200237, People's Republic of China

e-mail: gmlu@ecust.edu.cn

discussed. The evaluation method is confirmed by applying the data of 14 typical passenger cars. The relationship between evaluation index E and relational parameters are discussed, and some comparison and analysis are carried out, the sensitivity of E value for varying of relational parameters values is demonstrated, and the sensitivity is acceptable. And according to the E value, the lightweight level of a car can be defined, which is from 1 to 5 stars. A requirement of integrated fuel consumption for lightweight star level based on car mass is presented to be as a modifier to modify the final star-rating results of a car. This evaluation regulation considers the modal, stiffness, and sizes of car body, and safety of cars, and fuel consumption which are associated with weight of car body and car mass. A conclusion is attained that the evaluation method of lightweight presented by this paper is feasible, however, the details of evaluation regulation of automotive lightweight will be studied further, and an official new car evaluation regulation of automotive lightweight will be presented. According to the evaluation results and stars rating, customers can choose to buy a more lightweight and energy-saving car. And based on the stars rating, governments can also improve energy saving and emission reduction of automotive industry, by encouraging the car makers which produce the lightweight cars.

Keywords Multi-objective · Lightweight · Evaluation · Safety · Star-rating

1 Introduction

Improvement of safety, reduction of energy consumption, and reduction of emission become one of the most highlighted issues for automotive industry in recent years. One of the most significant solutions, i.e. lightweight car has been described in this paper. Automotive lightweight is system engineering, and lightweight design and weight reduction of the car cannot always be measured in kilograms, but also has to be related to the achieved vehicle dimension and functional requirements. In order to benchmark the efforts for lightweight engineering, the specific lightweight coefficient L is developed [1, 2]. The ratio of structure weight of body-in-white (BIW) m_{Ger} (excluding glass) per static torsion stiffness C_t (with glass) and the associated footprint (track \times wheelbase) is evaluated as a customer relevant parameter. This lightweight coefficient indicates the weight savings of BIW, and the increased customer benefits are reflected in a decreased lightweight coefficient. However, the present specific lightweight coefficient is not taken all things into consideration, for example, the application of aluminium sheets in engine hood can reduce the weight and improve pedestrian protection, or the application of thinner high strength steel sheets in other covers

can reduce the weight of body, but the lightweight coefficient can't express and measure such a lightweight effect. What's more, the lightweight coefficient can express the lightweight of BIW but not for the whole vehicle. So it's necessary to present a new regulation to evaluate the lightweight effect of a car or BIW, and this evaluation regulation can improve the development of lightweight technology. Here, the lightweight evaluation was associated with the weight, eigenfrequency, stiffness of car body, safety, and mass and fuel consumption of whole car by this method.

2 Theory Analysis

2.1 *Natural Vibration Frequency*

The lower limit of material thickness occurs when the vehicle structure resonates at a frequency encountered within the driving range. In most automotive structures, it is desirable to have as high a natural frequency as possible. The limiting natural frequency of a structure is usually that which will occur at the maximum speed of the vehicle. For example, if the maximum speed of a car is 120 km/h, then the first order natural vibration frequency should not occur until a speed greater than 120 km/h. So improving the natural frequency of car body is an important aim during the development of a new model.

In automotive applications, one type of motion and resistance is cyclic motion-vehicle vibration resistance. The vibration resistance implies a wide range of dynamic modulus values and a wide range of tangent modulus values depending on the amplitude of stress applied and the yield strength of the material [3].

According to lots of analysis, a conclusion were attended about a relationship of thickness of materials, natural frequency of structure, yield strength of materials, and the stress amplitude acted on the structure. For the structures of constant yield strength, as thickness decreases, natural frequency decreases. And under the condition of constant cyclic load amplitude, for the structures or parts, as thickness decreases (constant yield strength), stress amplitude increases and natural frequency decreases. And if yield strength of materials increases, dynamic modulus increases and natural frequency increases.

So the natural vibration frequency of car body is correlative with thickness of materials and yield strength of materials, however, thickness decreases and yield strength increases of materials are the main methods for lightweight. So for these structures requiring weight reduction (thickness decreases), a conclusion has been got that with a 10–20 % decrease in thickness and a 50 % increase in yield strength, increased dynamic modulus will offset the decrease in section modulus thus allowing the natural vibration to remain constant. In a word, the natural vibration frequency of car body and lightweight is related closely.

2.2 Safety

The material gauge decrease of parts and property changes of materials may influence the safety performance of cars, so the passive safety performance is a key target for execution of automotive lightweight engineering, and passive safety must be improved or keep stable, or the decrease extent of passive safety performance is acceptable for some car. “How to Make a Car Lighter and Safer” has been discussed in literature [4], and a statistics conclusion is attained that increasing the amount of light-weight materials in a vehicle can lead to lighter, larger vehicles possessing all of the following concurrent characteristics: reduced risk to its occupants in two-vehicle crashes; reduced risk to occupants in other vehicles into which it crashes; reduced risk to its occupants in single-vehicle crashes.

However, the development of lighter and smaller passenger car has been a trend, so “how to make a car lighter, smaller and safer” is a challenge. The application of high strength materials is a solution, and the advantages in crush performance with increases in material yield strength have been well documented [5]. It makes no sense for a car which is lighter but not safe.

NCAP is always used to evaluate the safety performance of cars, and ENCAP is applied in Europe and CNCAP is applied in China.

2.3 Size of Vehicle

It is very easy to understand that there are some relationships between car mass and size of cars. The car mass increases generally along with increscent size of body, which is seen in Fig. 1, and the statistics between car mass and the integrated fuel consumption is seen in Fig. 2, and the incremental trend of the integrated fuel consumption can be seen along with weight enhancement of cars. So the approximate relationships among size of body, car mass and fuel consumption of cars can be presumed, that more fuel consumption for a car whose body size is bigger.

2.4 Stiffness

A very important vehicle structural requirement is stiffness. This was thought to be controlled by shape, thickness, and Young’s modulus. It is generally accepted that Young’s modulus for steel is fairly constant and independent of yield strength. Therefore, for a given component, any reduction in thickness should reduce stiffness, accordingly. However, Kasper [2] found that the thinner gage high strength steel vehicle was significantly stiffer than the comparable mild steel

Fig. 1 The statistics between car mass and the associated footprint

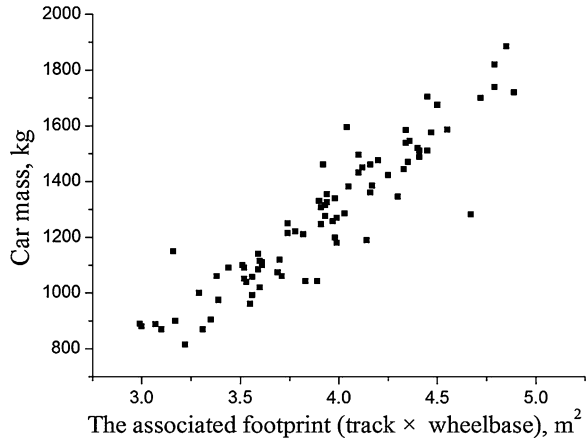
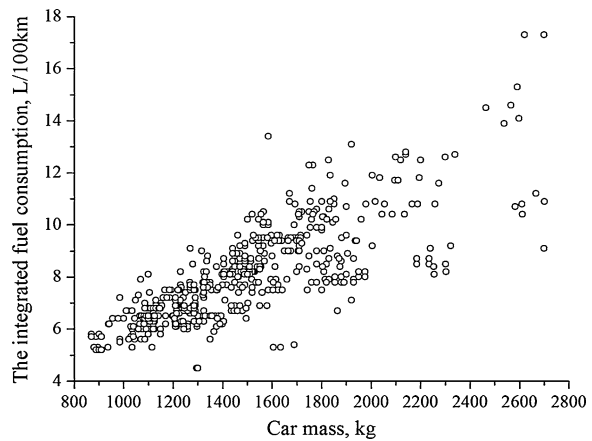


Fig. 2 The statistics between car mass and the integrated fuel consumption



vehicle and as stiff as the heavier production vehicle. Their studies show that high strength steel has higher dynamic stiffness and improved vibration response in structures as compared to that of lower strength steel. Thus, high strength steel can be used advantageously in stiffness controlled automotive structures to achieve greater weight reductions.

The primary goal for static design of the body-in-white is the optimization of the stiffness and strength for the quasi-static driving dynamics. Solid static characteristics lay the foundation for solid dynamic structural design. To keep the load on the bonded windscreen at acceptable levels and avoid stone damage from high surface tension, the stiffness of the body-in-white structure without glass must attain 2/3 of the target with the glass bonded into place.

Table 1 The lightweight comprehensive evaluation index E for 14 typical cars

Model	Car body weight with hang-on parts, kg	Car body weight without hang-on parts, kg	ENCAP total points ratio	The first torsion frequency of body, Hz	The static torsion stiffness of body, Nm/°	The specific lightweight coefficient L	The lightweight comprehensive evaluation index E
1	377	281	0.839	37.6	16,441	4.15	1.768
2	461	369.8	0.828	32.2	17,200	4.91	2.296
3	372	308	0.825	35	23,400	3.16	1.324
4	365	267	0.833	44	20,700	2.9	1.152
5	411.5	318	0.804	37	21,800	3.26	1.419
6	305	227	0.775	43	18,000	3.5	1.376
7	373.6	278	0.779	39	21,500	3.27	1.444
8	415.5	330.8	0.806	39.2	20,500	3.88	1.543
9	499	428	0.897	40	27,500	3	1.011
10	361.27	287.57	0.836	35.5	14,500	5.21	2.209
11	492	401	0.788	52	29,920	2.89	0.868
12	376.2	290.6	0.803	40.6	19,833	3.68	1.461
13	421.1	325	0.795	38.5	21,000	3.90	1.653
14	335	270.4	0.813	38.6	17,600	4.16	1.644

3 Lightweight Star-Rating Regulation

$$E = \frac{m_{Body}}{C_t \times A \times [ENCAP] \times F} \left[\frac{kg}{Nm/^\circ \times m^2 \times Hz} \times 10^4 \right] \tag{1}$$

Where E expresses the lightweight comprehensive evaluation index E, structure weight m_{body} (including hang-on parts but excluding glass) and C_t represents static torsion stiffness of car body without doors and closures but with class, parameter A represents the associated footprint (track \times wheelbase), and parameter F represents the first torsion eigenfrequency of body. Parameter [ENCAP] represents total points ratio of ENCAP after 2009, [ENCAP] can be got in formula 2,

$$[ENCAP] = X_1 \times 50 \% + X_2 \times 20 \% + X_3 \times 20 \% + X_4 \times 10 \% \tag{2}$$

Where X_1 represents adult occupant, X_2 represents child occupant, X_3 represents pedestrian, X_4 represents safety assist. And the conversion can be attained from CNCAP points to total point ratio of ENCAP by formula 3, so the formula 1 can be expressed by formula 4. And according to formula 1 and 4, and based on the data of 14 typical cars, the lightweight comprehensive evaluation index E is calculated, and the index E and relative parameters are shown in Table 1.

$$[ENCAP] = [CNCAP]/60 \tag{3}$$

$$E = \frac{m_{Body} \times 60}{C_t \times A \times [CNCAP] \times F} \left[\frac{kg}{Nm/^\circ \times m^2 \times Hz} \times 10^4 \right] \tag{4}$$

Table 2 Lightweight star rating standard







Level	The lightweight comprehensive evaluation index E
	$E \leq 1.0$
	$1.0 < E \leq 1.5$
	$1.5 < E \leq 2.0$
	$2.0 < E \leq 2.5$
	$2.5 < E \leq 3.0$
	$3.0 < E \leq 4.0$

Table 3 The requirement of integrated fuel consumption for lightweight star level based on Car Mass

Car mass kg	Car with two or less than two rows of seats, and equipped with manual transmission, L/100 km	Car with three or more than three rows of seats, or equipped with automatic transmission, L/100 km
$CM \leq 750$	4.8	5.2
$750 < CM \leq 865$	5.1	5.4
$865 < CM \leq 980$	5.3	5.7
$980 < CM \leq 1,090$	5.6	6.0
$1,090 < CM \leq 1,205$	6.0	6.3
$1,205 < CM \leq 1,320$	6.3	6.6
$1,320 < CM \leq 1,430$	6.7	6.9
$1,430 < CM \leq 1,540$	7.1	7.3
$1,540 < CM \leq 1,660$	7.5	7.7
$1,660 < CM \leq 1,770$	7.9	8.1
$1,770 < CM \leq 1,880$	8.3	8.5
$1,880 < CM \leq 2,000$	8.7	8.9
$2,000 < CM \leq 2,110$	9.1	9.4
$2,110 < CM \leq 2,280$	9.5	9.9
$2,280 < CM \leq 2,510$	10.2	10.5
$2,510 < CM$	10.9	11.3

According to Table 1, a propositional lightweight star level standard is presented in Table 2 in this paper. 5 lightweight star rating levels are presented according to the lightweight comprehensive evaluation index E.

The main aim of presenting evaluation regulation of automotive lightweight is to reduce the weight of car body and car mass. However, the final aim of the evaluation regulation of automotive lightweight is to improve energy saving and emission reduction of automotive product, in fact, the methods of improving energy saving and emission reduction are not only including lightweight technology, but also including engine, transmission, and other technologies. So for lightweight star level, the requirement of integrated fuel consumption basing on car mass must be considered, which is seen in Table 3, and this table will be as a modifier to confirm the final star-rating results of a car.

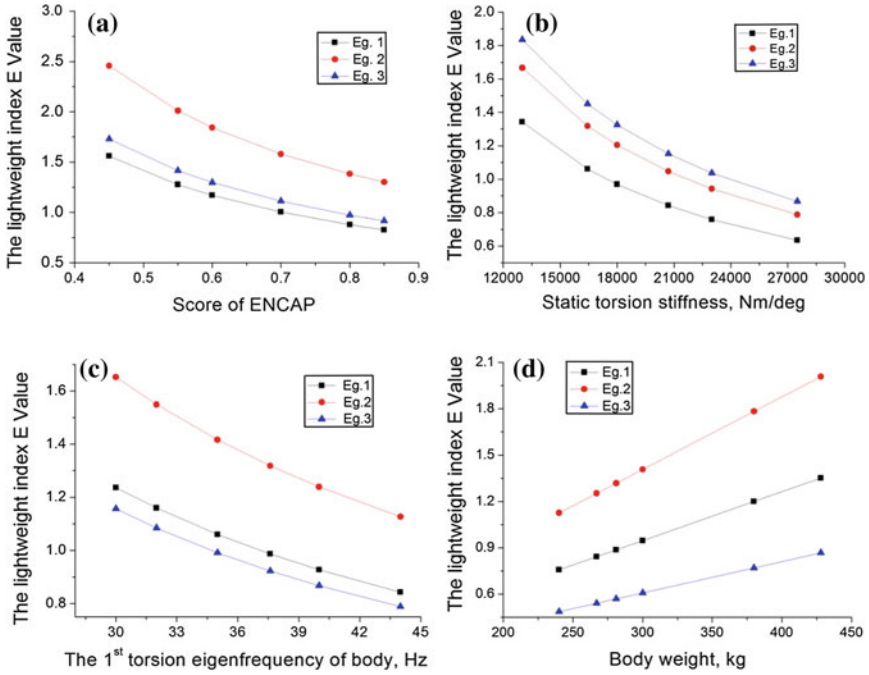


Fig. 3 The sensitivity of E value relative to the variation of relational parameters values, 3 typical car cases for example. **a** The curve of the lightweight index E values and the different scores of ENCAP. **b** The curve of the lightweight index E values and the different static torsion stiffness values. **c** The curve of the lightweight index E values and the different first torsion eigenfrequency values of body. **d** The curve of the lightweight index E values and the different body weight values

The Integrated fuel consumption value must be attended according to some universal standard, such as GB/T 19233-2008: measurement methods of fuel consumption for light-duty vehicles. The Integrated fuel consumption value is an important target, if the measure result of a car meets Table 2, and it has to meet Table 3, then a relative lightweight star rating level of Table 2 could be awarded for the car. And one-rating modifier will be applied if the measure result of a car meets Table 2, but it doesn't meet Table 3, then a degrading lightweight star level will be awarded for the car.

4 Discussion

Based on 3 typical car cases and according to the formula 1, the sensitivity of E value relative to the variation of relational parameters values is analyzed, which is shown in Fig. 3. For most car models, the score of ENCAP is in 0.6~0.8 scales, and the lightweight comprehensive evaluation index E value has a moderate variety in

Table 4 Performance parameters of car body

Weight of body with doors and closures (kg)	C-NCAP points	The torsion stiffness (Nm/deg)	The 1st torsion eigenfrequency of body (Hz)	Track × wheelbase m ²	Lightweight coefficient	Lightweight evaluation index E
367	46.5	18,598	43.36	4.1	3.63	1.43

this scale, see Fig. 3a. In order to improve passive safety of a car, the structure of car body must be optimized and more high strength steels or other good energy-absorbing materials should be used, and in this condition, thinner high strength steel sheets and lighter aluminium alloy will reduce the weight of the car.

Static torsion stiffness of car body and body weight are more sensitive for the lightweight index. The lightweight index E value has an obvious variety along with the change of the static torsion stiffness of car body and body weight parameters, which are seen in Fig. 3b and d. The static torsion stiffness of car body depends on structure and geometry section of parts, however, thinner materials or lower elastic modulus materials may decrease the stiffness and eigenfrequency. From Fig. 3c, the lightweight evaluation index E value has a moderate variety in 30~45 Hz scales.

Conclusively, the sensitivity of E value relative to varying of relational parameters values is demonstrated, and the sensitivity is acceptable.

A Chinese domestic car is analyzed to confirm the feasibility of the regulation mentioned above, whose parameters are in Table 4.

According to formula 2, the total point ratio of [ENCAP] of this car is equal to 0.775, and the lightweight comprehensive evaluation index of this car is 1.43, comparing to Table 2, 5 stars should be awarded for this car. However, the integrated fuel consumption for this car equipped with manual transmission is 7.3 L/100 km, and car mass is 1,265 kg. According to Table 3, the integrated fuel consumption for this car is higher than the standard of Table 3, so one-rating degrading modifier will be applied for this car, and finally, 4 stars can be awarded for this car. According to this evaluation result and regulation, some improvements can be presented for this car for getting better lightweight level, for example, the weight of body should be reduced further using more high strength materials or lighter alloys, and structure should be optimized, and what’s important is to optimize the vehicle power system, so a energy-saving engine and better engine matching and calibration should be applied.

However, there are several limitations of this evaluation regulation, firstly the more rational level of star-rating needs to be redefined later, and if possible, it’s better not to use the results value of NCAP, because the X₄of NCAP represents the active safety of automobiles, and an another passive safety evaluation parameter should be applied instead of NCAP in formula 1. The evaluation regulation in this

paper is mainly for traditional fuel consumption passenger cars, however, the car mass of new energy cars should be reduced to balance out the weight increment due to the heavier batteries and electric machines, so the modifier which is seen in Table 3 should be redefined for lightweight evaluation of new energy cars.

The standardization of data acquisition and testing methods of relational parameters in formula 1 and 4 are of importance, and some existing testing standards will be used and some new testing standards will be established for this evaluation regulation. For example, the value of the static torsion stiffness is measured on a torsion test stand with a torque of 4,000 N/m, and the static torsion stiffness is the rotational moment needed to rotate the body-in-white at the spring domes along its longitudinal axis. And these uniform testing standards must be carried out to make the results comparable.

5 Conclusion

The aim of the evaluation regulation of automotive lightweight is to improve energy saving and emission reduction of automotive products. This paper presents an innovative evaluation method and the lightweight comprehensive evaluation index E , which is expressed by following formula $E = \frac{m_{\text{body}}}{C_t \times A \times [\text{ENCAP}] \times F} \left[\frac{\text{kg}}{\text{Nm}^\circ \times \text{m}^2 \times \text{Hz}} \times 10^4 \right]$, and the formula considers the modal, stiffness, and sizes of car body, and safety of cars, which are associated with weight of car body. According to the evaluation formula, an evaluation regulation of the lightweight is presented including the star-rating level of a car, which is from 1 to 5 stars. A requirement of integrated fuel consumption for lightweight star level based on car mass is presented to be as a modifier to modify the final star-rating results of a car. The sensitivity of E value relative to varying of relational parameters values is demonstrated, and the sensitivity is acceptable.

References

1. Zipse O, Luedke B (1999) Functional design of lightweight body-in-white structures: how to determine body-in-white materials according to structural requirements. JSAE Annu Congr no 18–99, AGE.1–4
2. Mingu M, Hongliang Y, Hongzhou L, Xinming W (2012) On the automobile lightweight. Eng Sci 10(2):71–77
3. Kasper AS, Swenson WE, Dinda S, Cheng F-L (1979) Kinetic modulus of steel: a new automotive design parameter. SAE Technical Paper 790003. doi:10.4271/790003
4. Evans L (2004) How to make a car lighter and safer. SAE technical paper 2004-01-1172, 2004, SAE 2004 world congress and exhibition, March 2004, Detroit, session: achieving light weight vehicles (part 1 and 2)
5. VanKuren RC, Scott JE (1977) Energy absorption of high-strength steel tubes. Paper 770213 presented at SAE automotive engineering Congress. Detroit, Feb 1977

Future Mobility Requires Advanced Car Concepts and Power Train

Sven Augustin

Abstract *Research and/or Engineering Questions/Objective* Mobility is essential for well performing economy. One Billion vehicles are on the road globally. In 20 years the fleet is estimated to double. Global crude oil demand and prices are growing. To secure economy by well performing mobility there are only two main routes to go. (1) Broader range of different power train. (2) Energy Efficiency Measures. Besides power train efficiency the curb weight reduction is an effective solution applicable for all energy and vehicle types. In 2007 Evonik Industries started to evaluate a variety of polymers and material concepts for different automotive applications. The variety of polymers, reinforcement fibres, core materials and processes represent a huge number of potential solutions competing with established materials. On the other hand this complexity is an excellent opportunities for cost effective parts. Applying new composite material technologies also offer new design options such as large and complex body parts manufactured in “one shot”. *Methodology* All existing and coming up material concepts, different production processes of those and different applications for automotive serial application were studied. The Target was to find out the best combination relating cost, performance and weight reduction potential. The material concepts were proofed under severe conditions on the race track and in parallel with a road approved car. *Results* The factors weight reduction, performance, costs and annual production volume of lightweight parts were evaluated in detail to meet automotive targets. In this process Sandwich Composite Bodywork and Polymer Glazing were identified as promising future applications of novel material concepts. For automotive application new efficient processes have to be developed with adjusted chemistry to meet automotive quality and serial volume capability. *Limitations of This*

F2012-E09-025

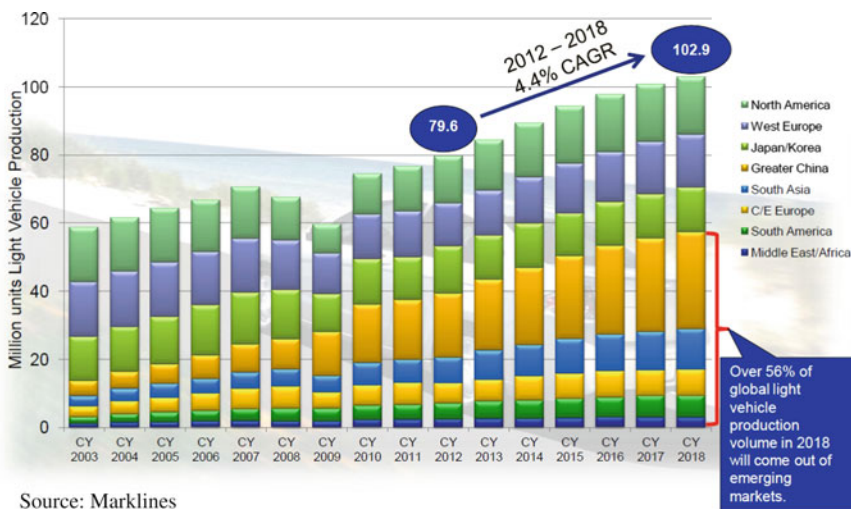
S. Augustin (✉)
Evonik Industries AG, Essen, Germany
e-mail: sven.augustin@evonik.com

Study Evonik is supporting the new process technology developments for the new material concepts in co-operations. The developments are highly confidential and cannot be disclosed. *What does the Paper Offer That is New in the Field in Comparison to Other Works of the Author* The paper includes the potential of polymer lightweight material concepts and the gaps to be closed to succeed for automotive serial application. The paper shows very promising routes and also the very fast testing of those routes at demonstration cars. *Conclusion* To demonstrate the feasibility two sport cars were built with Evonik material concepts. Features are light weight body, polymer screens, friction reduced engine oil, low weight and rolling resistant tires and additional measures. This electric powered demonstration car achieves a better balance of performance, range and cost by development and application of new material concepts. In comparison to the Tesla the Evonik E-Elise is 255 kg lighter and has 3/5 of battery capacity.

Keywords Lightweight design · Electric power train · Composite · Polymer glazing · Li-ion battery

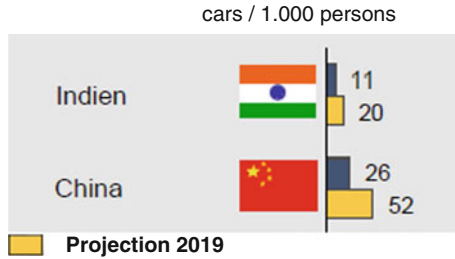
From 2002–2006 the SEPARION Team of Degussa developed Lithium-Ion battery separators for large format cells. There had been close contacts to global potential Lithium-Ion battery companies and automotive OEMs working on Hybrid-Electric- and Battery-Electric-Vehicles. There was coming up a new challenge additionally to the very complex battery technology. The Hybrid-Power train increases weight of the car—the Full-Electric Power train even more. This is contra productive to fuel saving of this power train.

2007–2008 the automotive team was running a corporate lightweight design project to find solutions with polymer material concepts which extremely reduce weight and could be manufactured at acceptable costs.

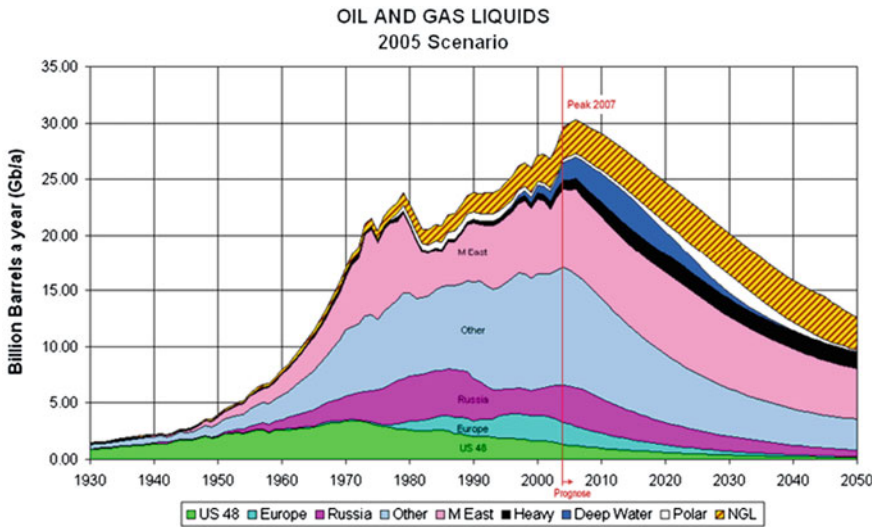


Source: Marklines

The projection of global car production is more than 100 Mio/a for year 2018. 56 % thereof are estimated to be produced in emerging markets, China, Thailand, Malaysia, Brasil and India. China and India have a very huge domestic demand for emerging car density.

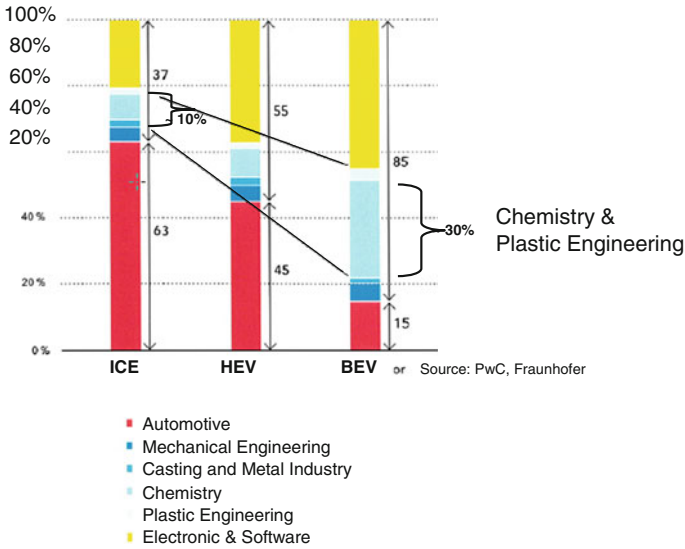


Crude Oil is limited and the price will increase. Alternative fuels will become more important in future to realize global mobility, economy growth and life style.

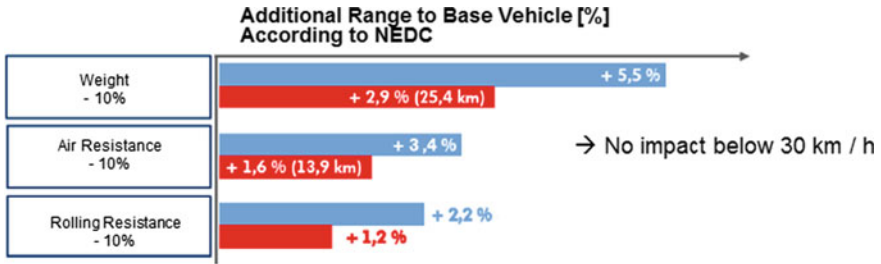


The other and more important route is fuel saving. The power train efficiency is the most important parameter to succeed. Additional measurements are the rolling resistance of tires, the aerodynamic and the weight.

Multi material concepts are needed to extremely reduce the weight. The production processes for the new polymer solution are very complex as mechanical engineering, simulation-technology, chemistry, tooling, automated processing and automotive production line integration know how is needed. New company co-operations have to be realized and should work very close together. The connection of the different materials and long term behaviour are additional topics to be find out and developed.



The whole value chain for Battery-Electric-Vehicles is new and not really existing. Know how for that type of cars at the OEM is currently limited.



BEV in Mega Cities: Impact of Weight & Rolling Resistance are even more

Base Vehicle	Golf 1.4L/90 kW TSI MQ	Golf Blue-e-Motion 85 kW
Weight	1215 kg	1554 kg
Range	887 km	150 km

Source: Dr. Ing. Klaus Rohde-Brandenburger, Volkswagen AG, Karosseriebauteile Hamburg, ATZ live, 2012, May 11th

Especially for the Battery-Electric-Vehicles the weight is key to cut the total costs of the cars and the needed range. By reducing the weight of the car less battery capacity is needed which reduces the weight additionally as the battery power train by itself reduces range caused by weight.

New tires are getting also very important. The requirements for Battery-Electric-Vehicle Tires which drive in Mega Cities should be worked out very soon to reduce battery capacity.

The automotive team together with the Evonik Business Units and external experts developed and build up a battery electric powered car with 31 kWh capacity.

The Body is made of carbon fibre reinforced sandwich composite material which reduces the weight by 60 % to traditional steel.

Special hardening systems for epoxy resin infusion process were developed and processed in vacuum infusion process. This system could be transferred to high performance resin transfer moulding processes.

For high stiffness requirements special structural core foam was used to reduce the carbon fibre content at that area. With this special foam a fast curing process is possible.

The mineral glass screens were replaced by a new developed polymer grade to reduce weight by 50 %. The screens are abrasion resistant coated. This PMMA material is UV resistant and keeps the transparency long term. The acoustic behaviour is excellent.

Further new tires with special inorganic materials are assembled which improved the rolling resistance by 30 % to the conventional used tire.

In total this demonstration car has additional 10 % range–22 km by above mentioned measurements.

Body work:

CFR-Epoxy Sandwich

Side screens: PMMA

Tires: with Silica/Silane

Powertrain: 40 Ah Li-ion cells

Curb weight: 1.062 kg

Power: limited to 130 kW

Capacity: 31 kWh

NEDC- Range: 240 km

4,6 sec. for 0 - 100 km/h*

limited to 200 km/h

manual 6 speed

* calculated value



A Lightweight Optimization Method of Vehicle Body Structure Design

Zhixiang Li and Jifa Mei

Abstract Lightweight body is effective for reducing the concentration of pollutant in emissions, improving crashworthiness performance and dynamic performance. Lightweight Index, which is proportional to body mass and inversely proportional to torsion stiffness, is used to evaluate the lightweight degree of body structure. Lightweight index can be reduced according to increasing torsion stiffness and reducing mass. The calculation of body stiffness is a linear process, which can be simulated by finite element analysis with high precision. In this paper, the torsion stiffness of a vehicle body was studied by using CAE analysis software. After simulation, the lightweight index was calculated according to body mass and torsion stiffness. For the purpose of improving lightweight index, body structure should be optimized to improve torsion stiffness and decrease body weight. At first, using sensitivity analysis, this paper studied the influence of 50 main parts' gauge to torsion stiffness and body weight, these parts thickness were set as variables in optimization. Then, after optimization, by comparing sensitivities of torsion stiffness and body weight, this paper identified key parts of a car body, according to optimizing the gauges of parts, the body weight decreased 3.1 kg, while torsion stiffness increased 38 Nm/deg. Comparing with part thickness, part structure has greater affection to the stiffness property, topography optimization can be used to optimize the design of part structure and shape. In this paper, coat rack structure was studied, through topography optimization to find the best optimized structure with manufacturing requirement. Vehicle parts are designed not only considering stiffness performance, but also taking into account strength, crashworthiness, NVH performance and so on, only body torsion stiffness for study has limitation. Topography optimization can

F2012-E09-026

Z. Li (✉) · J. Mei
SAIC MOTOR Technical Center, Shanghai, China
e-mail: lizhixiang@saicmotor.com

only find optimal part structure, however, manufacturing costs and feasibility should be considered. In this paper, CAE software tools were used to perform sensitivity analysis and optimization, parts gauges were set as variables to optimize body stiffness and weight, and topography optimization was used to optimize rib structure and position of coat rack, which gave a simple way to lightweight body design and optimize.

Keywords Lightweight · Torsion stiffness · Topographic optimization · Sensitivity analysis · Coat rack

1 Foreword

Body mass is a major component of the whole mass of a vehicle, usually accounts for more than 30 % of the whole mass. Automotive weight directly influences vehicle passive safety performance, NVH performance, exhaust emissions and vehicle handling performance [1]. With the national vehicle emission regulations and safety regulations more and more stringent, the requirement for automotive weight become stricter, and how to design automotive products to meet all laws and regulations on the premise of with minimize body mass, has become one of the main research directions of the automotive industry.

The lightweight vehicle body design method, which is using advanced production technology, innovative materials and optimal design technique to optimize body structure of the initial design to meet the target design performance with optimal mass of the body structure [2]. When a car is traveling on the road, it will bears a variety of loads from uneven road, these loads can be divided into bending load and torsion load, while torsion loads on the structure of a vehicle are more serious, they may cause door deformation, sealing strips off, local deformation of body structure or even local cracks, so body torsion rigidity is one of the most basic and important performance of the body structure. In this paper, using finite element analysis optimization method, the torsion rigidity of a car body was studied to get optimized parts gauge and structure to improve body torsion stiffness and reduce body mass.

Torsion stiffness of vehicle body can be analyzed using the simulation analysis and experimental analysis, simulation analysis is use finite element method to build model of actual torsion stiffness experiment, and then calculate its stiffness by compute. The performance of current computer can be timely and effectively calculate a highly detailed finite element car body model with satisfied accuracy. Thanks to CAE method, it will save much of the test cost, timely guide the design of the body structure, and propose optimization approach; finite element method has become indispensable in the process of design and analysis of car body property [3].

During the structural optimization, at first, sensitivity analysis should be conducted to determine the sensitivity of the design variables to the objective [4], and then modify design variables according to the sensitivity to gain optimal design goal with constraints condition. The sensitivities of design variables are relative to

the objective function, which are measured by the change of objective caused by the change of unit design variables, sensitivity analysis is the basis of the optimization analysis, optimization of structure can be carried out based on sensitivity analysis, which will save a lot of computing time and improve the optimization efficiency.

2 Basic Theory of Sensitivity Analysis

The structural analysis can be divided into two aspects of dynamic analysis and static analysis, the structure sensitivity analysis can also be divided into dynamic sensitivity analysis and static sensitivity analysis. Dynamic sensitivity analysis including eigenvalue sensitivity analysis, transfer function sensitivity analysis and dynamic response sensitivity analysis. The static sensitivity analysis can be stress, displacement and so on. For the car, the sensitivity analysis refers to body stiffness, strength, free mode and sensitivity analysis of the strain energy, part structural parameters including material, thickness, and cross-sectional moment of inertia [5].

The sensitivity of the shell element thickness to static stiffness can be expressed as follows:

$$\{u_{,h}\}_{n \times 1} = -[K]_{n \times n}^{-1} \sum [k_{,h}^e]_{ne \times ne} \{u^e\}_{ne \times 1}$$

In the expression: $\{u^e\}_{ne \times 1}$ is the component of element in $\{u\}_{n \times 1}$, ne is the freedom of element; h is element thickness, $[K_{,h}^e]_{ne \times ne}$ is extended element stiffness matrix

$$[K^e]_{ne \times ne} = [K_m^e]_{ne \times ne} + [K_b^e]_{ne \times ne} = Eh [K_1^e]_{ne \times ne} + Eh^3 [K_2^e]_{ne \times ne}$$

In the expression: $[K_m^e]_{ne \times ne}$ and $[K_b^e]_{ne \times ne}$ are the membrane stiffness and bending stiffness of shell element, E is material elastic modulus, $[K_1^e]_{ne \times ne}$ and $[K_2^e]_{ne \times ne}$ are independent on E and h , and:

$$[K_{,h}^e]_{ne \times ne} = E [K_1^e]_{ne \times ne} + 3Eh^2 [K_2^e]_{ne \times ne} = Fc [K_1^e]_{ne \times ne} + Fc^3 [K_2^e]_{ne \times ne}$$

In which, $c = \sqrt{3h}$, $F = \frac{E}{c}$, so the sensitivity of elements thickness to element displacement can be gained by re-calculate the element stiffness matrix.

There are two types of method to calculate sensitivity, derivation method and the accompanying structure method. Direct derivation method, which was proposed by Fox. R. L and Kapoor M. P, and then developed and promoted by many people in a wide range of areas. Direct derivation method has clear physical concept, simple mathematical theory, convenient to calculate and can be extended from the first-order sensitivity to the high-order sensitivity, therefore, it is widely utilized in industry areas [6].

3 BIW Torsion Stiffness Analyses

Finite element model of a car BIW is shown in Fig. 1, which consists of 769 862 elements including triangular elements and quadrilateral elements, the overall weight is 371.2 kg.

In order to compare with the vehicle torsion stiffness test process, finite element analysis model required to use beam element with diameter of 50 mm to simulate the test equipment such as Fig. 2. The boundary conditions of finite element analysis model is shown in Fig. 3, both the left and the right rear shock towers hard point are constrained at X, Y, Z translation DOF, the left and the right front shock absorber towers are constrained at X direction DOF. The loads are applied to the center of both front shock towers in the vertical direction, which are equal but with opposite direction. The load is obtained by the formula $F = M/L$, where M is the test torque value, L is distance between the center of right and left front shock tower. The stiffness result has nothing to do with the imposed torque, but for the purpose of compare with test result, the applied torque is 4,000 Nm, the test process is shown in Fig. 4.

The Z direction displacements of the left and right load point are exported to compute torsion stiffness value, torsion stiffness K_t is calculated using formula as follows:

$$K_t = \frac{M}{\arctg[(\Delta Z_L + \Delta Z_R)/L]}$$

M is imposed torque; ΔZ_L and ΔZ_R are Z direction displacement of load points; L is the distance between load points.

The lightweight index [7], which is one of the key factors to evaluate the performance of body structure, is calculated by body torsion stiffness and mass, the less the better. Light weight index is proportional to body mass and the inversely proportional to torsion stiffness, therefore to reduce the lightweight index, the most effective way is increase the torsion stiffness while reducing body mass, body lightweight index is calculated as follows formula.

$$L = \frac{M}{K_t \times A} \frac{kg}{Nm/^\circ \times m^2} \times 10^3$$

In the formula: M is the body mass; K_t is torsion stiffness; A is body project area (wheelbase \times tread).

Through analysis and calculation with finite element software, the stiffness of the body is shown in Table 1, the contours display of body Z direction is shown in Fig. 5, according to the figure, the displacement of the body is changed continuously, in line with the expected load case.

Fig. 1 FEA model of BIW

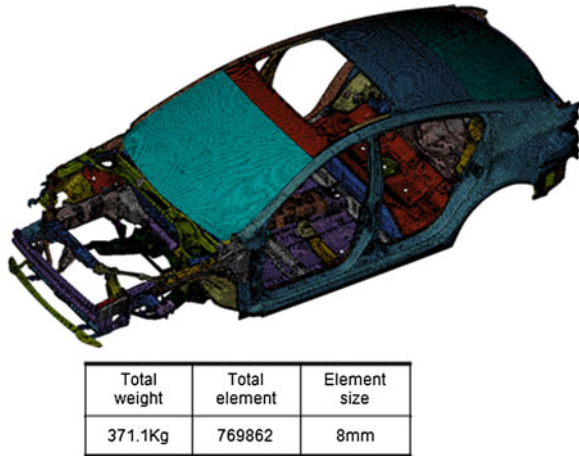


Fig. 2 FEA model of test equipment

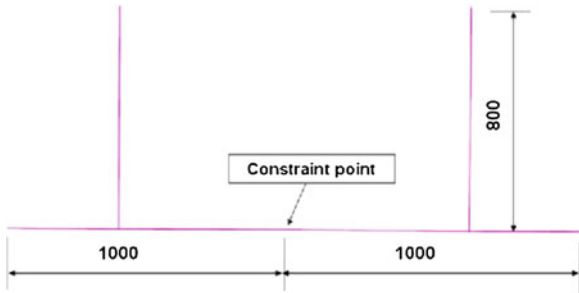
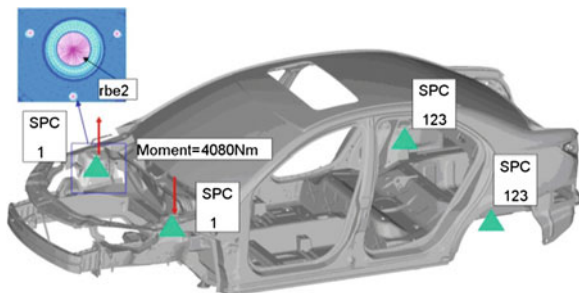


Fig. 3 Boundary condition of stiffness analysis



4 BIW Structure Stiffness Sensitivity Analysis and Optimize

According to sensitivity analysis, the influence of various parts gauge to relevant performance can be judged, the sensitivity greater means the part thickness is more important for the corresponding property, therefore, key components can be determined and then optimized. The main features of the parts including structure,

Fig. 4 Stiffness test process**Table 1** Torsion case result

Displacement (mm)		Distance (mm)	Torsion angle (degree)	Applied moment (Nm)	Torsion stiffness (Nm/degree)	Lightweight index Kg/((Nm/degree)·m ²)
Point 1	Point 2					
-2.865	2.868	1178.295	0.2788	4,000	14,634	5.237

shape, thickness, material properties, processability and so on, for linear analysis such as torsion stiffness, nonlinear characteristics of the material does not affect the torsion stiffness performance, the structure shape and size of the parts is the main factors of torsion stiffness. The body torsion stiffness mainly depends on connector section properties and geometric characteristics of vehicle body components, and part thickness is one of the factors that determine the geometric characteristics of parts, so it is one of the main factors affecting the torsion stiffness. By finite element analysis, the affection of parts thicknesses on the torsion stiffness can be studied conveniently. In this paper, 50 parts of the body (including symmetrical parts) are setup for sensitivity analysis, in the analysis, only one side of the symmetrical components are selected for analyze, finally 39 thickness variables are chose in sensitivity analysis. Components which are chose show in Fig. 6.

In the stiffness sensitivity optimization analysis, the minimum mass is set as the optimization objective and Z displacement of left load point as constraints, the sensitivities of parts thickness relative to torsion stiffness and whole vehicle mass are shown in Figs. 7 and 8. Sensitivities which are larger have more impact on the target performance, and target property can be effectively increase by enhance thickness, the same part may has great influence on both torsion stiffness and vehicle mass, when increase the thickness to improve the torsion stiffness will also result in the improve of vehicle mass, such types of parts are not suitable for optimizing torsion stiffness by increasing the thickness. The contribution of

Fig. 5 Contours display of body Z direction

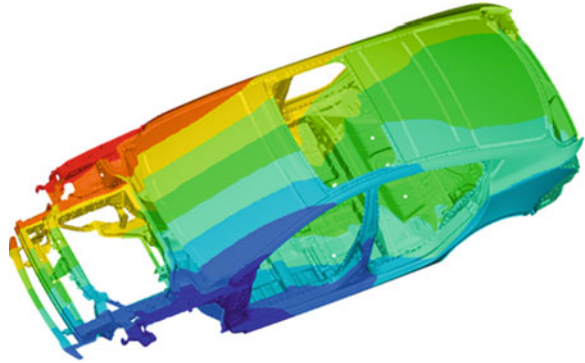
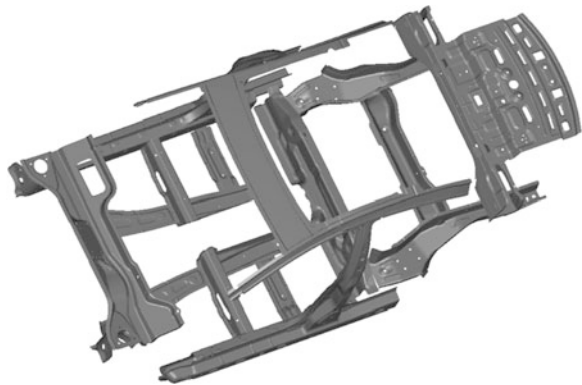


Fig. 6 Components chose for sensitivity analyze



different parts to the torsion stiffness and mass are diverse, how to choose suitable parts for thickness optimization to improve torsion stiffness while does not influence much on body weight is refer to the problem of optimization efficiency, which can be expressed by the compare of torsion stiffness sensitivity and mass sensitivity, the compare sensitivity of a part is larger means relative to other parts, changing its thickness can improve torsion stiffness but less enhance vehicle mass than others. The comparison sensitivity optimization efficiency is shown in Fig. 9. In order to improve torsion stiffness and decrease vehicle mass, the final optimization measures can be taken to is increase the thickness of parts which have larger comparison sensitivity, and decrease thickness of components which have less comparison sensitivity.

Parts gauge are optimized according to Fig. 9, and torsion stiffness is recalculated in Table 2, in relative to original model, the torsion stiffness increase 38 Nm/degree, and whole weight reduce 3.1 kg, lightweight index decrease 0.061.

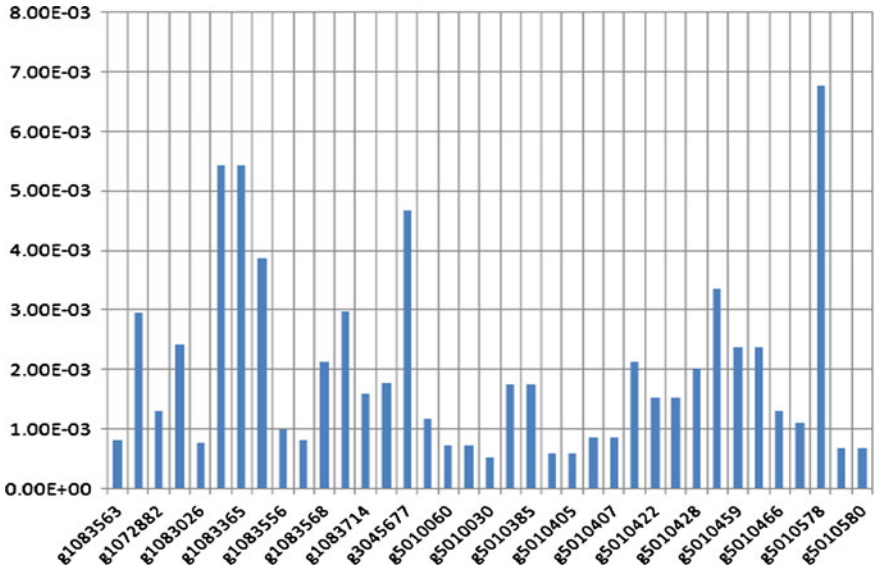


Fig. 7 Stiffness sensitivities of parts

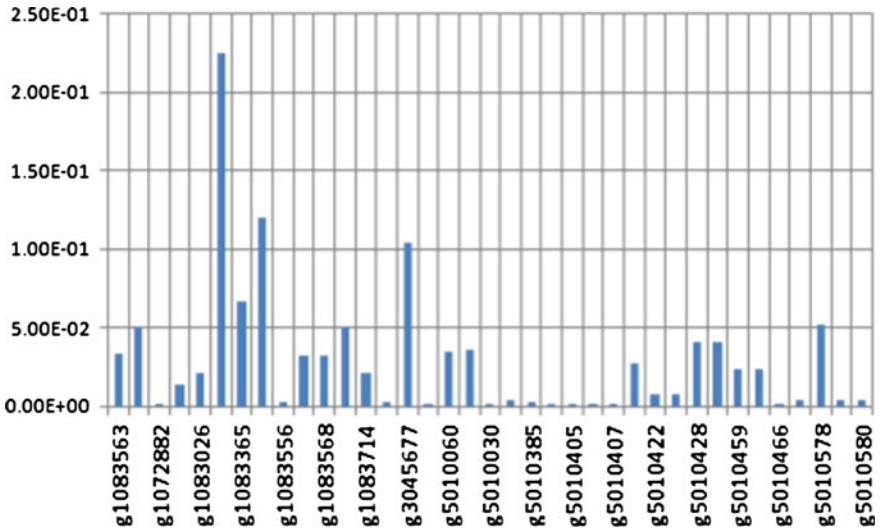


Fig. 8 Mass sensitivities of parts

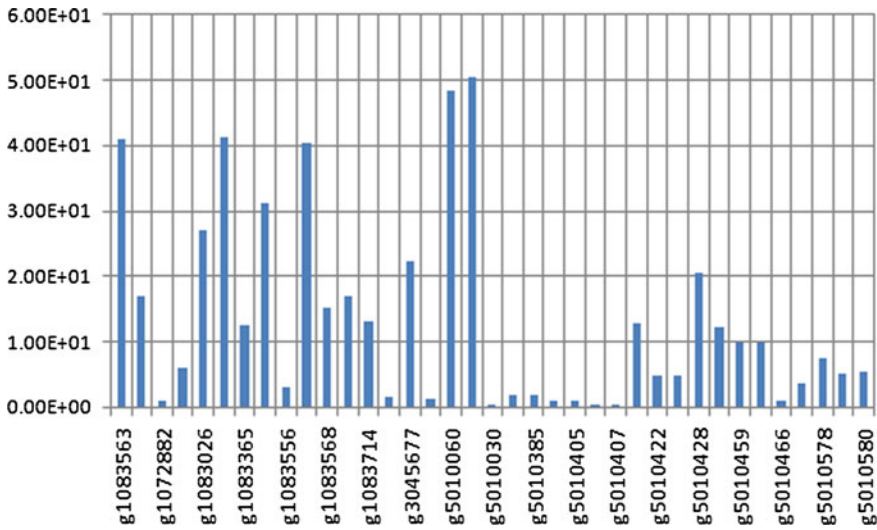


Fig. 9 Comparison sensitivities of parts

Table 2 The stiffness result after optimization

Displacement (mm)		Distance (mm)	Torsion angle (degree)	Applied moment (Nm)	Torsion stiffness (Nm/degree)	Lightweight index Kg/((Nm/degree)·m ²)
Point 1	Point 2					
-2.862	2.857	1178.295	0.2781	4,080	14,672	5.176

5 Coat Rack Topography Optimization

Topography optimization, which is optimize sheet metal structure by optimizing the distribution and size of rib structure, can be utilized to optimize parts strength and stiffness while reducing weight, supplying a optimization method for sheet metal part design. In the design area, topography optimization determines the best position and optimized parameters of ribs by elements nodes perturbation, since mass and volume are not sensitive to element change in topography optimization, therefore, the mass and volume do not set as constraints or objective in topography optimization. There are three components in optimization process, namely the design variables, objective function and constraints, design variables are parameters that changed during the optimization process to improve the performance objective, they are the variables in objective function, and constraints are limitation to design, they are the requirements of design variables and other performance [8].

Fig. 10 Topography optimization zone

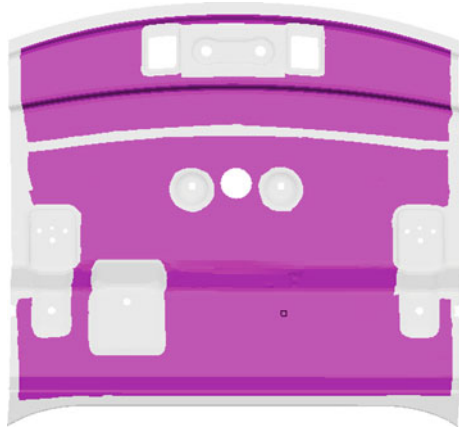


Fig. 11 Topography optimization result

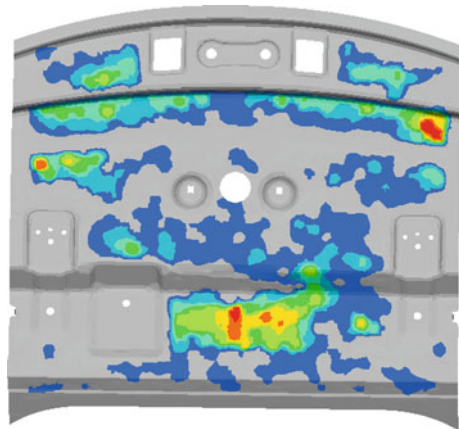


Fig. 12 Optimized coat rack structure

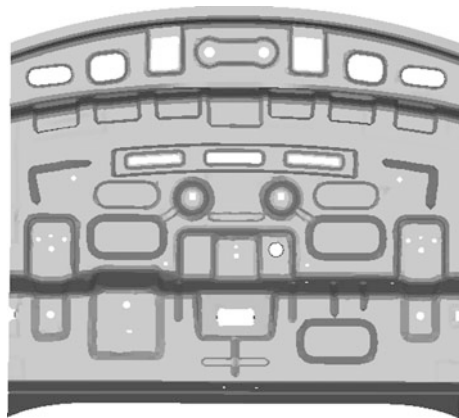


Table 3 The comparable result before and after topography optimization

Topography optimization	Displacement (mm)		Distance (mm)	Torsion angle (degree)	Applied moment (Nm)	Torsion stiffness (Nm/degree)
	Point 1	Point 2				
Before	-2.865	2.868	1178.295	0.2781	4,080	14,672
After	-2.821	2.816	1178.295	0.2741	4,080	14,885

Coat rack is one of the key components of vehicle torsion stiffness, and its quality is 3.81 kg, therefore, it is necessary to optimize coat rack structure to get optimal structure by topography optimization. In this paper, to perform topography optimization, minimum load point displacement is setup as objective, and the optimization zone is selected from original coat rack structure, which is shown in Fig. 10.

It is convergence after 11 iterations by the finite element analysis software, and the topography optimization result is shown in Fig. 11, the coat rack structure is re-designed according to the optimize result, the new structure is shown in Fig. 12, the comparable torsion stiffness and mass result of original and topography optimized coat rack structure is shown in Table 3, after optimization, the mass of coat rack structure is 3.24 kg, reducing 0.57 kg, and torsion stiffness increase 213 Nm/degree.

6 Conclusion

The sensitivity analysis method can effectively analyze the influence of each part gauge to required performance, and can easily identify the key components for further optimization. Gauge optimization and sensitivity analysis technology are basic method for lightweight design, at first, sensitivity analysis determines the key parts, and then gauge and topography optimization optimize parts gauge and structure, appropriate performance can be achieved with minimum quality requirements. In this paper, sensitivity analysis and gauge optimization method are used to determine the key components to torsion stiffness and mass, supplying a simple method for such case. Parts gauge optimization have limited contribution to lightweight vehicle design, torsion stiffness can be effectively improve by optimizing the performance of joint area stiffness and main sections. The lightweight body structure design is a very complex process, requiring a combinative consideration of vehicle safety, fuel economy and other performance, utilizing new materials, new processes, and new assembly method to achieve the ultimate lightweight design purpose.

References

1. Hu Z (2003) Minibuses body stiffness sensitivity analysis and optimization. *Mech Strength* 25(1):067–070
2. HyperMesh A (2003) The basic training course. Altair Engineering Software Co., Ltd, Shanghai
3. Zhang S (2008) The structure optimization design techniques based on the hyperworks. Mechanical Industry Press, Beijing
4. Zhang H (2004) Finite element analysis and CAE technology foundation. Tsinghua University Press, Beijing, p 95–136
5. Li C, Zhang S (2008) Hyperworks analysis instances. Machinery Industry Press, Beijing
6. Lu C (2007) Automotive lightweight technology development and implementation. Shanghai Automotive, Shanghai
7. Yang J (2010) Determinants coefficients of body lightweight index and optimization, automotive technology
8. Duan Y (2010) Car body lightweight based on stiffness and modal sensitivity analysis, noise and vibration control

Analysis of the Transient Thermomechanical Behaviour of a Lightweight Brake Disc for a Regenerative Braking System

S. Sarip, A. J. Day, P. Olley and H. S. Qi

Abstract Regenerative braking would extend the working range of an EV or HV provided that any extra energy consumption from increased vehicle mass and system losses did not outweigh the saving from energy recuperation, also reduce duty levels on the brakes themselves, giving advantages including extended brake rotor and friction material life, but more importantly reduced brake mass, minimise brake pad wear. The objective of this research is to define thermal performance on lightweight disc brake models. Thermal performance was a key factor which was studied using the 3D model in FEA simulations. Ultimately a design method for lightweight brakes suitable for use on any car-sized hybrid vehicle was used from previous analysis. The design requirement, including reducing the thickness, would affect the temperature distribution and increase stress at the critical area. Based on the relationship obtained between rotor weight, thickness, undercut effect and offset between hat and friction ring, criteria have been established for designing lightweight brake discs in a vehicle with regenerative braking.

Keywords Brakes · Friction · Regenerative · Automotive · Modelling · Thermal · Finite element analysis · Lightweight

F2012-E09-028

S. Sarip (✉)

UTM Razak School of Engineering and Advanced Technology, UTM Kuala Lumpur, 54100

Jalan Semarak, KL, Malaysia

e-mail: shamsul@ic.utm.my

A. J. Day · P. Olley · H. S. Qi

School of Engineering, Design and Technology, University of Bradford, West Yorkshire

BD7 1DP, UK

1 Introduction

It has been estimated that up to 70 % of the kinetic energy of a passenger car could be dissipated through the friction brakes and the other (up to) 30 % of the energy could be recuperated e.g. in the form of electrical power [1] and [2]. The need for conversion from kinetic energy to thermal energy by friction brakes therefore will decrease once regenerative braking is present in the system. The rest of the energy can be converted e.g. to electrical energy via a motor/generator (M/G). For a car with regenerative braking under a single stop braking event, where the energy dissipated via the front disc brakes is estimated as 70 % of the total kinetic energy.

The automotive industry has for many years identified weight reduction as a way of improving product competitiveness and thus achieving commercial success. To achieve reduction in weight, components made of materials such as iron and steel can be replaced with re-designed components made of lighter materials such as polymers and aluminium. One area that has been examined for weight reduction is the brake system, e.g. aluminium and associated composite materials such as ‘metal matrix composites’ (MMC) for brake rotors have been studied extensively. Although aluminium is increasingly used in modern brake components, the frictional and thermal requirements of a modern automotive brake have limited its use for brake discs [3]. Friction brakes get hot when used and the heat energy is dissipated by forced convection, conduction and radiation from the exposed surfaces of the brake. Over-heating can cause malfunction of the braking system and present a safety hazard. Much theoretical work has been done to calculate accurately the temperature rise during braking for different speeds and designs of brake discs. A. J. Day et al. [3–8] so the extent of the thermal loading on brake discs (rotors) is well-known.

Disc brakes are widely used on cars because of their better heat dissipation ability; a direct result of the exposed friction surface. The friction surface of a drum brake is inside and heat dissipation relies upon heat being conducted through the drum so car manufacturers fit drum brakes only on the rear axle of “low” performance cars. Additionally a drum brake provides a very effective parking brake. In commercial vehicles, drum brakes are still widely used across the world, being robust, durable and easy to maintain but in Europe most heavy goods vehicles now use disc brakes [9].

Furthermore, the performance requirement is not just for one isolated brake application, but for a series of high deceleration brake applications which form the part of the performance assessment known as the ‘fade’ test. So, the front brakes of a typical passenger car have to be designed to provide large amounts of braking torque, and withstand large amounts of heat generated, heat transfer, high temperatures and thermal loading. The size (and weight) of a car’s disc brake therefore depends upon the performance required, specifically the braking torque, energy dissipation and power. It is possible to generate high braking torque from a smaller brake, but the energy and power involved may overload the brake and cause physical damage. Lightweight disc brakes (smaller in size using lighter materials designed for

lower duty) have potential for passenger cars with regenerative braking. Regenerative braking is a feature of a hybrid and pure electric power train to recoup some of the energy dissipated during braking [10]. Electric vehicles (EVs), and hybrid electric vehicles (HEVs) have the ability to recover significant amounts of braking energy using the electrical part of the power train as a regenerative braking system (RBS). However, even with regenerative braking, friction brakes are required to provide the necessary high duty braking performance, e.g. in the event of an emergency stop being required. Regenerative braking therefore has to work alongside a conventional friction system because the braking power in an emergency is too high for a purely electrical regenerative system: this is primarily due to the limited energy transfer rate of electrical energy storage devices. Regenerative braking does however take work off the friction brakes of a vehicle, thereby extending brake disc life, minimising disc rotor weight, minimising brake pad wear and extending the working range of an EV or HEV.

Regenerative braking in an EV cannot be used when the batteries are fully charged, or when the battery is at a high temperature because this could damage the battery. At low vehicle speeds regenerative braking could generate high braking torque causing vehicle instability (if a continuously variable transmission (CVT) is used to keep the M/G at its optimum operating speed); this needs to be carefully controlled to avoid poor braking 'feel'. Braking energy recuperation for hybrid vehicles has been investigated by Ehsani et al. [2] using computer simulation to analyse the relationship between the recuperated braking energy from front wheels to the total braking energy available in a typical urban driving cycle. The results showed that 50–60 % of braking energy could be recovered by regenerative braking in urban driving. Regenerative braking can recover about 45 % of total kinetic energy for a city bus [11].

2 Single Stop and Drag Braking Analysis

For the work presented here, a test car has been used to investigate duty levels and braking performance. Legislation requires that the car can decelerate to rest at a minimum of 6.43 m/s^2 or 0.66 g from speeds up to 100 km/h (vehicles of category M1—cars) although manufacturers' own specifications often far exceed this. For a Type 0 test on this particular car, with the engine disconnected (as defined in Regulation 13 H, Annex 4), the total kinetic energy to be dissipated by each front brake is 231 kJ . The axle brake torque for each front brake is 1154 Nm providing a brake force (FB) of 3845 N . The vehicle stops from 100 km/h in 4.3 s and develops an initial braking power of 107 kW .

The simulation wheel rotational speed was set to 93 rad/s equivalent to 100 km/h for single stop braking with the initial disc temperature at $20 \text{ }^\circ\text{C}$. Heat was generated by pressing each pad on the disc with a uniform pressure of 6 MPa on the piston which created a rapid temperature rise in the disc; in an actual car this would be approximately equivalent to a 60 \% g deceleration. For the drag braking,

Table 1 Material properties of disc brake components. Adapted from Day [8]

Properties Material	Density, ρ (kg/m ³)	Young's Modulus	Poisson's ratio, ν	Conductivity k (W/mK)	Specific Heat, Cp (J/kgK)	Thermal Expansion, (K ⁻¹)
Cast iron (brake disc)	7,050	116 GPa	0.27	53.3	550	11.0×10^{-6}
Stainless steel (Brake disc)	7,800	200 GPa	0.29	25	460	11.0×10^{-6}
NAO friction material	2,620	210 MPa	0.29	2.0	1,100	16.1×10^{-6}
Backplate	7,850	210 GPa	0.30	32.0	595	–
Piston	7,887	210 GPa	0.30	32.0	595	–

loading and boundary conditions were set to represent a constant wheel rotational speed of 28.6 rad/s equal to 30 km/h vehicle speed under drag braking with an initial disc temperature of 20 °C. Tyre rolling radius was calculated from the tyre rolling circumference of the test car which was 1,860 mm, giving a tyre rolling radius of 0.29 m. The value of heat transfer coefficient used was 90 W/m²K based on the experimental results [12]. The material properties of 3D model are shown in Table 1.

3 Lightweight Disc Models

Vehicle mass is a critical parameter for a lightweight brake disc design. It is necessary to complete thermal stress prediction under two conditions of usage i.e. single stop braking and drag braking for the models for the best solution of effective lightweight disc design. Eight solid disc models were designed based on a prototype disc concept and these were used in the analysis to study the relationship between disc weight, geometry and energy loading (vehicle mass and speed). The materials used in these models were cast iron and stainless steel. Each model was given a name e.g. Ss-A (Model A made of stainless steel), Gi-B (Model B made of cast iron), etc., and the geometries of the solid discs rotor are given in Fig. 1.

4 Analysis

A fully coupled thermomechanical model was set up to predict the temperature changes of the brake disc shape caused by axial and radial deformation. Thermal conduction and convective heat transfer were the two modes of heat transfer considered. The convection heat transfer coefficient was 90 W/m²K over all exposed surfaces, and radiative heat transfer was considered negligible [12].

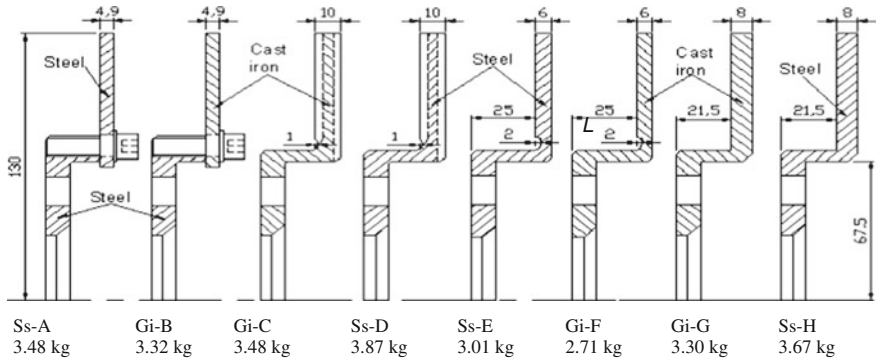


Fig. 1 Cross-section of the brake discs

5 Result: Test 1—Single-Stop Braking

Braking power in a single stop brake was computed assuming no slip at the tyre/ground interface and that heat is generated at the friction interface of the brake. The models were analysed based on a minimum vehicle mass of 1,000 kg to compare thermal stress results in medium conditions for single stop. Maximum surface temperatures were predicted at nodes on the disc, e.g. at the effective radius. Figure 2 shows the temperature distributions predicted from the models.

The lower temperatures predicted (below 200 °C) were on models Gi-C, Gi-G and Ss-H. Model Gi-C and Gi-G were made of cast iron, while model Ss-H, was made of stainless steel (Fig. 3). This shows that model Gi-G was the most suitable model in terms of low temperature rise, thermal stress and disc coning.

The comprehensive stresses associated with these temperature rises can cause yielding in compression of the material in the disc surfaces. Lower thermal stress, below 150 MPa, was predicted on all except model Ss-A (Fig. 3). Higher values of thermal stress were considered acceptable in lower duty of braking, hence all models were analysed further.

The deformation of the brake disc due to thermal loading is apparent when viewed through the disc cross section. The deformation of the brake disc region is primarily attributed to the thermal expansion of the disc. The magnitude of the coning displacement was calculated from the thermal stress analysis throughout the simulated brake schedule. Model Gi-C and Ss-D in Fig. 3c showed unacceptable thermal deformation.

The result from a sensitivity study of thermal deflection with respect to the disc mass at the end of braking (4 s) is shown in Fig. 4 for model Gi-F. Axial displacement (coning) was approximately 0.3 mm. Overall coning prediction was between 0.17 and 0.38 mm for all models except the externally vented designs (model Gi-C and Ss-D) which had a greater axial displacement up to 1.22 mm. Model Ss-E, Gi-F and Ss-H showed a small amount of axial displacement at the end of braking. Disc coning has to be reduced as well as reducing stresses to

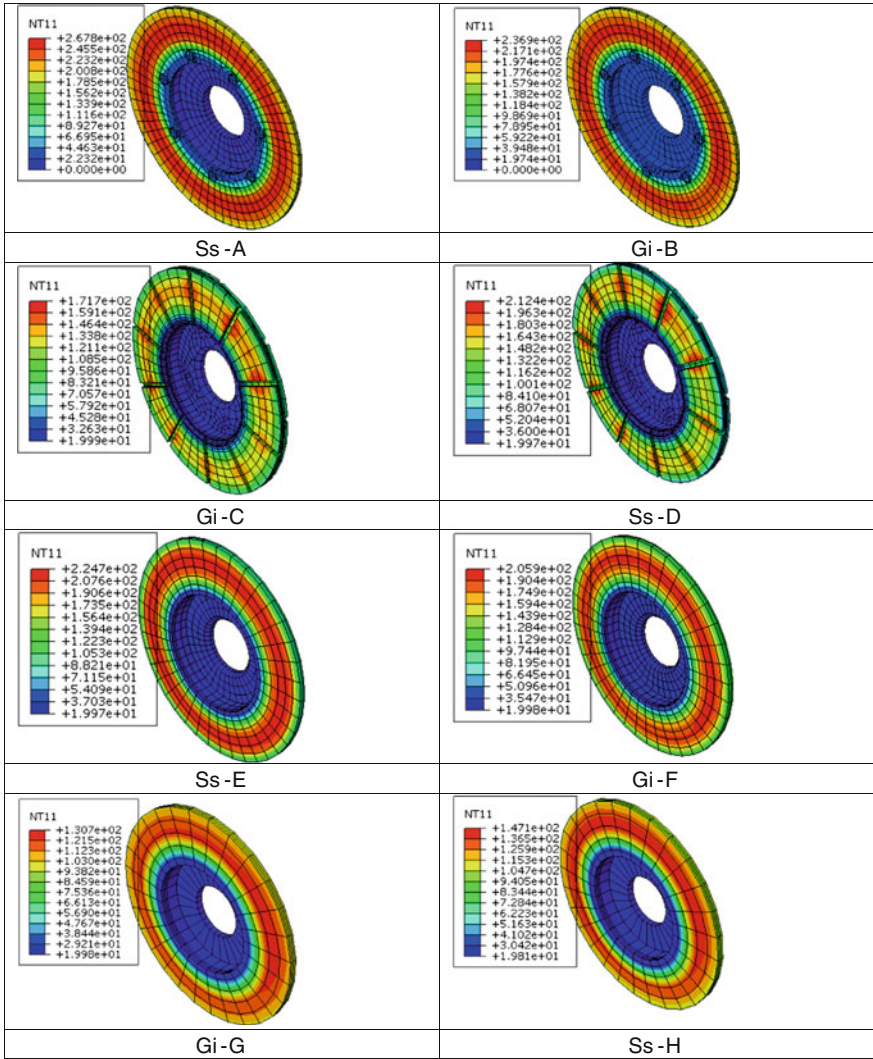


Fig. 2 Temperature contour plots

minimise disc cracking and instability of a lightweight disc. A further improvement to reduce disc coning is to create slot depth or undercut between friction ring and the hat and adequate design of the disc ring/top hat transition area should be considered. The reason for the undercut is to reduce the stiffness of the joint between the friction disc and the hat (Table 2).

Maximum temperatures obtained from the thermomechanical analyses show the superiority of cast iron over stainless steel in reducing surface temperature and thermally induced stress (Fig. 3a, b). In order to absorb and transmit the heat generated at the friction interface, cast iron has a high volumetric heat capacity

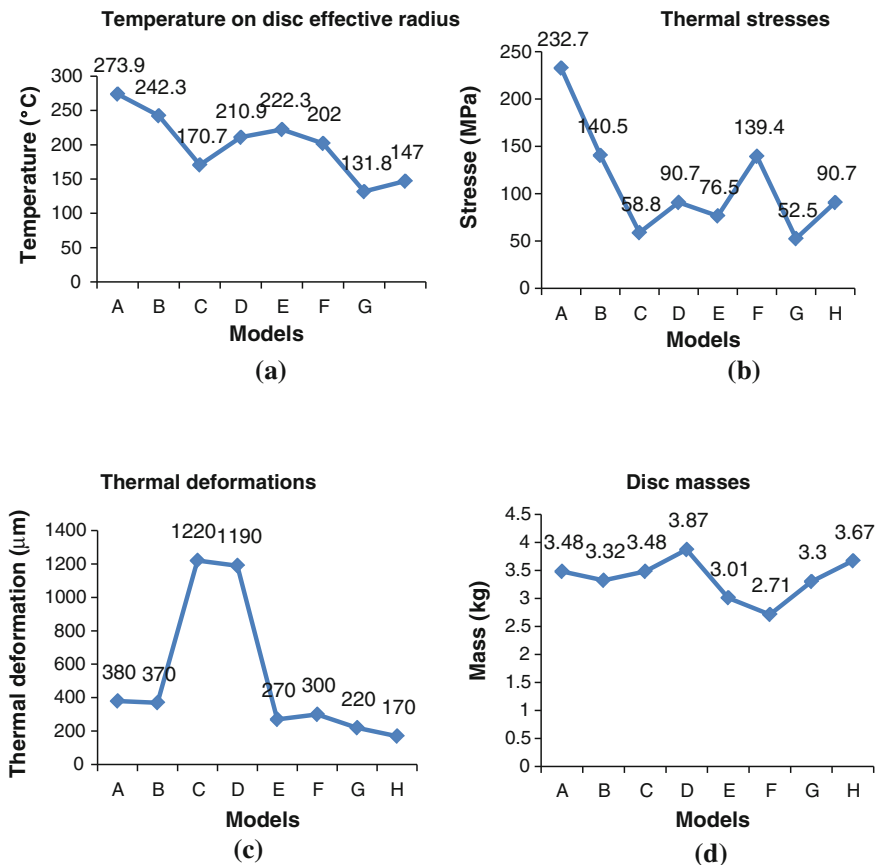


Fig. 3 Single stop braking analyse. **a** Maximum temperatures at 4 s of braking, **b** von-mises stress contour plots (4 s), **c** thermal deformation at the end of braking, **d** different disc masses between 2.71 and 3.87 kg

(ρC_p) and good thermal conductivity compared to stainless steel. Although stainless steel has a low coefficient of thermal expansion to minimise disc coning, it has higher density compared to cast iron.

Two models were proposed to replace model Gi-G. These were model Ss-E and Gi-F. Model Gi-F was made of cast iron and had good compressive strength, but at the same time it had low tensile strength as the material was brittle and prone to microcracking in tension. Model Ss-E was not practical to use in regenerative braking because of its weight i.e. model Gi-F, was more suitable to use in RBS because 30 % of the energy is recuperated in the system and this will reduce thermal duty and hence temperature rise, thermal stress and thermal deformation during braking. From the thermomechanical analyses in single stop braking, a disc made of cast iron (which is the disc Gi-F) was selected as a design model for vehicle masses lower than 1,500 kg that are equipped with regenerative braking.

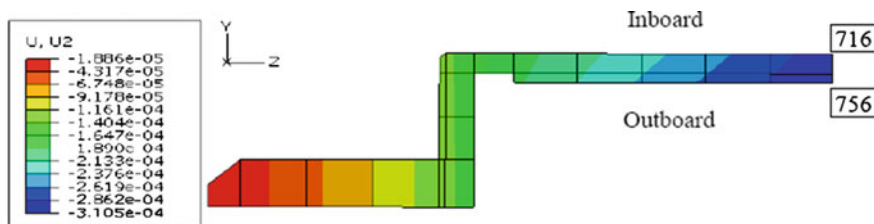
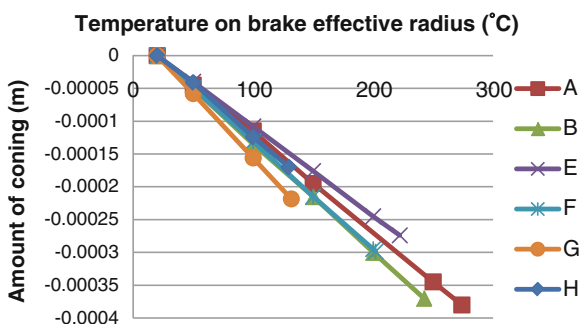


Fig. 4 Example of thermal deformation on model Gi-F in axial outboard direction

Table 2 Simulation results for deflections of the rotor edge

Model	Ss-A	Gi-B	Gi-C	Ss-D	Ss-E	Gi-F	Gi-G	Ss-H
δ (μm)	380	370	1,220	1,190	270	300	220	170

Fig. 5 Different amount of thermal coning between all models except model Gi-C and Ss-D



Disc deflection was investigated for all models except models Gi-C and Ss-D as shown in Fig. 5. The results show negative values indicating that all models deformed in an axially outward direction. Model Ss-H had a disc thickness of 8 mm and was made of stainless steel, and this showed the least amount of thermal coning (0.17 mm) of most models but slightly more coning than model Ss-E when the temperature reached 50 °C. This clearly indicated the effect of the undercut on the friction disc and the “top hat” transition region. Models Gi-G and Ss-H (without undercut) revealed the largest amount of coning between temperatures of 50–150 °C. Reducing the thermal coning of a brake disc needs an adequate amount of undercut between the transition ring/top hat. Model Ss-H has the lowest thermal coning, however, this model was not further considered because it was too heavy with a mass of 3.67 kg.

6 Result: Test 2—Drag Braking

Figure 6 shows that model Gi-G with 8 mm of disc thickness shows a good analysis result in the thermomechanical analysis. The results also showed a similarity under single stop braking. Therefore model Gi-F was selected as the

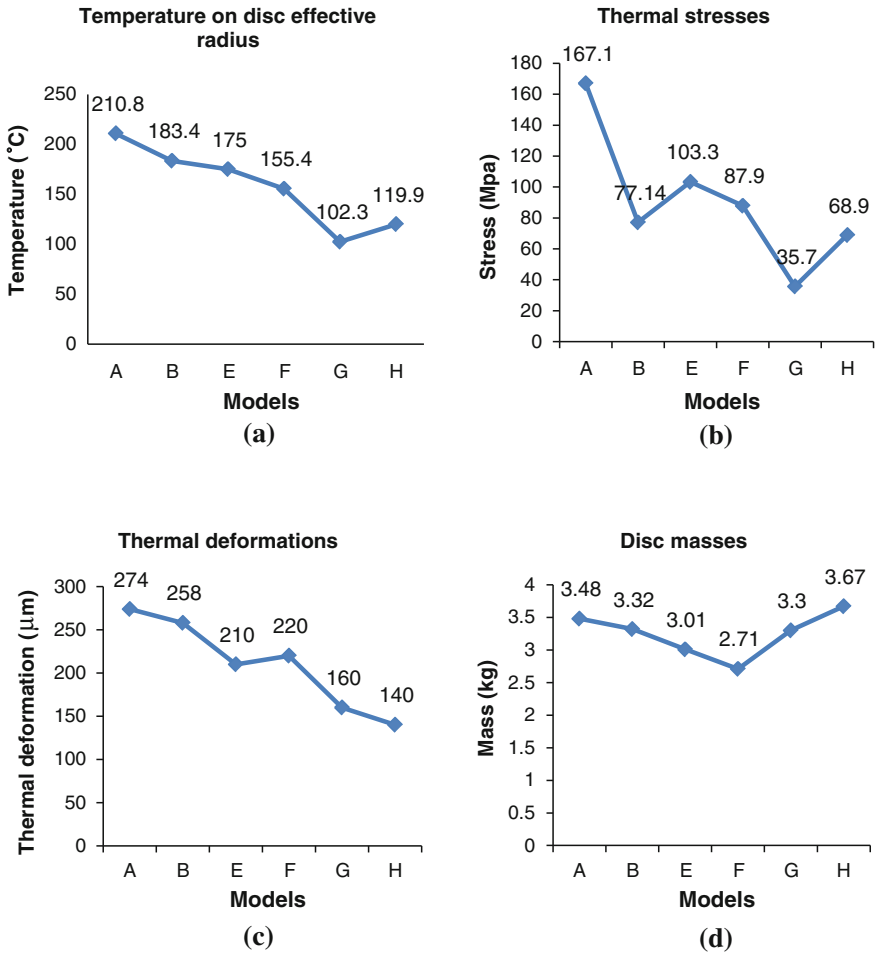


Fig. 6 Drag braking analysis. **a** Maximum temperatures for 10 s of drag braking, **b** von mises stress contour plots 10 s of drag braking, **c** thermal deformation at 10 s of drag braking, **d** different disc masses between 2.71 and 3.67 kg

prototype lightweight disc because its mass was only 2.71 kg. Model Gi-G was not suitable to use as a lightweight disc because it was heavy compared to model Gi-F.

The total amount of disc coning is shown in Fig. 7. Although model Gi-G gives the second lowest disc coning compared to Ss-H, it shows faster time of axial deformation at 50 °C (Fig. 7), which has the lowest disc coning. This is because disc Ss-H is made of stainless steel which has a higher tensile strength but lower thermal conductivity. Table 3 shows the thermal conductivity relationship between cast iron and stainless steel.

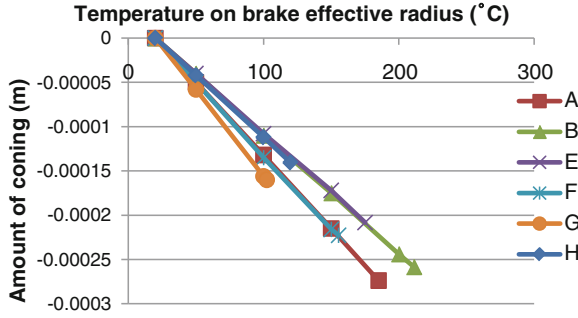


Fig. 7 Different amount of thermal coning between all models

Table 3 Maximum stresses and conductivity. Adapted from Gere to Timoshenko [14]

Discs	Min. Tensile Strength (MPa)	Conductivity (W/mK)
Cast iron	310	53.3
Stainless steel	910	25.0

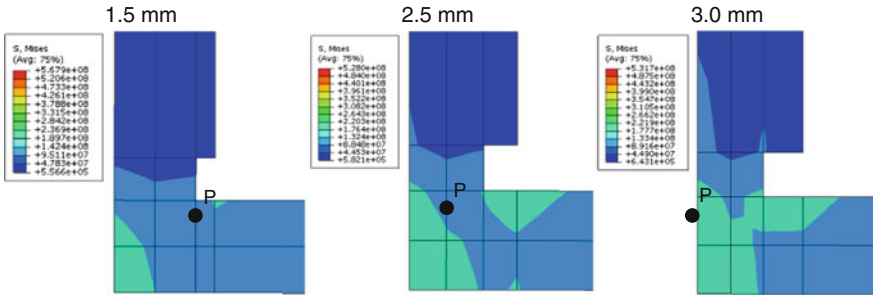


Fig. 8 Undercut values (1.5, 2.5 and 3.0 mm) and stress profile at the critical area at point P

7 Undercut Effects

From the results of temperature distribution prediction, the 8 mm thickness of the model Gi-G without undercut showed very little disc coning due to the lower temperature rise. Therefore three different undercuts were modelled for the Gi-G disc to analyse disc coning and mechanical stresses of the discs (Fig. 8).

The simulation was based on a maximum vehicle mass of 2,000 kg to predict disc coning under maximum braking duty for single stop braking. The results showed that disc coning increased with the decrease of the undercut depth 1.5 mm

Fig. 9 Variation of disc coning with undercut

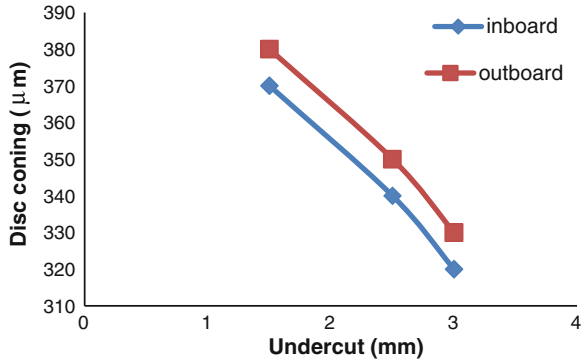
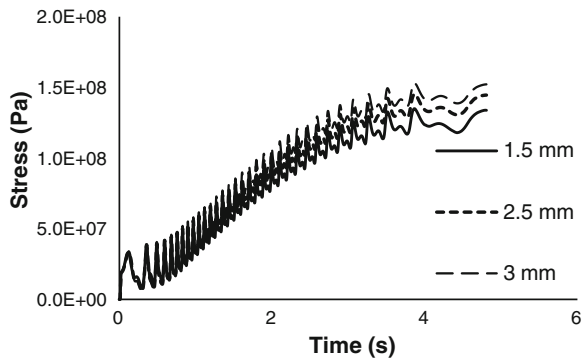


Fig. 10 Stress of the element at P



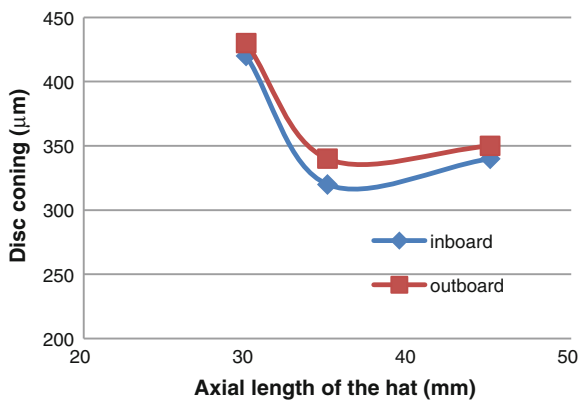
(Fig. 9) and the outboard side shows a higher value than the inboard side. The optimum value was found to be 3.0 mm depth of undercut which gave a lower stress at the critical area (Fig. 10), below 153 MPa. This value was acceptable since the tensile strength of cast iron is twice the predicted value of Von Mises stress in the region at point P. Therefore, for a lightweight disc design with 8 mm thickness, an undercut value of 3 mm was predicted as the optimum value to control disc coning.

8 Offset Between Hat and Friction Ring

The distance between the hat and the friction ring or hat axial length (L) affects the thermal deformation. Three types of the hat axial length (L) were investigated (30, 35 and 45 mm) to assess the deformation of inboard and outboard outer diameters. Figure 11 shows the result of disc coning for three values of hat axial length.

A theory of disc coning by Okamura [13] predicted that the larger the hat axial length, the smaller the disc coning but this theory is not numerically confirmed. From the FEA results, it is shown that the disc coning reduced from 420 to 320 µm

Fig. 11 Effect of hat axial length on disc coning



as the axial length was increased from 30 to 35 mm but after that disc coning increased to 340 μm with any further increase of the hat axial length. It was therefore considered that the larger value of L will force internal movement and increase bending moments in the hat wall for the longest hat length considered. The hat length of 35 mm was seen to be the most suitable length and thus was selected for the design for a lightweight disc for regenerative braking.

9 Discussion

The nearest designs to the prototype disc were Model Ss-A and Gi-B. From the thermal stress analysis, considering temperature predictions for Model Ss-A and Gi-B: both models showed high temperature rises at the disc effective radius for both test methods. The maximum temperatures were 274 and 211 $^{\circ}\text{C}$ for both discs. Using cast iron as the material, both test methods showed a lower value of temperature rise at 242 and 183 $^{\circ}\text{C}$, respectively. From the thermomechanical analysis investigation on the prototype disc, the maximum (permissible) operating temperature (MOT) was set to be 400 $^{\circ}\text{C}$ for stainless steel. The MOT of cast iron also was set to the same value of 400 $^{\circ}\text{C}$ to prevent the disc surface getting hotter. This means that maximum mass of the vehicle must be set below 1,000 kg and maximum speed must be limited to a maximum of 80 km/h for 4.9 mm disc thickness.

The maximum disc surface temperatures and thermal stresses for model Ss-C and Gi-D were predicted to have unacceptable values, in the form of very high temperature rise near the area of the external vents that is caused by the contact with the friction material. These designs were not analysed under drag braking because of the unacceptable axial thermal displacement. The brake disc flange remained substantially cooler than the friction surfaces, and radial expansion of the

friction rings was restricted. Stresses were increased in the brake disc and conical deformation occurred in the brake disc flange. In addition, the brake disc surface temperatures were uneven so the disc became deformed unevenly (Fig. 3a, b).

10 Conclusions

The design of the connection between the friction ring and the hub is important in a lightweight brake disc. The importance of this connection has been recognised and understood for many years [13] and car brake disc designers pay careful attention to the design of the so-called “top hat” region of the disc. Which friction face is mounted to the top hat, and the design of “undercut” both enable coning to be controlled within acceptable limits. However, the lightweight brake disc of the type proposed here has a completely different temperature profile, both in terms of the magnitude of the temperatures reached during braking, and the distribution of temperature in the disc. This is also known from the use of lightweight discs on motorcycles but, again, the duty levels are much different. This work predicts the magnitude and distribution of temperature in a lightweight brake disc for a passenger car and consequently the expected coning. It therefore provides an indication of what design steps must be taken to keep coning to acceptable levels in operation.

It can be concluded that stainless steel is a suitable material for a lightweight brake disc in terms of mechanical and thermal strength, provided that the tribological characteristics are suitable (e.g. it might be advantageous to use different pad materials). Stainless steel is suitable to be used for disc thicknesses less than 8 mm because stainless steel has three times the tensile strength of cast iron (Table 3). For disc thicknesses of 8 mm or greater cast iron is suitable because of its high thermal conductivity and low Young’s modulus, which limit the amount of disc damage caused by the heat flux generated by friction.

When choosing the best disc material, aside from the properties which have been referred to in Table 1, the heat capacity of the material has been shown to be as significant as the thermal conductivity. Disc material with higher heat capacity can decrease both the maximum surface temperature and the maximum stress applied to the disc surface. But stainless steel seems to be a good material for a lightweight disc, and it is better than Al-MMC because of its higher MOT. A disc made of stainless steel is designed to minimise stresses and distortion.

The contribution made by this research work to the field of vehicle braking is twofold. Firstly, the friction brakes can be downsized on a car with regenerative braking. Reducing the mass of the brake disc must consider temperatures, stresses, wear, deformation and durability. Second the example developed in this research illustrates that it is possible to reduce the brake disc mass by using a lightweight solid disc. The paper also presents a design approach for a lightweight brake disc based on mathematical and numerical (CAE) analysis with than associated experimental investigation. Conclusions relating to the scientific knowledge;

1. A lightweight friction brake can be used on a small passenger car with regenerative braking using the design approach.
2. Stainless steel disc thickness less than 8 mm and cast iron disc thickness greater than 8 mm are chosen in passenger car with regenerative braking.
3. A brake disc material with higher capacity can decrease both maximum surface temperature and maximum stress on the disc friction surface.

References

1. Zaini Z et al (2010) Mixed-mode braking for road vehicles with regenerative braking. In: Proceedings of 6th European conference on braking, pp 101–108
2. Ehsani M et al Modern electric, hybrid electric, and fuel cell vehicles fundamentals, theory, and design, Second Edn New York, CRC Press
3. Day AJ, Newcomb TP (1984) The dissipation of frictional energy from the interface of an annular disc brake. In: proceedings of the institution of mechanical engineers, part D: transport engineering 1984–1988 (vols 198–202). vol 198, pp. 201–209
4. Newcomb TP (1981) Stopping revolutions developments in the braking of cars from the earliest days. In: Proceedings of the institution of mechanical engineers 1847–1982. Vol 195, pp 139–150
5. Newcomb TP, Millner N (1965) Cooling rates of brake drums and discs. In: Proceedings of the institution of mechanical engineers. Automobile Division 1947–1970, vol 180, pp 191–205
6. Day AJ et al (1979) A finite element approach to drum brake analysis. In: Proceedings of the institution of mechanical engineers 1847–1982 (vols 1–196).vol 193, pp. 401–406
7. Hoffman T, Druten R (2004) Energy analysis of hybrid vehicle powertrains. In: Presented at the Proceedings IEEE international symposium vehicle power propulsion
8. Day AJ (1991) Drum brake interface pressure distributions. In: Proceedings of the institution of mechanical engineers Part D Journal of Automobile Engineering 1989–1996 (vols 203–210), vol. 205, pp 127–136
9. Fasci N (2008) Legislation and type approval braking of road vehicles 2008
10. Jefferson CM, Barnard RH (2002) Hybrid vehicle propulsion. WIT Press, Southampton
11. Chicurel R (1999) A compromise solution for energy recovery in vehicle braking. Elsevier Science Ltd, Kidlington vol Energy 24, pp 1029–1034
12. Sarip SB (2011) Lightweight friction brakes for a road vehicle with regenerative braking Ph.D. thesis, Engineering, Design and Technology, Bradford University, Bradford
13. Okamura T, Yumoto H (2006) Fundamental study on thermal behaviour of brake discs. SAE International vol 2006-01-3203
14. Gere JM (1999) Timoshenko SP mechanics of materials. Stanley Thorne, Cheltenham

Concept Analysis of Automotive Aluminium Alloy Bumper

Xinming Wan, Xiao Zhi, Qingjiang Zhao, Guangyao Wang
and Xiaofei Xu

Abstract One style of aluminium alloy bumper was developed for a passenger car. Firstly, strength performance objective was obtained through three-point static pressure simulation analysis and test on steel bumper of a target vehicle. In order to provide reference for aluminium alloy bumper on the design of structure and performance, benchmark analysis was applied on a reference aluminium alloy bumper. Then, the cross-section shape and dimension parameters of aluminium alloy bumper of target vehicle were obtained with OptiStruct topology optimization and size optimization, so that the material, process method and processing parameters of components of the production can be determined, among which, 6,061 aluminium alloy was employed for producing bumper beam with hot extrusion process, and 6,101 aluminium alloy was employed for producing crash box and flange with hot extrusion process. At last, low-speed collision simulation and test were used to analyze the energy absorption capacity of steel and aluminium alloy bumper. It has been found that: in the process of head-on collision, the energy absorption of aluminium alloy bumper is higher than that of steel bumper with increasing 5 %; the absorption per unit mass of aluminium bumper is significantly greater than that of steel bumper, and its deformation is 110 mm less than the permission displacement. Consequently, it is concluded that the crash-worthiness of aluminium alloy is better than that of steel bumper. In this paper, an aluminium alloy bumper was designed by using topology optimization and size

F2012-E09-030

X. Wan (✉) · Q. Zhao · G. Wang · X. Xu
China Automotive Engineering Research Institute Co., Ltd, Chongqing, China
e-mail: xinming_wan@126.com

X. Zhi
State Key Laboratory of Advanced Design and Manufacturing for Vehicle Body,
Hunan, China

optimization method, which has better performance, compacter structure and lighter weight than that of steel bumper. However, in view of the complexity of the actual working conditions applied by bumper, higher requirements should be taken into account in design process. Therefore, in subsequent structural optimization research, integration of additional conditions needs to be considered, such as collision, etc.

Keywords Aluminium alloy bumper · Three-point static pressure · Benchmark analysis · Structure optimization · Collision analysis

1 Introduction

Since 1970s oil crisis, the automotive lightweight was realized gradually as one of the important methods of energy saving, environmental protection. Studies showed that one-time weight loss effect of typical aluminium parts could be up to 30 ~ 40 %, and second-time weight loss can be further increased to 50 %, while 10 percent lighter equals 6 percent more fuel efficient. In addition, each kilo of aluminium used in a car can save 20 kg exhaust emission. Therefore, developing aluminium auto parts is an important way to the development of automotive lightweight [1, 2].

Bumper system is an important part of car body, which protects the body when collision happens. Facing with the development of automotive lightweight and based on the functional requirement, automotive researchers and manufacturers pay more attention to developing lighter bumper [3]. In this paper, simulation and test of three-point static pressure have been achieved on the target vehicle to get intensity objectives for developing aluminium alloy bumper. And benchmark analysis has been achieved on aluminium alloy bumper of reference vehicle to get basic parameters. Based on the basic parameters, a new aluminium alloy bumper has been developed by using structure optimization technology. The process methods and parameters for producing the aluminium alloy bumper have been presented. Lastly, collision simulation and test have been achieved to evaluate the new developed aluminium alloy bumper.

2 Analysis of Performance Target

2.1 Static Pressure Analysis of Steel Bumper

One of the important role of the bumper is ensuring as could as possible the transmission of collision force and collision energy backward along crash box on the condition of frontal collision and off-set collision. In order to achieve the above functions, it is necessary to propose strength requirement when design bumper.

Fig. 1 Three-dimensional diagram of steel bumper

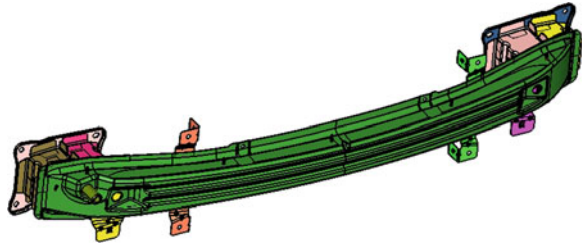
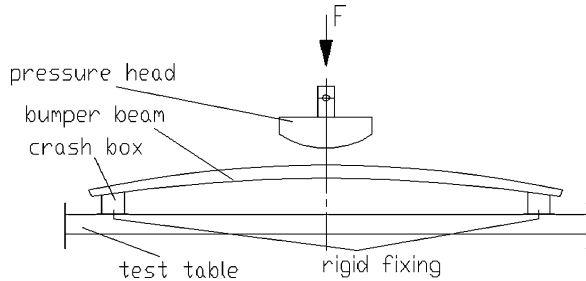


Fig. 2 Three-point static pressure simulation analysis diagram



Firstly, strength properties of steel bumper beam used on target automotive have been studied with simulation and test of three-point static pressure, reaction forces as indicators to test its strength properties. And the reaction force of steel bumper was employed to optimize the new aluminium alloy bumper.

Simulation analysis was employed for steel bumper. Firstly, the three-dimensional point cloud data has been achieved through scanning the steel bumper with Hexagon scanner, and then three-dimensional diagram was achieved with CATIA, which is shown in Fig. 1.

In order to achieve simulation analysis data of three-point static pressure, the above geometry was meshed using Belytschko-Tsay shell element with 5 mm mesh size. And the properties of 24# material provided by LS-DYNA were employed in simulation. Figure 2 shows three-point static pressure simulation analysis diagram. Figure 3 shows the model of three-point static pressure simulation. Full constraint was imposed on the base of each crash box in Hypermesh analysis, and a cylinder rigid body with 152 mm diameter was employed as pressure head. In order to simulate the must static pressure process, the middle of the bumper beam was moved forcibly 100 mm by pressure head with a constant velocity. During the simulation, the load stopped after pressure head descended 100 mm.

And three-point static pressure test has been finished under normal temperature and pressure, and Electro-hydraulic servo component test system PLS-L50B4 and high speed static strain gauge were chosen as equipments of test. In addition, the same working condition was selected for the test condition as the same as for the simulation.

Reaction force displacement curves of three-point static pressure simulation and test on steel bumper are shown in Fig. 4, respectively. It shows that pressure

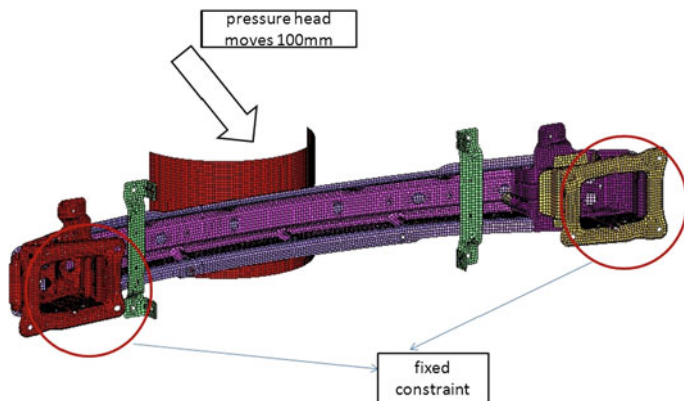
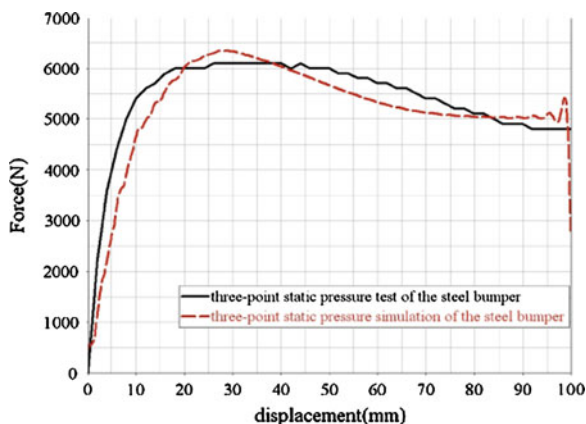


Fig. 3 Model of three-point static pressure simulation

Fig. 4 Reaction force–displacement curves of three-point static pressure simulation and test on steel bumper



peaks of test and simulation are, respectively, 6.1 and 6.35KN, of which the error is 4 %. Consequently, the correctness of the finite element model and simulation analysis was verified.

In order to ensure that the strength property of the developing aluminium alloy bumper is not less than steel bumper, 6.35KN was adopted as the strength property target in the development process of aluminium alloy beam.

3 Benchmark Analysis of Reference Aluminium Alloy Bumper

At present, aluminium alloy bumper has been applied in high-end passenger vehicles. In order to design a new type of aluminium alloy bumper possessing more excellent performance, the structure, material and strength property of a

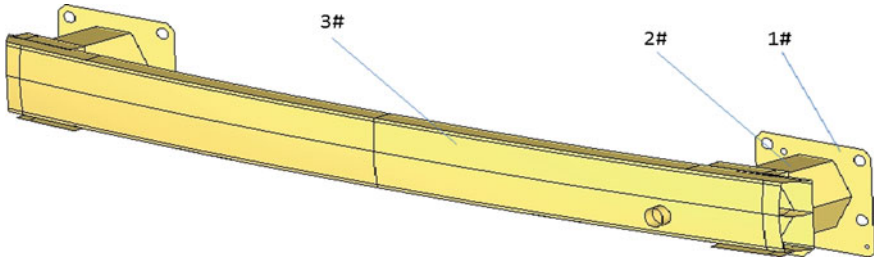


Fig. 5 3 D model of reference aluminium alloy bumper(1#-flange, 2#-crash box, 3#-bumper beam)

Table 1 Results of material component

Component	Metal component					Impurity component							
	Si	Mg	Fe	Cu	Cr	Fe	Cu	Mn	Cr	Zn	B	Ti	
1#	0.70	0.38											
2#	0.39	0.41	0.17				<0.05	<0.01					
3#	0.46	0.85		0.29	0.09	0.28							

Table 2 Strength property of 1#, 2# and 3# component

Component	Yield strength/MPa	Tensile strength/MPa	Percentage elongation after fracture/ %
1#	206.7	235.1	15.5
2#	211.3	239.8	15.1
3#	331.6	352.1	12.8

reference aluminium alloy bumper have been analyzed. The 3D model of reference aluminium alloy bumper is shown in Fig. 5. According to the symmetrical structure of the reference aluminium alloy bumper, material compositions in 1#, 2# and 3# position have been analyzed, and the results are presented in Table 1, which shows that the 6××× aluminium alloy is employed for producing the reference bumper. And the strength properties of 1#, 2# and 3# components have been tested, respectively. The results are presented in Table 2.

Table 2 shows that different component of the reference aluminium alloy bumper has different strength property, among which, high strength aluminium alloy is employed for producing bumper beam to meet the requirement of high strength property, and low strength aluminium alloy is employed for producing energy absorbing box to meet the requirement of high energy absorbing property. Because of different material for meeting different property requirement, the role of each part will be more sufficient exploited in the collision process.

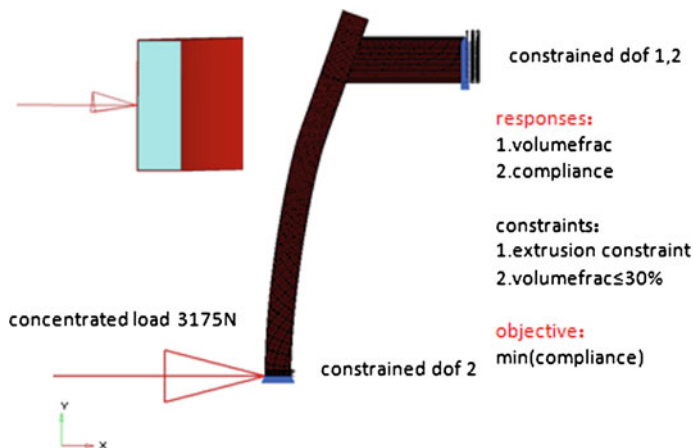


Fig. 6 Model of topology optimization analysis

4 Structure Design and Production Process

4.1 Design of Structure Optimization

Based on the structure analysis on the reference aluminium alloy bumper, it is known that thin-wall extrusion parts are employed for producing the bumper. Because of varies of properties with varies of cross-section shapes for aluminium alloy profiles, therefore, it is totally possible to optimize the aluminium alloy bumper from the view of structure and size.

In order to obtain deal cross-section shape of bumper beam, topology optimization analysis has been employed with OptiStruct in concept design stage. Because of the symmetry structure of the bumper, only a half of optimization model has been established, resulting in reduction of calculation time. In the paper, the shell of the bumper, 1 mm thick, was non-design space (red field shown in Fig. 6), and the rest area was design space (blue field shown in Fig. 6). In the simulation process, a half of pressure peak of three-point static, 3175KN, was intensively loaded on the forefront of bumper beam, minimizing strain energy and remaining volume fraction less than 30 % as the goal of optimization design, and extrusion constraint was imposed. Model of topology optimization analysis is shown in Fig. 6.

Figure 7 shows the result of topology optimization analysis. “□” style was employed as the cross section of the developing aluminium alloy bumper beam. Considering space limit to the crash box, “□” style was employed as the cross section of the new developing aluminium alloy bumper.

After that, the size parameters of aluminium alloy bumper were optimized with the OptiStruct software. In the size optimization process, under the premise of no more than 3.3 kg in weight, the strain energy was minimized through changing the

Fig. 7 Result of topology optimization analysis

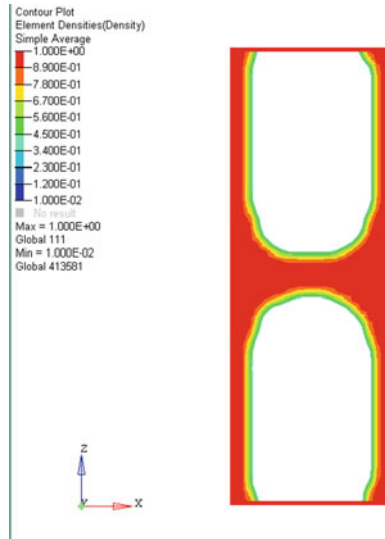
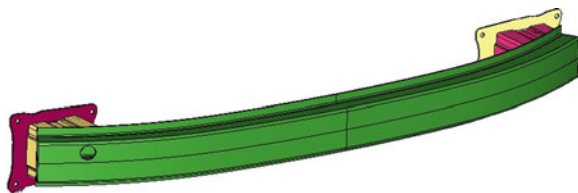


Fig. 8 3-D diagram of the developing aluminium alloy bumper



thickness size of the bumper. And the loading method in the size optimization process was the same as that in the topology optimization process. Figure 8 shows that the result of size optimization. The weight of new developing aluminium alloy bumper is 3.1 kg, reducing about 31 % of weight of the steel bumper beam used on target automotive.

5 Production Process

According to the benchmark analysis on the reference aluminium alloy bumper, in this paper, 6,061 aluminium alloy was employed for producing bumper beam with hot extrusion process, and 6,101 aluminium alloy was employed for producing crash box and flange with hot extrusion process, which process is hot extrusion → straightening, intercepting → solution treatment → bending → artificial aging. And the production process parameters were presented in Tables 3, 4.

Table 3 Hot extrusion parameters of 6,061 and 6,101 aluminium alloy

Brand	Extrusion velocity/ mm·s ⁻¹	Material outlet temperature/°C	Mold preheat temperature/°C	Extrusion temperature/°C
6,061	30	550	350	350
6,101	30	525	350	350

Table 4 Heat treatment parameters of 6,061 and 6,101 aluminium alloy

Brand	Solution treatment temperature/°C	Solution treatment time/min	Cooling medium	Cooling temperature/ °C	Artificial aging temperature/°C	Artificial aging time/ h
6,061	530	45	Water	20	175	7
6,101	510	35	Water	20	178	7

Note that, because of large composition range of 6,061 and 6,101 aluminium alloy, properly processing parameters need to be changed according to actual condition

6 Collision Performance Test

In order to test if the developing aluminium bumper meets collision performance requirement [4], collision simulation and test for the developing aluminium bumper and steel bumper have been finished, and the results were analyzed.

In the process of low velocity collision, permanent deformation and damage should only happen to bumper components. Bumper failure is defined as the displacement of relative deformation exceeds the permit displacement between bumper and radiator [5], which is 110 mm in this paper.

Simulation analysis of head-on collision and 40 % front offset collision on the developing aluminium bumper and the steel bumper have been finished. In the simulation and test process, sled weighted 1Ton, after accelerated to 9 km·h⁻¹, collided the bumper, and sled was free to rebound after collision. Diagrams of 40 percent offset collision simulation are shown in Fig. 9.

Figure 10 shows the simulation and test results of head-on collision on aluminium bumper and steel bumper. It shows that the maximum displacements happen, respectively, in the middle of aluminium bumper and steel bumper. However, the maximum displacement of steel bumper is 185 mm, exceeding seriously the permissive displacement, while the maximum displacement of aluminium alloy bumper is 103 mm. In addition, in the head-on collision process, the left side deceleration peak of the aluminium alloy bumper is 6.4 g, while that of the steel bumper is 8.3 g.

Similarly, the simulation and test results of 40 % front offset collision on the aluminium bumper and the steel bumper show that the maximum displacements happen, respectively, in the middle of the aluminium bumper and the steel bumper, and for the both bumpers, the maximum displacement is less than the permissive displacement. However, in 40 % front offset collision, the left deceleration peak of

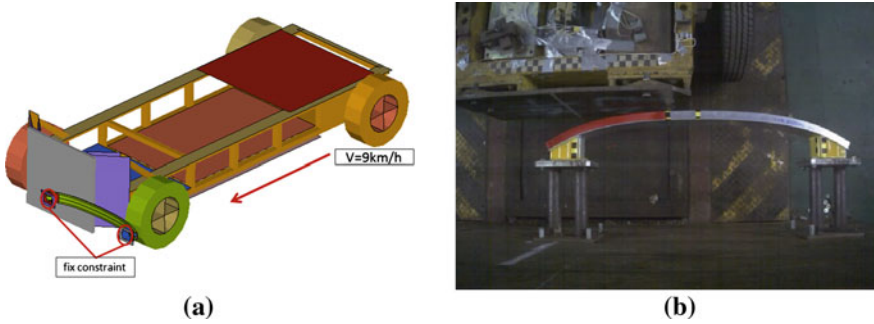


Fig. 9 Diagrams of 40 % offset collision a simulation b test



Fig. 10 Simulation and test results of head-on collision on aluminium bumper and steel a simulation result of aluminium alloy bumper, b test result of aluminium alloy bumper, c simulation result of steel bumper, d test result of steel bumper

the aluminium alloy bumper is 5.7 g, less than that of the steel bumper which is 7.1 g. Therefore, the aluminium bumper can provide better cushioning effect than the steel bumper in low-speed collision condition.

In the premise of not exceeding the permissive displacement, the more energy absorbed means the better collision performance in the low-speed collision process. Table 5 shows the energy absorbed results of aluminium alloy bumper components and steel bumper components in head-on collision and 40 % front offset collision process.

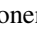
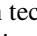
Table 5 shows that in head-on collision process, the amount of energy absorbed by aluminium alloy bumper is 2.56 kJ, which increases 5 % more than that by steel bumper. In addition, the energy absorption performance of aluminium alloy bumper beam is better than that of steel bumper beam. In 40 % front offset collision process, although the amount of energy absorbed by aluminium alloy bumper is almost equal to that by steel bumper, aluminium alloy bumper beam absorbs more energy than steel bumper beam, which is more favorable to protect the rear structure. And from Table 5, it has been found that, in head-on collision and 40 % front offset collision process, the amount of energy absorbed per kilogram of aluminium alloy bumper is much more than that of steel bumper. In addition, the weight of aluminium alloy bumper is lighter about 31 % than that of steel bumper.

Table 5 Energy absorbed results of aluminium alloy bumper components and steel bumper components in head-on collision and 40 percent front offset collision process

Weight: aluminium bumper 3.1 kg; steel bumper 4.5 kg	Left crash box		Right crash box		Bumper beam		Total energy absorbed/ N·mm	Energy absorbed per kg/ N·mm·kg ⁻¹
	Energy absorbed/ N·mm	Percent of energy absorbed (%)	Energy absorbed/ N·mm	Percent of energy absorbed (%)	Energy absorbed/ N·mm	Percent of energy absorbed (%)		
Head-on collision of aluminium alloy bumper	99,853	3.9	99,836	3.9	2.36e ⁶	92.2	2.56e ⁶	8.26e ⁵
Head-on collision of steel bumper	158,589	6.5	111,783	4.6	2.17 e ⁶	88.9	2.44 e ⁶	5.42 e ⁵
40 percent front offset collision of aluminium alloy bumper	234,554	11.3	9,350	0.45	1.83e ⁶	88.4	2.07e ⁶	6.68e ⁵
40 % front offset collision of steel bumper	506,905	24.1	14,084	0.67	1.58 e ⁶	75.2	2.10 e ⁶	4.67 e ⁵

Through the simulation and test analysis of low-speed collision absorption performance on the aluminium alloy bumper and the steel bumper, it can be seen that the collision absorption performance of the aluminium alloy bumper is much better than that of the steel bumper.

7 Conclusion

- (1) According to the idea of different structures corresponding to different bumper components, “” shape and “” shape, respectively, were employed as the cross section of the bumper beam and the crash box with topology optimization technology. And the size of the aluminium alloy bumper was optimized with size optimization technology, leading to reduction of weight by 31 %. In addition, different materials were employed to produce different bumper components, among which, 6,061 aluminium alloy was employed for producing bumper beam with hot extrusion process, and 6101 aluminium alloy was employed for producing crash box and flange with hot extrusion process.
- (2) In head-on collision process, the amount of energy absorbed by the aluminium alloy bumper increases 5 % more than that by the steel bumper. And in head-on collision and 40 % front offset collision process, the amount of energy absorbed per kilogram of the aluminium alloy bumper is much more than that of the steel bumper. The collision absorption performance of the new developing aluminium alloy bumper is much better than that of the steel bumper.

Acknowledgments Authors are thankful to State Key Laboratory of Advanced Design and Manufacturing for Vehicle Body for the partial support on this project through “The Research of Light Weighting Based on Key Component of Vehicle Body Benchmark (31015011)”.

References

1. Zhiwen W (2009) The development of automotive lightweight technology. *Automobile Technol Mater* 2:1–6
2. Mingtu Ma, Luxia Ma (2008) The application and advanced technology of the aluminium alloy in automotive lightweight. *Adv Mater Indus* 9:43–50
3. Zaoyun J (2008) Lightweight design of automotive bumper. *Dev Appl Mater* 10:56–59
4. Gu L, Zhongqian L, Zhao Y et al (2003) Investigation of low speed impact test for car bumpers. *J Shanghai Jiaotong Univ* 37(1):137–140
5. Haijiang L, Xia Z, Lifang X (2011) Collision simulation analysis of 7075 aluminium alloy car bumper based on LS-DYNA. *J Mach Des* 28(2):18–22
6. Yaqing X, Shuisheng X, Jing’an L, Tao W et al (2006) Practical manual of aluminium technology. Metallurgical Industry Press, Beijing, pp 168–170
7. GB/T6892-2006, Wrought aluminium and aluminium alloys extruded profiles for general engineering. China Standards Press, Beijing, 2006

Study on Lightweight of Vehicle Body Structure Based on Implicit Parametric Model

Jiyou Zhang, Shudan Liu, Hong Peng, Yongxin Men
and Fuquan Zhao

Abstract In the early development phase of a passenger car, the implicit parametric model of the lower body of BIW was built by SFE CONCEPT and combined with the finite element model of other parts of BIW to compose the parametric BIW model. On an Optimus workflow including BIW stiffness and vibration mode, design variables and their effective range were defined based on engineering experiences and vehicle features. A Response Surface Model (RSM) was created through Design of Experiments (DOE), and effects of key parameters of BIW structure on the stiffness and vibration mode were analyzed. Finally global optimization was conducted, and the lightweight vehicle body structure in compliance with performance requirements of modal and stiffness purposes was obtained, which saved 11.35 kg (154.55 → 143.20 kg) and lightweight effect was 7.34 %.

Keywords Body-in-white · Implicit parametric model · Stiffness · Vibration mode

1 Introduction

According to statistics, fuel consumption can be reduced by 6–8 % if vehicle weight is reduced by 10 % of the total mass. With the help of vehicle lightweight technology, developing body structure that meets multi-disciplinary (structure, NVH and crash safety) performance requirements has become a standard approach

F2012-E09-031

J. Zhang (✉) · S. Liu · H. Peng · Y. Men · F. Zhao
Zhejiang Geely Automobile Research Institute Co. Ltd, Hangzhou, China
e-mail: zhangjy@rd.geely.com

in the automotive world. At present, the lightweight development of the body structure in Geely Automobile Company can be divided into two phases: (1) in the initial conceptual design stage, the concept parametric body model is built to achieve lightweight body structure through optimizing the structure, shape, topology, material, thickness, etc.; (2) in the engineering design phase, the body weight is further reduced by optimizing the thickness of body parts. In this study, according to the project R&D requirement, the modal and stiffness performance optimization of a BIW structure in early conceptual design stage was carried out via one parameterization tool (SFE CONCEPT) and one optimization platform (Optimus).

2 Model Description

2.1 Introduction of Implicit Parametric Model

For a long time, the CAE analysis of the product structure can begin only after the complete CAD model is built, which needs a lot of geometry cleanup when it is imported into CAE software. Adopting the idea of “Analysis-driven Design”, SFE CONCEPT can quickly create the detailed geometric model and analysis model without CAD model. In this case, CAE is not just only playing the role of verification tool, but also playing a guiding role for engineers in early design stage. So engineers can put forward more optimization design schemes in the early design stage making use of the advantages of larger design space.

The parametric geometry of traditional CAD model is formed of a series of abstract parameters, and the relationship between the geometries is described by linear equations, and it is called “explicit”. The SFE model is implicit parametric model, in which geometry of single model is controlled by three types of parameters (control point location, line curvature and cross-section shape), and system-level models are connected by topological relationship. Once any of the above parameters is modified, the associated geometries will produce corresponding change [1]. Shown in Fig. 1, when the cross-section width of the threshold beam changes, the geometric continuity of the explicit parameter model will be damaged, but the implicit parametric model can maintain the topological relationships and geometric continuity.

Conventional morphing techniques modify the shape of the geometric model by modifying the finite element mesh [2, 3]. But this technique is only subject to minor change, and will easily cause distortion for the new element mesh which will affect the calculation accuracy and even leads to failure calculation. The solution of SFE CONCEPT is superior to morphing. When detecting the mesh quality doesn't meet the requirements, it will generate high-quality finite element mesh with correct connections according to the new geometric model.

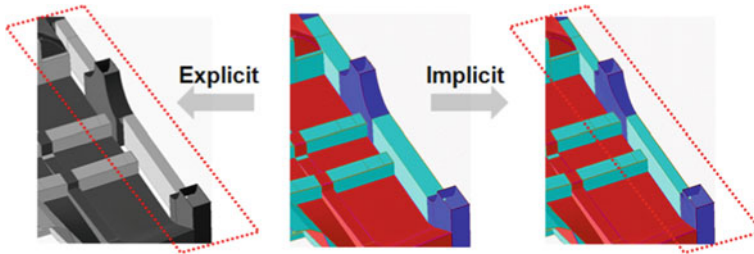


Fig. 1 Explicit (CAD) versus implicit (SFE CONCEPT)

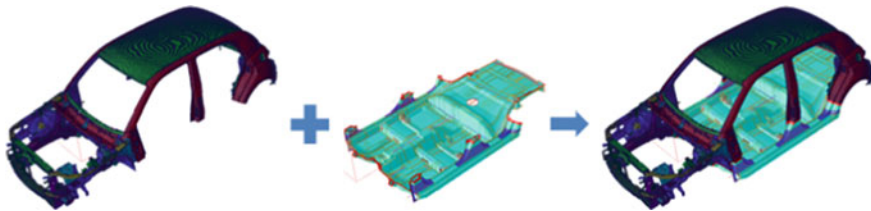


Fig. 2 BIW model assembly process

2.2 Implicit Parametric Model of BIW

Because the changing parts are lower body of BIW in this study, only the implicit parametric model of lower body was built to save modelling time. As shown in Fig. 2, the parametric model of lower body was established in the SFE CONCEPT firstly, then other assembly finite element model of BIW was imported, and the parametric model body of BIW was assembled by node coupling. The parametric design for lower body can be carried out through modification of the control parameters of node and the topological relationship.

2.3 Load Cases

Load cases in this study were consisted of BIW modal analysis and stiffness analysis. The element number of the BIW finite element model was about 600,000, and the format of the model was NASTRAN. The BIW stiffness analysis was consisted of torsion stiffness analysis and bending stiffness analysis, as shown in Fig. 3. In the working conditions of torsion stiffness analysis, translational degree freedoms of rear shock absorbers were restricted, and a MPC was placed in the mounting holes of two front shock absorbers, which made the displacement of installation holes has equal value and opposite directions. A force in the Z axis direction for 9,584 N was placed on the installation hole of the left front shock

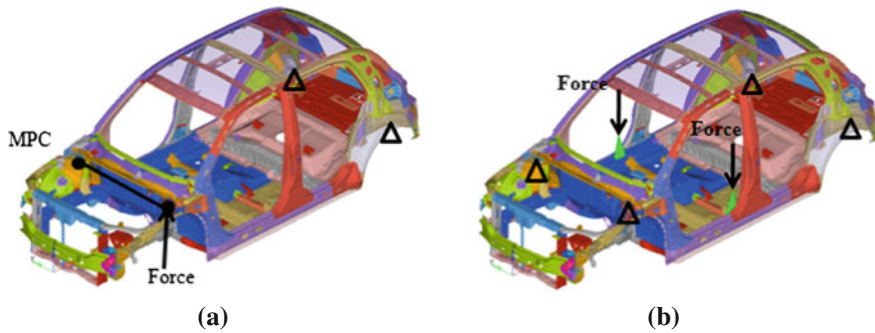


Fig. 3 Load cases **a** Torsion stiffness load case **b** Bending stiffness load case

Table 1 Comparison of BIW NVH simulation results

–		FEM model	SFE model	Error (%)
Mass	Lower body of BIW (kg)	156.66	154.55	–1.35
Mode	1st torsion mode (Hz)	39.62	39.16	–1.16
	1st bending mode (Hz)	42.05	41.55	–1.19
Stiffness	Torsion stiffness (KN·m/deg)	15.12	14.60	–3.34
	Bending stiffness (KN/mm)	10.33	10.66	3.19

absorber, which made an equivalent torque for 5,643 N m. In the working conditions of bending stiffness analysis, translational degree freedoms of front and rear shock absorbers was restricted, and loads of 3,332 N in the direction of Z axis were placed separately above the left and right thresholds.

Because the finite element model of low parts of BIW was reconstructed by the parametric model in SFE CONCEPT, it is necessary to examine the accuracy and rationality of the parametric model. In this study, the comparative results between the original FEM model and SFE model of the initial design state are shown in Table 1. As shown in Table 1, it was known that the error of the mass, mode and stiffness of the original FEM model and SFE model was within 4 %, which means that the parametric model was accurate and can be used for the optimization in the later study.

3 Optimization

3.1 Optimization Object and Process

Optimization object of this study was the minimum of the mass of the lower body of BIW, and constraints were stiffness and mode performance index of the BIW model provided by the design departments. The design variables included the main section of structure, structure shape, thickness and material.

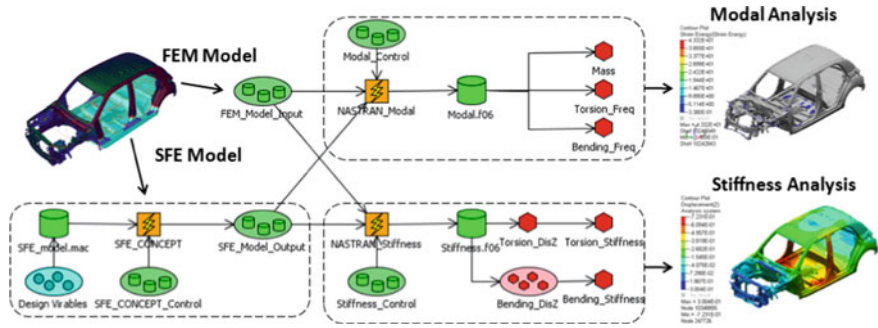


Fig. 4 Optimization workflow

With the help of Optimus optimization platform, the BIW modal and stiffness performance optimization process was established, as shown in Fig. 4. The optimization process mainly included two aspects: (1) using SEF CONCEPT to achieve the design variables changes, setting all design variables, and change the parametric model into finite element model automatically; (2) NASTRAN solver was invoked to carry out iterative calculations of the modal analysis model and stiffness analysis model in order to calculate mass of lower body, 1st torsion mode, 1st bending mode, torsion stiffness and bending stiffness. Mathematical model of process optimization can be expressed as:

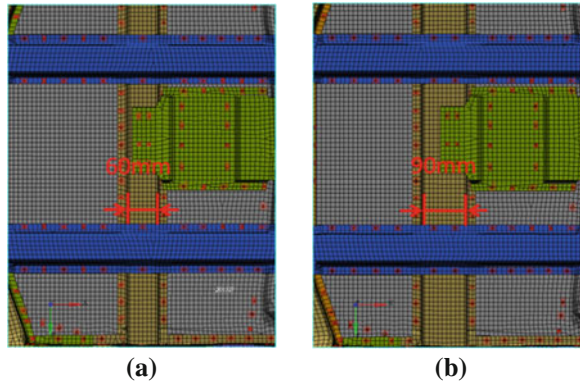
- DV01–DV39
- min Mass
- s. t. Torsion_Freq > 39 Hz
 - Bending_Freq > 41 Hz
 - Torsion_Stiffness > 12 K N m/deg
 - Bending_Stiffness > 11 K N/mm

where DV01–DV39 are all design variables (including shape design variables and gauge design variables), Mass means the mass of lower body of BIW, Torsion_Freq and Bending_Freq are 1st torsion mode and 1st bending mode respectively, Torsion_Stiffness and Bending_Stiffness stand for torsion stiffness and bending stiffness respectively.

3.2 Design Variables Sensitivity Analysis

This study had established 39 design variables (including 15 shape design variables and 24 gauge design variables). These design variables are required to conduct sensitivity analysis to knock out design variables which had less effect on optimization results. According to lower and upper bound, each variable was divided into 2–4 levels and used to calculate. The effect of the calculation result

Fig. 5 Lower and upper bound of DV14 **a** Beam width = 60 mm **b** Beam width = 90 mm



change would decide the sensitivity of each design variable. The shape variable DV14, shown in Fig. 5, was the width measurement of No. 6 beam section in the X axis direction. As shown in Table 2, when the beam width changed from 60 into 90 mm, the mass of lower body increased by only 0.10 %, modal and bending stiffness basically unchanged, and torsion stiffness increased by 1 %. Those show that cross-section variation of the beam had great influence on torsion stiffness, which means the design variable would be applied in the late optimization. After the sensitivity analysis, 20 effective design variables (including 6 design variables and 14 gauge design variables) were chosen, and would be involved in the late stage of the optimization calculation.

3.3 Optimization Calculation

This study selected 20 effective design variables to build the DOE matrix of 125 samples based on the type of Latin-Hypercube. Iterative computation is processed on the Optimus platform by invoking parametric tool SFE CONCEPT and solver NASTRAN. Based on the above DOE matrix, a constructive neural network approximation model (RBF, Radial Basis Functions) was obtained by using interpolation methods. As shown in Table 3, the R^2_{Press} values of the output parameters of RSM were all close to 1, which means the model response surface model (RSM) accuracy was high, and the RSM model could be used as the foundation of the optimization calculation.

Based on the establishment of the approximate model of this study, the initial state of the design variables were chosen as the starting point of the optimization. The global optimum of the mass of lower body is solved by adopting Self-Adaptive Evolutionary algorithm. And optimization results of some design variables were shown in Table 4. After that, the design variables of optimum case of RSM model were imported into the FEM model and calculated. Comparison of RSM results and simulation results were shown in Table 5. Finally, the lightweight

Table 2 Comparison of BIW NVH simulation results

–		Beam width = 60 mm	Beam width = 90 mm	Variance
Mass	Lower body of BIW (kg)	154.55	154.71	0.10 %
Mode	1st torsion mode (Hz)	39.16	39.23	0.18 %
	1st bending mode (Hz)	41.55	41.55	0
Stiffness	Torsion stiffness (KN·m / deg)	14.52	14.66	1.00 %
	Bending stiffness (KN / mm)	10.60	10.60	0

Table 3 RSM error results

Output	Mass	Torsion_freq	Bending_freq	Torsion_stiffness	Bending_stiffness
R^2_Press	0.9993	0.9555	0.9547	0.9343	0.9777

Table 4 Optimization results

Design variables/mm	Baseline	Optimum	Lower bound	Upper bound
DV04 (location)	0	8.5	−20	50
...
DV14 (Size)	0	24	0	30
...
DV16 (Gauge)	1.8	1.2	2.2	1.4
...
DV39 (Gauge)	1.5	1.8	1.0	2.0

Table 5 Comparison of RSM results and simulation results

–		Target	RSM results	Simulation results	Error (%)
Mass	Lower body of BIW (kg)	≤154.55	142.75	143.20	−0.31
Mode	1st torsion mode (Hz)	≥39	39.20	39.15	0.13
	1st bending mode (Hz)	≥41	41.36	41.28	0.19
Stiffness	Torsion stiffness (KN·m / deg)	≥13	13.92	13.86	−0.43
	Bending stiffness (KN / mm)	≥11	11.00	11.02	0.18

vehicle body structure which saved 11.35 kg (154.55 → 143.20 kg) met the performance requirements of modal and stiffness purposes, and the lightweight effect was 7.34 %.

Taking into account the reasonable application of computing resources, this study carried out the modal and stiffness properties of the BIW optimization firstly, not yet involved in the crash safety performance optimization, which will be carried out at a later stage.

4 Conclusion

This chapter introduces the concept of implicit parameters and a conceptual parametric model of lower body of a BIW structure was built to achieve lightweight body structure, which meet the modal and stiffness properties, through the optimization of the structure and shape, topology, material, thickness, etc. Finally, the lightweight vehicle body structure in compliance with performance requirements of modal and stiffness purposes was obtained, which saved 11.35 kg (154.55 → 143.20 kg) and lightweight effect was 7.34 %.

References

1. SFE GmbH (2010) SFE CONCEPT users' guide v4.2, p 2
2. Benedyk J (2000) Light metals in automotive application. *Light Met Age* 58(10):34–35
3. Noesis Solutions NV (2010) Optimus theoretical background rev. 10.1, p 4

Lightweight Design and Evaluation for Cab-in-White of Heavy-Duty Truck

Xinyu Wang, Dengfeng Wang, Wanlai Sun and Peiwu Liu

Abstract The weight of a heavy-duty-truck is one of the most important indexes to evaluate the lightweight design level of the cab. The domestic heavy-duty-truck studied in this chapter is high-roof with one and a half seat space, which is overweight by 10 % compared with the same type of truck aboard. In order to reduce vehicle weight, improve fuel economy, the lightweight design of the cab is carried out. In this chapter, topology optimization and size optimization methods are applied to realize the lightweight design for the cab-in-white of a heavy-duty-truck, and the weight is reduced by 46 kg. Next, the comparative analysis show that the strength, stiffness and the natural vibration characteristics of lightweight designed cab are essentially the same with the original, and the passive safety meets ECE R29 regulatory requirements. On this basis, this chapter proposes the lightweight coefficient of the cab-in-white of a heavy-duty-truck as a evaluation index for lightweight design, used in the lightweight analysis and evaluation for cab-in-white of a heavy-duty-truck.

Keywords Heavy-duty truck · Cab-in-white · Topology optimization · Lightweight design

F2012-E09-034

X. Wang (✉) · W. Sun · P. Liu
R&D Center, China FAW Co.,Ltd, Changchun, China
e-mail: wangxinyu@rdc.faw.com.cn

D. Wang
State Key Laboratory of Automotive Simulation and Control, Jilin University, Jilin, China

1 Introduction

Data from a literature review showed that, for vehicles with internal combustion engine, a 10 % curb weight reduction is equal to 4.5–6 % increase in fuel efficiency. With the energy crisis is increasing, lightweight design become the most important thing to consider during the development of truck production [1–4]. The lightweight design consists mainly of structural optimization and using of lightweight materials and new technology. In this chapter the structural optimization is performed to reduce the weight of cab-in-white of a heavy-duty-truck [5–8].

1.1 The Lightweight Coefficient of the Cab-In-White

According to lightweight coefficient of passenger cars, this chapter presents the commercial vehicle lightweight coefficient to evaluate the lightweight level of a cab. The definition of lightweight coefficient is:

$$L = \frac{M}{C_T \times V} \times 10^4. \quad (1)$$

In Eq. (1), L is the vehicle lightweight coefficient, M is the weight of cab-in-white, C_T is the static torsional stiffness of cab-in-white, V is the volume of cab-in-white.

According to the above definition, the comparative analysis between the studied cab and foreign cab is shown in Table 1.

Based to the foreign cab, we determine to reduce 40 kg weight of original cab, and the lightweight coefficient shall not be more than 8.8.

1.2 Modal Analysis of the Cab-In-White

Due to 3D CAD model, the FE model of the cab-in-white was built using shell elements and the elements size was 15 mm. The eventually established finite element model of the cab, shown in Fig. 1, contains 124 components and has a total of 191 877 elements and 196 022 nodes.

The first five modes of the cab were obtained from the finite element modal analysis. Natural vibration frequencies and modal shapes are shown in Table 2, and the natural frequency of the first overall torsional mode is 20.9 Hz meeting the modal stiffness design requirements. Cab-in-white first four mode shapes are shown in Fig. 2.

Table 1 The comparative analysis between the studied cab and foreign cab

	Weight (kg)	Stiffness (Nm/°)	Volume (length × width × height) (m ³)	Coefficient
Studied cab	346	34,934	2.310 × 2.465 × 1.760	9.883
Foreign cab	302	36,346	2.310 × 2.465 × 1.760	8.291

Fig. 1 FE model of the cab-in-white

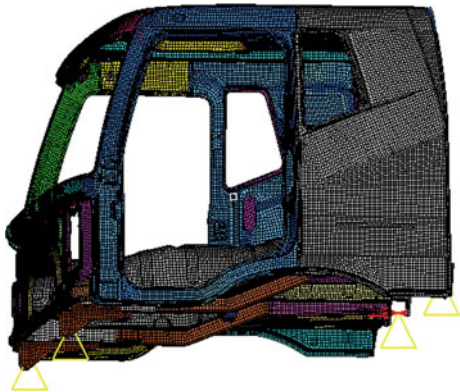


Table 2 First ten modal frequencies

Order	Frequency (Hz)
1	18.0
2	33.4
3	37.2
4	38.2
5	38.7
6	40.4
7	41.4
8	42.3
9	43.5
10	44.2

1.3 Topology Optimization of the Cab-In-White

Based on the actual structure low-order modal frequencies, the 3D topology optimization analysis model of the cab-in-white was established by using HyperWorks/OptiStruct optimization module.

In order to reduce the calculation scale and help for optimization analysis, the cab was divided into roof, side walls, front wall and floor these four blocks and they were analyzed separately.

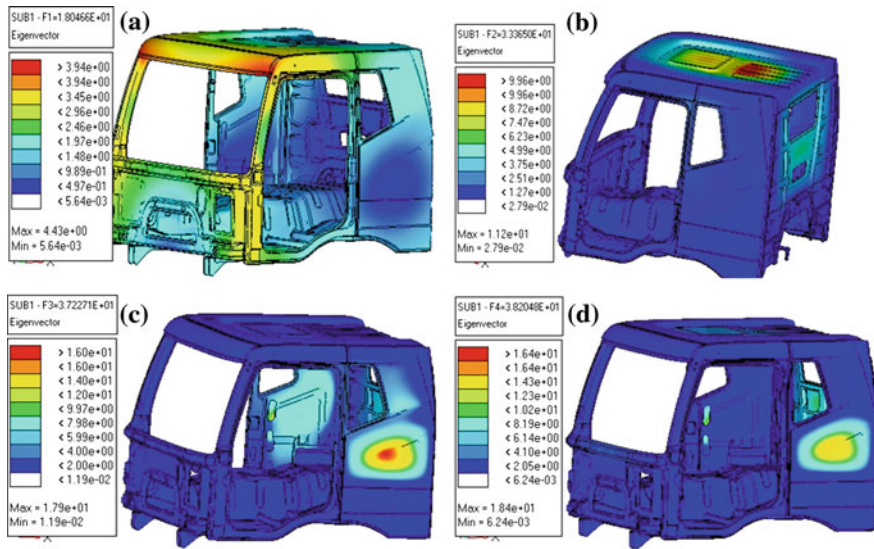


Fig. 2 First four modal shapes of the cab-in-white. **a** First order mode (18.0 Hz). **b** Second order mode (33.4 Hz). **c** Third order mode (37.2 Hz). **d** Fourth order mode (38.2 Hz)

1.3.1 Topology Optimization Analysis of the Roof

The topology optimization result of the cab roof is shown in Fig. 3. According to the result above and the structural features of the original cab, the improved design of the cab roof was proposed, reducing 12.1 kg than the original structure.

1.3.2 Topology Optimization Analysis of the Side Wall Panels

The result of the topology optimization analysis of the cab side walls is shown in Fig. 4. According to the result above improved the structure design of the cab both side walls: add reinforcing ribs to the inner panel, decrease the thickness of both inner and outer panels and simultaneously connect these two separated panels. After taking modifications the weight of both side walls is reduced by 17.3 kg.

1.3.3 Topology Optimization Analysis of the Front Wall

The result of the topology optimization analysis of the front wall is shown in Fig. 5. Considering the result above, for the front wall, completed structural improvements of the reinforced beams and ribs layout. At the same time decreased the thickness of the front wall. The improved front wall has a weight deduction of 6.4 kg.

Fig. 3 Optimization result of the roof

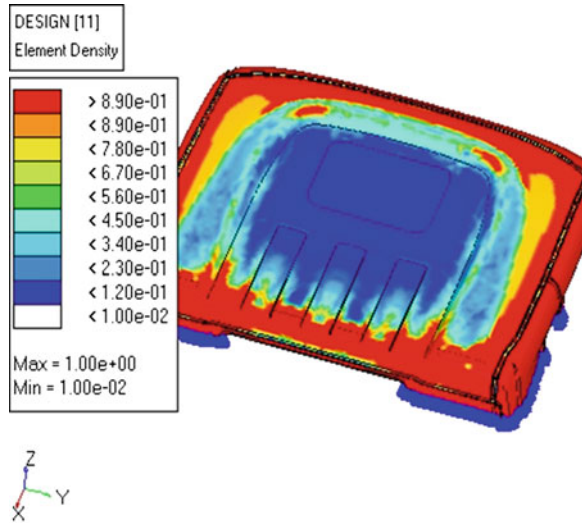
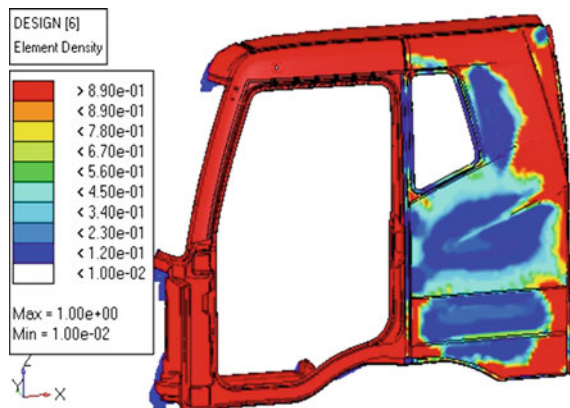


Fig. 4 Optimization result of the side wall panels



1.3.4 Lightweight Design of the Floor

The result of the topology optimization analysis of the cab floor is shown in Fig. 6. Accordingly the programs of adding ribs and decreasing wall thickness are applied to the rear part of the cab floor. The weight of the floor keeps the same with the initial structure.

After all of the lightweight designs above, the assembled lightweight cab is shown in Fig. 7. Without changing cab materials, the cab-in-white realizes a weight decrease of 46 kg, from 346 to 300 kg.

Comparative Analysis of Cab Modes Before and After Lightweight design.

Fig. 5 Optimization result of the front wall panels

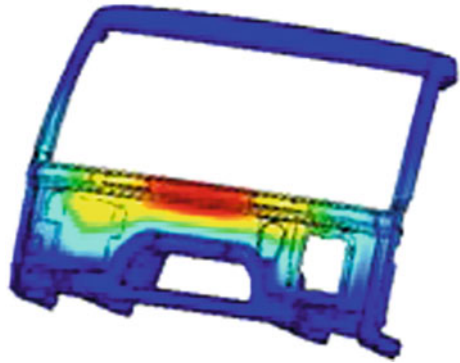


Fig. 6 Optimization result of the floor

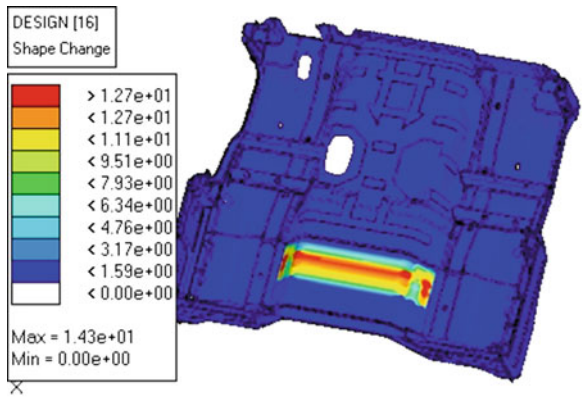
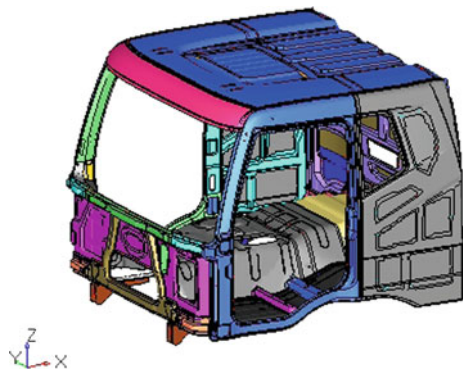


Fig. 7 Lightweight cab-in-white



1.3.5 Modal Analysis

The free modal analysis of the lightweight cab was executed and then compared analysis results with those of initial structure, as shown in Table 3 and Fig. 8.

Table 3 Frequency comparison between the initial and lightweight cabs

Order	Initial cab	Lightweight cab	Ratio of change (%)
1	18.0	19.0	5.6
2	33.4	35.3	5.7
3	37.2	38.8	4.3
4	38.2	44.6	16.8
5	38.7	45.8	18.3

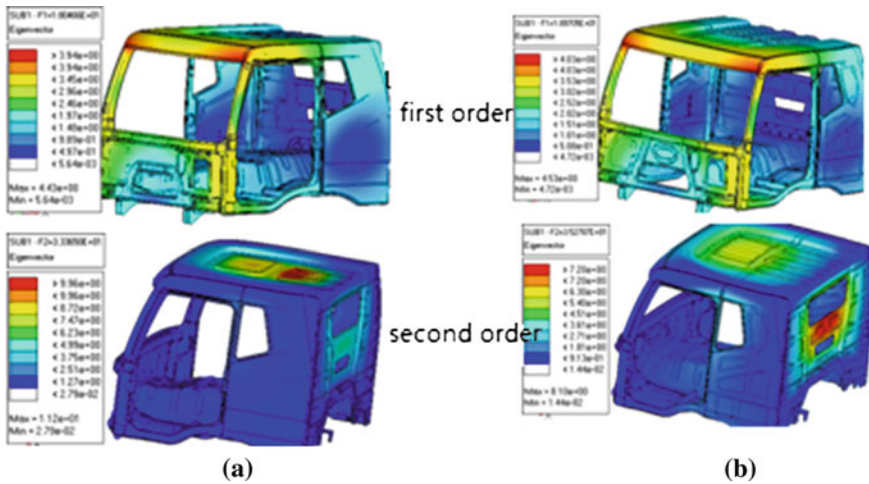


Fig. 8 Modal shapes comparison between the initial and lightweight cabs. **a** Initial cab. **b** Lightweight cab

Table 4 Stiffness comparison between the original and lightweight cabs

	Original cab	Lightweight cab	Ratio of change (%)
Torsional stiffness (Nm/°)	34,934	35,697	2.2
Bending stiffness (N/mm)	14,599	14,187	2.8

Table 3 indicates the first five natural vibration frequencies of the lightweight cab all have a certain increase compared with these of the original cab, meaning the modal stiffness of the lightweight cab has improved significantly.

1.3.6 The Static Stiffness Analysis

As shown in Table 4 and Fig. 9, the comparative results of simulation show that the static stiffness is increased.

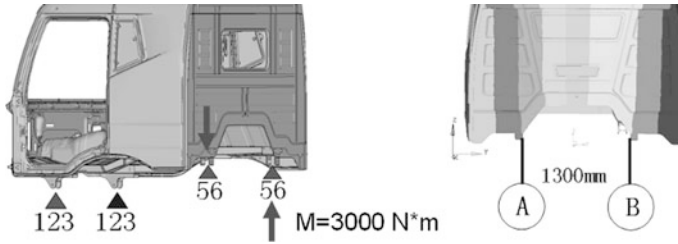


Fig. 9 The load and constraint conditions of the torsional stiffness

Fig. 10 Comparison of the survival space after impact



1.4 Passive Safety Tests of the Lightweight Cab

For validation to meet requirements of ECE R29, tests on passive safety were conducted in the national quality inspection center.

In front impact tests, the lightweight cab has a large Space under front pendulum impacts, and none of the cab inelastic components contact with the dummy, therefore lightweight cab meets the requirements of the occupant survival space during the front impacts. Test analysis results are shown in Fig. 10.

The Rear-end test results show that the maximum deformation of the rear part of lightweight cab is 33 mm, the small deformation of the lightweight cab satisfies the requirements for the driver's living space of rear-end push tests specified in ECE R29, the results shown in Fig. 11.

Carried out top-pressure tests of the lightweight cab, as shown in Fig. 12. The results show that there's still a 191 mm distance between the dummy head and cab roof, satisfying the requirements for occupants' survival space.



Fig. 11 Rear-end pushing tests of the lightweight cab



Fig. 12 Front view of the lightweight cab under top-pressure

Table 5 The comparative analysis between the studied cab and foreign cab

	Weight(kg)	Stiffness (Nm/°)	Volume (length × width × height) (m ³)	Coefficient
Original cab	346	34,934	2.310 × 2.465 × 1.760	9.883
Foreign cab	302	36,346	2.310 × 2.465 × 1.760	8.291
Lightweight cab	300	35,697	2.310 × 2.465 × 1.760	8.422

2 Conclusions

This chapter focused on the lightweight design of a heavy-duty truck cab. Lightweight design improvements and test verifications are performed using the topology optimization. The conclusions are as follows:

1. The weight was reduced by 46 kg.
2. The strength, stiffness and the natural vibration characteristics of lightweight designed cab are essentially the same with the original.

3. The qualified passive safety tests indicated that the lightweight designed cab could meet the requirements of passive safety of ECE R29.
4. After lightweight design, the lightweight coefficient declined to 8.422 (see Table 5).

References

1. Duonian Y, Dengfeng W, zhenhua W et al (2009) Light weight design of heavy duty truck cab based on topology optimization. *Automobile Technol* 9:18–21
2. Yupeng H, Xinming W, Shanpo W et al (2010) Sensitivity analysis based weight-reducing for cabs. *Constr Mach Equip* 41(7):16–18(48)
3. Xinming W, Yang L, Yupeng H et al (2011) Light weight design of heavy duty truck cab for the goal of safety. *Chin J Automot Eng* 1(2):134–139
4. Hojnacki HE, Taka G (2011) Light-weight automotive seating system. SAE paper 2011-01-0424
5. Iyer RS, Montroy T, Morgans S, Gustafson K (2011) application of advanced high strength stainless steel for mass reduction in automotive structures—A front bumper beam case study. SAE paper 2011-01-1054
6. Chiu Huang CK, Chang MY, Chi SH (2010) The lightweight chassis sub-frame design by applying hydro forming technology. SAE paper 2010-01-0989
7. 青山公彦, 櫻田澈 (2002) Lightweight technology for commercial vehicle. *Light Automobile Technol* 8:25–29
8. Jinghong Y (2009) How European manufacturers realized the lightweight of their tractors. *Commercial Veh* 8: 90–93

Research on Parameterized Structural Modeling for Carbody Lightweighting

Xin Chen, Fangwu Ma, Dengfeng Wang, Yongxin Men,
Qiang Liu, Zaiqi Yao, Junlong Zhou and Chen Xie

Abstract The method of parameterized structural modeling and design based on SFE CONCEPT makes it is available for fast modification and multi-performance rapid integration optimization on carbody structure. A structural SFE model is built from a car structural FE model in concept development stage, which is validated by some design simulation data. The validated SFE structural model can be used for rapid optimization and multi-performance evaluation for different design variation. This engineering parameterized design method on carbody structure has the obvious practical advantage to improve the efficiency of lightweighting design.

Keywords Carbody · Lightweighting · Structural modeling · Parameterized design

1 Introduction

Lightweight body can cut down the fuel cost and is good for environment protection. The weight of BIW (Body-in-white) is about 30–40 % of the total car, so carbody lightweighting plays an important role in reducing the entire car weight

F2012-E09-038

X. Chen (✉) · F. Ma · Y. Men · Q. Liu · Z. Yao
Zhejiang Geely Automobile Research Institute CO. LTD, Hangzhou, China
e-mail: cx@jlu.edu.cn

X. Chen · D. Wang · J. Zhou · C. Xie
State Key Laboratory of Automotive Simulation and Control, Jilin University,
Changchun, China

[1]. Structural lightweighting design is a practical way, besides the methods about manufacture processing and body materials, to get lighter weight of the whole car for the auto companies [2].

In order to reduce the carbody weight at most, the structural lightweighting design idea should be integrated into the early concept body model in the car concept development stage. Under the structural lightweighting design idea, the engineers can determine a series of varieties and plans for analysis and evaluation by CAE (Computer Aided Engineering) technology on the initial concept structure.

2 CAE Technology for Lightweighting Design

CAE technology based on FEM (Finite Element Method) provides a good solution to analyze and simulate the lightweighting case instead of components experiment. The prevalent structural lightweighting design needs a complicated FE model including the much more detailed structure, which will cost very long time for building and preprocessing. And, whatever the CAD or FEM model, those are not flexible enough to adjust to ceaseless modification in the concept development stage, since that geometry modifications are difficult to realize modify synchronization from CAD model to FE model.

Parameterized structure design by SFE CONCEPT idea is put forward for the structure fast update of car body lightweight structure. Rather than common CAD or FEM model, the SFE model is composed of engineering parameterized structure, which is built by SFE CONCEPT software. This parameterized model can be applied for the structure revision from detail to entire body with fewer design parameters, which can also quickly generate the FE model and provide better technical support for body structure multi-performance optimization. The SFE parameterized modeling method can shorten the modification period of CAE model, which has the obvious advantage of putting CAE in a position to lead the design activity instead of reacting to it [3]. This parameterized lightweighting method is very effective to help engineers to determine the best design way and balance the shape, size and thickness by the integrated analysis and optimization with the parameterized model.

3 Parameterized Structure Lightweighting

In SFE CONCEPT modeling idea, the parameterized structure should be constructed by many simply elements [4]. The geometry of the generated model is a result of the topological description, which is not constructed from a CAD tool or a CAE tool. The typical elements in SFE CONCEPT are influenced by points, base

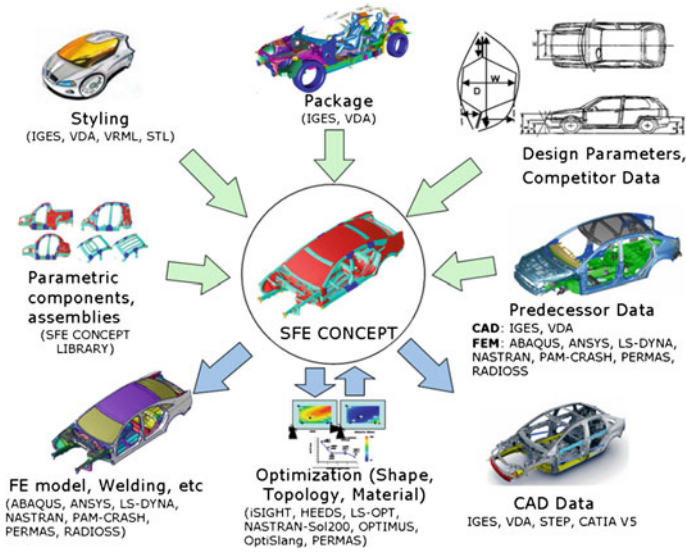


Fig. 1 Parameterized body structure

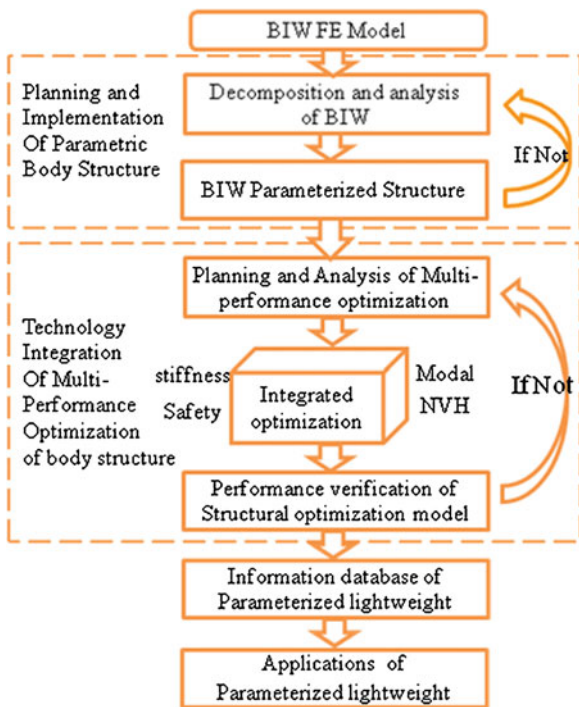
lines, cross sections, beams, joints, simple surface domains, and so on. The relations between these elements allow generating the complete and consistent surface of the model. The description is fully parametric and permits topological and/or geometrical modifications in a very fast and efficient manner.

The SFE parameterized geometrical model generated by SFE CONCEPT enables a good approximation to the target design geometry components, which is also required validation. This processing required much early product knowledge of a new design in the early design phase. Figure 1 shows the design ideas of parameterized body structure.

The SFE model built by point location, line curvature and the shape of cross-section is assembled by established mappings. All the parts of the SFE model are united logically by the engineering parameters. Each parameter change will automatically drive the change of other associated parameters. The whole SFE model is assembled by hundreds of parts which can be changed rapidly by the logical parametric change for some simulation.

Lightweighting design required the engineers devise the optimization factors in SFE model based on design performance and experience, such as material properties, thickness, section shape, size, the relative location of the parts. According to the predetermined engineering parameters, the SFE CONCEPT could quickly generate the FE model of BIW for the analysis on modal, stiffness, safety, and so on. Under the optimization tools drive, the SFE model can continuous change the structural parameters for FE model to analyze the multi-performance of body structure with the calculate solver. The optimization result can help the engineers

Fig. 2 Structural lightweight processes



find the best balance between body structural performances and body’s lightweight. The implementation process of parameterized structural design for car-body lightweighting is shown in Fig. 2.

4 A Case of SFE Structural Modeling and Validation

A new SFE structural parameterized model can be built from a FE model or a CAD model. Usually, an existing FE model is more available for the building of SFE structural engineering parameterized model [5].

SFE model building is about 9 steps.

(1) Topological Analysis of the Car FE-model and Splitting into Logical Parts

By the initially identify method and structural topological analysis process, the car structure is divided into many assemblies, and then split into many components. Finally, the SFE model will be established and assembled by all the parts.

(2) Creating Influence Points and Base Lines

Create influence points at flange or significant design edges, and then create base lines with those influence points.

(3) Creating Cross-sections

Fig. 3 Roof assembly SFE model

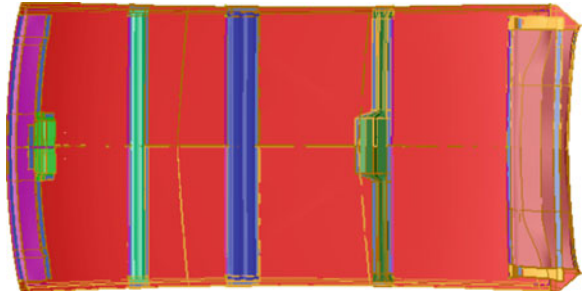
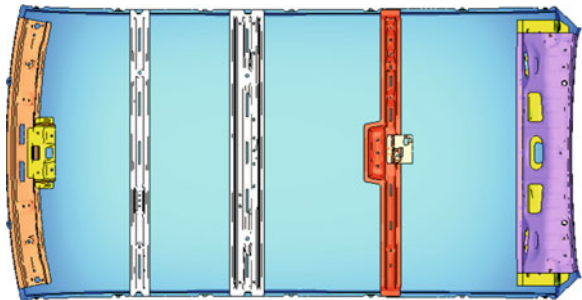


Fig. 4 Initial roof assembly FE model



In SFE model, cross-section is divided into base-section and local-section.

(4) Creating Beams

Establish an initial beam through the guide lines and the base-sections, and increase the local-sections according to the structural profiles in the corresponding locations.

(5) Creating Joints

Joints are complex beam connections, which show good consistency between SFE model and initial FE model.

(6) Creating SFE Surfaces

Surfaces are defined by closed loop lines, which are the edges of the surface.

(7) Assigning PIDs

In SFE model, the material properties are defined on IDs, which are assigned to the surfaces of the SFE model. Therefore, engineers should setup PIDs of different materials and thickness according to the parts characteristics.

(8) Mapping

Mapping is a unique feature in the SFE software, which is to project objects onto other objects. After that, the welding and assembly relations between parts can be defined.

Fig. 5 Modal analysis results on roof assembly

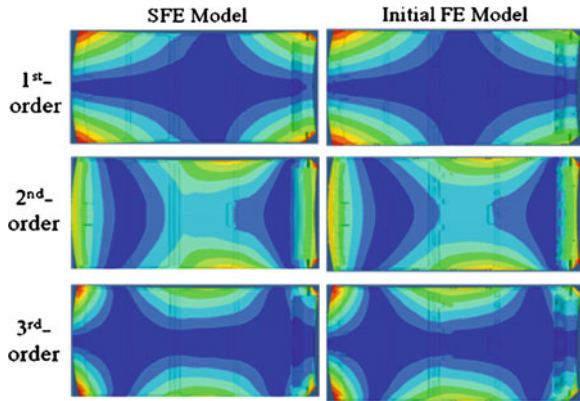


Fig. 6 SFE model of a car

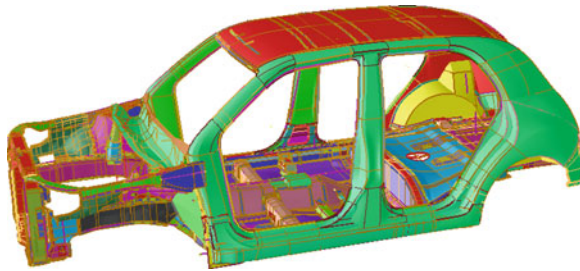
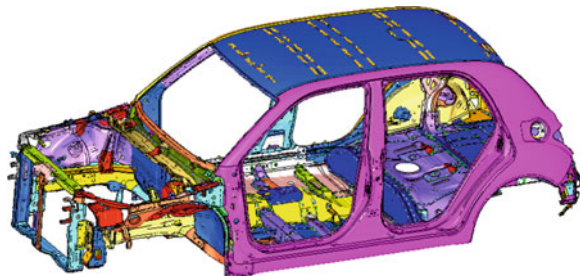


Fig. 7 The original FE model



(9) Generating the FE-mesh by SFE CONCEPT

The FE model can be generated by SFE CONCEPT from complete SFE model.

Figure 3 shows the SFE model of roof assembly. Figure 4 shows the initial FE model. From the two figures, it could be easily to find that SFE model could accurately reflect the body structure and details.

A validation process is about 6 steps.

- (1) Select an existing carbody FE model which is a detailed validated finite element simulation model. (As the initial roof assembly FE model shown in Fig. 4).

Table 1 The contrast data

Performance		The disparity from FE model generated by SFE model and the original FE model (%)
Mass	Body structure mass(kg)	-0.62
Modal	1st order torsion(Hz)	-1.16
	1st order bending(Hz)	-1.19
Stiffness	Torsion (kN m/deg)	-3.34
	Bending (kN/mm)	3.19

- (2) Create a parameterized SFE CONCEPT roof model. (As the roof assembly SFE model shown in Fig. 3).
- (3) Generate a finite element mesh using SFE CONCEPT.
- (4) Calculate the modal characteristics between the two models.
- (5) Compare the results from the SFE CONCEPT generated mesh to those of the validated finite element model.
- (6) Analyze the differences, and modify the SFE model further, in order to achieve a good consistency.

Figure 5 shows modal comparison of SFE model and SFE model. It can be easily to know that they have an excellent consistency.

Figure 6 is the SFE model of a car. Figure 7 is the original FE model.

The Table 1 is the contrast analysis data from FE model generated by SFE mode to the original FE model. All the disparity is less than 5 %. So that the parameterized structural SFE model generates FE model is available for further CAE optimization.

After the construction and validation, the SFE model can reflect the real structural performance of the body structure, so that can be used in the further analysis. One advantage of SFE CONCEPT parameterized model is that can implement structure change quickly and followed FE generating quickly. The grid generated rapidly from SFE model can be used for analysis of modal, stiffness, security, and so on. Driven by iSIGHT or OPTIMUS, the SFE CONCEPT can linked by solver, such as NASTRAN, ABAQUS, ANSYS, LS-DYNA, PAM-CRASH, and so on. Therefore, the multi-objective optimization analysis is available by SFE CONCEPT model and multiple solvers.

Figure 8 shows an optimization loop. Using such an optimization loop, the response relationship can be obtained between each lightweighting parameter and multi-performance of body structure, which can guide the carbody structural lightweighting design. If putting the lightest body weight as the target and multi-performance as constraints, the solver’s eventually calculation should be a good engineering parameters combination for carbody structural lightweighting design. Figure 9 is a lightweighting optimization flow chart.

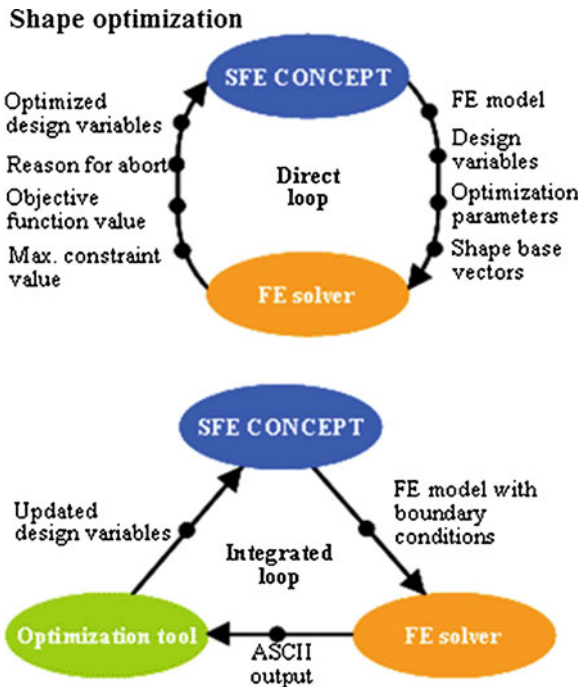


Fig. 8 Optimization loop

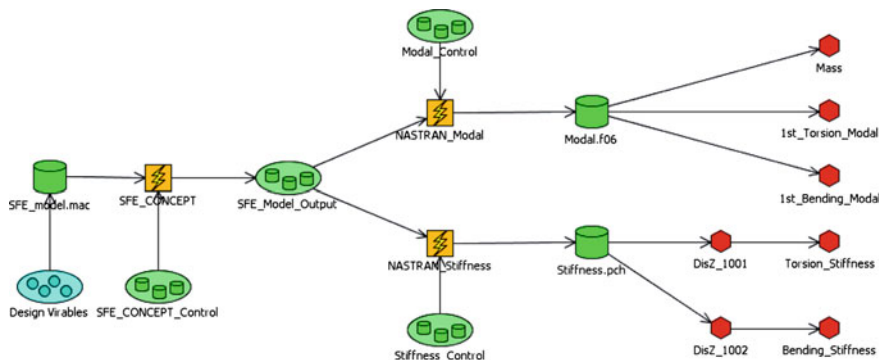


Fig. 9 A lightweighting optimization flow chart

5 Conclusions

Compared with traditional structural lightweighting process, this SFE engineering parameterized lightweighting design method has several advantages as follows.

- (1) Full engineering parameterization of the carbody geometry structure is possible.
- (2) The compared calculation results from SFE to the validated FE model show that the SFE model's validity is believable.
- (3) The automatic lightweight optimization can be carried out with engineering parameterized SFE model combined the tools of optimization and solver.
- (4) Save development time and cut down the cost, quickly optimize structural multi -performance objects.

Engineering parameterized structure lightweighting is a new method for reduce the carbody weight in the early structural concept development stage.

Acknowledgments The authors would like to express their appreciations to National Science and Technology Planning Project (No. 2011BAG03B02) and National Natural Science Foundation of China (No.51175214) for their supports to the research.

References

1. Wei zhou (2011) Structural lightweight design of bus frame. Jilin University, Changchun
2. Simon Xu (2007) Use of topology design exploration and parametric shape optimization process to development highly efficient and light weight vehicle body structure. General Motors Corporation.GM Global CAE conference. Sept 2007
3. Schelkle Erich, Elsenhans Herbert (2001) Virtual vehicle development in the concept stage-current of CAE and outlook on the future. 3rd MSC Worldwide Aerospace Conference & Technology Show Case, Toulouse, September 24–26
4. SFE GmbH (2010) SFE COCEPT reference manual v4.2
5. Zimmer H, Umlauf U (2000) Use of SFE CONCEPT in developing FEA models without CAD. SAE paper 2000-01-2706

Reliability-Based Topology Optimization of Control Arm of Suspension for Lightweight Design

Qinghai Zhao, Xiaokai Chen and Yi Lin

Abstract The existing uncertainties and the inducing factors for control arm are presented under the position of its function and requirements. Reliability-based topology optimization is proposed that integrate reliability analysis into topology optimization to design control arm subject to random inputs, such as random external loads. A single loop method is implemented to consider the reliability levels by combination deterministic topology optimization software. The first-order reliability method is adopted to approximate the failure probability constraint at most probable point. The random variables are transformed into deterministic boundary conditions for topology optimization by reliability index approach. Optimal topologies of control arm obtained from reliability-based topology optimization are compared to result from traditional deterministic topology optimization.

Keywords Reliability-based topology optimization · Control arm · Lightweight design · First-order reliability method · Reliability index approach

F2012-E09-039

Q. Zhao (✉) · X. Chen · Y. Lin
School of Mechanical Engineering, Beijing Institute of Technology, No.5 Zhongguancun
South Street 100081 Beijing, China
e-mail: zqh2006.1985@163.com

Y. Lin
Beijing Automotive Technology Center, No.10 Huaweili, Beijing 100021, China

1 Introduction

The aim of the deterministic topology optimization (DTO) is to obtain optimal material distribution that minimizes/maximizes the given objective while subjected to prescribed deterministic constraints. However, the solutions don't account for the effects of uncertainties such as material properties (Young's modulus, allowable stress, etc.), loading conditions and geometry. Therefore, deterministic designs couldn't ensure the target reliability level for the performance functions. For that reason, reliability-based topology optimization (RBTO) [1, 2] is proposed to integrate probabilistic constraints into topology optimization. The purpose of RBTO is to take into account the randomness of the applied loads, the assignment of material properties and the description of the geometry, and the solutions of RBTO could obtain the best compromise between cost and safety.

Different from in deterministic topology optimization, the variables in reliability-based topology optimization could be distinguished into three categories:

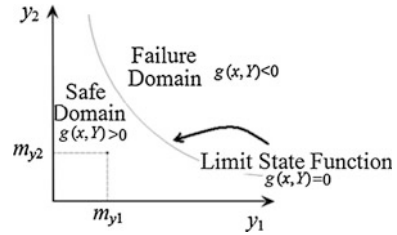
- (1) The deterministic variables x , which are the element design variables.
- (2) The random variables y , which represent the uncertainties, characterized by probabilistic distributions.
- (3) The normalized variables u , which represent the mean values and standard deviations in relevant with random variables.

Reliability analysis needs a model of the designed system that describes its behavior under various variables. The behavior is defined by a function $g(x, Y)$, where Y , represented as (y_1, y_2, \dots, y_n) is the vector of random variables defining loads, material properties and geometry. Let the limit between the state of failure $g(x, Y) < 0$ and the state of safety $g(x, Y) > 0$ is known as the limit state surface $g(x, Y) = 0$ shown in Fig. 1. So that the failure probability is evaluated by

$$P_f = P_r[g(x, Y) \leq 0] = \int_{g(x, Y) \leq 0} f_Y(y) dy_1 dy_2 \cdots dy_n$$

where P_f is the failure probability, $f_Y(y)$ is the probability distribution function of the random variables Y , and $P_r[\cdot]$ is the probability operator. The evaluation of the above integral is difficulty, because it represents a very small quantity and the limit state function may be unknown. For this reason, response surface method (RSM) [3] and standard response surface method (SRSM) [4] are used to generate an approximate limit state function where the chosen random variables are independent of each other. Obviously SRSM needs much fewer experimental points than traditional RSM in quadratic form. Besides, the necessary information for the probability distribution function may be not available. Therefore, several different approximate algorithms have been adopted to evaluate the reliability constraints, which can be done either by stochastic simulations or by moment methods. Monte Carlo simulation [5, 6] as basic sampling method can be used to evaluate reliability. Although the implement of MCS is relatively simple, this reliability analysis is

Fig. 1 Physical space



computationally expensive because this method requires a great number of structural responses. The moment methods, the first order reliability method (FORM) [7] and the third order approximation (TOA) [5], were applied to estimate the failure probability based on the reliability index concept. FORM involves the process of obtaining the most probable point (MPP) by a hyperplane which is tangent to the failure surface at that point. In TOA the failure surface is approximated by a more accurate cubic hypersurface at MPP. The higher-order failure surface approximations are generally considered to predict high precision of failure probability at the expense of computing cost. The reliability index approach (RIA) [8, 9] and the performance measure approach (PMA) [10–12], are two main formulations consisting in FORM. RIA and PMA can be divided into two-level approaches, where the outer loop aims to solving the optimization problem in terms of design variables x and the inner loop aims at solving the reliability problem in terms of random variables Y . Thus when applying the principle of the above approach to topology optimization, the problem becomes bigger because the computing time will increase significantly and the reliability analysis in each iteration of the topology optimization procedure will represent a very complex task.

In this paper, we will introduce a new different strategy of a sequential procedure, which employs a single-loop strategy that decouples the outer design optimization from the inner reliability analysis without increasing the computational time. The DTO software is used to solve the RBTO analysis of control arm. For simplify, the objective of control arm is minimize the weight equivalent to volume with the applied loads considered as random variables. The paper is organized as follows: the various uncertainties of control arm are presented with detail characterization in Sect. 2. Section 3 discusses the RBTO algorithm for control arm and the solution strategy for reliability analysis. In Sect. 4, the optimal results of control arm based on RBTO and DTO are compared with new reliable and applicable resulting topologies.

2 Uncertainties of Control Arm

Suspension system, an indispensable vehicle assembly, has greatly impact the quality characteristic of dynamic performances such as handling and stability. As an important portion of the complete suspension system, control arm has the function

not only to control the movement of the wheel and transmit propulsion, braking, lateral, and vertical forces from the tire's contact patch with the roadway to the vehicle's chassis, but also to fulfill the requirements of compactness and lightweight.

Nowadays, the design of control arm generally begins with the preexisting conditions including the hardpoints, link types, joint types and the available design space, where structural optimization is then considered to design optimized configuration that satisfies various demands such as strength, stiffness and cost. However, most of the current work is focused on deterministic optimization where the design is determined without taking the effects of uncertainties concerning materials, geometry, and loading into account. Actually, the geometrical dimensions of control arm are random variables due to manufacture and installation errors. Because of manufacture environment, technical conditions and polyphase structural features, material characteristics are uncertainties. Especially, the load boundary conditions for control arm are delivered by ball joints, rubber bushings or hydraulic bushings with strong nonlinear mechanical properties, which lead to the applied external loading randomness. Therefore, in order to improve the reliability level of control arm without increasing its weight significantly and result more reasonable structure, topology optimization need integrate reliability analysis by considering the randomness of the main variables of the control arm.

3 Reliability-Based Topology Optimization Problem

The topology optimization for control arm subjected to random loads is considered in this paper. The RBTO of control arm problem consists of minimizing the weight subject to the failure probability. The material densities are used as deterministic design variables. Using the SIMP approach, the problem can be expressed as:

$$\begin{aligned}
 \min_{x_e} \quad & V(x_e) = \sum_{e=1}^N x_e v_0 \\
 \text{s.t.} \quad & P_f \leq P_f^* \\
 & KU_{y_i} = F_{y_i} \\
 & 0 < x_{\text{Min}} \leq x \leq 1
 \end{aligned} \tag{1}$$

where V is the control arm volume, U_{y_i} and F_{y_i} are the global displacement and force vectors considering the randomness of the applied loads, respectively, K is the global stiffness matrix, x is the vector of design variables, x_{min} is a very small vector assigned to void regions in order to prevent singularity, N is the number of elements used to discretize the control arm, v_0 are the element volume, P_f^* is the target failure probability, where P_f must be less than or equal to it.

3.1 Failure Probability Conversion

Using FORM to calculate the failure probability of control arm, the limit state function can be approximate expanded by Taylor formulation at the most probable failure point (MPP):

$$\hat{g} \approx g(Y_{MPP}) + \nabla g(Y_{MPP}) \cdot (Y - Y_{MPP})^T \quad (2)$$

Suppose that probability distribution of the expanded limit state function satisfies Gaussian distribution, the mean value and standard deviation can be calculated from (2) as follows:

$$\mu_g = g(Y_{MPP}) \quad (3)$$

$$\sigma_g^2 = \sum_{i=1}^n \left(\frac{\partial g}{\partial y_i} \right)^2 \sigma_{y_i}^2 \quad (4)$$

Therefore, the failure probability constraint can be expressed as follows:

$$P_f = \Phi \left(-\frac{u_g}{\sigma_g} \right) \quad (5)$$

where $\Phi(\bullet)$ is the standard Gaussian cumulated function. The reliability index β is introduced, which is defined as:

$$\beta = \frac{u_g}{\sigma_g} \quad (6)$$

Then, the failure probability is simply evaluated by:

$$P_f = \Phi(-\beta) \Rightarrow P_f^* = \Phi(-\beta_t) \quad (7)$$

For practical engineering, the reliability index gives a sufficiently accurate estimation of the failure probability. The failure probability constraint could be replaced by expression of reliability index as follows:

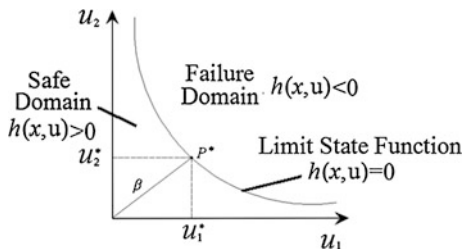
$$P_f \leq P_f^* \Rightarrow \beta \geq \beta_t \quad (8)$$

3.2 Reliability Index Evaluation

In order to calculate reliability index efficiently, the transformation from the random variables Y to uncorrelated normalized variables U is given by:

$$u_i = \frac{y_i - m_{y_i}}{\sigma_{y_i}} \quad (9)$$

Fig. 2 Normalized space



After the probabilistic transformation operation, the space with respect to the normalized variables is shown in Fig. 2.

The evaluation of the reliability index β can be carried out by a particular optimization procedure. The index is the minimum distance between the limit state and the origin in the normalized space as shown in Fig. 2. The reliability index is computed by solving the constrained optimization problem by reliability index approach (RIA) as follows:

$$\begin{aligned} \text{Min}_u \beta &= d(u) = \sqrt{\sum u_i^2} & (10) \\ \text{s.t } \beta &\geq \beta_t \end{aligned}$$

During the optimization procedure, the derivative of the index β with respect to u_i by:

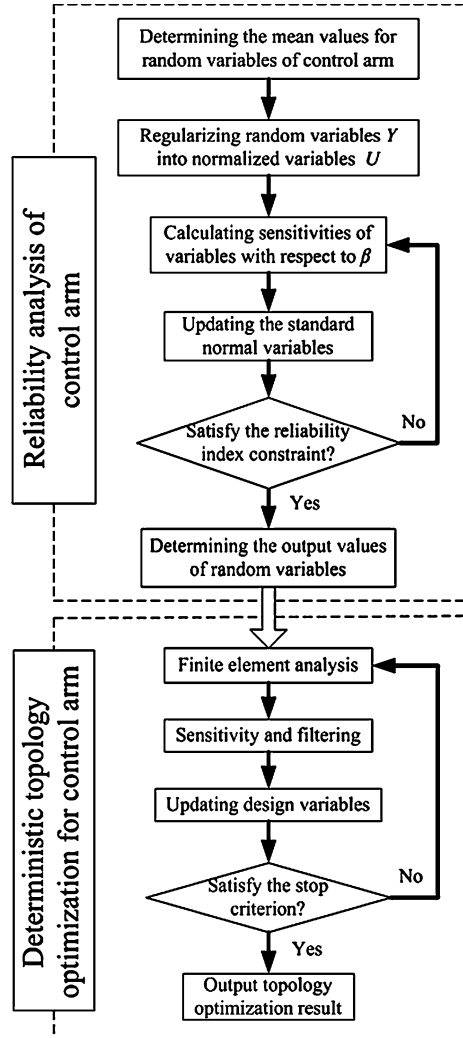
$$\frac{\partial \beta}{\partial u_i} = \frac{u_i}{d(u)} \tag{11}$$

The solution u^* is the so-called MPP, which will be used to evaluate the random variables Y by using inverse change (9) with the standard deviations given by $\sigma_{y_i} = 0.1m_{y_i}$.

3.3 Design Process for RBTO

The RBTO model contains two main successive processes: reliability index evaluation and the topology optimization process as shown in Fig. 3. Each one of these processes is considered as an independent loop that is called as a sequential procedure, which is more appropriate than the coupled procedures that contain nested optimization and reliability loops. First, the mean value of random variable is determined that concerns the applied loads of control arm. Secondly, the target reliability index β_t is evaluated by satisfying the failure probability constraint. Then the normalized variables U are calculated to formulate the random variables Y as deterministic boundary conditions for topology optimization. Finally, using the deterministic values of variables Y , the SIMP approach is applied to obtain the reliable and optimal solution of the control arm.

Fig. 3 RBTO procedure for control arm



4 Control Arm Example

To solve the topology optimization problem for control arm, OptiStruct software from Altair Engineering [13] is used. The control arm is optimized to minimize weight with displacement constraints and failure probability constraint in relation to corresponding three external random loads, including braking force, lateral force and wheel hop force. The geometry model of control arm with designable region and non-designable region is shown in Fig. 4. The non-designable region is assigned to the bushings, because the function for them is mainly connect and transfer the loads. In order to ensure the manufacturing process and reduce cost for

Fig. 4 The geometry of control arm

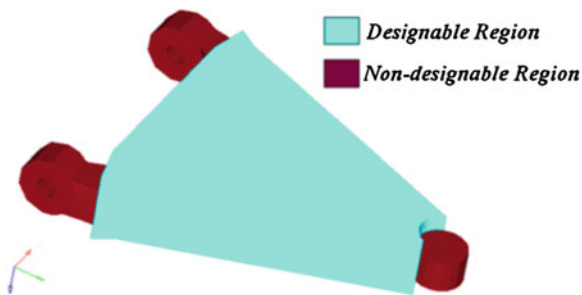
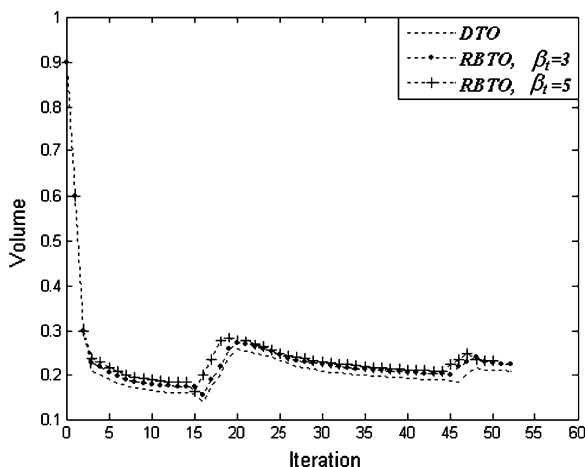


Fig. 5 Optimal volumes for control arm by RBTO and DTO



control arm, manufacturing constraints, involving symmetry and stripping constraints, is imposed on the control arm during RBTO process, which eliminate discrete result, asymmetric design and casting problem. After 52 step iterative optimization loop, the change of the volume with respect to optimization iteration and the optimal results by DTO and RBTO are shown in Fig. 5. Compared with the results obtained by DTO, the volume for control arm is increase by 7 and 11 % when $\beta_t = 3$ and $\beta_t = 5$ at RBTO design process, respectively. There are two main improvements for DTO and RBTO design results, where the connections between the bushings and the body of control arm are strengthened, and similar to ribs is appearance to firm the carrying capacity when random loads transform at an interval. The optimal topologies for DTO and RBTO with different reliability indexes are shown in Fig. 6.

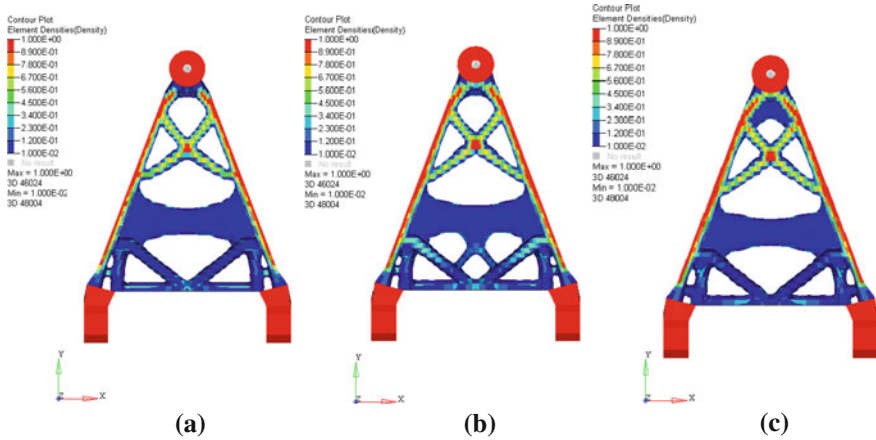


Fig. 6 Optimal topologies of DTO (a) RBTO $\beta_r = 3$ (b) and RBTO $\beta_r = 5$ (c) for control arm

5 Conclusions

Reliability-based topology optimization for control arm is performed, which is to minimize the weight while considering the randomness of the applied loads by using a single loop method that compatible with readily available topology optimization software. However, the random variables are calculated into deterministic boundary conditions with the help of predefined target failure probability by FORM. At the same time, the nature of the reliability constraint is retention while the solution for topology optimization problems. The methodology can be applied more generally with reliability analysis in advance and effectively overcome the limitations of the deterministic topology optimization design. The most advantage of the RBTO model is that the resulting optimal topologies are more reliable than the deterministic topologies. This method can be extended to other parts of vehicle, such as chassis and body design.

References

1. Kharmanda G, Olhoff N, Mohamed A (2004) Reliability-based topology optimization. *Struct Multidiscip Optim* 26:295–307
2. Kharmanda G, Olhoff N (2001b) Reliability-based topology optimization. Institute of Mechanical Engineering, Aalborg University, Denmark. Report No. 110, Dec 2001
3. Kwang-Sun Y, Young-Sop E, Jae-Yong P (2011) Reliability-based topology optimization using successive standard response surface method. *Finite Elem Anal Des* 7:843–849
4. Young-Sop E, Kwang-Sun Y, Jae-Yong P (2011) Reliability-based topology optimization using a standard response surface method for three-dimensional structures. *Struct Multidisciplinary Optim* 32:287–295

5. Mostafa M, Eysa S, Javad S (2012) Reliability-based topology optimization of double layer grids using a two-stage optimization method. *Struct Multidisciplinary Optim* 45:815–833
6. Nguyen TH, Song J, Paulino GH (2011) Single-loop system reliability-based topology optimization considering statistical dependence between limit-states. *Struct Multidisciplinary Optim* 44:593–611
7. Katsuya M, Shinji N, Kazuhiro I (2006) Reliability-based structural optimization of frame structures for multiple failure criteria using topology optimization techniques. *Struct Multidisciplinary Optim* 32:299–311
8. Kim C, Wang SY, Bae KR (2006) Reliability-based topology optimization with uncertainties. *J Mech Sci Technol* 20:494–504
9. Mariana Silva, Tortorelli DA, Norato JA (2010) Component and system reliability-based topology optimization using a single-loop method. *Struct Multidisciplinary Optim* 41:87–106
10. Cho K-H, Park J-Y, Ryu S-P (2011) Reliability-based topology optimization based on bidirectional evolutionary structural optimization using multi-objective sensitivity numbers. *Int J Automot Technol* 6:849–856
11. Jung HS, Cho S (2004) Reliability-based topology optimization of geometrically nonlinear structures with loading and material uncertainties. *Finite Elem Anal Des* 3:311–331
12. Maute K, Frangopol DM (2003) Reliability-based design of MEMS mechanisms by topology optimization. *Comput Struct* 81:813–824
13. Altair OptiStruct: user guide. Altair Engineering, Troy, 2007

Structural Lightweight Design of Engine Connecting Rod

Fuxiang Huo, Jun Li, Yu Xu, Bing Wu, Yepeng Han, Peng Li
and Qun Zhang

Abstract The connecting rod is one of the key components of an automotive engine; it works under dynamic loads with complex uncertainties. The reliability of a connecting rod is critical for an engine design. For traditional deterministic numerical simulations of connecting rods, which neglect some uncertain factors, the reliability is guaranteed by introducing overly conservative safety factors, and it normally results in a safe but over weighted and suboptimal design. In this paper a framework for the sensitivity analysis and reliability based design optimization of a connecting rod is proposed. The most advanced reliability based design optimization and simulation software integration methods will be employed in this research; it seamlessly integrates a sensitivity and reliability analysis driver, a parameter driven CAD tool, and an advanced nonlinear structural analysis CAE software package. The entire process will be conducted automatically by command scripts. Using the proposed reliability based analysis framework the weight of the connecting rod is reduced by 3.7 % without compromising reliability.

Keywords Connecting rod · Sensitivity · Reliability · Optimization design · ISIGHT integration

F2012-E09-042

F. Huo (✉) · J. Li · B. Wu · P. Li
The First Automobile Group Co., Ltd R&D Center, Changchun, China
e-mail: huofuxiang@rdc.faw.com.cn

Y. Xu · Y. Han · Q. Zhang
INTESIM (Dalian) Co., Ltd, Dalian, China

1 Introduction

Reliability problems originate from the existence of uncertainties in the actual engineering problems. It is essential to consider these uncertainties to achieve a reliability design for mechanical structure [1]. The connecting rod works under dynamic loads with complex uncertainties such as the geometrical dimensions, material properties and the external loads. Traditionally the reliability problem of the connecting rod is addressed by introducing a safety factor, which is artificial and arbitrary and usually results in a conservative and over weighted design.

There have been many research papers about reliability based design optimization (RBDO) for the connecting rod, but most of these research papers are limited to 2D analysis or restricted to the investigation for a simplified theoretical solution [2–4]. Some researchers have carried out the RBDO analysis for the 3D connecting rod but with cumbersome manual sampling.

To this author's knowledge, this is the first study of building a 3D parametric model to perform RBDO in consideration of uncertainties for a real connecting rod. An integrated and fully automatic parameterization and RBDO framework for the real 3D connecting rod is established in this study.

The most advanced RBDO and simulation software integration methods are employed in this research; it seamlessly integrates a sensitivity and reliability analysis driver—ISIGHT, a parameter driven CAD tool—CATIA, and an advanced nonlinear structural analysis CAE software—ABAQUS. The entire process is conducted automatically by command scripts. The distributions of the uncertain parameters and the ranges of the design parameters of the connecting rod are investigated and used in this research. The sensitivities of the design goals such as the total weight, maximum stress, and the deformation of the rod with respect to the key design parameters are studied. The deterministic design optimization and reliability based design optimization are carried out and the advantage of reliability based design optimization over the deterministic design optimization is discussed. The key conclusion for this research is that by using the proposed reliability based analysis framework the weight of the connecting rod is reduced by 3.7 % without compromising reliability.

2 Integration System

Figure 1 shows the integrated RBDO framework proposed in this research. In this framework CATIA with Excel are used as 3D parametric modeling tools, HyperMesh is adopted as the automatic meshing software, and ABAQUS is employed for the nonlinear structure analysis. There are some post processing modules to produce the mass, stress, deformation, etc. In this framework, all of the modules are controlled by the script language; it makes the entire process fully automatic.

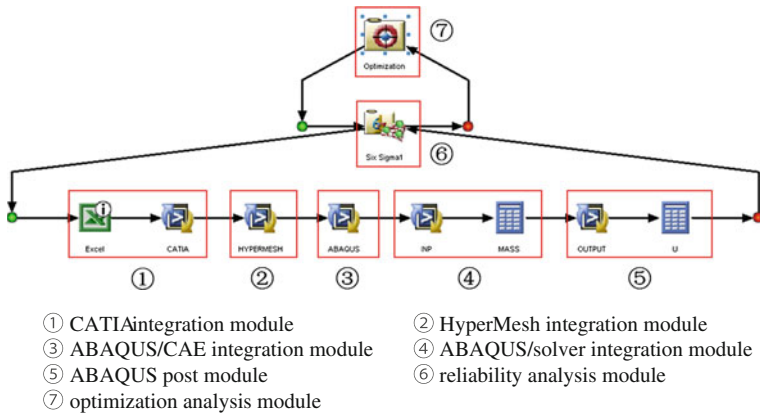


Fig. 1 RBDO integration system

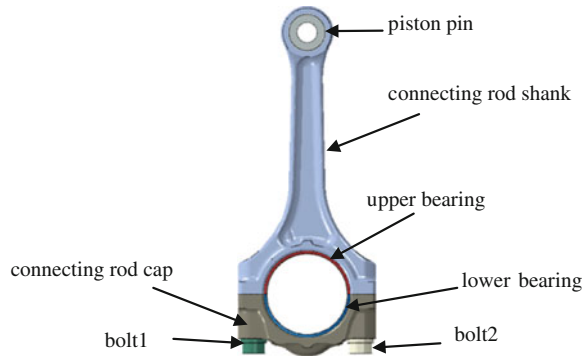
In this framework, the CATIA module with the parameter list defined in an Excel file is firstly launched to create and output the parameterized 3D model. The meshes are generated in the HyperMesh module; nodes and surface sets for interaction and boundary settings are also created. In ABAQUS/CAE module, the assembly process of the connecting rod is accomplished, and the analysis conditions are also set. In ABAQUS/solver module, random variables such as the material properties and external loads conditions are defined, then the finite element analysis is conducted, next the total weight of connecting rod is set as the target parameter. Finally in ABAQUS post-processing module, the results of finite element analysis are read, and the stress and deformation values in the monitoring locations are obtained.

The process control module in Fig. 1 includes the reliability analysis module and the optimization analysis module. The method for reliability analysis and the distribution type for the random parameters are set in this module, and then the reliability index for the stress and deformation in the monitoring locations are calculated. The optimization design module controls the global optimization analysis, the optimization algorithm, constraint conditions and optimization goals will be setup here, it drives the optimization directions and finally achieves an optimization design with the satisfactions of the constraint conditions.

3 Numerical Analysis

In order to perform the lightweight design for the connecting rod, deterministic finite element analysis (FEA), parameter sensitivity studies, deterministic design optimization, and RBDO are carried out orderly.

Fig. 2 Assembly model of connecting rod



3.1 Deterministic Finite Element Analysis

3.1.1 Finite Element Analysis Model

The assembly model of the connecting rod is shown in Fig. 2; it consists of the connecting rod shank, connecting rod cap, piston pin, bearings, and bolts. There are seven contact pairs defined in this model, that include piston pin to connecting rod shank, shank to upper bearing, connecting rod cap to lower bearing, bolt1 to connecting rod cap, bolt2 to connecting rod cap, connecting rod shank to connecting rod cap, and upper bearing to lower bearing.

The interference preload of bolts are considered in the deterministic analysis. In order to approximate the oil film pressure between the connecting rod and bearings, the line spring elements are created between the connecting rod and bearings. To obtain accurate finite element analysis results with a reasonable number of meshes, tetrahedron element C3D10 M is used for connecting rod shank and connecting rod cap, while hexahedron element C3D8I are generated for the other parts.

3.1.2 Load and Boundary Conditions

The connecting rod works under periodic loads, the maximum compression state occurs at the top dead center (TDC) position in the expansion stroke, and the maximum tension state occurs at the top dead center (TDC) position in the intake stroke. The deterministic FEA analysis is performed for these two extreme working conditions in the lightweight design process [5–7].

3.1.3 Results and Discussion of Deterministic Analysis

The von-Mises stress contour plots at the maximum tension and the maximum compression conditions are given in Fig. 3. The monitoring locations for von-

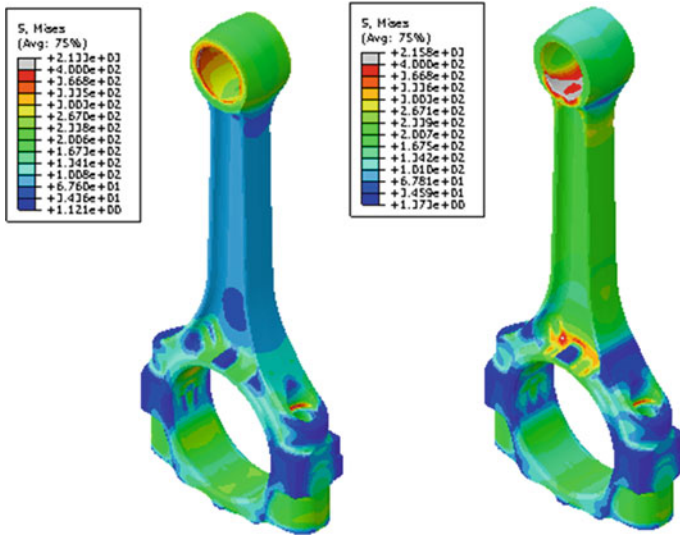


Fig. 3 Von-Mises stress contour plots at maximum tension (*left*) and maximum compression states (*right*)

Mises stress are demonstrated in Fig. 4 and the minimum and maximum stress σ_{\min} and σ_{\max} will be reported for these locations.

In this research the КИНАСОШИЛИ method [8] is employed for calculating the limit stress constraints. Figure 5 shows the graphical demonstrate for КИНАСОШИЛИ method. The coordinates of interaction point E_e and the boundary angle β_{E_e} can be calculated as below for steel material.

$$\sigma_{mEe} = \frac{K_\sigma \sigma_S - \sigma_{-1}}{K_\sigma - \psi_\sigma} = 308.9 \tag{1}$$

$$\sigma_{aEe} = \frac{\sigma_{-1} - \psi_\sigma \sigma_S}{K_\sigma - \psi_\sigma} = 511.1 \tag{2}$$

$$\beta_{Ee} = \arctan \frac{\sigma_{aEe}}{\sigma_{mEe}} = 58.85^\circ \tag{3}$$

Where, σ_{-1} is the symmetrical cycle fatigue limit of material, for steel the value is 440 MPa; σ_S is yield limit of the material, and 820 MPa is for steel; K_σ is comprehensive stress influence coefficient, the value is 0.74; ψ_σ is equivalent coefficient, the value is 0.2.

Equation (4) is used to calculate the boundary angle β

$$\beta = \arctan \frac{\sigma_a}{\sigma_m} \tag{4}$$

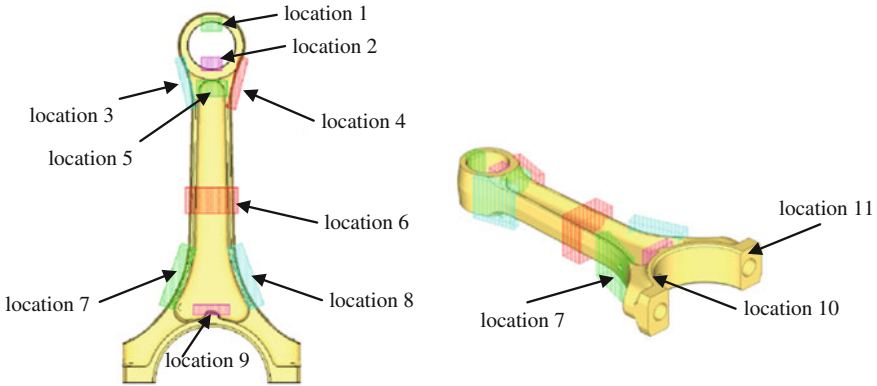
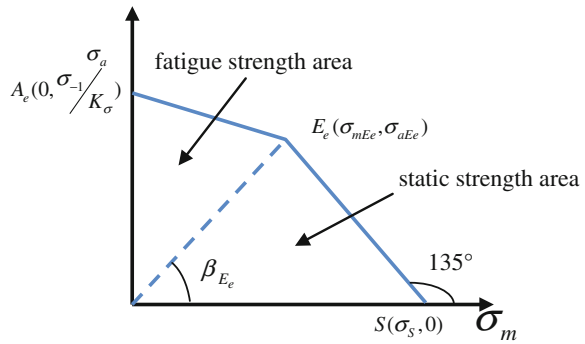


Fig. 4 Monitoring locations of Von-Mises stress

Fig. 5 КИНАСОШ.П.ИИ method of fatigue strength



where,

$$\sigma_m = \frac{\sigma_{\min} + \sigma_{\max}}{2}, \tag{5}$$

$$\sigma_a = \frac{\sigma_{\max} - \sigma_{\min}}{2}. \tag{6}$$

Substitute the minimum and maximum stress from FEA calculation into Eq. (4); we can obtain the boundary angle β for each monitoring location (Table 1). By comparing the value of β with β_{E_e} , we understand that locations 3–8 are in the fatigue strength area, the limit stress can be calculated by Eqs. (7) and (8), although the other locations are in the static strength area, the yield limit σ_s is used as $\sigma_{\lim e}$. The limit stress $\sigma_{\lim e}$ for all the monitoring locations are listed in Table 1, the constraint values (the last row in Table 1) that are used as constraint conditions in design optimization analysis are further limited than the value of $\sigma_{\lim e}$. In Table 1,

$$r = \frac{\sigma_{\min}}{\sigma_{\max}} \tag{7}$$

Table 1 Constraint values of each observation location

Location	r	β	σ lime	Constraint value
1	0.71	9.65°		820
2	0.46	20.30°		820
3	-0.25	58.93°	546.04	500
4	-0.25	58.93°	546.04	500
5	-0.32	62.49°	528.22	500
6	-0.36	64.95°	516.21	500
7	-0.79	83.30°	429.34	400
8	-0.34	64.00°	521.25	500
9	0.56	15.64°		820
10	0.58	15.11°		820
11	0.98	0.57°		820

$$\sigma_{\text{lime}} = \frac{2\sigma_{-1}}{K_{\sigma}(1-r) + \psi_{\sigma}(1+r)} / [S_{\sigma}] \quad (8)$$

S_{σ} is the safety coefficient, the value is 1.5.

According to Table 1, the smallest constraint stress value is located at location 7 (oil hole), this is consistent with the failure location from the actual fatigue strength test. This shows the validity of the use of КИНАСОШИ.ПИ method in this research (Fig. 6).

3.2 Parameter Sensitivity Analysis

Due to the complexity of the geometry of the connecting rod, there are more than 30 design parameters that need to be considered in the design optimization process and it is not practical for the huge computation demands. As a solution, parametric sensitivity studies need to be performed firstly to select the more influential parameters on the weight, stress and deformation of the connecting rod.

In the parameter sensitivity studies, the important parameters such as chamfer, the cross section of the I-beam and fillet radius are obtained by manual numerical testing, and then a full parameter sensitivity analysis was conducted for various combinations of those selected parameters. According to the analysis, there are 8 parameters shown in Fig. 7 are discovered to be the most influential ones which will be treated as design objects in the following design optimizations process. The corresponding design variable name, the original value and the variation range are given in Table 2.

In Table 2, L2, D1, D2, R3, R4 F5 and H1 are the most sensitive parameters to the weight of connecting rod, L1, L2, D1, D2, R3 are more sensitive to the stress, but L1 and R3 are more influential on the deformation of connecting rod.

Table 2 Design variables and variation range

Design variable	Description	Original value (mm)	Variation range (mm)
1. (L1)	Length	15.5	15.2–15.6
2. (L2)	Length	17.0	16.4–17.0
3. (D1)	Depth	7.5	7.5–7.9
4. (D2)	Depth	3.5	3.5–3.8
5. (R3)	Arc	24.5	24.5–25.0
6. (R4)	Arc	5.0	4.0–5.0
7. (F5)	Fillet	4.0	3.0–4.0
8. (H1)	Height	6.0	5.0–6.0



Fig. 6 Damaged location of connecting rod from experiment

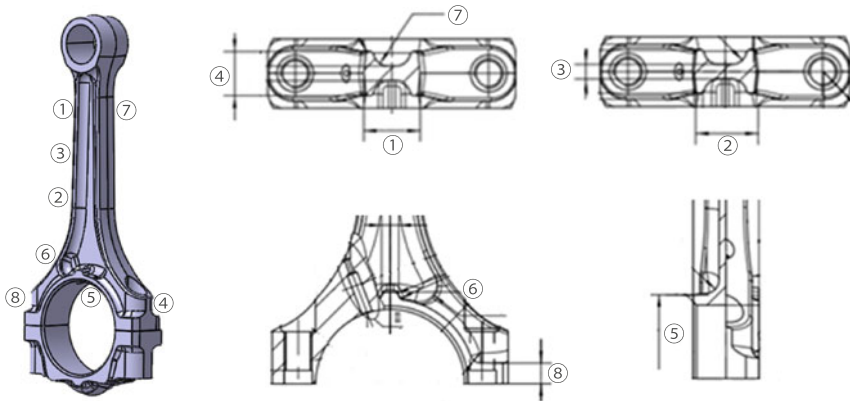


Fig. 7 Design variables locations

3.3 Deterministic Design Optimization

For the deterministic design optimization, the original values and the variation ranges of design variables are given in Table 2. In this analysis, limit stress constraints for each monitoring location are set with КИНАСОШИЛИ method, the

Table 3 Optimization result comparison

Parameter	Original value	DDO	RBDO
1. (L1)	15.5	15.4	15.2
2. (L2)	17	16.4	16.4
3. (D1)	7.5	7.9	7.8
4. (D2)	3.5	3.8	3.7
5. (R3)	24.5	24.5	25.0
6. (R4)	5.0	4.0	4.0 (fixed)
7. (F5)	4.0	3.0	3.0 (fixed)
8. (H1)	6.0	5.0	5.0 (fixed)
Reliability index for the worst location (%)	93.7	86.4	95.8
Weight/weight reduction(g)	331.3/0	313.8/17.5	319.0/12.3
Weight reduction percent (%)	0	5.3	3.7

deformation of the new design must be less than the corresponding value of the original design, and the objective of the design is to minimize the total weight. In this analysis the sequential quadratic programming optimization algorithm is employed. In order to improve the calculation efficiency, the response surface method is adopted with this design optimization method. Finally the optimal solution in the design space is obtained with the satisfaction of accuracy requirement of response surface representation.

The deterministic optimal designs are listed in Table 3; the total weight of the connecting rod is reduced by 5.3 % (or 17.5 g) which satisfies all constraint conditions.

3.4 Reliability Based Design Optimization

In the reliability based design optimization, the material properties and the loads are treated as random variables. According to the existing statistical results, the distribution type of these random variables can be approximated as normal distribution and the coefficient of variation is about 3 %. The reliability index for the stress on each monitoring location and the deformation of the crank end and the piston end are calculated by Monte Carlo method. In the RBDO analysis the constraint conditions for the reliability index are set to 95 % for all constraints, while the other settings remained the same as those in the DDO analysis.

Due to the large number of the total random and design variables, it will cost several days to establish the response surface as thousands of times of 3D nonlinear FEA calculations are needed. To reduce the computation time with minimum compromising on the accuracy, for the geometric parameters which are sensitive to weight but insensitive to the stress and deformation, such as R4, F5 and H1, are directly treated as the deterministic parameter with the value from DDO, and for the

other geometric parameters, such as L1 and L2, D1, D2 and R3, are retained as design variables with the same variation ranges as in the DDO analysis.

The RBDO analysis for the connecting rod is conducted using the settings described above, and the optimal design in Table 3 is obtained which satisfies the reliability requirements.

The comparisons between the original design, the optimal design from the DDO, and the optimal design from RBDO analysis are given in Table 3. From this table we know that the RBDO produces an optimal design with 12.3 g (or 3.7 %) less weight and higher reliability index than the original design. The DDO can reduce more weight (17.5 g or 5.3 %) than the RBDO analysis, but it results in an unreliable design than the original design.

4 Conclusion

1. An integrated and fully automatic numerical frame is presented for the parameter sensitivity analysis, DDO, and RBDO analysis.
2. Through the parameter sensitivity studies for the connecting rod, the important parameters which are sensitive to the weight, stress, and deformation of connecting rod are obtained, this information is used in optimization design.
3. The necessity of considering the uncertainties to perform RBDO analysis other than the traditional DDO was clarified from the analysis results.
4. With the proposed method, the weight of the connecting rod is reduced by 3.7 % without compromising the reliability.

References

1. Rui Y, Fu G (2007) Modern design reliability. National Defence Industry Press, Beijing
2. Yimin Z, Xiangdu H, Qiaoling Liu, Bangchun W (2004) Reliability-based optimizing design of connecting rod under the incomplete probability information. *Trans CSICE* 22(1):86–90
3. Kaymaz I, McMahon CA (2004) A probabilistic design system for reliability-based design optimization. *Struct Multidisc Optim* 28:416–426
4. Michael TL, Roger AK, Christopher CH, Dan HD, Alex Antoc MAHLE Industries Inc. (2010) Advanced connecting rod design for mass optimization. In: SAE Technical Paper 2010-01-0420
5. Mohammad RAAA, Mohammad R, Behnam ND (2011) Dynamic load analysis and optimization of connecting rod of samand engine. *Aust J Basic Appl Sci* 5(12):1830–1838
6. Li Y, Yuan Z, Zeng J (2010) The finite element analysis of connecting rod in 4 v-105 diesel engine based on ABAQUS[J]. *Mech Trans* 34(8):9–42
7. Jianwei Y, Shouguang S, Min L (2009) Fatigue strength analysis of petrol engine connecting-rod with an interference fit using FEM. In: Proceedings of the 2nd international conference on transportation engineering Vol 345., pp 1933–1938
8. Shen J (1994) Mechanical design. Shanghai Jiaotong University Press, Shanghai

Part X
Design for Recycling

Development of Environmental Assessment System of Vehicle

Moosang Yu and Yunjong Kim

Abstract Vehicles can lead to the environmental impact throughout their whole life cycle—from production, use, to disposal. Therefore, analyzing the whole life's environmental profile and setting up advanced environmental performance target for each vehicle within vehicle development process is the basis of 'Eco-design'. In this respect, Life Cycle Assessment (LCA) is a useful tool for analyzing the environmental profile. However, it is very time and manpower consuming work to collect and process the huge amounts of data related to material and energy flows during whole life cycle of a vehicle in the LCA process, due the number of components that a vehicle is made from. Therefore, environmental assessment system of vehicle is developed by GM Korea Company to help manage this problem based on automated and standardized data management and processing methods.

Keywords Vehicle environmental assessment · Environmental assessment system · Vehicle LCA · LCA · Eco-design

1 Introduction

Vehicles can lead to resource and energy consumption and waste discharge from raw material production, through their production and use, to final disposal. So, in order to reduce the environmental pollution induced by vehicles, environmental

F2012-E10-001

M. Yu (✉) · Y. Kim
GM Korea Company, Incheon, Korea
e-mail: moosang.yu@gm.com

regulations related to the each environmental issue are being enforced globally such as fuel efficiency, exhaust emissions, substance content and recycling. Automotive manufacturers make a great effort to develop environment-friendly vehicles for this reason.

In this respect, 'eco-design' that means an approach to a product design with consideration for the environmental impacts of the product during its whole life is important. To implement 'eco-design', comprehensive and objective assessment for environmental impact of a product in the early stage of design is needed. Also, verification for final vehicle in the product launch stage and setting up advanced environmental performance target for next vehicle is important for continuous improvement. This study focuses on development the support tool for environmental assessment that can be used in the vehicle development process.

2 Basic Concept of Environmental Assessment of Vehicle

Comprehensive and objective features that are needed to vehicle environmental assessment can be described in more detail below.

- Comprehensive features
 - Life cycle thinking (consideration for products' whole life cycle)
 - Multi-criteria (global warming, resource depletion, acidification, etc.)
- Objective features
 - Methodology based on scientific background
 - Use of high quality data
 - Quantitative analysis

Life Cycle Assessment (LCA), that is standardized ISO 14040s, is a well-known as useful tool for product environmental assessment that meets the above requirements. Product leads to 'flows in human activity (called intermediate flows)' such as raw material production, energy use, waste treatment, and these intermediate flows bring about 'flows between human activity and environment (called elementary flows)' such as the extraction of natural resources and primary energy, emissions to air or water and landfill wastes. Elementary flows finally induce the environmental impact (global warming, resource depletion, etc.). So, identification of these flows and translation to environmental impact value based on scientific methodology is the basic concept of LCA. Following Fig. 1 shows these processes [1].

LCA study basically consists of following 4 phases to produce the result.

1. Goal and scope definition
2. Inventory analysis
3. Impact assessment
4. Interpretation

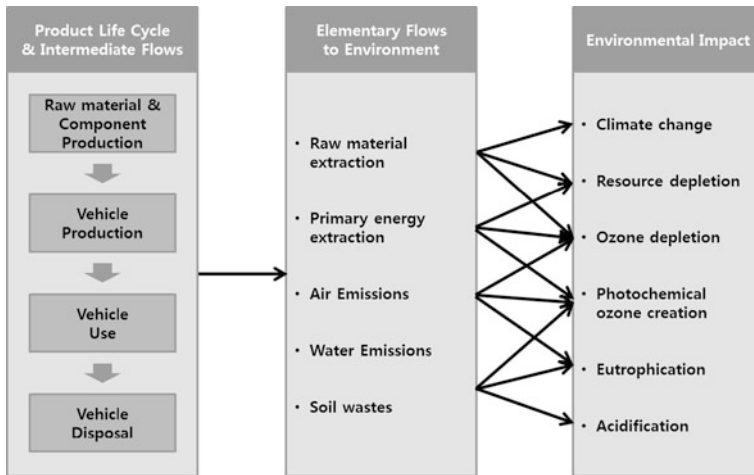


Fig. 1 Material and other flows and environmental impact induced by product during its life cycle [5]

First, subject, intended use, depth and breadth of LCA study are decided, and second, all of related data are collected, verified and calculated to identify intermediate and elementary flows. Third, environmental impact result is produced based on above flows using scientific impact assessment methodology, finally the result is analysed and reach to the conclusion.

The result based on above phases mostly meets the requirements of comprehensive and objective features. However, to do this, collection and processing for huge amount of data during whole life cycle is needed in the inventory analysis phase. GM Korea has tried to apply various alternatives to solve these problems.

3 Initial Process and Problems

Since the mid-1990s, GM Korea has tried to conduct environmental assessment for vehicles and their components based on LCA concept. At the beginning, the studies focused on each component (bumper, IP, seat, panel) [2], and then assessment process for whole vehicle was developed and published in 1998 [3]. Following Fig. 2 shows this initial process.

In this process, vehicle options are set up according to the goal of study (ex, basic/recycling worst case/eco-friendly models) and life cycle phase to be included and assumptions are decided. Then all of relevant data are collected and processed by manual work including component list of a vehicle (so-called 'BOM'), plant energy consumption, etc. As a result intermediate flows are identified. But additional work are needed to find further up and down flows to identify elementary flows, these works generally use existing Life Cycle Inventory Database (LCI DB) that are made on the basis of each material, energy and process— 1 kg steel production basis, 1 kg polypropylene incineration. So, LCA practitioner

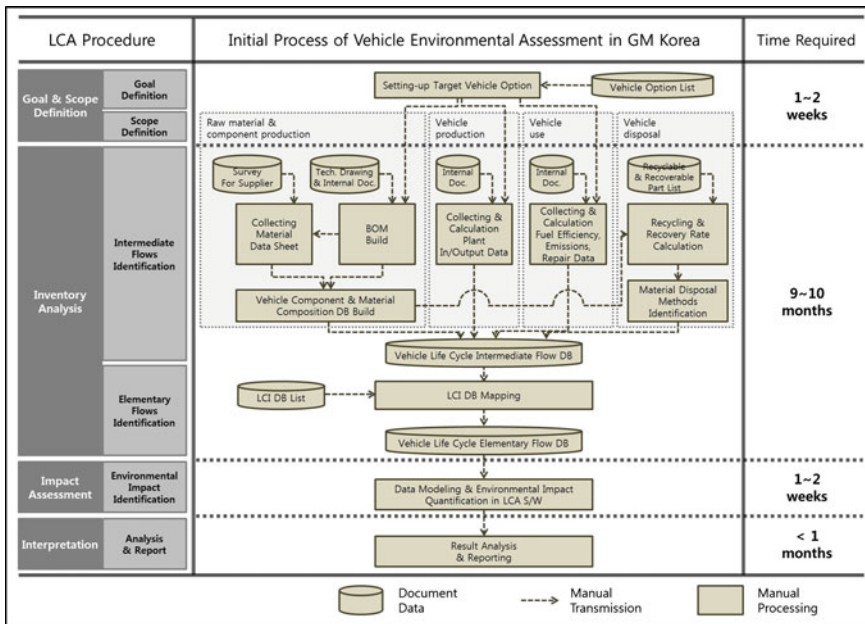


Fig. 2 Initial vehicle environmental assessment process in GM Korea

has to apply the most appropriate LCI DB for each material and process and there's needed expert knowledge. These works are called 'LCI DB Mapping' in this study. After mapping, elementary flows are identified. And following third and final phase are same as other general LCA study.

Furthermore, some improvements are applied to the initial process to reduce time required in inventory analysis such as build and use the LCI DB for commonized modules/components, application cut-off rule for minor environmental significance materials, etc. However, despite all these efforts, most data collection and process are based on manual work. Therefore, additional improvements are needed to use this process in the vehicle development process.

4 Development of Environmental Assessment System of Vehicle

4.1 Technological Breakthrough on Data Collection and Processing

By the 2000s IT system and Intranet are used for almost corporation works, so there are also many changes on the situation of environmental assessment field. Due to the computerization, building vehicle BOM that takes several months

before just finish within few days, and other works such as design, plant management, purchasing also use IT system to build, store, transmit and manage data as a form of electrical document. Therefore the speed of data collection and processing has increased.

But the most important change is the launch of International Material Data System (IMDS) that is developed in response to the 'EU-End of Life Vehicle regulation' by collective effort of many automotive OEMs (mainly European OEMs). It is web-based system to collect material/weight data of each component, and use of this system can reduce the time required to collect data for the inventory analysis. Also IMDS provides an advantage on standardization of data format.

Furthermore, without any help from professional IT system or programmer, some data processing work can be automated using general office program (ex, Microsoft Excel), as a result the groundwork has been laid to automate most of work in environmental assessment.

4.2 Development of Environmental Assessment System

According to improvement of IT technology, GM Korea tried to develop environmental assessment system of a vehicle that can be used in vehicle development process with advanced speed and reliability. It is based on LCA concept, and computerization and standardization concept for most of data processing is also used. These concepts are applied to two steps of inventory analysis that is intermediate and elementary flows identification.

4.2.1 Intermediate Flow Identification on Each Life Cycle Phase

Raw Material and Component Production Phase

Identification of intermediate flows in raw material and component production phase consists of following 3 steps, identification of vehicle BOM (step ①) and identification of material/weight structure of each component (step ②) and integration of two data (step ③).

In the step ①, a specific target vehicle is encoded and entered GM in-house vehicle description system, and BOM is produced. Verification of data is conducted using dedicated Excel Macro program developed by GM Korea. Finally, completed BOM is produced.

After step ①, material/weight data for each component is collected based on above BOM in step ② and all of data is collected as IMDS form. To do this, firstly existence of IMDS for each component is checked and if not, IMDS will be requested to suppliers and internal department. Collection is conducted till 100 % IMDS are obtained. Moreover, collected IMDS is also verified based on internal system data.

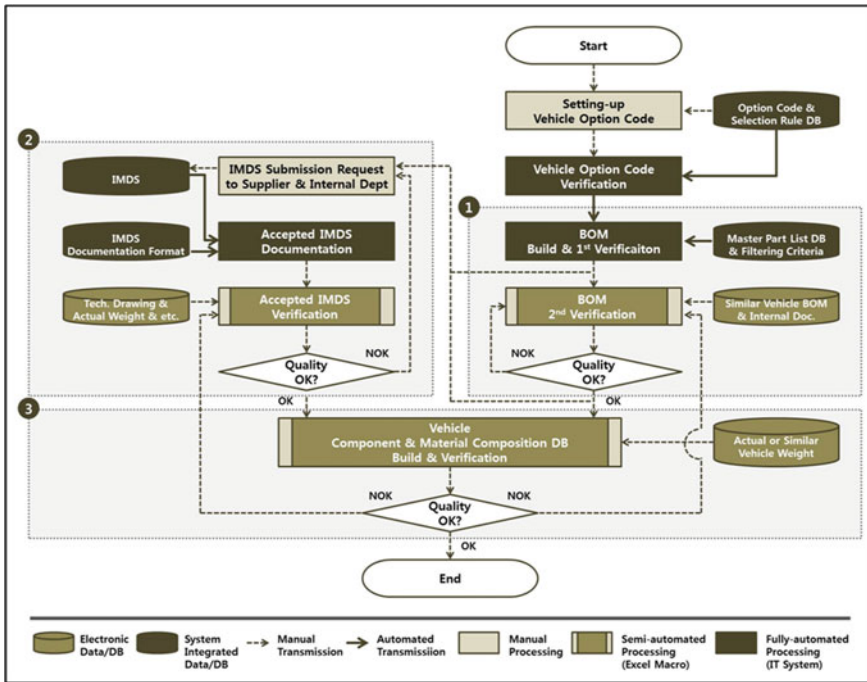


Fig. 3 Automated process in raw material and component production phase

Through above 2 steps, after completed BOM and IMDS are obtained, and then integration of two data is conducted to analyse hierarchy structure of component/material for target vehicle in the step ③. Using the Macro developed by GM Korea, this work is finished within few times, as a result vehicle component and material composition DB is built. And verification is also conducted to the this DB using actual/similar vehicle weight, therefore if some problem is found, the process goes back to the step ① and ②, verification of BOM and IMDS is re-conducted. All of works in each step are shown in Fig. 3.

This phase needs to most of time and manpower in the initial process due to the complexity and huge amount of data to collect, but now the time required is reduced by automated data collection and processing. Moreover, in respect of the data quality, the quality of each data is maintained by adding the verification work at each step.

Vehicle Production and Use Phase

In these phases, identification of electricity and fuel consumption, quantity of plant waste and repair component, etc. are needed, but main improvement is occurred in data production more than data transmit or process. For example, each of the working areas of plant such as raw and ancillary material purchasing, energy and

utility management, pollutant discharge management, use the in-house IT system to produce and store data as electronic document, so it can be more easily used by the 2000s. Also, environmental data in plant is continuously collected and stored as a database for further use such as ISO 14000s certification and greenhouse gases inventory. But it is difficult to automate for data transmission, calculation and verification due to the various data type and source, therefore, it's still remain as a manual work by LCA practitioner.

Vehicle Disposal Phase

Treatment method of End-of-Life Vehicle (ELV) differs little from country to country, but dismantling-based technology is generally used as following procedures.

1. Pretreatment
2. Dismantling
3. Shredding and metal separation
4. Non-metallic residue treatment

Several components such as airbag and vehicle fluids are removed in pre-treatment step, and dismantlable and economically valuable components are dismantled in dismantling step. After dismantling, vehicle goes to the shredder machine and shredded to small pieces, and then metallic materials that are recyclable are separated. Finally, non-metallic residues are further treated. In Europe, in order to reduce landfill waste, recycling technology for non-metallic residue has been developed and removing dismantling step to reduce time required. This method in Europe is called post-shredder technology in this study.

So, in order to identify how each component/material consists of ELV should be treated, treatment method has to be selected between dismantling-based and post-shredder technology firstly. And then calculation should proceed based on vehicle component and material composition DB that is produced first phase. The calculation method is standardized ISO 22628 [4], so the calculation in this study is based on ISO standard and is conducted automatically using the Macro developed by GM Korea. Following Fig. 4 shows this automated process.

4.2.2 Elementary Flow Identification with LCI DB Mapping

After identification of all intermediate flows at each life cycle phase according to above processes, elementary flows are identified using LCI DB Mapping based on intermediate flows. In case of initial process, mapping is also conducted by manual work, and especially mapping for vehicle component and material composition DB leads to lots of time required and errors. Furthermore, mapping needs to expert knowledge for material/process in intermediate flows—ex. interpretation for steel material standard (STS 305_KS spec., X5CrNi1812_DIN spec., etc.)—so there is

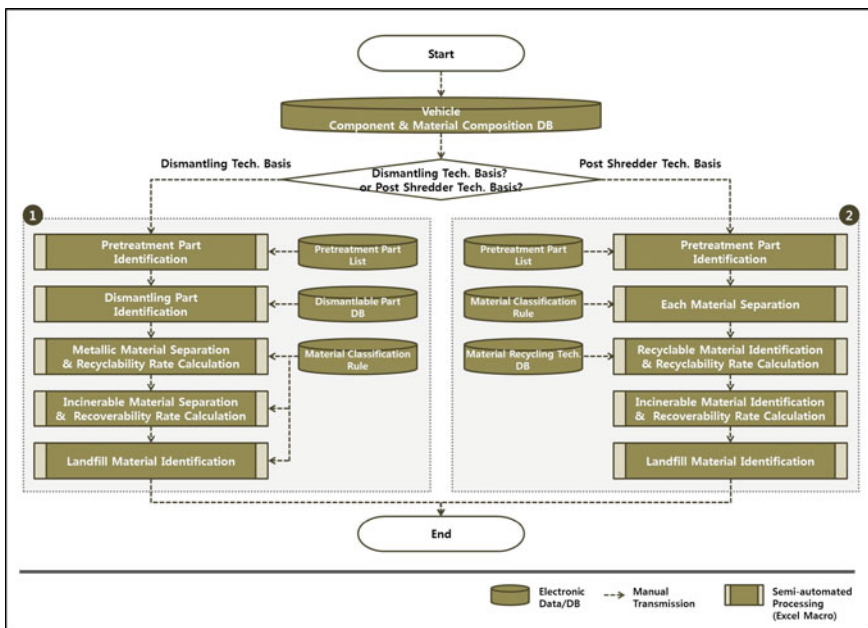


Fig. 4 Automated process in vehicle disposal phase

possible occurrence of deviation for quality of the result according to LCA practitioner’s level. Therefore, to solve these problems, the improvement working was conducted to following two aspects.

First is standardization for material name. The amounts of material type used in vehicle life cycle are about hundreds and thousands. Also, there’re lots of potential material names used by suppliers to identify a material such as popular name, trade name, public or private standard name.

Material type	KS	AISI/SAE	BS	DIN	ISO
Stainless Steel	STS 305	305	305 S 19	X5CrNi1812	13
Material type	Popular name	Other name 1	Other name 2	Trade name 1	Trade name 2
Polyamide	Polyamide 6.6	PA 6.6	Polyamid66	Nylon 6.6	Zytel

Therefore, standardization for each material name is full of help for mapping that needs to interpret various material name and match to the LCI DB. So, standardization work was conducted to the all of the different material names. And if the material name is not included this standardization DB, additional standardization was conduct as a result standardization DB is continuously updated. Following Fig. 5 is an example of standardization.

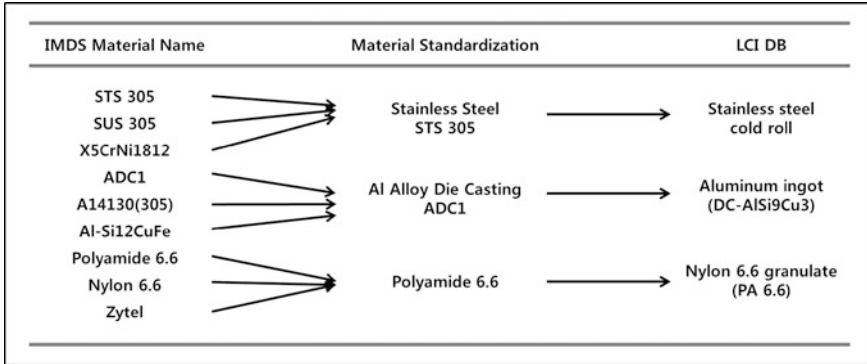


Fig. 5 Standardization for each material name

If there is the material names that cannot be identified due to uncertain information, for example, ‘metal, additives, wire, coating’, substance of material is used to estimate and if this is also impossible, information for classification of material (ex. VDA code in IMDS) is used.

Second is development of automated system to reduce the time required in mapping. The Macro developed by GM Korea automates all of mapping based on above standardization DB.

5 Results and Conclusions

The important target in this study—that is improvement of speed and reliability of vehicle environmental assessment—is achieved by automated system development. Following Fig. 6 is a new system’s process.

As a result, time required is reduced from 1 year to 3 or 4 months by the automated system. Also, standardization for data format and material name in mapping and verification process of each data are full of help for improvement of accuracy and reliability of result.

However, there’re still several limitations. First is using Excel Macro, so data transmission is still conducted by manual work. And second is not fully automated for several processes. Therefore, in order to achieve additional speed upgrade, 1 integrated system is required that can collect and process all of the data, and have to link with other systems as needed. And this new system only uses IMDS as a material/weight data of each component, so in the early stage of vehicle development process, that cannot be used. As a result usage or linkage with other database such as design and virtual assessment tool (CAD, CAE) is required instead of IMDS.

Nevertheless, this new system helps reduce the time for assessment and produce reliable result, so vehicle environmental assessment and analysis of its cause,

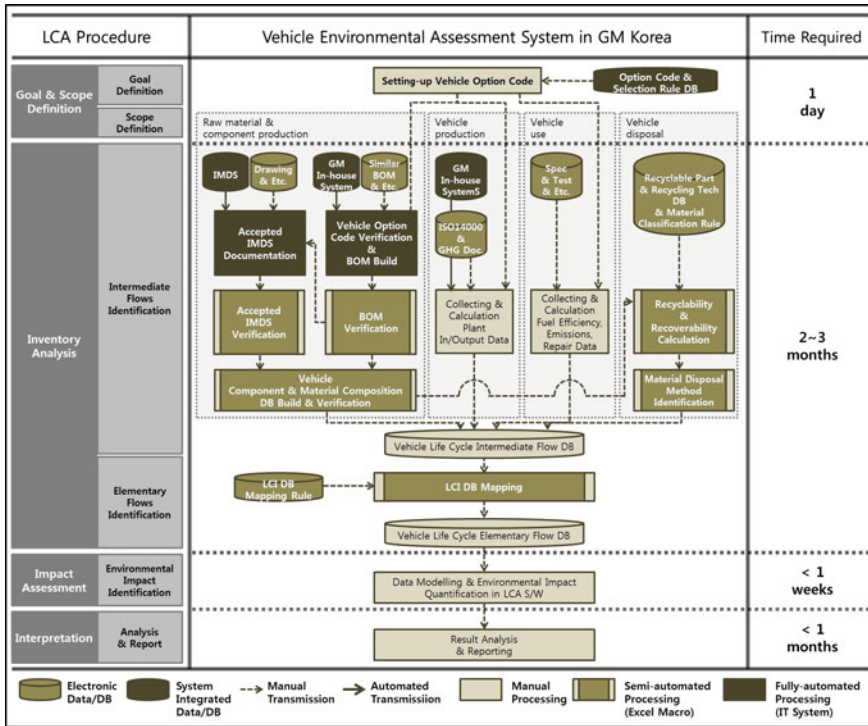


Fig. 6 New process of vehicle environmental assessment

identification of effective improvement in the vehicle development process are much easier than before. As a result, this tool can help to develop ‘environmental-friendly vehicle’.

References

1. ISO 14040, 14044. Geneva, international organisation for standardization, 2006
2. Ha J (1998) Life cycle assessment study of a bumper. SAE Technical Paper, 982175
3. Ha J (1998) Practical life cycle assessment methodology for a whole automobile. SAE Technical Paper, 982188
4. ISO 22628 (2002) Geneva, international organisation for standardization
5. Sonnemann G (2011) Global guidance principles for life cycle assessment databases. UNEP/ SETAC

Research on Hydraulic Regenerative Braking System for Pure Electric Vehicle Based on AMESim

Junping Jiang, Xiaobin Ning, Yaoting Xu, Qiucheng Wang, Wei Liu, Zhijie Pan and Fuquan Zhao

Abstract In order to increase the regenerative braking energy recovery and the dynamic performance of vehicle, the hydraulic braking energy recovery system is confirmed to use with the storage battery braking energy recovery system after comparing kinds of regenerative braking recovery plan and energy storage methods. Through PID control, simulation under ECE-15 cycle working mode and analysis of vehicle dynamic performance and energy recovery efficiency are conducted. The system simulation and analysis results show that using hydraulic regenerative braking system in pure electric vehicle can significantly improve the ability of vehicle's start-acceleration and the increase in vehicle driving range reaches around 28 %.

Keywords Pure electric vehicle · Hydraulic regenerative braking system · PID control · AMESim

1 Introduction

The electric machinery regenerative braking system (which referred to as ERBS in this paper) has significant effect in recycling brake energy for pure electric vehicle (EV) and advantages of simple structure and low cost. But it still has some difficulties and disadvantages: (1) the braking power and force are limited to be

F2012-E10-002

J. Jiang (✉) · W. Liu · Z. Pan · F. Zhao
Zhejiang Geely Automobile Research Institute CO. LTD, Hangzhou, China
e-mail: junping2007@163.com

X. Ning · Y. Xu · Q. Wang
Zhejiang University of Technology, Hangzhou, China

provided (2) there are large fluctuations in the regenerative braking performance dynamic; (3) braking energy recycling is limited; because the regenerative braking belongs to the electronic system and the braking element is more, so its reliability is generally lower than the dynamics of mechanical systems [1]. The power density of hydraulic pressure accumulator is higher than electric energy storage, suitable for load changes frequently in the city road conditions. Under the same conditions, the hydraulic auxiliary system for vehicles to provide greater auxiliary power (ability to solve the problem of insufficient power of EV), which has higher energy efficiency, faster energy storage and release rate, and more energy recovery, and the relative increase vehicle mileage [2]. When using hydraulic regenerative braking system (which referred to as HRBS in this paper), the load at battery levelled off, so that the service life of battery has also been a corresponding extension.

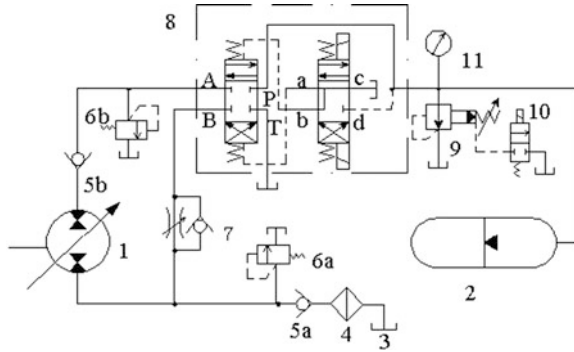
At present, all the countries in the world research and develop the hydraulic energy saving vehicles have different structural forms. They can be divided into three structure based on the different ways of the power transmission system configuration and combination. (1) Series structure form, which has the advantages of simple structure and easy implementation of system for different parameters control, such as Rexroth two hydrostatic drive system of Germany M.A.N Company. (2) Parallel structure form, which has the advantages of simple control, small automobile change, and high energy utilization efficiency, such as Cumulo drive system of Swedish Volvo Company. (3) Hybrid structure form, which has the best energy-saving effect, but the most complex system structure and the greatest difficulty to control, such as the CPS system of Japan Mitsubishi Company [3].

2 Develop Hydraulic System Scheme

HRBS's mission is to convert the loss mechanical energy to hydraulic pressure energy and store in the accumulator when the vehicle in deceleration and downhill condition, and release the storage hydraulic pressure energy into mechanical energy at the condition of acceleration or upslope, help the electric machinery to drive a vehicle. It demands the quick system response, stable operation, safety and reliability, long service life, the quality of small, compact structure, low cost and etc. [4]. Considering the above factors, the hydraulic system is designed as in Fig. 1.

Reversible hydraulic pump/motor 1 is selected for the execution component of HRBS. Electro-hydraulic reversing valve 8 is used to control the flow direction of hydraulic fluid at time of energy release and recovery. Some relief valves are used to buffer system's instantaneous high pressure. Pilot-operated pressure relief valve 9 can stabilize the hydraulic circuit of the role, but also used with two positions two way valves 10 for compulsion release of pressure in the system repair [5].

Fig. 1 Hydraulic system structure drawing



3 System Main Parameters Design

3.1 Pump/Motor

This paper selects a certain type of EV as the research object. If the vehicle is moving in a straight line, and the pump/motor separately drives the vehicle, the driven equilibrium equation can be expressed as Eq. 1.

$$T_{\rho/m} = \frac{Fr}{i_b i_o \eta_T} \tag{1}$$

Where, $T_{\rho/m}$ is pump/motor output torque (Nm), η_T is system efficiency, i_b is torque coupler ratio, i_o is rear axle main reducer ratio, and r is wheel rolling radius (m).

Without considering the energy loss of pump/motor in the energy conversion process, the pump/motor’s input power should be equal to the output power as

$$P_t = \Delta p \cdot q_t = \Delta p \frac{nV}{60} T_t \frac{2\pi n}{60} \tag{2}$$

Type of pump/motor parameters: Δp is the pressure difference between inlet and outlet (Mpa), q_t is theoretical flow (m^3/s), V is displacement (ml/r), T_t is theoretical output torque (Nm), n is rotational speed (r/min).

Because the average city vehicle travel speed is relatively slow, the air resistance is negligible, and then the displacement and power calculation method are as shown in the following three types [6].

$$V = \frac{2\pi T_t}{\Delta p} = \frac{2\pi r(mgf \cos \alpha + mg \sin \alpha + \delta ma)}{i_b i_o \Delta p} \tag{3}$$

$$P_{\rho/m} = T_{\rho/m} \cdot n = \frac{Fr}{i_b i_o \eta_T} n = \frac{Fv}{\eta_T} \tag{4}$$

$$(P_{\rho/m})_{\max} = \frac{1}{36,00\eta_T} \left[Gf + \frac{C_D A v_{\max}^2}{21.15} \right] v_{\max} \quad (5)$$

where, α is road slope, v is vehicle speed (m/s), a is vehicle acceleration (m/s²), $P_{\rho/m}$ is pump/motor output power (kW), G is vehicle fully loaded weight (N), C_D is drag coefficient, and A is windward area (m²). The maximum power $P_{\rho/m,\max}$ is to calculate a horizontal road with the maximum speed v_{\max} based on the vehicle traveling.

3.2 Hydraulic Pressure Accumulator

The main parameters of hydraulic pressure accumulator are inflation pressure p_0 , inflation volume V_0 , minimum/maximum working pressure p_1/p_2 , and gas polytropic index n (the isothermal process is 1, the adiabatic process is 1.4). p_1 and p_2 are determined by the Eqs. 6 and 7. And the inflation pressure is computed by the commonly used empirical formula (for folding type accumulator: $p_0 \approx (0.8-0.85) p_1$).

$$\frac{2\pi \left(Gf + \frac{C_D A}{21.15} v_a^2 \right)}{i_b i_0 V_{\rho/m,\max}} \leq p_1 \leq p_a \quad (6)$$

$$\frac{2\pi \left(Gf \cos \alpha + G \sin \alpha + \frac{C_D A}{21.15} v_g^2 \right)}{i_b i_0 V_{\rho/m,\max}} \leq p_2 \leq p_{\max} \quad (7)$$

Where, v_a is the average vehicle speed (m/s), v_g is the car ramp rate (m/s), p_a is the average working pressure of hydraulic system (Mpa), and p_{\max} is the maximum working pressure of hydraulic system (Mpa).

The energy recovered by hydraulic system is directly decided by the capacity of the hydraulic pressure accumulator. If the minimum working volume V_1 is to be decided, the inflation V_0 can be calculated by Eq. 8 from the Boyle's law. In the braking energy recovery process by the accumulator, V_1 is to be calculated by Eq. 9 from the first law of thermodynamics [7]. The energy recovered by pump/motor E_1 and the hydraulic system transmission efficiency η_1 multiply to the energy recovered by accumulator ΔE , where E_1 is to be calculated by Eq. 10 from the vehicle braking energy balance equation (automobile with initial velocity v_0 slowed to a stop through the braking deceleration a_1 , and forward sliding distance S).

$$V_0 = V_1 \left(\frac{p_1}{p_2} \right)^{1/n} \quad (8)$$

$$\Delta E = - \int_{V_1}^{V_2} p dV = - \int_{V_1}^{V_2} p_1 \left(\frac{V_1}{V} \right) dV = \frac{p_1 V_1}{1-n} \left[1 - \left(\frac{p_1}{p_2} \right)^{(1-n)/n} \right] \quad (9)$$

$$E_1 = \frac{1}{2} \delta m (v_0^2 - v_1^2) - mgfS - \frac{C_D A}{21.15} (v_0 - a_1 t)^2 \quad (10)$$

3.3 Torque Coupler

Coupler ratio should keep the pump/motor's rotational speed not to surpass its allowable maximum speed n_{max} . If the wheel rotational speed ω or vehicle speed v is known, the torque coupler ratio is decided by Eq. 11.

$$i_b \leq \frac{n_{max}}{\omega i_0} = 2\pi \times 60 \times 10^{-3} \times \frac{r_{max}}{v i_o} \quad (11)$$

4 The Speed Control of Energy Release and Recovery Process

When HRBS is recovering the braking energy, the pump/motor's working torque should be controlled to make sure that pilot has well braking performance. The accumulator will release recovery energy to drive the vehicle at the process of starting acceleration or climbing, the key is to control the pump/motor's output torque or speed timely to meet the external load changes.

In the practical engineering, the most widely used regulator control law is proportional-integral-differential control, also known as the PID regulator. PID is used to control the pump/motor's torque and speed in order to make the hydraulic system work timely and normally in this paper. The given value $r(t)$ is the feedback value of road cycle speed, the real-time vehicle speed is selected for feedback object $f(t)$, and the control objective is that the vehicle travel condition as close as possible to the standard cycle condition. According to project installation law, determines PID controller's proportional coefficient K_p , integration time T_I and differential time T_D in turn [8].

5 System Simulation and Analysis

AMESim provides an integrity platform of system engineering design, and allows the user to build complex multidisciplinary field system model in a platform and then carry on the simulation computation and the thorough analysis [9]. Building

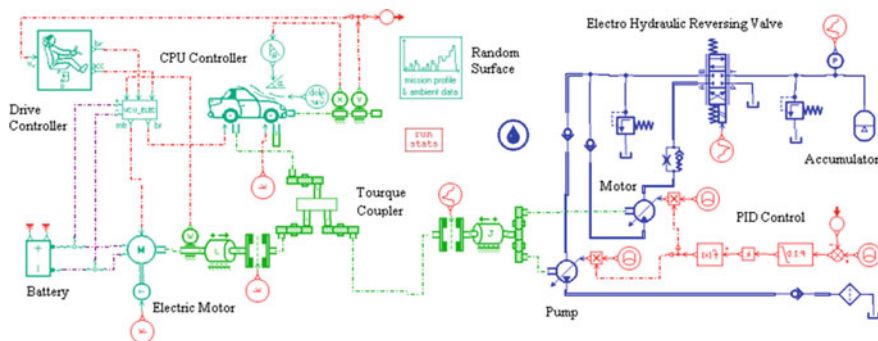


Fig. 2 Complex regenerative braking system simulation model

the regenerative braking system of EV on AMESim (see Fig. 2) needs hydraulic library, mechanical library, signal and control library and IFP drive library. The main simulation parameters are as shown in Table 1.

5.1 Common Start Acceleration

Simulation parameters are as follows: the electrical machinery output torque is the maximum torque of 1,350 Nm, the initial pressure of hydraulic accumulator is 315 bar, the stop-working pressure of hydraulic accumulator is 265, 250 and 235 bar. HRBS provides the driving force at beginning, until the accumulator pressure is lower than the set value. The velocity and displacement comparison curves drawn are obtained as in Fig. 3 after simulation.

From the picture, the ability of vehicle's starting and acceleration is significantly better when the electrical machinery works together with HRBS. Obviously, the vehicle dynamic performances are different at different stop-working pressures. When the stop-working pressure of accumulator is 265 bar, the velocity and displacement characteristics of hybrid vehicle (HEV) which is actuated by HRBS and electrical machinery are significantly better than EV. When the stop-working pressure of accumulator is 250 bar, the velocity characteristic of HEV is closed to EV after 4 s, while the displacement characteristic of HEV is slightly higher than EV. When the stop-working pressure is 235 bar, the velocity characteristic of HEV is slightly lower than EV after 4 s, and the displacement characteristic are similar.

The above describes that using HRBS in pure electric vehicle significantly improve vehicle starting acceleration capacity, thereby solving the pure electric vehicle driving torque shortage in a certain extent. Reasonable stock and release accumulator energy are related to the vehicle speed characteristics and displacement characteristics, which illustrates the influence to vehicle stability by HRBS.

Table 1 Complex regenerative braking system parameters

Name (unit)	Parameter value	Name (unit)	Parameter value
Vehicle loaded with quality (kg)	17,067	Main reducer ratio	5.13
Tire model	275/70R22.5	Transmission ratio	6.22/1.82
Battery capacity (Ah)	600	Battery voltage (V)	388.8
Max. torque of motor (Nm)	1,350	Max. power of motor (kW)	160
Pump/motor displacement (ml)	355	Pump/motor rpm (r/min)	2,440
Accumulator inflation pressure(bar)	150	Accumulator volume (L)	80

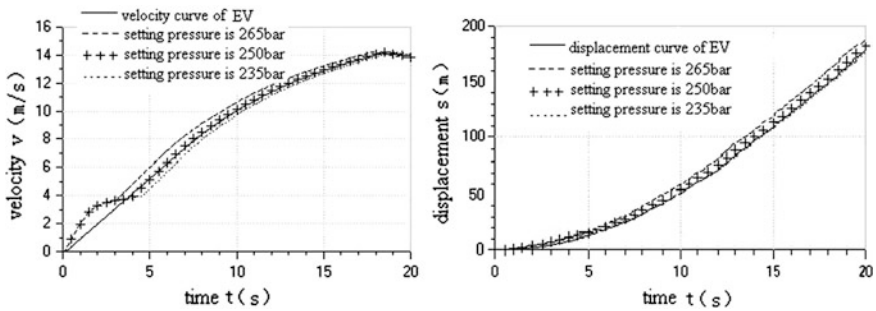


Fig. 3 Velocity and displacement curves in different stop-working of accumulator

5.2 Operating Condition Simulation

In order to test the energy saving effect of energy recovery system, the European ECE-15 working condition is selected to conduct the vehicle road simulation in full load, simulation time is 840 s [10]. Simulation of three different situations: firstly, the vehicle brakes without regenerative braking system to recover the brake energy; secondly, ERBS is used alone to recover the brake energy; thirdly, ERBS and HRBS are used together to recover the brake energy.

The working principle of HRBS is divided into two parts. In starting acceleration stage, HRBS releases energy to drive vehicle with electric machinery until the accumulator gas pressure drops to a setting value (245 bar is the best value by simulation and comparison). In braking stage, HRBS recovers the braking energy with electric machinery, and the braking torque distribution is controlled by PID controller and CPU controller until the accumulator gas pressure rises to a setting value 315 bar (in vehicle braking station, CPU controller can use ERBS to charge battery at a set principle of AMESim).

Figure 4 illustrates that the acceleration strength of HEV is relatively small and the change is relatively smooth, the max electric machinery output torque of EV is 1.21×10^3 N m and the max electric machinery output torque of HEV is 0.90×10^3 N m. The load change of electric machinery is relatively reduced by

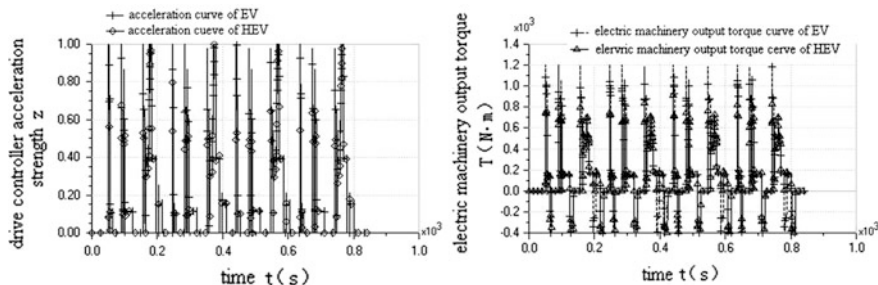
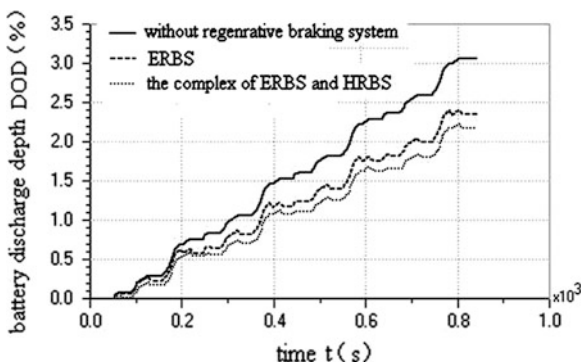


Fig. 4 Comparison curves of acceleration and electric machinery output torque

Fig. 5 Contrast curve of battery discharge depth

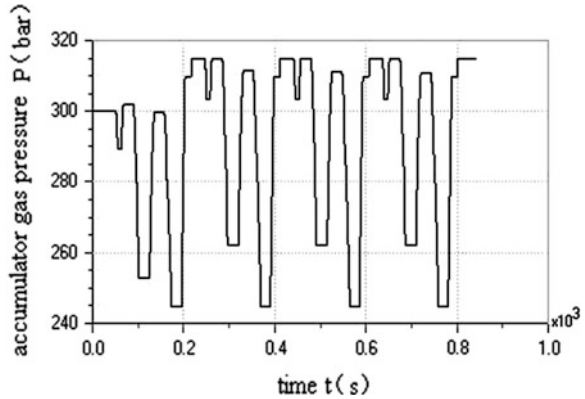


using HRBS, and the service lift of the electric machinery can be prolonged. In summary, the PID controller of system has to meet the vehicle obtaining ideal velocity curve and good braking performance.

From Fig. 5, the battery discharge depth of HEV is lower and more stable. After one ECE-15 working condition, the battery discharge depth of EV is 3.06 % without ERBS, the battery discharge depth of EV is 2.35 with ERBS, and the battery discharge depth of HEV is 2.18 % with the complex working of ERBS and HRBS. This can extend the service life of storage battery. Such as in percentage terms, the EV with ERBS can prolong the vehicle mileage of around 21 %, and the HEV with the complex working of ERBS and HRBS can prolong the vehicle mileage of around 28 %.

As shown in Fig. 6, HRBS always stops to recover the braking energy for the accumulator gas pressure reaching the max value. If HRBS can offer the driving force with electric machinery in the time of 203–216 s while the vehicle driving in constant speed after braking. Then the accumulator will release energy to drive pump/motor to work, the accumulator gas pressure dropping again for storing more hydraulic energy in the next braking condition. Therefore, HRBS will not stop to recover braking energy too early while in continuous braking of vehicle. In this time, HRBS can recover and utilize more braking energy in order to improve vehicle mileage.

Fig. 6 Accumulator gas pressure curve



6 Summary

Because the pump/motor can rapidly provide larger rotational torque to drive the vehicle in starting acceleration phase, the use of HBRS in EV solves the problem of starting slowly and torque insufficient by electric machinery. Moreover, the load of electric machinery is reduced and the max load is much lower than the max output torque, not only reduces the loss of electric machinery, but also prolongs the service life of the battery. Most importantly, using HBRS with EBRS working together can extend 28 % of EV mileage by a charging.

PID controller cannot distribute braking force and conduct energy management ideally, so that the braking energy recovery and utilization do not reach maximization. In future work, the primary work is to design an ideal brake force distribution strategy and establish a good energy management system for the complex system of HBRS and EBRS.

References

1. Liu H, Zhao W-P, Lv F-Y (2009) CA6700EV study on regenerative braking control strategy for pure electric passenger car. *Automot Technol* 08:25–30
2. Peng D, Zhang Y et al (2007) Design of hybrid electric vehicle braking control system with target wheel slip ratio control. SAE, 2007-01-1515
3. Erlston LJ, Miles MD (2008) Retrofittable regenerative braking in heavy applications. SAE, 2008-01-2558
4. Nakazawa N et al Development of a braking energy regeneration system for city buses. SAE, 872265
5. Nanjing Institute of Technology (2009) The use of hydraulic braking energy regeneration device in pure electric vehicle. China Patent: 0,082,016,074,7.3, 2009-08-26
6. Aoki Y, Shirase T et al (2007) Development of hydraulic servo brake system for cooperative control with regenerative brake. SAE, 2007-01-0868
7. Li X-S, Chang S (2007) Study on characteristics of energy storage element for a new vehicle with electronic control and hydraulic drive. *China Mech Eng* 18(10):1244–1247

8. Yonghua T (2005) The new PID control and its application. Machinery Industry Press, Beijing
9. Fu Y-Ling, Qi X (2006) AMESim system modeling and simulation—from entry to master. Beihang University Press, Beijing
10. Hu X (2009) Analysis and simulation of parallel hydraulic hybrid heavy vehicle. Jilin University of Mechanical Science and Engineering, Changchun

Part XI
Dynamic Modeling

Main Problems of Creating Surface Traction-Transport Vehicles with Mechatronic Systems

Belousov Boris and Ksenevich Tatiana

The article enumerates the main problems encountered in creating main traction-transport vehicles (TTV) units as mechatronic systems. The authors review the results of the comprehensive theoretical and experimental studies of creating TTVs—automobiles and tractors of the future based on mechatronic systems. The analysis of the results shows that TTV progress is only possible based on a broad introduction of mechatronic modules into vehicle designs. This significantly increases the role of electronics and control systems.

The paper shows that TTVs with mechatronic systems cannot be unambiguously described mathematically based on the existing theory of applied mechanics—the theory of automobile/tractor. We need a theory describing the laws governing the functioning both of individual TTV systems with their interrelationships, and of the object as a whole.

The importance is now given to the problem of creating the algorithmic and software support of the devices for power conversion and control, coordination and achievement of the systemic compatibility of parameters, for example, of electric equipment, electronics, and hydraulic, pneumatic, and hydro-pneumatic TTV systems, based on this theory. The development of such a theory as a refinement of the existing theory of automobile/tractor is one of the main tasks of the applied mechanics.

F2012-E11-001

B. Boris (✉)

N. E. Bauman Moscow State Technical University, Moscow, Russia
e-mail: BelousovBN@yandex.ru

K. Tatiana (✉)

A. M. Prokhorov General Physics Institute of Russian Academy of Sciences,
Moscow, Russia
e-mail: taxen@mail.ru

The main conclusion of the studies, conducted by the authors, is that TTVs of the future should be built as a module-based complex of mechatronic systems; and ideally, it should be a mobile robot intended for various functional applications.

1 Introduction

In early 2000s, pages of many journals were full of debates among engineers about the automobiles, with which the world would enter the 22 century. The debates have identified three groups of basic factors, which may affect the design of automobiles in the future. These groups are as follows: political factors (coordination of legislation, technical regulation, establishment of the united economic space, etc.); economic factors (fuel reserves and infrastructure of utilization thereof, level and distribution of wealth, degree of urbanization or sub-urbanization; validity/cost ratio of current technologies, including those related to transport safety, etc.); social factors (models of people's behaviour, leisure-time activities, cost of motor vehicles and fuel, environmental problems (to the extent the society perceives them), social standards adopted in relation to transport means, etc.).

However, the debates did not touch on the systemic technical factors of possible development of an automobile-tractor. This was an impetus for the collective of the Scientific and Production Centre "Special Machine-Building" (SPC SMB) of the N. E. Bauman Moscow State Technical University to pay attention to studying the systemic complex technical problem of creating a traction-transport vehicle (TTV)—the automobile-tractor of the future. By that time, the SPC SMB had performed a series of fundamental and applied studies related to development of transport vehicles.

A detailed study of all the aspects highlighted in the course of debates allowed us to formulate the main problem, which has its external and internal contradictions; namely: the modern automotive and tractor engineering is facing a global problem—creation of a TTV (automobile and tractor) of the future. The external contradictions include the need to observe the legislative requirements on the TTV active and ecological safety, since TTVs are among most popular objects used by the society at present. The ability of TTVs to ensure the current and future demands on active and ecological safety is the basic condition, which defines all the remaining consumer properties of the automobile and tractor, and, therefore, their competitive strength. It should be noted here that these demands are steadily becoming more and more severe.

Thus, the automotive and tractor engineering faces the problems, which cannot be solved by traditional methods and technical solutions. We need radically new solutions in TTV designs, able to ensure response to current and future consumer demands. These technical solutions cannot be developed today, since there are no developed respective scientific provisions, regularities and principles of the applied science—the Theory of Automobile and Tractor. This is the essence of the internal contradictions of the above global problem.

Furthermore, we should note here that the problem is of an interdisciplinary character and covers practically all the aspects of human life.

2 Objective

The studies conducted by the SPC SMB during the last decade allowed us to systemically formulate our views on the solution of the global problem, as well as on the solution of the local problems and scientific tasks, aimed to resolve the internal contradictions of the global problem.

1. We have revealed the stable process of changing the design of surface traction-transport vehicles (TTVs), qualitative changes of their structure and composition of their main power units based on integration of electronic, electric, hydraulic and mechanical elements and significant increase of the role of the electronics and control systems, i.e., a broad introduction of mechatronic systems and modules into the design of the automobile-tractor.

Mechatronics began its introduction into designs of transport means (TMs) with the simplest things—with introduction of functional components of controlled systems. First of all, these were sensors and transducers, then—drives. The next stage was a symbiosis of the mechatronics and mechanical, hydraulic, electro-mechanical and other systems of TMs. This process is at full swing and is stimulated, first of all, by the constant toughening of legislative requirements to TMs on their active and ecological safety. This stage can be characterized as a transition from the modular design of technical systems, based on decomposition, to systemically optimized unified TM structures. The process started from penetration of certain components into the TM design. Then, these components merged into a unified structure, which implements functional components within the united target function, similar to multi-agent systems in computer networks. This trend is advancing further and covering power units, which is proved by many examples.

Thus, the main systems of a traction-transport vehicle (TTV), namely, a power unit, transmission, steering, springing and braking systems, etc., embody complex technical solutions, built on different physical principles, and in terms of mechanics are hybrids and cannot be identically described by mathematic means. Besides, even the terminology lacks any unanimous approach and interpretation. The use of unified terminology in designing TTVs with mechatronic systems is one of the important problems of applied mechanics. In other words, a modern TTV is a complex system of mechatronic modules. This factor defines the technical interdisciplinary character of the problem.

2. The designing of the non-mechanical part (electronic, electric, hydraulic, pneumatic, etc.) of TTV systems is on specialists from the respective fields of knowledge. However, with respect to the object, i.e., to a TTV, the basic technical requirements and principles, the methodology of using hybrid systems in the design of an automobile, for example, as a system of mechatronic

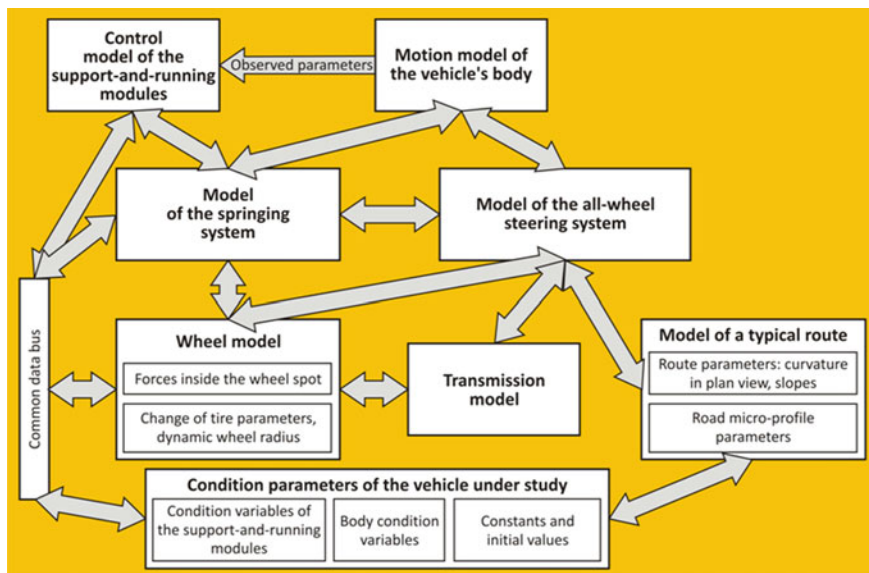


Fig. 1 Block diagram of the complex mathematical model (CMM)

modules, are formulated by automobile mechanics. Here, a huge designing experience has been accumulated, which needs generalization and apprehension. Even now, this experience allows making a key conclusion: a perfunctory use of achievements of mechatronics cannot bring any positive effect. We need a theory describing functionality regularities and interrelations both of individual TTV systems and of the object as a whole. Only based on these regularities we can build the algorithmic support and software for the efficient operation of the TTV mechatronic systems. Elaboration of this sort of theory as an update of the current automobile and tractor theory is one of the basic tasks of applied mechanics. With this aim in mind, the Scientific and Production Centre “Special Machine-Building” (SPC SMB) of the N. E. Bauman Moscow State Technical University has developed an original Complex Mathematic Model (CMM), which allows simulating different interaction patterns of all TTV systems (Fig. 1), including with account of the contact (tribological) interaction of the wheel with the supporting surface [1–3]. Based on the CMM, we have studied the operation of such hybrid TTV subsystems as: the internal-combustion engine—electric generator—electric drive with a motorized wheel, all-wheel steering control with an electro-hydraulic servo drive, and also a controlled wheel springing system, an on-board information and control system (OBI&CS), and the system “tire-supporting surface” with account of tribological links.

Any theory of applied science is directed towards ensuring consumer properties of the object, which is created based thereof. When projecting TTVs, the consumer

properties are taken into account (set) in specifications. The development process of an applied science is directly dependent on the formation process of new consumer properties or increased level of the current requirements. This interrelation is reflected in the contents of specifications.

For example, today, all over the world, the problem of automobiles' impact on the environment is becoming most important in designs of new automobile models.

At present, the most well-known TTV mechatronic system is the braking system of a modern motor vehicle.

Thus, the main development route from the current TTV design to the TTV of the future is through broad use of mechatronic modules and systems. The efficient use of them requires a strict algorithmic and software support based on the applied mechanics—the theory of automobile (tractor).

3. With account of the TTV development directions, when speaking about energy, we imply the need to design on-board energy complex (OBEC) of a traction-transport vehicle (TTV). Many automobile builders have made their choice—already at the Euro-4 stage—in favour of the following mechatronic systems: SCR—Selective Catalyst Reduction, and EGR—Exhaust Gas Recirculation, as new technologies. However, with requirement toughening at Euro-5, Euro-6 and higher, quite a new power generating system will be needed, for example, an electrochemical generator (ECG) based on fuel elements. The drawbacks of TTV power generating systems based on primary thermal engines stem from the fact that any thermal machine has its principal efficiency limitation (the maximum of thermal efficiency according to the Carnot cycle is 30 %). Apart from other circumstances, any further application of traditional thermal machines will be defined by the quality/cost ratio. Therefore, a great attention is now paid to combined power generating systems (PGSSs). This process can be viewed only as the first step in the transition to the radically new PGSSs. The English-language literature has the tradition to treat TTVs with combined PGSSs as hybrid electric vehicles: hybrid, because the power generating system makes use of different types of sources (instead of a thermal engine, some electrochemical source, for example, battery or fuel elements can be used); electric, because they have a distinctive element of electric transport means—a traction electric drive. In Russia, a bit different terminology is preferred: if a thermal engine is used as the main energy source of the vehicle, it is usually called an automobile with a combined power generating system (CPGS); otherwise, if any other power source is used instead of a thermal engine, for example, an electrochemical generator, the vehicle is treated as an electromobile with a CPGS.

An example of combined power generating systems is an automobile with a CPGS and a traction electric drive [3], Fig. 2a. Here, the power interaction goes along the chain: an internal-combustion engine (ICE), a traction generator (TG), a power accumulation unit (PAU) and a traction inverter (TI); while the information and control interaction goes along the following chain: a CAN-bus of data

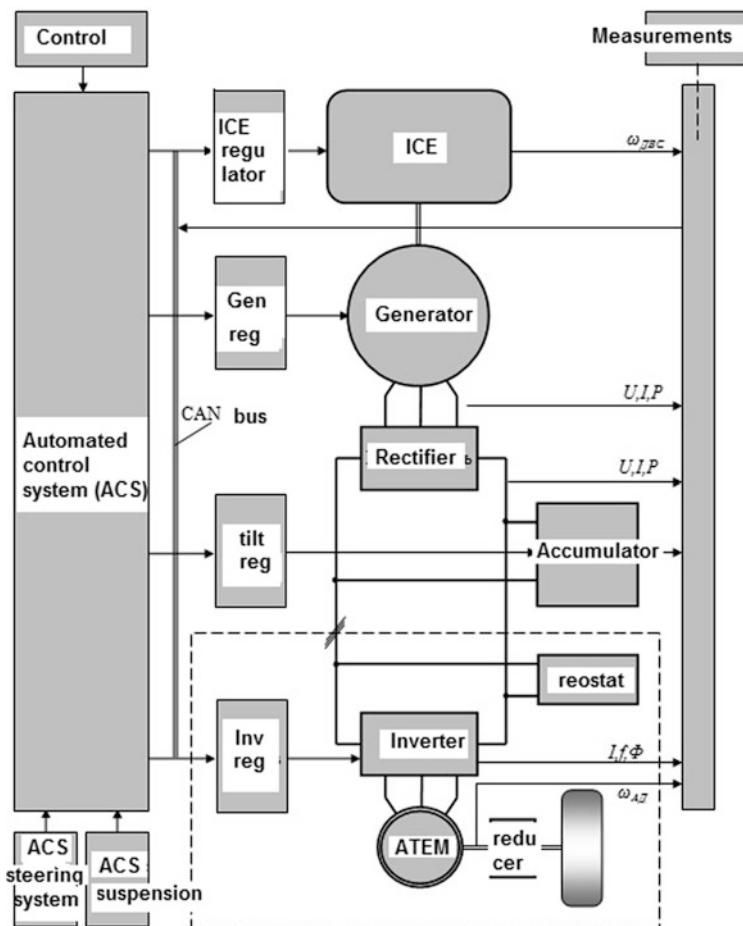


Fig. 2 a Main diagram of an automobile with a combined power generating system: enlarged generalized structural diagram of the traction drive structure. **b** Main diagram of an automobile with a combined power generating system: main diagram of the automated control system (ACS) of the electric drive

exchange and through their electronic regulators; each of them has and performs its own operation algorithm. The general control diagram of the traction drive of a single-link vehicle is presented in Fig. 2b.

The diagram of Fig. 2a is an enlarged generalized structural layout of the traction drive, connections of its elements, and a diagram of information communication and signal exchange system between the automated control system (ACS) and OBEC, on the one hand, and the automated regulation systems (ARSs) of the power drive.

Figure 2b presents all the three individual automated regulation systems present in the control structure: the ARS of the ICE, which controls—through the ICE

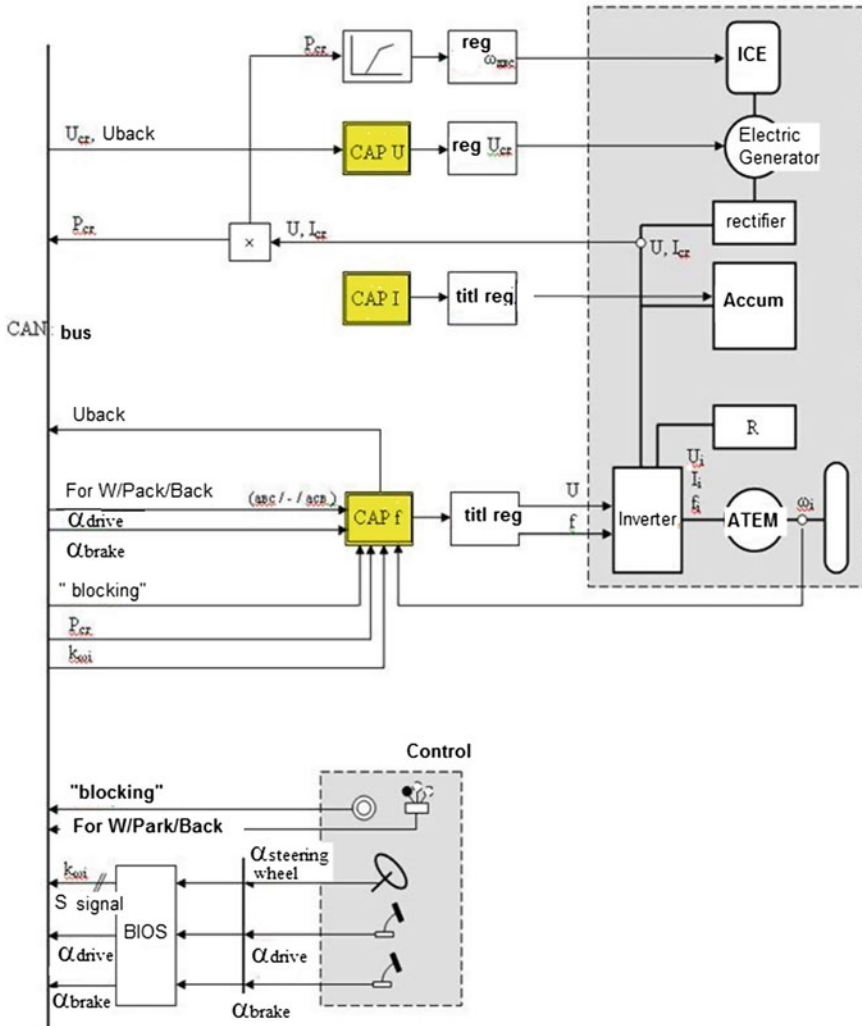


Fig. 2 (continued)

regulator—the engine rotation rate; the ACS of the U-generator; the ACS I—automatics of the PAU; and ACS f—automatics for managing the output parameters of the inventor.

The figure also shows the basic connections and information parameters of the system.

The DC bus (DCB) is connected to the PAU, which either stores power, or delivers it to the bus, depending on the preset operation mode and according to control commands. The PAU consists of super-capacitors and traction accumulation batteries.

The accumulator is controlled by its own power key element, commanded by current and voltage regulator. The control signal to the accumulator's regulator comes from the ARS of the drive in the form of a signal ordering to connect the PAU into operation, or disconnect it from the DCB. The central DCB is powering the TIs of each of the motorized wheels. An individual TI is powering and controlling the asynchronous traction electric motor (ATEM) connected to it. The transfer of the torques from the ATEM to the wheels with increase up to traction torque values is ensured with the help of wheel-hub drives (WHDs) with fixed transmission ratios. When the TTV is braked, the braking energy from the ATEM through the TI is accumulated by the PAU, and in case it is impossible, the braking resistors (BRs) come into play and convert and dissipate the electric energy received from the ATEM as heat.

This diagram can be considered only as the first stage (step) in the transition to the design of an automobile/tractor of the future. The efficiency of this design is defined by the efficiency of the PGS used.

As opposed to the ICE, fuel elements have incomparable advantages when used as a PGS. Fuel elements directly transform the energy of chemical bonds into electricity. At present, batteries of fuel elements, when used as PGSs, are bulky and able to work on hydrogen and oxygen only, which need to be carried on by the automobile. In prospect, they will become the main driving force of the second half of the 21st and the 22nd centuries and double the energy reserves of the mankind. At the same time, the use of batteries of fuel elements will essentially reduce CO₂ emissions into the atmosphere, since the final product of the exothermal reaction in them is water, unlike of end products of the ICE—exhaust gases, containing mainly a mix of CO₂, water and soot.

It is interesting to look at solutions of mechatronic modules when an OBEC is built based on an ECG. We present below (Fig. 3) a typical layout of the traction-power equipment of a hybrid automobile with fuel elements. The power layout is sequential: a battery of fuel elements—a DC matching step-up converter—a buffer accumulation battery—a traction drive inverter—a traction electric motor of motorized wheels. The battery of fuel elements is the main source of motion power; its power is enough to cover the average power consumed by the traction drive in the cycle (or preset mode) of motion.

The DC matching step-up converter serves to regulate the power consumed from the battery of fuel elements (the current value of the average consumed power may be less than the maximum battery power) and to charge the buffer source, which covers the peak power consumption (the values of peak power, for example, at acceleration, may multiply (by the factor of three and more) exceed the average power of the battery of fuel elements). At the same time, the buffer source serves to receive the power, returned from the traction drive in the vehicle's braking mode. The inverter converts the DC of the buffer battery into the 3-phase AC, powering the traction motor (the direction of power flow can be from the battery to the motor in the traction mode and back—in the braking mode. The DC matching step-up converter is feeding, apart from the buffer battery, individual devices (auxiliary devices of the battery of fuel elements) and charging its own

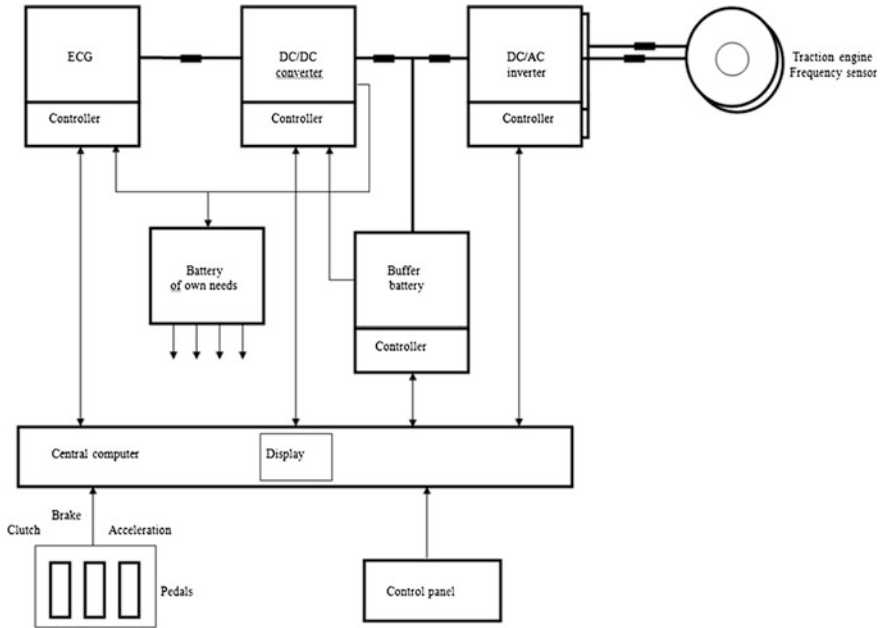


Fig. 3 Composition and structure of the powering and controlling traction equipment

battery (used to power automobile devices: illumination, signalling, etc.). The own battery is also used to initially start the equipment (the battery of fuel elements).

Further progress of TTVs has to do with mechatronic systems and use of new ways of power distribution and transfer from the ICE to the wheel based thereon. At present, we see an obvious ongoing transformation of TTV designs, qualitative changes of their structure and composition of main power units, integration of electronic and mechanical elements and increase of the role of electronics (both power and control) and control systems, that is, a broad introduction of mechatronic modules into TTV designs.

No perfunctory use of mechatronics' achievements can have any positive effect on TTVs. What we need is a theory, which describes functional regularities of both individual TTV systems with their interrelations and the object as a whole. Only based on these regularities, we can build the algorithmic and software support of efficient work of TTV mechatronic systems. Development of such theory as an update of the existing automobile-tractor theory is one of the basic missions of applied mechanics. Mechatronics is highly beneficial—both technically and economically—for automobile and tractor engineering.

In the nearest foreseen future, it is difficult to imagine appearance of any radically new power generating system for traction-transport vehicles.

The biggest efforts in the global automobile and tractor engineering are spent on improving the operation of these engines, development of electrochemical power generators and invention of combined power generating systems based on traditional engines, traction electric generators, and power accumulators.

The design of the future TTV has to do with various types of combined power generating systems based on ECGs in combination with traction hydro or electric drives of the wheeled mover.

A TTV of the future is a multifunctional mobile robot. Its design embodiment is impossible without developing the automobile-tractor theory and integrating the respective spheres of science and engineering.

References

1. Belousov BN, Popov SD (2006) Wheeled transport vehicles of super-high capacity. Construction. Theory. Calculation. Publishing House of N. E. Bauman Moscow State Technical University, Moscow
2. Belousov BN, Bannikova EB, Shvetsov AM (2010) Account of influence on oscillations in active safety systems of characteristics and parameters of actuation mechanism of control loop of electrohydraulic drive in steering control systems and springing of complex systems—wheeled transport-traction vehicles. Proceedings of international scientific-technical conference “innovations in machine-building”, Minsk, 87–93
3. Belousov BN (2011) Applied mechanics of surface traction-transport vehicles with mechatronic systems. Ulianovskiy Dom Pechati, Ulianovsk

Wheelbase Filtering Effect on Vehicle Ride Dynamics

Kang Song, Xiaokai Chen and Yi Lin

Abstract The time delay of rear wheel input relative to front one acts to filter the amplitude of vehicle motion. Through reference to a half-car pitch plane model, mechanism of wheelbase filtering was investigated. Amplitude of FRF between a motion and road input could be divided into two parts: steady part and variable part. Steady part that is determined by natural property of vehicle does not change with outer input condition. However, variable part fluctuates frequently because of cosine function item of itself, which is closely related to velocity of vehicle. It is variable part that modulates the amplitude of vehicle motion. In addition, wheelbase filtering effect varies greatly at different locations on the body. Filtering effect on work space and dynamic tire load of suspension was also studied. Results show that rear road input hardly influences front suspension motion and vice versa, so variable part is much smaller than steady part and filtering effect in suspension motion is not obvious.

Keywords Wheelbase filtering · Ride dynamics · Body motion · Suspension motion · Frequency response function (FRF)

F2012-E11-007

K. Song · X. Chen (✉)

School of Mechanical Engineering, Beijing Institute of Technology, Beijing, China
e-mail: chenxiaokai@263.net

Y. Lin

Beijing Automotive Technology Center, Beijing, China

1 Introduction

Wheelbase filtering is an effect which is caused by a time delay of front wheel input relative to rear one [1]. This effect has a function of modulating some motions of vehicle. In these motions, some are related to vehicle ride behavior, such as bounce acceleration and pitch angular acceleration of body, work space and dynamic tire load of suspension.

The effect of wheelbase filtering on vehicle dynamics has been proposed in many papers. However, these papers usually involved other topics and wheelbase filtering was only a part of these topics. At the same time, much attention was paid to the result of wheelbase filtering effect on vehicle dynamics.

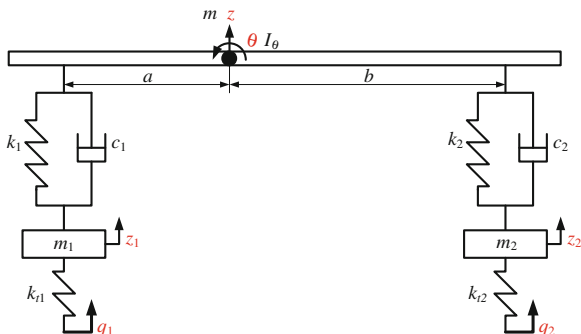
Sharp [2] investigated suspension tuning to minimize the pitch motion of body by calculating frequency response for the half-car over a wide range of speeds and design conditions. Wheelbase filtering effect was considered in suspension tuning. Cao Dongpu et al. [3] investigated the characteristics of different random road profiles considering wheelbase filtering effect. They used quarter-car and pitch-plane models to analyze the combined influence of random road roughness and wheelbase filtering on vehicle dynamics. Fu Wenkui et al. [4] compared the difference of wheelbase filtering effect and suspension tuning between two-axle and tri-axle vehicle and summarized advantage and disadvantage of Olley criteria in suspension tuning at higher and lower speed. Vittore Cossalter et al. [5] proposed a method for evaluating ride comfort of a motorcycle in frequency domain. Wheelbase filtering effect on longitudinal and vertical saddle motion was considered and this effect was introduced as a mean value by integration in this new method. In addition, in vehicle localization [6] and evaluating the dynamic-wheel-load performance of heavy commercial vehicle suspensions [7], wheelbase filtering was also considered.

In this paper, wheelbase filtering effect on ride behavior was investigated through reference to a half-car pitch plane model. Vertical acceleration at the mass center of body was taken for example to study the mechanism of wheelbase filtering. With this mechanism, the effect of wheelbase filtering on pitch motion of body and suspension motion were analyzed. In addition, relation between filtering effect and location on the body was discussed.

2 Modelling

Four degrees of freedom half car, pitch plane model was built to investigate the effect of wheelbase filtering on ride performance. The selected generalized coordinates consist of vertical displacement z at the mass center and pitch angle θ of body, vertical displacement z_1 of front wheel and vertical displacement z_2 of rear wheel. Road inputs acting on front and rear wheel are q_1 and q_2 respectively. All parameters used in this paper are shown in Fig. 1.

Fig. 1 Half car, pitch plane model



Motion equation of this model is written in the matrix form.

$$M\ddot{x} + C\dot{x} + Kx = K_t q \tag{1}$$

in which

$$x = [z \ \theta \ z_1 \ z_2]^T, M = \text{diag}[m \ I_\theta \ m_1 \ m_2], C = \begin{bmatrix} c_1 + c_2 & -ac_1 + bc_2 & -c_1 & -c_2 \\ -ac_1 + bc_2 & a^2c_1 + b^2c_2 & ac_1 & -bc_2 \\ -c_1 & ac_1 & c_1 & 0 \\ -c_2 & -bc_2 & 0 & c_2 \end{bmatrix}$$

$$K = \begin{bmatrix} k_1 + k_2 & -ak_1 + bk_2 & -k_1 & -k_2 \\ -ak_1 + bk_2 & a^2k_1 + b^2k_2 & ak_1 & -bk_2 \\ -k_1 & ak_1 & k_1 + k_{t1} & 0 \\ -k_2 & -bk_2 & 0 & k_2 + k_{t2} \end{bmatrix}, K_t = \begin{bmatrix} 0 & 0 \\ 0 & 0 \\ k_{t1} & 0 \\ 0 & k_{t2} \end{bmatrix}, q = [q_1 \ q_2]^T$$

Fourier transform of motion equation is

$$(-\omega^2 M + j\omega C + K)X(\omega) = K_t Q(\omega) \tag{2}$$

So frequency response function (FRF) matrix between vehicle output and road input is

$$H(\omega) = \frac{X(\omega)}{Q(\omega)} = (-\omega^2 M + j\omega C + K)^{-1} K_t = \begin{bmatrix} H_{11}(\omega) & H_{12}(\omega) \\ H_{21}(\omega) & H_{22}(\omega) \\ H_{31}(\omega) & H_{32}(\omega) \\ H_{41}(\omega) & H_{42}(\omega) \end{bmatrix} \tag{3}$$

in which $H_{ij}(\omega)$ represents FRF between the i th output and the j th road input.

When the car passes a path, rear wheel is excited by the same unevenness as front one with a time delay. The time delay is proportional to wheelbase and inversely proportional to velocity. In frequency domain, this relation could be expressed as

$$q_2(\omega) = e^{-j\omega L} q_1(\omega) \tag{4}$$

in which t_L is the time delay.

With this relation in frequency domain, frequency response function matrix $\mathbf{H}(\omega)$ could be expressed as another form.

$$\mathbf{H}(\omega) = \begin{bmatrix} H_{11}(\omega) + e^{-j\omega t_L} H_{12}(\omega) \\ H_{21}(\omega) + e^{-j\omega t_L} H_{22}(\omega) \\ H_{31}(\omega) + e^{-j\omega t_L} H_{32}(\omega) \\ H_{41}(\omega) + e^{-j\omega t_L} H_{42}(\omega) \end{bmatrix} \quad (5)$$

This expression means that road inputs acting on system could be equivalent to only one input q , and equivalent input q is equal to front road input q_1 , that is $q = q_1$. So this two-input system could be equivalent to a single-input one.

3 Wheelbase Filtering Effect on Body Motion

The time delay of rear wheel input relative to front one acts to filter the bounce and pitch vibration amplitude, and this effect is called “wheelbase filtering”. The time delay t_L in time domain corresponds to phase delay ωt_L in frequency domain.

In building vehicle model, the selected coordinates to represent body motion are vertical displacement z at the mass center and pitch angle θ of body. But usually bounce acceleration and angular acceleration of body are used to evaluate ride behavior of vehicle. In the following, wheelbase filtering effect on vertical acceleration at the mass center and pitch angular acceleration of body is investigated.

3.1 Vertical Acceleration at the Mass Center of Body

FRF $H(\omega)_{z \sim q}$ between vertical displacement z at the mass center of body and road input q is expressed as $H_{11}(\omega) + e^{-j\omega t_L} H_{12}(\omega)$, so FRF $H(\omega)_{\ddot{z} \sim \dot{q}}$ between vertical acceleration \ddot{z} at the mass center of body and road velocity input \dot{q} could be obtained easily according to Fourier transform rules, that is $j\omega(H_{11}(\omega) + e^{-j\omega t_L} H_{12}(\omega))$. The magnitude of this FRF is calculated as follows.

$$\left| H(\omega)_{\ddot{z} \sim \dot{q}} \right| = \omega \sqrt{|H_{11}(\omega)|^2 + |H_{12}(\omega)|^2 + 2|H_{11}(\omega)||H_{12}(\omega)| \cos(\omega t_L + \varphi_z)} \quad (6)$$

in which φ_z is the phase difference between $H_{11}(\omega)$ and $H_{12}(\omega)$, the calculation equation of this phase difference is $\varphi_z = \text{phase}[H_{11}(\omega)] - \text{phase}[H_{12}(\omega)]$.

Equation (6) shows that the magnitude of FRF $H(\omega)_{\ddot{z} \sim \dot{q}}$ consists of two parts: steady part and variable part. These two parts are defined as follows.

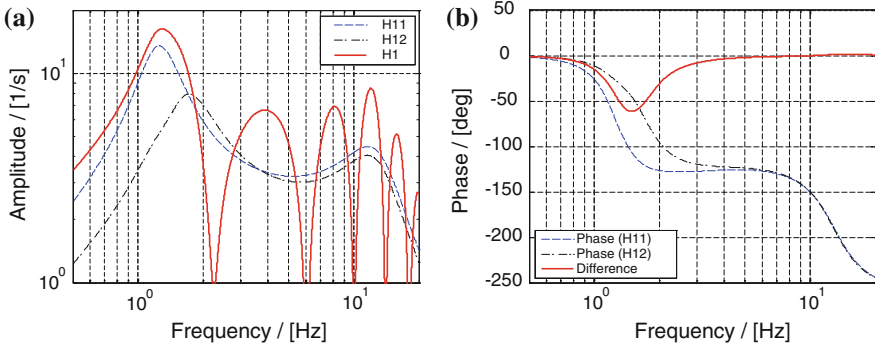


Fig. 2 Amplitudes (a) and phase angles (b) of FRFs between vertical acceleration and road input

$$\begin{aligned} \text{steady part} - part_1: part_1 &= \omega^2 \left(|H_{11}(\omega)|^2 + |H_{12}(\omega)|^2 \right) \\ \text{variable part} - part_2: part_2 &= \omega^2 \left(2|H_{11}(\omega)||H_{12}(\omega)| \cos(\omega t_L + \varphi_z) \right) \end{aligned}$$

In steady part, $H_{11}(\omega)$ and $H_{12}(\omega)$ are FRFs between vertical displacement and front and rear road input respectively, and both of them are determined by the vehicle model itself, which would not change with outer input condition. So steady part $part_1$ shows natural property of system. In variable part, introduction of cosine function $\cos(\omega t_L + \varphi_z)$ makes this part fluctuate frequently. In this cosine function, initial phase φ_z is the phase difference between $H_{11}(\omega)$ and $H_{12}(\omega)$, so it could also be seen as a “steady angle”. However, phase delay ωt_L of rear wheel input relative to front one is closely relative to velocity. So it is variable part— $part_2$ that is the way through which outer input condition influences system response. When phase delay ωt_L makes the cosine function reach its minimum, amplitude-frequency curve of $H(\omega)_{\ddot{z} \sim \dot{q}}$ would appear a trough.

According to classic mathematical inequation, steady part $part_1$ is greater than or equal to $2|H_{11}(\omega)||H_{12}(\omega)|$, and they are equal only with $|H_{11}(\omega)| = |H_{12}(\omega)|$. And $2|H_{11}(\omega)||H_{12}(\omega)|$ is greater than or equal to variable part $part_2$ because of inner cosine function item. So variable part $part_2$ is less than or equal to steady part $part_1$.

When the amplitudes of $H_{11}(\omega)$ and $H_{12}(\omega)$ are close to each other, amplitude-frequency curve of $H(\omega)_{\ddot{z} \sim \dot{q}}$ would appear obvious fluctuation. Otherwise, when the amplitudes of $H_{11}(\omega)$ and $H_{12}(\omega)$ are largely different, variable part would be much smaller than steady part and amplitude-frequency curve of $H(\omega)_{\ddot{z} \sim \dot{q}}$ would not show obvious fluctuation in the whole frequency range.

Amplitudes of $H_{11}(\omega)$, $H_{12}(\omega)$ and $H(\omega)_{\ddot{z} \sim \dot{q}}$ and phase angles of $H_{11}(\omega)$ and $H_{12}(\omega)$ are shown in Fig. 2, here velocity is 40 km/h.

Figure 2a indicates that amplitudes of $H_{11}(\omega)$ and $H_{12}(\omega)$ are close to each other, so the amplitude of $H(\omega)_{\ddot{z} \sim \dot{q}}$ shows obvious filtering effect, which means vertical acceleration at the mass center of body is greatly affected by outer input condition. Figure 2b indicates that phases of $H_{11}(\omega)$ and $H_{12}(\omega)$ decrease rapidly

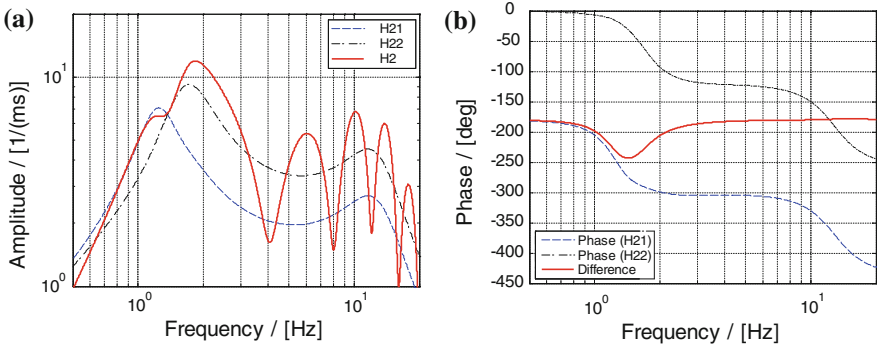


Fig. 3 Amplitude (a) and phase angles (b) of FRFs between pitch angular acceleration and road input

near the resonance frequency of body, and phase difference reaches its minimum in this range. In addition, in the low and high frequency ranges, phase difference is close to zero, which means front and rear road inputs have similar effect on vertical acceleration at the mass center of body.

3.2 Pitch Angular Acceleration of Body

According to Eq. (5), FRF $H(\omega)_{\theta \sim q}$ between pitch angle θ of body and road input q is $H_{21}(\omega) + e^{-j\omega t_L} H_{22}(\omega)$. Using the same approach in dealing with vertical acceleration, the magnitude of FRF $H(\omega)_{\ddot{\theta} \sim \dot{q}}$ between pitch angular acceleration and road velocity input is calculated as follows.

$$|H(\omega)_{\ddot{\theta} \sim \dot{q}}| = \omega \sqrt{|H_{21}(\omega)|^2 + |H_{22}(\omega)|^2 + 2|H_{21}(\omega)||H_{22}(\omega)| \cos(\omega t_L + \varphi_\theta)} \quad (7)$$

in which φ_θ is the phase difference between $H_{21}(\omega)$ and $H_{22}(\omega)$, the calculation equation of this phase difference is $\varphi_\theta = \text{phase}[H_{21}(\omega)] - \text{phase}[H_{22}(\omega)]$.

Amplitudes of $H_{21}(\omega)$, $H_{22}(\omega)$ and $H(\omega)_{\ddot{\theta} \sim \dot{q}}$ and phase angles of $H_{21}(\omega)$ and $H_{22}(\omega)$ are shown in Fig. 3, here velocity is 40 km/h.

Figure 3a indicates that there is a small difference between the amplitudes of $H_{21}(\omega)$ and $H_{22}(\omega)$, so the amplitude-frequency curve of $H(\omega)_{\ddot{\theta} \sim \dot{q}}$ does not show as large fluctuation as that of $H(\omega)_{\ddot{z} \sim \dot{q}}$, but filtering effect is still obvious. Figure 3b indicates that phase angle difference between $H_{11}(\omega)$ and $H_{12}(\omega)$ is close to 180°, which means front and rear road inputs have opposite effect on pitch angular acceleration of body.

3.3 Vertical Acceleration at Different Locations of Body

Pitch angular acceleration over the body is consistent; however, vertical accelerations at different locations of body are different, so analysis of vertical acceleration at the mass center doesn't represent general situation. As vertical acceleration of the body depends on location, it could be seen as a function of location, and effect of wheelbase filtering on vertical acceleration is also relevant to location. In the following, some typical locations on the body are selected to investigate the relation between wheelbase filtering effect and location.

Here seven locations on the body are selected to investigate effect of wheelbase filtering on vertical acceleration. They are respectively located in front of front axle (P_1), above front axle (P_2), between front axle and mass center (P_3), at the mass center (P_4), between rear axle and mass center (P_5), above rear axle (P_6) and in rear of rear axle (P_7).

Distance between a point P and mass center is defined as x_p . When a point is located in front of mass center, $x_p > 0$; when a point is located in rear of mass center, $x_p < 0$. Here list the distances between all selected points and mass center: $x_{P_1} = 1.5 * a$; $x_{P_2} = a$; $x_{P_3} = 0.5 * a$; $x_{P_4} = 0$; $x_{P_5} = -0.5 * b$; $x_{P_6} = -b$; $x_{P_7} = -1.5 * b$.

Vertical acceleration \ddot{z}_p at P point on the body could be expressed using the combination of vertical acceleration \ddot{z} at the mass center and pitch angular acceleration $\ddot{\theta}$.

$$\ddot{z}_p = \ddot{z} - x_p \ddot{\theta} \tag{8}$$

Based on this relation, $H(\omega)_{\ddot{z}_p \sim \ddot{q}}$ could be expressed using FRFs between body motion and road input. The final equation is written with phase delay item so as to easily investigate the effect of wheelbase filtering.

$$H(\omega)_{\ddot{z}_p \sim \ddot{q}} = j\omega \left[H_1(\omega)_{z_p \sim q} + e^{-j\omega t_L} H_2(\omega)_{z_p \sim q} \right] \tag{9}$$

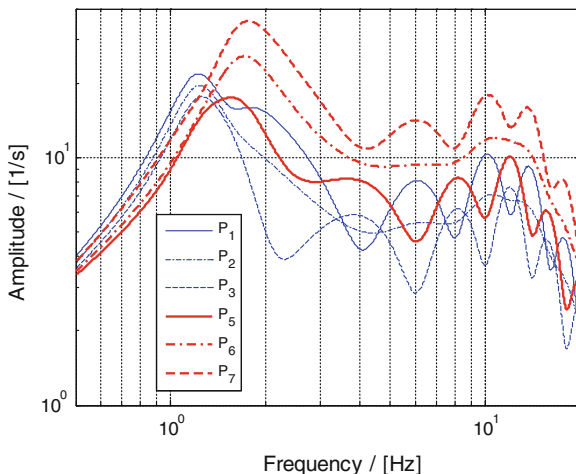
in which $H_1(\omega)_{z_p \sim q} = H_{11}(\omega) - x_p H_{21}(\omega)$, $H_2(\omega)_{z_p \sim q} = H_{12}(\omega) - x_p H_{22}(\omega)$. Here $H_1(\omega)_{z_p \sim q}$ represents FRF between vertical displacement and front road input and $H_2(\omega)_{z_p \sim q}$ represents FRF between vertical displacement and rear road input.

Amplitudes of FRFs between vertical accelerations at all selected points and road input are shown in Fig. 4, here velocity is 40 km/h.

Figure 4 indicates that vertical accelerations at P_2 and P_6 on the body do not show obvious filtering effect; however, vertical acceleration of body at P_1, P_3, P_5, P_7 show obvious filtering effect. This result means that when the point is above axle, filtering effect is not prominent; when the point is between two axles or out of wheelbase, filtering effect is prominent.

When dynamic index ($DI = I_0/mbc$) of vehicle is equal to one, front road input would not have any effect on rear suspension vibration and vice versa. In this

Fig. 4 Filtering effect of acceleration at different locations of body



situation, vertical acceleration of body above axle would not show any filtering effect. As dynamic index of actual vehicle is close to one, vertical acceleration of body above axle don't show obvious effect.

In addition, vertical acceleration of body at P_1 , P_7 and P_3 , P_5 show different phase, and their phase angles have a difference of 180° . This is because front road input and rear road input have the same effect on vertical acceleration of body between two axles (P_3 and P_5), and they have opposite effect on vertical acceleration of body out of wheelbase (P_1 and P_7).

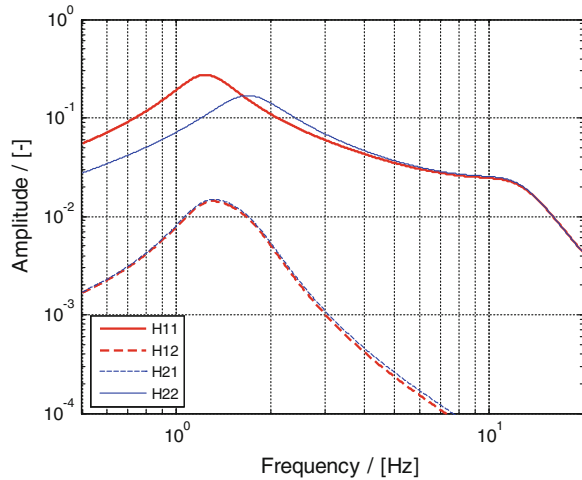
4 Wheelbase Filtering Effect on Suspension Motion

Both vertical acceleration and pitch angular acceleration show the motion of body. In the following, wheelbase filtering effect on suspension is investigated using suspension work space and dynamic tire load as evaluation indexes, both of which are usually utilized to evaluate ride behavior.

4.1 Suspension Work Space

In the running, suspension work space affects vehicle ride behavior. This is because suspension work space decides the probability of wheel striking limit block. If the design is not good enough, frequent wheel striking limit block would worsen ride behaviour of vehicle. So suspension work space is an important factor to evaluate ride behavior.

Fig. 5 Amplitude of FRFs between suspension work space and road input



Suspension work space f_d is defined as follows.

$$f_d = \begin{bmatrix} z - a\theta - z_1 \\ z + b\theta - z_2 \end{bmatrix} = \begin{bmatrix} 1 & -a & -1 & 0 \\ 1 & b & 0 & -1 \end{bmatrix} \mathbf{x} \tag{10}$$

To define transformation matrix T

$$T = \begin{bmatrix} 1 & -a & -1 & 0 \\ 1 & b & 0 & -1 \end{bmatrix}$$

FRF between suspension work space and front road velocity input is

$$\mathbf{H}(\omega)_{f_d \sim \dot{q}} = \frac{F[f_d]}{F[\dot{q}]} = \frac{f_d(\omega)}{j\omega q(\omega)} = \frac{\mathbf{TX}(\omega)}{j\omega q(\omega)} \tag{11}$$

Each element of $\mathbf{H}(\omega)_{f_d \sim \dot{q}}$ could be expressed as follows.

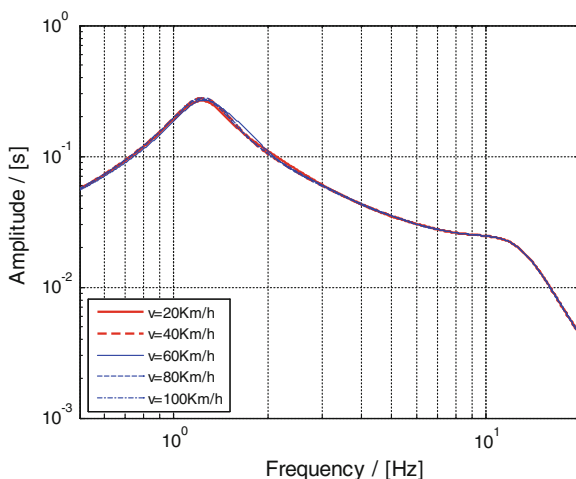
$$\begin{bmatrix} H(\omega)_{f_{d1} \sim \dot{q}} \\ H(\omega)_{f_{d2} \sim \dot{q}} \end{bmatrix} = \frac{1}{j\omega} \begin{bmatrix} H_1(\omega)_{f_{d1} \sim q} + e^{-j\omega t_L} H_2(\omega)_{f_{d1} \sim q} \\ H_1(\omega)_{f_{d2} \sim q} + e^{-j\omega t_L} H_2(\omega)_{f_{d2} \sim q} \end{bmatrix} \tag{12}$$

in which

$$\begin{aligned} H_1(\omega)_{f_{d1} \sim q} &= H_{11}(\omega) - aH_{21}(\omega) - H_{31}(\omega), & H_2(\omega)_{f_{d1} \sim q} \\ &= H_{12}(\omega) - aH_{22}(\omega) - H_{32}(\omega) \end{aligned}$$

$$\begin{aligned} H_1(\omega)_{f_{d2} \sim q} &= H_{11}(\omega) + bH_{21}(\omega) - H_{41}(\omega), & H_2(\omega)_{f_{d2} \sim q} \\ &= H_{12}(\omega) + bH_{22}(\omega) - H_{42}(\omega) \end{aligned}$$

Fig. 6 Amplitude of $H(\omega)_{f_{d1} \sim \dot{q}}$ at different velocity



Here $H_1(\omega)_{f_{d1} \sim q}$ is FRF between front suspension work space and front road input, and $H_2(\omega)_{f_{d1} \sim q}$ is FRF between front suspension work space and rear road input.

Amplitude of FRFs between suspension work space and road input are shown in Fig. 5.

Figure 5 indicates that amplitude of $H_2(\omega)_{f_{d1} \sim q}$ and $H_1(\omega)_{f_{d2} \sim q}$ is much smaller than that of $H_1(\omega)_{f_{d1} \sim q}$ and $H_2(\omega)_{f_{d2} \sim q}$. This means that rear road input has little influence on front suspension work space and front road input also hardly affects rear suspension work space. So suspension work space could be designed without considering coupling of front and rear suspension vibration in this situation.

The previous analysis show that amplitude of $H_2(\omega)_{f_{d1} \sim q}$ is much smaller than that of $H_1(\omega)_{f_{d1} \sim q}$, so $H(\omega)_{f_{d1} \sim \dot{q}}$ is greatly affected by $H_1(\omega)_{f_{d1} \sim q}$. As $H_1(\omega)_{f_{d1} \sim q}$ is determined by natural property of front suspension and it would not change with velocity, $H(\omega)_{f_{d1} \sim \dot{q}}$ would not change greatly. Figure 6 shows that $H(\omega)_{f_{d1} \sim \dot{q}}$ hardly change with velocity and five lines nearly coincide.

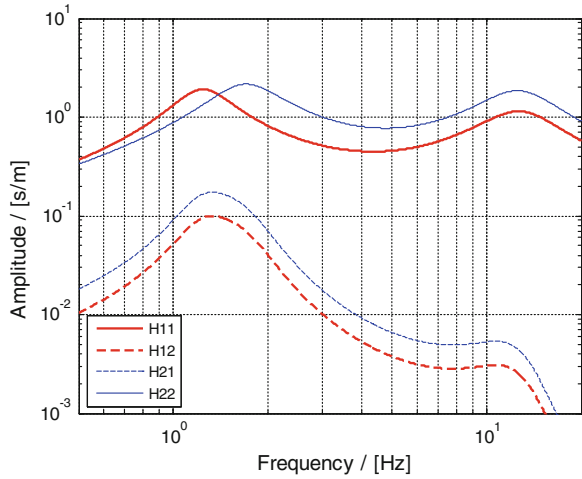
4.2 Dynamic Tire Load

Dynamic tire load influences the adhesion of tire and road. Good design of dynamic tire load contributes to improve handling and safety of vehicle. Dynamic tire load is another index to evaluate ride behaviour of vehicle.

Here dynamic tire load is analyzed using another form: relative dynamic tire load, which represents the relation between dynamic and static tire load.

Relative dynamic tire load F_d/G is defined as follows.

Fig. 7 Amplitude of FRFs between dynamic tire load and road input



$$\frac{\mathbf{F}_d}{\mathbf{G}} = \begin{bmatrix} \frac{k_{t1}(z_1 - q_1)}{(m_L^b + m_1)g} \\ \frac{k_{t2}(z_2 - q_2)}{(m_L^a + m_2)g} \end{bmatrix} = \begin{bmatrix} \frac{k_{t1}}{(m_L^b + m_1)g} & 0 \\ 0 & \frac{k_{t2}}{(m_L^a + m_2)g} \end{bmatrix} \left[\begin{bmatrix} 0 & 0 & 1 & 0 \\ 0 & 0 & 0 & 1 \end{bmatrix} \mathbf{x} - \begin{bmatrix} 1 & 0 \\ 0 & 1 \end{bmatrix} \mathbf{q} \right] \quad (13)$$

To define transformation matrix \mathbf{D}

$$\mathbf{D} = \begin{bmatrix} \frac{k_{t1}}{(m_L^b + m_1)g} & 0 \\ 0 & \frac{k_{t2}}{(m_L^a + m_2)g} \end{bmatrix}$$

FRF between dynamic tire load and front road velocity input is

$$\mathbf{H}(\omega)_{\frac{F_d}{G} \sim \dot{q}} = \frac{\mathbf{F}_d(\omega)}{j\omega} = \frac{\mathbf{D}}{j\omega} \left[\begin{bmatrix} 0 & 0 & 1 & 0 \\ 0 & 0 & 0 & 1 \end{bmatrix} \frac{\mathbf{X}(\omega)}{q(\omega)} - \begin{bmatrix} 1 & 0 \\ 0 & 1 \end{bmatrix} \right] \quad (14)$$

Each element of $\mathbf{H}(\omega)_{\frac{F_d}{G} \sim \dot{q}}$ could be expressed as follows.

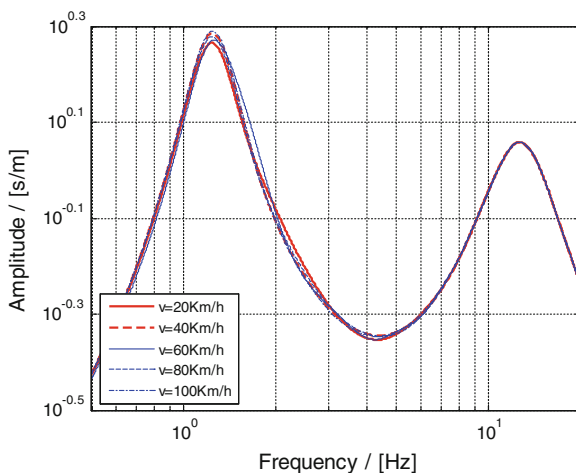
$$\begin{bmatrix} H(\omega)_{\frac{F_d}{G_1} \sim \dot{q}} \\ H(\omega)_{\frac{F_d}{G_2} \sim \dot{q}} \end{bmatrix} = \frac{1}{j\omega} \begin{bmatrix} H_1(\omega)_{\frac{F_d}{G_1} \sim q} + e^{-j\omega L} H_2(\omega)_{\frac{F_d}{G_1} \sim q} \\ H_1(\omega)_{\frac{F_d}{G_2} \sim q} + e^{-j\omega L} H_2(\omega)_{\frac{F_d}{G_2} \sim q} \end{bmatrix} \quad (15)$$

in which

$$H_1(\omega)_{\frac{F_d}{G_1} \sim q} = \frac{k_{t1}}{(m_L^b + m_1)g} (H_{31}(\omega) - 1), \quad H_2(\omega)_{\frac{F_d}{G_1} \sim q} = \frac{k_{t1}}{(m_L^b + m_1)g} H_{32}(\omega)$$

$$H_1(\omega)_{\frac{F_d}{G_2} \sim q} = \frac{k_{t2}}{(m_L^a + m_2)g} H_{41}(\omega), \quad H_2(\omega)_{\frac{F_d}{G_2} \sim q} = \frac{k_{t2}}{(m_L^a + m_2)g} (H_{42}(\omega) - 1)$$

Fig. 8 Amplitude of $H(\omega)_{\frac{F_d}{\sigma_1} \sim \dot{q}}$ at different velocity



Amplitude of FRFs between dynamic tire load and road input are shown in Fig. 7. Amplitude of $H(\omega)_{\frac{F_d}{\sigma_1} \sim \dot{q}}$ at different velocity is shown in Fig. 8. Figures 7 and 8 indicate that dynamic tire load shows similar characteristics to suspension work space. Front road input hardly affects rear dynamic tire load and vice versa. Amplitude of $H(\omega)_{\frac{F_d}{\sigma_1} \sim \dot{q}}$ could not change with velocity.

5 Conclusions

Wheelbase filtering effect exists in both body motion and suspension motion, but this effect varies greatly in different motions.

Amplitude of FRF between a motion and road input could be divided into two parts: steady part and variable part. Steady part would not change with outer input condition; however, variable part is closely related to velocity. When the amplitudes of FRFs between a motion and front and rear road input have a large difference, filtering effect in this motion is not obvious; otherwise, this motion would show obvious filtering effect.

Pitch motion of body shows obvious filtering effect, but filtering effect in bounce motion of body depends on location on the body. When a point is within or out of wheelbase, filtering effect at this point is obvious; however, when a point is near front or rear axle, filtering effect at this point is not obvious. The amplitudes of FRFs between suspension motion and front and rear road input have a large difference, so filtering effect in suspension motion is not obvious.

References

1. Gillespie T (1992) Fundamentals of vehicle dynamics. Society of Automotive Engineers Inc, USA
2. Sharp RS (2002) Wheelbase filtering and automobile suspension tuning for minimising motions in pitch. Proc Inst Mech Engineers Part D-J Automobile Eng 216(D12):933–946
3. Cao D, Khajepour A, Song X (2012) Wheelbase filtering and characterization of road profiles for vehicle dynamics. In: Proceedings of the ASME design engineering technical conference 4, pp 275–285
4. Fu W, Ling Fe, Peng M, et al. (2011) Comparison of wheelbase filtering effect and suspension tuning between two-axle and tri-axle vehicle with tandem suspension . In: The 2nd international conference on computer application and system modeling, Xiamen, China, pp 1124–1127
5. Cossalter V, Doria A, Garbin S et al (2006) Frequency-domain method for evaluating the ride comfort of a motorcycle. Veh Syst Dyn 44(4):339–355
6. Dean A, Martini R, Brennan S (2011) Terrain-based road vehicle localisation using particle filters. Veh Sys Dyn 49(8):1209–1223
7. Prem H, George R, McLean J (1998) Methods for evaluating the dynamic-wheel-load performance of heavy commercial vehicle suspensions. In: The 5th international symposium on heavy vehicle weights and dimensions, Maroochydore, Queensland, Australia, pp 252–278

Part XII
Simulation and Experimental Validation

Modeling and Experimental Research About a New Type of Vehicle Active Suspension Electromagnetic Actuator

Lai Fei and Huang Chaoqun

Abstract A new type of electromagnetic linear actuator for vehicle active suspension was designed, with the characteristics of large stroke and force and fast response. Combined with the finite element analysis software, the effects of actuator structure parameters such as gap thickness, the secondary stainless steel thickness, the secondary copper thickness, permeability and conductivity of insulation stall on actuator thrust size and speed response were studied. And the effects of actuator power parameters such as voltage, frequency and load mode on actuator thrust size and speed response were also studied. The results show that the electromagnetic force is closely related to structural parameters such as the gap thickness, except for the conductivity of insulation stall. And the electromagnetic force is proportional to the square of the voltage, and first increases and then decreases with the frequency, getting the maximum at 20 Hz. The mathematic model of the actuator was also built up. Based on the simulation results, a prototype of electromagnetic linear actuator with appropriate parameters was developed. And the electromagnetic force test of the actuator was done. By comparison of the finite element simulation results and the experimental data, it shows the corresponding results are consistent, indicating that the design and analysis of the electromagnetic actuator is correct.

F2012-E12-001

L. Fei (✉)

Chongqing Vehicle Test and Research Institute of National Bus Quality Supervision and Inspection Center, 401122 Chongqing, China
e-mail: laifeichq@163.com

H. Chaoqun

Department of Automotive Engineering of Chongqing Technology and Business Institute, 401520 Chongqing, China

Keywords Vehicle · Active suspension · Electromagnetic linear actuator · Modeling

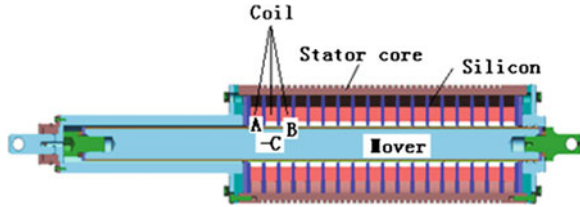
1 Introduction

Vehicle suspension must satisfy several conflicting purposes. It should isolate the body from vibrations resulting from road unevenness and maintain contact between the road and the tires. Electromagnetic linear actuators have several potential advantages for the generation of forces or motion when compared to pneumatic and hydraulic devices. The electrical actuators have very low static friction and the control of current through power electronics can be achieved rapidly and reliably so that force levels can be controlled.

Martins I. proposed a hybrid suspension system which combines the simplicity of the passive dampers with the performance of an electromagnetic active suspension [1]. Maintaining the passive damper, it is possible to keep the performance of the active suspension, but using a smaller electromagnetic actuator. Mirzaei S. introduced a novel passive suspension system for ground vehicles, which was based on a flexible electromagnetic shock absorber. The test results showed this system would have low cost and be controllable [2]. Bart L.J. used a tubular permanent magnet actuator together with a passive spring for vehicle active suspension system [3]. The quarter car test showed the active electromagnetic suspension vehicle can perform active roll and pitch control during cornering and braking as well as eliminating road irregularities. Seungho Lee used a direct-drive tubular linear brushless permanent magnet motor as a force generating component for active suspension [4]. Modified lead-lag control, linear quadratic servo control with a Kalman filter and a fuzzy control methodology were implemented for active suspension control. Both simulation and experimental results demonstrated the effectiveness of those control methodologies.

The main objective of this paper is to investigate the use of a new type of electromagnetic actuator for vehicle active suspension system. Firstly, it puts forward a suitable construction design of electromagnetic linear actuator. Secondly, it builds up the finite element model and mathematic model individually. After that, the actuator prototype is developed, and the steady state electromagnetic force and transient electromagnetic force are measured. The experimental data are also compared with the finite element model and mathematic model. It shows the correctness of the actuator design and the simulation results. Finally some conclusions can be obtained.

Fig. 1 Schematic of the electromagnetic linear actuator



2 Construction Design of Electromagnetic Linear Actuator

The 18-slot, 2-pole, and three phase induction electromagnetic linear actuator with modular winding is shown in Fig. 1. Each pole of the stator includes three different windings, for example, phase A, phase B and phase C. The Mover of the electromagnetic actuator comprises two layers, and the material of inner layer is 45# steel, which has high magnetic inductive capacity, and the material of outer layer is copper, which is use to conduct electric and yield the electromagnetic force.

3 The Modeling of the Electromagnetic Linear Actuator

As mentioned above, there are two ways to build up the model of the electromagnetic linear actuator. The first way is to use finite element software such as Flux, and the other way is to use mathematical model by Matlab/Simulink. The two different building ways are to make sure the model of electromagnetic linear actuator accurate.

3.1 The Building of Finite Element Model

The Actuator geometry and finite element model which is build up by finite element analysis software Flux are shown in Fig. 2a. The building process of the finite element model is very similar with other finite element software applications, for example, Ansys or Nastran. Basically it contains about six steps: (1) The building of actuator geometry, (2) The meshing of the actuator geometry, (3) The assignment of material attribute to the actuator mesh, (4) The circuit relation to the meshed model, (5) Load the boundary condition and solve and (6) Analysis the simulation results. The left part of Fig. 2 is the electromagnetic actuator geometry model, and the right part of Fig. 2 is the actuator finite element model, which contains about 26,508 nodes and 12,709 elements.

Once get the finite element model, some simulations can be analyzed. Before solving the finite element model, some boundary condition should be given. The boundary condition is: (1) give 0 m/s velocity to both the primary and the

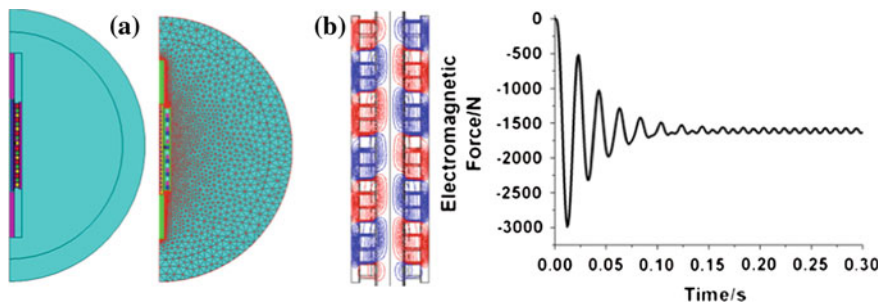


Fig. 2 The model and the electromagnetic force of the actuator (a) Geometry and finite element model (b) Magnetic flux and transient electromagnetic force response

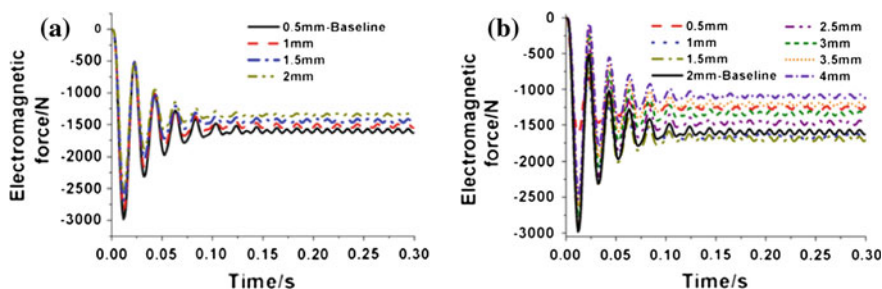


Fig. 3 Effect of air-gap thickness and secondary copper thickness to the electromagnetic force (a)Effect of air-gap thickness (b) Effect of secondary copper thickness

mover that means to fix the two sides of the electromagnetic linear actuator and (2) apply power voltage 220 V and power frequency 50 Hz of three phase Alternating Current electric to each winding, which has 120 degree delay in phase with each other. Figure 2b shows the magnetic flux distribution and transient electromagnetic force response of the electromagnetic actuator. It can be seen that the electromagnetic force amplitude is about 3000 N and it can reach steady state after 0.15 s, and the stationary force is about 1,609 N.

3.1.1 The Structure Parameter Effect to the Electromagnetic Force

The important structure parameters are the air-gap thickness and second copper thickness. Figure 3a shows the effect of air-gap thickness between primary and secondary to the electromagnetic force of actuator. It can be seen that the thicker of the gap is, the smaller of peak and steady force value is. When the gap is 0.5 mm, the peak value is 2,983 N, the steady value is 1,604 N. When the gap is 1 mm, the peak value is 2,873 N, the steady value is 1,524 N. When the gap is 1.5 mm, the peak value is 2,686 N, the steady value is 1,443 N. When the gap is 2 mm, the peak value is 2,518 N, the steady value is 1,350 N.

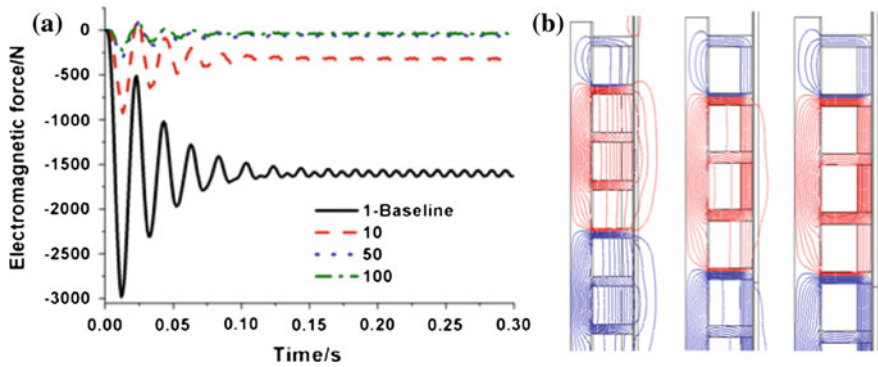
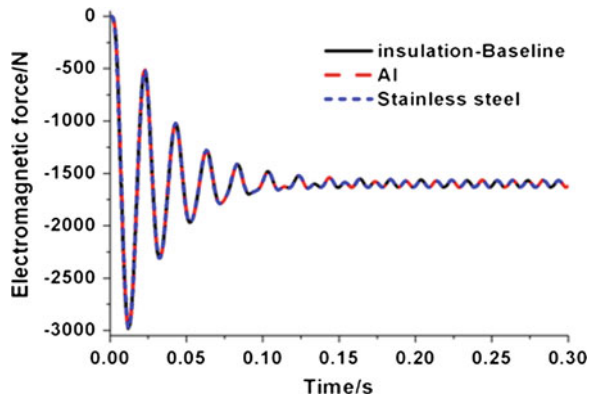


Fig. 4 Effect of insulation ring relative permeability to the electromagnetic force and magnetic flux distribution (a) Effect of insulation ring relative permeability (b) permeability 1\10\100

Fig. 5 Effect of insulation ring electrical conductivity performance to the electromagnetic force



The effect of secondary copper thickness to electromagnetic force is shown in Fig. 3b. When the copper thickness varies between 0.5 mm and 1.5 mm, the electromagnetic force varies corresponding with the copper thickness. When the copper thickness varies between 2 and 4 mm, the force varies opposite to the copper.

In addition to the air-gap thickness and copper thickness, the other important parameter to the electromagnetic force is the material property of insulation ring, which are the relative permeability performance and the electrical conductivity performance. Figures 4a and 5 show the effects of insulation ring relative permeability performance and electrical conductivity performance to the electromagnetic force individually. And Fig. 4b shows the effect of relative permeability performance to the magnetic flux. It can be seen that the relative permeability performance is important for the electromagnetic force, while the conductivity has no-effect to the electromagnetic force.

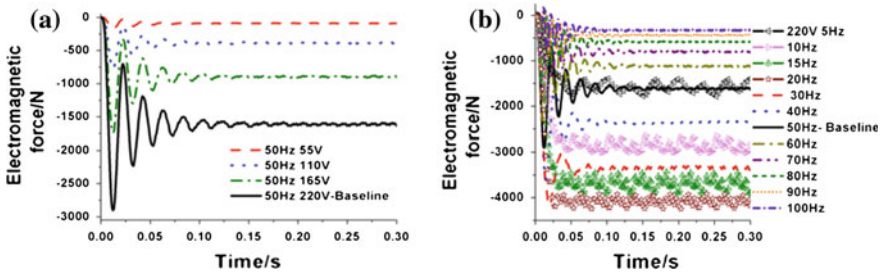


Fig. 6 Effect of power voltage and frequency to the electromagnetic force (a) Effect of power voltage at 50 Hz (b) Effect of power frequency at 220 V

3.1.2 The Power Parameter Effect to the Electromagnetic Force

The important power parameters are the power voltage and the power frequency. Figure 6a shows the effect of power voltage to electromagnetic force at 50 Hz. It can be that when the power frequency is fixed, the electromagnetic force increases with the power voltage. And it also can be seen that the electromagnetic force is about proportion to the square of power voltage. When the voltage is 220 V, the steady value is about 1,609 N. When the voltage is 165 V, the value is about 895 V. When the value is 110 V, the value is about 388 N. When the value is 55 V, the value is about 88 N.

The effect of power frequency to the electromagnetic force at 220 V is shown in Fig. 6b. It can be seen that when the power frequency is fixed, the electromagnetic force increases with the power frequency between 5 and 20 Hz, while decreases with the power frequency between 25 and 110 Hz. When the power frequency is at 20 Hz, the electromagnetic force achieves the maximum value, which is about 4000 N. When the power frequency is at 100 Hz, the electromagnetic force achieves the minimal value, which is about 330 N.

3.2 The Building of the Mathematical Model

To simulate the electromagnetic linear actuator, the simulation model should be built firstly. And some assumptions should be given to simplify the model, as follows: (1) The magnetic circuit is linear, and magnetic saturation is not considered, (2) The cogging force is not considered. The voltage equation of the electromagnetic linear actuator is given as follows.

$$U_{sd} = R_s \cdot i_{sd} + R_r \cdot f(Q)(i_{sd} + i_{rd}) + d\psi_{sd}/dt - w_1 \cdot \psi_{sq} \tag{1}$$

$$U_{sq} = R_s \cdot i_{sq} + R_r \cdot f(Q)(i_{sq} + i_{rq}) + d\psi_{sq}/dt + w_1 \cdot \psi_{sd} \tag{2}$$

$$U_{rd} = R_r \cdot i_{rd} + R_r \cdot f(Q)(i_{sd} + i_{rd}) + d\psi_{rd}/dt - w_s \cdot \psi_{rq} \quad (3)$$

$$U_{rq} = R_r \cdot i_{rq} + R_r \cdot f(Q)(i_{sq} + i_{rq}) + d\psi_{rq}/dt - w_s \cdot \psi_{rd} \quad (4)$$

The flux equation of the electromagnetic linear actuator is given as follows.

$$\psi_{sd} = (L_s - L_m \cdot f(Q))i_{sd} + L_m(1 - f(Q))i_{rd} \quad (5)$$

$$\psi_{sq} = (L_s - L_m \cdot f(Q))i_{sq} + L_m(1 - f(Q))i_{rq} \quad (6)$$

$$\psi_{rd} = L_m(1 - f(Q))i_{sd} + (L_r - L_m \cdot f(Q))i_{rd} \quad (7)$$

$$\psi_{rq} = L_m(1 - f(Q))i_{sq} + (L_r - L_m \cdot f(Q))i_{rq} \quad (8)$$

And the flux equation has inner relation with the voltage equation.

$$\psi_{sd} = \int (U_{sd} - R_s \cdot i_{sd} - R_r \cdot f(Q) \cdot (i_{sd} + i_{rd}) + w_1 \cdot \psi_{sq})dt \quad (9)$$

The other flux has similar relation above with the voltage, so ignored. The electric current equation can be solved by the flux equation, as follows.

$$i_{sd} = (\psi_{sd}[L_r - L_m f(Q)] - \psi_{rd}L_m[1 - f(Q)]) / [L_s L_r - L_m^2 + f(Q)(2L_m^2 - L_m L_r - L_s L_m)] \quad (10)$$

$$i_{sq} = (\psi_{sq}[L_r - L_m f(Q)] - \psi_{rq}L_m[1 - f(Q)]) / [L_s L_r - L_m^2 + f(Q)(2L_m^2 - L_m L_r - L_s L_m)] \quad (11)$$

$$i_{rd} = (\psi_{rd}[L_s - L_m f(Q)] - \psi_{sd}L_m[1 - f(Q)]) / [L_s L_r - L_m^2 + f(Q)(2L_m^2 - L_m L_r - L_s L_m)] \quad (12)$$

$$i_{rq} = (\psi_{rq}[L_s - L_m f(Q)] - \psi_{sq}L_m[1 - f(Q)]) / [L_s L_r - L_m^2 + f(Q)(2L_m^2 - L_m L_r - L_s L_m)] \quad (13)$$

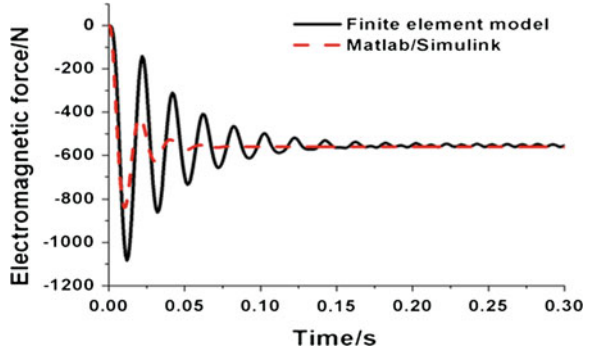
And the electromagnetic force of the actuator can be got as follows.

$$F_e = 3N_p \pi (\psi_{sd} \cdot i_{sq} - \psi_{sq} \cdot i_{sd}) / 4\tau \quad (14)$$

According to the Newton Second Law, the actuator dynamic equation can be got as follows.

$$a = dv/dt = (F_e - F_{load})/m \quad (15)$$

Fig. 7 Electromagnetic force of Finite element model vs Matlab/Simulink



$$v = v_0 + \int_{t_0}^t a dt \tag{16}$$

And the velocity has some relation with the angular velocity:

$$w_r = v \cdot \pi / \tau \tag{17}$$

In the above equation, U is the voltage, i is the current, ψ is the magnetic flux, d, q represent the dq coordinate system, s, r represent the primary and the secondary, R_s, R_r represent the equivalent electric resistance, L_s, L_m, L_r represent the primary self-inductance, mutual-inductance, secondary self-inductance, F_e is the electromagnetic force, N_p is the number of pole-pairs, τ is the polar pitch; F_{load} is the load, m is the load mass, a is the acceleration of the mover, v_0 is the initial velocity of the mover, v is the velocity of the mover, w_l is the primary magnetic field angular frequency, w_r is the secondary magnetic field angular frequency, $w_s = w_l - w_r$ is the slip angular frequency.

Once the mathematical model of the electromagnetic actuator is built, the simulation can be done at Matlab/Simulink environment. And the boundary condition is chosen as follows: (1) Fix both sides of the actuator, (2) apply the power voltage 120 V and power frequency 50 Hz. Figure 7 shows the result of finite element model and mathematical model in Matlab/Simulink. It can be seen that the results by different ways all get the same electromagnetic force. The peak value of finite element model is larger than that of mathematical model, and the main reason is that the material nonlinear is considered in finite element model, while at Matlab/Simulink it ignores the nonlinear property.

4 Experiment Data

In addition to do the simulation about the electromagnetic linear actuator, there is also very need to do some experiment to check the simulation results. The key step is to make designed electromagnetic actuator out. After that, some experiment could be done. Firstly, the steady electromagnetic force will be measured in the



Fig. 8 Experiment bench of Electromagnetic actuator

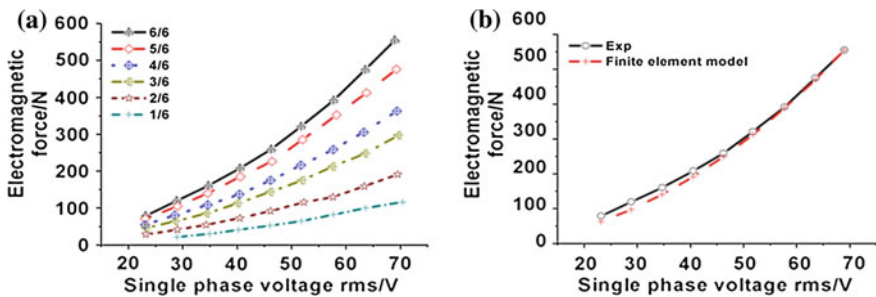


Fig. 9 Experiment vs Simulation (a) Actuator experiment data when secondary at different positions (b) Test vs simulation

experiment bench. After that the dynamic electromagnetic force will be measured in another experiment bench. All the experiment data will be checked out with the simulation result of Mathematical model.

4.1 The Steady Electromagnetic Force Experiment

The steady electromagnetic force is measured by the experiment bench, which is shown in Fig. 8. The left part is the side view, and the right part is the front view. The power voltage can be adjusted by the three phase voltage regulator, therefore different electromagnetic forces can be got at different voltages.

The experiment data of electromagnetic linear actuator is shown in Fig. 9a. The steady electromagnetic forces are measured at different power voltages which are

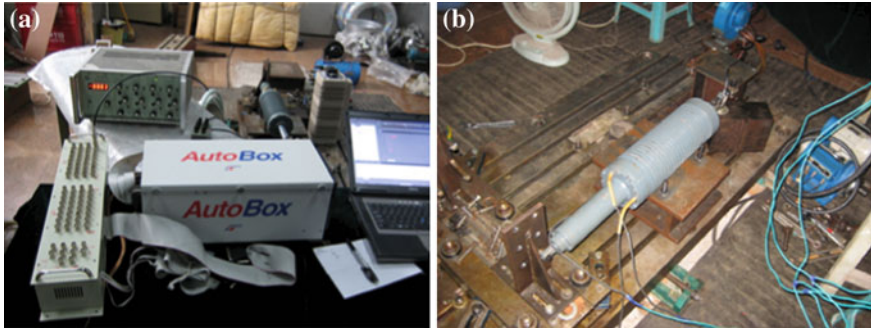


Fig. 10 The dynamic electromagnetic force experiment bench (a) Front view (b) Side view

adjusted by the type of GSGC2-6 three phase voltage regulator when secondary are at different positions. It can be seen that the electromagnetic force increases with the power voltage, which are similar with the simulation results. And it also can be seen that when the secondary is more in the stator, the electromagnetic force is also bigger.

In order to compare the simulation results and the experimental data, the condition that the secondary is full in the stator is compared, as shown in Fig. 9b. It can be seen that the simulation results are very correspondence with the experimental data. The condition that the secondary is at other position is also checked out. In order to save page, the results are ignored.

4.2 The Dynamic Electromagnetic Force Experiment

As mentioned before, the designed electromagnetic linear actuator will be used as a force generating component for vehicle active suspension system. So the dynamic characteristic of the electromagnetic actuator is very important, even more than that of the steady electromagnetic force measured above. In order to measure the dynamic force of the actuator, a simple experiment bench is built first. Figure 10 shows the front view and side view of the dynamic electromagnetic force experiment bench. It uses the type of ST35P-V-R-110-N-N three phase silicon-controlled rectifier (SCR) to control the power voltage, while it cannot change the power frequency. The AutoBox control unit is used to control the SCR.

Two cases are tested in the dynamic electromagnetic force experiment bench. One is the ramp control voltage load, and the other is the square wave control voltage load. Figure 11 shows the electromagnetic force between experiment and Matlab/Simulink under the ramp control voltage load. Figure 12 shows the force under the square wave control load. It shows the experiment result is corresponding with that of the mathematical model.

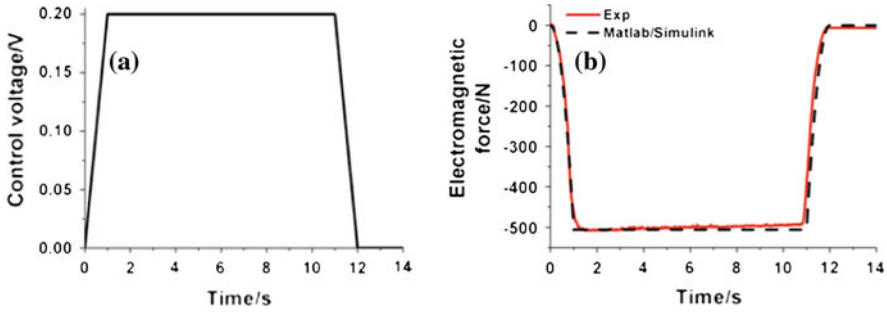


Fig. 11 The electromagnetic force of exp vs Matlab/Simulink under ramp voltage (a) ramp control voltage (b) Response of the electromagnetic force

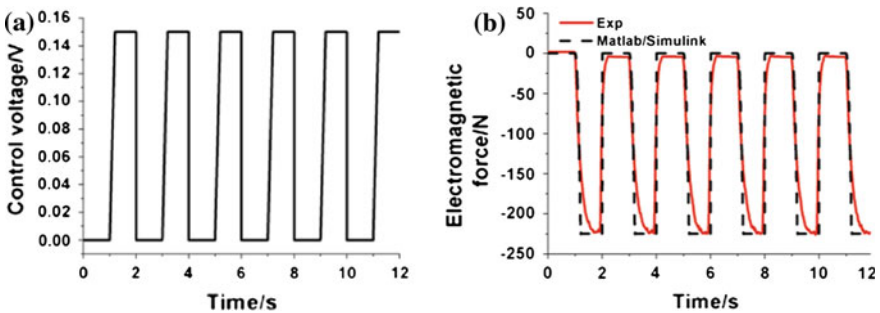


Fig. 12 The electromagnetic force of exp vs Matlab/Simulink under square wave scalar voltage (a) square wave control voltage (b) Response of the electromagnetic force

5 Conclusions

A new type of electromagnetic linear actuator is designed. The actuator model is built up through two different ways, one is the finite element model, and the other is the mathematical model. The simulation result shows they are corresponding with each other. The steady and dynamic electromagnetic force is tested under two different experiment benches. Compared with the mathematical model, it shows the correctness of modeling the electromagnetic linear actuator and the simulation results.

Acknowledgments The authors wish to express sincere gratitude to the reviewers for their invaluable suggestions and comments. And the authors also would like to thank Chongqing Bureau of Quality and Technology Supervision and Chongqing Shi Jiaoyu Weiyuanhui for their financial support.

References

1. Martins I, Esteves M, Pina F, et al. (1999) Electromagnetic hybrid active-passive vehicle suspension system. In: Vehicular technology conference, IEEE 49th, Vol 3., pp 2273–2277
2. Mirzaei S, Saghaiannejad SM, Tahani V, et al. (2001) Electromagnetic shock absorber. In: Electric machines and drives conference, IEEE international, pp 760–764
3. Bart LJ, Johannes JH, Jeroen LG, et al. (2008) Active electromagnetic suspension system for improved vehicle dynamics. In: IEEE vehicle power and propulsion conference, pp 1–6
4. Lee S, Kim W-J (2000) Active suspension control with direct-drive tubular linear brushless permanent-magnet motor. In: American control conference, Hyatt Regency Riverfront, St.Louis, Mo, USA, pp 5498–5503

Research on Nonlinear Characteristics of Hydro-Pneumatic Spring and Impact to Ride Performance of Vehicles

Junwei Zhang, Sizhong Chen, Zhicheng Wu, Lin Yang
and Bin Zhang

Abstract The relationship of nonlinear stiffness and natural frequency of vehicle body is analyzed. Nonlinear stiffness of hydro-pneumatic spring is modeled and simulated using the software Matlab/Simulink. The impact of two main parameters to the nonlinear stiffness is analyzed. The nonlinear stiffness is added into 2-DOFs vibration model and the results of simulation are compared with linear condition. The characteristics of two levels stiffness is verified by the bench test. Finally, some conclusions as to nonlinear characteristics and impact to ride performance are given.

Keywords Hydro-pneumatic spring · Nonlinear · Ride performance · Bench test

Hydro-pneumatic suspension had developed for dozens of years. It was well known for its superior characteristics of nonlinear and damping. It satisfied many kinds of vehicles and improved the ride performance and handling safety [1]. Hydro-pneumatic spring is the main part of hydro-pneumatic suspension, which is the aggregation of spring and shock absorber. It transfers power by means of oil and gas [2].

The vehicle ride performance is impacted by body natural frequency. And suspension stiffness is the main point to determine the body natural frequency. So the relationship between suspension stiffness and body natural frequency is studied in the first part of this paper. As for a kind of hydro-pneumatic spring which is used in a multiply axles heavy vehicle, its structure is described simply in this paper. The nonlinear characteristic of hydro-pneumatic spring is modeled and

F2012-E12-002

J. Zhang (✉) · S. Chen · Z. Wu · L. Yang · B. Zhang
Beijing Institute of Technology Vehicle Laboratory, Beijing, China
e-mail: zjw36927@163.com

simulated. The impact of nonlinear and linear stiffness to vehicle ride performance is compared each other. The vehicle 2-DOFs vibration model with nonlinear stiffness is simulated and the result is compared with linear model. The result shows that only part of evaluating indicators (body acceleration, wheel dynamic load and suspension deflection) are improved. In the end, some conclusions regarding nonlinear characteristics of hydro-pneumatic spring and vehicle ride performance are given.

1 Spring Stiffness and Body Natural Frequency

1.1 Body Natural Frequency

The demands of ride performance for different kinds of vehicle are different. The passenger vehicle requires more comfortable, while the lorry requires less. Generally, body natural frequency f_0 decreases with the increase of engine discharge.

The body acceleration grows down dramatically with the decrease of body natural frequency f_0 . But the suspension dynamic deflection is also increase, and it results in limit stroke f_d increase. We know that limit stroke is limited by the vehicle structure. So the body natural frequency is available decrease in a limit range. The available range body natural frequency f_0 , static deflection f_s , limit stroke f_d and damping rate ζ is listed in Table 1.

Sedan requires more comfort and drives on good road condition. The suspension dynamic deflection is not enough leading to crash onto the limit block. So body natural frequency chooses a low value. In another word, the spring of suspension system chooses a low value. While lorry and off-road vehicle require less comfort and road condition is rugged. The suspension dynamic deflection is huge. So in order to reduce the probability of crashing onto the limit block, the body natural frequency chooses a high value. It means that the spring stiffness choose big value.

The body natural frequency is deduced through vibration equation and described in Eq. 1.

$$f_0 = \frac{1}{2\pi} \sqrt{\frac{K}{m_s}} \quad (1)$$

Where

f_0 body natural frequency;

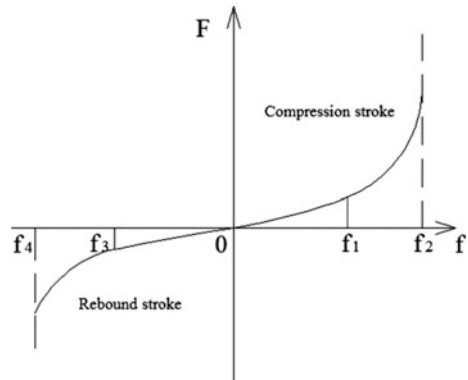
K spring stiffness;

m_s sprung mass

Table 1 The available range of f_0, f_s, f_d and ζ of suspension system [3]

Classification	f_0/Hz	f_s/cm	f_d/cm	ζ
Sedan	1.1 ~ 1.2	15 ~ 30	7 ~ 9	0.2 ~ 0.45
Lorry	1.5 ~ 2	6 ~ 11	6 ~ 9	
Coach	1.2 ~ 1.8	7 ~ 15	5 ~ 8	
Off-road	1.3 ~ 2	6 ~ 13	7 ~ 13	

Fig. 1 Elastic characteristic curve of suspension with nonlinear spring



1.2 Nonlinear Stiffness of Hydro-pneumatic Suspension

Elastic characteristics of spring are separated into linear (leaf spring and coil spring) and nonlinear (compound leaf spring, compound coil spring, air spring and hydro-pneumatic spring).

The elastic characteristic of linear spring is a straight line. Suspension distance f is in direct proportion to vertical force F . As for the load-carrying vehicle with huge mass change in empty and full load condition, body height and natural frequency have a huge change. They bring to unfavorable impact to vehicle ride performance and traffic-ability characteristic. However, the elastic characteristic of nonlinear spring is never a straight line. Suspension distance f is never in fixed proportion to vertical force F . The elastic characteristic curve of suspension with nonlinear spring is described in Fig. 1.

In Fig. 1, lateral axle stands for suspension distance f and ordinate axle stands for outside force F in vertical direction. The origin stands for equipoise under the full load condition. The part up the lateral axle is the compressed stroke, and the part below the lateral axle is the rebound stroke. The curves nears origin ($0 \rightarrow f_1, 0 \rightarrow f_3$) vary smoothly which means that spring stiffness is small. However, the curves far away from the origin ($f_1 \rightarrow f_2, f_3 \rightarrow f_4$) vary steep which means that spring stiffness is big. It brings to more dynamic capacity (Here dynamic capacity means that the capability of dissipating work from origin to the limit stroke f_d .) for nonlinear suspension than linear suspension within limit suspension dynamic deflection f_d . In another word, it decreases the probability of crashing onto the limit block and keeps the body height and body natural frequency in a reasonable range. In all, it improves the vehicle ride performance.

2 Model of Hydro-pneumatic Spring

2.1 Physical Model of Hydro-pneumatic Spring

Hydro-pneumatic spring transfers power by the oil and provides elastic force by the gas (Generally, it is inert gases such as Nitrogen.). It compounds with elastic component and damper. A kind of hydro-pneumatic spring is designed in this paper. Its structure is represented in Fig. 2.

The hydro-pneumatic spring is composed of cylinder, plunger, damping valve, electromagnetic valve, the main accumulator and vice accumulator. Of course, only the elastic characteristic is studied here. The cylinder is full of oil and accumulators are charged inert gas whose pressure is determined by real situation. There is a septum between the oil and the gas which prevents the two kinds of media from mixing each other.

In order to realize stiffness transfer function for two levels, the two accumulators are charged inert gas with different pressure. The vice accumulator is charged higher pressure than the main accumulator.

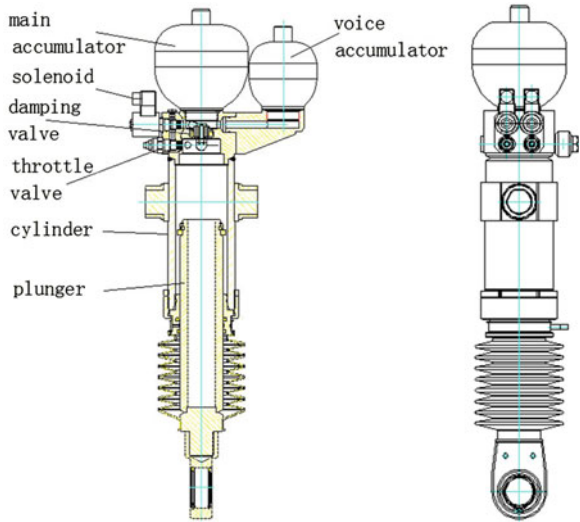
When vehicle with empty load drives on the smooth road, the plunger distance is slight. So the oil pressure is not enough to push the septum of vice accumulator. Only the main accumulator works under this condition. Here the elastic force curve is steep. When vehicle with full load drives on the rugged road, the plunger distance is huge. So the oil pressure is enough to push the septum of vice accumulator. Then both of the main accumulator and vice accumulator work together under this condition. Two accumulators increase the capacity of the whole system. It is equal to two spring connected in parallel way. Here the elastic force curve becomes smooth. Its function is to prevent the spring stiffness from increasing speed. The final purpose is showed in keeping the body height and body natural frequency in a reasonable range.

2.2 Mathematics Model of Nonlinear Stiffness

The accumulators are full of nitrogen which can be treated as ideal gas when both of pressure and working temperature have limit variation range [4]. We can treat it as isolated process and choose poly-tropic index of gas $k = 1.4$ in rapid loading process. Meanwhile, we treat it as isothermal process and choose poly-tropic index of gas $k = 1.0$. The actual process is treated as the condition which is between isolated and isothermal process and we choose $k = 1.2 : 1.3$ [5]. So, it is suitable to choose real gas equation of state to describe stiffness characteristic of hydro-pneumatic suspension in view of harsh working condition of off-road vehicle.

Elastic force equation of hydro-pneumatic spring in the equilibrium position can be derived:

Fig. 2 Structure diagram of hydro-pneumatic spring



$$F_{sp} = p_{sp}A_{sp} = \frac{1}{4}p_{sp}\pi d_s^2 \tag{2}$$

Where F_{sp} is elastic force, p_{sp} is gas pressure of accumulator, A_{sp} is area of plunger and d_s is diameter of cylinder.

The volume of gas inside accumulator in the process of suspension vibration is:

$$V_s = V_{sp} - \Delta V = V_{sp} - \pi\left(\frac{d_s}{2}\right)^2x \tag{3}$$

Where the V_s is the gas volume in the process of vibration and x is the piston displacement.

The suspension vibration can be treated as isolated process and choose polytropic index of gas $k = 1.4$. So, any time the gas pressure is:

$$p_s = p_{sp}\left(\frac{V_{sp}}{V_s}\right)^k \tag{4}$$

From “Eqs. 3 and 4” we can obtain:

$$p_s = p_{sp} \frac{V_{sp}^k}{\left(V_{sp} - \frac{1}{4}\pi d_s^2 x\right)^k} \tag{5}$$

So, the elastic force of hydro-pneumatic spring in the process of vibration is:

$$F_s = F_{sp} \frac{V_{sp}^k}{\left(V_{sp} - \frac{1}{4}\pi d_s^2 x\right)^k} \tag{6}$$

From R-K state equation, the volume of gas inside the accumulator when suspension is in the equilibrium position can be described:

Table 2 Parameters for elastic force simulation of single accumulator

p_0	3.2e6 Pa	V_0	$2e-3 \text{ m}^3$
d_s	0.096 m	F_{sp}	54, 953 N
T_0	288 K	T_{sp}	298 K
k	1.4		

$$V_{sp} = \left(\frac{p_0 T_{sp}}{p_{sp} T_0} \right)^{\frac{1}{k}} V_0 \quad (7)$$

We can treat it as isothermal process and choose poly-tropic index of gas $k = 1.0$, because the velocity is low from the original position to equilibrium position. So, Eq. 7 can be described:

$$V_{sp} = \frac{p_0 T_{sp} V_0}{p_{sp} T_0} \quad (8)$$

Where we define original pressure, volume and temperature as follows: p_0 , V_0 and T_0 .

Combining ‘‘Eqs. 6 and 8’’ we can obtain elastic force of hydro-pneumatic spring any time is:

$$F_s = F_{sp} \left(\frac{\frac{p_0 V_0 T_{sp}}{F_{sp} T_0}}{\frac{p_0 V_0 T_{sp}}{F_{sp} T_0} - x} \right)^k \quad (9)$$

3 Simulation and Analysis

3.1 Simulation of Nonlinear Stiffness

Simulating the model by means of Matlab based on the above mathematic model. The impact to nonlinear characteristic from main parameter is analyzed.

The impacts to nonlinear characteristic from p_0 and V_0 are analyzed. Let one parameter change, while the other parameters are constant. The parameters for simulation are listed in Table 2. The simulation results are described in Fig. 3.

From Fig. 3 we can obtain the following conclusions:

- (1) When the other parameters are constant, elastic force decreases with the increase of original gas pressure p_0 .
- (2) When the other parameters are constant, elastic force decreases with the increase of original gas volume V_0 .
- (3) The original gas volume V_0 impacts elastic force curve more dramatically than original gas pressure p_0 . So the elastic force curve becomes smooth quickly when both of the two accumulators work together.

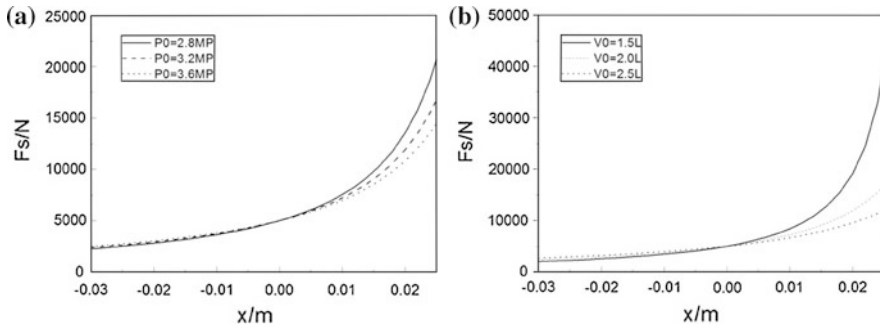


Fig. 3 Impacts to elastic force from P_0 and V_0 . **a** Original gas pressure p_0 . **b** Original gas volume V_0

Table 3 Parameters for elastic force simulation of two accumulators

p_{01}	$3.2e6$ Pa	V_{01}	$2e-3$ m ³
p_{02}	$6.4e6$ Pa	V_{02}	$1e-3$ m ³
d_s	0.09 m	F_{sp}	54,953 N
T_0	288 K	T_{sp}	298 K
k	1.4		

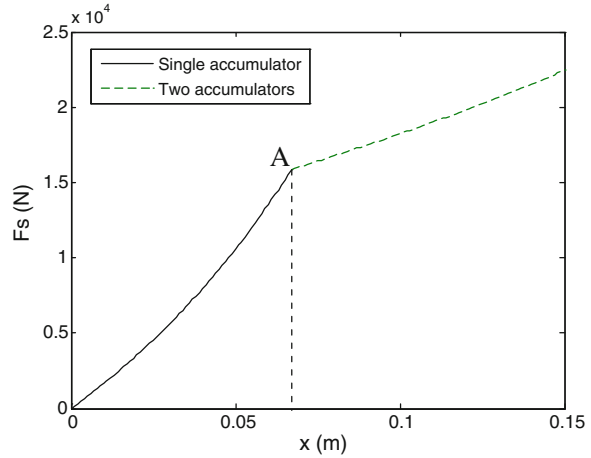
3.2 Simulation and Analysis of Two Levels Stiffness

The elastic force of two accumulators working together is described in Eq. (10). The $x_{transfer}$ is the plunger distance at the time of stiffness transformation. It can be calculated by the transformation pressure value. Simulating the elastic force characteristic of two accumulators and analyzing the simulation results. The parameters for simulation are listed in Table 3.

$$F_s = \begin{cases} F_{sp} \left[\frac{\frac{p_{01} V_{01} T_{sp}}{F_{sp} T_0}}{\frac{p_{01} V_{01} T_{sp}}{F_{sp} T_0} - x} \right]^k ; x < x_{transfer} \\ F_{sp} \left[\frac{\frac{p_{01} V_{01} T_{sp}}{F_{sp} T_0}}{\frac{p_{01} V_{01} T_{sp}}{F_{sp} T_0} - x_{transfer}} \right]^k + F_{sp} \left[\frac{\frac{p_{02} (V_{01} + V_{02}) T_{sp}}{F_{sp} T_0}}{\frac{p_{02} (V_{01} + V_{02}) T_{sp}}{F_{sp} T_0} - x} \right]^k ; x \geq x_{transfer} \end{cases} \quad (10)$$

The elastic force curve of two accumulators is represented in Fig. 4. The point A is the transformation point. Before point A, the plunger distance is small, and the oil pressure is not enough to push the septum of vice accumulator. Here only the main accumulator works under this condition. So the elastic force curve is steep. It keeps the body height and body natural frequency in a reasonable range in empty condition. After point A, the plunger distance is huge, and the oil pressure is able to push the septum of vice accumulator. Here both of the main accumulator and the vice accumulator work together under this condition. The elastic force curve

Fig. 4 Elastic force characteristic of two accumulators



becomes smooth with the increase of system capacity. It improves the vehicle ride performance when vehicle driving on the rugged road.

4 Modeling and Simulation of Vehicle 2-Dofs Vibration

4.1 Mathematic Model of Vehicle 2-DOFs Vibration

In order to build mathematical model of 2-DOFs vibration, we take some assumptions as follows: (1) Tires keep contact with ground and tires damping is neglected; (2) Weighting parameter is 1; (3) Pitch angle of body is neglected [6]. Look at the 2-DOFs vibration diagram in Fig. 5 and it is described by Eq. 11.

$$\begin{cases} m_2\ddot{z}_2 + F_s + C_s(\dot{z}_2 - \dot{z}_1) = 0 \\ m_1\ddot{z}_1 - F_s - C_s(\dot{z}_2 - \dot{z}_1) + k_t(z_1 - q) = 0 \end{cases} \quad (11)$$

Where F_s is elastic force. If it stands for linear elastic force, it is determined by Eq. 12. If it stands for nonlinear force, it is determined by Eq. 10.

$$F_s = K_s x \quad (12)$$

4.2 Simulink Model of Vehicle 2-DOFs Vibration

The vehicle two-dimensional Matlab/Simulink model is built using S-function block. It is described in Fig. 6.

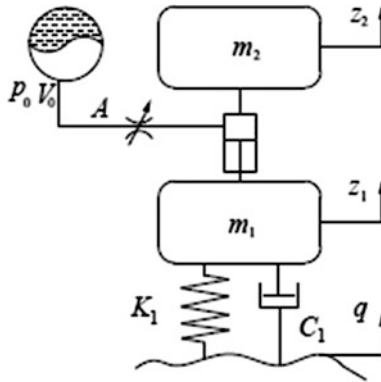


Fig. 5 2-DOFs vibration diagram

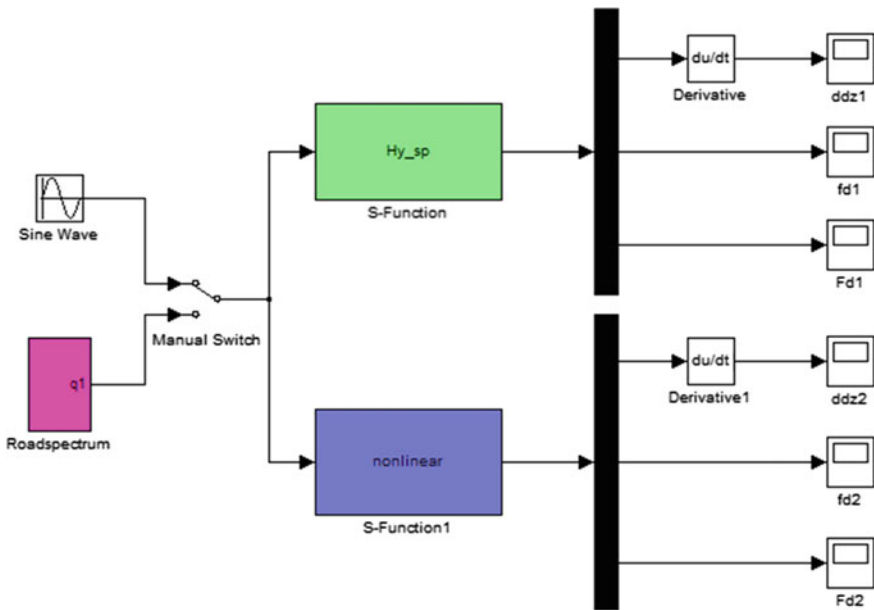


Fig. 6 Linear and nonlinear Simulink model of vehicle 2-DOFs vibration

4.3 Simulation Result and Analysis

A sine wave is inputted into the vehicle 2-DOFs vibration model with linear and nonlinear stiffness separately. Comparison of simulation result is showed in Fig. 7.

From Fig. 7 we can get that body acceleration peak value and wheel dynamic load peak value of nonlinear model are smaller than linear model. However, suspension deflection increases slightly, maybe owing to stiffness of hydro-

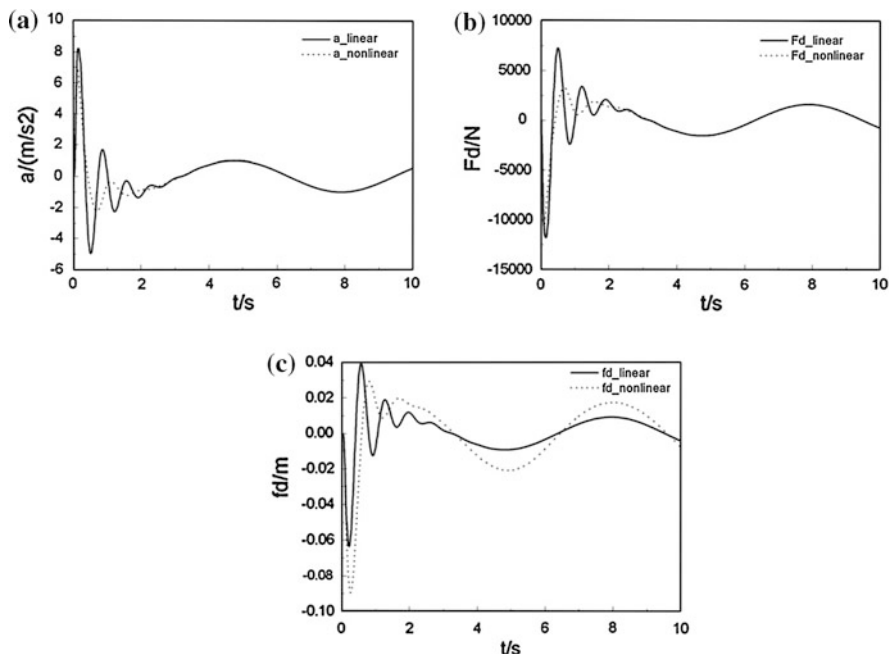


Fig. 7 Comparison of linear and nonlinear stiffness simulation results. **a** Body acceleration. **b** Wheel dynamic load. **c** Suspension deflection

pneumatic spring is small slightly. Meanwhile, the above three figures show that model with nonlinear stiffness has less peaks and tends to stability more rapidly.

The body acceleration becomes lower to some extent by reducing the hydro-pneumatic spring stiffness reasonably. But it is limited by the body height and natural frequency. If the spring stiffness is lower excessively, the probability of suspension distance exceeding limit stroke is increased hugely. In a word, if we want to improve every index, we must consider the matching of stiffness and damping synthetically.

5 Bench Test of Hydro-Pneumatic Spring with Two Accumulators

In order to verifying reasonable of structure design and two levels transformation characteristic, we did the bench test for hydro-pneumatic spring.

The two accumulators are charged Nitrogen with different pressure. The vice accumulator are charged higher pressure than main accumulator. The system input is sine wave. Before the test, pressing the plunger to a position as the balanced position. The load spectrum is described in Table 4.

Table 4 Load spectrum

	Excitation frequency (Hz)	Amplitude (mm)	Mean value (mm)	Excitation
Load spectrum	0.1	50	0	Sine
	0.1	60	0	Sine

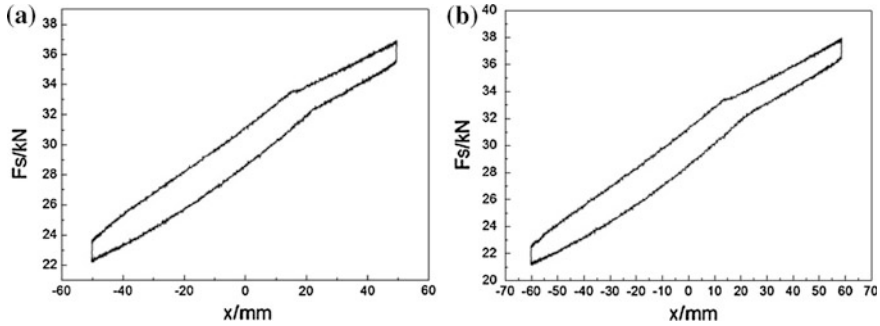


Fig. 8 Bench test of elastic force characteristic of two accumulators. **a** $f = 0.1$ Hz, $A = 50$ mm. **b** $f = 0.1$ Hz, $A = 60$ mm

The elastic force curves of bench test of two accumulators are described in Fig. 8. The output force curve of the bench test is treated as elastic force curve as the velocity of plunger is too small. From the picture we can see that only the main accumulator works for the system when plunger distance is below 20 mm. So the elastic force curve is steep. In another word, the suspension stiffness is big. When plunger distance reaches and exceeds 20 mm, both of main accumulator and vice accumulator work for the system in parallel. So the elastic force becomes smoothly. In another word, the suspension stiffness is small. Due to the original position is chose randomly, so the elastic force curve is unavailable to compare with the simulation results. It is just used to verify the two levels stiffness transformation characteristic of hydro-pneumatic spring with two accumulators. The bench test data shows that the stiffness transformation characteristic of two levels is good.

6 Conclusion

From the simulation and bench test we can obtain the following conclusions:

Hydro-pneumatic spring stiffness is in inverse proportion to original gas pressure P_0 and original gas volume V_0 . The stiffness of hydro-pneumatic spring can be reduced by increasing original charged pressure and original volume.

The hydro-pneumatic spring shows good function in reducing body acceleration and wheel dynamic load, but the suspension dynamic deflection has a slight

increase. We can deal with this problem by optimizing the matching between stiffness and damping rate.

The results of bench test verify show good characteristic of two levels stiffness transformation for hydro-pneumatic spring with two accumulators. When plunger distance reaches the setup value, main accumulator and vice accumulator work together for the system. The system capacity is increased. It prevents the spring stiffness from increasing speed. And it puts the purpose of improving vehicle ride performance.

References

1. Zhen Longxin (2005) Simulation, optimization and design calculation research of hydro-pneumatic suspension system. Beijing University of Science and Technology, Beijing
2. Wang Qidong, Wu Bofu, Chen Wuwei (2007) Integrated control of automobile active suspension and electrical power steering systems based on predictive control. Beijing: Trans Chin Soc Agric Mach 38(1):1–5
3. Yu Z (2006) Automobile theory. China Machine Press, Beijing, pp 237–245
4. Wu Renzhi (2000) Dynamic modeling, simulation and test study of hydro-pneumatic suspension. Zhejiang University, Zhejiang
5. Yoshimura T, Emoto Y (2003) Steering and suspension system of a full car model using fuzzy reasoning based on single input rule modules. *Int J Veh Auton Syst* 1(2):237–246
6. Wei Y, Yang J, Rong M (2000) A design to make the damp coefficient of a vehicles absorber suit the damp ratio of a suspension system. Hubei: *J Wuhan Automot Polytech Univ* 22(6): 22–25

Simulation Research on Car Suspension Durability Enhancement Test Based on Virtual Proving Ground

Zhenglin Cao, Jun Li and Konghui Guo

Abstract In this paper, a simulation model of flexible virtual proving ground (VPG) for a car was created in view of the shortcomings of long test cycle and high cost of traditional enhancement test for suspension durability at car development stage, with a variety of durability enhanced roads in the Nong'an Proving Ground as inputs. It solved a string of key technological problems regarding VPG applications. In addition, the time-history dynamic stress response of a car suspension system was analyzed, compared with the real vehicle durability test results obtained under the same conditions. The results of the simulation test and the real test are basically identical in terms of the trend of time and frequency domains. Furthermore, it demonstrates the effectiveness of the simulated suspension system's dynamic stress response for the flexible VPG technology, and realized the effective prediction for the suspension system durability in the development process.

Keywords Virtual proving ground (VPG) · Vehicle suspension · Durability · Enhancement test

F2012-E12-003

Z. Cao (✉) · J. Li
China FAW Co., Ltd R&D Center, Beijing, China
e-mail: caozhenglin@rdc.faw.com.cn

Z. Cao · J. Li · K. Guo
State Key Laboratory of Comprehensive Technology on Automobile Vibration
and Noise & Safety Control, Beijing, China

Z. Cao · K. Guo
Jinlin University, Jinlin, China

1 Introduction

The durability of automotive products is an important factor to affect their competitiveness; meanwhile, due to the long development cycle and huge costs at car development stage, the durability control in their conceptual design stage is in great need. The virtual proving ground (VPG) technology is therefore applied for the durability simulation research at an early stage, which makes it possible to conduct road test repeatedly without vehicle samples so as to further shorten test cycle and reduce costs. In the later stage of development, the VPG simulation test is an important supplement to real vehicle tests. The scientific research method and the inspection service system integrating VPG simulation and real vehicle test are the development trend of future testing grounds [1]. To this end, domestic and foreign major automobile companies have conducted the durability simulation research on VPG under conditions of the proving ground durability test. VPG research has been started earlier overseas: by employing the VPG technology, ArvinMeritor has successfully predicted the durability of a truck frame system [2]; and MIRA has explored the dynamic stress response of a vehicle suspension system [3].

The research on VPG technology involves a close combination of analysis, testing and test technology, which has rarely been covered by domestic researchers. In this paper, a simulation model of flexible VPG for a car was created in view of the shortcomings of long test cycle and high cost of traditional enhancement test for suspension durability at car development stage, with variety of durability enhanced roads in the Nong'an Proving Ground as inputs. It solved a string of key technological problems regarding VPG applications. In addition, the time-history dynamic stress response of a vehicle suspension system was analyzed, compared with the real vehicle test results obtained under the same conditions. The results of the simulation test and the real test are basically identical in terms of the trend of time and frequency domains. Furthermore, it demonstrates the effectiveness of the simulated suspension system's dynamic stress response for the flexible VPG technology, and realized the effective prediction for the suspension system durability in the development process.

2 Basic Theories of VPG Technology

The VPG Technology Simulation is a highly complex nonlinear dynamic process. It involves the contact nonlinear problems of parts as well as tires and the ground, together with the problems of tire and rubber mount materials and geometric nonlinear problems. Moreover, the flexible analysis of vehicle systems results in a relatively large computational model that needs a long calculation time causing the convergence difficulty. Thus, how to carry out a VPG technology simulation quickly and accurately has been a problem. And how to use mathematical

equations and a computer to describe and solve this complex problem is worth being discussed. The dynamic equations of the VPG system are as follows:

$$M\ddot{U}(t) + C\dot{U}(t) + R(t) = P(t) \tag{1}$$

Where: M , C represent the system mass and damping respectively; $\ddot{U}(t)$, $\dot{U}(t)$, $R(t)$ are the acceleration, speed and resilience respectively. If it is a linear system, $R(t) = KU(t)$ (where K is stiffness, $U(t)$ is displacement), $P(t)$ is the system external force. To solve the Eq. (1), explicit integration method and the implicit integration method could be used, described as below:

(1) Explicit integration method:

The iterative equation got from the central difference method is:

$$\bar{K}U_{i+1} = \bar{P}_i \tag{2}$$

Where: $\bar{K} = \frac{M}{(\Delta t)^2} + \frac{C}{2\Delta t}$

$$\bar{P}_i = P_i - \frac{M}{(\Delta t)^2}U_{i-1} - \frac{C}{2\Delta t}U_{i-1} - R_i + \frac{2M}{(\Delta t)^2}U_i$$

(2) Implicit integration method:

The iterative equation got from the Newmark- β method is:

$$\bar{K}_i\Delta U_i = \Delta\bar{P}_i \tag{3}$$

Where: $\bar{K}_i = \frac{M}{\beta\Delta t^2} + \frac{\gamma}{\beta\Delta t}C + K_i$,

$$\Delta\bar{P}_i = \Delta P_i + a\dot{U}_i + b\ddot{U}_i \quad a = \frac{M}{\beta\Delta t} + \frac{\gamma}{\beta}C \quad b = \frac{M}{2\beta} + \Delta t\left(\frac{\gamma}{2\beta} - 1\right)C$$

The solution of the above dynamic equations shows that applying the implicit integration method for solving Eq. (3) requires an inverse matrix operation for each time step in the process because \bar{K} contains a K matrix, which can be very difficult for solving a large or extremely nonlinear model problem. If the explicit integration method is applied to solve Eq. (2), no inverse matrix operation is needed for the constantly changing nonlinear stiffness in the calculation process, so the solution of such problems can be quite efficient. Via Eq. (2), the displacement response can be obtained; then according to the basic equation of the finite element theory, the values of strain and stress response is obtained. The VPG technology adopts the LS-DYNA program as its solver for the calculation.

Fig. 1 Tire stiffness test

3 Establishment of Vehicle Finite Element Models

3.1 VPG Dynamic Model for Tires

In this paper, P205/55R16 radial tires are adopted for the vehicle. The tire calculation model is composed of tread, sidewall, bead, spokes and rim. In the tire finite element model, the tire tread and bead adopt an eight-node solid unit, while the other parts adopt a shell unit. Through the tire stiffness test (see Fig. 1) and a comparative study of digital simulation, a VPG dynamic tire model that meets the accuracy requirements is established. See Fig. 2 [5] for the parameters of various tire component materials.

3.2 Suspension System Model

Some parts of suspension system pass the loading through kinematic pair(s). The loading transfer pathway of kinematic pairs is complex, so the kinematic pairs are simplified as hinges while establishing the finite element model, regardless of the internal friction and clearance. Figure 3 illustrates the front suspension system model; while the rear suspension system model is shown in Fig. 4.

3.3 Power Train Model

In this paper, the VPG simulation focuses on the suspension system durability prediction; as for the power Simulation Research on Car Suspension Durability Enhancement Test Based on Virtual Proving Ground train, inertia effect

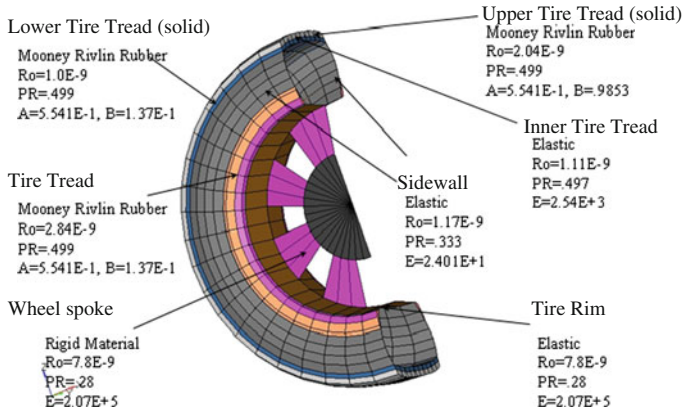


Fig. 2 Digital tire material parameters

Fig. 3 Front suspension system model

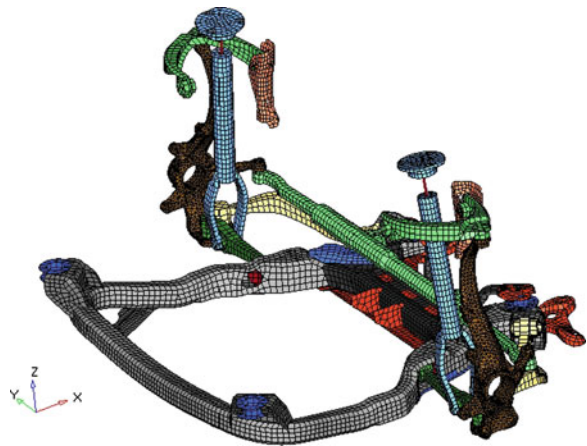


Fig. 4 Rear suspension system model

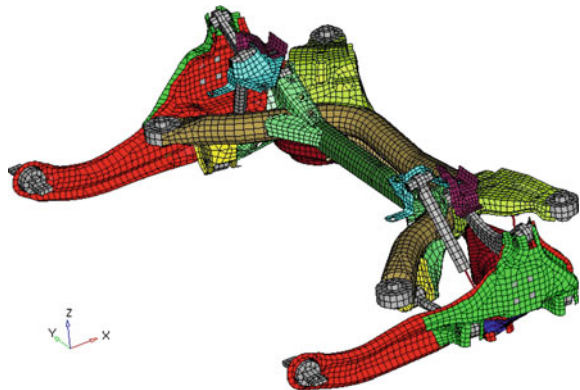
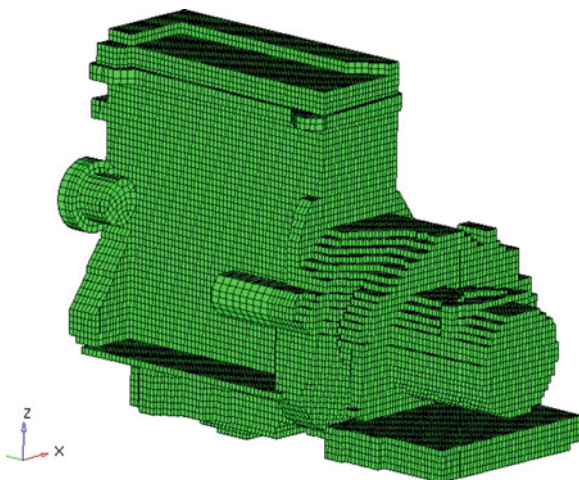


Fig. 5 Simplified power train model



consistency guarantee was needed. Via repeatedly comparing with the test results and debugging, a simplified model of the power train as shown in Fig. 5 was obtained.

3.4 Rubber Mount Stiffness Simulation

The rubber mount stiffness has been a difficulty in simulation analysis due to the nonlinear relationship between its material(s) and geometric height. Trial tests are mostly limited in the linear stage, while the stiffness curve in nonlinear stage cannot be obtained. In this paper, a digital model for rubber mounts was established (Fig. 6 indicates one type of rubber mounts). Through repeated simulation calculation, by guarantee the accurate fitting of rubber mount stiffness in the linear stage, rubber mount stiffness curve in the nonlinear stage (see Fig. 7) was got. The curve was used as the input for the VPG rubber mount stiffness curve.

3.5 Proving Ground Road Surface Model

The proving ground road surface model is the key that decides whether the VPG simulation of real vehicle road test can be reproduced and whether the simulation results can truly reflect the real situation of the vehicle loading. In order to compare with the real vehicle test results, the finite element model of durability standard road for the Nong'an Proving Ground was established, including the Belgium Road, twisting road, washboard road, fish-scale pit road, huge raised circle pavement, small-round-convex pavement, deceleration pavement, disrepair and twisting pavement (see Fig. 8).

Fig. 6 Rubber mount stiffness simulation

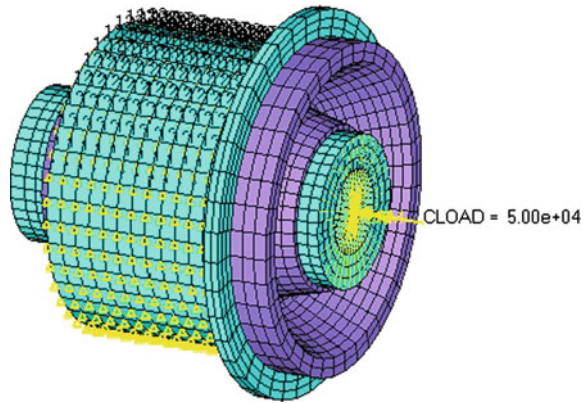
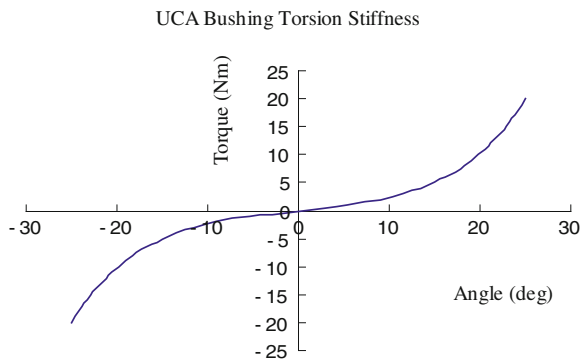


Fig. 7 Rubber mount stiffness curve



3.6 Vehicle Flexibility Model

The tires, pavements, front suspension system, rear suspension system, body and powertrain are assembled together according to the corresponding connection relationship to form a VPG simulation model of vehicle flexibility. The computational model is illustrated by Fig. 9, with 492,745 nodes and 488,148 units. The external loading of the computational model is the result of joint action of gravity acceleration and vehicle driving speed on the road. Mass scaling method adopted for the calculation controls the minimum time step within the magnitude of 10^{-6} s and the mass increase may not exceed 5 % [4, 5].

4 Proving Ground Durability Test

In order to improve the simulation accuracy of the VPG, a research method of comparison with the real vehicle test was adopted. The test points for measuring strain are set at the front left steering rod, the front left/right control arms,

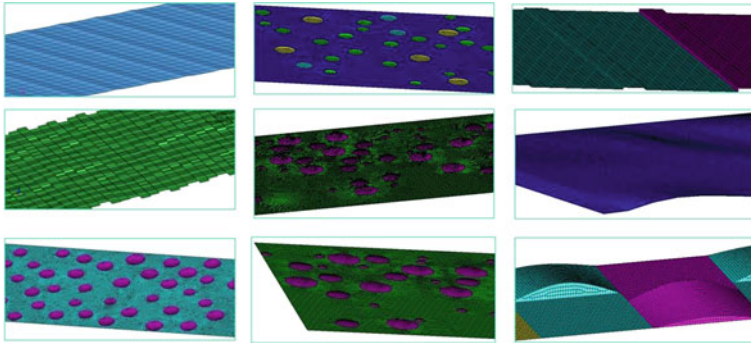


Fig. 8 Various proving ground road surface models

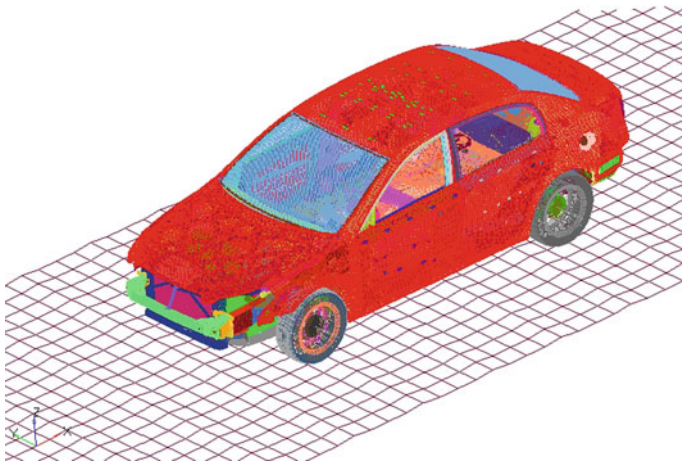


Fig. 9 Vehicle computational model

the front/rear stabilizer bars, the front/rear left/right coil springs, the right side bar of the rear suspension, the left steering knuckle of the front suspension, the upside of the rear left suspension upper arm and the rear trailing arm of the rear left suspension. An acceleration sensor is set at the heads of the wheel axles to test the acceleration. A six component force sensor is set at the wheel to test the force and torque in the three directions of the axle heads (see Fig. 10). A vehicle road test has been conducted on the durability enhanced pavement at the Nong'an VPG. Figure 11 illustrates the strain time-history response of the front right control arm test points, marked with the rough time intervals of some typical pavements. The vehicle driving speed on the particular pavements is figured out according to the proving ground pavement test data and the time intervals shown in Fig. 11 (see Table 1). These data will be used as the vehicle driving speed for VPG simulation calculation of vehicle systems.

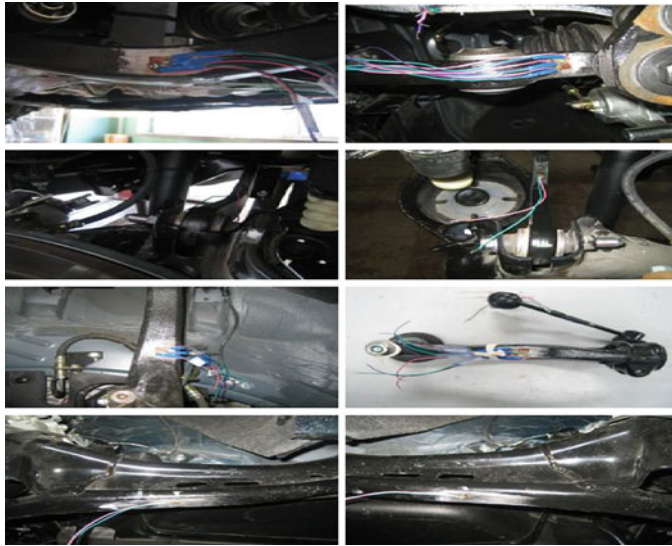


Fig. 10 Distribution of real vehicle road test points

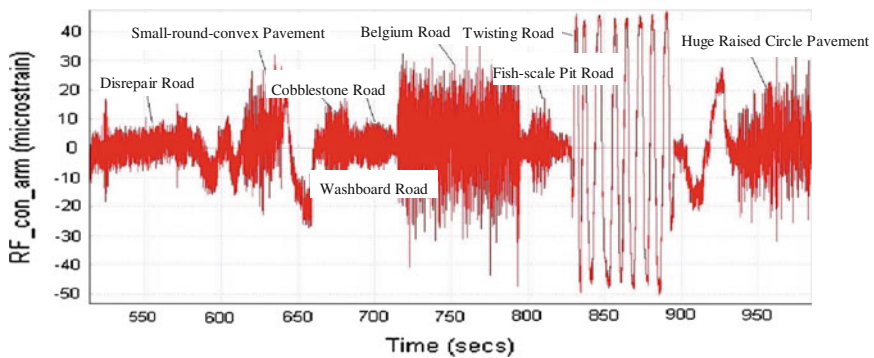


Fig. 11 Strain time-history response of front right control arm test points

Table 1 Driving speed of test vehicle

Road type	Speed (km/h)
Disrepair road	90
Deceleration strip	30
Small-round-convex pavement	20
Cobblestone road	50
Washboard road	75
Belgium road	30
Fish-scale pit road	65
Twisting road	10
Huge raised circle pavement	15

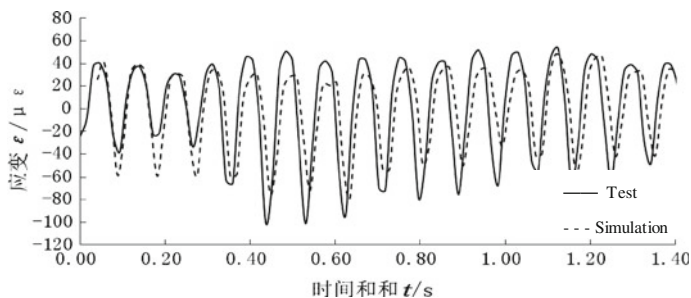


Fig. 12 Strain comparison of rear suspension trailing arm test points on the washboard road

5 Suspension Dynamic Stress Simulation and Experiment Comparison

The VPG simulation road models can be formed by combining the vehicle model with different proving ground pavement models. In this paper, the research by comparing the real vehicle test point strain response with the VPG simulation under the conditions of proving ground pavements including Belgium Road, twisting road, washboard road, fish-scale pit road, huge raised circle pavement has been conducted, small-round-convex pavement, deceleration pavement, disrepair pavement and twisting pavement. Figure 12 illustrates the strain comparison between the test point value and simulation calculation value of rear suspension trailing arm on the washboard road; Fig. 13 represents the self-power spectrum comparison of strain response between the test point value and simulation calculation value of rear suspension trailing arm on the washboard road. See Table 2 for the testing dynamic stress comparison between the VPG and real proving ground test on the washboard road.

It can be seen from the comparison between VPG test result and real proving round test result of typical suspension system components (see Figs. 12 and 13) and Table 2 that: the typical component test results at test points and the VPG simulation result are basically identical in terms of the trend of time and frequency domains, indicating the VPG technology can effectively simulate the dynamic stress response of vehicle components under conditions of various pavements of proving ground. It has laid a solid foundation for predicting the vehicle suspension system durability.

6 Vehicle Suspension System Durability Predication

On the basis of the better results of the time-history dynamic stress comparison between the real proving ground test and the VPG simulation, The prediction of the vehicle suspension system durability was adopted by the professional fatigue

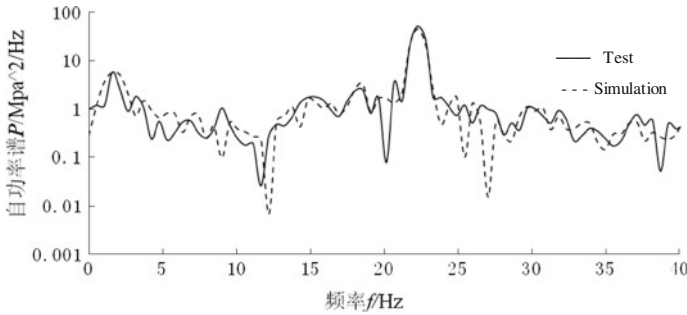


Fig. 13 Self-power spectrum comparison of rear suspension trailing arm test points on the washboard road

Table 2 Dynamic stress comparison on washboard road tests, MPa

No.	Component	Standard proving Ground-washboard			VPG			RMSE (%)
		Max.	Min.	RMS	Max.	Min.	RMS	
1	Front suspension lower right control arm (shake)(VonM)	28.090	2.064	5.297	31.503	0.000	6.341	-19.71
2	Front suspension lower right control arm (lift)(VonM)	34.467	0.725	6.881	40.054	5.784	6.319	8.17
3	Front suspension left knuckle (VonM)	18.043	1.923	4.188	30.055	0.000	5.369	-28.20
4	Front suspension right shock absorber lower poling (VonM)	9.406	3.145	1.173	11.000	0.000	1.274	-8.61
5	Rear left suspension upper arm (single direction)	25.708	-29.237	15.006	27.800	-23.400	13.395	10.74
6	Rear right suspension upper arm (single direction)	35.979	-33.429	15.499	29.242	-31.687	14.957	3.50
7	Rear left suspension trailing arm (single direction)	6.642	-8.737	3.990	10.800	-8.780	4.862	-21.85
8	Rear right suspension trailing arm (single direction)	12.438	-8.932	5.377	12.600	-11.800	4.644	13.63

analysis software FEMFAT4.7 in this paper. Table 3 represents the comparison of pseudo damage calculation of typical components of front/rear suspension in a test cycle on the proving ground pavement, with pseudo-damage ratios less than 200 %. Therefore, the specimens' damage is identical under the two working conditions was deemed, verifying the effectiveness of the suspension system durability predicted by the VPG technology.

Table 3 Comparison of pseudo damage calculation of typical components of front/rear suspension in a test cycle on the proving ground pavement

No.	Component	Pseudo damage of real proving ground	VPG damage simulation	Pseudo-damage ratio (%)	
1	Front suspension	Steering rod	9.31E-04	1.01E-03	108.81
2		Front control arm	9.13E-04	1.39E-04	15.18
3		Front sway bar	9.73E-04	1.57E-04	16.17
4	Rear suspension	Upper control arm	9.17E-04	2.47E-04	26.90
5		Beam	9.82E-04	3.98E-04	40.51
6		Trailing arm	9.28E-04	1.16E-03	125.15

7 Conclusion

In this paper, the flexible VPG simulation of vehicle suspension systems is achieved under the experimental conditions. The simulation and real test results are basically identical in terms of the time and frequency domain trends, demonstrating the VPG technology can effectively simulate the time-history dynamic stress response of the vehicle suspension system on various proving ground conditions. On this basis, the professional fatigue analysis software FEMFAT4.7 is applied to successfully predict the vehicle suspension system durability; thus, the suspension system design weaknesses can be identified clearly, and improve the design accordingly. Overall, this paper provides an effective approach for the suspension system durability evaluation in the initial stage of automobile product development.

References

1. Li W et al (2008) Research on stimulation of reliability enhancement test on washboard road of proving ground. SAE-China congress proceedings pp 1451–1455
2. Edara R, Shih S (2005) Heavy vehicle suspension frame durability analysis using virtual proving ground. SAE papers 2005-01-3609
3. Virtual proving ground—an integrated technology for vehicle analysis and simulation. MIRA—Motor Industry Research (c) 2008 MIRA Ltd
4. Fang J et al (2007) Virtual proving ground of tire mechanical characteristics. *Comput Simul* 6:243–247
5. Chen D, Shahidi B et al (2006) Correlation of explicit finite element road load calculations for vehicle durability simulations. SAE Papers 2006-01-1980

Simulation Research on Strong Fluid–Solid Interaction of Hydraulic Engine Mount

Zhenglin Cao, Jun Li, Konghui Guo and Qun Zhang

Abstract This paper sets the hydraulic engine mount (HEM) of a car as its research object and established the strong fluid–solid interaction finite element model for its property analysis by adopting the INTESIM strong fluid–solid finite element method. A stimulation analysis of the model’s static and translation dynamic stiffness characteristics was conducted, compared with the experimental result and the effectiveness of the simulation research findings was verified. The research demonstrates that the translation dynamic characteristics of the HEM can be effectively simulated by the INTESIM strong fluid–solid finite element method; on the basis of which, a preliminary discussion on its torsion dynamic stiffness characteristics was carried out also.

Keywords Hydraulic engine mount (HEM) · Strong fluid–solid interaction · Dynamic characteristics · INTESIM

F2012-E12-004

Z. Cao (✉) · J. Li
China FAW Co., Ltd R&D Center, Beijing, China
e-mail: caozhenglin@rdc.faw.com.cn

Z. Cao · J. Li · K. Guo
State Key Laboratory of Comprehensive Technology on Automobile Vibration
and Noise & Safety Control, Beijing, China

Z. Cao · K. Guo
Jinlin University, Jinlin, China

Q. Zhang
INTESIM (Dalian) Co., Ltd, Dalian, China

1 Introduction

In recent years, with the widespread use of the lightweight design and four-cylinder engine, the application of front engine and front-wheel drive in vehicles in particular, the impact of the engine mounting system on the driving smoothness has become more and more outstanding. The engine mounting system has two main functions: powertrain support and two-way vibration isolation. With much better elastic and damping properties compared to the ordinary rubber mount, the hydraulic engine mount (HEM) significantly improve the auto powertrain mounting system's properties of vibration isolation, noise reduction and shock absorption, making the HEM one of the major research targets on the vibration isolation of vehicles [1].

Under the high-frequency external excitation, the HEM will have complex fluid–solid interaction effect. Therefore, the numerical simulation of the HEM's mechanical property will encounter the following problems: the transformation from the rubber to the fluid, the strong fluid–solid interaction between hyper-elastic rubber and viscous fluid, high frequency domain with large scale. In recent years, with the notable improvement of fluid–solid interaction (FSI) analysis method and the calculation performance, the three-dimensional HEM dynamic simulation has been realized [2–5]. Lou Shaomin et al. [4] conducted the weak FSI analysis to the HEM by using ADAMS. Wenbin [1] used ADINA to pave the way for the mathematical analysis of the HEM, as well as the comprehensive application of the experimental study.

This paper sets the HEM of a car as its research object and established the strong FSI finite element model fortis property analysis by adopting the INTESIM strong fluid–solid finite element method. A stimulation analysis of the model's static and translation dynamic stiffness characteristics was conducted, compared with the experimental result and the effectiveness of the simulation research findings was verified. The research demonstrates that the translation dynamic characteristics of the HEM can be effectively simulated by the INTESIM strong fluid–solid finite element method; on the basis of which, a preliminary discussion was carried out on its torsion dynamic stiffness characteristics also.

2 Basic Theories of INTESIM Strong FSI

The basic characteristics of fluid and solid interaction are as follows: the surface force provided to the solid by the fluid forms the force boundary and leads to the deformation of the solid, by which the boundary and internal motions of the fluid are caused. The difficulty of FSI analysis is the nonlinearity of the N–S equation of fluid motions and the different describing forms of fluid and solid dynamical equations [6].

2.1 Arbitrary Lagrange's Equation

In Arbitrary Lagrange's Equation (ALE), the grids can be transformed randomly; hence, ALE fluid can be used directly to be interacted with solid and the interaction surface can be moved based on dynamic equilibrium. The derivatives of random variables are as follows:

$$\left. \frac{\partial(\cdot)}{\partial t} \right|_{\mathbf{x}} = \left. \frac{\partial(\cdot)}{\partial t} \right|_{\mathbf{x}} + (\mathbf{v} - \mathbf{v}_m) \cdot \nabla(\cdot) \quad (1)$$

Where: \mathbf{v}_m is the grid speed; $\partial(\cdot)/\partial t|_{\mathbf{x}}$ is the material derivative and $\partial(\cdot)/\partial t|_{\mathbf{x}}$ is the ALE derivative of the grid with the speed of \mathbf{v}_m . Provided that the viscous fluid has constant temperature and incompressible ($F(P, \rho) = 0$) with $\partial P/\partial \rho = B/\rho$, where B , P and ρ are the bulk modulus, pressure and density of the fluid respectively.

Corresponding ALE equation can be obtained by substituting (1) into the Euler form of Navier–Stokes equation:

$$\frac{1}{B} \left. \frac{\partial p}{\partial t} \right|_{\mathbf{x}} + \frac{1}{B} c_i \frac{\partial p}{\partial x_i} + \frac{\partial v_i}{\partial x_i} = 0 \quad \text{in } R_t^f \quad (2)$$

$$\rho \left. \frac{\partial v_i}{\partial t} \right|_{\mathbf{x}} + \rho c_j \frac{\partial v_i}{\partial x_j} = \frac{\partial \sigma_{ij}}{\partial x_j} + \rho g_i \quad \text{in } R_t^f \quad (3)$$

Where: σ is Cauchy stress tensor; \mathbf{g} is the acceleration of gravity, $\mathbf{c} = \mathbf{v} - \mathbf{v}_m$. R_t^f is the spatial domain determined by ∂R_t^f , the boundary condition at the time t and the superscript f stands for fluid. Provided that the Newtonian conditions are met:

$$\sigma_{ij} = -p\delta_{ij} + \frac{1}{2}\mu(v_{i,j} + v_{j,i}) \quad (4)$$

Where: δ is nominal tensor, μ is the coefficient of kinetic viscosity of the fluid. The boundary ∂R_t^f includes ∂R_t^g and ∂R_t^h corresponding to Dirichelett and Neumann.

$$v_i = g_i \quad \text{on } \partial R_t^g \quad (5)$$

$$\sigma_{ji}n_j = h_i \quad \text{on } \partial R_t^h \quad (6)$$

2.2 Finite Element Equation

Provided that Navier–Stokes Eqs. (2) and (3) with ALE form are described via Galerkin equation, i.e.:

$$\mathbf{M}^f \dot{\varphi}^f + \mathbf{C}^f \varphi^f = \mathbf{F}^f \tag{7}$$

Where:

$$\mathbf{M}^f = \begin{bmatrix} \mathbf{M}^P & \mathbf{0} \\ \mathbf{0} & \mathbf{M} \end{bmatrix}, \mathbf{C}^f = \begin{bmatrix} \mathbf{\Lambda}^P & \mathbf{G}^T \\ -\mathbf{G} & \mathbf{K}_\mu + \mathbf{\Lambda} \end{bmatrix}, \varphi^f = \begin{Bmatrix} \mathbf{P}^f \\ \mathbf{V}^f \end{Bmatrix}, \mathbf{F}^f = \begin{Bmatrix} \mathbf{0} \\ \mathbf{F}_v^f \end{Bmatrix} \tag{8}$$

\mathbf{M}^P and \mathbf{M} are mass matrixes of the pressure and speed respectively; $\mathbf{\Lambda}^P$ and $\mathbf{\Lambda}$ are convection matrixes of the pressure and speed respectively; \mathbf{K}_μ is the viscosity matrix of the fluid; \mathbf{G} is the divergence matrix; \mathbf{P}^f and \mathbf{V}^f are the vectors of the pressure and the speed; \mathbf{F}^f is the external force vector.

Equilibrium equation of the solid:

$$M^s \ddot{\mathbf{d}}^s + \mathbf{Q}^s(U^s, P^s) = F^s \tag{9}$$

Where:

$$\mathbf{M}^s = \begin{bmatrix} \mathbf{M}_v^s & \\ & \mathbf{0} \end{bmatrix}, \mathbf{d}^s = \begin{Bmatrix} \mathbf{U}^s \\ \mathbf{P}^s \end{Bmatrix}, \mathbf{Q}^s = \begin{Bmatrix} \mathbf{Q}_v^s \\ \mathbf{Q}_p^s \end{Bmatrix}, \mathbf{F}^s = \begin{Bmatrix} \mathbf{F}_v^s \\ \mathbf{0} \end{Bmatrix} \tag{10}$$

\mathbf{M}^s is the mass matrix; \mathbf{U}^s and \mathbf{P}^s are the displacement vector and the pressure vector respectively; \mathbf{Q}^s and \mathbf{F}^s are internal and external force vectors respectively. Subscript v and p stand for the values of corresponding speed and pressure respectively. In INTESIM, tangential stiffness matrix is iterated.

$$M^s \Delta \ddot{\mathbf{d}}^s + {}^t\mathbf{K}^s \Delta \mathbf{d}^s = {}^{t+\Delta t}F^s - {}^t\mathbf{Q}^s \tag{11}$$

Where: ${}^t\mathbf{K}^s$ is the tangential stiffness matrix at the time t ; Δ is the increment of the solid variable.

2.3 Mooney-Rivlin Material Model

Mooney-Rivlin material model can be described by the following equation:

$$\begin{aligned}
W_R^H &= c_1(\tilde{I}_C - 3) + c_2(\tilde{II}_C - 3) \\
&+ c_3(\tilde{I}_C - 3)^2 + c_4(\tilde{I}_C - 3)(\tilde{II}_C - 3) + c_5(\tilde{II}_C - 3)^2 \\
&+ c_6(\tilde{I}_C - 3)^3 + c_7(\tilde{I}_C - 3)^2(\tilde{II}_C - 3) + c_8(\tilde{I}_C - 3)(\tilde{II}_C - 3)^2 + c_9(\tilde{II}_C - 3)^3
\end{aligned} \tag{12}$$

$$\tilde{I}_C = \frac{I_C}{III_C^{1/3}}, \quad \tilde{II}_C = \frac{II_C}{III_C^{2/3}} \tag{13}$$

Where: I_C , II_C , and, III_C are three principal strains of $\mathbf{C}(\mathbf{E} = (\mathbf{C} - \mathbf{I}/2))$, the Cauchy-Green strain tensor. The parameter $c_1 \sim c_9$ is obtained through experiments.

2.4 FSI Equation

2.4.1 Boundary Conditions

With the complete FSI, the geometry deformation compatibility condition and equilibrium condition shall be met on the border. In INTESIM, provided that there is no slip on fluid–solid boundary, the deformation compatibility condition shall be:

$$v_i^f = v_i^s \quad (i = 1, 2, 3) \quad \text{on} \quad \partial R_i^c \tag{14}$$

The equilibrium condition shall be:

$$\sigma_{ji}^f n_j^f + \sigma_{ji}^s n_j^s = 0 \quad (i = 1, 2, 3) \quad \text{on} \quad \partial R_i^c \tag{15}$$

Where: \mathbf{n} is the outward normal vector; the superscripts f and s stand for the fluid and solid respectively; ∂R_i^c is the contact surface of the fluid and the solid.

2.4.2 Interaction Equation

In INTESIM, the deformation of the fluid–solid grids on the interaction boundary is provided to be coordinated. If the fluid and solid on the interaction boundary are described by Lagrangian, the variables of the interaction system can be divided into three parts:

$$\varphi^{fs} = \left\{ \begin{array}{l} \varphi_i^f \\ \varphi_c^{fs} \\ \varphi_i^s \end{array} \right\}, \quad \mathbf{d}^s = \left\{ \begin{array}{l} - \\ \mathbf{d}_c^{fs} \\ \mathbf{d}_i^s \end{array} \right\} \tag{16}$$

Where: φ_i^f ($\varphi_i^f = \{\mathbf{P}^f, \mathbf{V}_i^f\}^T$) is the speed and pressure vector within the fluid; φ_c^{fs} ($\varphi_c^{fs} = \mathbf{V}_c^{fs}$) is the speed vector on the interaction surface; φ_i^s ($\varphi_i^s = \{\mathbf{V}_i^s, \mathbf{P}^s\}^T$) is the speed vector and pressure vector within the solid; \mathbf{d}_c^{fs} (\mathbf{d}_c^{fs}) is the displacement vector of the interaction; \mathbf{d}_i^s ($\mathbf{d}_i^s = \{\mathbf{U}_i^s, \mathbf{P}^s\}^T$) is the displacement and pressure vector within the solid. Combined with the Eqs. (7) and (11), the interaction equation is as follows:

$$\mathbf{Q}^{fs} = \mathbf{F}^{fs} \quad (17)$$

Where: the internal force vector \mathbf{Q}^{fs} includes the internal force of the interaction system:

$$\mathbf{Q}^{fs} = \mathbf{M}^{fs} \varphi^{*fs} + \mathbf{C}^f \varphi^{fs} + \mathbf{Q}^s(\mathbf{d}^s) \quad (18)$$

\mathbf{F}^{fs} is the external force vector. \mathbf{M}^{fs} is the mass matrix of fluid and solid; \mathbf{C}^f is the viscosity coefficient and convection coefficient of the fluid.

3 FSI Model for the Dynamic Characteristics of the HEM

While carrying out finite element analysis for FSI system by the INTESIM software, the solid and fluid finite element models shall be established respectively. The grid density of the fluid shall be higher than that of the solid; and the FSI surface shall be defined as the contact surface of the fluid and solid. While solving FSI problems with the INTESIM, there are some common solutions to improve the convergence, such as applying appropriate grid density; applying relative small time step or automatic time step; and applying appropriate FSI boundary convergence criteria, etc.

The FSI model established in line with the HEM 3D CAD model is shown in Fig. 1. Please see Table 1 for relevant information of the components.

The rubber material model is determined by the tension and compression stress–strain experiment of test piece. Figure 2 shows the stress–strain curves of various rubber components in tension and Fig. 3 shows the stress–strain curves of various rubber components in compression. The parameters of various rubber materials of the HEM can be obtained by the least square method—see Table 2.

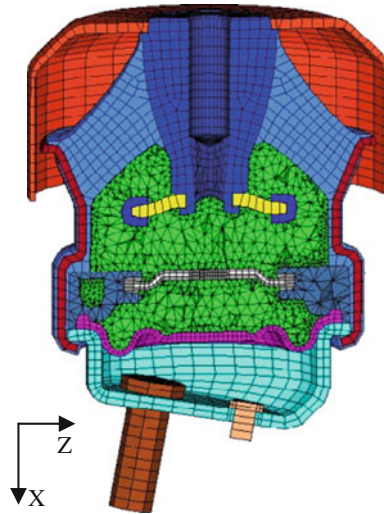


Fig. 1 HEM FSI model

Table 1 Node Information List of the HEM Grid Element

Name	Element type	Element number	Node number	Material feature
Heat shield	Hexahedron	896	1,856	Rubber
Main spring	Hexahedron	4,096	6,336	Rubber
Housing	Hexahedron	832	1,728	Steel
Inner core	Hexahedron	3,968	4,936	Steel
Agitator sulphide	Hexahedron	224	512	Rubber
Agitator metal	Hexahedron	224	512	Steel
Top runner plate	Tetrahedron	6,429	1,898	Aluminum
Down runner plate				
Decoupler	Hexahedron	1,504	2,564	Rubber
Decoupler metal	Hexahedron	352	768	Steel
Sealing cup	Hexahedron	2,016	3,059	Rubber
Left base	Hexahedron	1,210	1,858	Steel
Rivet, bolt	Hexahedron	436	684	Steel
Fluid	Tetrahedron	133,122	31,535	Glycol

4 Simulation Analysis of the HEM Properties

4.1 Static Features

Figure 4 shows the loading in the HEM property test. The HEM is loaded in experimental state and the loading scope shall be $-3,000$ – 500 N (the downward pressure is negative and the upward tension is positive). The static analysis of the HEM intends to find the relation between the vertical force and its displacement on

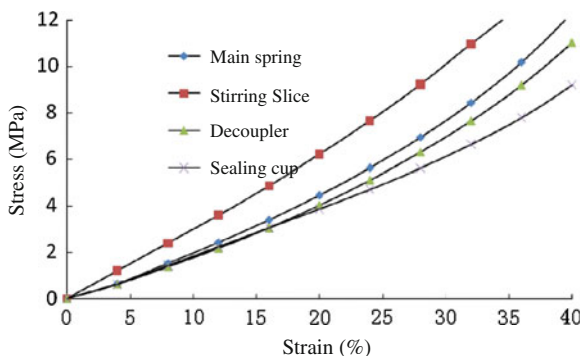


Fig. 2 Stress-strain curves of rubber components in tension

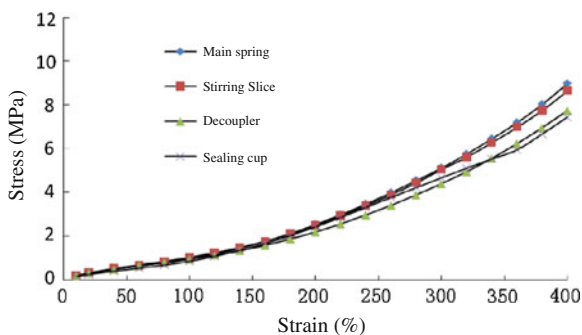


Fig. 3 Stress-strain curves of rubber components in compression

Table 2 Parameters of rubber materials

Component	Main spring	Agitator sulphide	Decoupler	Sealing cup
C01	0.2004	0.2463	0.2008	0.1983
C10	0.1183	0.0662	0.1057	0.0471

the surface of the main spring. Figure 5 shows the comparison curves of the calculated value and experimental value. It can be seen from Fig. 5 that these two values are in good agreement with each other. The numerical simulation can effectively calculate the static features of the HEM. Figure 6 shows the stress cloud chart of the solid structure Von Mises when the vertical force is 3,000 N; while Fig. 7 is the deformation cloud chart of the fluid field grids when the vertical force is 3,000 N.

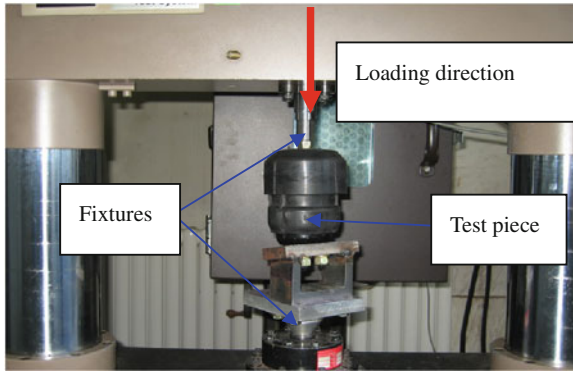


Fig. 4 Feature experiment of the HEM

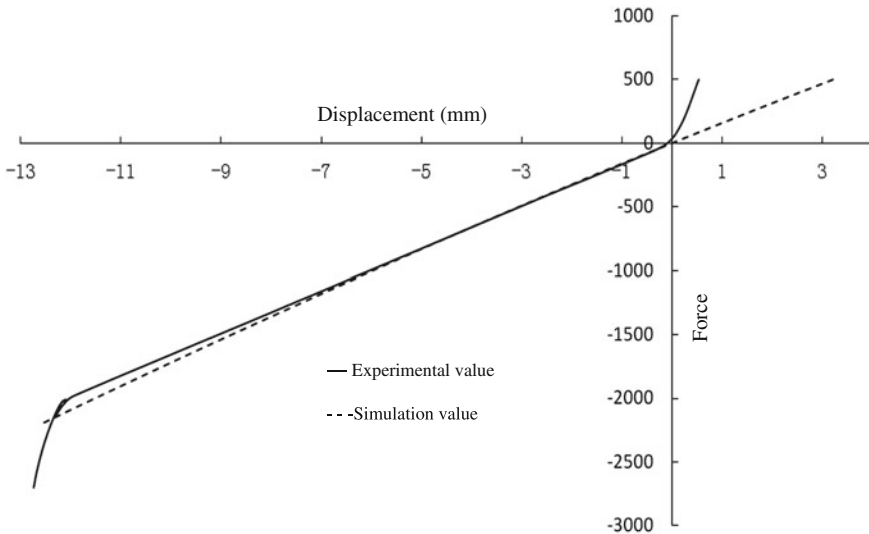


Fig. 5 Curves of the translational displacement and force in X direction

4.2 Dynamic Properties

While computing the dynamic characteristics, the periodic forced displacement load can be applied on the rubber main spring directly, the force of which can be calculated as follows:

$$x(t) = x_0 - A \cos(2\pi ft) \tag{19}$$

Where: x_0 is the displacement caused by the preload on the HEM and is in connection with the static working load of the HEM; A, f are the dynamic displacement excitation amplitudes and frequencies respectively.

Fig. 6 Mises stress cloud chart for solid structure

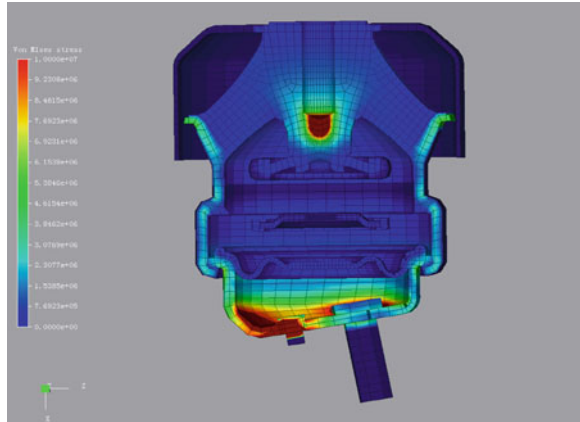
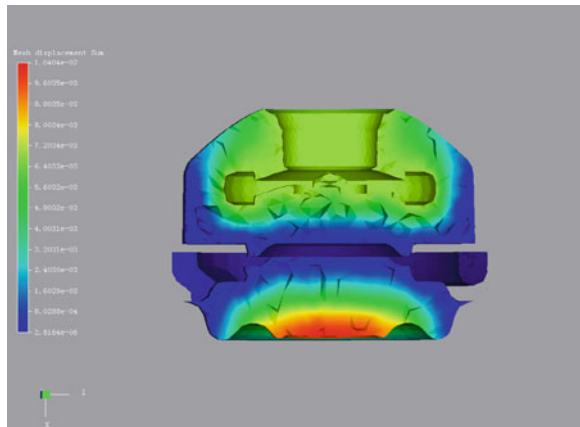


Fig. 7 Deformation cloud chart of the fluid field grids



Provided that $FT(t)$ is the constraint reaction of the characteristic node assembly and $XT(t)$ is the displacement of specified points, the dynamic stiffness and lag angle under a certain frequency can be obtained according to the definition of the complex stiffness; then the dynamic stiffness curve or lag angle curve can be made with the frequency value as the abscissa axis and the dynamic stiffness or lag angle value as the vertical axis on the basis of the dynamic stiffness value and lag angle value of each frequency.

$$\begin{aligned}
 K(j\omega 0) &= F(FT(t))/F(XT(t)) |_{\omega = \omega 0} \\
 &= K_1 + jK_2
 \end{aligned}
 \tag{20}$$

Definition of the dynamic stiffness: $K_d = \text{sqrt}(K_1 * K_1 + K_2 * K_2)$

Definition of the lag angle: $\Phi = \text{arctag}(K_2/K_1)$

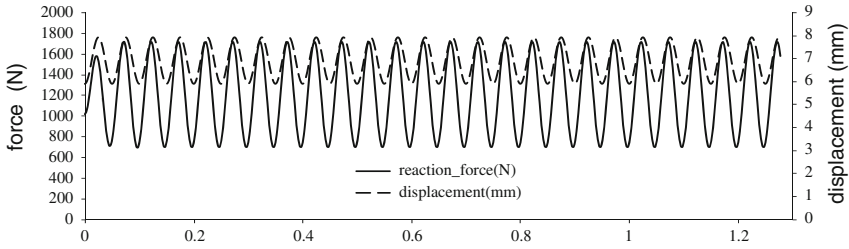


Fig. 8 Simulation results of excitation displacement and dynamic reaction force (20 Hz)

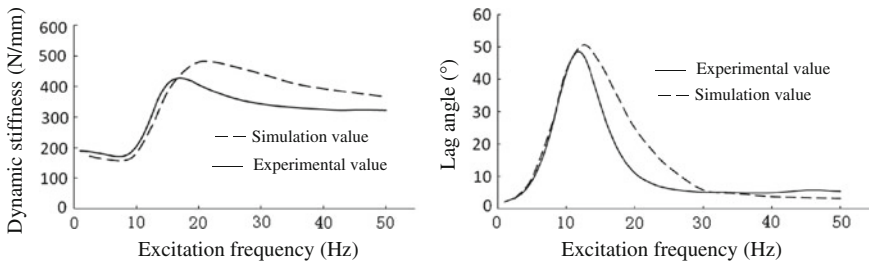


Fig. 9 Transition dynamic stiffness and lag angle curves in X direction

4.2.1 Translation Dynamic Stiffness in X Direction

When the excitation amplitude is 1.0 mm and the excitation frequency is 20 Hz, the excitation displacement and dynamic counterforce of the HEM is shown by Fig. 8. It can be seen from the figure that there is obvious lags exist between excitation displacement and dynamic counterforce, which can be obtained by using the Fourier transform method:

When $\omega = 20$ Hz,

$$K(j\omega 0) = 457.348 + 198.723j$$

$$K_d = 498.657 \text{ N/mm}, \Phi = 23.49^\circ$$

The HEM’s dynamic stiffness and lag angle curves can be obtained by this method within the frequency scope between 0 and 50 Hz, as shown in Fig. 9. It can be seen from the figure that the simulation results is in good agreement with the test results of the experiments, proving the effectiveness of the strong FSI method based on INTESIM in analyzing the dynamic characteristics of the HEM.

4.2.2 Torsion Dynamic Stiffness in X Direction

The torsion dynamic stiffness of the HEM can not be tested directly due to experimental limitations. The INTESIM is used to simulate the torsion dynamic

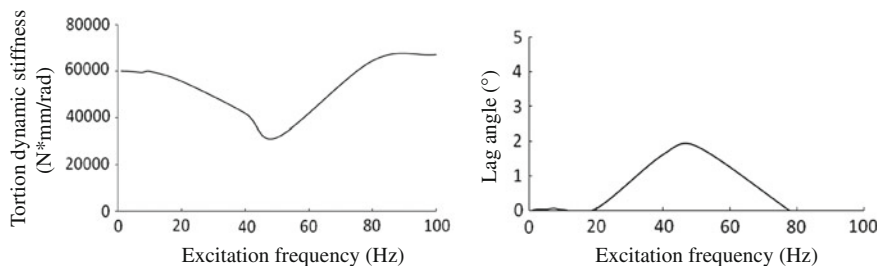


Fig. 10 Torsion dynamic stiffness and lag angle curves in X direction

stiffness of the HEM in X direction on the basis that the translation dynamic stiffness in X direction of INTESIM can be effectively simulated, through which the torsion dynamic stiffness and lag angle curves are obtained, as shown in Fig. 10. It can be seen from the figure that, with the increase of excitation amplitude, the torsion dynamic stiffness decreases gradually at the very beginning and begins to rise gradually after reaching the lowest level around the frequency of 45 Hz, indicating that the movement of the fluid may weaken the torsion stiffness of the HEM.

5 Conclusion

This paper established the strong FSI finite element model for a car's HEM property analysis by adopting the INTESIM strong fluid–solid finite element method and carried out simulation analysis on its static and dynamic stiffness characteristics. Therefore, the following conclusions are drawn:

- (1) The effectiveness of the simulation research is verified by comparing it with the experiment results, demonstrating that the use of INTESIM strong FSI finite element method can effectively simulate the static and dynamic characteristics of the HEM translation stiffness;
- (2) The torsion dynamic stiffness of the HEM will increase according to the excitation frequency; the torsion stiffness will decrease gradually and will rise when the lowest value is reached, indicating that the movement of the fluid may weaken the HEM torsion stiffness.

References

1. Wenbin S (2003) Simulation research on fluid-solid interaction dynamic characteristics of hydraulically rubber vibration isolator. Tsinghua University, Beijing
2. Bathe KJ, Zhang H, Ji S (1999) Finite element analysis of fluid flows fully coupled with structural interactions. *Comput Struct* 72(1–3):1–16

3. Stein K, Benney R, Kalro V, Tezduyar T, Leonard J, Accorsi M (2000) Parachute fluid-structure interactions: 3-D computation. *Comput Methods Appl Mech Eng* 190:373–386
4. Taylor CA, Hughes TJR, Zarins CK (1998) Finite element modeling of blood flow in arteries. *Comput Methods Appl Mech Eng* 158:158–196
5. Zhang Q, Hisada T (2001) Analysis of fluid-structure interaction problems with structural buckling and large domain changes by ALE finite element method. *Comput Methods Appl Mech Eng* 190:6341–6357
6. Wenbin S (2004) Simulation on fluid-solid interaction nonlinear dynamics of auto powertrain hydraulically damped engine mount. *Chin J Mech Eng* 80–86

A Study on Battery Model Verification Using Battery HILS

Hyun-Sik Song, Tae-Hoon Kim, Jin-Beom Jeong, Byoung-Hoon Kim, Dong-Hyun Shin, Baek-Haeng Lee and Hoon Heo

Abstract The development of technology for environmentally friendly cars such as plug-in hybrid electric vehicles (PHEVs) and electric vehicles (EVs) has increasingly progressed according to the conversion of vehicle development paradigms to energy issues, environmental regulations, the government's "New Deal" policies, and so on. As a result, the importance of the battery system that is the main power source for environmentally friendly cars has grown. The most effective way of the development of PHEVs and EVs is using battery hardware-in-the-loop simulation (HILS) to significantly reduce development costs and time in vehicle-level environments for the development and evaluation of battery systems, including a battery management system (BMS). Therefore, in the present study, a battery HILS was developed and tested. It was noted through the test that the developed battery HILS could be used as a method to assess the accuracy of battery modeling in real time by applying it to developed battery system models using the electrochemical impedance spectroscopy (EIS) method.

Keywords Battery HILS · Battery system model · PHEV · EIS · UDDS

F2012-E12-008

H.-S. Song (✉) · H. Heo
Korea University, Seoul, Korea
e-mail: hssong@katech.re.kr

T.-H. Kim · J.-B. Jeong · B.-H. Kim · D.-H. Shin · B.-H. Lee
Korea Automotive Technology Institute, Pohang, Korea

1 Introduction

As vehicle development paradigms have been changed due to the implementation of fossil energy consumption-reducing policies in response to the acceleration of fossil energy exhaustion, reinforced environmental regulations in relation to the aggravation of global warming problems, and “New Deal” policies that give priority to economic recovery and job creation the development of environmentally friendly cars such as PHEVs and EVs has been accelerated.

Accordingly, the importance of energy storage systems, which are major power sources of environment friendly cars, has further increased. The performance of environment friendly cars is directly affected by the performance of their energy storage systems. Therefore, to grasp the characteristics of environment friendly cars, the characteristics of energy storage systems should be grasped first. However, the assessment of battery systems that are used as energy storage systems require many tests and analyses. Grasping the characteristics of battery systems after installing them in actual vehicles in order to grasp the characteristics of battery systems when they have been installed in vehicles is practically very difficult. For instance, to grasp the characteristics of battery systems in harsh driving conditions, battery systems should be installed in actual environment friendly cars, and various driving environments should be utilized to analyze vehicle and battery system characteristics. It is clear that these kinds of experiments cannot be easily conducted because accurate characteristics data cannot be easily obtained, and also because battery system safety problems may occur.

Therefore, to support the efficient design and development of environment friendly cars, such as grasping the correlation between environment friendly cars and battery systems and significantly reducing development costs and time at actual vehicle-level environments, battery HILS systems that can simulate and assess battery systems are necessary.

In the present study, the development process for and assessment of battery HILSs were introduced, and the accuracy of battery system models made considering battery pack components based on large-capacity battery cell models developed using EIS was tested in real time at a level similar to actual vehicle environments through using battery HILSs.

2 Battery HILSs

2.1 Overview of Battery HILSs

Thanks to the development of electricity and electronics industries and to pursue users’ convenience and safety, controllers that serve diverse and complicated functions are installed in cars. Since considerable pressure for the reduction of development time and costs exists in the automobile industry, such controllers are

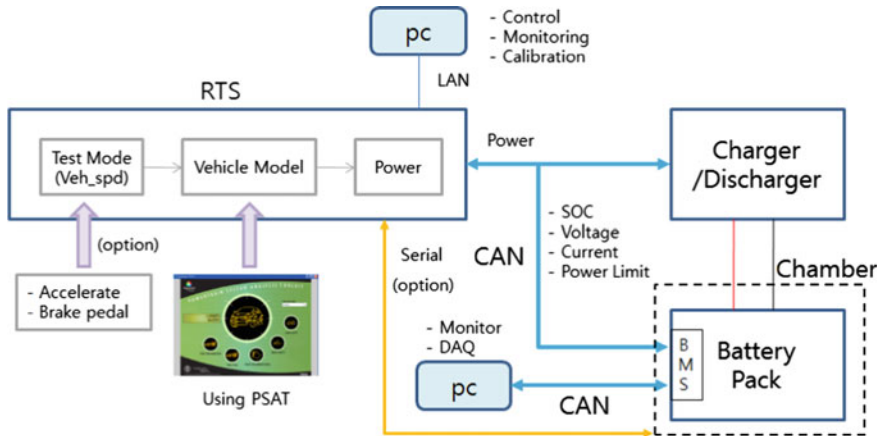


Fig. 1 Battery HILS configuration diagram

actively tested utilizing HILSs [1, 2]. A HILS is performed by replacing specific components in the control loop consisting of the controller and the plant with actual parts and other components with mathematical equations and algorithms. In vehicle development, a HILS is widely used as an alternative simulation when the plant component of a newly developed control algorithm does not yet exist. A HILS is also used for various testing conditions involving risk or danger that rarely occur in an actual vehicle, for implementing automated test procedures, and for situations in which manual testing requires a substantial amount of time [1, 3].

When a HILS is applied to a battery system, it is referred to as a *battery HILS*. The need for a battery HILS has been recognized, as the strong nonlinear characteristics of a battery make it difficult to model. With the active developments of environmentally friendly vehicles, research institutions and automobile manufacturers have implemented battery HILSs as the leading technology for vehicle design, performance, and reliability verification, as well as for developing optimal battery systems for vehicles and evaluating driving conditions in various environments.

2.2 Development of Battery HILSs

2.2.1 Configuration of Battery HILSs

A battery HILS consists of a battery system (the plant), a vehicle model implemented using a mathematical model of the dynamic characteristics of the vehicle excluding the plant, a real-time system (RTS) for calculating and processing the vehicle model, an interface for exchanging information between the plant and the vehicle model, a charger/discharger for simulating the power of the battery system, and an external environment chamber [4] (Fig. 1).

Table 1 Specification of batteries for battery HILSs

Item	Specification	Unit
Type	Li-ion	–
Capacity (nominal)	20	Ah
Energy (nominal)	6.9	kWh
Pack voltage (nominal)	360	V
Number of cells	96	ea

(1) RTS

RTSs can be configured with process boards, I/O boards, communications boards, and so on. In the present study, an RTS was configured by dSPACE (Paderborn, Germany) using a 2.6 GHz high-performance process board (DS1006) and a HIL I/O board (DS2202), combining multiple I/O and communications modules so that even complicated vehicle models could be processed in real time and using a case (PX10) having extra slots for later adding boards with additional functions. The RTS was also configured so that a PC could be connected to the RTS through a local area network for battery HILS control and monitoring.

(2) Charger/discharger

To be able to simulate the maximum rating of the battery packs for PHEVs and EVs, a charger/discharger was used that can provide 450 V 250 A (500 A in parallel connection) and can be controlled in terms of power/voltage/current using an external controller area network (CAN). Although general methods of power profile downloading into controllers in chargers/dischargers can respond within a maximum of 30 ms after a command, the method using a CAN takes at least 50 ms on average to respond because message buffering and processing time is additionally necessary when this method is used. In the present study, it was identified that current or power responses from the charger/discharger were given within 30–80 ms after current or power commands were transmitted from the RTS to the CAN.

(3) Battery system

The battery system used in the battery HILS was made using 6.9 kWh-grade lithium batteries for PHEVs, where 12 modules consisting of eight cells were connected in series; thus a total of 96 cells were connected in series. The battery system contains a BMS, and its power is controlled through a power relay assembly (PRA) (Table 1).

(4) Vehicle model

The vehicle model was constructed using a mid-sized PHEV model with a parallel structure provided by the Powertrain System Analysis Toolkit (PSAT), along with the models of the vehicle parts to which the battery system examined in this study can be applied, as based on the PSAT's library of vehicle parts 8 The

Table 2 PHEV specification reflected in the Model

Item	Specification
Environment friendly vehicle type	PHEV (medium-sized SUV)
Power train structure	Parallel type
Curb vehicle weight	1,988 kg
Engine	Gasoline, 1.8L, 104.2 kW
Motor	PM, continuous 25 kW, Peak 51.3 kW, maximum efficiency 95 %
Battery	Li-ion, 6.9 kWh, 96-cell, 20 Ah

major components of the constructed PHEV include a 1.8L, 105 kW gasoline engine from a Toyota Corolla; a 51.3 kW permanent magnet motor from a Toyota Prius (MY04) with the maximum power of a sport utility vehicle (SUV) and a curb weight of about 2 tons based on the Honda Accord body platform; and the 96-cell, 6.9 kWh LiPB system modeled in this study (Table 2).

2.2.2 Battery HILS development

(1) Battery HILS interface

A typical battery model, such as the one shown in Fig. 2, receives the current required by the vehicle (the current required by the motor + the current required by other electronic components) as inputs and outputs the calculated data, such as the voltage of the battery, the state of charge (SOC), and the temperature, based on the current requirements within the battery model block.

The battery model needs to be modified into an interface model for the battery HILS, which consists of the RTS, charger/discharger, and BMS. Data are exchanged among nodes over the CAN. The battery voltage, SOC, and maximum power monitored by the BMS are transmitted to the RTS, which multiplies the received voltage by the current requirement of the vehicle to calculate its power requirement. The charger/discharger charges and discharges the battery with the power required by the RTS to construct the battery interface model. The BMS measures the voltage and current of the battery system, estimates the SOC, and calculates the maximum output power.

The battery interface model, as shown in Fig. 3, is constructed using a configuration identical to that of the input and output of the battery system model, and the RTI CAN Blockset from dSPACE is used to apply the CAN. Using the charger/discharger, the CAN nodes are allocated as CAN TX (transmit) for transmitting the CAN data from the RTS to the charger/discharger, and CAN RX (receive) for receiving the CAN data at the BMS. Since the vehicle model used in this study is optimized for a 10 ms sampling time, the CAN RX block is identified using this sampling time, but the CAN TX block is given a transmission cycle of 100 ms to account for the response characteristics of the charger/discharger.

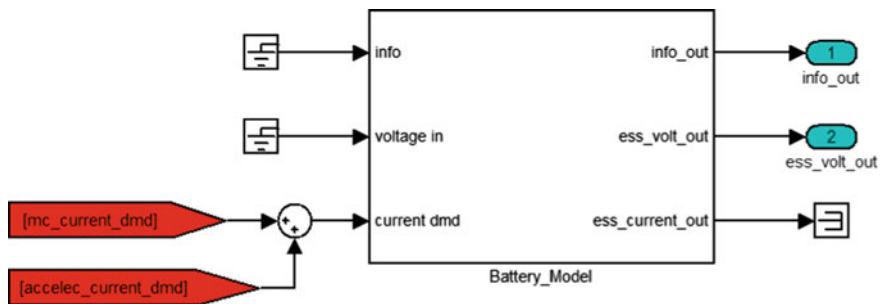


Fig. 2 General battery model input and output

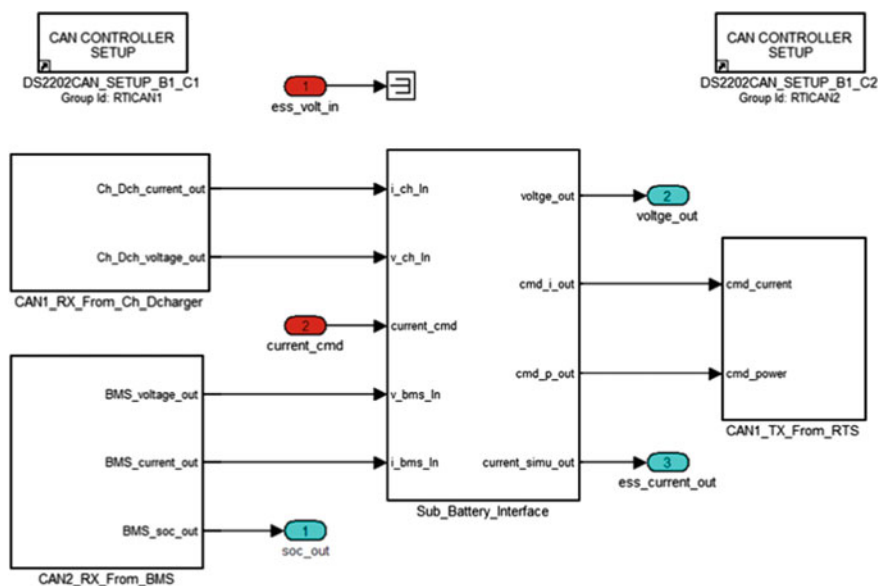


Fig. 3 Battery interface model

As shown in Fig. 4, the Sub_Battery_Interface model consists of a block to calculate required power using the required current calculated from the vehicle model and the voltage measured from the battery, plus a block to calculate the SOC using Ah counting in case the CAN data base (DB) of the BMS in the battery system is not known.

(2) Battery HILS control and fabrication

When the Battery_Model block has been changed into a Battery_Interface block for a battery HILS interface in the vehicle model, a real-time workshop (RTW) should be implemented so that the relevant model can be processed in real time by the processor in the RTS. Since battery HILSs should be processed in real

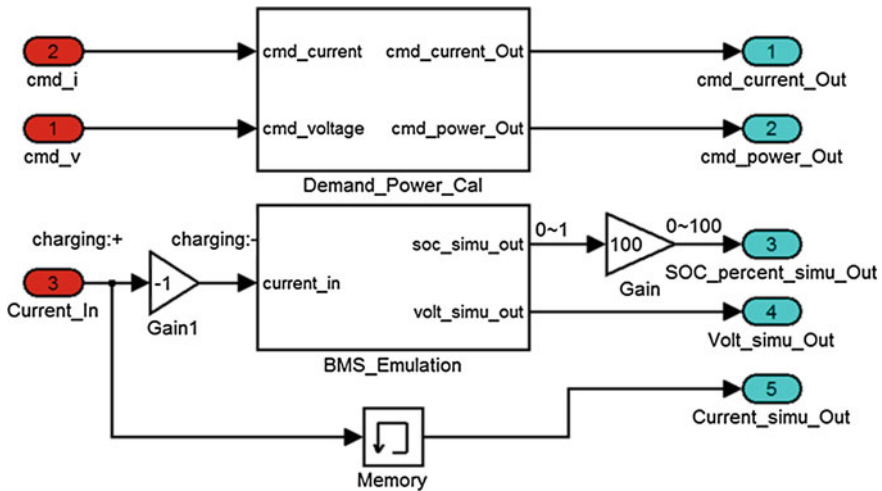


Fig. 4 Sub_Battery_Interface model

time by an embedded processor or controller, unlike pure simulations, fixed steps should be selected as the solver type, and the real-time mode should be selected as the execution mode among the real-time interface (RTI) simulation options. As a basic sample time, 10 ms was selected considering the operation speed of the RTS and the parameter reflecting speed of the model.

To easily grasp parameters used in the vehicle model utilizing the dSPACE ControlDesk for battery HILS control and monitoring, a layout was configured as shown in Fig. 5. The developed software was able to select a charge/discharge mode by CAN between the constant current (CC) and constant power (CP), operate cycle patterns for tests in the relevant mode, and conduct tests with speed data, such as the Urban Dynanometer Driving Schedule (UDDS) or US06. The developed software was also enabled to store and analyze parameters to be analyzed by the model and the CAN signals of the BMS and the charger/discharger.

The finally developed battery HILS is shown in Fig. 6.

2.3 Battery HILS Verification

Since verifying the developed battery HILS by connecting high-voltage batteries to the charger/discharger might be dangerous because the stability of the newly developed battery HILS had not been ensured, the developed battery HILS was first verified through simulations using the CAN of virtual interlocking between the RTS, the charger/discharger, and the BMS, and then verified after installing a 6.9 kWh-grade battery.

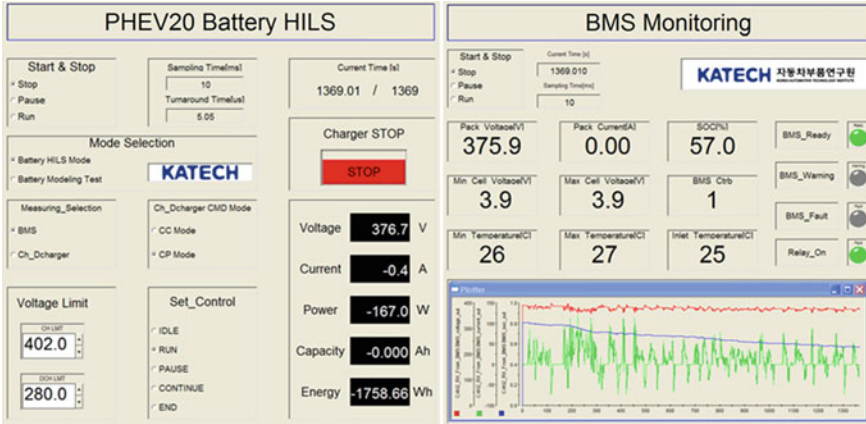


Fig. 5 Control and monitoring program for battery HILSs

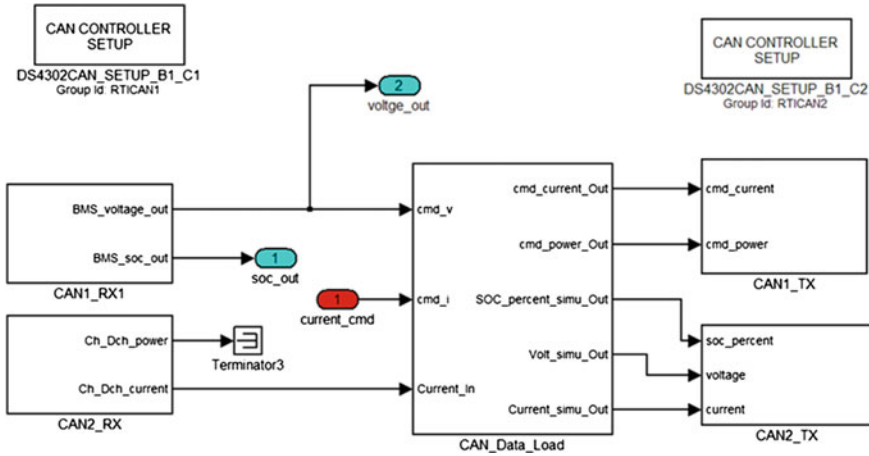


Fig. 6 Virtual battery_interface model using CAN

2.3.1 Verification by Simulations Using CAN of Virtual Battery HILS Interlocking

The simulation using the CAN of virtual battery HILS interlocking is a technique in which the charger/discharger and the BMS hardware were replaced by virtual CAN nodes. For the verification, a Virtual_Battery_Interface was configured, as shown in Fig. 7. The required current calculated from the vehicle model is sent by CAN1_TX, corresponding to the RTS. The CAN2_RX simulating the charger/discharger receives and then has a certain delay, and the CAN2_TX corresponding to the BMS applies the battery model used in the online simulation of the vehicle

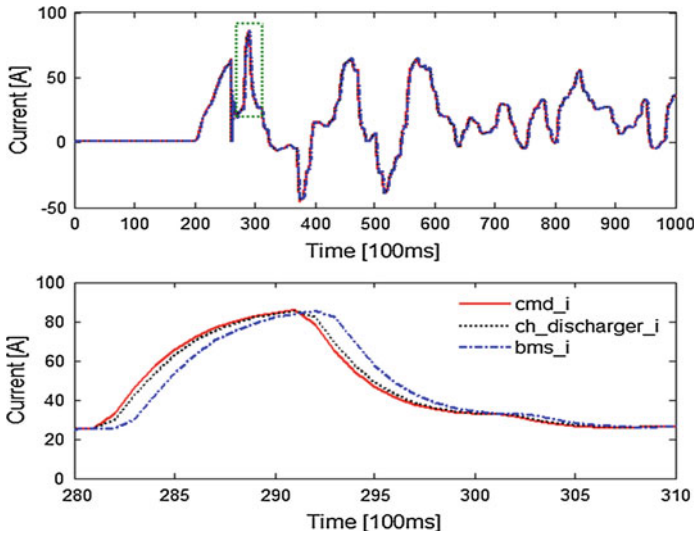


Fig. 7 Comparison of the currents of virtual battery HILS

model, as it is to send the SOC and voltage. Then, the RTS receives the SOC and voltage.

The simulation of virtual battery HILS interlocking was tested using UDDS at an SOC of 80 %. To reflect the response characteristics of the charger/discharger, the simulation was set to estimate the SOC and voltage from the current received from the RTS after a delay of 50 ms. From the results, compared to the required current, a delay of 50 ms was identified at the charger/discharger and a delay of 100 ms was identified at the BMS, as shown in Fig. 8. The voltage delay between the charger/discharger and the BMS was shown to be very small, and 0.5 % stepped data were identified because the length of each SOC CAN data was 8 bits.

2.3.2 Battery HILS Verification

After identifying the safety of battery HILSs, a 6.9 kWh-grade battery system was installed and simulations were conducted using UDDS at a SOC of 80 %. The current calculated from the vehicle model and the voltage measured by the BMS were received and used as the required power of the charger/discharger.

Figure 9 shows the required current calculated from the model, the currents actually charged and discharged by the charger/discharger, and the current measured by the BMS. Although the three current values involve delays depending on the CAN transmission speed, in general it can be seen that the currents were charged/discharged in accordance with the required current of the relevant model, and that the BMS normally fed back the SOC estimated by measuring currents and voltage. The battery HILS thus operated normally.

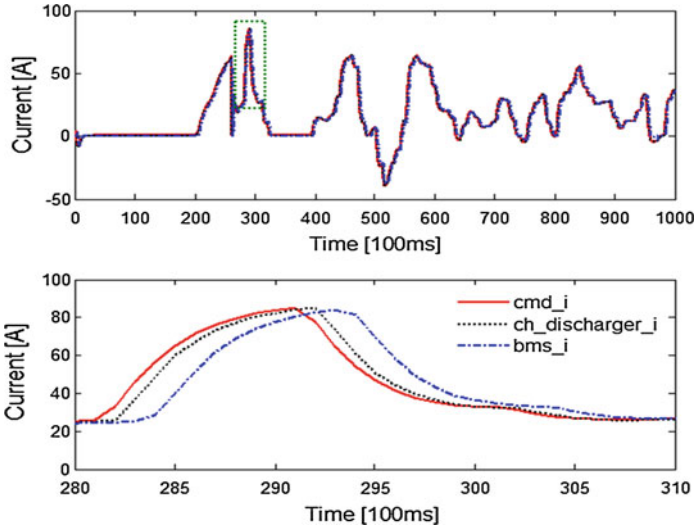


Fig. 8 Comparison of the currents of the battery HILS

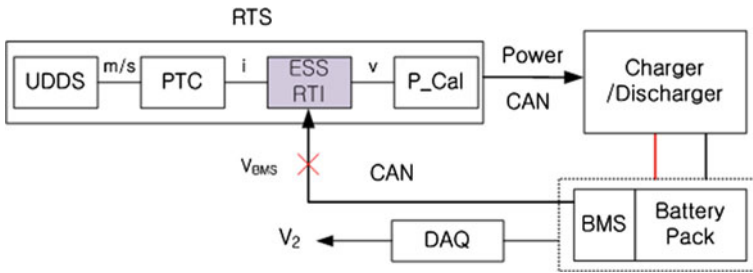


Fig. 9 Battery system model verification structure using a battery HILS

3 Battery Model Verification

One advantage—as well as a disadvantage—of battery HILSs is that, since tests are conducted in real time, considerable time is required to test every case. Therefore, to test diverse characteristics of battery systems within a short time, online simulations reflecting battery models are necessary even if the accuracy would be somewhat lower. Although the accuracy of the developed battery model can be tested by comparing data from tests conducted with actual batteries with the results of simulations conducted using the model, ultimately, battery behavior (voltage, SOC, and so on) should be compared with the behavior of the entire vehicle when the same input is given.

3.1 Battery Model for Verification

The battery system used in the present study is a 6.9 kWh-grade battery consisting of a total of 96 cells; 12 modules consisting of eight LiPBs connected in a series are connected with each other to constitute the battery. Its final output is delivered through a PRA. There are safety relays between the modules, and the BMS monitors the battery to control the cooling fan and other components as necessary.

The battery cell model was implemented utilizing EIS and a battery system model made considering the effects of the bus bar, connection cable, connectors and PRA, and so on, which were installed when the battery system model was changed from a module to a pack was used for verification. With the battery model for verification, it was noted that the voltage difference between the actual battery pack and the model was within 1 % on average, based on charging depleted cycle life (CDCL) profiles. It was discovered through error rate analyses that around 90 % of errors were concentrated within 0.5 % of voltage error.

3.2 Battery Model Verification Using the Battery HILS

The accuracy of a developed battery model is generally verified by comparing the results of tests conducted using cycle patterns reflecting battery characteristics and the results of battery model simulations. However, this method does not reflect the characteristics of the entire vehicle, nor does it accurately reflect a battery's dynamic characteristics. Therefore, even when a battery model is accurate in the relevant cycle pattern, it is possible in some cases for many errors to occur in other cycle patterns.

Therefore, to address this weakness, the accuracy of battery models can be verified using a battery HILS. As shown in Fig. 10, a battery HILS utilizes patterns such as the UDDS mode to receive vehicle speeds as an input to calculate the current required by the vehicle reflecting the behavioral characteristics of the entire vehicle at the powertrain controller (PTC) and calculates the final required power by estimating battery system voltage at the energy storage system (ESS) RTI based on the calculated current required by the vehicle. The calculated required power is delivered to the charger/discharger, and then the charger/discharger charges and discharges with the relevant power. Unlike the general characteristics of battery HILSs, the voltage measured by the BMS or the charger/discharger is not received as feedback, but the voltage estimated from the battery model is used. Since one of many test patterns can be selected and processed, and all parameters used in the model can be monitored in real time using HILS, the accuracy of the battery system model can be analyzed and grasped by comparing the voltage simulated by the battery model and the voltage measured from the battery system.

Fig. 10 Comparison of modeling accuracy (voltage) of UDSS using a battery HILS

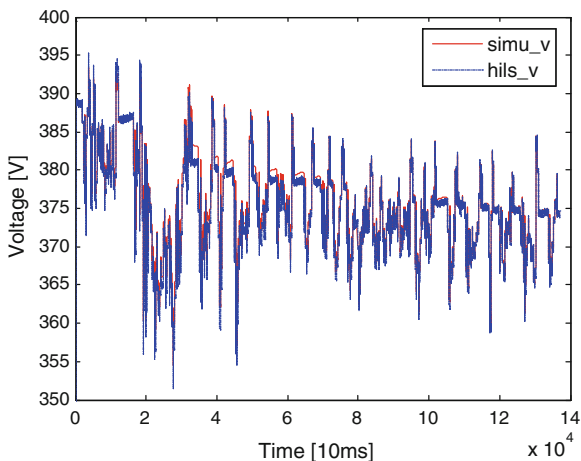
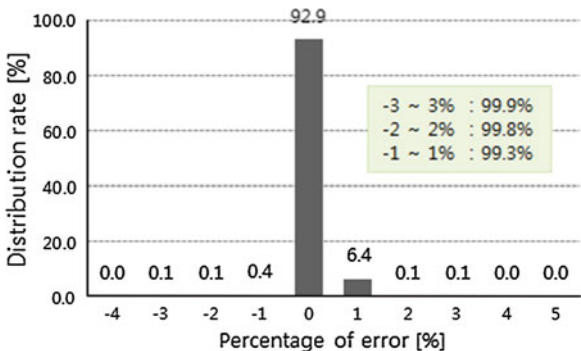


Fig. 11 Comparison of the error rates of the battery system models using the UDSS pattern



The developed battery system model was applied to a model for battery HILSs in order to compare the results of simulations by the battery model with the results of measurements by the battery HILS. The results compared were the voltage values of the battery system for the same input conditions. The battery modeling accuracy verification test utilizing the battery HILS was conducted using the UDSS pattern at a battery system SOC of 80 % and at a room temperature (25 °C).

Figure 11 shows a comparison between the voltage from the results of the simulation and the voltage of the actual load battery system using the battery HILS of the battery system model developed in this study and the UDSS pattern. The experimental results confirm that, when an identical current is applied, the average error between the voltage of the simulation and that of the battery system using a battery HILS is within 1 %. Furthermore, as shown in Fig. 12, the results of an error-rate analysis indicate that 92.9 % of the errors are distributed within an error rate of 1 %, confirming the idea that sufficient accuracy is secured for the moderate driving conditions of the UDSS pattern.

4 Results

A battery HILS consisting of a battery system, a charger/discharger, and a CAN interface was developed for medium-sized parallel PHEV models. The developed battery HILS was verified using virtual battery HILS interlocking simulations using CAN and a 6.9 kWh-grade lithium ion battery pack. The verification process identified that the developed battery HILS could be used as a method to assess the accuracy of battery modeling, and that the battery HILS could be applied to battery system models developed using EIS to verify the systems in real time.

References

1. Nabi S, Balike M, Allen J, Rzemien K (2004) An Overview of Hardware-In-the-Loop Testing at Visteon, SAE, 2004-01-1240
2. Tae JS, Lee KY, Lee W (2009) A Development of HILS System for MCU Testing, KSAE 2009, A0485
3. Shidore N, Lohse-Busch H, Smith RW, Bohn T, Sharer PB (2007) Component and subsystem evaluation in a systems context using hardware-in-the loop, vehicle power propulsion conference, pp 419–424
4. Song HS, Lee BH, Heo H et al (2011) A study on the development of battery HILS for green cars, KSAE 2011, A0540

Extended Flexible Environment and Vehicle Simulation for an Automated Validation

Albert Albers, Rolf Hettel, Matthias Behrendt, Tobias Düser
and Alexander Schwarz

Abstract In FISITA 2010 IPEK (Institute of Product Engineering) introduced the vehicle-in-the-loop platform based on its X-in-the-loop approach (F2010-C-177) (Albers and Düser, Implementation of a vehicle-in-the-loop development and validation platform, FISITA world automotive congress, Budapest, 2010). It offers a methodology for multi domain product development and validation as well focuses on its key hypothesis that validation is the main task in every step of product development process. An open hardware and software platform allows integration of different real components and simulation models as well as the usage of established tools and methods for measurement and validation. The platform is based on a common hardware-in-the-loop System using extended I/O-communication to the vehicle and the test bench. The application is done in C code and Matlab/Simulink so an easy exchange of modular simulation models and test cases is feasible. The architecture of model-, component- and test case implementation simplifies the scalability as well as the modularization. IPEK uses this platform amongst others for its improved fully automated validation environment which allows the optimization of operating time for determination of shifting quality on the chassis dynamometer. The task is to perform several hundred gearshifts under particular reproducible conditions automatically such as engine speed or even battery state of charge, which normally a real driver had to perform on a real test track. Compared to road tests on the rig it is possible to reach time benefits of over 80 % by using a special driver

F2012-E12-010

A. Albers · R. Hettel (✉) · M. Behrendt · A. Schwarz
IPEK—Institute of Product Engineering, Karlsruhe Institute of Technology (KIT),
Karlsruhe, Germany
e-mail: friedrich.brezger@kit.edu

T. Düser
AVL Zöllner GmbH, Bergisch Gladbach, Germany

model for acceleration (using gas pedal), deceleration (using dynamometer) and gear shifting (using tip signal at steering wheel). Since the vehicle behaviour on the road is constrained to different environmental conditions it is necessary to reproduce these conditions on the test bench accurately. Different resistances affect the vehicles responses such as shifting strategy, acceleration characteristics or fuel consumption which results in altering test results. State of the art for simulating environmental conditions and vehicle characteristics on the chassis dynamometer is the Road-Load-Simulation (RLS) which uses measured vehicle coast downs to map the static resistances of a real car on a real track onto the test bench. These coast downs have to be redone every single time components of the car or the environment changes. In addition, changing resistances during test like air drag due to headwind and rolling drag due to tire temperature or abrasion can't be simulated based on that static coast down. This paper shows an approach for simulating all kind of resistances that can appear and vary during the test such as air drag (wind), road gradient, road friction, curve resistance etc. in real-time. It can be used to drive test cases like the determination of characteristic shifting map in a more realistic way to perform better validated results. Central point is a configurable vehicle and environment model which has to be parameterized with data from the real car and track and then calculates the necessary dynamometer responses. Applied with a four roller dynamometer (two or even four driven axles) it offers the possibility to perform complex all-wheel manoeuvres e.g. such as μ -split or cornering with independent wheel behaviour and slip. Besides the advantages of this approach, an analysis of different influencing factors is shown in this paper.

Keywords Vehicle-in-the-loop • X-in-the-loop (XiL) • Model based testing • Environment simulation • Vehicle simulation • Road load simulation • Chassis dynamometer

1 Introduction

Vehicle testing in early stages of product development became state of the art for new vehicles. Including driving tests on the road, or the chassis dynamometer it got more and more important to know the exact vehicle behaviour, fuel consumption or other characteristic values as soon as possible in the product development process. Because most parameters of the complex system vehicle, which always stands in interaction with environmental influences, still can't be simulated reliable, tests with prototypes or pre-series cars are necessary.

Tests on the road are time-consuming (the prototypes, the staff and all the measuring equipment have to be transported to the test track) and not very reproducible (due to human deficiency in reaching defined operation points, which in consequence causes an higher amount of repetitions as well as weather conditions and curves). On the chassis dynamometer a robot can be used to drive the vehicle reproducible in every situation and independent of many unpredictable

environmental influences like temperature, weather or road surface. The measuring equipment can be placed right beside the vehicle on the test bench, which makes special measurement setup in the vehicle dispensable.

However, influences of the environment are highly important for a realistic measurement of parameters like fuel consumption or driving performance, these influences have to be simulated on the test bench. Therefore, the state of the art solutions use static coast down measurements to extract the driving resistances and emulate them on the test bench. The problem with that is the extracted driving resistances are only valid for the exact same car (same powertrain components, aerodynamic form, tire pattern, wheel pressure, etc.) with the exact same environmental influences (same wind direction, road surface, temperature, etc.). If even one parameter changes, the driving behaviour on the test bench changes too, which could make the measured results invalid. So every time a parameter changes a new coast down has to be done, because there is no direct mathematical relation between the parameters of the resistance force curve and the physical phenomenon it's caused by.

A new method has to be found to optimize the determination of driving resistances on the chassis dynamometer without using these static coast downs so that in every vehicle configuration and driving situation the resistances are comparable to the ones on the road. It should also give the operator the possibility to interact with the resistances so he can vary specific resistances, always with the direct physical parameter which influences it.

2 State of the Art

2.1 Driving Resistances on the Road

The most important resistances on the road that influence the vehicle coast down behaviour are:

- air resistance (air drag and wind)
- rolling resistance (wheel contact on the road)
- power train losses (e.g. bearing losses, gearbox losses, motor drag)
- grade resistance (slope of the road)
- curve resistance (course of the road)

The driving resistances on the road are very well known and described in many different state of the art sources (see [1, 2]). Therefore the different resistances are mentioned only for the sake of completeness.

2.2 Driving Resistances on the Chassis Dynamometer

The resistances on the chassis dynamometer differ from the ones on the test track. Because the vehicle is not moving lateral or longitudinal, there is no air drag like on the road, where it has a wide influence. Due to vehicle fixation, all forces

caused by air blower or external cooling fans have no influence on the driving behaviour of the vehicle on the test bed.

The roller surface is not plane but curved. That causes a higher rolling resistance for the wheel compared to the (almost) flat road surface. The differing rolling resistance on the chassis dynamometer can be calculated approximately with formula (1), where F_x is the rolling resistance on the road, r the wheel radius, R the roller radius [3].

$$F_{xR} = F_x \left(1 + \frac{r}{R}\right)^{\frac{1}{2}} \quad (1)$$

All the powertrain losses are (nearly) the same for the chassis dynamometer and for the test track. The vehicle uses all the same hardware components in both cases.

Grade resistances can be simulated on the test bed as well as curve resistances. Slopes and curves are not physically existent on the test bed but can be simulated by applying additional forces to the rollers.

2.3 Road Load Simulation

The standard method for transferring the real vehicle behaviour from the test track to the chassis dynamometer is the so called road load simulation (RLS) according to SAE J2264 [4]. It's a fast method for calculation of driving resistances on the chassis dynamometer. It's based on a pre-measured vehicle coast down and uses a simple mathematical approximation for computing-time reduction.

The Pros beside fast calculation and fast closed loop control are simple mathematics, robust and fail safe dynamometer operation and the possibility to simulate road gradients.

The key fact, which makes the big difference to the presented approach, is the way the dynamometers are operated. The road load simulation uses torque resp. force control. That means the output signal of the calculation is the dynamometer torque not the speed. The dyno controller then adjusts the dyno torque, applied to the rollers. That results in a roller speed change corresponding to formula (1), where $M(t)$ is the torque, J is the mass moment of inertia and $\ddot{\varphi}(t)$ is the rotational speed.

$$M(t) = J \cdot \ddot{\varphi}(t) \quad (2)$$

2.4 Approach to Calculate the Required Torque

First of all a coast down curve has to be recorded. Therefore, it is important to use exactly the vehicle which should be tested on the test bench. There must not be any differences in aerodynamics, mass, tires etc. It's clearly visible that changes in one

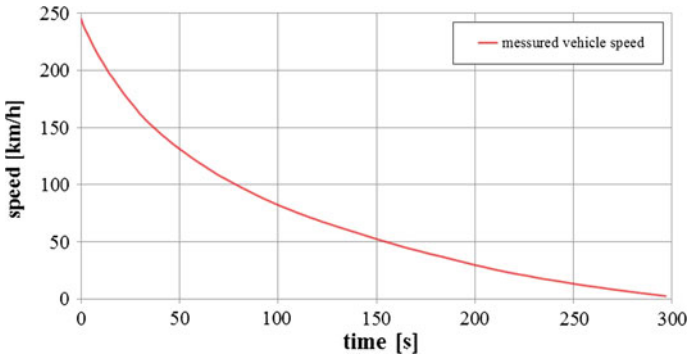


Fig. 1 Measured coast down curve $v(t)$

of these parameters affect the driving resistances (mentioned above) and therefore the coast down curve [5].

In Fig. 1 is shown a coast down curve of a common passenger car. It was measured on the test track with neutral gear position an approximated for high speeds. Some of the cars specs are:

- vehicle mass (with driver) $m = 1600kg$
- drag coefficient $c_w = 0.3$
- reference area $A = 2.05m^2$
- summer tires

With the coast down curve it is possible to calculate the effective driving resistance at each time. That includes air resistance (wind could be included), rolling resistance, rest powertrain resistances (of not uncoupled powertrain components like differential and axle bearings), tire bearing resistances and possible grade resistance (both not effective in this special case) of that specific vehicle configuration.

According to famous formula (1), where $F(t)$ is the sum of retarding forces, m the vehicle mass and $a(t)$ the vehicle acceleration, the reacting Force can be calculated. The acceleration results from differentiating the velocity plot.

$$F(t) = m \cdot a(t) \tag{3}$$

Figure 2 shows the calculated forces plotted over the corresponding vehicle speed $F(v)$.

By using a least square approach, the force over speed curve can be approximated in a wide speed range. As basic function serves a quadratic equation according to formula (1), where F_0, F_1, F_2 are unknown parameters which have to be estimated.

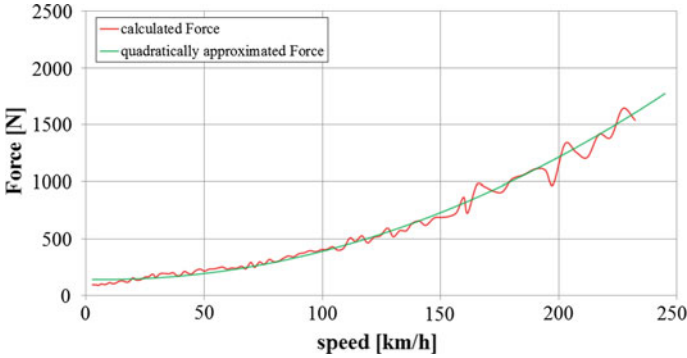


Fig. 2 Calculated and quadratically approximated force in tire contact point

$$F(v) = F_2 \cdot v^2 + F_1 \cdot v + F_0 \quad (4)$$

Applied to the curve shown in Fig. 2, the parameters for the least square approach result in $F_0 = 142$, $F_1 = -0.407 \frac{N \cdot h}{km}$ and $F_2 = 0.0289 \frac{N \cdot h^2}{km^2}$.

These parameters can be used to calibrate the test bench. Before it's possible to drive with the vehicle on the test bench it's necessary to do a parameter correction. The parameters calculated above are valid for the vehicle driving on the real test track. But when the vehicle drives on the test bench some influences on the vehicle coast down behaviour drop out and some come along. For example the air resistance drops out and an additional rolling resistance due to curved roller surface comes along. To adopt these changings it's necessary to measure the difference in coast down behaviour of the vehicle on the track and on the test bench without changing any parameters. This difference is also transformed into another Force over speed curve represented by another set of test bench parameters. In an iterative process these test bench parameters are adopted to match the coast down curve with the vehicle on the test bench with the one from the road.

Finally with these two sets of parameters every speed is attributed to one Force which then can be transformed into a torque resp. force with the radius of the roller. This torque is provided directly to the dynos.

3 Extended Validation Platform

As described above, the state of the art process to apply a road load simulation on the chassis dynamometer is based on a static coast down curve, and an iterative but static parameter adaption.

The here shown method uses a real time based vehicle and environment model to calculate all the driving resistances on the test bed without using a measured coast down. Goal of the model is to build up a simulation which can be parameterized with few characteristic values which are easy to find out and to produce a realistic driving behaviour. For example these parameters could be vehicle mass, tire size, tire type and air drag coefficient. Furthermore it should offer more possibilities to vary the driving behaviour due to different road and vehicle influences and it should be easy to parameterize.

In the paper F2010-C-177 from FISITA 2010 [6] the IPEK introduced the vehicle-in-the-loop platform based on its X-in-the-loop approach. The described platform is now used to build up the simulation of driving resistances. AVL InMotion powered by IPG CarMaker is chosen for the environment and vehicle simulation. In addition a model based on Matlab/Simulink was used for the vehicle which considers all driving resistances but does not use a vehicle model in an environment. The resistances are calculated directly with the corresponding equations.

3.1 Components of the Simulation Platform

At first there's the chassis dynamometer which in this special case is a 4×2 roller test bench (4 rollers, 2 driven axles). So it's possible to carry four wheel drive vehicles but the simulation is then limited in its possibilities (see below) compared to a 4×4 roller test bench (4 separately driven rollers). The dyno provides a rotary speed which is given by the simulation model. The speed of each driven roller is regulated separately so different speeds can be provided. The dyno controller is running in mode 'speed control', which allows the simulation to regulate the roller speed directly, not by regulating the torque.

The vehicle is mounted on the chassis dynamometer and fixated with a wheel hub fixation. The wheel hub fixation induces the less chassis movement and does not allow much longitudinal movement of the wheel relative to the roller apex. That improves the measurement of the dyno torque which in consequence improves the simulation results. Other vehicle fixations are feasible as well. The resulting chassis movement does not correlate with the one on the road which was neglected in the first step. The here shown tests are done with a front driven vehicle with approximately 66 kW. It has winter tires mounted and regular aerodynamic characteristics.

On the other hand there is AVL InMotion powered by IPG CarMaker [7] which runs the vehicle and environment model and represents the base for maneuver based testing on the chassis dynamometer.

The simulation uses a freely configurable vehicle model (based on the IPGCar [8]) which includes a powertrain, tire, chassis suspension, steering and aerodynamic model beside others. These simple physical models are sufficient for the performed tests what was shown by the received results. The model gets

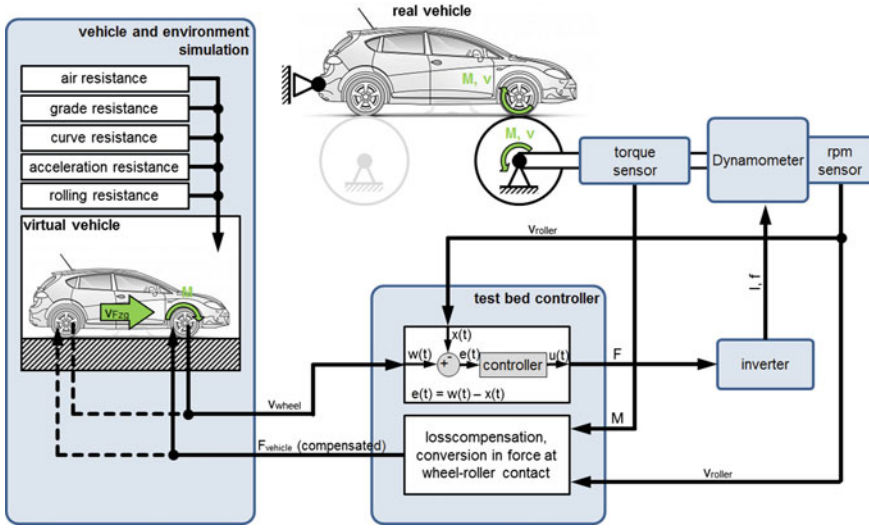


Fig. 3 Components of the simulation environment

parameterized with the parameters from the real car used for the tests. The most important parameters with the greatest influence can all be found very easy in data sheets or on the manufacturer’s homepage. Less important parameters have to be measured or can be used from comparable vehicles. For easy vehicle creation, the software provides the so called Vehicle Generator.

The virtual car drives in a virtual environment which induces resulting forces to the car. Beside air drag caused by aerodynamic coefficient and wind, the road has a big influence on the resulting forces. For example a downhill slope causes positive forces, air drag, rolling resistances and steering causes negative forces.

Figure 3 shows the build-up of the simulation environment with its components and interfaces schematically. The build-up is similar for each driven roller but here shown only for one roller. The torque from the dynos torque sensor is measured and serves as input for the simulation. The torque signal is converted to a Force at the wheel contact and the roller losses (bearings) are compensated in the test bed controller.

This measured force is added to the forces at the virtual wheel in the simulation which causes the virtual vehicle to accelerate or decelerate. The resulting new speed from the virtual car serves as set value for the test bed controller. The test bed controller then regulates the speed of the dynos. Based on the virtual car driving curves or occurring wheel slip, the speed of each roller is regulated individually, corresponding to the virtual wheels in the simulation.

Figure 4 shows a comparison of the different approaches. The red graph represents the reference coast down measured on the real test track. The green graph shows the results on the test bench with the Simulink model which was used in the first step. All parameters in the model were taken from the vehicle that was used

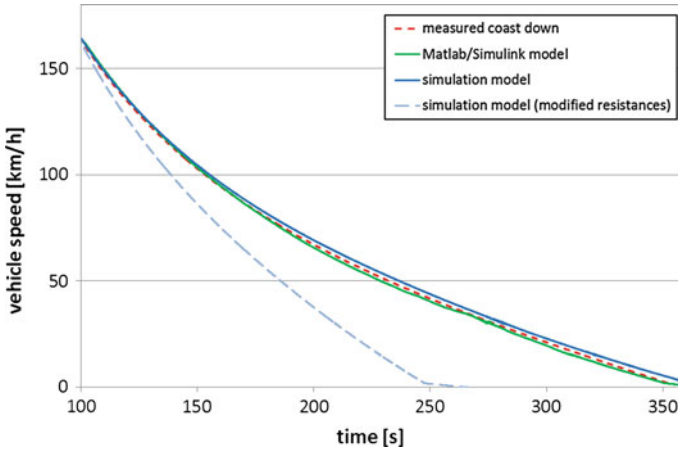


Fig. 4 Comparison of the different approaches and the measured coast down on the road

for the reference coast down. The blue graph shows the new approach using the simulation model for calculating the driving resistances (including vehicle and environment simulation). It matches the reference coast down very good revealing the validity of the presented approach. Finally the light blue graph shows the result with simulation model using slightly modified rolling resistances. Increasing the rolling resistance shortens the coast down and vice versa.

3.2 Characteristics of the Simulation

The new method for simulating the driving resistances has all the functionalities of the state of the art road load simulation and brings along many others. Some are mentioned below.

The virtual environment in which the virtual car is driving gives the information of slope and curves. In case the virtual car is driving uphill or in a curve the simulation raises the torque given to the virtual wheel hub which causes a reduction of the vehicle speed. When driving curves in the simulation the wheel speeds can be calculated independently to realise the different speed of the inner and outer wheels. On a four wheel dyno it is possible to analyse the behaviour of differentials while driving curves without the need to steer (which is not possible on a normal chassis dynamometer).

Because the vehicle model uses a simple air drag calculation (a real fluid simulation is not implemented yet due to performance reasons and the limitations given by the real time environment) it is possible to change aerodynamic parameters like drag coefficient or reference area while the simulation is running and the car driving on the test bed. A change in aerodynamics could be caused by rear spoiler which comes out at 80 km/h on the Porsche 911.

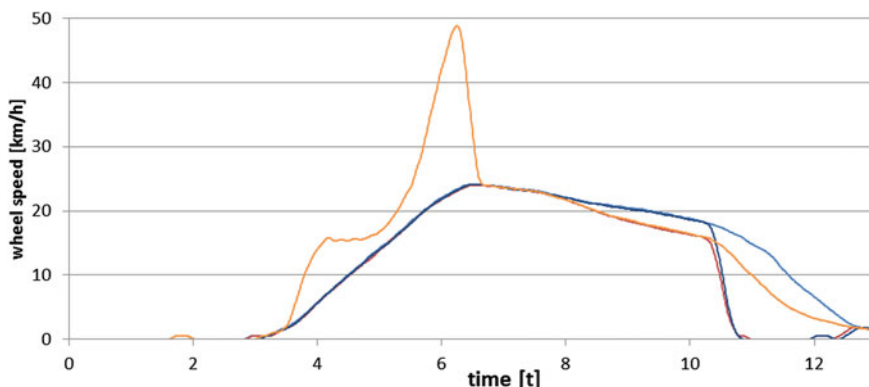


Fig. 5 Acceleration on ice (*left wheels on ice, right wheels on asphalt*), *front left wheel slipping; curve to the left (with slip) and blocked rear wheels*

A wind simulation makes it possible to simulate different wind directions and therefore the varying air drag in driving direction.

The simulation is based on a physical model where parameters like vehicle mass, center of mass or even trailer mass have an influence on the virtual driving behaviour and the real torque applied to the test bed. Because the mass although has an influence on the coast down it can be used to compensate weight influences like measuring equipment or driver which are installed on the test vehicle but should not be considered in the resulting driveability. Simulating trailer load could although be a use case for this simulation.

Many applications on the test bed make it necessary to use special roller tires (e.g. for acoustic measurements). The changed tire pattern causes a differing rolling resistance. To obtain the same coast down curve as with normal tires it's possible to change the tire model in the simulation.

Depending on the roller count, dynamometer power and the roller inertia it is possible to simulate different road surfaces (friction coefficients). These could be caused by changing weather in the environment simulation e.g. rain, snow or ice or other changes of the road surface like asphalt or gravel. It's not possible to simulate the real slip between tire and roller with this method but by allowing high accelerations of the roller the wheel slip can be played to the vehicle ECU. The higher the acceleration of the free spinning wheel is, the stronger the dyno has to be (for the tested car the slipping wheel acceleration on ice is about 10 m/s, see Fig. 1). For Example it's possible to simulate a slipping front axle on a slippery road (in the dynamic limits of the test bench) and use it to analyse the vehicles ESP. On a 4×4 roller chassis dynamometer where each wheel is controlled separately, μ -split drive can be simulated as well as blocked wheels (Fig. 5).

4 Summary and Outlook

In the paper was shown a method to calculate driving resistances based on a real time vehicle and environment model and use these to simulate the driving resistances on the chassis dynamometer.

The model is simple to parameterize as it's based on physical correlations and not on a measured coast down. It considers the important driving resistances and has many benefits compared to the road load simulation.

First comparisons of driving test on the road and the chassis dynamometer show good correlations between the results from the test track and the chassis dynamometer. The new simulation approach performs good compared to the measured coast down and the state of the art road load simulation.

Furthermore there's a good usability of this method for many other applications on the chassis dynamometer e.g. analysis as well as optimization of shifting strategies and the corresponding gear shifting quality [9]. Another application could be the use for calibrating or conceptual tests of vehicles using torque vectoring.

References

1. Haken KL (2008) Grundlagen der Kraftfahrzeugtechnik. Carl Hanser Verlag, München
2. Halfmann C, Holzmann H (2003) Adaptive modelle für die kraftfahrzeugdynamik. Springer, Heidelberg
3. Düser T, Olms H, Haase A, von Gave R, Schmidt C, Schmidt U (2011) Vehicle Chassis Dynamometers—from certification through to a mechatronic development platform. Süddeutscher Verlag onpact GmbH, München
4. SAE international (1995) chassis dynamometer simulation of roads load using coastdown techniques, recommended practice. SAE J2264
5. Isermann R (2006) Fahrdynamik-regelung—modellbildung, fahrerassistenzsysteme, mechatronik. GWV Fachverlage GmbH, Wiesbaden
6. Albers A, Düser T (2010) Implementation of a vehicle-in-the-loop development and validation platform, FISITA World automotive congress; Budapest
7. Düser T, Schmidt C, Schmidt U, Pfister F (2012) Chassis dynamometers for vehicle and powertrain concepts of tomorrow, ATZ 04/2012, Vol 114. Springer, Berlin
8. IPG Automotive GmbH, CarMaker—Reference Manual Version 3.5", 201111] Albers A, Schwarz A, Hettel R, Behrendt M (2011) Method for the time-saving capturing of characteristic gear shifting diagrams of vehicles on the rollertest bench carried out with dual clutch transmissions, 6th international CTI symposium and exhibition North America
9. Albers A, Schwarz A (2012) A operating system for the optimization of technical systems using the example of the calibration of transmissions, FISITA World automotive congress; Beijing

Application of Energy Distribution Analysis During the Vehicle Development

Yongsheng Long, Jianpeng Shi, Li Xin, Xueen Zhang, Jun Wang and Shaoju Qu

Abstract Faced with rising vehicle energy saving and environmental protection requirements, if you rely solely on a field of energy saving and consumption reducing, it is hard to get the required amount of goals to improve. And how will the vehicle fuel consumption reduction target value that you want the correct segmentation into fuel consumption reduction target values in various fields, will be the key to compliance. This research goal is to establish a decomposition model of vehicle fuel economy of consumption, by decomposition on vehicle fuel consumption target value, make of vehicle fuel consumption reduction target value easier to reach. Product development, will CAE simulation technology combined with the variety of real train test data, is to reduce the cost of development, an effective method to shorten the development cycle. Research methods in this chapter is through CAE simulation analysis of establishing vehicle fuel economy of consumption model, is allocated for vehicle fuel consumption management, vehicle fuel economy of consumption is divided into the following energy consumption model: engine loses energy consumption model, brake system energy consumption model, train energy consumption model, model of energy consumption of air resistance, rolling resistance model of energy consumption. And verified using experimental data on the energy decomposition model, continually modified and improved the energy decomposition model. Establishment of decomposition technique system of passenger automobile fuel economy, correctly grasp the body and chassis drive, engine and vehicle technology in reducing fuel consumption, energy distribution practices. In the development of a model of the company, through the use of energy consumption distribution model of the study

F2012-E12-012

Y. Long (✉) · J. Shi · L. Xin · X. Zhang · J. Wang · S. Qu
Technical Center, Dongfeng Motor Corporation, Wuhan, China
e-mail: longys@dfmc.com.cn

on rational allocation of vehicle fuel economy target values for confirmed their fuel economy target of the project model, allowing the automobile to standard three phase fuel consumption limit values easier. Due to the lack of product development experience and development data, may result in the model decomposition energy consumption of different automobiles in different degrees of error model, even its accuracy may also apply only to the model developed by the model. But with the development experience and data accumulated, the study on the establishment of decomposition models will continue to improve vehicle fuel economy, shorten the development cycle, reduce development costs of this research will play a key role. Vehicle fuel economy reflect the model of comprehensive performance indicators. Must be involved in all areas, such as: transmission of body and chassis, engine and vehicle technology in terms of performance and match the overall optimization. This innovative approach of the study is established through the CAE simulation model for vehicle fuel consumption, and using reasonable collection of test data and optimized using experimental data for model validation, and constantly improve the vehicle's energy consumption model with the. By establishing a decomposition model of vehicle fuel economy, vehicle involves different areas of the development of a rational energy consumption objectives, can greatly shorten the development cycle and reduce development costs. Therefore, in the future of the company's new product development, the study on the establishment of the vehicle fuel economy decomposition model will become an indispensable development tool.

Keywords Energy distribution • Fuel consumption • Simulation • Optimization

1 Introduction

Environment and energy is always what human take automobiles, also a international topic which influences worldwide development. Automobiles are related to environment and energy closely, which cost 80 % of total petroleum [1, 2]. As the number of automobiles increases, our economy and culture is developing, but we have to face to the environment pollution and resource problem which automobiles cause. How to deal with this problems is a worldwide question [3, 4].

Therefore, in order to protect environment and resource, each country builds up standards about the performance of automobiles' consumption and emission. Also, as the biggest market, our country releases 《GB 27999-2011 fuel consumption evaluation methods and targets for passenger cars》. It informs the limit of fuel consumption for passenger cars after 2015, showed at Table 1 as followed for example. So decreasing vehicle fuel consumption is absolutely essential in using multiple technique, for being satisfied with official standards.

Table 1 Fuel consumption target for passenger cars in 2015

Crub weight (CM) (kg)	Fuel consumption (L/100 km)
1090 < CM ≤ 1205	6.5
1205 < CM ≤ 1320	6.9
...	...

2 Summarize of Wordwide Advanced Technique

To satisfy the more and more rigorous rules of fuel consumption and emission, the worldwide auto industry is researching more advanced vehicle energy saving technique. So far, as is known to all, there are five ways for the vehicle energy saving, which is high efficient engine technique, drive and transmission technique, vehicle design and optimization technique, hybrid and electric vehicle technique, new fuel technique. Because electric vehicle and new fuel technique is not mature, the most feasible technique is high efficient engine and vehicle design and optimization technique.

2.1 High Efficient Engine Technique

Improving the fuel consumption of engine can exactly improve vehicle fuel consumption. From engine fundamentals, we know that engine fuel consumption depends on its efficiency and mechanical loss. The methods of increasing engine efficiency and decreasing mechanical loss include less friction loss, high compress ratio, EGR, VVT, turbo charge, GDI, HCCI, downsizing and so on.

2.1.1 EGR

EGR (exhaust gas recirculation) means bringing the exhaust gas into intake pipe to combustion again. This technique doesn't only decrease NO_x emission, but also improve fuel consumption. Because there are much double-atom molecules, just like CO₂, inside the exhaust gas, after these molecules return to cylinder, the specific heat ratio of mixed gas is increased, what improves efficiency. Besides, because of the "volume dilution" and "density dilution" influence, mechanical loss is reduced. In addition, by reducing combustion rate and temperature, the heat transfer loss is reduced. So engine fuel consumption is reduced.

2.1.2 VVT

VVT technique is able to bring up intake volume efficiency, cause mixed gas formed and ensure to combust steadily. This technique doesn't only improve performance and fuel consumption, but also reduce emission. The fuel consumption of vehicles is obviously decreased using VVT, which is more and more applied by automobile manufacturer.

2.1.3 High Compress Ratio

High compress ratio brings engine heat efficiency up, what improves fuel consumption. Why heat efficiency of diesel engine is higher than gasoline engine is that the compress ratio of the former is higher than the latter. Because of "knock", compress ratio is limited. However, as GDI, HCCI technique is applied, it is very possible that gasoline engine compress ratio may be increased a lot.

2.2 Vehicle Design and Optimization Technique

Besides engine loss and transmission loss, vehicle loss contains tire rolling resistance, air resistance, acceleration and climbing resistance loss. By optimizing tire, designing vehicle shape and decreasing vehicle weight, these loss may be reduced.

2.2.1 Tire Optimization Technique

Tire looks like foot of vehicle. Vehicle runs by the friction force between tire and road, but will be resisted by rolling resistance caused by "tire elasticity delay". Rolling resistance factor evaluates whether the resistance is big or not. Rolling resistance factor is smaller, rolling resistance is smaller, so vehicle fuel consumption is lower. There are much methods of decreasing rolling resistance factor, such as strengthening tire pressure, increasing tire width and decreasing number of tire layer and so on.

2.2.2 Vehicle Body Shaping Technique

Whether air resistance is big or small depends on vehicle shape, which is named "drag coefficient" that evaluates air resistance. Drag coefficient is smaller, rolling resistance is smaller, so vehicle fuel consumption is lower. Methods of decreasing drag coefficient contains designing plumb curved and streamlined shape with CFD simulation technique.

2.2.3 Vehicle Weight Decreasing Technique

As is known to us, vehicle is more weighty, running resistance is bigger, fuel consumption is higher. So decreasing vehicle weight is very import. Usually, using a mass of synthetic glass, engineering plastics, aluminium alloy and so on instead of steel, is quite efficient. On the other hand, decreasing components' volume is usable, too.

As is said above, fuel loss is various, methods of vehicle energy saving is various, too. If using only one of methods, it is difficult to achieve the target of vehicle fuel consumption, so multiple technique is required to be applied together. However, which methods to choose, what is the percentage of each system such as powertrain, body, chassis and vehicle, how to distribute target of each system, is a question to automobile industry. This thesis tells that by establishing a decomposition model of vehicle fuel economy of consumption, by decomposition on vehicle fuel consumption target value, make it easier to make of vehicle fuel consumption reduction target value to reach.

3 Vehicle Energy Distribution

This part discusses two points, one is whether vehicle simulation model is accurate, and the other is analysis for vehicle energy distribution.

3.1 *Establishing and Verifying the Decomposition Model of Vehicle Fuel Economy of Consumption*

This vehicle model is build up with AVL Cruise, showed in Fig. 1 as followed. Parameters required come from a developing vehicle.

After finishing modeling, add constant drive consumption task, and run. Simulation and test results are showed in Table 2, looking at engine speed, torque and fuel consumption, the inaccuracy is under 3 %, so the simulation model is considered accurate.

3.2 *Analysis for Vehicle Energy Distribution*

Running NEDC cycle by simulation, energy cost for each component is showed in Table 3 and Fig. 2.

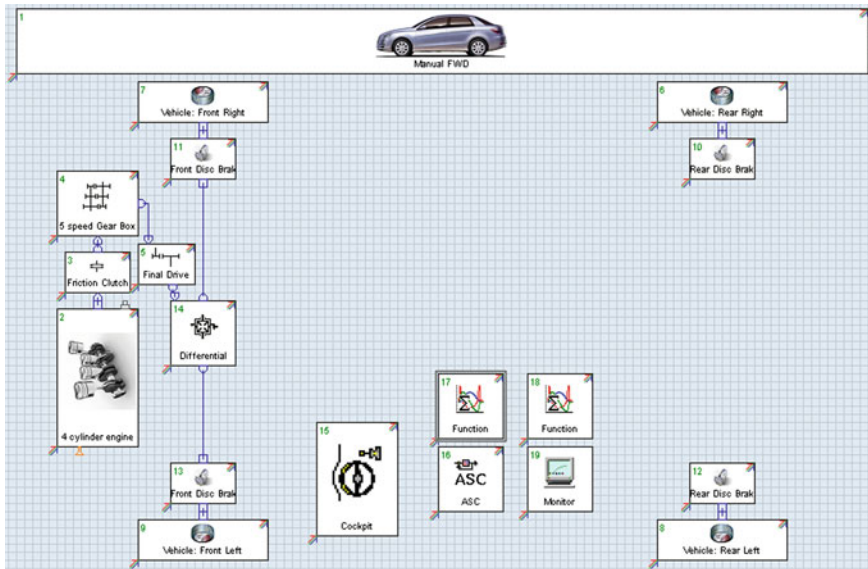


Fig. 1 Vehicle model with AVL cruise

Table 2 Constant drive simulation and test data

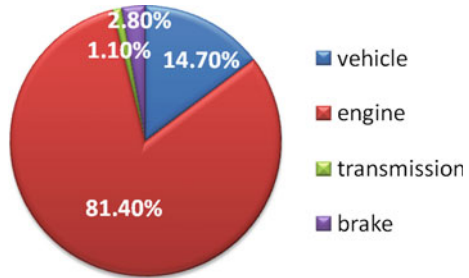
Data	Engine speed (rpm)			Engine torque (Nm)			Fuel consumption (kg/h)		
	Simulation	Test	Inaccuracy (%)	Simulation	Test	Inaccuracy (%)	Simulation	Test	Inaccuracy (%)
50 km/h @ gear4	1854	1860	0.32	19.67	20	1.65	1.68	1.66	1.20
70 km/h @ gear4	2595	2604	0.35	25.34	25.7	1.40	2.69	2.64	1.89
70 km/h @ gear5	2030	2041	0.54	32.21	32.2	0.03	2.34	2.38	1.68
100 km/h @ gear5	2916	2926	0.34	47.56	49	2.94	4.34	4.37	0.69

Obviously, engine energy cost is the most, up to 81.4 %. Therefore, the first way to solve vehicle fuel consumption, is to improve engine economy of fuel consumption.

Table 3 NEDC cycle energy distribution

Cycle	NEDC	
Component	Energy cost (kJ)	Percentage
Vehicle	3715	14.7
Engine	20600	81.4
Transmission	287	1.1
Brake	703	2.8
Total	25305	100

Fig. 2 NEDC cycle energy distribution



4 Engine Energy Distribution

Improving engine economy of fuel consumption is to decrease vehicle fuel consumption. So it is signality to research the energy distribution for each system of engine.

4.1 Establishing and Verifying the Decomposition Model of Engine Fuel Economy of Consumption

As mentioned, this engine is a gasoline one whose displacement is 1.6 l.

This engine model is build up with GT-power, showed in Fig. 3. The left stands for intake side, right for exhaust side and middle for cylinder. The combustion model is Si-wiebe, air fuel ratio is 14.7, the intake and exhaust pipe is modeled by simplifying 3D mechanical structure, which comes from the factual engine.

Referenced to four vehicle constant drive cycle, the engine working point is showed in Table 4.

Comparing with test data, the simulation result of fuel consumption is close, showed in Fig. 4.

So engine simulation model is believable.

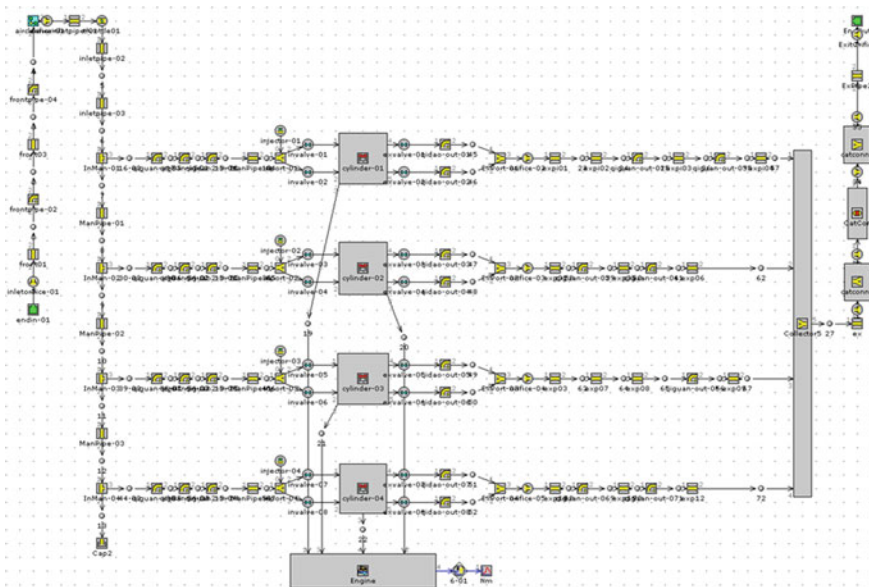


Fig. 3 Engine model with GT-power

Table 4 Engine working point

Cycle	Engine speed (rpm)	Engine torque (Nm)	Fuel consumption (kg/h)
50 km/h @ gear4	1860	20	1.66
70 km/h @ gear4	2604	25.7	2.64
70 km/h @ gear5	2041	32.2	2.38
100 km/h @ gear5	2926	49	4.37

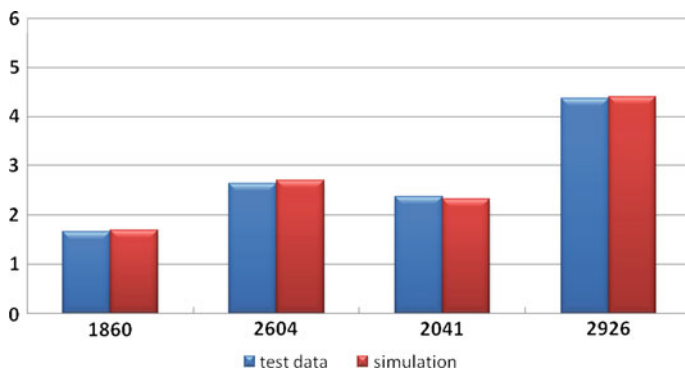


Fig. 4 Engine fuel consumption of test and simulation

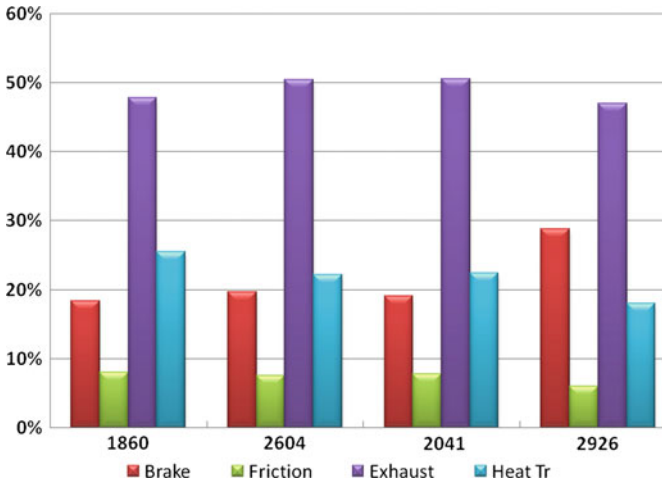


Fig. 5 Engine energy cost distribution

4.2 Analysis for Engine Energy Distribution

Engine energy cost includes brake, friction, exhaust and heat transfer, the distribution for the four cycle is showed in Fig. 5.

It is obvious that engine loss mainly contains friction loss, exhaust loss and heat loss while brake is the power output.

5 Improving Economy of Fuel

Vehicle fuel consumption depends on the engine efficiency in a great measure, which depends on friction loss, exhaust loss and heat transfer loss. As mentioned above, EGR, VVT and high compress ratio technique just makes the engine loss reduced. Therefore, the solution for improving economy of fuel is clear that improving engine economy of fuel by using EGR, VVT and high compress ratio technique, thus vehicle economy of fuel is improved.

5.1 Contribution for Engine Economy of Fuel with Advanced Technique

Filtering out five working points that can stand for engine map and then running above-mentioned engine simulation model, it is predictable that how much engine

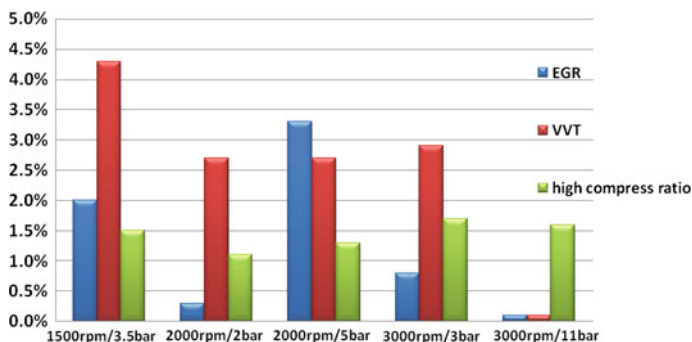


Fig. 6 Percentages of BSFC reduction with EGR, VVT or high compress ratio technology

BSFC decreases by using EGR or VVT or high compress ratio technique, as showed in Fig. 6.

When load is at middle zone such as 2000 rpm/5 bar, effect of EGR is very good, while BSFC is reduced 6 g/kwh, about 3 %. But when load is low, to avoid unstable combustion, EGR doesn't work. When load is heavy, EGR doesn't work too, to make sure that power output is plenteous. So effect of EGR is less better than that load at middle zone.

By using VVT technique, intake kinetic energy is able to be made use, and mechanical loss is decreased. Especially, BSFC shall be reduced from 8 to 12 g/kwh while load is at middle zone.

When compress ratio is raised from 10.3 to 11.0, heat efficiency should be increasing, So BSFC is reduced about 4 or 5 g/kwh at whole zone.

Meanwhile, 3 technique is made application together, BSFC of engine is reduced about 5.2 %, showed in Fig. 7.

5.2 Contribution for Vehicle Economy of Fuel with Advanced Technique

Three technique is made application together, engine economy of fuel is improved a lot. Simultaneously, vehicle economy of fuel is improved too. After being optimized, the vehicle fuel consumption for NEDC cycle is reduced 5 %. The effect is very satisfying, showed in Fig. 8.

Observing the vehicle energy distribution model, engine energy cost is reduced, thus total vehicle energy cost is reduced, so other system cost divided by total vehicle energy is raised, showed in Fig. 9. Because of engine efficiency is higher, energy loss is reduced, so the target for vehicle energy saving is reaching.

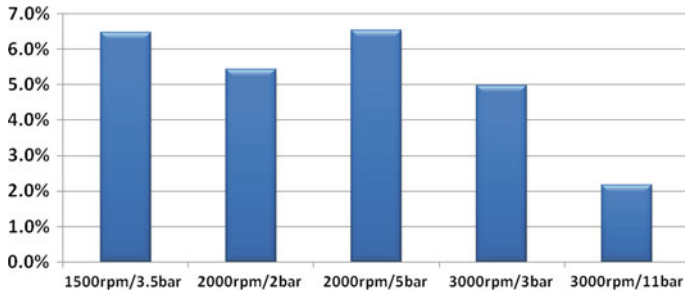


Fig. 7 Percentages of BSFC reduction with EGR, VVT and high compress ratio technology together

Fig. 8 Vehicle fuel consumption for NEDC cycle

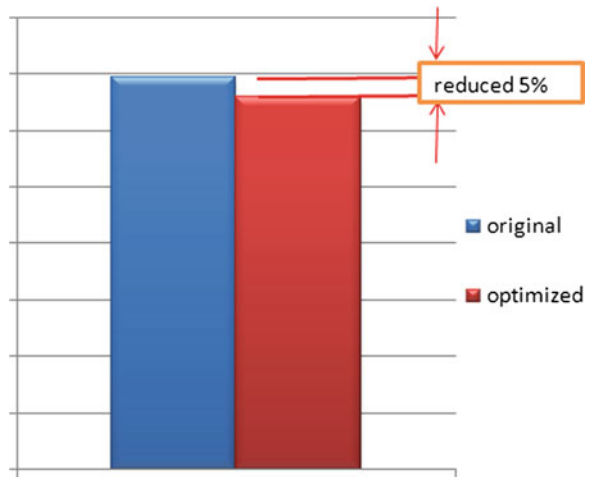
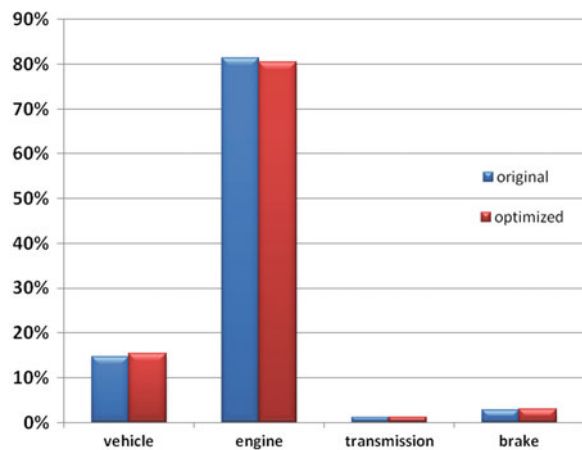


Fig. 9 Vehicle energy distribution for NEDC cycle



6 Conclusion

By establishing a decomposition model of vehicle fuel economy, vehicle involves different areas of the development of a rational energy consumption objectives, can greatly shorten the development cycle and reduce development costs. Therefore, in the future of the company's new product development, the study on the establishment of the vehicle fuel economy decomposition model will become an indispensable development tool.

References

1. AVL. Cruise UserGuid
2. Zhisheng Y (2009) Automobile theory. China Machine Press
3. Shijin S (2011) Automotive engine fundamentals. QingHua University
4. Ping H (2009) Optimized methods of vehicle fuel economy. Automobile engineer

Simulation and Correlation of Commercial Axle Banjo Housing Fracture Under Braking Fatigue Test

Ajay Guddeti and Abhijit Nilangekar

Abstract Three samples of commercial automotive axles were fractured prematurely in lab under braking fatigue test. Crack has initiated at similar location in all three samples. Investigation of fracture was done using Finite Element (FE) approach. Finite element model was validated with strain values which were obtained prior to fatigue test. Correlated model was further utilized for fatigue life prediction. Strain-life approach was used for fatigue life prediction. Fatigue material properties were approximated using Four Point approximation method. Fatigue life estimation was done and compared with braking fatigue test data. Design modifications were suggested to improve the fatigue life. FE analysis and fatigue life was re-evaluated virtually on modified design to endorse the conclusion.

Keywords Rear axle housing · Finite element analysis · Simulation · Braking · Fatigue

1 Introduction

In order to carry and protect the various driving unit of differential and axle shafts from dirt as well as to act as support for various bearings, a substantial enclosing structure known as axle casing or axle housing is used. Provisions are also made in it to attach springs and brake flanges from the stationary member of the brake

F2012-E12-013

A. Guddeti (✉) · A. Nilangekar
AAM Services India Pvt. Ltd, Pune, India
e-mail: ajay.guddeti@aam.com

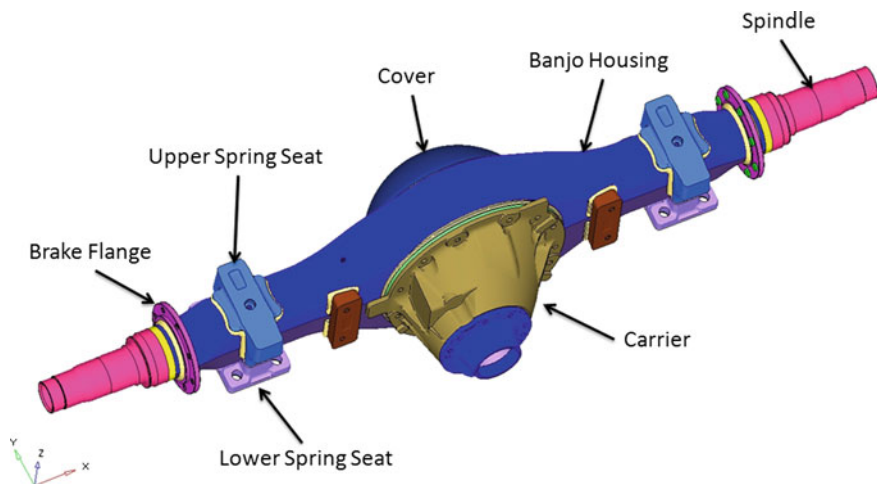


Fig. 1 Commercial automotive rear axle

assembly. Banjo type axle housing is the most widely used axle housing for commercial vehicles. Figure 1 shows typical commercial full float axle.

During the vehicle operation, road surface irregularity causes cyclic fluctuation of stresses on the axle housing, which is the main load carrying member [1]. Therefore it is imperative to make sure whether the axle housing resists against the fatigue fracture for a predicted service life. Axle housing experiences different loads in different direction, primarily vertical load due to curb weight and payload, torsional load because of drive/reverse torque, cornering load due to vehicle negotiating a corner and braking load caused by application of brakes. In real life scenario all these loads vary with time (road-load data). Performing physical test with road-load data is costly, time consuming and sometimes it is not feasible. So there is a necessity to calculate equivalent loading in different direction and acceptable cycles for the same. Most of the OEM's and axle manufacturers have developed this data based on their experience and road load data collected from other axle applications. Usually these loading are converted to sinusoidal type, hence can be easily applied by actuators in the lab.

2 Physical Testing

For the current study, fracture of axle housing under brake flange fatigue test was considered. For this test, axle was placed upside down on fixture for ease of testing. Axle was held fixed at both the spring seat locations. A special brake lever was made to apply braking load to brake flange. Load was applied by servo-hydraulic actuator and load cell at static loaded radius (SLR) in horizontal direction to simulate braking load of vehicle. This test was done on only one side

Fig. 2 Braking fatigue test setup



of axle. Figure 2 shows the test setup. Test was conducted in two phases, first was static test to acquire strain data and second was fatigue test for damage accumulation. Axle was strain gauged at four locations on brake flange and banjo, as shown in Fig. 3. Stacked rosette with 45° was used. Surfaces were prepared before pasting strain gauges. Load was gradually applied on brake lever from 0 to 40,235 N at SLR. Load vs strain data was recorded on one sample during the test. After the static test, strain gauge setup was removed and the same axle and the setup were used for fatigue testing. Half sinusoidal load from 3,591–40,235–3,591 N was applied on brake lever for fatigue loading. Dye penetration test was conducted at regular intervals for crack identification. Also, axle was visually monitored periodically for any cracks or fractures. Three samples were tested for fatigue loading.

Figures 4, 5 and 6 show the banjo housing fracture pictures under braking fatigue test. Crack has observed close to spring seat weld on banjo housing in 45° in all three samples. Sample #1 and #2 were testing on RH side brake flange and sample #3 was tested on LH side, therefore crack orientation in sample #1 and #2 were opposite of sample #3. Crack observation cycles and average test cycles are tabulated in Table 1.

3 Simulation

3.1 Preprocessing

A CAD model of axle and the fixture was used as an input to FEA. Banjo housing and spindle were meshed with linear brick elements. Both spring seats, brake flange, brake lever and fixture base plate were meshed with linear tetrahedral element. Weld was also modelled with linear tetrahedral elements. Bolt head and

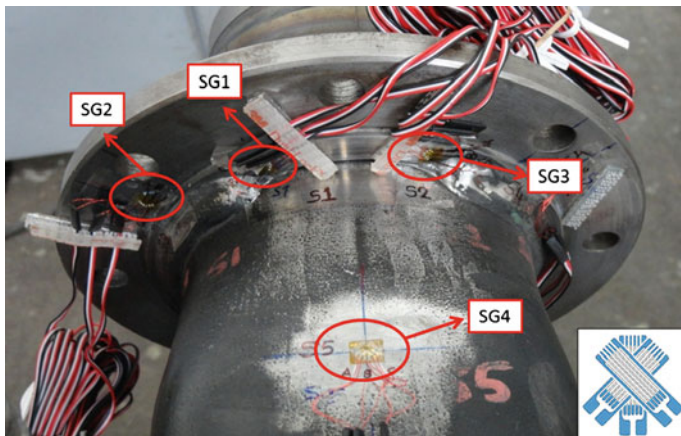


Fig. 3 Strain gauge locations on brake flange and banjo housing



Fig. 4 Sample 1, crack observed after 261,696 cycles

threads are modelled by rigid elements spiders. These spiders are then connected by beam (1-D) elements. Bolt pretension was defined for bolting connection of brake lever to brake flange. In testing both spring seats were clamped to fixture base plate, so at this location also bolt pretention was defined. Contact has been defined for interaction between different parts wherever appropriate.

Figure 7 shows meshed model and FEA setup of braking load case simulation. Braking force 40,235 N was applied in horizontal direction on brake lever using rigid element. Load was applied at SLR. Outer four holes of fixture base plate were held fixed in all degree of freedom using rigid elements to replicate testing condition. ABAQUS software was used for stress analysis.

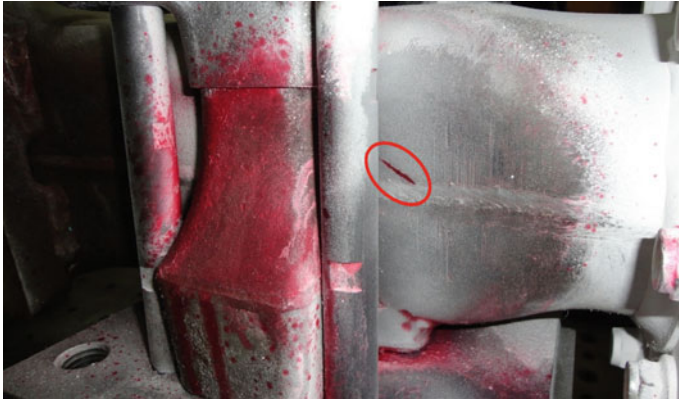


Fig. 5 Sample 2, crack observed after 296,707 cycles



Fig. 6 Sample 3, crack observed after 136,186 cycles

Table 1 Brake fatigue test results

	Crack observed after	
Sample 1	261,696	Cycles
Sample 2	296,707	Cycles
Sample 3	136,186	Cycles
Average	231,530	Cycles

3.2 Approximation of Fatigue Material Properties

In the absence of adequate data on constant strain-amplitude, it is often necessary to approximate the strain-life curve from monotonic tensile properties [2]. For this reason one of the banjo housing which was fractured in braking test was selected

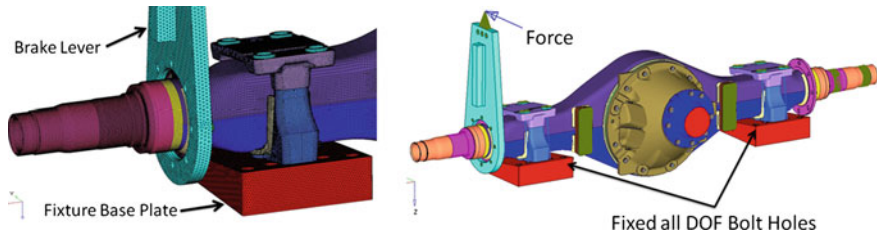


Fig. 7 Meshed model and FEA setup of braking fatigue

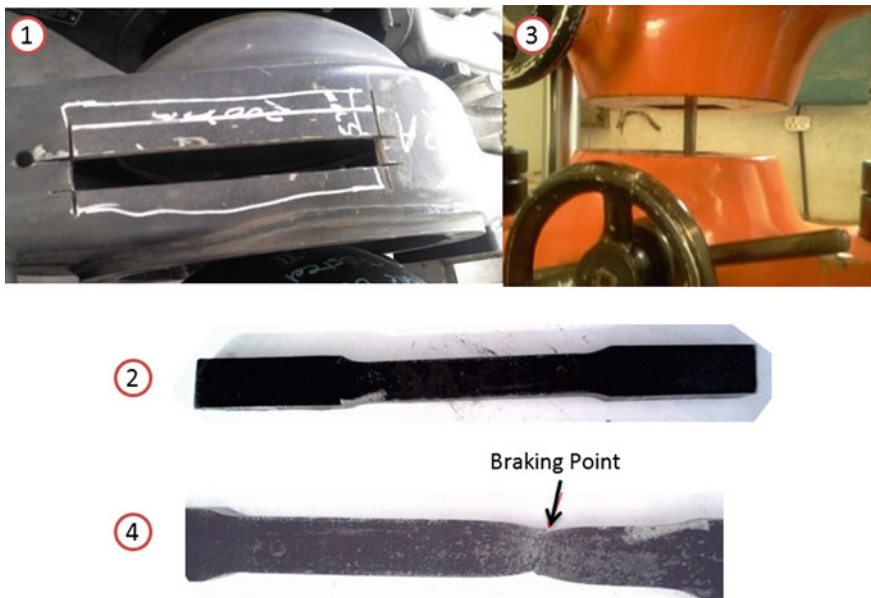


Fig. 8 1 Banjo housing trim for tensile test specimen, 2 tensile test specimen, 3 test specimen on tensile test machine, 4 test sample after fracture

for extracting tensile test specimen. The specimen was cut from the flat portion of the bowl region which was not under braking load path. This is shown in Fig. 8. This was then tested on tensile test machine for monotonic properties.

Tensile test results for the extracted specimen are shown in Table 2. These results were further used in approximating fatigue material properties.

For fatigue analysis, strain-life (ϵ -N) approach was used. Strain-life approach offers greater diversity of materials. Because it does not necessarily attempt to relate to total failure (separation) of the part, but can rely on what has become known as “initiation” for defining failure. It includes plastic response, addresses finite-lived situations on a sounder technical basis and has greater adaptability to variable amplitude situations [2].

Table 2 Tensile test results

Width	Thickness	Initial gauge length	Final gauge length	Yield load	Ultimate load	Yield stress	Ultimate stress	% Elongation	% Reduction in area
mm	mm	mm	mm	kN	kN	N/mm ²	N/mm ²		
15	10	70	87.8	64.2	82.16	428	547.7	25.4	61.17

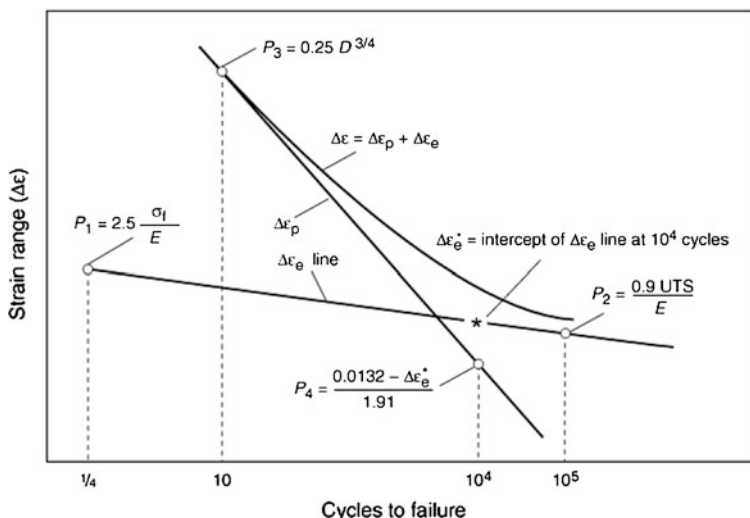


Fig. 9 Schematic of fatigue life curve with the manson four-point criteria [2]

It has long been recognized that fatigue data, when resolved into elastic and plastic terms, can be represented as linear functions of life on a logarithmic scale. Figure 9 schematically shows this representation of elastic and plastic components, which together define the total fatigue life curve of a material [2].

The fatigue-life relations for elastic and plastic strain amplitude are expressed in terms of the strain range, is as follows:

$$\frac{\Delta \epsilon_e}{2} = \frac{\sigma'_f}{E} (2N_f)^b \tag{1}$$

$$\frac{\Delta \epsilon_p}{2} = \epsilon'_f (2N_f)^c \tag{2}$$

Therefore, the total strain amplitude can be expressed as the sum of Eqs. 1 and 2 such that:

$$\frac{\Delta \epsilon}{2} = \frac{\sigma'_f}{E} (2N_f)^b + \epsilon'_f (2N_f)^c \tag{3}$$

where,

- Δε/2 Strain amplitude
- 2N_f Number of Reversals
- Δε_e Elastic Strain Range
- Δε_p Plastic Strain Range
- σ'_f Fatigue Strength Coefficient
- b Fatigue Strength Exponent
- ε'_f Fatigue Ductility Coefficient

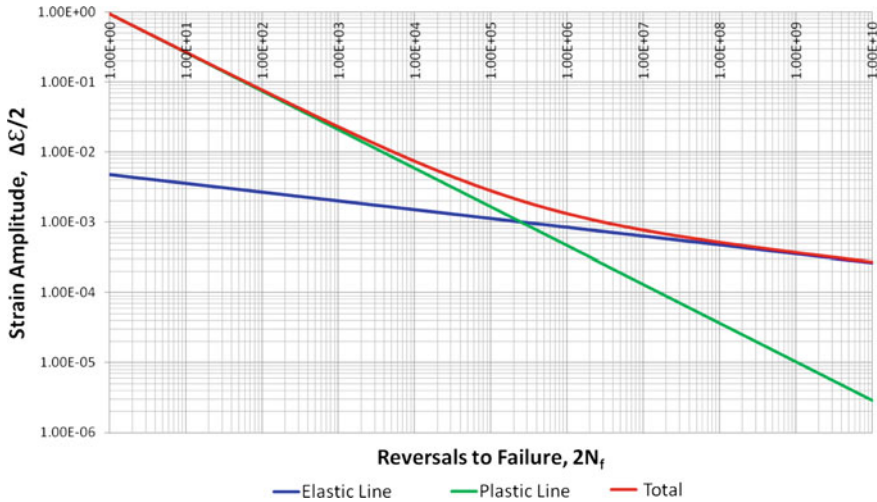


Fig. 10 Approximated strain-life curve for banjo housing material

- c Fatigue Ductility Exponent
- σ_f Fracture Stress in a Tensile Test
- E Elastic Modulus
- UTS Conventional Ultimate Strength
- R_A Percent Reduction in Area of Tensile Test Specimen
- ϵ_f and D Conventional Logarithmic Ductility

3.2.1 Strain-Based Four-Point Method

The Four Point method initially was developed in terms of strain range by Manson. The four points in Fig. 9 are determined as follows [2]:

- Point P_1 on the elastic strain line is positioned at $N_f = 0.25$ cycles and at an elastic strain range of $2.5 \sigma_f/E$
- Point P_2 on the elastic strain line is positioned at $N_f = 10^5$ cycles and at an elastic strain range of $0.9 UTS/E$
- Point P_3 on the plastic strain line is positioned at $N_f = 10$ cycles, where the plastic strain range is $0.25D^{3/4}$, where D is $\ln(1/1-R_A)$
- Point P_4 on the plastic strain line is positioned at $N_f = 10^4$ cycles, where the plastic strain range is given by $0.0069-0.525 \Delta\epsilon_e$.

With the above Four Point method strain-life curve for banjo housing material was constructed and same is shown in Fig. 10.

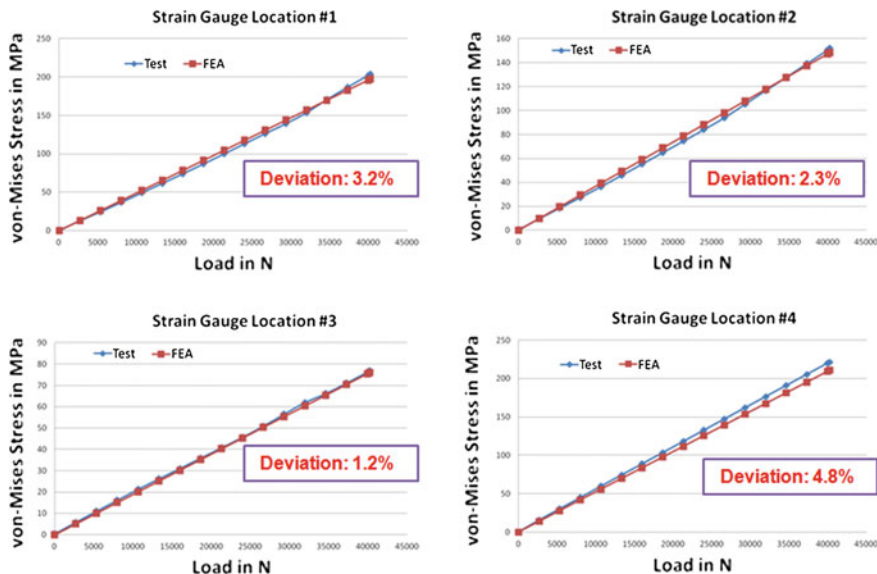


Fig. 11 Test to FEA correlation results for static braking load

Value of Fatigue Strength Exponent, “b” varies between -0.05 and -0.12 and Fatigue Ductility Exponent “c” varies between -0.5 and -0.7 . The Fatigue Strength Coefficient, σ'_f , is approximately equal to σ_f for many metals and Fatigue Ductility Coefficient ϵ'_f is approximately equal to ϵ_f [2].

4 Results and Discussions

4.1 Braking Test Strain Correlation

Following graphs (Fig. 11) shows Test to FEA correlation for static braking load. von-Mises stresses were calculated from strain data [3] and the same was compared with von-Mises stresses obtained from FEA. Stress deviation is below 5 % in all four locations. This validates FEA model.

Max-Principal stress contour of static braking analysis is shown in Fig. 12. High stress region was observed at spring seat weld end location on banjo housing. The weld is under tensile load.

Direction of max principal stress tensor in FEA is shown in Fig. 13; expected crack direction will be perpendicular to max principal tensor direction, which is correlating with the test. Sample #1 and #2 were testing on RH side brake flange and sample #3 was tested on LH side, therefore crack orientation in sample #1 and #2 were opposite of sample #3.

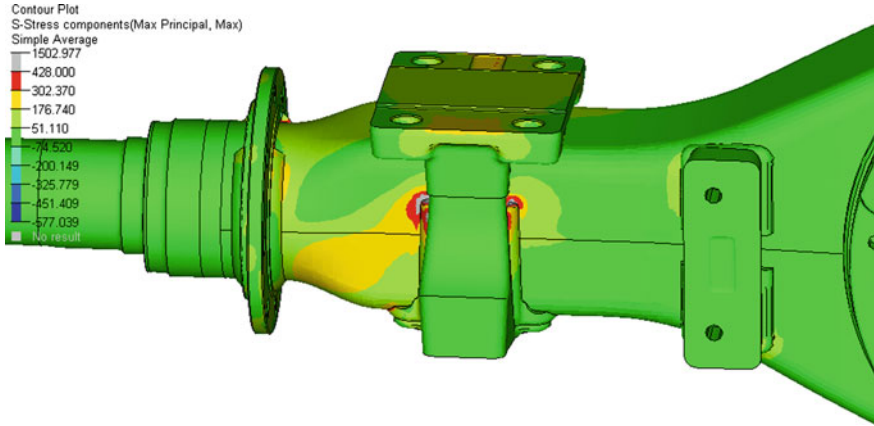


Fig. 12 Max-principal stress contour for static braking load case simulation

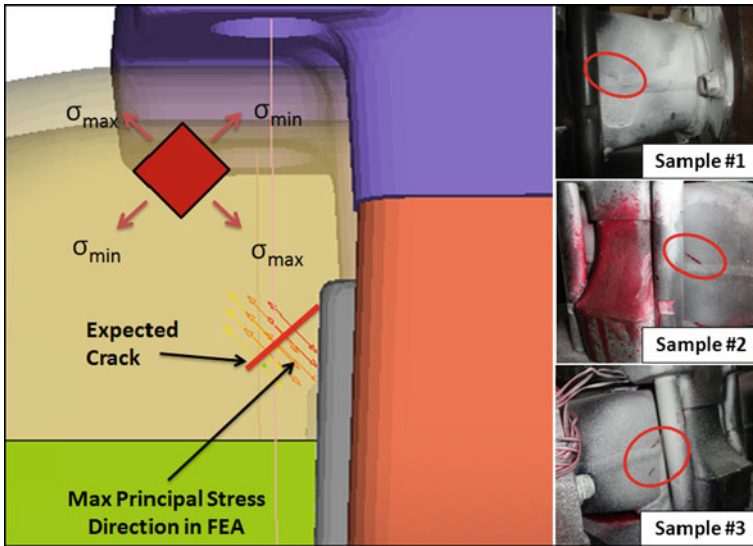


Fig. 13 Correlation of expected crack direction in FEA vs test

Table 3 Approximated fatigue material properties for banjo housing using four point method

Fatigue strength coefficient, σ_f'	995.79
Fatigue strength exponent, b	-0.12554
Fatigue ductility coefficient, ϵ_f'	0.94597
Fatigue ductility exponent, c	-0.55135

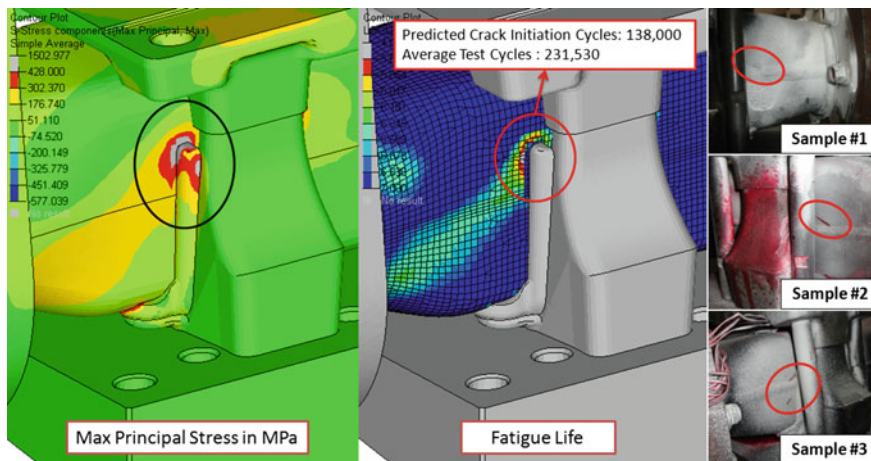


Fig. 14 Max principal stress and crack initiation cycles

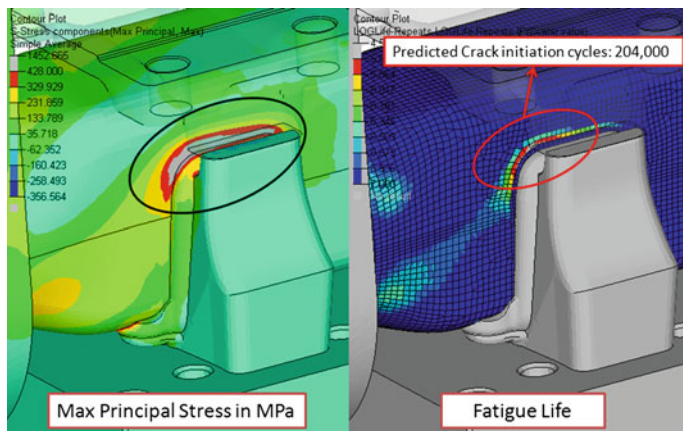


Fig. 15 Max principal stress and crack initiation cycles for improved design

4.2 Fatigue Correlation

To simulate the cyclic load applied on brake lever in test, fatigue analysis was done using fatigue properties shown in Table 3. The load was cycled from min to max braking load (3,591–40,235–3,591 N). Fe-safe was used to perform fatigue analysis. The spring seat weld end has undergone a cyclic tensile stress. As the high stresses were observed around weld end location, fatigue life was also low at the same location. Figure 14 shows predicted crack initiation cycles of 138,000 cycles where as average test cycles were 231,530 cycles and minimum test cycles were 136,000 cycles. The difference between predicted cycles and average test

cycles can be attributed to crack propagation in actual test sample; hence good correlation has been established.

To make the design better it has been proposed to make a small cut out in spring seat and continue the weld all around the spring seat. With this design modification stress concentration at weld end has reduced and it has been spread across the length of banjo housing. This has improved fatigue life by 48 %. Figure 15 shows the max principal stress and crack initiation cycles.

5 Summary and Conclusion

Fracture of three commercial axle banjo housings under braking fatigue test were investigated by finite element analysis. Finite element model was developed for simulation of this fracture. Model was first correlated with strain gauge values from static test. Very good correlation has been established with developed model. The same model was further utilized for fatigue analysis. High stress region was observed on banjo at weld termination region. FEA has accurately predicted the fracture location through fatigue analysis. Also good correlation was established for crack initiation cycles. Hence, approximated fatigue material properties through monotonic tensile test were validated. These fatigue properties can further be used to simulate other fatigue load cases such as beaming, cornering etc. Alternate approach has been suggested to increase fatigue life by simply continuing/extending weld on banjo housing in linear direction.

References

1. Topaç MM, Günal H, Kuralay NS (2009) Fatigue failure prediction of a rear axle housing prototype by using finite element analysis. *Eng Fail Anal* 16: 1474–1482 (Turkey)
2. (1996) ASM handbook, fatigue and fracture, vol 19. ASM Publication, ISBN 0-87170-385-8
3. Gere JM (2001) *Mechanics of materials*, 5th edn. Thomson Books/Cole Publication. 2004, ISBN 981-254-863-7

Development of a Vehicle Simulator Based on a Real Car for Research and Education Purposes

Zsolt Szalay, Péter Gáspár, Zoltán Kánya and Dávid Nagy

Abstract The chapter presents a hardware-in-the-loop simulation environment, which is built in such a way that the simulator tends to the real vehicle functions as much as possible. The simulation system contains several components such as an Human Machine Interface (HMI), a high-accuracy validated simulation software operated on a PC and a visual system with real-time graphics. The simulator is equally suitable for educational and research purposes. All the vehicle engineer students use the simulator system during their curriculum, enabling the thorough understanding of modern vehicle functions, thus improving the competence of future generations of engineers. Moreover, the simulator system projects ahead the opportunity of new vehicle research that induces considerable additional scientific results.

Keywords Vehicle simulator · Embedded functions · Driver assistance systems

F2012-E12-015

Z. Szalay (✉)

Department of Automobiles, Budapest University of Technology
and Economics, Budapest, Hungary
e-mail: zsolt.szalay@auto.bme.hu

P. Gáspár · D. Nagy

Systems and Control Laboratory, Computer and Automation
Research Institute, Budapest, Hungary

Z. Kánya

Inventure Automotive Electronics R&D, Budapest, Hungary

1 Introduction

A vehicle simulator system which is based on a real car (Audi TT Coupe) is developed. The simulator system is unique because it uses a real car for receiving the input signals of the driver and displaying information about the simulation. The real car can be switched to simulation mode by a push-button switch. The system is safe: the additional electronic units are isolated galvanically from the original electrical system of the vehicle and in the simulation mode the vehicle engine cannot be started (Fig. 1).

The purpose of the simulator system is twofold. One is the integration of the simulator system into the education of vehicle engineering. The simulator system is based on a real vehicle, and it uses high technology solutions which are applied in modern vehicles.

Modern technology and the realistic driving experience of the simulator increase the motivation of the students, and the simulator system ensures the better understanding of the vehicle dynamics, vehicle control systems, the system design methods and the electrical, computational and communication systems. The modular and flexible structure of the system enables the implementation of a number of vehicle control systems on the simulator, and additional electronic control units (ECU) and sensors can also be installed. On the other hand, the vehicle simulator is also a basis for research activities. The achievements of vehicle control research can be demonstrated and tested on the system, and a number of measurements can be carried out on the simulator—e.g., for investigating driver behavior. Furthermore the modular structure ensures that optional equipment (e.g., additional ECUs, sensors or actuators) can be fitted into the system for running hardware-in-the-loop simulations.

2 Structure of the Vehicle Simulator

The main concept of the vehicle simulator is shown in Fig. 2. The driver sits in the driver seat and controls the accelerator and brake pedals, the steering wheels and the transmission selector lever such as in real life, but the vehicle does not move. The simulation of the vehicle model and the environment (road, terrain, etc.) are run on the simulator PC. The simulation software calculates the vehicle motions by validated vehicle models then the scene is visualized in real time. The visualization of the vehicle and the environment are projected in front of the driver by a projector.

The specialty of the system is that the driver's cabin of the simulator is set up on the base of a real car and with one single switch the simulator can be converted back to a conventional road vehicle. The challenge is to keep the original vehicle functions intact while implementing simulation functions. For this reason the control of the vehicle's communication network has been taken over by the vehicle control panel, implementing full RBS simulation for the instrument cluster in



Fig. 1 Vehicle simulator system

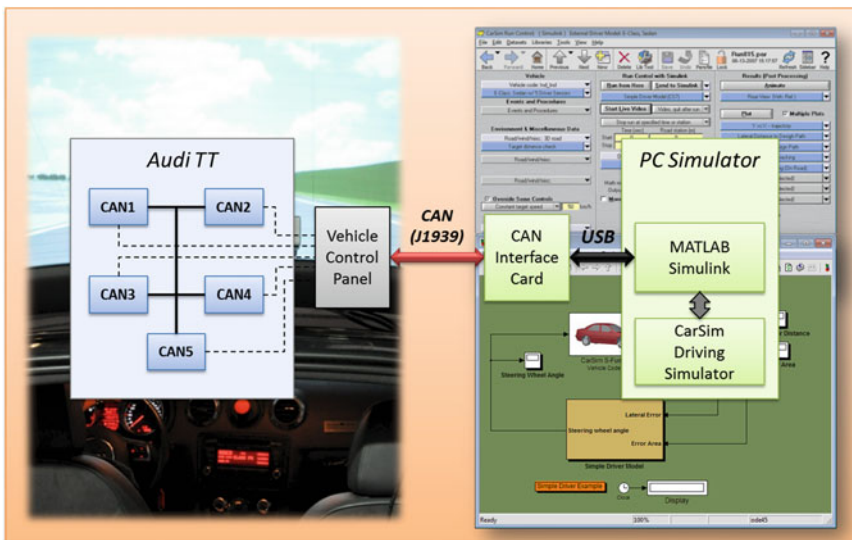


Fig. 2 The concept of the vehicle simulator

simulation mode. The standing vehicle can be ‘driven’ exactly the same way as on a test track: there is engine sound and screech while skidding; the dash panel displays the current speed and the engine rpm and one can shift gears just like in real life.

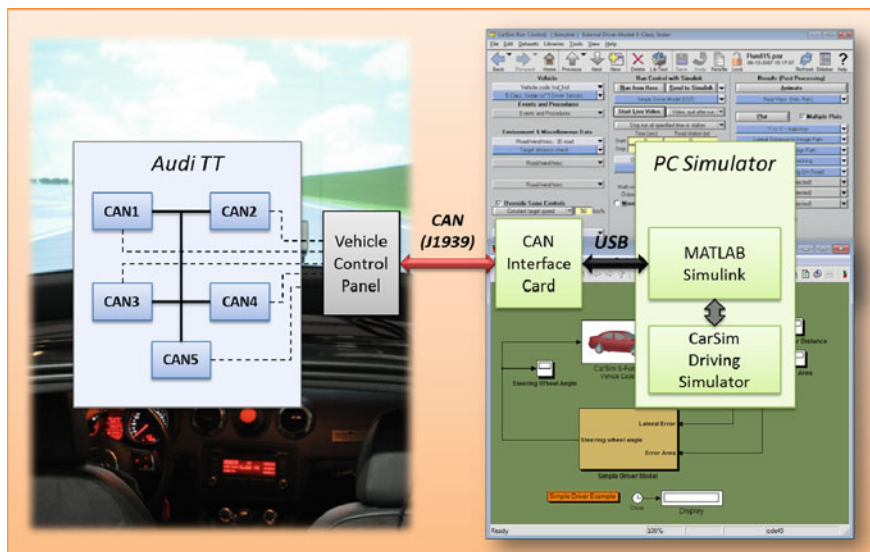


Fig. 3 Structure of vehicle simulator

The main advantage of keeping the original vehicle functions is that the system allows further educational and research opportunities. Keeping the moving capability of the vehicle enables real dynamic measurements on a test track, which induce more research projects; e.g., control-oriented vehicle model identification tasks or implementation of novel vehicle dynamic control algorithms. Modular and multilevel system architectures are applied at the development of the simulator components for ensuring simple further extensions of the system.

The structure of the vehicle simulator system is shown in Fig. 3. The simulation consists of two parts. One is the vehicle incorporating Human Machine Interface (HMI) functions, the other is a simulator application based on a PC which implements the physical model of the vehicle and the environment. As vehicle simulations are carried out with the engine switched off the missing internal signals are also generated in the vehicle to ensure the basic functions. During the modification of the electronic system of the vehicle crucial requirement was to provide plausible sensor signals which are necessary for control using the electronic systems of the real AUDI TT Coupe test vehicle. A standard (J1939), duplex and real-time CAN communication line was built between the vehicle control panel and the simulation PC. The simulation PC uses a standard CAN interface card for receiving and transmitting the specific input and output signals of the simulation.

The driver can induce various vehicle maneuvers by using the steering wheel, the accelerator/brake pedals of the real car. The vehicle model and the simulation environment are built in the complex vehicle dynamics software CarSim. The models are implemented in MATLAB/Simulink environment because it enables

the simple extension of the model with the CAN communication, the control systems and optional additional system models. The simulation is run in MATLAB/Simulink environment using the differential equation solvers of MATLAB. The MATLAB/Simulink simulation communicates with CarSim which visualizes the scene in quasi real-time. Based on the excitations and the control signals of the driver, the MATLAB/Simulink model generates the signals of the vehicle motions during the simulation. Then the CarSim Driving Simulator shows the vehicle maneuvers by quasi real-time graphics projected in front of the vehicle, and it provides the signals during the journey. Since the conditions of the simulation can change various simulation experiences are achieved.

3 Vehicle Control Panel

During the development of the vehicle control panel, it was a basic requirement to reach the essential sensor information of the electronic system of the vehicle. The specific signals (e.g., pedal and steering wheel positions) are sent to the simulation PC via the vehicle control panel. The control panel contains standard J1939 duplex CAN gateway electronics, and it is extended with other components which ensure the comfort and safe operation of the simulator system such as an engine sound generator and operation mode selector electronics. The cockpit and the vehicle control panel are shown in Fig. 4.

Besides the gateway function, the other important task of the control panel is taking over the control of the vehicle dashboard in the simulation modes. It requires that the control panel simulate the full electronic system of the vehicle in order to display the vehicle speed, the engine rpm, the engine temperature and the actual gear on the dashboard without any error messages. The residual bus simulation (RBS) is implemented on the vehicle control panel, and it emulates a real vehicle electronic environment to the dashboard electronics. The vehicle control panel receives signals from the simulation PC via the CAN bus then displays them on the dashboard.

Furthermore the vehicle control panel ensures the safety of the system. In normal vehicle operating mode, it galvanically decouples the additionally installed electronic devices from the original electronic system of the vehicle. The control panel makes the simulation safe as well with by preventing the engine from being started in simulation operation mode.

3.1 Operating Modes of the Vehicle Control Panel

The vehicle control panel installed on the Audi TT Coupe has the following operating modes.

Fig. 4 The cockpit and the vehicle control panel



1. Normal mode

In normal mode the vehicle operates 'normally', i.e., like a conventional road vehicle. This mode is safe: the additional electronic devices installed subsequently are isolated galvanically from the original electronic system of the vehicle. This mode is used for regular travelling. If the emergency switch placed in the middle of the vehicle console is pushed, the system returns into this mode.

2. Sensor test mode

In the sensor test mode a simple and quick test of the control panel and the communication system can be run without any other devices (e.g., a PC). In this mode, the accelerator and brake pedal position, the steering wheel angle and the selected gear are displayed on the vehicle dashboard.

3. Demonstration mode

In demonstration mode, the embedded software of the control panel runs a demo which demonstrates the main outputs (e.g., dashboard functions and sound generator) of the gateway without any additional devices.

4. Autonomous simulation mode

In this mode, the control panel simulates a simplified vehicle model in order to test the main functions and the communication of the simulation system without any additional devices such as a simulation PC. The accelerator and brake pedals, the steering wheel, the transmission selector lever and the simulation function of the dashboard can be checked easily in this operating mode; the sound generator provides the engine sound, as well.

5. PC simulation mode

The PC simulation mode is the most relevant operating mode in the vehicle simulator system. In this mode the vehicle is used as an HMI of the simulation run on the simulation PC. Furthermore it provides a feedback of some information to the driver by displaying the vehicle speed, engine rpm, etc. on the dashboard.

The simulation mode is safe: the vehicle engine cannot be started in this mode. The vehicle control panel transmits the following signals to the simulation PC:

- Accelerator pedal position and kick-down switch status
- Brake pedal position, pedal status
- Steering wheel angle
- Gearbox selector lever position
- Parking brake status
- Battery voltage

The signals received from the electronic system of the vehicle are read and transmitted continuously by the control panel; the most important signals (e.g., pedal and steering wheel positions) are sent with 10 ms sampling time and the less important signals (e.g. engine temperature and battery voltage) with 50–100 ms. The duplex CAN gateway can also receive CAN messages from the simulation PC and the relevant information is displayed on the vehicle dashboard. The MATLAB/Simulink simulation calculates the motion of the vehicle and the following signals are sent back to the vehicle control panel in order to be displayed on the dashboard in quasi real-time:

- Vehicle speed
- Engine speed
- Selected gear
- Engine coolant temperature
- Other indicator or error lights

In PC Simulation mode the engine and tire sound are generated by the CarSim, and the sound signals are fed into the original audio system of the vehicle. The system provides realistic driving experience while the driver is sitting in a real car; see Fig. 5.

6. Measurement mode

In the measurement mode the vehicle operates in the same way as in normal mode but the vehicle control panel still has the contact with the electronic system of the vehicle. In this mode, the vehicle control panel functions as a gateway; it reads the CAN messages on the five separate CAN buses of the vehicle and the additional sensor modules, then transmits the relevant messages to the PC CAN interface card. For safe operation, it is forbidden to send any messages towards the vehicle. The structure of the measurement system is shown in Fig. 6. The PC logs the CAN data received by the CAN interface card.

4 Simulation Software

The vehicle model, the road, the environment and the scenario of the simulation are built in CarSim. CarSim is a stand-alone simulation software which contains a



Fig. 5 Full in-car driving experience

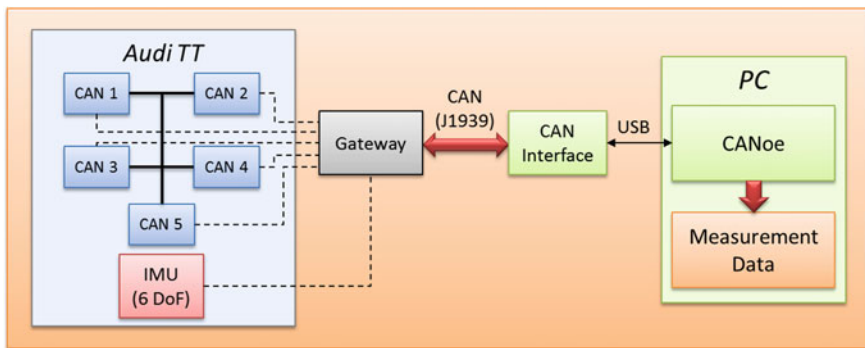


Fig. 6 The structure of the measurement system

number of validated complex vehicle models of passenger cars, racecars, light trucks and utility vehicles. Custom vehicle component models can be built as well or even replaced by external custom models; e.g., models built in Simulink or even written in C programming language. The software is able to use its own solver and cooperate with external software such as MATLAB. Other software components are available for the basic CarSim environment; modules for modeling flexible chassis, for using dSpace AutoBox for hardware-in-the-loop (HIL) simulations and so on. For the vehicle simulator the basic CarSim is extended with a Driving Simulator. This extension module ensures the real-time running and visualization of the scene. The vehicle model generated by CarSim is embedded in a Simulink model.

The Simulink model also contains the communication functions which receive and transmit the CAN messages by the CAN interface card. The positions of the pedals, the steering wheel and the transmission selector lever are fed into the

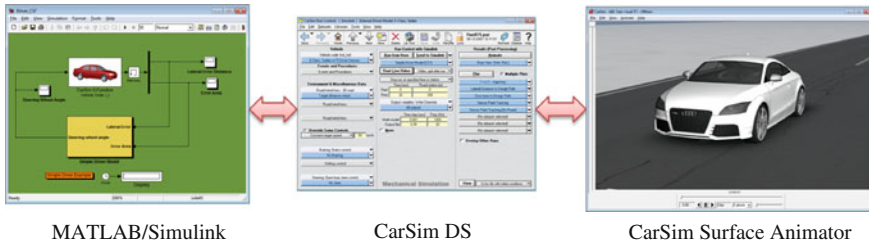


Fig. 7 Screenshots of the simulation software

vehicle model. Any signals of the vehicle model (e.g., positions, velocities and accelerations) can be read and used by the control systems. Vehicle control systems, designed in MATLAB/Simulink, are added to the simulation model. Figure 7 shows the screenshots of the simulation software.

The vehicle simulator uses mainly a custom vehicle model which is built for simulating the real Audi TT. Other built-in CarSim vehicle models are used for testing vehicle control algorithms as well. The purpose is to build a more sophisticated vehicle model for the simulator which converges to the real car. The validation of the vehicle model is carried out by measurements.

5 Education Purposes of the System

When the topic of ‘Systems and Control Theory’ is taught the theoretical methods can be illustrated in a simulation environment, see [1–3]. An important topic is the demonstration of the control design methods applied in the industry [4]. For example, the operation of an ABS/ESP or a ROP (Roll Over Prevention) control can be presented. The effect of changes in the control parameters can be further analyzed. Moreover, the simulation system supports the training of the driver. Different driver behaviors can be simulated and analyzed. Different responses to emergencies during vehicle maneuvers can be compared and the cause-effect relationships can be explored. In this way the appropriate response can be practiced.

Using the simulator system during lectures of “Automotive Communication Systems” students can understand how the CAN networks of vehicles are structured and what residual bus simulation means in practice. As the complete CAN communication to the instrument panel is taken over by the control panel in simulation mode, high level understanding of the operation is demonstrated.

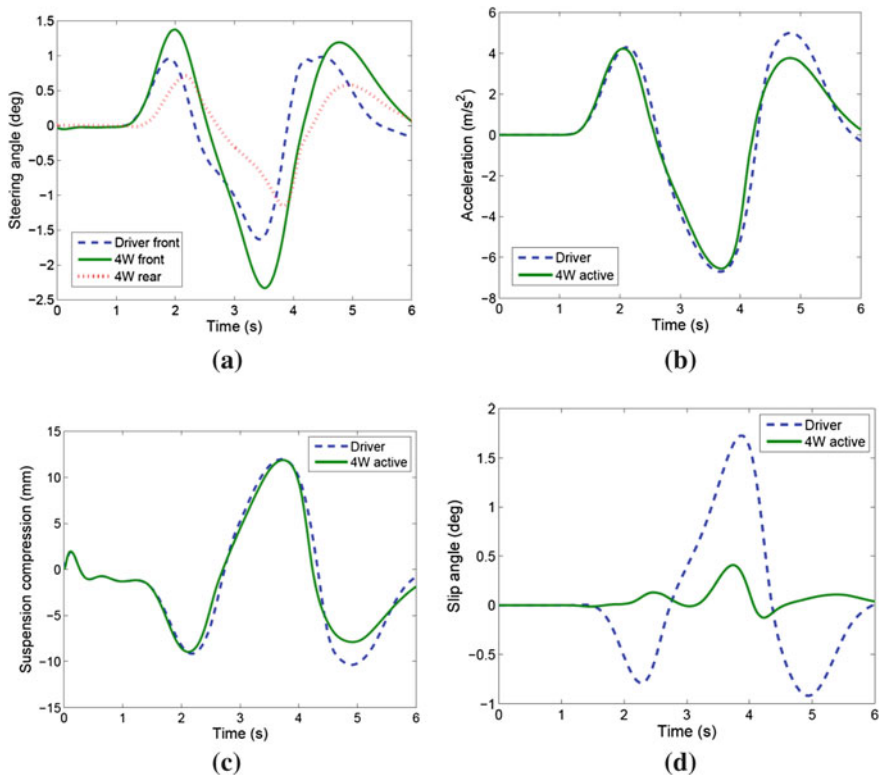


Fig. 8 Example of a trajectory tracking control algorithm tested on the vehicle simulator (steering angle, acceleration, suspension compression, slip angle)

6 Research Activities of the System

The vehicle simulator is also a basis for research activities. Various journey scenarios can be generated by the simulation system. The advantage of the system is that besides measuring various signals, i.e., the steering angle, the positions of the accelerator and the brake pedal or the gear level, in principle any signals can be monitored during the simulations. In this way signals which are not measurable in practice can be obtained for analysis purposes. Below some research directions are presented.

A. Trajectory tracking

The purpose of trajectory tracking is to follow road geometry at a predefined velocity and guarantee the road stability of the vehicle simultaneously. Several vehicle control components can be applied such as the brake or the steering. In the control design the interaction and priorities between the controllers must be taken into consideration. The time responses of the trajectory tracking algorithm based on 4WS (Four Wheel Steering) implemented on the simulator are illustrated in Fig. 8.

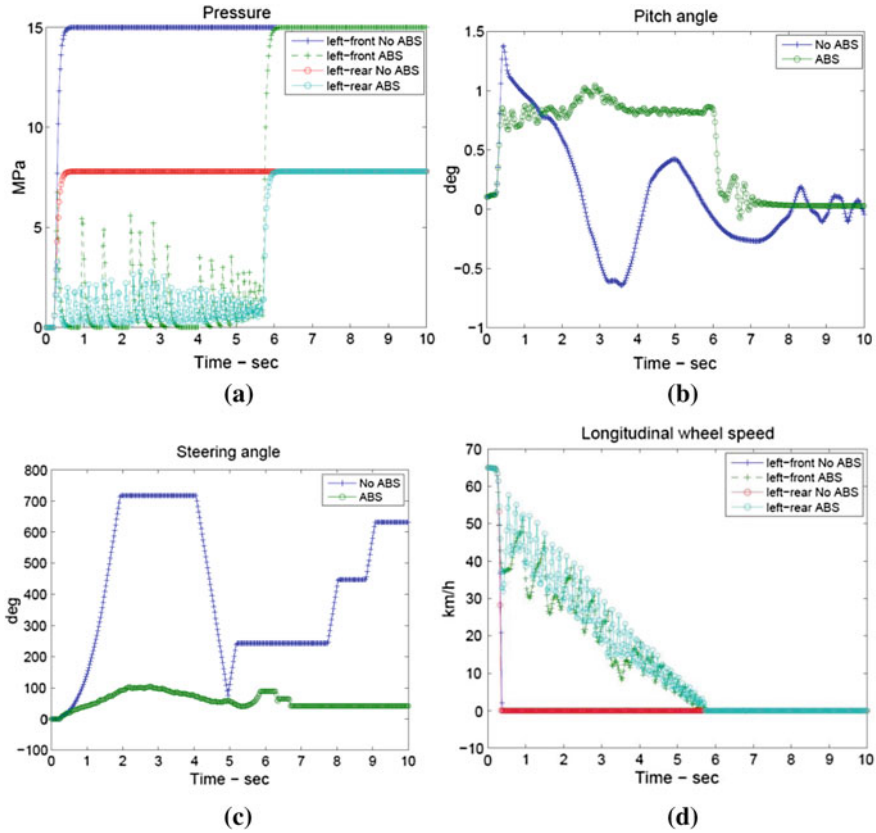


Fig. 9 Example of a vehicle stability control algorithm tested on the vehicle simulator (brake pressures, pitch angle, steering angle, longitudinal speed)

B. Mu-split control

When hard braking is taking place on a road on which friction significantly differs between the left and the right wheel paths (mu-split), the vehicle may rotate over the wheel path. There are several control methods which are able to handle this emergency. As an example the time responses of the operation of the brake control are depicted in Fig. 9.

C. Driver assistance systems

Driver assistance systems usually support the driver activities, since they have more information about the vehicles, the road (adhesion) and the environment (traffic signs, speed limit). A general solution is that the driver requirements are built into the automatic control system, e.g., sport and comfort style. In a typical sport mode the steering responses are sharper, the ride is firmer and the driving response improves. In comfort mode, these features are considerably less sharp. An example of the vehicle control algorithm can be seen in Fig. 10.

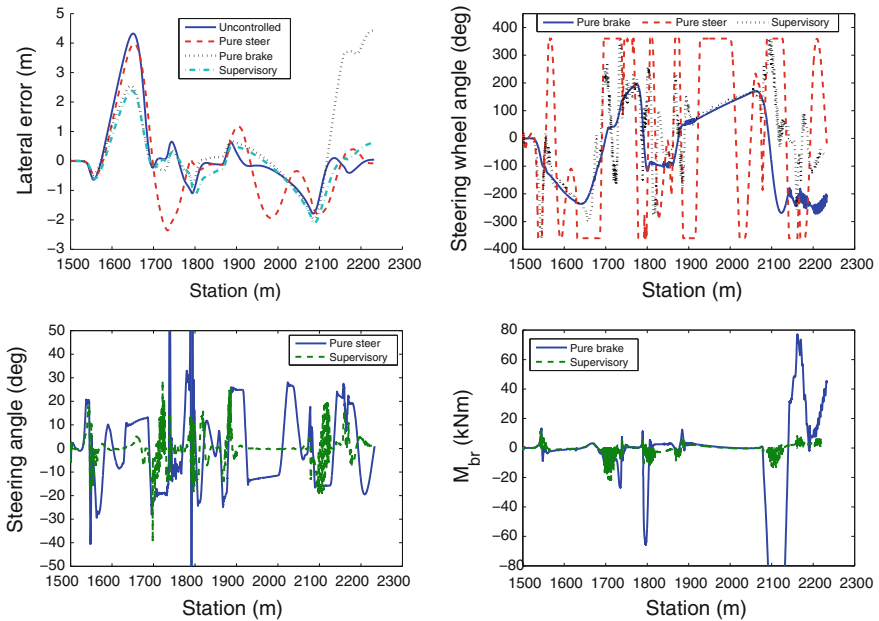


Fig. 10 Example of an integrated vehicle control algorithm tested on the vehicle simulator (lateral error, steering wheel angle, steering angle, brake yaw moment)

7 Conclusions

A real-vehicle-based simulator has been developed and tested, with the advantage of simultaneous use in education and scientific research on virtual or real test tracks. The unique feature of this simulator system is that the HMI of the simulator is a cockpit of a real car, which can also be driven as a normal vehicle on the real test track. The significance of such a simulator in university education is that the students are much more motivated in this environment, while the researchers are enabled to implement autonomous driving functions on the running vehicle.

Acknowledgments The development was supported by the project of Vehicle technology, transport and logistics (JKL) Research University Program by grants TÁMOP-4.2.1/B-09/KMR-2010-0002 and TÁMOP-4.2.2.B-10/1-2010-0009.

References

1. Gillespie T (1992) Fundamentals of vehicle dynamics. Society of Automotive Engineers Inc., Warrendale
2. Pacejka HB (2004) Tyre and vehicle dynamics. Elsevier Butterworth-Heinemann, Oxford
3. Rajamani R (2005) Vehicle dynamics and control. Springer, New York
4. Trachtler A (2004) Integrated vehicle dynamics control using active brake, steering and suspension systems. *Int J Veh Des* 36:1–12

Early Verification of Complex Distributed Systems Using Model Driven Development and Virtual Engineering

Lance Brooks, Jun Wu and Darrell Teegarden

Abstract *Research and/or Engineering Questions/Objectives* System-level modeling accelerates the development of distributed mechatronic systems by automating tasks and maintaining the integrity of validated executable specifications and test benches. This paper presents a systematic distributed embedded system development methodology that provides abstraction of hardware and software concerns, facilitates communication via highly accessible models, and promotes reliable early development of both hardware and software. The focus is on the development of complex mechatronic systems with specific emphasis placed on early development and subsequent reuse of hardware-dependent software components and on the concurrent and independent development of embedded electronic hardware, software, and physical plants. *Methodology* Complex interactions between physical plants and distributed embedded computing components make developing mechatronic systems very difficult—even when everything is fully specified. New technology options add further complications and require diversified skills from system developers. Designers must deal with embedded software, electronic control units (ECUs), electro-mechanical subsystems (mechatronics), and the networks through which they communicate. In order to manage change and accelerate development, collaboration within disparate groups of people is essential; various cross-sections of engineering disciplines must be allowed to work independently from each other without incurring huge integration costs in subsequent development phases. Model Driven Development (MDD) has been a term used in our industry for some time, but it has had a hard time achieving widespread adoption and respect as the most effective way to drive

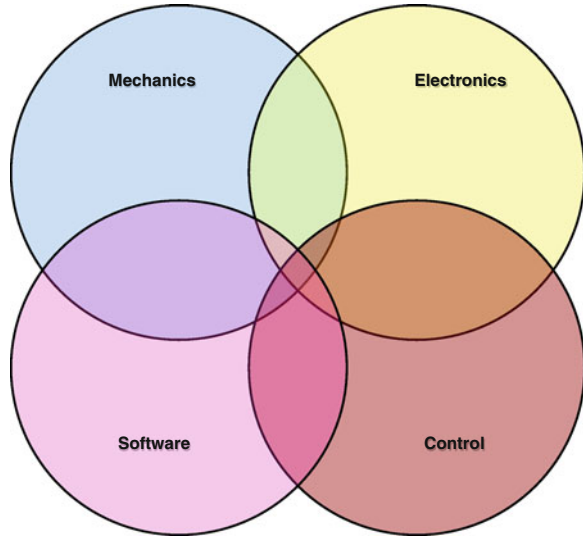
F2012-E12-020

L. Brooks · J. Wu (✉) · D. Teegarden
Mentor Graphics Corporation, Wilsonville, OR 97070, USA
e-mail: amy_knutson@mentor.com

a design process. It accelerates the creation, verification, and validation of embedded software using models as the primary engineering deliverable. *Results* Domain experts use MDD techniques to complete application-specific tasks early, using highly accurate mechatronic models. As projects progress through architectural design, functional partitioning, and detailed component design, the coherence of a system's model is maintained via communication abstractions, reuse of standard system-level architectures, and automatic C/C++ code generation. These capabilities decouple the decision points and ease regression testing to accelerate development as early confirmed strategies are successively verified when networks, actuators and sensors, real-time operating systems, embedded processors, and other sub-systems change. Models are captured using standard modeling languages such as xtUML and can be transformed, automatically, into production-ready C/C++ embedded software. Virtual Engineering augments MDD to provide a realistic modeling alternative—using modeling standards such as VHDL-AMS—to the physical electronics, mechanical devices, and other hardware that make up the typical environment that surrounds software under development. *Limitations of this Study* The technology boundaries inherent in such systems pose two main problems for design teams: compatibility between tools and communication between specialists. Conventional simulation tools cannot adequately deal with diverse modeling requirements; also, technology specialists speak a unique design language that is tailored to his/her specialty. As systems become more complex, contractors who once specialized in narrow technical areas are being forced to act as systems integrators and in turn, are contracting subsystems to a global network of subcontractors. It adds up to significant potential for misunderstandings, errors, and omissions due to communication challenges across language and cultural boundaries. *What does the paper offer that is new in the field in comparison to other works of the author* MDD provides an approach to the challenge of technology change by separating the application portions of a system from underlying platform technology. This technology promotes early, independent, and concurrent development by empowering designers to focus on application models without regard to platform-specific details. This is the difference between MDD and model-based development. MDD completely preserves early application modeling artefacts; the latter repeats modeling efforts for each platform variant. *Conclusions* This paper describes the capabilities of a virtual system integration environment that supports conceptual system development used early in the design cycle, as well as complete distributed system development on final embedded computing hardware. It describes how MDD improves productivity in the design cycle, automatically generating parts of a design, thus improving quality by bringing in repeatability and standards compliance. It shows how design team members working on complex projects in disparate locations can effectively collaborate using a common modeling and analysis environment, allowing a common modeling and analysis environment to act as a communications vehicle for the entire team.

Keywords Model driven development · Virtual engineering · AUTOSAR · Distributed systems · Verification

Fig. 1 Mechatronics—collaborating engineering disciplines



1 Introduction

It is essential that collaborating yet disparate groups of people from various cross sections of engineering disciplines are allowed to effectively work independently from each other without incurring huge integration costs in subsequent development phases. Cooperating mechatronic domain engineers are challenged in this regard since their idiosyncratic development progresses at different life-cycle rates [1] (Fig. 1).

The focus of this paper is on the development of complex mechatronic systems with specific emphasis placed on *early* development through cooperative reuse of software components and on the concurrent and independent development of embedded electronic hardware, software, and the rest of the physics-based system.

2 Electronic Throttle Control Example

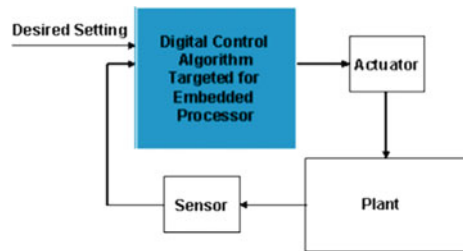
To provide a realistic context, we use an example—the development of an electronically controlled engine throttle body. Several good references discuss the intricate development issues and trade-offs related to electronic throttle control [2–6] (Fig. 2).

An electronic throttle is a good example of a complex mechatronic system found within a vehicle. This important sub-system consists of a physical plant



Fig. 2 Electronic throttle control

Fig. 3 Typical closed-loop control system configuration



(electronic throttle body), sensors (pedal and plate position), actuators (dc motor), and embedded electronic hardware (ECU) and software (digital control algorithm) arranged in a closed-loop configuration (Fig. 3).

3 Disparate Engineering Domains

Over time, various domain engineers develop subsystems of the electronic throttle system specific to their particular problem areas. Each uses different programming and modeling languages and develop their contributions on significantly different timelines.

3.1 Application Engineering

At the heart of a system is the application it realizes. The application lives above the implementation and indeed the same system can be (re-)implemented using different technologies over time. The methodology presented in this paper captures the system's application independent of any particular technical realization.

Standard technologies and formally compliant automated development tools break barriers during the development of the application aspects of the throttle system and allow disparate engineering teams to collaborate to solve:

- *Mechanical Problems*—the mechanical aspects of the throttle system are determined *early*. The dynamics that affect control software and electronics are captured using the VHDL-AMS modeling language [7].
- *Sensor and Actuator Problems*—sensor and actuator choices are made *early* which is ideal because they may introduce dynamics into the system that could affect the control system adversely. The sensor and actuator dynamics that affect control software and electronics are captured using the VHDL-AMS modeling language.
- *Control Problems*—control algorithms are developed *early* against VHDL-AMS models of the mechanical plants and related physics of the sensors and actuators that affect control. In our example, the control algorithm is developed using Simulink.

3.2 Test Engineering

Core to MDD is the concept of regression testing: application models that are the result of a model transformation (that typically defines the transition from one engineering phase to another) are retested using the identical test used to validate the system *early*. The engineering of regression test suites is a problem domain unique with dedicated testing languages and techniques.

Cross-domain modeling and simulation that includes testing languages further breaks barriers during the development of the test of the throttle system and allows disparate engineering teams to collaborate to solve:

- *Testing Problems*—the testing aspects of the throttle system are determined *early*. A LabVIEW test is instrumented at a strategic level of abstraction within the methodology: *the level that remains throughout the MDD workflow and captures the metrics needed to validate whether or not the system meets requirements.*

LabVIEW has test and validation features that are attractive throughout the overall system engineering workflow. It is used during early verification and the same LabVIEW tests are subsequently reused throughout the downstream engineering and system validation activities, including in the lab using real data acquisition and control equipment. Using SVX, the test directly monitors and stimulates the appropriate signals in the overall LabVIEW, Simulink, VHDL-AMS, AUTOSAR, and C/C++ system model and determines if the system meets requirements.

3.3 System Validation

The whole system is simulated *early* using only application- and test-specific model partitions: the plant, sensors and actuators, control algorithm, and test. System requirements are validated—and the system model serves as an executable specification for downstream engineering activities. In the methodology presented in this paper, the test model is directly reused in a regression testing manner as more detailed models that represent more of the ultimate system implementation emerge; this further breaks down discipline barriers.

3.4 Embedded Computing Platform Engineering

Embedded software problems are difficult and automatic generation of correct software provides significant advantages in terms of reuse, development speed, and quality. The development methodology outlined in this paper further breaks down development barriers and allows disparate engineering teams to collaborate to solve:

- *Embedded Software and Electronic Hardware Problems*—the methodology outlined in this paper leverages architectural embedded software standards, e.g. AUTOSAR [8, 9], in order to formally separate embedded hardware and software concerns and support industry standard reuse through architecturally compliant C/C++ source code generation that targets standard hardware platforms.

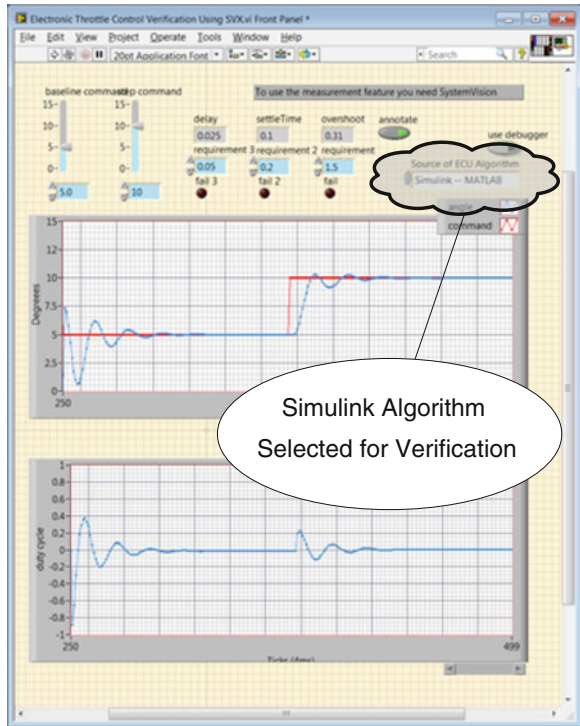
4 Model Driven Development and Early Verification

The methodology is straight forward: the Simulink throttle control algorithm is first validated using the LabVIEW automated test. The test automatically subjects the Simulink algorithm against the high-fidelity detailed application-level VHDL-AMS model of the throttle body executing in SystemVision (Fig. 4).

Then, correct-by-construction production-ready AUTOSAR-compliant C/C++ embedded software is automatically generated (and auto-configured using AUTOSAR configuration generators) using these validated analysis level models as input, and the result is automatically regression tested against the high-fidelity mechatronic model (the same VHDL-AMS model used to validate the system using the Simulink controller) (Fig. 5).

The model transformation and test workflow is completely automated, including the loading and subsequent execution of the system models in the

Fig. 4 Validation of electronic throttle control algorithm in Simulink



various modeling tools and the analysis needed for pass/fail determination. The AUTOSAR algorithm is executed within the Mentor Graphics AUTOSAR execution environment: Volcano Vehicle Systems Integrator (VSI) (Fig. 6).

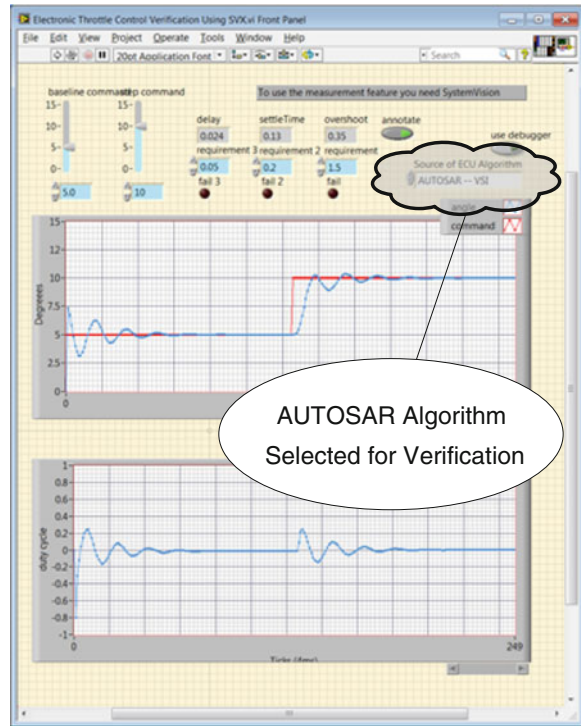
4.1 Electronic Throttle Component Models

Components that represent the final system are modeled so the overall system can be simulated together as a whole. Developers interact with the executing system model by tweaking model parameters and interpreting results (Fig. 7).

4.1.1 Physical Plant

The electronic throttle body consists of a throttle valve, gears, springs, stops, and a motor. The model of the plant was derived from previous work at Visteon [5, 6]. It was augmented using the VHDL-AMS modeling language to provide versatile models at multiple levels of fidelity (high- or low-level as necessary to solve specific problems) (Fig. 8).

Fig. 5 Validation of electronic throttle control algorithm in AUTOSAR (C/C++)



4.1.2 Digital Control Algorithm

The control algorithm is implemented using Simulink and is architected in a classic proportional, derivative, and integral (PID) controller configuration. In the field, it executes as software running on an embedded processor connected to real sensors and actuators that are bound to the plant (Fig. 9).

4.1.3 Signal Delivery Paths

Sense and actuation signals are delivered to and fed back from the plant and the digital control algorithm through very complex signal-delivery paths consisting of distributed embedded electronics hardware and software [3, 4, 10] (Fig. 10).

Signals “travel” through transducers, signal conditioning circuitry, Analog-to-Digital (A/D) and Digital-to-Analog (D/A) converters, and hardware-dependent device and driver software executing on an embedded processor located on an Electronic Control Unit (ECU) (Fig. 11).

The methodology presented in this paper abstracts the details of signal delivery paths in order to separate the development of the control system from the

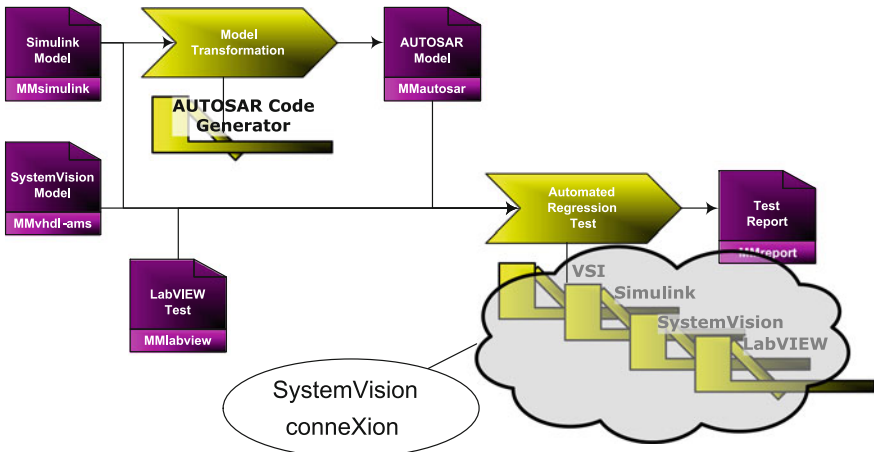


Fig. 6 Automated testing using model driven development

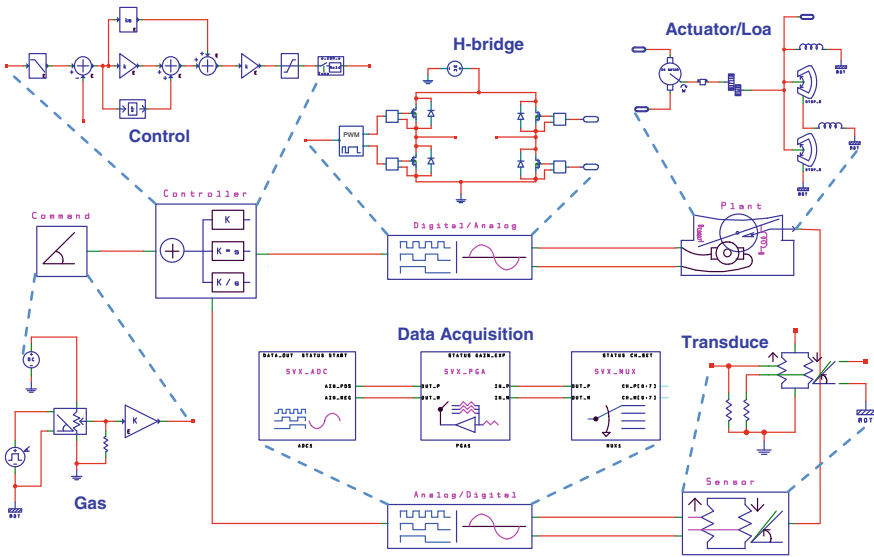
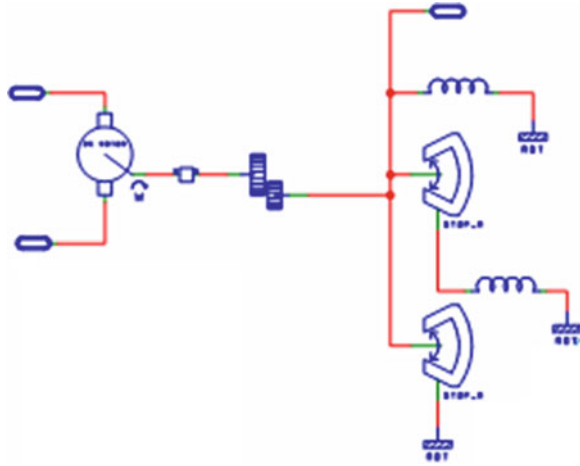


Fig. 7 Electronic throttle schematic

development of electronics hardware and embedded software subsystems that are shared at the system level. The details of variance can be significant and system development can bog down without MDD and virtual engineering techniques that develop around architectural standards.

Fig. 8 Electronic throttle body sub-system schematic



5 Leveraging Embedded Systems Architectural Standards

There is significant advantage leveraging embedded software architectural standards, for example AUTOSAR, that formalize the concept of hardware: sensors, actuators, and electrical input and output; behind an embedded software standard. This affords the ability to reuse standard hardware/software platforms *engineered on different timelines*.

A very advantageous benefit is the embedded hardware platform standards have associated embedded software interface counterparts. These embedded software APIs provide a *target for automated correct-by-construction C/C++ code generation* (Fig. 12).

The essence is the ability for disparate domain engineers to collaborate around a tight industry standard and the ability to cooperate across development timelines using reusable models and cross-domain modeling and simulation tools. Our example leverages the AUTOSAR embedded software and hardware architectural standard through the use of SystemVision conneXion (SVX) for AUTOSAR in order to develop around the AUTOSAR sensor, actuator, and electrical I/O architectural standard.

The subtlety can easily be lost: the details of embedded hardware and firmware, automotive networks such as CAN and FlexRay, and the integration of other functions, are all abstracted away (decoupled) from the problem of validating the *final* AUTOSAR production electronic throttle control software with very high fidelity. The final result can be downstream tested on real electronic hardware—including distributed electronics—with a high degree of confidence and visibility.

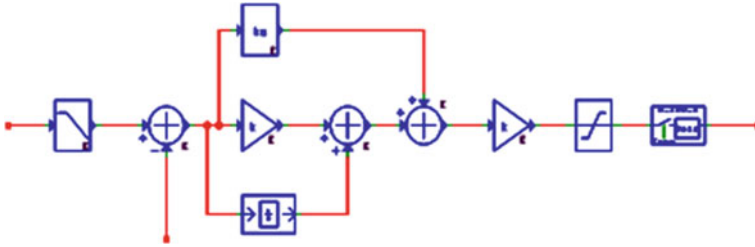


Fig. 9 Control algorithm sub-system schematic

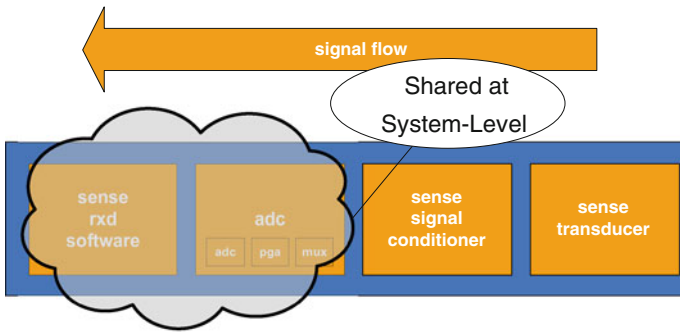


Fig. 10 Sensor complex signal delivery path

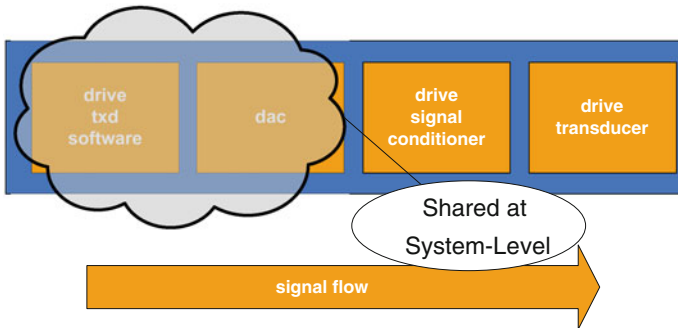


Fig. 11 Actuator complex signal delivery path

6 Cross-Domain Modeling and Simulation Tools

Since each domain typically uses its own modeling and programming languages, it is important for the tools to support collaboration, ideally through model-transformation and co-simulation.

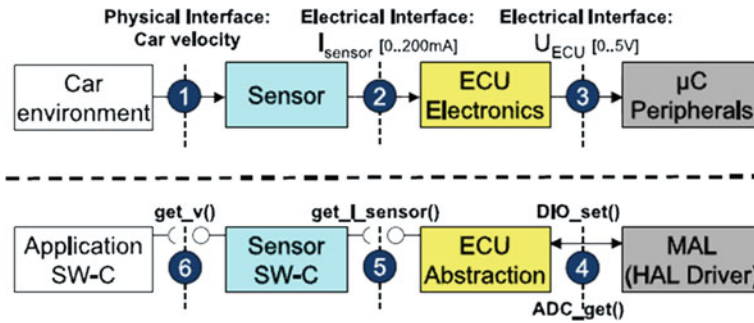


Fig. 12 AUTOSAR standardizes sensor, actuator, and electrical I/O interfaces

Model-transformation supports the need to transform models from one domain to another when the intent is to validate an artefact more appropriately against the goal or role of an engineering phase. For example, model transformation from a Simulink model to an AUTOSAR C/C++ model is a transformation from a control domain oriented model to an embedded software domain oriented model. This is needed in order to validate the algorithm artefact realized as C/C++ software in a downstream engineering activity (dynamic control algorithms and embedded software development typically occurs in different engineering phases—by engineers in different organizations with disparate skills).

Co-simulation supports the need to execute models in native forms to prevent the need for model transformation or re-authoring into single domain models for execution and analysis. Models from one engineering phase can be directly executed in future engineering phases without transformation if the tools support cross-domain modeling (for example SystemVision connexion supports the ability to co-simulate models native to Simulink, SystemVision, LabVIEW, C/C++, Java, SystemC, VHDL, and/or AUTOSAR).

7 Conclusion

A good distributed mechatronic system development methodology provides abstraction of hardware and software concerns, facilitates communication via highly accessible models, and promotes reliable early development of both hardware and software.

System-level modeling accelerates the development of distributed mechatronic systems by automating tasks and maintaining the integrity of validated executable specifications and test benches. Domain experts use MDD techniques to complete application specific tasks early using highly accurate mechatronic models. As projects progress through architectural design, functional partitioning, and detailed component design, the coherence of a system's architectural model is maintained via communication abstractions, reuse of standard system-level architectures, and

automatic C/C++ code generation. These capabilities decouple the decision points and ease regression testing to accelerate development as early confirmed strategies are successively verified as networks, sensors and actuators, real-time operating systems, embedded processors, and other sub-systems change.

References

1. Donnelly M (2004) Improving collaboration in automotive system design. Retrieved from Mentor Graphics Corporation: <http://www.mentor.com/products/sm/techpubs/index.cfm>
2. Hsu M, El-Jaroudi M, Bender E (2004) Accelerated life cycle development for electronic throttle control software using model-based/auto-code technology 2004-01-0276. SAE Technical Paper Series. Society of Automotive Engineers
3. Pechlaner A, Steurich B (2001) Electronic throttle control with contactless position sensor and smart power full-bridge 2001-01-0984. SAE Technical Paper Series. Society of Automotive Engineers
4. Pechlaner A, Kern H, Auer F (1999) System engineering automotive application note: throttle control with smart power bridges and microcontrollers of the C500 and the C16x-families. System Engineering Automotive 08.99, Rel 01
5. Pursifull R, Keener H (2003) Motorized throttle positioning simulation model 2003-01-0222. SAE Technical Paper Series. Society of Automotive Engineers
6. Yang C (2004) Model-based analysis and tuning of electronic throttle Controllers 2004-01-0524. SAE Technical Paper Series. Society of Automotive Engineers
7. Ashenden PJ, Peterson GD, Teegarden DA (2002) The system designer's guide to VHDL-AMS: analog, mixed-signal, and mixed-technology modeling. Morgan Kaufmann, London
8. AUTOSAR (n.d.) Retrieved from <http://www.AUTOSAR.org>
9. Heinecke H, Schnelle K-P, Fennel H, Bortolazzi J, Lundh L, Leflour J et al (n.d.) Automotive open system architecture—an industry-wide initiative to manage the complexity of emerging automotive E/E-architectures 2004-21-0042. SAE Technical Paper Series. Society of Automotive Engineers
10. Bogden D, Grimes M, Michaels L, Amann R (2004) Robust electronic control system design requires signal delivery analysis 2004-01-0892. SAE Technical Paper Series. Society of Automotive Engineers
11. Authors V, Bailey B, Martin G, Anderson T (2005) Taxonomies for the development and verification of digital systems. Springer, Berlin
12. Christensen CM, Raynor ME (2003) The innovator's solution. Harvard Business School Press, Boston
13. Gerke T, Schanze C (2005) A software component architecture for improving vehicle software quality and integration SP-1918. SAE Technical Paper Series. Society of Automotive Engineers
14. Heurung T (2005) Use of Matlab generated C code models in VHDL-AMS with VeriasHDLTM. ASIM workshop. Modellierung und Simulation technischer Systeme, Dresden
15. Madrid NM, Peralías E, Acosta A, Rueda A (2001) Analog/mixed-signal IP modeling for design reuse 1530-1591/01. In: Proceedings of design, automation, and test in Europe
16. Model Driven Architecture (n.d.) Retrieved from OMG: <http://www.omg.org/mda/>
17. Rushton G, Baillargeon R (2005) Model-driven product line software development process 2005-01-1288. SAE Technical Paper Series. Society of Automotive Engineers

Research in the Impact of Curtain Airbag Deployment on Interior

Shuyuan Zhou, Liangming Xiang, Jie Lou, Wenwei Zhang
and Min Xu

Abstract In this paper, Hypermesh and LS-DYNA were used for simulation modeling of complex curtain airbag based on particle method. A static detonation slider impact test was designed to verify the validity of the simulation model. The paper focused on the impact of curtain airbag deployment on the surrounding interior. The results showed that: curtain airbag simulation model based on particle method was reasonable and valid; during the curtain airbag deployment process, trim panels on the edge of B-pillar and C-pillar received more concentrated stress and strain; the opposite direction aircraft had a major impact on the curtain airbag, and deformation of the trim panels on edge of B-pillar and C-pillar was bigger without guide frame. The research results provide effective ways and reference for the design of curtain airbag and interior system.

Keywords Curtain airbag · Interior · Simulation · Particle method

F2012-E12-021

S. Zhou (✉) · L. Xiang · J. Lou
Pan Asia Technical Automotive Center Co., Ltd, Shanghai,
People's Republic of China
e-mail: shuyuan_zhou@patac.com.cn

W. Zhang · M. Xu
School of Aeronautic Science and Engineering, Beihang University,
Beijing, People's Republic of China

1 Introduction

Side curtain airbags are quite popular in recent years with more and more focus on front and side impact performance. A lot of side curtain airbag deployment issues are found in vehicle crash tests, they are: B-pillar trim panel cracked or torn caused by deployed side curtain airbags impact; B-pillar clips crack or doghouse crack, lead to B-pillar warp or detach; Side airbag deployment delay caused by too strong material or structure of trim panel and clips. A lot of physical tests are required and we have to modify the tool to update the structure and change the material for trial without any verification. Although we have some experience implemented on several production vehicles, we are still lack of rules or guideline, impact parameters and impact sequence is still under investigation.

Simulation is an important tool used in airbag design and research. Many scholars did a lot of research work on side curtain airbag simulation: In 2002, Balavich and Nayef [1] studied the effect on dummy's head during side curtain airbag deployments; In 2004, Zhang etc. [2] designed side curtain airbag based on CAE simulation; In 2007, Kaneko etc. [3] optimized the side curtain airbag system using Genetic Algorithm tool and Madymo simulation technology; In 2008, Pei etc. [4] build curtain airbag simulation model based on Uniform Pressure Algorithm using Hypermesh and Madymo software, verify the model using deployment parameters in airbag static deployment and head movement parameter curve in dynamic deployment; In 2009, Lu etc. [5] build up curtain airbag simulation model based on Arbitrary Lagrange Euler algorithm, verify this model using LS-DYNA software, and preliminarily apply the curtain airbag ALE model in side crash simulation on a certain car.

The purpose of this paper is to use simulation forecast the potential failures of the system and optimize the design before tooling kickoff. In this paper, Hypermesh and LS-DYNA were used for simulation modeling of complex curtain airbag based on particle method. A static detonation slider impact test was designed to verify the correlation of the simulation model and the physical test. The paper focused on the impact of curtain airbag deployment on the surrounding interior, offers guideline for side curtain airbag and interior design reference.

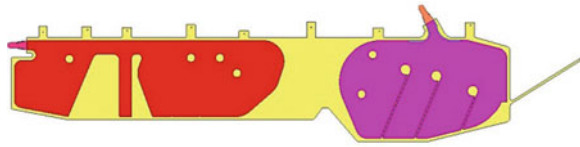
2 Simulation Model Creation Using Partical Method

2.1 Side Curtain Airbag Model

The side curtain airbag in this paper consists of two independent airbags, located front and rear, which are connected with textiles. Every airbag includes inflator, fill tube, fill tunnel, cushion and strap etc.

The bag is meshed by triangular membrane cells and use single cell of 6 mm. We fold the cushion along the specified folding line to reduce initial stress and

Fig. 1 Flat simulation model of a side curtain airbags



strain. Fill tubes and fill tunnels are key components in side curtain airbag, which distribute the air consistently to front and back cushions and keep the internal pressure even, to avoid cushion tore broken by extreme large pressure. In order to efficiently simulate the flow characteristics inside the tube, we divide fill tube and fill tunnel to smaller triangular cells of 4 mm. The strap is made from textile and are transfer to similar model as cushions. Figure 1 is the flat simulation model of a side curtain airbags.

2.2 Corpuscular Particle Method

Corpuscular Particle Method (CPM) is based on Kinetic Molecular Theory, its basic unit—particle is made of many molecules. We assume that every particle is spherical and the interaction between particle to particle and particle to structure are perfect elastic collision. And every particle has translational kinetic energy and rotational kinetic energy, the proportion is defined directly by heat capacity [6]. The air static pressure is the direct function of molecule’s translational kinetic energy. They are considered:

$$p = \frac{2}{3} \frac{\bar{W}_k}{V} \tag{1}$$

$$\bar{W}_k = \frac{1}{2} \sum_{N_p} \bar{m}_i \bar{v}_i^2 = \frac{1}{2} \sum_{N_m} m_i v_i^2 \tag{2}$$

p, V, \bar{W}_k are air pressure, volume and the total kinetic energy. $N_p, N_m, \bar{m}_i, \bar{v}_i, m_i, v_i$ are number of particles, number of molecules, mass of particle, velocity of particle, mass of molecule and velocity of molecule accordingly. For adiabatic expansion process, it is considered:

$$\frac{dp}{dV} = - \frac{C_p \cdot p}{C_v \cdot V} \tag{3}$$

C_p, C_v are air constant pressure specific heat and constant volume specific heat accordingly.

Fig. 2 Side curtain airbag model after folding and bending



2.3 Model Assembly

Curtain airbag model assembly includes side curtain airbag folding, folded model bending and assemble of side curtain airbag and interior components. AIRBAG FOLD module in LS-PREPOST is taken to simulate side curtain airbag folding. The way to folded model bending is firstly extract bending curve from corresponding car frame where side curtain airbag installed, secondly bend the folded side curtain airbag based on the bending curve taken by previous step, at last assemble the side curtain airbag into car frame and interior model (Fig. 2). To ensure side curtain airbag accurately assembled in the compressed space between car frame and interiors, the curtain airbag is to be folded as smaller as possible, and adjust the base bending curve partially.

2.4 Contact Realization

There are three different contact algorithms used for interface slide and collide. They are: node restrain method, symmetric penalized-function method, distributed parameter method. The first algorithms only apply for sticky contacts, the third algorithms apply for slide contacts. In this paper, we use two contact algorithms for distributed parameter method: * contact_airbag_single_surface is applied on the single surface contacts within curtain airbag, * contact_automatic_surface_to_surface is applied for surface to surface contacts between curtain airbag and body frame.

2.5 Side Curtain Airbag Simulation Verification Test

We designed side curtain airbag static detonation impact test to verify the effectiveness of the side curtain airbag simulation model. From kinematics point of view, we correlate side curtain airbag inflation process, include the inflation time and deployment shape etc. From dynamics point of view, we compare physical parameter variation, include the acceleration slide block colliding with curtain airbag.

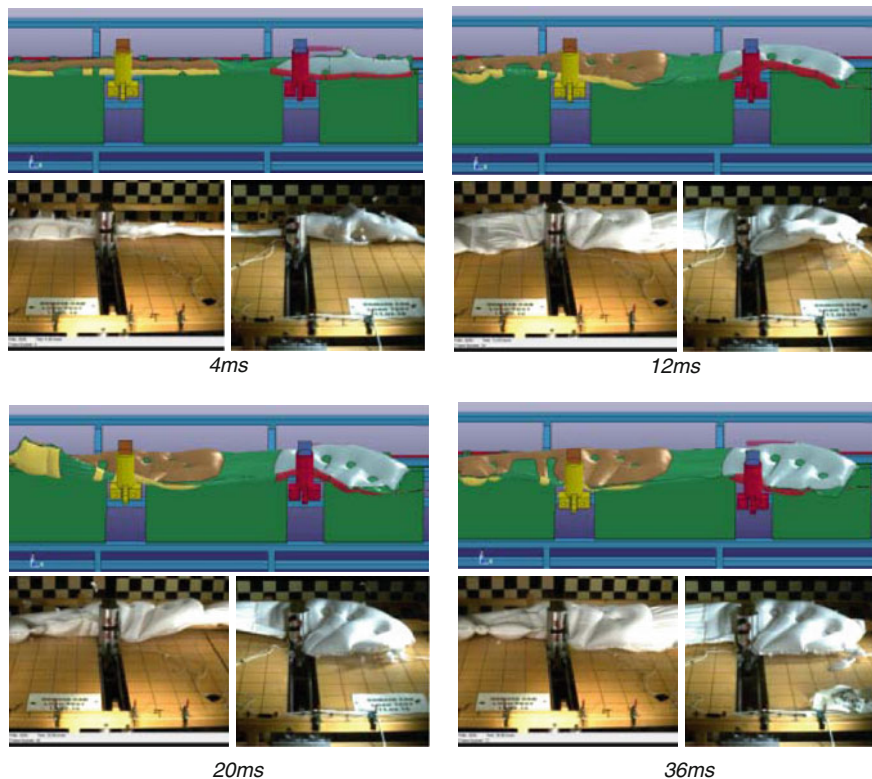
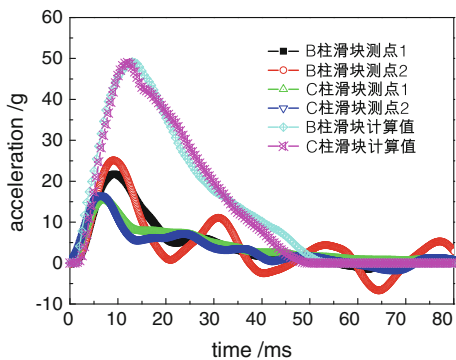


Fig. 3 Comparison of side curtain airbag inflation process simulation and experiment

Fig. 4 Comparison of slide block acceleration simulation and experiment

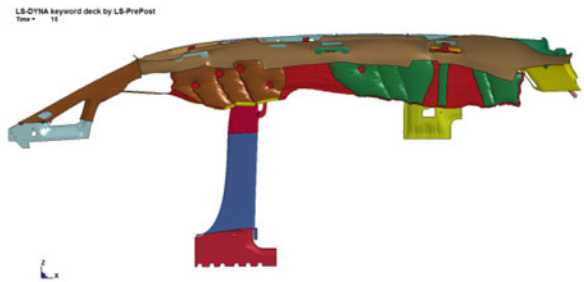


Comparison of side curtain airbag inflation process shows as Fig. 3. The shape of inflated curtain airbag simulated by particle model simulation is very close to the result of experiment with some difference in some position.

Fig. 5 Intergeration simulation model



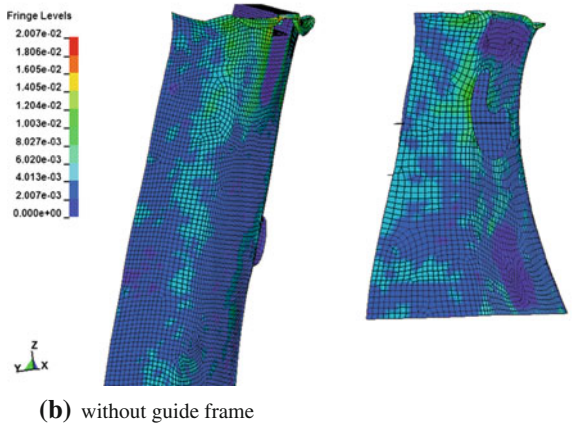
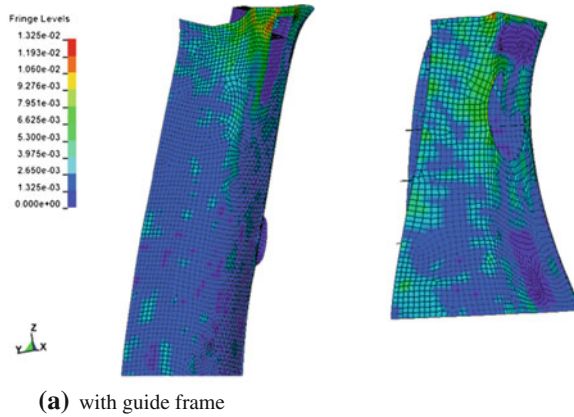
Fig. 6 The side curtain airbag inflation literature, $T = 15$ ms. **a** Deployment with guide ramp. **b** Deployment without guide ramp



The comparison of calculated and experimental slide block acceleration show as Fig. 4. The time of inflation by simulation is close to the experiment. When $T = 50$ ms, The acceleration of slide block is almost zero; the slide acceleration curve is close to the physical; The time when the C pillar acceleration achieve peak value is earlier that the B pillar measurement point. The slide acceleration value correlated well within the first 10 ms, while after 10 ms, the simulation result is bigger than physical test value.

The reason why the simulation result is different from experiment is: (1) In simulation there is so little friction on the assumed slide block on slide rail that slide friction is omitted while there's some friction during physical test; (2) The experiment frame is defined as rigid body in simulation but actually the 2 mm thick steel sheet for the frame will be deformed and absorb some energy when curtain airbag inflates; (3) In this paper, only symmetric penalized-function method is used for contact algorithms, the related contact friction coefficient should be acquired by try out method [5].

Fig. 7 Deformation of B-pillar and C-pillar, 15 ms **a** with guide frame, **b** without guide frame



3 The Preliminary Study of Effect on Interior Caused By Inflation

The intention of side curtain airbag is designed to protect passenger from injury as much as possible. But to be pointed out, curtain airbag detonation is a coupled process involves inner flow structure, body structure, interior and human structure. Curtain airbag inflation impacts interior components, which result in interior damage or curtain airbag deployment failure, leads to passengers injury. In this paper, particle method simulation model is taken to study the effect of side curtain airbag on interior during airbag inflation.

As indicated in Fig. 5, finite-element model for car frame and interior is build up according to above model assembly method.

Figure 6 shows the calculated results of integration simulation model with and without guide frame when $T = 15$ ms. The inflation with guide ramp is more quickly than the inflation without guide ramp, because the side curtain airbag greatly interacts with B-pillar and C-pillar if there is no guide ramp. The ramp can guide the curtain airbag deploy in the right way.

Figure 7 shows the deformation of integration simulation model with and without guide ramp when $T = 15$ ms. (1) The deformation of upper part of B-pillar and C-pillar is much bigger than the lower portion, so the impact of side curtain airbag inflation mainly apply on upper especially the upper end; (2) The deformation of the model without guide ramp is bigger than the model with guide ramp. The upper end of B-pillar and C-pillar is completely destroyed.

4 Conclusion

The finite element simulation model of complex side curtain airbag is establish and the particle method simulation model is testified by static impact test, which offers e-guideline for side curtain airbag and interior design.

Among side curtain airbag, car frame and interior system, the stress and deformation mainly available on upper end of B-pillar and C-pillar. The guide ramp is very important for side curtain airbag smooth inflation. Otherwise, more deformation of upper end of B-pillar and C-pillar and more possibility of deployment delay.

Guide ramp is recommended to be designed as necessary, at the same time reinforcement ribs or rib package can also be considered for better deployment performance. Further research can be focused more on how to design the guide ramp and how to optimize B and C pillar reinforcement structures.

References

1. Balavich KM, Nayef A (2002) Dummy head kinematics in tripped rollover tests and a test method to evaluate the effect of curtain airbag deployment. SAE Technical Paper Series, Paper No. 2002-01-0690
2. Zhang H, Ma D, Raman SV (2004) CAE-based side curtain airbag design. SAE Technical Paper Series, Paper No. 2004-01-0841
3. Kaneko N, Taguchi S, Motoki M, Ogawa S (2007) Optimization of the side airbag system using MADYMO simulations. SAE Technical Paper Series, Paper No. 2007-01-0345
4. Pei Y, Wu X, Zhao H (2008) Computer simulation research on curtain airbags. Liaoning Indus Univ Acad J 28(4):253–256

5. Lu S, Liping D, Chen G (2009) Curtain airbags deployment simulation based on arbitrary lagrange euler algorithm. *Automot Eng* 31(12):1158–1161
6. Hirth A, Haufe A, Olovsson L (2007) Airbag simulation with LS-DYNA past—present—future. In: 6th European LS-DYNA users conference, pp 23–46, Frankenthal, Germany, 11–22 Oct 2007

Multi-Domain Modeling and Simulation of Automotive Air Conditioning System Based On Modelica

Jing Li, Yunqing Zhang and Wei Chen

Abstract The automotive air conditioning (AC) systems are complex systems where two-phase flow, pneumatic, mechanical and electrical components are coupled. Such systems coupled with various physical domains have great influence on comfort and dynamic performance of the vehicle, such as cooling performance, driveability, fuel economy, etc. This paper presents a detailed model of AC system, including the condenser, evaporator, compressor, expansion device, etc. The simulation was carried out to study the performance of the AC systems, and the effect on the vehicle performance was studied.

Keywords Multi-domain · Air conditioning · Modeling · Simulation · Modelica

1 Introduction

An automotive AC system is the primary element in controlling environmental temperatures and humidity of an enclosed vehicle cabin. The automotive AC systems are complex systems where two-phase flow, pneumatic, mechanical and electrical components are coupled. Such systems coupled with various physical domains have great influence on comfort and dynamic performance of the vehicle, such as cooling performance, driveability, fuel economy, etc. In order to analyze the thermodynamic and thermo hydraulic process of the automotive AC systems

F2012-E12-024

J. Li (✉) · Y. Zhang · W. Chen
Center for Computer-Aided Design, Huazhong University of Science and Technology,
Wuhan, China
e-mail: 398864062@qq.com

and improve the efficiency of the systems, system simulations of automotive refrigeration cycles are necessary.

Eborn [1] and Limperich [2] presented dynamic simulations of automotive refrigeration cycles as parts of the design process based on a modelica library for dynamic simulation of AC systems. The process behavior of cooling capacity and compressor power during the New European Driving Cycle were predicted, and the simulation was proved to be able to support the design of refrigeration cycles for automotive applications. Li and Chung [3] provided a framework for automotive air-conditioning analysis and simulation. With the temperature and humidity dynamics derived, effects of air conditioning under different control policies can be simulated in the proposed simulation environment and compared directly on psychrometric chart. Rasmussen [4] showed a dynamic modeling framework for subcritical and transcritical vapor compression cycles. The models are derived using a lumped parameter, moving boundary model that captures the salient dynamic behavior, while remaining sufficiently tractable to be useful for model based control synthesis. The models are validated with experimental data, and are then used for designing and evaluating model based control strategies. However, many previous works considered the vehicle air conditioning system as an ideal system and always used a lookup table to represent the character of the AC system. And the effect of AC system to the vehicle acceleration and fuel economy performance were not studied in these works.

In order to analyze the interaction of AC system and vehicle acceleration and fuel economy performance, an automotive AC system composed of components from multi-domains like mechanical and pneumatic system, two-phase flow system was built in the paper. Modelica/MWorks (a software platform developed based on modelica programming language) was chosen for the task. A new automotive AC system library consisted of various components such as the compressor, condenser, evaporator, expansion valve, vehicle cabin, pipe, etc. was developed in this paper. With these models in the library, the AC system one-dimensional (1D) model was built and simulated.

2 Automotive Air Conditioning System

The basic components of the automotive AC system are the same as other AC systems. These components are a compressor, condenser, evaporator and expansion device as shown in Fig. 1. The difference between automotive and conventional AC system is in their operation and servicing. In a typical automotive AC system, the belt-driven compressor is mounted on the engine. The condenser is mounted ahead of the vehicle radiator, which allows cooling air to flow over it. The evaporator is mounted inside the plenum chamber in the passenger compartment.

For the reason of the environmental protection, R134a become the most commonly used refrigerant in the automotive AC systems. The R134a refrigeration

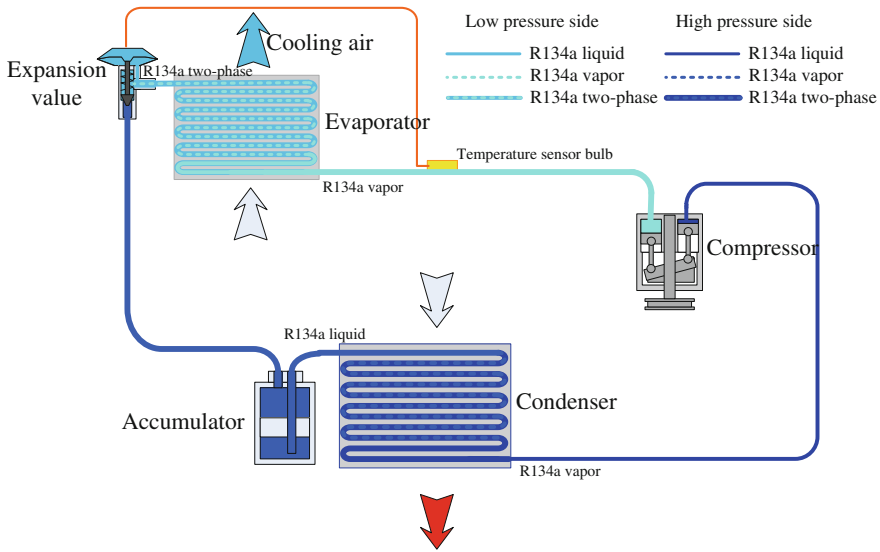


Fig. 1 An automotive AC system

AC system is a subcritical vapor process, as shown in Fig. 2. The numbers 1-5-6-3-7-4-8 show the different state points and thermodynamic processes of the R134a in the ph-diagram. A R134a cycle consists of four processes—the isentropic compression for generating high-pressure steam (1-2), the isobaric condensation for heat rejection (2-3), the adiabatic expansion for reducing the refrigerant pressure to the evaporation pressure (3-4) and the isobaric evaporation for cooling the inlet air temperature of the cabin (4-1). The R134a have five state in the cycle—saturated vapor (5,7), saturated liquid (6,7), superheated vapor (8-1-2-2), supercooled liquid (6-3-7) and two-phase state (5-6,7-4-8) [5].

Air conditioning compressors are driven directly by the engine crankshaft though belt drives in vehicles without auxiliary engines. And the changes in engine speed leads to the instability of the compressor speed and the cooling performance of the AC system. At the same time, the compressor will occupy a large part of the engine shaft power (about 10 ~ 15 %), and affect the vehicle acceleration and fuel economy performance significantly. Due to the interaction of the AC system performance and the vehicle acceleration and fuel economy performance, the multi-domain simulation of automotive AC system and power train system is necessary.

3 Components Modeling

The automotive AC system library consisted of various components such as the compressor, condenser, evaporator, expansion valve, vehicle cabin, pipe, and etc. is developed in this paper. Due to the library allowing user to built system models

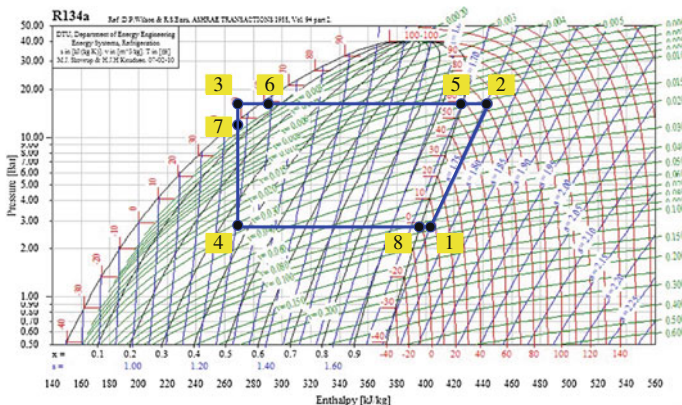


Fig. 2 Ideal case of R134a refrigeration cycle

by drag-and-drop flow, it will reduce the time cost for the modeling of different AC systems. In the AC system simulations, refrigerant flow should be considered as the two-phase flow, and the air flow’s moisture should be simulated, too. These make the AC system a complicated system, and the modeling of the refrigerant flow and moist air flow become the base of the component models in AC system library. The modeling approach will be introduced in the following sections.

3.1 Heat Exchanger Models

In automotive AC system refrigeration cycles, heat is absorbed at the low temperature level of the cabin inlet air (Fig. 2.1, 4-1) and rejected at the discharge level of the ambient (Fig. 2.1, 2-3). The isobaric evaporation for heat absorption (4-1) is taking place in the evaporator, while the isobaric condensation for heat rejection (2-3) is happening in the condenser. In order to get a accurate simulation result, detailed models of both main heat exchangers, condenser and evaporator, are required. Currently, air-cooled condenser and evaporator are commonly used in the R134a AC systems, and the compact cross flow heat exchanger structures that use finned flat tubes with internal microchannels (Fig. 3) are applied in both condenser and evaporator.

Due to the similarity of the structure and working process of the condenser and the evaporator, a generic heat exchanger model which can be used for the evaporator on the low pressure as well as for the condenser in the high pressure side is built up in this study. According to the principle of modular modeling method, the heat exchanger is divided into three parts—refrigerant side, air side and the heat transfer wall.

Fig. 3 Compact cross flow heat exchanger

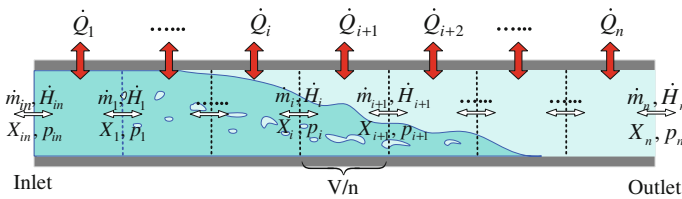
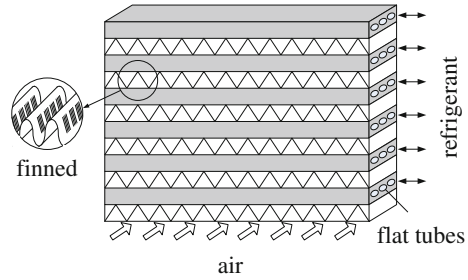


Fig. 4 Refrigerant side grid discretization

3.1.1 Refrigerant Side Models

The two-phase flow on the refrigerant side is based on the control volume model which is similar to the “staggered grid” model [6]. In this model, component refrigerant side is dispersed into several segments as shown in Fig. 4, and each grid have a same volume: V/n . The variables $\dot{m}_{in}, \dot{H}_{in}, X_{in}$ and p_{in} denote the inlet mass flow rate, heat flow rate, dryness (the proportion of vapor share) and pressure of the component. Similarly, variables $\dot{m}_i, \dot{H}_i, X_i, p_i$ and \dot{Q}_i denote the outlet mass flow rate, heat flow rate, dryness, pressure and heat exchange flow rate of each segment. And obviously, the n-th segment outlet data is also the outlet data of the component. All the fluxes such as mass flow rate, heat flow rate, heat exchange flow rate and some intensive quantities such as pressure, dryness are calculated on the border of each grid, and other intensive quantities such as density, mass, temperature are calculated in the center of the grid.

The calculation begins at the inlet interface, and the variables $\dot{m}_{in}, \dot{H}_{in}, X_{in}$ and p_{in} is the results of the upstream component model. The first step is the status distinguishing of the refrigerant flow. It is simple to know the status according to the input variable X_{in} , when $0 < X_{in} < 1$, the status corresponds to two-phase flow; when $X_{in} = 0$, the status corresponds to liquid phase flow; and when $X_{in} = 1$, the status corresponds to vapor phase flow. Then the temperature of the input flow can be calculated according to the flow status by the following equations.

Two-phase flow status:

$$\bar{h} = X_{in} \cdot h_{saturated_vapor}(T) + (1 - X_{in}) \cdot h_{saturated_liquid}(T) \tag{1}$$

Liquid phase flow status:

$$h_{liquid} = h_{saturated_liquid}(T_{saturated}) + \int_{T_{saturated}}^T c_{p_liquid}(T)dT \quad (2)$$

Vapor phase flow status:

$$h_{vapor} = h_{saturated_vapor}(T_{saturated}) + \int_{T_{saturated}}^T c_{p_vapor}(T)dT \quad (3)$$

In the equations, \bar{h} is the mean specific enthalpy of the inlet liquid and vapor refrigerant. $h_{saturated_liquid}$, h_{liquid} and c_{p_liquid} denote the saturated specific enthalpy of the liquid refrigerant, the specific enthalpy of supercooled liquid refrigerant and the isobaric heat capacity of liquid refrigerant. $h_{saturated_vapor}$, h_{vapor} and c_{p_vapor} denote the saturated specific enthalpy of the vapor refrigerant, the specific enthalpy of superheated vapor refrigerant and the isobaric heat capacity of vapor refrigerant. $T_{saturated}$ is the saturated temperature under the inlet pressure.

Then the outlet variables such as p_{out} , \dot{m}_{out} , \dot{H}_{out} of the first grid will be calculated by following equations.

Mass balance equation:

$$\dot{m}_{in} + \dot{m}_{out} + \dot{m}_v = 0 \quad (4)$$

Energy balance equation:

$$\dot{H}_{in} + \dot{H}_{out} + \dot{Q} = \int_{T_0}^T c_v(T)m(T)dT \quad (5)$$

Heat transfer equation:

$$\dot{Q} = \alpha A(T_{wall} - \bar{T}) \quad (6)$$

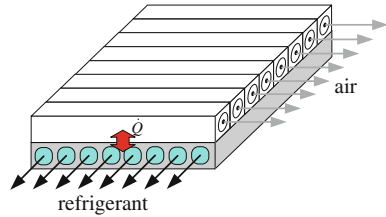
Pressure drop equation:

$$p_{in} - p_{out} = f(\dot{m}_{out}, S, L, \bar{T}, Re, \lambda) \quad (7)$$

The variables \dot{m}_v , S , L , Re , \bar{T} and λ denote the refrigerant mass change rate in the control volume, the mean cross-sectional area of the grid, the length of the grid along the flow direction, the Reynolds number of the flow, the mean temperature in the grid and the surface roughness of the grid.

Since the outlet variables of the grid is the inlet variables next grid, the variables will be calculated grid by grid until the last grid.

Fig. 5 Air side discretization



3.1.2 Air Side Models

The air side flow in the heat exchanger model can be treated as a simple compressible gas flow. However, due to the importance of dehumidification and its influence to the cooling performance, the moisture change of the air should be considered. In this study, air side model is dispersed into several segments along the refrigerant flow direction in order to correspond to the discretization of refrigerant side, as shown in Fig. 5.

The convective heat transfer formula, $\dot{Q} = \alpha A(T_{wall} - \bar{T})$, is used to calculate the heat transfer between the air and the heat exchanger wall. Some hydrodynamics formulas are used in the model to compute the flow characteristics. And the condensation of water vapor is based on the following equation,

$$\dot{m}_{cond} = \dot{m}_{air}(moisture - saturated_moisture(T))$$

where \dot{m}_{cond} is the condensation rate, \dot{m}_{air} is the mass flow rate of the dry air, *moisture* is the moisture of inlet air and the *saturated_moisture* is the saturated moisture of outlet air.

The energy balance on the air side can be calculated from

$$\dot{H}_{in} + \dot{H}_{out} + \dot{Q} + \dot{m}_{cond}h_{latent} = \int_{T_0}^T c_v(T)m(T)dT \tag{8}$$

with h_{latent} is the latent heat of the condensation.

3.1.3 Heat Transfer Wall Models

Models for heat transfer walls which are in thermal contact with the fluids are simple to treat. Two phenomena are considered when modeling walls: their capacity to store heat and their resistance to heat transfer. In the heat exchanger, heat transfer walls are the connector of the refrigerant side and the air side. The heat resistances and capacitances in a heat transfer wall are shown in Fig. 3.5.

The energy balance equation of the wall can be written as

$$m \frac{d(C_p T)}{dt} = \dot{Q}_1 + \dot{Q}_2 \quad (9)$$

Where $\dot{Q}_1 = 0.5R(T_m - T_a)$, $\dot{Q}_2 = 0.5R(T_m - T_b)$, R denote the resistances of the wall, and C_p denote the capacitance of the wall.

3.2 Compressor Models

In the AC system library, the swash plate compressor is modeled as a steady-state map that relates suction–discharge states and mass flow. The model uses three functions to characterize the compressor efficiencies—the volumetric efficiency η_v , the effective isentropic efficiency η_{eff} and the isentropic efficiency η_{is} . The key variables in the model are calculated by the following equations.

Shaft power of the compressor

$$Torque_{shaft} = \frac{(h_{is}(p, s) - h_{in}) \cdot \rho(p, T) \cdot \eta_v \cdot D}{2\pi\eta_{eff}} \quad (10)$$

Mass flow rate through the compressor

$$\dot{m} = \eta_v \cdot D \cdot n \cdot \rho(p, T) \quad (11)$$

The specific enthalpy of the output flow

$$h_{out} = \frac{h_{is}(p, s) - h_{in}}{\eta_{is}} + h_{in} \quad (12)$$

The compressor efficiencies η_v , η_{eff} and η_{is} in the model are considered as the functions of the compressor shaft speed, and fixed by measurement data.

3.3 Expansion Device Models

The AC library includes different expansion device (TXV) models such as simple orifice and thermostatic expansion valve models. In this study, a TXV model is selected to be the throttle device. The TXV model consists of a valve model, a sensor bulb and a PI-controller. Due to the complication of the refrigerant flow model and the possibility of the nonlinear equations have no solutions, the TXV model is simplified to empirical model based on the formula,

$$\Delta p = \frac{\dot{m}^2 \Delta p_0 \rho_0}{y^2 \dot{m}_0^2 \rho} \quad (13)$$

where y is the opening ratio of the valve, Δp_0 , ρ_0 and \dot{m}_0^2 is the measured pressure drop, density and the mass flow rate when the valve is fully opening.

3.4 Vehicle Power Train Models

A vehicle power train library has been built in previous work [7] [8]. The main components in the library include engine, brake, clutch, gearbox, wheel, driver and driving cycle. Vehicle power train system can be set up by drag components from the library. With the model, the fuel consumption and the dynamic performance of the vehicle can be simulated.

Due to the same programming language environment (Modelica) of the automotive AC system library and the vehicle power train library, the multi-domain modeling of the automotive AC system and the power train system can be realized on the same platform.

4 Simulation and Results

In this study, component models in the automotive AC system are validated respectively, the validation of the evaporator will be introduced. Then a Multi-domain model including automotive AC system and power train system is built and simulated, and the effect of AC system to vehicle dynamic performance is analyzed.

4.1 Validation of Models

The models in the automotive AC system are validated before the multi-domain modeling system is built, and the validation of the evaporator is chosen to be introduced (Fig. 6). The parameters in the model are set according to a certain evaporator, and the boundary conditions of the model are set by the actual experimental data of the evaporator. In addition, the evaporator model in this validation is divided into 10 segments, in order to get a satisfactory simulation result.

After the parameters and the boundary conditions setting are completed, a steady-state simulation is taken. And the results or the simulation are acceptable compared to the experiment data as shown in Table 1. Dryness and temperature of the refrigerant in the different evaporator segments are picked up and plotted as curves (Fig. 7), in order to reflect the state of the refrigerant in the evaporator.

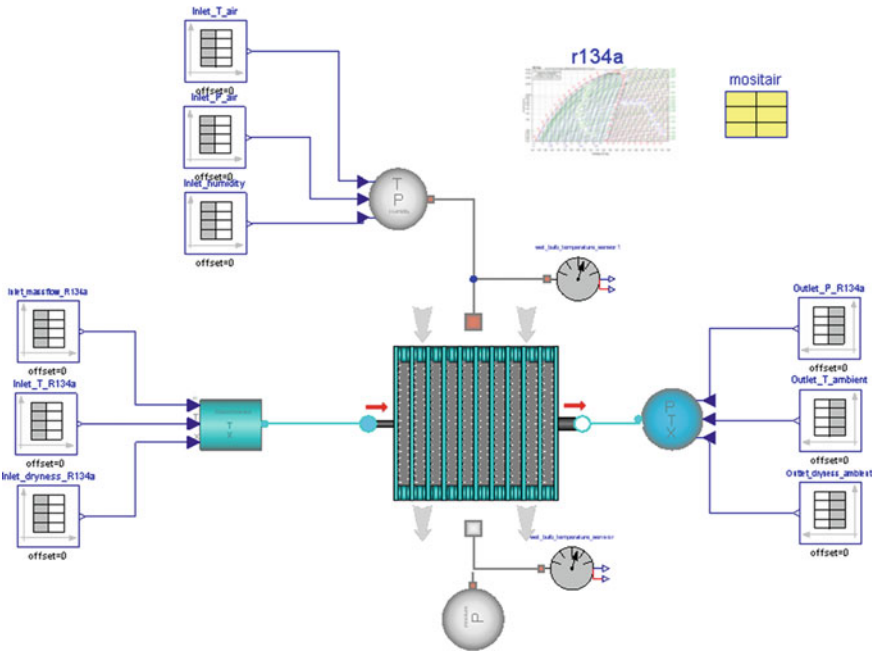


Fig. 6 Validation of evaporator model

The other component models in the library such as condenser, compressor and expansion device models are validated by the same approach. And the validation processes will not be repeated in this paper.

4.2 Multi-Domain Simulation and Results

After the validation of component models, a multi-domain model consists of the AC system and power train system is built by the models in the library. The components in the system such as compressor, condenser, evaporator, expansion valve, vehicle cabin, pipe, clutch, engine, gearbox, wheels and etc. are connected according to the transmission power flow, refrigerant flow, air flow and control logic (Fig. 8).

In order to study the influence of the AC system to dynamic performance, a dynamic simulation is taken in two conditions at first. One condition is the vehicle accelerates from zero to maximum speed with the AC turn off, and another condition is the vehicle accelerates from zero to maximum speed with the AC turn on. The vehicle parameter and acceleration control strategy remain unchanged. And a variable displacement compressor is used in the AC system, and the rated displacement is 160 ml. The results show that the AC system has a comparatively

Table 1

Air-Side			Refrigerant-Side				
Measured data	Experiment	Simulation	Remarks	Measured data	Experiment	Simulation	Remarks
Mass flow rate (kg/h)	674.42	674.42		Mass flow rate (kg/h)	126.3	126.3	
Intel dry bulb temperature (°C)	27.1	27.1	Settings	Intel temperature (°C)	273.8	273.8	Settings
Intel relative humidity	49 %	49 %		Intel dryness	0.33	0.33	
Intel wet bulb temperature (°C)	19.49	19.46		Outlet pressure (MPa)	0.262	0.262	
Outlet dry bulb temperature (°C)	12.79	12.19		Outlet temperature (°C)	5.09	4.79	
Outlet wet bulb temperature (°C)	11.3	12.19	Results	Outlet dryness	1	1	Results
Outlet relative humidity	86 %	100 %		Outlet specific enthalpy (kJ/kg)	404.35	403.74	
Dehumidification capacity (kg/h)	2.27	1.76		Outlet superheat (°C)	8.1	7.8	
Air-Side Heat exchange capacity (W)	4401.29	4222.4		RI-side Heat exchange capacity (W)	5000	4828.6	

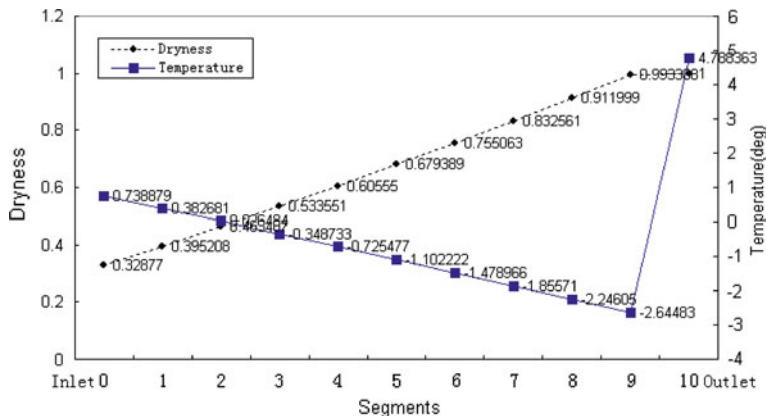


Fig. 7 The dryness and temperature in the evaporator

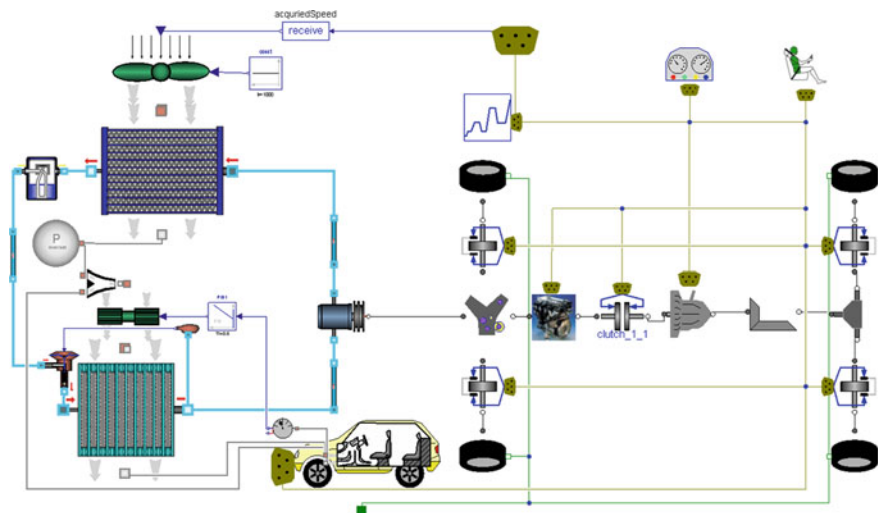


Fig. 8 Automotive air conditioning system one-dimensional model based on Modelica

large effect to vehicle dynamic performance. The maximum speed reduces from 211.3 to 199.5 km/h and the 100 km/h acceleration time increase 3.3 s, when the AC system is working as shown in Fig. 9. And Fig. 10 shows that the AC compressor shaft power occupy a significant part of engine power, especially when the engine speed is low.

Then several steady-state simulations are taken, in order to shown the effect of engine speed to the AC cooling performance. Two different kinds of swash plate compressor are used in the system—a fixed displacement compressor (rated displacement 40 ml) and a variable displacement compressor (rated displacement 160 ml). Simulation results such as the refrigerant mass flow rate, the compressor

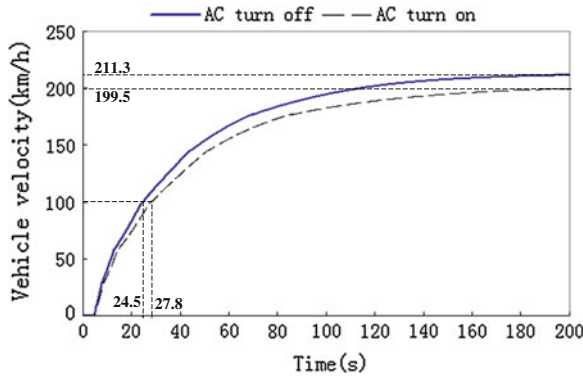


Fig. 9 Acceleration performance

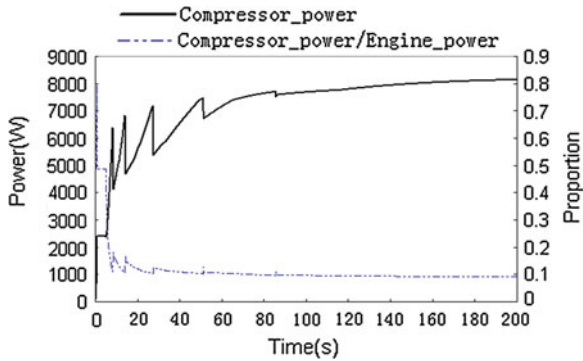


Fig. 10 AC compressor power response

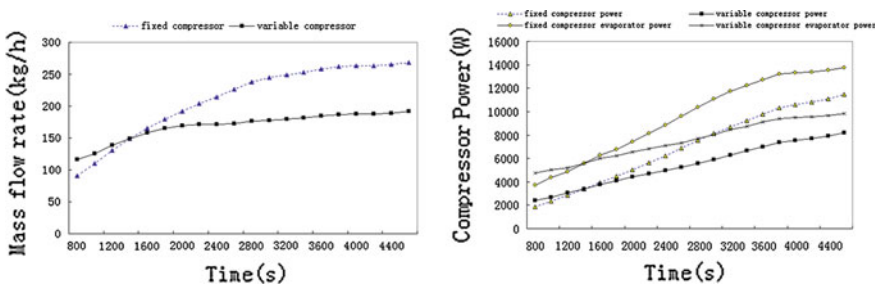


Fig. 11 Performance comparison of AC system with two different compressors

power and the evaporator power under two different compressors are presented as function of engine speed (Fig. 11).

From the simulation results, we can draw the conclusion that the use of the variable displacement compressor makes the cooling performance of the

automotive AC system changed smaller than the fixed compressor AC system. With this feature, a variable displacement compressor AC system can avoid inadequate cooling at low engine speed and over cooling at high engine speed. And this conclusion is also consistent with the fact.

5 Conclusions

The paper presents the modeling of a multi-domain system including automotive AC system and power train system. All the components of the refrigeration cycle and power transmission cycle, such as compressor, condenser, evaporator, expansion valve, engine, gearbox, clutch, and etc., have been considered. The simulation results show the multi-domain AC system can be used to estimate cooling performance, the influence of the AC system on vehicle performance and the effect of engine speed on the AC system. In addition, the model can also be used for automotive AC system components match assessment, the compressor performance evaluation and the automotive AC system fuel economy prediction. These will be studied in future work.

References

1. Eborn J, Tummescheit H, Prolß K (2005) Airconditioning-a modelica library for dynamic simulation of AC systems. In: Proceedings of the 4th international modelica conference, pp 185–192
2. Limperich D, Braun M, DaimlerChrysler AG (2005) System simulation of automotive refrigeration cycles. In: Proceedings of the 4th international modelica conference, pp 193–199
3. Li C, Chung S (2009) Modeling of automobile air conditioning systems. In: 2009 Chinese control and decision conference, pp 974–979
4. Rasmussen BP (2005) Dynamic modeling and advanced control of air conditioning and refrigeration systems. PhD Thesis, University of Illinois at Urbana-Champaign Graduate College, Champaign, USA
5. Que X, Chen J (2003) Automotive air conditioning practical technology. Mechanical Industry Press, Beijing
6. Tummescheit H (2002) Design and implementation of object-oriented model libraries using modelica. PhD Thesis, Department of Automatic Control, Lund Institute of Technology, Sweden
7. Chen W, Chen H, Zhang Y (2009) Modeling and optimization of vehicle acceleration and fuel economy performance with uncertainty based on modelica. SAE paper, 2009, NO.01-0232
8. Jiang M, Chen W, Zhang Y (2009) Multi-domain modeling and simulation of clutch actuation system based on modelica. SAE paper, NO 01-1141

Predictive Energy Management Strategies in Virtual Driving Tests: Early Evaluation of Networked Controller Functions in Realistic Use Cases

Andreas Kunz, Bernhard Schick and Steffen Lange

Abstract *Research and/or Engineering Questions/Objective* The evaluation of vehicle characteristics at an early phase of functional development is a key task in the definition of a viable system and function architecture. Today this is complicated by the fact that full vehicle characteristics, in particular those of modern hybrid and electric vehicles, are dependent on a broad range of electrical, mechanical, thermal and control-related partial aspects. In addition to the current driving status and information on the environment, modern energy management systems (e.g. control systems, range, charging and thermal management) also require predictive information on the driving route to be expected. This includes, for example, uphill road grades, curve radii, speed limits, number of lanes, urban and residential areas, intersections and traffic lights. All together, the intelligent fusion of this information provides for increased safety and energy efficiency. *Methodology* These additional functions however result in additional complexity in the development process, which must be controlled. Nevertheless many questions already arise in a very early phase of development, in particular in the interaction with the actual utilization profile, such as route, driver and environment characteristics in the various target regions of the future vehicle. This article shows new ways and methods of how the functions and total vehicle characteristics can be evaluated in virtual driving tests in the early phase of development. The method provides a major support for the development and evaluation of energy management systems in the complete vehicle environment with corresponding system

F2012-E12-027

A. Kunz (✉) · B. Schick
IPG Automotive GmbH, Mainz-Kastel, Germany
e-mail: edith.toepell@ipg.de

S. Lange
AVL Deutschland GmbH, Mainz-Kastel, Germany

interactions: The evaluation of energy states, losses and fuel consumptions in realistic utilization profiles, such as route, driver and environment characteristics in the various target regions of the future vehicle. *Results* In addition to the evaluation of the individual target functions in a broad range of different scenarios, the correct designs of the individual system components in the complete vehicle can also be verified. The performance and robustness of the operating strategy, as well as the corresponding fuel consumption or CO₂ emission values in the range of worldwide conditions of use can also be predicted with the different choice of route and driver types and the amount of traffic typical for the region. *Limitations of this study* Furthermore, positive fuel consumption effects are identified in the virtual driving test which cannot be recognized due to the insufficient repetitive accuracy in actual traffic. During this, the method can be consistently and uniformly used in the x-in-the-loop development process. As soon as hardware components like the engine, drive train or battery are available, these actual components can already be tested in the virtual driving test in combination with the virtual vehicle in accordance with the principles described. *Conclusion* As a result, the system and functional architecture can already be comprehensively evaluated in a very early development phase and the degree of integration maturity in the later, actual integration levels can be raised to a considerably higher standard, minimizing time-consuming, expensive development loops.

Keywords Modeling and Simulation • Energy Management • Vehicle Dynamics

1 Introduction

The evaluation of vehicle characteristics at an early phase of functional development is a key task in the definition of a viable system and function architecture. Today, this is complicated by the fact that full vehicle characteristics, in particular those of modern hybrid and electric vehicles, are dependent on a broad range of electrical, mechanical, thermal and control-related partial aspects. In addition to the current driving status and information on the environment, modern energy management systems (e.g. control systems, range, charging and thermal management) also require predictive information on the driving route to be expected. This includes, for example, uphill road grades, curve radii, speed limits, number of lanes, urban areas, and traffic lights. All together, the intelligent fusion of this information provides increased safety and energy efficiency.

2 Challenge

These additional functions however result in additional complexity in the development process, which must be controlled. Nevertheless many questions already arise in a very early phase of development, in particular in the interaction with the actual utilization profile, such as route, driver and environment characteristics in the various target regions of the future vehicle. This article shows new ways and methods of how the functions and total vehicle characteristics can be evaluated in virtual driving tests in the early phase of development.

In hybrid and electric vehicle, especially these interactions with the utilization profile are of major importance due to the multiple drive units and energy storage modules combined with complex control and function concepts:

- Is the system design and the operating strategy suitable for the various customer use conditions?
- How reliable are the networked hybrid functions in realistic driving scenarios?
- Is the determined fuel efficiency realistic? Which consumption variance results from different route profiles?
- Which emission levels result from full vehicle testing in realistic driving scenarios?
- How often does the change between electric driving and driving with the internal combustion engine occur?

3 Research Method

Innovative virtual methods are to enable different subsystems to be integrated in the complete vehicle in order to evaluate the complete vehicle characteristics in virtual driving tests. Therefore, a powerful, interdisciplinary, multi-domain modeling and simulation environment like CarMaker is required in order to model the complex systems and to make these use cases in the complete vehicle, which are as realistic as possible, available in the virtual driving test.

This virtual driving test is to be established according to the same basic principles as the actual driving test. Here a virtual driver carries out the test instructions in a complete vehicle and an environment as realistically as possible. In addition, the virtual driver shall be capable of independently driving a broad range of different 3D routes, of maintaining distance to a vehicle ahead, and of controlling innovative systems.

For example, the virtual driver must be able to follow driving recommendations, such as “foot off the accelerator” in order to use the sailing function and the ACC function (on/off, distance, GreenACC function, etc.). In addition, the choice of driver types (sporty, normal, energy-saving, defensive, etc.) is to simulate the entire range of customer use later.

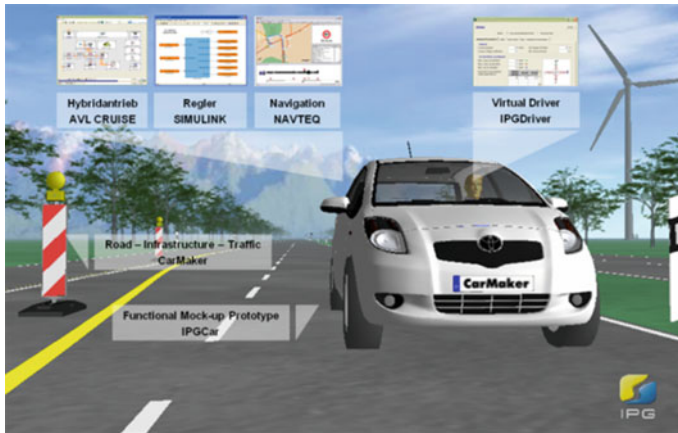


Fig. 1 Virtual integration of hybrid powertrain, controller and navigation in a complete vehicle

4 Open Integration and Test Platform

The integration of a hybrid drive train, predictive energy management, driver assistance system and navigation in the complete vehicle simulation is illustrated using the example of a hybrid vehicle. Here a hybrid powertrain based on the AVL CRUISE drive train simulation was integrated in the functional mock-up prototype of the CarMaker total vehicle simulation [1]. In addition, the complete vehicle was expanded with the energy management and driver assistance functions by means of MATLAB/SIMULINK. To provide the predictive energy management functions with the information of detailed digital maps and an anticipatory horizon (most probable path) in advance, the NAVTEQ ADAS RP development platform was integrated in the full vehicle simulation ([3, 4], Fig. 1). With this virtual hybrid vehicle virtual driving tests were then conducted in a wide variety of scenarios in order to evaluate the functions and vehicle characteristics in realistic use cases.

5 Functional Mock-Up Prototype

The full vehicle model is a completely non-linear 3D driving dynamics model with a body, axles, suspension, steering, engine mounts, powertrain, service brakes, tires and aerodynamics. In addition, the vehicle is equipped with a freely scalable sensor kit for slip angle/side-slip, IMUs (inertia measurement units), ADAS sensors (radar, lidar, ultrasonic) and a RoadPreView sensor. The concept of the ModelManager, with which models of different domains can be integrated in the complete vehicle, is of major importance.

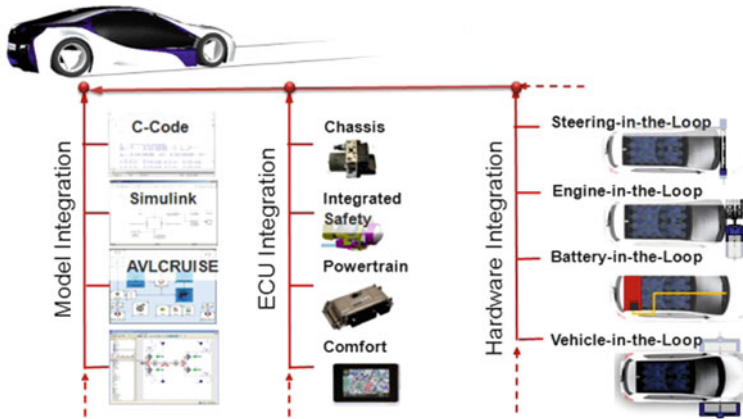


Fig. 2 Functional mock-up prototype “to integrate system components

Therefore different model classes were defined with standardized signal interfaces (I/O) and naming conventions. The models can be automatically generated for CarMaker from different environments and can be assigned to the corresponding model classes. The simulation environment automatically registers these models through cyclical monitoring of the model library. This makes it possible to manage and organize many different models at the same time. These can be conveniently changed over with the user interface or “on the fly” within the test automation. The parameterization, the initialization, the cyclical call and the concluding clean-up are automatically assumed by the ModelManager. The models, but also hardware components and systems (e.g. different control units, engines, drive train, steering) can be integrated very simply in the functional mock-up prototype from a hardware-in-the-loop (HIL) environment (Fig. 2, [2, 5].

6 Powertrain Model

To make a statement which influences preview functions have on the energy management in the vehicle in the driving maneuver, it is necessary to simulate the complexity of modern drive trains in a suitable degree of detail. This is the precondition for taking these functions into account in the virtual driving test or for being able to actively influence an increase in efficiency using control and closed-loop control algorithms. The goal is to create a uniform, bidirectional information structure which permits communication between the driver, the vehicle, the drive train and control and closed-loop control algorithms in such a way that route indicators determined in advance [4] (e.g. speed limitations, uphill grade, light signals) can have a direct effect on the engine management and therefore in turn significantly affect the maneuver retroactively. Due to the almost exclusive

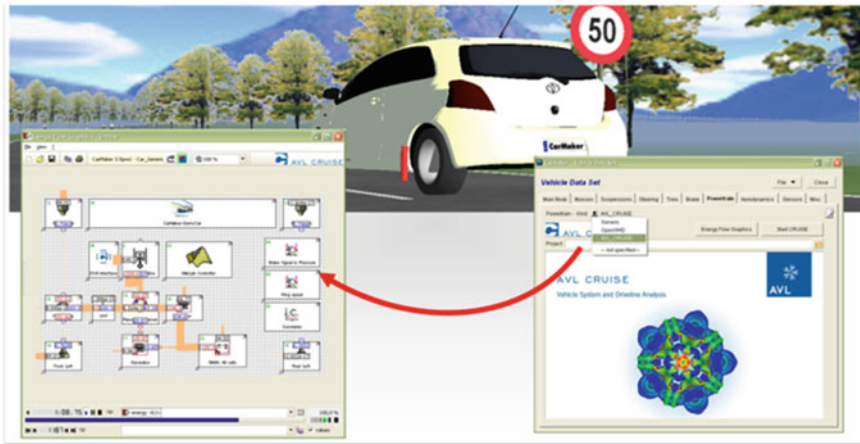


Fig. 3 Integration of hybrid drive in CarMaker and visualization of energy flows in AVL CRUISE

consideration of longitudinal dynamics and the evaluation based on standardized cycles, most attempts so far are no longer suitable for simulating realistic driving with realistic route, driver and regional information. The load requirements are unrealistic and in some cases faulty, which can lead to poorer efficiency, higher expenses and at worst to incorrect designs.

A complete replacement of the longitudinal dynamics simulation approaches used up until now would be justified by the established development phases in the product development cycle; however, this would not lead to success. As the evaluation based on standardized cycles for the concept analysis, basic design, component development and homologation of new vehicles will continue to play an important role in the future, AVL CRUISE was expanded so that it can be easily integrated in the CarMaker integration and test platform. In this context, the previous scope of software functions can be completely used “stand alone”, but it can also be integrated in a complete vehicle “at a click of the mouse” (Fig. 3). This is possible both in the pure office application and in real-time applications like CarMaker/HIL, AVL InMotion or on drive train test benches by means of PUMA Open. To do this, a fully-developed interface concept was required on both sides in order to not only exchange values on the signal level, but instead also messages for driver information, log functions, error handling, etc. By evaluating preview information from the realistic driving scenario, this system concept offers the option of completely taking the complex system and subsystem interaction into account.

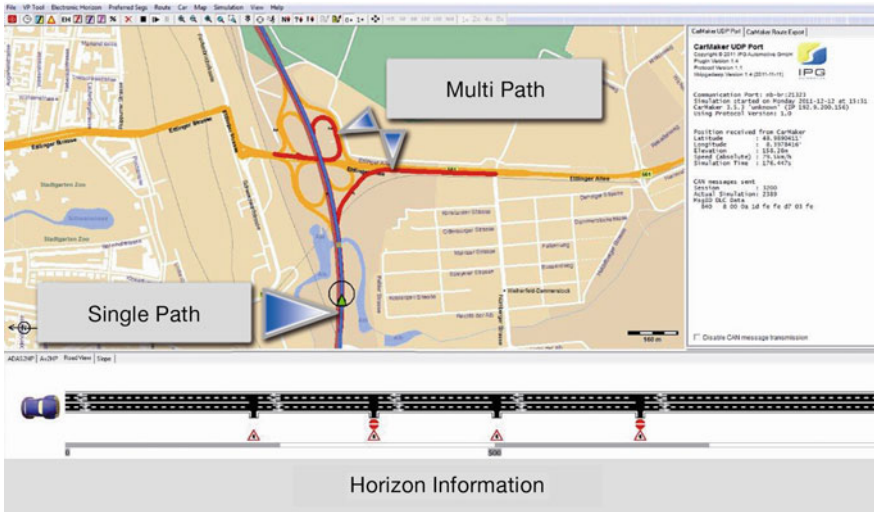


Fig. 4 Transfer of horizon, single path (1D) and multi path (2D) information from ADAS RP to the simulation environment CarMaker

7 Connecting Digital Maps

To supply these functions with the necessary information about the “most probable” future, digital maps, navigation devices and algorithms are required (MPP; Most Probable Path) and make it available to the controller functions and control units as a corresponding “horizon” [4]. The connection to ADAS RP from NAVTEQ, a development platform for functions of digital cards, was realized for this purpose. In the process, the map data of the actual course of the road are imported into simulation environment (Fig. 4). As a result the complete detailed geo data of customer-specific test routes as well as that of any route are available for the simulation. The route data also contain information on the road infrastructure (e.g. signing, curve characteristics). The data are available in such a high quality that they can be used directly in the simulation environment: The virtual driver can start the virtual vehicle immediately for the desired test drive. It drives the specified route completely independently and observes the traffic signs. Both the driving and the course strategy are parameterized quite simply. To exchange the information of the digital maps a connection to the CAN-based ADASIS protocol was realized [3]. The virtual vehicle transfers the GPS position with a corresponding emulation of the GPS receiver and receives the MPP back from the navigation device (horizon provider). Here, a distinction is made between the single path (1D horizon) and multi path (2D horizon).

8 Different Driving Strategies

Different drivers use different driving strategies (e.g. defensive, fuel-efficient, sporty, and aggressive). Each of them affects certain vehicle functions. If this effect is ignored, this will lead to altered results when determining fuel consumption values or when examining battery charging states. The drivers are distinguished by a different selection of trajectory, course steering, steering, braking and acceleration strategies. To be able to make valid statements on the fuel consumption, it is important that the virtual driver model can realistically simulate these differences. For this reason, a main focus of the development of the IPG driver model was on the realistic reconstruction of the driver input. Therefore IPGDriver was equipped with a repertoire of driving styles and driving strategies which the user selects with the user interface. The new traffic follow model plays an important role here. The virtual driver is now capable of “seeing” so that it can actively follow a preceding vehicle. Among other things, the temporal and spatial distance window and the desired following strategy are freely defined. The possible driving styles range from fuel-saving gliders to the gas-guzzler. Together these parameters lead to different fuel consumption. These options make systematic testing of integrated functions and of anticipatory energy management strategies possible for different driver types. The high adaptability of the driver model provides for a very exact simulation of reality in the virtual driving test.

9 Virtual Driving Test for Actual Use Cases

To effectively test the target functions, they must be assigned to corresponding actual use cases. There are situations in which the function is to work as desired and situations in which it must “not” work. In addition, there are error events (e.g. incomplete information or incorrect reactions of the driver) which the function must react to. The reconstruction of the actual use case can mainly take place in three different ways:

1. Maneuver and event-based scenarios for evaluating the target function with permanent assignment of the function and the driving maneuver.
2. Unobstructed driving on long city, country and motorway routes with different driver types and driving strategies for the integral evaluation of the complete vehicle characteristic (e.g. emission, fuel consumption, share of electric driving).
3. Combination of unobstructed driving with maneuver and event-based scenarios plus situations and events that are purposely included to integrally evaluate the full vehicle characteristic.

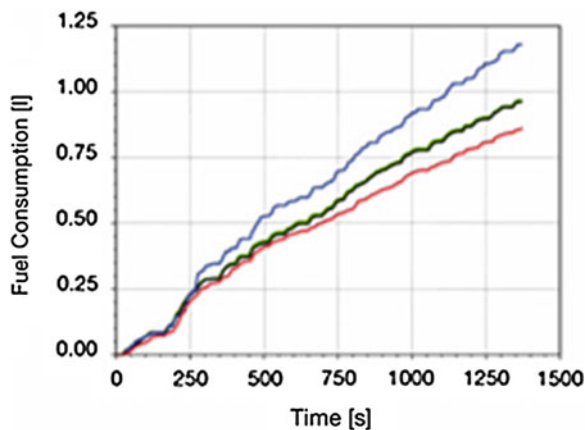


Fig. 5 Example scenario: approaching an uphill grade

10 Predictive Operating Strategy of Hybrid Vehicles

With hybrid vehicles, the central operating strategy, especially the SOC—State of Charge strategy of the battery—is very important. This operating strategy and controller functions were integrated in the complete vehicle. Here the predictive hybrid strategies are tested. In the process it is possible, for example, to use the

Fig. 6 Fuel efficiency impact of different styles of driving (*follow-to-car*)



route as a decision-making criterion for how much energy must be provided for boosting. If an uphill grade is anticipated, as much energy as possible will get stored in the battery, e.g. for electric drive support (Fig. 5). On the other hand, with probable downhill grades, the operating strategy can foresee that, despite a low SOC, no load point increase of the engine is necessary, as energy is fed into the battery through recuperation anyway when driving downhill. Thus the SOC span can be optimally utilized. And with a knowledge of upcoming city zones it is possible to increase the SOC in due time in order to glide through these zones electrically with little noise and emissions.

With the methods and tools created, the interaction with the actual utilization profile, such as route, driver and environment characteristics [6], can also be evaluated for the different target regions of the future vehicle. For this purpose, the vehicle concept complete with different driver types is sent on virtual test drives in various target regions. For example, Fig. 6 shows how fuel consumption varies depending on how different driver types maintain the distance to a preceding car.

11 Conclusion

The method presented here provides a major support for the development of energy management systems in the complete vehicle environment with corresponding system interactions: The evaluation of energy states, losses and fuel consumptions in realistic utilization profiles, such as route, driver and environment characteristics in the various target regions of the future vehicle. In addition the correct designs of the individual system components in the complete vehicle can also be verified.

The performance and robustness of the operating strategy, as well as the energy consumption or CO₂ emission values in the range of worldwide conditions of use can also be predicted—with different routes, driver types and the amount of traffic. During this, the method can be consistently and uniformly used in the x-in-the-loop development process. As soon as hardware components like the engine, drive train or battery are available, these actual components can already be tested in the virtual driving test in combination with the virtual vehicle in accordance with the principles described [2].

As a result, the system and functional architecture can already be comprehensively evaluated in a very early development phase and the degree of integration maturity in the later, actual integration levels can be raised to a higher standard, minimizing time-consuming, expensive development loops.

References

1. Bernhard Schick, Leonhard V, Klein-Ridder B, IPG Automotive GmbH, Karlsruhe (2008) Holistic inspection of hybrid drivetrains and chassis control systems in a continuous Mil/Sil/Hil Process. In: AVEC 2008 Kobe/Japan
2. Christian Schyr, Thomas Schaden, Stefan Jakubek, Bernhard Schick (2008) New frontloading potentials through coupling of hil-simulation and engine test bed. In: FISITA world congress 2008 Munich
3. Christian Ress, Dirk Balzer, Alexander Bracht, Sinisa Durekovic, Jan Löwenau on behalf of the ADASIS Forum Adasis protocol for advanced in-vehicle applications
4. Wilde A, Schneider J, Herzog H-G (2008) Fahrstil- und fahrsituationsabhängige ladestrategie bei hybridfahrzeugen, In: ATZ 110, pp 412–421
5. Pfister F, AVL List GmbH, Graz; Schick B, IPG Automotive GmbH, Karlsruhe (2011) The future has a sensor. location awareness meets powertrain controls. In: 4th international symposium on development methodology, Wiesbaden
6. Tetsunori H, Toyota Motor Corporation (2011) Reducing fuel consumption by improved vehicle efficiency. In: ATZ 113(2011) No. 4, pp 274–279

Evaluation of Video-Based Driver Assistance Systems with Sensor Data Fusion by Using Virtual Test Driving

Bernhard Schick and Steffen Schmidt

Abstract *Research and/or Engineering Questions/Objective* The vehicle of the future will support its driver by advising him regarding potential hazards. Essential prerequisite therefore is the sensor based perception of the traffic situation. For the recognition of traffic related objects, camera based sensors, deepness cameras, vehicle sensors as well as radar and lidar sensors are used. For the future development of ADAS the fusion of multiple sensor data to a consistent environmental picture will play a key role. The evaluation approach of real world driving tests will no longer be sufficient due to the complexity of the system interactions. New simulation methods are needed to evaluate ADAS by using virtual test driving with realistic vehicle behavior and complex traffic environment. *Methodology* Therefore it is important to integrate camera based components in a “closed loop”-simulation platform to be able to test sensor data fusion technologies under realistic conditions. To test new driver assistance systems in a simulation environment today animation data is filmed, subsequently this data is used to test an image processing algorithm or a fusion algorithm. But this method cannot be applied if wide-angle cameras such as cameras with fisheye lenses will be used. Within a research frame work for autonomous driving functions a new simulation technology was developed to integrate virtual cameras beside the well know environment sensor in the vehicle dynamic simulation CarMaker. For this purpose the real-time animation was extended with a sophisticated virtual camera model so called “VideoDataStream” to generate simultaneous video data (also PMD for 3D images). The camera positions as well as the camera properties could be applied individually. Additionally it is possible to freely define the type of the camera lens

F2012-E12-028

B. Schick (✉) · S. Schmidt
IPG Automotive GmbH, Karlsruhe, Germany
e-mail: edith.toepell@ipg.de

(e.g. fisheye) with lens settings like opening angle and the typical lens failures (e.g. distortion and vignetting). With this new technology it is possible that e.g. camera and radar data can be provided time and place synchronal for the fusion algorithm which should be tested! *Results* The video data could be used for evaluating image processing and sensor data fusion in Model-/Software-/Hardware-in-the-Loop applications within virtual test driving conditions. Here the created method and examples of image based perception of the vehicle environment as well as sensor data fusion algorithms shall be presented. Among others this covers first of all the recognition of traffic lanes, traffic signs and other traffic partners as well as the fusion of the single information up to a comprehensive environment picture. A further field of application will be the conjunction with navigation systems and digital maps, by which the virtual vehicle supports the navigation system with related GPS position and gets back the “MPP—Most Probable Path” with the “electronic horizon”, which is a type of predictive sensor, with all related preview information in front of the vehicle which are defined in the ADASIS protocol. *Conclusion* By using the introduced method the capability and efficiency of function development and testing in the area of Advanced Driver Assistant Systems will significantly be improved. Due to a powerful simulation environment a broad range of validation tests can be shifted into simulation because also complex test scenarios can be replicated and the tests are reproducible. The simulation data can be provided time and place synchronal, which is absolutely important, e.g. for a fusion algorithm which should be tested.

Keywords Sensor data fusion • ADAS • Virtual simulation technology • Vehicle dynamics • Image processing

1 Introduction

For recognition of traffic related objects, the usage of camera based sensors (e.g. gray scale, color cameras) and depth cameras (e.g. PMD 3D cameras) will increase in addition to the commonly known vehicle sensors like radar and lidar environment sensors. A wide range of image-based systems is currently being used in the field for purposes like traffic sign recognition and lane tracking to realize adaptive speed control systems and lane departure warning systems. To achieve further progress with future ADAS (Advanced Driver Assistance Systems), the fusion of multiple sensor data to create a consistent overall environmental picture will play a key role—primarily with respect to situation recognition and interpretation. The integration of multiple systems will lead to new driver assistance functionalities to improve safety, comfort and fuel-efficient driving. In addition to the commonly known safety aspects, environment perception also can be used as a source of information for foresighted driving strategies to improve fuel economy [1–3].

Nevertheless, the complexity of integrated systems will lead to a significant increase in development and validation effort. The current evaluation approach of

using real-world test driving will no longer be sufficient due to the high complexity of the system interactions. New simulation methods are needed to test and evaluate ADAS, using virtual test driving with realistic vehicle behavior and a complex traffic environment. On the one hand, the simulation should closely model the real-world traffic situation and on the other it should enable repeatable and comparable test conditions. Therefore, it is very important to also integrate camera-based components in the total “closed-loop” test and integration platform in order to enable testing of sensor data fusion technologies under realistic conditions.

2 Benefits of Information Fusion

Generally speaking, information fusion represents an important trend. The benefit is obvious: Merging of individual sensor data aims to increase the information content in order to capture the environment in more detail, at higher accuracy and with improved reliability. This will lead to a higher degree of safety, comfort and energy efficiency. The benefit associated with fusion can be illustrated best by means of a concrete example: radar and camera. Both systems have a high level of diversity. As a result, both data sources combined represent a major gain in complementary information and higher quality. Whereas radar generates a high level of precision and far-forward view in longitudinal direction, the camera precisely resolves the transverse and vertical direction and, in addition, recognizes the sizes of objects.

By bundling the strengths of the sensors for the acquisition of information and eliminating the weaknesses, the capability and efficiency of functional development will be significantly improved.

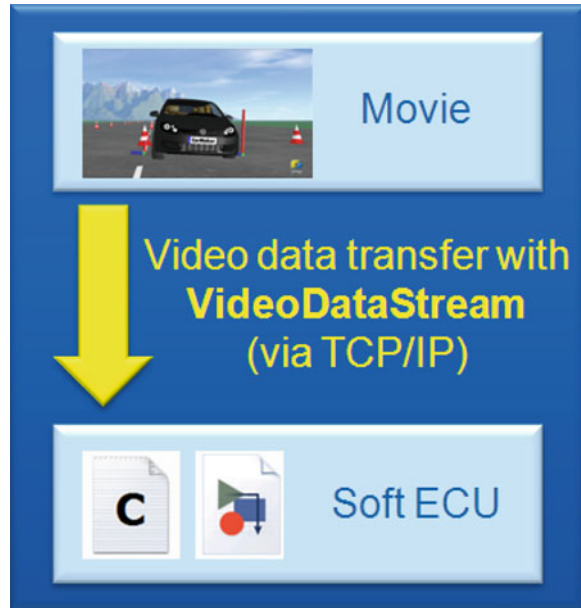
The different types of sensors have individual strengths and weaknesses. The radar-system offers a good determination of the distance of objects (even at night and fog), while the camera is very good determining the size and motion of objects—which walks along with a reduced visibility at night and in fog.

3 How to Test Sensors

To test new driver assistance systems or new software versions without using a simulation environment, it is common that thousands of test kilometers will be driven and recorded. But not every single relevant traffic situation can be covered by this method. Furthermore, once made driving situations can not be modified or repeated under the same test conditions with different parameter settings (such as different control parameters or algorithms). This leads to the fact, that this is not the most desirable solution.

There are many requirements concerning a suitable simulation environment. It must be possible to integrate controllers (hard- and/or software) as well as fusion

Fig. 1 Data transfer using VDS



algorithms. Sensors like radar, lidar and ultrasonic as well as the camera must be available as detailed models. Furthermore, the sensor data must be provided in a time and place synchronously manner for the fusion algorithm. To put an end to it, a possibility to set up also very complex test scenarios is mandatory.

3.1 Testing Software (MIL/SIL)

In an early stage of development or in cases where it is not necessary to test the real existing hardware, it is completely sufficient to test the software/algorithm itself. Within a research work in autonomous driving functions, a new Software-in-the-Loop/Model-in-the-Loop simulation technology was developed to integrate virtual cameras beside the well known environment sensor (radar, lidar, ultrasonic) in the open integration and test platform CarMaker. For this purpose, the realtime animation was extended by a sophisticated camera model which is called “VideoDataStream” (VDS) to generate simultaneous video data such as grey scale, color or stereo pictures as well as deepness maps (e.g. PMD) for 3D images.

Furthermore, it is possible to configure the resolution, frame rate, optic, sensor properties as well as the position and direction of the camera. The video data is transferred via the TCP/IP network interface to the controller or image processing algorithm under test (Fig. 1).

Fig. 2 Testing a LDW using a real camera



3.2 Testing ECUs (HIL)

The common way to test real existing ECUs e.g. for lane departure warning systems (LDW) is to install a camera and a monitor in a black box (Fig. 2).

In this case, an original camera from the vehicle is capturing the animation on the screen. This construction brings along many problems. The biggest one is the construction itself, which makes it very complicated to prevent the camera of interfering light.

As mentioned before, camera systems are getting cheaper and vehicles will be equipped with more than one camera system. It is obvious that evaluating multiple cameras carry along multiple costs.

A serious problem is the missing synchronization between the display and the camera, which leads to asynchronous pictures (Fig. 3).

Furthermore, the delay from the PC to the display, the internal delay from the display electronics to the LCD panel, the delay from the display to the camera and finally the delay from the camera to the ECU make it impossible to merge signals from different sensors because the signals will not be frame synchron.

Because more and more fisheye lenses are installed in modern cars, another problem arises. Real cameras equipped with panorama lenses can not be tested using the black box method described above—the display itself and its environment would be displayed in the picture. Therefore, it is necessary to find a method to reach a pleasant way of simulation.

Fig. 3 Sync-delay leading to interferences



Fig. 4 The principle of the VideoInterfaceBox



A new possibility to test real existing components, which means Hardware-in-the-Loop, is to transfer the video signals to the ECU via the VideoInterfaceBox. The necessary video signals are generated by a PC based on the images provided by IPGMovie.

The VideoInterfaceBox is designed to split and convert the input video signals from the computer into separate video signals, which correspond e.g. to the front, left and right camera images (Fig. 4).

Using the VideoInterfaceBox as well as the VideoDataStream, the camera positions and properties can be applied individually for more than 6 cameras—which are simulated fully synchronized in real-time. The integration of multiple cameras creates many new opportunities. These cameras can be freely configured with optical properties such as viewing angles up to 250° and lens faults like vignetting or distortion, which are clarified in chapter “Fisheye Settings”. Challenging applications like the fusion of cameras for e.g. 360° park view systems can be validated reliably this way.

Fisheye lenses are often used to realize parking assistance systems (Fig. 5). Installed at the front and the back of the car as well as at the side mirrors, the cameras offer an all-around-visibility. Due to the field of view it is even possible to simulate the view from the top of the car, which is called surround-view. To realize this, the pictures of the different cameras are put together and rectified digitally.

Fig. 5 Parking assistant using Fisheye-Lenses



The extracted, processed und fused environment information can be retransferred to the controller unit. According to this it is now possible to test sensor data fusion algorithms under realistic use case conditions by conduction of virtual test driving with the open integration and test platform CarMaker. And this virtual test driving can be reproduced in a synchronous (same time/same place) closed loop process.

This method allows the application of a wide scope of relevant situations with relatively small effort, which could be used for systematic evaluation. This covers very complex as well as infrequent real world situations, too.

4 Types of Fisheye Lenses

There are four important functions of representation of fisheye lenses on the market. All of them can be simulated in IPGMovie.

4.1 Fisheye Equidistant, Linear

Transforms the object angle of view linearly into a distance with respect to the image center point. With circular fisheye lenses, the image is circular and generally inscribed in the camera sensor area, hence the black area in the frame corners. This fish eye lens models can be classified according to their mapping function, i.e. the way the image is distorted.

4.2 Fisheye Equal Area

This model applies for lenses that use an equal-area or equi-solid-angle projection as a mapping function. It means that equal solid angles in three-dimensional space project into equal areas in the image plane.

4.3 Fisheye Orthographic

The mapping function for this lens model is an orthographic projection which is a form of parallel projection. All the projection lines are orthogonal to the projection plane, resulting in every plane of the scene appearing in affine transformation on the viewing surface. The result of this projection would be the view of a sphere, with the view mapped to the outside, seen from a far distance.

4.4 Fisheye Stereographic

This lens model uses a stereographic projection which is a mapping that projects a sphere onto a plane. The projection is defined on the entire sphere, except at one point (projection point). This mapping preserves angles but neither the distances nor the area of objects.

5 Fisheye Settings

The fisheye lenses integrated in IPGMovie can be configured in any possible way. The camera field of view can be specified in the range 90–250°. Let us have a look at the fundamentally options.

IPGMovie offers the possibility to configure the view in different modes.

In the x-mode, the fisheye circle is adapted to fill the window in the horizontal direction. This mode is typically used to simulate the cameras mounted on the vehicle (Fig. 6).

Using the y-mode, the fisheye circle is adapted to fit the vertical dimension (Fig. 7), while the full fisheye circle is displayed and fits the smaller dimension (horizontal or vertical) using the xy-mode.

To adapt the fisheye circle to the length of the window diagonal, the diagonal-mode can be selected (Fig. 8).

Another option is to set up the scale and offset of the lens in different modes.

The Scale-mode is a scaling factor for the fisheye image. Offset X + Y enable the user to shift the fisheye image in the horizontal/vertical direction.

Fig. 6 X-Mode View in IPGMovie



Fig. 7 Y-Mode View in IPGMovie



Furthermore, IPGMovie can simulate the most common lens faults in a realistic way, distortion and vignetting.

The distortion is a geometric aberration which leads to a local change of the image scale. In addition to the mapping function of the fisheye lens, the distortion can be defined by a polynomial up to the 5th degree whose coefficients are adjustable.

The vignetting is an unintended effect that consists of a reduction of the brightness or saturation at the image border compared to the image center (Fig. 9).

It is caused by angle-dependence of the camera sensor. Light incident on the sensor at a right angle produces a stronger signal than light hitting it at an oblique angle. This effect can be modeled with a polynomial up to the 4th degree whose coefficients are adjustable.

Fig. 8 Diagonal-Mode View in IPGMovie



Fig. 9 Vignetting-Effect in IPGMovie



6 Merging of Navigation Data

So far, we only talked about the fact that camera data can be merged with radar data. But there are also systems like sign recognition systems, which rely on navigation data. The data from a navigation system is static while the data from a camera is dynamic and situational. This data is very important, for example to recognize temporary speed limits within one day construction sites.

Therefore IPG realized a coupling to a research platform for map based ADAS which is called ADAS-RP. CarMaker sends the GPS position to ADAS-RP and gets back the electronic horizon and the most probable path (Fig. 10).

In Future, drivers will get more and more acoustic, optical and haptic guidance. In (Fig. 11), this is illustrated using the example of the electronic horizon which

Fig. 10 ADAS RP – CM – Google Earth

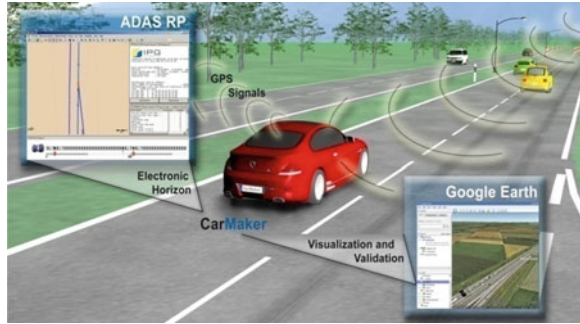


Fig. 11 HUD using Sensor Data Fusion



contains much important information like the current velocity, speed limits and dangerous spots like sharp curves.

In this case the driver is warned by the system against a sharp curve, while the current speed limit was detected by a camera.

7 Conclusion

The usage of camera based sensors in the automotive sector is steadily growing. This will lead to a significant increase in development and validation effort, so that the real world testing will no longer be sufficient. To achieve further progress with future ADAS, the fusion of multiple sensor data like radar and camera will play a key role. The merging of sensor data aims to increase the information content, but there are many requirements concerning a suitable simulation environment which must be considered. For use-cases where MIL or SIL tests are sufficient for the development, the VideoDataStream was developed by IPG. The VDS is a sophisticated camera model integrated in IPGMovie, which generates simultaneous video data.

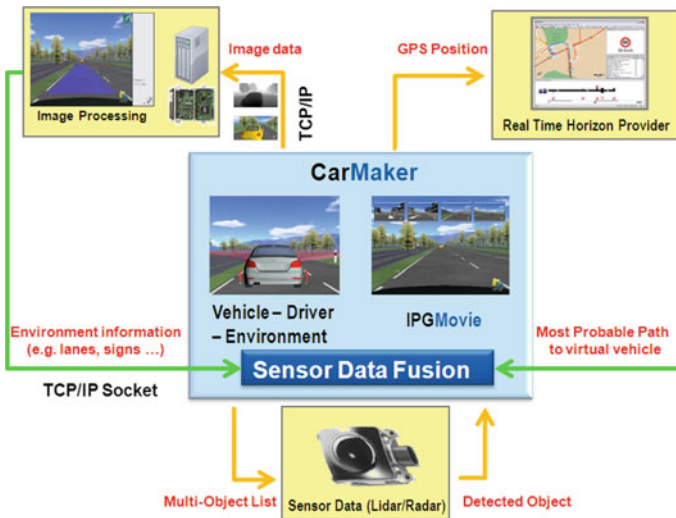


Fig. 12 Communication for SDF

If HIL tests are required, the common way to test the hardware is unsuitable because of many problems like interfering light and asynchronous pictures. A new possibility to test hardware components is the VideoInterfaceBox, which uses video signals generated by a computer. The whole signal consists of up to four different simulated cameras and is splitted into single signals to simulate real existing cameras. All camera signals are fully synchronized in real-time and configurable individually. The extracted, processed and fused environment information can then be retransferred to the ECU, finally. IPGMovie supports the simulation of all four important fisheye-lens types, which are available on the market. This solves the problems which occur if real fisheye-cameras are used.

To enable CarMaker to test Sensor Data Fusion algorithms, several techniques are required (Fig. 12).

Via the VideoDataStream, video data can be send out of CarMaker to an image processing algorithm. The information of detected driving lanes, signs, and traffic objects will be returned to CarMaker. The different sensor models integrated in CarMaker provide information of detected and important objects.

By transmitting the GPS position of the virtual prototype out of CarMaker to a navigation system, the most probable as well as the electronic horizon will be given back to CarMaker.

References

1. Schmidt S, Schick B (2011) Evaluation of video based driver assistance systems with sensor data fusion by using virtual test driving. IPG Automotive GmbH, Karlsruhe, AUTOREG 2011, Baden, Germany
2. Müller S-O, Brand M, Wachendorf S, Wolfsburg VAG, Schröder H (2009) Integration vernetzter fahrerassistenz-funktionen mit hil für den vw passat cc. t-Systems ES GmbH Wolfsburg, Thomas Szot, IAV GmbH Gifhorn, Sebastian Schwab, Birgit Kremer, IPG Automotive GmbH, ATZ extra Automotive Engineering Partners
3. Schick B, Klein-Ridder B, zur Heiden M, Henning J (2008) Simulation methods to evaluate and verify functions, quality and safety of advanced driver assistance systems. AVEC2008

Vehicle Warm-Up Analysis with Experimental and Co-Simulation Methods

Daniel Ghebru, Christian Donn, Wolfgang Zulehner, Heiko Kubach,
Uwe Wagner, Ulrich Spicher, Wolfgang Puntigam
and Klaus Strasser

Abstract A high accuracy of full-vehicle thermal models are required to predict the vehicle heat-up behaviour at every conceivable combination of driving cycle and ambient air temperature down to $-20\text{ }^{\circ}\text{C}$. Within this work a methodology for modelling the thermal behaviour of an IC-engine is presented. The focus lies on the heat-path beginning with the combustion process followed by heat conduction through the combustion chamber walls and convective heat transfer between engine structure and coolant. The thermal engine model is coupled with other models (HVAC-system, powertrain, etc.) by an independent co-simulation platform in order to describe the virtual vehicle as a whole. Finally, the model validation is performed with two different driving cycles at two different start temperatures. Using the described full-vehicle model the potential of a heat storage system is discussed for several heat-up strategies.

Keywords Full-vehicle simulation · Thermal engine model · Co-simulation · Thermal management · Warm-up behaviour

Nomenclature

A_w	Combustion chamber surface area (m^2)
c_m	Mean piston speed (m/s)
c_p	Specific heat capacity ($\text{J}/(\text{kgK})$)
d	Diameter (m)

F2012-E12-029

D. Ghebru (✉) · C. Donn · W. Zulehner · H. Kubach · U. Wagner · U. Spicher
Karlsruhe Institute of Technology, Institut für Kolbenmaschinen, Karlsruhe, Germany
e-mail: daniel.ghebru@kit.edu

W. Puntigam · K. Strasser
AUDI AG, Ingolstadt, Germany

Eu	Euler number (-)
η	Viscosity (kg/(ms))
h_c	Heat transfer coefficient (coolant-side) (W/(m ² K))
h_w	Heat transfer coefficient (gas-side) (W/(m ² K))
L	Length (fundamental unit) (m)
λ	Thermal conductivity (W/(mK))
M	Mass (fundamental unit) (kg)
\dot{m}	Mass flow rate (kg/s)
p_{cyl}	Cylinder pressure (bar)
Pe	Péclet number (-)
Pr	Prandtl number (-)
\dot{Q}_w	Wall heat flow rate (W)
\dot{Q}_{HSS}	Additional heat flow rate(W)
Re	Reynolds number (-)
ρ	Density (kg/m ³)
St	Stanton number (-)
T_{cyl}	Mean gas temperature (K)
T_w	Wall temperature (K)
T	Time (fundamental unit) (s)
Θ	Temperature (fundamental unit) (K)
u	Flow velocity (m/s)
V_{cyl}	Cylinder volume (m ³)

1 Introduction

Due to high friction losses within the engine and powertrain at low temperatures, vehicle fuel consumption increases with decreasing start temperatures, see Fig. 1. The right diagram shows the additional fuel consumption due to cold start conditions as a function of ambient temperature. Therefore, warm-up strategies have to be developed which are able to shorten warm-up time in order to reduce fuel consumption and thus CO₂ emissions.

Since experimental tests in a climatic wind tunnel are very time-consuming and cost-intensive, the expectations with regard to accuracy on modern simulation methods increase continuously. Numerical investigations of thermal systems must consider the interaction between the networked subsystems [9]. For instance, the power consumption of the blower affects both, the heat transfer of the air passing the heater core as well as the generator power output. Both have an impact on engine warm-up behaviour. Therefore, an investigation of an isolated subsystem, without taking the interaction to nearby subsystems into account, is not recommended. Against this background, all thermal sub-systems are modelled in detail before being coupled with an independent, superordinated co-simulation platform [8].

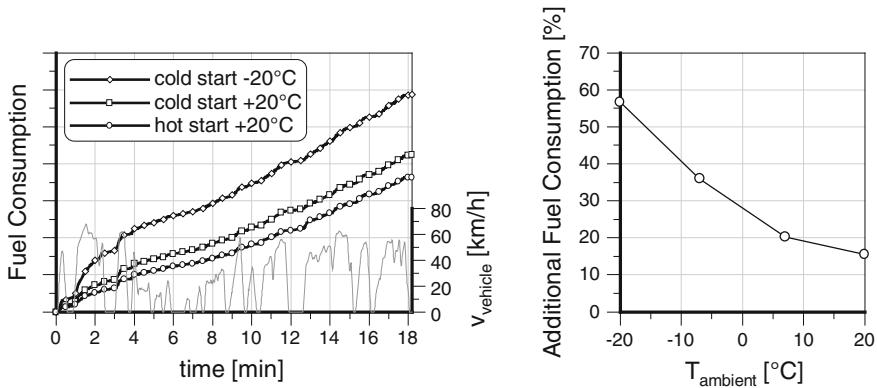


Fig. 1 Cold-start fuel consumption depending on ambient temperature

The major advantage of this approach is that for each thermal system the most qualified CAE-tool can be chosen.

The presented thermal full-vehicle model fulfils the requirement to predict the heat-up behaviour and fuel consumption not only for one special driving cycle at one certain ambient temperature, but also for every possible combination of driving cycle and start temperature down to $-20\text{ }^{\circ}\text{C}$. On basis of this model the impact of a heat storage system is investigated.

2 System Modeling

The focus of this paper is the warm-up behaviour of an internal combustion engine and its effect on overall vehicle energy efficiency. Therefore, the modelling of the heat path beginning with the combustion process, heat conduction through the combustion chamber walls and convective heat transfer between engine structure and coolant is described.

The calculation of the heat flow from combustion gas into the engine structure is crucial for every thermal engine simulation. The combustion process is simulated by an in-cylinder pressure based model whereby the injection process represents the most important controlling factor for the heat release [2]. This model is implemented in dSpace ASM [11], which is a completely open Simulink model, so that user-defined model extensions can be easily added. The model is parameterized with engine measurement data presented in [3] and [4]. Afterwards a model-based parameter optimization is performed [10]. Thus, the wall heat flux is not a finite value from an engine map, but is calculated for every single combustion cycle during a transient warm-up simulation according to the following equation:

$$\dot{Q}_W = \sum_i h_W \cdot A_{W,i} \cdot (T_{cyl} - T_{W,i}) \tag{1}$$

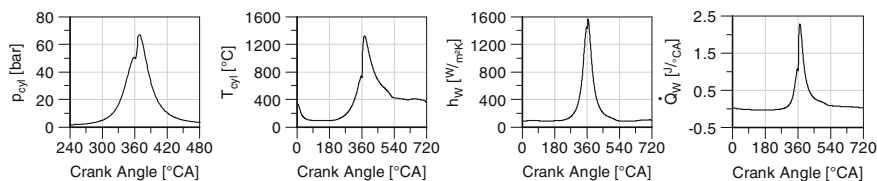


Fig. 2 Simulated pressure trace, in-cylinder mean gas temperature, heat-transfer coefficient and wall heat at 5.3 bar IMEP and 1500 rpm

with $i =$ cylinder head, piston, liner.

For describing the heat transfer coefficient h_w the empirical correlation of Hohenberg [6] is implemented:

$$h_w = 130 \cdot V_{cyl}^{-0.06} \cdot p_{cyl}^{0.8} \cdot T_{cyl}^{-0.4} \cdot (c_m + 1.4)^{0.8} \quad (2)$$

As a consequence the cylinder model has to be able to calculate the thermodynamic state variables p_{cyl} and T_{cyl} crank-angle based for every single working cycle in order to determine the wall heat transfer coefficient and thus, the wall heat flux, see Eq. 1 (Fig. 2).

Finally, the cumulated wall heat flux is one of the target values which are sent to an independent co-simulation platform. From there, these values can be picked up by other simulation models, e.g. thermal engine network and wall temperature model.

From Eq. 1 follows that the wall heat flux depends on the difference in temperature between combustion gas and combustion chamber walls. Hence, the combustion chamber wall temperatures (cylinder head, liner, piston) are of particular interest, especially in the context of engine warm-up simulation. The authors point out that the wall temperature should not be assumed to be geometrically constant. If so, the coolant-side heat transfer coefficients have to be adjusted ($h_{coolant, corr}$) as illustrated in Fig. 3. The temperature distribution can be solved analytically by Laplace transform with a numerical inversion method [7] or by the use of a simple FE-approach with a sufficient number of discrete masses.

At this point, the knowledge about the heat transfer coefficients between engine structure and coolant is crucial. The geometry of the cooling ducts inside the engine is complex. This fact induces varying flow velocities which have a significant influence on the formation of the flow boundary layer and thermal boundary layer. This in turn leads to an inhomogeneous distribution of the heat transfer coefficients inside the engine. On the other hand, information gained with heat flux sensors are only locally valid and the usage of extrapolation methods is not recommended, since the gained information are highly limited due to the arbitrariness of the sensor position. In the context of a transient warm-up engine model the simulation of the heat transfer coefficients between coolant and engine structure at any possible operating point is a major challenge. The impact of continuously varying flow velocities caused by changed engine speed as well as the impact of continuously changing thermophysical properties of the coolant due

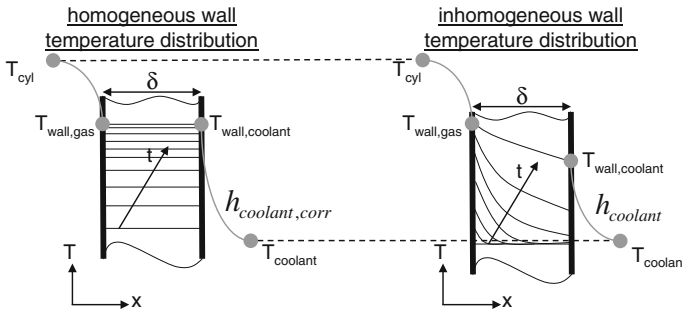


Fig. 3 Transient temperature distribution in cylinder wall (lumped mass approach vs. one-dimensional heat-conduction)

to increasing temperature must be taken into consideration when modelling such a thermal system.

In order to describe the convective heat transfer in a dimensionless form the authors recommend the following procedure:

1. Dimensional analysis of the heat transfer phenomena
2. Determining the area standardized heat transfer coefficients
3. Function analysis for 1d-CFD application.

2.1 Dimensional Analysis of the Heat Transfer Phenomena

In order to determine the dimensionless quantities which describe the heat transfer in the cooling ducts within the engine the *Buckingham II-Theorem* [1] is used. Therefore, the dependencies of the heat transfer coefficient have to be described at first:

$$h_c = f(u, d, \rho, \eta, c_p, \lambda) \tag{3}$$

Equation 3 shows that the heat transfer phenomena can be described by $k = 7$ parameters. Moreover, there are $r = 4$ fundamental physical units (M, L, T, Θ). Thus, the heat transfer can be described by $k-r = 3$ dimensionless parameters, so the dimensionality of the problem is reduced from 7 to 3, see Eq. 4. This corresponds to a high compression level of the underlying information.

$$\Pi_1 = f(\Pi_2, \Pi_3) \tag{4}$$

In order to gather the wanted parameters, 4 reference parameters have to be chosen. Great care has to be taken to ensure that the reference parameters are dimensional independent from each other. Therefore, it can be helpful to set up a dimensional matrix. Finally, the dimensional quantities can be formulated which leads to three linear systems of equations. The solutions, and thus the obtained dimensionless parameters are given below:

$$\Pi_1 = \frac{\alpha}{u\rho c_p} = \text{St} \quad (5)$$

$$\Pi_2 = \frac{\eta}{ud\rho} = \frac{1}{\text{Re}} \quad (6)$$

$$\Pi_3 = \frac{\lambda}{ud\rho c_p} = \frac{1}{\text{Pe}} = \frac{1}{\text{Re} \cdot \text{Pr}} \quad (7)$$

In summary it can be stated, that the investigated heat transfer phenomena can be described by the Stanton, Reynolds and Prandtl number. Before those dimensionless numbers can be interrelated, the area standardized heat transfer coefficients have to be determined at first.

2.2 Determining the Area Standardized Heat Transfer Coefficients

In order to determine the absolute values of the occurring heat transfer coefficients 3d-CFD simulations were performed. The boundary conditions of the investigated 16 cases have been selected to cover the relevant range of 700–4000 rpm and –20 to +110 °C. Figure 4 shows an excerpt of the heat transfer coefficient's distribution using the example of the cylinder head.

As expected, the heat transfer coefficient increases with rising engine speed, since higher flow rates reinforce turbulences within the boundary layer. The maximum ratio of the heat transfer coefficient at constant temperature is 4.17 at all contemplated cases. More attention should be given to the fact that the heat transfer coefficient is also significantly affected by coolant temperature. The response on temperature variation concerning maximum ratio of the heat transfer coefficients is on a similar scale (ratio = 4.33) compared to the flow rate variation. Thus, the coolant temperature's influence on the heat transfer must not be neglected, provided that the heat up behaviour of a water-cooled engine is of particular interest.

2.3 Function Analysis for 1d-CFD Application

The information generated by 3d-CFD simulations must be compressed to make them usable in one-dimensional simulation environments. Therefore, a function analysis has to be performed, so that the convective heat transfer phenomena can be described by the obtained dimensionless numbers Stanton, Reynolds and Prandtl. This approach leads to empirical relationships for the heat exchange surfaces *cylinder head*, *liner* and *crank case* listed in Eqs. 8, 9 and 10:

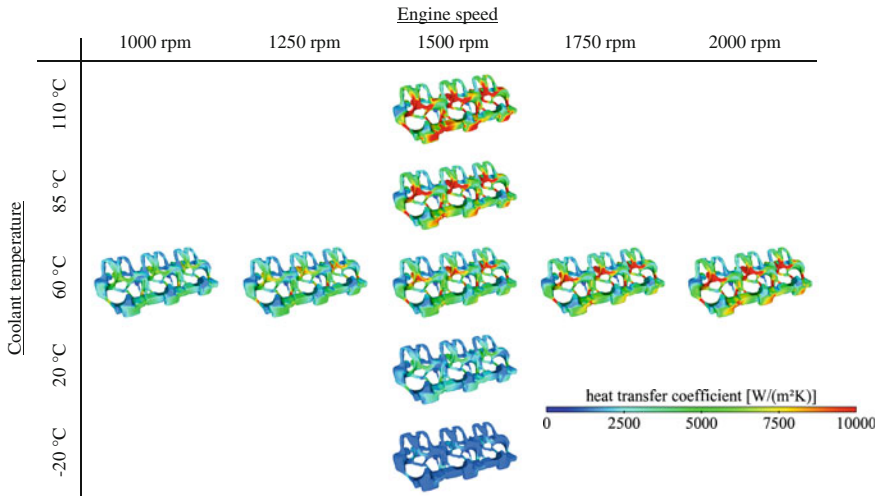


Fig. 4 3d-CFD analysis of the coolant-side heat transfer coefficient (cylinder head)

Cylinder Head:

$$St = \frac{0.076}{Re \cdot Pr} \cdot (Re^{1.013} + 4500) \cdot \left(1.073 - \frac{-0.0563}{Pr} \right) \quad (8)$$

Liner:

$$St = \frac{3.13 \cdot 10^{-3}}{Re \cdot Pr} \cdot (Re^{1.018} + 29000) \cdot \left(1.092 - \frac{-0.5706}{Pr} \right) \quad (9)$$

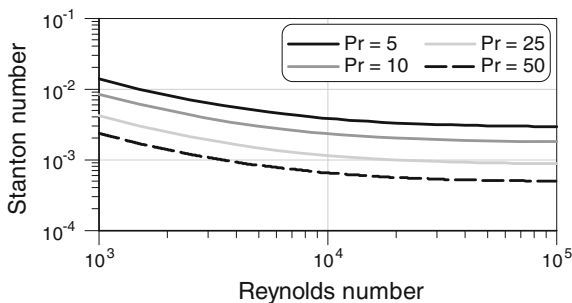
Crank Case:

$$St = \frac{0.0123}{Re \cdot Pr} \cdot (0.01 \cdot Re^{1.013} + 12350) \cdot \left(0.561 - \frac{-1.671}{Pr} \right) \quad (10)$$

Using the example of the heat transfer behaviour between coolant and cooling ducts within the cylinder head, the Stanton number over Reynolds number is plotted for different Prandtl numbers, see Fig. 5.

A validation over all operating points lead to a mean error smaller than 0.12 %. At this point should be noted that operating points have been considered, which were not used as an input for the function analysis. The presented correlations can be implemented in 1d-CFD code in order to predict the occurring heat transfer coefficients not only for all possible combinations of temperature and flow rates but also for different mixtures of water/antifreeze fluids or even alternative cooling fluids whose substance properties are known.

Fig. 5 Area standardized Stanton number (cylinder head)



The gained knowledge is important for every transient warm-up simulation. The necessity of this fact is demonstrated by a clear example shown in Fig. 6. In this example the area standardized heat transfer coefficients, the mass flow rate through the cylinder head and the coolant outlet temperature as a function of time are plotted for a warm-up run out of $-20\text{ }^{\circ}\text{C}$ at constant vehicle speed. While the mass flow rate through the cylinder head reaches steady-state conditions quite fast, the coolant temperature is increasing much slower. Attention should be paid to the fact that the area standardized heat transfer coefficients are increasing even though the mass flow rate is constant. In summary can be stated, that the influence of the coolant temperature is not negligible.

The knowledge about the hydraulic flow conditions within the engine’s cooling ducts is a basic requirement. On the one hand the Reynolds number is required for calculating the heat transfer, on the other hand the coolant mass flow distribution within the engine as well as the accurate simulation of the coolant mass flow through heat exchangers like EGR-cooler, ATF-cooler or engine oil-cooler, which directly affects the transferred heat quantity, is needed as well. The simulation model has to satisfy high requirements: Temperature variation, all possible water-pump feed rates, thermostat opening as well as changing pressure-drop circumstances within the cooling circuit due to changing valve positions controlled by the engine control unit must be considered adequately. As established before, a dimensional analysis of the hydraulic properties follows. This time the *method of differential equations* is used with the aim to reduce the dimension of the problem without loss of accuracy. As before, the complete range of $-20\text{--}110\text{ }^{\circ}\text{C}$ and $700\text{--}4000\text{ rpm}$ engine speed must be covered.

The flow conditions within the engine’s cooling ducts can be expressed by the Navier–Stokes equations for incompressible fluids under steady-state conditions where other body forces are neglected due to dominating pressure forces. The dimensional analysis applied on this problem leads to conservation of momentum in x-direction written in the following dimensionless form:

$$\bar{u} \frac{\partial \bar{u}}{\partial \bar{x}} + \bar{v} \frac{\partial \bar{u}}{\partial \bar{y}} = - \underbrace{\frac{\Delta p}{\rho u_{\infty}^2}}_{Eu} \frac{\partial \bar{p}}{\partial \bar{x}} + \underbrace{\frac{\eta}{\rho u_{\infty} d}}_{1/Re} \left(\frac{\partial^2 \bar{u}}{\partial \bar{x}^2} + \frac{\partial^2 \bar{u}}{\partial \bar{y}^2} \right) \tag{11}$$

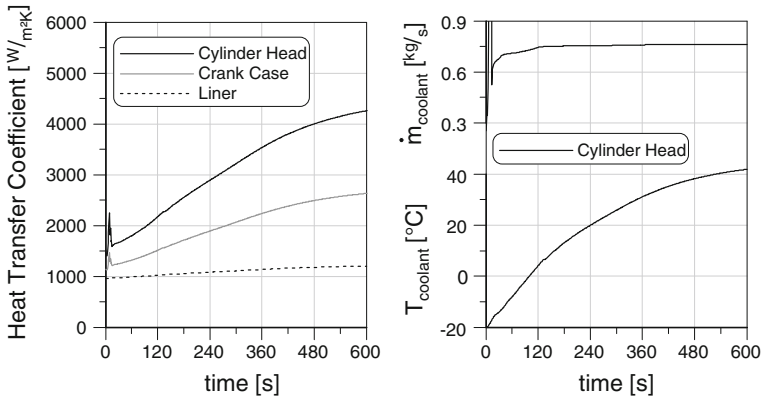


Fig. 6 Heat transfer coefficients dependency on coolant temperature

This basically means that every discrete length within the inner-engine cooling circuit can be described by interrelating the Euler number (ratio of pressure forces to inertial forces) and Reynolds number in the following form:

$$Eu = C_1 + C_2 \cdot Re^m \tag{12}$$

The coefficients C_1 , C_2 and the exponent m have to be determined by analyzing the results generated by 3d-CFD simulations. In this case the hydraulic properties of the system are described by 25 discrete pressure losses, see Fig. 7.

Another very important heat input into the engine structure and thus into the coolant and oil is the heat exchange through the inlet and exhaust ports. Based on Zapf’s Nusselt correlations [12] the authors formulate the heat transfer coefficient as follows:

Inlet port:

$$\alpha_{IP} = 1.342 \cdot \left(1 - 0.765 \cdot \frac{h_v}{D_i} \right) \cdot \dot{m}_{IP}^{0.68} \cdot D_{IP}^{-1.68} \cdot T_{IP}^{0.358} \tag{13}$$

Exhaust port:

$$\alpha_{EP} = 0.987 \cdot \left(1 - 0.797 \cdot \frac{h_v}{D_i} \right) \cdot \dot{m}_{EP}^{0.5} \cdot D_{EP}^{-1.5} \cdot T_{EP}^{0.498} \tag{14}$$

where the ratio of valve lift (h_v) to valve-seat diameter (D_i) is integrated over one working cycle.

Beside the heat input from the exhaust gas to the ports, the heat input caused by friction has to be considered. Since the frictional losses within the investigated engine are known by extensive strip-measurements on a climate test chamber, a friction table could be generated. Thus, heat input as a result of friction is depended on structure temperature, engine oil temperature as well as engine speed and load.

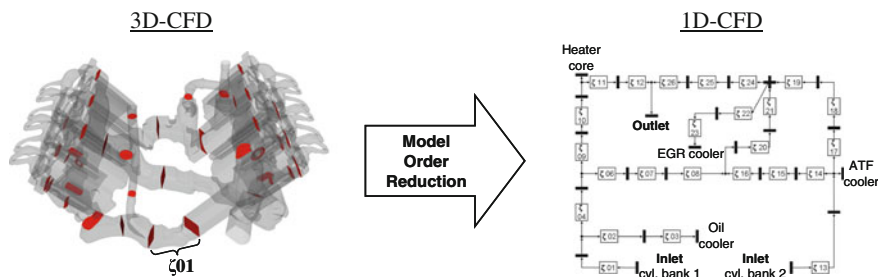


Fig. 7 Abstraction of 3d-coolant flow for the hydraulic 1d-model

3 Model Validation

In the framework of the presented investigations a test vehicle was set up. The test vehicle is equipped with 200 temperature sensors, 7 turbine flowmeters, a mobile fuel consumption measurement system and in-cylinder pressure sensors. The test engine is a turbocharged 3.0 L V6 Diesel engine with split cooling concept, high pressure EGR and common rail injection system. The presented measurements were performed in a climatic wind tunnel which can be cooled down to $-25\text{ }^{\circ}\text{C}$.

The authors point out, that the full-vehicle thermal model has to meet highest requirements in order to simulate every conceivable combination of driving cycle and ambient air temperature adequately. This means that the model can not be calibrated for one special case. Every single model taking part in the full-vehicle simulation has to be as physical as possible in order to be valid in a wide range. Therefore, the validation of the model is based on two different driving cycles at two different initial temperatures.

Figure 8 shows the simulation results compared to measured data for the NEDC at $+20$ and $-20\text{ }^{\circ}\text{C}$, respectively. For reasons of clarity the volumetric coolant flow rate is plotted only at $T_{\text{init}} = +20\text{ }^{\circ}\text{C}$, whereas the cabin temperature is plotted at $T_{\text{init}} = -20\text{ }^{\circ}\text{C}$. The used HVAC-model is not further described within this paper but can be looked up in [5]. Particular attention should be paid to the simulated coolant flow rate through the EGR-cooler. If the simulation would deviate from the reality, the simulation of the entire warm-up would certainly fail, due to the high amount of heat transferred in the EGR-cooler [3]. In Fig. 9 simulation results are compared to measured data again at $T_{\text{init}} = -20$ and $T_{\text{init}} = +20\text{ }^{\circ}\text{C}$. In contrast to above an intra-urban real world driving cycle is shown.

Overall it can be seen, that the gained simulation results match the measured data very well. On that basis, the simulation model is suitable for the investigation of several warm-up strategies before testing the best-case scenarios in a climatic wind tunnel or field tests under real conditions.

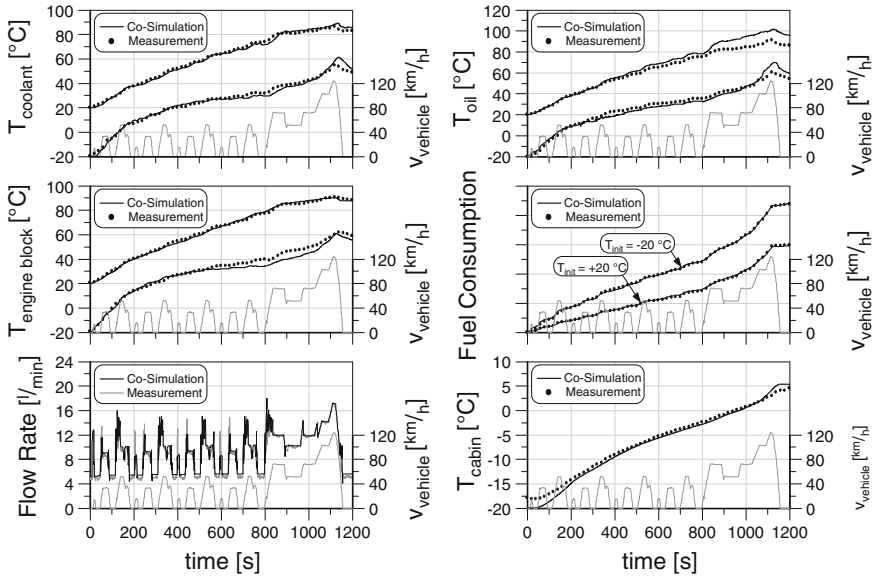


Fig. 8 Validation NEDC at different ambient temperatures

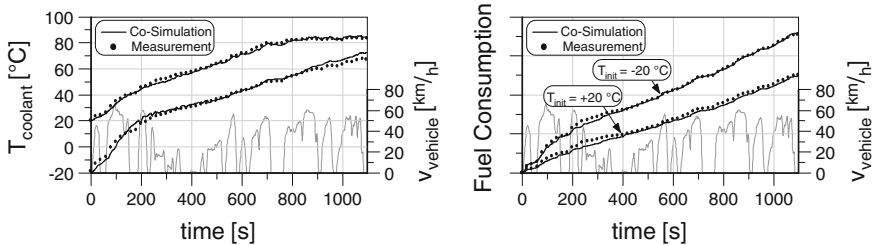


Fig. 9 Validation real-world driving cycle (intra-urban) at different ambient temperatures

4 Warm-Up Strategies

For further investigations the effects of a heat storage system (HSS) on warm-up behaviour and fuel consumption at an real-world driving cycle ($T_{init} = +20\text{ °C}$) will be discussed. The driving cycle has a length of 8.07 km and duration of 1,095 s. Without additional heat supply the thermostat opens after 800 s and 862 kJ heat are rejected at the radiator in total.

The aim is to identify a warm-up strategy on the supposition that 600 kJ of the stored heat can be recovered from former vehicle operation. As can be seen in Fig. 10, six different strategies are simulated. On the right diagram the net heat input $E_{HSS,net}$ is shown, which describes the difference between total heat input E_{HSS} and the reduction of the heat input caused by reduced wall heat flux (load

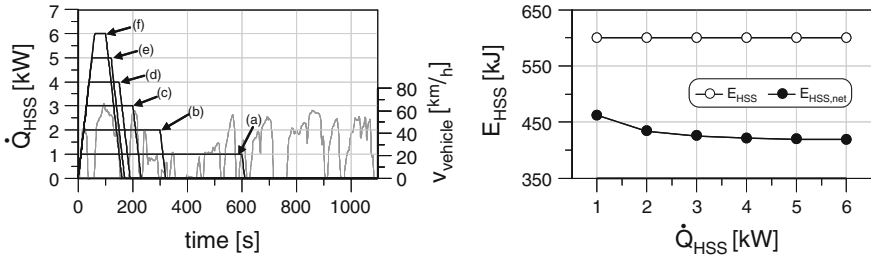


Fig. 10 Additional heat supply

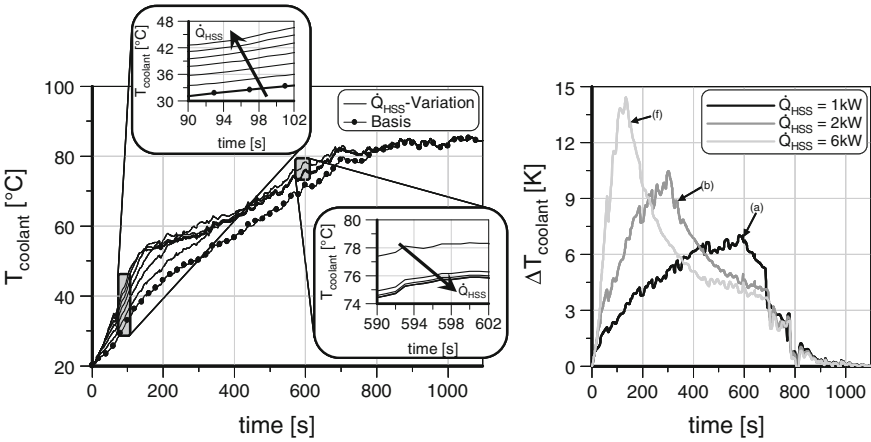


Fig. 11 Impact of heating strategy on coolant temperature development

reduction), reduced heat exchange between exhaust gas and port walls (decreasing exhaust temperature) as well as rising convection losses at the engine surface. Nevertheless, with respect to Fig. 11 it seems to be more important at which moment the heat is supplied within a warm-up simulation. The diagram shows the coolant temperature as a function of time for different warm-up strategies.

As expected the coolant temperature increases faster with higher heat input rates. On the right diagram the coolant temperature difference between the cases (a), (b) and (f) compared to basis is plotted. The temperature difference of case (b) exceeds after 220 s the temperature difference of case (f). This fact shows that the overall temperature level of the engine is higher and thus the friction losses are reduced. Figure 12 shows the FMEP-development over time for the different strategies.

The frictional losses can be reduced by the additional heat input of the HSS. Consequently, this leads to an overall reduction in fuel consumption and thus in CO₂ emissions, see Fig. 13.

Figure 13 shows the CO₂ emission reduction as a function of the heating strategy. Despite the fact that the net heat input decreases with higher heat input

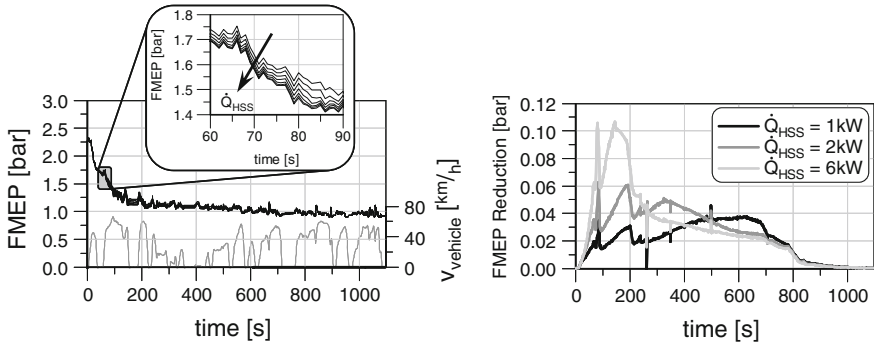
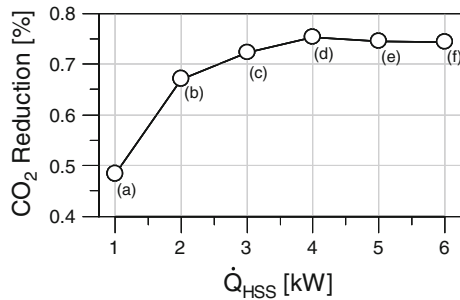


Fig. 12 Impact of heating strategy on FMEP reduction

Fig. 13 Impact of heating strategy on CO₂ emission reduction



rates (see Fig. 10), heating strategy (d) represents the most efficient heating strategy considering the interaction between every relevant systems within the vehicle.

Within the presented thermal full-vehicle simulation model the entire vehicle mass is considered in the driving resistance calculation. Therefore, the total vehicle mass was raised due to the additional mass of the heat storage system. In the framework of a holistic investigation the additional mass has to be considered at any time, even if the HSS can not be charged. This scenario must be considered since the CO₂ emissions would be raised by 0.2 % if the overall system can not benefit of the additional heat input. That is especially the case if the thermostat does not open due to very low ambient temperatures or shortened routes.

5 Conclusion and Outlook

In this paper the development process for a thermal engine model is presented which is used within a co-simulation environment of a full-vehicle model. The focus lies on modelling the heat-path beginning with the combustion process followed by heat conduction through the combustion chamber walls and

convective heat transfer between engine structure and coolant. CFD simulations have shown that heat transfer coefficients on the coolant-side not only depend on flow velocity but also on the coolant temperature. Particularly with regard to warm-up simulations this fact has to be considered. Thus, the information gained with 3d-CFD simulations were compressed to make them usable for 1d-CFD application by the usage of dimensionless quantities. The thermal sub-systems are coupled with an independent co-simulation platform. The major advantage of this approach is that for each thermal system the most qualified CAE-tool can be used.

The benefit of a heat storage system during an intra-urban real-world driving-cycle is shown. However, thermal management measures like the presented one should not be investigated at only one ambient temperature or one driving cycle. Therefore, a thermal full-vehicle model with highest accuracy is needed in order to gain information about the behaviour of interacting thermal systems and predict impact on heat-up behaviour and fuel-consumption.

References

1. Buckingham E (1914) On physically similar systems; illustrations of the use of dimensional equations. *Phys Rev* 4(4):345–376
2. Chmela FG, Orthaber GC (1999) Rate of heat release prediction for direct injection diesel engines based on purely mixing controlled combustion. SAE1999-01-0186
3. Donn C, Zulehner W, Ghebru D, Spicher U, Honzen M (2011) Experimental heat flux analysis of an automotive diesel engine in steady-state operation and during warm-up. SAE2011-24-0067
4. Donn C, Ghebru D, Zulehner W, Wagner U, Spicher U, Honzen M (2012) Influence of operating parameters on the thermal behaviour and energy balance of an automotive diesel engine, FISITA 2012 World automotive congress F2012-A07-014
5. Ghebru D, Donn C, Zulehner W, Spicher U, Puntigam W, Strasser K (2011) Numerical investigation of energy-efficient heat-up strategies considering a comprehensive HVAC-system, VTMS10, institution of mechanical engineers
6. Hohenberg G (1979) Advanced approaches for heat transfer calculations, SAE790825
7. Hollenbeck, KJ (1998) A matlab function for numerical inversion of Laplace transforms by the de Hoog algorithm
8. Kossel R, Loeffler M, Strupp NC, Tegethoff WJ (2011) Distributed energy system simulation of a vehicle, VTMS 10, institution of mechanical engineers
9. Puntigam W, Balic J, Almbauer R, Hager J (2006) Transient co-simulation of comprehensive vehicle models by time dependent coupling. SAE2006-01-1604
10. Püschl T, Schulze T, Schütte H (2009) Model-based parameter optimization for in-cylinder pressure based realtime engine models, Aachen colloquium automobile and engine technology
11. Schulze T, Wiedemeier M, Schuette H (2007) Crank angle-based diesel engine modeling for hardware-in-the-loop applications with in-cylinder pressure sensors. SAE2007-01-1303
12. Zapf H (1968) Untersuchung des Wärmeüberganges in einem Viertakt-Dieselmotor während der Ansaug- und Ausschubphase, PhD-Thesis, Technische Universitaet Muenchen

Modelling and Simulation of AMT Truck Clutch Actuating Mechanism

Yanying Guo, Xintian Lu, Tao Yan and Zhonghui Sun

Abstract The phenomenon of excessive separation and combination for clutch is caused by characteristics of pneumatic actuator itself when a heavy-duty AMT truck is starting and shifting. In order to solve this control problem, it was the first time to establish mathematic model of a heavy-duty truck clutch pneumatic actuator based on clutch pneumatic actuators working principle and gas dynamics basic theory, set the clutch cylinder piston target location in separation and combination, and make the simulation research in this paper. The validity of clutch pneumatic actuators model was verified using bench test. The basis for the preliminary work has laid for heavy trucks AMT control systems application program and the control strategies development.

Keywords AMT truck · Clutch · Pneumatic actuators · Model · Bench test

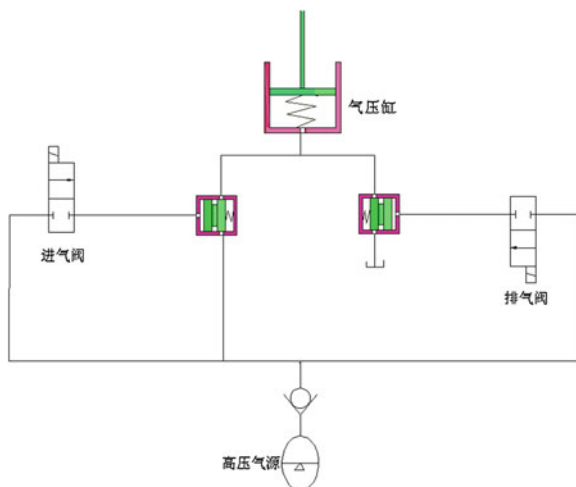
1 Introduction

Electronically controlled mechanical automatic transmission (AMT), occupies an important position in the automatic transmission family, with high transmission efficiency of the manual transmission, and low manufacturing costs, and its production can follow the production line of the manual transmission, the small investment in equipment, the products are high cost performance, very suitable for the development of China's automobile industry reality, with the prospects of the

F2012-E12-030

Y. Guo (✉) · X. Lu · T. Yan · Z. Sun
China FAW Co., Ltd R&D Center, Changchun, China
e-mail: guoyanying@rdc.faw.com.cn

Fig. 1 The clutch pneumatic actuator principle sketch



industry and a broad range of applications. As an important part of the transmission system, the clutch control effect is an important aspect of the evaluation of vehicle start-up and shift quality. The Clutch control is not only the core and the difficulty of the control system, but also the bottleneck of the development of heavy AMT truck. The complexity of the pneumatic actuator system, the strongly nonlinear and compression of medium gas, results in the clutch release bearing can not be stopped at the predetermined position, namely, exists the excessive separation or excessive engagement phenomenon when heavy-duty trucks in the start-up and shifting process. To solve this problem, we need to fully understand and master the clutch pneumatic actuator current working conditions. So, a mathematical model has been established, analysed in the chapter, and has been validated by the test bench, which well prepared for the development of the system control strategy.

2 The Actuator Working Principle and Model Theory Basis

The pneumatic actuator of the clutch in the paper comprises with the two 2/2-way normally closed solenoid valve and its valve block and a single-acting cylinder, which principle shows in Fig. 1.

1. When the intake valve is powered, the gas push the valve piston shifted to the right and entered into the clutch cylinder by the intake valve block, then push the clutch cylinder piston moved to overcome the diaphragm spring force, so the clutch disengaged.
2. When the exhaust valve is powered, the clutch cylinder gas was been exhausted into the atmosphere though the exhaust valve block by the clutch diaphragm spring force and the clutch engaged.

3. The intake valve and exhaust valve was powered off when the system keep pressure.

The correctness of the actuator model plays a vital role for the study of the control system. In accordance with the clutch pneumatic actuator work principle, the models have been simplified and make the following assumptions:

1. Pneumatic actuator doesn't leak;
2. The gas source state is regarded as the gas stagnation state;
3. Airflow within the actuator and the gas pipeline does not exchange of heat and power with the outside, that is, the friction between the pipe wall and gas has been ignored.
4. Ignore the gravitational potential energy due to gas weight is very small;
5. In pneumatic actuator system, the change of the gas pipeline cross-sectional area along the flow direction is small. The radius of curvature of the pipe axis is much larger than the pipe radius, so that the cross-section perpendicular to the flow direction airflow parameters (temperature, density, pressure, speed, etc.) is uniform [1] that is the pipe flow is one-dimensional steady flow.
6. The viscosity of air is very small, the energy loss which gas flow through throttle hole is much less than its total energy, so the energy loss in the gas flow is ignored and the gas flow has been seen as isentropic flow.
7. Temperature effects are ignored.

To research the clutch actuator media is mainly based on the gas dynamic theory basis. In the process gas flows from the gas source into the cylinder, before the gas cylinder fills with the gas quality Q_m , supposing, the gas pressure in cylinder is P_1 , the gas density in cylinder is ρ_1 , the volume of cylinder is V_1 , the gas mass in cylinder is m_1 . When the gas cylinder has filled with the gas quality Q_m , the gas pressure in cylinder is $P_1 + P$, the volume of cylinder is $V_1 + V$, the gas mass in cylinder is $m_1 + Q_m$, and the displacement of cylinder piston is x , the area of cylinder piston is A_{gang} .

Based on the ideal gas state equation [1]. Before the cylinder filled:

$$\frac{P_1}{\rho_1} = RT = \frac{P_1}{\frac{m_1}{V_1}} \Rightarrow P_1 V_1 = m_1 RT \tag{1}$$

After the cylinder filled:

$$\frac{P_1 + P}{\frac{m_1 + Q_m}{V_1 + A_{gang}x}} = RT \Rightarrow (P_1 + P)(V_1 + A_{gang}x) = RT(m_1 + Q_m) \tag{2}$$

The formula (1) into formula (2) and finishing as follow:

$$P(V_1 + A_{gang}x) = RTQ_m - P_1 A_{gang}x \tag{3}$$

Derivative formula (3) can get formula (4), consequently, get the cylinder pressure and piston displacement:

$$\frac{dP}{dt}(V_1 + A_{gang}x) = RTq_m - P_1A_{gang}u \tag{4}$$

There into: u —the cylinder piston velocity.

The volume of compressible gas flow through the throttle hole in unit time q_m which should divide into velocity and subsonic district [1] as the calculation.

When $P_H > 1.893P_L$ (P_H is gas source pressure, P_L is gas pressure in cylinder), the gas velocity is in velocity district and $M_a = 1, \lambda = 1$. So volume function [2] is shown as follow:

$$q(\lambda) = \left(\frac{k+1}{2}\right)^{\frac{1}{k-1}} \lambda \left(1 - \frac{k-1}{k+1} \lambda^2\right)^{\frac{1}{k-1}}$$

Here, the volume of compressible gas flow through the throttle hole in unit time is shown as follow:

$$q_m = \sqrt{\frac{2}{k+1} \frac{k}{R}} \left(\frac{2}{k+1}\right)^{\frac{1}{k-1}} q(\lambda) \frac{P_H a_{gang}}{\sqrt{T}} = \left(\frac{2}{2.4}\right)^{\frac{0.4}{0.4}} a_{gang} P_H \sqrt{\frac{2 \times 1.4}{287 \times 2.4 \times T}}$$

When $P_H = (1 \sim 1.893)P_L$, the velocity is in subsonic district [2], so:

$$\frac{P_L}{P_H} = \left(1 - \frac{k-1}{k+1} \lambda^2\right)^{\frac{k}{k-1}}$$

So:

$$\lambda = \sqrt{\frac{k+1}{k-1} \left[1 - \left(\frac{P_L}{P_H}\right)^{\frac{k-1}{k}}\right]}$$

Therefore, the volume function in the subsonic district is shown as follow:

$$q(\lambda) = \left(\frac{k+1}{2}\right)^{\frac{1}{k-1}} \cdot \sqrt{\frac{k+1}{k-1} \left[1 - \left(\frac{P_L}{P_H}\right)^{\frac{k-1}{k}}\right]} \cdot \left(\frac{P_L}{P_H}\right)^{\frac{1}{k}}$$

Here, the volume of compressible gas flow through the throttle hole in unit time is shown as follow:

$$\begin{aligned} q_m &= \frac{P_H a_{gang}}{\sqrt{T}} \cdot \sqrt{\frac{k}{R} \cdot \frac{2}{k-1} \left[\left(\frac{P_L}{P_H}\right)^{\frac{2}{k}} - \left(\frac{P_L}{P_H}\right)^{\frac{k+1}{k}} \right]} \\ &= \frac{P_H a_{gang}}{\sqrt{T}} \sqrt{\frac{1.4 \times 2}{287 \times 0.4} \left[\left(\frac{P_L}{P_H}\right)^{\frac{2}{1.4}} - \left(\frac{P_L}{P_H}\right)^{\frac{2.4}{1.4}} \right]} \end{aligned}$$

Namely:

$$q_m = \frac{P_H a_{gang}}{\sqrt{T}} \sqrt{0.0244 \times \left[\left(\frac{P_L}{P_H} \right)^{\frac{2}{1.4}} - \left(\frac{P_L}{P_H} \right)^{\frac{2.47}{1.4}} \right]}$$

There into:

- k Ratio of specific heats
- a_{gang} cross-sectional area of cylinder intake and vent
- T gas temperature

3 Clutch Actuator Model

Base on the Newton secondly law, homeostasis equation of cylinder piston is shown as follow:

$$m\ddot{x}_{piston} + c\dot{x}_{piston} + kx_{piston} = P_{gang} \cdot S - F$$

The displacement relation of clutch cylinder piston and disengagement bearing is shown as follow:

$$x_{clutchBearing} = i \cdot x_{piston}$$

Based on the moment balance principle, it can be get as follow:

$$F_{disengagement} \cdot x_{clutchBearing} = F \cdot x_{piston}$$

Thereinto:

- m piston equivalent mass, which is relevant with itself quality, piston rod and actuator coupling
- x_{piston} piston displacement
- c damp coefficient during piston movement
- k clutch cylinder spring stiffness coefficient
- P_{gang} gas pressure in clutch cylinder
- S piston force area
- F Discounted the diaphragm spring disengagement force to the piston force
- i clutch disengagement fork lever ratio
- $x_{clutchBearing}$ clutch disengagement bearing displacement
- $F_{disengagement}$ diaphragm spring disengagement force.

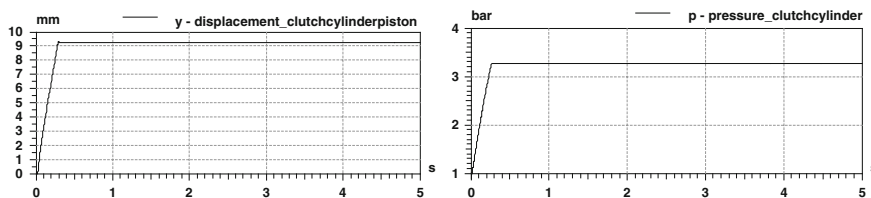


Fig. 2 The simulation curve of piston target location with 9 mm in disengagement process

4 Clutch Actuator Simulation Study

According to the clutch actuator principle [3], the model has been predigested. The action of intake valve and valve block has been predigested for the action of the intake valve. The action of exhaust valve and valve block has been predigested for the action of the exhaust valve. The gas pressure of source in the simulation model is 6 bar, which is the same with the bench test. Simulation set the target position of the clutch piston, inflate and deflate to clutch cylinder. Turn off the solenoid valve when the piston moves to the target location, i.e., during the disengagement process, when the actual location of the clutch piston reaches the target position, close the intake valve; Similarly, in the engagement process, when the actual location of the clutch piston to reach the target position, close the exhaust valve.

In Figs. 2 and 3, it has respectively set the clutch piston target location in the disengagement process with 9 and 16 mm. In Figs. 4 and 5, it has respectively set the clutch piston target location in the engagement process with 5 and 16 mm. The clutch piston actual displacement curves and the cylinder pressure curves have been shown in the figure, the results can be seen from the simulation figure as follow:

1. When the target disengagement and engagement position set value is smaller, which results are shown in Figs. 2 and 4, the piston can be basically stopped in the setting target position. Because of the compressibility of gas and the piston inertia in the movement, the piston actual position is slightly ahead of theory position, which is inevitable existence and realistic. The curves in Fig. 2 are the clutch disengagement process curves, when the piston reaches the smaller the target location, the gas pressure in the cylinder, the piston acceleration and velocity are not large, the piston can basically stop at the predetermined position after closing the intake valve; The curves in Fig. 4 are the clutch engagement process curves, when the piston reaches the target location, the gas pressure in the cylinder and the piston acceleration are very small, the piston can basically stop at the predetermined position after closing the exhaust valve.
2. When the target disengagement and engagement position set value is larger, the piston can not reach the specified location accurately as controlling the relevant solenoid valve separately. The curves in Fig. 3 is the disengagement process curves, the piston can't stop at the predetermined position if only closing the intake valve. When the piston reaches the target location, the piston

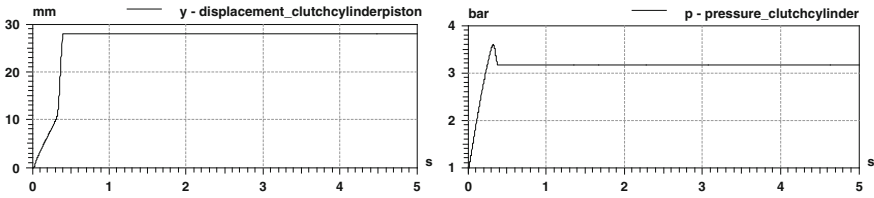


Fig. 3 The simulation curve of piston target location with 16 mm in disengagement process

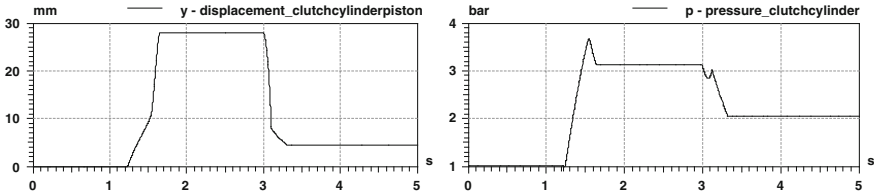


Fig. 4 The simulation curve of piston target location with 5 mm in engagement process

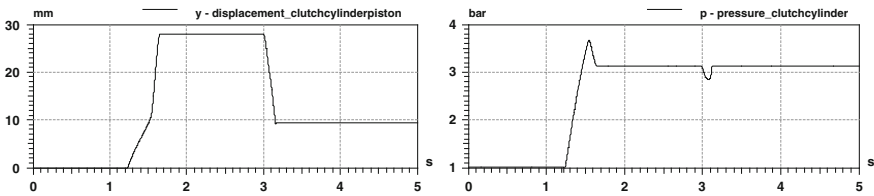


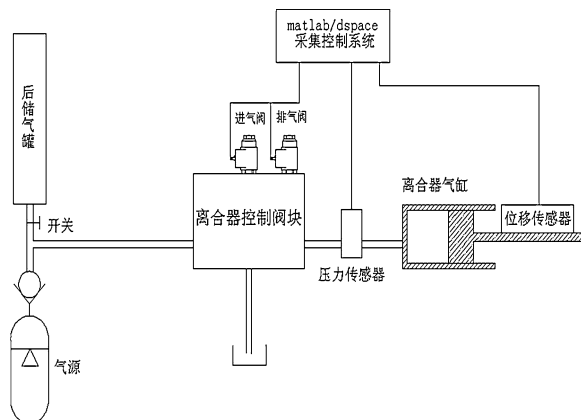
Fig. 5 The simulation curve of piston target location with 16 mm in engagement process

acceleration and velocity is not zero, the cylinder pressure is large, and the compressibility of gas is strong, the gas will push the piston move continually until it reaches its force balance position. The curves in Fig. 5 are the clutch engagement process curves, when the piston reaches the larger target location, the piston acceleration and velocity are large, the piston will move continually until it reaches its force balance position if only closing the exhaust valve. Therefore, in the starting and shifting process of heavy AMT truck, it is very easy to result the clutch excessive separation or combination, and this is the control difficulties and key of the heavy AMT truck clutch.

5 Clutch Actuator Bench Test

In order to validate the simulation model, the clutch actuator static bench tests have been done, the test principium figure is shown in Fig. 6. The control order is emitted by ControlDesk to dSPACE, then is conversed for controlling voltage with

Fig. 6 The bench test principle figure



0–5 V by dSPACE, then magnifying controlling signal voltage with 0–24 V by Hydforce signal magnify board, which acts on clutch solenoid valve and the clutch cylinder can intake and exhaust gas. The clutch can disengage and engage.

The clutch cylinder piston target disengagement location has been set with 9 and 16 mm, the target engagement location has been set with 5 and 16 mm in the bench test. The results are shown in Figs. 7, 8, 9 and 10.

The test result curves in Fig. 7 are compared with the simulation result curves in Fig. 2, we can see that the piston stopped at 9.3 mm and the cylinder pressure is 3.27 bar in the simulation result curves; the piston stopped at 9.5 mm and the cylinder pressure is 3.3 bar in test result curves.

The test result curves in Fig. 8 are compared with the simulation result curves in Fig. 3, we can see that the piston stopped at maximum displacement and the cylinder pressure is 3.16 bar in the simulation result curves; the piston stopped at maximum displacement and the cylinder pressure is 3.1 bar in test result curves.

The test result curves in Fig. 9 are compared with the simulation result curves in Fig. 4, we can see that the piston stopped at 4.3 mm and the cylinder pressure is 2.05 bar in the simulation result curves; the piston stopped at 4.1 mm and the cylinder pressure is 1.9 bar in test result curves.

The test result curves in Fig. 10 are compared with the simulation result curves in Fig. 5, we can see that the piston stopped at 9.28 mm and the cylinder pressure is 3.12 bar in the simulation result curves; the piston stopped at 9.5 mm and the cylinder pressure is 3.2 bar in test result curves.

Therefore, it can be seen that the simulation results and test results are basically consistent. Because of seal oil, seals, other damping effects of the pneumatic actuator system and the gas compressibility, the results error of simulation and test are inevitable [4, 5].

Fig. 7 The test curve of piston target location with 9 mm in disengagement process

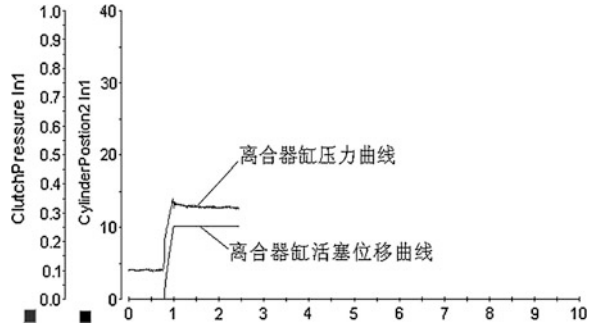


Fig. 8 The test curve of piston target location with 16 mm in disengagement process

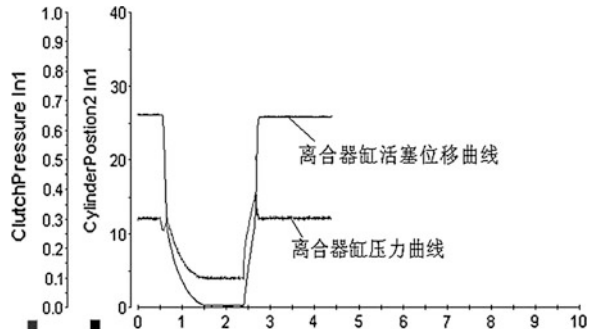


Fig. 9 The test curve of piston target location with 5 mm in engagement process

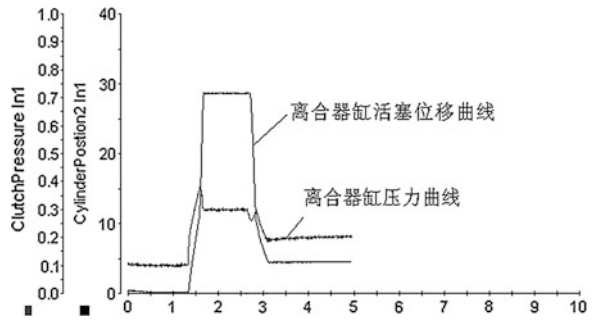
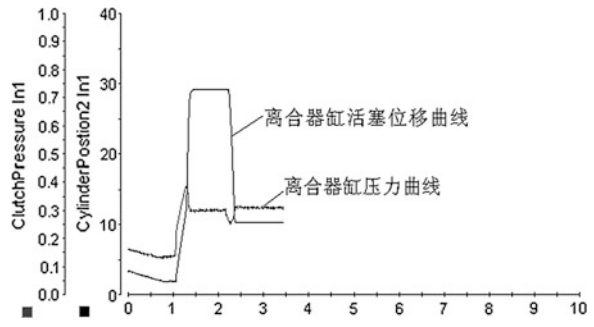


Fig. 10 The test curve of piston target location with 16 mm in engagement process



6 Conclusion

It is firstly created a mathematical model of a heavy-duty truck clutch pneumatic actuator in the paper. The clutch piston target locations of clutch disengagement and engagement process are setting in the simulation and test. The simulation studies have shown when the target location is smaller, individually controlled solenoid valve, the piston can be basically stopped at the predetermined position; and when the target location is larger, individually controlled solenoid valve, the system overshoot, increased the difficulty of the clutch control. Static bench test results and simulation results are consistent and the simulation model is available, which can be used for simulating the clutch actuator action and designing the clutch actuator control system.

References

1. Wang W (2007) Mechanism design manual [M], vol 4. Mechanical Industry Press, Beijing, pp 16–24
2. Wang X (2006) Gas dynamics basis[M], vol 70. Northwest Industry University Press, Xian, pp 122–124
3. Xi J (2009) Pressure-driven automatic clutch control technology[J], vol 1. Harbin Institute of Technology Transaction, Harbin, pp 122–125
4. Xuan S (2005) Automobile clutch[M]. Tsinghua University Press, Beijing
5. Gean L (1998) The best engagement regularity of Clutch[J]. Automotive Eng 10(2):54–65

Vibration Fatigue Analysis of Adaptive Front Lighting System

Yeon Gyoo Lee, Seungryul Choi and Tae Ryong Jeon

Abstract This chapter discusses the computer simulation methodology to predict the crack initiation fatigue life cycle of automotive Adaptive Front Lighting System (AFLS) under vibration. The AFLS improves visibility by changing the beam pattern of an automotive headlamp in accordance with various driving conditions. As the mechanical linkages consisting of projection module of the AFLS are slender and light-weight for functionality, packaging and fuel economy, the AFLS might exhibit nonlinear dynamic behavior by external vibration that the traditional Finite Element (FE) based frequency response analysis fails to simulate. By including kinematic behavior such as the leveling and the swiveling of the projection module and the nonlinear stiffness of pivot sockets into analysis model, the combination of Finite Element Analysis (FEA) and flexible multi-body dynamics (MBD) analysis can show more realistic vibration characteristics and predict the reliable fatigue life cycle of the AFLS.

Keywords Adaptive front lighting system · Finite element analysis · Multi-body dynamics · Vibration · Fatigue

F2012-E12-031

Y. G. Lee (✉) · S. Choi · T. R. Jeon
Hyundai Mobis, Suwon, Korea
e-mail: yonq@mobis.co.kr

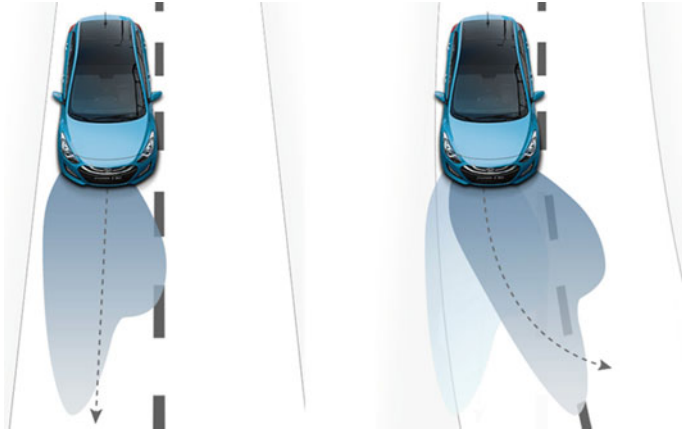


Fig. 1 The AFLS improves visibility in a curve

1 Introduction

In recent years, automotive industry has been increasingly introducing the AFLS to improve safety when driving at night. The AFLS improves visibility for the driver by changing the low beam angle of a headlamp in accordance with the steering angle and vehicle speed (Fig. 1).

Most of the AFLS in the current market have mechanical linkage to redirect low beam headlamp unit. The links and connections of the linkage must have enough stiffness for the low beam unit to remain firmly in position and to be aimed properly even under the influence of impact and vibration when driving. Over time, the vibration can also loosen or break the connections or adjustment screws, allowing the headlight to shift to an ineffective position.

Although the stiffness of the linkage is important for the functionality and durability of the AFLS, some constraints make it challenging to design links with sufficient stiffness. Headlamps can introduce an important styling attribute to a vehicle and enhance aerodynamic performance. The AFLS should be compact in size enough to provide flexibility in the front-end styling of vehicles. Since the AFLS has more components such as frame, brackets, sensors, ECU, intelligent stepping motor and electromechanical solenoid, reducing weight by using light-weight material and optimizing design is of the utmost importance for fuel economy.

For example, the projection module for low beam of the AFLS is fixed to the headlamp main housing by guide brackets for vertical/horizontal aiming, the shape of which might be slender under given functionality and packaging constraints. In addition, typical material for the brackets is light-weight engineering thermoplastic such as Polyoxymethylene (POM) to reduce the system weight. Improper design of the brackets might increase susceptibility of the projection module to vibration and result in material fatigue failure as well as poor beam pattern (Fig. 2).

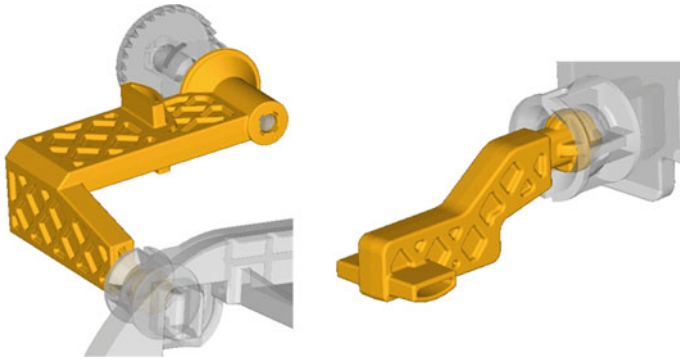


Fig. 2 Plastic guide brackets connecting housing and frame

It is of utmost importance to verify the structural stability and resistance to vibration of the AFLS before manufacturing. Computer simulation is a very efficient way of proving design before building expensive prototypes. Frequency response analysis (FRA) using FEA is common practice for understanding the basic dynamic behavior of the conventional headlamp [1]. In the case of the AFLS, however, the FRA assuming linear system cannot simulate dynamic behavior since the lightweight flexible linkage for leveling and swiveling mechanism of the AFLS could cause local non-linear rigid-body motion at joints.

This study proposes the computer simulation method for the realistic prediction of the vibration behavior and the fatigue life of the AFLS. The basic idea is using the flexible MBD analysis. The projection module of the AFLS is separated as an independent body and connected to main housing with pivot or sliding joints implemented with nonlinear stiffness characteristics for reducing model complexity. Each body is modeled as flexible body or concentrated mass to achieve balance between model accuracy and analysis cost. As the engineering plastic is increasingly used for headlamps for reducing weight and increasing fuel efficiency, various plastics are tested with specialized fatigue testing equipment to acquire stress-life curve used for fatigue analysis.

2 Structure of AFLS

The typical headlamp system has low beam and high beam units fixed to main housing with steel aiming screws or plastic guide brackets of various shapes and size. The low beam unit provides a distribution of light designed to provide adequate forward and lateral illumination with a sharp, asymmetric cut-off preventing significant amounts of light from being cast into oncoming cars. As the low beam of high-intensity discharge (HID) lamp produces more light than halogen, the dynamic leveling system of the AFLS ensures correct beam settings by rotating about a horizontal pivot axis depending on vehicle acceleration.

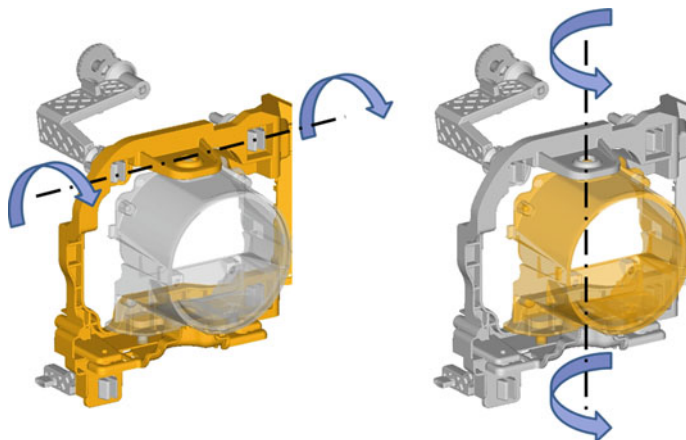


Fig. 3 Leveling (*left*) and swiveling of AFLS

The projection module of the AFLS also rotates about a vertical pivot axis of a frame. This swiveling movement is controlled by a microcomputer according to the steering angle and speed of the vehicle. As the swiveling movement must operate with the utmost precision to meet the high safety standards, the structural components such as frame, guide brackets, aiming screws and pivot sockets should have sufficient stiffness to overcome resonance from vibration. Dimensional tolerance of the components should be controlled to make sure sufficient stiffness as well (Fig. 3).

The swiveling movement are actuated by intelligent stepping motor fixed to the frame. A bi-xenon headlamp offers both low and high beam lighting from one bulb by rotating a shield with solenoid. The increase of weight with the motor and solenoid might cause local rigid body rotation and translation at joints if the frame, supporting brackets and screws are not stiff enough to overcome vibration.

3 Frequency Response Analysis

The dynamic behavior of a structure can be determined both in the time and frequency domains. Dynamic analysis in the time domain, however, involves a complicated and often lengthy transient analysis, which is not suitable for the headlamp system of large number of degrees of freedom. The analysis in the frequency domain can simplify the problem considerably. The modal FRA utilizes the mode shapes of the headlamp to reduce and uncouple the equations of motion with modal damping assumption. The FRA on the finite element model of the headlamp is performed to determine frequency response function (FRF) between external loading and stress in the headlamp for each frequency. If the external

Table 1 Resonance frequencies from FRA and MBD

Headlamp analysis	A (AFLS—bi-xenon)	B (conventional—HID)	C (conventional—halogen)
FRA	33	38	92
MBD	30	38	92

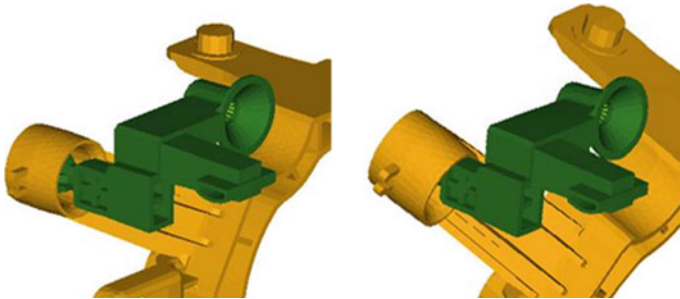


Fig. 4 The 1st resonance mode of the AFLS A

loading is given as power spectral density (PSD), statistical methods such as Lalanne are used to predict the probability density function (PDF) of stress range, and hence the rainflow cycle counting used for fatigue life prediction of the headlamp.

The main limitation of the FRA is its linear system assumption. Although the FRA works well with the conventional headlamp, it sometimes fails to describe dynamic characteristics of the AFLS. Table 1 compares the 1st resonance frequencies calculated from FRA and MBD for different types of headlamps. Whilst the two different analysis methods produce the same resonance frequencies for the conventional headlamps B and C, they produce different frequencies for the AFLS A.

The 1st resonance mode of the AFLS A is the rotation of the frame about the pivot point of a guide bracket as shown in the Fig. 4. The rigid body rotation is nonlinear phenomena which is hard to predict by using the linear analysis.

The reaction forces from the two different analysis methods are different as well. The Fig. 5 compares the reaction forces acting at a joint from the two analysis methods. While the both methods predict same reaction force for the conventional headlamp C, they show different forces for the AFLS A.

Table 2 compares the fatigue life of some components of the AFLS A from the two different analysis methods. As the MBD analysis can implement nonlinear behavior of pivot rotation in the analysis model, the MBD analysis predicts more realistic stress response and fatigue life than that of FRA.

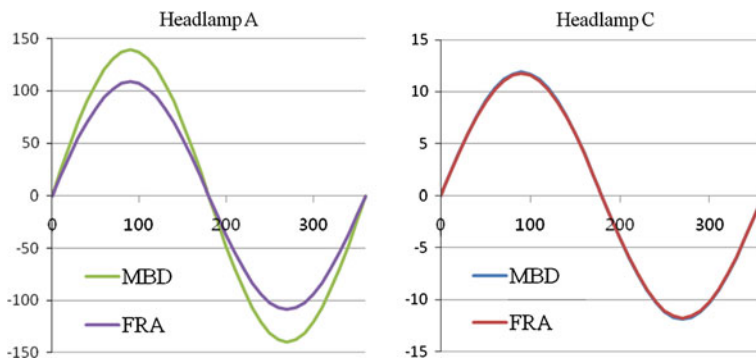


Fig. 5 Reaction forces from FRA and MBD

Table 2 Fatigue life (hour) to crack initiation of AFLS A

Component	Vibration 1		Vibration 2	
	MBD	FRA	MBD	FRA
Housing	1.5	0.1	No crack	Static failure
Guide bracket	Static failure	Static failure	4.7	Static failure
Frame	Static failure	Static failure	3,700	Static failure

4 Fatigue Analysis of AFLS

The FRA can help understanding the basic dynamic behavior of the conventional headlamp. In the case of the AFLS, however, the FRA with linear system assumption cannot simulate dynamic behavior since the lightweight flexible linkage for leveling and swiveling movement of the AFLS could cause local nonlinear rigid-body motion at joints.

For the realistic vibration simulation of the AFLS, the flexible MBD analysis is adopted. The projection module of the AFLS is separated as an independent flexible body and connected to headlamp housing with pivot joints implemented with nonlinear stiffness characteristics for reducing model complexity. The new analysis method can simulate nonlinear high-frequency responses that the linear analysis fails to predict, which increases reliability of fatigue life estimation of the AFLS.

4.1 MBD Analysis Model

The flexible MBD model consists of rigid and flexible bodies. The flexible body is represented by a set of vibration modes which are obtained from the FE modal analysis of the flexible body. The dynamics equations of the flexible body are

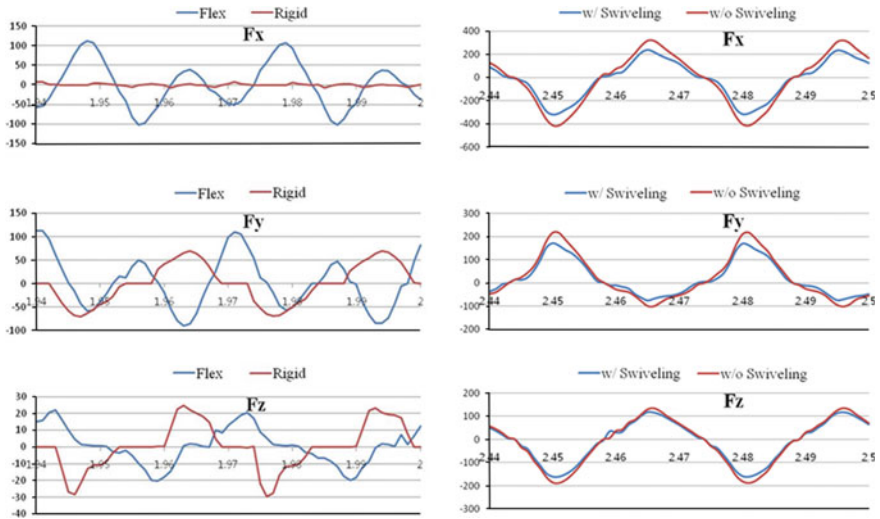


Fig. 6 Effect of frame stiffness (*left*) and swiveling mechanism on reaction forces

coupled to those of the rigid bodies of the MBD. The strain and stress should be represented by modal vectors and modal coordinates if resonance is expected. The MBD formulation is based on the assumption that the period of large rotations of the body is much larger than the period of oscillations due to deformation, which is not typical for the conventional headlamp but possible for the AFLS if resonance occurs from the frame and guide bracket of insufficient stiffness.

The flexibility action of the frame and guide brackets has very important influence on the dynamics characteristic of the AFLS. The Fig. 6 (left graph) shows the reaction forces are different depending on the modelling methods of the frame. Swiveling mechanism of the frame must be implemented in the MBD model. The Fig. 6 (right graph) shows that modelling swiveling mechanism makes difference for the reaction forces.

Bezel assembly that is attached to the outer lens of headlamp and functions as trim or finishers around the headlamp produces significant contribution to the stiffness and mass of the AFLS. Basically it is not necessary to separate the high beam unit as a body. The resonance of bulb shield, however, should be carefully checked which is possible even with the conventional FRA [2]. Each body is modelled as flexible body or concentrated mass with rotational inertia to achieve balance between analysis accuracy and cost. The pivot joints connecting each body are simplified to the ideal constraint used in the dynamics simulation. The Fig. 7 represents an example of the MBD modelling scheme for an AFLS.

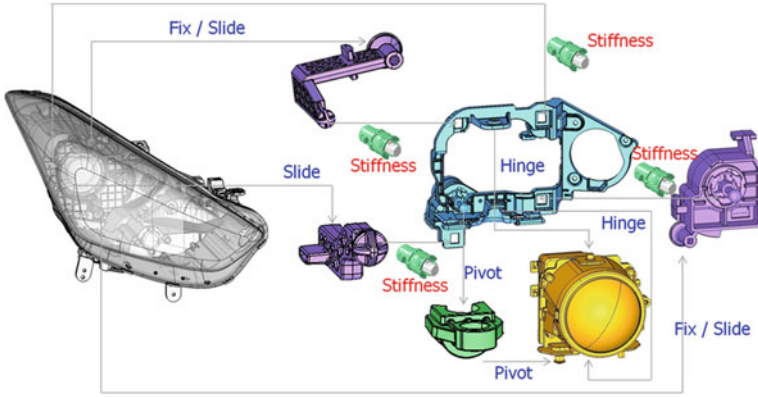


Fig. 7 Constraints and stiffness connecting the bodies of AFLS

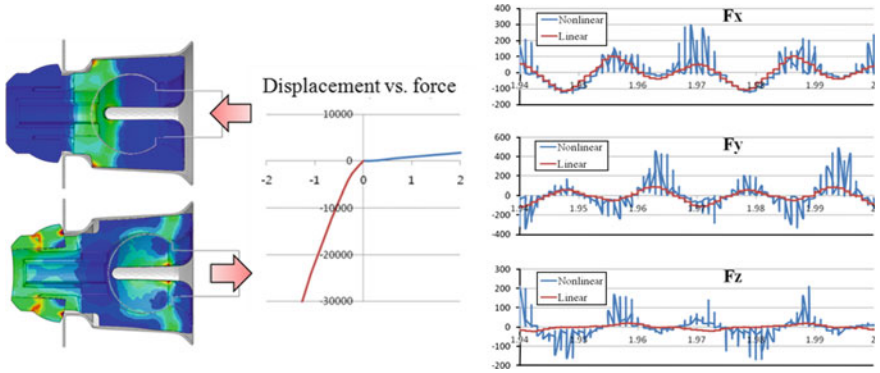


Fig. 8 Axial stiffness of a pivot socket (left) and its effect on reaction forces (right)

4.2 Stiffness of Pivot Socket

The main frame of projection module is fixed to aiming screws and brackets of lamp housing by plastic sockets. The stiffness of pivot socket, assembly clearance and rotation limit of joint are very important factors to decide reaction force acting at projection module. They must be incorporated into the MBD analysis model.

Modelling the pivot socket as an independent body with contact algorithm is inefficient; it will dramatically increase analysis model complexity and make it difficult to obtain converged solution. It is more efficient to replace the pivot socket with nonlinear spring element. Translational/rotational stiffness of pivot socket is measured with independent nonlinear stiffness analysis, which considers geometric nonlinearity such as large deformation and contact (Fig. 8).

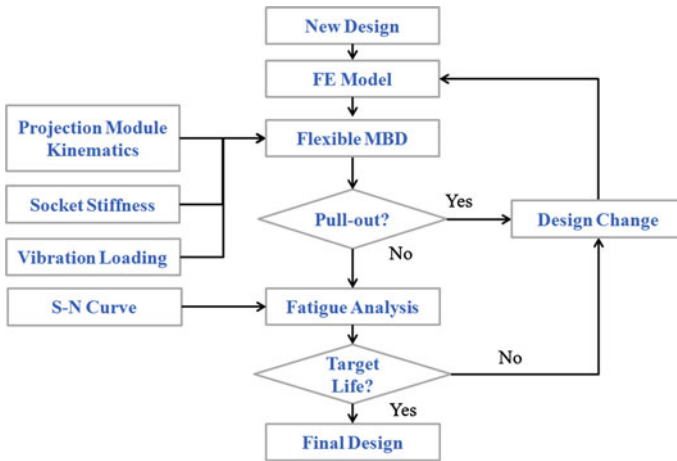


Fig. 9 Procedure of AFLS vibration fatigue analysis

A ball joint can escape from loosened pivot socket during vibration test, which is difficult to simulate in the simulation. It is more efficient to prepare the pull-out forces/moments of each pivot socket in advance before the MBD analysis. The algorithm can be implemented that analysis would stop if a reaction force exceeds the pull-out force of the pivot socket.

4.3 Fatigue Property of Engineering Plastics

Engineering plastics are increasingly adopted for various types of headlamp components. For realistic fatigue analysis, various plastics are tested with specialized fatigue testing equipment [3] to acquire stress-life curve used for fatigue analysis (Fig. 9).

4.4 Procedure of AFLS Vibration Fatigue Analysis

5 Conclusion

New analysis procedure using the flexible MBD analysis for simulating dynamic behavior of the AFLS has been proposed. The fatigue life estimation of the AFLS with the new method is more accurate than the existing FRA.

1. The FRA is still valid to predict the resonance of conventional headlamp system. If nonlinear dynamic characteristic is expected, the flexible MBD analysis has to be performed for more realistic simulation of dynamic behavior of the AFLS.
2. In the flexible MBD modeling, the frame of projection module and plastic brackets supporting the frame must be modeled with flexible bodies. Each body is connected by nonlinear stiffness characteristics representing pivot sockets.
3. The kinematic mechanism of swiveling and leveling of projection module should be implemented in the analysis model. They help to simulate the local rigid body rotation from insufficient stiffness of the mechanical linkages of the AFLS.

There is a significant time penalty to build the FE model of the AFLS. As the suggested analysis method is a holistic approach, it is necessary to develop component-based analysis method to increase analysis efficiency.

References

1. Schrader CD, Hilburger FKN (2005) Development and correlation of three axes random vibration simulation on automotive lighting, SAE Technical Paper, 2005-01-1570
2. Zhang Y, Usman M (1999) Life prediction for lighting bulb shield designs subjected to random vibration, SAE Technical Paper, 1999-01-0705
3. Jeon T, Koo J, Kim BW (2009) Study on the Derivation of fatigue properties of engineering plastics for fatigue analysis, KSAE annual conference, KSAE09-A0445

Application of Two-Chamber Muffler to Reduce Car Noise in Engine Intake System

Zhihong Tang, Zhenying Zhu, Yongxin Men and Fuquan Zhao

Abstract There is obvious noise while a vehicle accelerating, under the engine speed at 2410 rpm and 3,650 rpm. Based on tests it is found that noise is induced by engine intake system. In order to reduce the noise level a Helmholtz resonance muffler is introduced, which is widely used in engine intake system. Generally, several resonance mufflers are needed to reduce the same number of noise peaks. This way is not good for cost control and space arrangement. In this paper, the theory of Helmholtz resonance muffler with two chambers is applied and transmission loss analysis is done to determine the chambers' sizes to reduce the noise level effectively. A sample of intake system is made based on the simulation results, and validation tests are conducted to confirm the improvement in car noise reduction.

Keywords Intake system · Helmholtz resonance muffler · Two-chamber muffler · NVH · Transmission loss

1 Introduction

Intake system noise is a most important noise source of vehicle. Intake system is close to the cabin, which means it has a great influence on the inside noise level. Besides, intake system noise at the inlet is also a part of the pass-by noise [1]. Therefore, noise control of intake system is very important to the NVH quality of full vehicle.

F2012-E12-040

Z. Tang (✉) · Z. Zhu · Y. Men · F. Zhao
Geely Automobile Research Institute, Hong Kong, China

Intake system noise of engine contains periodic pressure fluctuation noise, vortex noise, Helmholtz resonance noise of cylinder and inlet gas column etc. [2]. There are two main ways to reduce intake system noise, namely, to reduce the engine noise levels and improve noise reduction capability of intake system. Generally, the second one is considered after engine design is complete. In this case to add resonance box is one of the most effective method.

The usual muffler component and transmission loss analysis of intake system is introduced in literature [3]. The multi-chamber muffler numerical optimization is discussed in literature [4].

2 Theory of Helmholtz Resonance Muffler

The Helmholtz muffler is composed by a rigid container and a connected neck, shown in Fig. 1.

When the sound waves spread into the neck hole, sound energy translates into heat energy because of the friction damping, so that sound is attenuated. When the sound wave frequency close to the resonator's natural frequency, the air column vibration at resonator neck hole is particularly strong, and sound energy can be absorbed a lot; otherwise, sound energy is absorbed little. Helmholtz resonator has narrow absorption band, and the maximum absorption is at the resonance frequency, which is calculated by the following formula:

$$f_0 = \frac{c}{2\pi} \sqrt{\frac{\pi R^2}{V(L + \frac{\pi}{2}R)}} \quad (1)$$

in the formula, V is the volume of the resonator (m^3), L is the length of the neck (m), R is the radius of the neck hole (m), c is the sound speed (m/s).

3 Structure and Characteristics of Two-Chamber Helmholtz Muffler

Helmholtz muffler can only absorb the noise of the particular frequency and the band close to it. In addition to traditional single-chamber structure, there is also two-chamber Helmholtz muffler. It is shown respectively in Fig. 2a and b that two chambers are in outside and internal tandem series.

Two-frequency noise can be eliminated by two-chamber Helmholtz muffler. If the two-chamber muffler with a same volume of single-chamber muffler, then the two-chamber muffler transmission loss corresponding to the peak to be lower. Figure 3 shows transmission loss contrast of single chamber and two-chamber Helmholtz muffler.

Fig. 1 Helmholtz muffler

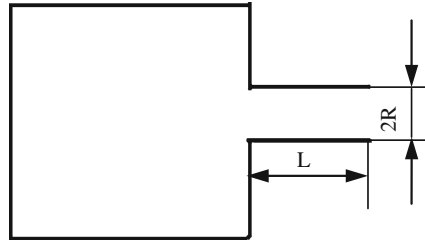


Fig. 2 Two-chamber Helmholtz muffler [1]

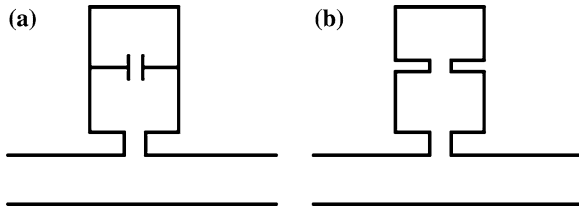
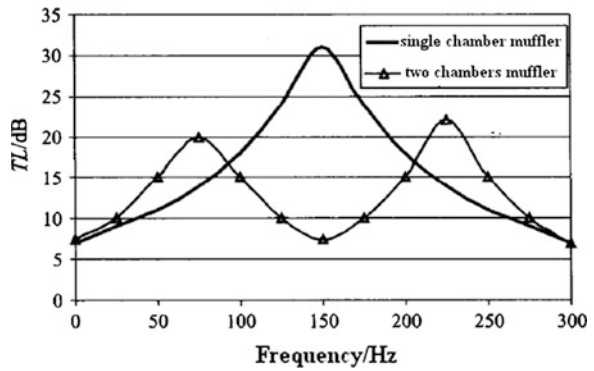


Fig. 3 Transmission loss contrast of single chamber and two-chamber Helmholtz muffler [1]



4 Application of Two-Chamber Muffler

4.1 The Problem: Intake Noise Problem of a Vehicle in Accelerating Condition

In tests it is found that there are obvious noise of a vehicle, when the engine is at 2410 and 3650 rpm in accelerating condition, which are mainly caused by the intake noise. The frequency of the SPL peak is about 245 Hz, shown in Fig. 4.

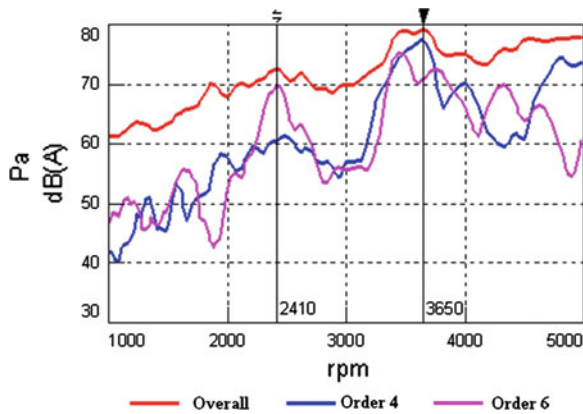


Fig. 4 Noise order map of driver's left ear in accelerating condition

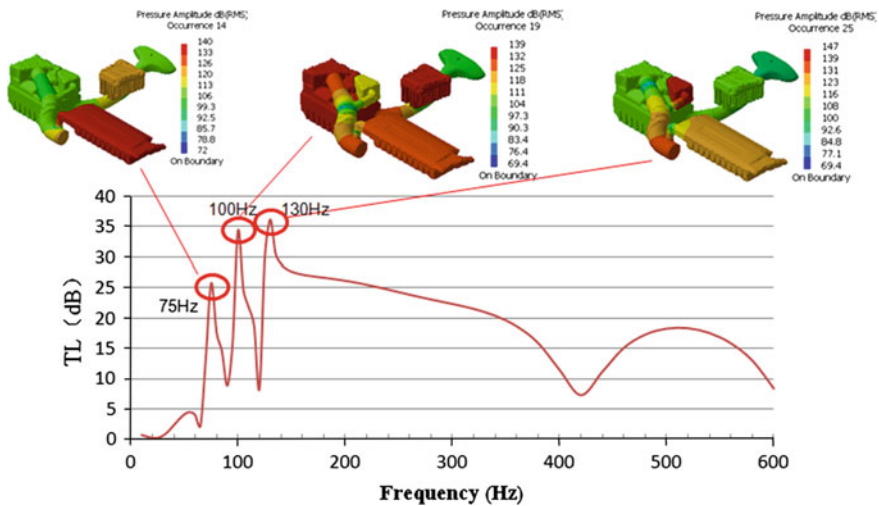


Fig. 5 Transmission loss result of original intake system

4.2 Improving Method: Using Helmholtz Muffler with Two Chambers

First, transmission loss analysis is done to the original intake system to determine whether a design flaw exist or not. The analysis result is shown in Fig. 5.

Transmission loss curve does not appear a trough at about 245 Hz, which determine the non-intake system design flaws, but by the engine itself, there is noise peak in this frequency. The improving method is to add a Helmholtz

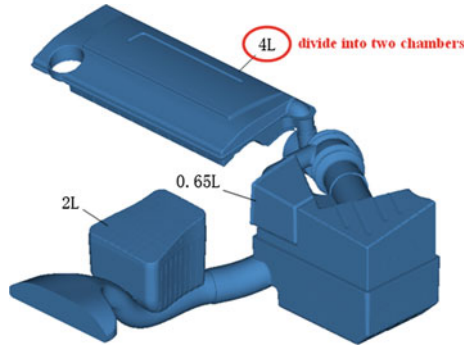


Fig. 6 Original intake system

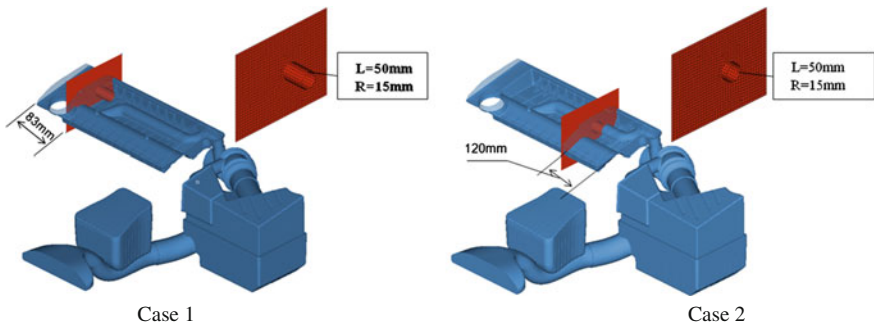


Fig. 7 Case of intake system

resonance box with the resonance frequency of 245 Hz for the noise peak. For the original intake system has three resonance box, considering the layout of space, mold changes, and cost control, to divide the resonance box with the volume of 4L into two chambers is a good way, shown in Fig. 6.

Based on the theory of Helmholtz muffler, a clapboard with a pipe is put into the resonance box. For different position of the clapboard, two cases is considered, and the position and dimension of the clapboard are shown in Fig. 7. In case 1, the smaller resonance box is far from the intake main pipe, its volume $V = 0.48L$, the length of the neck $L = 50$ mm, and the radius of the neck $R = 15$ mm. The resonance frequency $f_0 = 245$ Hz, which is calculated by the formula (1). In case 2, the smaller resonance box is close to the intake main pipe, the neck is same with the original 4L resonance box, and its volume is 1.05L by calculating. The transmission loss results of two cases are shown in Figs. 8 and 9.

Comparing the results of two cases, it shows that the band which the resonance box effects is too narrow in case 1, that means the noise reduction capability is probably not enough. The band is wider in case 2, and it may satisfy the improvement desire.

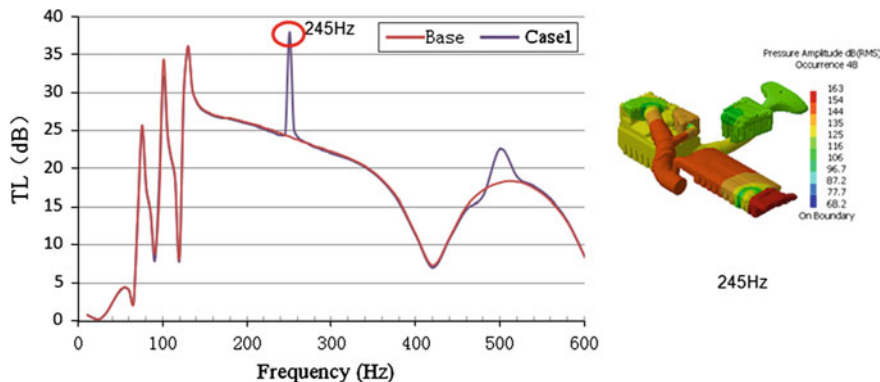


Fig. 8 Transmission loss result of intake system case 1

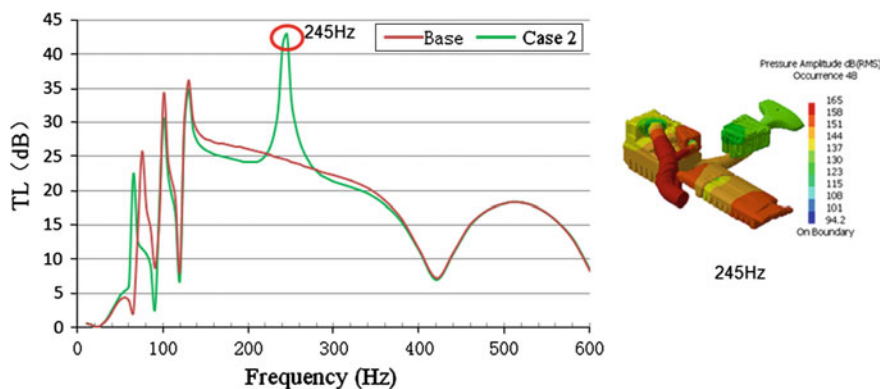


Fig. 9 Transmission loss result of intake system case 2

Besides, the transmission loss result is rarely affected in case 1, but the amplitude and frequency are both lower in case 2. A particular resonance box model is created to study this phenomenon, shown in Fig. 10.

The resonance is divided into two chambers by a clipboard with a pipe. The clipboard close to the main pipe is position A, and the other is position B. The smaller chamber has a close volume in two cases. The transmission loss results are shown in Fig. 11. It is similar to the above intake system improvement cases. Besides, the influence of scaling relation between the volume of two chambers is worth to take a further study.

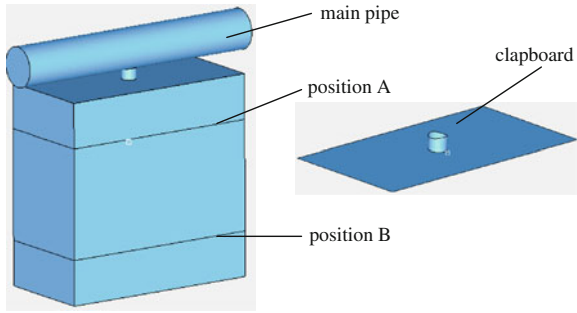


Fig. 10 Two-chamber model with different position of clapboard

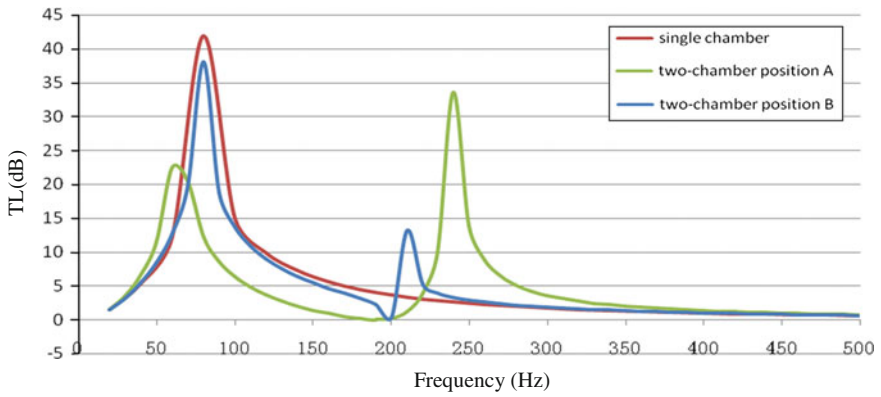


Fig. 11 Two-chamber model with different position of clapboard TL result

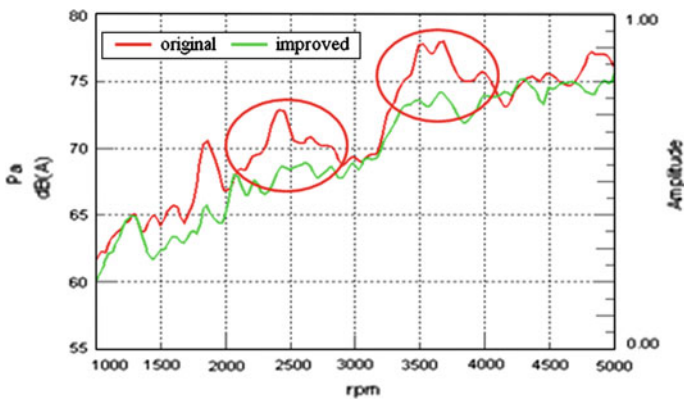


Fig. 12 Comparison of SPL at driver's left ear in accelerating condition

4.3 Validated by Test: Accelerating Noise Reduced Obviously

A sample of intake system based on case 2 is made, and tests are done. The results shows that the noise peak reduced obviously when the engine is near 2410 and 3650 rpm, see in Fig. 12. The effect is quite good.

5 Summary/Conclusions

The intake noise problem is solved effectively by separating the resonance box into two chambers. Compared with adding a single chamber muffler, it has several advantages:

- (1) do not influence the layout of space;
- (2) less mold changes;
- (3) less cost increasing per vehicle.

For the layout of space in cabin is limited, two-chamber resonance box has more advantages than traditional ones. So the two-chamber resonance box scheme should be considered first if the intake system needs more than one single chamber resonance box.

For dividing the resonance box into two chambers, the smaller chamber has a better noise reduction capability when it is near the main pipe than far away. But it also influence the transmission loss of the original resonance box more. The influence of scale relation between the volume of two chambers is worth to take a further study.

References

1. Jian P, Gang C, Hua H (2006) Noise and vibration of automobile. Beijing University of Technology Publisher, Beijing
2. Jinxiu L, Xiao L (1996) Air cleaner and intake system noise elimination. Vibr Noise 6
3. Zhihong T, Hong P (2009) Transmission loss analysis and optimization study of engine intake system. In: China SAE congress memoir. Beijing:Mechanical Industry Publisher
4. Chiu M-C (2010) Numerical optimization of a three-chamber muffler hybridized with a side inlet and a perforated tube by SA method. J Marine Sci Technol 18(4):484–495

Ergonomic Simulation and Optimization During the Body Assembly

Yanjun Gao, Xianbo Wei, Beifang Ma, Yang Yu,
Xingmin Wei and Fuquan Zhao

Abstract The ergonomic simulation is significantly important to reduce the cost and shorten the product development cycle in the vehicle development. In this paper, the technological design and simulation validation are performed with regard to assembly process of subframe subsystem and body structure on a particular vehicle. During the simulation, the problems are found as follows: (1) There is interference between dolly front pillar and spreader bottom when the subframe subsystem is transported; (2) The blind area happens to an operator at the static operating posture. The assembly operation needs to be accomplished by means of human body. Furthermore, the operator's neck and arms are subject to fatigue. When cyclic load is applied, fatigue usually appears on the operator's body. The analysis results indicate that interference can be avoided by optimizing the spreader structure and relative position or adjusting the dolly front pillar by nearby operator when the dolly goes through the spreader. By modifying the location of installation points, an easy assembly can be completely achieved, and fatigue can be substantially eliminated as well.

Keywords Ergonomics · Simulation verification · Static operating posture · Blind area · Fatigue

F2012-E12-041

Y. Gao (✉) · X. Wei · B. Ma · Y. Yu · X. Wei · F. Zhao
Geely Automobile Research Institute CO, LTD, Hangzhou, China
e-mail: yanjun.gao@yahoo.com.cn

1 Introduction

The simultaneous engineering (SE) of automobile manufacturing process goes throughout the different stages of vehicle development, such as the clay model making, the preliminary design and vehicle prototyping stage. The SE can greatly optimize the product structure, reduce process costs and shorten product development cycle, at the same time vehicle quality was controlled at early stage of the whole developing process [1, 2].

At the present time, varieties necessary technique information of tools, frocks, equipment, racks and carriers have established database by many Original Equipment Manufacturers (OEMs). However, the date storage is not standard normally, which result in inconvenient to use. SE analysis can't combine with the actual situation due to lack of production site information, which make SE analysis become meaningless. The static interference, the mis-assembling, assembly datum, assembly space were analysed by CATIA software in previous SE Analysis [3]. It is built on the basis of engineers' experience. The analysis of operating space whether meets the requirements is not accurate, because operating space analysis follows the rule of thumb when putting a tool to the operating position to determine whether reasonable. The operator of the vehicle production line often do the repetitive operations, which can easily result in the operation interfere, the operation fatigue, low productivity and even affect the tact [4]. SE work rarely involves the analysis of the above operating posture, vision and limb fatigue situation of operators.

To sum up the above arguments, SE analysis is not accurate enough for the lack of three-dimensional process simulation verification, which cause many problems in the actual production operation can't be found in the engineering design phase. This will can't only reach purposes of shorting the product development cycle, the vehicle quality, efficiency and cost can't be accurately controlled yet.

It takes assembly process of subframe subassembly and the body for example in this paper, standard database is established, process design and simulation verification of assembly process are included, adjustment suggestions are proposed. These are to direct practical production, reduce labour intensity and raise production capacity and quality.

2 Research Methods

The assembly reachability of parts, feasibility of assembly space, visibility of operator, convenience of operation and the fatigue in parts of body under various postures were analysed using DPE process planning platform and DPM simulation verification module of DELMIA software. The assembly simulation according to the process is under three-dimensional workshop environment.



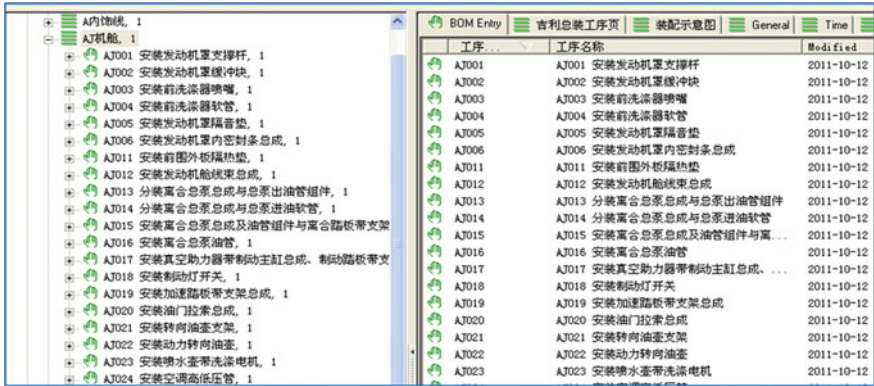
Fig. 1 Standard database

3 Simulation Process

3D simulation model of a vehicle was established early according to assembly process of subframe subassembly and the body structure at the vehicle development phase. Standard database of a variety of tools, frocks, equipment, racks and carriers (shows in Fig. 1), the library of standard working hours (shows in Fig. 2), three-dimensional model of the workshop (shows in Fig. 3) were established using DPE process planning platform of DELMIA software. They were associated in the DPE system, and then standard process templates and general assembly processes were established. First edition process was compiled quickly according to standard process templates and general assembly processes when analysis on SE of new products. Process, BOM and 3D model were associated. Assembly process of sub-assembly and body was simulated by the combining of DPE and DPM module of DELMIA software. There were four operators were involved in operating, the operational processes of operators are as follows:

The operator of split charging station hoisted the sub-assembly frame using light suspension crane and put it to the transport dolly which is used to co-load powertrain and body, and then it was transported to the underbody. Figure 4:

Three operators who were at co-mounted station were showed as Fig. 5, their operations are as follows: Three left bolts connected subframe and the body, three bolts connected steering low pressure tubing with the body were fixed by the left operator; two bolts which connected the left isolation pads of engine with the engine were fixed by the top operator. The top operator also should finished the installation of two bolts connected right isolation pads of engines with transmission, the assembly of left and right front pillars plate, the connected bolt of front pillar and body, assembly dust cover of left and right front pillars; three right bolts



工序	工序名称	Modif.ed
AJ001	安装发动机罩支撑杆	2011-10-12
AJ002	安装发动机罩缓冲块	2011-10-12
AJ003	安装前洗涤剂喷嘴	2011-10-12
AJ004	安装前洗涤剂软管	2011-10-12
AJ005	安装发动机罩隔音垫	2011-10-12
AJ006	安装发动机罩内密封条总成	2011-10-12
AJ011	安装前围外板隔热垫	2011-10-12
AJ012	安装发动机舱线束总成	2011-10-12
AJ013	分装离合器总成与油泵出油管组件	2011-10-12
AJ014	分装离合器总成与油泵进油软管	2011-10-12
AJ015	安装离合器总成及油管组件与离合器踏板支架	2011-10-12
AJ016	安装离合器油管	2011-10-12
AJ017	安装真空助力器带制动主缸总成、制动踏板支	2011-10-12
AJ018	安装制动灯开关	2011-10-12
AJ019	安装加速踏板支架总成	2011-10-12
AJ020	安装油门拉索总成	2011-10-12
AJ021	安装转向油泵支架	2011-10-12
AJ022	安装动力转向油泵	2011-10-12
AJ023	安装喷水壶带洗涤电机	2011-10-12

Fig. 2 Library of standard working hours

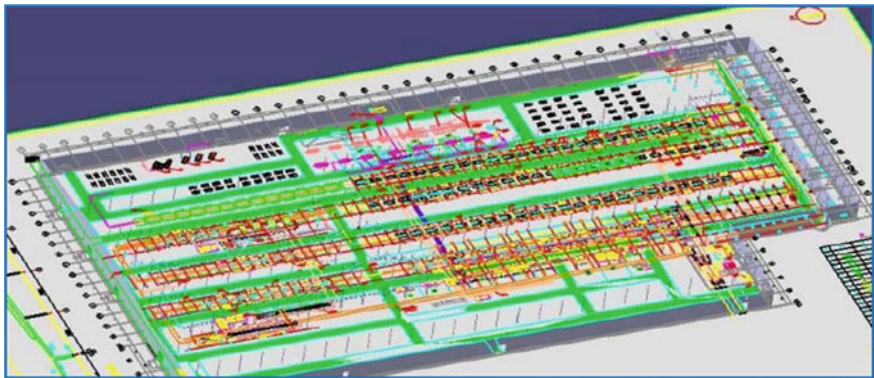


Fig. 3 Three-dimensional model of the workshop

Fig. 4 Packing station

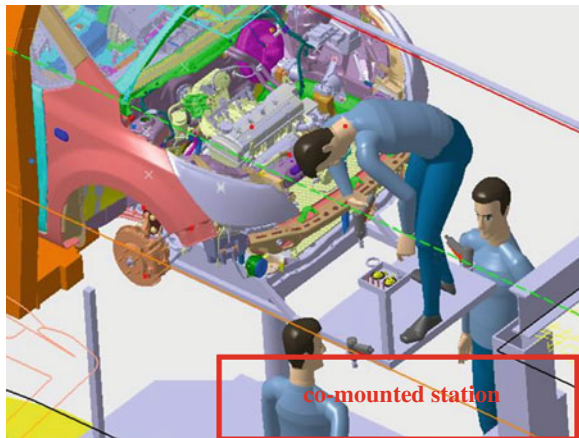
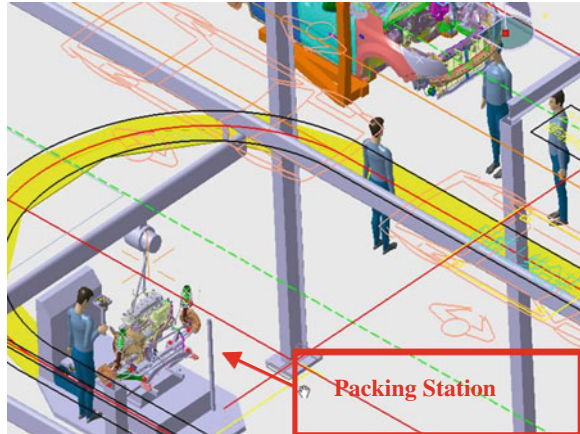


Fig. 5 Co-mounted station



connected the sub-frame and body were fixed by the right operator. The simulation and verification of the operative visual field convenience and fatigue strength of the operators were more concerned in this paper.

4 Simulation Results

Following questions were found during assembly process simulation:

Transport dolly interfered with bottom of the spreader when frame sub-assembly was in the transmission, which is shown in Fig. 6. The main reasons of this problem are that on the one hand, transport tooling was not analysed in the engineering design phase of SE works, on the other hand, tooling spreader and transport dolly working height were not reasonably matched.

The problem is solved by the following solutions:

The data of local transport trolley and spreader can be changed to re-match if transport dolly, its slide and the spreader are in the engineering design phase, the design are not frozen; if transport tooling and spreader have been finished developing, which can't be changed, it need the help of operator nearby station to press the front pillar when transport dolly go through the bottom of spreader to eliminate interference. The frock and spreader need not be re-developed with the help of operator and the cost was saved.

The reachability and the visibility of the operators are poor when the operators want to complete the assembly of low pressure tubing with left and right inside installation point of longitudinal beam during simulation process. The necks of operators are prone to fatigue when they do mass production.

The operator vision is blind and the installation point deviates from the vision under the existing posture shows in the Fig. 7, which has serious visual influence on bolt installation later. Installation of this bolt needs human arm spanning due to

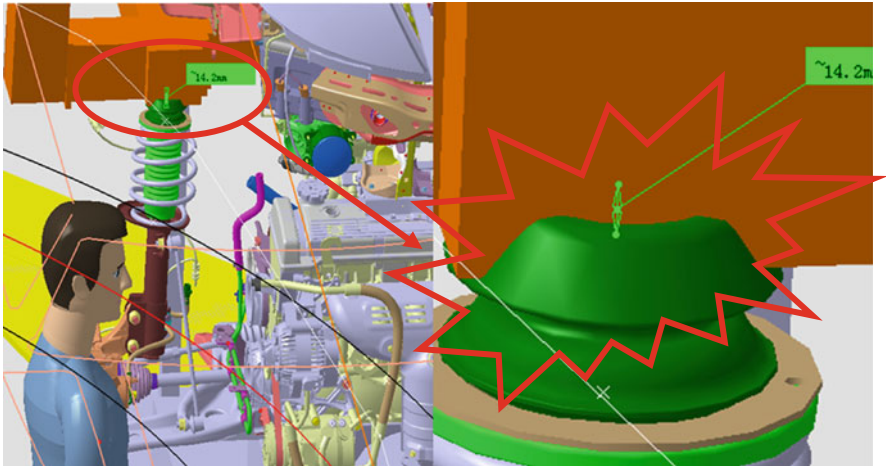


Fig. 6 Interference of front pillar of transport dolly with the bottom of spreader



Fig. 7 Vision analysis

poor visibility. If position of the connection installation is in the range of the human arm spanning, human body will not be fatigue. However, it is necessary to finish the operation by mean of body movements when the installation point is out the scope of the arm spanning. Varying degrees fatigue of other parts of the body is caused in this case.

It must be with the help of the neck movement and arm spanning to install accurately according to the location of the existing installation point for the existing of visual blind spots. It can be seen from the Fig. 8 that the vision is more open with the help of body movements. Connectivity installing is convenient,

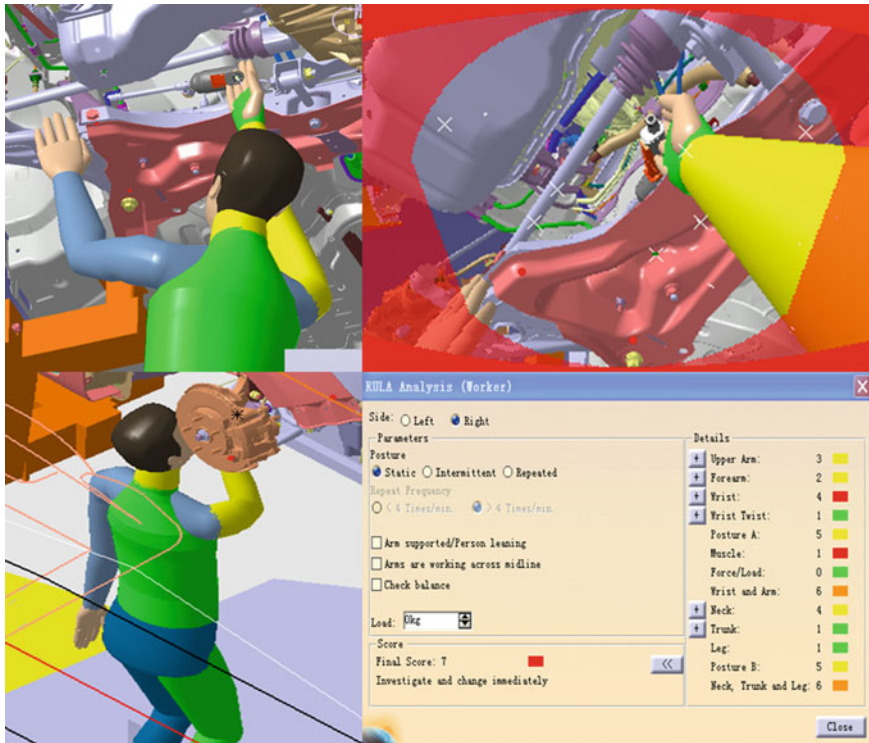


Fig. 8 Posture analysis

but the colour of person’s neck, hands holding tools and legs changes can be seen from the table in Fig. 8, which show that different degree of fatigue symptoms occurred.

The position of hands or feet is determined by the formula (1) in the motion analysis of human model. Concrete method is to establish three-dimensional coordinate system (X, Y, Z) firstly and then establish relative coordinate (x_n, y_n, z_n) on every movement limbs. The position of hands or feet is represented by the base coordinate system which is transformed by following coordinate transformation when the human body is during exercise [5].

$$\begin{Bmatrix} X_n \\ Y_n \\ Z_n \end{Bmatrix} = [T_n] \cdot \begin{Bmatrix} x_n \\ y_n \\ z_n \end{Bmatrix} + [P_n] \tag{1}$$

$$[T]_n = \begin{pmatrix} \cos \gamma & -\sin \gamma & 0 \\ \sin \gamma & \cos \gamma & 0 \\ 0 & 0 & 0 \end{pmatrix} \begin{pmatrix} \cos \beta & 0 & \sin \beta \\ 0 & 1 & 0 \\ -\sin \beta & 0 & \cos \beta \end{pmatrix} \begin{pmatrix} 1 & 0 & 0 \\ 0 & \cos \alpha & -\sin \alpha \\ 0 & \sin \alpha & \cos \alpha \end{pmatrix} \tag{2}$$



Fig. 9 Fatigue analysis

The $[P_n]$ is the coordinate origin of (x_n, y_n, z_n) in the base coordinate system, $[T_n]$ is transformation matrix of (X, Y, Z) and (x_n, y_n, z_n) , $[T_n]$ is obtained by rotating the coordinate system (x_n, y_n, z_n) around the axis of x_n, y_n, z_n , the rotation angle are α, β, γ .

The human model is established closely to the human model of Chinese, Japanese or Korean in the DPM module of DELMIA software. The action of human model was set during the simulation. A variety of different colours represent different fatigue levels when the human model is in different working actions after grabbing objects. The colour of the human model change from green to yellow shows that this kind of action lead operator feel fatigue during simulation process. It can be explained this kind of action will make people feel very fatigue if the colour changes to red. The fatigue will gradually increase with weight of grabbed objects increase.

Person in the existing model was set as being not absorb load and in static state (current position). Fatigue is easy to occur in the arm and neck in existing static which can be seen from the simulation results. Local joints have turned to red which shows that it has produced severe fatigue which can be seen from the simulation report. The arm holding tool is forced to do tightening operations in the process of actual installation. The operator repeated this operation online production. The colour changes of the human model took place in many locations when the arm was set force to finish the tightening operation and repeat the action such as in actual operation shown in Fig. 9: this means that many parts of the body is very tired.

The installation point was adjusted direct against the above situation. The fixed point after adjusting is at the bottom of stringer, which was at right angles to that before adjusting. The vision is open when the fixed point was adjusted, and the body help is not needed. The fatigue is not occurred even if the body withstand cyclic loading.

5 Conclusions

By using the DPE and DPM modules of DELMIA software, the results of ergonomic simulation for body assembly process are as follows:

1. There is interference between transport dolly with spreader bottom when the subframe subsystem is transported. On one hand, this problem can be solved by modifying the spreader structure or relative position. On the other hand, it can be solved by pressing the dolly front pillar with the help of nearby operator as well.
2. The operating visibility is poor or even blind at current simulation state. The operator has to execute assembly operation with the help of his body, and the neck and arms are subject to fatigue when they are without cyclic loading. Furthermore, Fatigue appears on many parts of body if simulated with cyclic loading. For this reason, an easy assembly and can be achieved and fatigue can be eliminated by modifying the location of installation points and assembly direction.

References

1. Dang H (2011) The application of SE analysis. *Welding technology*, vol 40, issue 4
2. Zheng S (2000) Discussing the application of SE in product development. *Product development*
3. Li L (2008) The application of SE in developing of Chang an automobile. *Technology research*
4. Pan C, Zhao F, Chen L (2011) SE of the engineering design phase. *Agric Equip Veh Eng* 1(234):1673–3142
5. Yang M, Yi M (2009) Ergonomics simulation and application in virtual assembly based on DELMIA. *Research in agriculture development*, pp 1673–9205

Test and Analysis of the Mechanical Properties for Laser-Welding Seams and Spot-Welding Joints

Liling Zhang, Xuefeng Chen, Qing Jiang and Xu Wang

1 Introduction

Laser welding seams and Spot-welding Joints are wide used in auto body design. It is important for the body design engineers and CAE engineers to understand the mechanical behaviors of spot-weld joints and laser-welding seams. The objective of this paper is to introduce a test method to study the mechanical properties for laser-welding seams and spot-welding Joints by test and simulation.

In this paper, different welding joint samples are designed considering the application in auto body joint design, and the methods for measuring the mechanical properties for Laser-Welding Seams in tailor welded blanks and Spot-welding Joints are presented. Two size TWBs (tailor welded blanks) tensile test samples with longitudinal laser-welding seams and three kinds of spot-welding joints with different thickness blanks are designed and tested. The strength and mechanical properties of these welding joints are determined by manipulating a mathematical model. The effects of sample size on the calculating mechanical properties of the weld metal are assessed. The obtained mechanical properties are used to a FEM model and are proved to be useful in assess the joint strength by comparing results of the simulation and test.

F2012-E12-046

L. Zhang (✉) · X. Chen · Q. Jiang · X. Wang
Beijing Automotive Technology Center, Beijing, China
e-mail: zhangll@beijing-atc.com.cn

2 Mechanical Properties Test of Laser-Welding Seams in TWB

2.1 The Mathematical Model of ‘Iso-Strain’ Method

In this paper, the main processes of “Iso-strain Method” to get the mechanical property of weld metal are shown as Fig. 1. The weld metal in TWB sample is paralleled to tensile load direction. The mechanical properties of weld metal could be obtained by calculating the assumption Eq. (1) in conjunction with force equilibrium Eq. (2). Because the hardening behavior of weld metal vary along the cross section, that is the weld metal show anisotropic characteristic. The σ_w which is calculated from Eq. (2) is an averaged stress on weld metal.

$$\varepsilon_1 = \varepsilon_2 = \varepsilon_w \quad (1)$$

$$\sigma_w = \frac{P - k_1 \varepsilon_1^{n_1} A_1 - k_2 \varepsilon_2^{n_2} A_2}{A_w} \quad (2)$$

Among the equation:

σ_w	Stress of weld metal
P	Tensile force of TWB sample
$\varepsilon_1, \varepsilon_2, \varepsilon_w$	Strain of base material 1, base material 2 and weld metal
k_1, k_2, n_1, n_2	Material parameters of base material 1 and base material 2
A_1, A_2, A_w	Cross section area of base material 1, base material 2 and weld metal.

2.2 Test Method and Test Plan

The dimensions of base material tensile sample are chosen on the basis of ASTM E8 standard. The sample are selected and arranged in three directions which are 0°, 45°, 90°. Because there is no international standard for tensile sample of TWB, the sample with two kinds of dimensions are chosen to do the research based on the present experimental conditions in this paper. The first TWB sample has the same shape and dimensions with base material. The gauge length and parallel width of the first TWB sample which is called full-scale size sample are 50 and 12.5 mm separately. The dimension of the second TWB, whose gauge length and parallel width are 25 and 6 mm separately, is called subsize TWB sample. The two kinds of samples are cut from the same tailor welded blanks. The thicknesses of base materials are 0.8 and 1.5 mm separately, and the materials are 08Al.

Rofino DC25 and CO₂ laser weld equipment, which have a weld power of 20 KW and weld speed of 1.5 mm/s, are used to weld the tailor welded blanks. All the samples are manufactured by using the wire-electrode cutting. The photo of

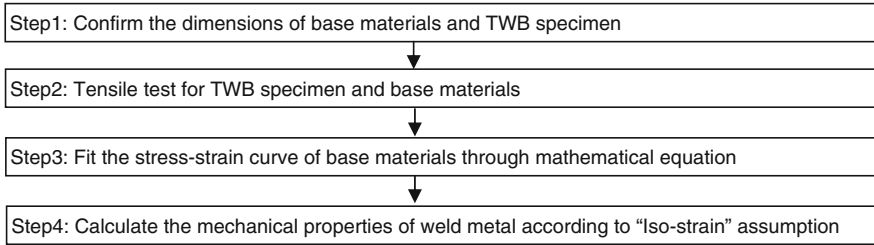


Fig. 1 The flow chart of ‘iso-strain’ method

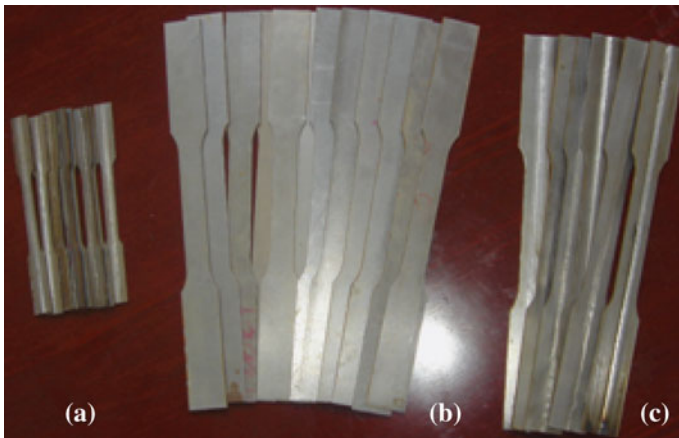


Fig. 2 Tensile test samples **a** subsize TWB samples; **b** base material samples; **c** full-scale size TWB samples

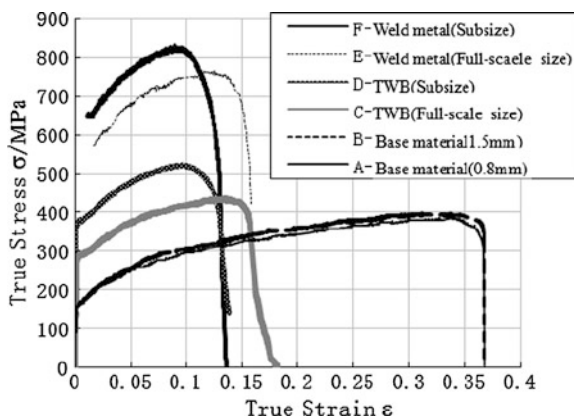
tensile test samples is shown as Fig. 2. The tensile test is carried out on test equipment of MTS880 100KN. The extensometers of 50 and 25 mm are used which could collect 10 data per second.

2.3 Test Data Analysis

The average value of the weld metal width on top and bottom surface in TWB sample are collected as the calculation weld width based on the tensile test data of base materials and TWB sample. The area of weld metal cross section is calculated by multiply the width of weld metal and average thickness of two base materials. The mechanical properties (strength coefficient B and hardening exponent n) of weld metal are get by calculating Eq. (2), as shown in Table 1. The stress–strain curve of weld metal is shown as Fig. 3. Curve A, B, C, D represent stress–strain curve which are measured from 0.8 mm base materials, 1.5 mm base materials,

Table 1 Mechanical properties data from tensile test

Sample type		Strength coefficient (K/MPa)	Hardening exponent (n)
Base material A (Thickness 0.8 mm)		498.17	0.2237
Base material B (Thickness 1.5 mm)		507.49	0.2177
Full-scale size sample (Thickness ratio 1.5/0.8)	TWB	642.61	0.17939
	Weld metal	1025.97	0.1396
Subsize TWB sample (Thickness ratio 1.5/0.8)	TWB	739.35	0.1457
	Weld metal	1138.29	0.1332

Fig. 3 True stress–strain curves of base material, tailor-welded blank and the weld

full-scales size sample with parallel width of 12.5 mm and subsize TWB sample with parallel width of 6 mm separately in tensile test. Curve E is the weld metal properties of full-scale size sample which is get on the basis of curve A, B and C. Curve F is the weld metal properties of subsize TWB sample which is obtained based on curve A, B and D. From Table 1 and Fig. 3, it could be seen that the strength of the weld metal is much higher than that of base materials, while the plasticity property is lower than that of base materials. The elongation of weld metal obtained from subsize TWB sample (curve F) is lower than that of curve E, and is 36.93 and 42.87 % of two base materials elongation separately (curve A and B). It should be noticed that the stress–strain curve of weld metal for curve E differ greatly from curve F due to the difference of TWB sample dimensions.

2.4 The Comparison of Simulation and Test Result

In order to assess the practical application of weld metal mechanical properties calculated from “Iso-strain Method”, the weld mechanical properties listed in Table 1 are used in tensile test FEM model of subsize TWB sample. The shell

Fig. 4 As-formed subsize TWB sample and FEM model

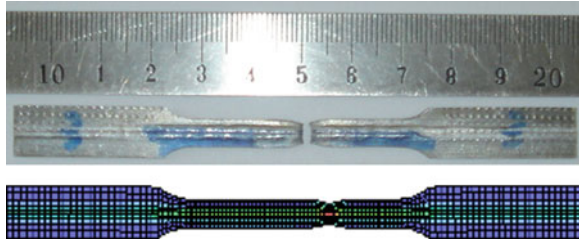
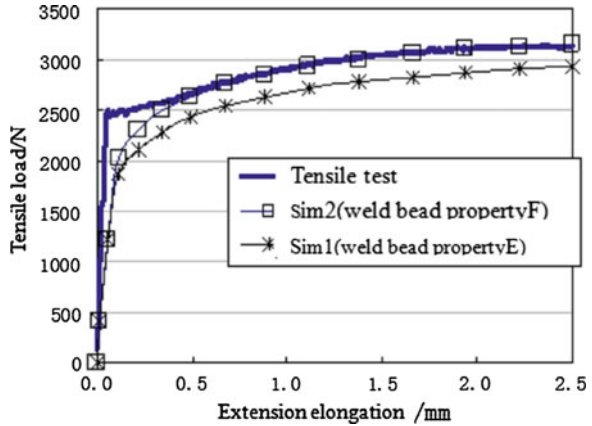


Fig. 5 The curves of tensile load versus extension elongation by simulation and test



elements are used to create weld metal FEM model and nine integration points are chosen along thickness direction. LS-DYNA software is used to simulate and analyze the model. The failure mode of shell element where the necking occurs in tensile process is similar to the actual transformation of subsize TWB sample. The photos are shown in Fig. 4.

The curves of tensile load versus extension elongation calculated from experiment and simulation method are shown in Fig. 5. It could be seen that the curve of FEM model Sim 2 which is created using weld metal mechanical properties from subsize TWB sample are very similar to the curves of tensile load versus extension elongation from actual test. While the tensile loads of FEM model Sim 1 which is created using weld metal mechanical properties from full-scale size sample have some difference with the test data. This further indicates that the calculation accuracy of subsize TWB sample is higher than that of full-scale size sample. It is also proved that the weld metal mechanical properties from “Iso-strain Method” in this paper could be applied directly in FEM analysis and this measurement method for weld metal properties has some practical application.

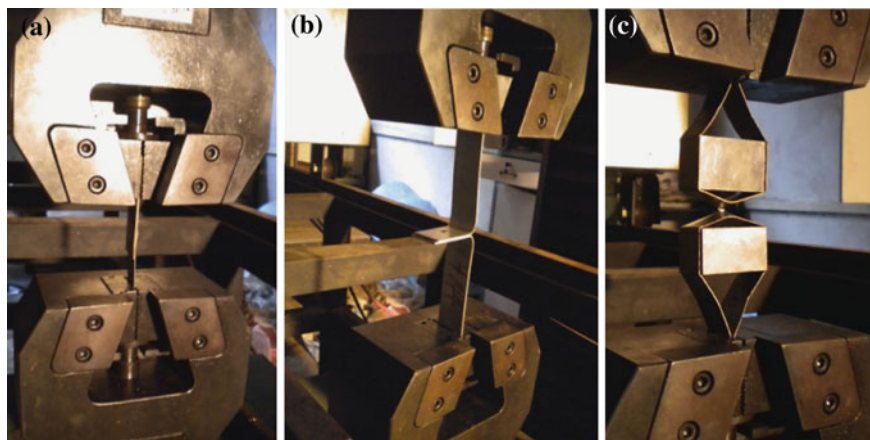


Fig. 6 Spot weld tensile test under different loading cases. **a** II type, **b** L type, **c** O type

3 Spot Weld Strength Test

Three kinds of spot weld test specimen are designed (type “II”, type “L”, type “O”), shown as Fig. 6. Type “II” sample is testing shearing force resistance ability of weld nugget and jointing strength between weld nugget and metal sheet around. The test on spot weld tearing resistance ability using the common spot loading mode is showed in type “L” sample. Type “O” sample is the test on spot weld pulling resistance ability (shearing resistance ability of metal sheet around weld nugget and elongation resistance ability of weld nugget). The spot weld specimens listed in Table 2 are manufactured in order to carry on the spot weld test under the loading cases described before.



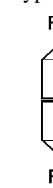

3.1 Deformation Mode Analysis

The typical specimen photos after the tests are shown in Fig. 7.

It could be seen from the photos that in spot weld shearing test of specimen type II majority of weld nuggets are damaged by shearing force. But one specimen whose strength is relatively lower than another specimen would be tearing along spot weld. This is because the weld nuggets become reversal under the tensile force on both sides. When the weld nugget length becomes longer and the welding thickness is thicker, the two specimens jointed by spot weld are much easier to be teared.

From the picture, it could be seen that basically parts of the specimen are damaged by shearing force at the side that the spot weld is closer to tensile force in the L type specimen. The region at the side of spot weld becomes tearing.

Table 2 Spot weld specimen type

Series No.	Specimen combination	Welding method	Specimen Thickness-1	Specimen thickness-2	Spot-weld diameter	Specimen type	
D1-1	144 + 144	O	2.00	2.14	6.70		
D1-2	144 + 144	O	2.00	2.05	6.80		
D1-11	144 + 144	L	2.00	2.00	7.00		
D1-12	144 + 144	L	1.99	1.98	7.00		
D1-21	144 + 144	II	1.99	2.00	6.80		
D1-22	144 + 144	II	1.96	1.99	6.90		
D2-11	DC01 + B250	L	1.51	1.96	6.30		
D2-21	DC01 + B250	II	1.51	1.97	6.50		
D2-22	DC01 + B250	II	1.51	1.96	6.70		
D2-12	DC01 + B250	L	1.51	1.98	6.90		
D3-21	139 + 145	II	1.20	1.25	5.90		
D3-22	139 + 145	II	1.21	1.23	5.70		
D3-11	139 + 145	L	1.20	1.22	6.00		
D3-12	139 + 145	L	1.19	1.24	5.70		
D3-1	139 + 145	O	1.19	1.23	5.60		
D3-2	139 + 145	O	1.19	1.24	5.80		
D4-21	145 + 145	I	1.21	1.23	5.80		
D4-11	145 + 145	L	1.24	1.24	6.00		
D4-12	145 + 145	L	1.22	1.21	5.80		
D4-1	145 + 145	O	1.22	1.23	5.50		
D5-1	550 + 145	O	1.21	1.36	6.40		
D5-11	550 + 145	L	1.24	1.34	5.50		
D5-21	550 + 145	I	1.24	1.32	6.20		

D5 and D11 specimen in O type specimen are totally break by shearing force around the spot weld, while other specimens are partly break. The reason is the D5 and D11 are added the holding block in the middle of specimen in the test in order to guarantee the edge containing the spot weld would not fold in the tensile process. The region around spot weld could support the force evenly and be break by shearing force at the same time. Because of the size problem of other specimen, the holding block could not be added in the middle of specimen. The edge containing spot weld bend and fold in tensile process. The forces around spot weld are not uniform. Parts of the specimen where force concentrated around spot weld are breaking by shearing force first and then other parts break along fracture.



Fig. 7 Typical specimen deformation mode after test

3.2 The Test Data Analysis

The spot weld test data is shown in Fig. 8.

From Fig. 8, the tensile force that specimen II supports is the highest while the tensile force that specimen L supports is the lowest. Because the welding thicknesses of D1 and D2 specimen are the thickest and they have the biggest weld nugget, they could support higher tensile force than other spot welds with smaller nugget diameter. The bigger the spot weld diameter is, the higher the shearing resistance force which spot weld could support (tensile force resistance of II type specimen).

From the tensile test curves of three II types specimen D3, D4 and D5, it could be found that the maximum tensile force which specimen could support is only related to the materials with lower strength. Between the 139-145 specimen and 145-145 specimen, because the strength of 139 is lower than 145, the maximum tensile force which the former specimen could support is smaller than the latter one. Between the 145-145 specimen and 550-145 specimen, the strength of 145 is lower than 550, so the two specimens could support similar maximum tensile force.

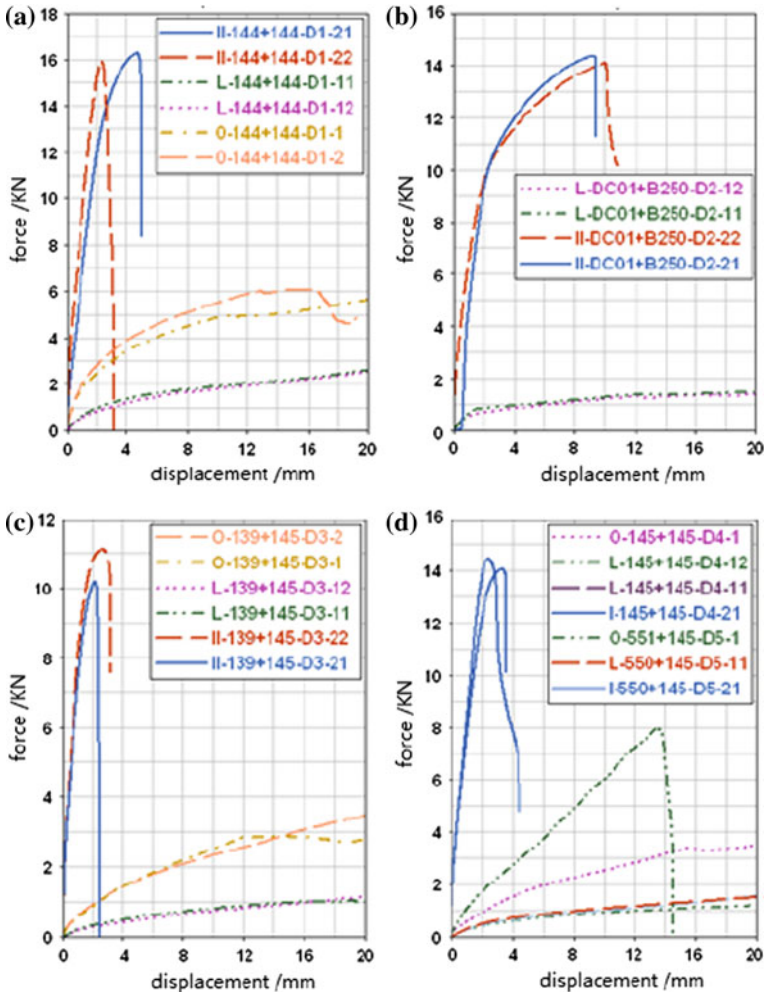


Fig. 8 Force–displacement curves in spot weld strength test. a D1, b D2, c D3, d D4–D5

From the II type specimen with the same spot weld diameter, because the strength of D1 specimen is higher than that of D2 specimen, while the strength of D4 and D5 specimen are higher than the specimen of D3 specimen, the maximum tensile force which D1 specimen could support is higher than D2 and the maximum tensile forces which D4 and D5 specimen could support are higher than D3. That means when the strength of welding material is higher, the tensile force resistance of II type specimen would become bigger.

From the II type specimen curve in Fig. 8, it could be seen that the shape of D2 curve is obviously different from other curves. The elongation of D2 is relatively high, and yield phenomenon happens in the later stage. This is because D2 welding

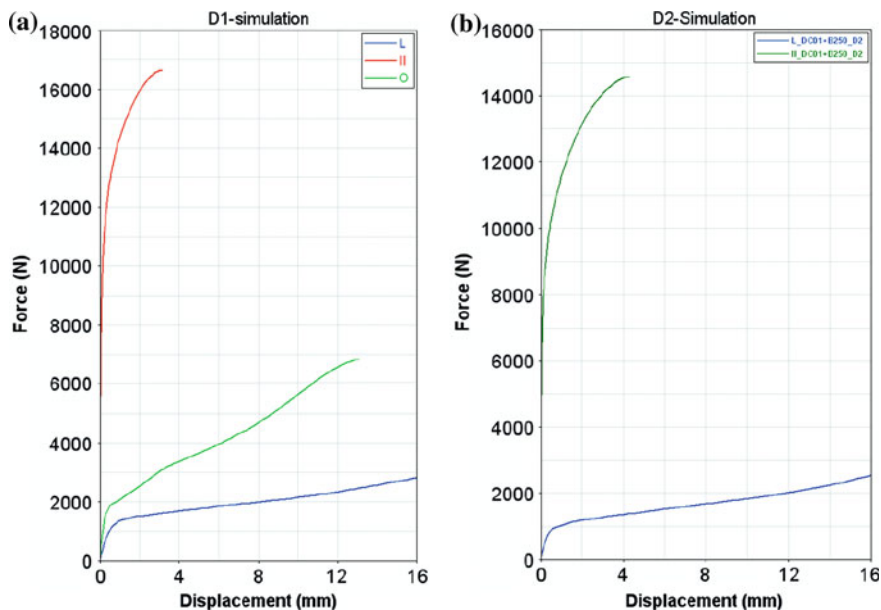


Fig. 9 Curves of force–displacement in simulation. **a** D1, **b** D2

material is the soft steel with low strength, and other welding materials are high-strength steel which have high strength.

The tensile force resistance of L type specimen has direct proportion to the thickness and strength of the weakest material in specimen. The thicker the thicknesses are, the bigger the tensile force resistance is. And when material strength is higher, the tensile force resistance becomes bigger.

In O type specimens, the test forces do not have obvious inflection point in rising process and could reach to a high value because D5 break around the weld nugget at the same time.

The comparison of simulation and test result were done, the curve of force–displacement and deformation mode is similar, the actual transformation of sub-size TWB specimen, shown in Figs. 9 and 10.

4 Conclusion

1. In this paper, different welding joint samples are designed considering the application in auto body joint design, and the methods for measuring the mechanical properties for Laser-Welding Seams in tailor welded blanks and Spot-welding Joints are presented. Two sizes TWBs tensile test samples with longitudinal laser-welding seams and three kinds of spot-welding joints with different thickness blanks are designed and tested. The strength and mechanical

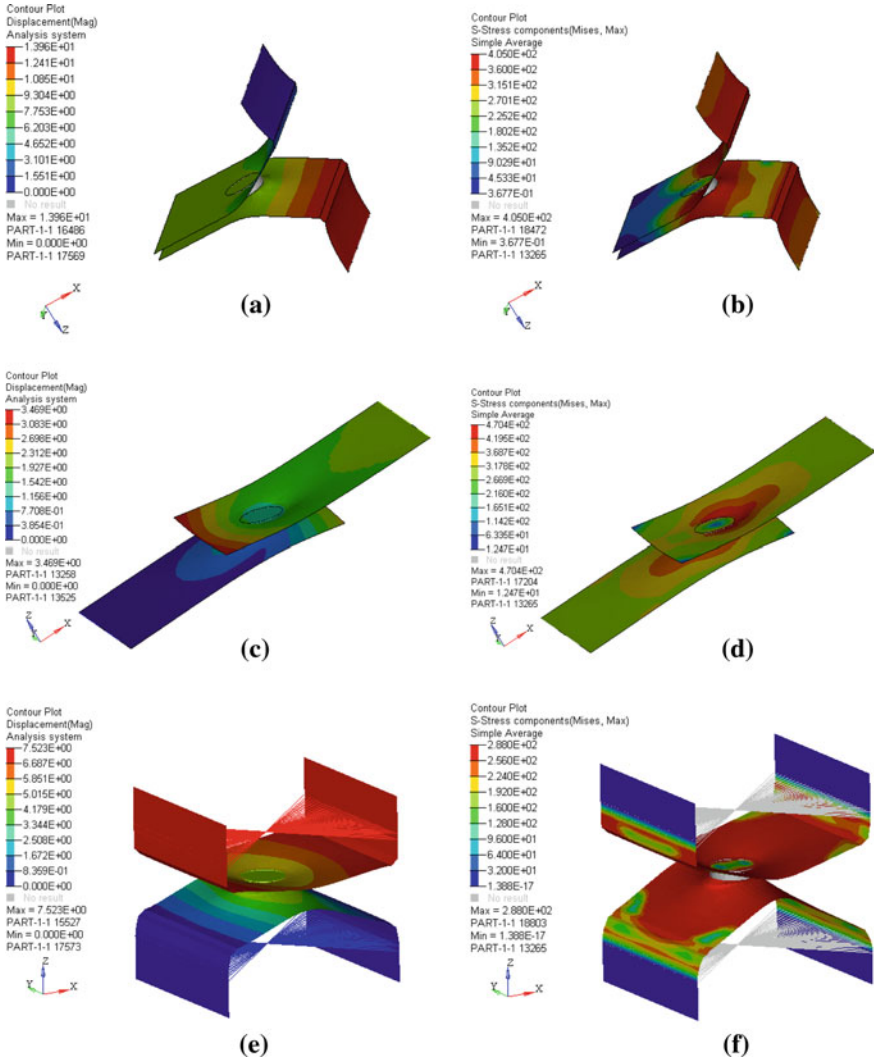


Fig. 10 Distribution of stress and displacement in simulation. **a** displacement distribution in L type, **b** stress distribution in L type, **c** displacement distribution in II type, **d** stress distribution in II type, **e** displacement distribution in O type, **f** stress distribution in O type

properties of these welding joints are determined by manipulating a mathematical model. The obtained mechanical properties are used to a FEM model and are proved to be useful in assess the joint strength by comparing results of the simulation and test.

- Spot-weld is the most popular jointing technology to weld metal sheet in automobile manufacture field, whose strength and density directly influence the car body strength and stiffness. The research on single spot weld strength and

damage type under different loading conditions could be used on the arrangement of spot weld spacing and optimization of selecting spot weld materials. From the spot weld tensile test under three loading cases, it could be concluded that:

- A. In the actual structure, when the loading mode of spot weld is similar with II type specimen, the weld nugget would be broken by shearing force if the strength of two jointing plate are similar. The shearing resistance strength of weld nugget is obviously higher than that of welding plate. The tear will happen at the plate with lower strength. The tearing force of structure could be estimated according to the strength of weaker plate.
- B. In the actual structure, when the loading mode of spot weld is similar with L type specimen, the weld nugget and weak plate are broken and separated with welding plate by shearing force at the side that the spot weld is closer to loading force. The loading force which structure could support could be estimated according to the bending resistance ability and shearing resistance strength of weak welding plate.
- C. In the actual structure, when the loading mode of spot weld is similar with O type specimen, if the plate around spot weld do not bend and fold making use of spot weld as bending line, then the weld nugget would be broken and separated from the weak plate by shearing force. The loading force which structure could support could be estimated through the shearing resistance strength of weak plate material. If the plate around spot weld would have obvious bending on the basis of spot weld, the failure mode of spot weld would be similar to the mode that two L type specimen are jointed using the spot weld as jointing line. The loading force which structure could support correlates closely with the bending resistance ability of welding plate.

Aerodynamic Design and Numerical Simulation Analysis of a Passenger Car's Defrosting Duct

Bo Yang, Li-na Huang and Fengtao Ren

Abstract Many cars are equipped with the same Heating, Ventilation and Air Conditioning (HVAC) system with different outlet flow rates, shapes, sizes and positions etc. according to modern automobile modular and platform design strategies. Consequently, the aerodynamic design of airflow duct has become an important issue of the automobile HVAC system. In this research, the HVAC defrosting airflow canal of a passenger car was designed using Computational Fluid Dynamics (CFD) method. The HVAC defrosting outlets' sizes and positions were considered as design variables. The mass flow rate distribution and the cabin flow structure were considered as design targets. The steady Reynolds Averaged Navier–Stokes (RANS) method was adopted because it is an efficient way to help select possible good designs in the early stage of new product development without time consuming and huge computational cost of the unsteady methods. Various duct design configurations were evaluated by analyzing the defrosting mass flow distribution of each flow outlet and by visualizing the flow structure near the windshield and the front left side window. The CFD results showed that the total area of the outlets near the rain wipers was a decisive parameter for mass flow distribution in this duct design. The defrosting flow structure near side windows were difficult to be improved only by enlarging the area of the outlet. The effective flow structure was realized by choosing proper angles of the vanes skirt of the outlets to defrost the windshield region. The overall performance of HVAC system, such as defrosting time and cabin temperature distribution, could not only be predicted based on the results of the steady RANS method. It was shown that the important parameters including the mass flow distribution of each outlets and

F2012-E12-048

B. Yang (✉) · L. Huang · F. Ren

State Key Laboratory of Automotive Simulation and Control, Jilin University, Jilin, China

e-mail: yang_bo@jlu.edu.cn

the flow structure near the windshield and side windows could be quickly evaluated from the steady state CFD simulation results in the early design stage.

Keywords Defrosting duct · CFD · Aerodynamic design · Steady RANS · Passenger car

1 Introduction

The Heating, Ventilation and Air Conditioning (HVAC) system performance is a critical factor which is highly related to potential consumer's payment decision in the modern passenger car market. In General, manufacturers need to update the exterior and interior trim designs of their car products periodically. And in these updating works, the airflow outlet's shapes and positions were very likely changed with regard to a car's interior trim. Unfortunately, there would be impacts on the HVAC system performance caused by these changes, even without changing the HVAC compressor. Therefore, automotive engineers would like to know the modified HVAC performance before it was manufactured [1–3]. And CFD methods were chosen in this early design stage. However, transient simulation, considering cabin temperature distribution or phase changing, need a lot of computational resources and time due to the complicated geometry model and millions of CFD model cells. Based on the motivation of pre-evaluating the HVAC system performance in the early design stage, the steady state CFD simulation of a passenger car's defrosting duct was carried out.

2 Computational Models

2.1 Geometry Model

In this research, only the defrosting duct was analysed without the air conditioning ducts of the HVAC system. The whole geometry model for CFD simulation, shown in Fig. 1, consists of the defrosting duct, interior trim, seats, cabin, two front passengers and almost all the cabin accessories. All parts were described by feature curves.

Basically, the defrosting duct of this passenger car has five outlets regions, shown in Fig. 2, which are the left side window outlet (LSWO), the right side window outlet (RSWO) the windshield left part outlet (WLPO), the windshield right part outlet (WRPO) and the wiper outlets (WIO).

Undoubtedly, the outlets' areas and their positions will influence the defrosting airflow. Therefore, area and position design variables were analyzed. As far as the designs of these variables are concerned, there is one important rule of not

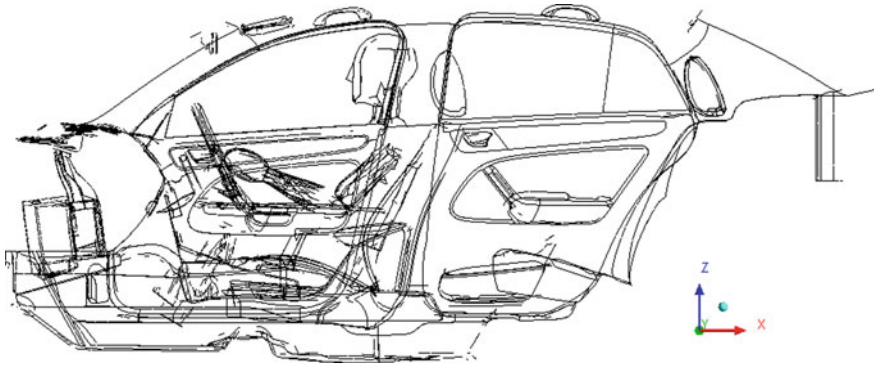


Fig. 1 The whole geometry model

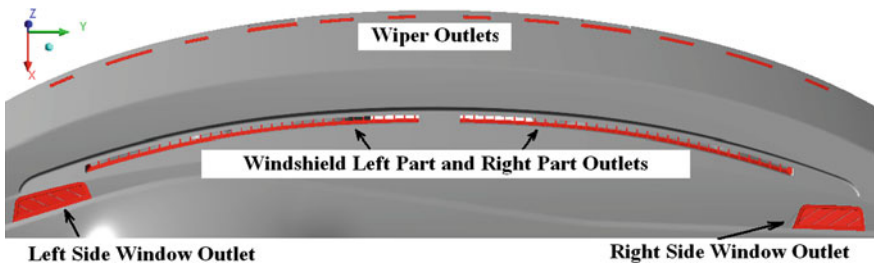


Fig. 2 Five outlets regions (in red color)

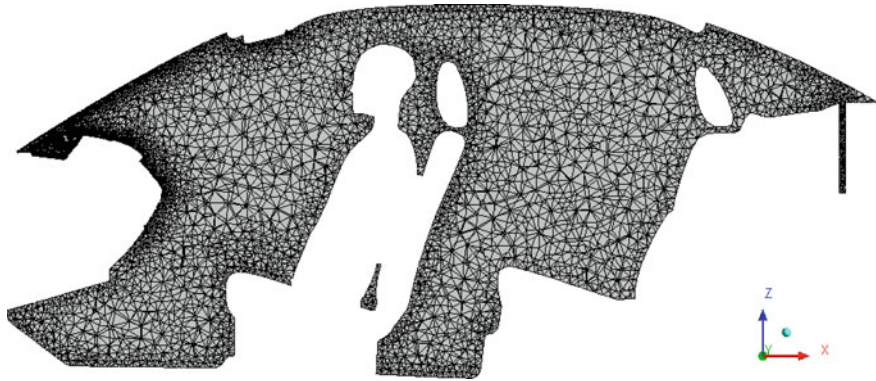
modifying the whole cabin interior trim styling theme. Four design variables were analysed, including the total area of the WIO (S_{wio}), the total area (S_{lsw}) and position (P_{lsw}) of the LSWO and the angle between the air flow guiding vane skirt and the vertical direction of the WLPO and the WRPO (A_{wo}). Six cases simulations were carried out, including the original design case and other five cases. The cases and variables settings were listed in Table 1. In Case 1, total area of the WIO was around 50 % of the Original Design. In Case 2, the total area of the LSWO was around 120 % of the Original Design. The position of the LSWO of Case 3 was moving 55 mm along X direction based on the Original Design. And in Case 4, the angle between the air flow guiding vane skirt and the vertical direction of the WLPO and the WRPO was decreased 10° based on Case 1. The last case, Case 5, combined all of the variable changes from Case 1 to Case 4.

2.2 Turbulent Model, Computational Mesh and Boundary Conditions

Generally, the defrost duct shape is complex and a lot of vortices will be generated in the duct. For this reason, the k-omega SST turbulent model was chosen to

Table 1 Design variables and cases

Cases	Variables settings			
	S_{wio}	S_{IswO}	P_{IswO}	A_{wo}
Original design	S_{wio}	S_{IswO}	P_{IswO}	A_{wo}
Case 1	$0.5*S_{wio}$	S_{IswO}	P_{IswO}	A_{wo}
Case 2	S_{wio}	$1.2*S_{IswO}$	P_{IswO}	A_{wo}
Case 3	S_{wio}	S_{IswO}	$P_{IswO} + 55 \text{ mm}$	A_{wo}
Case 4	$0.5*S_{wio}$	S_{IswO}	P_{IswO}	$A_{wo} - 10^\circ$
Case 5	$0.5*S_{wio}$	$1.2*S_{IswO}$	$P_{IswO} + 55 \text{ mm}$	$A_{wo} - 10^\circ$

**Fig. 3** A vertical mesh cutting plane**Table 2** Boundary conditions

Position	Boundary conditions	Settings
Defrosting duct inlet	Volume flow inlet	$0.09673 \text{ m}^3/\text{s}$
Carbin air outlet	Pressure outlet	Gauge pressure 0 Pa
Others	Wall	Default settings

simulate the turbulent flow field [4, 5]. The numerical simulations were carried out using a commercial CFD code, ANSYS Fluent.

In each case, the computational domain was filled by all tetrahedral cells because of the complex shapes and small size defrosting duct features (1 mm). There are around 13 million volume cells of each case, which around 7 million in the defrosting duct and around 6 million in the cabin. A horizontal volume mesh cutting plane was illustrated in Fig. 3. Boundary conditions were shown in Table 2.

3 Results and Discussion

3.1 Mass Flow Rate

The average mass flow rates of five defrosting outlet regions of each case were illustrated in Table 3. And the mass flow rate distributions of the five defrosting regions were plotted in Fig. 4. It was shown that the Case 1 WIO mass flow rate decreased from 26.33 to 17.14 % by reducing around 50 % the WIO areas compared with the Original Design. And in Case 2, the LSWO mass flow rate increased from 4.99 to 5.84 % by adding 20 % area compared with the Original Design. With regard to Case 3, the mass flow rates of each outlet region were almost the same as the Original Design. The possible reason was that each area of the five outlet regions of Case 3 was not changed compared with the Original Design. That means the area of the outlet is a decisive factor of the mass flow rate distribution of the defrosting duct. In Case 4, the mass flow rates of each outlet region were similar as the Case 1. The differences between Case 4 and Case 1 were caused by the variable A_{wo} . Finally, as for Case 5, the mass flow rate of LSWO was increased from 4.99 to 7.06 % compared with the Original Design. The mass flow rates of other outlet regions were similar as the values of Case 1.

3.2 Flow Field Structure

Defrosting air flow structure inside the cabin is really important to the defrosting performance. A good defrosting duct design means not only the mass flow rate distribution of each outlet is reasonable, but also the air flow could reach the locations where needed. Obviously, the windshield, the left and the right side windows are crucial locations as far as a passenger car is concerned. It was shown in Fig. 5 that the air flow comes from LSWO cannot reach the left side window effectively in the Original Design and Case 2. It could be seen from Fig. 5, Case 2, that the flow structure could not be improved only by enlarging the total area (S_{lswo}) of the LSWO. After changing the position of the LSWO (P_{lswo}), it could be found in Case 3, the flow field structure near the left side window was much better than flow structure in the Original Design and Case 2. So does the Case 5. It was also illustrated in Fig. 5, Case 5, that most of the air flow comes from the LSWO could reach and attach the left side window.

As for the flow structure near the windshield, it was described in Fig. 6, the air flows come from the WLPO and WRPO were lifted in Case 4 compared with the Original Design and Case 1. That means the angle between the air flow guiding vane skirt and the vertical direction (A_{wo}) was a helpful variable for improving the flow structure. Similar phenomenon could be found in Fig. 6, Case 5.

Table 3 Five outlet region mass flow rates of six cases

Outlet region	Mass flow rates					
	Original design (%)	Case 1 (%)	Case 2 (%)	Case 3 (%)	Case 4 (%)	Case 5 (%)
LSWO	4.99	5.67	5.84	5.07	5.05	7.06
WLPO	30.41	34.69	30.91	31.13	34.59	36.33
WRPO	31.54	35.28	31.19	31.35	37.97	34.76
RSWO	6.73	7.22	6.35	6.47	6.47	7.34
WIO	26.33	17.14	25.72	25.67	15.91	14.51

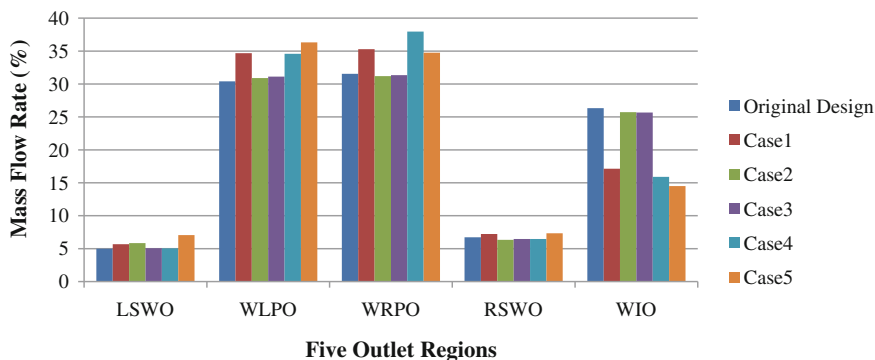


Fig. 4 Mass flow rate distribution of six cases

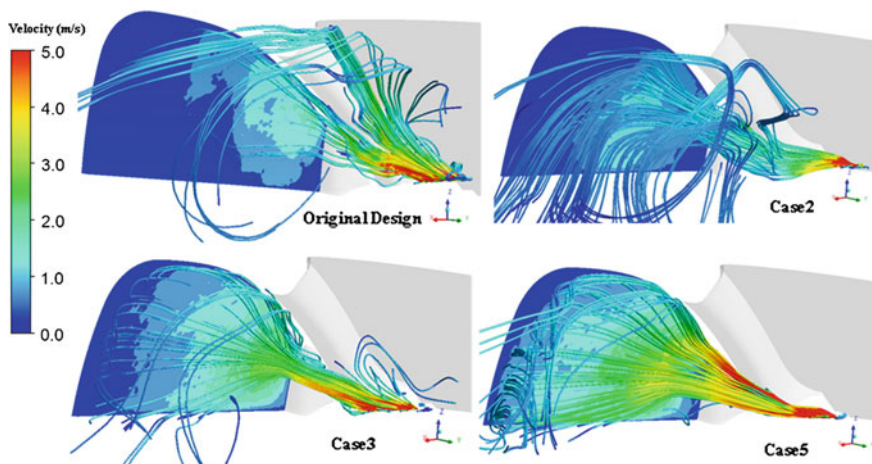


Fig. 5 Streamlines from the LSWO and velocity magnitude on the *left side window*

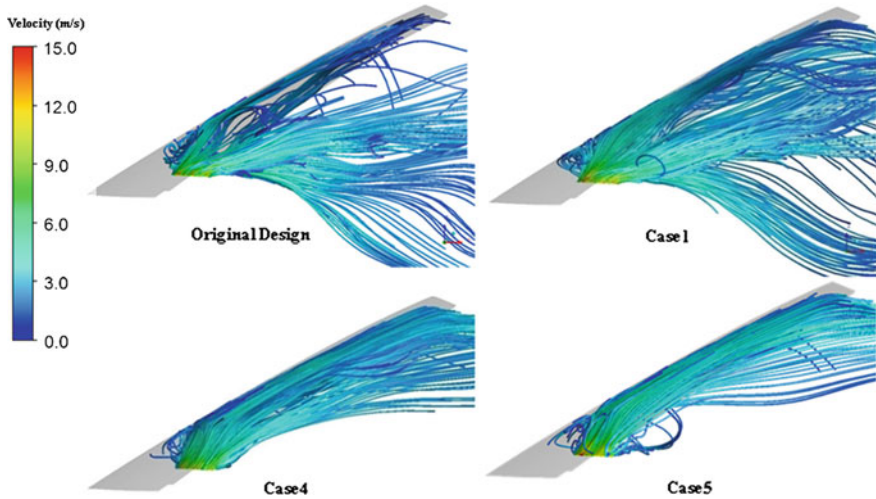


Fig. 6 Streamlines from the WLPO and the WRPO

4 Conclusion

The flow field inside the HVAC defrosting airflow canal and the passenger car cabin was analyzed using the steady RANS method. The aerodynamic design variables were defrosting outlets' sizes and positions. And the aerodynamic design targets were reasonable mass flow rate distribution and the good flow structure.

The CFD results showed that the total area of the WIO (S_{wio}) was a decisive variable for mass flow distribution in this duct design. The mass flow rate of the LSWO could be increased by enlarging its area (S_{lsw}), but the flow structure near side windows cannot be improved only by enlarging S_{lsw} . The LSWO's position (P_{lsw}) was also needed to be modified. Good flow structure was realized by choosing proper angle (A_{wo}) of the vanes skirt of the WLPO and WRPO.

It is true that the HVAC system performance data, such as defrosting time and cabin temperature distribution, could not only be obtained based on the results of the steady RANS method. However, the mass flow distribution of each outlets and the flow structure near the windshield and side windows could be evaluated using the method of this work.

Acknowledgments Thanks for the supports from National Science Foundation of China (50905070), Development Programs in Science and Technology of Jilin Province (20100175, 20110724), Foundation of State Key Laboratory of Automobile Dynamics Simulation and Basic Science and Research foundation of Jilin University.

References

1. Srinivasan RC, Karim NJ (2004) A numerically-based parametric study of heat transfer off an inclined surface subject to impinging airflow [J]. *Int J Heat Mass Transf* 23(47):4967–4977
2. Roy S, Karim NJ, Patel P, AbdulNour B (2002) An experimental and numerical study of heat transfer off an inclined surface subject to an impinging airflow [J]. *Int J Heat Mass Transf* 8(45):1615–1629
3. Roy S, Kumar H, Anderson R (2005) Efficient defrosting of an inclined flat surface [J]. *Int J Heat Mass Transf* 12(48):2613–2624
4. Menter FR, Kuntz M, Langtry R (2003) Ten years of industrial experience with the SST turbulence model [M]. *Turbul Heat Mass Transf* 4 (Begell House, Inc.)
5. Menter FR (1993) Zonal two equation k-omega turbulence models for aerodynamic flows [C]. In: AIAA 24th fluid dynamics conference, 6–9 July 1993, Orlando, Florida, AIAA-93-2906

An Operating System for the Optimization of Technical Systems Using the Example of Transmission Calibration

Albert Albers, Alexander Schwarz, Matthias Behrendt
and Rolf Hettel

Abstract Technical systems must be continuously improved so that they can remain competitive in the market. The duration and the costs of the development process are important factors of success for a company. Therefore practical methods and processes have to be provided to create an efficient optimization process. Within this paper an operation system for a time efficient, test based optimization of technical systems will be presented. Therefore methods from simulations and tests are being combined. Based on the X-in-the-Loop approach (XiL) it is possible to examine the Unit under Test (UuT) on an overall vehicle level in interaction with the environment and the driver. This way, even complex interactions between the systems can be emulated concerning examination- and optimization- goals. This also allows validating and optimizing modern, strongly interconnected drive systems. Especially hybrid powertrains present major challenges to the test because the additional state variables like SOC as well as engine and operating temperatures have to be considered and adjusted if necessary. This operation system provides the methods to reduce the time of conventional test runs as well as methods for model based optimization. Conventional approaches use non-physical models like polynomial-approaches or artificial neural networks for the optimization. In contrast, the presented approach allows the use of models partly consisting of physical parts. Thereby, the model quality and the expenditure of time for testing can be reduced significantly. Even conventional test runs with various measuring points, like monitoring of shifting quality, can be shortened significantly by this operation system. In the example of the gear shifting

F2012-E12-051

A. Albers · A. Schwarz (✉) · M. Behrendt · R. Hettel
IPEK–Institute of Product Engineering at the KIT–Karlsruhe Institute of Technology,
Karlsruhe, Germany
e-mail: alexander.schwarz@kit.edu

evaluation of a dual clutch transmission the expenditure of time can be reduced by 80 %. Therefore, several measuring points are being defined throughout the different shifting modes (different accelerator pedal positions, rpms, gears, driving situations and driving maneuvers) and put into an ideal order. This means, the system calculates the order for a minimum time of conditioning between the measuring points (reaching the desired initial condition).

Keywords Hybrid · X-in-the-Loop · Time-efficient model based validation · Optimization · Identification of physical models

1 Introduction

Shorter shifting duration, higher energy efficiency and a higher gear shifting comfort are only few criteria of modern powertrain systems that will be faced with stronger requirements in the future. For succeeding in the market, technical systems have to be improved continuously. Thereby, even with increasing complexity, the development time of technical systems has to decrease in order to ensure the profitability for the company. For reaching this goal by so-called ‘frontloading’, new methods and processes are needed.

A central activity of the product development process is the validation and optimization. An important part is still the test based optimization. In this thesis the validation and optimization of the shifting curve and shifting points in a vehicle with a seven gear dual clutch transmission and a mild hybrid will serve as an example. The shifting quality and the energy efficiency depend on a variety of parameters of the transmission control unit. The examination is based on test data from an acoustic roller test bench (see Fig. 1) with Vehicle-in-the-Loop technology. Depending on the test, environmental influences like traffic, turns, slopes and the driver can be simulated. This test bench is capable of drivability examinations due to an axial vehicle fixture through a load cell. The signal of the load cell can be used for calculating a high-frequency, longitudinal acceleration for evaluating the comfort. Another advantage of the Vehicle-in-the-Loop environment is the possibility of using the real-time simulation system as a virtual driver. Thereby, shifting can be done fast, reproducible and regardless of weather conditions.

2 Motivation and Development Goals

Goal of this operating system is to identify the design parameters for a perfect behavior of the technical system concerning the target function. The target function describes the interaction of several evaluation criteria and sub-criteria. In this example, energy efficiency is one criterion. Sub-criteria are for example the fuel consumption during the NEFZ (new European driving cycle) as well as the real fuel consumption according to customer specific cycles or the “Auto Motor Sport Normalrunde”.

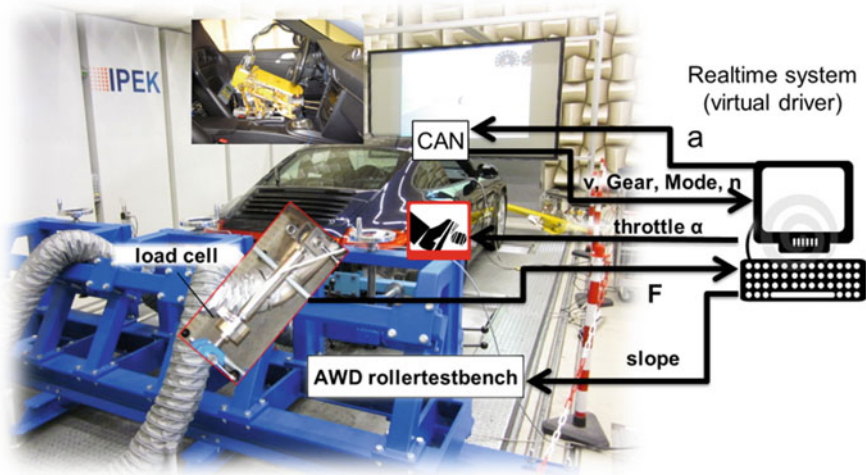


Fig. 1 Acoustic roller test bench with vehicle-in-the-loop technology

The design parameters are the parameters supposed to be optimized in this development step. In this example it is the definition of shifting curves and shifting strategy. State of the art is the static test planning using non-physical models like polynomial models or artificial neural networks for test based optimization. With the help of Design of Experiments (DoE, see [1]) the design parameters are being varied specifically and the evaluation criteria for every variation are being determined. With the target function it is possible to calculate the target function value for every variation. This data (design parameters and target function values) is used to determine the parameters of the non-physical model. This model is then used for optimization. In the end the new parameter adjustments have to be verified through testing and the model structure has to be adjusted if necessary, and further variations have to be done. Therefore, this approach has to consider the interdependence between the target function value and the design parameters. This procedure is especially qualified under the following conditions:

- Small number of design parameters.
- Quick variation of the design parameters is possible.
- Criteria can be determined quickly through testing.

If one or more conditions are not fulfilled, test time increases rapidly. For the full fractional test the following relations are deemed:

$$totaltestduration = numberofvariations * durationofvariation \tag{1}$$

$$numberofvariations = numberofvariationsteps^{numberofdesignparameters}$$

$$durationofvariation = durationadjusting\ designparameters \tag{2}$$

$$+ duration\ capturing\ evaluation\ criteria$$

In modern drive systems even more strong interactions exist between the several subsystems. Therefore, the amount of design parameters increases strongly. The number and duration of evaluation criteria increases steadily as well. In this example one “Auto Motor Sport Normalrunde” (173 miles) for each variation is required. The duration of every adjustment of the design parameters also has a large influence on the test duration. Unlike the control unit parameters, transmission ratio parameters can only be varied with huge test effort. Therefore, the goal of this operation system is to create a more efficient way of solving optimization problems by extending the approach.

3 X-in-the-Loop Validation Environment

For this test the X-in-the-Loop-Validation environment (Fig. 2) is used (for additional information see [2–4]). Using corresponding rest vehicle simulation the Unit under Test (UUT) is being completed to a full vehicle. Thereby, the rest vehicle simulation can contain real test bench components as well as simulation models. This allows the examination of the working surface pairs, from the single subsystems up to the complete vehicle in the overall system context. This also means that the interactions between the systems driver, environment and vehicle are being considered.

4 Operation System for the Test Based Optimization

A model concept of the system is frequently available before the test based optimization, but one or more parameters, like frictional coefficients, which could not be calculated before the construction or at least not without excessive effort, are often missing. This model structure shall be used in the following to improve and shorten the optimization process. This process consists of the following steps (see Fig. 3):

- Definition of the optimization problem and choice of optimization approach.

In this step the optimization problem is defined. Depending on the technical system and the boundary conditions, a suitable approach must be chosen for the optimization process in order to be able to optimize as efficiently as possible. First the model structure, the individual variable groups such as parameters, which need to be identified or are already known, and the design parameters have to be defined.

This is where the additional boundary conditions like the installation space or the assessment maneuvers are being defined.

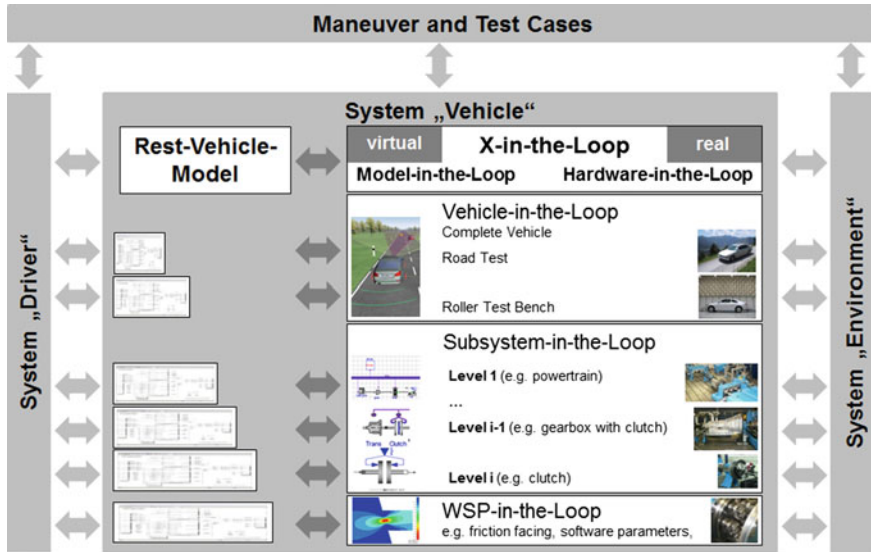


Fig. 2 X-in-the-loop-validation environment

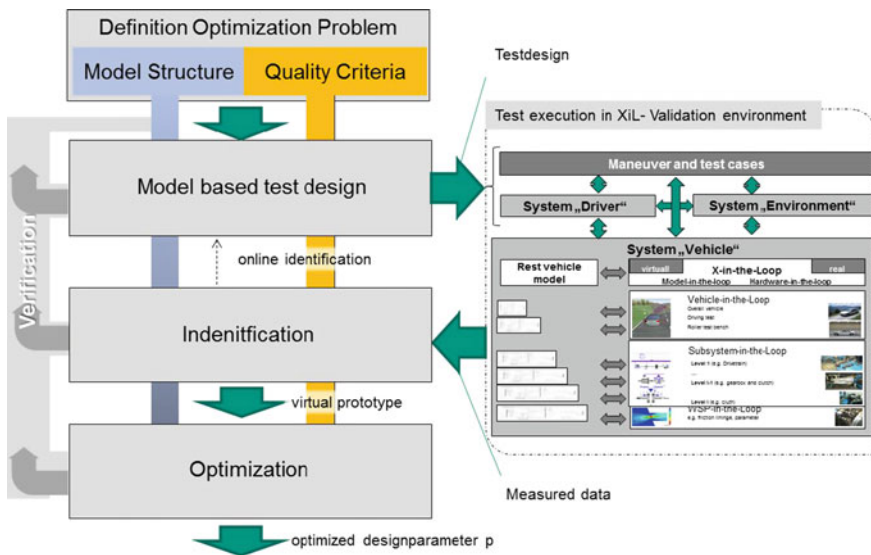


Fig. 3 Operation system for test based optimization

- Model based test design/test execution.

In this step the test design based on the definition of the optimization problem is determined. This means, suitable maneuvers (input parameters) as well as suitable test points are being defined or calculated. In this process, model

assumptions as well as online identified models are already used for the calculation of time and cost efficient test design.

The essential factors are:

- Choice of the measuring points.
 - Calculation of the measuring points.
 - Calculation of the order of the measuring points.
- Automated identification.

From the test data, a model of the system is identified. This means, unknown parameters are calculated based on the measurement data. The result is a complete parameterized and virtual test object which acts in the same manner as the real test object.

- Automated optimization of design parameters.

In this step the design parameters are calculated, in order to optimize the system with regards to the defined objective functions as well as the defined boundary conditions.

The advantage of using virtual prototypes is that evaluation criteria whose site identification took very much longer in the real test, for example the “Auto Motor Sport Normalrunde”, can be evaluated much faster in the simulation and without using a test bench at all.

5 Definition of the Optimization Problem

The optimization problem is defined in this phase. This means that the variables of the model structure must be assigned.

The same variable can appear in several groups:

- Known parameters.
Some parameters, like natural constants, which are contained in the model structure, are already known before the real test. It makes sense to define many parameters before the test execution in order to reduce the test and computing time.
- Input quantities.
The input quantity is flow data such as sets of measuring points which will appear in the system. If system parameters are varied by a DOE plan they also become input quantities.
- Output quantities.
All system answers are denominated as output quantity.
- State variables taken into account.
The flow data is also taken in account for the identification. This prevents that the virtual prototype from acting non-physically, even at a high model quality regarding the criteria.

- **Unknown parameters.**
Unknown parameters are the parameters which must be calculated during the identification. Additionally, it is helpful to define limits in which these parameters are acting.
Depending on applied algorithm additional start values can be indicated for these parameters. In this way the calculation time can be reduced.
- **Design parameters**
The design parameters are optimized according to the defined valuation criteria in the optimization phase.

In addition to the variables, the model structure has to be defined as well. The possible model structures are:

5.1 Closed Model

A closed model exists in the linked simulation environment. The usage of these models requires that all unknown parameters can be controlled by the identification algorithm. That allows using models which contain domain-specific sub-models.

5.2 Non-Physical Models

Additional possibilities are special predefined equations which simulate the behaviour of the system non-physically. Examples for such structures are polynomial models or artificial neural networks.

5.3 Nonlinear System of Equations

An open model structure in the form of equations offers the most efficient way for the identification algorithms.

6 Test Design

In some cases measured data of the vehicle or the technical system is available. In this case the data can be directly used to identify a model. Even if there is no adequate model based on this data, this model can be used to shorten the testing process. Ideally, the measuring data is used online during the testing process to improve the model. This model can be used for the optimization of the testing process. In general, the following possibilities for each examination and model structure exist:

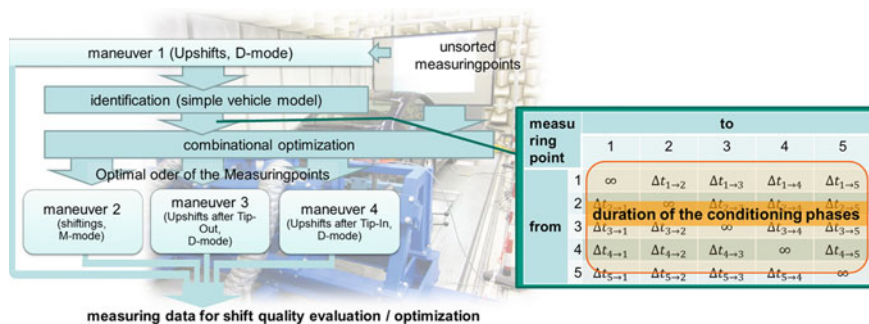


Fig. 4 Method for shortening of measuring point based test runs

6.1 Measuring Point Based Test Runs

The test time of measurement-based test runs can be reduced by optimizing the order of the measuring points if different initial and end condition are being reached. For the shifting quality evaluation this approach can be used to put the shiftings into order in order to reduce the overall duration of the conditioning phases. For a seven gear dual clutch vehicle, up to 80 % of the test time can be saved in comparison to an experienced test driver. For the gear shift quality evaluation there are four interesting shifting types which can be initiated by four driving maneuvers. The first maneuver (upshifting) is used to parameterize a simple model of the vehicle (see Fig. 4). This model is used to calculate the duration of conditioning between the measuring points (see table in Fig. 4). With a combinational optimizer the ideal order of the points is calculated for the remaining maneuvers. For more details see [5].

6.2 Test Runs for Identifying Models with Physical Structures

The calculation of the input signal is based on the identification of models with physical structures. An optimizer is used to calculate the optimal input signals. During the test process the used model can be improved.

7 Automatic Identification

In the phase of identification the unknown parameters are determined in a way that the model acts like the real test object. That means the algorithms are used to calculate the model parameters so that the model behaves like the unit under test regarding specific criteria but also in regard to the state variables. For calculating the parameters the following types of algorithms exist:

7.1 Algorithms for Solving Systems of Equations

If the equations of the model structure are accessible, the parameters can be determined with a suitable solution algorithm. Many technical systems can be described in the following shape:

$$\vec{y} + \vec{\epsilon}_a = \vec{H} * \vec{\alpha} \tag{3}$$

with

- $\vec{y} = y_k = (\dot{:})$ estimate(s) (filtered measuring data)
- $k = 1..ke$ control variable of the measuring points
- $\vec{\epsilon} = \epsilon_{ak} = (\dot{:})$ absolute offset from model value to test value
- $\vec{H} = H_{kl} = (\ddot{:})$ design matrix with combined state variables
- $l = 1..le$ control variable state variables
- $\vec{\alpha} = \alpha_l = \begin{pmatrix} f_1(\vec{p}) \\ \vdots \\ f_l(\vec{p}) \end{pmatrix}$ combined parameter vector
- $\vec{p} = p_q = (\dot{:})$ parameter vector
- $\vec{q} = 1..qe$ control variable parameter

If several state variables and conditions are considered in the identification the equation looks like this:

$$\begin{pmatrix} \frac{\bar{y}_{1,1}}{\bar{b}_1} \\ \frac{\bar{y}_{1,2}}{\bar{b}_1} \\ \vdots \\ \frac{\bar{y}_{2,1}}{\bar{b}_2} \\ \frac{\bar{y}_{2,2}}{\bar{b}_2} \\ \vdots \end{pmatrix} + \vec{\epsilon} = \begin{pmatrix} Hzust1 & \begin{pmatrix} 0 & \dots & 0 \\ \vdots & \ddots & \vdots \\ 0 & \dots & 0 \end{pmatrix} \\ \begin{pmatrix} 0 & \dots & 0 \\ \vdots & \ddots & \vdots \\ 0 & \dots & 0 \end{pmatrix} & Hzust2 \end{pmatrix} \begin{pmatrix} \frac{\bar{z}_{zust1}}{\bar{b}_1} \\ \frac{\alpha_{zust1}}{\bar{b}_2} \end{pmatrix} \tag{4}$$

The vector \bar{b}_z is a scale factor which brings the different state variables on one level and weighs them against each other. This equation can be used to minimize the error according to the least square method.

$$\min_p \left(\sum_k \hat{e}_k^2 \right) = \min_p (\vec{\epsilon}^T \vec{\epsilon}) \tag{5}$$

Usually the following system of equations has to be solved:

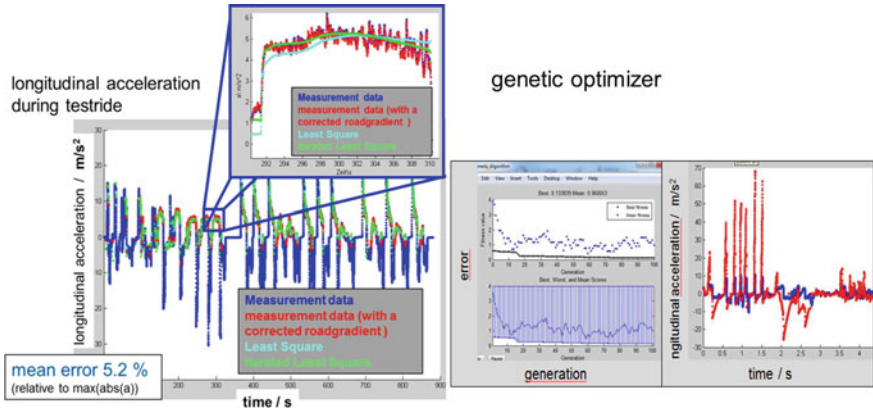


Fig. 5 Result of least squares estimator (left) and genetic optimizer (right)

$$\frac{\partial(\vec{\varepsilon}^T \vec{\varepsilon})}{\partial \vec{p}} = 2 \frac{\partial \vec{\alpha}^T}{\partial \vec{p}} \left(\vec{H}^T \vec{H} \vec{\alpha} - \vec{H}^T \vec{y} \right) = 0 \tag{6}$$

Therefore algorithms can be used to solve nonlinear systems of equations depending on the structure.

7.2 Estimator

In the case of $\vec{\alpha} = \vec{p}$ or the possibility of solving directly for the vector $\vec{\alpha}$ different estimators are available for solving the system of equations:

- Least squares estimators e.g. weighted, iterated
- Ransac estimator [6]
- ...

7.3 Optimizer

If the system cannot be described in this form or the model exists as a closed model, optimization algorithms like generic optimizer or search patters can be used.

7.4 Results

For the test of the algorithms a model of a automatic powertrain was used with real measurement data. Figure 5 shows the comparison of the longitudinal acceleration of the vehicle for the identified and real measurement data during a test drive.

The high frequencies can't be reproduced by the model because the used model structure does not contain elastic properties. The model structure has to be adapted if the high frequencies are important for the determination. In this case an iterated least-square estimator provides better results, because it is less influenced by outliers. The genetic optimizer is simple to implement but provides less accuracy regarding the computation time in this case.

8 Optimization

The identification results in a model that performs like the real system in regard to the examined criteria. This model can be used to optimize the design parameters. Standard optimization procedures can be used for this step. Genetic optimization procedures are often suited for this task, because they are able to find global minima without needing adequate initial values. After finding the optimal design parameters, the model can be adjusted specifically with respective experiments.

9 Conclusion

This contribution introduces an operation system which allows finding the optimal design parameters for a given model structure with the help of respective experiments. The advantage of this operation system is that the design parameters are only varied within the simulation model and not in real tests. This allows optimizing design parameters, which could only be varied slowly in real experiments. Also, criteria with very long cycles/maneuvers can be used for the target function, like the NEDC or "Auto Motor Sport Normalrunde". In contrast to non-physical modeling, the statistical test planning allows to safely predict the model limits. The required tests can be shortened by specifically optimizing the order of the measuring points within a test run. When evaluating the shifting quality, this course of action can reduce the expenditure of time by 80 %.

10 Outlook

The next step is to improve the identification procedure. Especially the computation effort must be minimized by using specialized algorithms. Besides that, the selection of manoeuvres and measuring points shall be automated in the case of the statistical test planning in regard to the model structure as well as the quality criteria.

References

1. Roy Ranjit K (2001) Design of experiments using the taguchi approach
2. Albers A, Düser T (2009) Integration von Simulation und Test am Beispiel Vehicle-in-the loop auf dem Rollenprüfstand und im Fahrversuch
3. Albers A, Behrendt Ott S (2010) Validation—central activity to ensure individual mobility. In: FISITA world automotive congress, Budapest, Hungary
4. Albers A et al. (2012) System-oriented validation aspects of a driver assistance system based on an accelerator-force-feedback-pedal. In: FISITA world automotive congress, Beijing, 2012 F2012-I04-003
5. Albers A, Schwarz A, Hettel R, Behrendt M (2012) Method for the time-saving capturing of vehicles on the roller test bench carried out with dual clutch transmissions”, 6th International CTI Symposium and Exhibition North America
6. Hartley R, Zisserman A (2003) Multiple view geometry in computer vision. University Press, Cambridge

Model Structure, Realization and Learning Process For a Driver Model Being Capable to Improve Performance with Learning by Itself

Kazuhide Togai and Hisashi Tamaki

Abstract Vehicle electrification has been extended rapidly in a recent few years and development work for those has been added to conventional vehicles. Model based development (MBD) methodologies have been adopted widely. A dynamic driver model is required for controller design considering driver's behaviour and for verification with SiLS and HiLs in the MBD process. Some higher response and multi-variable control systems can be constructed with electronic devices. However, human control is not so quicker and not capable to handle multi states. There have been a lot of published papers regarding to driver models. Structure of the driver model with constrains of human property and learning process seems to be under study. Authors have investigated driver models for target speed tracking driving in emission test cycles in which the target is clearly defined. Taking account of constrains with driver's response and information processing capability, a driver model structure, feed forward operation based on prediction and additional error feedback correction, is introduced. A learning algorithm to obtain inverse vehicle property for the feed forward control is proposed. Knowledge which enables to select features to be learned and condition for stable learning process are discussed. Numerical simulation illustrates driving behaviour from a beginner to an expert with the driver model. Further, it is shown that speed tracing driving performance with a novice driver model could be improved when vehicle property is changed, e.g. an IC engine is replaced by an electric motor. It is supposed that the proposed method is also applicable to development process for a lower order and lower sample rate controller with adaptation functionality.

F2012-E12-052

K. Togai (✉) · H. Tamaki
Kobe University, Hyōgo, Japan
e-mail: kazuhide.togai@mitsubishi-motors.com

Keywords Driver model · Learning control · Software in the loop simulation · Rapid prototyping · Emission test cycle

1 Introduction

Current automobiles are designed and tested on the premise of electronic controllers and control theory. However, automobiles were put into practical use in 18 century when those controller and theory were not developed yet. Basic vehicle control such as to run, stop and steer has been done by human drivers since the invention, while a lot of control have been took placed by electronic control e.g. for engine starting, ignition and fuel injection. Automatic operation has been applied widely to airplanes, trains and also applied to automotive for specific purposes.

Vehicle electrification has been extended rapidly in a few years, and vehicle R&D work load has been increasing in addition to that of IC engines. Model based development (MBD) methods have been widely adopted and driver models are required for design considering drivers dynamics and for evaluation with model simulation.

Driver models have been published mainly for steering since 1960s. Macadam surveyed related papers widely up to 2003 and introduced some typical concept including driver's response delay from acknowledgement to operation and target prediction. Relationship between driver's response time and prediction time for stable steering control was also introduced [1]. Kageyama has proposed a driver model which consists of feed forward and feedback for steering and has described driver behaviour depending on response time and in various environments in his series of papers [2].

Driver model application to vehicle evaluation has proposed recently. Behaviour of a river model combined with a specified vehicle was investigated. Sometimes a PID controller is called a driver model. Even if the model could track the target, the operation would be different from that of human drivers. Target speed and actual speed are inputs and operational amplitudes of apparatus are output. The input—output relationship is common for a machine controller and a human driver. But, internal information processing principles are different. A human driver can learn and obtain better skill. An expertise process of driver consists of increase of accuracy, efficiency of acknowledgement—judgment and smoother operation and rather accurate operation with smaller operating energy.

Purposes of our study are to distinguish driving behaviour between a human driver and an electronic controller and to represent the human behaviour in mathematical equations or in controller model. Driving behaviour during target speed tracing in emission test cycles was selected for the study. Because the tracking target is well defined and driving behaviour is easily evaluated. At first, a powertrain—vehicle model from driving operation to vehicle speed is derived within required frequency. Then, driving behaviour of an expert and a beginner

based on measurement is compared and analyzed. Allowed human driver control is to be identified from response constraints. It is predicted that driver's control is based on mainly feed forward and learning is required to increase accuracy of feed forward.

To find clue of learning method, iterative learning strategy, in which knowledge of plant is not required and operation correction for each cycle is calculated only with tracking error, is applied to a driver model. If specific property of the plant would be obtained during the iterative learning, fewer parameters would be learned systematically based on the knowledge found. That enables robust and accurate feed forward control. During further learning, a driver takes correct operation without thinking on looking a specific target profile. The process may be explained with Rasmussen's SRK model.

A human driver is inferior to an electronic controller in response and multiple variable processing, but can learn and can be expertise. If human learning process would be modelled, it is expected that the model would be applied to human—vehicle design and evaluation, lower order controller design with fewer parameters and autonomous distributed control system.

2 Vehicle: Controller System Property for Test Cycle Driving

Vehicle speed response to accelerator/brake is derived in frequency domain to formulate driving operation as the control input.

3 Vehicle System Response in Time Domain and Frequency Domain

An engine of the test vehicle is an internal combustion (IC) engine. There are some detail engine model such as fuel chemical reaction with fluid dynamics in 3D, while, some detail six degree of freedom vehicle dynamic model containing frame deformation. Engine output torque can be obtained with an engine speed and accelerator position map which is the simplest engine model. Frequency response up to 10 Hz is required to analyze the speed tracing driving behavior. A mass represents the vehicle and a powertrain, i.e. engine and transmission, can be described as first order or second order delay system with time constant up to 0.5 s [3]. Vehicle acceleration or deceleration is not linear to acceleration or brake operation amplitude respectively.

A stroke mean value model [4] is applied for torque generation process where air flow regulated by a throttle is taken to combustion chamber and the air—fuel mixed gas generates torque proportional to intake air mass after expansion stroke. Air flow response from the throttle to combustion chamber through plenum chamber is a first order system and the time constant of the system is proportional to the volume of the chamber and reverse proportional to engine speed.

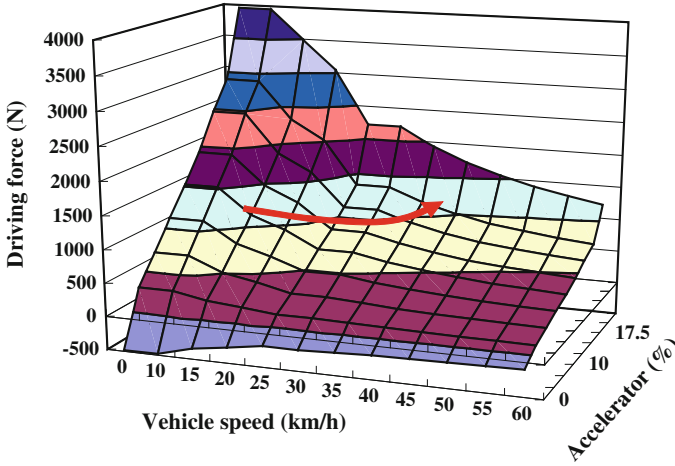


Fig. 1 Accelerator position for constant acceleration shown as the red arrow

Engine output is transferred to the transmission through a torque converter. The torque converter output torque is proportional to engine speed square [5]. Sufficient torque for acceleration cannot be obtained until the speed reaching at a certain speed. Torque transfer response, i.e. time constant, is depending on engine speed increasing rate [6]. A CVT is selected as the transmission for the modelling. It is assumed that gear ration change response delay is negligibly-small in the emission test cycle driving, even if gear ratio change response is not quicker enough when target gear ratio changes largely.

Vehicle speed response to driving force can be approximated by first order delay. Air resistance of the vehicle is proportional to vehicle speed square and the resistance is a feedback to the force. The response property can be replaced by integration (1/s) at lower vehicle speed. Major time constants are contained in the engine and the torque converter until being locked up and in the engine after the lock up. Frequency response property from an accelerator to vehicle speed is shown in Fig. 1 [7].

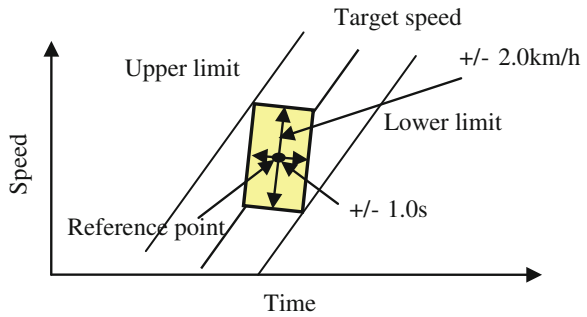
Transfer function from engine torque demand by the driver to vehicle speed is well approximated in Eq. (1) for emission test speed tracking analysis.

$$G_v(s) = \frac{K_e}{1 + T_e s} \frac{K_{tm}}{1 + T_{tm} s} \frac{1}{Ms} \tag{1}$$

Where

- K_e engine torque gain,
- T_e engine time constant,
- K_{tm} transmission gear ratio,
- T_{tm} transmission time constant for un-lockup,
- M vehicle weight.

Fig. 2 Tracking error tolerances in a test cycle



4 Non Linearity in Vehicle Speed Response Property

Non linearity in torque transfer from driver operation to driving force exists mainly in acceleration side. Driving force is affected by the torque converter during launch. Gear ratio is shifted as vehicle speed increasing, so that the same driving force is not obtained if the accelerator position is kept at constant for all vehicle speed. Accelerator position to generate constant driving force to compensate gear ratio shift is shown in Fig. 1.

Braking force to brake pedal force is nearly linear. Engine brake force is added to running resistance when fuel is cut during deceleration. Creeping force, which is proportional to idle engine speed square, acts as driving force just before the test vehicle stop. Those forces should be considered when brake is applied.

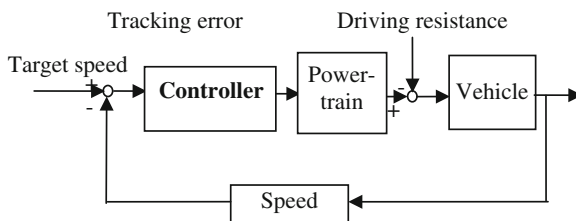
5 Test Cycle Speed Tracking

Target speed tracking problem is defined as driving a test vehicle within allowed speed error to target speed specified by laws for emission test cycles. Some speed tracking error is allowed as shown in Fig. 2. Values in the figure are for a Japanese test cycle. Higher tracking accuracy than specified is not required.

Smoother operation within the tolerance is preferable. Rapid operation with frequent WOT or close throttle could lead to deterioration of emission and fuel economy. A speed controller for a vehicle has target speed and measured speed inputs and accelerator or brake outputs. That is the same for an electronic controller and a human driver as shown in Fig. 3. The controller block can be replaced by a human driver or an electronic device.

The controller can be assumed as a simple proportional controller for tracking performance evaluation. The control gain is set to be K for unit vehicle weight. Time response of the closed vehicle—controller system to the speed target can be calculated analytically with the transfer function described in Eq. (1). For constant

Fig. 3 Target speed tracking control system



acceleration target, steady state speed error of the system is multiply $1/K$ by the target acceleration. The gain K should be greater than 2.0 at least to keep the vehicle speed within the allowed error as shown in Fig. 2.

6 Drivers' Behavior and Feasible Control

A vehicle was run on a chassis dynamo by a number of drivers to trace the Japanese 10–15 mode emission test cycle. The test vehicle was a 2.0 L gasoline CVT passenger car.

7 Comparison of Driving Behaviors

Two people were selected for comparison in consideration of their experience. One was an inexperienced first-timer, and the other was well experienced in this kind of test. The driving operations and target tracking errors of these drivers were measured. The first-timer drove the test cycle three times to measure driving behaviour change. The comparison results are shown in Figs. 4 and 5. The expert tracked the target with smaller error and stable operation, while the beginner deviated largely from the target and changed accelerator or brake pedal positions frequently and unstably [8].

8 Feasible Control with Constrains of Human Driving Property

Target speed tracking is a driving control based on visual information which includes target speed and current speed error. There is delay time from visual information acknowledgement to operation by a driver. Kageyama reported that the delay time is 0.3–0.5 s and may not be reduced by learning or training [9]. Feedback control performance, e.g. stability, in human driving is mainly governed by response of the controller.

Fig. 4 Target speed tracking behaviour in a test cycle

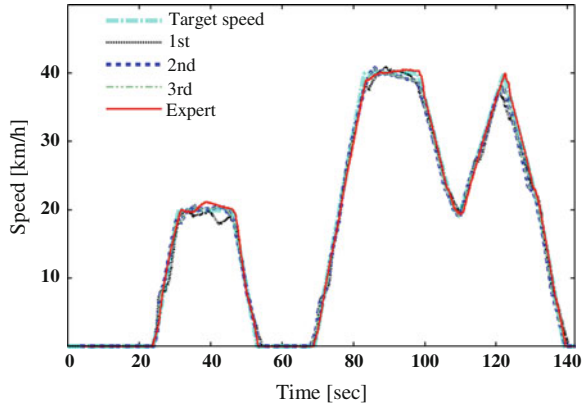
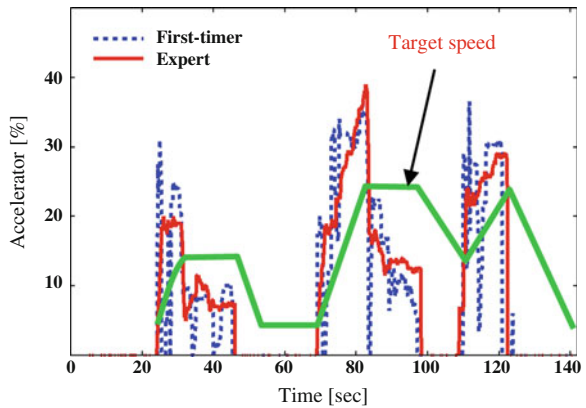


Fig. 5 Accelerator operation: expert and beginner



Frequency response of an electronic controller with 0.05 s dead time and a control system which include a human driver with 0.5 s dead time is shown in Fig. 6. Where, both controls are assumed to be proportional feed back control with gain 1. Dead time in a control loop deteriorates the system stability significantly and allowed feedback compensation amount inversely proportional to the dead time in the control loop. The electronic system (A) has allowed gain 33 dB at the frequency where phase delay exceeds -180° , while, the human control system (B) has 13 dB gain margin at the same phase delay. The proportional gain in the controller is required to be greater than 2.0 as described in the previous chapter. In this case, A has still 26 dB margin, however, B has only 7 dB margin. Although, B system seems to be still stable, proportional gain 2.0 is not sufficient for smaller tracking error. That means feed back error compensation is not be a major control means for a human driver.

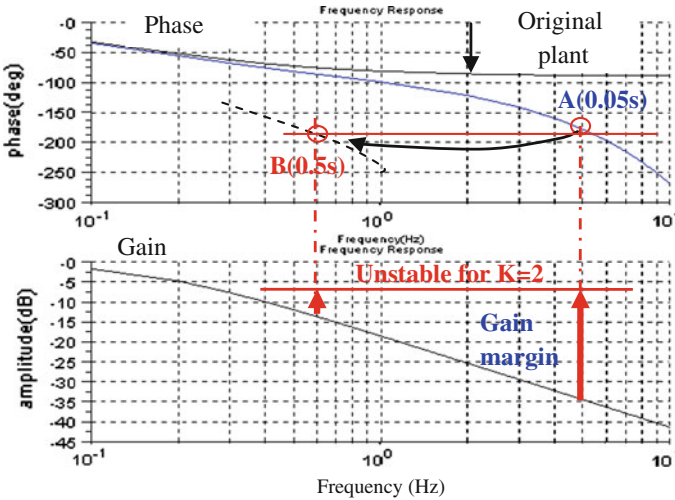


Fig. 6 Stable threshold gain is reduced as the dead time become large

9 Advanced Operation with Prediction to Compensate Delay

Even if an accelerator is positioned at a target position at the time when the target speed changes, the vehicle stays nearly stand still for a certain period of time which consists of engine response dead time, engine time constant and torque converter time constant. Some response delay can be compensated with feedback, however large compensation with larger input is not feasible due to limitation of input operation i.e. engine output torque is finite. If the target profile would be known in advance, the target could be well tracked with advanced operation by the response delay time as shown in Fig. 7. A methodology developed as predictive digital control also indicates that when amplitude of input operation is limited, optimal response is obtained by input in advance to the target change [10].

10 Learning Process in a Driver

Driving a car is a process in which information coming from environment and the car is processed and apparatus are operated by hands or feets based on the information. The process has been explained as acknowledgement, judgment and operation processes shown in Fig. 8. Where, $V(t)$: vehicle speed, $V(t)'$: recognized vehicle speed, $a(t)$: acceleration, $f(t)$: operation force for output. Each block has own delay (τ) and error (ϵ). How the information is handled in each block and how the process is described as a control system have not explained clearly, because it is challenging to observe information processing in human brain.

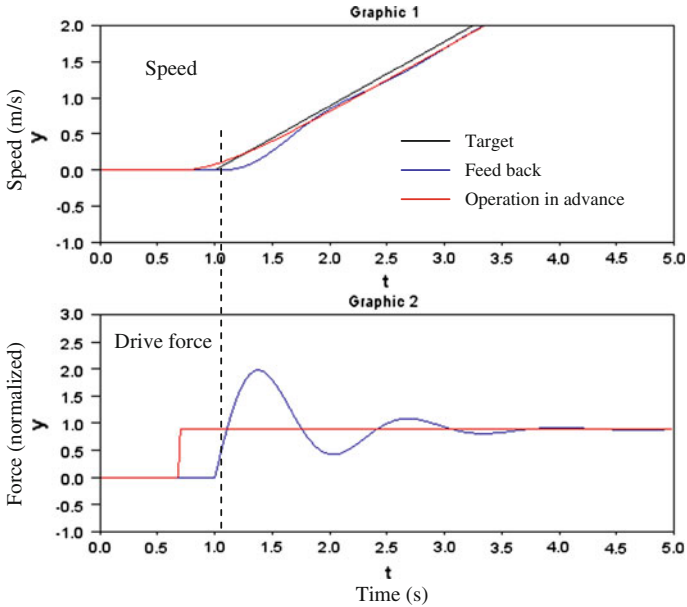
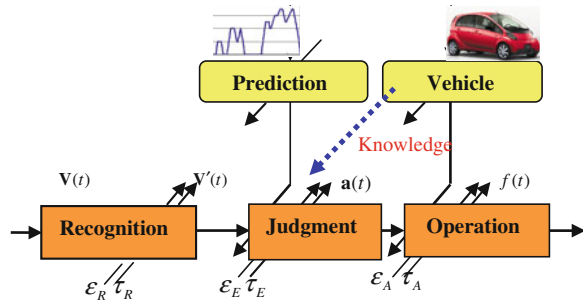


Fig. 7 Advanced operation and feedback compensation

Fig. 8 Information transfer in the driving agent



11 Inner Model of the Target Plant in a Brain

A control concept with an inner model in human brain was introduced [11]. A driver model based on knowledge level and skill level was adopted [12].

Target plant has an input response property as;

$$y(t) = f(x, u, t)$$

Where u: input, x: state, y: output

If controller has an inverse property described as the following equation,

$$u(t) = f^{-1}(x, y, t)$$

Fig. 9 Inverse system to generate an input for the target

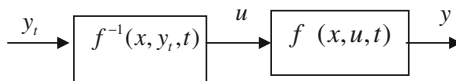
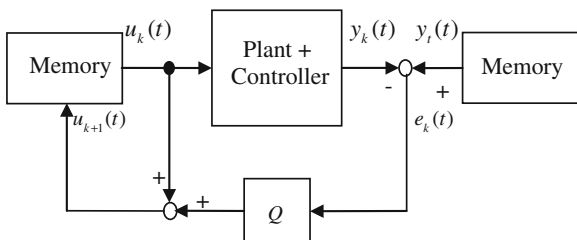


Fig. 10 Iterative learning control law



An input vector is derived from the target using the inverse function, generally as shown in (Fig. 9). However, realization of the inverse function is not always guaranteed due to irrevocableness of time.

12 Features Extraction in the Target Plant

Beginners may not understand vehicle response property at first. But, they may have knowledge, such that, acceleration or deceleration is proportional to accelerator or brake position and can recognize target tracking error. It is well known that target error feedback to next time operation input makes the output converging to an input profile which drives the car with smaller tracking error. Arimoto introduced the control scheme in Robotics [13]. The control strategy is shown in a block diagram as Fig. 10. The strategy does not require knowledge of the target plant construct and parameters. Operation input is replaced by previous time operation and error.

$$u_{k+1} = u_k + Q(y_t - y_k)$$

Where u_k : kth input data profile, y_k : kth output, y_t : target profile, Q : feedback gain (Matrix).

The strategy is applied to the target speed tracking. A constant accelerator position for target acceleration and a constant brake position for target deceleration regardless of the target speed are set at the beginning as Fig. 11. After ten time driving and learning iterations, resulted speed approaches to the target as shown in Fig. 12. Further learning up to 100 times reduced the tracking error. However, that does not mean the optimal learning to be feasible. It is required to memorize operation input and error every a certain interval. The number is huge and the task may be more difficult than to memorize pi up to 1,000 digits.

Furthermore, as the input operation profile is depending on the target vehicle property, once the vehicle would be changed, then the same learning would be required again. Even if all the input profile could be memorized, structure of the

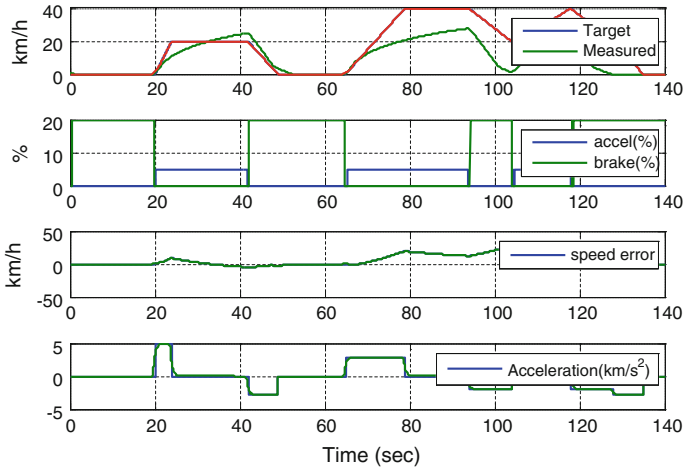


Fig. 11 Driving behaviour with initial values

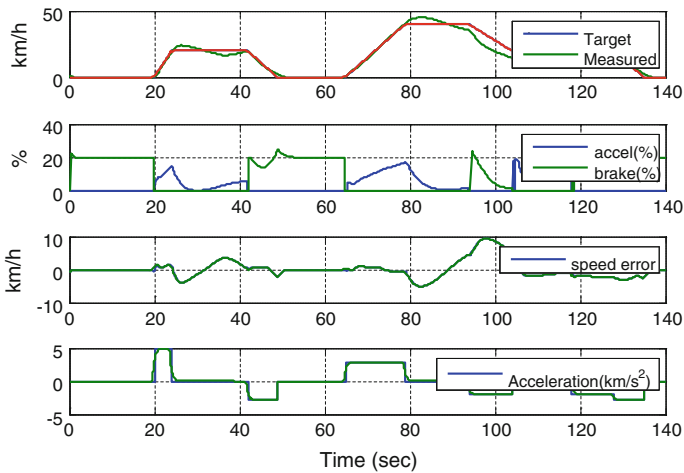
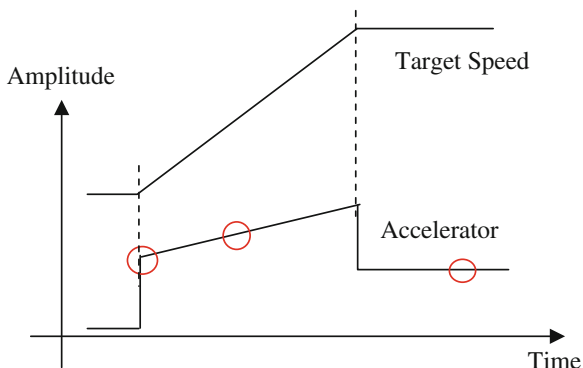


Fig. 12 Driving result after 10 times of irrelative learning

target plant would not be obtained with this strategy only and the learning result would not be applied to different vehicles.

Relationship between driver operation and response comes out gradually as resulted output becoming close to the target. Some features of the target plant may be found, for example, accelerator position increasing as speed increasing, and those can be hint to next stage learning which includes rule making. Advice might be given by expert during beginner status.

Fig. 13 Operation pattern and parameters



13 Finding Rules and Learning with Knowledge on a Vehicle

If the driver would know vehicle response to driving operation, the person could learn parameters which represent character of the vehicle. Then, learning can be done systematically and be completed within fewer times. That is said to be a pattern matching between a specific vehicle speed target profile and a specified operation profile. After some target speed tracking driving of a car equipped with an IC engine and a transmission, a driver would find empirically that vehicle acceleration is accelerator position dependent, the required position is increasing as vehicle speed increasing, accelerator position at constant speed depends on vehicle speed and further braking force is required just before the vehicle stop.

Those early learned knowledge was used to select features of vehicle speed response to driving operation and to construct a driver model which updates model learning parameter using target speed, resulted speed and speed error. Operation output profile is generated characteristic parameters, e.g. three parameters shown in Fig. 13 for start from stand still, acceleration and constant speed cruising. The model parameters can be learned as the following.

Initial accelerator position setting was arbitral with no speed increase correction for acceleration as shown in Fig. 14. Then, acceleration dependent initial accelerator position was learned to adjust vehicle speed at a certain speed to the target as in Fig. 15. In the third step, speed dependent increment of the accelerator position was learned to meet speed increasing rate to that of the target (Fig. 16). Finally, Accelerator position at constant speed cruising, where driving force is equivalent to running resistance, was learned from speed error and speed gradient as in Fig. 17. There is still speed error larger than allowed, and the error is reduced by small gain feedback compensation.

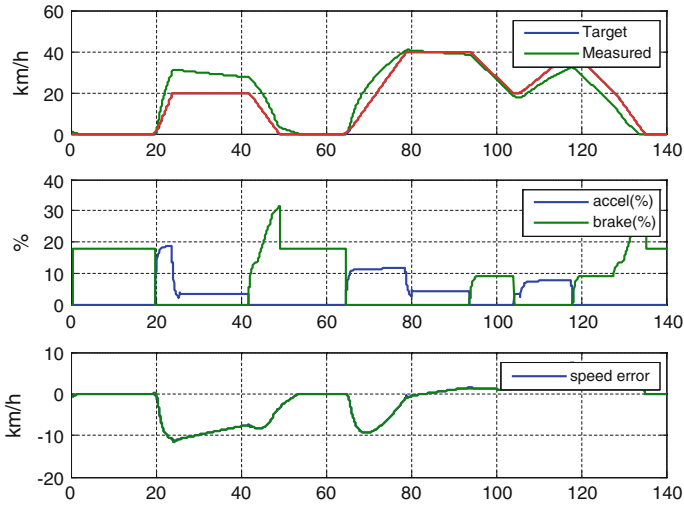


Fig. 14 Driving behaviour with initial value

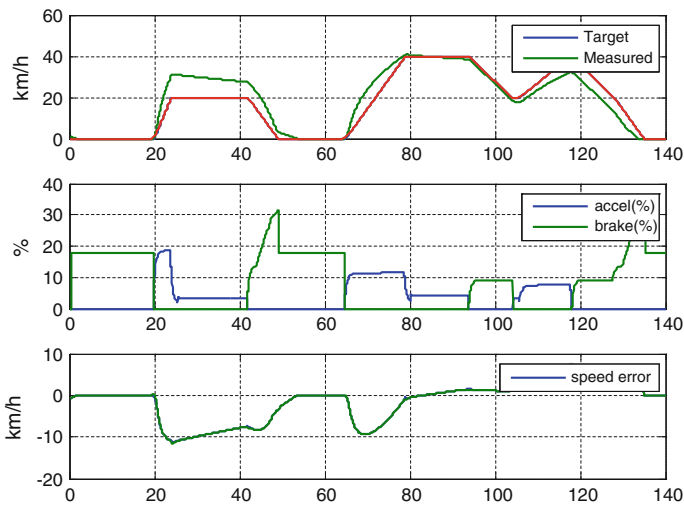


Fig. 15 Driving behaviour after acceleration gain learning

14 Learning for Response Delay

It is not so complicated to compensate vehicle starting delay including driver response delay, because consequence is clear and measurement by driver may be easy. Target speed prediction algorithm for driver operation can be implemented in an electronic—mechanical system controller as shown in Fig. 18.

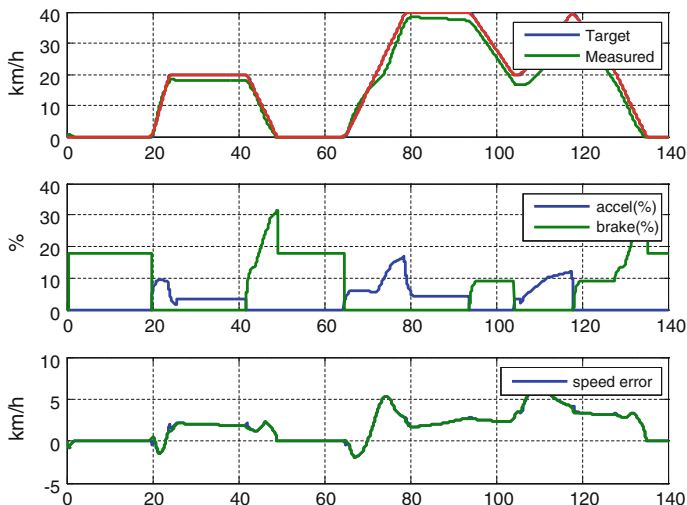


Fig. 16 Driving after speed dependent gain learning

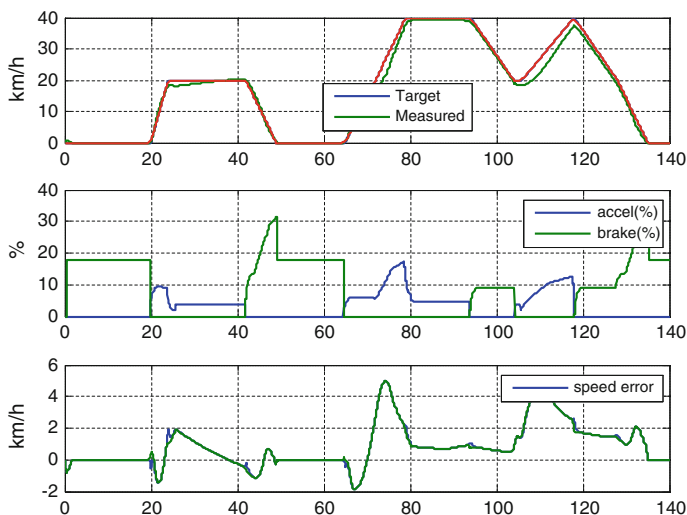


Fig. 17 Driving behaviour after road load gain learning

15 Being Proficient Level Where a Driver Operate Without Thinking on Looking the Target

Driver's behaviour can be evaluated with speed tracking index and stable operation index [14].

Learning process shown in Figs. 14, 15, 16, 17 had no feedback, but there is small feedback compensation available additionally in actual driving. A model

Fig. 18 Operation timing learning

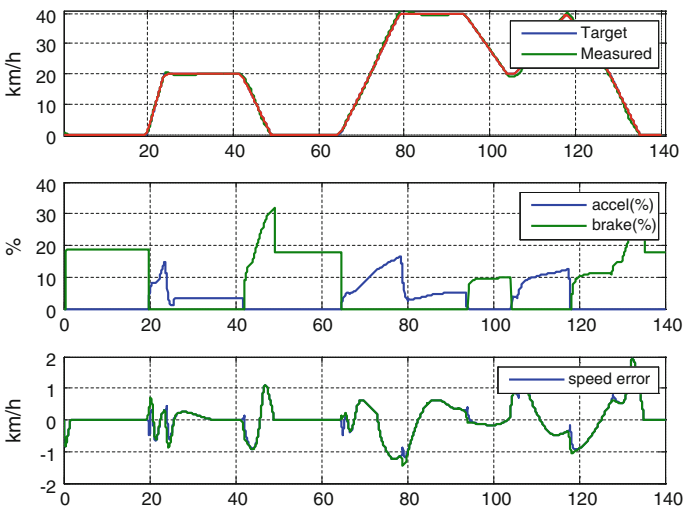
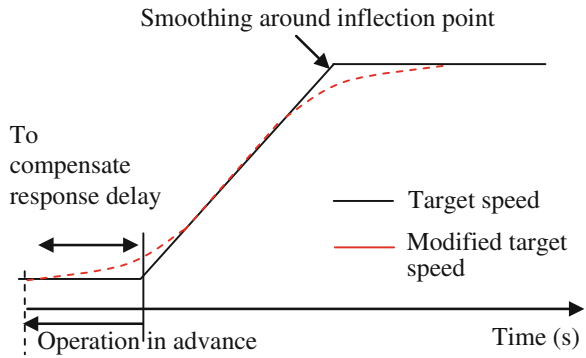


Fig. 19 Expert driving behaviour with the model

expert drove as shown Fig. 19. Beginner’s un-stable operation is well represented with the model as shown in Fig. 20.

16 Summary/Conclusions

A control system which can be realized within ordinal human driver capability for an emission test cycle driving was studied.

Response property of a vehicle from driver operation to vehicle speed was derived based on mathematical models within the frequency range required by speed tracking performance. The response consist of first order delay with dead time in an IC engine, first order delay in torque converter (during start and low

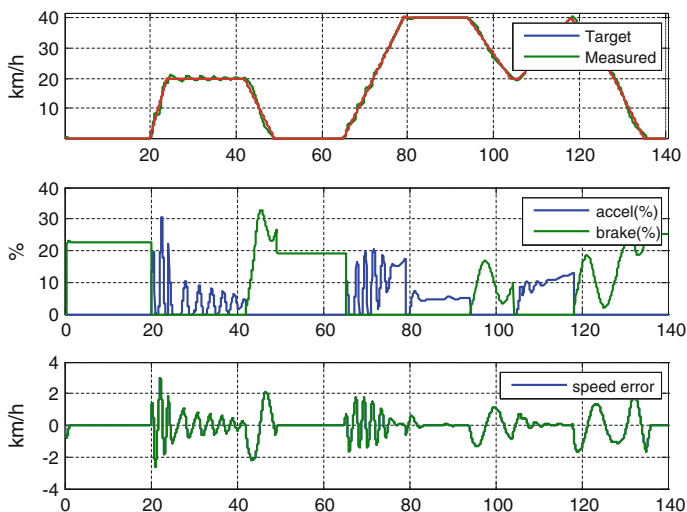


Fig. 20 Beginner's driving behaviour with the model

speed) and non-linearity of speed dependant gear ratio and braking force. The allowed tracking error is ± 2 km/h for the test cycle. When a controller consists of proportional control with a gain K for unit vehicle mass, resulted speed tracking error is $1/K$ for steady state acceleration. That requires the gain K should be greater than 2 at least to keep the error within the allowance.

Driving behaviour difference between a beginner and an expert driver in a test cycle driving was compared. The former's speed tracking performance is not so good despite of frequent accelerator or brake pedal position change, while the latter drives the vehicle within allowed speed error with smoother and stable operation. The beginner depends on speed error feedback largely and an expert mainly operates based on feed forward. Relatively large dead time of 0.5 s approximately exists in speed error feedback through visual information. It is proven that the closed loop driver—vehicle system is closed to the stability limit when feedback gain greater than 2.0 is required. Therefore, Feed forward control becomes the main operation to make the speed tracking stable and smoother operation for a human driver. While, similar result is also shown by above mentioned experiment.

Feed forward rules are not given to a driver from the first time, so that the driver has to find appropriate rules and learn parameters. It is illustrated with simulations that an input sequence for the speed tracking can be obtained with an iterative learning. The learning cannot be applicable to human driver learning, however, rules of operation can be found from the result. Rule of operation and parameters are selected for example acceleration proportional gain and speed dependent gain representing gear ratio. It is shown that those parameters can be adapted by a few times driving with simulation. The beginner's driving behaviour is represented with the proposed model.

References

1. Macadam CC (2003) Understanding and modeling the human driver, vehicle system dynamics. Taylor & Francis, UK
2. Kageyama I (2007) Construction of driver model for analyzing driver behavior, JSAE20075284, JSAE annual congress 2007 Spring
3. Togai K (2010) Powertrain model selection and reduction for real time control algorithm design and verification in rapid controller prototyping environment SAE2010-01-0236
4. Hendrics E (1991) SI engine controls and mean value engine modeling. SAE910258
5. Kotwicki AJ (1982) Dynamic models for torque converter equipped vehicles. SAE820393
6. Danno Y, Togai K (1989) Powertrain control by DBW system: strategy and modeling. SAE 890760, pp 85–98, SP788
7. Togai K, Tamaki H (2010) Human driving behaviour analysis and model representation acquisition of meta-knowledge and expertise acquiring process. AVEC'10
8. Togai K, Tamaki H (2008) Emission test cycle driving agent and expertise in driving behavior. Rev Automot Eng JSAE 29(3):93–97
9. Kageyama I (2005) Study on evaluation of driver's behavior at running on narrow road. Proc JSAE Annu Congr Autumn 2005
10. Lio F, Egami T, Tsuchiya T, Yu X (1996) On general type of digital optimal preview servo system. Appl Math Mech 17(5):423–436
11. Arimoto S, Kawamura S (1984) Bettering operation of robotics. J Rob Syst 1–2:123–140
12. Ito M (2009) Control mechanisms that we learn from the brain. J Soc Automot Eng Jpn 63(5)
13. Carlo Cacciabue P (eds) (2007) Modelling driver behaviour in automotive environments: critical issues in driver interactions with intelligent transport systems. Springer, New York
14. Togak K, Tamaki H (2011) Human driving behavior analysis and model representation with expertise acquiring process for controller rapid prototyping. SAE2011-01-0051

Part XIII
Virtual Design, Testing and Validation

The Suspension Optimization of FSAE Racing Car Based on Virtual Prototyping Technology

Jun Ni, Sizhong Chen and Zhicheng Wu

Abstract Research and/or Engineering Questions/Objective: One important design goal of racing car suspension is to keep the tire perpendicular to the ground which needs an accurate kinematic design of suspension. This paper details the simulation method of FSAE racing car based on MSC.ADAMS and VI-Motorsport, then the optimization of suspension kinematic characteristic could be conducted. Meanwhile, the paper will show the effect of suspension kinematic characteristic on lap time. Then the problem that the developing period of FSAE racing car is not long enough to conduct sample prototype test can be solved by the performance prediction and optimization by virtual prototyping technology. *Methodology:* The virtual prototyping model of BIT FSAE racing car and a certain race track were built by multi-body dynamics simulation software MSC.ADAMS and professional racing car simulation software VI-Motorsport. During the modelling process, the non-linear mechanical characteristic of tires was taken into consideration by the tire data provided by FSAE TTC, as well as the aerodynamic characteristics. The correctness of the model was verified by the “g-g” diagram collected by data logger in competition, then the further analysis and optimization could be conducted based on these. The comparison of lap time between the original race car and the race car after optimization was also conducted by simulation. *Results:* The comparison of lap time simulation results shows that the grip of tire during turn is increased after optimization of suspension, and the lap time is reduced. *Limitations of this study:* The simulation is based on multi-body dynamics simulation which assumes the chassis and suspension as rigid body. It brings some errors because the compliance characteristic of chassis and suspension

F2012-E13-002

J. Ni (✉) · S. Chen · Z. Wu
Beijing Institute of Technology, Beijing, People's Republic of China
e-mail: wjyyjsbb@163.com

is ignored. What does the paper offer that is new in the field in comparison to other works of the author: In previous technical papers in FSAE racing car field, there is no precise comparison between simulation results and actual data. But in this paper, the correctness of the model was verified by the comparison between simulation results and actual data collected in competition. And in this paper, the “g-g” diagram of FSAE racing car was first presented and discussed which is vital important of racing car performance. *Conclusion:* The simulation of FSAE racing car lap time based on MSC.ADAMS and VI-Motorsport has a high accuracy which could provide a possibility of performance prediction. It can shorten the developing period of FSAE racing car and improve the performance of FSAE racing car. Furthermore, the designers can adjust the kinematic design of suspension to meet different requirements in different race tracks by the proposed method.

Keywords FSAE racing car · Virtual prototyping technology · Race track · “g-g” diagram · Suspension optimization

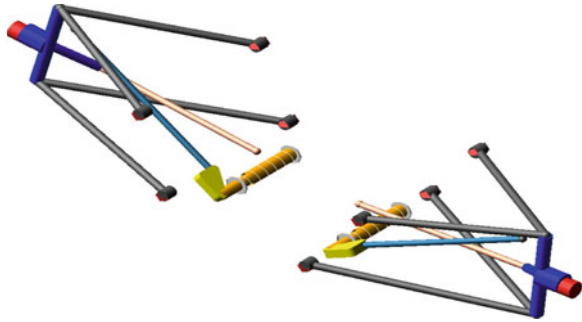
1 Introduction

The student competition Formula SAE(FSAE) which is sponsored by the Society of Automotive Engineers(SAE), motivates students to design, build and compete with a small formula style race car. The competition is separated into static and dynamic events. The static events include the cost analysis, sales presentation, and engineering design. The dynamic portions of the competition are the 15.25 m diameter skid-pad, 91.44 m acceleration event, 0.8 km autocross, 44 km endurance race and fuel economy[1].

The suspension system is one of the most important systems when designing a FSAE car. All accelerations, either lateral or longitudinal, must be put to the ground through the tires, which are held in contact with the ground by the suspension. In other words, the most important design goal of suspension system is that to keep the largest contact tire patch at all the times, especially in a turn. When a race car is moving in a turn, the camber angle will turn positive because of the chassis roll which can be determined from roll stiffness. So a proper negative camber gain is needed to compensate that to keep the tire perpendicular to the ground, so that the tire could provide enough grip. This paper aims at the kinematic characteristic of “proper camber gain”.

Camber gain is usually obtained by having different length upper and lower control arms. And the camber gain is truly a non-linear function of link geometry. For a race car, maybe there is no “optimum design”, but there is a “most proper” design for particular race track, that’s because a race car with high performance on a certain race track maybe won’t behave pretty well on another race track. And you can’t modify your design after the manufacture and the assembly is done. So, the performance prediction and optimization based on virtual prototyping

Fig. 1 Model of front suspension



technology is a good choice. This paper assumes a basic knowledge of vehicle and suspension design and it is based on the previous work of the author.

2 Modelling of Bit FSAE Race Car

The virtual prototyping model of BIT FSAE race car is built by multi-body dynamics simulation software MSC.ADAMS. Due to space limitation, the modelling process won't be introduced in detail which could be seen in literature [2, 3].

2.1 Modelling of Suspension and Steer Systems

The front and rear suspensions are both double wish-bone suspension which is composed of upper and lower control arms, upright, hub, push rod, shock absorber, spring and bellcrank. The structure parameters are obtained by CAD software. In total, the front suspension system includes 3 cylindrical joints, 4 revolute joints, 8 spherical joints, 9 fixed joints, 8 constant velocity joints and one in-plane joint. The rear suspension includes 3 cylindrical joints, 4 revolute joints, 8 spherical joints, 2 translational joints, 11 fixed joints, 4 constant velocity joints and one in-plane joint.

Structure parameters of pinion-and-rack steering system are obtained by three-dimension model as well. The variables such as max displacement of rack, max torque of steering wheel are set up according to design value (Figs. 1, 2 and 3).

2.2 Modelling of Powertrain System

In MSC.ADAMS, powertrain system represents transmission, clutch, engine and differential. Several spline elements represent engine's steady-state torque versus engine speed which is obtained by bench test. Transmission ratio is set up according to design value.

Fig. 2 Model of rear suspension

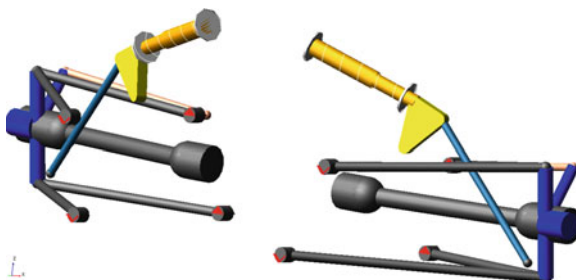
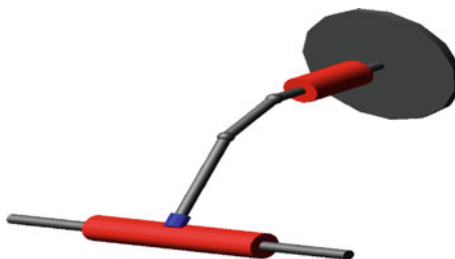


Fig. 3 Model of steer system



2.3 Modelling of Tire

MSC.ADAMS provides several tire models including UA, Fiala and so on. In this paper, MF_5.2 is selected which fits experiment data by trigonometric function. It has high precision to formulate tire properties, such as the longitudinal force, lateral force, overturning torque, as well as the combined effect condition. The magic formula is expressed as follow[4]:

$$Y(x) = D\sin[\text{Carctan}\{ Bx - E(Bx - \arctan(Bx))\}] \tag{1}$$

In Eq. 1: x is the slip ratio or lateral slip angle; $Y(x)$ is the adhesive coefficient or tire force or torque; B is the stiffness factor; C is the shape factor; D is the peak factor; E is the curvature factor.

According to the experiment data of Hoosier $18 \times 6-10$ tire, the property file could be conveniently built by MF_5.2. Raw data of longitudinal force and lateral force provided by FSAE TTC are shown in Figs. 4 and 5.

2.4 Modelling of Full Vehicle and Race Track

Some main parameters are obtained by three-dimension model, such as mass, center of mass and moment of inertia. The full vehicle model has 73 moving parts and 47 DOF. Main parameters of full vehicle are listed in Table 1.

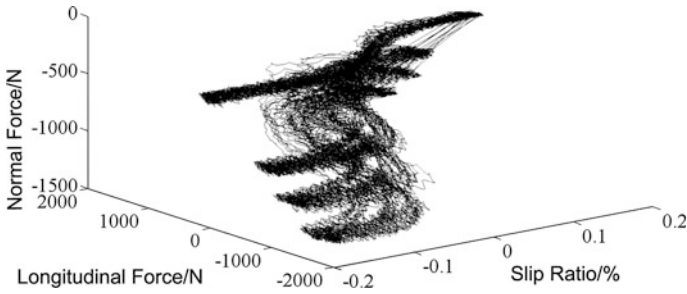


Fig. 4 Raw data of longitudinal force provided by FSAE TTC

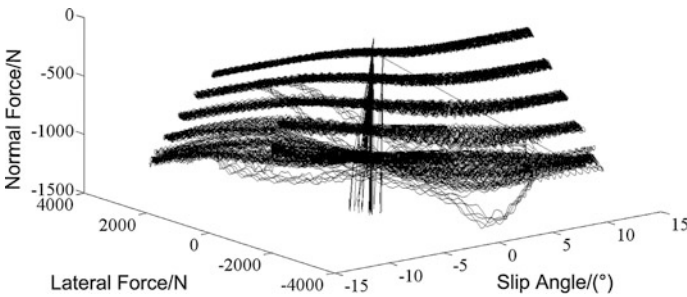


Fig. 5 Raw data of lateral force provided by FSAE TTC

Table 1 Main parameters of full vehicle

Parameter	Value
Mass/kg	218.1
Wheel base/mm	1,550
Front track width/mm	1,210
Rear track width/mm	1,230
Inertia around X axis/(kg/mm ²)	5.17×10^7
Inertia around Y axis/(kg/mm ²)	2.40×10^8
Inertia around Z axis/(kg/mm ²)	2.41×10^8

The model of race track is shown in Fig. 7 which is built by VI-Motorsport with 2400 m long. For convenience, several points marked A, B, C, D and E is illustrated in Figs. 6 and 7.

3 Simulation Result Analysis

According to race car theory, a race car won't keep a constant velocity in the race, in other words, there is always acceleration or deceleration [5]. A race car should brake into a turn and accelerate out of a turn, accompany with lateral acceleration.

Fig. 6 Model of full vehicle

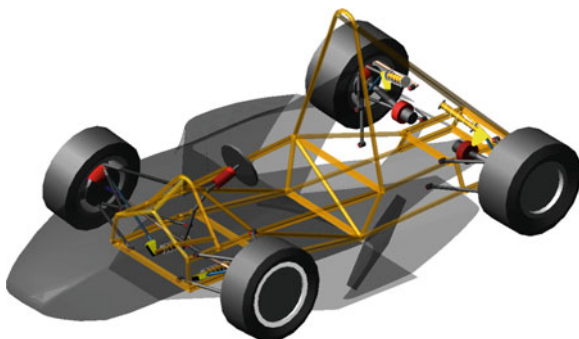
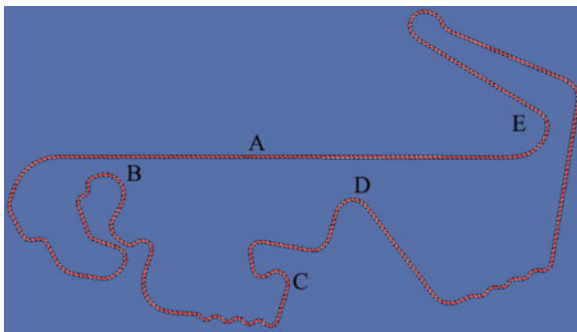


Fig. 7 Model of race track built by VI-motorsport



One should increase speed at a maximum acceleration out of each turn and continue to the point where, with maximum deceleration the speed can just be brought down to the maximum speed for the next corner. Figure 8 shows the speed simulation result. The race car started at point A, and accelerated in straightline, before braking into the first turn its speed increased as 130 km/h. Then it passed through point B, C and D, began to accelerate after leaving “turn E” and the speed peaks 150 km/h when back to point A. And the lap time is 134.06 s.

The “g-g” diagram is an important concept in race car field which is obtained by recording the longitudinal and lateral acceleration [5]. These data points indicate the levels and combinations of longitudinal and lateral acceleration that driver used in negotiating the circuit, and it will show the acceleration limits of the race car which indicates the “performance capability”. The “g-g” diagram obtained by the simulation is shown in Fig. 9, and the “g-g” diagram obtained by actual data from 2011 China FSAE competition is shown in Fig. 10.

When the race car brakes into a turn, there would be a combination of negative longitudinal acceleration and lateral acceleration(negative for left-hand turn and positive for right-hand turn). When the race car accelerates out of a turn, there would be a combination of positive longitudinal acceleration and lateral acceleration. So the “g-g” diagram is presented in 4 quadrants. According to Figs. 9 and 10, it can be concluded that there is a great consistency between the virtual race car and actual race car. They have almost the same performance capability

Fig. 8 Speed simulation result

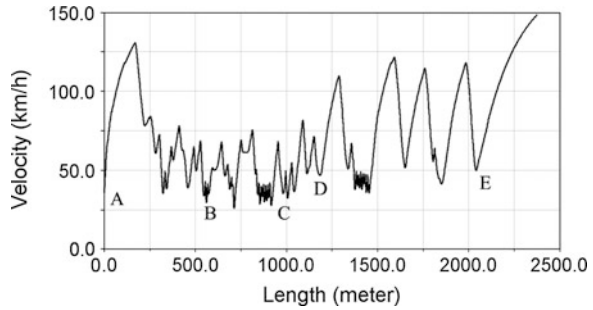


Fig. 9 “g-g” diagram obtained by simulation

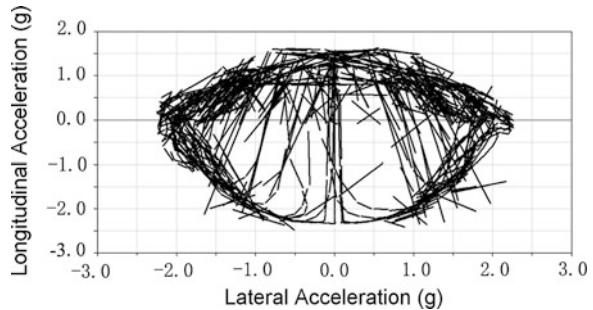
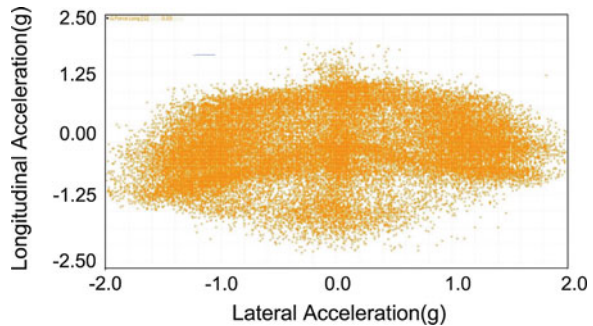


Fig. 10 Actual “g-g” diagram obtained by data logger

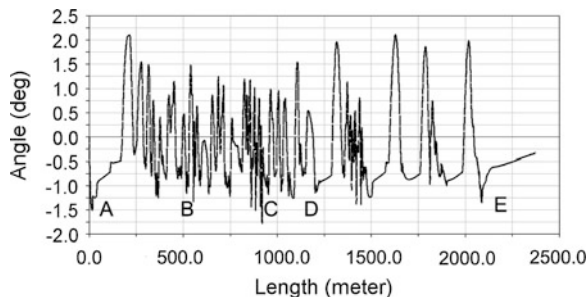


which the “g-g” diagrams indicate. In other words, the virtual model of FSAE race car has a great accuracy which could be used in performance prediction and optimization.

The inclination angle of tire plays a very important role in turning performance of the race car, the lateral force provided by the tire increases with the contact patch increases. In other words, the inclination angle of tire should be as little as possible in the turn which can be adjusted by design of “camber gain”. In fact, the outside tire is more important than the inside one due to lateral weight transfer.

When body rolls in a turn, the outside tire will have a “positive camber” tendency, it is called “roll camber”. To keep the tire perpendicular to the ground, a kind of so-called “short and long arms” double wishbone suspension is often used

Fig. 11 Inclination angle during lap race of front left tire



in race car design which could provide a negative “camber gain” to compensate the “roll camber”. The amount of camber compensation or gain for vertical wheel movement is determined by the control arm configuration. With different length control arms, the ball joints move through different arcs relative to the chassis, the angle of the control arms relative of each other also influences the amount of camber gain. Because camber gain is a non-linear function of link geometry, the virtual prototyping technology usually is used to analyzing it. Figure 11 shows the inclination angle of front left tire during the lap race, it can be seen that during the turn B, C, D and E the inclination angle of front left tire peaks about -1.5° .

4 Optimization and Comparison

As mentioned above, we hope the inclination angles in turn could be as little as possible so that the tire contact patch can be largest. According to Fig. 11, we know that if we can reduce the inclination angle in turn, then the higher lateral force can be provided by the tire, so the race car can get higher lateral acceleration and less lap time. The optimization design process is omitted because the paper doesn't aim at it. After the adjustment of link geometry, the optimization is done. Then the camber gain curves of original race car and race car after optimization are shown in Fig. 12.

According to the analysis of simulation result, it is found that the roll camber is not obvious. That is because the race car has a low mass centre location and equipped with anti-roll bar. According to Fig. 12, the original camber gain of suspension is about 2 to -2° which is beyond the range of roll camber, so the inclination angle of outside tire tends to be negative which decreases the grip of tire [6]. Furthermore, the maximum lateral force will be reduced and the lap time will be prolonged, so the amount of “negative camber gain” should be decreased. Based on above, the optimization of suspension kinematic characteristic is conducted, the location of suspension hard point is adjusted and the camber gain of the suspension after optimization is shown. The details of suspension kinematic design and link geometry design can be seen in [7, 8].

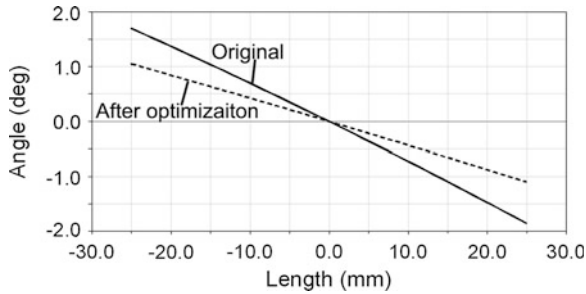


Fig. 12 Camber gain comparison

Table 2 Comparison between original race car and the race car after optimization

Turn	Original race car		After optimization	
	Inclination angle/(°)	Lateral force/N	Inclination angle/(°)	Lateral force/N
B	-1.25	1,000	-0.99	1,038
C	-1.98	1,261	-1.34	1,317
D	-1.21	829	-0.75	871
E	-1.27	820	-0.97	854

For comparison, the same simulation of race car after optimization was conducted. The comparison of inclination angle during circuit was presented, the inclination angle in turn B, C, D and E is becomes smaller and higher lateral force is produced. They are shown in Table 2 because the differences of curves are difficult to observe.

According to Table 2, the optimization has achieved the goal which reduces the inclination angle and produces higher lateral force during turn B, C, D and E. With higher lateral acceleration in turn B, C, D and E, the race car can finish the lap in a higher speed and less lap time. The speed comparison in turn B, C, D and E is shown below.

According to Fig. 13, we can see that the speed has increased in turn B, C, D and E. The conclusion from Table 1 is verified by Fig. 13 from other point of view. The lap time after optimization is 133.46 s, 0.6 s less than the race car before optimization. For a race car competition, 0.6 s is really a big improvement.

5 Conclusion

This paper shows the process of suspension optimization by MSC.ADAMS and VI-Motorsport. The correctness of virtual prototyping model was verified by “g-g” diagram. The comparison between the simulation result and actual data shows the great accuracy of virtual prototyping model. It is convenience to do the performance prediction and optimization by MSC.ADAMS and VI- Motorsport.

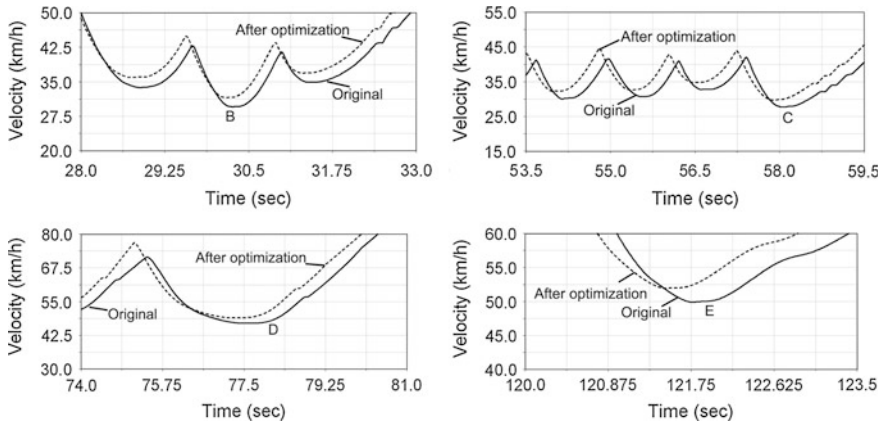


Fig. 13 Speed comparison in turn B, C, D and E

Moreover, the paper shows the effect of suspension camber gain on lap time. With optimized camber gain, the lap time could be reduced by about 0.6 s on the race track proposed by the author. And the camber gain should be adjusted to compete in different race track, the concept of proper design aims at particular race track is very important to race car.

Acknowledgments The authors gratefully acknowledge the FSAE TTC and the Calspan Tire Research Facility for providing FSAE teams with tire data, despite the cost. A proper suspension design is impossible without tire data. Especially acknowledge Douglas. Milliken, who is also the author of < Race Car Vehicle Dynamics >, he has helped a lot in registering FSAE TTC.

The authors also thank to VI-Motorsprot. During the design process of BIT FSAE race car, VI-Motorsport has provided lots of help as a professional race car simulation software. And also, VI-grade is a sponsor of BIT FSAE race car team, which gives us lots of help in research of race car dynamics.

References

1. Gaffney EF, Salinas AR (1997) Introduction to formula SAE suspension and frame design. SAE, 971584
2. Ni J, Xu B (2011) Modelling and handling stability simulation of a FSAE racing car based on ADAMS. *J Eng Des* (in Chinese) 18(5):354–358
3. Jun N, Chen S, Da Feng et al (2012) Research on crosswind stability of FSAE racing car with rear wing at different attack angles. *Appl Mech Mater* 152:737–742
4. Pacejka HB (2002) Tyre and vehicle dynamics. Butterworth-Heinemann, Waltham
5. Milliken WF, Milliken DL (1995) Race car vehicle dynamics. SAE, Warrendale
6. de Paula Eduardo G (2005) Formula SAE suspension design. SAE, 2005-01-3994
7. Robertson D, George J (2010) Delagrammatikas. The Suspension system of the 2009 Cooper Union FSAE vehicle: a comprehensive design review. SAE, 2010-01-0311
8. Jawad BA, Baumann J (2002) Design of formula SAE suspension. SAE, 2002-01-3310

The Study of the Impact of Aluminum Formability Parameters on its Stamping Formability

Jian Zhang, Mingtu Ma and Hongzhou Lu

Abstract To find parameters to estimate stamping formability of aluminum alloy sheet in autobody, simulate the cylinder components stamping process by LS-DYNA software based on dynamic explicit method; Study the impact of the material parameters (Yield stress RPS, hardening exponent n and anisotropy parameter r) and the process parameters (the blank-holding force and friction coefficient) on the stamping formability of the aluminum alloy sheet; Analyze the corresponding relationship between the research targets (material and process parameters) and the drawing properties through the Regression Analysis. The results indicate that the n values of the material parameters and all of the process parameters in this paper are remarkably correlated with the drawing properties of aluminum alloy, while the r values of the material parameters have little correlation with it.

Keywords Aluminum alloy sheet · The material parameters · The process parameters · The drawing properties · The regression analysis

1 Introduction

Energy saving, environmental protection and safety are the important topics in today's automobile industry and the lightweight is an important way to achieve the three goals. Research shows that reducing vehicle weight for every 10 %, fuel

F2012-E13-003

J. Zhang (✉) · M. Ma · H. Lu
China Automobile Engineering Research Institute Co., Ltd, Mainland, China
e-mail: gean_zhang@163.com

consumption can be reduced by 6–8 % [1]. The autobody weight accounts for 40 % of the whole automobile, therefore reducing the body weight plays an important role in the vehicle lightweight.

The automotive lightweight can be achieved in mainly three ways: the first is to optimize the automobile structure, the second is to use high-strength lightweight materials and the third is to use advanced processing technology. Optimizing the automobile structure has made great progress through continuous research and development. With the development of science and technology and the emergency of the new materials and new process, high-strength lightweight materials explores a great space for the vehicle lightweight [2]. Among all the high-strength lightweight materials, Aluminum sheet, with the merit of low density, high strength and corrosion resistance, has become an important material in automotive lightweight technology.

As some characteristics of the aluminum alloy sheet are different from that of the steel sheet, the experience in the steel stamping process can not be borrowed to aluminum alloy stamping process, which makes it necessary to study the forming method and the relevant influencing factors according to the characteristics of the aluminum alloy sheet [3–7]. Kurosaki thought that the total elongation and the limited tensile ratio are related [8]; Hayashi pointed out that between the n value and r value, n value is more relevant to the limited tensile depth ratio of the aluminum alloy sheet [9]. The formability parameters of 5,000 and 6,000 series aluminum alloy sheet based on the uniaxial tension property from Alcoa [10] show that when automotive aluminum alloy sheet is compared to steel materials in the same intensity, the uniform elongation and r value of the former are lower than the latter, but the n value and FLD value of the former are higher. The researches above studied the correspondence between material parameters and drawability but few aluminum species were involved and little was reported on material and process parameters. Therefore, further study on the influence of material parameters and process parameters on aluminum alloy sheet formability is rather significant to autobody panel production.

In this paper, finite element analysis is used on cylinder components stamping process simulation and the influence of certain material parameters and process parameters on aluminum alloy sheet formability is analyzed. On this basis, the degree of the influence on the aluminum sheets drawability from these data is analyzed, which provides a reliable evidence for a reasonable choice of materials, process conditions and formability prediction in stamping process.

2 The Selection of Material Parameters and Process Parameters

Material parameters is an important indicator that would influence the component forming, which includes yield strength, tensile strength, uniform elongation, after

Table 1 The material parameters of aluminum alloy obtained by uniaxial tensile tests

Mat.	State	Thickness (mm)	R _{PS} /MPa	σ _b /MPa	\bar{n}	\bar{r}	EL/ %	FLD ₀ / %
6,016		0.9	142.1	239.0	0.21	0.59	26.9	23.7
6,111	T ₄ PD	0.9	146.0	290.0	0.23	0.65	25.0	22.8
6,022	T ₄ PD	0.9	122.0	238.0	0.25	0.66	30.0	23.2
5,182	O	0.9	123.0	276.0	0.32	0.82	25.6	22.2
5,023	O	0.9	124.0	280.0	0.31	0.85	32.0	26.5

breakage percent elongation, hardness, n value, r value and so on. The research on the formability of sheet metal both at home and abroad in recent decades shows that the yield strength, n value and r value were the most important parameters which would influence the sheet stamping [11], [12]. Therefore, the selection of yield strength, n value and r value as object of study is in line with the actual situation of the product.

Process parameters, including stamping speed, friction coefficient, blank holder force, and so on, also have important influence on sheet metal formability. Generally speaking, the smaller the stamping speed, the better the deformation of the uniform distribution. The small stamping speed would help to improve the material forming, but its influence is limited. Friction and lubrication are commonly used to control sheet flow in stamping process, but the current research on friction and lubrication is mainly focused on the friction model and the test of friction coefficient. Blank holder force (BHF) is also an important factor affecting the sheet flow and the best values of blank holder force should also ensure that sheets do not produce cracking and wrinkling. Therefore, selecting the friction coefficient and BHF as the object of the research on process parameters could reflect the major problems in stamping process.

3 The Determination of Materials and Processes Parameters

Aluminum alloy material used in autobody panels is mainly of 5XXX and 6XXX series, the former is mainly used for processing inner autobody panel and the latter for the outside autobody panel. The test materials in the research are the aluminum alloy sheets of a domestic factory; the material parameters are obtained by uniaxial tensile tests (uniaxial tensile test carried out according to standard GB/T228-2002). Table 1 lists the 5,000 and 6,000 series aluminum alloy material parameters, where n value and r value is the average of three directions.

When the size of the components used in cylinder component stamping is defined, the main factors affecting the limit drawing modulus include the material parameters, BHF and friction coefficient. Material parameters mainly include the yield strength, n value and r value and these values are selected according to the material parameters in Table 1. The BHF value is selected through trial calculation in the premise that blank does not produce wrinkles. The trial result shows that

Table 2 Factors and levels of deep drawing orthogonal analysis

Levels	Factors				
	A BHF (MPa)	B Friction coefficient	C Yield stress (MPa)	D r	E n
1	3.0	0.12	122.0	0.59	0.21
2	3.5	0.15	128.0	0.655	0.235
3	4.0	0.18	134.0	0.72	0.26
4	4.5	0.21	140.0	0.785	0.285
5	5.0	0.24	146.0	0.85	0.31

Note The friction coefficient of the blank is in accordance with that of punch, die and blank holder

when the BHF is greater than $3 \text{ MPa} \times \text{unit area}$, there would be no wrinkles. Five different friction coefficients are selected according to different lubrication conditions. The five-factor five-level orthogonal test is shown in Table 2. In order to better reflect the various factors in Table 2 the impact of the evaluation will be reasonable and a gradient of change factor for selection. In order to better reflect the impact of various factors on evaluating indicators, the selection of the various factors is reasonable and gradient.

4 The Establishment of the Simulation Model and the Comparison of the Test

As cylinder components are the simplest but the most typical pieces, the basic principles of drawing could be well understood through the analysis of cylindrical deep drawing process. In this paper, the test device in deep drawing and stretch forming of automotive aluminum alloy sheet by Jain et al. [13] is used to establish a cylinder drawing model.

The cracking site of the drawing components is usually at the punch corner. Given the symmetry of the cylinder components and to save simulation time, only 1/4 of the model is taken to analyze. Figure 1 is the finite element model of cylinder component drawing; Fig. 2 is the 2D scheme of the blank and mold in testing and simulation:

In order to clarify the relationship between aluminum sheet thinning and cracking in simulation, FLD curve is adopted to reversely infer the cracking thinning. The specific steps of the reverse inference are: first to use the material parameters in Table 1 to simulate the cylinder components drawing, then to determine the cracking time through the FLD curve, the maximum thinning of the sheet at this time is the cracking thinning. Figure 3 is the forming limit diagram of 6,016 aluminum alloy sheet in cracking; Fig. 4 is the thinning contour of 6,016 aluminum alloy sheet in cracking.

The same method can be used to clarify the relationship between aluminum alloy sheet cracking and thinning of the other aluminum alloys in Table 1 in

Fig. 1 The finite element model of cylinder component drawing

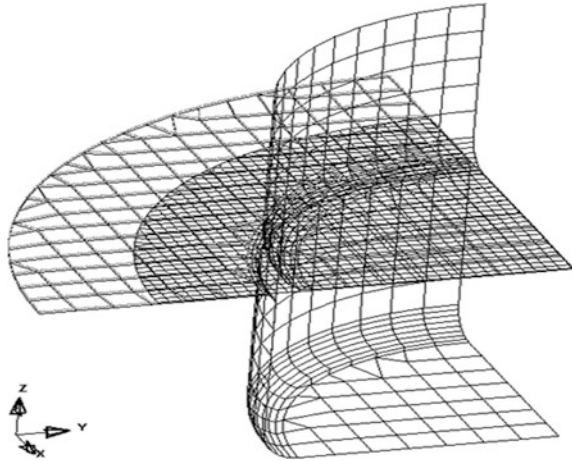
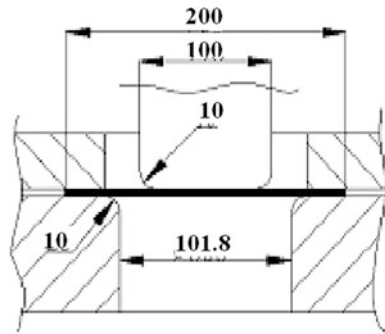


Fig. 2 The 2D scheme of the blank and mold



simulation. Table 3 is the list of relationship between aluminum alloy sheet cracking and thinning in Table 1.

As can be seen from the table, in the set test of cylinder components drawing in this paper, although the aluminum material properties are different, the cracking thinning is concentrated in a rather small range of 19.4–20.4 %. Since the changing range of the set factors in Table 2 is all in the range of the materials listed above, therefore, in simulation, when the thinning is considered greater than 19.9 %, the cracking appears and the punch stroke is the limit punch stroke(LPS).

In the test, firstly use 6,016 aluminum alloy to study the relationship between the blank holder force and stroke distance. Drawing properties indicators can be represented by LPS in the cylinder drawing test. LPS is defined as punch stroke distance during the cylinder component drawing when the cracking appears. 5 tests are carried out on the working condition of each BHF to identify the specimens with similar cracking positions and get their average LPS.

In the simulation, use LS-DYNA software to simulate. The yield criterion of the material is that of Barlat-Lian, the sheet thickness is $t_0 = 0.9 \text{ mm}$ and the gap of mould is $S = 1.1 \times t_0$. The material parameters are the 6,016 aluminum alloy

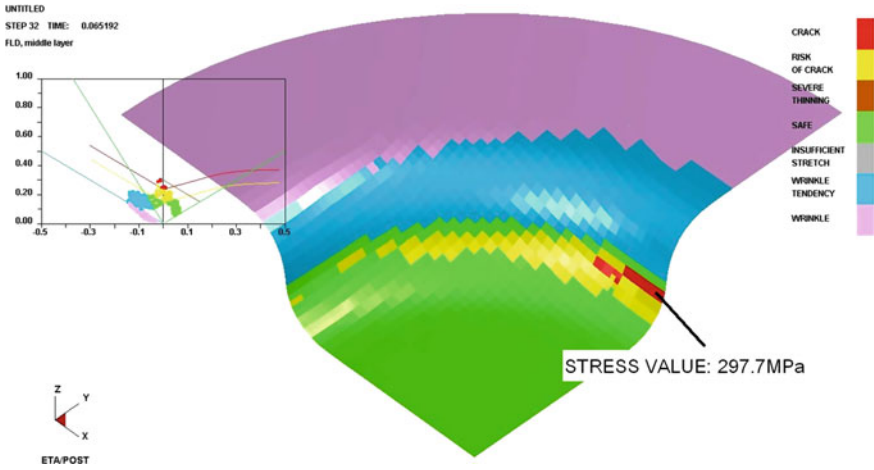


Fig. 3 The FLD of 6016 aluminum alloy sheet

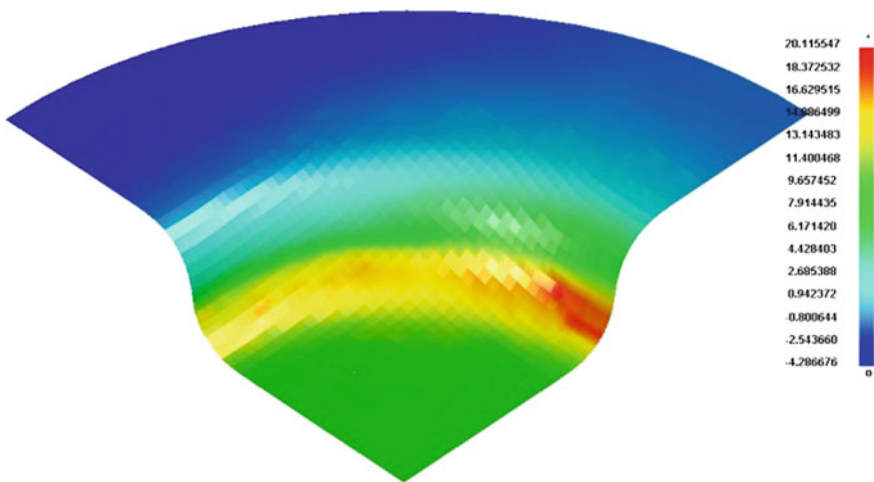


Fig. 4 The thinning contour of 6016 aluminum alloy sheet

Table 3 The list of relationship between aluminum alloy sheet cracking and thinning

Mat.	Thickness (mm)	FLD ₀ / %	Cracking thinning (%)
6,016	0.9	23.7	20.1
6,111	0.9	22.8	19.5
6,022	0.9	23.2	19.7
5,182	0.9	22.2	19.4
5,023	0.9	26.5	20.4

Table 4 The comparison between the result of test and simulation about the impact on the stamping formability from BHF

BHF (MPa)	Average value in test (mm)	Simulation value (mm)	Relative error (%)
3.0	30.0	28.865	3.8
3.5	25.6	26.352	2.9
4.0	24.0	24.497	2.1
4.5	23.2	22.782	1.8
5.0	22.0	21.294	3.2

material parameters (in Table 1). The friction coefficient is determined as 0.125 through trial and error.

The comparison between the result of test and simulation is listed in Table 4.

As can be seen from the table, relative errors are less than 5 % and there exists good consistency between the simulation result and the test result. This demonstrates that the boundary conditions of the simulation in this paper meets the project accuracy requirement and can be used for the simulation of other material and process parameters under changes.

5 The Simulation Evaluation on Formability

In order to find the most remarkable influencing factors on forming properties from the material and process parameters above, mathematical statistical method is used to conduct unitary linear regression analysis on the samples obtained [14]. Use formula (1) to calculate the correlation coefficient r_c of each parameter. And if $|r_c| \geq r_{0.01}$ (i.e. $|r_c| \geq 0.99$), the linear relationship is the most remarkable; if $r_{0.01} > |r_c| \geq r_{0.05}$, the linear relationship is remarkable; if $|r_c| < r_{0.05}$, the linear relationship is not remarkable, i.e. Irrelevant.

$$r_c = \frac{\sum_i (x_i - \bar{x})(y_i - \bar{y})}{\sqrt{\sum_i (x_i - \bar{x})^2} \sqrt{\sum_i (y_i - \bar{y})^2}} \tag{1}$$

In the formula above, x_i is the factor parameter, \bar{x} is the mean of all factors; y_i is the limit punch stroke, \bar{y} is the mean of all the limit punch stroke.

Use the above simulation model to conduct stamping simulation. In each simulation, only one of the five parameters, including R_{PS} , r , n , friction coefficient and blank holder force, is changed; variation is based on the data in Table 2. After each simulation, determine the cracking time from the thinning contour and measure the displacement of the punch in Z direction, i.e. LPS. Figures 5, 6, 7, 8, 9 present the result of the relationship between all the factors and LPS.

In the five figures above, the abscissa is the various material and process parameters, the vertical axis is the LPS. To accurately describe the correlation degree of the linear relationship between material and process parameters and

Fig. 5 The relationship between R_{PS} and LPS

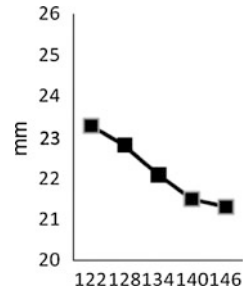


Fig. 6 The relationship between n value and LPS

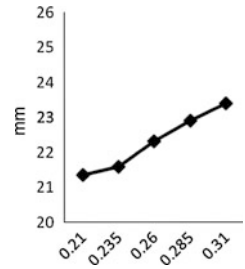


Fig. 7 The relationship between r value and LPS

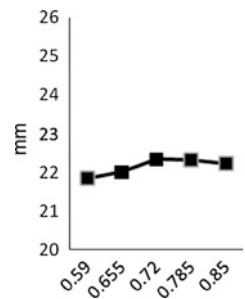
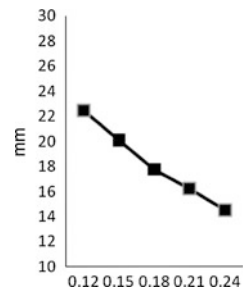


Fig. 8 The relationship between friction coefficient and LPS



LPS, use Eq. (1) to calculate the $|r_c|$ value of all factors and get the significance level. The results are presented in Table 5.

As can be seen from the series of results in Table 5, the correlation between the yield strength, n value, BHF and friction coefficient and LPS is remarkable, while

Fig. 9 The relationship between BHF and LPS

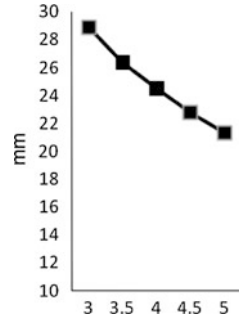


Table 5 Correlation coefficient results list

Factors	$ r_c $	Correlation degree
BHF	0.995	Most remarkable
Friction coefficient	0.996	Most remarkable
n	0.992	Most remarkable
r	0.785	Not remarkable
R_{PS}	0.986	Remarkable

the correlation between r value and LPS is not remarkable. In addition, as the yield strength, the blank holder force and friction coefficient increases, the limit punch stroke will decrease; as n value increases, the limit punch stroke will increase; there is no clear single increasing or decreasing trend between r value and LPS.

In summary, n value can be used to evaluate the drawability of aluminum alloy sheet from the perspective of materials but r value can be hardly used to evaluate it. Meanwhile, the BHF and friction coefficient can directly reflect the drawability of the aluminum alloy sheets.

6 Conclusion

This paper has conducted research on the formability of cylinder component of the commonly used 5 and 6 Series aluminum alloy sheet on autobody panels and evaluated the impact of series of material and process parameters on the drawability of cylinder components. The following conclusion can be drawn:

1. Within a certain range of materials, by simulation, the cracking thinning of aluminum alloy sheet can be effectively achieved through the reverse inference from the given FLD curve, which thereby determines the LPS.
2. Series of reliable sample data can be achieved conveniently through the test-based simulation on the cylinder components of aluminum alloy sheets.
3. Unitary linear regression analysis has been adopted in this paper to ensure the most remarkable correlation between the BHF and friction coefficient and

formability, their correlation coefficient are greater than that of material parameters. Therefore, in actual production, when material parameters meet the limited value in a certain range, adjustment to the lubrication and BHF would be a direct and effective way to improve the formability.

4. Unitary linear regression analysis has been adopted in this paper to study the indicators that influence the formability of aluminum alloy sheet. The n value of material parameters is the most effective factor that could be directly used to evaluate the drawing formability of aluminum alloy sheet; while the yield strength, secondary to n value, could also be used to evaluate, but the r value could hardly be used to evaluate. All these study results could provide a reliable foundation for the control, choice and prediction of formability of the aluminum alloy sheet in automotive sheet stamping.

References

1. Zhu P, Zhang Y, Ge L (2005) Research on lightweight of auto-body material based on crashworthiness simulation. *Chin J Mech Eng* 41(9):207–211
2. Jing-an L (2005) Make great efforts to develop aluminum parts industry and promote the modernization progress of automobile industry. *Alum Fab* 162(3):8–12
3. Xue-chun L, Yu-ying Y, Jun B, Shun-ping L (2000) Relationship between elastic modulus and plastic deformation. *J Harbin Inst Technol* 32(5):54–56
4. Barlat F, Berm JC (2003) Plane stress yield function for aluminum alloy sheets. *Int J Plast* 19(9):1297–1339
5. Yang YY, YU ZQ (2003) A new ductile fracture criterion and its application to the prediction of forming limit in deep drawing. *J Mater Sci Technol* 19:217–219
6. Ming-tu M, Xiang-yu B, Jiang-hai Y, Hong-zhou. L (2010) Research progress of property and its application of aluminum alloy auto sheet. *Mater Mech Eng* 32(6):1–32
7. Zhuo-chao H, Yan-dong L, De-fen Z et al (2004) Effect of lubrication on evolution of through thickness texture in cold rolled 3104 aluminum alloy sheets. *Chin J Nonferrous Metals* 14(3):410–417
8. Kurosaki Y (1980) Some consideration on formability parameters in deep-drawing and stretch-forming. *J Jpn Soc Technol Plast* 21:189–196
9. Hayashi H, Nakagawa T (1994) Recent trends in sheet metals and their formability in manufacturing automotive panels. *J Mater Process Technol* 46:455–487
10. ALCOA (2006) Material Property. Beijing
11. Xiao-gang Q (2004) The influence of friction coefficient and material parameters on the bulging forming. *Metal Form Technol* 22(3):51–54
12. Shuo-ben L (2002) The theory and new technology of stamping process. Science Press, Beijing
13. Jain M, Allin J, Bull MJ (1998) Deep drawing characteristics of automotive aluminum alloys. *Mater Sci Eng A* 256:69–82
14. Kai-tai F, Hui Q (1988) Applied regression analysis. Science Press, Beijing

Calculation of Shrinkage Rate for Injection Molding Based on Moldflow

Fangcheng Xiao, Lei Chen and Xiao Wang

Abstract During the process of injection molding, shrinkage rate varies on plastic type, product structure, processing parameter, flow gate size and location. Traditional shrinkage rate estimated from mold designer's experience makes it quite difficult to meet the accuracy requirements on products, especially in terms of big size items like automotive interior and exterior. This paper introduces the accurate calculation of shrinkage rate for injection molding by computer simulation via MOLDFLOW software, and researches the factors influencing shrinkage rate, which holds guiding significance on improving the pass rate of big size injection molded items.

Keywords MOLDFLOW · Shrinkage rate · Mold design · Injection molding · Computer simulation

1 Foreword

The shrinkage rate of the traditional injection molding products is based on the experience of mold engineers who just select an empirical value, or on the intermediate value from the range of shrinkage rate provided by the material manufacturer. This means that as long as the plastic type is the same, the same shrinkage rate is adopted for all the injection molded parts and all the locations of

F2012-E13-007

F. Xiao (✉) · L. Chen · X. Wang
Department of Polymer Product Performance Development, Changan Automobile Global R&D Center, 401120 ChongQing, People's Republic of China
e-mail: sunqiemail@163.com

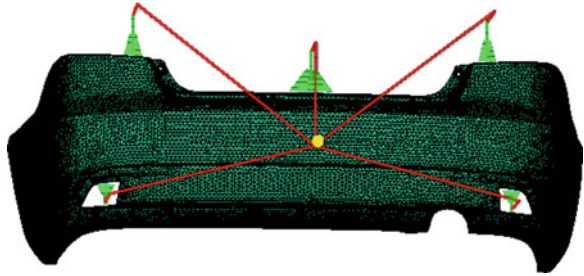
that part, in spite the fact that the product shape, mold structure, number, location, and size of gates may vary a lot. In fact, shrinkage rate of injection molded product varies according to many influencing factors such as plastic types, product structure, processing parameter, and size and location of gates, etc. [1]. Therefore, great errors exist between the actual shrinkage rate and the shrinkage rate adopted, and therefore it becomes difficult to control the size of large injection molding parts. Especially in terms of injection molding for automobile interior and exterior, if the size is not properly controlled, gaps and rat-holes will appear, which will seriously affect the grade of the product.

For the purpose of better dimensional accuracy and surface quality of injection molding parts, a more accurate shrinkage rate is needed. Yet, neither the traditional empirical estimation of the engineer nor the plastic supplier could provide a shrinkage rate against the part's structure and specific material which is highly close to the actual shrinkage. However, this can be realized by simulating the injection molding process with MOLDFLOW software. Using this simulation, a shrinkage rate highly close to the actual shrinkage can be calculated out with comprehensive consideration on the influence of product structure, material type, gate number and location, and process parameter on the molding shrinkage. The shrinkage mechanism of injection molding products, the calculation method and influencing factors of shrinkage rate will be introduced in the following text from examples of simulation calculation on automobile exterior and interior.

2 The Shrinking Mechanism of Injection Molding Parts

When the injection molding machine injects the plastic melt into the mold cavity through nozzle, runner, and gate, polymers orient along the melt-flow direction and the conformational entropy reduces. But this kind of orientation does not happen in the whole polymer chain as the polymer is formed by a number of chain segments and entanglement between those segments determines that orientation stretch could only happen in some segments.

After the mold cavity is fully filled and the pressure feeding stage is ended, the shear stress along the flow direction gradually disappears. According to the principle of entropy increase, the polymer chain tends to the largest natural curly conformation entropy state, resulting in disorientation. At the same time, when the cavity pressure drops to the equal value of the atmospheric pressure, post-mold shrinkage process begins. As the volume of the polymer is composed by the volume of the polymer chains and gaps between these polymer chains, volume shrinkage (including thermal shrinkage and crystal shrinkage) in plastic product is mainly the result of the gap-narrowing between the molecules, which is realized by polymer chain's constant exchanging places with the gaps and gradually transferring the gaps to the surface of the plastic piece [2, 3]. Therefore, the motion state of polymers on the surface layer of the plastic product controls its volume shrinkage. During the shrinking process of the plastic product, disorientation determines that

Fig. 1 Mesh of rear bumper I

polymers contract along the flow direction; while in the thickness direction, driven by the intermolecular attractive force, polymers on the plastic surface layer move closer to the core of the plastic product, which means that shrinkage in the thickness direction points from the plastic product's surface to the core.

3 Processing Parameter Setting

After the structure design of the rear bumper I for a certain car was completed in CATIA, the pre-treatments of meshing, mesh repair, and runner establishment were completed in MOLDFLOW. The product size is 735 mm*1610 mm*540 mm. The product is 3.0 mm thick. Figure 1 shows the product structure and the runner system. The material was PP filled with 10 % talc. Molding shrinkage rate in parallel direction provided by the manufacturer was 0.4538 ~ 0.9043 %, and that of the perpendicular direction was 0.7559 ~ 1.367 %. The mold temperature was 35 °C. The melt temperature was 205 °C. The injection time was 5 s. Before the calculation of the cavity shrinkage dimension, a reference dimension was needed to be set, as shown in Fig. 2. The reference dimension was set according to the size of the tolerance. After the calculation was completed, the results were compared with the tolerance range to judge whether the molding shrinkage rate selected was qualified.

4 Calculation of Shrinkage Rate

In order to calculate the shrinkage rate of a specific material, process parameter and product structure, a simulated calculation of Fill + Pack + Shrink in MOLDFLOW was needed. After the calculation was completed, MOLDFLOW would provide the entire product's molding shrinkage rate, as shown in Fig. 3. The molding shrinkage rate of the rear bumper I was 1.1 ± 0.16 %. Molding shrinkage rate in all directions was shown in the product molding shrinkage report, as shown in Fig. 4, together with the rear bumper I's recommended molding shrinkage rate range.

Fig. 2 Reference dimension of rear bumper I

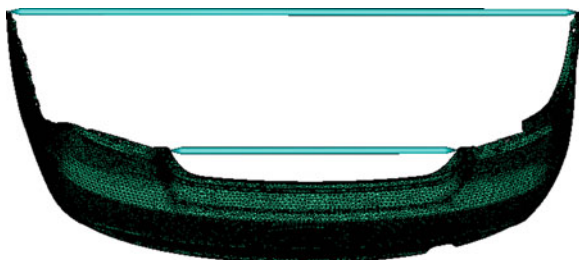


Fig. 3 Molding shrinkage rate of rear bumper I

Recommended Shrinkage Allowance Report- Entire Model

Total = 1.10 +/- 0.16 %

Fig. 4 Molding shrinkage rate of rear bumper I

Component Shrinkages Report

Dir.	Single Value		Predicted Shrinkage Tolerance	Shrinkage Min:Max
	Recomm. [%]	Validity Range [%]		
X	0.84	0.30:1.39	0.55	0.00:1.71
Y	0.98	0.39:1.57	0.59	0.00:2.02
Z	0.99	0.40:1.58	0.59	0.00:1.87
Total	1.10	0.83:1.36	0.27	0.54:1.58

The mold design engineer could calculate the mold processing size in X, Y, Z direction according to this table, and thus improve the machining accuracy of the critical dimensions of the injection molding product in all directions.

For the recommended shrinkage rate of $1.1 \pm 0.16\%$, MOLDFLOW calculated whether the size of different position of the simulated product met the requirement, as shown in Fig. 5. Green means the recommended product shrinkage rate could meet the requirement of the product’s size. Red means it could not meet the requirement size of the product. Yellow means size of this part needs to be treated with caution. It is between “could meet the requirement” and “could not meet the requirement”. As shown in Fig. 5, by adopting the molding shrinkage rate of $1.1 \pm 0.16\%$, most part of the rear bumper was green, which meant this size met the requirement. Two installation holes’ (point A and point B in the picture) size was red. The two holes were kidney-shaped, and the size deviation was of ± 3 mm. This size was set as the reference size to perform the simulation analysis. As shown in Fig. 6, the distance between A and B was 807.39 mm. After injection molding, the predicted distance was 805.24 ~ 809.54 mm which was within the tolerance range and met the operation requirement.

Fig. 5 Shrinkage rate of rear bumper I

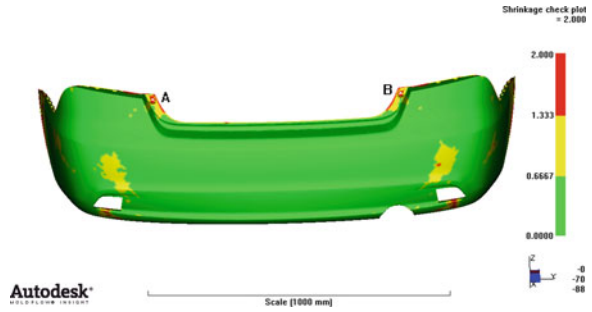
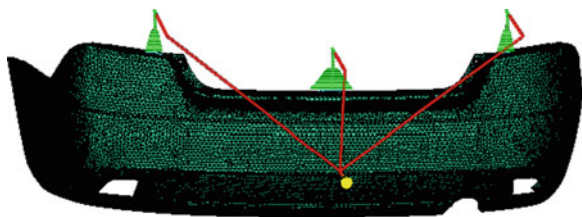


Fig. 6 Reference dimension report of rear bumper I

Dimension Summary Report
(Using Recommended Shrinkage Allowance)

Desired Part Dimension(-/+ Tol) (mm)	Required Mold Dimension(Tol) (mm)	Predicted Part Warning Dimension Range (mm)
Dim#1 Node A =14238/Node B =14261		
807.39	-3.00:3.00	816.26 0.86 **Met** 805.24:809.54

Fig. 7 Running system of rear bumper I



5 The Influencing Factors on Molding Shrinkage Rate

5.1 Gate's Influence on Molding Shrinkage Rate

In terms of injection mold design, it is known that with fixed product structure and material, the structure of the mold gates is a key influencing factor on the product's molding shrinkage rate [4–8]. To research on the influence of gates on molding shrinkage rate, the product structure, material, and processing parameter were kept the same, and the gate's number was reduced to 3. As shown in Fig. 7, the size and location of the 3 gates were set the same with the corresponding gates in Fig. 1.

The simulation calculation result was shown in Figs. 8 and 9. It could be seen that after the adoption of 3 gates, the recommend molding shrinkage rate of the rear bumper lowered 0.03 %, and shrinkage rate in X, Y, Z direction changed too. In Z direction, the decrease was the most obvious of 0.03 %. In X direction, the molding shrinkage rate increased 0.01 %. Therefore, when the mold was designed, key dimension in X and Z direction should be seriously considered to ensure the product size precision.

Fig. 8 Shrinkage rate of rear bumper after using 3 gates

Component Shrinkages Report				
Dir.	Single Value	Predicted	Shrinkage	
	Recomm. [%]	Validity Range [%]	Tolerance [%]	Min:Max
X	0.85	0.30:1.39	0.55	0.00:1.57
Y	0.96	0.40:1.51	0.55	0.00:1.78
Z	0.96	0.39:1.53	0.57	0.00:1.76
Total	1.07	0.82:1.31	0.25	0.59:1.41

Fig. 9 Molding shrinkage rate in X, Y, Z direction of rear bumper I after using 3 gates

Recommended Shrinkage Allowance Report- Entire Model	
Total	= 1.07 +/- 0.16 %

Fig. 10 Molding shrinkage rate of rear bumper after changing material

Recommended Shrinkage Allowance Report- Entire Model	
Total	= 0.64 +/- 0.06 %

5.2 Material's Influence on Molding Shrinkage Rate

Materials have significant influence on the molding shrinkage rate. Crystalline material's molding shrinkage rate is generally far larger than amorphous materials'. Different types of materials have different molding shrinkage rates. Even for the same type of material, the molding shrinkage rate could be different as crystallizability of the material, filler type and quantity, orientation of the polymer chain segment will affect molding shrinkage rate.

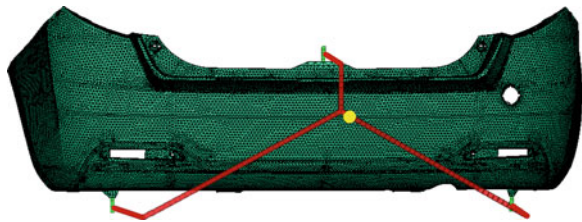
After keeping the gate's location and size, process parameter, and product structure the same and changing the molding material into modified PP filled with 13 % talc, the simulation calculation result of MOLDFLOW was shown in Figs. 10 and 11.

With a comparison of the calculation result of Figs. 10 and 11 with that of Figs. 3 and 4, it is concluded that the molding shrinkage rate of the rear bumper I decreased 0.46 % after using modified PP filled with 13 % talc, and the molding shrinkage rate in X, Y, Z direction also greatly decreased. Therefore, it can be concluded that different material's molding shrinkage rate varies a lot. Therefore, when the mold is designed, as long as the material changes, the molding shrinkage rate recommended by simulation calculation in MOLDFLOW with the material used in production should be adopted. Otherwise the accuracy requirement of the product can not be achieved.

Fig. 11 Molding shrinkage rate in X, Y, Z direction of rear bumper I after changing material

Component Shrinkages Report					
Dir.	Single Value	Predicted	Shrinkage		
Recomm.	Validity	Range	Tolerance	Min:Max	
[%]	[%]	[%]	[%]	[%]	
X	0.50	0.21:0.80	0.29	0.00:1.00	
Y	0.58	0.26:0.90	0.32	0.00:1.03	
Z	0.58	0.27:0.90	0.32	0.00:0.99	
Total	0.64	0.54:0.74	0.10	0.57:0.90	

Fig. 12 Mesh and runner system of rear bumper II



5.3 Cooling System’s Influence on Molding Shrinkage Rate

After keeping the gate’s location and size, processing parameter, molding material, and product structure the same as shown in Fig. 12, the molding shrinkage rate of rear bumper II was analyzed separately when core temperature was kept the same with cavity temperature and adopting cooling system as shown in Fig. 13.

The MOLDFLOW calculation result was shown in Figs. 14 and 15. Comparing the two Figures, we can see the molding shrinkage rate of rear bumper II increased 0.15 %, and that in Y direction increased 18 %. The Y direction is the length direction of rear bumper II, whose size is a key size of the product. If size in this direction can not meet the product accuracy requirement, a gap will appear after it is installed into the car, which will reduce the grade of the car.

5.4 Product Structure’s Influence on Molding Shrinkage Rate

Keeping the processing parameter, molding material, and other conditions the same, the product structure’s influence on molding shrinkage rate was researched when runner system of rear bumper II was kept same with that of rear bumper I.

MOLDFLOW’s simulation calculation result was shown in Fig. 16. Comparing Fig. 16 with Figs. 3 and 4, it can be seen that the molding shrinkage rate of rear bumper II increased 0.06 % compared with that of rear bumper I. The shrinkage rate in X, Y, Z direction all increased. Especially in Y direction it increased 0.1 %.

Fig. 13 Cooling system diagram of rear bumper II

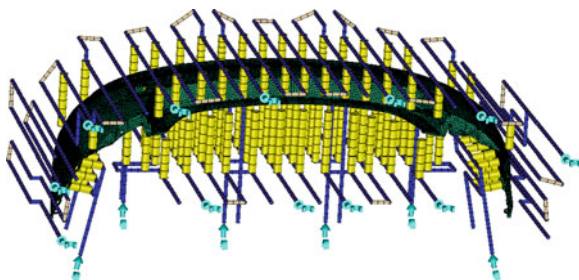


Fig. 14 Molding shrinkage rate of rear bumper II

Recommended Shrinkage Allowance Report- Entire Model

Total = 1.23 +/- 0.16 %

Component Shrinkages Report

Dir.	Single Value Recomm. [%]	Predicted Validity Range [%]	Shrinkage Tolerance [%]	Min:Max [%]
X	1.06	0.39:1.73	0.67	0.00:2.20
Y	1.12	0.54:1.70	0.58	0.00:2.31
Z	1.07	0.47:1.68	0.60	0.00:2.04
Total	1.23	0.95:1.51	0.28	0.67:1.90

Fig. 15 Molding shrinkage rate diagram of rear bumper II after using cooling system

Recommended Shrinkage Allowance Report- Entire Model

Total = 1.38 +/- 0.16 %

Component Shrinkages Report

Dir.	Single Value Recomm. [%]	Predicted Validity Range [%]	Shrinkage Tolerance [%]	Min:Max [%]
X	1.19	0.43:1.96	0.76	0.00:2.97
Y	1.30	0.61:1.98	0.69	0.00:2.94
Z	1.14	0.50:1.79	0.64	0.00:3.36
Total	1.38	1.07:1.70	0.31	0.80:2.62

This proves that product structure will influence its molding shrinkage rate. Accordingly, when the mold is designed, the same molding shrinkage rate should not be used just because the product material is the same.

Fig. 16 Molding shrinkage rate diagram of rear bumper II after using cooling system

Component Shrinkages Report				
Dir.	Single Value Recomm. [%]	Validity Range [%]	Predicted Shrinkage Tolerance [%]	Shrinkage Min:Max [%]
X	0.89	0.30:1.48	0.59	0.00:2.19
Y	1.08	0.49:1.67	0.59	0.00:2.27
Z	1.07	0.44:1.70	0.63	0.00:1.90
Total	1.16	0.91:1.41	0.25	0.65:1.91

6 Conclusion

1. Using MOLDFLOW simulation analysis, molding material, gate location, gate number and size, product structure, and cooling system’s influence on molding shrinkage rate can be thoroughly considered in order to calculate out the product’s proper molding shrinkage rate. On this basis, the molding result of the key size can be predicted. Accordingly, the mold engineer can adjust the mold’s dimension to improve product accuracy.
2. Molding material is an important influencing factor on molding shrinkage rate of injection molding products. Different material’s molding shrinkage rate varies a lot. Before designing the mold, simulation calculation on the molding shrinkage of the selected material should be conducted.
3. Different gate location, quantity and size will affect the orientation and crystallization of the polymer chains and the feeding of the packing stage. Thus, location, quantity and size of the gates have a significant influence on molding shrinkage rate.
4. Cooling system is another key influencing factor of molding shrinkage rate. Therefore, when the mold is designed, the molding shrinkage rate can be adjusted by optimizing the mold’s cooling system.
5. Product structure is one of the important influencing factors on the injection molding shrinkage rate. The same molding shrinkage rate should not be used just because the molding material is the same. Simulation calculation of Cool + Fill + Park + Shrink in MOLDFLOW should be carried out. The recommended molding shrinkage rate should be adopted with consideration on product structure and other influencing factors.

References

1. Song M, Huang Y, Zhao D (2003) Injection mold design and manufacture. Machinery Industry Press
2. Zhao H, Jiaodong J, Wu D, Minshao T (1994) Polymer physics. Textile Industry Press 107–110
3. Zhu T, Wang M (2001) Shrinking rules of injection molding products. *J Plast Eng* 8(14):72–76
4. Gao Y, Xichen W (2006) Design optimization progress of injection molding product's bending. *China Plastics* 20(11):8–10
5. Li H, Gu Y, Shen C (2002) Bending analysis and molding size predict of injection. *China Mach Eng* 13(10):820–822
6. Dong B, Shen C, Li Q (2005) Shrinking and bending reasons of thin injection molding products. *J Chem Eng* 56(4):730–731
7. Leo V, Curelliez Ch (1996) The effect of the packing parameters, gate geometry and mold elasticity on the final dimensions of molded part. *Polym Eng Sci* 36:1961–1969
8. Guo Z, Li D (2001) Research on bend deformity of injection molding products. *Plast Sci* 1:22–24

Author Biography

XIAO Fangcheng Master, who graduated from Sichuan University in 2009, and majored in material processing engineering, he has published 8 papers. Now he is working for the department of polymer product performance and development in Changan Automobile Global R&D Center. He is engaged in MOLDFLOW analysis and CAE work.

A Study of Contact Condition in Vehicle Transmission Virtual Assembly System

Yan Chen, Shouwen Yao and Fei Liu

Abstract Facing violent market competition, how to push new product into market with the fastest speed is the key to the survival of the enterprises. Virtual Assembly is the trend of the manufacturing development today. Data glove, as a human computer interactive tool in Virtual Reality, is an important device in virtual assembly. In this paper, the principle and functions of the data glove are studied. Data glove and virtual part's contact condition detect is done. An interaction and control module of data glove is designed, with which man can assemble the transmission in virtual environment conveniently.

Keywords Visual assembly · Data glove · Vehicle transmission · Virtual model · Collision detection

1 Introduction

With the accelerated competition in global market, the enterprises must accelerate the speed of product development in order to survive in the keen competition of market. But traditional assembly has high cost and long cycle, for it cannot dispense the process radically that the prototyping has to be manufactured again and again during product development [1].

F2012-E13-010

Y. Chen (✉) · S. Yao · F. Liu
School of Mechanical Engineering, Beijing Institute of Technology, Beijing, China
e-mail: cydragon1988@163.com

S. Yao
Science and Technology on Vehicle Transmission Laboratory, Beijing, China

Virtual prototyping, as a kind of new products development approach, compares with traditional design method, it cannot merely revise and design conveniently through virtual prototype before making physics prototype actually, shorten products development period, lower costs, and can also improve the properties of product, strengthen the market competitiveness, accelerate the transformation from new technology to new products [2].

Virtual assembling can assist to shake off the excessive reliance of physical prototype to test and assemble [3]. It can improve the quality and velocity of product modeling and assembling, benefit in decreasing product developing cost and reducing product developing cycle.

In virtual assembly (VA) system, it is an important method to use data glove to manipulate virtual objects [4]. Data glove is one of the devices in Virtual Reality Technology, and the implementation of the data glove is important in virtual manufacturing design [5]. Through virtual hand modeling and collecting the data from data glove, the hand gesture mapping between the virtual hand and the real hand is realized, and the collision detection between virtual hand and virtual objects is implemented by using Bounding Volume Hierarchy.

2 Virtual Assembly System Platforms

2.1 Hardware Structure of Virtual Assembly System Platform

Based on the analysis on the virtual assembly system, the integrated two-channel visual simulation platform (Fig. 1) has been putting up by selected hardware system with excellent performance and advanced technology. The platform includes computer software and hardware subsystems, projection subsystem, central control subsystem, interactive subsystem, and several other major components.

The system with advanced visual simulation technology has significant features as described in the following.

- The system has the ability of powerful graphics processing, data exchange and calculation. By using PC-Cluster architecture, the system has more expansibility and high maintenance.
- By using plate rear projectors of two-channel projection, the system realizes a 1:1 ratio stereoscopic display for vehicle transmission system, with the characteristics of more details and high resolution in features exhibition.
- The virtual assembly system makes the projector, computer, audio, lighting, video and electromechanical equipment as a integration.
- Peripheral equipment of virtual assembly system is complete for the need of human-computer interaction. The system can meet the position tracking, roaming, stereo image watching and virtual assembly operations of product.
- The system implements stereoscopic display by means of spectra stereo, high quality and light wave band filtration technologies.

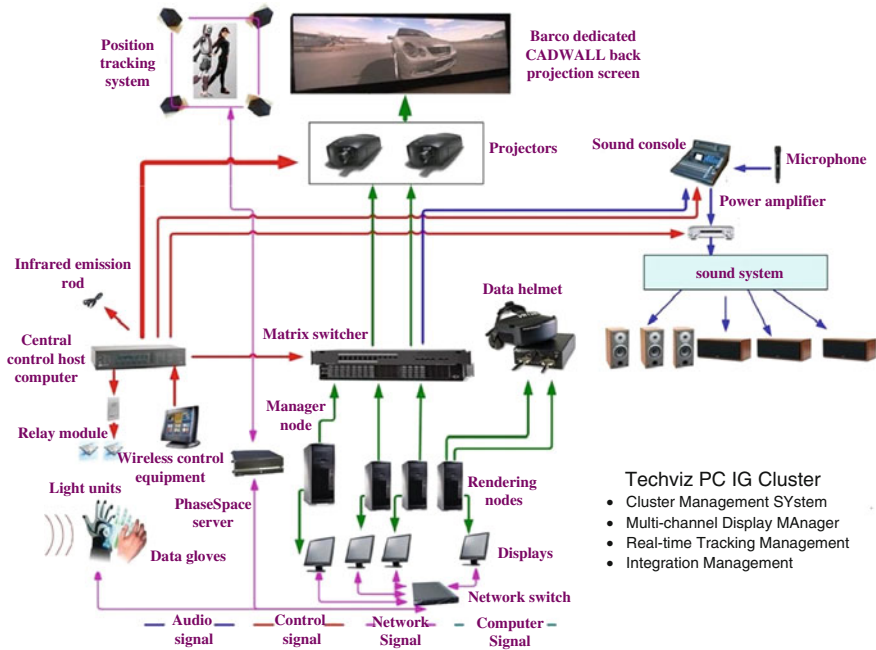


Fig. 1 System architecture diagram of virtual assembly platform

2.2 Software Structure of Virtual Assembly System Platform

Virtual environment (Table 1) of virtual assembly platform has been established by using the visual simulation software Virtools, combined with secondary development of Virtools SDK package to achieve function integration for the assembly system. The models needed for the assembly system come from Pro/E software. The conversion from solid geometry models to virtual models have been accomplished by intermediate conversion. The extraction of non-geometry information relative to virtual assembly to model information database has been realized by secondary development technology. Data bottom has been implemented by relational database. The association of geometric models with assembly information has been realized by Visual C++ programming. This system develops and runs on Windows XP Server system, takes VC++ 6.0 as the integration development environment and Pro/E WildFire 3.0 as the secondary development platform.

Table 1 Development and running environment of virtual assembly system

Category	Software name
Virtual reality platform	VIRTOOLS 5.0
Secondary-development tool kit	Pro/TOOLKIT, VIRTOOLS SDK
Development platform	VC++ 2006
CAD design tools	Pro/E WildFire version 3.0
Operation system	Windows XP

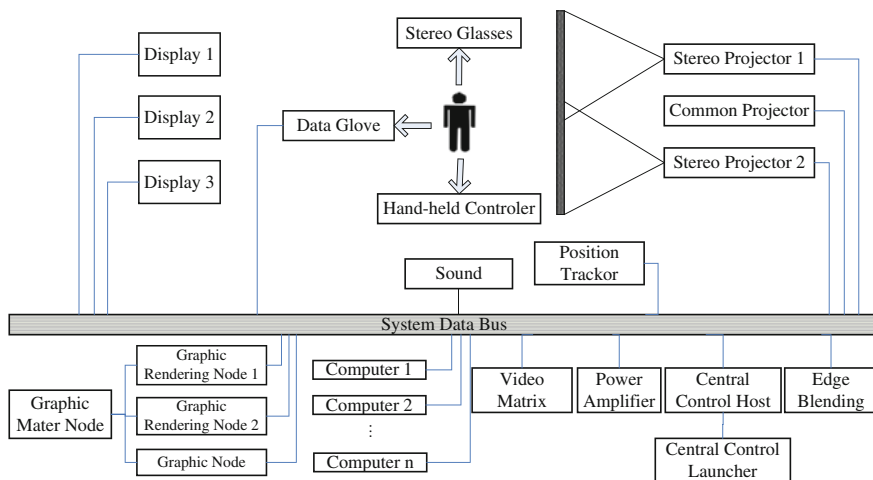


Fig. 2 Virtual assembly system architecture based on data glove

3 Overall Design of Virtual Assembly System Based on Data Glove

The virtual assembly platform (Fig. 2) is designed for virtual assembly for transmission system, which includes virtual assembly function of transmission system, virtual display of transmission system and strong sense of immersion and other functions. The architecture of virtual assembly has been established to achieve functional requirements.

In this paper, a frame of vehicle transmission visual assembly system (Fig. 3) is constructed. The content includes visual assembly scene construction and software secondary development. Finally, a vehicle transmission visual assembly system based on visual simulation platform is implemented by using data glove, position tracker and other virtual reality hardware devices. Users can naturally interact with transmission parts in the form of operating virtual hand immersing in the visual assembly system.

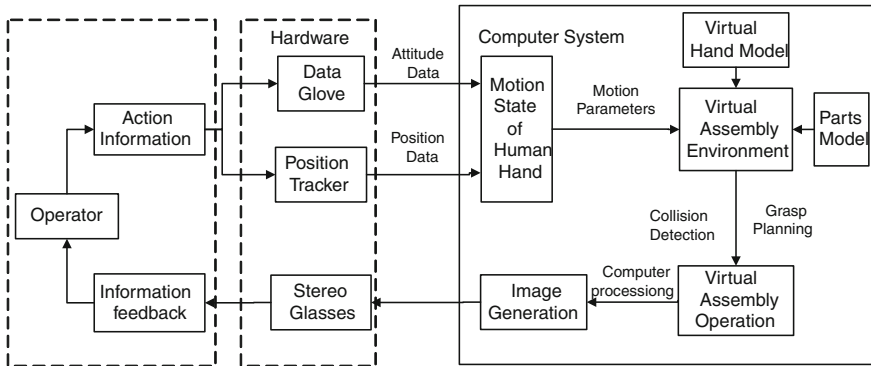
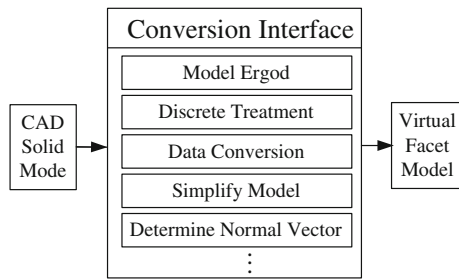


Fig. 3 Data glove operation process in virtual assembly system

Fig. 4 Model information acquisition process



4 Virtual Modeling Based on Reconstruction of Virtual Assembly Feature

The differences between solid model in CAD and facet model in virtual environment are studied [6], and the assembly model information database of transmission device is established based on the relational data model [7, 8]. CAD models of transmission device transformed into virtual assembly models is achieved which provides the data support for virtual assembly system (Fig. 4).

According to information constitutes of virtual assembly features, the technology of secondary development of Pro/E is used to realize assembly information acquisition. Three kinds of methods are contrastively analyzed to use for mapping between geometric elements and triangular facets, and the integrated information feature models of virtual assembly are created based on model information database. Under the VC++ 6.0 environment, using Pro/Toolkit procedure development technology to carry on secondary development in Pro/E, and building the vehicle transmission visual assembly model oriented to Virtools visual platform.

Using 3DS file as a neutral file, we import the Pro/E models into Virtools environment to complete transform of geometric model. Pro/Engineering provides the API function library of the underlying data to develop. The secondary development tools can extract assembly information using a recursive method for

Table 2 Some of functions of Pro/ToolKIT API library and their descriptions

Function name	Descriptions
ProMdlCurrentGet	Get handle of current model
ProMdlDataGet	Get name and type
ProSolidMassPropertyGet	Get physical properties
ProSolidSurfaceVisit	Traverse all surfaces of model
prodb_get_surface_props	Get properties of the surface
ProAsmcompConstraintsGet	Get constraint information
ProAsmcomppathTrfGet	Get relative transformation matrix

product assembly structure tree, and write to model information database. Just as mentioned above methods, between the triangle models and acquired semantic information are independent, which should be mapped in the virtual environment.

Pro/TOOLKIT provides a series of API functions (Table 2) to traverse each node of assembly tree, in it of which the function ProSolidFeatVisit can visit all nodes of assembly (or sub-assembly), which has a function parameter, named Action Function, that can extract the node name, type, attribute information, constraint information, etc. Recursive process can be performed by called the function ProSolidFeatVisit in function Action. Table 2 lists some of the API functions and their descriptions.

5 Second Development of Virtools and Data Glove

Virtools second development of technology is studied; Visual C++ 6.0 and Virtools SDK development tools are used to realize the second development of Virtools, data gloves (Fig. 5), and position tracker. The interactive operation between human and virtual environment is studied and developed either. And Real-time collision detection also realized by using Virtools SDK to do secondary development of Virtools inner building blocks (Fig. 6).

6 Example of Contact Condition in Virtual Assembly System

As to armored vehicle, such as tank, integrated transmission system plays a prominent role in vehicle maneuverability. The reasonableness of structure design and feasibility of assembly can be better investigated by using virtual assembly technology, with high practical value. In this paper, a type of integrated transmission system is taken as an example to study (Figs. 7, 8).

The mixed interference checking method is proposed based on assembly relationship characteristics, which has a layered detection feature. The virtual assembly system uses an algorithm for collision detection using hybrid bounding

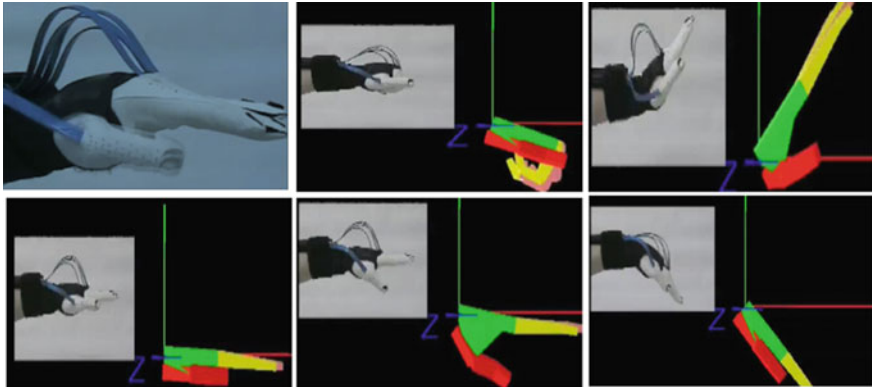


Fig. 5 Data glove pose alignment

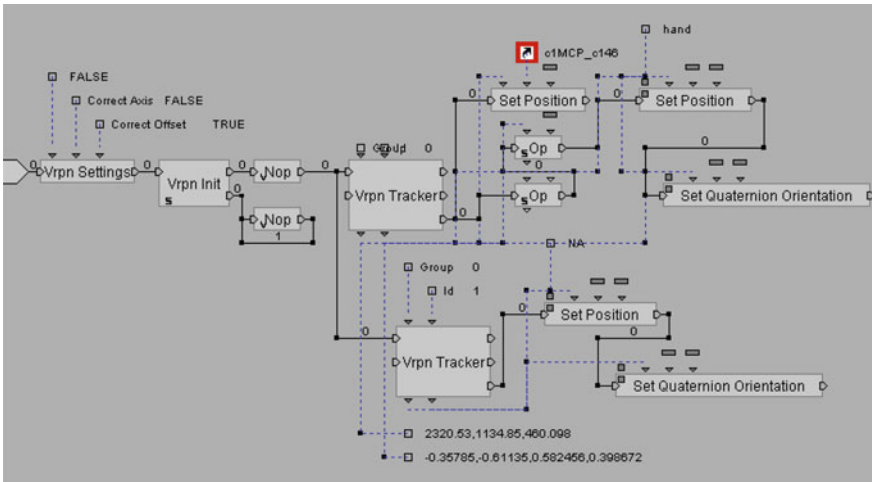


Fig. 6 Data glove development program module

box based on characteristics of assembly relation [9]. Different means of collision detection are adopted based on the differences of space distance, assembly constraints and other factors. Simple and rapid collision detection using hybrid bounding box is adopted for the parts without assembly constraints [10]. For the parts with assembly constraints, geometric elements of involved in assembly will be obtained for collision detections including the geometric surfaces and bounding boxes detection and geometric surfaces of different parts detection. This hybrid collision detection method can efficiently improve the efficiency of collision detection to satisfy real-time and authenticity of virtual assembly environment.



Fig. 7 Data glove operation

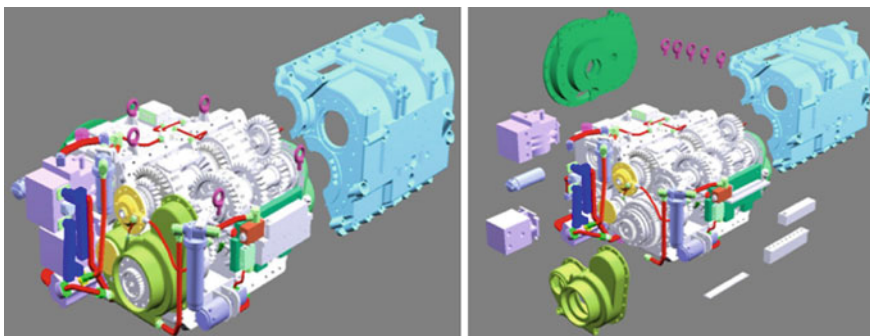


Fig. 8 Virtual assembly examples

7 Conclusions

In this paper, an interactive environment is constructed where users can naturally interact with transmission parts with data glove in the virtual assembly system. Result shows that the system can implement the motion mapping from human hand to virtual hand and the contact condition between virtual hand and virtual objects, and it can also meet the virtual hand 's operation requirement of virtual assembly system, and has a broad application in virtual assembly. But, Force feedback interface was not considered in the virtual assembly system which will be added in the further research.

References

1. Li M (2010) Applications of virtual reality technology in construction industry. Proceedings ICCET symposium. International conference on computer engineering and technology (ICCET 2010), IEEE Press, V4223–V4227, April 2010 doi: [10.1109/ICCET.2010.5486354](https://doi.org/10.1109/ICCET.2010.5486354)
2. Cao W, Chen D (2009) A research on the virtual assembly technology for automotive components. *Automot Eng* 31:561–564
3. Wang T, Li HC, Yan Q (2009) Study on virtual assembly of vehicle integrated transmission equipment. *Vehicle Power Technol* 116:16–17
4. Liu C, XU Q (2009) Design and application of interaction and control module for a data glove. *Comput Simul* 26:251–255
5. Liu J, Yao Y, Li J (2004) Virtual manipulation based on data glove in virtual assembly. *J Syst Simul* 16:1744–1747
6. Shah JJ, Rogers MT (1993) Assembly modeling as an extension of feature based design. *Res Eng Des* 3:218–237
7. Zheng T, He Y, Du J (2004) Study on virtual assembly based on virtual assembly features. *Mech Sci Technol* 23:872–875
8. Liu J, Yao J, Ning R (2005) Research on information integration technology between CAD system and virtual assembly system. *Comput Integr Manufact Syst* 11:44–47
9. Liu J, Ning R (2004) Research and realization of collision detection algorithm in virtual assembly environment. *J Syst Simul* 16:1775–1778
10. Hubbard PM (1995) Collision detection for interactive graphics applications. *IEEE Trans Vis Comput Graph* 1:218–230

The Multi-Properties Modeling Technologies of Virtual Assembly for Vehicle Transmission Based on the Design

Fei Liu, Qingdong Yan, Shouwen Yao and Xin Zheng

Abstract According to the design requirements of transmission system, the multi-properties model of virtual assembly was researched on the basis of physical properties. The multi-properties models of transmission system were established by multi-properties modeling techniques. Visualization simulation of virtual assembly process of transmission is realized by the accurate collision detection, structure analysis, large scene simulation platform and other technologies and methods. Simulation of virtual assembly for vehicle transmission is implemented combined with virtual visual scene. Related performance analysis of transmission based on virtual assembly was done in this paper. These analyses will play an important role on the structural design of transmission.

Keywords Multi-properties model · Virtual assembly · Vehicle transmission · Virtual assembly simulation · Performance analysis

1 Introduction

Virtual assembly based on virtual reality, which is an important way to solve the problems of assembly and design for complex products, has got considerable development in recent years. Current research on virtual assembly is mainly based

F2012- E13-011

F. Liu (✉) · Q. Yan · S. Yao · X. Zheng

School of Mechanical Engineering, Beijing Institute of Technology, Beijing, China
e-mail: liufei2007186@163.com

Q. Yan · S. Yao

Science and Technology on Vehicle Transmission Laboratory, Beijing, China

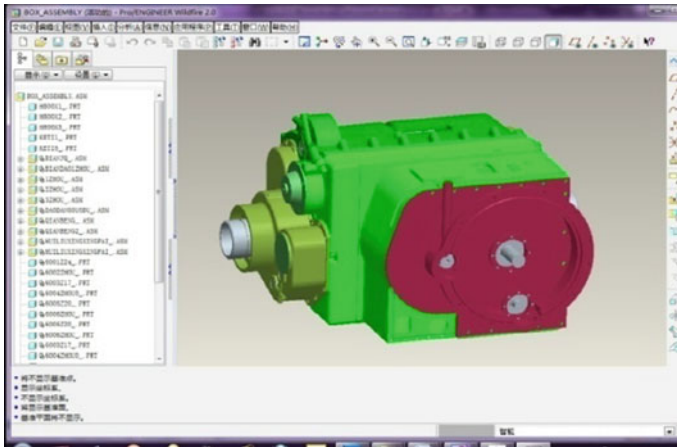


Fig. 1 The assembly drawing of vehicle transmission

on geometric models, in which assembly process simulation of products is realized through geometric constraint, collision detection and so on. The authenticity and validity of assembly process could not be guaranteed, which has certain limitations in solving practical engineering problems. In addition, the analysis of the assembly process is the main content of the virtual assembly simulation study [1]. The system dynamics simulation based on the system virtual assembly model is rarely studied [2]. Therefore, according to the transmission system design requirements, the system multi-properties model, which was based on the system geometric model, has been established to meet the requirements of practical engineering applications. The dynamics simulation analysis of the transmission system has been done after the completion of virtual assembly. These provide a certain theoretical and technical basis for complex mechanical system performance forecast design.

2 Establishment of System Geometric Property Model for Vehicle Transmission

In the virtual assembly system, the geometry property is an important part of the system, as well as the basis of the model properties. Generally, most of virtual reality and virtual assembly software do not have the solid modeling function; therefore, the modeling in the virtual assembly environment was not been directly established, but was established by CAD systems to create geometric property model. The geometric property modeling in CAD system was that the components were assembled by defining the assembly constraint to obtain complete assembly model of system. The assembly drawing of vehicle transmission was shown in Fig. 1.

3 Realization of Virtual Assembly Environment Based on Multi-Channel Projection

Virtual assembly environment, which directly affects the authenticity of the product virtual assembly, is a vector of the virtual assembly in the virtual assembly application. The assembly of armored vehicle transmission has the characteristics of pipeline and integration point. The parts of armored vehicle transmission are numerous, and the production of transmission is small batch. The assembly of armored vehicle transmission is to assemble the different assembly components according to integration point mode, and then the pipeline way was used [3].

According to the assembly characteristics of armored vehicle transmission, it is necessary to build a high resolution, large field of view and deep immersion sense virtual environment for the vehicle transmission system. The immersive features virtual assembly environment was established by stereoscopic display, PC cluster structure, geometric correction, synchronization mechanism, system software and hardware and other methods and technologies [4]. According to the segregation pattern, the common ways of stereoscopic projection are active and passive stereoscopic. The passive stereoscopic display, which includes polarization and spectra stereoscopic projection, is the main applied mean [5].

Because the polarization stereoscopic projection can not realize the application of multi-channel, the stereo of spectra stereoscopic projection was applied in the structure of virtual environment. The mixed geometric correction way of mechanic combined with software correction was proposed to satisfy the assembly environment in the paper. The primary application goal of virtual assembly environment for vehicle transmission was guaranteed by the consistency of each node. For the virtual assembly environment of vehicle transmission, the virtual scene was static. The Master-Slave mode could meet the need of information synchronization [6]. The display of virtual assembly scene images in system working was illustrated in Fig. 2.

4 Simulation of Virtual Assembly Process for Vehicle Transmission

For the establishment of virtual assembly model for vehicle transmission, the first step is to realize the data conversion between CAD and virtual assembly system. The assembly model information was mainly from the CAD system; therefore, integrating with the CAD system data was an important part of the virtual assembly modeling. The assembly information acquisition process was described in Fig. 3.

Virtual assembly properties model must have characteristics of integrity, flexibility, accuracy and real-time. The information of virtual assembly properties model was analyzed in this paper. Based on the relational data model,

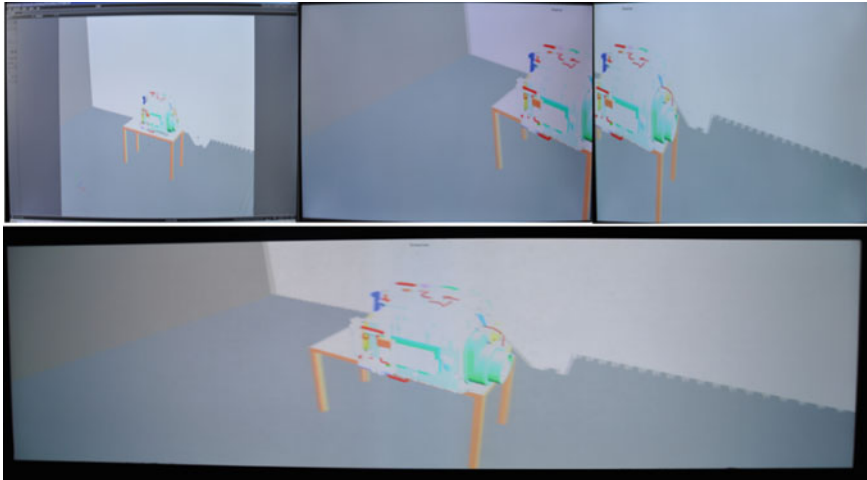


Fig. 2 The display of virtual assembly scene images in system working

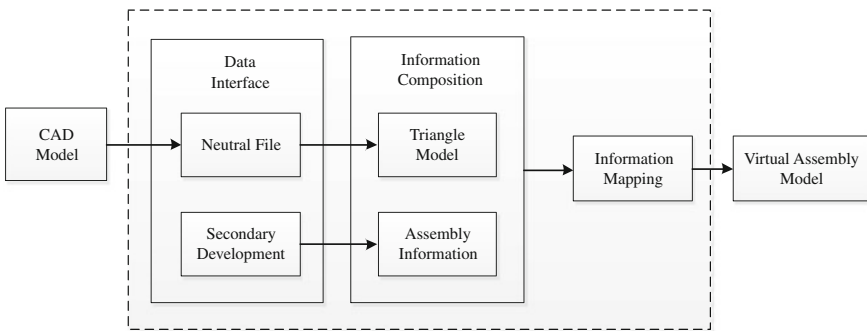


Fig. 3 The assembly information acquisition process

the assembly model information database was built to construct components property models for realizing association between the facet model and assembly information. The virtual assembly characteristics information set was established and virtual assembly characteristics was reconstructed in the virtual environment for the virtual assembly process.

The components and assembly geometric property model of vehicle transmission was established in CAD system. The CAD model was converted into virtual assembly environment by data conversion. The converted model in virtual assembly environment was shown in Fig. 4.

The model information database was built by SQL Server relational database in this paper. The extracted information was stored and managed in the database. Meanwhile, the database provided hierarchical organization and retrieval functions for models. The relational schema of vehicle transmission relational database

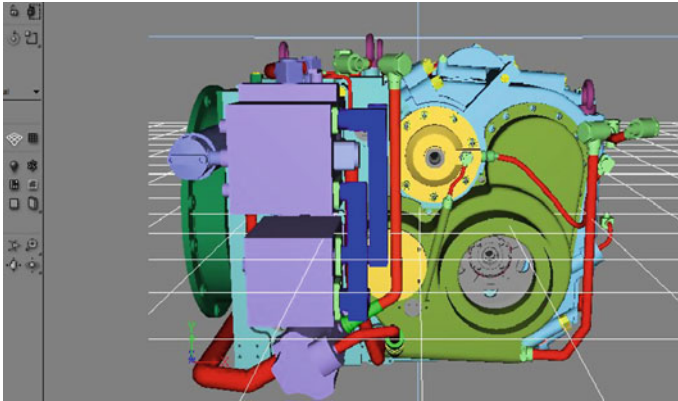


Fig. 4 The converted model in virtual assembly environment

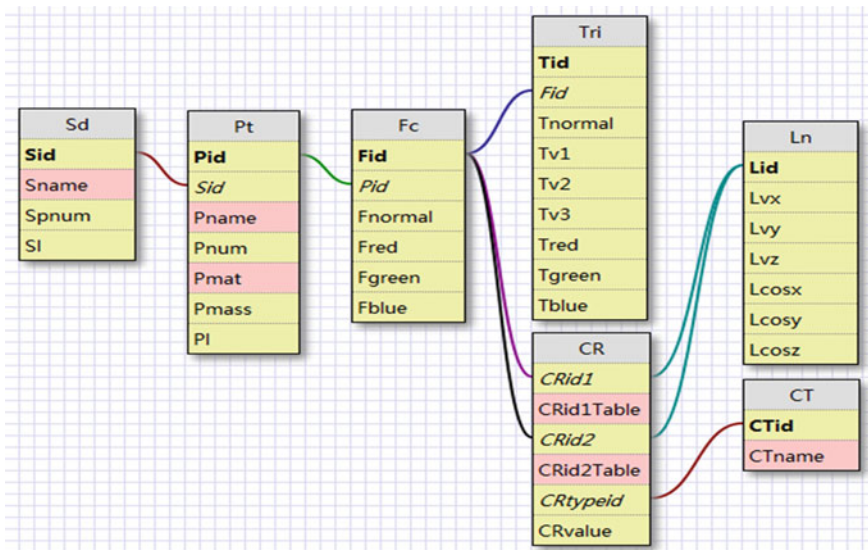


Fig. 5 The connection relations of the relational schema

described the relationship of transmission hierarchical structure. The connection relations of the relational schema were illustrated in Fig. 5.

According to the before-mentioned connection relations of the relational schema and the structure of vehicle transmission, the relational database structure of vehicle transmission and model information management system were respectively described in Figs. 6 and 7.

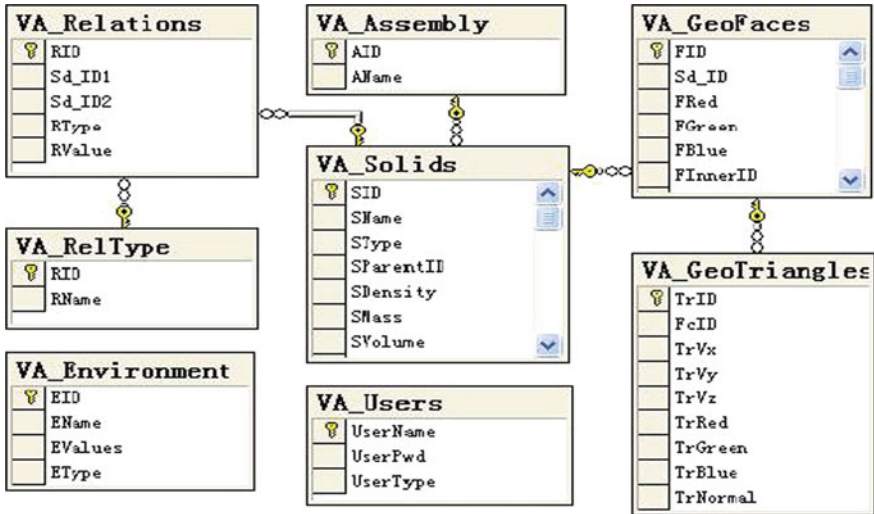


Fig. 6 The relational database structure of vehicle transmission

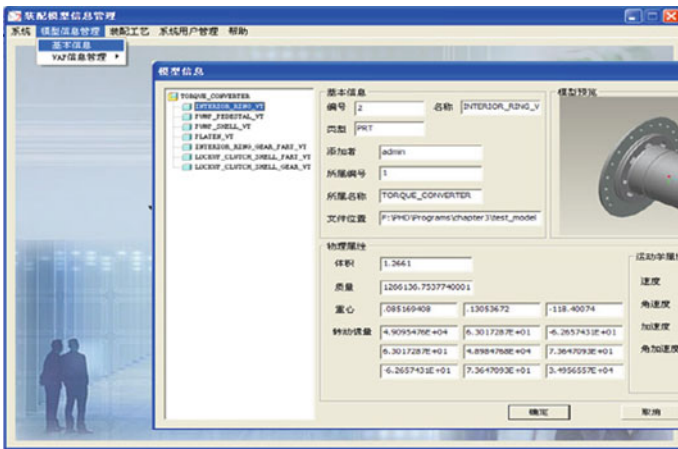


Fig. 7 The model information management system

There are a large number of components in vehicle transmission. Therefore, the sub-assembly pre-identified strategies were applied in this paper to make the process of identifying and judging the feasibility for sub-assembly move forward. This method can effectively improve efficiency of algorithm analysis reduce the combinatorial explosion problems in virtual assembly sequence planning [7].

Simple and rapid collision detection using hybrid bounding box was adopted for the parts without assembly constraints. For the parts with assembly constraints, geometric elements of involved in assembly will be obtained for collision

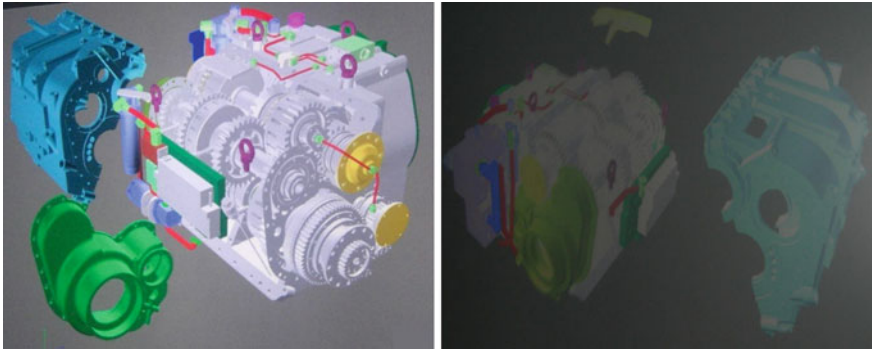


Fig. 8 The virtual assembly process simulation of vehicle transmission

```

VtVector3 pos1(0,0,0);
VtVector3 scale(0.01,0.01,0.01);
float colorRed[4] = {1.0f, 0.1f, 0.1f, 1.0f};
std::string fileName1("../resources/Gear/gear_1.flt");

mGearAsset = new VtFileGraphicAsset("Gear1");
mGearAsset->setFilename(fileName1);
mGearAsset->setScale(scale);
mGearAsset->setTranslation(pos);
VtNode gearNode1 = mGearAsset->getNode(0);
sceneGraph->addNode(gearNode1);
gearNode1.setColor(colorRed);

VtTriangleMesh* gear1Geom = VtTriangleMesh::createFromNode(gearNode1);

mFixedPart = new VtPart(0);
mFixedPart->addGeometry(gear1Geom, 0);
mFixedPart->setName("FixedPart");
mFixedPart->setNode(gearNode1);
mUniverse->addEntity(mFixedPart);

// create gear1
VtVector3 pos2(0,0,0);
VtVector3 scale2(0.01,0.01,0.01);
float colorGreen[4] = {0.1f, 1.0f, 0.1f, 1.0f};
std::string fileName2("../resources/Gear/gear_2.flt");

mGearAsset = new VtFileGraphicAsset("Gear2");
mGearAsset->setFilename(fileName2);
mGearAsset->setScale(scale2);
mGearAsset->setTranslation(pos2);
VtNode gearNode2 = mGearAsset->getNode(0);
sceneGraph->addNode(gearNode2);
gearNode2.setColor(colorGreen);

VtTriangleMesh* gear2Geom = VtTriangleMesh::createFromNode(gearNode2);

const VtReal massPart2 = 0.0;
mMovingPart = new VtPart(massPart2);
mMovingPart->setName("movingPart");
mMovingPart->addGeometry(gear2Geom, 0);
mMovingPart->setNode(gearNode2);
//mMovingPart->setPosition(1, 0, 0);
mUniverse->addEntity(mMovingPart);

mUniverse->disablePairIntersect(mMovingPart,mFixedPart);

```

Fig. 9 The defining process of components multi-properties

detections including the geometric surfaces and bounding boxes detection and geometric surfaces of different parts detection. This hybrid collision detection method was used in this paper, which can efficiently improve the efficiency of collision detection to satisfy real-time and authenticity of virtual assembly environment [8].

With these technologies and methods, the virtual assembly process simulation was implemented. The virtual assembly process simulation was shown in Fig. 8.

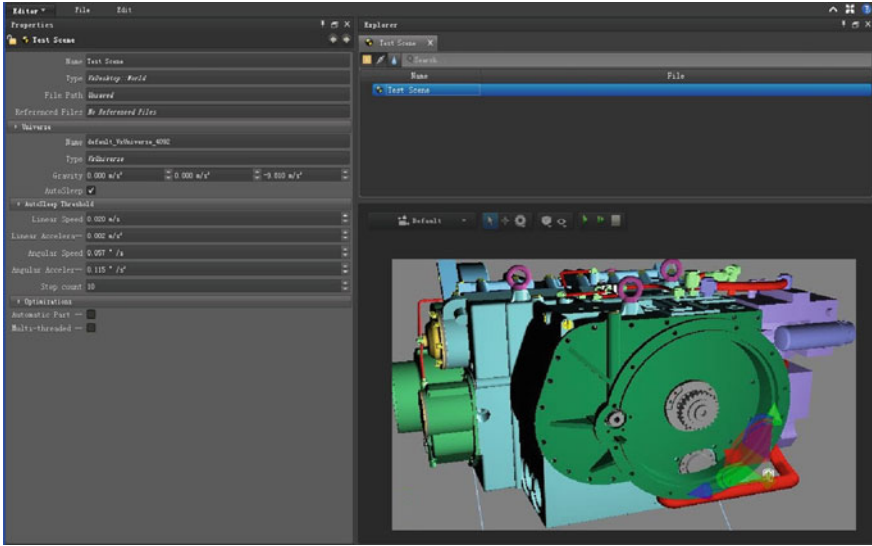


Fig. 10 The defining process of scene properties for system performance analysis

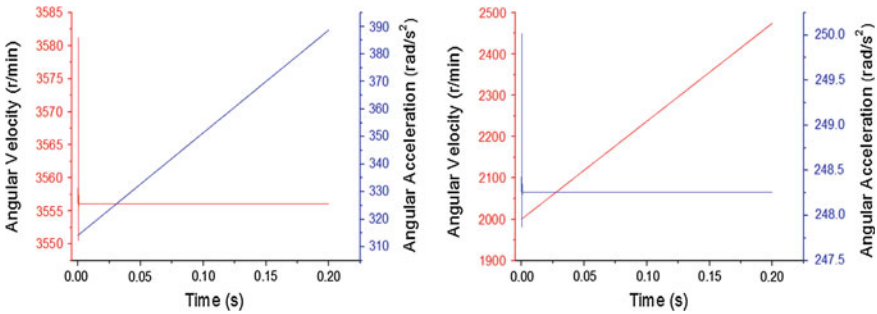


Fig. 11 The diagram of input and output dynamic performance of one gear

5 Performance Analysis of Vehicle Transmission Based on Virtual Assembly

Based on the model that had been assembled by the virtual assembly, the multi-properties model was established. The components of vehicle transmission multi-properties were defined in the virtual assembly environment, such as material properties, centroids, qualities, inertia tensors, positions, directions, velocities, torques, constraints between components, and so on. The defining process of components multi-properties was illustrated in Fig. 9.

The scene properties of system performance analysis were defined after the model multi-properties had been completed. The defining process of scene properties for system performance analysis was explained in Fig. 10.

The system performance analysis was done after the defining of components multi-properties and scene properties. The research contents of vehicle transmission performance analysis were more. Taking into account the real-time of systems analysis based on the virtual assembly model, the input and output dynamic performance of one gear for vehicle transmission was analyzed in this paper. The diagram of input and output dynamic performance of one gear was shown in Fig. 11.

6 Conclusion

The geometry property model of vehicle transmission and dual channel projection were established for providing the base of modeling in virtual assembly environment; the data conversion between CAD and virtual assembly system was realized by model information database and reconstruction technology and method; the virtual assembly process was completed with collision detection and the sub-assembly pre-identified strategies assembly sequence planning; With these bases, the multi-properties model was established by multi-properties defining and scene properties building. Based on these technologies and methods, the input and output dynamic performance of one gear for vehicle transmission was verified. The results showed that the multi-properties modeling technologies were feasible. These technologies could provide a certain bases for the designing of vehicle transmission.

References

1. Liu J, Hou W, Shang W (2009) Integrated virtual assembly process planning system. *Chin J Mech Eng* 22(5):717–728
2. Wang T, Yan Q-D, Li H-C (2010) Research on method of virtual modeling based on reconstruction of virtual assembly feature. 2010 International Conference on audio, language and image processing, pp 1295–1301
3. Pingjun X, Yuedong L, Cheng L (2008) Study on virtual assembly technology for complex products. *Mech Sci Technol Aerosp Eng* 27:1001–1004
4. Liu GH, Yao YX (2006) Development of a new virtual environment system for assembly. *Key Eng Mater* 316:556–560
5. Liu Z, Tan J (2007) Constrained behavior manipulation for interactive assembly in a virtual environment. *Int J Manuf Technol* 32:797–810
6. Liu Z, Shi J, Peng H (2006) A survey of cluster-based parallel rendering system. *J Syst Simul* 18:70–72
7. Liu F, Yan Q, Shouwen Y (2012) Research on virtual assembly platform realization technology of vehicle transmission system. *Appl Mech Mater* 135:856–861
8. Gaoliang P, Yu H, Gongdong W (2008) Fast collision detection approach to facilitate interactive modular fixture assembly design in VE. *Int Conf Adv Intell Mechatron (AIM 08)* 8: 856–861

New Technologies in Driving Dynamics Performance Simulation

Cibrario Valerio and Cugnon Frederic

Abstract Today's vehicle dynamics engineers are facing many different challenges at the same time, such as achieving full vehicle response target requirements for ride and handling, simulating accurate road loads prediction, developing and integrating chassis subsystems (such as steering, brake, damper) and even the more complex active safety systems, keeping a good balancing compromised solution with other vehicle performances such as road noise, passive safety and NVH. In order to answer to such complex panorama, vehicle dynamics engineers are using CAE for the development of a vehicle with usage of 1D modelling and 3D MBS and FEA. The concurrent use of all these technologies represents a standard in the automotive industry, depending on the frequency range and on the vehicle development stage. However, the current simulation process is not efficient because there is very limited integration between the different approaches. In addition local geometrical and material nonlinearities are not accurately modelled in classical MBS software. This paper introduces an integrated methodology for vehicle dynamics simulation with particular application to MBS nonlinear FEA environment. The integration of MBS capabilities in one single nonlinear FEA environment enables an accurate modelling of nonlinearity in vehicles. The advantages of using the "Motion in FEA" simulation capabilities are demonstrated with relevant vehicle dynamics examples. The "Motion in FEA" approach is very accurate since it can describe all the non-linear effects present in the vehicle. As they are not limited to low frequencies or connection modes, results are more accurate. With respect to the engineering process

F2012-E13-012

C. Valerio (✉) · C. Frederic
LMS Italiana S.r.l, Novara, Italy
e-mail: valerio.cibrario@lmsintl.com

efficiency the “Motion in FEA” model also allows eliminating unnecessary iterations between local separate mechanical models, improving productivity during the complete vehicle development process.

Keywords Driving dynamics • 1D • 3D Multi-body • Nonlinear FEA • Multi-attribute

1 Introduction

Despite the increased focus on fuel efficiency and environmental issues, much of the attention from customers is focused on vehicle performance—acceleration, braking, cornering and ride. Those characterizations, which are responsible for the direction taken when designing and developing new vehicles in the automotive industry today, are challenged by questions about the quality desired in the product by the customer:

- How can the handling of a newly designed vehicle be guaranteed to match a given target vehicle without compromising comfort or noise performance?
- How can the contribution of body and sub-frame flexibility (i.e. modes, local/global deformation, etc.) be taken into account when optimizing the ride and handling performance of a car?
- How can active safety systems, such as ABS or ESP, be taken into account in the routine dynamic simulations with high accuracy?
- How can a multi-body simulation model be made from a vehicle in a modular way, assembling suspensions, steering system, braking system and driveline from separate sub-models?
- How can the ride and handling simulation process be standardized on a corporate level to capture invaluable engineering insight and experience in a knowledge-based environment?
- How can local geometrical and material nonlinearities be assessed with sufficient accuracy?
- How can reliable and correct loads be predicted in order to guarantee durability performances when prototypes are not yet available?

Furthermore, today’s vehicle dynamics engineers are facing all of the above challenges while ensuring that safety and fuel economy targets are not hindered. A dedicated analysis solution, including 1D and 3D multi-body and FEA simulation methodology, will provide invaluable help in the chassis systems and full vehicle design process.

2 Integrated Simulation Process

Considering the overall domain of simulation in mechanical engineering, different levels of modelling complexity are available depending on the level of performance requirements (see Fig. 1):

- The simplest model is a bicycle model. This is a component oriented model, possibly extended with nonlinear parameters either updated live or estimated a posteriori. All the parameters are condensed to simulate a nonlinear side force map.
- A 4 wheeled model is developed in the form of block diagram. The suspension characteristics are represented by look-up tables. It is used mainly for real-time applications for Software in the Loop (SIL), Hardware in the Loop (HIL) or driving simulators.
- An MBS model is well adapted in the early phase of the full vehicle project development and can be used to evaluate the effect of design changes. It is slower in term of CPU solver time compared to the previous types of model. Nevertheless this kind of model is limited in terms of frequency and cannot make proper usage of advanced tire models.
- MBS model with super elements: this represents the current standard for vehicle dynamics simulation as the flexibility can be taken into account without compromising the CPU solver time too much. With this kind of linear model, the tire models can be better exploited. Nevertheless this approach is still limited as local 3D non-linearity cannot be taken into account, bearing in mind that lumped models of non-linearity cannot capture true 3D phenomena in detail.
- MBS model within nonlinear FEA: there has been increasing interest shown in this approach in the recent years, especially to simulate the local structural non linearity in the suspension (contact with elastomer insulator or side load spring in McPherson strut) [1].
- MBS model within nonlinear FEA and meshed tires: this is clearly the highest level of complexity which can be simulated as the level of details modelled is very high.

The complexity of the model used depends on the data available to the end user but also on the level of accuracy required. There is a compromise between the accuracy and the CPU time. On top of that, it can also be useful to integrate the control system into the MBS environment. For instance active suspension or ABS and ESP systems introduce strong coupling between the vehicle model and the controller [2].

Typically each modelization is independent from each other, meaning engineers are facing considerable effort to pass from one model to the other. Input data is also not exchangeable, adding uncertainty to the consistency and even correctness of the input data during model creation.

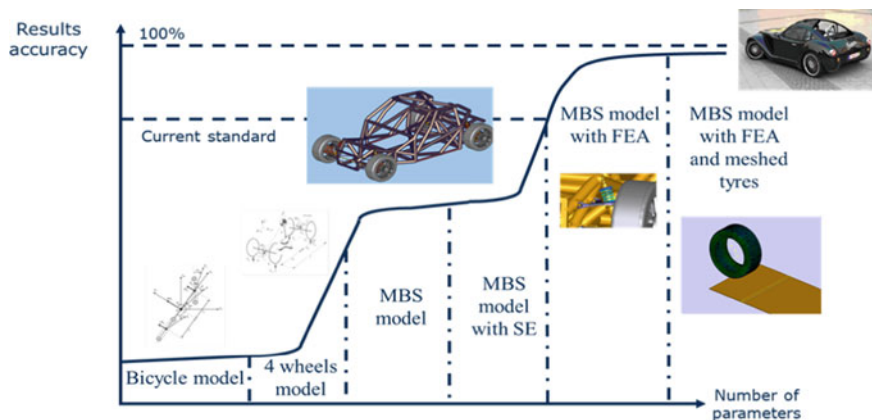


Fig. 1 Driving dynamics modelling hierarchy

The need of an integrated simulation solution represents a fundamental step to ensure increased productivity and guaranteed consistency.

2.1 1D Modelling

LMS Imagine.Lab Vehicle System Dynamics (see Fig. 2) offers dedicated capabilities to design individual chassis system components (such as brakes, suspension, steering, anti-roll system and the vehicle itself) and integrate them in a single system model in order to simulate and validate global chassis control strategies.

With LMS Imagine.Lab Braking System, LMS Imagine.Lab Power Steering and LMS Imagine.Lab Suspension and Anti-Roll, LMS provides reliable and accurate models to design robust chassis systems and components (booster, valves, active dampers, etc.) early in the process as well as validate and test control strategies using model-in-the-loop, software-in-the-loop and hardware-in-the-loop methods [16]. These can give the Engineer an understanding of issues specific to each sub-system, such as the noise and vibration behaviour of braking systems, shimmy phenomenon of power steering systems and improved damper design versus cavitation.

In addition, LMS Imagine.Lab Vehicle Dynamics offers a comprehensive vehicle dynamics library for real-time simulation or real-time hardware, including parametric functions to modify the shape of kinematic tables in order to optimize the vehicle behaviour.

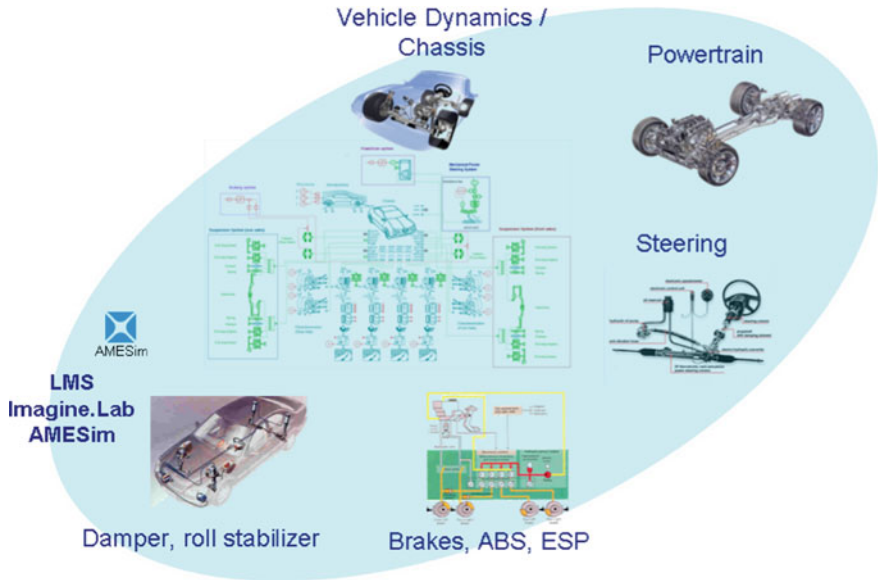


Fig. 2 Positioning of LMS Imagine.Lab AMESim for vehicle system dynamics

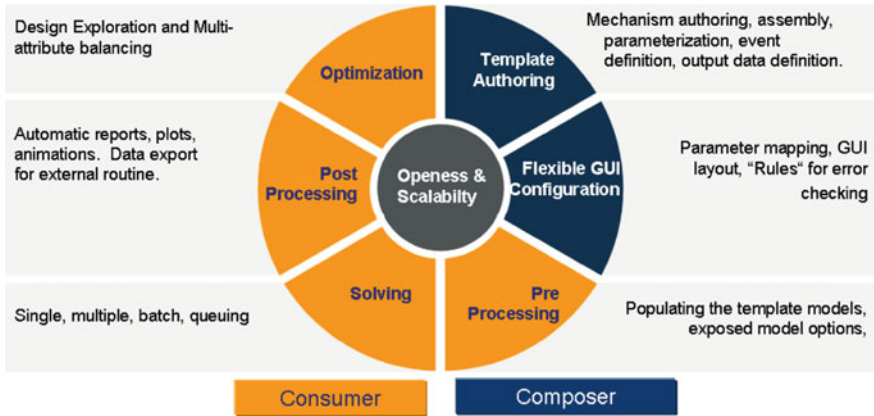


Fig. 3 Driving dynamics solution with LMS Virtual.Lab motion

2.2 3D MBS

LMS Virtual.Lab Vehicle Motion (see Fig. 3) simulates all types of vehicles' ride and handling behaviour, from passenger cars and motor sport vehicles to multi-axle vehicles like trucks and buses [12, 13].

Front- and rear-axle suspension models created in LMS Virtual.Lab Suspension can easily be integrated into a full-vehicle model. The time-domain analysis covers

everything from the conceptual rigid body model evaluation to high-fidelity model performance with full trimmed body details and various kinds of non-linear effects. The out-of-the-box vehicle solution's predefined templates allow efficient simulations of multiple runs with standardized events, for quarter-vehicle, half-vehicle and full-vehicle events. The available library of pre-defined vehicle events, including ISO manoeuvres, can be extended by any user-defined event. The car can be driven through a kinematic driver or through a path-following control algorithm implemented in LMS Virtual.Lab Motion or the IPG Driver model, including complex driver-vehicle interaction to include human reactions.

LMS Virtual.Lab Vehicle Motion Real Time guarantees high fidelity full vehicle multi-body models, potentially beyond 150 DOF, fully interfaced in any available hardware system [14].

Today, LMS Virtual.Lab Motion is available in a fully integrated Plug'n'Play automated solution thanks to LMS Virtual.Lab Composer and VBA (Visual Basic Applications) journaling and scripting. LMS Virtual.Lab Composer enables customization without coding and contains all of the requisite building blocks for accessing core solver technologies with simple drag-and-drop functionality. Together with VBA scripts, it automates any repeatable process, saving a large amount of time by eliminating highly repetitive tasks and concretely allowing the optimization of the design.

Accurate tire and road modelling are vital when using motion simulations as input for downstream durability and comfort analysis with LMS Virtual.Lab Durability and LMS Virtual.Lab Noise and Vibration. LMS Virtual.Lab Motion offers a set of tire models dedicated to specific applications going from basic ride and handling analysis at low frequencies up to more complex comfort and durability analysis at higher frequencies: TNO MF-Tire and TNO MF-SWIFT, LMS-LBF CDT tire and COSIN F-Tire formats are supported.

To provide realistic road load data without the availability of detailed tire models or a digital road surface, LMS has developed a methodology based on Time Waveform Replication (TWR) in cooperation with leading automotive manufacturers. The LMS Hybrid Road Methodology, fully integrated in LMS Virtual.Lab Motion-TWR, translates measured road inputs on a predecessor vehicle to an equivalent road load data to be applied in simulation models of next-generation vehicles. Applying the road load cascading process on an unconstrained vehicle guarantees correct load input time histories at all interface hard point locations of any subsystem and component of the suspensions or of the body.

2.3 3D MBS Nonlinear FEA

LMS-SAMCEF Mecano (see Fig. 4) is the proper tool for simulating combined multi-body nonlinearities with FE solver, allowing higher accuracy. Many components in the automotive domain require additional modelling details, and have impact on the direct driver feeling:

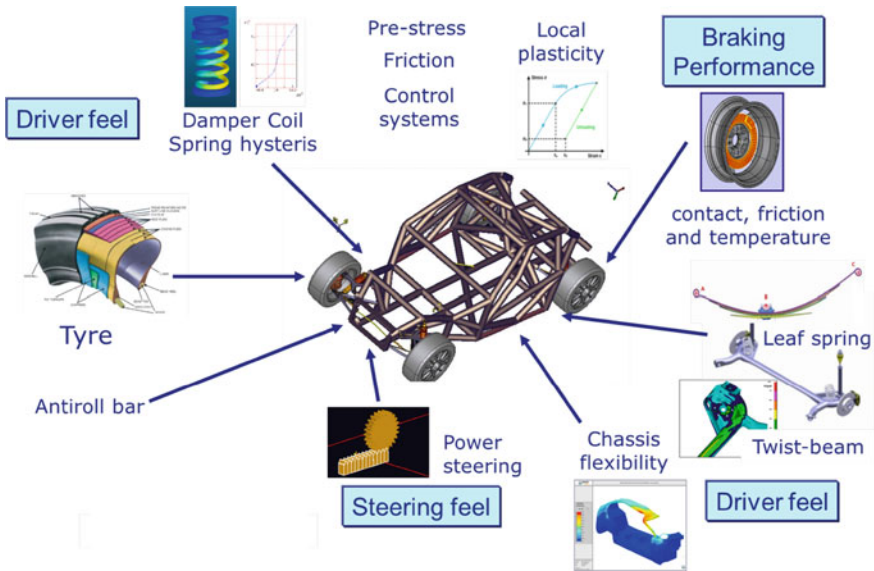


Fig. 4 Non-linearity for modelling accuracy with LMS-SAMCEF Mecano

- on the suspension geometry effect the twist beam architecture model;
- on the suspension hysteresis the bushing non-linearity and coil spring—or leafspring;
- on the steering feeling the contact, friction forces and free play in the steering rack;
- on the braking judder and squeal the detail modelling of the brake temperature effect;
- on the transmission the detail representation for differentials, steering wheels, drive shaft joint, etc.

LMS-SAMCEF Mecano uses a finite element approach with an implicit solver, augmented by Lagrangian method and rotation vector theory. Non-linear FE capabilities include geometric nonlinearities (large deflections and rotations and large strains), non-linear material laws (elasto-plasticity, visco-elasticity, hyper-elasticity, etc.), temperature dependency and frictional contacts. Thus covering the entire range of nonlinearities in one single environment and avoiding the exchange of data between standalone MBS and FEA software.

2.4 Integration in the 1D-3D Environments

Efficiency in simulation can be achieved from the proper application of 1D physics based and 3D geometry simulation. The combination of LMS Virtual.Lab Motion and LMS Imagine.Lab AMESim allows an efficient scalable simulation process

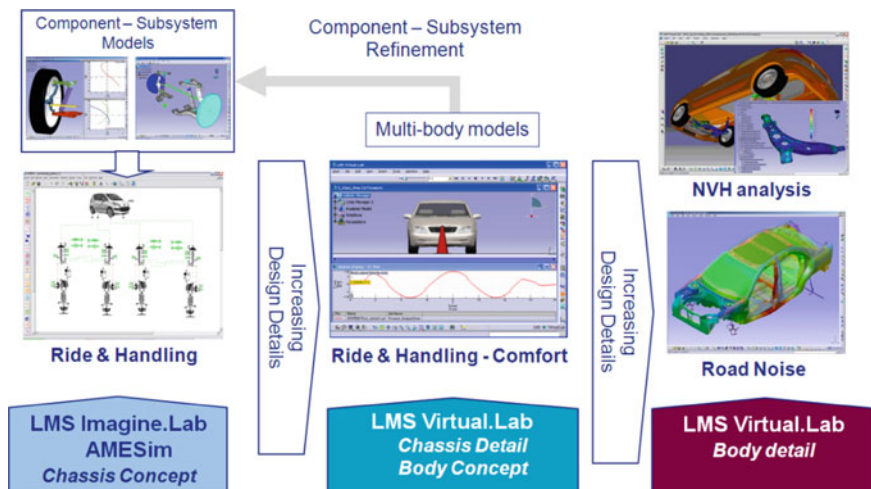


Fig. 5 Scalable 1D-3D simulation process for vehicle dynamics

(see Fig. 5). In LMS Imagine.Lab AMESim models can be built for chassis concept analysis, based on libraries for suspension components (elasto-kinematic representation). Many different layouts and variations of suspensions can be studied for many different vehicle configurations—for instance, loading. As detailed designs become available for the actual suspension, and body concept is available, one can further transit to a 3D model in LMS Virtual.Lab, expanding also the realism of the simulation including ride comfort—by taking into account flexibility of subframes, vehicle body, and appropriate tire modelling.

Direct co-simulation between LMS Imagine.Lab AMESim and LMS Virtual.Lab Motion enables complex chassis interactions to be tackled, such as those between the mechanical and the hydraulic systems, or analysing the shimmy phenomenon or the steering handling.

3 Modelling of Structural Nonlinearity

Even with the integration of Super-Elements, structural nonlinearity cannot be accurately simulated in MBS environment [5, 9, 15]. It is clear that medium frequency vehicle dynamics simulation can only be performed with nonlinear FEA software [6, 7, 10].

The sources of local non-linearity are numerous in vehicle dynamics: pre-stress, bushings, contacts, tires... One of the easiest ways to treat non-linearity is to use semi empirical models such as the well-known “Magic Formula” developed by Pacejka [1] for the tire models or spline curves for suspension stiffness. A similar methodology is applied to model bushings and dampers. Nevertheless, as the model is empirical and not physical uncertainties about the quality of the model

are always present. A tuning of the model is also difficult as the model is not physical and consequently relies more on experience than on pure analytical techniques. These alternative methods provide therefore little or no direction on what is needed to solve. Furthermore, for higher non-linearity and frequency, the uncertainty can become very important and have a non-negligible impact on the validity of the simulation results. This is typically the case for the modelling of phenomenon that cannot be handled by classical MBS package, due to its lack of nonlinear FEA capabilities for local structural nonlinearity such as contact between surfaces or material non-linearity. These phenomena have to be modelled as geometrical effect such as elasto-kinematics of a twist-beam suspension, or even for combined effects such as in the leaf-spring modelization.

This deficiency in current MBS simulation software shows the need for a new solution procedure capable of simulating such phenomenon while also including the classical methodology.

3.1 Formulation of the Motion in FEA Problem

In the nonlinear finite element method, the system of equations to be solved is given in Eq. (1):

$$M.\ddot{q} = g(q, \dot{q}, t) \tag{1}$$

where:

- M mass matrix
- q displacement
- g forces (internal and external)

When constraints Φ are considered (e.g. relations between degrees of freedom to make a motion useful for a desired purpose, i.e. kinematical constraints or joints), the problem to be solved is based on the stationary of an augmented Lagrangian defined by the kinetic and potential energies and two additional terms related to the constraints including a penalty factor and the Lagrangian multipliers λ . It turns that the system of nonlinear equations to be solved is given by Eq. (2):

$$\begin{cases} M.\ddot{q} + B^T.(k.\lambda + p.\Phi) = g(q, \dot{q}, t) \\ \Phi(q, t) = 0 \end{cases} \tag{2}$$

where:

- Φ constraints
- λ Lagrangian multipliers
- p penalty factor
- k scaling factor
- $B = \frac{\partial \Phi}{\partial q}$ Gradients of the constraints

The relations between the degrees of freedom representing each joint are added to the global system of equations usually solved in the nonlinear finite element method. These are written in the Motion of FEA formulation. Detailed equations and solution procedures can be found in [3, 4].

3.2 Implicit Time Scheme Integration

The Newmark or the HHT schemes are used for the time integration. These two methods are implicit time integration methods. They offer the advantages of being unconditionally stable compared to explicit integration methods. Indeed the stability of the explicit method depends on the time step. Above a certain time step, dependent on the mesh size, convergence issues may arise. Consequently a small time step has to be chosen which makes the calculation time very long. The implicit integration method does not suffer this drawback and is therefore well adapted for vehicle structural dynamics simulation. For each time step, the nonlinear system is solved by the Newton–Raphson method.

Several possibilities are available for the integration of dynamic nonlinear system divided in two families of different solvers: explicit methods and implicit methods. LMS-SAMCEF Mecano uses the Hilber-Hughes-Taylor (HHT) method (also known as the alpha-method). This method will be shortly described.

A precursor of the HHT method is the Newmark method in which the integration formulas depend on two parameters β and γ (see Eq. 1).

$$\mathbf{q}_{n+1} = \mathbf{q}_n + \mathbf{h} \cdot \dot{\mathbf{q}}_n + \frac{\mathbf{h}^2}{2} [(1 - 2\beta) \cdot \ddot{\mathbf{q}}_n + 2\beta \cdot \ddot{\mathbf{q}}_{n+1}] \quad (1a)$$

$$\dot{\mathbf{q}}_{n+1} = \dot{\mathbf{q}}_n + \mathbf{h} \cdot [(1 - \gamma) \cdot \ddot{\mathbf{q}}_n + \gamma \cdot \ddot{\mathbf{q}}_{n+1}] \quad (1b)$$

with \mathbf{q} , \mathbf{q}' and \mathbf{q}'' respectively displacement, velocity and acceleration vector.

The Newmark method is explicit at the position and velocity at time t_{n+1} depend on the acceleration at time t_{n+1} .

This Newmark method is implicitly stable provided:

$$\gamma \geq 1/2 \quad (2a)$$

$$\beta \geq \frac{(\gamma + 1/2)^2}{4} \quad (2b)$$

The HHT method is unconditionally stable provided $\alpha \in [0, 1/3]$ and:

$$\gamma = \frac{1 + 2 \cdot \alpha^2}{2} \quad (3a)$$

$$\beta = \frac{(1 + \alpha)^2}{4} \quad (3b)$$

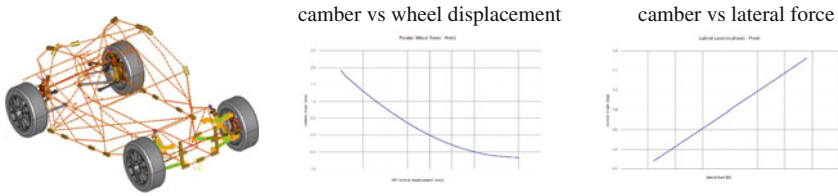


Fig. 6 Compliance with meshed parts

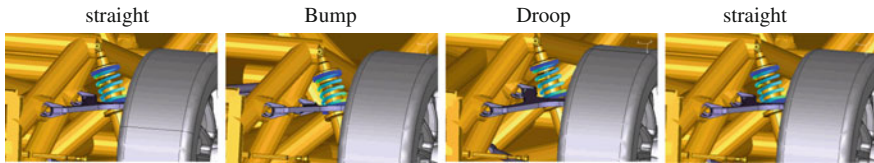


Fig. 7 Main spring in different front suspension set-up configurations

The advantage of the HHT method is the numerical damping which has a stabilizing effect on the time integration procedure. The smaller the value of α , the more damping is induced in the numerical solution. Note that in the limit, the choice $\alpha = 0$ leads to no numerical damping while $\alpha = 1/3$ generates maximum damping. In LMS-SAMCEF Mecano, it is generally recommended to use an intermediate value ($\alpha = 0.05$ for example).

This problem is solved iteratively using Newton’s method for each time step. As the HHT integration method is unconditionally stable there is no limit on the size of the time increment. In general, implicit methods are stable for larger time steps than explicit methods. This leads to a reduced number of function evaluations and therefore a more efficient algorithm. Consequently the use of HHT is perfectly suited for the simulation of vehicle dynamics.

4 Applications and Examples

A list of examples showing the need of combined MBS and FEA approach in vehicle dynamics is presented in the following sections.

4.1 Suspension Compliance Prediction

Suspension compliance results from the application of the tire forces at the contact patch. They lead to deformation of the suspension (see Figs. 6, 7). Suspension compliance is known to affect both handling and comfort. Predicting and optimising the suspension compliance is a very complex task as forces and moments

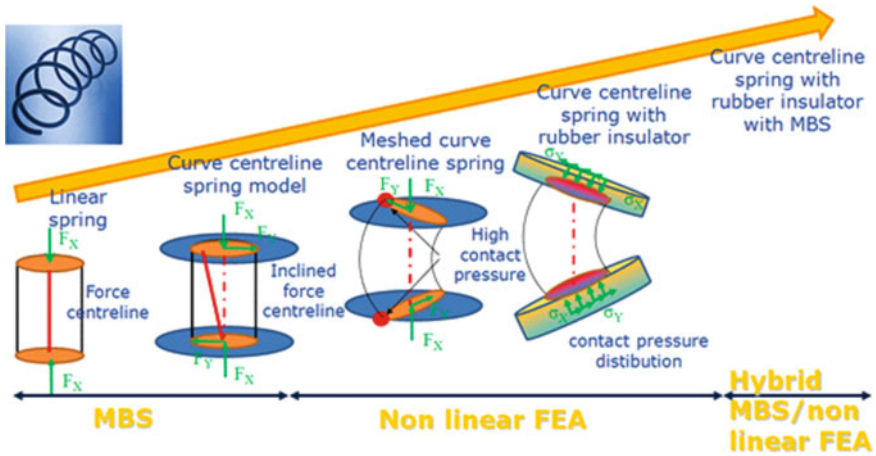


Fig. 8 Spring model complexity

are applied in the tire contact patch. On top of that, the requirements are most of the time contradictory for ride (soft) and handling (stiff). The differences between test rig and simulation reveal the importance and necessity of using a nonlinear FE model (even simply using deformable beam elements) to include the component flexibility in vehicle chassis/suspension dynamic analysis.

Theoretically kinematics and compliance should not be assessed separately from one another as the attachment points of the suspension are affected with a first order effect of the motion of the suspension but also affect the flexibility with a second order. In current MBS simulation, the hysteresis cannot be accurately modelled because it results from complex 3D contact/friction with elastomer parts, pre-stresses and non-linear material interactions.

4.2 Curved Centreline Spring in McPherson Strut

Undesired lateral force inevitably exists in a MacPherson suspension system leading to friction in the damper tube because of bending moment (Fig. 8).

This bending moment has a consequence on the ride performance but also leads to an excessive wear of the damper tube (see Fig. 9).

To minimize or even eliminate this problem, one possible solution requires tilting the coil spring with regards to the damper. This solution is nevertheless not always feasible for packaging reasons. Another solution to avoid conflicting with the packaging is the substitution of the conventional coil spring with a new side load spring with curved centreline (see Fig. 9) sometimes called side-load spring. With an appropriate design of the curvature such a spring can generate a side load when compressed or elongated. The side-load spring itself but also the integration of the side-load spring in the suspension system needs to be optimised all together

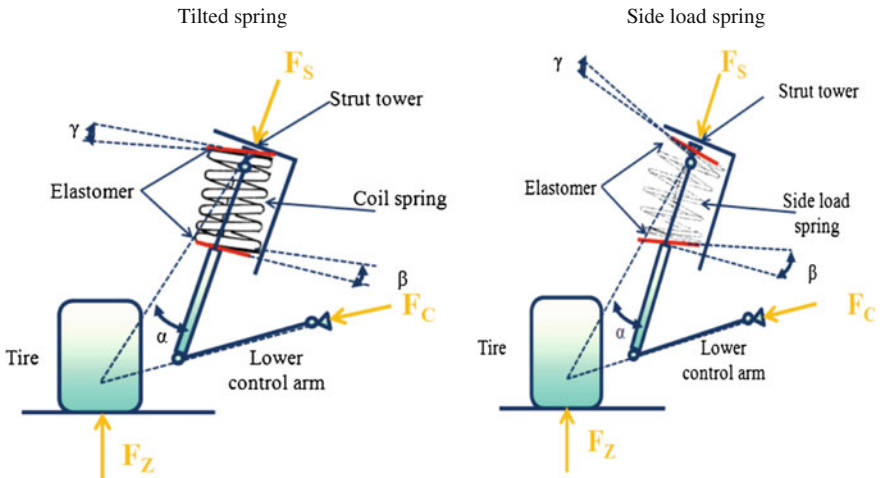


Fig. 9 McPherson sketch

as the position of the attachments points are of critical importance. Indeed for a curve centreline spring, the force is no longer in the axis of the spring but can have transverse components and also moment components. It is clear that alternative methods to FEA can be used to calculate the response of such a spring. Nevertheless it will not give accurate results. Optimization will not be robust as it will be based on simulation results that lack accuracy. Consequently tuning will be needed on the physical prototype. With such a spring, it is therefore mandatory to use a combined nonlinear FEA/MBS approach to have an accurate numerical simulation. Otherwise data exchanges between the MBS and FEA software will be needed and the fine tuning will be time inefficient and maybe even not converging.

4.3 Interaction Between Coil Spring and Rubber Insulator

As seen in the previous section, the friction in the suspension has a direct impact on ride comfort and alternatives need to be found to classical suspension design to optimise the comfort. Again for the particular case of the McPherson suspension, the position of the spring on the rubber insulator is therefore of critical importance with regard to comfort and low frequency vibration.

There are different sources of non-linearity in the McPherson suspension taking into account the rubber insulator:

- large strain of the rubber,
- large displacements of the coil spring
- contact between the spring and the elastomer and possibly between the coils. These contacts present significant difficulties in achieving numerical convergence during the solution process.

Fig. 10 Coil spring integrated in the vehicle model



The spring and the insulator were first modelled separately with nonlinear FEA before being integrated in a classical MBS model once validated (see Fig. 10). The complete model of the car contains rigid bodies, Super-Elements and also meshed parts to represent the different parts of the vehicle. It was decided to use rigid body for some components as they were not of direct interest for the study. This enables a better computing efficiency.

Thanks to the combined non-linear FEA/MBS approach, the effects of some design parameters can be investigated:

- the orientation of the upper spring seat,
- the orientation of the lower spring seat,

the translational offset of the lower spring seat in the lateral direction; with the possibility to calculate the hysteresis of the entire suspension, as mainly due to the parasitic forces (lateral forces) acting on the main spring.

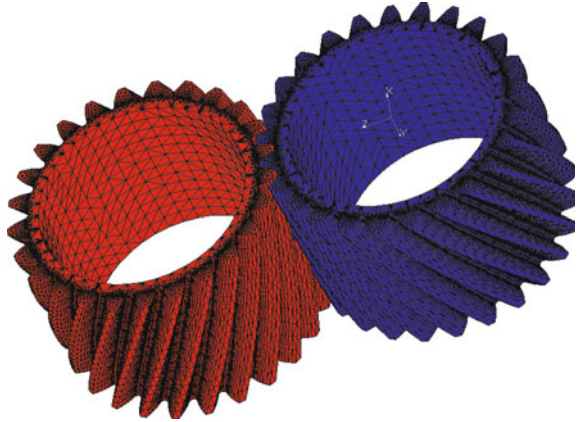
It can be seen that the properties of the elastomer of the insulator enable a reduction of:

- the axial resonances of the spring;
- the force transmitted to the body;
- the amplitude of the vibration of the coils and therefore the risk of contact between the coils.

The bending of the spring generates in fact an additional moment which cannot be simulated with classical MBS software. The hybrid non-linear FEA/MBS approach also enables estimation of the contact pressure with the rubber insulator. This helps by indicating the high contact pressure location and can therefore help in optimising the shape of the rubber insulator for better noise and vibration.

The results obtained underline the importance of integrating the rubber insulator into the suspension subsystem for the optimization of the MacPherson suspension. This study therefore opens the way to propose optimal solutions in terms of comfort and endurance. This optimal design cannot be investigated by classical MBS programs because of the complex nonlinearity. The problem can only be solved by the synergy of a MBS and a nonlinear FEA program as the kinematical joints are mandatory to simulate the compression of the spring because of suspension movements.

Fig. 11 Worn and worn wheel



4.4 Torsion Beam and Leaf Spring Suspension

Torsion beam and leafspring suspensions are widely used for rear suspension on front wheel drive passenger vehicle with small to medium size. Main advantages of these suspension geometries are the simplicity and the small number of components offering maximum space usage combined with a low manufacturing cost. Despite the simplicity, the accurate simulation requires nonlinear FEA as the torsion beam and leafspring can undergo significant nonlinear displacement for specific manoeuvres. Contact adds damping for the leafspring suspension which cannot be modelled with MBS software. The nonlinear deformation is further exaggerated for manoeuvres like braking on a pothole for one wheel as large rotation takes place in the beam section. Classical flexible MBS software can only support linear structural compliance and is therefore valid only for small deflections. For large structural deflections, non-linear structural compliance must be represented for accurate results using a non-linear FEA tool. With a combined non-linear FEA/MBS approach, a better prediction of the toe and camber compliance under longitudinal and lateral load will be possible. Otherwise only a linear compliance value will be computed. For small lateral acceleration manoeuvre, this is acceptable as the force generated by the tire is small but in the case of heavy cornering or heavy braking manoeuvres nonlinear deformations occur and the assumption of linear compliance is no longer valid.

4.5 Steering System

The steering system is a complex mechanical system involving either hydraulic or electric. Within classical MBS environment, rack and pinion steering system is modelled thanks to rigid body called gear element (see Fig. 11) which does not enable having the full dynamics of the steering system and the vibrations induced [8].

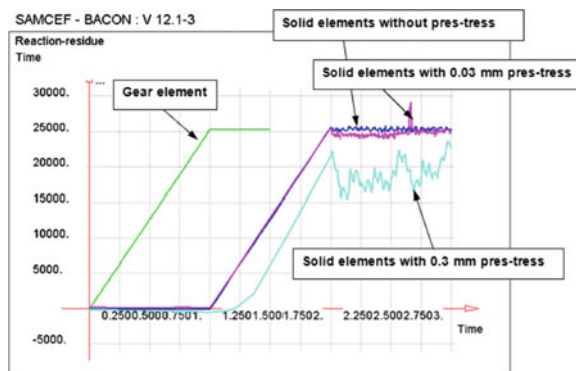


Fig. 12 Comparison of wheel torque reaction for the different quasi-static analyses

With a hybrid MBS/FEA approach, it is possible to mesh the gears and determine the influence of the level of pre stress.

Looking at results obtained with the four simulations (gear element, meshed gear with three different pre stress level), we can observe that the reaction forces, the transmission efficiency and the angular velocity are quite the same in the four different cases (see Fig. 12).

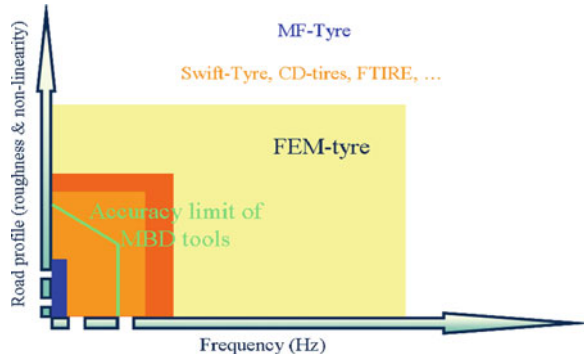
However, it is possible to observe that gear element is not able to simulate the high dynamic compared to meshed gear with pre-stress. The pre-stress induce a contact between several teeth that cannot be considered by classical gear element. As expected, the pre-stress of 0.03 mm decrease slightly (around 1,000 Nmm) the reaction torque. With a pre-stress of 0.3 mm, the assist torque requested to rotate the worm is much important (start at 1.2 s), the reaction torque decreases more and is much noisier.

4.6 Tire

The tire is the component of the vehicle having the most important influence on vehicle dynamics. The modelling of rubber tires involves many nonlinear phenomena: geometric material, contact... Several commercial tire models have been developed in order to extend the modelling capabilities for tire simulation [1] & [11]. All these models are said to be valid up to at least 100 Hz which is far beyond the capabilities of rigid MBS software (see Fig. 13).

Therefore, the capabilities of advanced tire models are often limited by the capabilities of the MBS software. Traditional MBS software is not able to simulate up to a suitably high frequency and must be supplemented by flexible components such as FEM or even non-linear FEM model components. For certain applications, the commercial tire models are not accurate enough and a complete FEM tire model is imperative. For such simulation a hybrid FEM/FMD approach is needed.

Fig. 13 Tire models validity



4.6.1 Optimization

With the aim of reducing components weight, optimization has become very popular in the automotive industry. Optimization can involve either topology or shape. In the case of the part shape optimization, the modification of the part also implies the modification of its mechanical properties like stiffness, inertia and natural frequencies. Consequently a change in the part affects the overall dynamics of the mechanical system that contains this part. Additional complexity can come from the interaction with the control systems.

For an optimization criteria based on fatigue analysis, the load/time histories of the stress is of critical importance. As a consequence, the load extracted from a MBS will no longer be accurate if used for a shape optimization and that can lead to erroneous design.

The optimization of a single component is not robust as all the interactions with the other components are not accurately taken into account. The next step in optimization is to optimize not only the sub-system in which the part is included but also the complete system. The optimization of the global complex system can only be done thanks to the coupling of non-linear FEA/MBS approach as otherwise too much data exchange will be needed between the different platforms: 1D functional modelling, MBS, linear FEA, non-linear FEA and eventually fatigue software.

This new procedure will obviously be at a cost of increasing CPU time but the gain with the reduction of building prototypes can more than compensate this increase.

5 Conclusions

The competitive environment in the automotive market requires early assessment in the design interaction between the parts and systems. For vehicle dynamics, this interaction between the different elements of a vehicle can only be done through a

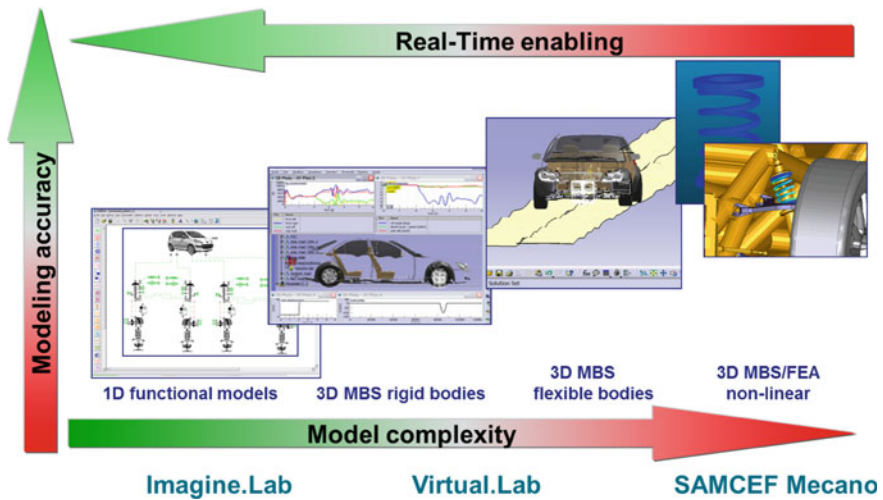


Fig. 14 Driving dynamics integrated simulation solutions

monolithic non-linear FEA approach embedding MBS when local structural non-linear phenomena occur. LMS-SAMCEF Mecano enables modelling a wide range of problems in vehicle dynamics in one single environment. However, this method can also be used for classical MBS or FEA analyses, with the big advantage that the same simulation tool can be used from early pre-design activities (mechanism synthesis, kinematics, load estimation) to detailed stress analysis. An integrated 1D-3D solution with easy-to-use data exchange becomes then fundamental for improving modelling productivity (see Fig. 14).

The Finite Element approach complemented with MBS developed in LMS-SAMCEF Mecano allows extending the field of dynamics simulations to medium frequency range and to systems involving higher level of non-linearity.

References

1. Pacejka HB (2002) *Tire and Vehicle Dynamics* 2nd ed, Butterworth-Heinemann Ltd, London
2. Wissart T, Trost P, Grosgeorge S (2011) Multi body systems inside FEA for structural nonlinearity in vehicle dynamics simulation, 13. Internationale VDI-Tagung mit Fachausstellung, VDI, Hannover, 25–26 Oct 2011
3. Zienkiewicz OC (1977) *The finite element method*, 3rd edn. McGraw-Hill, New York
4. Craig R, Bampton M (1968) Coupling of substructures for dynamic analyses, *AIAA J*, 6(7): 1313–1319
5. Géradin M, Cardona A (2001) *Flexible multi-body dynamics: a finite element approach*, Wiley, New York
6. SAMCEF: Système d'Analyse des Milieux Continus par Eléments Finis, www.samtech.com

7. Voss B, Cugnon F, Prétot Ph, Granville D, Bruyneel M (2009) Advances in vehicle dynamics simulation with SAMCEF Mecano. In: 15th International conference on vehicle dynamics, SIA, Lyon, 23–24 Sept, 2009
8. Virlez G, Brüls O, Poulet N, Duysinx P Multi-body dynamics analysis of differentials in vehicle drivetrains. In: The 1st joint international conference on multi-body system dynamics
9. Fischer E (2007) Standard multi-body system software in the vehicle development process. IMechE Part K J Multi-body Dyn 221(1): 13–20
10. Cugnon F, Cardona A, Selvi A, Palenczny C, Pucheta M (2008) Synthesis and optimization of flexible mechanisms. Multi-body dynamics, book Series on computational methods in applied sciences, vol 12, Springer, Netherlands
11. www.cosin.eu
12. Gubitosa M, Cugini U, De Cuyper J (2007) A virtual prototyping approach to vehicle dynamics using a CAD based MBS simulation software, MSc Thesis at Politecnico di Milano, Milan
13. De Cuyper J, Furmann M, Kading D, Gubitosa M (2007) Vehicle dynamics with LMS Virtual.Lab Motion. Vehicle Syst Dyn, 45(S1): 199–206
14. Prescott WC (1999) Numerical integration technique for multi-body dynamic system software. In: Symposium on international automotive technology, Pune, Jan 1999
15. Blundell M, Harty D (2004) The multi-body systems approach to vehicle dynamics. Society of Automotive Engineers, Inc. 400 Commonwealth Drive, Warrendale
16. Alirand M, Lebrun M, Richards CW (2001) Front wheel vibrations: A hydraulic point of view—models and first results, SAE Paper n° 2001-01-0490, pp 1–14

Transmission System Design and Manufacture in FSC Racing Vehicle

Zhenpo Wang, Changfu Zou, Lei Yue and Lei Zhang

Abstract This paper is mainly devoted to transmission system design and manufacture in FSC vehicle. Based on the rules of FSC and design goals on the vehicle, the principle for FSC transmission system design is proposed. The optimal transmission ratio is gained from both the classic formula of vehicle dynamic and analysis in Matlab. Chain transmission system and the idea of its integrated design are adopted. To optimize the system, different scenarios are considered including various constraints and configuration through modelling and simulating in Solidworks. With a balance among lightweight, stiffness and strength, we build up a transmission system fitting to FSC vehicle, and the results of long-term test show that it is reasonable and efficient. Finally, some practical problems and their solutions are discussed and references for the future relative research are provided.

Keywords FSC · Racing vehicle · Chain transmission system · Dynamic performance · Optimization

1 Introduction

FSAE is initiated by the U.S. With more than 30 years' development, it has become an annual grand event for young engineers from global top universities. Formula Student China (FSC) is a new competition, carefully orchestrated by

F2012-E13-014

Z. Wang (✉) · C. Zou · L. Yue · L. Zhang
National Engineering Laboratory for Electric Vehicles, Beijing Institute of Technology,
Beijing, China

SAE-China and its cooperating societies after learning and summarizing relative experience from America, Japan, German and other countries. University students are required to design and manufacture an amateur leisure racing car comprehensively considering vehicle performance, cost and market value while satisfying certain rules. FSC vehicle is popular for its power acceleration and smart steering ability. To provide such performance, a reliable, stable and efficient transmission system is greatly important, especially at extreme speed, urgent acceleration and sharp turns. There are few academic papers researching FSC vehicle transmission system. This chapter takes the second FSC vehicle from Beijing Institute of Technology as the example to discuss and analyze engineering design and the requirements of competition.

2 Design Goals and Scenario

Besides normal function [1], transmission system in FSC vehicle needs to have the following characteristics. It should steadily delivery power to wheels. Its power loss and moment of inertia should be as small as possible. Meanwhile, it should possess high efficiency and smart response. According to the above analysis, the principle of transmission design is summarized as follow: meeting the dynamic requirement in acceleration time, maximum speed and maximum grade ability, conforming to reliable transmission, smart response and lightweight design, and satisfying the FSC rules [2].

With given engine characteristic and wheels' parameters, transmission design not only includes parameters calculation and modelling for the whole system, but also need to be in harmony with frame and suspension. After analysis of design goals on dynamic performance, transmission ratio can be gained. Then, a reasonable transmission mode is proposed and a main reduction is designed. Finally, we design and match all components and parts assembled in drive shafts, and their layouts is further determined.

3 Overall Design of Transmission System

In "Black Shark II", the FSC vehicle of Beijing Institute of Technology, CBR600F4i engine is applied, with a six-gear mechanic gearbox inside. The characteristic of engine and ratios of each gear in gearbox are known. Transmission ratio can be designed according to overall parameters. Considering the accuracy and flexibility of driver's operation at some complex conditions, six gears are too many while three or four ones are proper. Four gears are utilized in practical design. Important overall parameters are listed in Table 1.

Table 1 Overall parameters of vehicle design

Maximum speed	>= 120 km/h	75 m acceleration time	<= 4 s
Maximum grade ability	10 %	Complete vehicle kerb mass	<240 kg
Number of gears	4	Minimum ground clearance	25.4
Axle distance	1,550	Rear wheel distance	1,170
Transmission efficiency	>90 %	Spline fit precision	>H6

3.1 Transmission Ratio

Main reduction is designed to reduce rotate speed and accelerate torque delivered to wheels. Generally speaking, in a certain range, if transmission ratio is bigger, the speed will be lower and the acceleration ability will be better, vice versa. However, both maximum speed and acceleration ability are key factors of vehicle dynamic performance. Thus, it is necessary to find an appropriate ratio to accomplish the competition in minimum time.

Firstly, we attempt to calculate the transmission ratio in accordance with the maximum speed. There are five different dynamic events judging the FSC vehicle, i.e. 75 m Linear Acceleration, Skidpad Event, Autocross Event, Endurance Event and Fuel Economy Event. According to our experience, the maximum speed is about 120 km/h. It is sufficient and reasonable to primarily set it to 130 km/h. Based on speed formula [3] in Vehicle Kinematics, we can get the maximum speed $u_{a,max}$:

$$u_{a,max} = \frac{0.377r \cdot n_{max}}{i_{g,min}i_0} \quad (1)$$

From the above equation, it is easy to deduce i_0 :

$$i_0 = \frac{0.377r \cdot n_{max}}{u_{a,max} \cdot i_{g,min}} \quad (2)$$

where, n_{max} is the highest engine speed. r is radius of wheel. $u_{a,max}$ is the maximum speed, $i_{g,min}$ is the largest transmission ratio of gearbox, i_0 is main conduction ratio. Substituting the known data to Eq. (2), we can achieve the relationship between the main reduction ratio and the maximum speed at different gears. Comparing different main reduction ratios, when it is 3.5, the maximum speed is approaching the aimed maximum speed, so we can make it as the primary value, and the result is tabulated in Table 2.

Secondly, the main reduction ratio is calculated on the basis of acceleration time. The design goal for 75 m linear acceleration time is within 4 s, which is indicated in Table 1. Synthesizing force balance equation and the definition of power factor, we can derive:

Table 2 The relationship of final reduction and speed

Gears	Maximum rotating speed/rmin ⁻¹	Main reduction ratio	Gear ratio	Wheel diameter/in.	Speed/km h ⁻¹
4th gear	13,500	3.5	2.605	18	128
3rd gear	13,500	3.5	3.019	18	110
2nd gear	13,500	3.5	3.780	18	88
1st gear	13,500	3.5	5.193	18	64

$$\begin{cases} \frac{T_{ig} i_g \cdot i_0 \eta_T}{r} = mgf + \frac{C_D A}{21.15} u^2 + \delta m \frac{du}{dt} \\ D = \frac{F_t - F_w}{G} \end{cases} \quad (3)$$

By solving Eq. (3), the acceleration can be reached:

$$a = \frac{du}{dt} = \frac{g}{\delta} (D - f) = 9.423(D - f) \quad (4)$$

Meanwhile, it is easy to know that

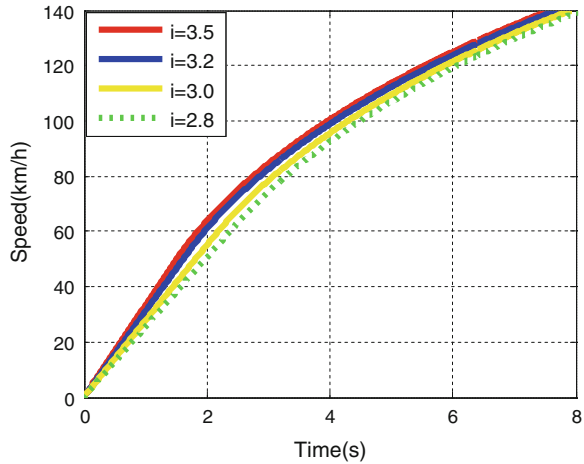
$$t = \int_0^t dt = \int_{u_1}^{u_2} \frac{1}{a} du \quad (5)$$

and acceleration distance

$$S = \int_0^t u(t) dt \quad (6).$$

Integrating Eqs. (4)–(6), we can gain two functions, acceleration time function of time and acceleration distance function of time. The acceleration time curve and acceleration distance curve are plotted with Matlab. It is obvious that acceleration time of any specific distance and speed can be found on the curves, which is shown in Fig. 1. To achieve optical solution, varieties of main reduction ratios are comparatively analyzed, and the results can be clearly seen in the below figure. If $i_0 \leq 3.5$, 100 km/h acceleration time will decrease when the value of i_0 increases. Additionally, the number of i_0 is more and the interval between adjacent two values is less, the main reduction ratio is more approaching the most optical solution.

Fig. 1 Speed to time under 4 different final reductions



3.2 Transmission Mode and Layout of Transmission System

It can be found in FSC rules [2] that axle distance should not be more than 1.525 m. Therefore, the layout of transmission system is demanded to be compact. Since engine capacity is not allowed to over 610 cc, lightweight design for transmission system is essential to enjoy perfect dynamic performance. After comparing with shaft transmission and belt transmission, we can find that chain transmission have distinct advantages: foremost, it will not present elastic slide and sliding phenomenon at work, so its average transmission ratio is accurate and its efficiency is higher than 95 % [4]. What's more, it can significantly ease shock vibration. Its size is compact and can be easily arranged. Low accuracy requirement for Installation and low cost are also its advantages. According to the above analysis, we can draw a conclusion for transmission mode “Gearbox + chain transmission”.

Besides engine which is mounted transversely and chain transmission system, drive axle including differential, halfshafts, CV joints, etc. needs to be arranged. In order to make the figuration more impact and the weight lighter, as well as increase the stiffness of powertrain system, integrated design is employed, i.e. to combine transmission system and engine into a whole, which can be seen in Fig. 2.

4 Design for Components and Parts

4.1 Design for Chain and Chain Wheel

From the point of lightweight design, chain wheels said the smaller the better while satisfying the requirements of strength and stiffness, meanwhile, it enables to

Fig. 2 Layout of transmission system. 1 Big chain wheel, 2 differential, 3 engine, 4 connecting piece, 5 tension mechanism, 6 joint, 7 halfshaft, 8 frame, 9 suspension

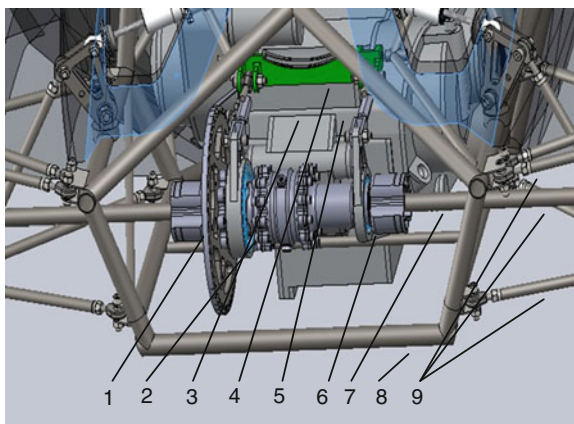
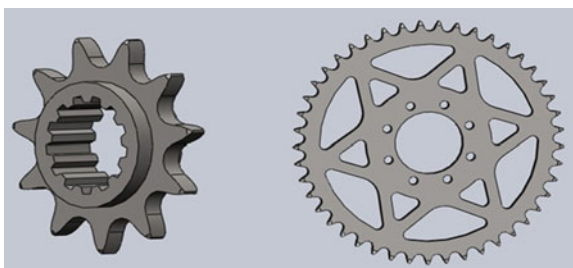


Fig. 3 Small chain wheel's model and big chain wheel's model



reduce size interference and facilitate the arrangement of the whole system. During the detailed process, small chain wheel can be firstly designed. To protect the small chain, its wrap angle should not exceed 120° and the number of teeth meshing with chain at the same time is no less than 3. Obviously, the total number of teeth is larger than or equal to 9. On the other hand, if the teeth number of both chain wheels is chosen to be odd and prime, these chain wheels will be worn uniformly at work. Apart from the above general principles, the specific number of teeth can be reached by force analysis and check calculation on their models. After getting the data of splines of engine's output shaft, models of 9, 11, 13 and 15 teethes are respectively built up, and the small chain wheel's model of 9 teethes and its corresponding big chain wheel are showed in Fig. 3.

Because of $i_0 = \frac{z_2}{z_1}$, where z_1 and z_2 respectively refer to the number of teethes of small chain wheel and big chain wheel. In market, there are kinds of standardized chain wheels but they usually cannot meet the requirements of strength in racing car because they may be made of 45 steel, 20 Cr or other ordinary materials. Moreover, their size and mass are too big for our small FSC car. After check calculation, it is found that the big chain wheel made from aluminium alloy 7075-T6 whose mass is relatively light can sufficiently meet our requirements. Thus, it has been made by ourselves and used in our car. Furthermore, to pursue for

Table 3 Parameters of small and big chain wheel

Tooth of chain wheel	Pitch/p	Pitch diameter	Tip diameter/damax	Root diameter/damin	Chain number
11	15.875	56.3478	66.03153	59.7537	520
39	15.875	197.287	206.9707	202.3506	520

extreme lightweight design, many weight loss holes and grooves are arranged in chain wheel after considerate force analysis, as displayed in Fig. 3.

The basic variables like pitch/p, pitch number and centre distance need to be confirmed in chain design. After studying and summarizing the experience of the first FSC car and international top FSAE cars, No. 520 chain wheel is selected. And then the pitch, pitch number, array pitch can be looked up in the Machinery’s Handbook. Centre distance a_0 can be preliminarily chosen based on the arrangement of engine in frame and positions of front and rear axles. Therefore, pitch number L_p can be derived from the geometrical relationship in [5].

$$L_p = \frac{2a_0}{p} + \frac{z_1 + z_2}{2} + \frac{p}{a_0} \left(\frac{z_2 - z_1}{2\pi} \right)^2 \tag{7}$$

When p and L_p are known, based on the theoretical calculation formula of a_0 , we can get:

$$a = \frac{p}{4} \left[\left(L_p - \frac{z_1 + z_2}{2} \right) + \sqrt{\left(L_p - \frac{z_1 + z_2}{2} \right)^2 - 8 \left(\frac{z_2 - z_1}{2\pi} \right)^2} \right] \tag{8}$$

To guarantee the transmission loose edge has certain prolapse, the final center distance a_0 is smaller than a about 2–5 mm. And a round number from the value of a_0 is what we want. Main parameters of chain wheel and chain are listed in Table 3.

4.2 Differential

Tracks are full of many turns such as hairpin turns, chicanes and multiple turns in Skidpad Event, Autocross Event, Endurance Event and Fuel Economy Event. A proper differential to improve steering ability and control stability, and use the wheels efficiently, is of great importance. After comparing the three kinds of differential: Cross-axle, Torsen and Drexler, the type of Drexler V3 is used. Inside of this differential, there are several couples of friction plates, spring steel plates, thrust plates and V type cant, which can help to adjust locking factor. What’s more, its size and mass is small, and it is easy to cool and lubricate. So this differential will make great contribution to perfect performance in the above turns.

Table 4 Properties of materials chose for halfshafts

Materials	Tensile strength/ksi	Yield strength/ksi	Fracture spin rate/ %	Fracture toughness/ksi in ^{0.5}	Density/lbin ⁻²
Aermet 100	302	258	14.2	115	0.285
AISI4340	175.1	166.1	14.2	92	0.284
AISI4130	161	138	14.7	74.6	0.284
AL6061-T6	45	40	12	26.4	0.0975

4.3 Halfshaft

Main goals in halfshaft design are to confirm reliable driving, long life and small moment of inertia. Two scenarios are considered: one is carbon fiber halfshaft, the other is steel halfshaft. Presently, carbon fiber halfshafts are becoming more and more popular in FSC cars because its lightweight and high strength can reduce moment of inertia greatly. However, their shortages such as high price, relatively difficult machining of spline and high probability in producing crack, cannot be ignored. Under the condition of immature technology, they are not adopted in this work. There are series of high-strength steel and aluminum, as shown in Table 4. Ultra high-strength alloy steel, AerMet100, is chosen finally for its comprehensive performance to manufacture halfshafts.

4.4 Check and Optimization

Check analysis is an important part in transmission system design. Force analysis is processed in Solidworks/Simulation. New counting cases are created 2 with static limit load and fatigue dynamical load, respectively. Whilst, materials and models are set up based on the above choices. Stress, strain, displacement and safety factor are come out as results of these counting cases. Stress Analysis of a CV joint is showed in Fig. 3. Where, the value 1 is usually set to be the dividing line. For one thing, if safety factor is too small, reliability is poor, which demonstrates the design is too radical or not reasonable. For another, if safety factor is too large, then the design is too conservative that it does not meet the principle of lightweight design, as well as cause material waste. Each component is checked to keep excellent performance for the whole system.

Results of check and analysis provide good help to optimization including optimization in materials and design. Whilst, there are many aspects as follow in design optimization: correct wrong design, choose right size according to the different parts of the safety factor, increase fillets or chamfers to get rid of stress concentration, add weight loss holes or change the form of them, so that each part is correct and reasonable.

5 Typical Practical Problems and Their Solutions

5.1 Design for Tension Mechanism

The loosening phenomena in chain will appear in the following two situations: Due to the existence of gaps between chain pitches, chain will be elongated to a big extent when it is used for the first time. After a long period of operation, the supporting components in chain will be deformed and pitches will be further tightened to make the chain loose again. Therefore, chain needs to be regularly inspected and tensioned. In our car, we design a tension mechanism, as shown in Fig. 4, to make tightness of the chain adjustable. It is designed based on the layout of the transmission system playing roles of connectivity and support (Fig. 5).

5.2 Heat Treatments and Surface Treatments

Chain wheel made of alloy aluminum is poor in corrosion resistance and soft in texture, so it is easy to be worn for constant contact and impact with the steel chain. Clearly, the hardening process of the surface is necessary, and there the anode treatment to chain wheel's surfaces is employed. After treated, on the surfaces of chain wheel, a dense layer of aluminum anodic oxide film has been formed, whose wear resistance and corrosion resistance is five times higher than before, up to HV500 [6]. There are also colorful surface treatments which in accordance with gorgeous appearance of the FSC car producing an excellent visual effect. While, the small chain wheel and halfshafts made of alloy steel, bearing large impact load and operating at high-speed for long time, are dealt with the processes of thermal refining, quenching and tempering to prevent the fatigue fracture of tooth body.

5.3 Assemble of Chain Wheels

Centreline of the matched chain wheels must installed in the same plane, otherwise transmission imbalance will present when they operate at high speed, resulting in noise and vibration. What's worse, it may cause chain breaking. Based on [7] and practical experience, parallel degree of the same side of two matched chain wheels should lower than 0.05.

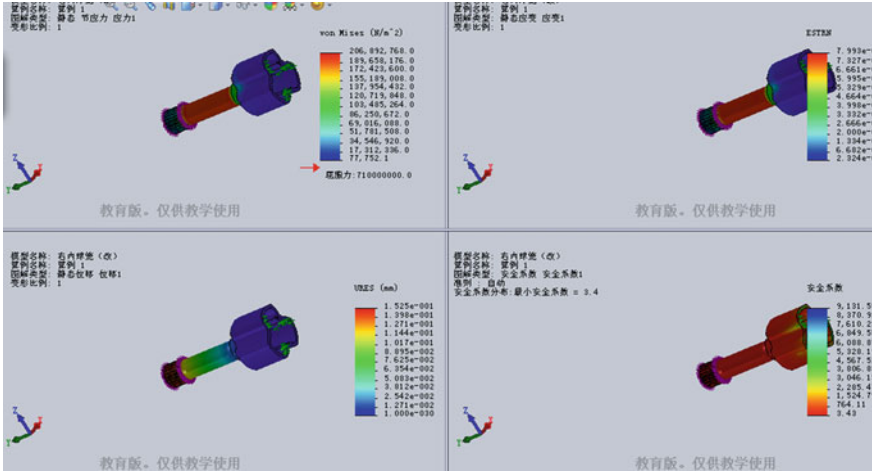
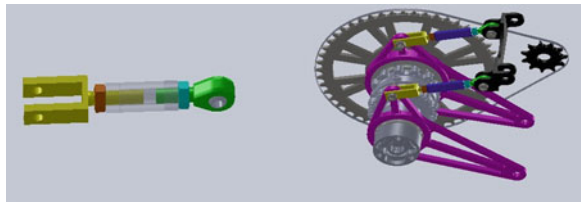


Fig. 4 Stress analysis of CV joint

Fig. 5 Tension mechanism for chain and its arrangement



5.4 Distance of Vacant Travel

Since processing errors exist absolutely, distance of vacant travel cannot be avoided in inside splines and outside splines. Distance of vacant travel brings a lot of drawbacks reducing the sensitivity of transmission system, increasing the impact load, and accelerating wear of components and parts. Therefore, the problem should fully take into account in design and manufacture process. Splines fit precision of components and parts is required to be better than H6, additionally, machining technology and the errors of tools themselves also should be given enough attention. For the racing car, metal curing adhesive can also be used to meet the specific needs in case of emergency.

6 Conclusion

A transmission system is designed for the FSC racing car and the ultimate performance parameters are as follow: the maximum speed is 128 km/h, 75 m acceleration time is 4.13 s, the largest climbing degree >25 %, Curb weight is

215 kg, efficiency of transmission system is 94 %, and spline fit precision is H5 level, which generally satisfied the proposed design objectives. Based on the above analysis, the following conclusions can be drawn:

Firstly, it is applicable and reasonable to use chain transmission in FSC vehicle because it can deliver power reliably and efficiently.

Secondly, transmission ratio is affected by both the maximum speed and acceleration time. In specific design case, series of ratios are chosen to simulation until the most optimal value is achieved.

Thirdly, the idea of integrated layout is throughout the transmission design which makes the construction much more compact and increases the stiffness and strength of the whole system largely.

Last, compared to these products, components and parts designed and manufactured by ourselves have distinct advantages in shape, size, materials and machining technology, which can greatly reduce weight while keeping the enough strength and stiffness.

References

1. Chen J (2002) Vehicle mechanics [M]. China Communications Press, Beijing
2. Li L, Ding K, Niu X, et al (2011) 2011 China student formula rules [S]. SAE-China
3. Yu Z (2009) Vehicle theory [M]. Mechanical industry press, Beijing
4. Kong L, Wang X (2005) Machine design [M]. Beijing Institute of Technology Press, Beijing
5. Wen B (2010) Manual of machine design [M]. Mechanical industry press, Beijing
6. Ma S (2005) Basic machining technology [M]. Mechanical industry press, Beijing
7. He Y (2006) Geometric accuracy specification-the second version [M]. Beijing Institute of Technology Press, Beijing

Parallel Design Optimization of Articulated Heavy Vehicles with Active Safety Systems

Manjurul Md. Islam, Steve Mikaric, Yuping He and Thomas Hu

Abstract This paper presents a parallel design optimization method for multi-trailer articulated heavy vehicles (MTAHVs) with active safety systems (ASSs). It is a challenge to deal with the trade-off between high-speed stability and low-speed maneuverability. Evolutionary algorithms have been used for the design optimization of MTAHVs, but the computation efficiency is low. To address the problem, a parallel computing technique with a master-slave system is proposed. Active trailer steering, differential braking and anti-roll sub-systems are combined in an integrated ASS. Considering the interactions of Driver-Vehicle-ASS, the method simultaneously searches optimal active and passive variables of the ASS controllers, the driver model, and the trailers using a master-slave computing system. Simulation results indicate that the proposed method provides an effective approach to the design synthesis of MTAHVs with ASSs.

Keywords Multi-trailer articulated heavy vehicles · Active safety systems · Design optimization · Parallel computing · Closed-loop dynamic simulation

F2012-E13-015

M. Md. Islam · S. Mikaric · Y. He (✉) · T. Hu
Faculty of Engineering and Applied Science, University
of Ontario Institute of Technology, Oshawa, ON L1H 7K4, Canada
e-mail: yuping.he@uoit.ca

1 Introduction

In closed-loop dynamic simulation-based design of multi-trailer articulated heavy vehicles (MTAHVs), the design criteria and constraints are evaluated using numerical integration of the governing equations of motion of the vehicle-driver-road system [1]. The optimization of MTAHV requires a large number of expensive fitness function evaluations. For MTAHVs with active safety system (ASS), additional difficulties arise because of the interactions among the plant and controllers. The design problem may involve even more expensive computation loads. The resulting design problem may also contain non-differential points and numerous local minima.

For the design optimization of complex multibody systems, such as MTAHVs, convexity of the optimization cannot be guaranteed and conventional search algorithms often get trapped at local optima [2]. Compared with deterministic algorithms, evolutionary methods, such as genetic algorithms (GAs), are better suited to the design optimization of these systems [3]. However, evolutionary methods are known for their computational inefficiency when compared with traditional nonlinear programming methods. Fortunately, for GAs and many other evolutionary methods, individual designs are evaluated independently and these algorithms are well suited for parallel computing. Thus, this paper proposes a parallel design optimization method for MTAHVs with ASSs. To improve the parallel efficiency, a simple dynamic load-balancing scheme is used in the cases of uneven computation loads.

To investigate the performance of the parallel optimization, an MTAHV with ASS is optimized in high-speed lateral stability and low-speed manoeuvrability. A 3-D yaw-roll model is generated to represent the MTAHV with a tractor/double-semi-trailer configuration. The ASS is constructed as an integrated control system that consists of the sub-systems of active trailer steering (ATS), differential braking (DB) and anti-roll (AR). To evaluate the stability and manoeuvrability, a high-speed single-lane change and a low-speed 90-degree intersection turn are emulated [4]. In the closed-loop simulations, the driver, modelled as a PID controller, 'drives' the virtual vehicle following the specified testing procedures. In the combined plant/controller design optimization, the design variables for the plant, the ASS controllers, and the driver model are optimized simultaneously in order to improve the stability and manoeuvrability.

2 Vehicle System Model

2.1 Vehicle Model

The MTAHV to be designed consists of a tractor and two semi-trailers, which are connected by fifth wheels. A 7 DOF yaw-roll model is generated to represent the MTAHV. As shown in Fig. 1, each axle is represented by a single wheel. Based on

2.2 Driver Model

To assess road vehicle directional performance, two types of tests, namely, open-loop and closed-loop, are frequently conducted [5]. In open-loop tests, specific steering inputs are predefined and they are not dependent on the response of the vehicle. These tests can be conducted with high repeatability and they are used for the purpose of characterizing only vehicle responses. In closed-loop tests, a desired vehicle motion or trajectory is achieved by continuously monitoring vehicle response and adjusting steering actions accordingly. Because of the cost and safety concerns, it may not be practical to perform field testing during the concept design phase. Simulation assessment thus may be more practical in certain situations. In past studies on ASSs for AHVs, the open-loop tests were frequently simulated to evaluate the vehicles directional performance measures. Numerous numerical experiments demonstrate that the open-loop dynamic simulation is difficult to accurately simulate the well-defined single lane-change maneuver defined by SAE J2179 for evaluating the rearward amplification (RWA) ratio. Note that RWA ratio is defined as the ratio of the peak lateral acceleration at the rearmost trailer's center of gravity (CG) to that of the towing unit in an obstacle avoidance lane-change maneuver [6]. Thus, the simplified driver model reported in Ref. [7] is introduced and two closed-loop tests will be simulated for evaluating AHVs' directional performance under well-defined test procedures.

2.3 Test Maneuvers Emulated

For measuring high-speed RWA ratio and low-speed maneuverability of AHVs, Two test maneuvers, namely, and the high-speed single-lane change specified in SAE J2179 [8] and the 90-degree intersection turn maneuver [9], respectively, are widely accepted. To effectively represent the low-speed maneuverability, a unified measure, called path-following off-tracking (PFOT), is introduced, which is defined as the maximum radial offset between the path of the tractor's front axle center and that of the rearmost trailer's rear axle center during the 90-degree intersection turn test procedure. In each of the maneuvers, the vehicle tested is required to follow a precisely prescribed path at a specified speed and the driver should continuously monitor and adjust steering actions accordingly. In the current research, the recommended single lane-change test procedure has been simulated for determining the high-speed RWA ratio. In this simulation, the vehicle is travelling at the speed of 88.0 km/h along a straight path section. Then, a sudden lane-change is conducted. The lateral displacement of the vehicle in the lane-change is 1.46 m. The maneuver emulated during the design process for measuring low-speed PFOT value is based on the 90-degree intersection turn test. In the case, the center of tractor front axle is required to travel along a specified path. The vehicle travels at the speed of 4.0 km/h.

3 Controller for the Active Safety System

In the design of the proposed controller, the active trailer steering (ATS), differential braking (DB), and anti-roll (AR) sub-systems are combined as an integrated ASS controller. With the ASS, the trailer axles are steerable and active steering angles are δ_{2f} , δ_{2m} , δ_{2r} , δ_{3f} , δ_{3m} , and δ_{3r} as shown in Fig. 1; the active anti-roll moments u_{c1} , u_{c2} , and u_{c3} are applied to the sprung masses of tractor, lead semi-trailer and second semi-trailer, respectively; the active yaw moments M_1 , M_2 , and M_3 are also applied to the sprung masses of tractor and semi-trailers, accordingly. In order to control the trailer axle steering angles, anti-roll moments, and yaw moments, the ASS controller is designed with respect to two design criteria, i.e., improving low-speed maneuverability and enhancing high-speed stability. In other words, the ASS controller has two operating modes, namely, PFOT and RWA.

In the RWA mode design, the performance index is constructed as follows,

$$\begin{aligned}
 J_{RWA} = \int_0^\infty [& q_{RWA1} \left(U_1 (\dot{\beta}_1 + \dot{\psi}_1) - \frac{m_{s1}}{m_1} (h_{s1} - h_{r1}) \ddot{\phi}_1 \right)^2 + q_{RWA2} \left(U_2 (\dot{\beta}_2 + \dot{\psi}_2) - \frac{m_{s2}}{m_2} (h_{s2} - h_{r2}) \ddot{\phi}_2 \right)^2 \\
 & + q_{RWA3} \left(U_3 (\dot{\beta}_3 + \dot{\psi}_3) - \frac{m_{s3}}{m_3} (h_{s3} - h_{r3}) \ddot{\phi}_3 \right)^2 + q_{RWA4} \delta_{2f}^2 + q_{RWA5} \delta_{2m}^2 + q_{RWA6} \delta_{2r}^2 + q_{RWA7} \delta_{3f}^2 \\
 & + q_{RWA8} \delta_{3m}^2 + q_{RWA9} \delta_{3r}^2 + q_{RWA10} M_1^2 + q_{RWA11} M_2^2 + q_{RWA12} M_3^2 + q_{RWA13} u_{c1}^2 + q_{RWA14} u_{c2}^2 \\
 & + q_{RWA15} u_{c3}^2] dt
 \end{aligned} \tag{4}$$

subjected to Eq. (1). By solving the algebraic Riccati equation, the solution of the optimization problem is the control vector of the form

$$\mathbf{u} = -\mathbf{K}_{RWA} \mathbf{x} \tag{5}$$

where \mathbf{K}_{RWA} is the control matrix with a dimension of 12×15 , \mathbf{x} and \mathbf{u} are the state and control variable vectors defined by Eqs. (2) and (3), respectively.

In Eq. (4), q_{RWAi} , where $i = 1, 2, \dots, 15$, are weighting factors that impose penalties upon the magnitude and duration of the lateral acceleration at the tractor CG, the lateral acceleration at the trailer CG, the trailer steering angles, the yaw moments, and the anti-roll torques, respectively. Note that the third to the ninth terms on the right hand side of Eq. (3) represent the energy consumption of the control system.

Similarly, in the PFOT mode design, the performance index takes the following form

$$\begin{aligned}
 J_{PFOT} = \int_0^{\infty} & \left[q_{PFOT1}\phi_1^2 + q_{PFOT2}\dot{\phi}_1^2 + q_{PFOT3}\beta_1^2 + q_{PFOT4}\dot{\psi}_1^2 + q_{PFOT5}\phi_2^2 + q_{PFOT6}\dot{\phi}_2^2 + q_{PFOT7}\beta_2^2 \right. \\
 & + q_{PFOT8}\dot{\psi}_2^2 + q_{PFOT9}\phi_3^2 + q_{PFOT10}\dot{\phi}_3^2 + q_{PFOT11}\beta_3^2 + q_{PFOT12}\dot{\psi}_3^2 + q_{PFOT13}\phi_{11}^2 + q_{PFOT14}\phi_{12}^2 \\
 & + q_{PFOT15}\phi_{13}^2 + q_{PFOT16}\delta_{2r}^2 + q_{PFOT17}\delta_{2m}^2 + q_{PFOT18}\delta_{2r}^2 + q_{PFOT19}\delta_{3r}^2 + q_{PFOT20}\delta_{3m}^2 + q_{PFOT21}\delta_{3r}^2 \\
 & \left. + q_{PFOT22}M_1^2 + q_{PFOT23}M_2^2 + q_{PFOT24}M_2^2 + q_{PFOT25}u_{c1}^2 + q_{PFOT26}u_{c2}^2 + q_{PFOT27}u_{c2}^2 \right] dt
 \end{aligned} \tag{6}$$

subjected to Eq. (1). Since at the low speeds, the lateral accelerations at tractor and trailer CG are negligible, in construction of the performance index for the PFOT mode, the acceleration terms are ignored. By solving the algebraic Riccati equation, the solution of the optimization problem is the control vector of the following form

$$\mathbf{u} = -\mathbf{K}_{PFOT} \mathbf{x} \tag{7}$$

where K_{PFOT} is the feedback control gain matrix with a dimension of 12×15 , \mathbf{x} and \mathbf{u} are the state and control variable vectors defined by Eqs. (2) and (3), respectively. In Eq. (6), q_{PFOTi} , where $i = 1, 2, \dots, 27$, are weighting factors that impose penalties upon the magnitude and duration of the each state valuable of state vector \mathbf{x} defined by Eq. (2).

4 Proposed Design Method

To implement the parallel numerical optimization of MTAHVs with the ASS with respect to both high-speed stability and low-speed maneuverability, the GA is executed on a master/salve computer system that consists of one master node and twenty salve nodes. Each slave node contains one central processing unit (CPU), whereas the master node contains two CPUs. In both master and slave nodes, each CPU consists of four cores. All available cores form a pool from which a core is assigned to a demanding computing job. At any instant of time, one process is executed by only one core based on the availability. However, it is possible that a task/process is completed by multiple cores, one by one consecutively. Among the Matlab workers, each one takes one core from the pool of CPU cores at any instant of time. All the task executions are done dynamically among the cores.

Figure 2 shows the cluster architecture in Matlab environment. The user is directly connected to the parallel computation toolbox (PCT). The Matlab scheduler receives user instruction or task from PCT. This Matlab scheduler stays on the master node and manages the entire parallel computation job. The scheduler assigns tasks to the Matlab distributed computation server (MDCS) agent. Each MDCS agent is connected to a worker. The agent send computation task to Matlab worker. When the computation task is done, the agent collects and sends the result back to PCT via scheduler. Then the agent waits for the next instruction from the scheduler. Underneath Matlab Matlab Distributed Computing Server (MDCS) is

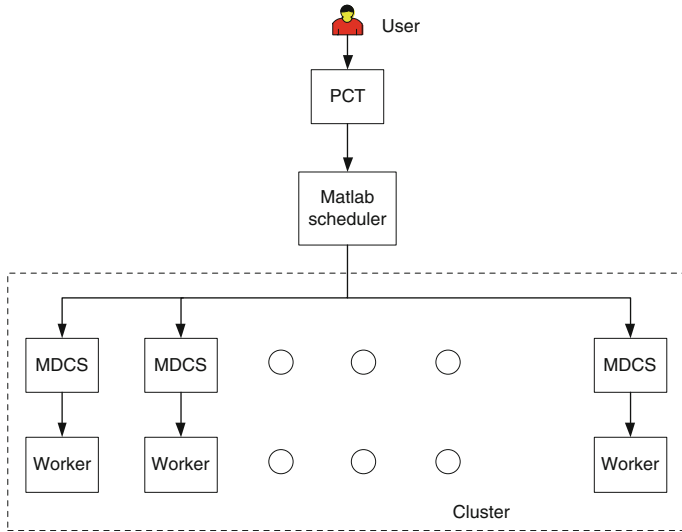


Fig. 2 Cluster architecture in Matlab environment

Beowulf cluster using Message Passing Interface (MPI) for interconnect communication among cluster nodes.

The objective of designing the ASS is to improve the tractor and double semi-trailer combination’s low-speed maneuverability and high-speed lateral stability. The test maneuvers of the 90-degree intersection turn and the single lane-change are emulated to evaluate the vehicle’s low-speed maneuverability and high-speed stability, respectively.

The proposed framework of the design optimization method using the parallel computation technique with the master–slave system is shown in Fig. 3. The proposed method offers a multi-objective formulation approach to the design optimization of integrated active systems for MTAHVs. The design optimization of MTAHVs is implemented using a parallel genetic algorithm (GA) in Matlab. The MTAHV model may be generated using multibody dynamic programs, e.g., ADAMS and TruckSim. The ASS controller based on LQR technique and the driver model can be constructed in Matlab. Then, the combined vehicle model, ASS controller and/or driver model are optimized simultaneously using the GA in the master–slave parallel computing system. The master–slave computing system, with one master and twenty slave quad-core processors, runs the Matlab distributed computing software in Linux operating system.

As shown in Fig. 3, in each iteration of the optimization design, the high-speed lane change (HSLC) and the low-speed path-following (LSPF) testing maneuvers can be simulated concurrently. For instance, in an iteration, a design variable set X_h is sent to the HSLC simulation module. X_h consists of X_{SYS} , X_{DR} , and X_{RWA} . Note that X_{SYS} represents passive vehicle system parameters, such as the tractor and semi-trailer geometric and inertia parameters, X_{DR} denotes driver model parameters for HSLC maneuver, e.g., K_p , K_i and K_d described in Ref. [7], and

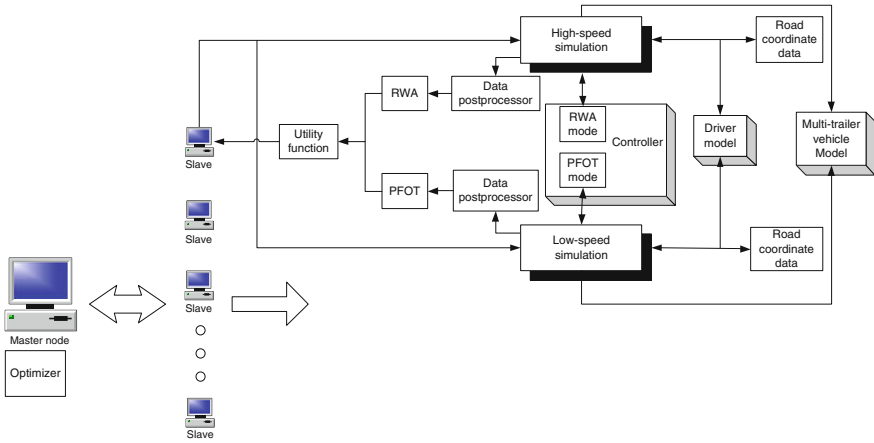


Fig. 3 Design framework using a master–slave system in the design synthesis of MTAHVs with ATS systems

X_{RWA} denotes RWA controller parameters. The RWA controller is designed to enhance the high-speed lateral stability of AHVs. The linear quadratic regular (LQR) technique is applied to the design of the RWA controller. Given the design variable set X_h , including X_{DR} , X_{SYS} and X_{RWA} for the driver model, vehicle model and RWA controller, respectively, these three models are integrated and the HSLC test maneuver can be simulated.

With the feedback position error between the current target path and the actual vehicle trajectory, the driver ‘drives’ the vehicle model by means of manipulating the steering angle (δ_{lf}). Given the current vehicle state variables x that can be achieved through a sensor system, the RWA controller determines the control variables u in order to get the desired active trailer steering angles, anti-roll torques, and yaw moments. In this process, the driver drives the vehicle following the test procedure specified in SAE J2179 [8]. After the numerical simulation of the HSLC test maneuver, the performance measure can be achieved, which emphasizes the improvement of the high-speed stability.

Similarly, in the iteration, a design variable set X_l is sent to the LSPF simulation module. Design variable set X_l consists of X_{SYS} , X_{DP} and X_{PFOT} . Note that X_{DP} denotes driver model parameters for the LSPE maneuver, i.e., K_p , K_i and K_d shown in Ref. [7], and X_{PFOT} stands for PFOT controller parameters. The PFOT controller is designed to improve the low-speed maneuverability of AHVs. The LQR technique is also applied to the design of the PFOT controller. Given the design variable set X_l , including X_{DP} , and X_{PFOT} for the driver model, vehicle model and PFOT controller, respectively, these three models are integrated and the LSPE test maneuver can be simulated. During the process, the driver drives the vehicle based on the low-speed path-following maneuver (90-degree intersection turn). After the simulation of the LSPF test maneuver, the performance measure can be obtained, which emphasizes the enhancement of the low-speed maneuverability.

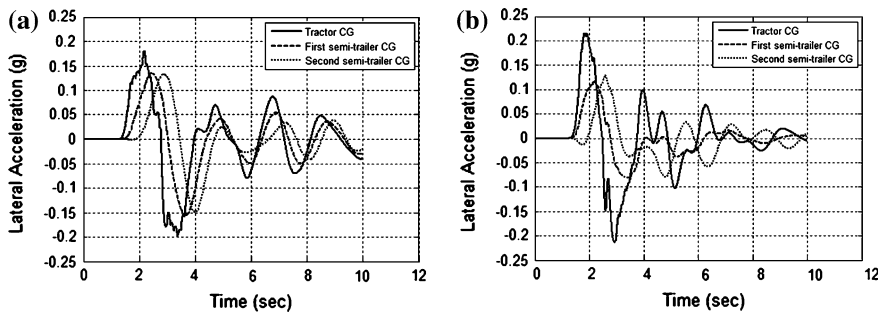


Fig. 4 Lateral acceleration at CG of tractor and two semi-trailers versus time in high-speed lane change maneuver for: **a** baseline design; **b** optimal design

As shown in Fig. 4, with the completion of this iteration’s HSLC and LSPF simulations, one is faced with a vector optimization problem with the two design criteria, and, and corresponding constraints. Using the technique of scalarization reported in Ref. [10], the vector optimization problem is reduced to a scalar optimization problem that can be formulated in the following format:

$$\begin{aligned}
 & \text{minimize} && \sigma_1 \tilde{\mu}_{RWA}(\mathbf{X}_h) + \sigma_2 \tilde{\mu}_{PFOT}(\mathbf{X}_l) \\
 & \text{with respect to} && \mathbf{X}_h^T = [\mathbf{X}_{SYS}^T \quad \mathbf{X}_{DR}^T \quad \mathbf{X}_{RWA}^T], \\
 & && \mathbf{X}_l^T = [\mathbf{X}_{SYS}^T \quad \mathbf{X}_{DP}^T \quad \mathbf{X}_{PFOT}^T]
 \end{aligned} \tag{8}$$

where σ_1 and σ_2 are weighting factors, $\tilde{\mu}_{RWA}(\mathbf{X}_h)$ and $\tilde{\mu}_{PFOT}(\mathbf{X}_l)$ consider the corresponding performance measures, $\bar{\mu}_{RWA}(\mathbf{X}_h)$ and $\bar{\mu}_{PFOT}(\mathbf{X}_l)$ as well as the respective constraints. The parallel genetic algorithm is used as the optimizer to resolve the trade-off relation between the high-speed lateral stability and the low-speed maneuverability. To improve the parallel efficiency, the simple dynamic load-balancing scheme is to choose the population size of GA as the number of available cores for numerical simulation multiplied by a suitable natural number.

5 Results and Discussion

To examine the efficacy of proposed design method, it has been applied to the design of the MTAHV using the 7 DOF model and the resulting design is compared with the baseline design. During the design optimization using the proposed method, the design variables are permitted to vary by 5 % from their nominal values. In this section, the integrated ASS system, including the sub-systems of ATS, DB and AR, will be investigated by analyzing the numerical results derived from the simulated high-speed lane change (HSLC) and low speed path-following (LSPF) test maneuvers. For both cases, in the HSLC simulation module, the baseline driver model parameters are assigned the following values $K_p = 0.7680$,

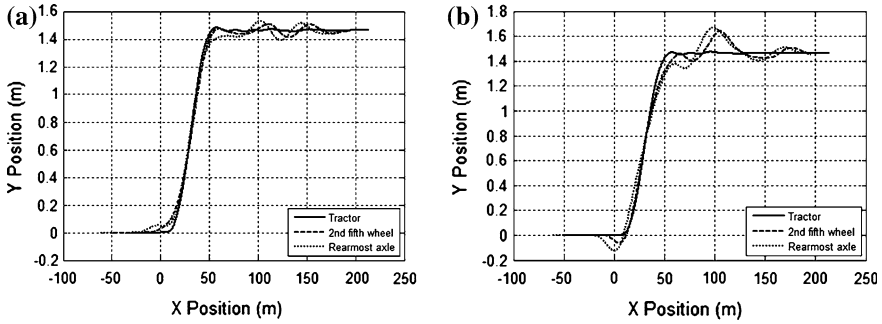


Fig. 5 Trajectory of tractor front axle center, 2nd fifth wheel and second semi-trailer rear axle center in high-speed lane change maneuver for: **a** baseline design; **b** optimal design

$K_i = 0.7862$, and $K_d = 0.2060$; in the LSPF simulation module, $K_p = 4.0$, $K_i = 0.1$, and $K_d = 0.1$. These six PID controller gains are optimized, simultaneously with the other design variables, in the range of -70 to $+70$ % of their nominal values.

In the case of the optimal design, the design variables are the trailer geometric parameters, trailer inertia parameters, weighting factor vectors q_{RWAi} where $i = 1, 2, \dots, 15$, and q_{PFOTj} where $j = 1, 2, \dots, 27$. Note that the weighting factors are used to construct the LQR controllers corresponding to the RWA and PFOT modes of the ASS controller. The passive design variables include sprung mass of lead semi-trailer m_{s2} , sprung mass of second semi-trailer m_{s3} , roll moment of inertia of lead semi-trailer I_{xx2} , roll moment of inertia of second semi-trailer I_{xx3} , yaw moment of inertia of lead semi-trailer I_{zz2} , yaw moment of inertia of second semi-trailer I_{zz3} , height of roll center of lead semi-trailer sprung mass h_{r2} , height of roll center of second semi-trailer sprung mass h_{r3} , height of lead semi-trailer sprung mass h_{s2} , height of second semi-trailer sprung mass h_{s3} , height of the coupling point connecting the tractor and the lead semi-trailer h_{c2} , height of the coupling point connecting the lead semi-trailer and the second semi-trailer h_{c3} , horizontal distance between the lead semi-trailer sprung mass CG and first coupling point l_{c2} , horizontal distance between the second semi-trailer sprung mass CG and second coupling point l_{c3} , horizontal distance between lead trailer semi-trailer sprung mass and mid axle of its tridem axle set b_{25} , and horizontal distance between second trailer semi-trailer sprung mass and mid axle of its tridem axle set b_{38} . In the design optimization, the optimized values of all the above design variables are searched in the range from -5 to $+5$ % of their nominal values.

In the optimal and baseline cases, the selected vehicle dynamic responses are illustrated in Figs. 4, 5, and 6. Figure 4a and b show the time history of the lateral accelerations at the tractor and semi-trailer CGs in the high-speed lane-change maneuver for the baseline design and optimal design, respectively. Due to the RWA control mode of the ASS and the optimal passive design variables derived from the proposed method, the RWA ratio of the optimal design decreases

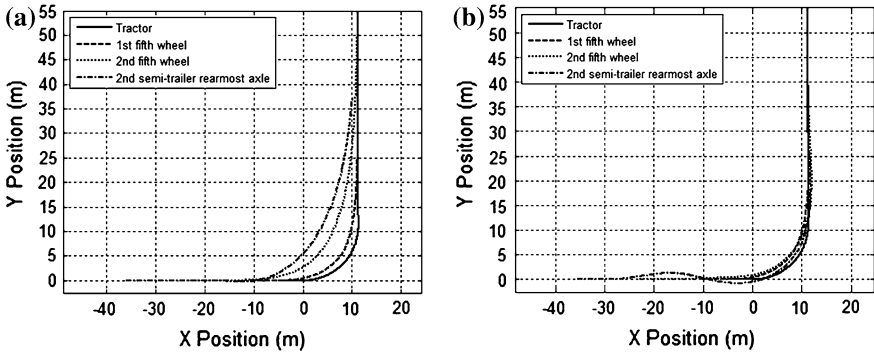


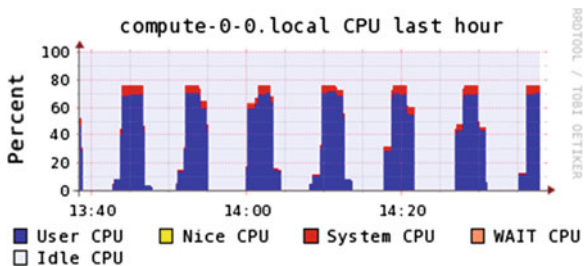
Fig. 6 Trajectory of tractor front axle center, 1st fifth wheel, 2nd fifth wheel, and second semi-trailer rearmost axle center in low-speed 90-degree intersection turn maneuver for: **a** baseline design; **b** optimal design

22.06 % from the baseline value of 0.7649–0.5962. The drop of the RWA ratio will greatly improve the high-speed lateral stability of the resulting optimal design. Figure 5a and b provide useful simulation results for investigating whether the rear axle of second semi-trailer can follow the tractor’s trajectory accurately in the high-speed lane-change maneuver. Compared with the baseline design, in the case of the optimal design, during high-speed lane change, the ability of the rearmost axle of second semi-trailer to follow the trajectory of tractor front axle is decreased by 118.26 % from the maximum transient off-tracking of baseline case of 0.0734 m to the optimal case of 0.1602 m. Results shown in Figs. 4–5 imply that with respect to the baseline design, the optimal design has higher lateral stability, lower path-following performance in high-speed obstacle avoidance maneuvers.

With the simulation results shown in Fig. 6, the optimal design’s low-speed maneuverability can be examined and evaluated. Figure 6a shows the simulation result of the baseline design, illustrating the trajectory of the tractor’s front axle center and that of the second semi-trailer rear axle center in the low-speed 90-degree intersection turn maneuver. Figure 6b shows the corresponding simulation result for the optimal design. A close observation of the simulation results reveals that compared with the baseline design, for the optimal design, the rearmost axle of second semi-trailer can track the tractor front axle’s trajectory more closely. For the optimal design, the maximum PFOT value drops 89.91 % from the baseline value of 7.5727 to 0.7639 m. The low-speed performance improvement of the optimal design is attributed to the PFOT mode of the ASS controller and the optimal passive design variables derived from this design method. Regarding the ASS system power consumption, the simulation results of the optimal design are not comparable with those of the baseline vehicle.

Figure 7 shows a time history of a typical work load of a slave node. As mentioned previously, each slave node has one CPU and each CPU has four cores in the pool. However, only three of the cores from the pool at any instant will be

Fig. 7 Time history of a typical work load pattern of a slave node during the design optimization process



available for simulation. Allocation of these three cores, however, is always changing with time and the remaining core is allocated for the operating systems and other overheads. Each node can run three different simulations in parallel. It can be seen from the Fig. 7 that there is a repeated pattern of idle times in for the CPU. This idle time corresponds to the computation of next generation of design variables by the master nodes.

Note that in the case of optimal design, the optimal results shown in this table has been derived from the proposed design method and a single run of the GA. In the design optimization using the GA, the population size and total number of generations took the values of 244 and 100, respectively. The optimization process using the parallel computing cluster system with 61 cores of available processor units only requires 10.10 h.

6 Conclusions

This paper presents a parallel design optimization approach for MTAHVs with ASSs. The design method has the following important features: (1) a parallel computation technique with a master–slave system is introduced to improve computation efficiency; (2) a formulation for the optimization problem of MTAVHs with ASSs is recommended; (3) in the design process, to evaluate the vehicle performance measures, a driver model is incorporated; and (4) the optimal active and passive design variables of the ASS, the trailers, and the driver model are searched simultaneously.

The proposed design method has been applied to the design of a MTAHV with an ASS. Numerical simulation results show that the resulting optimal design is superior to the baseline design in the performance measures of high-speed lateral stability and low-speed path-following. The proposed method may be used for identifying desired design variables and predicting performance envelopes in the early design stages of AHVs with ASSs.

References

1. Islam MM, Ding X, He Y (2011) A closed-loop dynamic simulation-based design method for articulated heavy vehicles with active trailer steering systems. *Vehicle System Dynamics*. doi:[10.1080/00423114.2011.622904](https://doi.org/10.1080/00423114.2011.622904)
2. He Y, McPhee J (2005) A design methodology for mechatronic vehicles: application of multidisciplinary optimization. *Multibody Generic Algorithms Veh Sys Dyn* 43(10):697–733
3. Cantú-Paz E (1997) A survey of parallel genetic algorithms. Department of Computer Science, University of Illinois at Urbana-Champaign
4. He Y, Islam MM (2012) An automated design method for active trailer steering systems of articulated heavy vehicles. *ASME J Mech Des*. doi:[10.1115/1.4006047](https://doi.org/10.1115/1.4006047)
5. Prem H, Ramsay E, Pont J, McLean J, Woodrooffe J (2001) Comparison of modelling systems for performance based assessments of heavy vehicles (performance based standards—NRTC/Austrroads project A3 and A4). In: Working paper, The National Road Transport Commission (NRTC), October, Melbourne
6. He Y, Islam M, Webster T (2010) An integrated design method for articulated heavy vehicles with active trailer steering systems. *SAE Int J Passeng Cars Mech Sys* 119–6:158–174
7. Islam M, Ding X, He Y (2012) A closed-loop dynamic simulation based design method for articulated heavy vehicles with active trailer steering systems. *Veh Sys Dyn*. doi:[10.1080/00423114.2011.622904](https://doi.org/10.1080/00423114.2011.622904) (Manuscript ID: NVSD-2011-0014)
8. SAE (1994) A test for evaluating the rearward amplification of multi-articulated vehicles. SAE Recommended Practice J2179, Warrendale, USA
9. Fancher P, Winkler C (2007) Directional performance issues in evaluation and design of articulated heavy vehicles. *Veh Sys Dyn* 45:607–647
10. He Y, Islam M (2012) An automated design method for active trailer steering systems of articulated heavy vehicles. *ASME J Mech Des* 134(041002):1–15

The Application of Dual Limit Analysis Method in Physical Performance Characteristics Defining and Structural Designing

Chi Luo

Abstract Dual limit analysis method that can be widely used in stress analysis and judgment for the mechanical components, including the movement mechanics and finite element static mechanical analysis; and can be used in the social sciences, economics decision-making for the event, events, game, life choices, the program decision-making. To the dual limit analysis, we can use the coordinate system to express their inherent relationship. Because the event or project components, does not exist in the negative, so it can not be expressed with the traditional Cartesian coordinate system, we need to create a cross positive coordinate system to express. So, dual limit analysis method in the event judgment is a fuzzy analysis method to judge, but with the constantly adding the more parameters, this ambiguity will turn to clarity, add some precise value allows the results get closer to the clear. Dual limit analysis method has a great impact especially on fuzzy mathematics.

Keywords Fuzzy mathematics · Quantum coherence · The equation of the dual limit analysis · Fuzzy value range · Finite element

1 Introduction

In Engineering Mechanics, especially involving various performance parameters of Engineering Mechanics, different parameters cause the different states of operating. How to select the appropriate parameters, and to minimize cost and

F2012-E13-016

C. Luo (✉)

Automotive Electronics Department, Shanghai Haima Automobile R&D CO., LTD, 201201 Shanghai, China

calculation, so that the parts' running under the best condition and keep the service life maximum, which is the subject of engineering community has been studying.

2 The Optimal Value Principle and Fuzzy Mathematics in Engineering Mechanics

2.1 Optimal Value Principle

A performance parameter "a", if the value is too large or too small is not conducive to the actual working conditions, then there must be an optimal value between the maximum and minimum working conditions to achieve the optimal state [1, 2].

This optimal value can be calculated. If this parameter is linear, we can direct access to the middle value is optimal; if it's non-linear relationship. It can be calculated by calculus. This is a precise mathematical and stochastic mathematical area.

2.2 Engineering Mechanics Fuzzy Math Application Requirements

Practical applications, some performance parameters' defining, do not require such a precise calculation to get this optimal value. Because too many parameters involved, will lead to a heavy calculations increased. Then the heavy calculations will add an excessive workload and the resulting increase in process cost, and difficult to control the actual process operation to a specific precise value. The performance parameters are generally selected a vague range of values is enough, which to be called fuzzy value range.

So, some of the performance parameters of the choice of engineering applications, are related to the scope of fuzzy mathematics. Judgment and choice of the fuzzy mathematics also need to use the specific method of analysis and judgment in order to determine this fuzzy value range. It's a confirmation of the value of membership function in fuzzy mathematics.

For example, the conductivity of the steel bars of pressure from the wiper blade inside, if the rigidity is too weak, the pressure will pass on uneven; if too hard, because the front windshield glass is curved surface, so it will lead to both ends of the tilt of the blade, and pressure can not be passed to the two tips. Under these two states, the wiper cannot reach a good scraping effect.

To calculate the optimal value, you need to calculate the coefficient of elasticity of the steel bar, steel bar thickness, but also into the curvature of the front windshield glass to carry out heavy calculations. It leads to a heavy calculation, and the actual process can not achieve accurate control, technical costs also increased. Therefore, in practical used, we are actually only need to determine a

fuzzy value range. But if we have no specific method of analysis, you can not select the exactly range of this fuzzy value range, and even steel bars should be a “harder” or “softer”, which is a fuzzy judgment, we have no way of knowing, let alone “how hard” and “how soft” to decreased the ambiguity range of judgment. A dual limit analysis method is to set to deal with this problem, to judge and analysis to determine the fuzzy value range, but also to determine the membership function value. This is also a fuzzy definition process.

3 Application and Calculation of the Dual Limit Analysis Method

3.1 Dual Limit Analysis Method of Generation

In our macro-reality world, the probability of a range of $[0, 1]$, the value can not be less than 0 or greater than 1. If outside this range, do not conform to the logic of the macro-social reality, social reality is not allow the existence of such an event [3, 4]. However, in the quantum world, the probability can be beyond the scope. A microscopic particle can spin in two opposite directions at the same time, two states added together. The most typical example is the famous Schrödinger cat conjecture experiment. This conjecture experiment, the cat is in the state of life and death at the same time, then the probability of life is 1, the dead probability is 1 too, coexistence and superposition of two states, the cat is both alive and dead. From the mathematical view, the probability is “2”. The range of membership function of fuzzy mathematics is $[0, 2]$. Here, life and death this is the logic state of the two deterministic, but in this conjecture experiment, because of the characteristics of the quantum, it's to achieve a superposition exist.

This is a feature of the quantum, called quantum coherence, quantum superposition of two repulsive states exist. Quantum coherence exists only in the microscopic quantum world.

If we assume that quantum coherence is also macro-real world exists, and then separate the results of the comparison of the two state events, which is available for us to make analysis and judgment, and can quickly thus making the right choice and judgment. So here we get an entirely new method of analysis and judgment. This is the Dual limit analysis method.

Dual limit analysis method is not only the above-mentioned two states contrasted, it must set the probability of the two states to 1, and all parameters are pushed to the maximum and minimum limits of the two tips, in order to carry out contrast. Then contrast the working conditions or status of components or events in the two limit states, and then make a judgment or choice.

3.2 Dual Limit Analysis Method's Definition and Equation

Dual limit analysis method that can be widely used in stress analysis and judgment for the mechanical components, including the movement mechanics and finite element static mechanical analysis; and can be used in the social sciences, economics decision-making for the event, events, game, life choices, the program decision-making.

3.2.1 When the Object of Study for is the Physical Components

For a performance parameters "x", this parameter determines the operating condition of the parts, that the operating condition has a expression of function P (x). Set "x" to be the maximum value of what it can be, which is "max x", the working conditions of the components is "P (max x)"; at the same time, set "x" to be the minimum "min x", the components of working conditions is P (min x); comparison of two conditions, to take a better working condition. That is, $P \max = \{P (\max x), P (\min x)\}$. At this point the inverse function of x is expressed as $x (P \max x)$. Thus we can conclude that the fuzzy value range we have to select at least meet the $x < x (P \max)$.

3.2.2 When the Object of Study for is the Event

An event P there are two options A and B, we can make it run to the A state, or make it run to the B state, A and B are two repulsion of the state, they cannot happened in the macroscopic world at the same time. That is, $A + B = 1$, $A \cap B = 0$. What we need to do is to determine A and B which one is better. Now we set $A = 1$, $B = 1$, the quantum coherence appears, then A and B exist at the same time. Under the A state, assuming that event A there are two extreme conditions, if A happened, optimal state $E_{A \max}$ and the worst state $E_{A \min}$ also reached at the same time; in the state of the B state, Suppose B event has two extreme states, so we have optimal state $E_{B \max}$ and the worst state $E_{B \min}$. We compare the Σ_A and Σ_B , the larger one, is the program which we want to select.

Dual limit analysis equations:

$$\begin{aligned} P \text{ optimal} &= \max\{(E_{A \max} + E_{A \min}), (E_{B \max} + E_{B \min})\} \\ &= \text{MAX} \{\Sigma_A, \Sigma_B\} \end{aligned} \quad (1)$$

where, P is the best options for the most reasonable choice program; $E_{A \max}$ is the optimal state the A program can achieve; $E_{A \min}$ is the worst state A program can achieve; $E_{B \max}$ is the optimal state B program can achieve; $E_{B \min}$ is the worst state B program can achieve; Σ_A is the algebraic sum of A program of the best and the worst two extreme states; Σ_B is the algebraic sum of B program of the best and the worst two extreme states.

We have to judge that the option A or option B, which is the optimal solution. It can be assumed that these two states simultaneously, and the respective state, while taking the optimal value and the worst value, then add into the above formula to compare, we can quickly make the right choice. Here, the probability of event A and event B is not known.

If there are more than two programs, the above expression is still applicable. The dual limit analysis equation of more than 2:

$$P \text{ optimal} = \max\{\Sigma_A, \Sigma_B \dots \Sigma_n\} \tag{2}$$

Where, P is the best options for the most reasonable choice program; n is the number of programs; Σ_A is the algebraic sum of A program of the best and the worst extreme states; Σ_B is the algebraic sum of B program of the best and the worst extreme states; Σ_n is the algebraic sum of n program of the best and the worst extreme states.

From this definition, the dual limit analysis method for the event, we do not need to know the probability of an event’s good and bad states, we can quickly make the best judgment. That is, from the exact value must be informed that the event occurred, to judge precise mathematical judgment method, converted to use fuzzy math to judge the program which does not need to know the probability of events. We can quickly determine and make the workload greatly reduced by this method.

3.3 Dual Limit Analysis Method of the Mathematical Expression

To the dual limit analysis, we can use the coordinate system to express their inherent relationship. Because the event or project components, does not exist in the negative, so it can not be expressed with the traditional Cartesian coordinate system, we need to create a cross positive coordinate system to express.

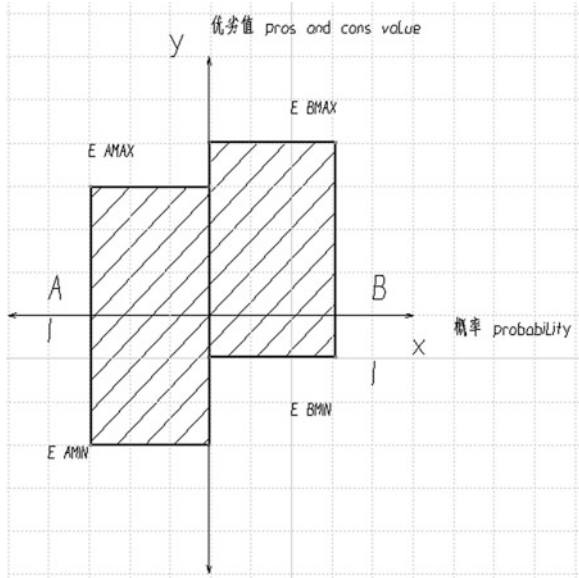
3.3.1 The Cross Positive Coordinate System for Event

The State of Unknown the Probability of Program Optimal and Worst

Two options as shown below, A and B are the program of event P; $E_{A\text{MAX}}$ is the optimal state the A program can achieve; $E_{A\text{MIN}}$ is the worst state A program can achieve; $E_{B\text{MAX}}$ is the optimal state B program can achieve; $E_{B\text{MIN}}$ is the worst state B program can achieve;

The abscissa is the probability, if unknown the probability of occurrence of programs A and B respective optimal and worst situation, they all can be set by a value of 1.

Fig. 1 Probability unknown event double limit cross coordinate system expression



The vertical axis is the value of the program that it can reach. Area indicates the value when their probability is same.

X coordinate of the upper half of the figure represents the optimal state, the lower half of show inferior state. The larger the area, the more excellent it is.

Because the coordinate units are positive, so though the bottom half is inferior value, still the larger the area, the more superior, then inferior value smaller; Conversely, the smaller the area, the greater of inferior value. However, if the inferior value is to a certain extent, maybe smaller than 0, it can move to the top of the formation of negative to cut the part of the area of merit. Now the inferior value is proportional to the area.

The form shown in Fig. 1:

Parameters taken into the coordinate system, we now can calculate ΣA and ΣB .

From Fig. 2 we can see $E_{AMAX} = 3$; $E_{AMIN} = 3$; $E_{BMAX} = 4$; $E_{BMIN} = 1$.

We can get: $P_{optimal} = \max \{ \Sigma_A, \Sigma_B \} = \max \{ 6, 5 \} = 6$.

So the conclusion is: A program is better than program B.

3.3.2 When the Probability of Optimal and Worst of Program is Known, Coordinate System is Expressed

Though as usual, we will not know the probability of occurrence of the respective optimal and worst state of A and B programs, but in a few cases, the probability can be informed. So this time we can put the probability of substitution into the coordinate system equation in our calculations, this could make analysis accuracy.

Fig. 2 Negative value reduction event double limit cross coordinate system expression

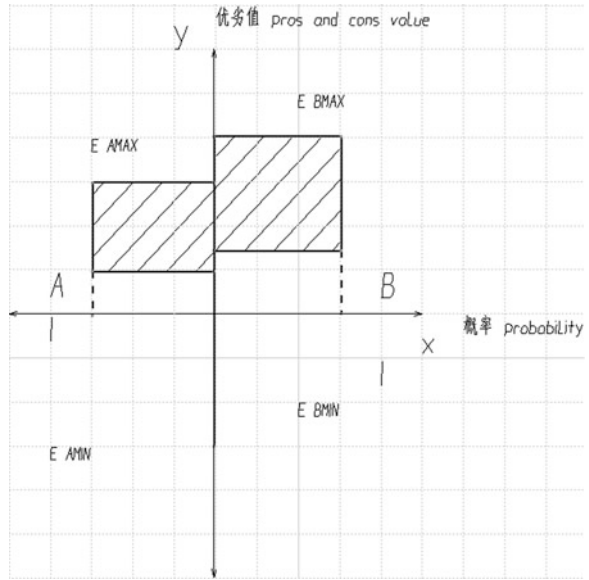
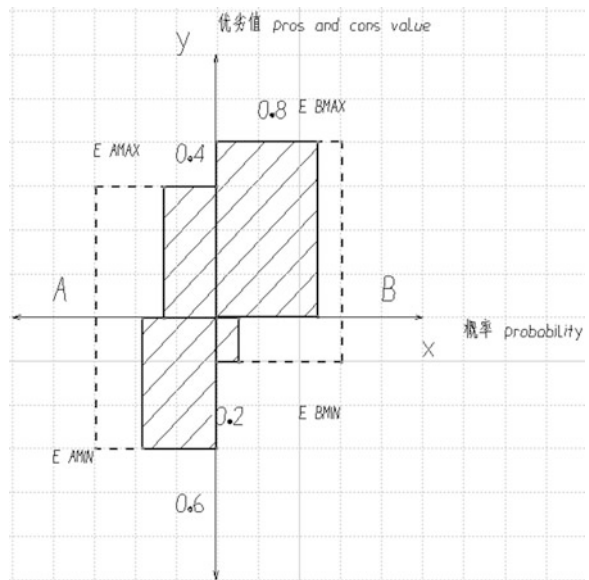
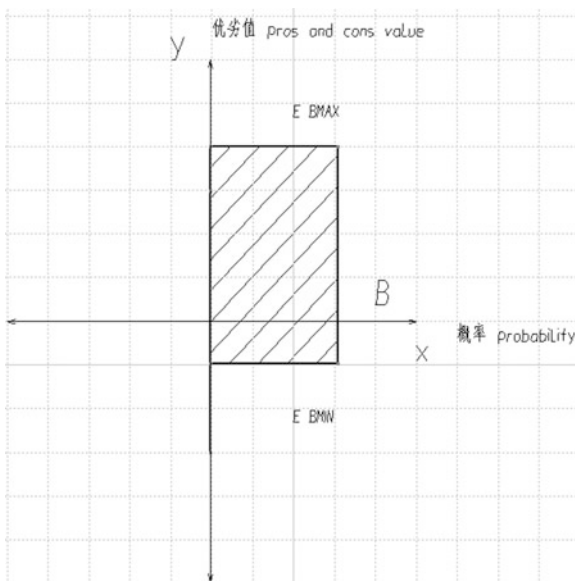


Fig. 3 Probability known event double limit cross coordinate system expression



Suppose we know that the optimal state of option A, $E_{A_{MAX}}$, it's probability of occurrence I_1 is 0.4, the probability of occurrence of the worst state of the program A, $E_{A_{MIN}}$, $I_2 = 1 - 0.4 = 0.6$; Option B best state $E_{B_{MAX}}$ probability of occurrence I_3 is 0.8, So the probability of occurrence of the worst state of B option, $E_{B_{MIN}}$, $I_4 = 1 - 0.8 = 0.2$.

Fig. 4 The engineering components double limit cross coordinate system limit expression



Probability taken into the original probability set for an area will decreased the area in accordance with the corresponding probability, as shown in (Fig. 3).

We can get that: $E_{AMAX} = 9 \times 0.4 = 3.6$; $E_{AMIN} = 9 \times 0.6 = 5.4$; $E_{BMAX} = 12 \times 0.8 = 9.6$; $E_{BMIN} = 3 \times 0.2 = 0.6$; namely $\Sigma_A = E_{AMAX} + E_{AMIN} = 3.6 + 5.4 = 9$; $\Sigma_B = E_{BMAX} + E_{BMIN} = 9.6 + 0.6 = 10.2$.

Taken into the equation of dual limit method, $P \text{ optimal} = \max \{ \Sigma_A, \Sigma_B \} = \max \{ 9, 10.2 \} = 10.2$.

So the conclusion is: program B is better than program A.

So, dual limit analysis method in the event judgment is a fuzzy analysis method to judge, but with the constantly adding the more parameters, this ambiguity will turn to clarity, add some precise value allows the results get closer to the clear. Before reach the absolute clarity, the dual limit analysis method does not guarantee an absolutely correct judgment. With the keep on taking in of the new parameters, the results may change.

3.3.3 The Cross Positive Coordinate System for Parts

If the subject of study is parts, the analysis method is similar with the event analysis, only the difference is, it has only one program. Not like the event analysis, as there will be two or more programs. So, cut it into half, and we can get the engineering parts of the dual limit analysis coordinate expression.

As shown in Fig. 4: Now what we need to compare is no longer the Σ_A and Σ_B , but E_{BMAX} and E_{BMIN} .

So the dual limit analysis method equation for parts:

$$P \text{ optimal} = \text{MAX} \{E_{\text{BMAX}}, E_{\text{BMIN}}\} \tag{3}$$

Where, P optimal is the best options for the most reasonable choice program; E_{BMAX} is the optimal state B program can achieve; E_{BMIN} is the worst state B program can achieve; Here we focused on the steel elastic modulus selected case in the wiper blade of the aforementioned mentioned for analysis.

Set selecting wiper blade steel modulus of elasticity for the event B, then next step we have to determine is values of E_{BMAX} and E_{BMIN} .

For event analysis, the dual-limit we have chosen is the best and the worst; but for parts, is to take the maximum and minimum values of the two values compared.

Thus, For E_{BMAX} , we assume that the elastic modulus of the steel bars is infinite at this time, so steel bars is an ideal rigid body, so the wiper blade pressure distribution is the absolute smooth state, that is every points in blade equal force. Because the front windshield glass is a certain curvature of the surface, but the curvature is low, very close to the plane, so the front windshield wiper blade pressure distribution is absolutely smooth. Due to transformable wiper blade, except two tips will be local tilt, the central region of blade can be pressed on the front windshield, so 70 % of the central part of about regional wiper is available.

And For E_{BMIN} , we assume that the minimum modulus of elasticity of steel rigid body, which is equal to 0, then, steel is absolute soft, equivalent to not pass any pressure. As shown below, the steel bar loses its elasticity, the pressure from the blade rods can not transmit pressure to all parts of the blade, as Fig. 4, only claw frame is under pressure, while each claw has only two points of force, so in this state, the blade is only 8 points by force.

So contrast E_{BMAX} and E_{BMIN} , the E_{BMAX} is 70 % of the area has a smooth pressure distribution, and it is a surface contact; the E_{BMIN} , only eight points have pressure, others do not have any pressure, and it is a point contact. If the wiper driven, the E_{BMIN} has 70 % of the area scraping clean, while the E_{BMIN} only 8 points get scraping.

By contrast, we get that: $E_{\text{BMAX}} > E_{\text{BMIN}}$. That is, $P \text{ optimal} = \max \{E_{\text{BMAX}}, E_{\text{BMIN}}\} = E_{\text{BMAX}}$.

The conclusion is that to the steel bars within the wiper blade, we should choose a more rigid steel bar, and the elastic modulus depending on the size of the curvature of the front windshield glass to choose based on experience. The smaller the curvature of glass is, the more of elastic modulus selected for the steel bars.

In the actual production, the choice of the wiper blade steel modulus of elasticity, but also a fuzzy selection process. We do not need to accurately calculate the elastic modulus, but through the selection of classification, we can select the appropriate wiper blade steel bars (Fig. 5).

Dual limit analysis method can effectively help of finite element analysis. Finite element analysis is through the establishment of the mathematical model consisting of a number of small units infinitely to get close to the objects of real, this is also a vague unlimited clear process. To compare parameters pushed to the limits in both directions, in order to determine the actual impact of this parameter range.

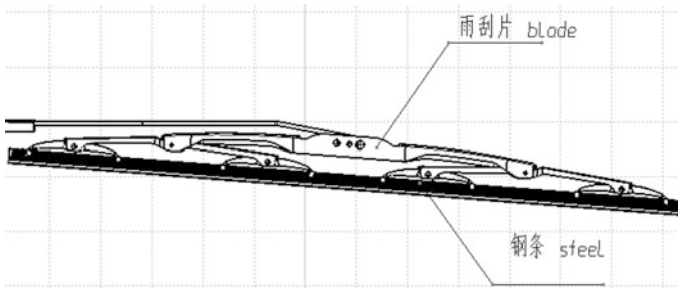


Fig. 5 Wiper blade structure diagram

Structure designing, using the dual limit analysis, we can determine the impact of a mechanical structure on the overall structural strength and to determine the structure of a reasonable size range.

Include wiper structural designing and the sheet metal structural designing, and so on.

4 Conclusion

Dual limit analysis method is mainly used in the two areas, one is the analysis and judgment of events and programs, the other is a mechanical engineering components analysis and judgment. But at the same time it across the two areas of social sciences and natural sciences, and it is a widely used of the edge of judgment and analysis methods. Dual limit analysis method has a great impact especially on fuzzy mathematics. As Dual limit analysis, fuzzy control, fuzzy pattern recognition, fuzzy cluster analysis, fuzzy decision, fuzzy evaluation easier, to reduce the computational workload, and greatly increase accuracy.

References

1. Kaufman A (1975) Introduction to the theory of fuzzy subsets fundamental theoretical elements, vol 1. Academic, New York
2. Wang Guo jun L (1988) Fuzzy topology space theory. Shan xi Normal University press, Xi' an
3. Chang K (2000) Here, there and everywhere: a quantum state of mind. The New York Times, 11 July 2000: D3
4. Blatter G (2000) Schrödinger's cat is now fat. Nature 406:25–26

Predicting Battery Pack Thermal and Electrical Performance in a Vehicle Using Realistic Drive Cycle Power Profiles

Allen Curran and Scott Peck

Abstract The heat generated during battery charge and discharge cycles is a major design issue, particularly since the performance of a battery depends on its operating temperature. As a consequence, robust thermal management systems are required to provide the operating conditions needed to assure the performance and reliability of the battery packs. Subsequently, computer-aided engineering tools that model the thermal behaviour of a battery are needed to assist with the design and integration of battery packs into vehicles. To meet this need, we have developed a coupled thermal-electric model for battery systems. This paper describes the development and use a computational model to predict battery pack thermal and electrical performance in a vehicle undergoing a realistic drive cycle.

Keywords Electric vehicle · Battery · Thermal modelling

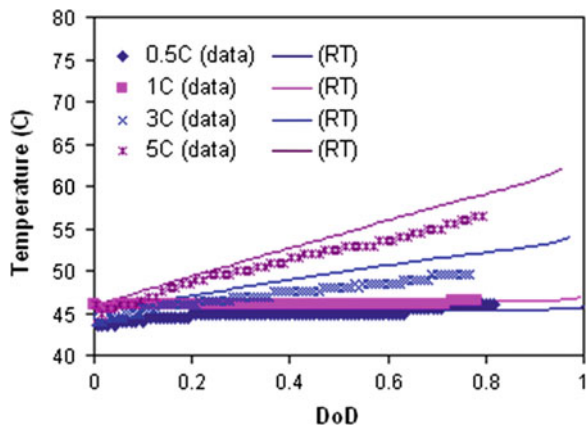
1 Introduction

We have previously developed a battery model that employs an empirical approach to capture discharge behaviour as a function of current density and the depth-of-discharge (or charge depletion) on an electrode [1]. This approach is combined with Poisson's equation, which represents voltage distribution on a 2D plate, to compute voltage and current distribution over the electrodes of a cell

F2012-E13-017

A. Curran (✉) · S. Peck
ThermoAnalytics, Inc, Calumet Township, USA
e-mail: arc@thermoanalytics.com

Fig. 1 Average cell temperature predictions compared to measured data in a controlled 45 °C environment



during charge or discharge. The model developed includes a two-way coupling between electrical and thermal predictions.

Measurements on a lithium-ion cell were made to provide data for validation of the battery thermal-electric model [2]. Terminal voltage and cell surface temperature were measured during constant current discharges in a controlled environment. The cell was simulated in the RadTherm software environment [3] using the model described above; the output of the model was compared to the measurements (Fig. 1).

2 Methodology

A computationally-efficient, equivalent-circuit type model based on the “distributed current density” thermal model described above was developed for use in more computationally demanding simulations. In the equivalent-circuit model, the current density is assumed to be uniform across the cell; each cell is modelled by an internal voltage source, U , and an internal resistance, R , (Fig. 2). In our previous work, the cell was described by an internal voltage and an internal conductance, Y , which is equal to the inverse of the internal resistance. Both U and R are considered to be functions of the cell’s state of charge and temperature, and can be determined experimentally [1].

The power required by the vehicle causes a current draw, I , through each cell in a battery pack (Fig. 3). This produces a voltage drop across the internal resistance of the cell; the cell voltage, V , can be calculated from $V = U - IR$. When the cell voltage drops below a specified cut-off voltage, the cell is considered to be discharged. The power supplied to the vehicle is equal to the product of the current drawn from battery pack and the voltage of the battery pack.

During a thermal-electric simulation, we must calculate each cell’s state of charge and temperature, since the cell’s behaviour (i.e., voltage and internal

Fig. 2 Equivalent circuit representation of a single cell

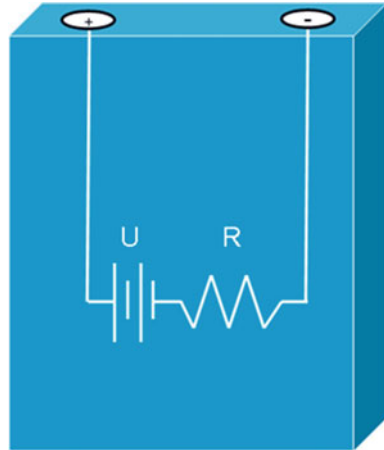
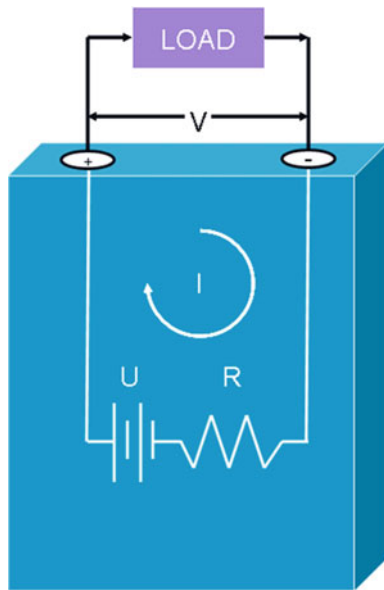


Fig. 3 Equivalent circuit representation of a single cell under load



resistance) depends on both of these quantities. The state of charge is calculated by summing the cell current multiplied by the time-step size for each time step of the simulation. The temperature is calculated by applying the time-varying joule heating, $Q = I^2 R$, to a transient thermal model of the cell. The process for calculating cell voltage and heating when the battery pack is being charged is virtually identical to what is described above for cell discharge.

The performance of the equivalent circuit model was compared to the original battery thermal-electric model by comparing average cell temperature for a 1 C (Fig. 4) and 5 C discharge (Fig. 5).

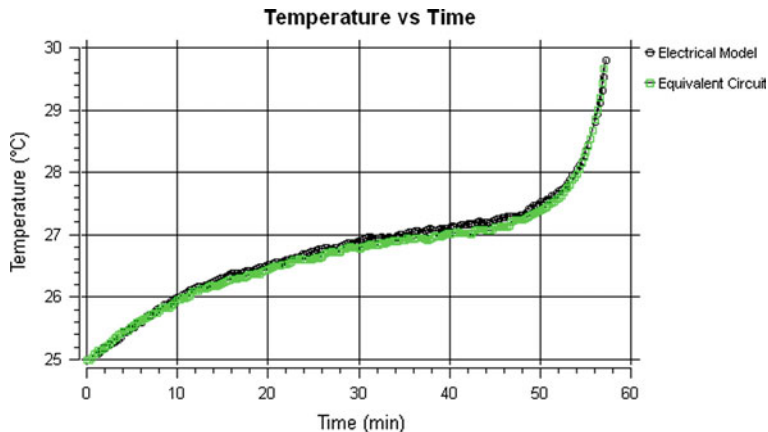


Fig. 4 Average cell temperature for a 1 °C discharge in a controlled, 25 °C environment

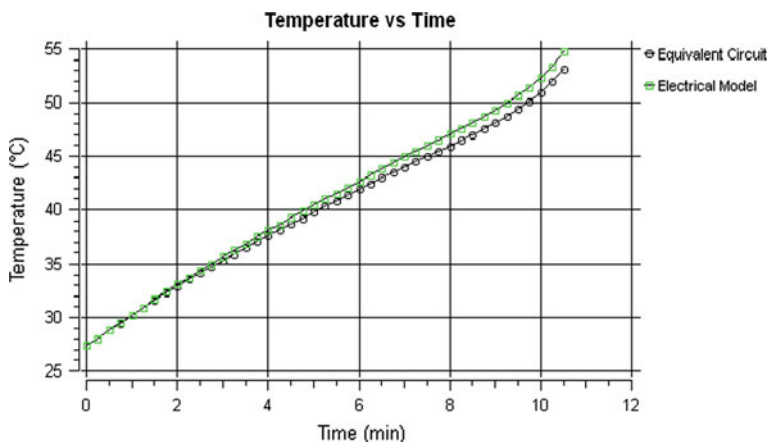


Fig. 5 Average cell temperature for a 5 °C discharge in a controlled, (nominally) 25 °C environment

3 Results

The two battery modelling approaches were applied to a 64 cell battery pack that was placed into a full-vehicle model of a plug-in hybrid. Figure 6 illustrates the model, showing the battery pack in a ducted enclosure behind the passenger compartment above the exhaust pipes.

The 64 cells are connected in series; each cell is 348 × 225 mm, and has a capacity of 45.7 A-h (not intended to represent an existing cell). The pack is placed in an enclosure to shield it from thermal radiation from the surrounding thermal environment, and a serpentine cooling channel is placed underneath the

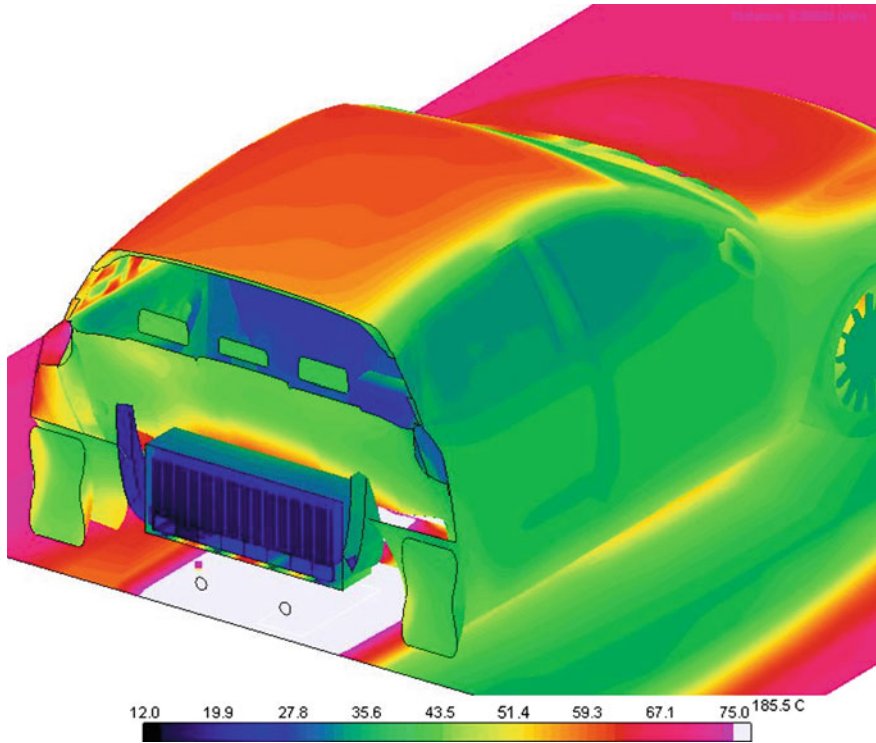


Fig. 6 A cutaway view of a battery pack installed in a plug-in hybrid vehicle

pack. A RadTherm fluid stream is placed in the cooling channel to simulate air flowing at 600 L/min with an inlet temperature of 7 °C. The vehicle was simulated driving on a hot summer day in the Southwest United States.

A transient load was imposed on the battery, based on the power requirements of the URB1 drive cycle described in Ref. [4]. The power profile provided by the battery is shown in Fig. 7. A battery controller script determines the instantaneous current draw on the battery during the simulation. The current is obtained by dividing the power for a given simulation time by the instantaneous voltage across the battery pack terminals. The instantaneous terminal voltage is derived from the collective state of the cells in the pack, as determined by the depth of discharge and local ambient temperature of each cell.

The simulation was performed for a brief drive cycle. The first 20 min were used to initialize the thermal state of the vehicle, followed by three min driving, followed by a short quiescent period. The temperature responses of the cells at the ends of the pack and in the middle of the pack are shown in Fig. 8 for both the original distributed current density battery model and the equivalent circuit battery model. The two modelling approaches predict very similar average temperature rises for the respective cells.

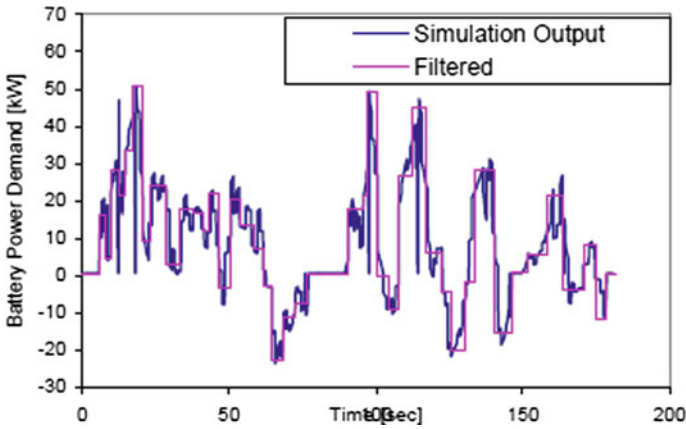


Fig. 7 The power profile derived from the URB1 drive cycle [4]

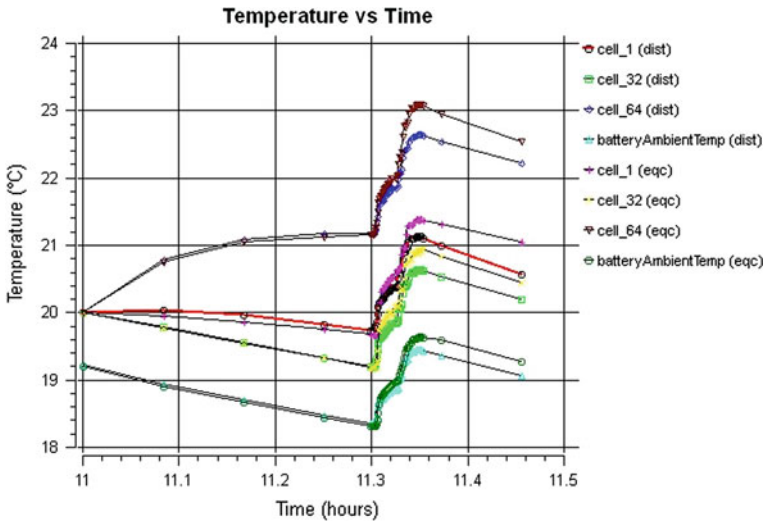


Fig. 8 Cell temperature predicted by the computationally efficient equivalent circuit (*eqc*) model and the original distributed current density (*dist*) model for a hot environment

The temperature distribution over the face of the cells is shown in Fig. 9. The equivalent circuit model, which uses an uniform current density assumption, produces a temperature distribution prediction nearly identical to that of the distributed model, which uses a detailed calculation of current density and local heating.

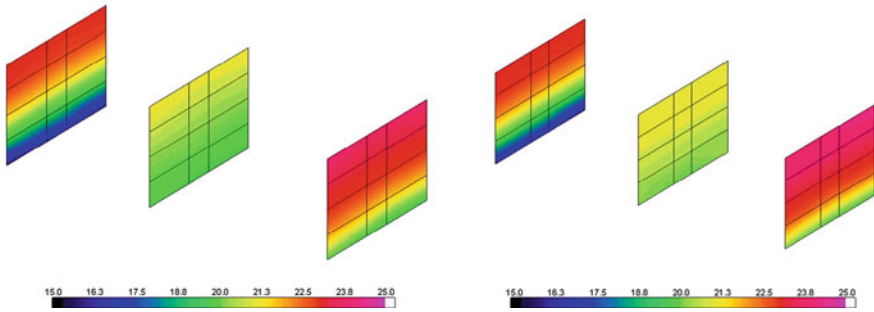


Fig. 9 Predicted cell temperature from the distributed model (*left*) and the equivalent circuit model (*right*) for a hot environment. The cells from both ends of the pack are shown as well as from the *middle* of the pack

4 Conclusions

Computer-aided engineering tools that model the thermal behaviour of a battery are needed to assist with the design and integration of battery packs into vehicles. To meet that need, two coupled thermal-electric models for battery systems have been added to the thermal modelling software RadTherm. The distributed current density battery model can be applied at a high level of detail to address individual cell design issues while the equivalent circuit battery model can be used for lower level of detail studies, e.g. for large cell packs. In the latter case, long transient simulations of a full vehicle become practical. We have shown that the simple equivalent circuit model can adequately predict the temperature distribution of cells in a pack without the additional computational overhead associated with the distributed model. It is also possible to combine the two modelling approaches within the same thermal model.

References

1. Peck S, Pierce M (2012) Development of a temperature-dependent Li-ion battery thermal model, SAE Technical Paper 2012-01-0117, doi:[10.4271/2012-01-0117](https://doi.org/10.4271/2012-01-0117)
2. Peck S, Olszanski T, Zanardelli S, Pierce M (2012) Validation of a thermal-electric li-ion battery model. SAE Int J Passenger Cars—Electron Electr Syst 5(1):154–163. doi:[10.4271/2012-01-0332](https://doi.org/10.4271/2012-01-0332)
3. <http://www.thermoanalytics.com/products/radtherm/>, Thermo analytics, Inc. Retrieved 22 July 2012
4. Duvall M (2005) Battery evaluation for plug-in hybrid electric vehicles. Vehicle power and propulsion 2005 IEEE conference, Sept 2005

Virtual Test Drive in the Application Process of ESP[®]-Systems to Ensure Performance and Robustness

Albert Lutz, Fabien Macaire and Walter My

Abstract Vehicle dynamics simulation is a well established tool in the function development and in software testing of ESP[®]—the Electronic Stability Program. Due to an increase of vehicle variants, additional ESP[®] features, legal requirements and the pressure to increase the overall efficiency in the development process vehicle dynamics simulation is becoming more and more a part of the ESP[®] application process. For this purpose increased requirements of the simulation models, the set-up process of the simulation environment and finally the test cases have to be met. This paper describes the ESP[®] specific simulation methods, the environment and the related process between OEM and supplier to set-up and run the simulation platform commonly. Examples are presented which are applied in two phases in the application process. One is the frontloading process to set-up an initial mature software (SW) supported with simulation. The other one is the handling of projects with a large amount of vehicle variants. In both cases simulation is used to ensure the performance and robustness of the overall vehicle and ESP[®] system.

Keywords ESC · ESP[®] · Application process · Simulation · Sine with dwell test

F2012-E13-019

A. Lutz (✉)
Robert Bosch GmbH, Stuttgart, Germany
e-mail: albert.lutz@de.bosch.com

F. Macaire
Robert Bosch (France) SAS, St ouen, France

W. My
Robert Bosch (Australia) Pty. Ltd, Melbourne, Australia

1 Introduction

For many years, vehicle dynamics simulation at Bosch has been laid out for active safety systems improvements, especially since the beginning of the ESP[®] in 1995 [1]. Nowadays the development of such systems handles an increasing combination of items.

One is the increase of systems complexity due to additional functions called VAFs (Value Added Function). These functions could be either system additions (e.g.: Roll Over Mitigation, Trailer Sway Mitigation, ...) or be part of a networked control system (e.g.: Adaptive Cruise Control, Lane Departure Assist, ...) [2]. This complexity requires more tests to develop and validate all the additional features.

The other one is that the number of vehicles equipped with ESP[®]—also called ESC (Electronic Stability Control) has raised steadily, ref. Fig. 1. While in the premium and medium car segment ESP[®] has long been considered a standard fitment, in small cars it was only pro-posed as an option or not available at all.

However, ESP[®] is just as important for small cars as it is for the premium and medium car segment. Moreover, it is becoming a standard feature for vehicles since the European Parliament decided to make ESP[®] mandatory for new passenger-cars and commercial-vehicles registered in the European Union starting from 2011 [3]. Other regions of the world, currently facing a high growth of their automotive industry, are contributing to the increase of ESP[®]-projects too. And finally the growing number of variants inside of the projects are requiring additional parameter sets and testing effort.

Due to the mandatory fitting of vehicles with ESP[®] an increasing number of tests and ratings have to be performed for certification requirements, both for manufacturers of ESP[®] systems and OEMs. Nowadays according to the ECE R13H Annex 9 the homologation of ESP[®] systems can be supported by vehicle dynamics simulation [4]. Either using simulation as support and complementing physical tests [5] and for in-stance verification of vehicle variants of a project [6].

Finally the worldwide competition leads to permanent pressure to reduce costs and development time. Vehicle dynamics simulation itself, based on a continuous improvement, seems the key to meet those challenges as shown by the number of publications on this topic.

Bosch has been using vehicle dynamics simulation since the mid of the 1980s for function development and software tests and later on for the support of homologation tests. The challenge is now to use simulation for application series projects. Initially the following chapters present methods, tools and processes provided by Bosch to set-up and operate a common simulation environment together with the OEM. The final part of the paper will highlight examples and results showing the potential of vehicle dynamics simulation to support the application engineer focusing on the vehicle dynamic controller (VDC) inside of ESP[®]. The last chapter gives a summary with conclusions and an outlook.

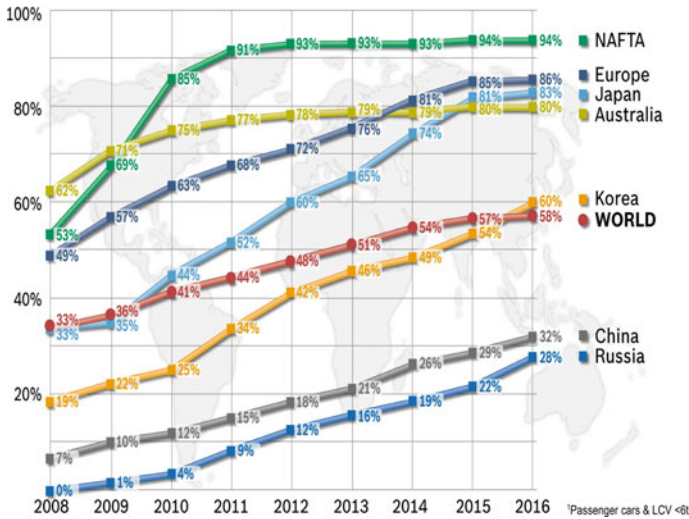


Fig. 1 ESP® installation rates—based on production (Bosch 08/2011)

2 Application Process of ESP® Systems

The ESP® system supports the driver in critical driving situations by controlling brake forces and the engine torque to ensure that the vehicle can be driven in a stable, steerable and safe manner [2]. The application of the ESP® system for all vehicle variants has to ensure that the performance requirements are fulfilled. This means interventions are early enough and well adapted. Equally the robustness has to be guaranteed, too. This means no interventions are accepted as long as the vehicle is not in a critical situation. As a result to this there is a conflict in the targets, interventions and driver feeling. Figure 2 shows both the main targets of the application process which have to be ensured according to the specification of the OEM and the workflow which guarantees that the targets are fulfilled in all vehicle projects at all Bosch locations. The workflow starts with a project definition phase followed by the delivery of test vehicles. A first major step is the preparation phase divided into two paths. One path is the SW set-up phase with an initial parameter set followed by testing in the laboratory to ensure a mature SW is being applied to the car. The other path contains the equipment of the vehicle with ESP® specific components and measurement equipment. At the end of this phase the vehicle can be taken into operation. The next main phase is the basic application where vehicle specific characteristics are determined by tests on the bench or test track. Afterwards, the tuning of the ESP® takes place in an iterative process on high and low- μ conditions. At the end of each tuning phase a new software baseline is generated and released by a standardized verification procedure based on the Bosch Vehicle Test Catalogue (VTC).

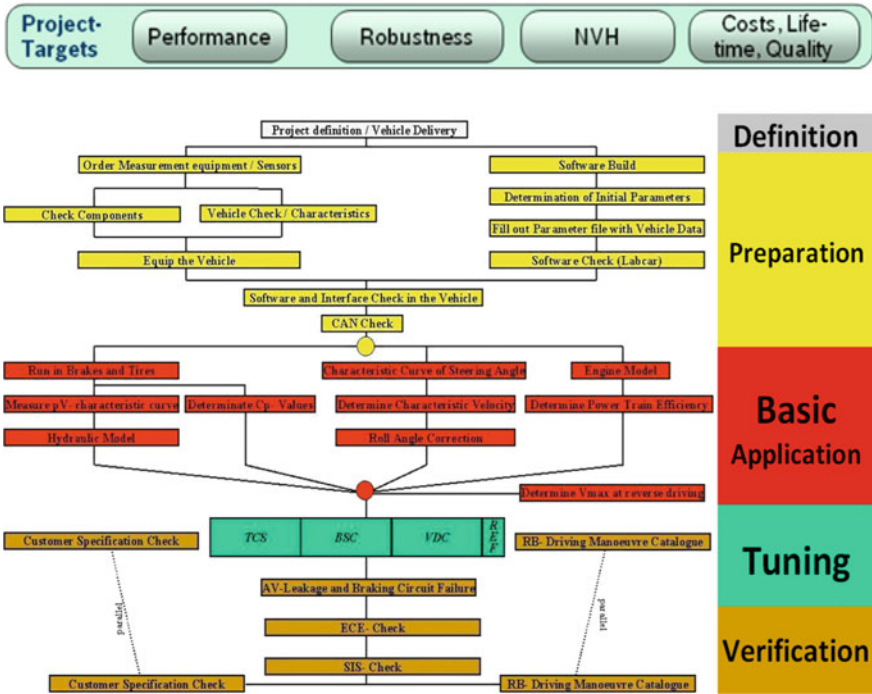


Fig. 2 Workflow of the ESP® application process

The application phases (basic application, tuning and verification) are today mainly based on vehicle tests. The target is to transfer as many tests as possible to the virtual world, wherever it makes sense and improves the efficiency. Major focus is frontloading by providing a mature software and substitution of missing vehicle variants. For both approaches tests with objective criteria are needed.

3 Simulation Process and Technical Solutions

3.1 Simulation in the Project Development Cycle

In the development and application process of the ESP® system simulation is used along the entire V-model (see Fig. 3). Different methods like Model in the Loop (MiL), Software in the Loop (SiL) and Hardware in the Loop (HiL) are applied.

This paper is focusing on the SiL simulation which has two characteristics:

- Usage of simplified, generic models for function and software development and test.

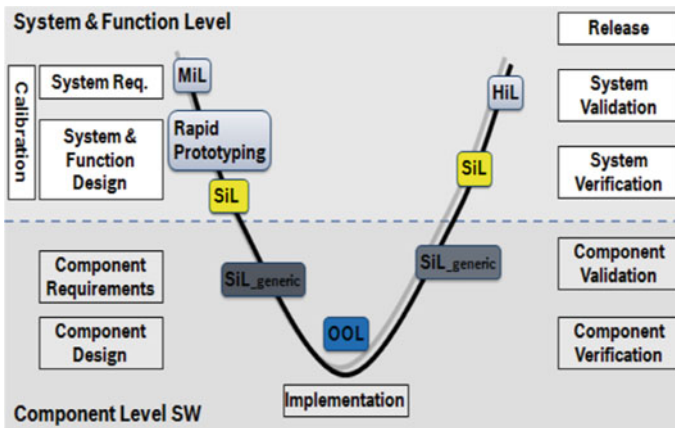


Fig. 3 Simulation in the V-model

- Project specific, validated models from the OEM are used to support robustness and performance tuning and tests by using the so-called Virtual Test Drive (see Sect. 3.4).

Bosch supports a variety of SiL vehicle dynamics simulation tools e.g. Car-Maker, veDYNA, CarSim and also Multibody Systems (MBS) e.g. Adams, SIMPACK.

3.2 Project Definition and Simulation Environment Set-Up

The use of simulation must be agreed upon by both Bosch and the OEM during the acquisition phase. This includes a clear definition of the targets and responsibilities. The simulation activities have also to be embedded in the project plan and in the Bosch and OEM teams as shown in Fig. 4. Project milestones such as SW releases, test phases and vehicle deliveries are adapted to the planned simulation activities. Updates of the simulation environment with ESP[®] models and/or virtual prototypes are also defined in advance by the project teams.

Technical solutions have to be specified during the acquisition phase with details like OEM simulation environment, simulation tools including versions, model-, file types and inputs/outputs of the models including units. Furthermore tools and information exchanges must be protected by non-disclosure agreements.

After defining the simulation project the set-up of the simulation environment can commence. Depending on the targets both the OEM and Bosch have to provide models and their parameter sets based on the defined tools:

- OEM: Vehicle parameter sets including tire and power-train model.
- Bosch: ESP[®] controller model incl. sensors, actuation and parameter sets.

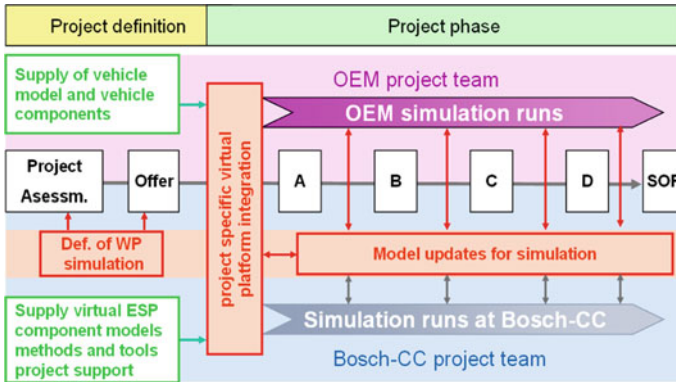


Fig. 4 Simulation embedded in the project plan

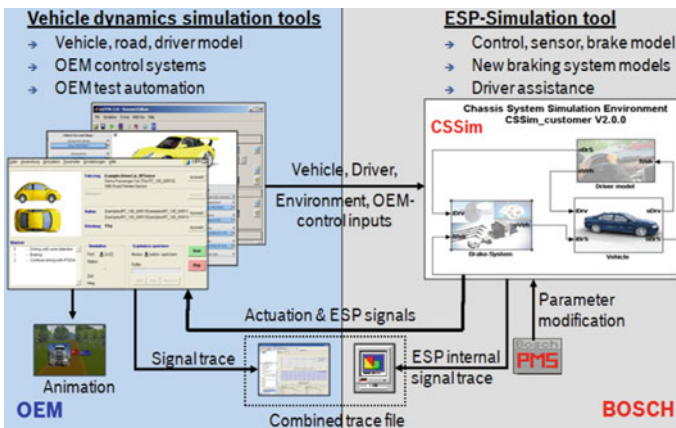


Fig. 5 Set-up simulation environment

Figure 5 shows the working principle of a simulation environment. The OEM vehicle dynamics simulation tool inter-faces with the BOSCH internal simulation tool CSSim which includes the ESP[®] controller software as an S-function. In addition to that it also includes a generic vehicle, a driver model and environmental models which are unused when coupled with OEM tools. The Simulink based CSSim is used at Bosch for:

- Vehicle dynamics function development and integration tests.
- Investigations of functional chains.
- Integration of third-party models.
- Base for ESP[®] controller integration in OEM simulation environments.

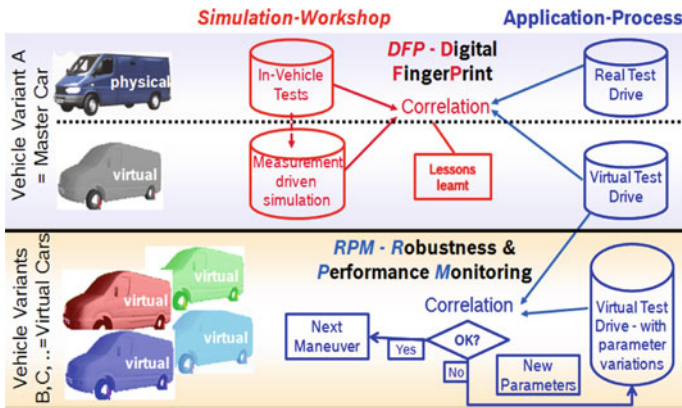


Fig. 6 Master car approach

The simulation environment is specified in such a way that the interface between application engineer and the ESP® system in the simulation is identical to the vehicle. For this purpose, the same ESP® output files are used in the simulation to enable identical post processing independent from vehicle test or simulation. Additionally the parameter modification tool used in the vehicle is also implemented in the simulation environment.

3.3 Simulation Workshop

Necessary for achieving the desired targets is a high quality simulation environment. The quality can be assessed by following the correlation process that Bosch offers to their OEMs, which has been adapted and improved in multiple collaborations over the past years. Therefore, after the simulation has been set-up, a simulation workshop takes place on a proving ground as a joint activity for the duration of usually four days. The purpose is to validate the simulation environment, to identify its capability and to check the quality against the defined targets, see Fig. 6. In a first step reference data is collected by tests on an existing prototype—the so-called master car. After that, the driver inputs from the real maneuvers are used as inputs to the simulation environment, where the same vehicle is available as a virtual proto-type. Both results are then automatically compared and assessed. This assessment is called DFP (Digital Finger Print) as it helps to characterize the current capability of the simulation environment. An important point for the success of this process is to understand why a deviation of the results may have occurred and to document the findings in a lessons learnt database. Also, it is necessary to update the data acquisition process and to set-up quality gates if necessary. In doing that, a high degree of confidence as to the

quality of virtual prototypes that are generated with the same process and tool chain can be obtained.

3.4 Virtual Test Drive

In contrast to the real testing environment on proving grounds, the simulation environment offers perfect conditions for application, i.e. no unintended environmental or vehicle variations and changes during testing occurs. Depending on the quality of the simulation environment some application process steps can be automated by using a scripted based version of the Bosch parameter modification tool, objective criteria and optimization tools [7]. Test results from missing vehicles can be checked versus the virtual master car using objective or mathematical criteria, ref. Fig. 6. Focus of the check is performance and also robustness aspects of the ESP[®] tuning. If this is done we are talking about Performance and Robustness Monitoring (RPM). Furthermore verification and robustness checks can be done by modify-ing the relevant system parameters.

To assist the application engineer a graphical user interface has been developed which is based on the application process of ESP[®] systems and independent from the used vehicle dynamics simulation tool. Main features include:

- Testing on digitalized tracks
- Measurement driven simulation
- Testing based on VTC maneuvers and on Objective Performance Release criteria (OPR)
- Automated application steps.

The utilization of the RPM inside of the Virtual Test Drive concept means that missing prototypes are checked virtually and continuously against the virtual Master Car with each SW release or prototype model update. In the following chapter some examples for the frontloading process and the variant handling phase will be explained in detail.

4 Examples

This chapter will describe examples of maneuvers currently performed at Bosch: First of all tuning maneuvers of the VDC basic application phase, then the sine with dwell maneuver whose results assess performance of the VDC, and finally the threshold consumption and banked curves test whose results give an insight as to the robustness of the VDC.

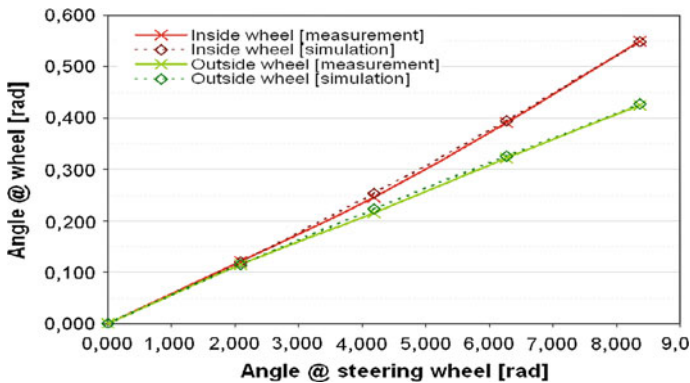


Fig. 7 Wheel angle values versus steering wheel angle

4.1 Initial Tuning

In the basic application phase, frontloading consists of selecting project specific data as well as initial ESP[®] parameter sets from predecessor projects and the determination of some vehicle characteristics with the aim of providing a mature SW for initial implementation in the car. Thanks to results from maneuvers performed in SiL simulation—rather than on a physical prototype—some of the vehicle characteristics can be determined. This gives the supplier more flexibility to cope with the availability of prototypes.

The steering characteristic consists of identifying first of all the relationship between the steering wheel angle versus the steering angle at each front wheel, and also versus the average angle values of front wheels. The results are analyzed with the same tool as for physical proto-type tests. Today, the correlation between SiL and the physical results is very accurate for most of the OEMs as shown in Fig. 7. The difference between physical and SiL tests is less than 3 %.

To allow the VDC controller of the ESP[®] to calculate a target yaw rate of the vehicle, a para-meter named “characteristic velocity” must be determined and used in the so-called Acker-mann equation [2]. This characteristic velocity gives a plausible yaw rate value for linear and steady-state driving conditions at constant speed. Today, the correlation between SiL and physical results is quite good for most of the OEMs with a difference of less than 10 % between physical and SiL tests which is sufficient to calculate the target yaw rate of the vehicle with a good precision.

4.2 Performance Check and Tuning

The ESP[®] has to ensure the stability as well as the steerability of the vehicle. To ensure those features the NHTSA established the FMVSS126-test for the

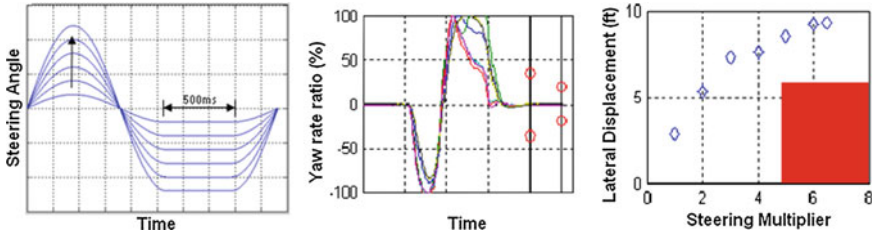


Fig. 8 Sine with dwell maneuver steering inputs and analysis

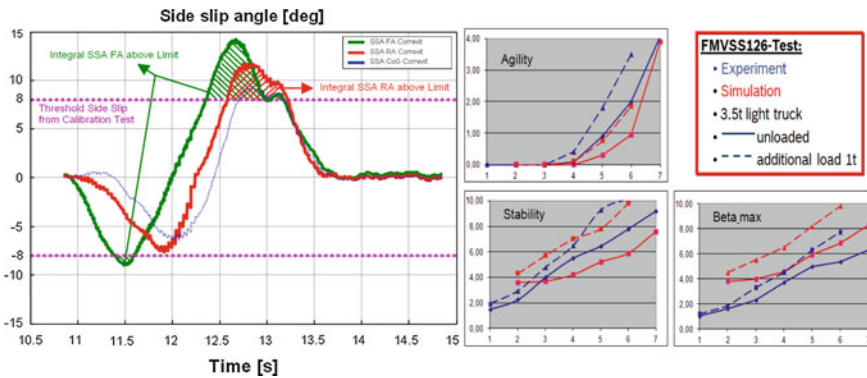


Fig. 9 Definition of side slip based criteria (left) and comparison of measured and simulated stability, agility, beta_max values versus steering multiplier (right)

homologation of ESP[®] systems. The test which has to be performed by a steering robot is a so-called sine with dwell with multiple amplitudes and it is the main test of ECE R13H homologation for ESP[®]. For more details please see [4, 8,9] and Fig. 8.

The evaluation of the tests is done by analyzing the yaw rate on one hand. 1 s after the end of the maneuver the yaw rate has to be below 35 % and at 1.75 s 20 % below the maximum peak yaw rate. On the other hand the lateral displacement of a vehicle (<3500 kg) must be greater than 1.83 m (6 ft), see Fig. 8.

More information on the performance of the ESP[®] system can be gained from the criteria developed by Bosch [10], based on the sine with dwell maneuver. The evaluation uses side slip values. For this a threshold value is defined by determining the side slip angle at 0.3 g lateral acceleration. Then three criteria are derived as detailed in Fig. 9:

- Stability criteria: integral of the rear side slip angle exceeding the threshold value.
- Agility criteria: difference of the integrals of the front and rear side slip angle exceeding the threshold value.
- Beta max criteria: maximum of the side slip angle at the center of gravity.

Due to the objective criteria the test case is well suited to be used by simulation to check the performance of the VDC controller of variants which are not available at Bosch teams or even to use it to improve the ESP® performance in the frontloading process. Figure 9 shows a comparison of an analysis based on measured and simulated results for a light truck without and with loading. For both cases—unloaded and loaded—the simulation shows a quite good correlation with measured results.

4.3 Robustness Check

Finally the VDC of the ESP® has to ensure robustness and safety to avoid mis- or early interventions. This means active interventions are only allowed if conditions are fulfilled and indicators of events are exceeded.

4.3.1 Threshold Consumption

To guarantee the robustness of ESP® systems, physical tests are performed on cross-country roads, driving according to the speed limits and a lateral acceleration up to ± 0.6 g and with a continuous analysis of ESP® internal signals. Meanwhile those maneuvers can be transferred to the virtual test drive too, using GPS-based tracks. The signals analyzed are the calculated target and the current measured yaw rate. The threshold consumption value (TC) for VDC interventions is an indicator of an over- or under-steering behavior of the vehicle. Over-steering behavior is calculated according to Eq. (1)

$$TC = 100\% \frac{|\Delta\dot{\psi}|}{\dot{\psi}_{threshold}} \quad (1)$$

With:

- $\Delta\dot{\psi}$ = deviation between calculated target yaw rate and current measured yaw rate.
- $\dot{\psi}_{threshold}$ = threshold of the VDC controller on which intervention are based.
- TC = 0 % : no over-steering situation, not regarded.
- TC = 0...100 % : over-steering situation without ESP® intervention.
- TC > 100 % : controller release, intervention by ESP®.

For a robust tuning of the ESP® no interventions should occur during a normal driving situation. In contrast, projects showing high values of TC are not robust enough and have to be re-tuned.

This robustness test is analyzed using different panels as shown in Fig. 10. The left one indicates to the user the driving conditions (longitudinal speed versus

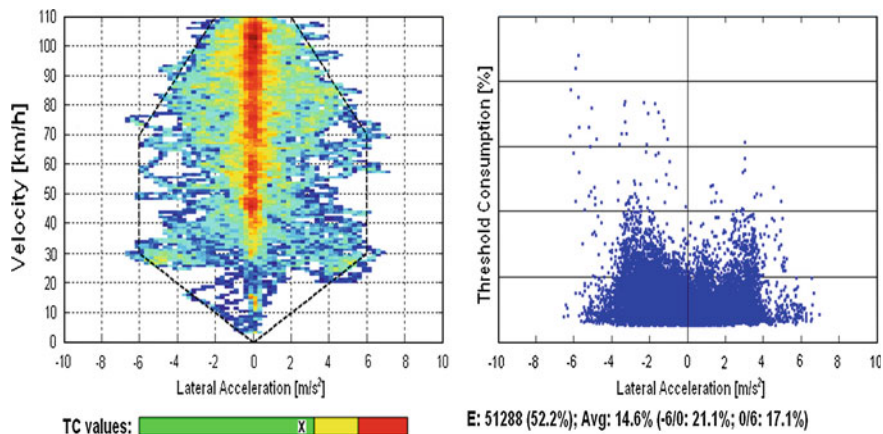


Fig. 10 Visualization of the TC results

lateral acceleration) identified by colors: in blue, driving situations where the vehicle is only occasionally and in red where the vehicle is very often. The test is valid if the driving conditions are mostly inside the black dashed area to ensure that all relevant driving situations are covered. The right panel indicates the TC level for each event versus the lateral acceleration.

Gyro colors assess the calculated average TC-values:

- green: good
- yellow: to be inspected carefully
- red: predicts an insufficient robustness of the ESP[®] system.

Below this information some TC digits indicate the number of events, the TC global average and the average for left and right turn. The user is also able to display these TC values versus other signals like for instance the vehicle speed or the yaw rate. All these features offer the flexibility to analyze different conditions in order to ensure the best robustness level of the ESP[®] system.

To cope with the increasing amount of vehicle variants and additional functions, the current focus is to obtain the TC values from the laboratory. This needs a validated vehicle model, an accurate modeling of the track based on GPS measurements and an efficient driver model. Figure 11 shows real road scenarios and a related virtual part. Interesting to note is that although there are some visible differences in the vehicle speed versus lateral acceleration plots, the related TC-values derived vary only in a negligible way. Also the correlation between measurement #1 and the simulation is quite good.

Numerical simulation is able to provide information on the TC tendency. Figure 12 shows a correlation between both experimental and simulation tests done using different tire configurations using summer (ST) and winter tires (WT). The more over-steering behavior (higher TC value) expected using ST on the front axle and WT on the rear axle is also predicted by simulation and confirmed by

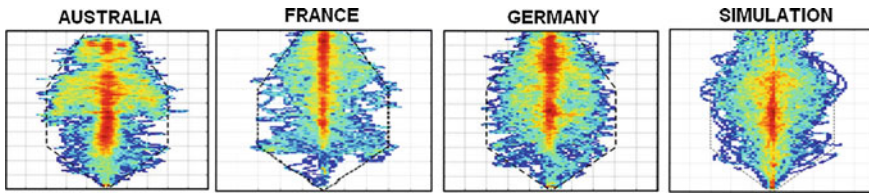
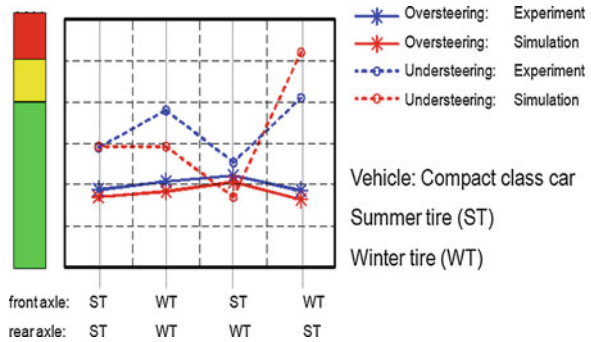


Fig. 11 Velocity—lateral acceleration profile (*left* measurements from different Bosch regions—*right* picture simulation results of Australian profile)

Fig. 12 Measured and simulated TC values (tire study)



experiment. Conversely, a more under-steering behavior is obtained using WT on the front and ST on the rear axle.

4.3.2 Detection of Banked Curves

ESP® checks consistently the plausibility of sensor signals. On banked curves this plausibility is no longer given as such curves can be driven without any lateral acceleration. Therefore, banked curves have to be detected by adequate measures to avoid mis-interventions or even unintended system shutdowns. This is the reason why a lot of effort has to be spent on this topic. An issue is that the availability of different banked curves around the world is limited. To support these tests by simulation existing tracks but also synthetic tracks like s-curves have been modeled. In addition to real tests the parameters of the tracks (radius, elevation, curvature, height,...) and also of the car (center of gravity, mass,...) can be varied inside user defined limits automatically in the simulation which increases the depth of testing, ref. Fig. 13. An evaluation is done based on the standard methods which are applied to real tests, too. Analogous to the TC method critical configurations of the system are indicated to the application engineer by color codes. In a first step real tests are prepared with the test method. Depending on the experience in a second step tests with vehicle variants might be substituted.



Fig. 13 Modeling of banked curves and comparison of measured and simulated quantities

5 Summary, Conclusions and Outlook

Pilot projects have shown the potential of vehicle dynamics simulation in the application process of ESP[®] systems. Based on a well defined process the OEM and supplier are able to build-up and maintain a common simulation platform using validated project specific vehicle models from the OEM. Objective or mathematical criteria enable us to check in an automated way real vehicle variants to a virtual reference with focus on performance and robustness. The major benefits can be seen today for the ESP[®] functions VDC and ABS, and also for VAFs. A transfer to the TCS function requires more detailed and accurate modeling. Applied in different stages of the application process it leads to a win-win-situation for both partners. The development of objective criteria for the automated evaluation of simulation results are the big challenges for the future.

Acknowledgments A special thank you to all Bosch colleagues around the world for supporting the simulation activities. Their efforts in analyzing tool developments and simulation results have been indispensable to the success of these activities. Of course, also big credit is due to the Bosch management for motivating and supporting the simulation teams, especially to mention is Dr. Liebemann, Mr. Liersch, Mr. Villemin and Mr. Langhorst.

References

1. van Zanten A, Erhardt R, Lutz A, Neuwald W, Bartels H (1996) Simulation for the development of the Bosch-VDC—SAE960486, SAE-conference, USA
2. Winner H et al. (2009) Handbuch fahrerassistenzsysteme, Vieweg+Teubner, GW Fachverlage GmbH, Wiesbaden
3. Regulation (EC) No. 661/2009 of the European Parliament and Council of 13 July 2009
4. ECE Regulation No. 13-H: <http://live.unece.org/fileadmin/DAM/trans/main/wp29/wp29regs/r013hr1a2e.pdf>
5. Reymend G et al (2006) Validation of renault's dynamic simulator for adaptive cruise control experiments, RENAULT, Research Department, 78288 Guyancourt Cedex, France
6. Fuhr F (2010) Variant validation in the development process of chassis control systems using CarMaker for simulink. IPG technology conference apply and innovate 2010, Karlsruhe

7. Knödler K, Ruf M (2008) Calibration of Vehicle stability controllers based on active learning methods in vehicle dynamics simulation. FISITA, München
8. Holzmann H, Webb J (2012) Simulation-based homologation of ESC-systems according to ECE-R 13-H, 12. Int. Stuttgarter symposium, Automobil- u- Motorentechnik, Stuttgart
9. Wüst K, Lutz A (2012) Simulation-aided homologation of ESP systems for NAFTA vans by software-in-the-loop methods. IPG technology conference apply and innovate 2012, Karlsruhe
10. Gerdes M, Dittrich S (2006) Objective assessment of vehicle stability with ESP. VDI-Berichte Nr 1931:249–258

The Test and Analysis of Car's Brake Noise

Qinghai Sui

Abstract With the development of the car industry and the rising of consumer's requirements for comfort, brake noise gradually becomes one of the important factors to appraise the comfort of vehicle. This paper, aiming at solving the noise problem of the passenger car, researches the mechanism of brake noise's generation and the ways to optimize it in order to reduce the noise. The brake noise is tested according to the road test standard. The frequency and intensity of the noise are recorded in the vehicle test. At the same time, the relation of speed and the noise's frequency is recorded. The brake noise is divided into Squeal noise and Groan noise based on the test results of the car. Squeal noise: It is important to collect more information in the dynamometer which used suspension assembly to analyze the character of noise. The noise mechanism is analyzed and the optimum direction is found through the computer CAE technique. Groan noise: Based on the calculation and analysis of the test results, the main influencing factors of the noise are found and the optimum scheme is designed. Finally the performance of brake noise is validated in the dynamometer and the vehicle test. Computer analysis and test results show that Squeal noise is caused by the resonance of the brake system. In this paper, brake noise is reduced by reducing the stiffness of the brake disc by an average of 5 %, optimizing the inherent character of the brake system and improving the stability of the brake system. Based on the test and the analysis, the main cause of the Groan noise is that the structure of brake pad and brake disc's ventilation is designed with defects. Groan noise is related to the structure of brake pad and brake disc's ventilation. It is effective to reduce noise by optimizing brake pad's structure.

Keywords Brake noise · Squeal · Groan · Brake system

F2012-E13-020

Q. Sui (✉)

China Faw Co., Ltd. R&D Center, Beijing, People's Republic of China

e-mail: suiqinghai@rdc.faw.com.cn

Fig. 1 The information and statistics of assessment of Squeal

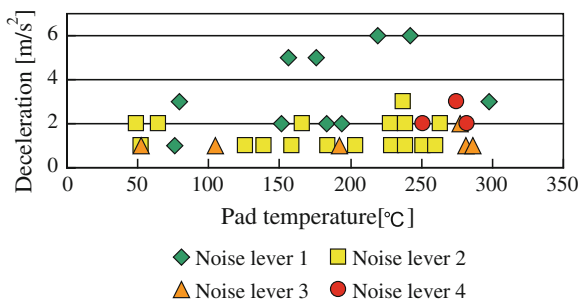
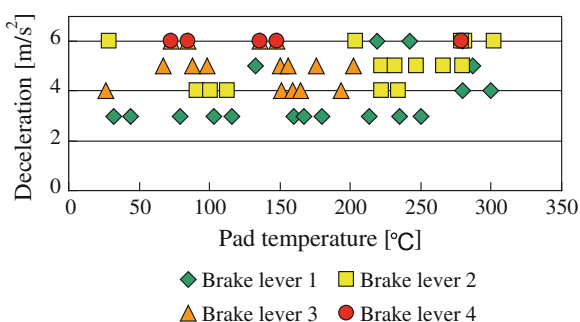


Fig. 2 The information and statistics of assessment of Groan



1 Brake Noise Test

Brake noise test contains the road test and the dynamometer test [1]. The performance of brake noise in the vehicle would be truthfully reflected in the road test [2]. Drivers could evaluate the brake noise from customers’ point of view in the road test which is made the basis for final acceptance. Through the dynamometer test, more information of noise could be got. It combined with the results on the computer analysis, provides effective means for the analysis of noise problem and the verification of the optimum scheme [3, 4].

The car is evaluated according to the road test standard. The results are shown in Figs. 1 and 2. The frequency of noise in Fig. 1 is more than 1000 Hz and it’s called the Squeal. The frequency of noise in Fig. 2 is less than 1000 Hz and it’s called the Groan. As shown in Figs. 1 and 2, the probability of the two kinds of noise is very high. “Noise of level 4” appears in both of the figures (The noise level is from 1 to 4, the greater the value is, the worse the noise is. The “noise of level 4” is not acceptable). There are differences between two kinds of noises. The Squeal mainly appears in the situation of low-intensity brake and the Groan mainly appears in the situation of high-intensity brake. The greater the brake strength is, the worse the Squeal and Groan noise level are.

Fig. 3 The brake noise test on vehicle

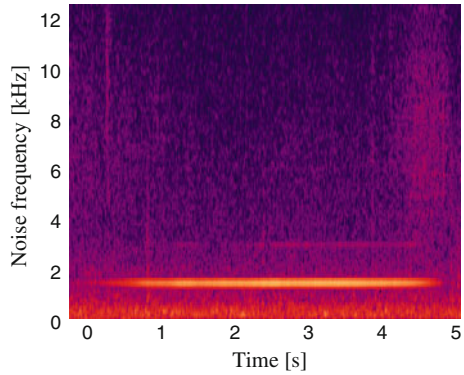
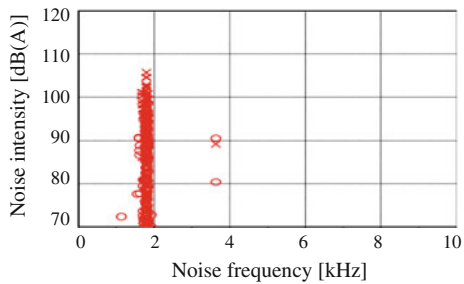


Fig. 4 The brake noise test on dynamometer



2 Noise Analysis

2.1 Squeal Noise Analysis



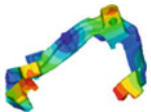
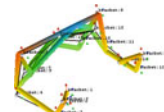
The information of vehicle Squeal noise test is shown in Fig. 3. The frequency of squeal noise is 1800 Hz or so, and the intensity of noise is 100 dB (A) above.

The squeal noise is tested in the dynamometer according to the standard of “SAE 2521”, the result is shown in Fig. 4. The frequency of the squeal noise tested in the dynamometer is 1800 Hz or so. Test data shows that the probability of the noise above 70 dB (A) is 29 %. The probability of the noise would increase if the temperature reaches 100 ~ 300 °C and hydraulic pressure reaches 15 ~ 25 bar. The temperature and hydraulic pressure at which noise occurs may affect the comfort of vehicle.

According to the test results, it is known that the frequency of squeal noise is mainly 1800 Hz or so. If the noise was caused by the resonance of the brake system, there may be intrinsic mode which is close to 1800 Hz of brake caliper and brake disc. The intrinsic mode of brake caliper and brake disc is analyzed in the Computer and tested in the dynamometer. The results are shown in Table 1.

According to the CAE analysis’ results, the frequency of the 5th vibration modes in the intrinsic mode of the brake caliper is 2082 Hz, the frequency of the

Table 1 Information and statistics of brake caliper and brake disc' intrinsic mode

	CAE modal		Testing modal	
	style	Frequency (Hz)	style	Frequency (Hz)
3ed vibration modes		1693		1734
5th vibration modes		2082		2114

3ed vibration modes in the of the brake disc is 1693 Hz. According to the test results, the frequency of the 5th vibration modes in the intrinsic mode of the brake caliper is 2114 Hz, The frequency of the 3ed vibration modes in the of the brake disc is 1734 Hz. Both of brake disc and brake caliper have the intrinsic mode whose frequency are close to 1800 Hz. The system may resonate when there is some incentive.

The brake system model was built in order to further analyze the brake system's stability in CAE. The negative damping coefficient indicates the stability of the complex modal of the brake system in a certain intrinsic frequency. The greater the negative damping coefficient value is, the more unstable the system is, the higher the probability of the noise is.

According to the CAE analysis' results, when the vibrant frequency of complex modal is 1800 Hz, the negative damping coefficient is 0.025. The negative damping coefficient is below 0.005 except the vibrant frequency is 1800 Hz. The resonance of system may be one of the reasons that cause Squeal noise problem.

Based on analysis results above, changing the intrinsic modal of brake parts may improve the stability of the system. In this paper, the intrinsic modal of brake disc is changed by adjusting the elastic modulus. The elastic modulus of brake disc is E. The elastic modulus is adjusted to E+10 % and E-10 %. The relationship between elastic modulus of brake disc and the negative damping coefficient of the system is shown in Fig. 5.

The results indicated that the negative damping coefficient is reduced by decreasing or increasing the stiffness of brake disc; in the same stiffness variation condition, reducing the stiffness of brake disc is more effective to reduce negative damping coefficient of the system.

The stiffness of brake disc decreases by optimizing the structure of the brake disc's ventilation. The stiffness of the brake disc has been reduced by 5 % in the analysis of the brake disc's intrinsic modal; the analysis of the complex modal of system shows that, when the vibrant frequency of complex modal is 1800 Hz the negative damping coefficient is 0.008. The brake system tends to be stability (Table 2).

Fig. 5 The relationship between the elastic modulus of brake disc and the negative damping coefficient of system

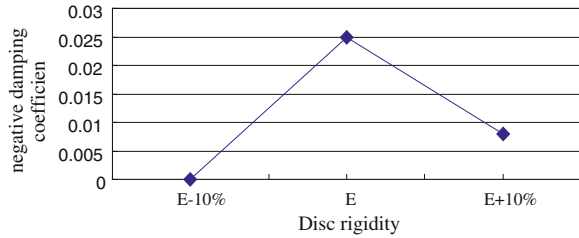
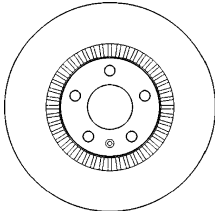
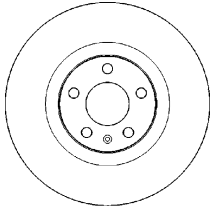


Table 2 Brake disc structure contrast

Brake disc original structure	Brake disc optimization structure
	

Dynamometer test of optimization structure: The main frequency of brake noise is 1800 Hz. The maximum intensity of the noise is below 100 dB (A). The probability that noise appeared is less than 1 %. It's shown in Fig. 6.

2.2 Groan Noise Analysis

The frequency and intensity of the noise and the relationship between frequency and speed are tested in the vehicle. As shown in Fig. 7, the frequency of the Groan noise is between 80 and 120 Hz, and it changes with the speed of the vehicle. The maximum intensity of noise is 50 dB (A) or so. By processing the data, we can get the curve as shown in Fig. 8.

The straight line in Fig. 8 can be expressed by the following formula:

$$f_{(Hz)} = (5 \sim 7)V_{(km/h)} \tag{1}$$

The low-frequency noise usually has strong correlation with the structure of the parts. The friction surface of brake disc is separated by soft and hard area, as shown in Fig. 9. There are 44 ventilations in the brake disc of the car, so the surface is divided into 44 areas in average. In the brake process, brake pad periodically contact soft and hard area of brake disc with the rotation of the wheel, which causes the change of brake force periodically, The change of the force may cause the vibration of the force.

Fig. 6 The brake noise test result on dynamometer after optimization

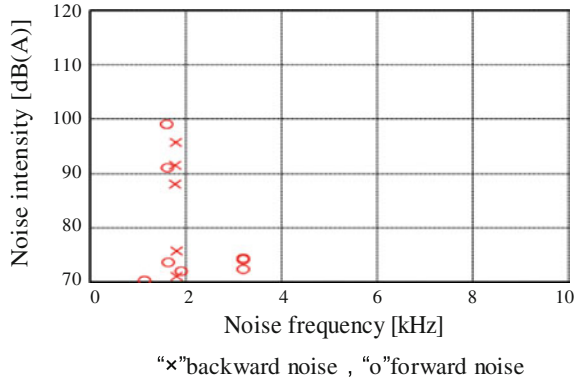


Fig. 7 Groan noise test

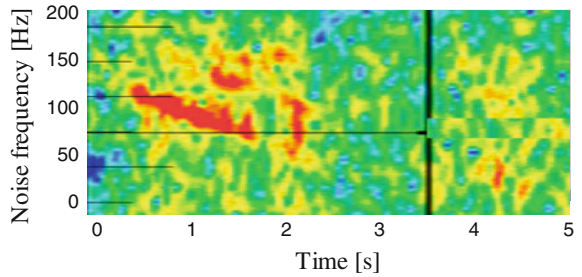
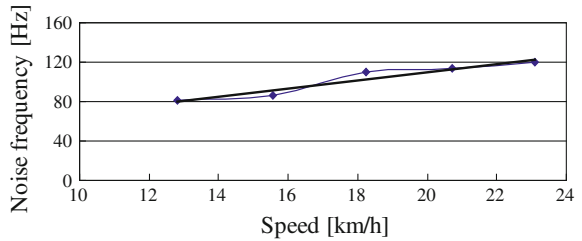


Fig. 8 The relationship of noise frequency and the speed



If the analysis above was tenable, there should be certain relations between the ventilation’s frequency rotating with wheel and the frequency of brake noise. Assuming that the noise is caused by the structure of the brake disc’s ventilation and the time that the brake disc rotates a circle is 1 s, the frequency of the noise is 44 Hz.

The following formula would be got through the assumptions above:

$$n_{(r/s)} = \frac{V_{(km/h)}}{3.6 \times R} \tag{2}$$

$$n = \frac{V_{(km/h)}}{2\pi \times 3.6 \times R} = \frac{V_{(km/h)}}{7.45} \tag{3}$$

Fig. 9 Brake disc structure

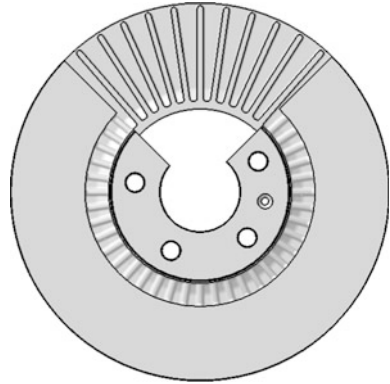
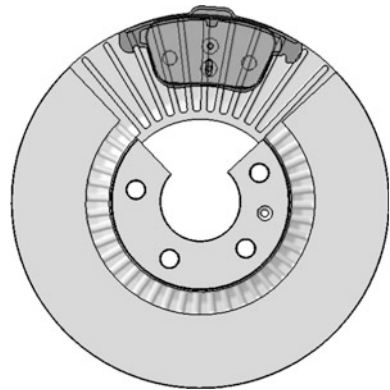


Fig. 10 The relationship between brake pad structure and brake disc structure



$$f_{(Hz)} = 44 \times n = 44 \times \frac{V_{(km/h)}}{7.45} = 5.9V_{(km/h)} \tag{4}$$

- $n_{(r/s)}$ Angular velocity of the brake disc [rad/s]
- R Wheel rolling radius [m]
- n Brake disc's speed [circle/s]
- $f_{(Hz)}$ Frequency of brake disc's ventilation passed by brake pad [Hz]
- $V_{(km/h)}$ Speed of the vehicle.

It is shown that the formula 1 is similar to formula 4 in the calculation results. Preliminary judgment: the coordination between ventilation's structure and the structure of the brake pad is a factor which affects the groan noise.

Noise is caused by vibrations, and vibration is due to the periodic fluctuations of the force, the strength of the force would affect the intensity of the vibration. One side of brake pad's contour line and the direction of the ventilation are in the same direction. In the braking process, the overall soft and hard area of brake disc's surface pass through one side of the brake pad's contour line, which can cause fluctuation of the brake force. It is shown in Fig. 10.

Table 3 Optimization scheme of brake pad’s structure






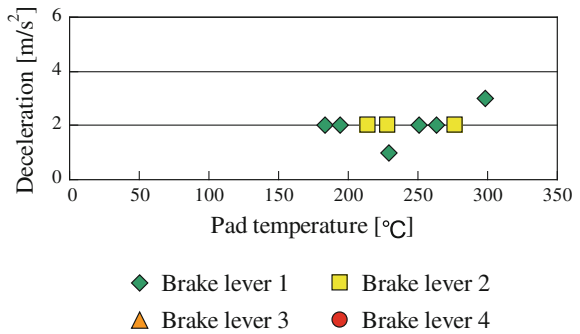
Original scheme	Design scheme		Optimum scheme
	Name	Schematic	
No chamfer			Parallel chamfer
	“V” chamfer		
	“A” chamfer		
	Parallel chamfer		

Fig. 11 Information and statistics of the assessment of Squeal



Based on the analysis above, by changing the structure of the brake pad, the coordination between the brake pad and the disc is optimized. There is certain transition when the soft and hard areas of the brake disc’s surface pass through the brake pad’s contour line, which can reduce the effect of the structure of ventilation on the fluctuation of the break force. Finally, it reduces the vibration. The new design scheme of the brake pad’s structure is shown in Table 3. According to the vehicle test, three kinds of schemes for noise all have the optimization effect, and the parallel chamfer scheme is the best of all.

3 Road Test of Brake Noise

The road test result is shown in Fig. 11: The probability of the Squeal noise appearing is low. There is no noise above 100 dB (A). The noise is mainly appears when the deceleration is 2 m/s² or so and the temperature is from 180 to 275 °C. The Groan noise didn’t appear.

4 Conclusion

Different kind of noise is affected by different factors. High frequency noise is mainly caused by the resonance of the brake system stimulated from the friction surface. Low frequency noise is related to the structure of brake components.

The car's brake Squeal noise is caused by the resonance of the brake system which is caused by the friction surface. Optimizing the negative damping character of system can reduce brake noise. By increasing or reducing the stiffness of brake disc, the negative damping coefficient can be decreased and the system stability can be improved, but the optimum results are uncertain. It shows better effect in reducing the brake noise to reducing the brake disc's stiffness in the car.

The car's Groan noise is related to the copulation of the structure of brake pad and the structure of the disc. The frictional surface is divided into 44 sections by ventilation's structure of brake disc. In the braking process, brake pads periodically contact soft and hard area of brake disc with the rotation of the wheel, which causes the fluctuation of brake force periodically. The fluctuation may cause brake system's vibrating. When the vibration of brake system is shifted to somewhere such as body, it makes sound.

It may influence the stability of brake system if the intrinsic frequency of various parts is mismatched. To avoid the resonance of brake system in brake process, the intrinsic frequency of one part should not overlap another. It should to be considered that the periodic change with wheel's rotation of the structure may influence the vibration and the noise of the system. In order to avoid vibration and noise problems, the factors that influence fluctuation of brake torque should be avoided.

References

1. DiHua G, XinDong S (2004) An overview on brake vibrations and noise. Engineering mechanics. Tsinghua University, Beijing
2. Xiaoyue C (1988) A study of drum brake judder. Qinghua University, Beijing
3. Zhang L, Weijia M, Zhuoping Y (2008) Experimental investigation into friction vibration coupling characteristics of vehicle disc brake. Tribology. Tongji University, Shanghai
4. Zheng FL, Jianmin Ge (2008) The experiment and analysis of brake squeal of automobile. Tribology. Technique Acoustic, Shanghai

Thermal Management Simulation of Passenger Car with Naturally Aspirated and Turbocharged Gasoline Engine

Haie Chen, Hongzhou Li, Xinxin Dai, Qun Chen and Kang Li

Abstract The passenger car thermal management is studied in this chapter by simulation method. The underhood air flow is simulated by CFD in order to optimize engine cabin layout. The whole cooling system is modeled by 1D flow simulation in order to matching the critical components in the system. The thermal analysis is carried out by the coupling of 3D CFD and 1D simulation including radiation. The two type of gasoline engines -naturally aspirated (V6 PFI 3.0L) and turbo-charged direct injection (TGDI 2.0L) are layout in the same car underhood separately, and both have good thermal management performance. The thermal balance test and temperature measurement are carried out in order to validate the simulation.

Keywords Passenger car · Underhood · Thermal management · CFD · Coupled thermal analysis

1 Research Background

With the increasingly strong requirement for the energy saving and exhaust reducing in the global range, the front grill opening and underhood spacing are decreased as for the design trend of passenger car inclined to small and lower streamlined body. It results in the heat dissipation is more difficult. Thus the

F2012-E13-021

H. Chen (✉) · H. Li · X. Dai · Q. Chen · K. Li (✉)
R&D Center, FAW Co., Ltd., Changchun, China
e-mail: chenhaie@rdc.faw.com.cn

thermal management is becoming more and more important in the vehicle development processing [1]. The passenger car in China is facing the trend from matching naturally aspirated engine to turbo-charged direct injection engine in order to decreasing the fuel consumption. The cooling performance requirements are increased correspondingly because the additional cooling components such as intercooler are added in the limited underhood space. Meanwhile, the thermal protection problems are needed to be solved urgently as for the higher temperature of exhaust pipe and turbo-charger.

The underhood thermal management which influences the vehicle quality straightly is one of the important steps during the vehicle development process. The authors study the thermal simulation methods on underhood flow field, temperature field and 1D cooling system matching analysis. And the two types of gasoline engine naturally aspirated (V6 PFI 3.0L) and turbo-charged direct injection (TGDI 2.0L) are layout in the same car underhood separately, and both of them have good thermal management performance.

2 Methodology

It costs too much time and money to do the underhood thermal management test because it needs proto car and has special requirement for the test ambient, and the biggest problem is that the design deficiency cannot be found in time. With the development of calculation fluid dynamic (CFD) and the improvement of computer hardware performance, the simulation method is more and more applied on the underhood design and layout. It can find the design risk in time and guides the structure modification to improve the design quality, reduce the development period and test costs [2]. The three simulation methods used in this chapter are introduced below.

2.1 Introduction of the Underhood Flow Simulation Method

The underhood flow field is simulated by the software STAR-CCM+ [3] in this chapter. The interface process from CAD geometry to CFD model is built according to the very complicated cabin layout. The time cost of finishing the flow field simulation shortens much by the way of reasonable geometry partition and surface wrapping. The process of building simulation model is shown in Fig. 1. It costs only 3 weeks for one case of underhood flow field simulation which costs 3 months before, thus it can meet the vehicle development requirements.

The calculation zone is similar to the wind-tunnel test environment in order to simulate the underhood flow field more accuracy. The calculation zone size is defined as follows: the distance between inlet and the front of passenger car is 3 times of vehicle length, the distance between outlet and the rear of passenger car is

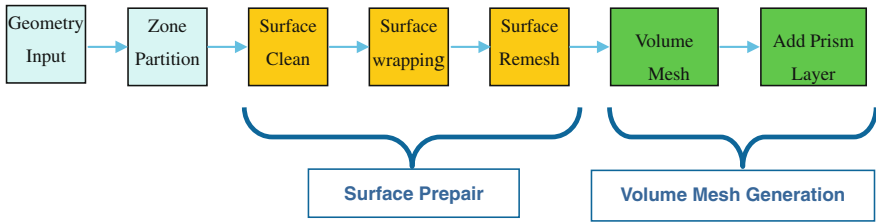


Fig. 1 Process of building the simulation model

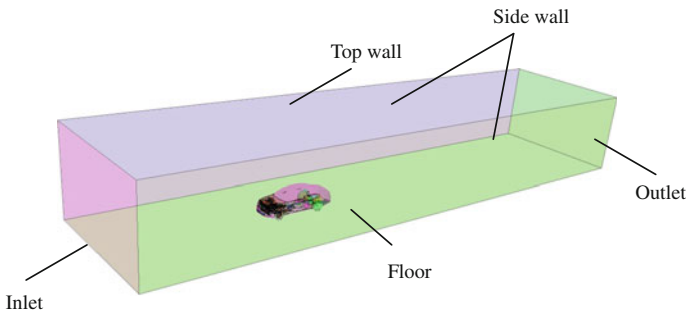


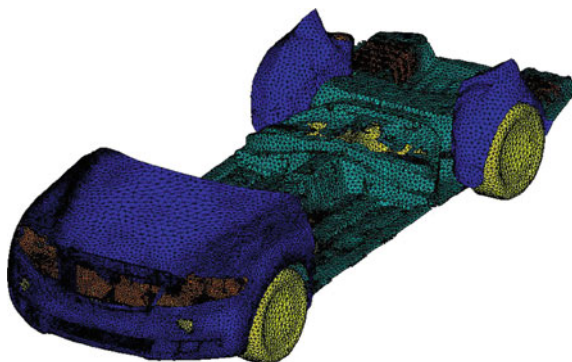
Fig. 2 Calculation zone of underhood CFD simulation

5 times of vehicle length, the top wall is 5 times of vehicle height away from the passenger car top and the two side walls are both 5 times of the vehicle width away from the passenger car side, the calculation zone structure is shown in Fig. 2.

The air flow is assumed to be incompressible turbulent flow during the calculation. The $k-\omega$ turbulence model is adopted and standard wall function is solved. The porous model is used for the heat exchanger such as radiator and condenser. And the fan is simulated by the MRF model. The input boundary conditions for calculation are as follows: (1) The inlet boundary is assigned velocity which is the same as vehicle speed; (2) The walls are not slip; (3) The outlet boundary is assigned pressure.

The flow field informations from the CFD simulation such as velocity, mass flow rate and pressure etc. in the key locations are used to not only evaluate the underhood layout and improve structure but also provide the boundary condition for 1D cooling system simulation.

Fig. 3 RadTherm simulation model



2.2 Introduction of the Underhood Thermal Coupled Simulation Method

It costs too much time to do the preprocessing and calculation if we simulate the underhood temperature field by 3D CFD method. A new method coupled the 3D CFD analysis and 1D radiation thermal analysis is studied in this chapter in order to obtain underhood temperature field at lower cost. The heat transfer rate of the thermal components, such as radiator and intercooler etc., and the exhaust pipe temperature are assigned based on the flow simulation results according to the engine operation condition. The heat transfer rate of condenser is also assigned according to the AC operation condition.

The conduction heat transfer of the fluid itself and convection heat transfer between fluid and wall are simulated by 3D software STAR-CCM+, and the calculation model is the flow simulation model mentioned above. The radiation between the solids is simulated by RadTherm [4] software. The radiation simulation model is shown in Fig. 3. The radiation heat transfer model is mainly including the components in the underhood, parts around the exhaust pipe and car floor etc. The RadTherm model is only built by components surface mesh, and the components in the model are simulated by defining some parameters such as material, thickness etc.

The process of underhood thermal coupled simulation is shown in Fig. 4. The temperature distribution can be got when the coupled simulation is finished by repeating the process. If the temperature of monitored elements is changed less than 0.5 °C between two successive results during the calculation, the temperature field is stable, and the coupled simulation is converged.

The main result of the coupled simulation in the underhood is the temperature distribution. Usually we pay more attention to the components temperature around the exhaust pipe, the maximum temperature of the other thermal sensitive components etc.

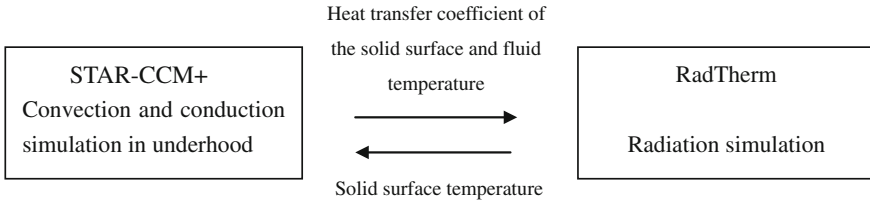


Fig. 4 Process of coupled temperature simulation between STAR-CCM+ and RadTherm

2.3 Introduction of the 1D Cooling System Matching Simulation

The cooling system matching analysis is conducted by 1D software FLOW-MASTER [5], the basic simulation process is shown in Fig. 5. The simulation model is built according to the exact vehicle cooling layout. Usually the components in the cooling system include coolant pump, engine water core, oil cooler, thermostat, radiator, cabin heater and connection pipes etc., the intercooler, condenser, EGR cooler, transmission oil cooler and other components are also be considered in some cases according to the vehicle layout.

The air conditions (flow rate and temperature) of the radiator needed during the simulation come from the results of the underhood CFD flow simulation and thermal coupled simulation.

The aim of results analysis is primarily evaluate the coolant flow distribution, pressure drop and the maximum coolant temperature, and draw the conclusion whether the cooling system matching is reasonable. The guidelines are as follows: (1) the coolant flow rate distributed of the key parts can meet the requirement under the special engine operation conditions; (2) the maximum coolant temperature should not exceed the maximum allowable temperature.

3 Analysis of the Underhood Thermal Management Simulation Result

3.1 Analysis of Thermal Management Simulation Results Matched with V6 3.0 L NA Gasoline Engine

V6 NA gasoline engine is matched in this passenger car, and the simulation conditions are as the same as the vehicle thermal balance test listed in Table 1. The simulation results analysis are as follows.

The air flow distribution of the underhood can be found from the CFD result directly. Figure 6 shows the air flow path lines in the underhood from grill. It can be seen from the figure that the incoming air from the grill mostly flows away from the both sides of the underhood, and it is not utilized by the radiator efficiently. So,

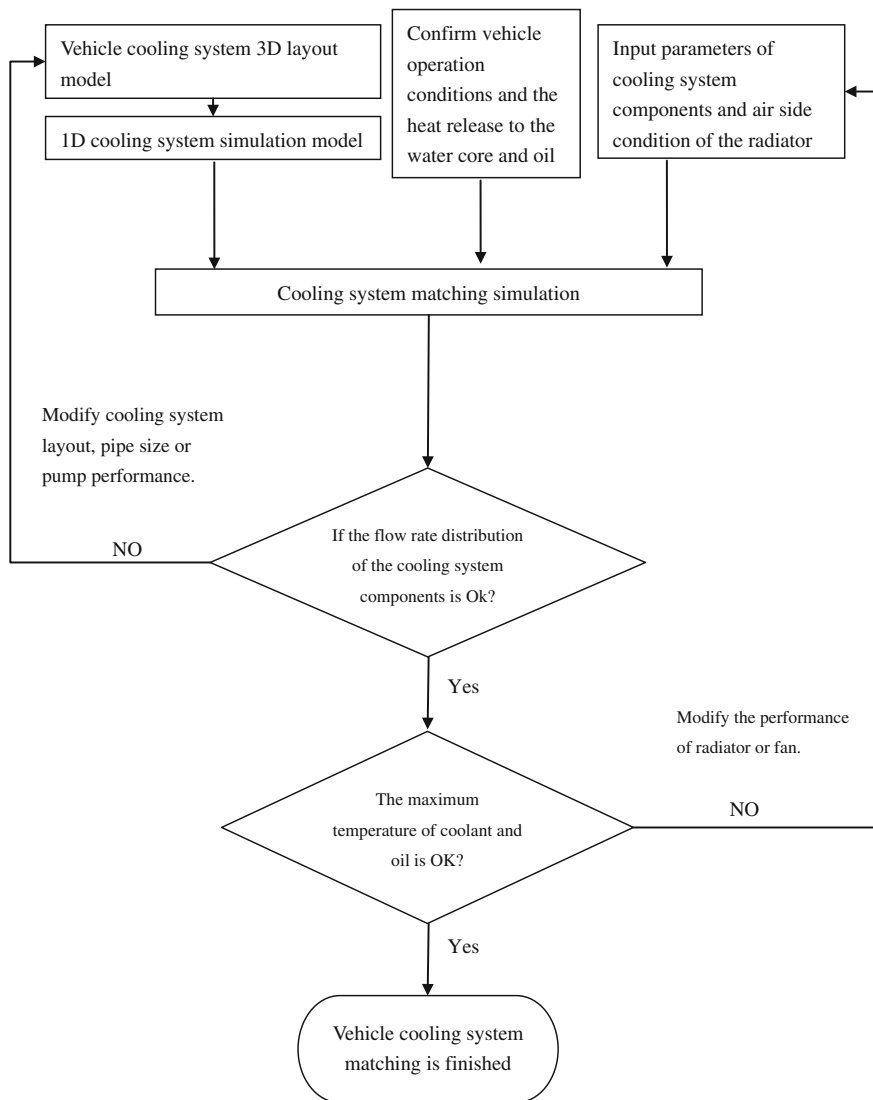


Fig. 5 Process of the cooling system matching analysis

Table 1 Analysis operation conditions for V6 3.0L NA gasoline engine

Conditions		Vehicle speed (km/h)	Engine speed (r/min)
Condition 1	2 shift, 9 % gradient	63	3900
Condition 2	90 km/h, 5.5 % gradient	90	3805
Condition 3	5 shift, 140 km/h	140	3055

Fig. 6 Air flow path line in underhood with baffle

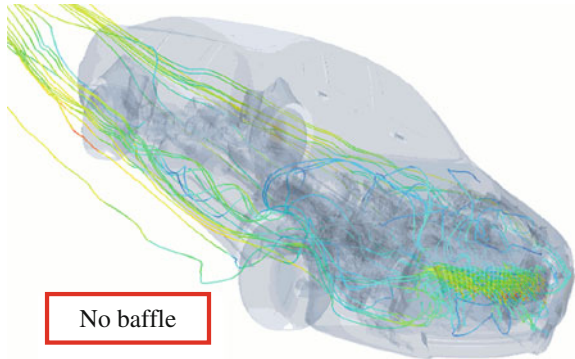
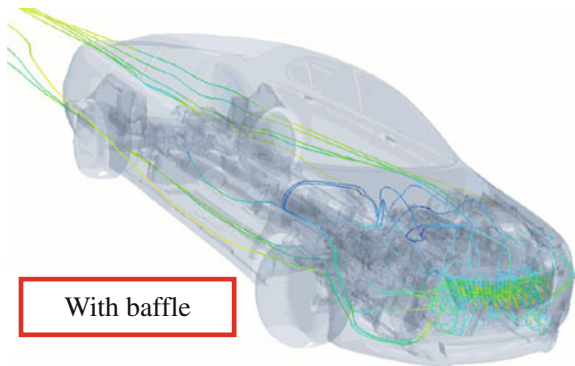


Fig. 7 Air flow path line in underhood without baffle



it is necessary to take some measures to reduce the air flow which go away from both sides. Usually adding some sealing strips and baffle are very useful to prevent the air flow away from both sides of the channel, which can make the air comes from the grill goes through the radiator as much as possible. The comparison of the air flow path line in the underhood with/without baffle is shown in Fig. 7. It can be seen obviously that the baffle reduces the air flow to both sides effectively and increases the air flow rate went through the radiator.

Figure 8a is the velocity distribution of radiator inlet under original layout. It can be seen that the velocity distribution of radiator surface under original scheme is very uneven, which can reduce the heat transfer efficiency of radiator. It can be found via the flow field analysis that this result is caused by the unreasonable design of fan shoulder. The uniformity of velocity distribution front the radiator is greatly improved by optimizing the structure of fan shoulder and fan blades, which is shown in Fig. 8b.

The exhaust pipe is a high-temperature component in the underhood. Its high temperature radiation has great affects on the temperature of other components in the underhood. Figure 9 shows the surface velocity distribution of engine and

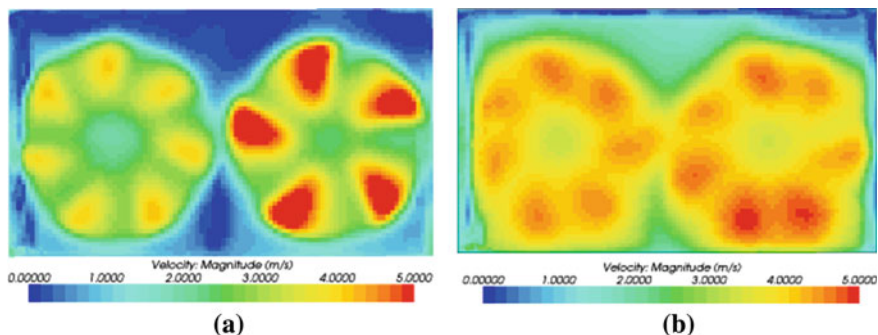


Fig. 8 Comparison of velocity distribution in radiator front surface under different fan schemes. **a** Original fan scheme. **b** Optimized fan scheme

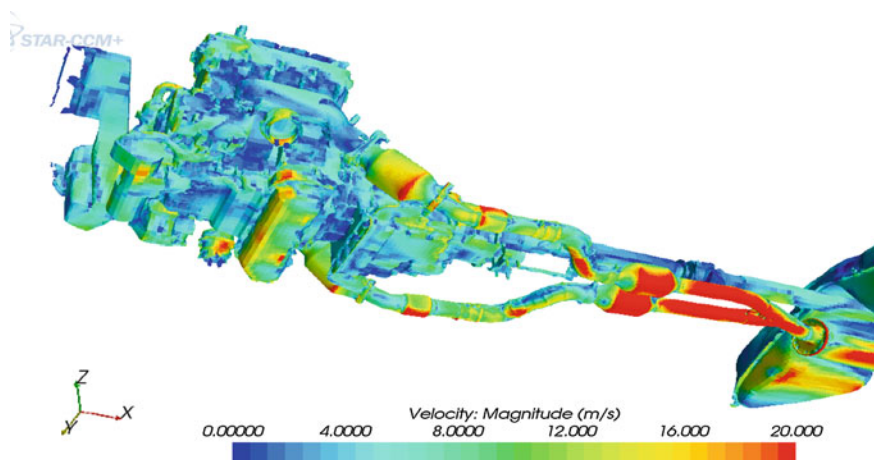


Fig. 9 Velocity distribution of engine and exhaust pipe surface

exhaust pipe. It can be noticed that the exhaust pipe of V-type engine is arranged in the bottom of the underhood which reduces the high-temperature radiation effect on other components in the underhood. Meanwhile, a larger space in the bottom of the underhood makes the airflow relatively smoother and the flow velocity of exhaust pipe surface relatively higher, which is benefit to heat release. In addition, the gas flow velocity of engine sump surface is high enough to cool the oil.

3.1.1 Results of Cooling System 1D Simulation

The main study object of whole vehicle cooling system matching analysis is cooling system itself, and the interaction among lubrication system, engine and cooling system should also be think about together. The components included in

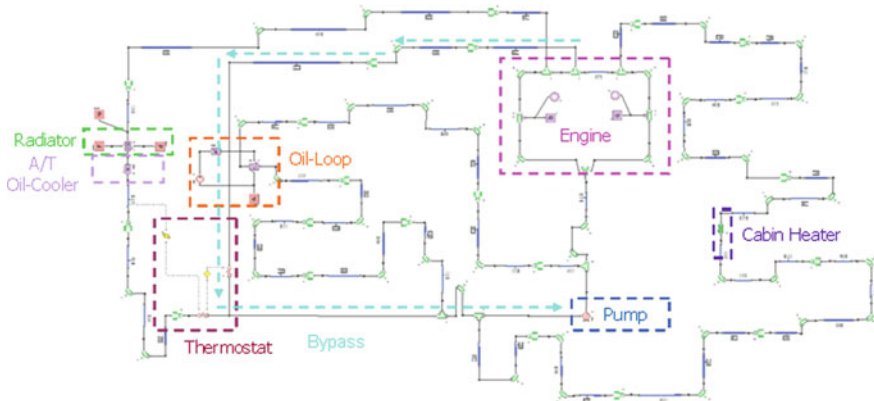


Fig. 10 1D network model of cooling system for V6 3.0 L NA gasoline engine

Table 2 Simulation results of cooling system matching for original scheme

Conditions	Maximum coolant temperature (°C)	Maximum oil temperature (°C)	Ambient temperature (°C)
Condition 1	121.90	129.19	35
Condition 2	107.85	115.29	35
Condition 3	107.57	118.80	35

cooling system are different according to the engine type and layout of the whole vehicle. For the V6 3.0 L NA gasoline engine studied in this chapter, the 1D network model of cooling system built according to the arrangement of actual vehicle is shown in Fig. 10. The coolant circuit is composed of water pump, engine water core, engine oil cooler, radiator, transmission oil cooler, thermostat, cabin heater and connecting pipes. The oil circuit is composed of oil pump and engine oil cooler. The coolant circuit and oil circuit are connected by engine oil cooler. Engine model is simplified. The input parameters of simulation are the components geometry parameters, resistance characteristic and heat-transfer characteristic.

The simulation results of cooling system matching for original scheme under three typical vehicle conditions are shown in Table 2. It can be noticed from the results that the coolant temperature exceeds the maximum allowable temperature 115 °C under condition 1. It indicates that the original scheme doesn't meet requirement.

In view of this situation, the author took a series of improvement measures which optimized by some corresponding thermal management analysis. Finally, the air flow rate passed through radiator is increased by two methods, one is increasing the belt wave length of radiator in order to reduce wind resistance, and the other is increasing the diameter of fan impeller and the number of blades in order to improve the performance of cooling fan. The problem of high coolant

Table 3 Simulation results of cooling system matching for improved scheme

Conditions	Maximum coolant temperature (°C)	Maximum oil temperature (°C)	Ambient temperature (°C)
Condition 1	107.185	124.797	35
Condition 2	100.298	119.74	35
Condition 3	96.515	113.11	35

Table 4 Comparison of simulation results and test data for V6 3.0L NA gasoline engine

Condition	Maximum coolant temperature (°C)			Maximum oil temperature (°C)			Ambient temperature (°C)
	Calculation	Test	Deviation (%)	Calculation	Test	Deviation (%)	
Condition 1	107.185	109.49	2.11	124.797	130.13	4.1	35
Condition 2	100.298	105.08	4.55	119.74	125.81	4.82	35
Condition 3	96.515	95.15	1.43	113.11	111.19	1.73	35

temperature is solved eventually. The simulation results of cooling system matching for improved scheme are shown in Table 3. From the results, we can notice that the temperature of coolant and oil are both below the maximum allowable temperature. In addition, the coolant volumetric flow rate of engine water jacket is 278 L/min which reaches the design requirement under rated power condition. It is thus clear that the improved scheme meets the cooling system requirement for V6 3.0 L NA gasoline engine.

The comparison of cooling system simulation results and the heat balance test data is presented in Table 4. It can be found that the maximum deviation of temperature between calculated results and test data is 4.55 and 4.82 % for coolant and oil separately. The maximum deviations are both in the permitted range of projects. Thus, the simulation method can be used for cooling component selection and determining the cooling system matching scheme.

3.2 Analysis of Thermal Management Simulation Results Matched with 2.0 L TC Gasoline Engine

This passenger car is also matched the smaller placement 2.0 L TC gasoline engine in order to decrease the fuel consumption. The simulation conditions are listed in Table 5.

The vehicle underhood spacing matched with TGDI 2.0L engine becomes more narrow compared to which matched with V6 NA engine. Firstly, because the TGDI 2.0L is inline 4 cylinders engine, and it's longitudinal length is larger than V6 engine. Meanwhile, the intercooler is added between the condenser and radiator which results in more compact layout in longitudinal direction and makes heat

Table 5 Simulation operation conditions for 2.0L TC gasoline engine

Conditions		Vehicle speed (km/h)	Engine speed (r/min)
Condition 1	2 shift, 9 % gradient	60	3935
Condition 2	90 km/h, 5.5 % gradient	90	2714
Condition 3	5 shift, 140 km/h	140	3039

Table 6 Air flow rate through the radiator, intercooler and condenser for different TGDI 2.0L schemes

Vehicle speed (km/h)	Air flow rate through radiator (kg/s)			Air flow rate through intercooler (kg/s)			Air flow rate through condenser (kg/s)		
	Original fan	New fan		Original fan	New fan		Original fan	New fan	
	Original rad.	Original rad.	New rad.	Original rad.	Original rad.	New rad.	Original rad.	Original rad.	New rad.
0	0.468	0.670	0.720	0.402	0.575	0.623	0.377	0.539	0.584
28.3	0.496	0.681	0.729	0.449	0.599	0.644	0.409	0.551	0.595
43.6	0.578	0.754	0.803	0.563	0.691	0.734	0.507	0.627	0.668
140	1.155	1.240	1.297	1.328	1.365	1.412	1.164	1.192	1.239

release more difficulty. Secondly, the temperature of exhaust pipe is much higher for the turbo-charged engine. It is also beside the engine and in the middle of the underhood, and its radiation to the parts around is more significant. Thus, the temperature field analysis of the underhood matched with 2.0L TGDI is more important.

3.2.1 Analysis of Underhood Flow Simulation Results

It can be found that the main problem of underhood matched with TGDI 2.0L engine is the air flow rate passed through of the radiator and the intercooler is too small (see Table 6 of the original fan and the original radiator) to meet the needs of engine cooling. The suggestions are increasing the fan capacity and optimizing the radiator structure. In order to increase the capacity of the fan, its structure and layout are optimized. The comparison of the original fan and the optimized fan is shown in Fig. 11. The two impellers of the original fans are in the same diameter, while the new fans are optimized to change the main fan impeller diameter to the maximum value in the structure allowance, the diameter of the other impeller near the compensation tank side is designed smaller than original.

Figure 12 shows the comparison of velocity distribution on the radiator inlet surface under different fan schemes. Figure 13 shows the pressure distribution comparison on the middle section plane under different fan schemes. It can be seen from these two figures that the airflow velocity increases significantly due to the increasing capacity of the cooling fan. The lower pressure area near the fan will

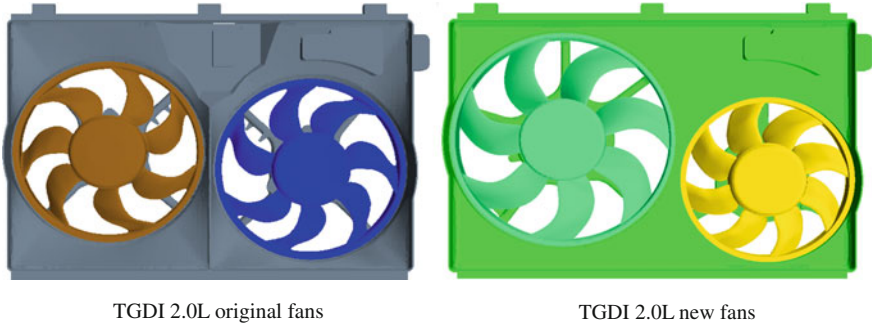


Fig. 11 Fan structure comparison for original fans and new fans

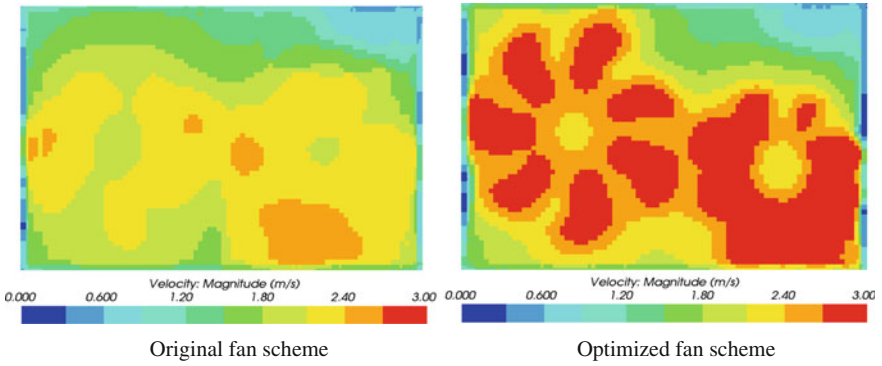


Fig. 12 Comparison of velocity distribution on the radiator inlet surface under different fan schemes

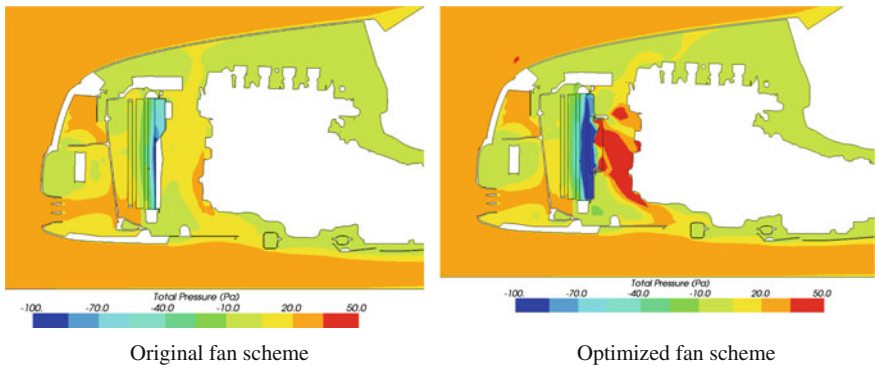


Fig. 13 Comparison of pressure distribution on the section plane under different fan schemes

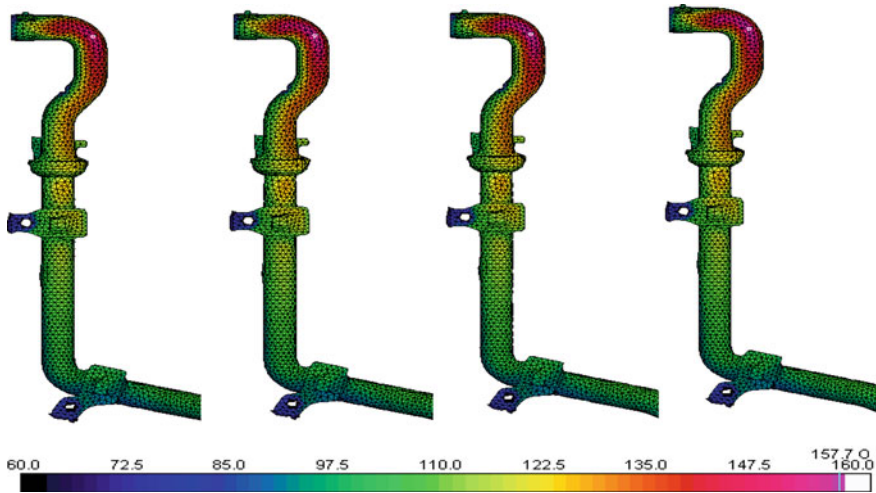


Fig. 14 Comparison of the crankcase ventilation pipe temperature distribution for four iterations

increase the air flow rate through the radiator, intercooler and condenser. It can also be seen clearly in Table 6 that the air flow rate through the radiator, intercooler and condenser has increased significantly with the fan optimized. The air flow rate can be increased 40 % especially at lower vehicle speed.

From the simulation of the cooling system matching, the air flow rate through the radiator is not enough with the new fans. It can not improve capability of the fan due to noise constraints. The next step needs to improve the capability of radiator. The method is to reduce the wind resistance and ensure the heat transfer capacity of radiator unchanged at the same time, which will increase the air flow rate through the radiator. It can be seen from Table 6 that the air flow rate through the radiator, intercooler and condenser all increased with the new fans and new radiator. Meanwhile, it can be found through the 1D cooling system simulation results that the maximum coolant temperature is below the maximum allowable temperature when the engine reaches thermal balance.

3.2.2 Temperature Field Analysis of Underhood

As previously mentioned, the monitored cell temperature change and comparison of temperature field between two iterations are used to judge whether the thermal coupled simulation is finished during the underhood temperature simulation. The comparison of crankcase ventilation pipe temperature distribution among four iterations is shown in Fig. 14. The cell numbered 457,500 is monitored, and its temperatures for four iterations are 153.2, 156.9, 157.6 and 57.7 °C separately. The temperature difference between the last two iterations is 0.1 °C. Thus we can confirm that the thermal coupled simulation is converged.

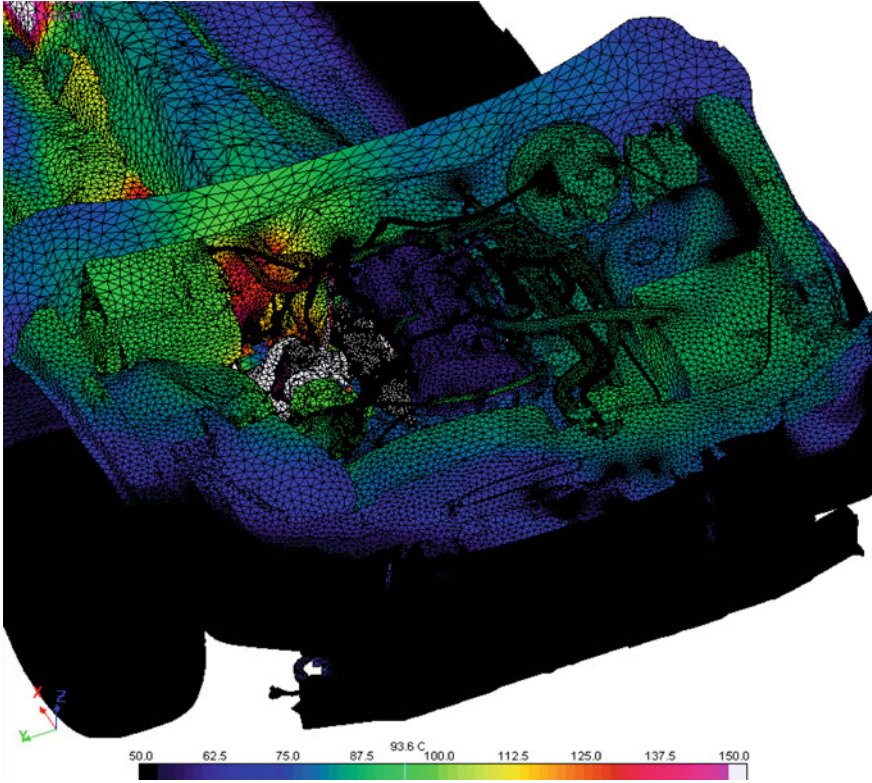


Fig. 15 Temperature distribution in underhood

The aiming of underhood temperature field simulation is to confirm whether the components temperature can meet the design requirements, take reasonable measures to decrease the parts temperature and choose suitable components material according to the temperature. The primary thermal protection measures are as follows: (1) Optimizing the underhood layout to keep the temperature sensitive components away from the high temperature exhaust pipe; (2) Choosing the high temperature resistance material; (3) Adding thermal shield to decrease the radiation from the high temperature parts. The underhood space of passenger car is very narrow and compact, which results in some thermal sensitive components cannot keep away from the higher temperature exhaust pipe, so the later two measures mentioned above are adopted to solve the thermal problem. Usually the thermal shield is firstly think about because the cost of high temperature resistance material is much higher.

The temperature field of underhood is shown in Fig. 15. The temperature of side near exhaust pipe is obviously higher than the other side because of the radiation of higher temperature exhaust pipe. The temperature in front and bottom of the underhood is basically same as the environment. The temperature around exhaust pipe is much higher than the other zone which can be found in Fig. 16. It

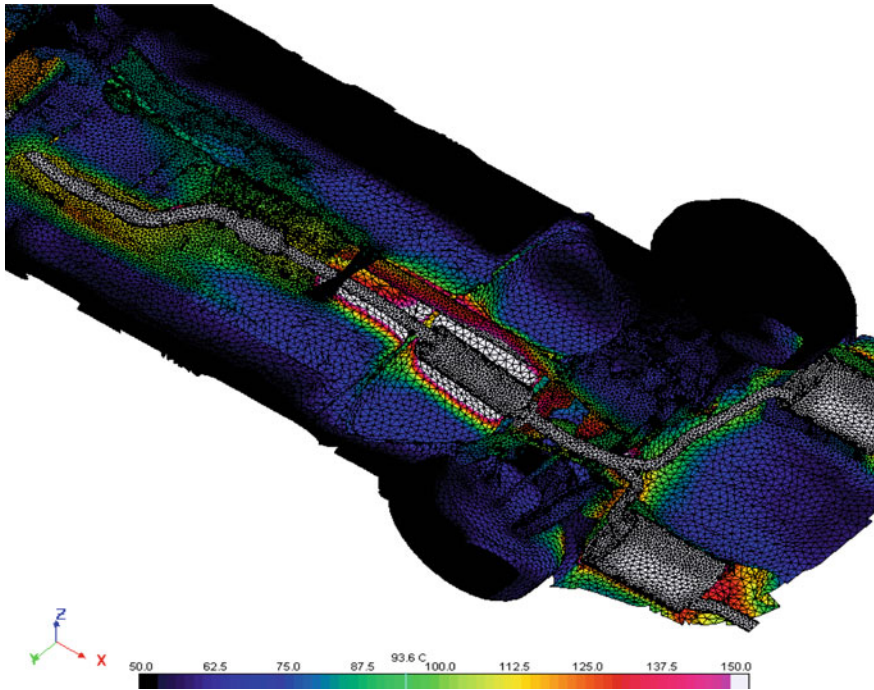


Fig. 16 Temperature around exhaust pipe

is a good way to decrease the underhood temperature by using thermal shield. The temperature in the zone with thermal shield is obviously lower than without it.

The temperature distribution near exhaust pipe is shown in Fig. 17. The components temperature are very higher and part of them exceed 150 °C because the temperature of exhaust pipe is above 500 °C. The temperature distribution of crankcase ventilation pipe is shown in Fig. 18. Its maximum temperature is 158 °C which is a little higher for the rubber material. The reason is the radiation of higher temperature exhaust pipe without the thermal shield after the turbocharger is great. The crankcase ventilation pipe temperature is decreased to 130 °C by the way of adding thermal shield and extending 5 mm between crankcase ventilation pipe and exhaust pipe.

The temperature distribution of wiring harness in underhood is shown in Fig. 19. The temperature of wiring harness far away from the exhaust pipe are around 85 °C, but the temperature of others near the exhaust pipe are very higher which partly exceed 160 °C, especially the temperature of electric pump wiring harness is near 315 °C which exceeds the maximum allowable temperature (160 °C). The reason is that the exhaust pipe after the turbocharger is not covered by the thermal shield. The temperature of wiring harness is decreased below 135 °C by adding thermal shield which is the only measure to take because of the fixed position of electric pump.

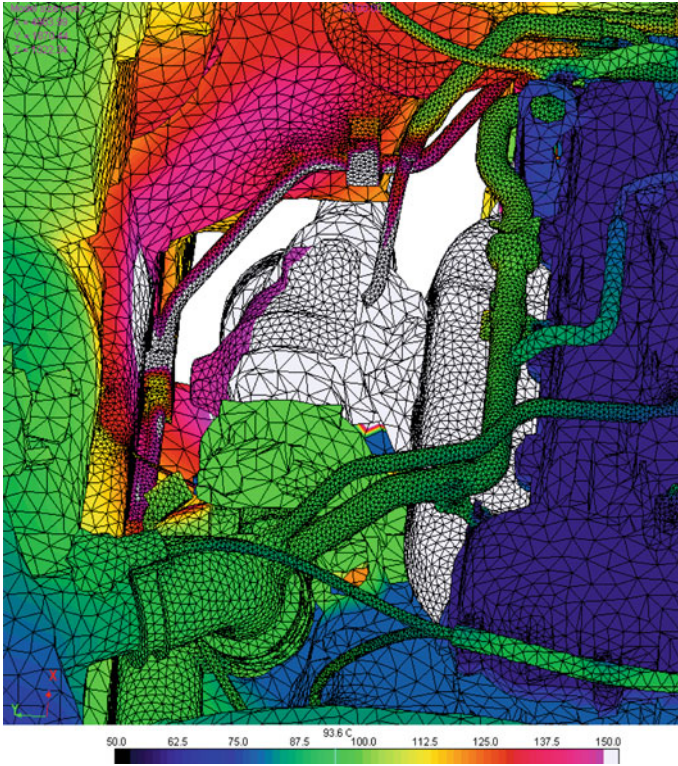


Fig. 17 Temperature distribution near exhaust pipe

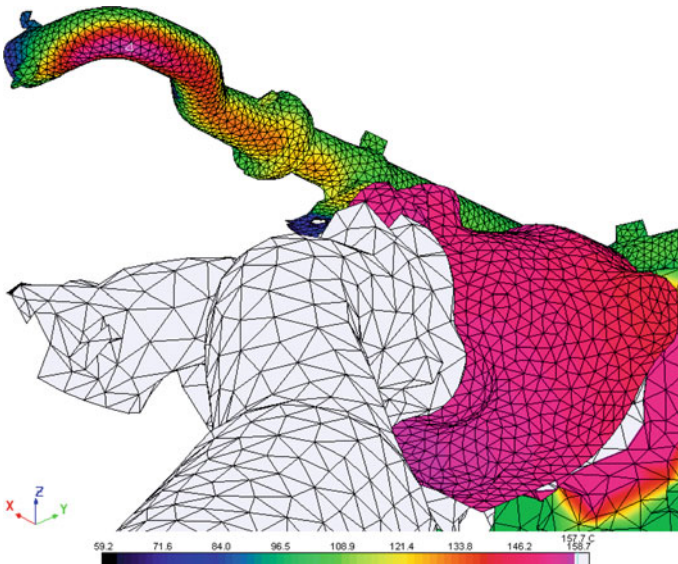


Fig. 18 Temperature distribution of crankcase ventilation pipe

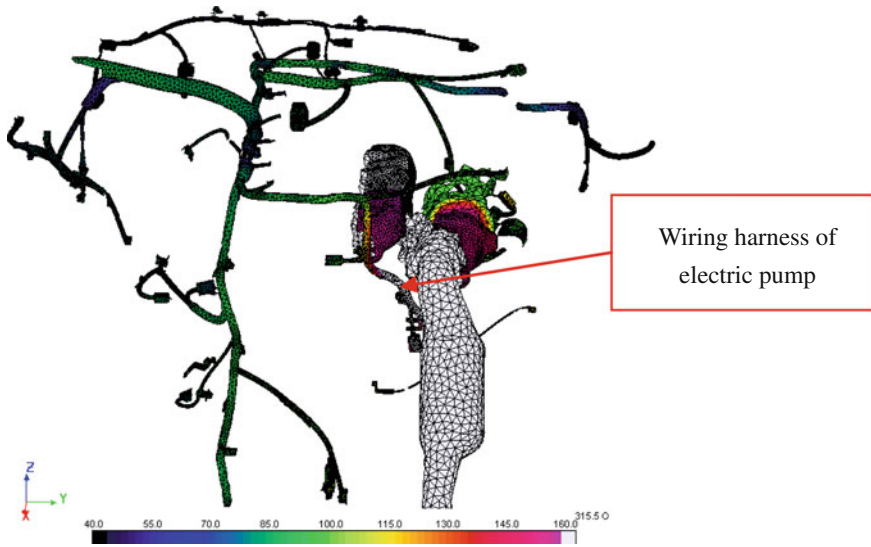


Fig. 19 Temperature distribution of the wiring harness in the underhood

The effect of adding thermal shield on decreasing underhood temperature is shown in Fig. 20. The radiation heat transfer rate from exhaust pipe to sump is very large before adding the thermal shield, and the maximum temperature of sump surface is 250 °C which exceeds the allowable temperature. The sump temperature can be decreased only by adding thermal shield because its location can not be changed. The maximum temperature of sump is decreased from 250 to 87 °C with the thermal shield added.

3.2.3 Results of Cooling System 1D Simulation

For the 2.0 L TC gasoline engine studied in this chapter, the 1D network model of cooling system built according to the layout of actual vehicle is shown in the Fig. 21. The cooling components constituted coolant circuit and oil circuit are the same as the components in cooling system of V6 3.0 L NA gasoline engine, but the components performance and connection type are different.

After the engine of this passenger car is changed from 3.0 L NA to 2.0 L TC, the engine heat load is approximately equal. For the same underhood space, although the engine size reduced, it not only increase the wind resistance but also make the arrangement space reduce along the radiator width direction because of the addition of intercooler and the layout of charged air piping, which eventually reduced the supply air rate and increase the air temperature into radiator. Therefore, the demand of cooling system for turbocharged engine is more rigorous compared to naturally aspirated engines.

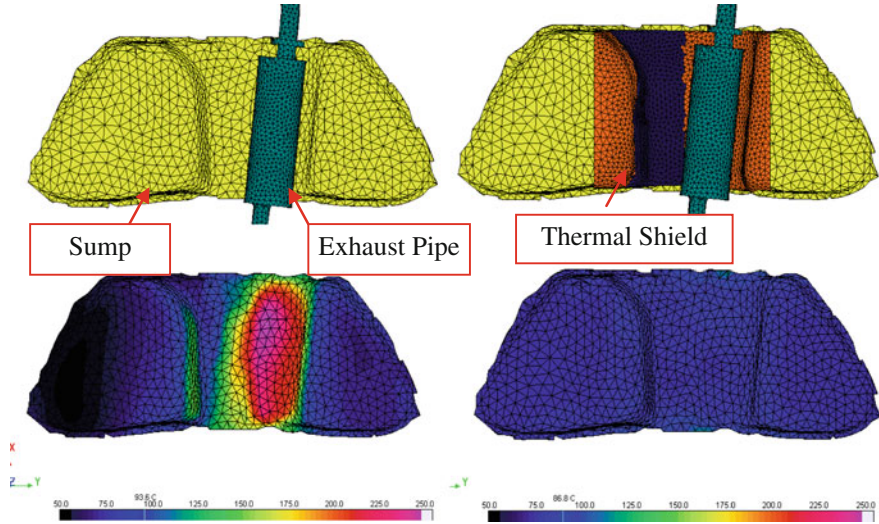


Fig. 20 Influence on the sump temperature with thermal shield

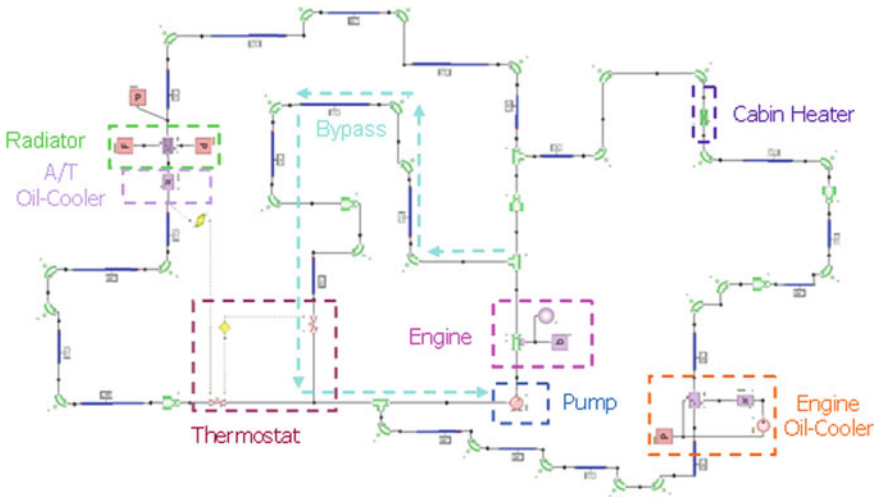


Fig. 21 1D network model of cooling system for 2.0 L TC gasoline engine

Comprehensively considering all of the above factors, the heat transfer performance of radiator for turbocharged engine must be better than for naturally aspirated engine in order to guarantee the reasonable matching of cooling system. Therefore, increasing the thickness of radiator and optimizing the structure of radiator fin properly are needed in order to improve the heat transfer performance. Meanwhile, optimizing the structure of fan and improving the fan performance are

Table 7 Comparison of simulation results and test data for 2.0L TC gasoline engine

Condition	Maximum coolant temperature (°C)			Maximum oil temperature (°C)			Ambient temperature (°C)
	Calculation	Test	Deviation (%)	Calculation	Test	Deviation (%)	
Condition 1	105.82	103.7	2.04	134.92	129.1	4.51	35
Condition 2	102.53	101.4	1.11	128.81	123.0	4.72	35
Condition 3	92.67	89.2	3.89	115.60	111.2	3.96	35

also needed in order to overcome the increased wind resistance caused by the addition of intercooler and the structure changing of radiator. After several rounds of improvement, the rational cooling system matching for 2.0 L TC gasoline engine is achieved finally.

The comparison of cooling system simulation results and the heat balance test data for 2.0 liter TC gasoline engine under three typical steady conditions is presented in Table 7. We can notice from these results that the deviations are all within 5 %, and it also shows good consistence with test data.

4 Conclusion

The studies conducted on the passenger car underhood thermal management in this chapter are summarized as follows:

1. The time of building the 3D underhood simulation model shortens much by the way of reasonable 3D CAD input and geometry clean method. It takes only 3 weeks to finish the underhood flow simulation which can meet the vehicle development requirement.
2. A new underhood temperature field simulation method is studied, and the calculation time is shorter by the way of coupled 3D CFD simulation and 1D radiation simulation, and the simulation results can meet the requirement of engineering accuracy.
3. The two types of gasoline engines (V6 PFI engine and 2.0TGDI engine) are matched in the same vehicle underhood space by the way of thermal management simulation. And the cooling system components are matched reasonable separately according to the two engines characteristics. Both of them reach the thermal balance targets.
4. The simulation results have good consistency with thermal balance test data, and the deviation of maximum coolant temperature is within 5 % which can meet the engineering requirements.

References

1. Costa E (2003) CFD approach on underhood thermal management of passenger cars and trucks. SAE Technical Paper 2003-01-3577
2. Bennion K, Thornto M (2010) Integrated vehicle thermal management for advanced vehicle propulsion technologies. SAE Technical Paper 2010-01-0836
3. STAR-CCM+ user manual
4. RadTherm user manual
5. FLOWMASTER user manual

Part XIV
Testing of Components, Systems and Full
Vehicle

Research on User Vehicle Operation Regularity

Zhonggao Yu, Yutan Zhang, Yonghong Xu, Gan Chen,
Jianguang Zhou, Jianxian Chen and Jie Bai

Abstract *Engineering Questions and Research Objective* During vehicle development, engineers often set vehicle design targets based on the reports from market investigation, benchmarking, testing or users' feedbacks. However, such reports, which can not provide quantitative, accurate data on vehicle running information, may cause over-design or insufficient design problems. In this paper, a method on how to collect vehicle running information and analyze user operation habits and cars' running regularity is researched in order to solve the problems. *Methodology* By investigating engineers' requirements and vehicle specifications, the information collection scheme was determined and analysis arithmetic was designed. Secondly, according to collection requirements analysis and network capacity analysis, the on-board information collection device was produced and background service system was built. Thirdly, database was established using the collected vehicle running information. Fourthly, vehicle operation regularity and user driving habits was found out by submitting enormous data to arithmetic program and analyzing it. *Results* Vehicle running analysis model was made and database was built. Analysis results provide the basis for vehicle top-down design and design improvement. *Limitations of this study* Due to the limitation number of vehicle samples, the analysis results represent only part of vehicle running information. What does the paper offer that is new in the field: The device can comprehensively collect signals from CAN/LIN BUS and from various sensors. The acquired data can be packed and uploaded to sever via 3G network. *Conclusion* This study proved the methodology of vehicle running information

F2012-E14-008

Z. Yu (✉) · Y. Zhang · Y. Xu · G. Chen · J. Zhou · J. Chen · J. Bai
Dong Feng Motor Corporation Technical Centre, Wuhan, China
e-mail: yuzg@dfmc.com.cn

collection and data process is feasible. The device could not only collect and store plenty of data, but also upload the data files to sever. By using the arithmetic program, data could be analyzed. The analysis results of user operation habits and vehicle running regularity provide important references for vehicle design. For long-term work, consistent and extensive collection work needs to be done in order to acquire more accurate statistical data.

Keywords Vehicle running information · Information collection · Data analysis model · Operation habit · Running regularity

1 Introduction

When designing a new passenger car, it is necessary to know how user will use it, or in other words what the target user's operation habits are, for these could be important references for forward development. However, acquiring these will consume long-time and need immense statistics. Because of lack of data, traditional experiences and benchmarking data are often consulted by domestic manufacturers to be design parameters. Obviously it isn't good for independent innovation nor can meet daily increasing consumer requirements. Thus, to develop a reliable vehicle operation data collection device and an accordingly data analyzing system have grate significance for vehicle corporations.

Right now, many enterprise and institutes home and abroad have made similar researches [1, 2]. For example, Intrepids's (American) product Neovi Fire and Vehicle Spy, which can collect and analyze BUS signals, have been widely used. However, these products can not universally being used because of the limit of collection range or the uploading capacity. What's more, most of the researches face vehicle arrangement other than face designing requirements.

This assay introduced technique of gathering passenger car's running information and method of analyzing data. Contents include the following aspects: requirements, hardware design, software design, analysis arithmetic design and data processing. It showed both the content of the idea and its feasibility all around. This essay provided significant references in this research field.

2 Method of Data Collection

Data collection is the basis of the whole system. Firstly the devise should collect data as comprehensively as possible on the condition of no influence to vehicle normal running. Secondly, the acquired data should be stored in the devise or be uploaded to severs via wireless network. Thirdly, the devise should be easy to be fixed in cars and collection work should be reliable and confidential. Besides of these, users could supervise the devise and adjust collection mode from far away.

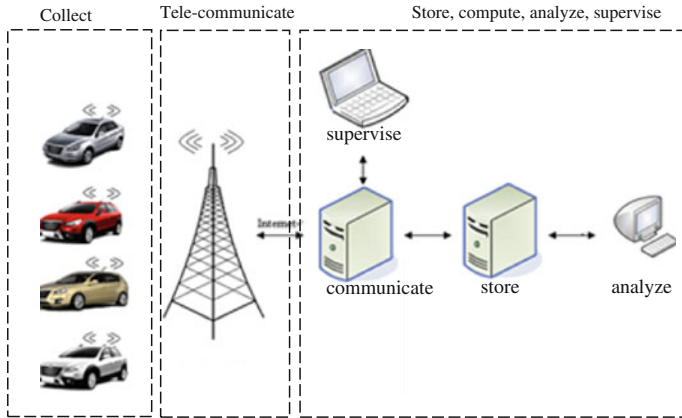


Fig. 1 Principle of the whole system

Figure 1 shows the principle of the whole system. This chapter introduces collection requirement, device function design, hardware design and software design in detail.

2.1 Collection Requirement Analysis

The collection requirement derives from all kinds of input borderline in vehicle design and development. For example, when designing the lock, it needs to know how many times the door will be opened and closed in car’s lifecycle, and when developing car’s economic performance, it is necessary to define its high-way and urban road’s speed range, and, in product planning phrase, it’s helpful to know different age user’s acceleration habits and brake habits in order to set developing goals. By investigating and analyzing engineers needs, the collection requirement was confirmed.

While most running information can be gained from the CAN BUS and LIN BUS, those which can not directly gained by this way should be transferred. For instance, engine power should be transferred by engine torque and engine speed. Some I/O information and A/D information that could not directly or indirectly gained from BUS, needed to be collected by extra sensors. In addition, information like road, temperature, 3 axles acceleration etc., have no direct relation with vehicle design, but are critical for running data analysis. So this kind of information should also be collected.

By analyzing the CAN/LIN BUS signal and feasibility of installing extra sensors, we fixed nearly 300 collection signals, containing engine, body, chassis, electronics and so on.

2.2 Device Function Design

The main function of collection box is to collect vehicle running signal according to the configuration file's control definition and to arrange the gained data to form a file and store it in the box. Besides, the box need to upload the stored files to server and receive instructions from server and feedback for them. Collection work should do no harm to vehicle's running and data won't leak.

2.2.1 Collection Function Design

Because BUS networks' speeds are not the same, the collection box should have different interfaces to suit different BUS. Thus, we confirmed several CAN interfaces and LIN interface according to development requirements. Be sure the box wouldn't affect BUS communication when listening. Taking into account the limit of BUS signals, it is necessary to fix several I/O interfaces to gather numeral information and several A/D interfaces to gather analogue signals. Except for this, gyroscope, 3 axles acceleration sensor, temperature sensor were installed in the box to gather angle speed, acceleration and temperature continuously.

Another important function of collection box is that it could accurately acquire required operation signals for different cars, no matter whether their network definition the same or not. Such function can be achieved by reading network definition files. Definition file for CAN is called DBC. It defined node name, signal name, message address, frame format, data field length, layout etc. Giving the box current car's DBC can it clearly know which signal in which message should collect. In addition, DBC also defined the transformation parameters between the realistic data and the transformed data thus secured data be confidential. The definition file for LIN is called LDF, collection mode for LIN is the same with CAN.

The sending period of different messages are different while for one message, its sending period is not exactly the same, so it is not appropriate to collect signals respectively, for this will bring CPU heavy burden and make data analysis difficult. Therefore, we made all CAN signals be collected in the same interval. Sampling frequency could be chosen from 1 to 100 Hz. Collecting signals from LIN, GPS, gyroscope, battery, temperature sensor were the same as CAN, while sampling frequency was from 1 to 400 Hz. But numerical and analogue data are collected individually depending on the collection conditions be meet. Although the same frequency will result in data repetition, compression technology will treat the redundancy [3].

The above collection function design made the box more compatible with cars and had comprehensive and flexible collection ability.

2.2.2 Storing Function Design

All signals of which length ranges from 1 to 24 bits were summed up to set storage capacity. The “recoding” and “non-recoding” methods were used to evaluate bits flow. Assuming that there are 2 times data expansion needs and 50 % compress rate, the bits flow is 8 kB/s. If 6 h a day, 30 days a month the collection box works, there is 5G bits should be stored. Thus, the storing chip embedded in the device should no less than 32 G capacity in order to ensure enough local storing.

2.2.3 Uploading Function Design

Data files were firstly stored locally, then it was uploaded to sever via 3G network. Speed and stability test was done between 3 kinds of network and the best was chosen to be the transmission media. Then, a drive test was made in several kinds of road in Wuhan to assure the stability of 3G’s transmission. Test results showed that transmission speed had no relation with vehicle speed, but was largely affected by the driving area. And switching to another base station would make transmission break off. So the collection box should have “resume break transfer” function. That means as soon as the network again connected, the broken files should be uploaded from the broken point, and sequential files waited orderly by its time [4]. Files were marked after uploaded.

Device configure files were also transferred via 3G network. Contents of the configure file are sampling frequency, uploading regularity, BUS baud rate, file size and so on.

2.3 Hardware Design

According to function analysis, we designed collection box’ hardware structure and confirmed chips’ standard. Figure 2 shows how each module combines and communicates. Among them, the most important module is processor. Its functions were: interpret configure files, collect signals from BUS, I/o, A/D, acceleration sensor, gyroscope, temperature sensor, pack data and define transmission mode.

Key hardware’s standards are as follows:

1. CPU should have higher clock frequency and the ability of parallel computing, in order to meet 100 Hz sampling frequency and can put enormous data into files;
2. Memory was 256 M or above, to meet huge data requirement;
3. FlashRom was no less than 32 G, to meet enough storage needs.

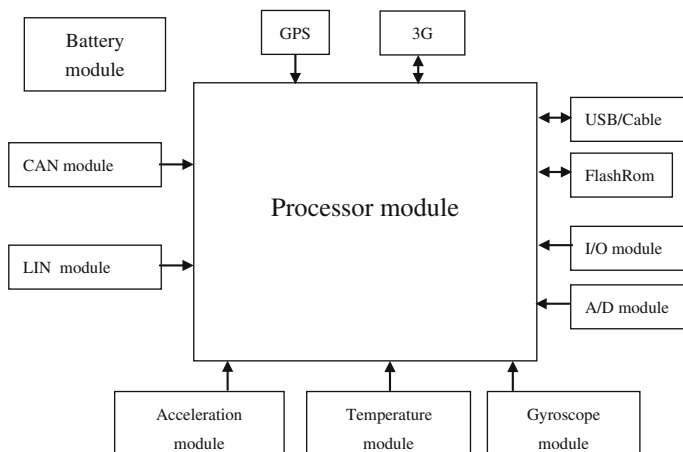


Fig. 2 Device system modules

2.4 Software Design

Box software design includes base software's collection function design and upper software's data processing function design. Server software design is to realize the function of data file receiving, storing, data computing, control file transmitting and supervising.

2.4.1 Base Software and Upper Software Functions Design

Single-chip computer was in charge of collecting base data and packing them to FlashRom memory. The stored files could be transferred through wire or wireless ways. Before the connection with CPU had done, MCU stored data in ferroelectric. As soon as connected, MCU abandoned the control for ferroelectric and packed stored data to CPU, CPU wrote data to files and transferred them to FlashRom. When device started, CPU read configuration file from ferroelectric and configure system. Figure 3 shows box' three layers construction, they are physical layer, application layer and transmission layer.

After started, collection box firstly required connection for sever and then checked whether current configure file was the newest. If it wasn't, the box would require to the server for renewing and reset system parameters. After initialization, the box collected required signals periodically. These signals data were packed in a certain frame formula and encrypted, encased, compressed and stored. With the "resume break transfer" function, files could be uploaded through 3G. They could also be downloaded of course. While connected, the box would report to sever device's state and vehicle's state which included vehicle speed, location, failures, temperature and voltage. The box should response control order from sever in time. If network failure

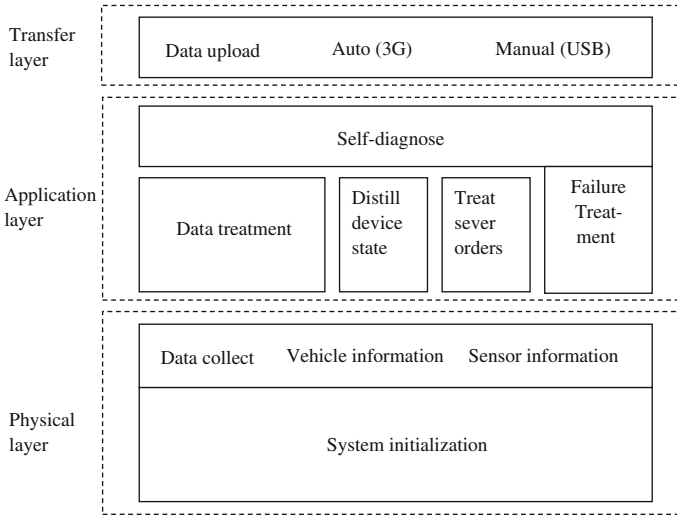


Fig. 3 Sever program modules

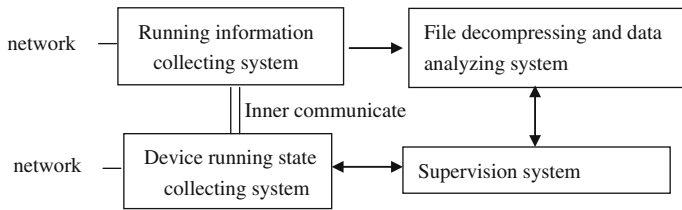


Fig. 4 Sever program modules

appeared or device running became wrong or order processing delayed, the box would do self-diagnose, deal with the faults and report them to sever.

2.4.2 Sever Software Function Design

Sever software design is to realize the function of data file receiving, storing, data computing, control file transmitting and supervising. Figure 4 shows sever program modules.

The files sever received would be decompressed, decoded and converted to revert to real running data. These data were recorded in specific files. All files recorded the number of the box, the number of the car, file version and the date.

The supervision end displayed vehicle running information and realized several data analysis, display, replay and record. Information displayed in this end is real-time speed, average speed, average fuel consumption, longitude, latitude, voltage and alarm.

3 Arithmetic Design

There is a huge database storing enormous running information data in sever. How to analyzing those data to find intrinsic laws and relations between them [5, 6] on the purpose of knowing vehicle performance and operation regularity so as to supply references to development work is the keynote of whole collection system. This chapter introduces the arithmetic designing principle and method, as well as cites typical arithmetic to explain how to design it.

3.1 Arithmetic Designing Principle and Scheme

Data analysis arithmetic designing principle:

1. Arithmetic should be comprehensive.

Comprehensive means that arithmetic should meet all vehicle development needs. On the result of collection requirement analysis, we confirmed several sorts of parameters. They are power parameters, economic parameters, driving parameters, safety parameters, comfort parameters, reliability parameters and other parameters. Each parameter was a kind of factor that would affect car's performance. One parameter may indicate one or more signal. For example, torque parameter indicated engine indication torque, flywheel torque, friction torque, driver needed torque.

Firstly, we tried to think out all potential arithmetic needs for every single parameter. Secondly, we used a matrix to put all parameters in the first row and all of them in the first column to try to find all potential arithmetic needs for parameter mutual relations by scanning every parameter in the matrix. For instance, torque parameter from the power sort and engine speed from economic sort may bring to arithmetic that is the relation between the two parameters. This scheme made arithmetic designing work ordinal, comprehensive and modifiable.

2. Arithmetic langue should be general

When compiling arithmetic, it was necessary to consider file format and langue accuracy. Besides, while different cars have different definition for some certain signals, we made a "data unit list" to ensure all the output data have same meaning.

3.2 Typical Arithmetic

For single parameter, arithmetic was manly about finding data changing regulation. So detailed arithmetic were data distilling, data transferring, computing

extreme value, computing average/median value, computing standard deviation and drawing distribution diagram. For several parameters, arithmetic was mainly about drawing curves and distribution diagrams in order to find the relations. The meanings of arithmetic are as follows:

Data distil: Take requirement accuracy, computing time and capacity into account, it is necessary to distil data from database. Sampling frequency is decided by requirement accuracy.

Data transfer: Some data need to be transferred to have reference value.

Extreme value and valid range: Abnormal, extreme value which would do harm to data analysis should be eliminated. So data in 5–95 % of the whole range are distilled to be the valid range.

Average/median value: In order to realize the average level of a set of data.

Standard deviation: In order to realize the deviation level of a set of data.

Distribution diagram: We designed 5 kinds of distribution diagram, named A, B, C, D and E (see Fig. 5). A diagram shows parameter 2’s value in every section of parameter 1; B shows the percentage of every section in parameter 1; while C is the scatter diagram of parameter 1 and parameter 2, the relation between them can be drawn by linking these points; D tells parameter 3’s percentage (or value) when parameter 1 and parameter 2 are in some certain section; E illustrates parameter 1’s distribution respectively in condition 1 and condition 2.

3.3 Introduction for Several Arithmetic

This essay takes “gear distribution” and “location-gear-fuel consumption-vehicle speed” for examples to explain arithmetic of data distilling, data transformation and data distribution in detail.

3.3.1 Gear Distribution

As the original data quantity was very huge, data distilling in the frequency of 20 ms/time was firstly done. For manual-transmission, gear position information is not generated in CAN BUS as auto-transmission is, so it must be transferred from vehicle speed and engine speed.

After acquired gear position sample, data distribution could be computed. All values were recorded in an EXCEL sheet. In a moment, we read the gear position value in the EXCLE file and assign it to parameter “GearPosition”. Define “n” as parameter and “ContX” as counter for X gear. (X = 1, 2, 3, 4, 5, 6, 11, 12, 13, 14),

If GearPosition = 1, then Cont1 ++, n ++;

If GearPosition = 2, then Cont2 ++, n ++;

...

After scanning all values, every ContX was used to multiply data distilling time interval to acquire gear usage time, and program will compute the distribution and drawing diagram B.

3.3.2 Location-Gear Position-Fuel Consumption-Vehicle Speed

This arithmetic is to acquire relation between vehicle speed and fuel consumption in all gears under different conditions of road level. Firstly program read GPS values (including highway, urban fast road, main road, sub-road, sub-sub-road), and then consulted road value's exact time to read gear position value, fuel consumption value, and vehicle speed value. Thirdly, program wrote these data into a new EXCEL file to be arithmetic sample.

If gear position value was 1 and vehicle speed was between 0 and 20 km/h, program would firstly compute driving distance and summed up fuel consumption to forecast 1 kilometre's fuel consumption under this speed. Secondly, program forecasted 1 kilometre's fuel consumption under 20–40, 40–60, 60–80, 80–100, 100–120 km/h vehicle speed in the same way. Thirdly, fuel consumption distribution was computed. When the car was in other gear, program computed fuel consumption distribution accordingly. Finally, C diagram was drawn according to these analysis results.

4 Test Results Analysis

Connection box was installed in car for 6 months for road test to collect its operation information. Test conditions were as follows: First, road types were urban main Rd, urban sub-Rd, urban sub-sub-Rd, expressway, high way, national Rd, provincial Rd, and country Rd. Second, temperature ranged from 5–40 °C. Third, collection forms were daily go to work collection, usual roads drive collection and unusually roads drive collection. Forth, driver was male, 35 years old with 8 years driving experience. Initial parameter's setting derived from configure file. The collected data was put to arithmetic program and then vehicle running analysis results was acquired.

This essay illustrates the result of vehicle speed distribution under different road level to show how car's operation data analysis could help passenger car design and development.

4.1 Collection Result and Analysis

Sampled vehicle speed and engine speed data was acquired after data distilment. The data was then submit to analysis program. The following diagram shows that when engine speed ranges separately in (500, 1000) (1000, 1500) (1500, 2000) (2000,

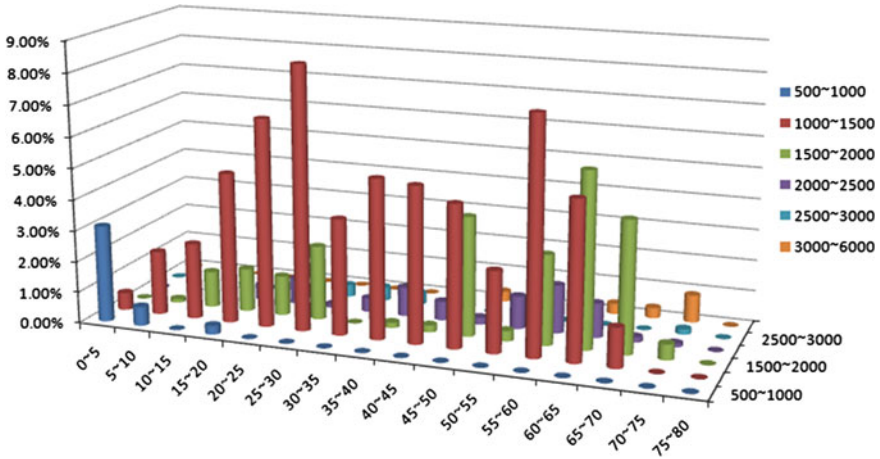


Fig. 5 Relation between engine speed and vehicle speed

2500) (2500, 3000) (3000, 5000), how corresponding vehicle speed distribute, see Fig. 5. Conclusions can be drawn that the engine frequently runs in 1,000–1,500 rpm, which accounts for 60 % of its whole running time. In addition, it also usually runs in 1,500–2,000 rpm. Vehicle speed distribute mostly in 15–60 km/s, and the driver tends to drive in 15–30 km/h on this road.

5 Conclusions

Method on how to collect vehicle driving data and how to analyze the data is given in this essay. Data collection device was produced according to this method, and vehicle test was done. The collected data was analyzed through arithmetic program. Conclusions can be drawn as follows:

1. The method is feasible and the device is useful. Data analyze results are valuable for vehicle design;
2. The device is compatible for all cars in the family and the collection scheme is designable;
3. Though for some reasons, such as cost, vehicle inner space limitation and user privacy and so on, specific data are not obtainable at present, the method to acquire them is the same as the essay states;
4. Analyze results are not only the reference for vehicle design and taxi fleet management, but also can give valuable recommends for forming good driving habits. So it has comprehensive application value.

References

1. Zong Y (2005) Development of data acquisition system for hybrid electric city bus. Wuhan University of Technology, Wuhan, p 3
2. Zhang Y, Yang Y, Ye X (2009) Design of signal recorder of automobile based on CAN bus. *Instrum Tech Sens* 2009:40–41
3. Chen C (2010) Research and design on data compression algorithm. Central South University of Technology
4. Chen Z, Guo J, Liu Z, Yuan Z (2012) Research on key technique of file transmission system with resume broken transfer. *Comput Eng* 12:14–16
5. Huang X, Xie B (2009) *Methods and Application for Statistics*. Renmin University
6. Messerschmidt WF, Muttart JW (2009) A statistical analysis of data from heavy vehicle event data recorders. SAE:2009-01-0880

Acoustic Mode and Structure Mode Analysis of Heavy Duty Truck Muffler

Guoquan Wang, Cheng Zhao, Liangcheng Zhang and Yong Chen

Abstract To reveal the muffler acoustic performances and structure vibration characteristics, the computational fluid dynamical (CFD) model and finite element method (FEM) model were established. Acoustic analysis results show that the muffler not only has complex acoustic vibration modes, but also the mode frequency approximately equals the engine's incentive frequency at rated speed, so the resonance may occur and the noise eliminating effect will be reduced. Structure vibration modal analysis shows that the muffler system has high natural frequency and the natural frequency is widely distributed. So while the engine runs at rated speed or idling speed, its natural frequencies are close to the engine exhausting incentive frequencies. It is the main cause that the muffler cannot reduce the noise effectively and needs further optimization.

Keywords Muffler · Acoustic mode · Structure vibration mode · Finite element method (FEM) · Modal test

F2012-E14-011

G. Wang · C. Zhao (✉) · Y. Chen
Beijing Information Science and Technology University, 100192 Beijing, China
e-mail: zhaocheng1007@sina.com

G. Wang
e-mail: wang.guoquan.ok@163.com

L. Zhang
Beijing Foton Motor Corp.Ltd, 102206 Beijing, China

1 Introduction

Noise level has become an important index to evaluate the heavy vehicle quality, the exhausting noise is one of the main sources of heavy duty truck, therefore reduce exhaust noise is an inevitable way to improve the NVH performance of heavy duty truck. Muffler is an effective device to reduce the engine noise. But the muffling effect depends on the acoustic performance, aerodynamics performance and structural parameter. A good muffler can not only muffler the given wavelength noise, but also ensures the exhaust flow smoothly as much as possible to reduce the pressure loss. At the same time, the overall dimension, structure stiffness, working life and the whole assembly also should be good. The muffler is a multi-cavity system made of welding steel plate, connected from beginning to end by the exhaust pipe and mounted on the truck frame by special hanger. During the working process, the muffler bear the exhaust gas exciting and the frame vibration exciting, which bring about acoustic resonance and structure vibration, then will reduce muffling effect and damage the life of the muffler system.

The principle of muffler dampening down the engine's noise is a sophisticated problem. It involves multi-disciplinary theories such as gas flow, heat transfer, acoustic and vibration, combustion of engine and its structure, etc. Traditional method of design muffler mainly rely on one dimension planer wave theory and the designer's experience as well as lot of repeated tests. Due to we cannot grasp the underlying cause of three dimension sound wave, it cost a large amount of money, and the muffling efficiency is discounted [1]. With the development of computational aero acoustics, muffling study is turning from the pure transfer matrix algorithm to the boundary element method and finite element method, especially to acoustics analysis; it is realized from plane wave to three-dimensional sound wave calculation, then the muffler acoustic performance analysis become more and more accurately. The results of calculation and analysis are close to the actual acoustic characteristics, and the multiple design schemes can be simulated or compared in a short cycle.

Based on the theory of fluid dynamics and structural dynamics, the paper presented the acoustic mode analysis and structural dynamics analysis using FEM, obtained the muffler system modal parameters, and established the foundation on muffler structural optimization and vibration noise reduction.

2 The Principle of Modal Analysis

Structure mode is characterized by specific vibration displacements of structure, and depicted by modal frequency, modal shape, modal damping as well as other modal parameters. Structure modal analysis is the base of spectrum analysis, transient analysis, harmonic response and other dynamic analysis [2].

Acoustic mode is characterized by the sound pressure distribution that is the orthogonal eigenvector of the surface vibration velocity matrix. It is similar to the

structure modes, and explained by natural frequency and modal shapes (Sound pressure distribution): at one acoustic modal frequency, the incident of air flow wave and reflection from muffler cavity boundary superimposed on each other or mutual cut in different part, then produce different pressure distribution [3, 4]. Acoustic modal provides very valuable information to avoid the occurrence of resonance of cavity wall [5]. The results can determine whether the cavity resonance is aroused and how to add resonant cavity to control sound pressure distribution [1], therefore the muffler performance was improved.

2.1 Theory of Acoustic Modal Analysis

Sound vibration is a macroscopic physical phenomena, it meets the fundamental laws of physics, including Newton's second law and Law of Conservation of energy, as well as the state equation of ideal gas to describe the relationship among pressure, temperature and density. To the ideal fluid medium, the three-dimensional wave equation of little amplitude sound wave is:

$$\nabla^2 p = \frac{1}{c_0^2} \frac{\partial^2 p}{\partial t^2} \quad (1)$$

Where ∇^2 is the Laplace operator; c_0 is the sound propagation speed in the air; p is the sound pressure function of arbitrary points in the sound field [6]. In linear space, acoustic mode is the characteristic value of acoustic quality matrix and acoustic stiffness matrix [7], considering the materials and boundary conditions combined, then got the acoustic modal analysis equation:

$$(\mathbf{K}_a - \omega^2 \mathbf{M}_a) \{\phi\} = \{0\} \quad (2)$$

Where $\{\mathbf{K}_a\}$ is an $n \times n$ acoustic equivalent stiffness matrix; $\{\mathbf{M}_a\}$ is the $n \times n$ acoustic equivalent mass matrix. Equation (2) can solve n linear independent characteristic values and n characteristic values $\omega_i^2 (i = 1, 2, \dots, n)$, and then any pressure vector $\{p_i\}$ can be Linear represented by $\{\phi_i\}$ as follow:

$$\{p_i\} = \lambda_1 \{\phi_1\} + \lambda_2 \{\phi_2\} + \dots + \lambda_n \{\phi_n\} = \Phi \{\lambda\} \quad (3)$$

Where $\Phi = [\phi_1 \ \phi_2 \ \dots \ \phi_n]$ is a modal matrix; $\{\lambda\} = \{\lambda_1 \ \lambda_2 \ \dots \ \lambda_n\}^T$ is a modal participation factor. The acoustics system equation is:

$$(\mathbf{K}_a + j\omega \mathbf{C}_a - \omega^2 \mathbf{M}_a) \cdot \{p_i\} = \{F_{ai}\} \quad (4)$$

Where \mathbf{C}_a is a $n \times n$ damping matrix; $\{F_{ai}\}$ is a acoustic excitation. Combining Eqs. (3 and 4), then multiply modal matrix Φ^T at both left of the new equation. Get a new equation:

$$(\Phi^T K_a \Phi + j\omega \Phi^T C_a \Phi - \omega^2 \Phi^T M_a \Phi) \cdot \{\lambda\} = \Phi^T \{F_{ai}\} \tag{5}$$

Where $\tilde{K}_a = \Phi^T K_a \Phi$ is the acoustic modal stiffness matrix; $\tilde{C}_a = \Phi^T C_a \Phi$ is the acoustic modal damping matrix; $\tilde{M}_a = \Phi^T M_a \Phi$ is the acoustic modal mass matrix; $\{\tilde{F}_{ai}\} = \Phi^T \{F_{ai}\}$ is the acoustic modal incentive vector, the new as follow:

$$(\tilde{K}_a + j\omega \tilde{C}_a - \omega^2 \tilde{M}_a) \cdot \{\lambda\} = \{\tilde{F}_{ai}\} \tag{6}$$

It only requires solving modal participation factor $\{\lambda\}$. The sound pressure value of each node can be solved through the Eq. (3), combined the shape function (relationship between the acoustic pressure and node pressure), then the acoustic pressure $p(x, y, z)$ of the arbitrary points in the sound field are got.

$$p(x, y, z) = N\{p_i\} = N\Phi\{\lambda\}. \tag{7}$$

2.2 Theory of Structure Modal Analysis

Finite element method is used to discrete the Physical structure into a n degrees of freedom linear elastic system. Any instantaneous movement patterns can be described by n independent generalized coordinates.

$$M\ddot{\delta} + C\dot{\delta} + K\delta = F(t) \tag{8}$$

Where K is a positive definite or semi-definite global stiffness matrix; M is a positive definite mass matrix; C is the damping matrix obtained by the damping unit; $F(t)$ is the time-varying dynamic loads. With regard to the non damping materials pure elastic body, while the excitation force is 0, the n freedoms system vibration equation will get:

$$M\ddot{\delta} + K\delta = 0 \tag{9}$$

The vibration of each node abided by simple harmonic vibration, and the displacement can be expressed as:

$$\delta(t) = \delta_0 \sin(\omega t + \varphi) \tag{10}$$

Here δ_0 is the amplitude vector of natural mode of vibration; ω is the natural frequency; φ is the phase angle.

Combining Eqs. (9 and 10) get the equation:

$$(K - \omega^2 M)\delta_0 = 0 \tag{11}$$

The condition of the Eq. (11) has solutions is:

$$\det(K - \omega^2 M) = 0 \tag{12}$$

So, both the structure modal frequencies ($[\omega_1 \ \omega_2 \ \omega_3 \ \dots \ \omega_n]$) and the modal shapes ($[\delta_{01} \ \delta_{02} \ \delta_{03} \ \dots \ \delta_{0n}]$) can be obtained by Eqs. (12 and 10) respectively.

3 The Muffler Calculating Modal Analysis

3.1 The Digital Modal of the Muffler

The research object is a type of heavy vehicle muffler with Cummins ISME385 30 engine, the model of the muffler brackets as shown in Fig. 1. The geometric parameters of the muffler is: $830 \times 556 \times 400$ mm, outer covering made by stainless steel, inside cavity was split into multiple cavities by perforation plates, the middle anechoic layer made of special heat-resistant and sound absorption material, the exhaust sound energy can be transformed to thermal energy. In order to improve the calculation efficiency, some details were simplified. Welding parts and the fold edges were removed, model as shown in Fig. 2.

3.2 Structural Modal Analysis

The finite element model of the muffler was imported into the HyperMesh10.0. The muffler's outer covering and the inner wall of each cavity used as benchmark, then extracted the internal surfaces which contact with air, and then formed a closed acoustic cavity. On the premise of ensuring the calculation precision the model was simplified [8]: the snap-in between plates, welding transition region, transition fillet, the groove of bracket U-shaped bolt and technical structures. These parts have little effect on the mechanical structure.

While meshing, the acoustic unit size should be consistent with the structure unit, in addition to, there are at least six acoustic units along the smallest wavelength range [7]. The smaller local mesh would not improve the calculation accuracy, because the calculation accuracy of the fluid model is controlled by majority unit, which is different to structural analysis. Assuming that the propagation velocity of sound is C , a unit length is L , then the unit can calculate the maximum frequency: $f_{\max} = C/6L$. The main incentive forces of the muffler are the engine exhaust and tires, the incentive frequency mostly are below 400 Hz. So all of the length of the unit should be meet: $L \leq C/6f_{\max}$, C takes $340m/s$, f_{\max} takes 400 Hz, then $L \leq 0.142$ meter. The longest length of the unit is 13 mm in Fig. 3, meet the requirements. Based on past experience, it is necessary to keep 1 mm distance between the different cavities to ensure the calculation precision. The cavities on both side of the perforated plate were connected by hexahedral units which through the holes of the perforated plate, as shown in Fig. 4.

Fig. 1 The muffler and the bracket assembly drawing

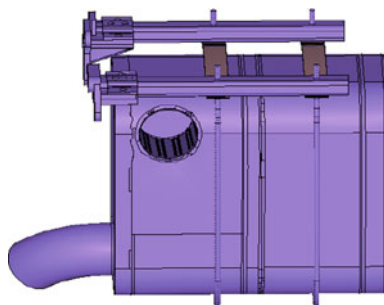


Fig. 2 Muffler geometry model

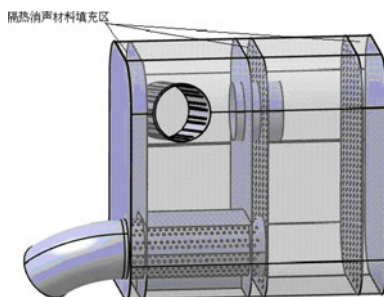
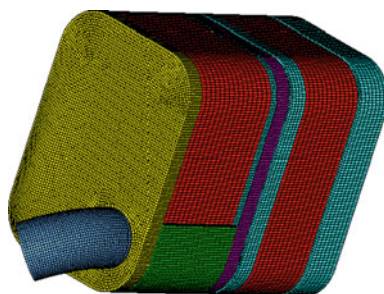


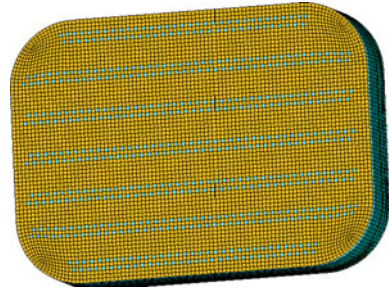
Fig. 3 Muffler acoustics meshes



Using the Lanczos algorithm in LMS Virtual Lab software, the acoustic mode of the muffler cavity was analysed, and then got the first ten order acoustic modes and frequencies, shown in Table 1.

Analysis shows that, the second, third and sixth-order mode shapes (Sound pressure distribution) are symmetrical and the peak sound pressure spread in the resonant cavity. First order is the rigid body mode and the natural frequency is 0 Hz. The second order and third order sound pressure peaks are respectively in the muffler's cavity on its left and the Helmholtz resonator on its right. The acoustic natural frequency (about 90 Hz) is similar to the bracket structure modal frequency. The fifth, seventh, eighth, ninth and tenth modes are mainly local mode,

Fig. 4 Meshes of the perforation plate



probably produced by the complex internal structure and the perforation plates. The fourth and seventh order modal peak pressure appeared in the muffler outlet, probably it was the local modes too, and as the acoustic modal frequency goes up, the pressure distribution becomes more and more complex.

3.3 The Muffler Structure Modal Analysis

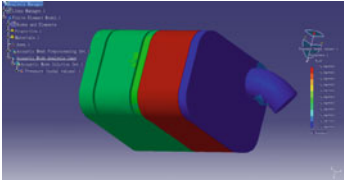
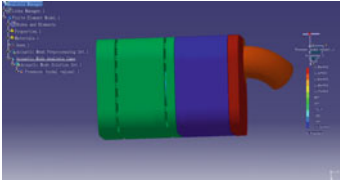
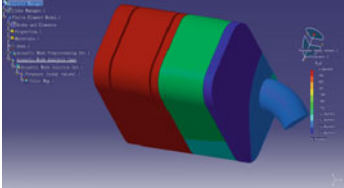
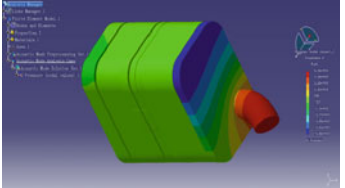
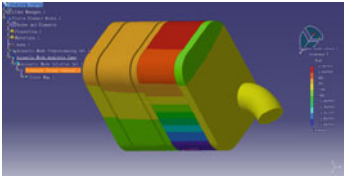
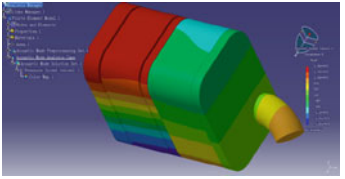
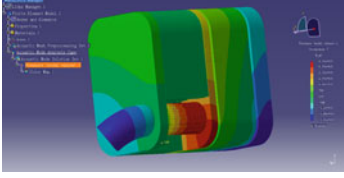
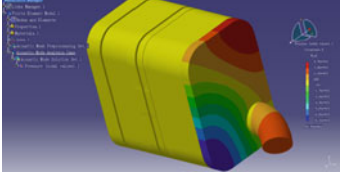
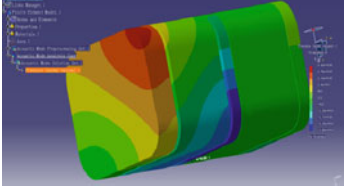
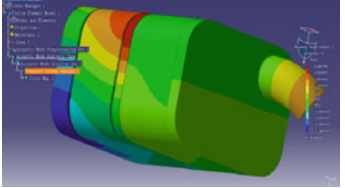
While establishing the muffler structural finite element model, the sound material was taken out, and the round holes of the exhaust pipe were replaced by small square holes. The muffler wall, brackets and steel strips were established by shell elements, the brackets support was established by hexahedral elements, as shown in Fig. 5a, b. Radioss solver of HyperWorks (10.0) and Lanczos arithmetic was used for calculating the structural mode [9].

4 Analysis of Structural Modal Test

To verify the results of finite element analysis, two kind of modal vibration tests were operated by using DASP software of China Orient Institute of Noise and Vibration: one was installed state experiment, and the other was free modal experiment. The test site was shown in Figs. 6 and 7.

Using hammering incentive during the muffler brackets modal test, and then the vibration of the muffler brackets were obtained. The actual structure was very complex, including the mounting brackets (divided into the upper straight segment and the lower curved section), the connecting plate of the mounting brackets and complex structures of heavy-duty trucks. In order to increase efficiency, here the upper straight section and the two horizontal connecting plates of the brackets were established. The single Input with Multi-point Output (SIMO) method was used, selected the NO. 2 node of the bracket structure chart as the origin admittance position, moved sensors, knocked 22 times and got 66 output signals. Same as the brackets test, 133 nodes of the muffler were elected, then connected these

Table 1 Results of muffler acoustic modal analysis

 <p>First order mode (0 Hz)</p>	 <p>Second order mode (70.067 Hz)</p>
 <p>Third order mode (90.026 Hz)</p>	 <p>Forth-order mode (244.268 Hz)</p>
 <p>Fifth-order mode (306.842 Hz)</p>	 <p>Six-order mode (321.062 Hz)</p>
 <p>Seventh-order mode (371.62 Hz)</p>	 <p>Eighth-order mode (391.917 Hz)</p>
 <p>Ninth-order mode (416.199 Hz)</p>	 <p>Tenth-order mode (437.408 Hz)</p>

nodes by straight lines and constituted the entire muffler structure. Figures 8 and 9 are the structure and the measuring point arrangement of the bracket and the muffler respectively.

The time domain method was used in test data processing. Time-domain signal processing including spectrum analysis, the transfer function estimates, filtering, impulse response measurement, correlation analysis, and so on.

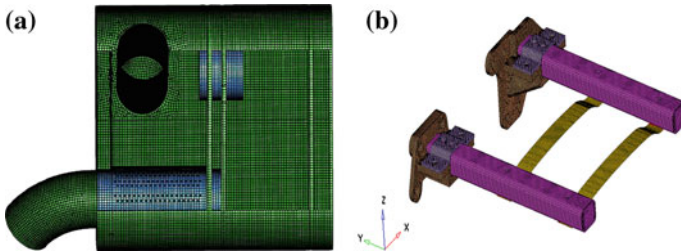


Fig. 5 Finite element model of muffler system

Fig. 6 Bracket modal test site



Fig. 7 Muffler modal test site



Calculated the impulse response function of the points, and then identified the modal shape by eigen system realization algorithm (ERA). The eigen system realization algorithm (ERA) method which according to the impulse response function, construct a generalized Hankel matrix and use the singular value

Fig. 8 Measuring points and structure of bracket

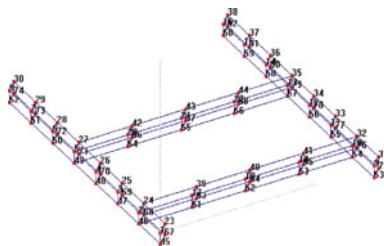
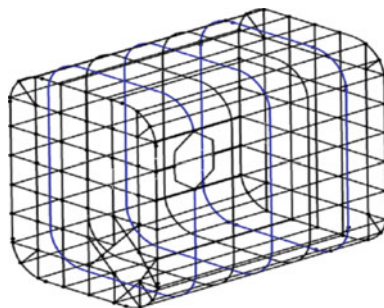


Fig. 9 Measuring points and structure of muffler



decomposition technique to get the minimal realization system that is the minimum order system matrix, and then identify the modal parameters of the system. ERA method has a good ability on identifying dense mode and the complex structure mode [10]. In DASP software, stability diagram showed that the MAC value was 1, so the input and output signals had good coherence, the data were credible.

5 Comparison with the Test Results and Calculated Results

Muffler and bracket modal test results and finite element analysis results were compared, as shown in Tables 2 and 3. As Table 3 shown, modal test analysis and finite element calculation not only have the similar modal frequency, but the vibration modes fits well. Few modes of the muffler system are failed to accurately identify, but the mode alright obtained are corresponding to the finite element analysis results, then the finite element analysis verified to be correct. The test results have more modes which may contain the U-shaped belt modes. The test results can characterize the vibration shapes of the bracket and the muffler very well, and besides, the test results match with finite element analysis very well. It is shown the test results are credible.

The finite element calculation results do not exactly equal the test, the possible causes were:

Table 2 Natural frequency comparison between modal test and finite element analysis

Order	Comparison between muffler test results and finite element analysis results			Comparison between bracket test results and finite element analysis results		
	Calculation results (Hz)	Test results (Hz)	Error (%)	Calculation results (Hz)	Test results (Hz)	Error (%)
1	53.98	52.51	2.8	7.24		
2	62.20	59.87	3.9	13.94	14.9	6.4
3	93.10	93.95	0.71	16.38	17.28	5
4	96.67	113.86		24.87		
5	110.97	124.38		28.49		
6	137.12	138.54	2.01	41.14	40.02	2.8
7	150.34	145.27	3.49	70.54	52.69	
8	158.10	153.73	2.86	85.77	83.36	2.9
9	168.78			90.56	106.41	
10	170.80	174.30	2.01	120.87	113.99	6

1. Parts of muffler system were welded or connected by steel sheet. While defining contact of the muffler in finite element model, the welding joint was merged into one node and the steel sheet was replaced by a certain thickness units.
2. The actual structure of the muffler had many geometric features which may affect the results. In order to improve the calculation efficiency, replaced the round holes with square holes, ignored the rolled-seam of tube and welding features.
3. In modal test process, some test points near the modal nodes, thus presents modal omission. In addition, test equipment, test environment, the operator, test method and so on various factors brought test error.

Muffler vibration source mainly come from three aspects: Vibration incentive from the engine; Vibrations incentives when exhaust airflow through the muffler; Ground incentive. Test and finite element calculation results shown that the frequency of the muffler and bracket widely distributed in 14.9–200 Hz range. This muffler was assembled to the Cummins ISME385 30 engine which idle speed between 600–800 r/min, the rated speed was 1,900 r/min and the maximum torque speed was 1,200 r/min. Then the engine exhaust vibration mainly frequency can be calculated:

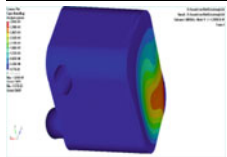
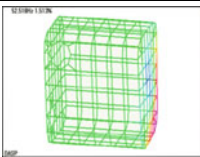
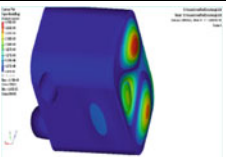
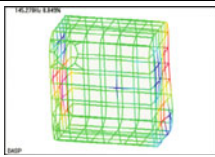
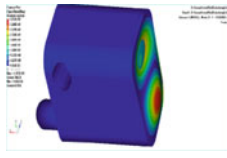
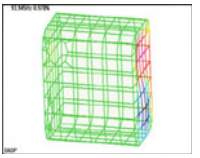
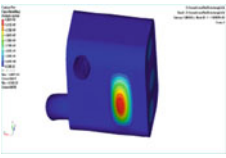
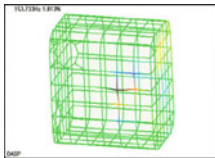
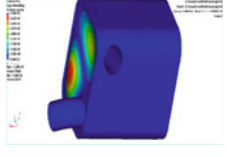
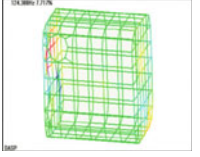
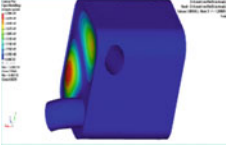
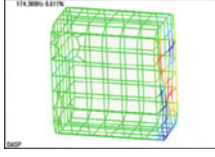
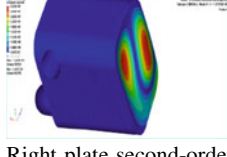
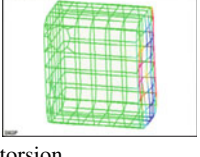
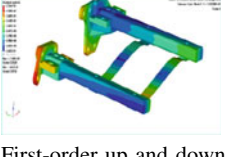



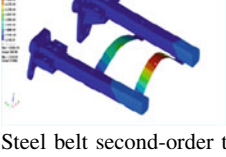
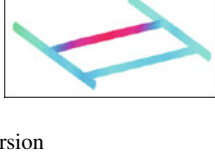
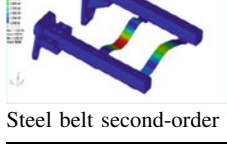

$$\text{Under idle condition: } f = \frac{2kn}{60T} = \frac{2 \times 6 \times 800}{60 \times 4} = 40\text{Hz}$$

$$\text{Under rated condition: } f = \frac{2kn}{60T} = \frac{2 \times 6 \times 1900}{60 \times 4} = 95\text{Hz}$$

Under maximum torque condition: $f = \frac{2kn}{60T} = \frac{2 \times 6 \times 1200}{60 \times 4} = 60\text{Hz}$ (k is the number of cylinder, n is engine speed, T is number of strokes)

It is clear that the engine exhaust frequency is close to the brackets second-order natural frequency (40.02 Hz) under the engine idle speed. The two low natural vibration frequency (14.9, 17.28 Hz) of brackets are in road excitation frequency range (1–20 Hz) in commonly used speed. Thus the brackets structure

Table 3 Vibration mode comparison between modal test and finite element analysis

Vibration mode of finite element calculation	Vibration mode of modal test	Vibration mode of finite element calculation	Vibration mode of modal test
			
Right plate first-order swing		Right plate third-order vibration	
			
Right plate second-order bending		Side plate first-order vibration	
			
Right plate second-order vibration		Right plate fourth-order vibration	
			
Right plate second-order torsion		First-order up and down swing	
			
Steel belt first-order bending		Steel belt second-order torsion	
			
Steel belt second-order bending			

need to be improved or the installation position should be improved in order to avoid resonance.

The main muffler structure modal distribution on the sides of the resonant cavity cover, these places and the overall framework of muffler are mainly connected by welding, in practical work may appear unsoldering phenomenon, so the

other connection method can be adopted or add other auxiliary device to reduce the damage. Under engine rated speed, the muffler third-order frequency (90.26 Hz) of acoustic mode is close to the exhaust excitation frequency and the peak of sound pressure distribution is located in the Helmholtz Resonator cavity. So resonance may occur and it will affect the muffler performance.

6 Conclusion

Based on the modal test method and finite element analysis method, the muffler system modal parameters were successfully obtained. It provided a very valuable theoretical basis for the muffler brackets installation and the muffler noise and vibration reduction. Structural vibration analysis and acoustic analysis found that resonance probably occur in some incentive frequency of engine exhaust. It is necessary to optimize the brackets installation method, to adjust the length of the exhaust pipes or increase the auxiliary device for improving the muffler performance.

Eternal excitation will cause the vibration of muffler's outer covering sheet and the inner cavity wall. The covering sheet and panel vibration also were affected by the muffler cavity fluid counterforce. Noise produced by wall vibration was amplified or attenuated in inner cavity, whereas the noise produced by muffler cavity also was amplified or attenuated at the covering sheet. So it is necessary to consider the coupling between muffler structure vibration and the inside cavity noise, but the early study ignored the coupling effect. In order to simulate interactions between muffler covering sheet and the internal cavity, and master coupling system dynamic characteristics, the muffler cavity and muffler structure coupling model needs to be established, this is the next step research focus.

Acknowledgments The authors would like to acknowledge the support of Beijing Municipal Commission of Education under the grant No. PXM2012_014224_000023 and Beijing Information Science & Technology University graduate innovation fund project under the grant No.5028211000.

References

1. Chengwu L, Dingjian H, Yong Z (2009) Modal analysis of interior acoustic cavity based on noise, vibration and harshness (NVH). *J Fujian Univ Technol* 7(4):347–350
2. Jian P, Gang S, Hua H (2006) *Automotive noise and vibration—principle and application*. Beijing Institute of Technology Press, Beijing
3. Xingda Z, Wenxue Z (2011) Analysis of acoustic performance resistance muffler based on acoustic mode. *J Yanbian Univ (Nat Sci)* 37(3):265–268
4. Chu CI, Hua HT, Liao IC (2001) Effects of three-dimensional modes on acoustic performance of reversal flow mufflers with rectangular cross-section. *Comput Struct* 79:883–890

5. Chen Y, Chengwu L (2008) Study and analysis on the car body NVH characteristics. *J Guangxi Univ Technol* 19(4):5–9
6. Gonghuan D, Zhemin Z, Xiufen G (2010) Acoustic foundation. Nanjing University Press, Nanjing
7. Zenggang L, Fuliang Z (2010) Virtual lab acoustics simulation calculation and advanced application example. National Defense Industry Press, Beijing
8. Lingyu S, Zhenhua L (2003) Discussions on modal analysis of interior acoustic field. *Automot Eng* 25(1):74–77
9. Chulin L, Shenglan Z, Yin F, Chaoyang Z (2008) Hyperworks analysis application example. Mechanical Industry Press, Beijing
10. Shuqian C, Wende Z, Longxiang X (2001) Vibration structure modal analysis—principle, experiment and application. Tianjin University Press, Tianjin

Transient Thermal Measurement of Electronic Components and Radiometric Characterization of LEDs

Boris Marovic and Alexandra Francois-Saint-Cyr

Abstract Changing requirements for HEVs and EVs (e.g., for IGBTs) and automotive lighting with LEDs are forcing component manufacturers to re-think designs, moulding techniques or packaging strategies. These changes can result in new unknown thermal behaviours that could lead to bad thermal characteristics, delamination, increased thermal resistance and failure. This chapter will address how thermal and radiometric testing and measuring to obtain accurate thermal characterization helps to increase component reliability. We used thermal and radiometric testing and measuring software/hardware products (T3Ster and TERALED) to obtain thermal characterization data of various electronic semiconductor components such as LEDs, IGBTs, and different chips for thermal simulation to understand the thermal and radiometric behaviour of the design to be able to eliminate the risks of component failure before production and also to deliver accurate thermal characterization data for thermal simulations. We obtained high-accuracy thermal and radiometric measurement values of LEDs with repeatable results. The radiometric measurements of LEDs enable a detailed characterization of various parameters, such as radiant flux and color coordinates depending on current and temperature. With this information, we were able to make selections from different vendors after researching the aging effects on these components and therefore their quality. In other tests, we were able to determine component and assembly defects that can appear either because of aging or during manufacturing of the component or the assembly, which results in changes in

F2012-E14-013

B. Marovic (✉)

Mentor Graphics (Deutschland) GmbH, München, Germany
e-mail: amy_knutson@mentor.com

A. Francois-Saint-Cyr

Mentor Graphics, Greenwood Village, CO 80111, USA

thermal resistance and worsens the thermal behaviour. The transient thermal measurement of electrical components is limited to semiconductor-based electrical components and their assembled state on the PCB in its environment. This chapter shows a new technology with never before reached accuracy of thermal and radiometric coupled characterization of semiconductor components that helps ensure designing and manufacturing best-in-class components and high reliability systems that use such components. A detailed thermal characterization enables optimized thermal design of the system rather than over-designing the system for thermal performance. With additional LED radiometric characterization, the same can be done for optimal performance of LEDs. This is especially important in future EV and HEV where energy consumption is critical to a higher efficiency and extended range of the vehicles.

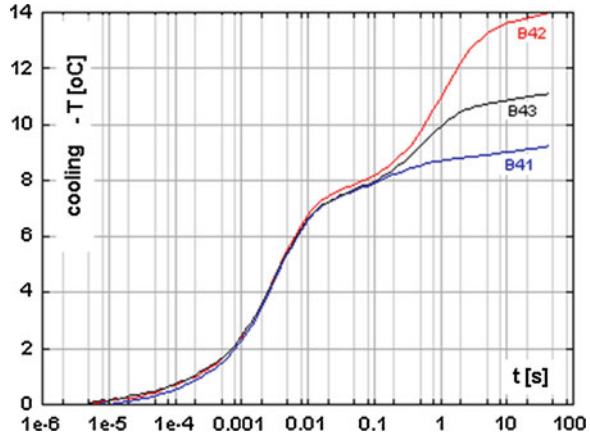
Keywords LED · IGBT · Thermal testing · Thermal characterization · Optical characterization

1 Thermal and Radiometric Characterization According to JEDEC Standards

When talking about thermal and radiometric characterization it is often unclear what is meant. Thermal and radiometric characterization means to get detailed thermal or radiometric information of a component such as an LED, chip or IGBT. Usually one can find some information in datasheets but often just rough data or for certain temperatures but not very detailed information on which important decisions in the component selection or design changes can be based. For example when selecting an LED the datasheet usually provides one with a value for the thermal resistance of Junction-to-Case ($R_{\theta JC}$) or the optical properties such as the Luminous Flux at a certain temperature and for a certain driving current. But the components are usually not working at these temperatures or different currents and can be subjected to much higher temperatures where these values are simply not valid anymore. But what are the values for these working conditions? And especially the higher temperatures are decreasing the lifetime of the components sometimes drastically and the components will degrade over time. But how and at which point in the structure of the component are they degraded?

These and more of these issues and questions will stay unanswered without any deeper research on the component. Thermal and radiometric characterizations can be done by component manufacturers and system designers and for different reasons such as in line testing of samples to check if the manufacturing process is still alright or for component selection in case of offers from different component vendors. That way the designer is able to select the best quality component he needs for his product, better than from just a few values and facts in a datasheet.

Fig. 1 Measured thermal response curve by T3Ster



1.1 Thermal Characterization According to JEDEC JESD 51-1 and 51-14

The thermal characterization in general is valid for semiconductor components and will measure thermal resistance and capacitance of the component. With T3Ster it is possible to achieve an incredible high accuracy and repeatability of this measurement and gain a structure function that will show the detailed structure with the thermal resistance and capacitance of each layer from junction to the environment. Even in an assembly such as a memory chip on a RAM module that is mounted on the motherboard, the whole heat flow path can be measured and analysed for weaknesses and bottlenecks in the design.

The advantage of this method compared to measurements with thermocouples is that thermocouples have a high potential error due to the alternate heat flow via the thermocouple itself and one would have to get direct access to the measuring location.

The thermal characterization according JEDEC Standard JESD 51-1 [1] and JESD 51-14 [2] works by leveraging the properties of the semiconductor which is the voltage change due to the changing temperature of the semiconductor at a constant current. If someone calibrates the measurement to this tie of voltage and temperature, he is able to activate the component and bring it to the hot steady state and when abruptly deactivating it to a point of only a small constant current, he can measure the thermal response (Fig. 1) of the component as it transitions to the cold steady state. This can be the diode forward voltage or the MOSFET threshold voltage that is measured to sense the change in temperature of the junction temperature directly. Here there are two ways possible, a dynamic (or pulsed) measurement or a static (or continuous) measurement.

From this measured thermal response curve which shows the temperature delta over the time, the structure function can be derived by some mathematical methods and in addition a Cauer ladder model can be derived. This detailed structure

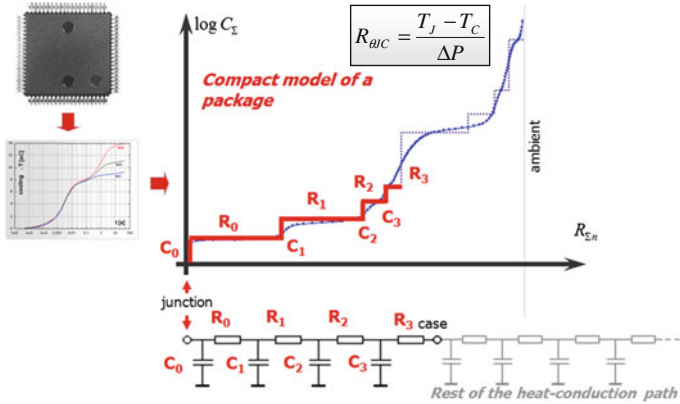


Fig. 2 Simplified process to get the structure function and the Cauer ladder model of the component

function (Fig. 2) gives detailed inside view in the structure of the component and the Cauer ladder model for a compact thermal representation of the component and can be used for more detailed thermal simulation models and result in higher simulation result accuracy than often less accurate data presented in the datasheets. The thermal resistance of Junction-to-Case is defined by the temperature difference between Junction (T_J) and Case (T_C) divided by the Power difference (ΔP).

1.2 Radiometric Characterization According to JEDEC JESD 51-51 and 51-52

The radiometric characterization of LEDs, according to JESD 51-51 [3] and 51-52 [4], is not only important to gain radiometric properties of the LED but also to measure the real thermal resistance. Because LEDs don't just create heat by the electrical power they consume but also light, the light output has to be considered for the real thermal resistance. Here the calculation of the real thermal resistance uses for the power difference $\Delta P = P_{el} - P_{opt}$ as the electrical power P_{el} that drives the LED is reduced by the optical power P_{opt} that is emitted by the LED. If this is not taken into account the deviation of the thermal resistance of a LED can vary up to 30 %, depending on the operating conditions such as temperature and current (Fig. 3).

A combined measurement of thermal and radiometric parameters (Fig. 4) enables an even more and easier linked combination of the data. The LED can be measured at different currents and temperatures and the corresponding data can be recorded and displayed with both dependencies for its radiometric parameters as shown in Fig. 5.

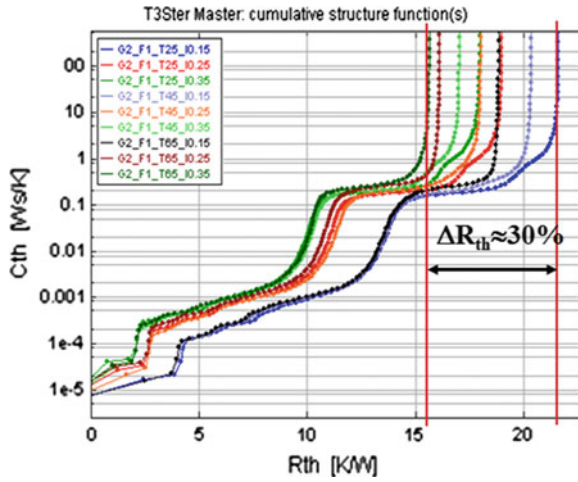


Fig. 3 Deviation of thermal resistance if optical power is not considered in the measurement

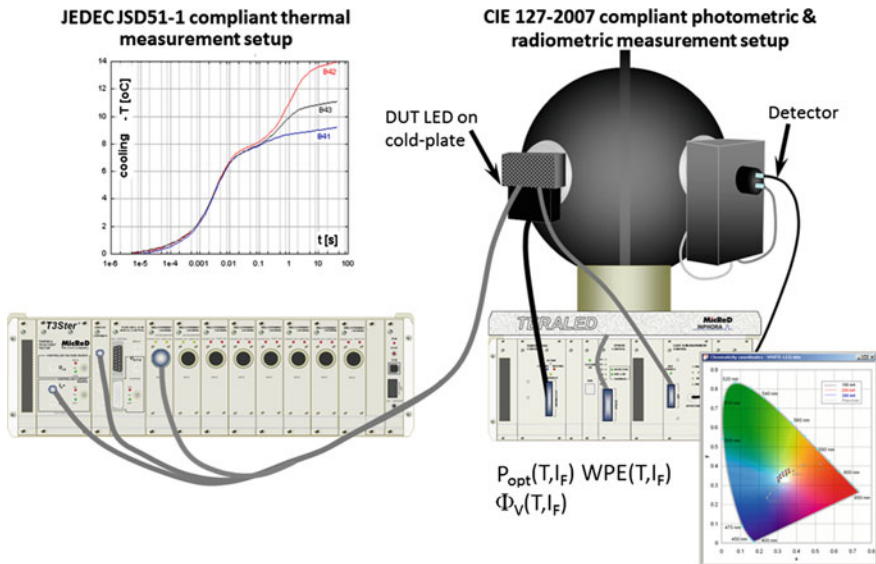


Fig. 4 Schematic of a combined thermal and radiometric characterization with T3Ster and TERALED

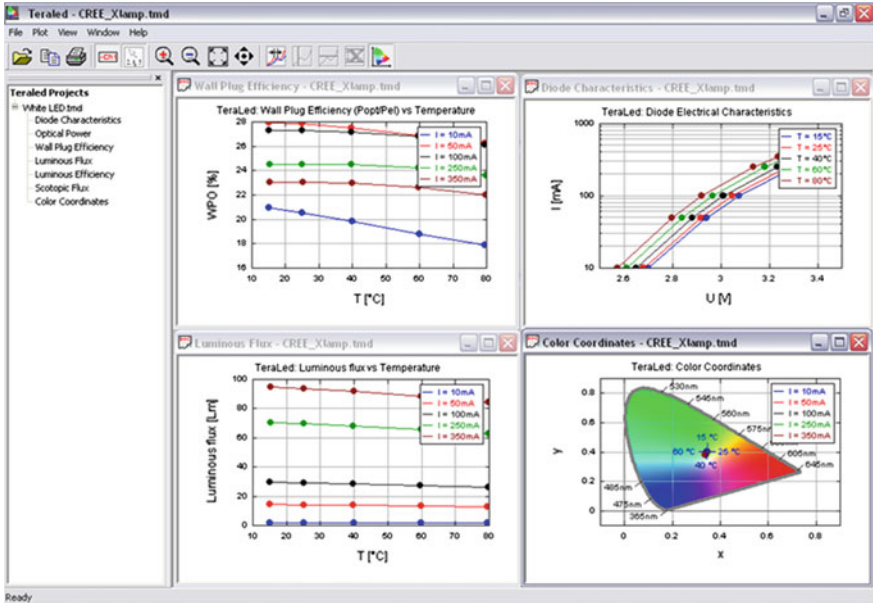
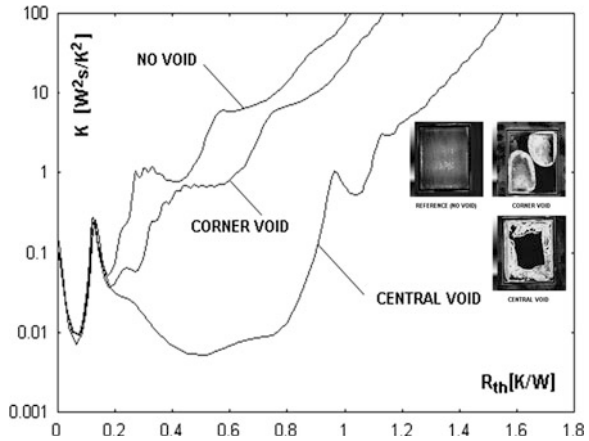


Fig. 5 Detailed radiometric characterization evaluation

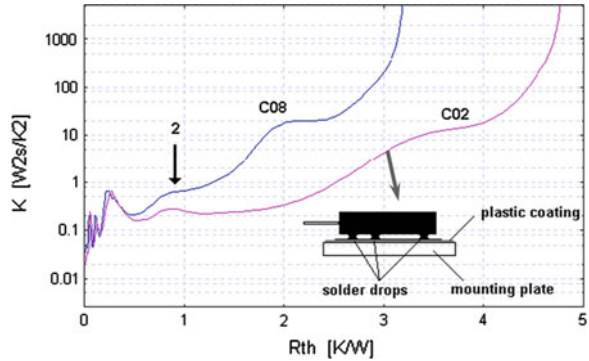
Fig. 6 Die delamination types and the corresponding structure function [1]



2 Examples Cases of Thermal and Radiometric Characterization

There are some uses of the structure functions. In the case of failure analysis the structure function can show the point in the structure where the component has failed (Fig. 6). The failure usually shows a shift in the thermal resistance or capacitance if a component is damaged or not in ideal health due to aging,

Fig. 7 Influence of a faulty soldering on the structure function



bad manufacturing process or excessive temperature exposure. Such failures can cause die delamination and overheating and at the end the terminal failure of the component.

Another example are detecting assembly failures. In Fig. 7 one can see the structure function for a good and bad soldering. In this case the bad soldering is represented by solder drops in a power JBT system which causes a bad thermal resistance because of the bad surface contact.

3 Conclusions

The thermal and radiometric characterization is a non-destructive method to get an insight view into the components structure and its failures. This enables manufacturers and system designers to test and compare different components or changes in the health of a component and use this detailed information for thermal simulations. Thus making the thermal simulation models more accurate than with the usual provided data in datasheets.

The application is wide, from quality assurance or assembly line control to failure analysis and component selection. This method can be used for semiconductors ranging from low power LEDs and chips to High Brightness LEDs and IGBTs in consumer electronics such as LED TVs to electric vehicles (EVs). It is an ideal method to assure reliability and quality of products by picking the best component and simulating the thermal management of the product with the highest accuracy.

References

1. Rencz M, Székely V, Morelli A, Villa C (2002) Determining partial thermal resistances with transient measurements and using the method to detect die attach discontinuities. In: Proceedings of 18th IEEE SEMI-THERM symposium, San Jose, pp 15–20
2. JEDEC Standard JESD51-1 (1995) Transient dual interface test method for the measurement of the thermal resistance junction-to-case of semiconductor devices with heat flow through a single path. <http://www.jedec.org/sites/default/files/docs/jesd51-1.pdf>, JEDEC
3. JEDEC Standard JESD51-14 (2010) Transient dual interface test method for the measurement of the thermal resistance junction-to-case of semiconductor devices with heat flow through a single path. http://www.jedec.org/sites/default/files/docs/JESD51-14_1.pdf, JEDEC
4. JEDEC Standard JESD51-51 (2012) Implementation of the electrical test method for the measurement of real thermal resistance and impedance of light-emitting diodes with exposed cooling. <http://www.jedec.org/sites/default/files/docs/JESD51-51.pdf>, JEDEC

Maneuver-Based Testing of Integrated, Highly Interconnected Safety Systems

Kathrin Sattler, Andreas Raith, Thomas Brandmeier,
Christian Schyr and Daouda Sadou

Abstract Active safety and passive safety were long viewed as separate entities of automotive safety systems, while current trends point toward networks and integration. In addition to signals from the crash phase, modern passive safety systems use pre-crash information from other systems (such as ESC). This new system interdependence leads to new development requirements. Whenever communication takes place across several levels such as different bus systems with many bus participants, reliability and data consistency have to be assured at all times. Network intensification and a large number of variants dramatically increase the complexities of fault protection and control unit tests during the development process. This requires new types of test systems with corresponding interfaces and advanced simulation tools for efficient, cost-effective and seamless testing. The test system presented here uses highly capable vehicle dynamics and driver simulations with integrated crash data and fault feed-in. Normal driving conditions as well as pre-crash and in-crash scenarios were implemented to conduct a realistic test (illustrated here by the example of a safety control unit). The test was run by defining the corresponding driving maneuvers in extensive test catalogs, analogous to real-world tests. This creates the basis for a highly capable, seamless test platform. In addition, testing depth and fault detection probability

F2012-E14-019

K. Sattler (✉) · A. Raith · T. Brandmeier
Institute for Applied Research (IAF) of Ingolstadt University of Applied Sciences,
Ingolstadt, Germany
e-mail: kathrin.sattler@haw-ingolstadt.de

C. Schyr
IPG Automotive GmbH, Berlin, Germany

D. Sadou
Continental Automotive GmbH, Berlin, Germany

can be significantly increased through a flexible and comprehensive selection of test cases.

Keywords Test system · Networks · ISO 26262 · Maneuver-based testing

1 Introduction

The automotive industry has traditionally been relying on two different, separate pillars with respect to safety systems: active and passive safety. The purpose of active safety systems, such as anti-lock braking systems, is to avoid accidents as far as possible. On the other hand, passive safety systems, such as airbags, serve to mitigate the consequences of accidents. As the improvement potential that lies in combining active and passive safety has lately been emerging with increasing clarity the trend now is to interlink and integrate the various systems with each other. Today, the control units in automobiles extensively exchange data via various bus systems such as CAN (Controller Area Network [1]) or FlexRay [2], with the information being used to calculate algorithms. While this approach yields advantages, such as avoidance of sensor redundancies and use of synergies among the control units, it poses new challenges as well. Particularly in the area of fault protection and the associated testing of the combined control units complexity due to the higher extent of networked systems has dramatically increased. Different bus systems communicate with each other across several levels or gateways and therefore heavily depend on the reliability of the bus systems and on data consistency (see Fig. 1). This integrated view of active and passive safety systems now makes it necessary to combine different types of tests. Consequently, for a comprehensive test, an integrated control unit like the safety control unit (SCU) has to be fed with vehicle dynamics data such as yaw rate, lateral acceleration and longitudinal speed as well as—at the time of an accident—with crash signals emitted by relevant sensors such as CISS- (Crash Impact Sound Sensing [3]), acceleration or pressure sensors. Such a seamless test system has not been available to date and still has to meet various requirements and challenges. Effective testing of a control unit such as the SCU examined below, which represents a networked and integrated safety system, at an early stage of the development process as realistically as possible in its subsequent environment requires a comprehensive test system that encompasses the development stages of a control unit. This means that such a test system has to cover the design phases in the form of Model-in-the-Loop (MiL), implementation as Software-in-the-Loop (SiL) and platform tests using Hardware-in-the-Loop (HiL) (compare [4, 5] for example). Furthermore, to realistically test an safety control unit, it must be possible to feed in the state of normal driving as well as pre-crash and in-crash scenarios. This requires a continuous supply of various types of data, which can be achieved by a

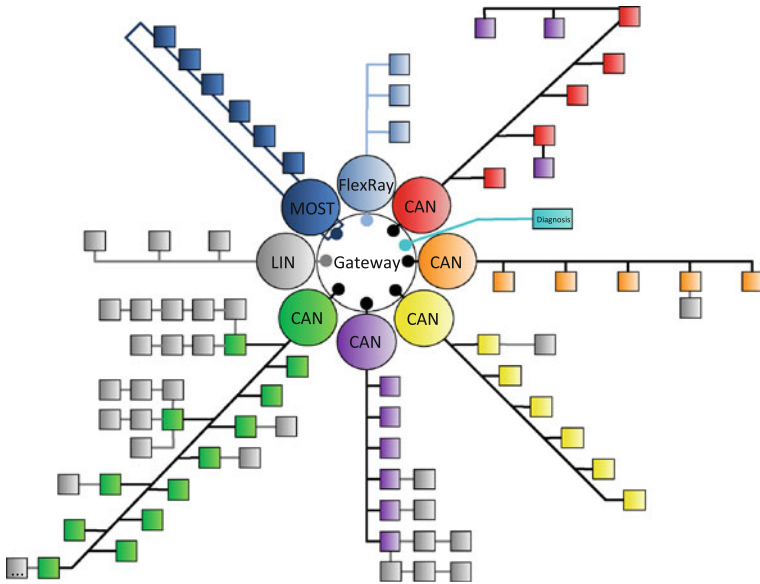


Fig. 1 Overview of the complexity of the electronic network of a contemporary vehicle based on [16]

vehicle dynamics simulation as realized by IPG’s CarMaker[®] multi-body simulations [6] in combination with crash data input.

Equally important is a comprehensive test strategy for the SCU as a networked safety system. As it is not possible to test all error combinations, intelligent and innovative test methodologies have to be used in order to achieve a sufficient depth of testing while minimizing the effort involved in the tests.

The generation of crash data input poses another problem. Vehicle dynamics simulation allows optional scenarios of different types of accidents to be flexibly simulated. The generation of real-world crash data by means of crash tests or the calculation of such data using FEM (Finite Element Method) simulation are very costly and time-consuming. Therefore, a method for crash data generation that produces new situation-conformant data from existing crash data by scaling and interpolating them is of great interest in this context.

2 Concept of the Test System

In our previous project VISAPS (networking and integration of safety systems of active and passive safety) a test system was developed that is intended to represent a comprehensive test platform for the SCU and resolve the aforementioned challenges. The aim is to be able to model all the faults which a SCU may experience in the real-world vehicle. This requires a multitude of interfaces and

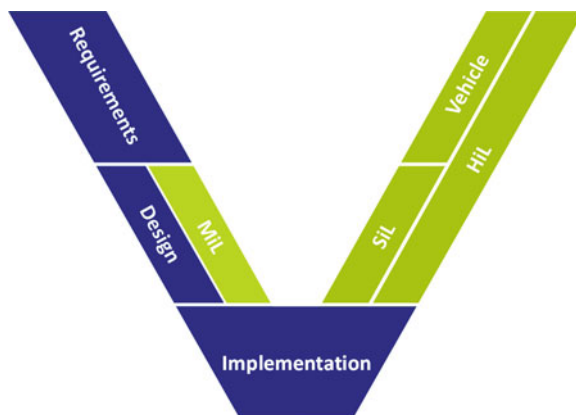


Fig. 2 The generally used V-cycle represents the development lifecycle of a control unit throughout the whole process. Also shown are different test methods used in different stages of the development. After the requirements are defined the design is verified by MiL tests. After implementation SiL and, if hardware prototypes are available, HiL tests are run. At the end of the development cycle vehicle test drives are conducted

manipulation options of a physical and peripheral nature. Depending on the current development state of the control unit's software and hardware (see Fig. 2) the test system that has been developed feeds a model (MiL), software (SiL) or a control unit (HiL) using a vehicle and environmental simulation or a corresponding residual bus simulation via various interfaces with data.

The requirement for seamless data input ranging from normal driving situations, critical pre-crash cases through to accidents with crash data poses another challenge when developing a test system for a highly networked safety system such as an SCU (see Fig. 3). These data can either be fed in by a vehicle dynamics simulation such as CarMaker[®] or as data recorded in a real-world road test or artificially recorded bus signals in the form of a trace. During a normal driving situation and during a pre-crash phase the vehicle dynamics data via CarMaker[®] or recorded data are fed in. In the case of an accident input of situation-conformant crash data from a crash database using a trigger which is integrated into the vehicle simulation is started. The crash data can either originate from real-world tests or FEM simulation. The future aim is for such data to also be artificially generated based on real-world crash data (see Section Crash Data). Input is possible in the MiL, SiL and HiL phases and allows test methods that have already been standardized for active and passive safety systems to be re-used while closing the gap for a consistent and seamless test procedure for integrated control units.

The concept explained above primarily includes maneuver-based test cases. Furthermore, communication-based testing is required. This means that all potential faults of a bus system in terms of data consistency and transmission errors must be tested. For this purpose, numerous interfaces of the SCU such as CAN or LIN for communication with other control units and SPI (Serial Peripheral

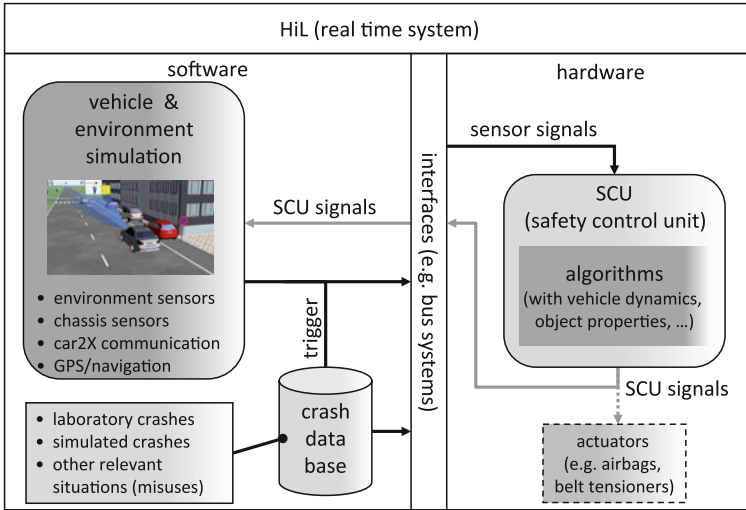


Fig. 3 Concept of the crash-capable HiL test system developed in the VISAPS project

Interface [7]) and PSI5 (Peripheral Sensor Interface 5 [8]) for exchange with internal and external sensors were entered into the test system and provided with diverse manipulation options. This makes it possible to confront the control unit with faults of the bus system and data from the periphery as well.

For the HiL test, it is possible to also test physical faults such as under-voltage or short circuits by means of an integrated failsafe tester. This way, the test object is embedded in the same physical environment as it would be in subsequent real-world use. The output signals such as the ignition circuits of the airbag can be monitored and their correct operation checked. Consequently, from the beginning of the development project, even before hardware is available and without a real-world road test, it is possible to test whether or not the developed algorithm, hardware and intercommunication with other components perform in accordance with the requirements.

For effective and comprehensive testing of the SCU, it is also necessary to offer a large number of data feed and manipulation options (see Fig. 4). In the area of the connected bus systems it is possible—via intelligent IO (Input Output)—to generate faults both on the physical level, with CAN such as checksum or timeout faults, and on the content-related signal level. The content faults represent the fault condition of a peripheral control unit. A relevant example in the case of a SCU would be a corrupted engine speed value transmitted by the engine control unit. Furthermore, in addition to the type of fault, the timing and duration of the feed-in are crucial. By means of precisely specified timing information faults can be specifically introduced into the SCU to check its behavior. Via analog and digital sensor interfaces (e.g. SPI and PSI5) fault conditions of the connected sensors can be simulated. Furthermore, the failsafe tester makes it possible to also manipulate

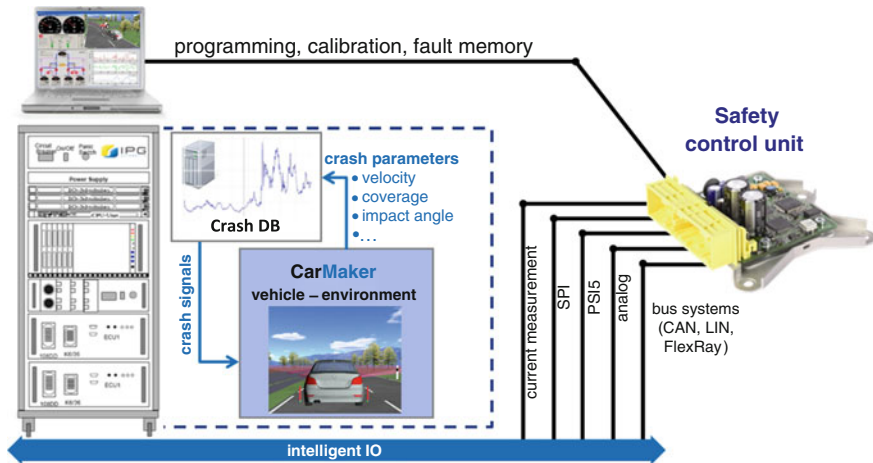


Fig. 4 Time-accurate fault conditions confronting the SCU can be created via the intelligent IO

or simulate physical signals such as voltage supply to the control unit or a sensor snap-off.

It is also possible to use different data sources as input for continuous data supply to the control unit. Three sources are currently envisioned. The first one is the previously described vehicle dynamics simulation via CarMaker[®], which can be used either with or without the combination with crash data feed via the crash database. In addition, a residual bus simulation with the option of systematically manipulating individual data can be fed in. As a third source, the reproduction of a recorded bus trace is possible. In this case, the process can take its course either with or without manipulation of data.

This architecture now makes it possible to model all fault conditions an SCU may experience in order to check its correct behavior relative to the situation.

3 Test Strategy

For efficient and reliable system testing in a functional safety project, it is important to use a test strategy that depends on the requirements assessed for the system and that defines the test activities. Figure 5 shows one possible approach for the combination of a test strategy and test activities.

After the requirements are defined in documents and tools the safety concept is derived from them. Depending on this concept a test strategy will be defined using different test methods with differing priorities. The most important pillar has to be test cases which are systematically identified. Here all test methods of Fig. 6 are highly recommended since they are part of ISO 26262 “Road vehicles—Functional safety” [9]. Other possible classification tree methods for finding test

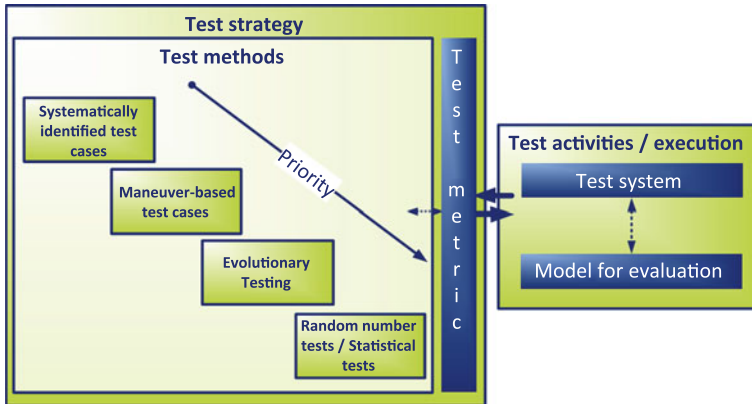


Fig. 5 Testing in a project should rely on a test strategy that depends on the requirements for the system and defines the test activities. The chosen test methods will always mostly rely on systematically identified test cases. A newer approach in the case of SCUs is the use of maneuver-based test cases. Evolutionary testing can either be combined with the maneuvers or used as stand-alone tests. Error detection can also be increased by using random number and statistical tests as additional efficiency-enhancing methods. A test metric can be used to assert the progress and quality of testing. All these tests have to be run on a flexible and powerful test system and evaluated based on knowledge of the system behavior and a model for localizing errors in the system

cases are equivalence classes, boundary value analysis and control flow analysis. The most important proposals are systematically identified test cases since they offer the highest error detection potential. By proceeding systematically, sufficient coverage of requirements, functions and architecture can be achieved. These methods are not only recommended but crucial for the system test and therefore already used extensively.

The second proposed pillar is maneuver-based test cases. Since later in the development cycle a large number of costly and lengthy vehicle tests are performed it is desirable to shift and reduce the effort as far as possible. Vehicle test drives are often simulated by injection signal traces into the system that were recorded in a vehicle. Unfortunately, the flexibility of this approach is very poor since only a small number of driving situations are recorded. An innovative method to enormously increase flexibility is maneuver-based testing. This means that test scenarios for the test object are defined and simulated in a suitable environment. In our specific case, a vehicle dynamics and environment simulation is used to create the necessary signals for the SCU. This is done since the safety algorithms depend mostly on sensor signals retrieved from vehicle dynamics and environment conditions detected by radar or camera systems, for instance. An example of a critical scenario could be braking and skidding on ice. The parameters for this scenario such as vehicle velocity, steering angles or brake pressure can be varied, resulting in a huge diversity of maneuvers which could never be achieved by real-world vehicle test drives. By combining this vehicle dynamics

Methods	System Integration				Meaning during System Integration
	A	B	C	D	
Requirements-based tests	++	++	++	++	Test cases derived of system requirement specification
Back-to-back tests	o	+	+	++	Comparison between behaviour of model and system
Tests of external interfaces	+	++	++	++	External interfaces (e.g. HMI) or data bus system
Interface consistency check	+	++	++	++	Focus on data bus system
Tests of internal interfaces	+	++	++	++	Internal interfaces (e.g. data bus system)
Communication tests	++	++	++	++	
Tests of interaction /communication	++	++	++	++	
Fault injection tests	+	+	++	++	Electrical faults , failure data bus , stimulation of fault detection mechanisms
Error guessing tests	+	+	++	++	Focus EE system
Tests derived from field experience	o	+	+	++	
Resource usage tests	o	+	+	++	
Performance tests	o	+	+	++	
Stress tests	o	+	+	++	
Tests for interference resistance /robustness and under certain environmental conditions	++	++	++	++	

Fig. 6 This figure shows the test methods for the system test of vehicle electrical and electronic systems proposed by the ISO 26262 standard for the various Automotive Safety Levels (ASIL) [9]. While a number of possible test methods is recommended the standard does not state how these methods shall be combined and to what extent they should be used

and environment simulation with crash data feeding as proposed in [10] it is even possible to simulate the whole course of an accident scenario. From normal driving situations to the pre-crash and in-crash phases all the bus systems and signal interfaces can be fed with plausible data in order to simulate an accident. Since vehicle test drives and crash tests are conducted separately this simulation approach is even more realistic than the physically driven tests as the whole course of events of an accident is represented. Maneuver-based testing is an innovative

The fourth pillar could be random number and statistical tests. These methods are almost not being used for system tests of control units or embedded systems. They are based on an extension of random number tests and use a model of the real-world usage of the testing object which is fed with random numbers [11]. Statistical tests are the only test class that can quantify software reliability. Here additional high potential lies ahead to optimize test strategies. For example Monte Carlo test methods (see [5] or [12]) use repeated executions of random number feeding to calculate very complex systems. Of course not only completely random numbers can be used but also pseudo-random numbers which are reproducible and random numbers within boundaries. This way, it is possible to come up with test cases which are not found systematically or that are not considered.

All these test cases should be considered in a test metric in order to measure the test progress [13]. Here a combination of requirements, architecture and error coverage will be developed in order to calculate a level of confidence for the system. This metric will give the testers an assertion about the quality and progress of the testing activities. Of course the tests ultimately have to be evaluated. Often this has to be manually done by the relevant functional experts since the creation of a test evaluation would take as long as the manual activity and would only be an additional effort without benefit. But most of the test cases can be evaluated automatically and therefore a lot of time and energy can be saved. In order to do this, an easy to handle measure has to be integrated into the test system. A model could be used to localize an error that has occurred in the system. Of course it is also possible to immediately use model-based approaches to derive test cases, but this will not be done here. The model will be a superficial model that is only used for test evaluation. One possible approach could be Petri Nets (see [4, 14] or [15]). Petri Nets are used as a modeling measure to represent parallel processes vividly. They could be used to display the current state of the system to show possible errors.

Overall, this proposed combination of test methods is one approach for an innovative test strategy for highly networked safety systems like the SCU. Of course other solutions are possible, and for some methods, their efficiency and feasibility in this context has yet to be proven.

4 Crash Data

The linking of the test system with the CarMaker[®] multi-body vehicle dynamics simulation tool allows optional driving and accident scenarios to be simulated and the SCU to be tested in relation to them. By using evolutionary testing and the related, systematic generation of critical driving maneuvers the scenarios to be tested are reduced. A multitude of accident scenarios can be simulated in the test system nonetheless. Testing the functions of the control unit during an accident requires crash data which must be fed into the test system. For each of the simulated scenarios a separate data record is necessary. Consequently, a large number

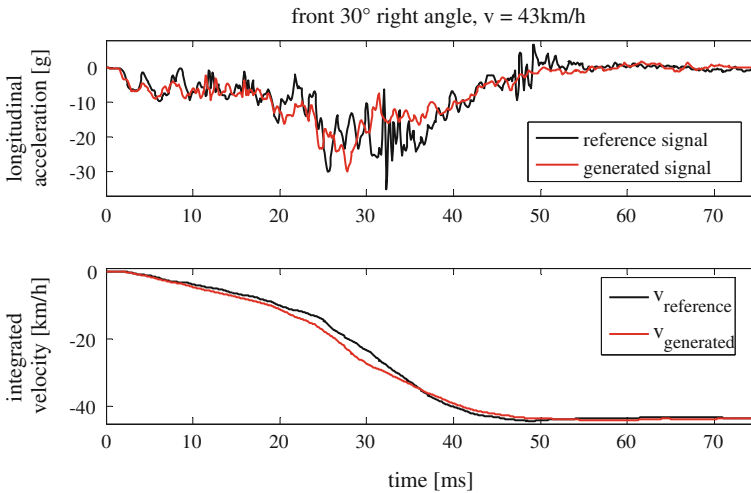


Fig. 8 Comparison of the signal curves of lateral acceleration and the resulting speed of a real-world crash test (red) with an artificially generated signal (blue) in an identical accident configuration

of crash data must be available which are stored in a database that is integrated with the test system. These crash data are divided into two different types: data which are artificially generated by simulation and real-world data.

Real-world crash data are obtained by recording the signal curves of the various sensors installed in the vehicle, such as acceleration or pressure sensors, during a crash test while artificial data are calculated by the Finite Element Method (FEM), for example.

Due to the high computing and resulting time intensity of an FEM simulation this method has only limited suitability for the real-time-capable test system that has been developed. Therefore, a new method is in development which generates a new data record by scaling and interpolating existing, physically driven crash data. The data record thus generated contains the required accident parameters and can be fed into the test system to test the SCU. The result (red signal curve) of an initial, speed-dependent method to scale and interpolate crash data is plotted in Fig. 8 based on the lateral acceleration data of a frontal impact on a wall with a 30° angle and compared to the acceleration data of a physically driven test with the same configuration (black signal curve).

The signals thus generated can be fed into the test system for testing the SCU. Due to the low computing requirements this method provides a cost-efficient and fast alternative to real-world crash tests and to the artificial generation of data using the Finite Element Method.

5 Future Work and Conclusion

One of the aims of the future work will be to achieve an improvement of the system test of highly interconnected safety systems through skillful selection and combination of different test methods and strategies. Furthermore, based on the example of the SCU, the aim is to investigate the potential that is inherent in different test methods and to explore how such potential leads to the optimization of test methods.

As initial investigations and the method for scaling and interpolating crash data that has been developed so far have produced promising results further relevant analyses will be performed. During the course of this work the existing method will continue to be optimized and extended from the purely speed-dependent scaling and interpolation to further accident parameters. These parameters, for instance, will include the impact angle, overlapping of the vehicle with the obstacle, nature of the obstacle etc.

The next steps to be taken will involve additional extensions and optimizations in preparation for future technologies, particularly the extension by bus protocols such as FlexRay and the associated manipulation and data feed options.

Another aim is to achieve the certification of the test system according to ISO 26262. Among other things, this standard establishes requirements for development and testing of software tools specifically in the automotive sector as protection against potential faults. ISO certification provides the benefit of the test system being validated and verified, and bearing a quality seal that confirms the quality of the test system.

The combination of a multi-body vehicle dynamics simulation and crash data feeding has produced a powerful test platform which provides a real-time-capable and seamless base for flexible and convenient testing across the entire development cycle (MiL, SiL, HiL). Due to the additionally integrated manifold interfaces, feed-in points and manipulation options it is possible to test the SCU in its subsequent environment at a very early stage of the development process and to thus be prepared for future developments.

Gefördert durch:



This research is being funded by the Federal Ministry of Economics and Technology (Grant Number KF2122306PR1) based on a decision of the German Bundestag. We would like to thank our partners IPG Automotive GmbH in Karlsruhe and Continental Automotive GmbH in Regensburg and our former partners Berner & Mattner Systemtechnik GmbH in Munich and Otto-von-Guericke University Magdeburg.

References

1. Lawrenz W, Bagschik P (1999) CAN—controller area network: grundlagen und praxis. Hüthig, Heidelberg
2. FlexRay (2012) The communications system for advanced automotive control applications. <http://www.flexray.com/>
3. Lauerer C Ein Beitrag zur Erhöhung des (2010) Insassenschutzes durch Körperschallmessung in der Crasherkenntung. Dissertation, Otto-von-Guericke-University Magdeburg
4. Cassandras CG, Lafortune S (2008) Ereignisdiskrete systeme. Springer Science + Business Media, New York
5. Fishman GS (1996) Monte carlo. Springer, New York
6. IPG Automotive GmbH, Karlsruhe. www.ipg.de, CarMaker® (2011) 3.5
7. Freescale Semiconductor Inc, Texas. www.freescale.com
8. PSi5 organization (2011) www.psi5.org, PSi5 V2.0
9. International Organization for Standardization. ISO 26262 (2011) Road vehicles—functional safety
10. Raith A, Sattler K, Ertlmeier R, Brandmeier T (2008) Networking and integration of active and passive safety systems. Ninth Workshop on intelligent solutions in embedded systems IEEE WISES 2011, conference Proceedings, 2011 University of Applied Sciences Regensburg 75–80
11. Wegener J (2001) Evolutionärer test des zeitverhaltens von realzeit-Systemen. Shaker, Aachen
12. Binder K, Heermann DW (2002) Monte carlo simulation in statistical physics. Springer, Berlin
13. Sneed HM, Baumgartner M, Seidel R (2012) Der systemtest. Carl Hanser, Munich
14. Lunze J (2006) Ereignisdiskrete systeme. Oldenbourg, Munich
15. Petri CA (1962) Kommunikation mit automaten. Schriften des Rheinisch-Westfälischen Institutes für instrumentelle Mathematik der Universität Bonn, Bonn
16. Kiesewetter T Der Touareg VW (2010) Karosserieelektronik und Infotainment. ATZextra, No. 2010-02, p 47
17. Reiner J, Meyer J (2010) Evolutionäres Testen von Steuergeräten. Elektronik automotive
18. Gerdes I, Klawonn F, Kruse R (2004) Evolutionäre algorithmen. Vieweg, Wiesbaden

Studying of Instantaneous Emissions Character for Hybrid Electric Vehicle

Yanxin Nie, Baocheng Du, Peng Wan and Jingsi Xie

Abstract By testing hybrid electric vehicle emissions under a variety of driving cycles, collect instantaneous emissions, battery current and the output voltage data and so on, and analyze these data to study emission characteristics of hybrid electric vehicle. The results showed that: this hybrid electric vehicle has many complex working modes, automatic start-stop technology can adopt about 7.2 % of carbon emissions, accelerating the warm up of engine is an effective means to reduce emissions further.

Keywords Instantaneous emissions · Character · Hybrid electric vehicle

Under China's automobile development of energy saving and environmental protection policy guidance, the electric vehicle development has become the focus of the domestic electric vehicle R&D [1, 2]. How to learn the advanced electric vehicle design philosophy, and gradually master these core technologies, will become the key point. Benchmarking advanced electric vehicle is important technical mean of understanding core technologies.

In this paper, test emissions of the vehicle under a variety of driving cycles; analyze typical working mode of the vehicle, the influence of engine state to emissions, and energy saving effect of automatic start-stop technology, etc.

F2012-E14-024

Y. Nie (✉) · B. Du · P. Wan · J. Xie

China Automotive Engineering Research Institute, Changchun, People's Republic of China
e-mail: nieyanxin2007@163.com

1 Design of Experiment

1.1 The Vehicle

The vehicle is MY2006 Honda Civic hybrid. The main technical characteristics include improvement of the engine and IMA system, maturely use of CVT, new type of three stage i-VTEC and VCM allowing all four cylinder deactivation, new type of brake system allowing the regenerative braking variable voltage in the slowdown, etc. The main technical specifications are shown below (Table1).

1.2 Test System and Main Set Parameters

Test system includes the environmental cell, chassis dynamometer, sampling system, emission analysis system, current sensor, voltage sensor etc.

At China auto testing field, conduct coast down testing of the vehicle, and gain target coefficient A, B and C by data processing. And gain set coefficient A, B and C at chassis dynamometer.

1.3 Test Items

According to the test requirements (1), precondition the test vehicle, “soak”, and emission test and data record under NEDC (1), US06 (2) and JAN10–15 (2).

2 Test Data Processing

According to design of experiment, test emissions of the Civic hybrid under different driving cycles. The testing records and gets time (s), speed (km/h), CO emission concentration (PPM), NOx emission concentration (PPM), HC emission concentration (PPM), CO₂ emission concentration (PPM), CVS flow (m³/min), CO background concentration (PPM), NOx background concentration (PPM), HC background concentration (PPM), CO₂ background concentration (PPM, battery current (A), battery voltage (V) data, etc [3]. There is the need to further deal with emission concentrations to gain emission rate (1).

Need to make a simultaneous match to vehicle emission data for driving cycle data. According to “START” point of the engine, let instantaneous emissions rates (HC, CO, NOx, CO₂), voltage signal, current signal and speed signal synchronization. Then give a quality control to these data (such as the processing of mutation value equality and adding value to missing values) to ensure the accuracy

Table 1 MY2006 Honda civic hybrid specifications

Hybrid system net power	110 hp @ 6000 rpm (85 kW) 123 lb-ft @ 2500 rpm (167 Nm)
Engine	1.3-L SOHC 8-valve i-VTEC 4-cylinder Variable Cylinder Management (VCM) 93hp @ 6000 rpm (70 kW) 89 lb-ft @ 4500 rpm (123 Nm)
Electric motor	
Power output	20 hp @ 2000 rpm (15 kW) 76 lb-ft @ 0–1160 rpm (103 Nm)
Motor type	Permanent magnet DC brushless motor
Traction battery	
Type	Ni-MH
Voltage	158 V
Transmission	Continuously Variable Transmission (CVT)
Brakes	Power-assisted ventilated front disc/solid rear disc brakes anti-lock braking system (ABS)/electronic brake distribution (EBD) with brake assist

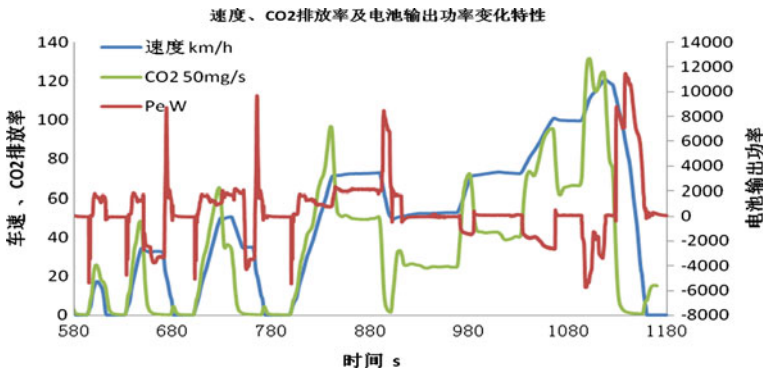


Fig. 1 After the synchronous process CO2 emission rate, battery power, speed curve with the change of time

of data. Draw after the synchronous process the CO2 emission rate, battery output power, speed curve with the change of time from 580 to 1180 s of NEDC. The figure is shown below (Fig. 1).

3 Analysis and Discussion

NEDC and JAN10–15 change more stable than US06. Under NEDC and JAN10–15, operation characteristics of Civic hybrid are similar. So choose NEDC to express and analyze Civic hybrid emission characteristics under relatively stable driving cycle, and choose US06 to express and analyze Civic hybrid emission characteristics under relatively drastic driving cycle.

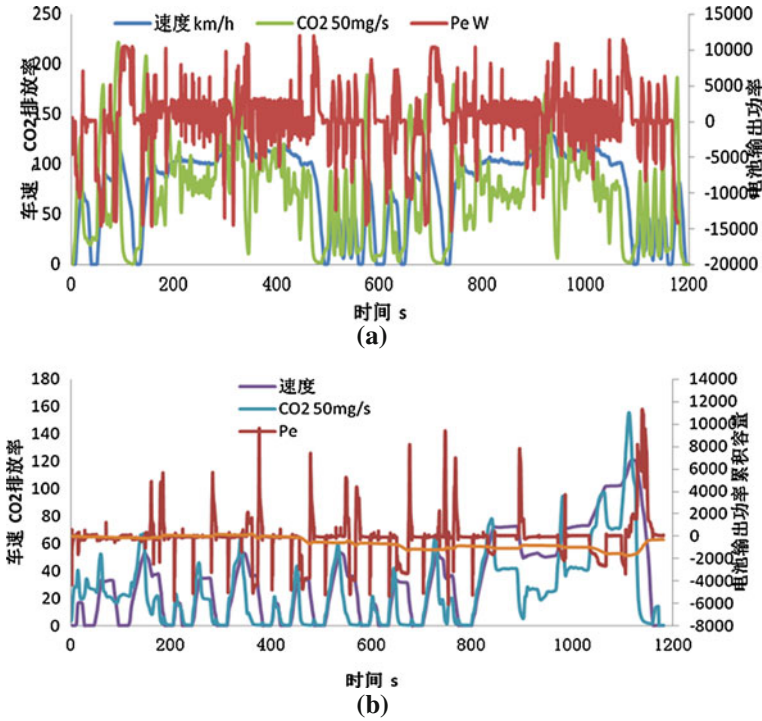


Fig. 2 Speed, CO2 emissions, battery output power and the battery cumulative charge capacity curve with the change of time under US06 or NEDC. a US06, b NEDC

3.1 Topic Working Mode

Figure 2(a) describes speed, CO2 emission rate, battery output power and the battery cumulative charge capacity curve with the change of time under US06. Figure 2(b) describes the same parameters curve with the change of time under NEDC. The parameters under US06 change too fierce, the switch of working mode is too fast, that goes against analysis of topic working mode. So use NEDC to analyze topic working mode.

The battery power can reflect the motor working state: when battery output power is positive, motor is charging; when battery power is negative, motor is driving. The CO2 emission rate can reflect the engine working state: when exist CO2 emission, engine is not either cylinder deactivation or stop state (0 rpm). By joint analysis of the battery output power, CO2 emission rate and speed can obviously observe topic working mode of Civic Hybrid.

3.1.1 IMA Motor Start-Up Mode

The vehicle has the starting demand (its speed from 0 began to increase), and at this time motor drives (battery power is positive), the engine starts (CO₂ emission rate has the increased trend).

When the whole IMA system in normal state (such as system trouble-free, battery SOC and temperature at the proper range), IMA motor automatic starts that happens at the first time vehicles starts (the ignition switch by the “ON” to “START”) and after idle stop. The vehicle has 12 V starter starting mode, used for IMA motor not normally starting.

A typical automatic IMA motor starting of Civic hybrid requests that the maximum battery output power is about 5 kW, time is about 0.16 s, output energy is $1.2 * 10^{-3}$ kWh.

3.1.2 Engine Idle Stop Mode

the vehicle is idle stop (0 km/h), and at this time the engine doesn't work (CO₂ emission rate close to or under 0), the motor doesn't work (motor output power close to 0). Just now, the vehicles can start and don't need through the ignition key from “ON” to “START”.

Data show that, when vehicle is in “D” gear and more than 12 km/h (speed according to the condition change), then press brake pedal to slow down, vehicle will happen idle stop. But there are many reasons to affect vehicle's idle stop, such as the engine cooling fluid temperature, IMA battery energy, the control from pilot (such as press accelerating pedals, and release the brake pedal and shift, etc.).

3.1.3 Motor Charging Mode

The vehicle works, and at this time the engine works and the motor charges. In order to make the engine work at good working condition (low fuel consumption, low emissions) or for charging the battery (battery SOC low), the vehicles will operate this mode.

3.1.4 Pure Motor Driving Mode

The vehicle is at the low speed cruise operation, such as the speed maintains 32 km/h, and at this time engine doesn't work, the motor drives.

When low speed cruise and SOC at more appropriate range, the vehicle operates this mode, the engine is at all four cylinder deactivation in order to reduce resistance.

3.1.5 Pure Engine Driving Mode

The vehicle is at the high speed cruise operation, such as the speed maintains 70 km/h, and at this time the engine works, the motor doesn't work.

3.1.6 Regenerative Braking Energy Recovery Mode

The vehicle with a certain speed (such as 15 km/h above) speeds down, and at this time motor charges, engine may be at a state of fuel-cut or cylinder deactivation.

When the vehicle speed at a certain range (such as 10–50 km/h) slows down, the engine will deactivate four cylinders.

3.1.7 Joint Driving Mode

The vehicle is at the large acceleration, and at this time the engine and motor work.

According to obtained information on Civic hybrid, the operating mode also can be refined. Such as engine driving mode, the vehicle will operate this mode at the high speed cruise or slowly speed up. Components working mode also can be constituted, such as engine working (CO₂ concentration higher than the environment), engine can work at low valve lift or high valve lift; such as engine no working (CO₂ concentration similar the environment), engine can work at stop state (0 rpm) or cylinder deactivation. In the future, will further increase sensors, that more detailed analyze and monitor working mode.

3.2 Emissions Competing

According to Fig. 3 and Table 2, emission pollutant is concentrated at the first ECE driving cycle, and the amount is very small in EUDC. The engine is cool at the first ECE driving cycle, which affect the emission pollutant. When the engine is cool, the electrical machine gets little involved in the driving and energy recovery (the vehicle is started firstly).

Except for the first ECE driving cycle, emission pollutant rate is very low. The relationship between emission pollutant rate and speed, acceleration, driving power (3), VSP (3) cannot be analyzed, or the meaning is not big.

The emission pollutant can be further reduced by accelerating the warm up of engine. By analyzing Jan10–15 and US06, similarly find this feature. Different is a number CO emission under US06, according to Fig. 4 and Table 3. The speed of US06 is higher than NEDC, and the acceleration is bigger. The writer believes that drastic variation of US06 cause the incomplete combustion, which results in the more CO emissions.

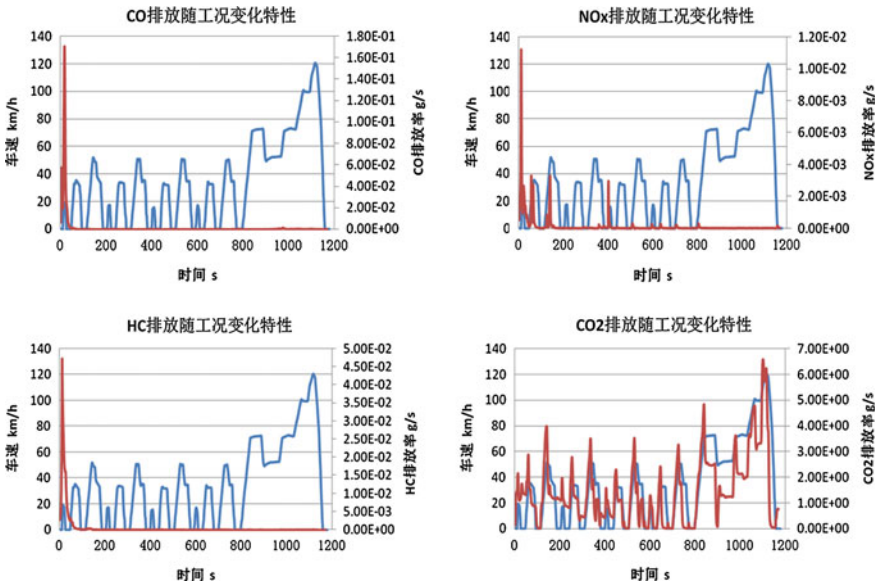


Fig. 3 Emissions rate with the change of time under NEDC

Table 2 Emissions of NEDC

Driving cycle	CO g	NOX g	HC g	CO2 g	Variation AH
ECE_1	1.841141	0.145029	0.687949	257.12	0.048627318
ECE_2	-0.0028	0.001365	-0.0062	235.1492	0.377871323
ECE_3	-0.00655	0.01176	-0.00801	186.8146	0.288352501
ECE_4	-0.00528	0.002797	-0.0091	128.3725	0.04038236
UDC	1.826504	0.16095	0.664636	807.4564	0.755233503
EUDC	0.043105	0.001439	-0.01917	891.1895	0.374386234
NEDC	1.86961	0.162389	0.645461	1698.646	1.129619737

3.3 Energy Saving Analyse

When the vehicle is stopped and is at normal condition (the oil temperature and the water temperature of the engine is at suitable range), and the engine is not stopped, the CO2 emission is 0.42 g/s at idle and discharge. Only with the start/stop function, Civic HEV can reduce the CO2 emission up to 123.06 g, 7.2 % (Fig. 5).

Note: the 100 km fuel consumption of 2012 Civic is 6.8 L/100 km, CO2 emission is 1710.6 g.

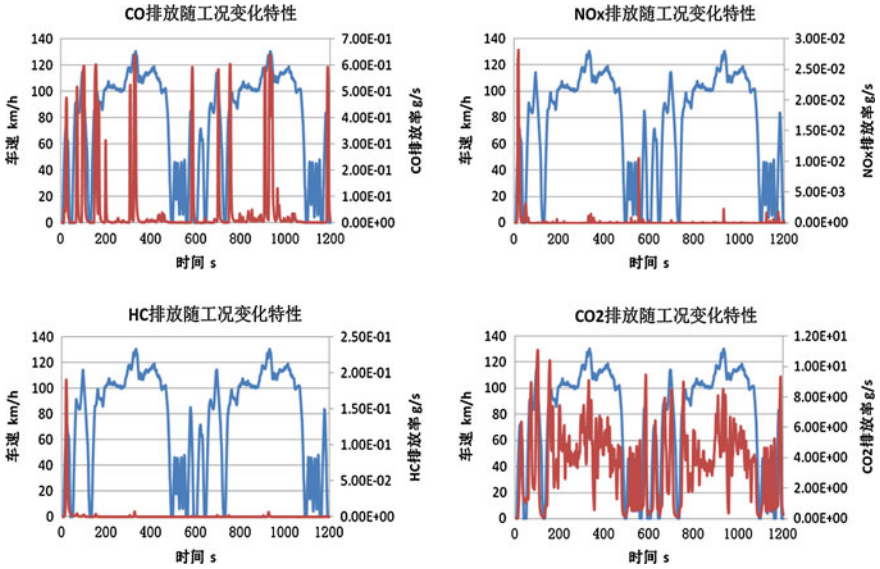


Fig. 4 Emissions rate with the change of time under US06

Table 3 Emissions of US06

工况	CO g	NOX g	HC g
US06_1	38.73562	0.292872	1.712374
US06_2	30.04794	0.027865	0.089941
US06	68.78356	0.320737	1.802315

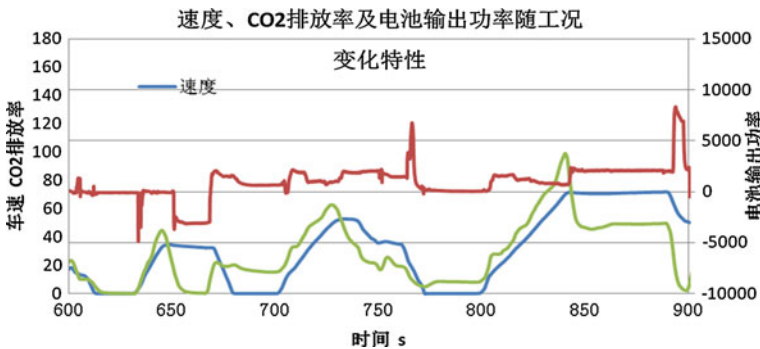


Fig. 5 Emissions rate with the change of time from 600 to 900 s of NEDC

4 Conclusion

Civic hybrid has many complex working modes, including IMA motor start-up, engine idle stop mode, motor charging mode, pure motor driving mode, pure engine driving mode, regenerative braking energy recovery mode, joint driving mode and so on.

The cool engine is the main reason cause many emission. So, accelerating the warm up of engine is a good method to reduce the emissions. The relationship between emission pollutant and speed, acceleration, driving power, VSP is low. So, the emission factor model is cannot established.

The CO₂ emission is reduced obviously by the start/stop, and Civic HEV reduced 7.2 % by using the technology.

References

1. GB/T19755-2005 Measurement methods for emissions from light-duty hybrid electric vehicles
2. ISO 23274-2007 Hybrid-electric road vehicles—Exhaust emissions and fuel consumption measurements—Non-externally chargeable vehicles
3. Mengliang Li (2010) A comparative study on emissions of hybrid electric bus and conventional bus, 32 (3):193–201

Effect of Cryogenic Treatment on Retained Austenite and Fatigue Life of Gcr15 Wheel-Hub Bearing

Qiucheng Wang, Xiaobin Ning, Qi Chen and Bintao Mao

Abstract *Research and/or Engineering Questions/Objective* There are many domestic enterprises that produce auto-hub bearings in China. But the majority of products are only applied in the after-sale market as the unstable quality of the domestic products can't meet the OEM's requirements. In order to improve fatigue life and dimensional stability of GCr15 steels, the cryogenic treatment was introduced to control the percentage of retained austenite of GCr15 bearing steel. *Methodology* The correlation between cryogenic treatment parameters and microstructure of the hub-bearing was studied. The percentage of retained austenite after different cryogenic treatments was measured by X-ray diffraction experimental. The equation was established to reveal the relationship between the percentage of retained austenite and cryogenic temperature. Finally, the fatigue life was performed by strengthen test according to JB/T 50013-2000 test rules of life and reliability of rolling bearings. *Results* After cryogenically treated in -40 , -80 , -120 , -160 , -196 °C chamber for 2 h, the investigation revealed that the retained austenite of the specimen surface is with proportional to the temperature decrease of deep cryogenic treatment. The specimens possess the maximum hardness and the minimum impact toughness during keeping at -80 °C deep cryogenic treatment temperature. *Limitations of this study* This study work has verified that the cryogenic treatment can improve the fatigue life and dimensional stability of wheel hub bearing. In order to obtain broader application and promotion, it requires further investigation on the characteristic properties of cryogenic treatment to be applied to *other* automotive bearings and *other kinds of* parts.

F2012-E14-025

Q. Wang (✉) · X. Ning · Q. Chen · B. Mao
Institute of Vehicle Engineering, Zhejiang University of Technology, Zhejiang, China
e-mail: wqc@zjut.edu.cn

What does the paper offer that is new in the field in comparison to other works of the author Since the mechanism of cryogenic treatment is not yet to be understood very well, So in general cryogenic treatment is still in the dormant level at present. In this study, we focus on investigating the mechanism and optimizing parameters of cryogenic treatment to improve the fatigue life of wheel-hub bearing. *Conclusion* The test results indicate the cryogenic treatment can improve the fatigue life of DAC 4007040 hub bearing, which runs 39.537 million revolutions, $Re = 99.22\%$ by optimizing cryogenic treatment. In the same load conditions, the fatigue life of DAC 4007040 hub bearing subjected to conventional heat treatment is only 21.79 million revolutions in average, $Re = 96.7\%$.

Keywords Wheel-hub bearing · Cryogenic treatment · Retained austenite fatigue life · Strengthen test

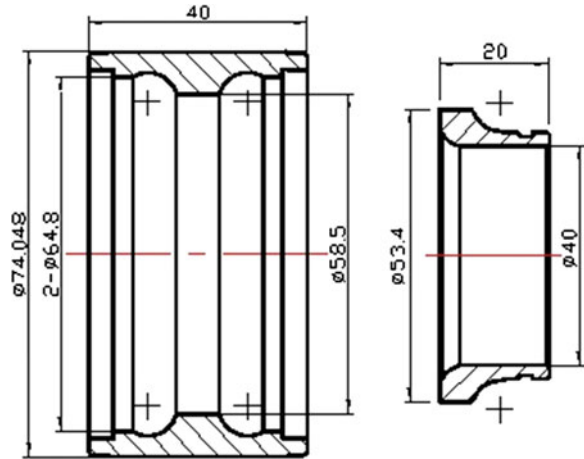
1 Introduction

There are many domestic enterprises that produce auto-hub bearings in China. But the majority of products are only sold to the after-sale market as the unstable quality of the domestic products can't meet the OEM's requirements. In our research work, The emerging technology of cryogenic processing (also known as cryogenic treating or tempering) is introduced to improve fatigue life and reliability of GCr15 steels wheel hub-bearings under the existing production conditions (production facilities, technology, technicians).

Cryogenic treatment can improve wear resistance of materials because it enhances the transformation of austenite (soft phase of iron) to martensite (a hard phase of iron) and appear finer microstructure. Cryogenic treatment usually arrange at the end of conventional quench treatment process but before tempering [1]. Also it is not a substitute process but rather a supplement to conventional heat treatment process. It has adopted the process in their production line itself to improve wear resistance and dimensional stability of their components in aerospace, automotive and electronic industries in USA, China and other developed countries [2]. In order to avoid confusion, cryogenic treatment has been classified into shallow cryogenic treatment (SCT) and deep cryogenic treatment (DCT) depending upon the temperatures in which the material is treated.

Since the mechanism of cryogenic treatment is not yet understood very well, this chapter focus on how to improve fatigue life and dimensional stability of GCr15 steels by optimize the cryogenic treatment parameters of GCr15 hub-bearing steel.

Fig. 1 Outer raceway and inner raceway of wheel bearing



2 Specimen and Heat Treatment

2.1 Sampling

A hub-wheel bearing comprises four basic components: two separate inner track rings, one outer track ring, two rows of steel balls and two holders. Under normal operating conditions, the inner raceway, the outer raceway and the steel balls are subject to load, and the holders play a role of separating and keeping the steel balls stable. Since failure of wheel bearings usually happens on the outer raceway or the inner raceway when subjected to load, our research work focus on how to improve the wear resistance and fatigue life of the inner track ring and outer track ring (are shown in Fig. 1).

The case carburized steel (GCr15) is selected as the raw material of the inner track ring and outer track ring for hub-bearing. The chemical composition is shown in Table 1.

The blank of case carburized GCr15 steel is bought in the forging condition. After the forging blank of the inner track ring and outer track ring are machined in the lathe, they are conventionally subjected to the quench treatment and tempering treatment (CHT). Finally, after grinding, they are assembled as a component of hub-wheel bearings.

2.2 Heat Treatment Schedule

In this study, deep cryogenic treatment (DCT) is added between the quench treatment and tempering treatment to improve the wear resistance and fatigue life of GCr15 steels. Six groups of specimens are subjected to different heat treatment Schedule shown as Table 2.

Table 1 Chemical composition of the GCr15 steel (weight %)

C	Si	Mn	Cr	Mo	P	S	Cu	Ni	Cu + Ni
0.95–1.05	0.15–0.35	0.25–0.45	1.40–1.65	≤0.10	≤0.025	≤0.025	≤0.25	≤0.30	≤0.50

Table 2 Heat treatment schedule

Sequence	Heat treatment
CHT 1	Austenitise at 840 °C, oil quench at 93 °C, then temper at 170 °C
DCT 1	Austenitise at 840 °C, oil quench at 93 °C, Cryo at –40 °C for 2 h, then temper at 170 °C
DCT 2	Austenitise at 840 °C, oil quench at 93 °C, Cryo at –80 °C for 2 h, then temper at 170 °C
DCT 3	Austenitise at 840 °C, oil quench at 93 °C, Cryo at –120 °C for 2 h, then temper at 170 °C
DCT 4	Austenitise at 840 °C, oil quench at 93 °C, Cryo at –160 °C for 2 h, then temper at 170 °C
DCT 5	Austenitise at 840 °C, oil quench at 93 °C, Cryo at –196 °C for 2 h, then temper at 170 °C

In the sequence 1 of conventional heat treatment (CHT), a group of specimens austenitized at 840 °C for 15 min in a tube furnace, followed by oil quenching at 93 °C. Then temper in a tube furnace at the temperatures of 120 °C for 4 h.

In the sequence 2–6 of DCT treatment, 5 groups of specimens were subjected to deep cryogenic treatment (DCT) including, austenitizing at 840 °C for 15 min in a tube furnace, followed by oil quenching at 93 °C. Then slowly cooling oil-quenched specimens to –40, –80, –120, –160 °C, or emerged at approximately –196 °C liquid nitrogen, and holding at this low temperature for 2 h and gradually bringing the specimens back to room temperature [3]. Finally temper in a tube furnace at 170 °C for 4 h. In this study, five different heat treating sequences were used to evaluate the response of the specimens to cryogenic treatment (as shown in Table 2).

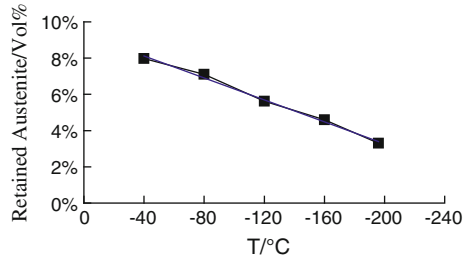
3 Results and Discussions

3.1 Retained Austenite Analysis

Since Austenite has a different crystal structure from Martensite and the other forms of steel (Ferrite, Bainite and Pearlite), the resulting diffraction pattern will be different also. Thus, we can estimate the amount of Retained Austenite by comparing the intensities of diffraction peaks arising from each of the phases.

The retained austenite content was determined by an X-ray diffraction technique according to the ASTM E975 standard [4]. Three points selected on outer track ring tracks, CrK α radiation was used to measure α Fe at (211) and (211) planes. The γ Fe is measured at (220) and (311) planes. A scan of 6° was done

Fig. 2 Effect of cryogenic treatment on retained austenite



around each peak with a 2θ step of 0.05° and a collection time of 10 s/point. The amount of retained austenite is estimated using intensity ratio of α (martensite) and γ (austenite).

The effect of cryogenic treatment on retained austenite is shown in Fig. 2. After cryogenically treated in -40 , -80 , -120 , -160 , -196 °C chamber for 2 h, the results obtained are represented as the volumetric fraction of retained austenite at the surface in specimens type DCT 1 to DCT 5. The retained austenite of the specimen surface is with proportional to the temperature decrease during deep cryogenic treatment.

3.2 Hardness Test

Hardness is the property of a material that enables it to resist plastic deformation, usually by penetration. In this study, the Rockwell hardness test method is selected to test the hardness of six groups of specimens. The Rockwell hardness test method consists of indenting the test material with a diamond cone or hardened steel ball indenter. Advantages of the Rockwell hardness method include the direct Rockwell hardness number readout and rapid testing time.

The effect of cryogenic treatment on sample's hardness is shown in Fig. 3. The specimens appear the maximum hardness when keeping at -80 °C temperature during deep cryogenic treatment.

3.3 Impact Energy

The Charpy impact test is selected to test the amount of energy absorbed by a material during fracture. The quantitative result of the impact tests the energy needed to fracture a material and can be used to measure the effect of deep cryogenic treatment on the yield strength of GCr15 steel. According to ASTM A370, Six groups of standard specimen is made as size $10 \times 10 \times 55$ mm subjected different cryogenic treatment processes for Charpy impact testing, three specimens in each group.

Fig. 3 Effect of cryogenic treatment on sample's hardness

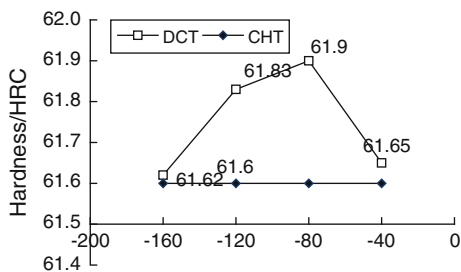
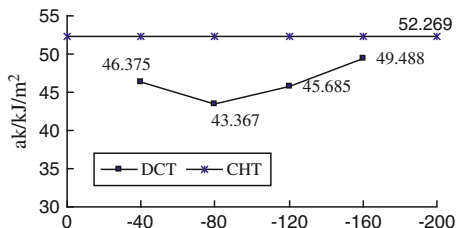


Fig. 4 Effect of cryogenic treatment on impact toughness



The results in Fig. 4 show the effect of cryogenic treatment on impact toughness. The minimum impact toughness happened when the specimens are held at – 80 °C for 2 h during deep cryogenic treatment.

4 Fatigue Life Test

As discussed above, different cryogenic treatment parameters were carried out after quenching the outer ring and inner ring of wheel-hub bearing. And their mechanical properties of different process parameters were tested. As we all know, the hardness has the most important role on wear resistance and fatigue on the outer/inner raceway of the wheel-hub bearing. The test results indicate that the DCT 2 specimen has the maximum hardness during keeping at –80 °C cryogenic treatment temperature.

Evidently, the best fatigue limits of the wheel-hub bearing are expected while the outer rings and inner rings are heated to 840 °C, quenched at 93 °C oil, cryogenic treated at –80 °C for 2 h, then tempered at 170 °C for 4 h.

To verify the improvement of fatigue life of wheel-hub bearing by the cryogenic treatment, the strengthen test of the hub bearing was utilized to test fatigue life of DAC407404840 wheel-hub bearing on the ABLT-1 type bearings fatigue life testing machines. The pure axial load (17.31 kN) is applied to the samples of the wheel-hub bearing [5].

To test fatigue life of Automobile hub bearings DAC407404840, two groups of hub-bearings, each group consist of 10 hub-bearing, are selected as the sample bearings at ABLT-1 Type Tester. Every of wheel-hub bearing will be applied 17.31 kN axial load and run at 2600 r/min. The test results as shown in Table 3

Table 3 Results of the fatigue life of the wheel-hub bearing

	Number of samples	Fatigue life(million revolutions)	Reliability (%)
DCT 2	10	29.35	99.22
CHT	10	21.79	96.7

indicate that their fatigue failure of the wheel-hub bearing, suffered $-80\text{ }^{\circ}\text{C}$ deep cryogenic treatment (DCT), happens after running 29.35 million revolutions in average, $Re = 99.22\%$. In the same load conditions, the fatigue life of conventional heat treatment (CHT) is only 21.79 million revolutions in average, $Re = 96.7\%$.

5 Conclusions

In this study, the effect of cryogenic treatment parameters on retained austenite, mechanical properties such as hardness, impact toughness and fatigue life are investigated. It is concluded the following results:

- (1) The retained austenite of the specimen surface is proportionally to the temperature decrease during cryogenic treatment.
- (2) The outer ring specimens for DCT 2 have the maximum hardness, among 5 kinds of cryogenic treatment schedule as shown in Table 2.
- (3) The test results indicate that the fatigue life of wheel-hub bearing for DCT 2 is as high as 29.35 million revolutions, improved by 34.7% over CHT.

Acknowledgments The authors are grateful for the financial support by Zhejiang Provincial Natural Science Foundation (Grant No. LZ12E05003).

References

1. Bensely A, Prabhakaran A, Mohan Lal D et al (2006) Enhancing the wear resistance of case carburized steel (En 353) by cryogenic treatment. *Cryogenics* 45:747–754
2. Zhirafar S, Rezaeian A, Pugh M (2007) Effect of cryogenic treatment on the mechanical properties of 4340 steel. *J Mater Process Technol* 186:298–303
3. Wang Q, Zhang Z, Lu W et al (2008) Transformation of microstructure of GCr15 steel under cryogenic treatment condition. *Cryogenics* 6:24–27
4. Lu J (1996) Handbook of measurement of residual stresses. Fainmont Press, Georgia
5. Wang Q, Wang L, Lin Q et al (2010) Strengthen test of hub bearing under cryogenic treatment. *Cryogenics* 2:28–31

A Study on Analysis Method of Motion Characteristics in the Crash Test Based on Computer Vision

Guohua Cao, Gang Han, Weiguo Liu and Fuquan Zhao

Abstract The actual vehicle crash test is the most basic and effective method in the development and validation of comprehensive vehicle safety performance. In the actual crash test, the optical measurement system can significantly record the motion form change through images on each target point. The image after-treatment can be performed by using the photographic measurement technology based on computer vision. The accurate motion characteristic information of the target points can be obtained through bundle adjustment of a series of frames, 3D photogrammetry and target tracking, as well as related calculation. The experimental results conducted at Zhejiang Key Laboratory of Automobile Safety Technology indicate that this method can particularly describe the motion characteristics of bodywork and dummy in the crash test with high sensitivity, quick speed and more data acquisition, thus satisfying the development requirements of vehicle safety performance.

Keywords 3D calibration · Binocular vision · Collision analysis · Motion characteristics

F2012-E14-029

G. Cao (✉) · G. Han · W. Liu · F. Zhao
Zhejiang Geely Automobile Research Institute CO., LTD, Hangzhou, China
e-mail: caoguohua@rd.geely.com

1 The Principle of Photography Measuring Technology

The camera image filmed in different Angle projection form can be regarded as the same image according to different rotate after turn to the same image Angle camera projection, which any two space right Angle coordinate system can convert all through the translation, rotation, zoom [1]. So just make sure the rotation between the various image parameters can be determined based on the reference form unknown form.

Set O1, O2 respectively, signifies the camera when shooting in two different locations of the two local coordinate system, they and parameters under the world coordinate system respectively are R1, t1, R2, t2. Any point P1, P2 under the world coordinate system, in the O1, O2 coordinates of the image respectively, are X01Y01, X02Y02, and coordinate diagram shown in Fig. 1 as follows:

Set space form O1 coordinates X02Y02 by a three-dimensional conformal affine transformation, that is the first translation (X0, Y0, Z0), then turn around the X-axis, Y-axis and the rotation of the Z-axis rotation ω, φ, κ . Finally, after scaling λ times, and the coordinate system coincides X01 Y01 under O2. Knowledge obtained by the following vector equation of projective geometry:

$$OX1 = Oo + oX1 \tag{1}$$

$$OY1 = Oo + OY1 \tag{2}$$

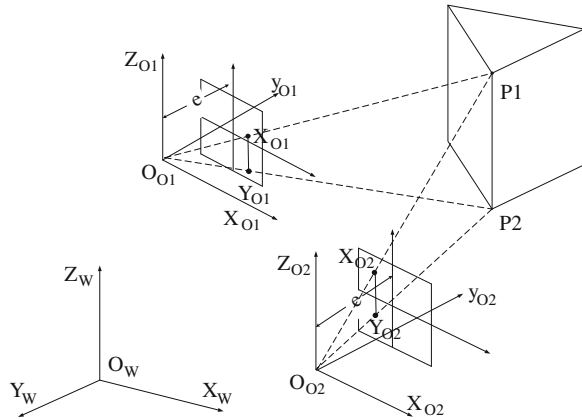
$$\left\{ \begin{array}{l} OP = \begin{bmatrix} X \\ Y \\ Z \end{bmatrix} \\ Oo = \begin{bmatrix} Xo \\ Yo \\ Zo \end{bmatrix} \\ oP = \frac{1}{\lambda} Mop = \frac{1}{\lambda} M \begin{bmatrix} x \\ y \\ z \end{bmatrix} \end{array} \right. \tag{3}$$

$$M = \begin{bmatrix} a1 & a2 & a3 \\ b1 & b2 & b3 \\ c1 & c2 & c3 \end{bmatrix} \tag{4}$$

Equation (4), M is the rotation matrix.

Equation (4) goes into Eq. (3), which gets a point P (X, Y, Z) and its corresponding point p (x, y, z) in oxyz has the following relationship:

Fig. 1 Coordinate diagram



$$\lambda \left\{ \begin{matrix} \begin{bmatrix} X \\ Y \\ Z \end{bmatrix} - \begin{bmatrix} X0 \\ Y0 \\ Z0 \end{bmatrix} \end{matrix} \right\} = M \begin{bmatrix} x \\ y \\ z \end{bmatrix} \tag{5}$$

Rotation matrix M is orthogonal matrix, M of the nine elements of three independent rotation angles ω , φ and κ the function. Because it is rotating around the axis of the linkage, it is a different angle in order; each element value is not the same. The use of ω , φ and κ corner sequence, into the value of each element, rotation matrix is:

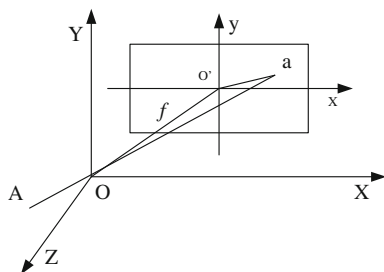
$$M = \begin{bmatrix} \cos \varphi \cos \kappa & -\cos \varphi \sin \kappa & \sin \varphi \\ \sin \omega \sin \varphi \cos \kappa + \cos \omega \sin \kappa & -\sin \omega \sin \varphi \sin \kappa + \cos \omega \cos \kappa & -\sin \omega \cos \varphi \\ -\cos \omega \sin \varphi \cos \kappa + \sin \omega \sin \kappa & \cos \omega \sin \varphi \sin \kappa + \sin \omega \cos \kappa & \cos \omega \cos \varphi \end{bmatrix} \tag{6}$$

Establish the relationship between the reference plane and three-dimensional shape the world coordinate system, so that the three-dimensional data measured in the same three-dimensional world coordinate system. Any two space Cartesian coordinate system can convert through translation, rotation, scaling.

2 Dual Machine Positioning of the Camera System

According to camera calibration technology [2], we can gain the image of the goal 3D information by the camera position and direction and its own some parameters. For example, according to the focal length of the camera image plane can correspond a scene point coordinates with the coordinates; calibration points can determine the relationship of two coordinates in the absolute coordinate system transformation, or determine the position and orientation of the distance sensors in the absolute coordinate system. The former is an external positioning, the latter is the absolute positioning, of which an important application is to determine the

Fig. 2 The corresponding relationship between A scene point and its image point



relationship between the binocular stereo vision system and the absolute coordinate system defined in the scene.

The relationship between camera optical system's the Lord coordinate system OXY and CCD image plane's the coordinate system O'X'Y' as shown in Fig. 2. The coordinate of point A calibrated in the CCD image is a (x_a, y_a). The focal length of optical system is f, which can get OA unit vector and azimuth A(ε_A, α_A).

$$\epsilon_A = \tan^{-1} \left(f / \sqrt{x_e^2 + y_e^2} \right) \tag{7}$$

$$a_A = \tan^{-1} (y_e / x_e) \tag{8}$$

OA vector of the unit vector is:

$$n_{OA} = (\cos \epsilon_A \cos a_A, \cos \epsilon_A \sin a_A, \sin \epsilon_A) \tag{9}$$

Assuming a point in the scene simultaneously imaging in two known position and orientation of the camera, then according to the binocular stereo vision measurement principle [3], we can determine the point's coordinates in the camera coordinate system, Principle shown in Fig. 3. Suppose point A in the camera image on the P1 and P2, which the distance between the origin of the coordinate system is L, the point OP1 azimuth in the coordinate system OXYZ | P2 is (ε_{P1}, α_{P1}). OP2 azimuth in the coordinate system OXYZ | P1 is (ε_{P2}, α_{P2}). By the unit vector n_{OP1OP2} and n_{OP2OP1} style can be. Two vectors the same coordinate system the angle between n_i and n_j formula is:

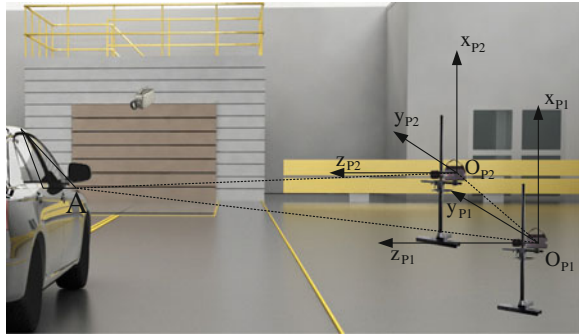
$$\cos \theta_{ij} = n_i \cdot n_j = \cos \epsilon_i \cos \epsilon_j (\cos a_i \cos a_j + \sin a_i \sin a_j) + \sin \epsilon_i \sin \epsilon_j \tag{10}$$

From (Eq. 10) can get the size of ∠ AOP1OP2 and ∠ AOP2OP1. The sine theorem:

$$\frac{\epsilon}{\sin A} = \frac{b}{\sin B} = \frac{e}{\sin C} \tag{11}$$

From (Eq. 11) can obtain that the coordinates of point A within the coordinate system OXYZ | P1 is:

Fig. 3 Standard fixed-point dual machine positioning principle



$$\frac{L}{\sin \angle O_{P1} A O_{P2}} \cdot \sin \angle O_{P1} O_{P2} A \cdot n_{O_{P1} A} \tag{12}$$

The coordinates of point A within the coordinate system OXYZ | P2 is:

$$\frac{L}{\sin \angle O_{P1} A O_{P2}} \cdot \sin \angle O_{P2} O_{P1} A \cdot n_{O_{P2} A} \tag{13}$$

3 Point Scale Attitude Measurement

If know the three known spatial coordinates of non-collinear points, you can determine a coordinate system. Therefore, to determine the attitude of moving targets on the target set at least three calibration points. To ensure the principle of two-plane positioning of the conditions—a standard point in the two cameras imaging the same time, on the top of the target can be shown by Fig. 4 shows the layout of calibration points.

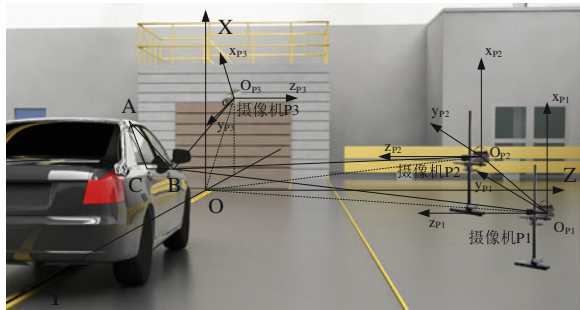
The principle of the measurement system shown in Fig. 5 shows three cameras, the objectives and the above three calibration points in the absolute coordinate system can be pre-position are measured. Target motion, the three cameras shooting simultaneously at some point calibration points to be like; According to dual-positioning principle, can determine the calibration points in the camera coordinate system relative coordinates, and then according to the camera and the absolute coordinate system transformation between the absolute calibration points derived from the three calibration points coordinates of the initial coordinates and measured values can be determine the three attitude angles.

A four-element method can describe that the rigid body transform between two coordinate systems. Coordinate translation and rotation as shown in Fig. 6.

Fig. 4 Schematic layout of calibration points



Fig. 5 Schematic diagram of the target attitude measurement coordinate system



Coordinate translation transformation matrix:

$$\text{Trans}(abc) = \begin{vmatrix} 1 & 0 & 0 & 0 \\ 0 & 1 & 0 & 0 \\ 0 & 0 & 1 & 0 \\ a & b & c & 1 \end{vmatrix} \tag{14}$$

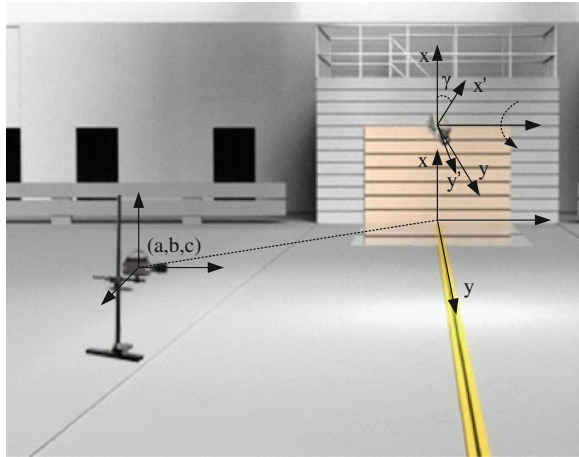
Around the x-axis rotation angle α of the transformation matrix:

$$\text{Rot}(x,a) = \begin{vmatrix} 1 & 0 & 0 & 0 \\ 0 & \cos a & -\sin a & 0 \\ 0 & \sin a & \cos a & 0 \\ 0 & 0 & 0 & 1 \end{vmatrix} \tag{15}$$

Around the y-axis rotation angle β of the transformation matrix:

$$\text{Rot}(y,\beta) = \begin{vmatrix} \cos \beta & 0 & \sin \beta & 0 \\ 0 & 1 & 0 & 0 \\ -\sin \beta & 0 & \cos \beta & 0 \\ 0 & 0 & 0 & 1 \end{vmatrix} \tag{16}$$

Fig. 6 Schematic diagram of coordinate system transformation



Here is the rotation around the z-axis angle γ transformation matrix:

$$\text{Rot}(z, \gamma) = \begin{bmatrix} \cos \gamma & -\sin \gamma & 0 & 0 \\ \sin \gamma & \cos \gamma & 0 & 0 \\ 0 & 0 & 1 & 0 \\ 0 & 0 & 0 & 1 \end{bmatrix} \quad (17)$$

In the target posture measurement, assuming that the coordinates of the initial target $A_0(x_0, y_0, z_0)$, pitch angle θ , yaw angle φ , roll angle Φ , the measured calibration point A of coordinates $A_h(x_h, y_h, z_h, 1)$, there are coordinate transformation method discussed above can be drawn from the initial position and the measured position of the corresponding relationship

$$A_h(x_h, y_h, z_h, 1) = A_0(x_0, y_0, z_0, 1)\text{Trans}(a,b,c)\text{Rot}(z, \theta)\text{Rot}(y, \varphi)\text{Rot}(x, \Phi) \quad (18)$$

Among them

$$\begin{aligned} & \text{Rot}(z, \theta)\text{Rot}(y, \varphi)\text{Rot}(x, \Phi) \\ &= \begin{bmatrix} \cos \theta \cos \varphi & -\sin \theta \cos \Phi + \cos \theta \sin \varphi \sin \Phi & \sin \theta \sin \Phi + \cos \theta \sin \varphi \cos \Phi & 0 \\ \sin \theta \cos \varphi & \cos \theta \cos \Phi + \sin \theta \sin \varphi \sin \Phi & -\cos \theta \sin \Phi + \sin \theta \sin \varphi \cos \Phi & 0 \\ -\sin \varphi & \cos \varphi \cos \Phi & \cos \varphi \cos \Phi & 0 \\ 0 & 0 & 0 & 1 \end{bmatrix} \end{aligned} \quad (19)$$

4 Building System in the Vehicle Crash Tests

4.1 The Requirements of Vehicle Crash Test

In the real car crash test vehicles preparation phase need to measure and record four wheels of the canter of the wheel and the round plate wheel section with the height of the intersection; Measured in the test needs to measure the steering



Fig. 7 Schematic diagram of experimental high-speed framing camera in the test

column in the longitudinal and vertical displacement; In the “H” point and the actual backrest angle determination process to be measured and recorded “H” point and the relative position of the vehicle fixed structure; In measuring the relative position of the dummy, the need to record the dummy and car interiors relative position.

According to the needs of vehicle safety R & D performance, the vehicle collision deformation measurement is an important vehicle crash test output parameters. These include bumper beams, A pillar, B pillar, the amount of deformation and intrusion of the engine compartment and so on. In the collision process, a potential safety hazard for dummy of objects state of motion analysis is the analysis content on the vehicle safety R & D performance, according to the collision of high-speed camera capture the image, you can analyze the speed of airbag opening parameters.

4.2 System Composition

The real vehicle crash tests which proceeds in the stage of the automotive research and development safety performance may proceed the construction of the high-speed camera acquisition system as shown Fig. 5, according to the needs to build a car, an off-board high-speed video acquisition system, at the time of high-speed camera choosing the scene and in order to facilitate this in the camera calibration, calibration points for attitude measurement and other work. Figure 7 shows the part high-speed camera of the framing plans in the system.

According to the method described in the text, images from the high-speed car under the A-pillar and the window edge of the calibration points for high-speed camera in a position calibration, positioning the high-speed digital camera system of the machine coordinates. Use of the image point in the calibration standard of known distance demarcates the distance of the test position.

In the crash test that done in Zhejiang Province, Key Laboratory of Automotive Safety Technology, we take a high-speed camera images for analysis. According to flight calibration, a view of the dummy movement patterns shows as in Fig. 8.



Fig. 8 Views of the high-speed camera images

After high-speed camera's position calibration, this position of 1,000 per second shooting speed, each time interval between images already determined. By the image tracking points on the dummy head to track the identity, and the use of three-dimensional calibration of the identity of each time point position coordinates calculated by each image after the time interval available to identify the point of the acceleration curve shown in Fig. 9 follows:

Similarly, According to in the image of the collision before and after the position coordinates of the marked point on A pillar can determined A column deformation in the test shown in Fig. 10 as follows:

5 Data Calibration and Error Analysis

Camera calibration [4] is a key step in the video image measurement, that is a solution to identify the point of physical space coordinates and image plane coordinate relational equations in the internal and external camera parameters. Calibration point setting and calibration material should be placed so that calibration points for easy identification and accurate positioning, and calibration object placement on the measurement results of no significant impact on the analysis from the measurement principle, the system measurement accuracy of the position profile major impact factors:

1. Moving target positioning accuracy of the calibration points on the impact of the calibration points to the relevant standard image processing algorithms to improve the positioning accuracy of the center point;
2. The moving target imaging camera system, the computer's clock there will be error, the error is generally a few microseconds;
3. In order to correctly identify the calibration points, with the CCD can be used to match the frequency response of a specific frequency of laser light source as calibration points;

Fig. 9 The acceleration curve of the identification point

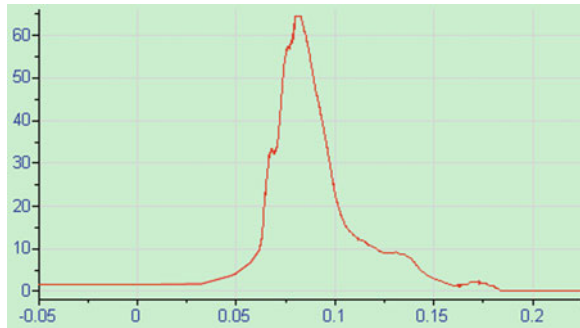
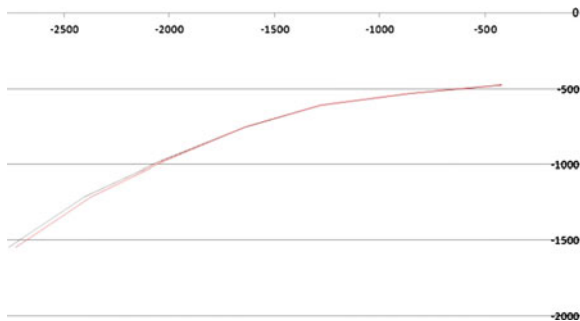


Fig. 10 The deformation of the marked point in the test before and after



4. Camera Lens error, distortion effects, optical lens may exist errors in the manufacture, performance in the work environment may change, this error and distortion can be corrected in the calibration of the system [5].

References

1. Songde Ma, Zhengou Z (1998) The computer vision. Science Press, Beijing
2. Zhengtao Z (2009) Based on the intelligent video camera of the high speed camera system and its visual target tracking algorithms. *Robots* 31(3):229–241
3. Mingjun S (2009) The target tracking under Multi-camera environment. *Mod electron technol* 12:61–70
4. Masoud O, Rogers S, Papanikolopoulos NP (2001) Monitoring weaving sections, CTS 01-06. ITS Institute, University of Minnesota, Minneapolis
5. Jensen K, Anastassiou D (1995) Subpixel edge localization and the interpolation of still images. *IEEE Trans Image Process* 4:285–295

Study of Optimized Tuning in Full AFLS Head Lamps

Doohyun Kim

Abstract Full AFLS (Adaptive Front Light System) is just on time headlamp-technology about varying driving-circumstances and vehicle speed using communication between vehicle's ECU and Headlamps' ECU. The objective of this study was to investigate optimized tuning method of AFLS headlamps in the real each car and matters that should be focused on.

Keywords Full AFLS · Class · Swiveling · Parameter

1 Introduction

Recently, in the field of headlamps better visibility and steering stability has to offer customers by using AFLS technology when driving at night. Nowadays many cars adapted advanced technology with changing class of headlamps' beam pattern according to vehicle's speed (or environment) it's called Full AFLS head lamps. It's beyond technology of simple swivelling function.

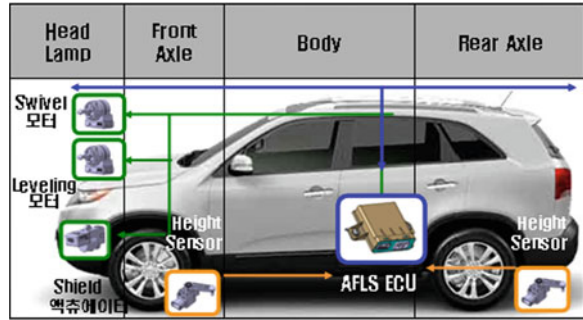
Full AFLS means on-time technology in optimized beam pattern, brightness, swivelling of lamp unit through the wireless connection between headlamp's ECU and vehicle's ECU.

In this study, proceed virtual test using Driving Simulator and analysis Tool with dynamic factor (Yaw Rate, SWA, Speed, and Environment). Also through the verify AFLS function in real car and real situation with optimized tuning, develop new test method that would contribute next-step development and setting direction.

F2012-E14-031

D. Kim (✉)
Hyundai-Kia Motor Company, Hwasung, South Korea
e-mail: kkorinn@hyundai.com

Fig. 1 Full AFLS diagram



2 Body

2.1 Full AFLS

2.1.1 Full AFLS Concepts

AFLS system controls not only headlamps unit’s movement through calculating vehicle’s front and rear wheels’ height differences, but also headlamp’s beam pattern using rotation of shield that inputted vehicle information. That information is vehicle speed, SWA. See the Fig. 1.

2.2 Swivelling Function

2.2.1 Swivelling Concept

Swivelling is basic function that obtains visibility of curve road. That means headlamp unit’s transverse rotation according to steering wheel angle when driving curve road. Thus, to tune the swivelling function, understand vehicle’s dynamic nature at first.

Vehicle’s dynamic nature has differentiated character according to each vehicle’s power train performance, weight, suspensions, and tires. Thus, we need to know unique dynamic nature each vehicle to tune swivelling performance. Main dynamic character of vehicle are vehicle speed (V), radius of gyration according to steering wheel angle (R’) and yaw rate (Y_R).

It has relationship with each other when vehicle driving at radius of gyration R.

$$R \propto \frac{V}{Y_R}$$

Fig. 2 Slow speed

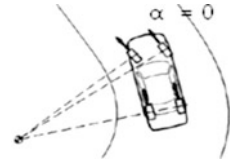
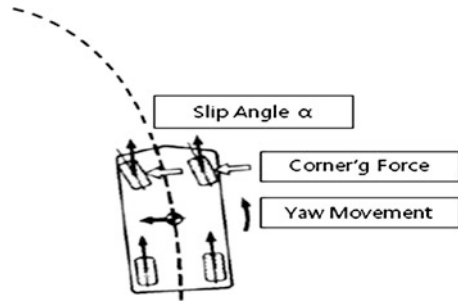


Fig. 3 General speed mechanism



Then, it will get different result of R' in same situation when driving same curvature road with same steering wheel angles. It is called characteristic difference.

So even if it is same setting vehicle in AFLS systems that unreferenced dynamic character, there will be big differences of visibility in curve road and movement of headlamp unit.

2.2.2 Vehicle’s Behavior when Turning Drive

If vehicle drives very slowly in curve road, there is no slip angle (α). Also, there is no yaw movement because it has same directions between vehicle and tire (Fig. 2).

But, in real driving situation most of vehicle drives faster. And the less vehicle has inertia the more vehicle has yaw movement. (for example, lightweight vehicle) Slip angle (α) makes cornering forces that causes yaw movement around vehicle’s center mass.

So, There is essential factor, vehicle speed (V), radius of gyration according to steering wheel angle (R') and yaw rate (Y_R), that need to be referred (Fig. 3).

2.2.3 Swivel Control

AFLS ECU monitors vehicle’s condition receiving many information, vehicle speed, power train data, yaw rate, accelerator-pedal data, brake pedal data and RPM of engine.

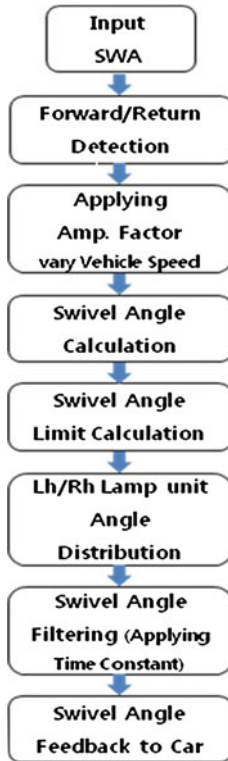


Chart 1 Swivel flow chart

And ECU sends final swivelling angle (θ) to the headlamps after calculates headlamp unit's swivelling angle with filtering process. Final swivelling angle (θ) is equivalent to kink point tracking angle (θ_k) (Chart 1) [1, 2].

2.2.4 Forward and Return Control Logic

Judgment of entering or returning on curve road is according to relationship between present SWA and ex-SWA.

In here, frequent and small SWA in very short term will not be activated headlamp's swivelling because zero angle filter (Fig. 4).

It will have smoother and safer visibility in S-shape curve road using logic control technology. For example, if vehicle drives general curve road, headlamp unit swivelling linearly. If vehicle drives S-shape curve road, headlamp unit swivelling non-linearly, because it is needed faster swivel at incoming entrance of 2nd corner than general curve road.

Fig. 4 Entering/returning swivel angle

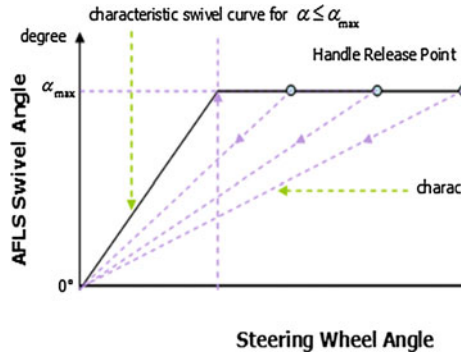
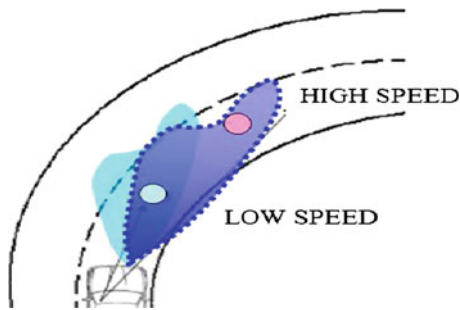


Fig. 5 Point of view



So in this study, it can improve the phenomenon of hesitation that every car applied AFLS system in S-shape curve road. It is more efficient logic, because there is no re-calculation process to return swivelling. In the parameters, there is logic control technology in there, For example, if No.11 has 0.25 values, there will be 4-times faster return swivelling than enter swivelling.

2.3 Dbl Parameter Tuning

2.3.1 Amplifying Factor Parameters

It means degree of headlamp unit’s swivelling according to vehicle speed. The more degree it takes in factor, the more swivelling angle out.

There is no meaning at vehicle speed 0 and 250 kph because amplifying factor value goes to 0. In mid-sector amplifying factor value is connected each other linearly. That can give steady swivelling angle(θ) according to vehicle speed.

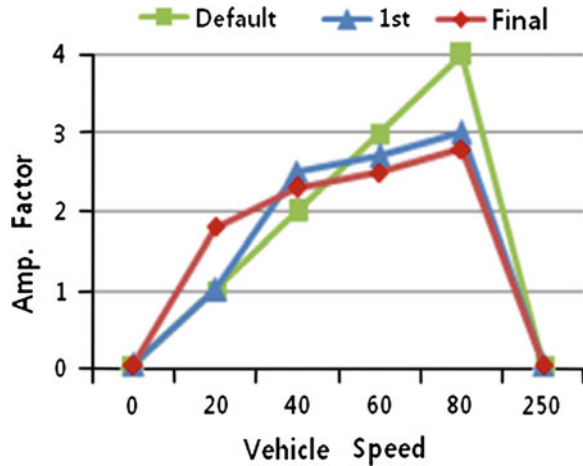
When driving at night, driver’s eye wants to see cut-off line of headlamps (It is called kink point) to obtain further visibility of night road. It was tracking with Eye-mark camera, it was instinctive behavior.

So, the more it gets vehicle speed in curve road, the more need swivelling angle(θ) (Fig. 5) [3].

Table 1 Amplifying factor setting

Speed	Initial	1st	2nd	Final
0	0.042	←	←	←
20	1	1	1.8	1.8
40	2	2.5	2.5	2.3
60	3	2.7	2.7	2.5
80	4	3	3	2.8
250	0.042	←	←	←

Graph 1 Amplifying factor



Above 80 kph, there is only steady turning driving, not rapid cornering. So there is no increase in amplifying factor. After all, it goes to 0 and also swivelling angle(θ) goes to 0.

In this study, It obtains 45 % improve of visibility in night driving at curve road with AFLS systems. It was tuned and targeted; kink point would be located on driver’s instinctive sight point. Final fixed parameter values are in Table 1. It got basic outline using Driving simulator facility (Virtual driving circumstance chamber).

After, 1st real car tuning process, there was insufficient visibility in low speed area and 2nd real car tuning process, there was intrusion of kink-point in opposing lane in mid-speed area. So, we fixed final parameters down below Graph 1.

2.3.2 Max/Min Swivel Adaption Parameters

This AFLS system’s max swivelling angle is 15° (outer side, θ_{out}) and 7° (inner side, θ_{in}). It has limitation of outer max angle because relationship of between θ_{out} and θ_{in} . If difference of θ_{out} and θ_{in} exceed 2-times θ_{in} , center area of cut-off line has dark spot that brings loss of visibility (Fig. 6).

Fig. 6 Dark spot

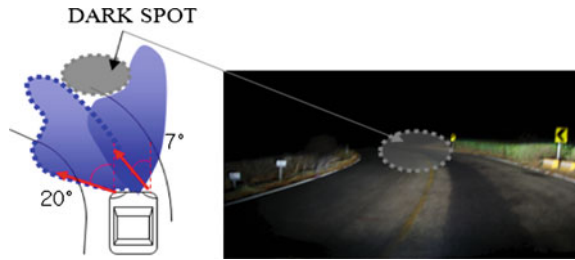
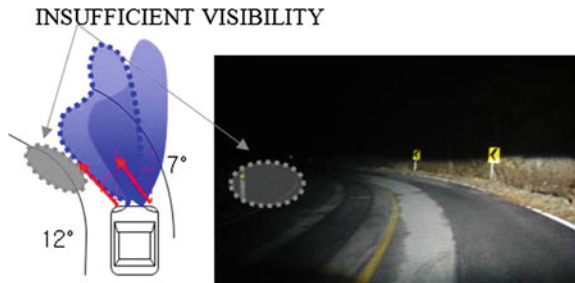


Fig. 7 Insufficient corner visibility



Also, excessive θ_{out} of swivelling is concerned to opposing incoming car glare regulations.

In contrast, If $\theta_{out} = 12^\circ$ applied to minimize loss visibility in center area, there was insufficient corner visibility when driving deep winding road ($R = 30$) (Fig. 7).

Thus, It was chosen $\theta_{out} = 14$ and relationships between θ_{out} and θ_{in} , $\theta_{in} = \theta_{out}/2$, to obtain the best optimized visibility of curve road.

$$\theta_{in} = \frac{1}{2}\theta_{out}.$$

2.3.3 Relationship of Master and Sub Beam

There are also significant relationships between master beam and sub beam.

As you can see the graph of relationship I, According to increasing SWA, there is increasing gap between master beam and sub beam. Under this condition, driver could sense master beam’s escaping feeling from sub beam at some moment (Graph 2) and (Fig. 8).

But, under relationship II, driver could sense steady angular speed from the start because it has linear relationship. So no more master beam’s escaping feeling in there (Graph 3) and (Fig. 9).

Graph 2 Relation of master and sub beam i

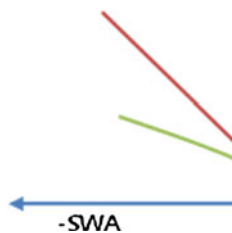
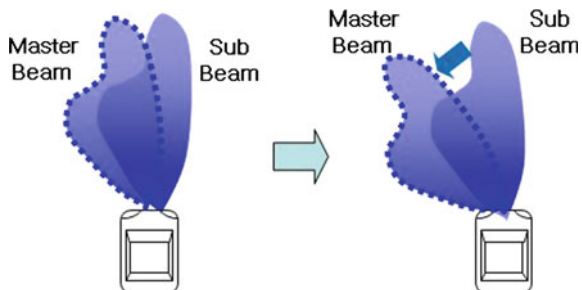
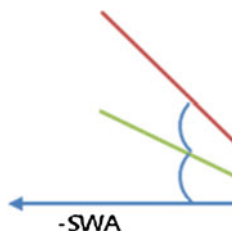


Fig. 8 Master beam escaping



Graph 3 Relation of master and sub beam ii

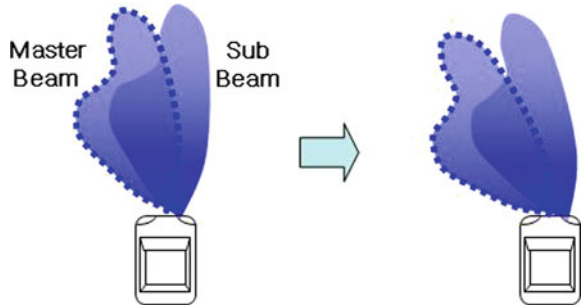


2.3.4 Time Constant Parameters

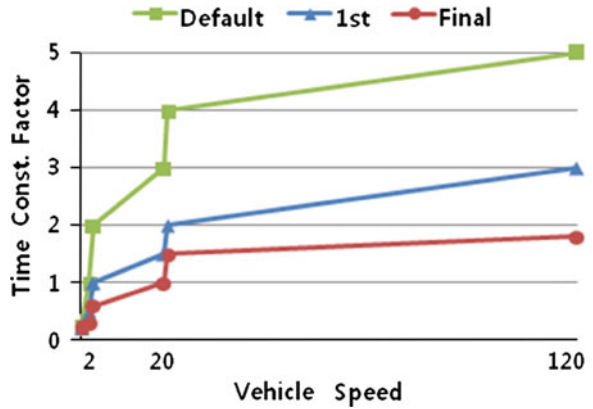
It means degree of headlamp unit's delay time according to vehicle speed. The more degree it takes in factor, the more it takes time to target at allocated swivelling angle(θ).

It also got basic outline using Driving simulator facility. In 1st real car tuning process, there was too slow responsiveness. In 2nd real car tuning process, there was too sheer feeling around 20 kph. At the early stage of real car tuning process, it had been thought; if it had faster movement of headlamp's unit, it would good to fun to drive feeling and appeal attractiveness.

Fig. 9 Linear relationship



Graph 4 Time constant factor



After panel group test (Include normal consumer driver and expert driver, 5 h drive, ages 20–50), it was found that excessive sheer movement feeling gives dizziness and fatigue to the human eyes.

There is big time-constant value at 120 kph because there is no deep curve road with radius of gyration R at vehicle speed over 120 kph. Unless it takes big time-constant, it can be dangerous and caused loss of visibility. General user condition, it was sufficient to obtain good visibility using time constant factor until 110 kph Graph 4.

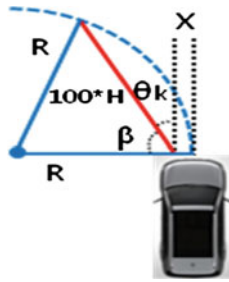
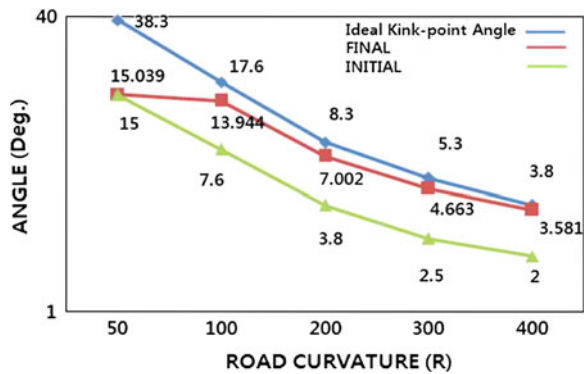


Fig. 10 Ideal kink point tracking angle. R Radius of road, X width of lamp, H Height of lamp, $100*H$ Max length of beam (regulation)

Graph 5 Swivelling tracking



2.4 Swivelling Parameter Verifying

2.4.1 Swivelling Parameter Tuning

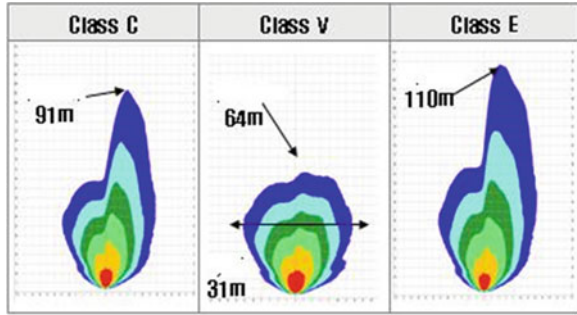
When vehicle drives curve road, ideal tracking angle(θ_k) of kink-point is satisfy below relation (Fig. 10).

It is possible to compare between ideal tracking angle(θ_k) and swivelling angle(θ) when real driving circumstance. And then it can compare and verify tracking ability of headlamps quantitatively.

As see the graph, there are good tracking ability lamps (Red) and poor tracking ability lamps (Green).

Final setting (Red) follows well ideal curvature of the curve road. In 50R curvature of road, there is some tracking gap. Because headlamp design layout doesn't allow swivelling movement Graph 5.

Fig. 11 Beam pattern



2.5 Class Change

2.5.1 Beam Pattern

Changing optimized beam pattern skill is core part of the Full AFLS systems with recognizing vehicle speed and driving circumstance. Generally, it is divided 3 classes.

First, basic beam pattern C-class (country mode). This pattern is basic class to obtain length of visibility.

Second, V-class (village mode). It is suit for low speed driving like urban cross road area. It is designed for wide view, for example, to see the pedestrian in side road.

Third, E-class (express way mode). It is suit for high speed driving like express way. It is designed for longer visibility and wide view.

In headlamp’s module Rotation of shield and longitudinal movement of cut-off line make change optimized beam pattern (Fig. 11).

2.5.2 Entering Class

After start up engine, it will go to V-class pattern to drive in low speed. And when vehicle drives faster over A kph, it will go to C-class pattern from A to B kph.

High speed mode, E-class start after allocated time duration over B kph condition. E-class brings power increasing in ballaster and raising cut-off line X degrees.

2.5.3 Returning Class

When driving condition, there is so many conditions to increase and to decrease speed. Process of returning beam pattern occur according to decreasing vehicle speed.

To avoid discomfort of beam pattern returning, it has time delay and vehicle speed buffer.

2.5.4 Feeling in Changing Process

It also found that fast and frequent change of beam pattern gives dizziness and fatigue to the human eyes. Thus, it was applied shield rotating type to change beam pattern that rotate smoothly and comfortably during Y sec.

2.5.5 Final Verifying Full AFLS System

It is strongly recommended real car and real circumstance test. Because it is impossible to reflect all of the dynamic nature, Hard ware character, point of view each vehicle and especially steering wheel feeling. In this study, It had tested in mountain winding road, express way and public road in Korea and Europe.

2.5.6 Extra Matters

It is also needed to verify durability test because there is so many working parts in headlamp's unit.

First, initial matching test—test for initial aiming of headlamps at start-up engine.

Second, return position after swivelling—test for after max swivelling, whether or not return initial aiming position.

Third, beam pattern test at each class—test for rotation of shield at each class.

At last, fun function test—test for headlamp's swivelling in idling stop condition (RH side only). It's only for recognition of system working. Because some of customer wants to know this AFLS system is working well.

3 Conclusion

Full AFLS headlamp is all round aggregation of headlamp's technology. It helps customer's safe and appeal the attractiveness of vehicle. Some conclusion has obtained down below with Driving simulator and real car and circumstance test.

- (1) It can compare and verify tracking ability of headlamps quantitatively using ideal tracking method. So test car follows real winding road with 94 % accuracy and there is max 45 % improvement in visibility of light.
- (2) Main tuning part of Full AFLS headlamp system is changing class of beam pattern and entering/returning each class. In hard-ware view, swivelling

actuator and cut-off line shield actuator. In soft-ware view, logic in entering/returning each class.

- (3) Main tuning part of swivelling is amplifying factor and time constant factor. That is related to swivelling angle(θ) referring vehicle speed, SWA, yaw rate.
- (4) It is needed to verify durability test because there is so many working parts in headlamp's unit.
- (5) This study will contribute improvement of understanding Full AFLS system to designer and engineer. It could demand details to the manufacturer in initial stage of design. So it could bring reduction of development time.

References

1. Ishiguro K, Control technology for bending mode AFS, SAE 2004-01-0441
2. Schmidt C, (2005) Adaptive systems for motor vehicle lighting First steps and future, SAE
3. Shibata Y, The Evaluation of AFS beam pattern using the movement of the driver's eye-fixation points, SAE 2006-01-0944

Improvements in Test Protocols for Electric Vehicles to Determine Range and Total Energy Consumption

Juhani Laurikko, Jukka Nuottimäki and Nils-Olof Nylund

Abstract As electric vehicles have entered the market fairly recently, test procedures have not yet been much adjusted to address their particular features. Mostly EVs are tested the same way as the ICE-driven cars with the exception that determining range is also part of the procedure. However, the current procedures address mainly primary energy consumption, i.e. energy needed to propel the vehicle, whereas the secondary energy, like energy used for cabin heating, cooling and ventilation, is not accounted properly. Main reason is probably the fact that a large proportion of this energy is catered by the waste or excess energy, but in an EV also this part of energy uses is drawn from the battery. Therefore, range of an EV may differ fairly strongly depending on ambient conditions, as in adverse conditions secondary energy use may rise considerably. Furthermore, unlike propulsion energy use that is mainly dependent on driving speed, secondary energy use is mostly dependent on ambient temperature and driving time, and energy is spend even when the vehicle is stopped. However, the challenge to determine a procedure that would more properly address the various parameters that affect range is quite substantial. Also any laboratory test procedure is always a compromise, because it is not possible in practice to replicate the real-life driving completely. Therefore, the authors call upon the engineering community to work on this subject. This chapter outlines our attempt to address this issue, and presents data from in-laboratory testing at normal and low ambient temperatures. It was found that cold driving at $-20\text{ }^{\circ}\text{C}$ ambient can shorten the range by about 20 %, even without cabin heating engaged, compared to normal ambient conditions. Using the electric cabin heater will shorten the range further by about 50 % in urban driving and some 20 % in road-type of driving with higher average speeds.

F2012-E14-032

J. Laurikko (✉) · J. Nuottimäki · N.-O. Nylund
VTT Technical Research Centre, P.O. Box 1000 FI-02044 Espoo, Finland

Keywords Electric vehicle · Range · Test procedures · Ambient conditions

1 Introduction

Electric-driven vehicles open up a possibility to use more renewable energy for transport. However, current battery technology is still quite embryonic and limits the capacity of the on-board energy storage to allow only some 100–200 km range. Furthermore, time needed to refuel an ICE car is some 5 min, whereas typical charging time for a BEV is 6–8 h, even if fast charging can bring charging time down to 30 min. Also if an ICE car runs out of fuel, it is fairly easy to bring fuel to it and refuel the car to allow driving to the next refuelling station. However, if an EV runs out of electricity, there is no straightforward way of replenishing the battery of a stranded EV on-road, although some innovative solutions for emergency charging has been developed [1]. Instead it must be transported to a charging station, because in most cases towing of an EV is not allowed, as it would impose a strong tractive resistance because of the regenerative features of the drivetrain.

All these factors together have led to certain uneasiness called “range anxiety” amongst the general public. Yet we firmly believe that a realistic estimate of the range is the most critical factor for EV’s success, but because of this disparity in range, the industry is tempted to quote optimistic figures. However, if the numbers given do not reflect the true performance, and the customers are in practice seeing drastically lower driving ranges than those advertised, there is a danger that the market-acceptance of EVs suffers strongly.

Therefore, assessing vehicle performance using most realistic driving patterns and weather conditions, including especially low ambient temperatures, is essential. Otherwise, this may even cause a severe backfire effect to the deployment of EVs.

Accurate and realistic information of range is also needed for the process of planning and calculating the capacity of the charging infrastructure, as well as spatial allocation of the charging points. Station-to-station distances need to be in relation to the actual ranges of the vehicles in all conditions. In extreme situations local conditions may lower the range of EVs, and the density of the charging network needs to be increased to guarantee all-year trouble-free operations.

2 Target and Objectives

For the reasons above, customers are very sensitive to the performance figures advertised, as if the EV falls short to meet their expectations, there is a danger that the whole technology will soon be labelled useless. Therefore, test procedures that are used to generate the information provided to the customers must be able to simulate real use enough to render figures that will honestly portray the performance, and will certainly not overestimate it.

As electric vehicles have entered the market fairly recently, test procedures have not yet been much adjusted to address their particular features. Mostly EVs are tested the same way as the ICE-driven cars with the exception that determining range is also part of the procedure. However, the current procedures address mainly primary energy consumption, i.e. energy needed to propel the vehicle, whereas the secondary energy, like energy used for cabin heating, cooling and ventilation, is not accounted properly. Main reason is probably the fact that a large proportion of this energy is catered by the waste or excess energy, but in an EV also this part of energy use is drawn from the battery. Therefore, range of an EV may differ fairly strongly depending on ambient conditions, as in adverse conditions secondary energy use may rise considerably. Furthermore, unlike propulsion energy use that is mainly dependent on driving speed, secondary energy use is mostly dependent on ambient temperature and driving time, and energy is spent even when the vehicle is stopped.

However, the challenge to determine a procedure that would more properly address the various parameters that affect range is quite substantial. Also any laboratory test procedure is always a compromise, because it is not possible in practice to replicate the real-life driving completely. Therefore, the authors call upon the engineering community to work on this subject. One attempt is already started in the form of a co-Nordic research project called RekkEVidde.

3 Status Quo and Development of the Test Procedures

3.1 Official Testing of EV Range

Today in the European Union, the energy use of cars, both ICE-driven and electrically-powered, is measured according to UN-ECE Reg. 101. It prescribes a laboratory test, performed in normal ambient conditions (temperature between +20 and +30 °C), and using a duty-cycle New European Driving Cycle (NEDC) composed of an urban and extra-urban sub-cycle originating from a pan-European exhaust emissions regulation (UNECE Reg. 83 and 98/69/EC).

Although primarily set to measure energy consumption, the protocol today includes also determination of range for electric-powered vehicles. As for normal ICE-driven cars, range is not an issue. Most of the cars will go more than 500 km on a tankful of fuel, and the extremely frugal diesels can today extend their range up to four digit figures. For an EV the range is the distance driven using the NEDC driving pattern until the car does not any more reach the speed of 50 km/h.

3.2 Official and OEM-Specific Figures for EV Range

In addition to the official figures, EV manufacturers have today started to quote also figures for range resulting from their own testing. However, those are not comparable to each other. For example for the “twinning” of Peugeot Ion/Citroën

C-Zero, the current range given by the manufacturer is 150 km [2]. However, it's worth noting the disclaimer which states, "Range varies according to climatic conditions, driving style, the use of electrical equipment, the frequency of normal or fast charges and ageing of the main battery".

On the other hand for the original "master-car", Mitsubishi iMiEV, the range quoted for the Japanese market is 160 km (100 miles) [3], even if they are all technically similar vehicles with equal battery capacity. The reference is then the Japanese 10.15 cycle having lower speeds than its European counterpart. For the recent entry to the U.S. market, the official EPA sanctioned range for MY 2012 cars is only 100 km (62 miles) when using the full five-cycle test protocol with climate control [3]. Yet, if driving is limited to LA4 driving cycle only and no A/C, the range goes up to 158 km (98 miles) [4], which is very comparable to the Japanese figures.

As for another market-ready EV, the Nissan Leaf, the manufacturer has originally quoted a 100 miles (160 km) range in EPA city driving cycle (LA4). However, when using the full official protocol EPA testing reached 117 km (73 miles) for the U.S. model, whereas the official European figure is 175 km (109 miles) [5].

Furthermore, Nissan has also released in U.S. new "unofficial" range figures referring to 6 different types of driving versus weather conditions, ending up to 6 different ranges between 47 and 138 miles depending on the particular case [6]. This type of information is very useful for the consumers to understand that range is quite sensitive to a host of conditions, primarily driving style and ambient temperature. However, there is a danger that every OEM will develop their own set of "supplemental procedures" to address this issue. Then the information will not be consistent from make to make. Therefore, it would be of great help if someone could coordinate this effort and help the industry to test their products in a harmonised way, instead of each having their own tests.

3.3 Future Activities

Under the auspices of United Nations Economic Council for Europe (UN-ECE), there are activities related to the development of world harmonised regulations for motor vehicles. The Group of Expert in Pollution and Energy (GRPE), working for the Working Party 29 (WP.29) that deals with technical regulations for motor vehicles has so far developed Global Technical Regulations (GTR) for heavy-duty vehicles (trucks and busses) and motorcycles, and work is underway also for an equivalent regulation for passenger cars. In its meeting in January 2012, GRPE received a joint proposal from US, EC and Japan of establishing an informal working group for electric vehicles. Under this initiative it was proposed to address both safety and environmental issues with the formation of two new informal groups one on Electric Vehicle Safety, and, another on Electric Vehicles and the Environment (EVE) under the GRPE [7].

Through this initiative, the co-sponsors aim to exchange information on current and future regulatory requirements for electric vehicles in different markets, minimize the differences between these regulatory requirements, with a view toward facilitating the development of vehicles to comply with such requirements, and where possible, develop common requirements in the form of one or more UN Global Technical Regulations (GTR). This is a very welcome act, and should be promoted and supported.

In North America a specific test procedure and protocol for battery-electric vehicles is being developed by the SAE International Committee on Electric Vehicle Energy Consumption and Range Test Procedure (SAE J1634). In that forum, the influence of the ambient conditions is being addressed in search for more representative results.

Another international forum for discussion on this topic is the Electric Vehicle Initiative (EVI), an activity of International Energy Agency (IEA) launched in October 2010 [8] by a team of eight countries. Currently, 14 countries are listed, and the topic of more realistic testing of EV performance is already an item on their common agenda.

4 Experimental Testing Activities

4.1 Laboratory Test Set-Up

Technical Research Centre of Finland (VTT) has a climatic test cell for passenger car energy and exhaust emission measurements. It is equipped with a single-roller dynamometer with 1.0 m diameter rollers. Ambient temperature in the cell can be controlled between +25 and −30 °C, and cooling air circulation is available at speeds up to 100 km/h, constant or relative to the roller speed equalling driving speed. The range for inertia simulation is from 450 to 2500 kg, which makes it suitable for testing of all kinds of EVs, also the light-weight concepts.

Initial laboratory testing for this project was imposed on a Citroën C-Zero. The car was factory standard with all optional heating and ventilation accessories. Before testing the car was run-in for some 1200 km on normal roads in Helsinki Metropolitan area in November–December 2011.

Figure 1 shows the car in the test cell with probes and other instrumentation for energy measurements also within the propulsion system itself.

4.1.1 Driving Cycles

To assess the effect of driving cycle a set of existing duty-cycles were exploited. The base cycle was the official test cycle (NEDC), i.e. European driving cycle consisting of urban part (ECE15) and an extra-urban part (EUDC). In addition, two local Finnish cycles were used, one for urban (Helsinki City) and one for road and

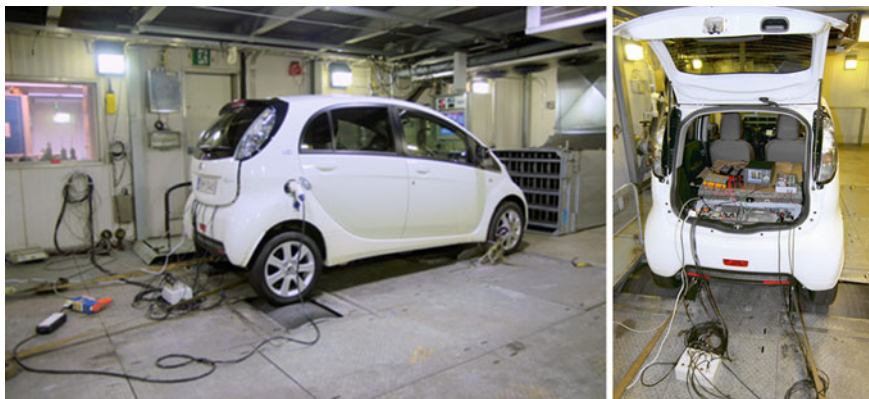


Fig. 1 Citroën C-Zero on in test cell at VTT

highway-type of driving (Highway.FIN). Both of these were developed by VTT based on measurements in traffic. Further three cycles were sourced from the European ARTEMIS-project that developed a set of “representative” cycles in early 2000 for measuring exhaust emissions from cars. They were supposed to portray urban, road and motorway driving. See [9] for more details. Figures 2, 3, 4, 5 illustrate all cycles imposed.

Table 1 lists main characteristics of the cycles used in this preliminary testing phase.

4.2 Test Conditions

The initial phase of the in-lab testing was conducted at two ambient temperatures. Those were +23 and -20 °C. Relative humidity in the test cell was controlled to agree with the requirements of ECE R-101.

Setting of the dynamometer road load was made against coast-down data obtained from a similar car on flat road conditions, and the final setting of the bench agreed with those coast-down times observed. Also the 0–100 km/h acceleration times equalled results from on-road measurements.

For the tests at -20 °C the air drag factor was increased by about 10 % to match with the increased density of the air at that given temperature compared to normal temperature. No other adjustments were made. However, in real conditions also rolling resistance would be higher, because road surface friction would probably increase due to the packing of the ice and snow. This effect will be investigated during the project later on with on-road measurements, and the effect shall be taken in also in the future lab measurements.

Furthermore, in this test series the on-board cabin heater was not used, even if the driving at low temperatures more than a few minutes surely requires it. This choice was made to more clearly differentiate the various contributions to the

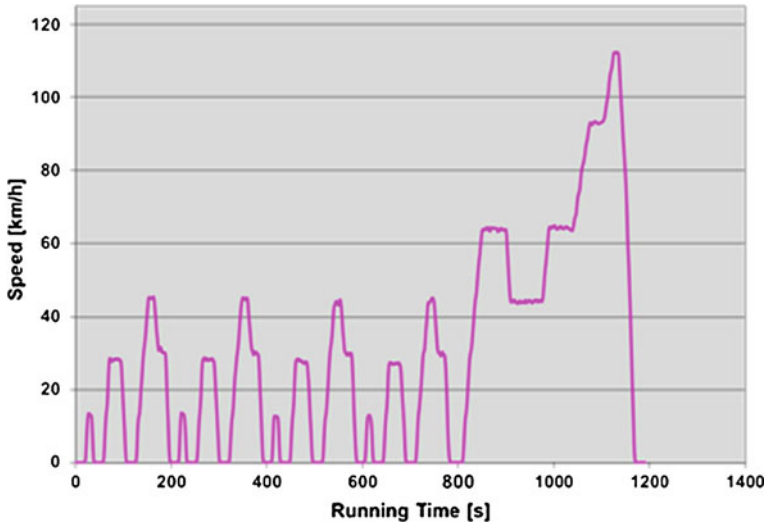


Fig. 2 New European driving cycle (NEDC)

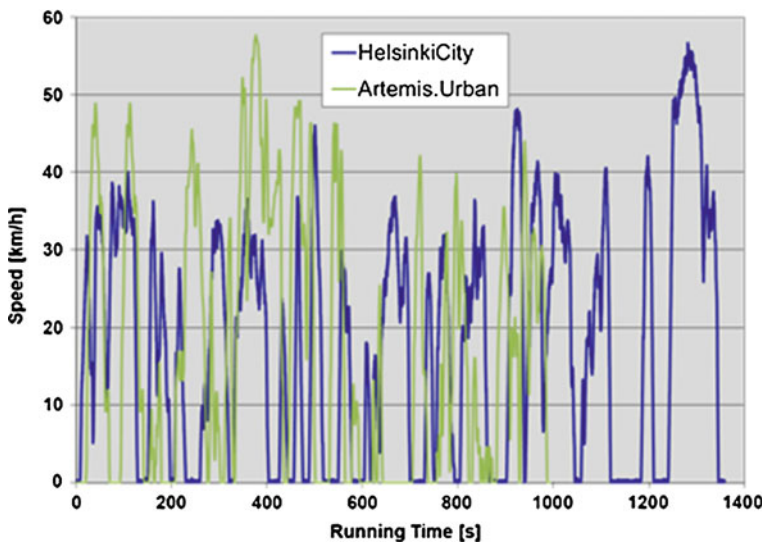


Fig. 3 Urban cycles Helsinki City and Artemis Urban

increase of total energy consumption, and its eventual effect on shortening of the range. Moreover, to make the driving conditions acceptable and to match the minimum ambient temperature limits of the instruments used in the exercise, a separate heater/blower using 230 V grid electricity was used. Energy use of the on-board cabin heater was measured separately, and its effect is superimposed on the results.

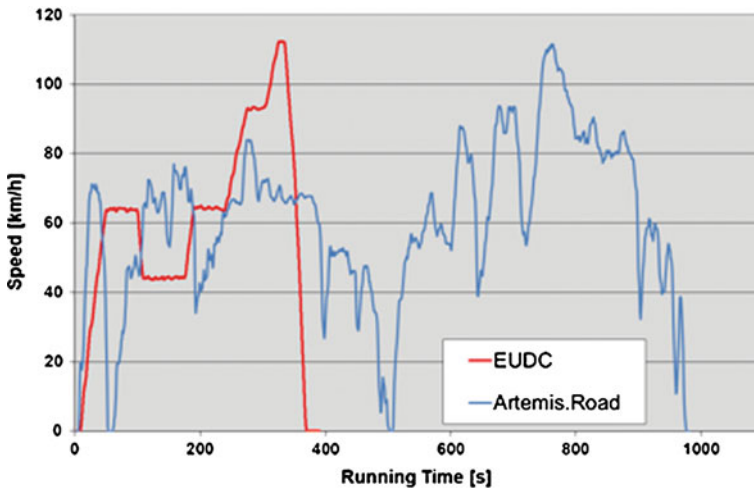


Fig. 4 Road cycles European extra-urban cycle (EUDC) and Artemis Road

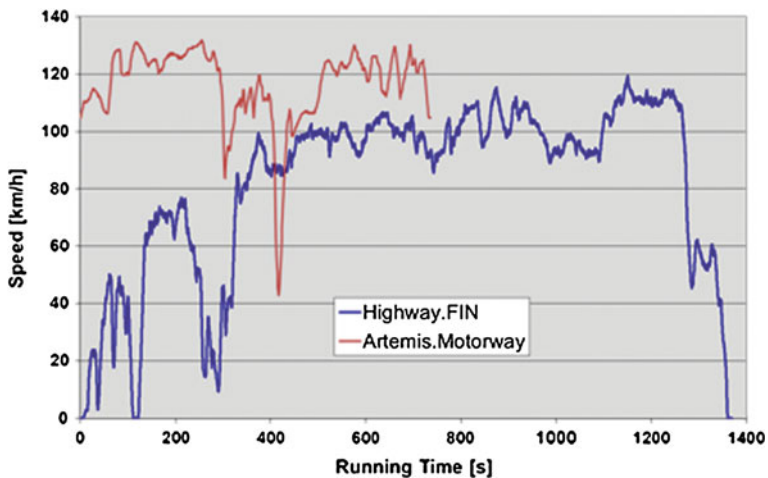


Fig. 5 Highway cycles Finnish Highway Cycle and Artemis Motorway

5 Results and Discussion

The analysis of the measurement results so far entail only comparison of gross energy use of the various driving cycles at both ambient temperatures, as well as calculation of range based on the amount of energy that the traction battery was able to deliver until fully drained.

Table 2 encompasses results for specific energy use over each cycle at both test temperatures. The energy use has been calculated from the uptake of grid

Table 1 Characteristics of the driving cycles

Cycle	Distance (km)	Average speed (km/h)	Maximum speed (km/h)	Stops during cycle	Running time (s)
NEDC	11.007	33.6	120	12	1180
ECE15	4.052	18.7	50	4	780
EUDC	6.955	62.6	120	0	400
Helsinki City	6.600	19.1	55	17	1360
Artemis Urban	4.488	17.6	58	19	993
Road, FIN	24.800	81.3	120	1	1370
Artemis Road, EV ^a	16.641	60.3	111	1	981
Artemis Motorway, EV ^a	23.793	105.6	130	0	736

^a EV denotes that warm-up part of the cycle is omitted

Table 2 Specific energy use (uptake from grid) for each cycle at +23 and −20 °C

Cycle	Energy use (grid)		Difference −20 versus +23 % (%)
	+23 °C kWh/km	−20 °C kWh/km	
NEDC	0.142	0.200	+41
Helsinki City	0.141	0.166	+18
Artemis Urban	0.178	0.239	+34
Road, FIN	0.193	0.251	+30
Artemis Road, EV ^a	0.157	0.195	+25
Artemis Motorway, EV ^a	0.244	0.329	+35
Average, all cycles	0.183	0.236	+29

^a EV denotes that warm-up part of the cycle is omitted

electricity after driving of each cycle three times in series with a 2 min pause in between. However, the Artemis. Motorway cycle was so demanding that traction battery was depleted before reaching the end of the third run. At normal temperature the car could reach $\frac{3}{4}$ of the cycle, but at sub-zero temperature, the third run was limited to a mere 1.4 km.

When we look at the figures in Table 2, and especially compare results measured at −20 we can see that need for energy uptake from the grid to cover energy need to run the given cycle increased on average by some 30 %, when ambient temperature during the test was lowered from +23 to −20 °C. Most notable increase was seen in New European Driving Cycle (+41 %), while in case of the Helsinki City “urban crawl” cycle we saw less than 20 % raise.

We have also calculated nominal ranges for each case by dividing the capacity of the traction battery measured at both conditions with the cycle-specific energy uptake. Even if the use of energy seemed to increase while the ambient temperature was lowered, traction battery capacity seemed to sustain at the same level. After fully depleting the battery for a few times at both temperatures, the amount of grid energy uptake was on average 17.6 kWh in both temperatures. However, somewhat longer time was needed at low temperature to reach 100 % SOC compared to normal ambient. The reason is the limiting of the charging current

Table 3 Estimated range for each cycle at +23 and $-20\text{ }^{\circ}\text{C}$

Cycle	Estimated range		Difference -20 versus $+23\text{ }^{\circ}\text{C}$ (%)
	$+23\text{ }^{\circ}\text{C}$ km	$-20\text{ }^{\circ}\text{C}$ km	
NEDC	124	87.732	-29
Helsinki City	125	105.567	-15
Artemis Urban	99	73.637	-26
Road, FIN	91	69.928	-23
Artemis Road, EV ^a	113	90.051	-20
Artemis Motorway, EV ^a	72	53.448	-26
Average, all cycles	100	78.526	-21

^a EV denotes that warm-up part of the cycle is omitted

that the car manufacturer has built in the system. Interestingly enough, according to the user manual it shuts down the charging completely at $-25\text{ }^{\circ}\text{C}$.

The calculated estimates for range in each case are shown in Table 3.

When looking at the results in Table 3, we see that the estimated range can differ from a high of 125 km for Helsinki City cycle at normal temperature to a low of 53 km in Artemis Motorway at $-20\text{ }^{\circ}\text{C}$. Also if we compare the relative shortening of the range in each cycle case, we see that the range will fall short by some 20 % on average, while at worst it can be as much as nearly 30 % shorter, when the weather is cold.

We can compare these results with data published in [10] from similar measurements performed for a Mitsubishi iMiev that is basically the same car as Citroën C-Zero. However, Mitsubishi has more advanced transmission with three driving modes (D), (Eco) and (B), whereas Citroën and Peugeot have only one (D). Therefore, we can compare our figures only to results achieved by driving the Mitsubishi in D-mode.

If we compare the estimated range for European driving cycle, the UK laboratory reports 116 km, whereas our figure was 124 km; about 7 % more. Also in Artemis Urban cycle, our result (99 km) is longer than the UK figure (93 km) relatively about as much. However, in road and motorway cycles our results are closer to the UK results, as our estimations were only some 2–3 % higher than those of the UK lab. Part of this difference may come from the fact that the Mitsubishi was of 2010 model, and the particular Citroën that was measured at VTT was MY 2011.

As said before, all these measurements were done without the heater on. If we would employ also the heater at low ambient conditions, a further reduction in range would be seen. The nominal power of the PTC-heater is some 4.5 kW, and taking into account the average speed in each cycle, we can estimate the heater will draw additionally some 0.25 kWh/km in slow urban cycles and around 0.06 kWh/km in road/motorway cycles with higher speed. This will raise the total energy use quite substantially, especially in urban crawl, where the total is more than doubled because of the heater.

Table 4 Energy use of PTC heater and its simulated impact on range at $-20\text{ }^{\circ}\text{C}$

At $-20\text{ }^{\circ}\text{C}$, 4.5 kW heater cycle	Heater energy (kWh)	Total energy (kWh)	Estimated range (km)	Relative impact (%)
NEDC	0.134	0.334	53	-40
Helsinki City	0.236	0.402	44	-59
Artemis Urban	0.256	0.494	36	-52
Road, FIN	0.055	0.307	57	-18
Artemis Road, EV ^a	0.075	0.270	65	-28
Artemis Motorway, EV ^a	0.043	0.371	47	-11

^a EV denotes that warm-up part of the cycle is omitted

Table 4 summarises the results of this exercise.

The eventual impact on the range is of course also marked, and employing the heater can further cut down the range by more than 50 % in urban driving and by some 20 % on road/motorway type of driving. At worst case the range can drop down to only 36 km (Artemis Urban) with the heater full on.

If we compare these figures with data found in literature, we see that similar level of impact was also reported in [11]. The Canadian laboratory has measured three BEVs according to the J1634 procedure at $+20$, -7 and $-20\text{ }^{\circ}\text{C}$, and found that the range will on average be 20 % shorter than normal at -7° , and a further 25 % shorter, if the cabin heating was used. With use of maximum cabin heating at $-20\text{ }^{\circ}\text{C}$ ambient the range was reduced by 55–60 % from normal value in their tests. This data corroborates our findings very well.

6 Further Work

The work within the Nordic Project “RekkEvidde” will continue with in-laboratory measurements, where the driving resistance will also be modulated to match the results of coast-down tests on different road surfaces and snow conditions performed in Arjeplog, Sweden in March 2012. Those measurements should give the best estimate how much the range will eventually be shortened in winter driving conditions.

In parallel the authors continue to keep the issue of “more honest range estimates” on the agenda of forums like the IEA EVI, and subsequently try to engage into co-operation with the organisations performing same type of work both in Europe and in North-America, as well.

Acknowledgments The author acknowledges the invaluable help and expertise of Mr. Mikko Kallio and Mr. Ari-Pekka Pellikka for their expert efforts, ingenuity and time put into the instrumentation for these measurements. Furthermore, last but not least we owe our gratitude to Mr. Tommi Hangas-maa and Mr. Reijo Mikkola for the execution of tests at sometimes freezing conditions.

References

1. Gell RJ (2012) The development of a mobile EV charge solution to support the EV driver and delivered by the global automotive clubs. Paper EVS26-4270406. In: Proceedings of EVS26 international battery, hybrid and fuel cell electric vehicle symposium. Los Angeles, USA
2. Peugeot iOn, technical brochure. Accessed 28 Feb 2012. <http://www.peugeot.co.uk/Resources/Content/brochures/technical/peugeot-ion-prices-and-specifications.pdf>
3. Battery-electric Mitsubishi i EPA-rated at 112 MPGe combined, 62 mile “real-world” range. Green Car Congress, July 2011, <http://www.greencarcongress.com/2011/07/i-20110708.html>
4. Gordon-Bloomfield N (2012) Mitsubishi i gets official ratings from EPA, gets 112 MPGe. http://www.greencarreports.com/news/1062836_2012-mitsubishi-i-gets-official-ratings-from-epa-gets-112-mpge
5. Nissan leaf in Wikipedia. http://en.wikipedia.org/wiki/Nissan_Leaf. Accessed 8 June 2012
6. Nissan pegs Leaf range between 47 and 138 miles, individual results may vary. <http://green.autoblog.com/2010/06/14/nissan-pegs-leaf-range-between-47-and-138-miles-individual-resu/>. Accessed 8 June 2012
7. Draft proposal for terms of reference for proposed informal working group on electric vehicles and environment (EVE); Informal document No. GRPE-63-13 (63rd GRPE, 17–20 Jan 2012). <http://www.unece.org/fileadmin/DAM/trans/doc/2012/wp29grpe/GRPE-63-13e.pdf>
8. IEA forum at Paris motor show launches electric vehicles initiative—commitments for greater international cooperation on electric vehicles. IEA Press release. http://www.iea.org/press/pressdetail.asp?PRESS_REL_ID=398
9. André M (2004) Real-world driving cycles for measuring cars pollutant emissions—Part A: the ARTEMIS European driving cycles. Report INRETS-LTE 0411, p 97 http://www.inrets.fr/ur/ite/publi-autresactions/fichesresultats/ficheartemis/road3/method31/Artemis_cycles_report_LTE0411.pdf
10. Walsh C (2010) EV range testing. Centre of excellence for low carbon and fuel cell technologies, UK. www.cenex.co.uk/resources
11. Meyer N, Whittal I, Christenson M (2012) The impact of driving cycle and climate on electrical consumption and range of fully electric passenger vehicles. In: Proceedings of EVS26 international battery, hybrid and fuel cell electric vehicle symposium, Los Angeles

New AMFM Test Method with Android Operation System

Yongqing Zhu, Kerun Xu, Lubing Zeng, Minjie Tian
and Chendong Wang

Abstract With the rapid evolution of Android system, a portable, low cost, self developed test device become possible. The vehicle engineer will be able to use the cell phone with Android system and portable test kit to do the vehicle level test. There are many possible applications, one of them is the AMFM test application. Compared with the traditional test method, there are some advantages. First of all, the cost of the test device is considerable lowered. With the traditional test method, an electrical tune table is required to test the signal strength in 360°. The tune table, including the mechanical, electrical and fundamental part, costs twenty to thirty thousand USD. Maintain cost shall be additionally considered. Android test system will be an application installed in infotainment head unit. The embedded compass will record the orientation and link the test result. Tune table will be replaced. Secondly, the inconvenience of the traditional test is remarkably relieved. The tune table is a huge, expensive device, so it has to be established in proving ground. Normally speaking, proving ground is several hundred miles away from technical center. In addition, engineering vehicle is strictly prohibited to access freeway. It makes the test very inconvenient. Without the tune table involved in the test, engineer may find a place much nearer to the technical center, and do the test whenever needed. Last but not least, the flexibility of the test content is tremendously improved. The traditional test device provides some interface to engineer, but there is no way for engineer to give any suggestion. Android system provides many accesses to programmer, who may be a contractor or a supplier working with engineer together, so it's possible for engineer to design the test content, formula, and interface.

F2012-E14-038

Y. Zhu (✉) · K. Xu · L. Zeng · M. Tian · C. Wang
Pan Asia Technical Automotive Center Co., Ltd, Shanghai, China
e-mail: yongqing_zhu@patac.com.cn

Keywords AMFM · Turn table · Android · Mobile phone application

The Android operation system is rapidly developed in the recent several years. Many applications are developed. The reason why so many applications are developed is there are many software programmers involved in. The application market is open to the 3rd software programmer, so any new idea can be realized as long as Android operation system provides the interface.

Android operation system provides many application interfaces, such as cameral, flash light, as well as AMFM reception device. AMFM is a mainstream entertainment method for more than half century. AMFM antenna system development is normally done in the vehicle level antenna test lab. Antenna test lab is a EMC isolated room big enough for a vehicle to be tested in it. The antenna test lab is very expensive to be built, besides the lab need a very large field without trees, building or any metal materials. This kind of equipment is rear indeed, normally one antenna company has only one vehicle level test lab [1, 2].

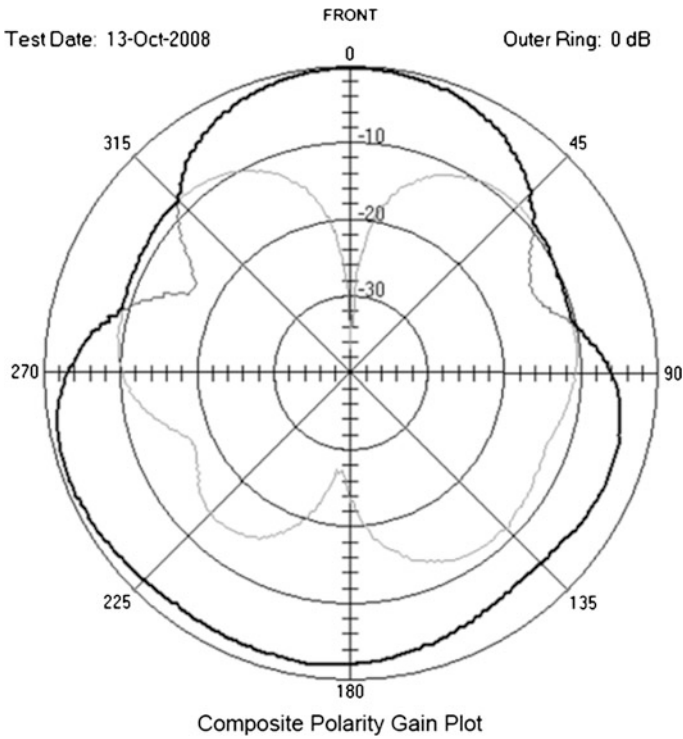
The proto type vehicle is built in the vehicle technical center. In order to develop the in vehicle antenna system, the proto type vehicle is to be shipped to the antenna test lab. But the vehicle level test lab is normally far away from the vehicle technical center, it's not convenient to ship the vehicle, not mention the difficulty of applying for moving a prototype car out of the technical center.

Android operation system in mobile phone provides a new method to settle this issue. One of the main purposes in AMFM test is to check the directionality of the antenna system. FM antenna system is sensitive to the direction. In some directions, the signal gain drop significantly. The customer will hear the noise when the vehicle turn to these directions. A good antenna system shall be not sensitive to the direction, so whatever the direction is the customer will not perceive any poor reception caused by direction [3, 4, 5].

In order to develop the non-direction sensitive antenna system, antenna engineer need to test the 360° reception gain and modify the antenna design to smooth the directionality. Due to the complexity of RF design, very few antenna system can be successfully designed without many rounds of modification, that's the reason why turn table is so widely used in the traditional antenna system design.

Because the tune table is a huge, expensive device, so it has to be established in proving ground. Normally speaking, proving ground is several hundred miles away from technical center. In addition, engineering vehicle is strictly prohibited to access freeway. It makes the test very inconvenient. Without the tune table involved in the test, engineer may find a place much nearer to the technical center, and do the test whenever needed.

The idea of developing AMFM test application in android operation system come from similar WIFI test application. There are many WIFI related application that help user to search WIFI source. For example, the WIFI hub will be show on the screen and the size of it indicates the signal strength. When the user turn around, a small WIFI hub picture will be moving in and out of the screen. When the user is facing directly to the WIFI hub, the WIFI hub picture will be right at the



Plot 1 360 Degree AMFM Signal Strength

center of the screen. That helps the user to locate the hub and a better place to surf online.

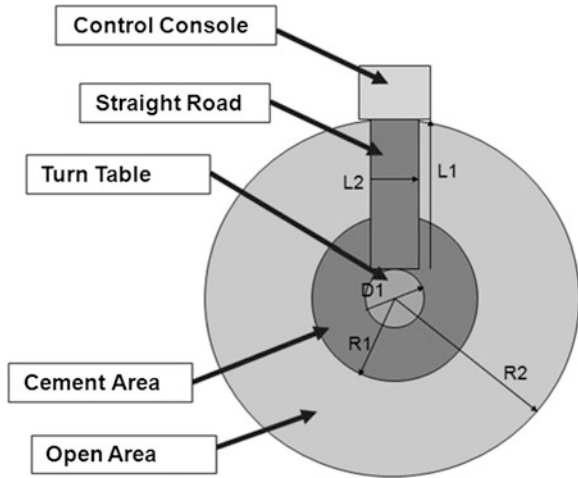
So why not to make a AMFM test application? The main reason that there is no AMFM test application in the open market is there is no customer requirement. A normal customer is not going to find out where and which direction the AMFM signal is stronger, and changes the location accordingly. But it's a very important function for an antenna engineer to know the signal strength and directionality.

Android operation system provides the compass API and AMFM API to the 3rd software programmer. Compass API able the programmer to develop the compass. AMFM API make the AMFM function possible. There are existing compass and AMFM radio applications in the open market.

As long as the direction information and the AMFM signal strength information is open to the software programmer, it's feasible to record the signal strength and its directionality at the same time. The purpose is to have a plot with AMFM signal stinger in 360° like Plot 1.

From the plot we can see that the signal strength in each direction varies significantly. This plot is normally need a turn table and some other RF test equipments. The turn table need some construction as Plot 2.

Plot 2 AMFM Turn Table
Design Concept



Control Console

Control Console controls the turn table with 1° per step. There shall be AC power outlet on or near control console. Distance from turn table to control console is $L1$, $L1 = 100$ m.

Straight Road

There shall be a straight road covered with asphalt or cement between turn table and control console. Length of road is $L1$, $L1 = 100$ m. Width of road is $L2$, $L2 = 15$ m.

Turn Table

Turn table is electric powered and controlled by control console with 1° per step. Turn table shall be capable to bear the weight of 5,000 kg. $D1$ is diameter of turn table. $D1 = 5.5$ m.

Cement Area

$R1$ is radius of the area covered with asphalt or cement. $R1 = 10$ m.

Open Area

$R2$ is radius of the area that shall be flat, without any building, vehicle, metal barrier or other reflecting constructions. $R2 = 100$ m.

It's quite expensive and time consuming to prepare such equipment, with the new android AMFM test application, the investigation will be cut and test itself can be much simplified. The main cost for the AMFM test application is to hire the 3rd software programmer to develop the application. Because the application is made for engineering development, instead of for final consumer, the interface doesn't need to be very good looking. Only the necessary data need to be recorded.

The necessary data is the AMFM signal strength, which is provided by AMFM radio API, and the orientation, which is provided by compass API. The data shall



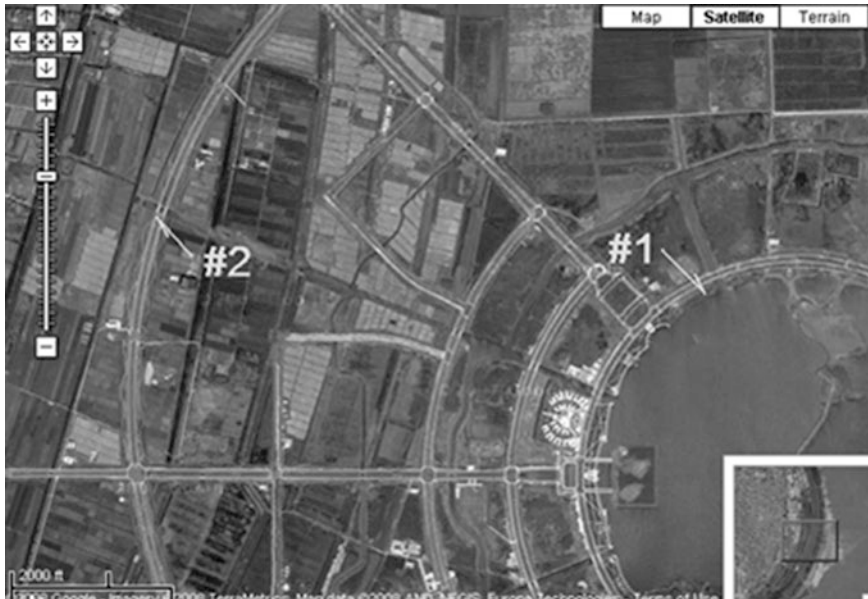
Plot 3 AMFM Field Test Site #2 in Google Map



Plot 4 AMFM Field Test Site on Site

be recorded and evened to increase the accuracy of the result. The test sample for each direction shall not be less than 10 samples. Before the test is being done, an open field shall be found like Plots 3 and 4.

The transmission tower is preferred to be set up. If there is no transmission tower, the existing AMFM radio station can be used as the signal source. Although the accuracy is not assured, the mainstream design can be investigated. Furthermore, antenna design may need to tune the antenna amplifier in the EE lab for



Plot 5 AMFM Field Test Site #1 in Google Map

several times. The EE lab is normally in the technical center, instead of in the proving ground. Going back to the technical center and then back to the proving ground may need a whole day, even more, not mention the risk of driving several hundred miles and the restriction of new vehicle in the public place.

Another advantage of using the existing AMFM radio station as signal source is it's far away from the test field. When the vehicle is moving, the radius of the circle can be ignored. If the transmission tower is set up by the antenna engineer, the distance between the transmission tower and vehicle will be no more than 100 m, while the radius of the moving vehicle shall be considered.

During the test, the in vehicle antenna system shall be connected to the Android device AMFM antenna. The Android device shall be firmly fixed in the vehicle, because the direction information, which is provided by the Android compass API, indicates the direction of the vehicle, and the direction of the antenna system as well.

The vehicle shall be moving slowly to make sure as many test samples as possible can be collected. The speed doesn't need to be even, because the recorded direction relies on the compass API, instead of the speed-orientation estimation method. In the case that the signal source is radio station, which is far away from the test field, a circle road can be used as show in plot, because the radius of the circle does not inference the test result. The circle road #1 in Plot 5, which is surrounding a round lake, is used to do the directionality test.

1 Conclusions

The traditional antenna test method needs the turn table and its infrastructure, as well as the test equipments, which is too expensive and too far away from the technical center, causing the antenna test not feasible. With the new in vehicle antenna test application, a table with the 360° orientation and signal strength can be formed. With the information in the table, the antenna system directionality plot can be made. The main purpose of this application is to replace the turn table and the equipments needed in the traditional antenna test method, so the antenna test is feasible.

References

1. Mitola J (1995) The software radio architecture. *IEEE Commun Mag* 5:26–38
2. Funderburk DM, Park S (1994) Digital receiver design for AMFM stereo signals using a general purpose digital signal processor. *IEEE Trans Consum Electron* 40(1):64–74
3. O’Leary P, Maloberti F (1991) A direct-digital synthesizer with improved spectral performance. *IEEE Trans Commun* 39(7):1046–1048
4. William S, Davis T, Rajkumar M (2005) *Operation systems: a systematic view*. Addison Wesley, U.S
5. Protocol buffers—google’s data interchange format: <http://code.google.com/p/protobuf/>

Part XV
Subjective and Objective Evaluation
of Performances

Ergonomic Evaluation System for Vehicle Package

Shihai Li, Yongqing Liu, Zhongxian Chen, Mengdong Mi, Hao Chen,
Weiwei Du, Tingchuan Song and Huang Jian

Abstract In the early days of automotive products design stage, validation of the package program primarily through the 3D virtual environment, and the 3D virtual environment is not virtualization specific enough and overall image; At the same time in the mid-term product development stage, rapid prototype production is completed, additional pay for rapid sample fixture to complete the production, transportation and installation, re-use is very low; Based on this, in order to validating the package program environment during the early days of automotive products design stage, in order to providing a platform for rapid sample during the mid-term product development stage, we need Ergonomic evaluation system. We have an introduction about the Ergonomic valuation system's research content, the Ergonomic valuation system should simulate the driver environment and other situation; including comfort machine, visibility, reach, entertainment establishment, including seat, paddles, steering wheel, console and so on. The Ergonomic valuation system's characteristics include multi-joint, high precision, enough interfaces for fast sample installation and safe for using. The Ergonomic valuation system can simulate the feasibility of ergonomic solutions in the early stages of project development; a multi-frame Ergonomic valuation system can reduce the cost of product development, because we don't need to make the base of the fast sample as before.

Keywords Ergonomic · Validation · Package solution · System · Project

F2012-E15-001

S. Li (✉) · Y. Liu · Z. Chen · M. Mi · H. Chen · W. Du · T. Song · H. Jian
Changan Auto Global R&D Centre of Changan Automobile Co. Ltd., Chongqing, China
e-mail: sunqiemail@163.com

1 Introduction

In the process of automotive products design stage, the way used to aiming at validating the ergonomic package project mainly through either the 3D virtual environment or reference automotive.

The virtual validation is the validated and analytical method that establishing the ergonomic project in the 3D environment. The virtual validation doesn't need actual parts to be processed or assembly, the cost of the virtual validation is very economical; at the same time; due to the 3D virtual environment, there is no error contrast with actual parts, at the same time, it can be used unlimitedly, besides, the state of environment is consistent; but the disadvantage is that the 3D environment can't completely exhibit the entire feeling such as the comfortable of ride, the feel of the space station.

The reference automotive validation is the method that the processing actual part based on ergonomic package project to validate [1]. It can completely exhibit the situation of the ergonomic package project, the effects of validating projects is the best [2]. But, in the beginning of the automotive products design stage, the projects can't be confirmed, the actual parts can't be processed, at the same time, the cost of the actual parts is so expensive that it can't be used widely [3].

So we need to build the Ergonomic evaluation system for vehicle package instead of the two methods above. By this machine, we can actual parts to validate the projects more impersonality, so that the result will be used to make the projects optimize. Finally, depress the risk of the whole automotive products design stage.

2 Necessary Functions

In order to evaluate all the ergonomic of vehicle, all the components can be located on the system; for example console, seat, roof etc. The following Table 1 shows all the components that ergonomic evaluation system can evaluate.

The content in the Table 1 include four types: vision roominess ingress/egress and comfort.

Vision: the vision of driver/front passenger/rear passengers. The vision must include two things, the driver or passengers can get information that form outside the vehicle; another thing is the components that driver or passengers should be observed.

Roominess: the roominess of driver/front passenger/rear passengers. The roominess is the distance for driver and passengers to drive and state in. The roominess also include the distance for user to operate the component.

Ingress/egress: all the vehicle need doors for user to get in or out. There need several passages that the user can easy to get in or out. So we must evaluate all the components that influence the ingress and egress.

Table 1 The functions of evaluation system

Vision	Roominess	Ingress/egress	Comfort
Direct view	Head room	Height of door cell	Comfort of seats
A pillar obstacle angle	Shoulder room	Location of A pillar	Comfort of pedals
Forward vision angle lower	Elbow room	Location of B pillar	Comfort of rest pedal
Forward vision angle upper	Hip room	Location of C pillar lower	Comfort of brake and gearshift
Rearward vision angle lower	Leg room	Location of C pillar upper	Comfort of armrest on console
Rearward vision angle upper	Knee room	Ingress and egress passage	Comfort of sun visor
Side view from side window for front passenger	Operate room of buttons on the steering wheel	Location of threshold	Comfort of steering wheel
Front view of rear passenger	Operate of pedals	Height of floor	Comfort of head lamp
Side view of rear passenger	Operate of sun visor		Comfort of safety belt
360° field of view	Operate room of buttons on the roof		Comfort of armrest on door
Cowl point and deck point	Operate room of release handle		Comfort of handle on door
Hood	The operate of the box on the door		Comfort of release handle
View field of cluster	Roominess of handles		Comfort of grab handle
Visibility of pedals	Roominess of grab handles		
Visibility of DVD	Operate roominess of brake and gearshift		
Visibility of buttons on dashboard	Operate roominess of cigarette lighter		
Visibility of brake	Operate roominess of seat		
Visibility of buttons on the door	Operate roominess of seat belt		
Visibility of cigarette lighter	Operate roominess of handle for side windows		
Visibility of combined switch	Operate roominess of combined switch		
Visibility of ashtray	Operate roominess of ignition switch		
Visibility of buttons on the console	Operate roominess of headlamp		
View field of outer mirror	Operate roominess of ashtray		
View field of inner mirror	Operate roominess of glass box		

Comfort: every vehicle has different dimensions, but the custom requirement will be also different, every component must be easy to see, every component must be easy to reach, every component must be easy to operate.

3 Key Factors

In order to evaluate the vehicle's ergonomic; the ergonomic evaluation system must own the following key factors.

First: the ergonomic evaluation system must be composed by the joints, all joint must be Adjusted. The joint on the Ergonomic evaluation system is the component that can be adjusted and locate automotive parts. The ordinary evaluation system don't have joint, so it can't be adjusted to evaluate different vehicle ergonomic proposal. The ordinary evaluation system will be cost because every project must spend the money to do the same work. The ergonomic evaluation system can save the money. Every joint on the ergonomic evaluation system must be length enough to adjust for different situation. For example the seat trace of different vehicle is different; if here need to evaluate the different vehicle's seat trace, the Adjustment range of the ergonomic evaluation system's seat adjust joint must as length as passable, but too length will be difficult to design the Ergonomic evaluation system, and will be cost. The number of the joints will decide. Over all the ergonomic evaluation system must be composed by joints; the number of joints should be the more the better; every the joint's adjustment range must be designed will carefully.

Second: the adjustment of the ergonomic evaluation system's joint must be quantified and polar adjust. There will be a lot of evaluation in the vehicle design, every evaluation proposal have different requirements, for the same joint need to adjust to different position, so the adjustment of joint must be polar adjust; the ergonomic evaluation system must be quantified, otherwise the user can't sure whether the joint have moved to the position where the proposal need. There will be another situation that every joint has moved to a position where the user don't required, but the proposal shows on the ergonomic evaluation system is quite good, all the position can be measured.

Third: the number of the ergonomic evaluation system's interface need as more as possibility. The interface of the ergonomic evaluation system is the fix position can fix vehicle part, Including bolt, screw, clamp and clamping device, Install the different parts form different vehicle to the Ergonomic evaluation system, A type of parts installed card access structure can also be a screw connection, With the location of the connection point of a connection is not the same. The Ergonomic evaluation system must have a large number of convenient interfaces.

The interfaces must have sufficient strength and stiffness.

Fourth: the ergonomic evaluation system. Many vehicle parts are installed on the Ergonomic evaluation system; the overall weight of the bench will be more

than 1 tons. Calculation and verification of structural strength is necessary, or the ergonomic evaluation system is easy to collapse in the running process; Stiffness of the calculation and verification is necessary, the Ergonomic evaluation system for a long time will be distorted, Evaluation of personnel and laboratory personnel will be a huge security risk. The component of the ergonomic evaluation system is made from metal. The high hardness of the parts will hurt people. It is necessary to consider the following two points in the design:

Materials Optimization: Easy wounding parts must be made of smaller hardness of the material, or use a smaller hardness of material to cover the greater hardness of the material. The easy wounding parts usually on the surface of the Ergonomic evaluation system, they are easy to reach people who use the Equipment. The smaller hardness metal includes Plastic, foam, fabric, etc.

Structural optimization: Reasonable structure to reduce harm, Adding specifications for construction support to ensure the bench do not collapse.

4 Main Structure

The Fig. 1 shows the preview of the ergonomic evaluation system. The ergonomic evaluation system is made by base, frame, roof, body.

The ergonomic evaluation system is composed by 16 functional units, each unit can simulate different ergonomic proposal. All the units are fix on the same base, the relationship between the units must be carefully conceded. All the units show the proposal that is useful for vehicle development. All the 16 functional units can simulate all ergonomic proposals in the Table 1.

Each unit is made up by joint. All joints can divide to two types, one is constitute by the screw, the interfaces on the joint can move along the screw; the other is rotating hinge, the interfaces on the joint can rotate by the joint. The ergonomic evaluation system includes 70 joints. Each joint has its own range of adjustment. We have done a survey of a large number of vehicles in the market. We can know how many is we need.

Simply here will show the seat unit structure as an example. Each seat unit include three joints, each joint is made by screw, so the seat can move along three directions; the directions are X direction Y direction, Z direction, each direction is drove by motor. Each seat unit includes one interface that can fix the seat on the joint. The interface on the joint is a metal panel which has a lot of holes on. Different kind of seat can be fixed on the metal panel. The following Table 2 is the information of the joint about driver and passenger.

The main structure of the seat functional unit shows as following Fig. 2. There are three joint in each seat unit, each joint can move along the crew. Here be a motor at the end of the crew which drive the crew. The green component in Fig. 2 is the interface of the seat unit. The seat can fix on the interface (Fig. 3).

Fig. 1 Preview view of the ergonomic evaluation system

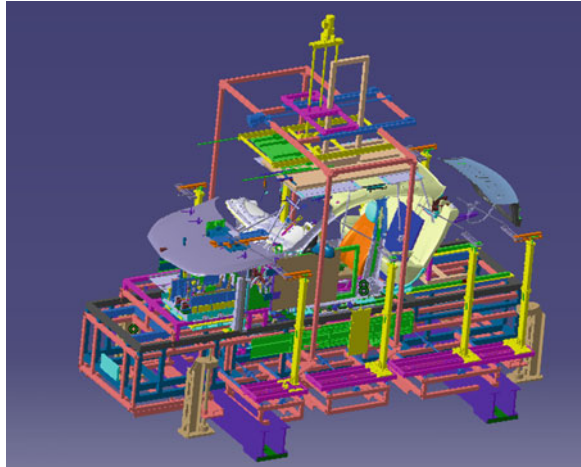


Table 2 The information about joints in seat unit

Joint name	Motor	Value
Driver seat X	Yes	460
Driver seat Y	Yes	150
Driver seat Z	Yes	100
Passenger seat X	Yes	150
Passenger seat Y	Yes	50
Passenger seat Z	Yes	200

Fig. 2 Side view of seat functional unit

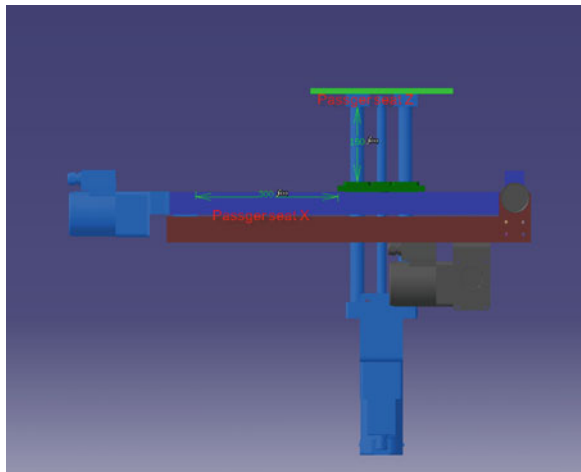


Fig. 3 Top view of seat functional unit

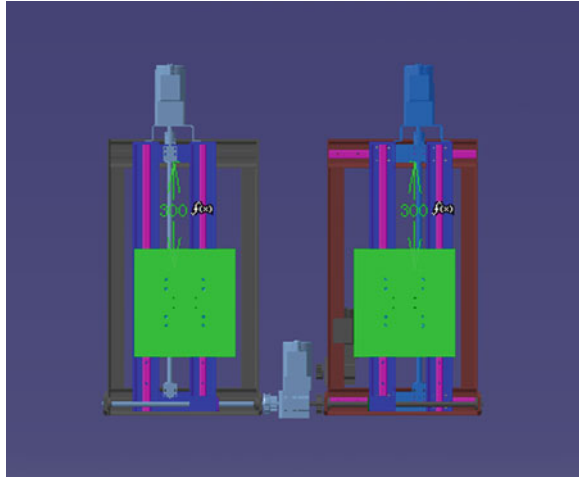


Table 3 The information about ergonomic proposal

Name	Vehicle	Value
Seat	EADON	
Roof	EADON	
Instrument panel	EADON	
Console	EADON	
Steering wheel	EADON	
A B C pillar	EADON	
Pedals	EADON	MT
Brake	EADON	

5 Accessibility

Here are too much joints to adjust, when we need to evaluate the ergonomic proposal. The adjustment will waste a lot of time and energy, a virtue ergonomic evaluation system is created in the CATIA, in order to save time. All the information of the ergonomic evaluation system is including, including joint structure, range of joint adjustment, and interface of the seat unit. It must be evaluation in the virtue ergonomic evaluation system before simulate in the ergonomic evaluation system.

6 Evaluation

Here will be a test to evaluation the ergonomic evaluation system.

The test progresses have 4 steps. First of all, the information of the ergonomic proposal must be ready. The following Table 3 is the information of the ergonomic proposal.

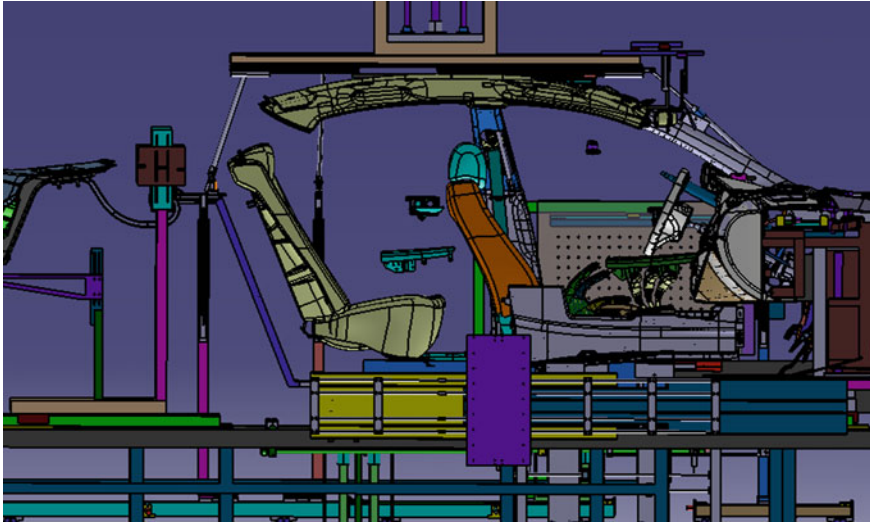


Fig. 4 Evaluation of the virtue evaluation system

The second step: the evaluation in the virtue ergonomic evaluation is required. The Fig. 4 is the evaluation of the test. All the parts of EADON can fix to the interface of the virtue ergonomic evaluation system.

The Table 4 is the value of the joint which have fixed the EADON's parts.

The third step: The parts of EADON must be fixed onto the ergonomic evaluation system, and adjust all the joints to the right position. The Fig. 5 is the preview of the ergonomic evaluation system after fixed the parts.

The fourth step: the measurement of the ergonomic evaluation system must be done. The Table 4 is the result of the measurement.

Results: The ergonomic evaluation system can simulate the ergonomic proposal.

7 Results

The virtual ergonomic evaluation system has setup in CATIA. First evaluate the ergonomic proposal in the CATIA virtual ergonomic evaluation system; we can get the value of the joints to adjust the ergonomic evaluation system, at last check the proposal shows on the ergonomic evaluation system. The ergonomic evaluation system can evaluate the ergonomic proposal.

We have fixed the parts on the ergonomic evaluation system, all the part are fixed by the interfaces in the right position and right way.

Table 4 The value of joints on the virtue ergonomic evaluation system

Name	Vehicle	Name	Value
Bottom Z	200	D Pillar-L X1	53
Roof X1	-26.5	D Pillar-L Z	18.5
Roof Z	350	D Pillar-L X2	30
Roof X2	434	D Pillar-L Y	30
A Pedal Y	33	CD Pillar-R Y	37
A Pedal Z	44.3	C Pillar-R X	820
A Pedal X	200	C Pillar-R Z	18.5
B Pedal Y	150	C Pillar-R Y	30
B Pedal Z	46	D Pillar-R X1	53
B Pedal X	228.9	D Pillar-R Z	18.5
C Pedal Y	19	D Pillar-R X2	30
C Pedal Z	44.3	D Pillar-R Y	30
C Pedal X	250	Sill-L Z	137
A Pillar-L Y1	37	Sill-R Z	137
A Pillar-L X1	41	Seat Occupation Seat Y	41
A Pillar-L Z	18.5	Seat Occupation Seat-L X	37
A Pillar-L X2	30	Seat Occupation Seat-L Z	29
A Pillar-L Y2	30	Seat Occupation Seat-R X	37
A Pillar-R Y1	37	Seat Occupation Seat-R Z	29
A Pillar-R X1	41	Shift X	44.1
A Pillar-R Z	18.5	Shift Z	7
A Pillar-R X2	30	Shift Y	2.522
A Pillar-R Y2	30	Hand Brake X	337.923
B Pillar-L Y1	37	Hand Brake Z	7
B Pillar-L X	50	Hand Brake Y	2.522
B Pillar-L Z	18.5	Driver seat X	460
B Pillar-L Y2	30	Driver seat Y	150
B Pillar-R Y1	37	Driver seat Z	100
B Pillar-R X	50	Passenger seat X	150
B Pillar-R Z	18.5	Passenger seat Y	50
B Pillar-R Y2	30	Passenger seat Z	200
CD Pillar-L Y	37	SW-Z	100
C Pillar-L X	820	SW-Y	310
C Pillar-L Z	18.5	SW-X1	10
C Pillar-L Y	30	SW-X2	10
		SW-ADEG-01	20

8 Innovations

The Innovations of The ergonomic evaluation system as following:

First: Build intuitive and specific physical environment that can simulate the ergonomic proposal;

Second: the ergonomic evaluation system can improve the correctness of the proposal;

Fig. 5 Preview of the ergonomic evaluation system after fixed seat



Third: the ergonomic evaluation system can save money; we don't need to make the rear vehicle to evaluate the ergonomic proposal;

Fourth: the interfaces of the ergonomic evaluation system can join different parts from different car, it is useful and convenient.

9 Limitations

First: Most of the joints on the ergonomic evaluation system must be manually adjust, because there is not enough money for this research topic. So we have to spend more Energy and more time to adjust the ergonomic evaluation system.

Second: The virtual ergonomic evaluation system in CATIA and The ergonomic evaluation system are independent of each other.

We will improve the system in the next research steps; we change the value of the joint in CATIA the ergonomic evaluation system will move to the position that shows in the CATIA. So we can improve the efficiency and save money.

10 Conclusions

In the early stages of vehicle development, we can not use the real vehicle to evaluate the ergonomic proposal; but the ergonomic evaluation system can easily simulate ergonomic proposal. We can obviously aware of the feasibility of the ergonomic proposal. So the ergonomic evaluation system can improve the efficiency of the vehicle development, it can save time. It can avoid trial and error of ergonomic proposal.

References

1. SAEJ1100-2002 vehicle dimensions
2. Ergonomic Chinese Construction Industry Press
3. Application of Ergonomic Mechanical Industry Press

Subjective and Objective Vehicle Tests, Two Parallel Vehicle Handling Evaluations

Eric Chabrier and Michel Grima

Abstract Subjective and objective tests have long been used for estimating on road vehicle handling, in DGA Angers, in order to address safety problems which can occur in risky configurations. On one part, objective tests are used to measure vehicle dynamics characteristics, in ISO tests and in specific manoeuvres, mainly: (1) Steady state turning at constant radius; (2) Double lane change tests. On the other part, trained drivers give ratings to vehicle handling and dynamics characteristics, in a more comprehensive way. The aim of this paper is to present completeness or links which exist between subjective and objective tests which are carried out in order to have a comprehensive evaluation of all kinds of vehicles tested in DGA Angers. With instrumented tests and ratings given by trained drivers, correlations have been researched based on available tests results in DGA Angers which is in charge of vehicle tests whose results are used for giving them driving agreement. These links are presented and discussed in this paper focused on evaluation of safety performance made on a large spectrum of vehicles.

Keywords Vehicle · Safety · Subjective · Objective · Tests

F2012-E15-004

E. Chabrier · M. Grima (✉)
DGA Angers, Angers, France
e-mail: migrima@wanadoo.fr

1 Introduction

In DGA Angers test center,¹ all tests which are carried out on vehicles, are designed in order, not only to assess mobility performances, but also, at the very beginning of the process, to make decision on the vehicle ability to be driven safely.

To do so, criteria related to vehicle safety in critical situations has been defined with threshold values.

Compliance of vehicle under test is evaluated with respect to objective and subjective performances requirements, which are expressed in term of threshold values for each criteria related respectively to subjective and objective vehicle performances.

The system which is under test, is composed of a test driver who imposes actions on the vehicle which react dynamically to road or terrain configurations and to meteorological conditions, as it is illustrated on Fig. 1.

In order to minimize the influence of the driver on test results, several drivers can carry out each elementary tests.

Handling limits of vehicles, in all configurations that can be encountered, has to be assessed in DGA Angers test center. So using subjective and objective tests, procedures have been defined for each elementary test of these two categories of test, these procedures are strictly applied by a team of test drivers who have more than 5 years of experience for driving a large spectrum of vehicle (light medium and heavy vehicles) up to their limits.

2 Literature Survey

Many works and research have been made in the past to address vehicle safety and handling evaluation.

An important topic is related to criteria used in subjective and objective tests which are to be carried out, in order to evaluate vehicle handling characteristics which can affect vehicle safety, with an exhaustive spectrum of tests.

Another important topic is related to the research of links and correlations between objective and subjective handling tests.

One can notice an interesting thesis [1] which studied these two testing approaches and their links. One aim of this thesis was to relate drivers subjective ratings with measurement results of objective tests.

For several configurations of a light vehicle, subjective and objective results have been studied for a large number of handling aspects, on the basis of tests carried out at MIRA with 8 drivers, for several configurations of a vehicle.

¹ French Ministry of Defence trial centre dedicated to testing land military vehicles.

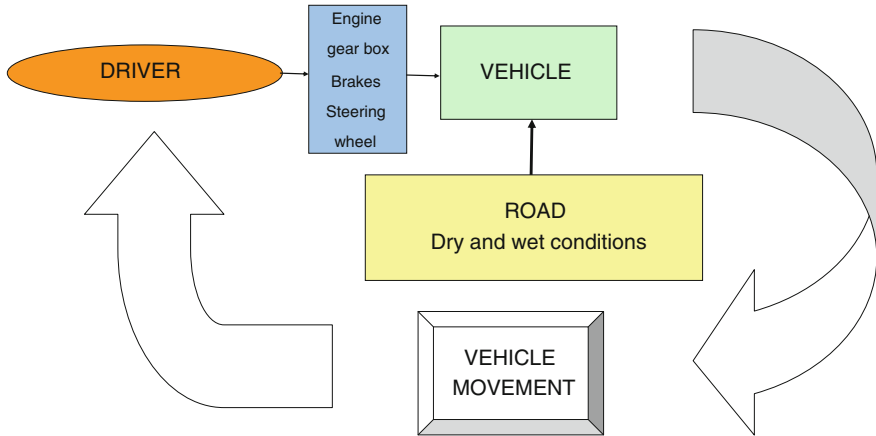


Fig. 1 Vehicle—driver—road system

This work described clearly a process which allows to compare and find relations between the two approaches.

Another study [2] based on D Chen works, Ash studied relations between objective metrics and subjective driver ratings of vehicle handling.

In DGA Angers test center, objective and subjective tests have been carried out together, to assess vehicle behaviour safety, even in off road conditions [3].

3 Objective Tests

On road objective tests are done, in DGA Angers test center, with instrumented vehicle, using standard test procedures, in order to collect data related to steering column, braking system, vehicle movement

In order to register during these objective test, time histories of physical parameters of interest, are registered with an on board measurement system (see Fig. 2) composed of a laptop connected to sensors, mainly:

- a fifth wheel fixed behind chassis vehicle which measure vehicle speed;
- a steering wheel sensor for measuring hand-wheel angle;
- a sensor for measuring force on brake pedal;
- a yaw rate sensor.

Objective tests for assessing vehicle dynamic behaviour safety are:

- Braking tests;
- Steady-state turning tests;
- Double lane change tests.

Fig. 2 Vehicle instrumentation

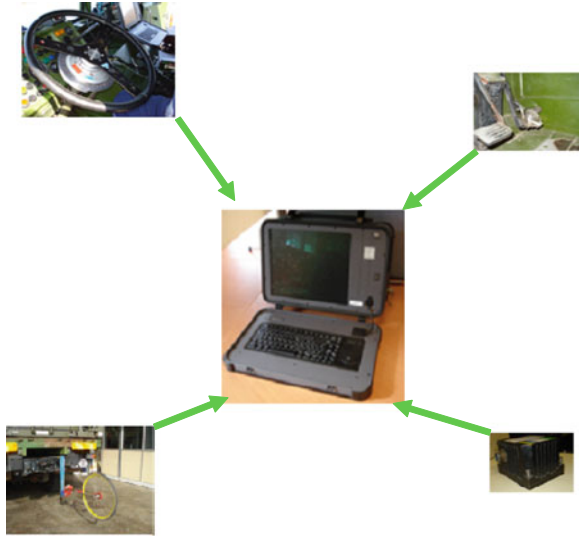


Fig. 3 Emergency brake test



- Braking tests in straight-line:

Two types of braking tests are made in straight-line, a first one to control the conformity, of the specimen under test, to regulation and standards, and a second one to evaluate the lateral deviation of vehicles after an emergency braking at maximal initial speed before vehicle braking (see Fig. 3).

- Braking tests in curve:

This test evaluates behaviour of a vehicle on a curve, disturbed by the braking action of the driver.

Transient evolution of the yaw rate is measured in order to evaluate the compliance of specimen to safety criteria which are estimated during braking phase

- Steady-state turning at constant radius (Fig. 4).

Fig. 4 Steady-state turning tests on dry and wet conditions



Fig. 5 Double lane change test



This test is realized on a 525 ft diameter circular pad, which can be totally sprayed to create wet conditions. Vehicle response to steering is identified through steady-state turning tests made at a constant turning radius, following ISO 4138 standard.

Results of this test are transverse acceleration limit and variation of hand-wheel angle versus lateral acceleration.

The hand wheel angle gradient can then be deduced, giving information about behaviour characteristics of vehicle on curves. Specimen can have under steer (for positive gradient) or over steer (for negative gradient) tendency, which gives information on their performances related to safety.

Required levels for steady-state turning performances assessment are given for each vehicle category and for the loading configuration of vehicle.

Vehicle Categories	M1 & N1		M2, M3, N2 & N3	
Loading condition	Empty	Full loaded	Empty	Full loaded
(ay)Lim (m/s ²)	≥ 6	≥ 5.5	≥ 4.5	≥ 3.75

- Double lane change (Fig. 5):

Evaluation of the stability of vehicles during an avoidance maneuver is made up to the maximal possible mean speed.

The test zone is defined by cones laid on the ground, on a hard and level surface, following AVTP standards 03-160, tests are carried out to check ability of vehicles to realize a double lane change.

The result of the test is the mean maximal achievable speed for crossing the test lane.

Required levels for double lane change performance are given for each vehicle category.

Vehicle Categories	M1 & N1	M2, M3 & N2	N3
Maximal mean speed for crossing the test lane	80 % of Vmax limited to 95 km/h	80 % of Vmax limited to 80 km/h	80 % of Vmax limited to 70 km/h

4 Subjective Tests

On road subjective tests are done with qualified drivers trained to analyse vehicle behaviour and to be able to translate their feelings of vehicle response in dynamic conditions in precise terms.

After rigorous defined elementary tests, these drivers produce indexed reports on dynamic behaviour of specimens under test, based on evaluation of criteria.

The aim of these tests being:

- to evaluate capability of vehicles to move safely during their missions or through road traffic;
- to put in evidence vehicle defaults related to its dynamic behaviour;
- and to identify their defaults origin.

This is done by defined subjective tests carried out by test driver teams, analysis of trained drivers lead to ratings for each elementary and in the end to a global rating of vehicle behaviour.

Subjective rating scales are used to give numerical values to their subjective analysis of particular vehicle characteristics.

Required levels of road subjective performance are given for each vehicle category.

Vehicle Categories	M1, N1	M2, M3, N2 & N3
Global rating	≥ 6	≥ 5

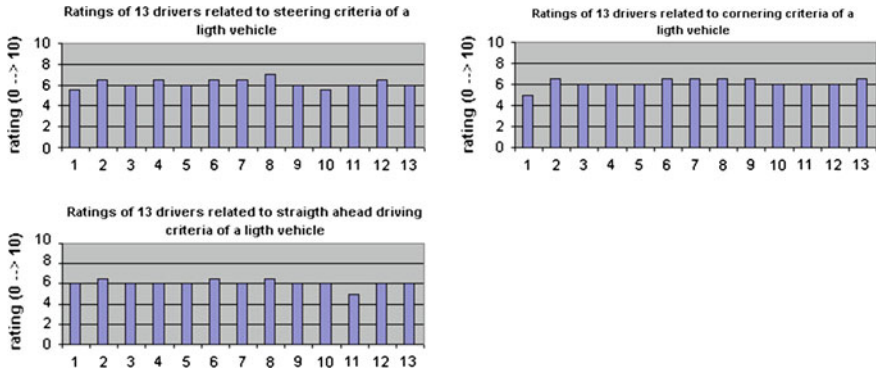


Fig. 6 Ratings obtained in a training session for a light vehicle

Trainings are regularly organized to maintain drivers ability to give ratings in accordance to what is expected for reference vehicles in defined configurations.

Two examples of ratings (Figs. 6 and 7) obtained for a light vehicle and for a 12 t truck, shows little discrepancies that can be observed between members of a test team who have regularly training sessions designed to maintain knowledge and know how on vehicle subjective tests.

5 Comparison Between Objective and Subjective Tests

Braking performances of vehicles are part of objective and subjective test carried out in DGA Angers test center, but they are not considered in this paper, only steady-state turning tests and double lane change tests results are compared to subjective tests global ratings.

Subjective tests global ratings are based on criteria ratings obtained with handling tests to assess mainly cornering, straight-line running and steering characteristics.

These two families of test are compared in order to put in evidence their relations.

From a global point of view, the two following graphics of Fig. 8 present objective and subjective test results obtained for a large spectrum of vehicles tested in DGA Angers test center, including for some of them several results obtained for the same vehicle for several configurations: empty, partially loaded and full loaded.

For a given vehicle in a given configuration, two objective tests results:

- double lane change test result;
- and steady-state turning (at constant radius) result, have been compared to global ratings of subjective tests, obtained with the same vehicle configuration.

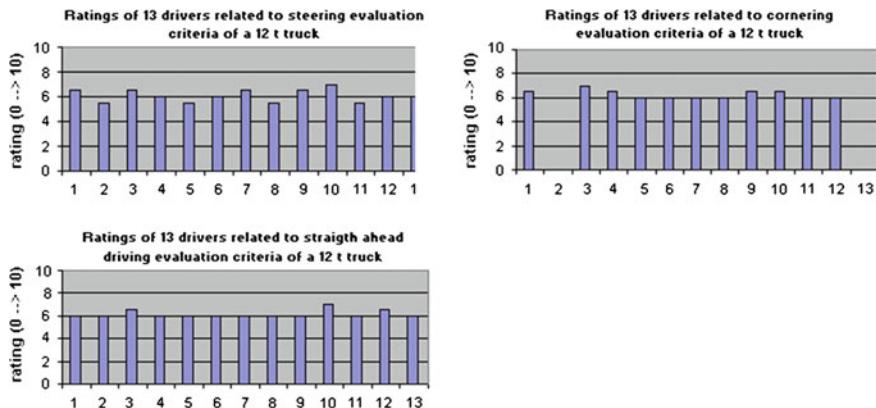


Fig. 7 Ratings obtained in a training session for a 12 t truck

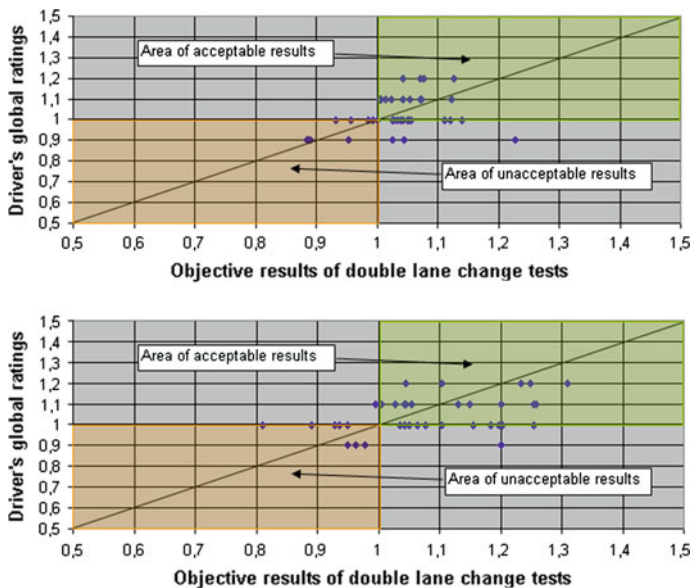


Fig. 8 Links between objective and subjective test results

Values are given in a normalized form, the borderline value (e.g., 1) corresponds to value of ratings or objective results equal to required level for the test.

It can be noticed that when vehicle objective performances are not compliant with minimum required performance, vehicle subjective tests put in evidence unacceptable ratings.

Conversely, when vehicle objective performances are compliant with minimum required performance, vehicle subjective tests put in evidence acceptable ratings in

almost all the case, except for some where subjective analysis put in evidence problem of handling in specific situations: e.g., straight-line running on uneven roads...

But there are no results on upper left sectors of graphics, thus giving confidence in the validity of subjective ratings.

6 Conclusion

Subjective and objective vehicle tests are two complementary approaches which can be used in order to evaluate vehicle handling performances. These two types of tests are carried out, in DGA Angers test center, in order to be sure, that vehicles under test behaviour are compliant to safety requirements.

In some cases, and in order to have a rapid evaluation of vehicle handling characteristics, subjective tests which are less time and cost consuming can be carried out especially to compare handling of a vehicle for different configurations.

Confidence we can give to subjective tests depends on driver's training and skill which must be maintained with recurrent training sequences and precise procedures which must be strictly applied by drivers.

For the future, understanding of links between subjective driver's ratings and objective test results must be improved by studies taking into account available vehicle objective and subjective test results gathered in a test results database.

In the end, drivers feelings and their subjective ratings must be considered as the most important statements about vehicle safety.

References

1. Chen DC (1997) Subjective and objective handling behaviour, PhD. Thesis, University of Leeds, England
2. Ash HAS (2002) Correlation of subjective and objective handling of vehicle behaviour, PhD thesis, University of Leeds, England
3. Chabrier E, Ramaen C (2003) Vehicle behaviour in all-terrain conditions, analysis methods and driver training, ISTVS, 9th European Conference, Harper Adams, UK

Subjective Evaluation and Modeling of Human Ride Comfort of Electric Vehicle Using Tools Based on Artificial Neural Networks

Lerspalungsanti Sarawut, Albers Albert and Ott Sascha

Abstract This article presents an application of the human comfort objectification tool developed based on the Artificial Neural Networks (ANNs) to support the development of drive train system. The main objective of this study is to apply the developed tool to predict the subjective comfort rating of different driver types during the start-up procedure, i.e. the process of starting to drive from standstill with releasing of the brake and reaching of constant travel speed. In this case, test drives performed by drivers representing potential customers are carried out with a commercial electric vehicle. The subjective evaluation in terms of customer satisfaction is executed based on the 5-digit scale. During the experimental investigation, the predefined objective parameters are captured. They are the resulting longitudinal acceleration measured at the different locations of the driver seat, the vehicle velocity, the vehicle acceleration as well as the standardized courses of the accelerator pedal and the brake pedal. The human sensation modeling is carried out by determination of the relationship between the objective parameters, like the power spectral density (PSD) values of the longitudinal acceleration captured at passenger seat and the subjective comfort ratings. An ANN is applied to interconnect output data (subjective rating) with input data (objective parameters) by “trained” weighted network connections. The results of the investigation have demonstrated that the objective values are efficiently correlated with the subjective

F2012-E15-005

L. Sarawut (✉)

National Metal and Materials Technology Center (MTEC), National Science and Technology Development Agency (NSTDA), Chiangmai, Thailand

A. Albert · O. Sascha

Institute of Product Engineering (IPEK), Karlsruhe Institute of Technology, Karlsruhe, Germany

sensation. Thus, the presented approach can be effectively applied to support the drive train development of electric vehicle.

Keywords Electric vehicle · Comfort evaluation · Objectification · Human sensation modeling · Artificial neural networks

1 Introduction

Nowadays, the large number of R&D activities regarding to transportation have emphasized the development of high-efficiency, clean, safe and sustainable transportation. Alternative energy vehicles such as electric vehicles (EVs) have been proposed to substitute conventional vehicles in the near future. One of challenges of today automotive industries is to develop the electric propulsion system of an EV which can sustain passenger demand of vibration comfort and safety during different driving situations such as start-up, acceleration and deceleration.

Many research projects related to the prediction of human comfort have been carried out for years by the IPEK—Institute of Product Engineering, Karlsruhe Institute of Technology (KIT). The aim is to develop methods and tools to identify the vehicle dynamic properties in the early stage of the product development process. This is achieved based on the prediction of the subjective comfort rating. The results of the investigation (i.e. vehicle start-up) have prior demonstrated that the objective values generating from test benches and simulation models are efficiently correlated with the subjective comfort evaluation [1–3]. The correlation is achieved by means of the developed method based on Artificial Neural Networks (ANNs) [3]. As described in [3], the prediction of the subjective evaluation from objective data which are captured from the real and virtual vehicle can be achieved by using the developed method of comfort objectification. The aim of the current study is to implement the developed ANN-based methods and tool, which are presented in Sect. 2, in the field of electric vehicle. In Sect. 3, the field test procedures and the experimental setup of the test vehicle are demonstrated. Sect. 4 refers to the human sensation modeling results for prediction of the customer comfort rating of various start-up characteristics, followed by a conclusion and prospect in Sect. 5.

2 Approach of Human Comfort Objectification Based on Artificial Neural Networks

This section presents the systematic procedure to identify and evaluate the dynamic features of vehicles or assemblies using ANNs.

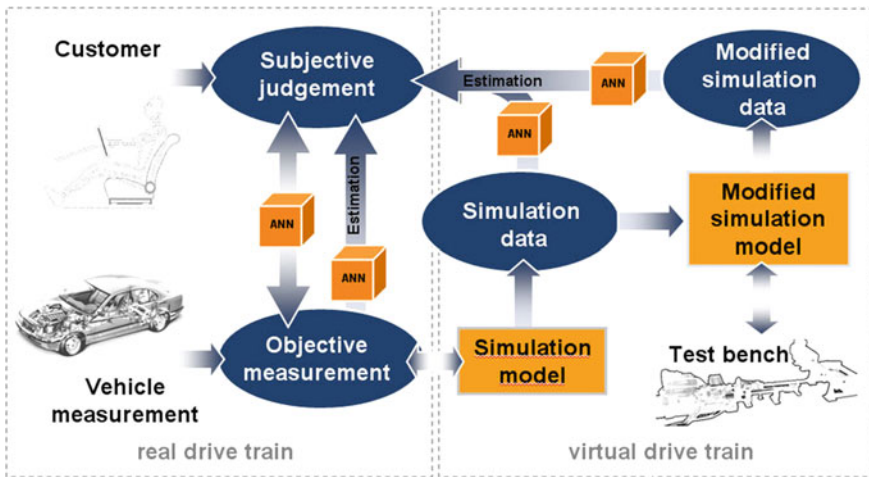


Fig. 1 Approach of comfort objectification based on integrated drive train development at the IPEK

2.1 Approach of Customer Comfort Prediction

A generic method to determine the dynamic features of drive train commonly requires drive tests with passenger and real prototypes. Consequently, these lead to time-consuming modification on real vehicle and additional costs. To partially compensate these disadvantages, an approach of comfort objectification [3] based on integrated drive train development is developed, as shown in Fig. 1.

From the situation analysis, the development concepts and the target customer group are to be determined on the basis of the defined requirements. Consequently, the potential solutions in form of concepts or ideas to achieve of the required comfort evaluation are to be concretized and converted by modifying drive train assemblies. To be able to estimate the comfort rating, the human sensation models based on Artificial Neural Networks (ANN) are elaborated. According to the virtual product development, the prediction of passenger subjective comfort assessment can be executed using the objective data. These can be either measured from the real prototype or generated from the numerical model. By means of the estimation of the subjective comfort rating and the customer acceptance, the suggestions for one or more alternatives for a solution pave a way for a decision to be taken by a developer. To assure the required product properties, the progress made with the design is needed to be continually approved. This is accomplished by means of vehicle tests, test benches and simulation models. By combination of simulation methods and experiments on test bench, the investigation of dynamic properties of the drive train can be carried out in an early stage of product development process.

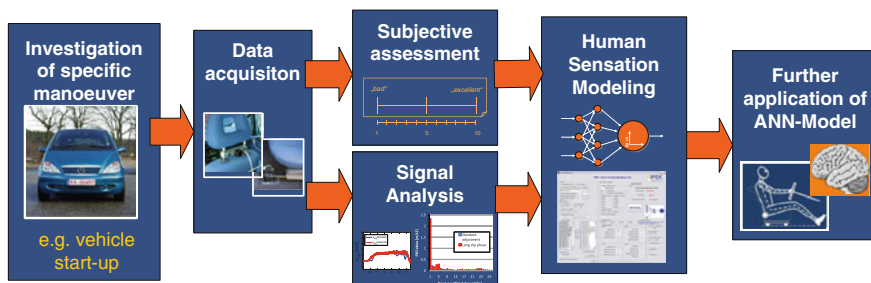


Fig. 2 Methodology for the development of the ANN-based human sensation model [2]

2.2 Modeling of Human Sensation

An Artificial Neural Network (ANN) is defined as a computational model mostly used either to find a relationship between inputs and outputs or to recognize a data pattern [4]. The ANN can be described with a simplified mathematical function $z(w, x)$, which is commonly defined by the nonlinear weight sum according to:

$$z(w, x) = f\left(\sum_k w_k \cdot x_k\right) \quad (1)$$

z denotes the output vector consisting of the data to be approximated. x represents the input vector consisting of k input nodes x_k . w denotes the vector of the connection weights w_k between the input node x_k and the output node z . The type of the function z is defined by the applied activation function f . This can be either linear or nonlinear function, such as the log-sigmoid function. In this case, the ANN-model is introduced to find a correlation between the objective data and a subjective comfort assessment from the individual customer point of view. The operating principle of ANN for the current research is illustrated in Fig. 2.

To objectify the human sensation according to each driving manoeuvre, the comfort-relevant characteristic values are to be predefined. After obtaining all data, both sets of objective value representing the input data and the subjective evaluation denoting the target data are combined into a “pattern file”. This is used as a data set for the driver sensation modeling. To simplify this process, the “Driver Comfort Modeling Tool” is developed as presented in [3]. To predict the subjective comfort rating of performed test drives, the “knowledge” of trained ANNs is applied. The modeling results are described in following section.

3 Test Programme and Data Acquisition

This section presents the modeling results of vehicle start-up evaluation. By means of the presented ANN-based tools, a non-linear relation of subjective comfort assessment and objective data of each driver can be found and applied to evaluate the vehicle start-up properties and its effect on human comfort sensation.

3.1 Vehicle Start-up Process

One particular driving situation which mostly influences the ride comfort is the start-up procedure of vehicle, i.e. the process of starting to drive from standstill with releasing of the brake and reaching of constant travel speed. Drive tests were performed by 50 laymen between 30 and 50 years of age representing average consumers; they should have not ever take part in any special training in terms of vehicle evaluation. Each person is asked to perform a total of 18 tests which consist of 2 start-up alternatives, the normal or D mode and the ECO drive mode [5]. Both test configurations are carried out at 3 different pedal values at 40, 80 % and maximum of pedal travel. A total of 3 courses for each configuration were carried out on the test track allowing repeatable driving conditions.

3.2 Experimental Set-up

This experimental set-up was developed to generate different variants of start-up characteristics of an intermediate-class commercial electric vehicle equipped with measurement system for data acquisition. The start-up characteristics are set to different variants by applying different levels of accelerator pedal limitation. Characteristic values are derived from data obtained in each test and the corresponding comfort ratings are captured.

During start-up process, all predefined characteristic values are captured. They are the resulting longitudinal acceleration measured at the seat rail $a_{seatrail}$, the longitudinal acceleration measured at the neck rest $a_{neckrest}$, the longitudinal acceleration captured under a seated person a_{seat} , the vehicle velocity $v_{vehicle}$ and the vehicle acceleration $a_{vehicle}$. In addition, the corresponding standardized course of the brake s_{brake} and those of the accelerator pedal s_{acc} are captured using the compact string potentiometer. Examples of the measurement of the longitudinal acceleration using piezoelectric accelerometers at the neck rest and the seat rail and the measurement of vehicle velocity during start-up process are shown in Fig. 3.

The following figures on the left are examples showing the standardised courses of the brake, those of the accelerator pedal and the resulting longitudinal

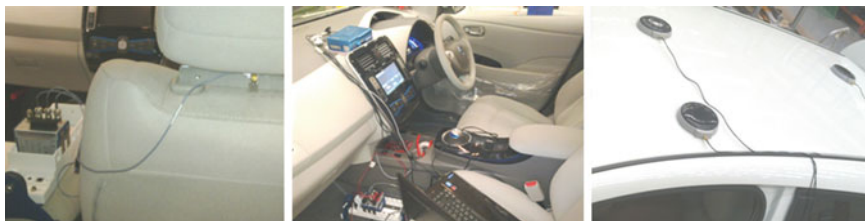


Fig. 3 Installation of accelerometer at neck rest (*left*); GPS-based vehicle velocity sensor and data acquisition system (*middle*); Installation of vehicle velocity sensor antenna (*right*)

acceleration measured at the neck rest. On the right, the corresponding time course of the vehicle velocity and corresponding acceleration in driving direction, obtained from the GPS-based speed sensor are presented.

Figures 4 and 5 demonstrate the curve corresponding to the alternative with normal drive mode and the one with the ECO drive mode, respectively. These indicate the different vehicle response due to a similar driver demand in terms of accelerator pedal travel of 40 %.

In this study, the subjective assessment has been performed on a basis of the 5-digit scale representing different levels of customer satisfaction. As illustrated in Fig. 6, the left endpoint marked as 1 stands for “unacceptable” and the right endpoint marked as 5 means “excellent”.

4 Model Application and Results

This section presents the capability of the objectification tools and the elaborated ANN models to estimate the customer comfort ratings of different start-up situations.

4.1 Human Sensation Modeling and Results

As illustrated in Fig. 7, an ANN is applied to interconnect input data (objective parameters) with output data (comfort evaluation) by “trained” weighted network connections as the way a test person makes his evaluation.

There are several alternatives to set a network structure defining human sensation model [3]. To reach the highest performance possible for each task, the appropriate network setting consisting of network topology, training algorithm or training parameters is required. The developed driver comfort modeling tool shown in [3] allows users to build different network structures. After the processes of training, validation and verification, the modeling results consisting of the performance value G [3], the sequence of weight initialisation and the number of

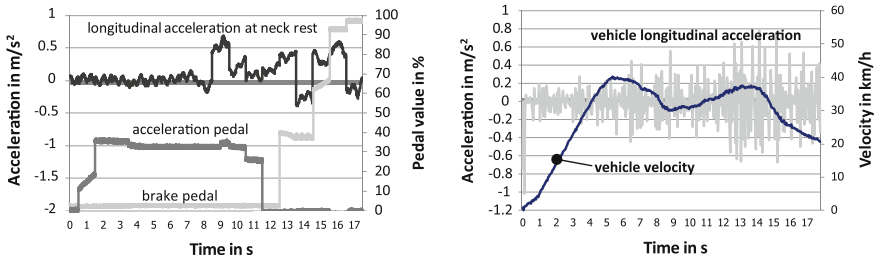


Fig. 4 Example time courses start-up with the normal drive mode @40 % pedal travel

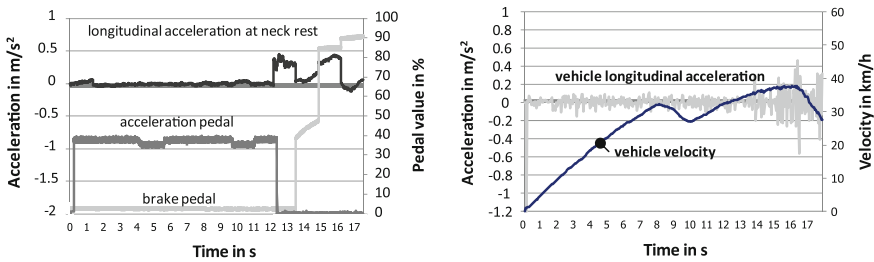


Fig. 5 Example time courses start-up with ECO drive mode @40 % pedal travel

Unacceptable	Improvement required	Satisfied	Good	Excellent
1	2	3	4	5

Fig. 6 5-digit scale for comfort evaluation

training epochs are obtained. In this case, the resulting prediction performance G of 87 % is achieved from the trained ANN with a total of 60 objective parameters derived from the start-up duration, the maximum longitudinal acceleration measured at all described locations of driver, the corresponding power spectral density from 0 to 100 Hz, the maximum longitudinal acceleration of the vehicle as well as the accelerator pedal speed representing driver demand in terms of the start-up. The elaborated ANN-model consists of 3 hidden neurons and an output neuron corresponding to a predicted comfort assessment by using the Levenberg–Marquardt algorithm. During the application stage, this ANN can be later applied to estimate the vehicle start-up comfort evaluation based on the generated objective data from other test alternatives.

Figure 8 demonstrates an example of comfort ratings performed by a test driver with the subjective comfort ratings on the abscissa and the ANN output values calculated using the corresponding ANN-model on the ordinate. If exact approximation was possible, all points would lie on the first bisecting line. By using the trained ANN with G of 87 %, a relatively good correlation of the subjective

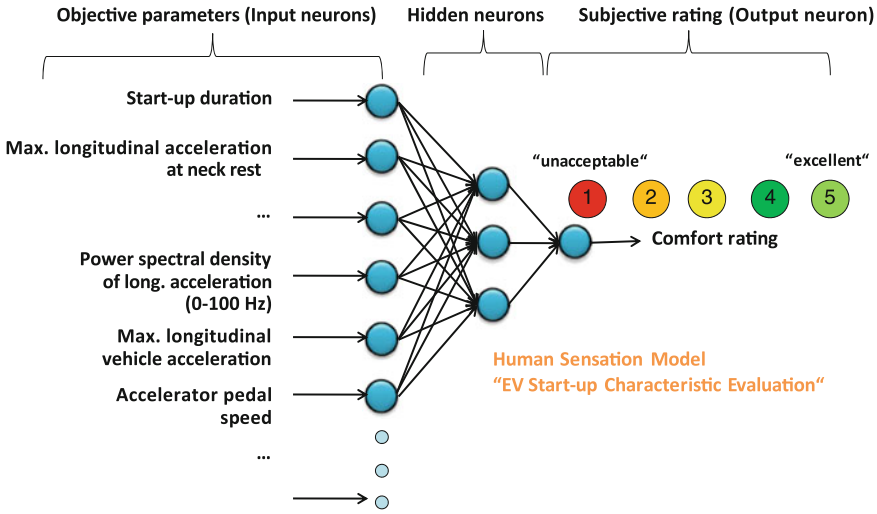
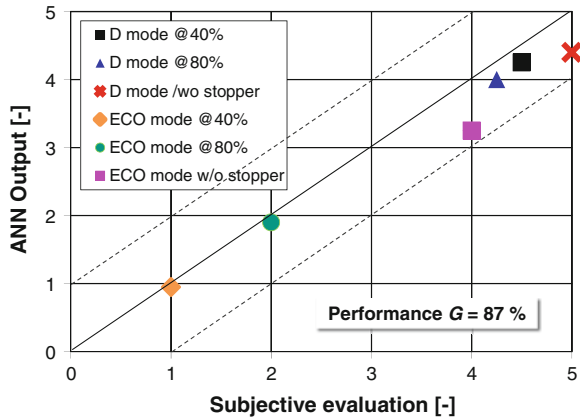


Fig. 7 Example of network topology for prediction of EV start-up comfort evaluation

Fig. 8 Application of the driver model and virtual drive train to estimate the subjective evaluation



evaluation and the calculated values is achieved. Concerning the satisfaction level, the same trends of comfort rating of start-up characteristics with “good” to “excellent” from tests with the normal or D-mode are attained. On the other hand, the same ANN rated the ECO-mode tests with limited maximum pedal value of 40, 80 % and without pedal limitation as “unacceptable”, “improvement required” and “satisfied”, respectively. The results indicate that the presented approach can be effectively applied to predict the customer satisfaction level of the start-up characteristic of the investigated drive train.

5 Conclusions and Prospect

This article presents the capability of the developed ANN-based tools to model the complex nonlinear relationships between the subjective evaluation and the objective parameters and to be applied to other automotive research fields, for example in the development process of the electric vehicle. The experimental set-up was developed to generate different variants of start-up characteristics of an intermediate-class commercial electric vehicle equipped with measurement system for data acquisition. The start-up characteristics are set to different variants by applying different levels of throttle pedal limitation. A total of 18 tests are performed by each layman. Characteristic values are derived from data obtained in each test and the corresponding comfort ratings are captured. The results of the human sensation modeling emphasizes that the selection of a suitable topology in views of input neuron type or used training algorithm has a significant effect on the prediction performance. Consequently, the objective values are efficiently correlated with the subjective sensation captured during each test. Thus, the presented approach can be efficiently applied to support the drive train design and development process of EV. To improve the start-up property of the entire drive train and to reach a higher customer satisfaction, new concepts emerged from influencing drive train parameters can be examined. The prediction of expected comfort rating using the presented tools is carried out by applying objective data from the simulation model. The following modification on EV drive train can be carried out in an early stage of development process. As a result, costly drive tests and cost-intensive prototypes can be partially replaced. In the long run, the first system prototype can be developed and the satisfying passenger comfort rating is obtained.

References

1. Albers A, Lerspalungsanti S, Dueser T, Ott S (2009) Design parameter investigation in customer-oriented drive train development using human sensation modeling tools, ASME IDETC:11th International conference on advanced vehicle and tire technologies (AVTT). San Diego, USA
2. Albers A, Lerspalungsanti S, Dueser T, Ott S (2008) Vehicle start-up simulation and subjective comfort evaluation of virtual drive train by means of new driver modeling tools based on artificial neural networks, FISITA 2008 world automotive congress. Munich, Germany
3. Lerspalungsanti S, Albers A, Dueser T, Ott S (2008) A systematic approach to supporting drive-train assembly design using new customer comfort objectifying tools, ASME IDETC:10th international conference on advanced vehicle and tire technologies (AVTT). USA, New York
4. Gurney K (1997) An introduction to neural networks. Routledge, London
5. Nissan Motor Co., LTD. (2012) Nissan Leaf Owner's Manual 2012, Publication No.: OM1E-OZE02, USA

Torque Vectoring Control Design Based on Objective Driving Dynamic Parameters

Michael Graf and Markus Lienkamp

Abstract Due to the good controllability of electric motors the possibilities of driving behaviour control are increased. The amount of applicable yaw moment on the car compared to previous systems is increased; therefore it is essential to investigate the possibilities of influencing the driving experiences. Thus the subjective impression of the vehicle dynamics can be improved although the narrow roll-resistant optimized tyres on electric cars have less lateral potential than conventional ones. The objective of this study is to find the key driving dynamic parameters to evaluate the behaviour already in the simulation and to adjust the torque vectoring control unit to improve the drivability. The vehicle dynamics evaluation of the small electric car is based on characteristic values from literature research and handling tests. Further dynamic simulations and test drives with different torque vectoring target specifications generate a range for each parameter, where the driving behaviour for the driver is still on a high level. A correlation between the objective parameters gives a detailed overview of their specific importance in different driving manoeuvres. Depending on the uncontrolled vehicle behaviour a recommendation for the design criteria of the torque vectoring control unit is given. Thus in the time intensive driving tests only the control target (the yaw rate) has to be validated and adjusted.

Keywords Torque vectoring · Control design · Control target specification · Objective driving dynamic parameters · Questionnaire for subjective assessment of the drivability

F2012-E15-006

M. Graf (✉) · M. Lienkamp
Technische Universität München, München, Germany
e-mail: graf@ftm.mw.tum.de

1 Introduction

After the car design, the quality of driving dynamics is the most important reason for purchasing a particular model. Due to the good controllability of electric motors compared to conventional systems, the potential for vehicle dynamics control systems is increasing. Therefore it is important to exploit the new opportunities. The rear wheel driven prototype on which this study is based has a driving motor and a torque vectoring motor [1]. This motor is able to distribute 90 % of the drive torque between the wheels of the rear axle with a superposition gear. The vehicle in question is a small city vehicle with two seats and a total weight of 600 kg. The rolling resistance of the tyres is optimized (115/70R16). An important goal during the development was to enhance safety and drivability.

Up to now, objectification studies have exclusively been undertaken with middle class vehicles. Therefore the results of the previous studies (e.g. [2–5]) have to be examined more closely before the torque vectoring control unit is designed. This chapter shows a possibility of designing the torque vectoring unit based on known characteristic values demonstrated on the manoeuvre step steer. Furthermore, new characteristic values are presented. These values are evaluated on the basis of their mutual correlation before the correlation to subjective assessment grades is formed.

2 Control System Analysis

The torque vectoring control system of this project is divided into two parts: the control target and the controller. The structure of the system is shown in Fig. 1.

The controller does not need to be especially fast because of the relatively high yaw eigenfrequency (1.43 Hz) and the control limits due to the low tyre performance in lateral and longitudinal direction. As long as eigenfrequency of the controller is approximately ten times faster than the eigenfrequency of the controlled system, it is only the target specification which has to be adjusted according to the desired driving behaviour. Graf et al. [6] describes the structure of the target specification. In non-critical driving situations, the torque vectoring improves the agility; the car feels sporty and direct. In critical situations, on the other hand, the torque vectoring helps the driver to stabilize the car and to increase driving safety. The system gauges the actual driving situation based on lateral acceleration and yaw rate level as well as its time derivations.

Due to the comparability requirement for the characteristic values, the lateral acceleration is limited to 4 m/s^2 . Most of the published objectification studies were made on this lateral acceleration level. The only manoeuvre which is also driven with higher lateral accelerations is the constant radius cornering.

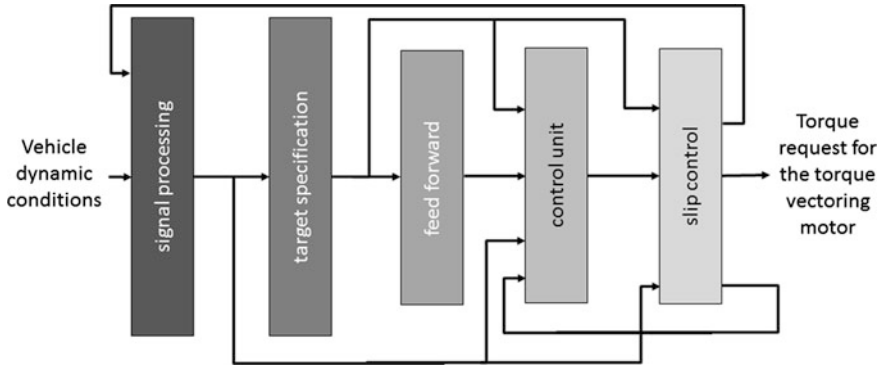


Fig. 1 Structure of the torque vectoring control unit

3 Driving Manoeuvres to Evaluate the Control Target Design

To ensure a holistic approach to driving behaviour, both stationary and non-stationary excitations in time and frequency domain are investigated.

Referring to the open-loop manoeuvres listed below the driving behaviour of the yaw-rate-controlled electric vehicle will be analysed:

- Step steer (ISO/DIS 7401-9)
- Constant radius cornering (ISO 4138)
- Weave test (ISO/FDIS 13674-1)
- Sine sweep (ISO/DIS 7401-13)
- Single sine (ISO/DIS 7401-10)

According to [5] the normal driver uses not more than 4 m/s^2 lateral acceleration while driving. In this range the tyre behaviour is approximately linear. Furthermore, the average driver has no experience with the behaviour of the vehicle in the physical limits and cannot rely on automation to stabilize the vehicle in critical situations [7].

The characteristic values are generated based on the measurement and simulation data and compared with known values from the literature. In a further subjective assessment study, the known and new generated values are evaluated in a correlation test.

The characteristic values can be seen as a concentration of the information within the measured and simulated data. They form the basis for a subsequent correlation analysis with the subjective parameters.

Figure 2 shows an example of defining the characteristic values of the yaw rate for the step steer. The same values can be found for the lateral acceleration a_y , side slip angle β , roll angle φ and steering torque M_h for the step steer manoeuvre.

The following part of the paper discusses characteristic values already known from other publications [3, 8, 9] are discussed as well as new defined ones. The goals of the control target design process for the torque vectoring unit are

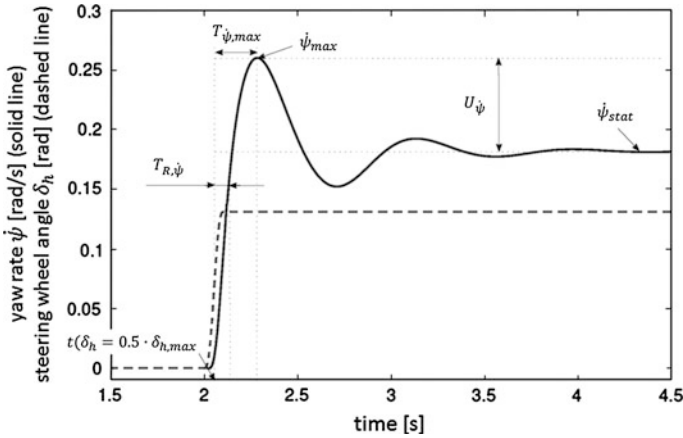


Fig. 2 Step steer manoeuvre with the characteristic values of the yaw rate

quantified essentially based on the published values and their ranges. Those figures are developed for middle class cars and not all of them can also be reached by a small electric car. In some cases, however, the reaction of the small electric car to defined inputs is faster. It cannot be assumed that the characteristic values always represent always an absolute maximum of subjective feeling; they show at least a local maximum within physical limits (e.g. yaw eigenfrequency, side slip stiffness) of the vehicle. After the basic design of the torque vectoring system the driving behaviour in an objectification study is conclusively tested. In this study both the known and the newly defined characteristic values are examined and evaluated on the basis of correlation studies with subjective judgments.

3.1 Characteristic Values of the Step Steer Manoeuvre

As far as the step steering input is concerned, the vehicle reaction is examined for a highly dynamical excitation. As this is an open-loop-manoevrue the driver’s impact can be ignored and there is a very high repeatability. Besides, both transient and stationary characteristic values can be investigated from the measurement data.

Figure 2 shows the yaw rate of the uncontrolled vehicle at the speed of 80 km/h. The steering angle is chosen in such a way that the stationary lateral acceleration is about 4 m/s². The yaw rate’s characteristic values are marked in the figure as an example of forming them in other manoeuvres as well.

In [5] a small, related transient overshoot of the yaw rate $U_{\dot{\psi}}$ is defined as subjectively good. However, in [4] a good response to steering inputs is equated with a high overshoot of the yaw rate. The torque vectoring control unit and the low yaw inertial torque of the car (yaw eigenfrequency of 1.43 Hz) form a good basis for further examinations to solve contradictions as mentioned above.

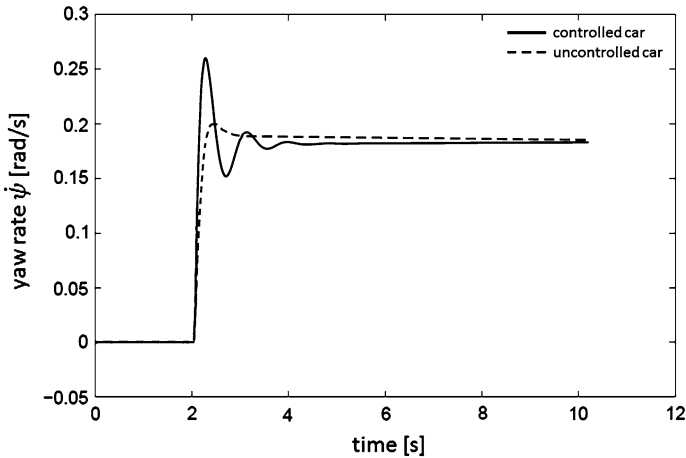


Fig. 3 Step steering input in passive-active comparison

Figure 3 shows the reaction of the vehicle with and without the torque vectoring control unit.

As can be seen in Fig. 3, the response of the uncontrolled car is slightly faster. The torque vectoring control unit tries to adjust the yaw intensification slightly towards the known characteristic ranges from the literature (e.g. [3, 8, 9]), therefore the reaction is somewhat slower (see first two lines of Table 1). The fast response of the uncontrolled car allows a wider space of influencing the driving dynamics on one hand and more configurations of the control target value during the objectification process on the other hand.

In Table 1 only those characteristic values are listed which correspond to the input speed of 80 km/h and the lateral acceleration of 4 m/s².

This input range builds the basis of the simulation and real driving tests. Higher speeds are not investigated since the prototype car is designed for a speed of 120 km/h and the power of the drive motor is at 15 kW. Published characteristic values for step steer manoeuvres at 100 km/h can be viewed in [7, 10] and [11].

The first yaw rate overshoot is reduced significantly by the torque vectoring unit to stabilize the car and to give the driver a precise steering feeling. This phenomenon is represented by the change in the characteristic value $U_{\dot{\psi}}$ from 1.42 to 1.08.

The yaw intensification value $V_{\dot{\psi}}$ ($V_{\dot{\psi}} = \dot{\psi}_{stat} / \delta_{h,stat}$) of the uncontrolled car fits into the range published in [3], the torque vectoring control unit nearly doubles it in the lower lateral acceleration range. With higher lateral accelerations this value is reduced again to have more stability reserve and to ensure safe driving behaviour. The previous observations can also be applied for the characteristic values of the lateral acceleration. The response times $T_{a_y,max}$ and T_{R,a_y} of the controlled car are higher because of the yaw damping effect. The overshoot of the lateral acceleration U_{a_y} is smaller, but only slightly, compared to the value of the yaw rate.

Table 1 Characteristic values of step steering input (for the meaning of the variables see Table 2)

Characteristic value	Known ranges			Uncontrolled car	Controlled car
	[3]	[8]	[9]		
$T_{R,\dot{\psi}} [s]$	0.12–0.3	0.12	0.1	0.09	0.20
$T_{\dot{\psi},\max} [s]$	0.2–0.5	0.22	0.2	0.24	0.39
$T_{R,a_y} [s]$	0.2–0.6	0.24	0.19	0.21	0.39
$T_{a_y,\max} [s]$	0.4–1.0	0.42	0.28	0.41	0.79
$U_{\dot{\psi}} [-]$	1.0–1.7	1.11	–	1.42	1.08
$V_{\dot{\psi}} \left[\frac{1}{s}\right]$	0.15–0.3	0.25–0.27	–	0.35	0.61
$U_{a_y} [-]$	1.0–1.4	1.11	–	1.23	1.05
$V_{a_y} \left[\frac{m}{s^2}\right]$	–	–	–	0.13	0.23
$\dot{\delta}_h [^\circ]$	200–500	–	1,000	188.8	110.1
$TB - value [s \cdot \text{deg}]$	0–2.0	–	–	0.18	0.49
$ \beta_{start} [^\circ]$	–	–	–	0.76	1.26

The stationary side slip angle is slightly increased due to the torque vectoring at the rear axle, which indirectly affects the yaw intensification. There are any value ranges found in the literature, so that the variation of this value has to be investigated in detail during the following objectification study. The steering wheel angle speed $\dot{\delta}_h$ to fulfill the request of the norm (0.15 s from straight to 4 m/s²) are both within the range of [3]. The declaration of [9] seems very high and can only be realized by using a steering robot.

3.2 New Characteristic Values for the Step Steer Manoeuvre

In previous publications (e.g. [2, 3]) the steering wheel torque M_h has not been treated with a great deal of importance. Since the driver receives the haptic feedback from the steering wheel, in addition to the lateral acceleration and the yaw rate, the steering wheel torque is examined in depth when forming the characteristic values and objectifying them later.

The characteristic values of Table 1 are consequently expanded. Response times, related over-shoots, intensification factors (maxima as well as stationary values) are defined for every measurand. The TB-value ($TB = T_{\dot{\psi},\max} \cdot \beta_{stat}$, discussed in [12]) is completed by the newly introduced TB_φ -value. The correlation with subjective assessment still has to be investigated, but according to [7] and [13] the driver reacts highly sensitively to the roll angle. Table 2 shows the complete list of the defined characteristic values.

Table 2 Complete list of characteristic values for the step steer manoeuvre

Complete list of characteristic values for the step steer	
Characteristic value	Annotation
$T_{R,\dot{\psi}}, T_{R,a_y}, T_{R,\beta}, T_{R,\varphi}, T_{R,M_h}$	Response time until 90 % of the stationary value
$T_{\dot{\psi},\max}, T_{a_y,\max}, T_{\beta,\max}, T_{\varphi,\max}, T_{M_h,\max}$	Response time until the maximum
$U_{\dot{\psi}}, U_{a_y}, U_{\beta}, U_{\varphi}, U_{M_h}$	Related overshoot
$V_{\dot{\psi}}, V_{a_y}, V_{\beta}, V_{\varphi}, V_{M_h}$	Intensification value
$\dot{\psi}_{\max}, a_{y,\max}, \beta_{\max}, \varphi_{\max}, M_{h,\max}$	Maximum value
$\dot{\psi}_{stat}, a_{y,stat}, \beta_{stat}, \varphi_{stat}, M_{h,stat}$	Stationary value
TB – value, TB $_{\varphi}$ – value	$T_{\dot{\psi},\max}$ times β_{stat} respectively φ_{stat}

To evaluate the new characteristic values in Table 2 12 variants of the target specification are examined with a validated multi-body vehicle model. The control unit is developed in MATLAB. Therefore a cosimulation framework is build for this study.

With this big number of values it is almost self-evident that some values correlate highly with each other. Therefore the list of independent or nearly independent values is shortened.

For the study the Pearson correlation coefficient (described in [14]) is built between every characteristic value over the different torque vectoring variants. The most significant results of the correlation study are discussed below.

The response times of the yaw rate $T_{\dot{\psi},\max}$ and $T_{R,\dot{\psi}}$ correlate strongly (correlation coefficient: $r = 0.975$).

$T_{R,\dot{\psi}}$ shows also a strong correlation with T_{R,a_y} , $T_{R,\beta}$ and $T_{R,\varphi}$. Hardly any correlation is given between $T_{R,\dot{\psi}}$ and T_{R,M_h} ($r = 0.022$). This is due to the fact that the steering torque shows a phase advance (0.04–0.07 s) because of the low friction in the steering system. With such short time intervals the simulation and measurement has to be very accurate to not influence the correlation coefficient too strongly. A simulation and measurement rate of 0.01 s is recommended here.

The response time of the yaw rate $T_{\dot{\psi},\max}$ has a low correlation to $T_{a_y,\max}$, $T_{\beta,\max}$ and $T_{\varphi,\max}$ therefore all of them need to be considered for the objectification study.

Furthermore the T_R -values except T_{R,M_h} show the same changes over the variants like the overshoot of the yaw rate $U_{\dot{\psi}}$. The low correlation between the T_R -values and the corresponding transient overshoot is noticeable.

U_{a_y} is also considered in the objectification even the high correlation with U_{β} respectively U_{φ} , because it lowly correlates with all other characteristic values.

The stationary values $a_{y,stat}$, $\dot{\psi}_{stat}$, β_{stat} and φ_{stat} significantly correlate with their corresponding intensification values V . This relation seems coherent because of the calculation of the intensification value: e.g., $V_{\dot{\psi}} = \dot{\psi} / \delta_h$.

Table 3 List of selected characteristic values for the step steer

List of selected characteristic values for the step steer

$T_{R,\dot{\psi}}$
$T_{\dot{\psi},\max}, T_{a_y,\max}, T_{\beta,\max}, T_{\varphi,\max}, T_{M_h,\max}$
$U_{\dot{\psi}}, U_{a_y}, U_{\beta}, U_{\varphi}, U_{M_h}$
$V_{\dot{\psi}}, V_{a_y}, V_{\beta}, V_{\varphi}, V_{M_h}$
$\dot{\psi}_{\max}, a_{y,\max}, \beta_{\max}, \varphi_{\max}, M_{h,\max}$
$M_{h,stat}$
$TB - value, TB_{\varphi} - value$

Since the steering wheel angle is kept constant at each manoeuvre execution, a direct relationship between the stationary values and the gain factors is given. Therefore all the stationary values are excluded from further investigations.

There is a medium to high correlation of the mentioned TB-value and the other values, however, this TB-value is not eliminated because of its high relevance to subjective assessments. The new build TB_{φ} -value (see Table 3) combines important values for the subjective impression of the vehicle dynamics: the response time to the maximum yaw rate and the stationary roll angle.

In conclusion the following characteristic values are selected for the further investigations:

4 Test Procedure for the Evaluation of the Characteristic Values

The procedure for the evaluation of the new characteristic values can be divided into two different sections: the procedure for generating the characteristic values with open-loop manoeuvres and the subjective evaluation with professional test drivers (closed-loop manoeuvres). The benefit of the separation of objective and subjective tests is that the test driver does not have to concentrate on the correct procedure of the manoeuvre, so that he has more time to assess the vehicle dynamics with different torque vectoring control variations. Secondly, the plan makes the procedure a bit more flexible and able to react faster to the availability of drivers and testing ground. An important constraint for this procedure is that the external conditions like track conditions, air temperature, tyre pressure and tyre wear have to be in a similar range for all test drives. Figure 4 shows the described approach.

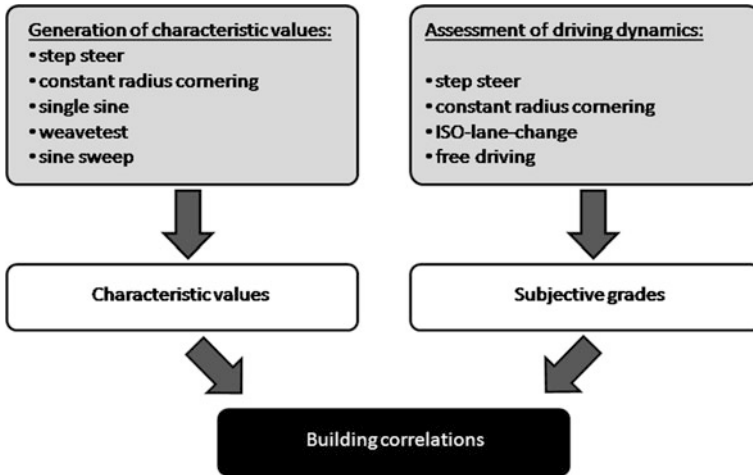


Fig. 4 Testing procedure for objectification

5 Conclusions

The ranges of the characteristic values can vary from publication to publication, because the amount of qualified test drivers is always (usually less than five). Another reason for the variation is that the expectation of the drivers on a vehicle changes with their experience. Once a driver is used to a certain vehicle behaviour, he assesses it better than unknown reactions [2].

The correlation study shown in this paper is applied also for the other driving manoeuvres: constant radius cornering, weave test, sine sweep and single sine with the same torque vectoring variants as for the step steer manoeuvre. With this method the significance evaluation of every characteristic value for the objectification can be shortened. As the expectations of the driver varies from category to category, the characteristic values and their explicit range has to be examined. This work will be done further in the project.

References

1. Höhn B-R, Stahl K, Lienkamp M, Wirth C, Kurth F, Wiesbeck F (2011) Electromechanical power train with torque vectoring for the electric vehicle MUTE of the TU München [J]. *Getriebe in Fahrzeugen 2011*, VDI-Verlag, pp 77–95
2. Decker M (2008) Zur Beurteilung der Querdynamik von Personenkraftwagen [M]. Technische Universität München, Munich, Dissertation
3. Zomotor A (1991) Fahrwerktechnik: Fahrverhalten [M]. Vogel Verlag, Würzburg
4. Schimmel C (2010) Entwicklung eines fahrerbasierten Werkzeugs zur Objektivierung subjektiver Fahreindrücke [M]. Technische Universität München, Munich, Dissertation

5. Heissing B, Ersoy M (2008) Fahrwerkhandbuch—Grundlagen, Fahrdynamik, Komponenten, Systeme, Mechatronik, Perspektiven [M]. Vieweg + Teubner Verlag, Wiesbaden
6. Graf M, Steinberg S, Lienkamp M (2011) Fahrdynamikregelung eines Elektrofahrzeuges: Sollwertvorgabe und Reibwertschätzung für die Torque-Vectoring-Regelung des Fahrzeuges MUTE [J]. AUTOREG 2011, VDI Verlag, pp 345–360
7. Stock G (2010) Handlingpotentialbewertung aktiver Systeme [M]. Technische Universität Carolo-Wilhelmina zu Braunschweig, Braunschweig, Dissertation
8. DTA—Drivability Testing Alliance (2011) Fahrdynamik-Testmanöver: Stationäre Kreisfahrt. <http://driveability-testing-alliance.com/download/datasheets/DTA-Stationaere-Kreisfahrt-DE-B090603g.pdf>. Checked on: 11.07.2012
9. Diermeyer F (2008) Methode zur Abstimmung von Fahrdynamikregelsystemen hinsichtlich Überschlagsicherheit und Agilität [M]. Technische Universität München, Munich, Dissertation
10. Mitschke M, Wallentowitz H (2004) Dynamik der Kraftfahrzeuge [M]. Springer, Berlin
11. Heissing B, Rompe K (1984) Objektive Testverfahren für die Fahreigenschaften von Kraftfahrzeugen [M]. Köln, Verlag TÜV Rheinland
12. Lincke W, Richter B, Schmidt R (1973) Simulation and measurement of driver vehicle handling performance [J]. SAE technical paper nr. 730489
13. Kraft C (2010) Gezielte Variation und Analyse des Fahrverhaltens von Kraftfahrzeugen mittels elektrischer Linearaktuatoren im Fahrwerksbereich [M]. Karlsruher Institut für Technologie (KIT), Karlsruhe, Dissertation
14. Hartung J (2009) Statistik [M]. Oldenbourg Verlag, München

Integrated State Estimation with Driving Dynamic Sensors and GPS Data to Evaluate Driving Dynamics Control Functions

Markus Bauer, Carlo Ackermann and Rolf Isermann

Abstract The aim of this research project is to investigate the use of GPS data for test drives. Based on data of a multi-antenna GPS system and vehicle dynamic sensors, an information platform is performed. This platform includes the merged sensor signals and an estimation of vehicle states that are not measurable. In a state estimator the lateral dynamic model is combined with a navigation model. The state estimation is accomplished by coupling the signals in an extended Kalman Filter (EKF) which is a variant of the Kalman Filter (KF) for nonlinear dynamic systems. The double-track approach with a linear tire force model is used to describe the lateral vehicle dynamics. Pitch and roll movements are analyzed separately from each other. The unknown or time-variant vehicle parameters are estimated online by recursive estimation methods. In addition to the presentation of the developed methods, results from test drives with the research vehicle (BMW 540i) at the testing area of the Technische Universität Darmstadt are presented.

Keywords Extended kalman filter · Fusion INS/GPS · Parameter and state estimation

1 Introduction and Motivation

The current vehicle development is characterized by an increasing variety and complexity. In addition, the vehicles are more and more individualized. Certain vehicle models are available in up to 100 variants with different engines, gears,

F2012-E15-013

M. Bauer (✉) · C. Ackermann · R. Isermann
Technische Universität Darmstadt, Darmstadt, Germany
e-mail: mbauer@iat.tu-darmstadt.de

chassis adjustments and control systems [1]. The resulting tuning and testing efforts challenge the vehicle development and testing. In ever-shorter development time a higher number of vehicle models have to be calibrated. To face these challenges, automated calibration processes and a shifting of development steps to simulations are required. For the efficient tuning of vehicle dynamics control systems, an accurate determination of the vehicle dynamics is necessary. Therefore, a method for the integration of GPS measurement technology with a dynamic gyro box data is developed for research vehicles. Hence, the GPS system is not only used for navigation but also to determine the vehicle dynamics response.

For several years, the use of GPS data for vehicle dynamics control systems has been studied [2–4]. The complementary characteristics of GPS data in terms of availability, long-term stability, and sampling frequency compared to vehicle dynamics sensors (VDS) motivate the use of GPS data to determine the dynamic state variables in addition to the actual navigation. In the research project “GNSS4FAS” [5] it could be proven in field test that the usability of GPS data (depending on the manufacturer) is up to 97 % on highway driving, 84 % on overland drives and 53 % on urban drives. It was also shown that the error components in yaw rate and velocity can be reduced significantly by the fusion of vehicle dynamics and GPS data. Further motivation is provided by the cost reduction of GPS systems. The technical developments regarding the efficiency, size and weight have opened, further markets for GPS technologies (mobile navigation in smartphones, geotagging, geocaching) in recent years [6]. Thus, GPS hardware has developed from a purely military application to a mass product.

The fusion is effected by a loosely coupled integration of the GPS and IMU data. The data are merged externally, i.e., the individual sensor data are not influenced on raw data base [6]. Advantages of this approach are the possibility of using existing sensors and the fast integration with already built-in signal data processing. The method is primarily intended for the development of vehicle dynamics control systems used in test vehicles.

This paper describes a method to estimate the positions and states of motion of a vehicle, based on vehicle dynamics sensors and GPS data. In the first part of the paper, the research vehicle and the information platform are presented. The second part shows the state estimation. Lateral and longitudinal position and velocity as well as the yaw rate and angle are estimated by fusion of vehicle dynamics sensor data and a three-antenna GPS system. In the last part results from real test drives are presented.

2 Integrated Sensor Platform

2.1 System and Sensor Properties

The arrangement of the sensors in the test vehicle is shown in Fig. 1. Wheel speed, brake pressure, steering angle, lateral and longitudinal acceleration sensors are series sensors and are recorded by the vehicle CAN bus. An inertial measurement unit is used to determine the rotation rates and accelerations. As reference sensor

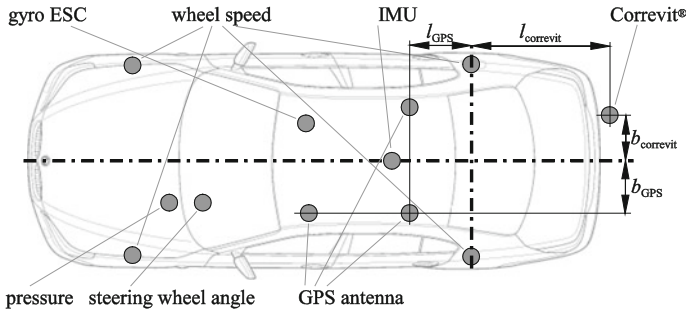


Fig. 1 Arrangement of the sensors

an optical cross-correlation sensor (Correivit®) for the determination of the longitudinal and lateral velocity is installed. On the roof of the vehicle, a multi-antenna GPS system is installed. This system not only measures the position but also the speed and orientation (pitch, roll, yaw) of the vehicle in space [7]. The reference sensors are connected to a separate CAN bus in the vehicle. All measured data are recorded with a notebook, using hard- and software of Vector Informatik. Further processing and algorithms are implemented in Matlab.

2.2 Information Platform

The signal flow of the information platform is depicted in Fig. 2. Input variables are the measured sensor signals of conventional vehicle sensors (ESC), the GPS system, the IMU and the Correivit® sensor. These measured data are first processed in a signal processing unit. This includes a filtering of the signals transformation of the speed signals into the center of gravity and an offset correction. In addition, a first driving state detection differs between standstill, stationary and dynamic maneuvers.

In the block “State estimation” the signals of the GPS system, the vehicle sensors and the IMU are merged. Output variables of this block are the rotation angle and rotation rates around the three main axes of the vehicle. In addition, a speed and slip angle signal from the vehicle sensors and GPS are determined [8, 9].

Based on the merged signals and further sensor signals, the parameters of drive dynamic models are determined [10]. The identifiable parameters depend on the maneuvers. All information about the movement of the vehicle is used in the block “Test drive evaluation”. To ensure reproducibility of the maneuvers only standardized maneuvers are used.

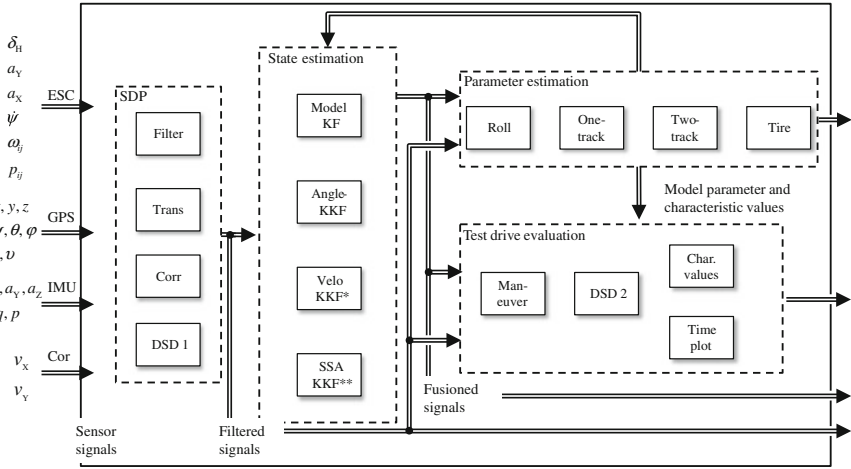


Fig. 2 Information platform: *published in [8] **published in [9]

3 Modelling and State Estimation

In this section, a model-based approach for the determination of dynamic state variables is presented. Figure 3 shows the input and output behavior. The input variables are the sensor signals from the ESC control unit $[\dot{\psi}, a_x, a_y, \omega_{i,j}, \delta_H]^{ESC}$ and the GPS system $[\psi, x_E, y_E, v]^{GPS}$. The speed in longitudinal and lateral direction (\hat{v}_X, \hat{v}_Y), the yaw rate $\hat{\psi}$ and navigation data ($\hat{\psi}, \hat{x}_E, \hat{y}_E$) have to be estimated. The filter runs with a sampling of $T_0 = 0.01 s$. The problem of different sampling of the input signals is treated in [8] and not further explained here.

The state estimation is processed by coupling a vehicle model and a navigation model in an extended Kalman Filter (EKF). The EKF is a variant of the Kalman filter (KF) for nonlinear dynamic systems, see [11, 12]. To use the KF algorithm the dynamic system has to be available in discrete state space:

$$\begin{aligned} \mathbf{x}_k &= \mathbf{f}(\mathbf{x}_{k-1}, \mathbf{u}_{k-1}) \\ \mathbf{y}_k &= \mathbf{h}(\mathbf{x}_k, \mathbf{u}_k). \end{aligned} \tag{1}$$

3.1 Process Model

The process model $\mathbf{x}_k = \mathbf{f}(\mathbf{x}_{k-1}, \mathbf{u}_{k-1})$ shows the dynamic behavior of the system. The vehicle dynamic is modeled with a two-track approach, see [13, 14].

Equation (2) describes the translational and rotational movements of the vehicle in the horizontal plane:



Fig. 3 Input/Output behavior of the extended kalman filter (EKF)

$$\dot{v}_{X_k} = a_{X_k} + \dot{\psi}_k v_{Y_k} \quad ; \quad \dot{v}_{Y_k} = a_{Y_k} + \dot{\psi}_k v_{X_k}. \tag{2}$$

Balancing longitudinal and lateral forces and the torque around the vertical axis leads to three differential equations, Fig. 4a:

$$\begin{aligned} f_1 &= v_{X_k} = v_{X_{k-1}} + T_0 \left(\left(F_{X,V_{FL,k-1}} + F_{X,V_{FR,k-1}} + F_{X,V_{RL,k-1}} + F_{X,V_{RR,k-1}} \right) \frac{1}{m} + \dot{\psi}_{k-1} v_{Y_{k-1}} \right) \\ f_2 &= v_{Y_k} = v_{Y_{k-1}} + T_0 \left(\left(F_{Y,V_{FL,k-1}} + F_{Y,V_{FR,k-1}} + F_{Y,V_{RL,k-1}} + F_{Y,V_{RR,k-1}} \right) \frac{1}{m} - \dot{\psi}_{k-1} v_{X_{k-1}} \right) \\ f_3 &= \dot{\psi}_k = \dot{\psi}_{k-1} + \frac{T_0}{J_Z} \left(\left(F_{Y,V_{FL,k-1}} + F_{Y,V_{FR,k-1}} \right) l_V - \left(F_{Y,V_{RL,k-1}} + F_{Y,V_{RR,k-1}} \right) l_H + \dots \right. \\ &\quad \left. \dots + \left(F_{X,V_{FR,k-1}} - F_{X,V_{FL,k-1}} \right) \frac{b_V}{2} + \left(F_{X,V_{RR,k-1}} - F_{X,V_{RL,k-1}} \right) \frac{b_H}{2} \right). \end{aligned} \tag{3}$$

The longitudinal and lateral forces ($F_{X,V}, F_{Y,V}$) in Eq. (3) can be expressed by the longitudinal and lateral tire forces ($F_{X,W}, F_{Y,W}$). The lateral tire forces are modeled as a rotary spring, with c_α denoting the cornering stiffness and α the slip angle at wheel:

$$F_{Y,W,i} = c_{\alpha,i} \underbrace{\left(\delta - \arctan \left(\frac{v_{Y,W,i}}{v_{X,W,i}} \right) \right)}_{\alpha_i} \quad \text{with } i = \text{FL, FR, RL, RR}. \tag{4}$$

The slip angle can be described by the steering angle δ and the wheel velocity ($v_{X,W,i}, v_{Y,W,i}$). A detailed description of this method is shown in [15].

The longitudinal tire forces are modeled with a lookup table estimated with the earlier measurements see Fig. 4d. Therefore, the slip is determined from the vehicle speed estimation and the wheel speed sensors [8]. To include the tire forces in Eq. (3) the forces have to be transformed into the vehicle coordinates.

To evaluate driving maneuvers the precise determination of the driven trajectory is important. Therefore, the EKF will be expanded by three other states. The yaw angle ψ , and the position of the center of gravity (COG) in earth fixed coordinates (x_E, y_E):

$$\begin{aligned} f_4 &= \psi_k = \psi_{k-1} + T_0 \dot{\psi}_{k-1} \\ f_5 &= x_{E_k} = x_{E_{k-1}} + T_0 (v_{X_{k-1}} \cos(\psi_{k-1}) - v_{Y_{k-1}} \sin(\psi_{k-1})) \\ f_6 &= y_{E_k} = y_{E_{k-1}} + T_0 (v_{X_{k-1}} \sin(\psi_{k-1}) + v_{Y_{k-1}} \cos(\psi_{k-1})). \end{aligned} \tag{5}$$

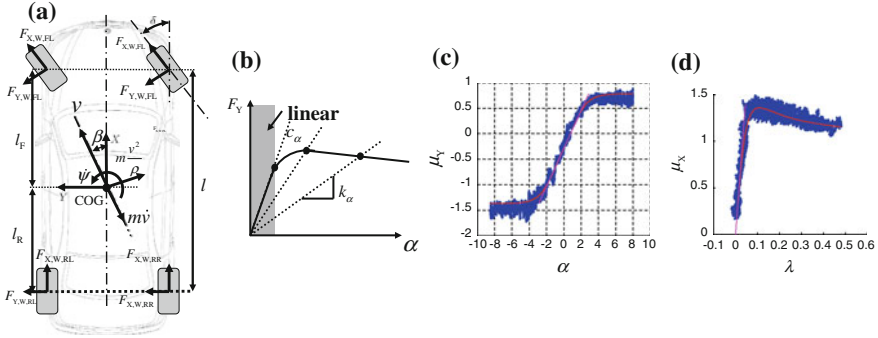


Fig. 4 Modelling vehicle dynamics: **a** two track model, **b** lateral wheel force, **c** lateral friction coefficient μ_Y over tire side slip angle α and **d** longitudinal friction coefficient μ_X over slip λ

3.2 Observation Model

The next step is to generate the observation model $\mathbf{y}_k = \mathbf{h}(\mathbf{x}_k, \mathbf{u}_k)$. Therefore, the sensor signals have to be modeled as algebraic functions of the state vector and the input vector. The sensor setup provides measurements of the lateral and longitudinal acceleration, wheel speeds, yaw rate, yaw angle and position:

$$\mathbf{y} = [a_X, a_Y, v_{FL}, v_{FR}, v_{RL}, v_{RR}, \dot{\psi}, \psi, x_E, y_E]^T. \quad (6)$$

The measured lateral and longitudinal acceleration can be modeled by balancing the forces, see Fig. 4:

$$\begin{aligned} h_1 &= a_{X_k} = \frac{1}{m} \sum_j F_{X_{k,j}} \\ h_2 &= a_{Y_k} = \frac{1}{m} \sum_j F_{Y_{k,j}}. \end{aligned} \quad (7)$$

The wheel speeds are modeled as rigid body and with the measurements of the velocity and yaw rate:

$$\begin{aligned} h_3 &= v_{FL} = v_X - \dot{\psi} \frac{b_F}{2}, & h_4 &= v_{FR} = v_X + \dot{\psi} \frac{b_F}{2} \\ h_5 &= v_{RL} = v_X - \dot{\psi} \frac{b_R}{2}, & h_6 &= v_{RR} = v_X + \dot{\psi} \frac{b_R}{2}. \end{aligned} \quad (8)$$

Yaw rate, yaw angle and the position are directly measured:

$$h_7 = \dot{\psi}, \quad h_8 = \psi, \quad h_9 = x_E, \quad h_{10} = y_E. \quad (9)$$

3.3 Vertical Wheel Force

To determine the lateral and longitudinal wheel forces an estimation of the vertical wheel forces is required. The vertical wheel forces of a driving vehicle are affected by vehicle acceleration and road undulations. Dynamic vertical wheel forces of a driving vehicle can only be directly determined by using additional sensor technology, e.g., power measuring rims. Due to the fact that our research vehicle is not equipped with such sensors, a well-known method to determine the wheel forces is used here:

It is assumed that the vehicle is a rigid body. As a result, dynamic effects of the wheel suspension are not considered. As studies have shown the consideration of these dynamic effects does not lead to increased model accuracy and therefore, the additional calculation effort is not useful [15]. Pitch and roll movements are analyzed separately from each other and gradients of the road are disregarded, see [14]. This leads to the following equations:

$$\begin{aligned} F_{Z_{FL}} &= m \left(\frac{l_R}{l} g - \frac{h_{COG}}{l} a_X \right) \left(\frac{1}{2} - \frac{h_{COG}}{b_F} \frac{a_Y}{g} \right); & F_{Z_{FR}} &= m \left(\frac{l_R}{l} g - \frac{h_{COG}}{l} a_X \right) \left(\frac{1}{2} + \frac{h_{COG}}{b_F} \frac{a_Y}{g} \right) \\ F_{Z_{RL}} &= m \left(\frac{l_F}{l} g + \frac{h_{COG}}{l} a_X \right) \left(\frac{1}{2} - \frac{h_{COG}}{b_R} \frac{a_Y}{g} \right); & F_{Z_{RR}} &= m \left(\frac{l_F}{l} g + \frac{h_{COG}}{l} a_X \right) \left(\frac{1}{2} + \frac{h_{COG}}{b_R} \frac{a_Y}{g} \right) \end{aligned} \quad (10)$$

The vehicle mass m , the track at front and rear axle $b_{F,R}$, the acceleration of gravity g , and the wheel base l are given. The position of the center of gravity $l_{F,R}$ and h_{COG} has to be estimated. The estimation approach is described in [16].

The entire signal flow of the estimator is shown in Fig. 5.

4 Identification

Some of the physical parameters in Eqs. (3)–(10) are known from construction data sets or can be determined by using approximation equations. Other parameters have to be identified from measurement data sets. It is assumed that the track width at front and rear axle $b_{F,R}$, the wheel base l and the mass m of the vehicle are known constructively. The position of the COG is estimated with parameter estimation according to [16] and in the following assumed to be known. According to [17] the cornering stiffness is the most time variant parameter in Eqs. (3)–(10). The cornering stiffness corresponds to the initial slope in $F_\alpha(\alpha)$ -characteristic curve, Fig. 4b. For small tire slip angles, the linear approximation is sufficient. For larger tire slip angles, the tire model is not accurate. Therefore, the cornering stiffness c_α is replaced in the adaptive model by a time-varying parameter k_α . The parameter k_α corresponds to the secant of the $F_\alpha(\alpha)$ characteristic curve. This online estimation is implemented with a recursive least square approach according to [16].

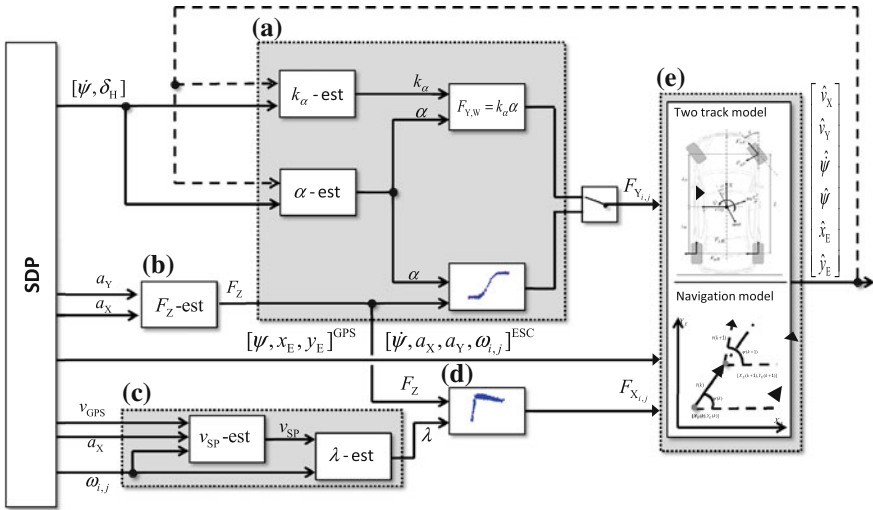


Fig. 5 Signal flow of the model based estimator: **a** Determination of the lateral forces using an estimation of the lateral tire stiffness or a previously defined characteristic map, **b** Estimation of the vertical forces (Eq. 10), **c** Determination of the slip of a velocity estimation and wheel speed sensors [8], **d** Determination of longitudinal tire forces by a characteristic diagram, and **e** Model-based state estimator Eqs. (3)–(9)

5 Results

In this chapter the results of the methods described above are presented. The estimator was tested in two configurations. In the first configuration (EKFrls_{GPS}) the estimator runs with the observation model presented in Eq. (6):

$$y = [a_x, a_y, v_{FL}, v_{FR}, v_{RL}, v_{RR}, \dot{\psi}, \psi, x_E, y_E]^T. \tag{11}$$

In the second configuration (EKFrls) the estimator runs with a reduced sensor configuration, without the GPS measurement:

$$y = [a_x, a_y, v_{FL}, v_{FR}, v_{RL}, v_{RR}, \dot{\psi}]^T. \tag{12}$$

Figure 6 shows the signals of a test drive with the research vehicle (BMW 540i). In (a) the driver inputs are illustrated. There were two sinusoidal driving maneuvers and two lane changes driven at nearly constant speed. The comparison of the two estimator configurations with a reference signal is depicted in Fig. 6b–d. To get a close look only 20 s of the test drive are shown. The estimations of the longitudinal velocity and the yaw rate are very accurate, Fig. 6b + d. The difference between the two configurations lies in the part per thousand range.

The additional information from the GPS system attached to those two states no improvement. In the lateral velocity Fig. 6c ($t = 45 - 60\text{ s}$), a significant

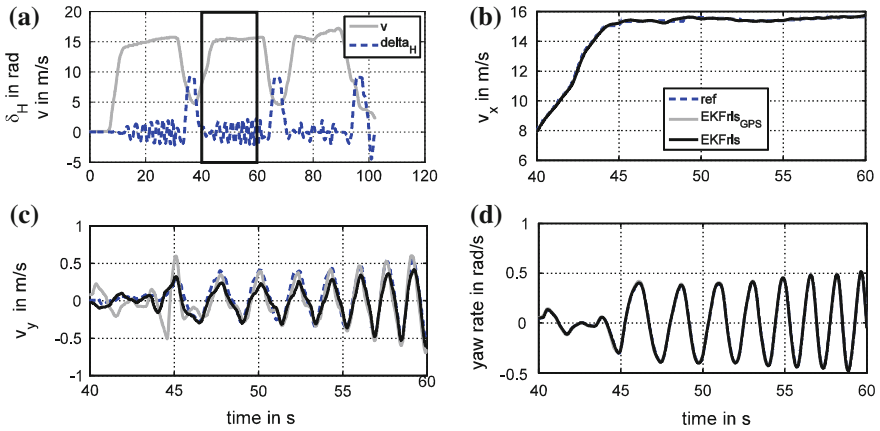


Fig. 6 Results from test drive: comparison between estimated and measured values. *ref* reference signal, *EKFrls_{GPS}* estimated signal with GPS sensors, *EKFrls* estimated signal without GPS sensors. **a** Driver input: Steering wheel angle δ_H and velocity v (from ESC), **b** zoom in **a**: longitudinal velocity v_x ; **c** zoom in **a**: lateral velocity v_y and **d** zoom in **a** yaw rate $\dot{\psi}$

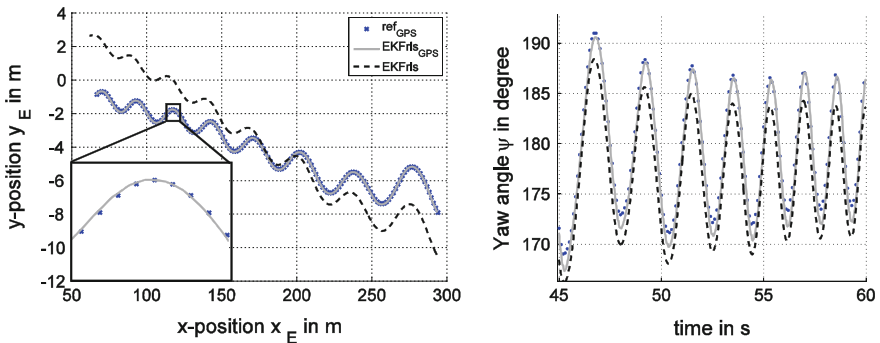


Fig. 7 Results from test drive. Estimation of the position and yaw angle

improvement in the estimation can be seen. Especially at high amplitudes, the estimation errors are reduced from 30 to 5 %.

The main benefit of the additional GPS sensor can be seen in Fig. 6. There, the trajectory and the yaw angle are shown. A small estimation error in the yaw angle results in an erroneous deflection of the vehicle. This bug is transmitted via the navigation model in the position estimation. Without a correction of the measured data, the estimation error of the navigation increases with the duration of measurement. In the correction step of the *EKFrls_{GPS}* configuration a readjustment of the estimation is made. Therefore, a robust estimation of the position is only possible through an update from the GPS measurement. Alternatively, the correction signal could also be generated also from measurement data by environmental sensors, see [18] (Fig. 7).

6 Conclusion

For the calibration and evaluation of vehicle dynamics control systems, an accurate determination of the vehicle dynamics and a precise reconstruction of the driven trajectory is necessary. Therefore, an information platform is performed, which provides the merged sensor signals and an estimation of not measurable vehicle states.

A method for the integration of GPS technology with dynamic gyro box data has been described. The multi-antenna GPS system serves not only for position data but also for the orientation of the vehicle in space. In an extended Kalman Filter the lateral dynamic model is combined with a navigation model. The unknown or time-variant vehicle parameters are estimated online by recursive estimation methods.

The algorithms have been implemented in a research vehicle. All developed methods have been evaluated at the testing area of the Technische Universität Darmstadt.

References

1. Bewersdorff S (2007) Simulation und Bewertung von Fahrdynameigenschaften im Grenzbereich. ATZ, Juni 2007
2. Bevlly DM (2010) GNSS for vehicle control. Artech House, Boston
3. Beiker S (2006) GPS augmented vehicle dynamics control. SAE International, Warrendale
4. Ryu J (2004) State and parameter estimation for vehicle dynamics control using GPS. Dissertation, Stanford University
5. Schmidt D (2010) Fehleranalyse und Datenfusion von Satellitennavigations- und Fahrdynamik-sensorsignalen, Bd. 719, Düsseldorf: VDI-Verlag
6. Wendel J (2007) Integrierte navigationssysteme. Oldenbourg, München
7. Septentrio. PolaRX@ Datenblatt 2009
8. Bauer M (2011) Bestimmung der Übergrundgeschwindigkeit aus Fahrdynamiksensoren und Satelliten-Navigationsdaten. AUTOREG, Baden-Baden
9. Bauer M (2012) Estimation of vehicle dynamic states using driving dynamics sensors and GPS data to evaluate driving control functions. Chassis Tech, München
10. Isermann R (2006) Hrsg. Fahrdynamik-Regelung. Wiesbaden. Friedr. Vieweg & Sohn Verlag | GWV Fachverlage GmbH Wiesbaden
11. Isermann R (ed) (2011) Identification of dynamic system. Springer, Berlin
12. Mitschke M (ed) (2004) Dynamik der Kraftfahrzeuge. Springer, Berlin
13. Kiencke U (2005) Automotive control systems. Springer, New York
14. Schorn M (2007) Quer- und Längsregelung eines Personenkraftwagens für ein Fahrer-assistenzsystem zur Unfallvermeidung. Bd. 651, VDI, Düsseldorf
15. Wesemeier D (2012) Modellbasierte Methoden zur Schätzung nicht messbarer Größen der Fahrzeugquerdynamik und des Reifenluftdrucks. VDI, Düsseldorf
16. Germann S (1997) Modellbildung und modellgestützte Regelung der Fahrzeuglängsdynamik. VDI, Düsseldorf
17. Börner M (2004) Adaptive Querdynamikmodelle für Personenkraftfahrzeuge—Fahrzustands-erkennung und Sensorfehlertoleranz. VDI, Düsseldorf
18. Schmitt K (2009) Vehicle state estimation in curved road coordinates for a driver assistance system for overtaking situations. IAVSD, Stockholm

Evaluation Tool for Current and Future Powertrains

Barak Adam

Abstract *Research and/or Engineering Questions/Objective* The paper describes a simulation tool for determination of vehicle energy consumption under dynamic conditions, suitable for early stages of design. It describes vehicle dynamics in longitudinal direction and the appropriate efficiencies of engine, transmission and accumulation components (if used). The simulation tool is targeted to the optimization of vehicle powertrains with respect to reducing the vehicle fuel consumption, CO₂ production and increasing the overall efficiency of the vehicle. It is also used to evaluate the possible benefits of new powertrain concepts. The objective of this paper is to demonstrate the possibilities of the developed tool on a comparison study of several powertrain layouts. *Methodology* The simulation tool is based on ordinary differential equations and a dynamic expandable library of vehicle component features. Various powertrain components are represented by a dynamically expandable library of component modules. Each module represents a particular component of a powertrain such as gearbox, engine, wheels, vehicle body etc. Modules may be modified to more complex models at any time or even replaced by different modules to represent different powertrain layouts. Mechanical part of the powertrain is modelled with multi body simulation approach. Particular powertrain elements are represented either by mass elements or stiffness/damping elements. Electric part of vehicle powertrain such as electric engines and battery models are based on simple circuit models and/or look-up table based models. All required input data may be obtained by targeted simulations using multi-dimensional methods or by experiments. *Results* The result of this study is a

F2012-E15-016

B. Adam (✉)

Faculty of Mechanical Engineering, Czech Technical University in Prague,
166 07 Praha 6, Technická 4, Prague, Czech Republic
e-mail: adam.barak@fs.cvut.cz

comparison of various less or more common powertrain layouts. Its aim is not to present accurate results that correspond to each powertrain type, but more to point out the advantages and disadvantages of particular powertrain types. The simulation tool itself should also be considered as a result, because it provides a powerful tool for powertrain evaluation, topology layout optimization and may be adapted for various simulation tasks. *Limitations of this study* This simulation tool is designed to provide quick initial estimates with minimal input data or to serve as a part of X in the loop (XiL) tests, where X stands usually for hardware, software, man, etc. Therefore a lot of simplifications must have been applied. However, the dynamically expandable library allows the replacement of any part of the model with a more sophisticated model if needed and thus adapt the simulation tool to various computational tasks. *What does the paper offer that is new in the field in comparison to other works of the author* This paper is more focused on less common powertrains, such as pure electric vehicles or fuel cell vehicles. Presented simulation approach is far more complex than ever before. The simulation environment is completely new as well. *Conclusion* The simulation tool that calculates quick initial estimates of vehicle qualities in a transient driving cycle was created in a specialized graphical programming language. The demand on its transparency and modularity was satisfied by a dynamic expandable library of vehicle component features. The great advantage of presented simulation tool is its low computational time and easy realization of XiL approach. Comparison of various less or more common powertrain layouts was performed with this simulation tool and its results are presented within the paper.

Keywords Powertrain simulation • Efficiency • Vehicle dynamics • Driving cycle • Fuel cell

1 Simulation Tool

The overall energy consumption, efficiency and CO₂ production of a vehicle are greatly influenced by the performance of the whole powertrain. A powertrain simulation tool is nowadays a must for the development of new cars and optimization of powertrain components. The importance of powertrain simulations becomes now especially important, because most car manufacturers are dealing with new powertrain concepts due to the on-going boom of hybrid and electric vehicles. The still rising number of powertrain layout options demands a modular simulation tool which is able to represent any vehicle.

Simulation models can be generally performed with different width and depth of accuracy. Simulation tools including mathematical modules for lateral and longitudinal dynamics have the highest level of physicality. On the other hand, more complex models lead to longer computational time, higher code complexity and more simulation input data are needed. Due to the previously mentioned reasons the model including only the longitudinal vehicle dynamics is used in this



Fig. 1 Model in labVIEW

case. The model is dedicated for calculation of system forces/torques, system states of motion (velocities, positions) and overall energy consumption during a vehicle ride in a predefined cycle such as New European Driving Cycle (NEDC) or Artemis [1].

The simulation tool was initially developed in the National Instruments LabVIEW using its Control, design and simulation toolkit and later was also adapted to Matlab/Simulink. It is built up of custom library swappable blocks that represent particular powertrain components. Each of these blocks represents a particular component of a powertrain such as wheels, gearbox, engine, vehicle body etc. Particular blocks may be whenever replaced with more complex models or even replaced by different blocks to represent different powertrain layouts. The LabVIEW version (Fig. 1) offers an easy hardware connectivity and thus easy hardware in the loop realisation. The Matlab/Simulink version (Fig. 2) offers more simulation possibilities, very good connectivity to 3rd party software and better post processing tools.

The simulation tool mathematically describes the behaviour of the complete vehicle by the multi body system (MBS) approach. MBS approach was chosen to describe the system for its low computational time. Driveline components are modelled with rigid bodies linked with elements like springs and dampers. Distributed system properties such as mass, inertia, stiffness and damping are concentrated on mass elements (mass, inertia) and link elements (stiffness, damping). The system is then mathematically described with n differential

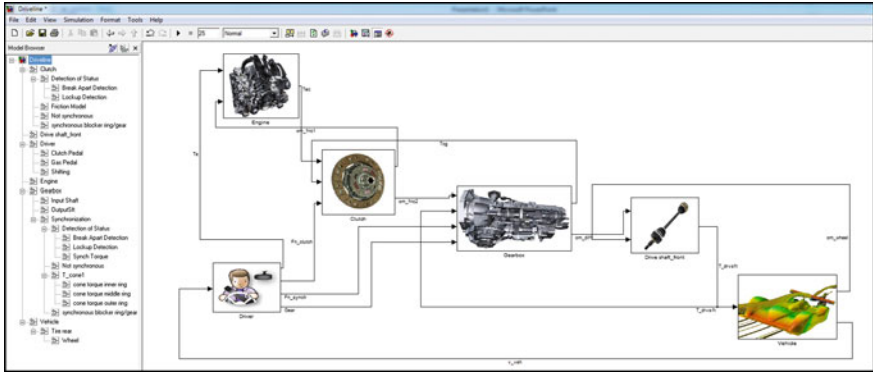


Fig. 2 Model in Matlab/Simulink

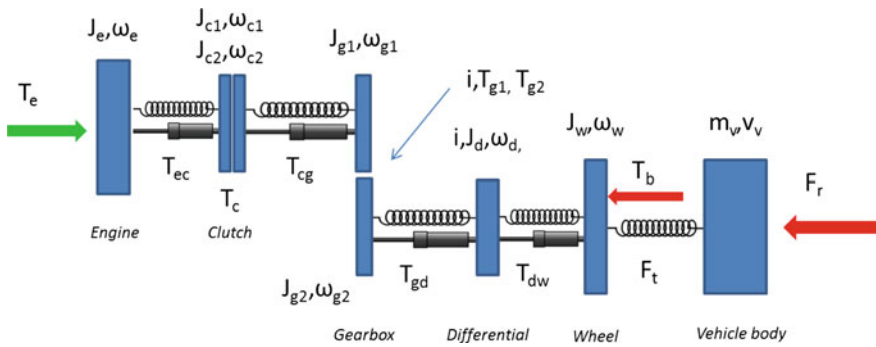


Fig. 3 MBS EV driveline model

equations (n degrees of freedom) that are solved by numeric integration algorithms in time domain using built in solvers of LabVIEW and Simulink.

The basic function of the simulation tool will be described on the example of powertrain that consists of engine, clutch, gearbox, differential, driveshaft, wheels and vehicle body.

1.1 Powertrain

Each driveline shaft is modelled as a set of two constant inertias connected with a spring-damper element (Fig. 3). Symbols used at Fig. 3 are J (inertia), ω (angular velocity), T (torque), F (force), m (weight), v (velocity). The meaning of symbol indexes is clear from the Fig. 3.

The dynamics of the system in Fig. 3 is accordingly to Newton’s law described by a set of Eq. (2):

$$\begin{aligned}
J_e \dot{\omega}_e &= T_e - T_{ec} \\
J_{c1} \dot{\omega}_{c1} &= T_{ec} - T_c \\
J_{c2} \dot{\omega}_{c2} &= T_c - T_{cg} \\
J_{g1} \dot{\omega}_{g1} &= T_{cg} - T_{g1} \\
J_{g2} \dot{\omega}_{g2} &= T_{g2} - T_{gd} \\
J_d \dot{\omega}_d &= T_{gd} - T_{dw} \\
J_w \dot{\omega}_w &= T_{dw} - F_t r_w \\
m_v \dot{v}_v &= F_t - F_v
\end{aligned} \tag{1}$$

Where:

$$\begin{aligned}
&T_{ec}, T_{cg}, T_{gd}, T_{dw} : \\
T_{xy} &= k_{xy} \Theta_{xy} + b_{xy} \omega_{xy} \\
\dot{\Theta}_{xy} &= \omega_{xy} = \omega_x - \omega_y.
\end{aligned} \tag{2}$$

1.2 Clutch

The clutch model is based on the Matlab/Simulink demo example. However, it must have been significantly modified to fulfil the model demands. Clutch model assumes a stick-slip friction model. Different equations for clutch torque are used with locked (3) and unlocked clutch (4). In the case of locked clutch, where $\omega_{c1} = \omega_{c2} \wedge |T_c| \leq T_{cM}(F_N)$:

$$T_c = \frac{J_{c1} J_{c2}}{J_{c1} + J_{c2}} \left(\frac{T_{ec}}{J_{c1}} + \frac{T_{cg}}{J_{c2}} \right) \tag{3}$$

Otherwise:

$$T_c = T_{cM}(F_N) \cdot \text{sign}(\omega_{c1} - \omega_{c2}) \tag{4}$$

$T_{cM}(F_N)$ is the maximum transmissible torque and depends on the axial force that is applied to the clutch plate. The clutch is calculated as coupled inertia when locked and as two inertias when unlocked. The state of the clutch thus changes the number of degrees of freedom of the system [2].

The torque transmitted by the driveshaft T_{dw} or braking torque T_b are not completely transmitted into traction force F_t that accelerates or decelerates the vehicle. The amount of torque transmitted to traction force is greatly dependent on the actual adhesive coefficient $\mu(\lambda)$. The adhesive coefficient is in the simulation considered to be a function of road surface and actual slip λ . Slip is the difference between wheel speed ω_w and vehicle speed ω_v [1].

$$\lambda = \frac{\omega_w - \omega_v}{\text{Max}(\omega_w, \omega_v)} \quad (5)$$

The actual adhesive coefficient is calculated using the Pacejka magic formula which is a respected approach of modeling tire characteristics. Various surface types may be simulated by varying the coefficients in Pacejka's formula. Tarmac, wet tarmac, snow and ice surface are predefined in the simulation tool [1].

Model respects basic resistances acting on a vehicle such as the air drag resistance, rolling resistance of wheels and hill resistance. The traction force F_T acting on a single wheel is a product of adhesive coefficient which is calculated with Pacejka's magic formula and the normal force F_n at the wheel.

$$F_T = \mu(\lambda) \cdot F_n \quad (6)$$

The air resistance force F_A acts on the vehicle body and depends on air density ρ_{air} , air drag coefficient c_x , frontal area of the vehicle S and mostly on the actual velocity v [1].

$$F_A = \frac{1}{2} \rho_{air} \cdot v^2 \cdot c_x \cdot S \quad (7)$$

The rolling resistance force F_R is considered to be independent on the vehicle velocity and is therefore a product of the actual normal force F_n at a single wheel and the rolling resistance coefficient f [1].

$$F_R = F_n \cdot f \quad (8)$$

Longitudinal dynamics of the vehicle are also respected and thus normal forces acting on front and rear wheels vary with acceleration and deceleration of the vehicle.

1.3 Power Sources

The powertrain model described in the previous chapter may be driven by various power sources. The simple models of combustion engine, traction motor, fuel cell and battery are explained in this chapter.

1.3.1 Combustion Engine

Combustion engine is simplified to an ideal torque generator acting on a constant inertia that is connected via rotor shaft to the clutch disk. The engine torque is limited by full load curve. Full load curve is realized by a look-up function that assigns the maximal value of torque to the actual value of engine speed. Look up table is also used to determine the brake specific fuel consumption *bsfc* at specified

speed and torque. The actual *bsfc* depends on current engine speed and torque and is interpolated from the map data. Fuel consumption is calculated from *bsfc* and current power (Eq. 9) and serves as the input for the equation describing the CO₂ production [1].

$$\dot{m}_f = P_e \cdot bsfc \quad (9)$$

Symbol \dot{m}_f is the actual mass flow rate of the fuel and P_e is the engine power.

1.3.2 Traction Motor

The traction motor is simplified to an ideal torque generator acting on constant inertia that is connected via rotor shaft to the clutch disk. The engine torque is limited by full load curves for both motor and generator mode. Full load curves are realized by a look-up function that assigns the maximal motoric or generator torque to the actual value of engine speed. Look up tables are also used to determine the power losses (motor efficiency) at specified speed and torque. The electrical power needed to run the motor is then calculated as the sum of mechanical power and actual power loss [3]:

$$P_{el} = P_{mech} + P_{loss} = T_m \cdot \omega_m + P_{loss} \quad (10)$$

The generator mode is calculated vice versa. The resulting motor efficiency is:

$$\eta_m = \frac{P_{mech}}{P_{el}} \quad (11)$$

The motor power loss look-up tables might also be modified to efficiency look-up tables, but it results in complications with determination of power losses along the zero torque line.

1.3.3 Fuel Cell

Electrical power of the fuel cell running at current density i is calculated using the polarisation curve:

$$P_e = U \cdot i \cdot A_{cell} \quad (12)$$

A is the overall area of the fuel cell. P_e is the power of the fuel cell without parasitic losses.

The fuel cell module also calculates parasitic losses for a turbo-compressor assembly, designed to maintain the optimal operating pressure of the fuel cell. The equations of compressor and turbine operation used in the fuel cell module are valid only for the following assumptions: the heat flow from the compressor is negligible and the change in the kinetic energy of the inlet and outlet gas is

negligible. The gas is considered to be a perfect gas with a constant specific heat capacity C_p . A reversible process of gas compression is as follows [4]:

$$\frac{T_2'}{T_1} = \left(\frac{p_2}{p_1}\right)^{\frac{\gamma-1}{\gamma}} \quad (13)$$

The upper index in the symbol T_2' indicates isentropic temperature change. The isentropic efficiency of compression (η_c) is defined by Eq. (14):

$$\eta_c = \frac{\text{isoentropic work}}{\text{real work}} = \frac{c_p(T_2' - T_1) \cdot m}{c_p(T_2 - T_1) \cdot m} = \frac{T_2' - T_1}{T_2 - T_1} = \frac{T_1}{T_2 - T_1} \left(\left(\frac{p_2}{p_1}\right)^{\frac{\gamma-1}{\gamma}} - 1 \right) \quad (14)$$

and so:

$$\Delta T = T_2 - T_1 = \frac{T_1}{\eta_c} \left(\left(\frac{p_2}{p_1}\right)^{\frac{\gamma-1}{\gamma}} - 1 \right) \quad (15)$$

The power needed to run the compressor is calculated from the temperature change and is divided by mechanical efficiency η_{mech} [4]:

$$P_{comp} = \frac{c_p \cdot \Delta T \cdot \dot{m}_{air}}{\eta_{mech}} = \frac{c_p \cdot \frac{T_1}{\eta_c} \left(\left(\frac{p_2}{p_1}\right)^{\frac{\gamma-1}{\gamma}} - 1 \right) \cdot \dot{m}_{air}}{\eta_{mech}} = c_p \cdot \frac{T_1}{\eta_{comp}} \left(\left(\frac{p_2}{p_1}\right)^{\frac{\gamma-1}{\gamma}} - 1 \right) \cdot \dot{m}_{air} \quad (16)$$

$$\eta_{comp} = \eta_c \cdot \eta_{mech}$$

The isentropic efficiency of the compressor may be estimated from compressor performance charts.

A similar procedure is applied in turbine power calculations. For turbine power to drive an external load, is derived and used the following formula (4):

$$P_{turb} = c_p \cdot \Delta T \cdot \dot{m}_{wet\ air} \cdot \eta_{mech} = c_p \cdot \eta_c \cdot T_1 \left(\left(\frac{p_2}{p_1}\right)^{\frac{\gamma-1}{\gamma}} - 1 \right) \cdot \dot{m}_{wet\ air} \cdot \eta_{mech} \quad (17)$$

$$= c_p \cdot \eta_{turb} \cdot T_1 \left(\left(\frac{p_2}{p_1}\right)^{\frac{\gamma-1}{\gamma}} - 1 \right) \cdot \dot{m}_{wet\ air}$$

More realistic performance $P_{turb.cond}$ is lower, because the wet exit air condensates in the turbine (4):

$$P_{turb.cond} = \frac{P_{turb}}{\text{condensation coefficient}} \quad (18)$$

Finally the power we get from the fuel cell after subtracting the parasitic losses is:

$$P_{FC} = P_e - (P_{comp} - P_{turb\ cond}). \quad (19)$$

1.3.4 Hydrogen and Air Usage Calculations

According to the working principle of a fuel cell four electrons are transferred for each mole of oxygen. The charge Q , generated by this electron motion, is equal to (5):

$$Q = 4 \cdot F \cdot \text{amount of } O_2 \quad (20)$$

Divided by time for a stack of n cells (5):

$$O_2\ usage = \frac{I \cdot n}{4 \cdot F} = \frac{P_e}{4 \cdot U_c \cdot F} = 8.29 \cdot 10^{-8} \frac{P_e}{U_c} \quad (21)$$

It is better to change moles/s to kg/s (5):

$$\dot{m}_{oxygen} = \frac{32 \cdot 10^{-3} \cdot P_e}{4 \cdot U_c \cdot F} \quad (22)$$

The Eq. (22) may be modified in order to get air usage. The molar mass of oxygen (32 g/mole) is exchanged by the molar mass of air (28.97 g/mole) and the whole Eq. (23) is divided by the molar proportion of oxygen in air (0.21). The air stoichiometry must also be considered here and included in the Eq. (23) [5]:

$$\dot{m}_{air} = \frac{28.97 \cdot 10^{-3} \cdot P_e}{0.21 \cdot 4 \cdot U_c \cdot F} \cdot \lambda = 3,57 \cdot 10^{-7} \frac{P_e}{U_c} \cdot \lambda \quad (23)$$

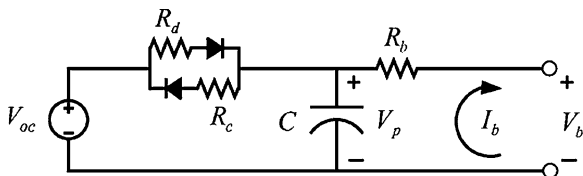
The exit air flow rate depends on the consumption of oxygen and is calculated as air inlet flow rate minus hydrogen usage. The formula is therefore (5):

$$\dot{m}_{air\ exit} = (3.57 \cdot 10^{-7} \cdot \lambda - 8.29 \cdot 10^{-8}) \cdot \frac{P_e}{U_c} \quad (24)$$

Hydrogen usage is calculated similarly as oxygen usage. The only difference is that there are only two electrons from each mole of hydrogen. The formula for hydrogen usage at stoichiometric operation therefore becomes (5):

$$\dot{m}_{hydrogen} = \frac{2.02 \cdot 10^{-3} \cdot P_e}{2 \cdot U_c \cdot F} = 1.05 \cdot 10^{-8} \frac{P_e}{U_c} \quad (25)$$

Fig. 4 Equivalent circuit battery model—Thevenin



1.3.5 Battery

Thevenin battery model is used to describe the battery behaviour. It is an equivalent circuit battery model that simplifies the battery processes to a simple electronic circuit (Fig. 4). It uses a capacitor to simulate the capacity C of the battery and resistors R to simulate the internal resistance of the battery [6].

Following equations describe the battery accordingly to Thevenin model [6]:

Discharging:

$$\dot{V}_p = -V_p \frac{1}{R_d C} + V_{OC} \frac{1}{R_d C} - I_b \frac{1}{C} \quad (26)$$

Charging:

$$\dot{V}_p = -V_p \frac{1}{R_c C} + V_{OC} \frac{1}{R_c C} - I_b \frac{1}{C} \quad (27)$$

Where the battery current I_b is:

$$I_b = \frac{V_p - V_{OC}}{R_b} \quad (28)$$

All parameters may be entered as constants or as a function to better describe the dependency of battery performance on state of charge, rate of charge/discharge or temperature. Data must be measured or supplied by the battery manufactures. The battery model also contains a simplified thermal model for a rough prediction of battery temperatures under load.

2 Case Study

A comparison study of three various powertrains was performed to demonstrate the functionality and possibilities of the developed simulation tool. The simulation tool was tested on a drivetrain based on Skoda Fabia 1.2 HTP 44 kW. The basic input data for the simulation were taken from the official technical specifications list and detailed data such as engine parameters, bsfc map, transmission parameters, wheel rolling resistance and inertias of rotating parts were obtained from the measurements done at the Josef Bozek research centre (Table 1).

Table 1 Vehicle data [7]

Vehicle type	Skoda fabia
Vehicle weight (kg)	900–1,700
Frontal area (m ²)	2
Air drag coefficient [1]	0.3
Wheel radius dynamic (m)	0.308
Rolling resistance coefficient [1]	0.012
I_{wheel} (kgm ²)	0.47
No of axles	2
Air density (kg/m ³)	1.2
Gearbox ratios (ICE only)	3.455; 1.955; 1.281; 0.927; 0.74
Fixed gear ratio (ICE only)	4.533

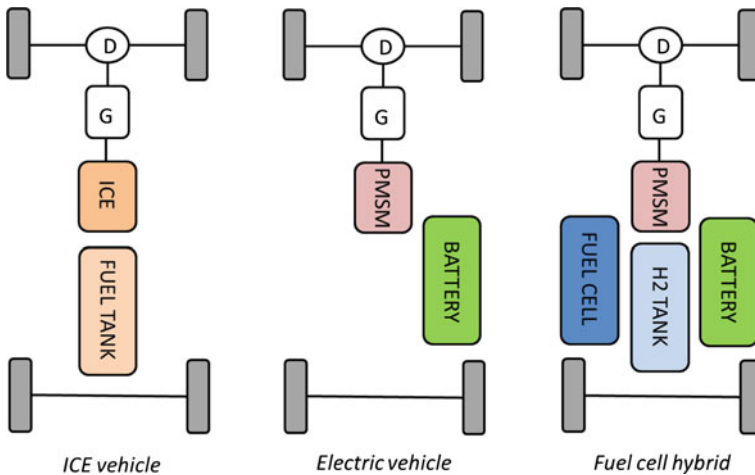


Fig. 5 Investigated powertrains

Conventional gasoline engine powertrain was compared to pure electric vehicle powered by one PMSM traction motor and further to fuel cell hybrid vehicle (Fig. 5). The rated power of three compared power units was chosen between 40 and 50 kW.

The control of the vehicle in a driving cycle is realized with a PID controller that compares actual and demanded speed and via virtual throttle pedal applies positive torque directly at the engine or motor inertia element. Negative torque is applied on inertias that represent wheels during braking. The shifting events are prescribed by the NEDC and realized by a clutch opening, throttle release and change of gear ratio. The control of electric powertrain is realized in a similar way, but without shifting events and with regenerative braking over the whole NEDC.

The control of the fuel cell hybrid vehicle is more complicated, because the electrical energy that drives the traction motor might be drawn either from the fuel cell, battery or the combination of both. The control strategy is determined by the current battery state of charge, speed and load (Table 2).

3 Results

The ride of the vehicle with a combustion engine powertrain was calculated in several driving cycles and compared to measurement results to approve the simulation tool. Selected resistance coefficients were validated by a comparison of model and real test results for the free deceleration test.

The consumption at a constant speed was tested at 90 and 120 km/h. New European Driving Cycle (NEDC) was selected to obtain the simulation results for the consumption and CO₂ production during a transient ride. Finally the top speed of the vehicle and 0–100 km/h acceleration were calculated and compared to the performance of a real vehicle. The official values of consumption at constant speed measured by the producer are 4.9 liters at 90 km/h and 6.9 liters at 120 km/h. Actual consumptions calculated with the simulation tool are 4.94 l/100 km at 90 km/h and 6.62 l/100 km at 120 km/h. Both measurement and simulation results were obtained with shifted 5th gear. The average vehicle consumption in NEDC calculated by the developed tool is 5.5 l/100 km (CO₂: 124 g/km), which is 0.4 l/100 km less than the official value for Skoda Fabia 1.2 HTP 44 kW according to EU99/100. The simulated vehicle can reach the maximum speed 154 km/h which may be compared to the measured top speed 151 km/h. The overview of results is in Table 3.

All powertrains were then evaluated over a range of vehicle curb weight to show the influence of weight on energetic consumption (Fig. 6) and driving range (Fig. 7). The results are based on calculations performed in NEDC. The biggest marker always indicated the default weight of the powertrain. The energy consumption graph shows the high efficiency of electric powertrains and pure efficiency of combustion engines over the whole range of vehicle mass. The energy consumption significantly increases and consequently vehicle range decreases with the increasing vehicle mass in all cases. Thus the weight of the vehicle should be reduced as much as possible to decrease its energy consumption in the case of each powertrain layout.

The range of the vehicle decreases with its increasing weight. This is especially crucial with pure electric vehicle powertrain, where its range becomes a limiting factor for everyday use.

Table 2 Fuel cell hybrid control strategy

		Demanded power		
		Power < 0	Power = 0	0 < Power < Max FC
State of charge	SOC = 0	Regenerative braking	Batteries are recharge by the FC power	FC power in use
	SOC < SOCmin	Regenerative braking	Batteries are recharge by the FC power	FC and battery power in use
	SOCmin > SOC < SOCmax	Regenerative braking	Batteries are recharge by the FC power	FC and battery power in use
	SOC > SOCmax			FC and battery power in use

Table 3 Comparison of simulation and measurement results

	Consumption at 90 km/h (l/100 km)	Consumption at 120 km/h (l/100 km)	NEDC cons. (l/100 km)	Top speed (km/h)
Skoda official Values	4.9	6.9	5.9	151
Simulation results	4.94	6.62	5.5	154

Fig. 6 Effect of curb weight on energy consumption

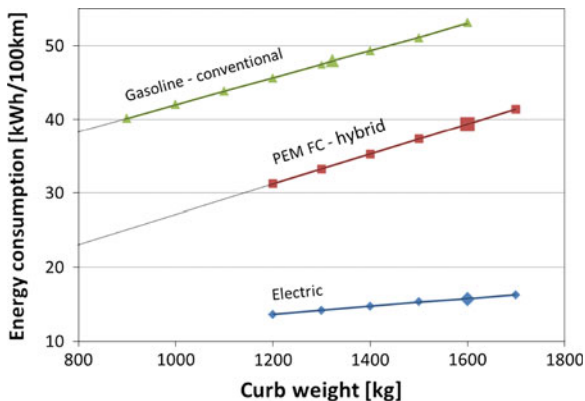
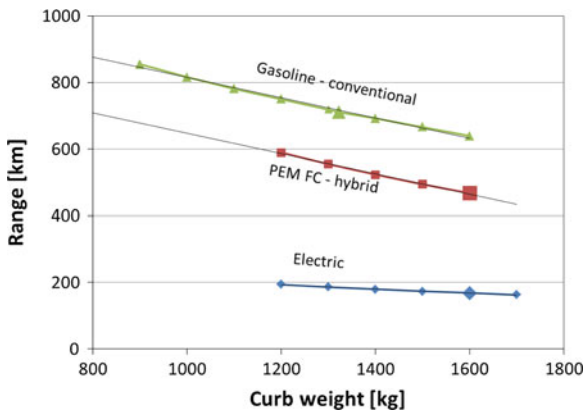


Fig. 7 Effect of curb weight on vehicle range



4 Conclusions

The simulation results for Skoda Fabia show good coincidence with real data regarding to the simplicity of the model. No calibration coefficients were used to fit simulation results on measured data. The developed simulation tool seems to provide good results for rough powertrain calculations. Its great advantage is its low computational time effort.

The comparison of conventional combustion engine powertrain, fuel cell hybrid powertrain and electric powertrain proved the high efficiency of electric powertrain at the cost of low range of electric vehicles. The influence of weight on the overall powertrain efficiency is very significant in all three cases.

The simulation tool is planned to be used for the optimization of vehicle powertrains with respect to reducing the vehicle consumption and thus also reducing the CO₂ production. It will be also used to evaluate the possible benefits of new powertrain concepts.

The next development steps will lead to the introduction of modules for other types of hybrid vehicle powertrains and existing modules may be updated with more complex models. The developed tool may due to its modularity also serve as a real time model for hardware in the loop simulations.

References

1. Barák A et al (2010) Powertrain simulation tool. MECCA—J Middle Eur Constr Design Cars. 2010/3-4, p 1-4, ISSN 1214-0821
2. Lucente G (2005) Modelling of a car driveline for servo-actuated gear shift control. University of Bologna, Bologna
3. Mindl P (2008) Hybridní automobily 1.část. [Online] 2008. http://www.inovace-dmt.fs.cvut.cz/studijni_materialy/Microsoft_PowerPoint_Prednaska_1.pdf
4. Larminie J, Dicks A (2003) Fuel cell systems explained, 2nd edn. Wiley, Chichester, p 424, ISBN 0-470-84857-X
5. Chiasson J (2005) Estimating the state of charge of a battery. IEEE Trans Control Syst Technol 13
6. Vávra J et al (2008) Simple tank-to-wheels analysis tool for future vehicle powertrains. [Online] http://www3.fs.cvut.cz/web/fileadmin/documents/12241-BOZEK/publikace/2008/2008_077_01.pdf
7. Barák A et al (2010) Model spotřeby hybridního vozidla v LabVIEW. AUTOMA- Časopis pro automatizační techniku, p 52-53, ISSN 12-10-9592

Part XVI
Other

Wet Handling Track: Utilities, Water System, Coefficient of Adherence

Pinilla Marc, Carbonell Abel and Arango Luz A

Abstract *Research and/or engineering questions/objective* A Wet Handling facility must assure a regular and controlled water film depth all along the track, homogeneity and an adequate coefficient of adherence of the asphaltic surface to allow maximum repeatability on tests. The study focused on defining the parts of the track and the construction procedures required to get the proper **coefficient of adherence** and to define the **basis of the design** of the watering system. The influence on the grip of the asphalt characteristics, the aging procedure of the track and the water treatment systems were tested and studied. The layout of the track, the design of the watering and the recovery elements (pianos, drainages, run-off areas) were done to get the safest conditions without affecting the tires and their behaviour. *Methodology* The Test Facilities Engineering department at IDIADA's Technical Centre has carried out a large number of studies on the asphalt characteristics to define the bituminous mixture and the grain size distribution of the aggregates to be paved in tracks with wet surfaces. The analysis of the cleaning, filtering and treatment systems for the water used in the track was done thinking on the influence of the presence of organic and non-organic particles on the grip. Based on the water study and on standard quality control tests, comparisons were made with the results obtained from other tracks. A procedure for aging the asphalt was studied and implemented for three months by means of repeated drive-through with test vehicles. The coefficient of adherence was measured every two weeks following internal braking procedure and complemented with the one indicated in the Regulation N° 13 ECE. The design of the watering system took into account that the watering system needed to be adapted to the “pianos” and kerb stones to

F2012-E16-005

P. Marc (✉) · C. Abel · A. L. A
IDIADA Automotive Technology, SA, Spain
e-mail: mpinilla@idiada.com

keep the desired water film depth and regularity without damaging the tires or affecting test vehicle trajectories. *Results* The asphalt's coefficient of adherence data obtained during the aging period and how this affects the results will be shown together with the test procedure used for the aging of the track, the basis for the design of the watering system and the water recovery system used. *Limitations of this study* The lack of testing regulation guidelines for these facilities gives no trustful ways to correlate the data obtained between different tracks. *What does the paper offer that is new in the field?* This new watering and recovering system designed and implemented gives an optimal control on the regularity of the water film depth along the track with a high percentage of water recovered on the system. *Conclusions* The Wet handling track utility system and pavement characteristics designed and constructed fulfil the most demanding premises in terms of water film depth regularity, coefficient of adherence of the track and water reservoir savings according to environment policies.

Keywords Coefficient of adherence • Watering system • Sprinklers • Asphalt pavement • Aging procedure

1 Scenario

The local environmental condition of the land where the track was built was one of the most important restriction points for designing a Wet Handling track. The special weather conditions at IDIADA, the huge quantity of water needed and also the target of recovering most of it were a handicap for the viability of the project.

The water introduced in the system comes from both rainfall and wells and its quality needs to be checked before introducing it into the system. The characteristics of the water (hardness, chemical components, presence of organic material,...) can affect the functioning of the track mainly by attacking the watering systems (which could be blocked and broken) and also affecting the coefficient of adherence of the track by means of algae and other components (like calcium) that can be settled in the surface of the track after the water has flown.

The Water Treatment Plant from the nearby Municipality is placed not far from IDIADA's site. From here, the rejected water can be drained out of the system and easily driven to it.

In the next years the system will get the water from the municipal Water Treatment Plant (from the 1st degree of treatment) instead of from the wells available nowadays. This is going to fulfil local environmental policies and will provide a bigger flow of water without depending on the well capacity.

2 Utilities

2.1 Water Supply

The amount of water needed for running the Wet Handling track was calculated according to the following hypothesis and formulas:

Track length (in m) = L (**1.565 m**)

Track width (in m) = W (**6 m**)

Track surface (in m²) = S (**9.390 m²**)

- Desired Rain Intensity (in mm/h) = RI (**64 mm/hour**—Pluviometry coefficient in Barcelona city (the average rainfall once per year during 20 min–62.4 mm/hour))

Other design criteria shall be decided at this time like:

Functional days per Year = D (**273 days**)

From here we can get:

Used Volume per year (in m³) UVY = **1.312.497 m³**

Considering that % of water recovery (%WR) is an experimental data according to the type of asphalts, slopes given to the roads and other parameters, a conservative, but at the same time quite real number for IDIADA special conditions is 70 % of water recovery. From here we obtain:

Water recovered Volume (in m³) WRV = UVY x %WR = **918.748 m³**.

So the volume of water that shall be taken from external sources (WES1) is:

WES1 = **393.749 m³**.

This WES is the conservative data to be considered as calculations, however, in order to check and validate this number more calculations and more hypothesis shall be confirmed.

Calculation Confirmation

Evaporation. The evaporation to be taken into consideration at IDIADA's zone is 5.000 mm/year, which means a total of = 52.500 m³ (TEY).

So the rainfall minus the evaporation (in m³) RME = UVY – TEY = **1.415.148 m³**.

The run coefficient according to [1] from the Spanish Road and Transport Ministry tables is 0.9 and the loss for water splash (in % of volume) is 5 %.

From here and applying these two coefficients it can be said that the volume of water that shall be taken from external sources (WES2) is: **257.696 m³**.

Comparing WES1 (**393.749 m³**) and WES2 (**257.696 m³**) it can be seen that value for WES1 is conservatively enough.

2.2 Dimensioning of the Water Tank

Due to the fact that the water usage is not constant, but follows a specific timetable pattern, this water shall be stored in order not to have a continuous external water supply with the necessary flow when needed.

The dimensioning of the water tank has been deducted from the hypothesis of a usage of 5 working days a week at 8 h per day. Then, a sixth day with only 2 working hours use and a seventh day for recovery. The loss is around 30 % (according to the experience of similar facilities). According to this the final external supply shall be enough to keep the water tank volume constant.

Finally, the data for the hydraulic dimensioning were as follows:

- External water flow 24 h 365 days: 743 692 m³/year, which is equivalent to an instantaneous flow of 85 m³/h. The demand to the official entity *l'Agència Catalana de l'Aigua (ACA)* was of 760.000 m³/year, in order to keep a security margin.
- Volume of the regulation tank: 5100 m³.
- Flow supply during 8 h per day 6.958 m³/d, equivalent to 870 m³/h.

2.3 Pumping Station

Water recovered from the drainage System is driven to a pumping station. From there the water will be pumped up to the tank in order to be re-used.

The pumping station was designed in three parts:

- Sand collector: It is the zone where the water first enters to the drainage System; it was dimensioned with the criterion of 10 min of hydraulic permanence in the System. In that way, the particles swept by the water from the track can decant. The bottom slab of the tank has a slope in order to accumulate the particles in one side of the tank, and in this way, the maintenance tasks become much more efficient.
- Aspiration: From the sand collector, the water passes to the aspiration zone through the drainpipe. The pumps are installed in this zone and by means of an ultrasonic water level they are switched on or off on the demand.
- Pumping station; this is the zone where the pumps and other equipment is installed (electrical switch cabinets, impulsion pipe, filtering System...).

The pumping station is totally underground with access to the pumps zone for maintenance Works (repairs and cleaning).

The recirculation System is composed by 3 pumps mounted in parallel with a frequency shifter in order to allow a soft switch on. Two of them are always running and the third is kept as spare. After each pump there is a medium size filter

Fig. 1 Manning Formula

Q	Flow
A	Area of the hydraulic section
N	Manning number
i	slope (in 1 per cent) obtained from combining the camber and the longitudinal slope of the axis
R_h	Hydraulic radius

in order to retain the bigger particles which have not been eliminated in the sand collector.

2.4 Water Piping

The object of the study was to check that with the previewed flow and the designed slopes of the track, the water film was 1 mm thick approximately. It was also required that the time needed for the water to run-through it was between 1 and 2 min. This value is extremely important because for longer times, the track would run out of water when the second car would pass over the same zone. On the contrary, for shorter times it would need a huge volume of water. For this reason it was decided to keep it between 1 and 2 min as an optimal time.

2.5 Water Film Calculation on the Surface of the Track

The wetting System was conceived with one nozzle at the side of the track every single meter. When the water, contacts the pavement, it moves by gravity to the recovery System according to the combination of slope and longitude. For the development of the project, a one-dimensional simulation of the water flow was carried out. The approach given to this hypothesis matches the reality considering the following:

- The watering System (nozzles) allows a uniform distribution of the flow along 1 m the distance between nozzles and
- From the impact with the pavement, the water will move though the maximum slope line.

For the water film depth calculation the Manning formula has been used: (Fig. 1).

$$Q = \frac{A}{n} (i)^{1/2} (R_h)^{2/3}$$

Pluviometry	64	mm/h
Width of the wet sector	1	m
Length to be crossed by the water	6	m
Moving water flow	0,384	m ³ /h/sector
	0,000107	m ³ /s/sector
	6,4	l/min/sector
	0,107	l/s/sector
Manning number	0,013	
Slope	0,005	
Depth	0,0015	m
Speed	0,071	m/s
Time used	84	s

Fig. 2 Calculations for a slope of 0.5 %

Fig. 3 Calculations for a slope of 2.5 %

Slope	0,025	
Depth	0,0009	m
Speed	0,115	m/s
Time used	52	s

Where:

The time needed for the water to cross the 6 m width of the track was also studied. The calculations were done considering the Manning number typically used for smooth pavement, and the minimal and maximal slope in the track and the results obtained were:

- Slope 0,5 %: In 1 ms of the length of the track the flow (transversal) is: (Fig. 2).
- Slope 2.5 %: In 1 m of the length of the track the flow (transversal) is: (Fig. 3).

It can be observed that the depth it is between 0,9 i 1,5 mm, and the time used by water is between 52 and 68 s. These values are acceptable keeping in mind that the System was designed with high regulation measures (pumps with variable speed and regulation valves for each nozzle). With these measures, the water flow could be adapted to the real needs for each point on the track.

2.6 Sprinklers at Water Level

The water reaches the track surface by means of a sprinkler as it is shown in the following pictures: (Fig. 4).

The sprinkler is placed inside a special designed concrete “piano” kerb that allows the flow expansion. At the same time, the sprinkler must be hidden inside the “piano” so it cannot be stepped on by a vehicle. The “piano” with its sprinkler is installed every meter for assuring the complete wetting of the surface of the track.

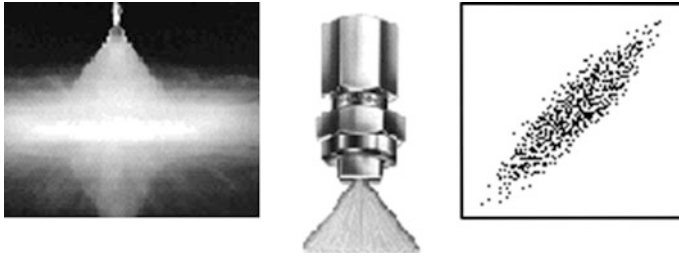


Fig. 4 Sprinkler's water flowing

The water flow depends on the pressure of the flow itself; for that reason a ball-valve has been installed in every sprinkler allowing the flow regulation on it. These manual regulations are only used as complement of the automatic regulations obtained from the regulation valves and the variation on the speed of the pumps.

2.7 Pressure System

The pressure system is composed by:

- 4 similar pumps mounted in parallel
- A frequency shifter for every pump

The pumps are switched on when a test in the track starts. The switch off of the pumps can be done also manually or when the pressure transduction elements installed in the pumping station can detect a raise on the pressure over a pre-selected value.

The switch on/off of the pumps is commanded in an alternative way from the electrical switch cabinet in a way that all the pumps are running the same number of hours. For this reason, each pump has its own frequency shifter for the switch on and also to control the speed of rotation and with this system the pumping height is managed. If the pressure level is below the pre-programmed one, the frequency shifter raises the turning speed of the pump. With this action the working point is giving more water flow. The frequency shifter is only working with one pump at a time “master” and the others are the “slaves”.

A simulation was done to check the functioning of the net with the chosen pumping system. The software EPANET, from U.S. Environmental Protection Agency, solves pressured water system at steady conditions. The software provides the flow and pressure in each point of the net under study.

Fig. 5 Manning strickler formula

Q (m³/s)	Drained flow.
V (m/s)	Average circulation speed.
S (m²)	Wet surface.
Rh (m²/m)	Hydraulic Radius.
J (m/m)	Longitudinal slope (in per one).
η	Manning Coefficient of roughness de Manning
η	η = 0,011 for plastic materials (PVC) pipes
η	η = 0,015 for concrete elements

2.8 Water Recovery System

In order to study the hydraulic capacity of the different elements the Manning–Strickler formula was used. This formula solves the relation between the pipe dimensions with the flow and its average speed. By combining them, the dimensioning of the elements is obtained. The formula is shown with the following expression:

$$Q = V s$$

$$Q = \frac{R^{2/3} J^{1/2} S}{\eta}$$

where: (Fig. 5).

3 Coefficient of Adherence

3.1 Pavement Definition

As starting point of the study and in order to try to do a first approach on the type of pavement to be chosen some benchmark test were performed in two existing European Wet Handling tracks using the same cars (medium FWD and medium RWD) to be taken as reference. Afterwards, same vehicles and tires were used for validation of the new track.

This Test procedure was specially designed and agreed with the future users so that all potential users could understand from scratch the results that were obtained.

So, after testing in the reference tracks the target to be obtained in the wet handling track was set at:

- BPN (British Pendulum Number) between 0.55 ± 0.3
- Braking distance ($30 \text{ m} \pm 1 \text{ m}$) and mean deceleration ($8 \text{ m/s}^2 \pm 0.5$) for 80–0 km/h.

With this information, the specific weather and environmental conditions at IDIADA together with our previous experience in pavement design, IDIADA

	Type of asphalt	Aggregates	Sand	Filler
Asphalt 1	Dense Bituminous Mixture with modified bitumen	Coarse aggregate: 4/12: alluvial (30%) Coarse aggregate: 12/18 porphyritic (16%)	Sand 0/4:Limestone (50%)	Limestone (4%)
Asphalt 2		Coarse aggregate: 4/12: alluvial (30%) Coarse aggregate: 12/18 porphyritic (16%)	Sand 0/4: Limestone (50%)	
Asphalt 3		Coarse aggregate: 4/12: alluvial (30%) Coarse aggregate: 12/18 porphyritic (16%)	Sand 0/4: Limestone (26%) Sand 0/6: Porphyritic (26%)	

Fig. 6 3 asphaltic mixtures characteristics

specified 3 different possible asphaltic mixtures with the following characteristics: (Fig. 6).

These trial sections were laid in one of IDIADA’s streets in order to check the adhesion coefficient and its evolution in time. Their dimensions were 50 × 5 m each and the measurements were taken in wet conditions. These sections were exposed during 6 months to daily traffic.

After this, measurements were taken according to the following test procedure: Each vehicle had to perform the following:

3.2 Brakes and Tyres Conditioning

- Burnish brake:
 - a. With new brakes and tyres perform at speed of 80 km/h and IBT < 100 °C and GVW:
 - b. 50 brakes at 2 m/s² + 50 brakes at 3 m/s² + 100 brakes at 5 m/s².
- Tyre run in: to drive 200 km at 120 km/h.
- Tyre bedding: 10 full stops following the procedure below.

3.3 Adhesion Measurements Performed Following ECE R13 09 Procedure (Performed with New Tyres) Stopping Distance Test Procedure (Performed with 50 % Worn and New Tyres) [2]

- Vehicle weight: Curb Weight + 150 kg
- Transmission posit: Neutral
- IBT: 65–100 °C (Performed at 100 °C)
- Init. vehicle speed: 90 km/h
- Speeds for calculation: 80 ÷ 20 km/h

	km	80-20	80-60	40-20
		[m/s ²]	[m/s ²]	[m/s ²]
Asphalt 1	1.049	8.89	10.25	9.66
Asphalt 2	1.068	9.33	10.14	9.97
Asphalt 3	1.081	8.98	9.97	9.58

Fig. 7 Table: longitudinal adhesion

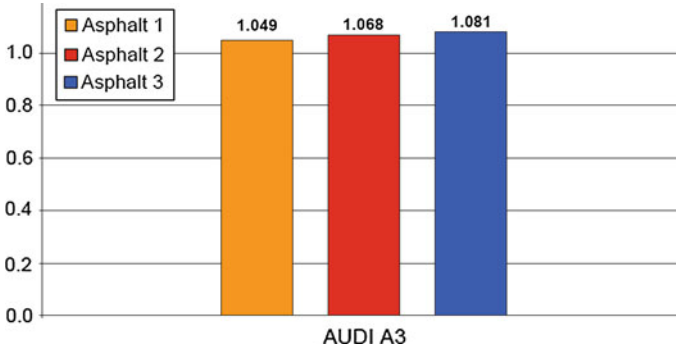


Fig. 8 Table: longitudinal adhesion

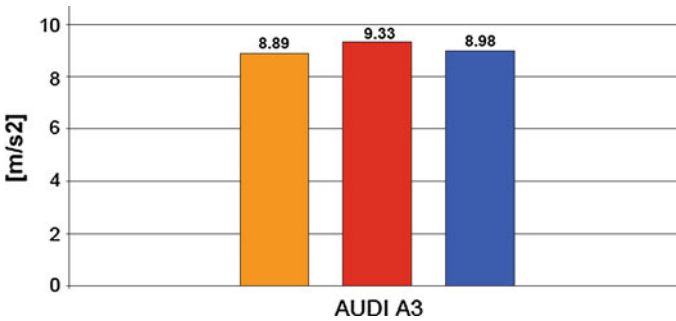


Fig. 9 Table: deceleration

- Brake pedal effort: > 500 N
- Pedal rate: 500 N within 0.15 s (3333 N/s)
- No. of stops: 10 brake stops

The averaged longitudinal adhesion coefficients, the maximum decelerations and the Stopping distances obtained, are compared as follows: (Figs. 7, 8, 9, 10)

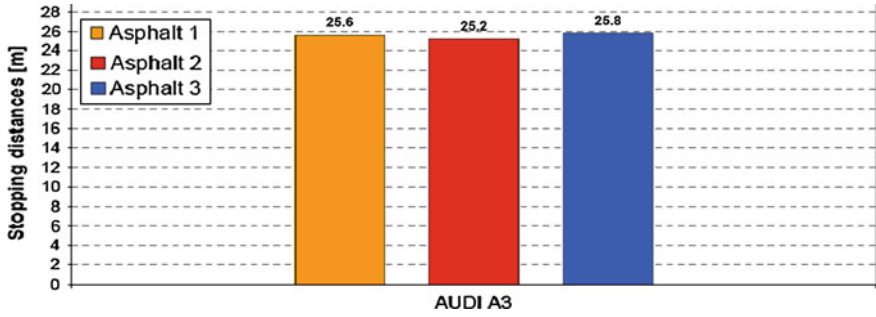


Fig. 10 Table: stopping distance (80–0 km/h with new tires)

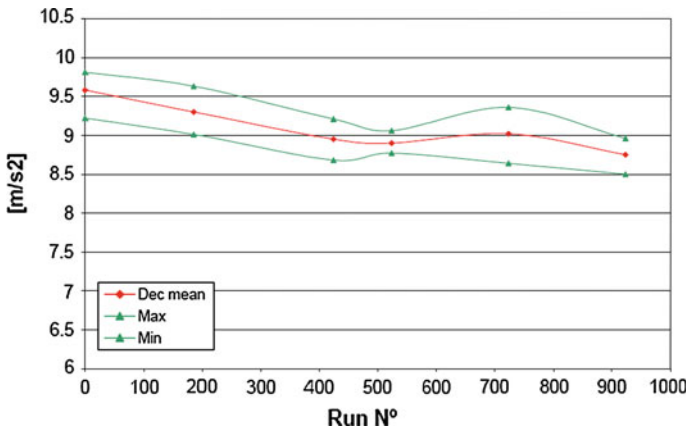


Fig. 11 Average deceleration vs run number

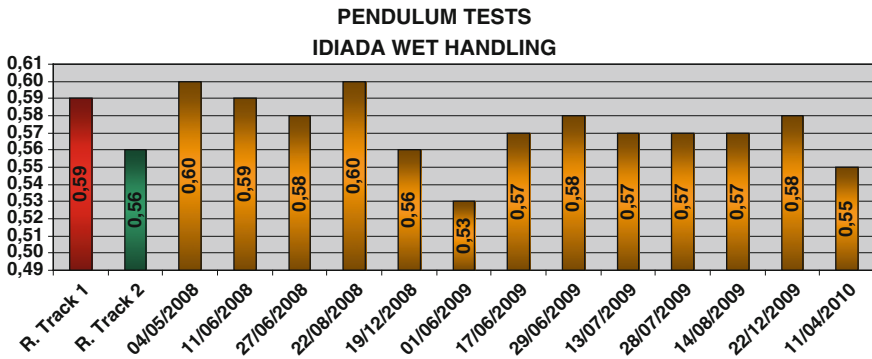


Fig. 12 Pendulum tests

3.4 Aging of the Pavement

Additional polishing was done with a special trailer in order to remove the bitumen and polish the soft aggregates. The number of polishing rounds was controlled and periodical measures were taken. The laps were polished by a tractor with a pneumatic trailer (Figs. 11, 12).

4 Conclusions

After the abovementioned studies and a deep analysis of the results, it was jointly decided together with the main Wet Handling track users that the best asphaltic mixture to be laid was the one called Asphalt 3.

It shall be remembered that the materials from Asphalt 3 are the ones available at IDIADA's surroundings and the characteristics of each type of stones and sand could vary from one place to another.

So in conclusion, the Wet handling track utility system and pavement characteristics designed and constructed, fulfil the most demanding premises in terms of water film depth regularity, coefficient of adherence of the track and water reservoir savings according to most advanced tire development testing needs as well as most demanding environment policies.

References

1. Instrucción 5.2-I.C. Drenaje Superficial, de la Dirección General de Carreteras, BOE núm. 123, de 23 de mayo de 1990
2. ECE R13 09 braking procedure, Approval of vehicles of categories M, N and O with regard to braking

The Development of an Auxiliary Unloading Device for Dump Trucks

Guoxing Li and Tie Wang

Abstract This chapter analyzes the roll-over mechanism of dump truck in the unloading operation, and then presents an auxiliary unloading device. The device consists of boosting mechanism and linkage mechanism. The driving force of the device originated from the geometric distortion produced in the process of lifting carriage. This chapter elaborates on the principle of device and establishes virtual prototype model of the device. Based on the established model, the validity and feasibility of the design has been verified.

Keywords Dump truck · Roll-over · Auxiliary device · Dynamic analysis · Centroid

1 Introduction

As one of the special-purpose engineering vehicles, the centroid of dump truck is higher than other trucks due to its structural features; therefore, the risk of roll-over is also higher than that of others [1]. When loading the powder, especially wet powder, the dump truck has a high probability of occurrence of roll-over accidents in that accumulation of goods caused by the adhesion with the carriage will lead to raising the carriage's centroid.

At present, many scholars have carried out many studies on the mechanism of dump truck roll-over. Considering the factors such as tires, suspension, using a

F2012-E16-006

G. Li (✉) · T. Wang
Taiyuan University of Technology, Taiyuan, China
e-mail: lgx0053@link.tyut.edu.cn

nonlinear model, Prem [2] carried out some studies on roll-over stability of large dump truck for mining by using a nonlinear model; Using the method of combining experiment and simulation, Ginzburg [3] analyzed the lateral stability of the dump truck; From the perspective of statics, Chen [4] analyzed the mechanism of heavy-duty dump trucks roll-over in the lifting process, and proposed the way that increases the stability of lifting by improving the structure of frame.

In view of the characteristics of dump truck unloading, this chapter analyzes the mechanism of dump truck roll-over, and presents an auxiliary unloading device with a simple structure.

2 Mechanism of Dump Truck Roll-Over

2.1 Analysis of Dump Truck Stability

Compared with the general trucks, dimensions parameters of dump truck chassis frame, subframe, carriage vice longitudinal beam and compartment lead to its higher centroid, generally between 2000 and 2200 mm. The dump truck's centroid is higher than the general truck, therefore, the risk of roll-over is also higher than that of others.

Figure 1 is the unloading schematic diagram of dump truck parked in the transverse slope β . When the dump truck suspension deforms, the left and right suspension result in different elastic deformations on account of the role of gravitational force component, which makes the carriage occur angular displacement α relative to the axle. In the process of dump truck lifting, the angular displacement α will change with the rising of the centroid of carriage and goods.

Calculation the height above ground of the dump truck's centroid H' :

$$H' = \frac{G_1 \times h + G_2 \times H}{G_1 + G_2} \quad (1)$$

In this formula

H The centroid height of compartment (mm);

H The centroid height of chassis (mm);

G_1 The total weight of dump truck chassis (kg);

G_2 The total weight dump truck compartment (kg).

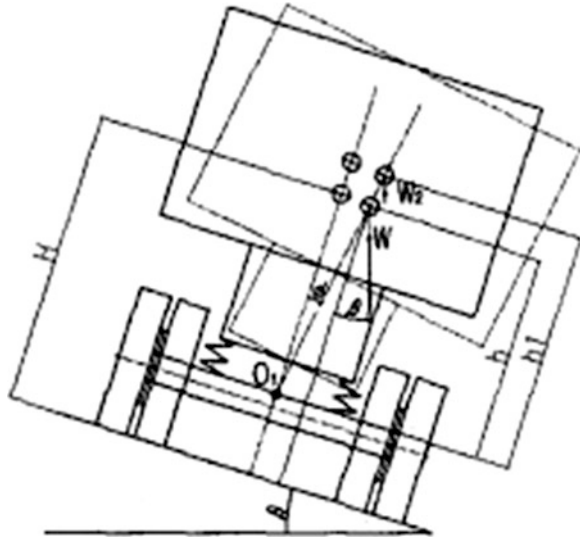
To prevent the dump truck roll-over occurs, the coordinates $(x_0, 0)$ of the intersection between the extension cords of vehicle gravity direction W and the ground, must satisfy the formula 2:

$$x_0 = H' \times \text{tg}\beta + (H' - h) \times \text{tg}\alpha < \frac{B}{2} \quad (2)$$

In this formula

B Width of the tires touching the ground (mm).

Fig. 1 Schematic of dump truck unloading



It can be seen from Eq. 2, factors affecting the stability of the dump truck operations, include wheel track, suspension stiffness, the vehicle centroid height and slope of operation site.

2.2 Effect of Carriage Lifting on the Stability of Vehicle

As shown in Fig. 2, during the unloading process, the centroid of the carriage and goods has increased to ΔH . Assume that the G_2 and the angle α does not change, substituted ΔH into Eq. 1, and the $\Delta H'$ can be got. Then, taking $\Delta H'$ into Eq. 3, the stable angle β would be get

$$\beta = \arctg\{[B/2 - (H' - h) \times tg\alpha]/H'\}. \tag{3}$$

3 The Principle of Auxiliary Unloading Device

3.1 The Mechanical Principle of the Device

The viscosity between the goods and dump truck carriage will lead to the elevation of vehicle centroid and increase the roll-over risk. The conventional counter-measure is the manual operation by the driver, keeping bodywork wobble up and down and making the inside goods concentrated and separated, which can promote

Fig. 2 Change of carriage centroid during the lifting process

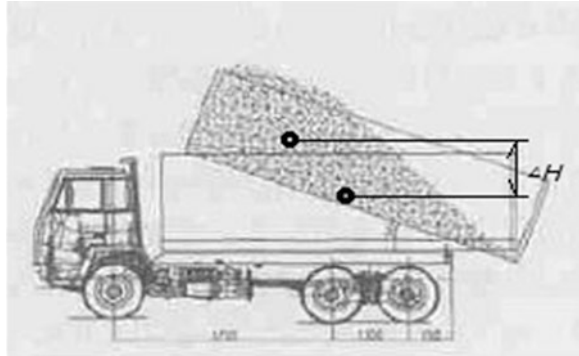
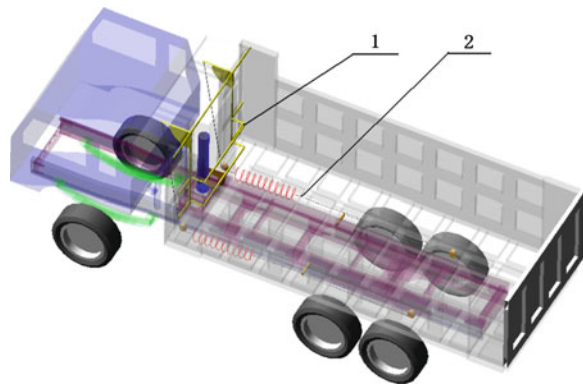


Fig. 3 Structure sketch of auxiliary device



the unloading process. However, this measure also has the risk of roll-over because the goods are deviated from the center of carriage; and dynamic operation may exacerbate this trend.

In response to this situation, in order to reduce the height of the centroid in the unloading process, this chapter presents an auxiliary unloading device.

Auxiliary device consists of boosting mechanism 1 and linkage mechanism 2. As shown in Fig. 3, boosting mechanism is placed in the front of the carriage inside which can rotate around the shaft at the top of the carriage. In the rotating process, boosting grid which attached to the carriage inside will impose thrust on goods. Attendant shredding force will contribute to the dispersion of goods, facilitating its unloading.

Driving force of boosting mechanism is provided by the linkage mechanism. Linkage mechanism consists of wire ropes, pulleys and springs. As shown in Fig. 4b and c, with the rising of the carriage, bottom of the carriage detached from the frame. Geometric changes make the wire ropes pulled tight. The leverage part of boosting mechanism which extends to the outside receives the pulling force down along the rope. Then the boosting grid gains the power.

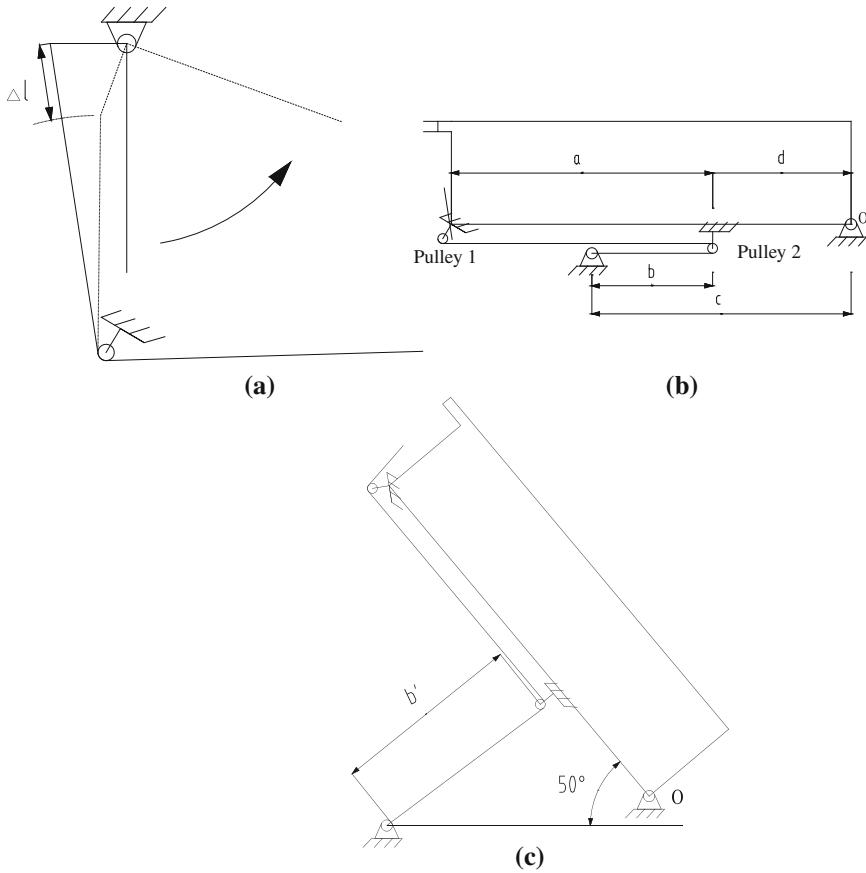


Fig. 4 a Changes in length of the wire rope during the taut process. b The layout of linkage mechanism. c The shape of wire rope when the angle equal to 50°

In order to make the boosting mechanism get the suitable promoting distance, the layout of the wire rope needs to be rationally calculated.

As shown in Fig. 4a, in the process of the carriage lifting, with the boosting mechanism rotating around the shaft, when leverage stays under the two extreme positions, the length difference of the corresponding wire rope is Δl .

As shown in Fig. 4b, pulley 1 is placed under the front side of carriage. Pulley 2 is similarly placed under the carriage, and the distance between the two pulleys is a . After rounding the pulley 2, wire rope is fixed outside of the frame. The distance between the fixed node and pulley 2 is b . The distance between fixed node and point O is c .

As shown in Fig. 4c, when the carriage is lifted in the extreme position, the angle from the carriage and car frame is taken as 50° . The distance between pulley 2 and fixed node will increase to b' .

In order to meet the length changes Δl of the wire rope, the locations of the pulley 2 and fixed node need to be satisfied the following conditions:

$$b' - b = \Delta l \quad (4)$$

The length of the carriage is known for 4900 mm, and $b' - b = 550$ mm. According to the given conditions, equations are available as follows:

$$\left. \begin{aligned} a - b + c &= a + d = 4900 \text{ mm} \\ (c^2 + d^2 - b^2) / (2 \times c \times d) &= \cos 50^\circ \\ c &= b + d \\ b' - b &= \Delta l \end{aligned} \right\} \quad (5)$$

Solve the equations, and select the appropriate solution from the solution set:

$$a = 3800, b = 1789 \text{ mm}$$

B is a variable. The time when boosting mechanism reaches the maximum can be adjusted by adjusting the values of B. The smaller the value of B is, the shorter action time of boosting mechanism is, the greater the thrust will be, the shorter unloading time is, the higher efficiency will be.

3.2 Application of Springs

In the early stage of carriage lifting, the angle between carriage and frame is tiny, and the component force of gravity along the sliding direction is very small, and then the load of the device is too large, which may cause the deformation and damage of the frame and wire rope. Therefore, in order to ease the large tension, set the spring 1 in the section a of wire rope.

The another function of the spring 1 is storing energy, changing the initial tensioning force into the potential energy of spring, then concentrated releasing it before carriage and goods reach the highest point, which can promote the unloading process.

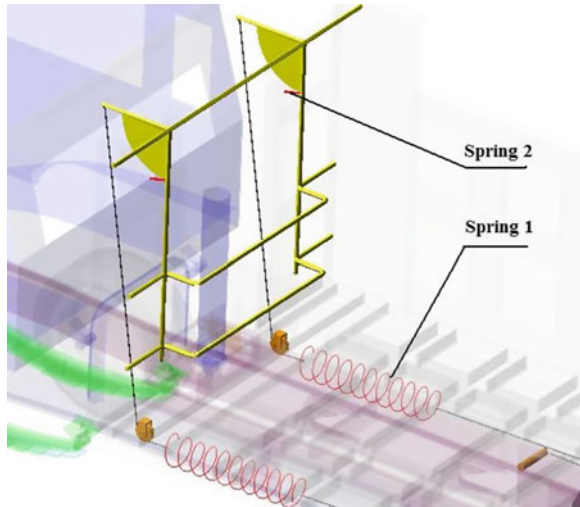
After the discharge of the goods, or during the no-load transport process, in order to restrict the boosting mechanism close to the inside of carriage, the pull-back spring 2 is set between the boosting grid and carriage (Fig. 5).

4 Dynamic Simulation of Auxiliary Unloading Device

4.1 Dynamic Model for Device

Establish the dynamic model for device through the widely used dynamic analysis software ADAMS (Automatic Dynamic Analysis of Mechanical System).

Fig. 5 Application of springs



Modelling three-dimensional model for the device, then import it into ADAMS/View in Parasolid format. Then define the material properties of the model, imposes additional constraints, sets friction parameters for contact.

In order to verify the effect of auxiliary devices for unloading, the prototype model has been simplified-models of tires and leaf springs have been omitted. Connect the lifting mechanism and carriage with the revolute joint. The other end of the hydraulic cylinder is connected with the subframe with revolute joint. The back fulcrum of carriage is connected with the subframe by using a revolute joint. Simplified representations of the goods are three cuboids 2000 × 1500 × 1000 mm. Set a contact pair with friction between goods and carriage. Choose the wire rope with D = 20 mm, Minimum Breaking Load of Rope = 239 KN, and establish a flexible model for the wire rope with the grid number = 1400 in ADAMS.

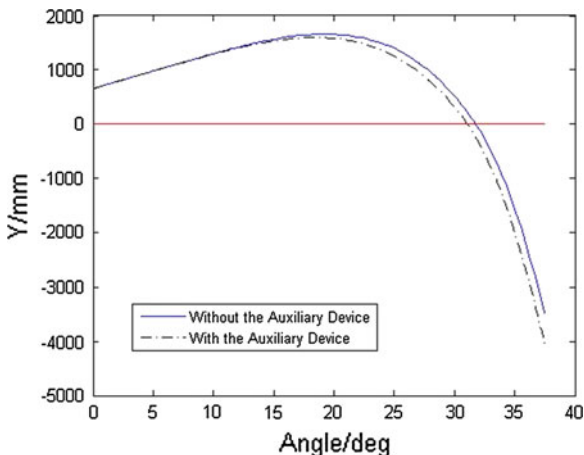
The definition of friction in ADAMS:

$$F = -N \cdot STEP(v, -V_s, -1, V_s, 1) \cdot STEP(ABS(v), V_s, C_{st}, V_{tr}, C_{dy}) \tag{6}$$

In the equation, N is the contact force in normal direction; V_s is the static friction velocity; V_{tr} is the dynamic friction velocity; C_{st} , C_{dy} are static friction coefficient and dynamic friction coefficient respectively. Select the friction parameters based on the material properties of surface [5]: $C_{st} = 0.3$, $C_{dy} = 0.25$, $V_s = 0.1$, $V_{tr} = 10$ m/s.

After selecting these parameters above, dynamic simulation can be started.

Fig. 6 The height variation curves of centroid of the goods



4.2 Dynamic Simulation of Device

4.2.1 Optimization of Stable Angle

Establish the models of dump truck with auxiliary device and without auxiliary device respectively. Driven by hydraulic cylinder, the carriage will be lifting from 0° to 50°, relative to the frame. Draw the height variation curves of centroid of the goods in the vertical direction (Y direction).

As shown in Fig. 6, the height of the contact surface between carriage and frame is 0 mm. When the centroid curve intersects $Y = 0$, it shows that goods is unloading below the plane of the frame, from which it can be judged that unload process has been finished. The real line is without the auxiliary device and the dotted line with the auxiliary device.

It can be seen from the Fig. 6 that the centroid of the goods in the vehicle installed with auxiliary device can reach the higher point in a shorter time and its highest point value is 70.44 mm lower than that without the auxiliary device. On 32°, the dotted line intersects $Y = 0$ and it finishes the unload at 2° in advance than the real line.

Combine the two maximum values of centroid of the goods and the carriage centroid respectively to get $G1_{max}$, and then take it into the formula 1 and calculate the biggest stable angle $\beta_1 = 20.2894^\circ$, $\beta_2 = 21.5838^\circ$.

The results show that the largest stable angle of the vehicle installed the device increases by 6.3797 %. The auxiliary device has a great effect on the stability of the vehicle. The repose angle of goods unloading reduces by 2°, the unloading time shortened and the work efficiency improved.

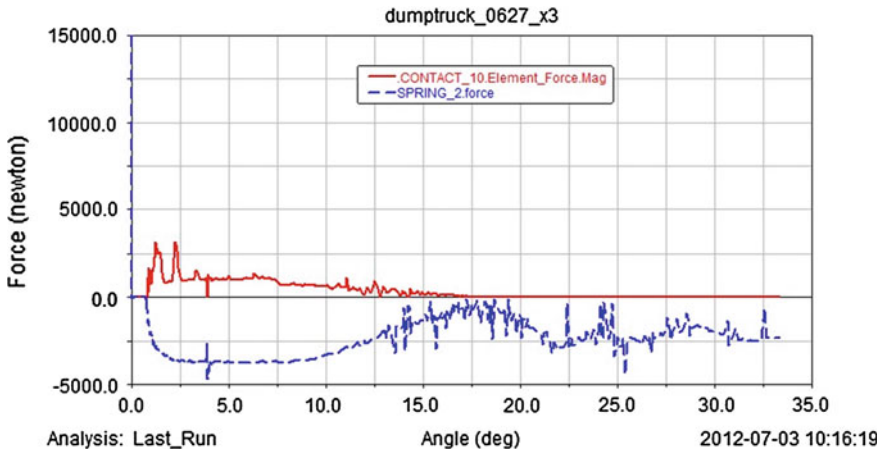


Fig. 7 The stress curves of boosting mechanism and spring 1

4.2.2 Mechanics Analysis

As shown in Fig. 7, the real line is the contact stress between the boosting grid and goods. The dotted line is the tension that the spring 1 bears in the process of dump truck lifting.

As shown in the Fig. 7, in the early stage of the carriage lifting, when the lifting angle $< 1^\circ$, the contact force between the boosting grid and goods is small because geometric distortion between the carriage and goods is small and the spring tension is not obvious. Along with further increase of the lifting angle, the spring begins to tighten stress and the thrust of the boosting grid to goods increases. It reaches the maximum value 3KN on 2° . After 17.5° , the goods in its own gravity finish unloading.

It is known from the curve, the maximum stress of the spring is 4.960 KN, which does not exceed the Minimum Breaking Load of Rope 239 KN; therefore, it is a reasonable and feasible scheme.

5 Conclusion

This chapter presents an auxiliary unloading device for dump trucks. It is known from the dynamic simulation analysis:

- (1) The structure of the device is designed simply and doesn't increase the driving equipment for special-purpose, which controls the application cost of the device effectively.

- (2) This design to modification and structural damage of the original vehicle is relative small. The application of springs avoids the destruction of big load on the body of the vehicle.
- (3) The auxiliary unloading device increases the stable angle of the roll-over of the whole vehicle, increases the stability of unloading work, and reduces the risk of roll-over.
- (4) The auxiliary device reduces the rest angle of the goods, speeds up the goods unloading, shortens the unloading time, and improves the work efficiency of the dump truck.

The structure of the device is simple and the cost is low. It can prevent the dump truck roll-over effectively and improve the efficiency and save energy. It has broad application prospects in the field of dump truck safety design.

References

1. Ning A, Qiu-mei L, Ye-hong Y (2009) Working stability analysis for dump truck based on ADAMS. *J Hubei University Technol* 1003–4684(2009)02-0031-03
2. Prem H, Dickerson AW (1992) A study of the steady state roll-response of a large rear-dump mining truck. *SAE Trans* 101(2):585–599
3. Ginzburg LL, Kisulenko BV, Nikul' Nikov EN (2002) Experimental and calculation method of evaluating the stability of dump truck with resistance to turning over in transverse plane. *Avtomobil'naya Promyshlennost* (10):35–37
4. Wenchao C (2004) Study on the heeling mechanism of heavy dump truck in lifting. *Equip Manuf Technol* 3:5–7
5. Shungang H, Guoquan Y, Tieming S (2006) Modeling and dynamic simulation of reducer virtual prototype based on ADAMS. *Mach Des Res* 1006–2343(2006)06-047-06